Graduate Texts in Physics

Marius Grundmann

The Physics of Semiconductors

An Introduction Including Nanophysics and Applications

Fourth Edition

Springer

Graduate Texts in Physics

Graduate Texts in Physics publishes core learning/teaching material for graduate- and advanced-level undergraduate courses on topics of current and emerging fields within physics, both pure and applied. These textbooks serve students at the MS- or PhD-level and their instructors as comprehensive sources of principles, definitions, derivations, experiments and applications (as relevant) for their mastery and teaching, respectively. International in scope and relevance, the textbooks correspond to course syllabi sufficiently to serve as required reading. Their didactic style, comprehensiveness and coverage of fundamental material also make them suitable as introductions or references for scientists entering, or requiring timely knowledge of, a research field.

More information about this series at http://www.springer.com/series/8431

Marius Grundmann

The Physics of Semiconductors

An Introduction Including Nanophysics and Applications

Fourth Edition

Springer

Marius Grundmann
Felix Bloch Institute for Solid State Physics
Universität Leipzig
Leipzig, Germany

ISSN 1868-4513 ISSN 1868-4521 (electronic)
Graduate Texts in Physics
ISBN 978-3-030-51568-3 ISBN 978-3-030-51569-0 (eBook)
https://doi.org/10.1007/978-3-030-51569-0

Cover Credit line: “Whispering gallery mode in circular cavity. Image: Th. Nobis, M. Grundmann, Universität Leipzig”

This Springer imprint is published by the registered company Springer Nature Switzerland AG
The registered company address is: Gewerbestrasse 11, 6330 Cham, Switzerland

To Michelle,
Sophia Charlotte
and Isabella Rose

Preface

Semiconductor electronics is commonplace in every household. Semiconductor devices have enabled economically reasonable fiber-based optical communication, optical storage and high-frequency amplification and have recently revolutionized photography, display technology and lighting. By now solar energy harvesting with photovoltaics contributes a significant portion to the energy mix. Along with these tremendous technological developments, semiconductors have changed the way we work, communicate, entertain and think. The technological progress of semiconductor materials and devices is evolving continuously with a large worldwide effort in human and monetary capital. For students, semiconductors offer a rich and exciting field with a great tradition, offering diverse fundamental and applied topics [1] and a bright future.

This book introduces students to semiconductor physics and semiconductor devices. It brings them to the point where they can specialize and enter supervised laboratory research. It is based on the two semester semiconductor physics course taught at Universität Leipzig in its Master of Science physics curriculum. Since the book can be followed with little or no pre-existing knowledge in solid-state physics and quantum mechanics, it is also suitable for undergraduate students. For the interested reader many additional topics are included in the book that can be covered in subsequent, more specialized courses. The material is selected to provide a balance between aspects of solid-state and semiconductor physics, the concepts of various semiconductor devices and modern applications in electronics and photonics.

The first semester contains the fundamentals of semiconductor physics (Part I, Chaps. 1–10) and selected topics from Part II (Chaps. 11–20). Besides important aspects of solid-state physics such as crystal structure, lattice vibrations and band structure, semiconductor specifics such as technologically relevant materials and their properties, doping and electronic defects, recombination, surfaces, hetero- and nanostructures are discussed. Semiconductors with electric polarization and magnetization are introduced. The emphasis is put on inorganic semiconductors, but a brief introduction to organic semiconductors is given in Chap. 18. Dielectric structures (Chap. 19) serve as mirrors, cavities and microcavities and are a vital part of many semiconductor devices. Other sections give introductions to 2D materials (Chap. 13) and transparent conductive oxides (TCOs) (Chap. 20). The third part (Part III—Chaps. 21–24) is dedicated to semiconductor applications and devices that are taught in the second semester of the course. After a general and detailed discussion of various diode types and their physical mechanisms, their applications in electrical circuits, photodetectors, solar cells, light-emitting diodes and lasers are treated. Finally, bipolar and field-effect transistors including thin film transistors are discussed.

In the present text of the fourth edition many passages have been revised and updated, e.g. lead halide perovskites, dipole scattering, anisotropic dielectric function, valley polarization, Dember field, new CMOS image sensors. A new chapter is devoted to 2D semiconductors and an appendix on tight-binding theory has been added. The concept of topological properties now permeates the book; it is introduced for mechanical vibrations in the diatomic linear chain model and appears in chapters on band structure and photonic dielectric structures. Last but not least a few errors and misprints have

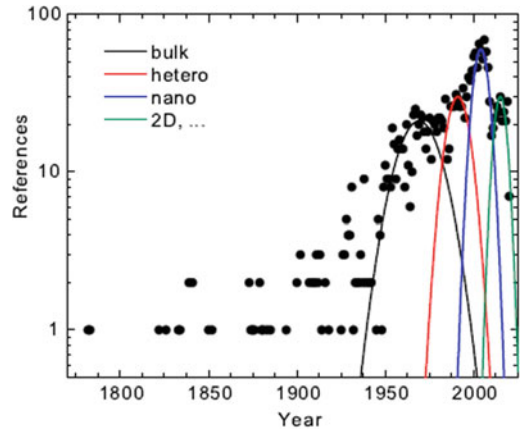

Fig. 1 Histogram of references in this book together with simplified fits visualizing major developments

been corrected. More than 300 additional references, some old and many brand new, have been included (compared to the third edition) and doi's for most of them are provided for easy retrieval. The references have been selected to (i) cover important historical and milestone papers, (ii) direct to reviews and topical books for further reading and (iii) give access to original literature and up-to-date research. In Fig. 1, a histogram of the references by year is shown. Roughly four phases of semiconductor physics and technology can be seen. Before the realization of the first transistor in 1947, only a few publications are noteworthy. Then an intense phase of understanding the physics of semiconductors and developing semiconductor technology and devices based on bulk semiconductors (mostly Ge, Si, GaAs) followed. At the end of the 1970s, a new era began with the advent of quantum wells and heterostructures, and later nanostructures (nanotubes, nanowires and quantum dots) and new materials (e.g. organic semiconductors, nitrides or graphene). Another peak develops with emerging topics such as 2D materials, topological insulators or novel amorphous semiconductors.

I would like to thank numerous colleagues for their various contributions to this book, in alphabetical order (if no affiliation is given, at the time at Universität Leipzig): Gabriele Benndorf, Klaus Bente, Rolf Böttcher, Matthias Brandt, Christian Czekalla, Christof Peter Dietrich, Pablo Esquinazi, Heiko Frenzel, Volker Gottschalch, Helena Hilmer, Axel Hoffmann (TU Berlin), Alois Krost† (Otto-von-Guericke Universität Magdeburg), Evgeny Krüger, Michael Lorenz, Stefan Müller, Thomas Nobis, Rainer Pickenhain, Hans-Joachim Queisser (Max-Planck-Institut für Festkörperforschung, Stuttgart), Bernd Rauschenbach, Bernd Rheinländer, Heidemarie Schmidt, Mathias Schmidt, Rüdiger Schmidt-Grund, Matthias Schubert, Jan Sellmann, Oliver Stier (TU Berlin), Chris Sturm, Florian Tendille (CNRS-CRHEA), Gerald Wagner, Eicke Weber (UC Berkeley), Holger von Wenckstern, Michael Ziese and Gregor Zimmermann. This book has benefitted from their comments, proof reading, experimental data and graphic material. Also, numerous helpful comments from my students on my lectures and the previous editions of this book are gratefully acknowledged.

I am also indebted to many other colleagues, in particular to (in alphabetical order) Gerhard Abstreiter, Zhores Alferov†, Martin Allen, Levon Asryan, Günther Bauer, Manfred Bayer, Friedhelm Bechstedt, Dieter Bimberg, Otto Breitenstein, Len Brillson, Fernando Briones, Immanuel Broser†, Jean-Michel Chauveau, Jürgen Christen, Philippe De Mierry, Steve Durbin, Laurence Eaves, Klaus Ellmer, Guy Feuillet, Elvira Fortunato, Ulrich Gösele†, Alfred Forchel, Manus Hayne, Frank Heinrichsdorff, Fritz Henneberger†, Detlev Heitmann, Robert Heitz†, Evamarie Hey-Hawkins, Detlef Hommel, Evgeni Kaidashev, Eli Kapon, Nils Kirstaedter, Claus Klingshirn, Fred Koch†, Jörg Kotthaus, Nikolai Ledentsov, Peter Littlewood, Dave Look, Axel Lorke, Anupam Madhukar, Jan

Meijer, Ingrid Mertig, Bruno Meyer†, David Mowbray, Hisao Nakashima, Jörg Neugebauer, Michael Oestreich, Louis Piper, Mats-Erik Pistol, Fred Pollak†, Emil V. Prodan, Volker Riede†, Bernd Rosenow, Hiroyuki Sakaki, Lars Samuelson, Darrell Schlom, Vitali Shchukin, Maurice Skolnick, Robert Suris, Volker Türck, Konrad Unger†, Victor Ustinov, Borge Vinter, Leonid Vorob'jev, Richard Warburton, Alexander Weber, Peter Werner, Wolf Widdra, Ulrike Woggon, Roland Zimmermann, Arthur Zrenner, Alex Zunger and Jesús Zúñiga-Pérez, with whom I have worked closely, had enjoyable discussions with and who have posed questions that stimulated me. It is my distinct privilege and joy that this list becomes longer as I pursue studies in semiconductor physics but sadly the number of †-symbols increases too rapidly from edition to edition.

Leipzig, Germany Marius Grundmann
May 2020

Contents

Part II Selected Topics

Abbreviations

0D	Zero-dimensional
1D	One-dimensional
2D	Two-dimensional
2DEG	Two-dimensional electron gas
3D	Three-dimensional
AAAS	American Association for the Advancement of Science
AB	Antibonding (position)
ac	Alternating current
ACS	American Chemical Society
ADF	Annular dark field (STEM method)
ADP	Acoustic deformation potential (scattering)
AFM	Atomic force microscopy
AHE	Anomalous Hall effect
AIP	American Institute of Physics
AM	Air mass
APD	Antiphase domain, avalanche photodiode
APS	American Physical Society
AR	Antireflection
ARPES	Angle-resolved photoemission spectroscopy
ASE	Amplified spontaneous emission
AVS	American Vacuum Society (The Science & Technology Society)
bc	Body-centered
BC	Bond center (position)
bcc	Body-centered cubic
BD	Blu-ray^{TM} disc
BEC	Bose–Einstein condensation
BGR	Band gap renormalization
BIA	Bulk inversion asymmetry
BJT	Bipolar junction transistor
BZ	Brillouin zone
CAS	Calorimetric absorption spectroscopy
CCD	Charge coupled device
CD	Compact disc
CEO	Cleaved-edge overgrowth
CIE	Commission Internationale de l'Éclairage
CIGS	$Cu(In,Ga)Se_2$ material
CIS	$CuInSe_2$ material, CMOS image sensor

CL	Cathodoluminescence
CMOS	Complementary metal–oxide–semiconductor
CMY	Cyan-magenta-yellow (color system)
CNL	Charge neutrality level
CNT	Carbon nanotube
COD	Catastrophical optical damage
CPU	Central processing unit
CRT	Cathode ray tube
CSL	Coincident site lattice
CVD	Chemical vapor deposition
cw	Continuous wave
CZ	Czochralski (growth)
DAP	Donor–acceptor pair
DBR	Distributed Bragg reflector
dc	Direct current
DF	Dielectric function
DFB	Distributed feedback
DH(S)	Double heterostructure
DLTS	Deep level transient spectroscopy
DMS	Diluted magnetic semiconductor
DOS	Density of states
DPSS	Diode-pumped solid-state (laser)
DRAM	Dynamic random access memory
DVD	Digital versatile disc
EA	Electron affinity
EBL	Electron blocking layer
EEPROM	Electrically erasable programmable read-only memory
EHL	Electron–hole liquid
EIL	Electron injection layer
EL	Electroluminescence
ELA	Excimer laser annealing
ELO	Epitaxial lateral overgrowth
EMA	Effective mass approximation
EML	Emission layer
EPR	Electron paramagnetic resonance
EPROM	Erasable programmable read-only memory
ESF	Extrinsic stacking fault
ESR	Electron spin resonance
ETL	Electron transport layer
EXAFS	Extended X-ray absorption fine structure
F_4-TCNQ	2,3,5,6-tetrafluoro-7,7,8,8-tetracyano-quinodimethane
FA	Formamidinium, $HC(NH_2)_2$
fc	Face-centered
fcc	Face-centered cubic
FeRAM	Ferroelectric random access memory
FET	Field-effect transistor
FIB	Focused ion beam
FIR	Far infrared
FKO	Franz–Keldysh oscillation
FLG	Few layer graphene

FPA	Focal plane array
FQHE	Fractional quantum Hall effect
FWHM	Full width at half-maximum
FZ	Float-zone (growth)
Gb	Gigabit
GIZO	GaInZnO
GLAD	Glancing-angle deposition
GRINSCH	Graded-index separate confinement heterostructure
GSMBE	Gas-source molecular beam epitaxy
GST	$Ge_2Sb_2Te_5$
HBL	Hole blocking layer
HBT	Heterobipolar transistor
hcp	Hexagonally close packed
HCSEL	Horizontal cavity surface-emitting laser
HEMT	High electron mobility transistor
HIGFET	Heterojunction insulating gate FET
hh	Heavy hole
HIL	Hole injection layer
HJFET	Heterojunction FET
HMM	Hyperbolic metamaterial
HOMO	Highest occupied molecular orbital
HOPG	Highly ordered pyrolithic graphite
HR	High reflection
HRTEM	High-resolution transmission electron microscopy
HTL	Hole transport layer
HWHM	Half-width at half-maximum
IBM	International Business Machines Corporation
IC	Integrated circuit
IDB	Inversion domain boundary
IE	Ionization energy
IEEE	Institute of Electrical and Electronics Engineers[1]
IF	Intermediate frequency
IOP	Institute of Physics
IPAP	Institute of Pure and Applied Physics, Tokyo
IQHE	Integral quantum Hall effect
IR	Infrared
ISF	Intrinsic stacking fault
ITO	Indium tin oxide
JDOS	Joint density of states
JFET	Junction field-effect transistor
KKR	Kramers–Kronig relation
KOH	Potassium hydroxide
KTP	$KTiOPO_4$ material
LA	Longitudinal acoustic (phonon)
LCD	Liquid crystal display
LDA	Local density approximation
LEC	Liquid encapsulated Czochralski (growth)
LED	Light-emitting diode

[1]pronounced Eye-triple-E.

lh	Light hole
LO	Longitudinal optical (phonon), local oscillator
LPCVD	Low-pressure chemical vapor deposition
LPE	Liquid phase epitaxy
LPP	Longitudinal phonon plasmon (mode)
LST	Lyddane–Sachs–Teller (relation)
LT	Low temperature
LUMO	Lowest unoccupied molecular orbital
LVM	Local vibrational mode
MA	Methylammonium, methylammonium
MBE	Molecular beam epitaxy
MEMS	Micro-electro-mechanical system
MHEMT	Metamorphic HEMT
MESFET	Metal–semiconductor field-effect transistor
MIGS	Midgap (surface) states
MILC	Metal-induced lateral crystallization
MIOS	Metal–insulator–oxide–semiconductor
MIR	Mid-infrared
MIS	Metal–insulator–semiconductor
MIT	Massachusetts Institute of Technology
ML	Monolayer
MLC	Multi-level cell
MMIC	Millimeter-wave integrated circuit
MO	Master oscillator
MOCVD	Metalorganic chemical vapor deposition
MODFET	Modulation-doped field-effect transistor
MOMBE	Metalorganic molecular beam epitaxy
MOPA	Master oscillator power amplifier
MOS	Metal–oxide–semiconductor
MOSFET	Metal–oxide–semiconductor field-effect transistor
MOVPE	Metalorganic chemical vapor deposition
MQW	Multiple quantum well
MRAM	Magnetic random access memory
MRS	Materials Research Society
MS	Metal–semiconductor (diode)
MSA	Mobility spectral analysis
MSM	Metal–semiconductor–metal (diode)
MTJ	Magneto-tunneling junction
MWNT	Multi-walled (carbon) nanotube
NDR	Negative differential resistance
NEP	Noise equivalent power
NIR	Near infrared
NMOS	n-channel metal–oxide–semiconductor (transistor)
NTSC	National television standard colors
OLED	Organic light emitting diode
OMC	Organic molecular crystals
ONO	Oxide/nitride/oxide
OPSL	Optically pumped semiconductor laser
PA	Power amplifier
PBG	Photonic band gap

pc	Primitive cubic
PCM	Phase change memory
PFM	Piezoresponse force microscopy
PHEMT	Pseudomorphic HEMT
PL	Photoluminescence
PLD	Pulsed laser deposition
PLE	Photoluminescence excitation (spectroscopy)
PMC	Programmable metallization cell
PMMA	Poly-methyl methacrylate
PMOS	p-channel metal–oxide–semiconductor (transistor)
PPC	Persistent photoconductivity
PPLN	Perodically poled lithium niobate
PV	Photovoltaic(s)
PWM	Pulsewidth modulation
PZT	$PbTi_xZr_{1-x}O_3$ material
QCL	Quantum cascade laser
QCSE	Quantum confined Stark effect
QD	Quantum dot
QHE	Quantum Hall effect
QW	Quantum well
QWIP	Quantum-well intersubband photodetector
QWR	Quantum wire
RAM	Random access memory
RAS	Reflection anisotropy spectroscopy
RF	Radio frequency
RFID	Radio frequency identification
RGB	Red-green-blue (color system)
RHEED	Reflection high-energy electron diffraction
RIE	Reactive ion etching
RKKY	Ruderman–Kittel–Kasuya–Yoshida (interaction)
rms	Root mean square
ROM	Read-only memory
RRAM	Resistance random access memory
RSC	The Royal Society of Chemistry
SAGB	Small-angle grain boundary
SAM	Separate absorption and amplification (structure)
sc	Simple cubic
SCH	Separate confinement heterostructure
SCLC	Space-charge limited current
SdH	Shubnikov-de Haas (oscillation)
SEL	Surface-emitting laser
SEM	Scanning electron microscopy
SET	Single-electron transistor, single electron tunneling
SGDBR	Sampled grating distributed Bragg reflector
SHG	Second-harmonic generation
si	Semi-insulating
SIA	Semiconductor Industry Association
SIA	Structural inversion asymmetry
SIMS	Secondary ion mass spectrometry
SL	Superlattice

SLC	Single-level cell
SLG	Single layer graphene
SNR	Signal-to-noise ratio
s-o	Spin-orbit (or split-off)
SOA	Semiconductor optical amplifier
SOFC	Solid-oxide fuel cells
SPD	Spectral power distribution
SPICE	Simulation Program with Integrated Circuit Emphasis
SPIE	Society of Photographic Instrumentation Engineers
SPP	Surface plasmon polariton
SPS	Short-period superlattice
sRGB	Standard RGB
SRH	Shockley–Read–Hall (kinetics)
SSH	Su–Schrieffer–Heeger (model)
SSR	Side-mode suppression ratio
STEM	Scanning transmission electron microscopy
STEM-ADF	Scanning transmission electron microscopy with annular dark field imaging
STM	Scanning tunneling microscopy
SWNT	Single-walled (carbon) nanotube
TA	Transverse acoustic (phonon)
TAS	Thermal admittance spectroscopy
TCO	Transparent conductive oxide
TE	transverse electric (polarization)
TED	transferred electron device
TEGFET	Two-dimensional electron gas field-effect transistor
TEM	Transmission electron microscopy
TES	Two-electron satellite
TF	Thermionic field emission
TFET	Transparent FET, tunneling FET
TFT	Thin film transistor
TM	Transverse magnetic (polarization)
TMAH	Tetramethyl-ammonium-hydroxide
TMDC	Transition metal dichalcogenide
TMR	Tunnel-magnetoresistance
TO	Transverse optical (phonon)
TOD	Turn-on delay (time)
TPA	Two-photon absorption
TSO	Transparent semiconducting oxide
UHV	Ultrahigh vacuum
UV	Ultraviolet
VCA	Virtual crystal approximation
VCO	Voltage-controlled oscillator
VCSEL	Vertical-cavity surface-emitting laser
VFF	Valence force field
VGF	Vertical gradient freeze (growth)
VIS	Visible
VLSI	Very large scale integration
WGM	Whispering gallery mode
WKB	Wentzel–Kramer–Brillouin (approximation or method)
WS	Wigner–Seitz (cell)

X	Exciton
XPS	X-ray photoelectron spectroscopy
XSTM	Cross-sectional STM
XX	Biexciton
YSZ	Yttria-stabilized zirconia (ZrO_2)
ZnPc	Zinc-phthalocyanine

Symbols

α	Madelung constant, disorder parameter, linewidth enhancement factor
$\alpha(\omega)$	absorption coefficient
α_{m}	mirror loss
α_{n}	electron ionization coefficient
α_{p}	hole ionization coefficient
α_{T}	base transport factor
β	used as abbreviation for $e/(k_{\mathrm{B}}T)$, spontaneous emission coefficient, two-photon absorption coefficient
γ	broadening parameter, Berry phase, Grüneisen parameter, emitter efficiency, tight-binding nearest-neighbor coupling parameter
Γ	broadening parameter
γ_1, γ_2, γ_3	Luttinger parameters
δ_{ij}	Kronecker symbol
Δ_0	spin-orbit splitting
$\epsilon(\omega)$	dielectric function
ϵ_0	permittivity of vacuum
ϵ_{i}	dielectric constant of insulator
ϵ_{r}	relative dielectric function
ϵ_{s}	dielectric function of semiconductor ($= \epsilon_{\mathrm{r}}\epsilon_0$)
ϵ_S	gain compression coefficient
ϵ_{ij}	components of strain tensor
η	quantum efficiency
η_{d}	differential quantum efficiency
η_{ext}	external quantum efficiency
η_{int}	internal quantum efficiency
η_{w}	wall-plug efficiency
θ	angle
Θ_{D}	Debye temperature
Θ_{B}	typical phonon energy parameter
κ	imaginary part of index of refraction, heat conductivity
λ	wavelength
λ_{p}	plasma wavelength
μ	mobility
μ_0	magnetic susceptibility of vacuum
μ_{h}	hole mobility
μ_{H}	Hall mobility
μ_{n}	electron mobility

ν	frequency, filling factor (QHE), winding number
Π	Peltier coefficient
π_{ij}	components of piezoresistivity tensor
ρ	mass density, charge density, resistivity
ρ_{ij}	components of resistivity tensor
ρ_{P}	polarization charge density (per volume)
σ	standard deviation, conductivity, stress, effective mass ratio
Σn	grain boundary type
σ_{ij}	components of stress tensor, conductivity tensor
σ_{n}	electron capture cross section
σ_{p}	hole capture cross section
σ_{P}	polarization charge density (per area)
τ	lifetime, time constant
τ_{n}	electron (minority carrier) lifetime
τ_{nr}	non-radiative lifetime
τ_{p}	hole (minority carrier) lifetime
τ_{r}	radiative lifetime
Θ_{D}	Debye temperature
ϕ	phase
Φ_0	photon flux
χ	electron affinity, electric susceptibility
χ_{ex}	light extraction efficiency
χ_{sc}	electron affinity (of semiconductor)
$\chi(\mathbf{r})$	envelope wavefunction
ψ	angle
$\Psi(\mathbf{r})$	wavefunction
ω	angular frequency
ω_{LO}	longitudinal optical phonon frequency
ω_{p}	plasma frequency
ω_{TO}	transverse optical phonon frequency
Ω	interaction parameter
a	hydrostatic deformation potential, lattice constant
$\mathbf{a}$	accelaration
A	atomic mass ($A = 12$ for ^{12}C)
A	area, band-impurity recombination coefficient
$\mathbf{A}$, A	vector potential
A^*	Richardson constant
a_0	(cubic) lattice constant
b	bowing parameter, deformation potential
$\mathbf{b}$	Burger's vector
B	bimolecular recombination coefficient, bandwidth
$\mathbf{B}$, B	magnetic induction field
c	velocity of light in vacuum, lattice constant (along c-axis)
C	capacitance, spring constant, Auger recombination coefficient
C_{n}, C_{p}	Auger recombination coefficient
C_{ij}, C_{ijkl}	elastic constants
d	distance, shear deformation potential
d_{i}	insulator thickness
D	density of states, diffusion coefficient
$\mathbf{D}$, D	electric displacement field

D^*	detectivity
$D_e(E)$	electron density of states
$D_h(E)$	hole density of states
D_n	electron diffusion coefficient
D_p	hole diffusion coefficient
e	elementary charge
e_i	strain components (Voigt notation)
E	energy
E, E	electric field
E_A	energy of acceptor level
E_A^b	acceptor ionization energy
E_C	energy of conduction-band edge
E_{xc}	exchange interaction energy
E_D	energy of donor level, Dirac energy (in graphene)
E_D^b	donor ionization energy
E_F	Fermi energy
E_g	band gap
E_i	intrinsic Fermi level
E_m	maximum electric field
E_P	energy parameter
E_V	energy of valence-band edge
E_{vac}	energy of vacuum level
E_X	exciton energy
E_X^b	exciton binding energy
E_{XX}	biexciton energy
f	oscillator strength
F	free energy
F, F	force
$F(M)$	excess noise factor
F_B	Schottky barrier height
f_e	Fermi–Dirac distribution function (for electrons)
f_i	ionicity
f_h	Fermi–Dirac distribution function for holes ($= 1 - f_e$)
F_n	electron quasi-Fermi energy
F_p	hole quasi-Fermi energy
F_P	Purcell factor
g	degeneracy, g-factor, gain
G	free enthalpy, generation rate
G, G	reciprocal lattice vector
g_m	transconductance
G_{th}	thermal generation rate
h	Planck constant
H	enthalpy, Hamiltonian
H, H	magnetic field
$\hbar$	$h/(2\pi)$
i	imaginary number
I	current, light intensity
I_D	drain current
I_s	saturation current
I_{sc}	short circuit current

I_{thr}	threshold current
$\boldsymbol{j}, j$	current density
j	total orbital momentum
j_{s}	saturation current density
j_{thr}	threshold current density
k	wavenumber, Boltzmann constant
$\mathbf{k}$	wavevector
k_{B}	Boltzmann constant
k_{F}	Fermi wavevector
l	angular orbital momentum
L	length of line element
$\mathbf{L}$	line vector (of dislocation)
L_{D}	diffusion length
L_{z}	quantum-well thickness
m	mass
m_0	free electron mass
m^*	effective mass
m^*_{ij}	effective mass tensor
m_{c}	cyclotron mass
M	mass, multiplication factor
$\mathbf{M}$, M	magnetization
m_{e}	effective electron mass
m_{h}	effective hole mass
m_{j}	magnetic quantum number
m_{l}	longitudinal mass
m_{r}	reduced mass
m_{t}	transverse mass
n	electron concentration (in conduction band), ideality factor
$\mathbf{n}$	normal vector
$N(E)$	number of states
n^*	complex index of refraction $(= n_{\mathrm{r}} + \mathrm{i}\kappa)$
N_{A}	acceptor concentration
N_{c}	critical doping concentration
N_{C}	conduction-band edge density of states
N_{D}	donor concentration
n_{i}	intrinsic electron concentration
n_{if}	ideality factor due to image force effect
n_{r}	index of refraction (real part)
n_{s}	sheet electron density
N_{t}	trap concentration
n_{tr}	transparency electron concentration
n_{thr}	threshold electron concentration
N_{V}	valence-band edge density of states
p	pressure, free hole density
$\mathbf{p}$, p	momentum
P	power
$\mathbf{P}$, P	electric polarization
p_{cv}	momentum matrix element
p_{i}	intrinsic hole concentration
q	charge

$\mathbf{q}$, q	heat flow
Q	charge, quality factor, impurity-bound exciton localization energy
r	radius
$\mathbf{r}$	spatial coordinate
R	resistance, radius, recombination rate
R_λ	responsivity
$\mathbf{R}$	vector of direct lattice
r_H	Hall factor
R_H	Hall coefficient
s	spin
S	entropy, Seebeck coefficient, total spin, surface index, surface recombination velocity
S_{ij}, S_{ijkl}	stiffness coefficients
t	time
t_ox	(gate) oxide thickness
T	temperature
u	displacement, cell-internal parameter
U	energy
u_{nk}	Bloch function
$\mathbf{v}$, v	velocity
V	volume, voltage, potential
$V(\lambda)$	(standardized) sensitivity of human eye
V_a	unit-cell volume
V_A	Early voltage
V_bi	built-in voltage
v_g	group velocity
V_G	gate voltage
V_oc	open circuit voltage
V_P	pinch-off voltage
v_s	velocity of sound, drift-saturation velocity
V_SD	source-drain voltage
v_th	thermal velocity
w	depletion-layer width, width
w_B	base width (bipolar transistor)
W_m	(metal) work function
X	electronegativity
Y	Young's module, CIE brightness parameter
Z	partition sum, atomic order number

Physical Constants

Constant	Symbol	Numerical value (new SI units)	Unit
Speed of light in vacuum	c_0	2.99792458×10^{8} (exact)	$\mathrm{m\,s^{-1}}$
Permeability of vacuum	μ_0	$4\pi \times 10^{-7}$	$\mathrm{N\,A^{-2}}$
Permittivity of vacuum	$\epsilon_0 = (\mu_0 c_0^2)^{-1}$	$8.854187817 \times 10^{-12}$	$\mathrm{F\,m^{-1}}$
Elementary charge	e	$1.602176634 \times 10^{-19}$ (exact)	C
Electron mass	m_e	$9.1093837 \times 10^{-31}$	kg
Planck constant	h	$6.62607015 \times 10^{-34}$ (exact)	J s
	$\hbar = h/(2\pi)$	$1.05457182 \times 10^{-34}$	J s
	$\hbar$	$6.58211957 \times 10^{-16}$	eV s
Boltzmann constant	k_B	1.380649×10^{-23} (exact)	$\mathrm{J\,K^{-1}}$
		8.6173333×10^{-5}	$\mathrm{meV\,K^{-1}}$
von-Klitzing constant	$R_\mathrm{K} = h/e^2$	25812.8075	Ω
Rydberg constant		13.605693123	eV
Bohr radius	a_B	$5.29177211 \times 10^{-11}$	m
Avogadro constant	N_A	$6.02214076 \times 10^{23}$ (exact)	$\mathrm{mol^{-1}}$

Chapter 1
Introduction

The proper conduct of science lies in the pursuit of Nature's puzzles, wherever they may lead.

J.M. Bishop [2]

Abstract Important dates and events in the history of semiconductors are chronologically listed, from the early days (Volta, Seebeck and Faraday) to the latest achievements like the blue and white LED. Many known and not so well known scientists are mentioned. Also a list of semiconductor related Nobel prizes and their winners is given.

The historic development of semiconductor physics and technology began in the second half of the 19th century. Interesting discussions of the history of the physics and chemistry of semiconductors can be found in [3–5]. The development of crystal growth is covered in [6]. The history of semiconductor industry can be followed in [7, 8]. In [9] 141 pioneering papers on semiconductor devices are compiled. In 1947, the commercial realization of the transistor was the impetus to a fast-paced development that created the electronics and photonics industries. Products founded on the basis of semiconductor devices such as computers (CPUs, memories), optical-storage media (lasers for CD, DVD), communication infrastructure (lasers and photodetectors for optical-fiber technology, high frequency electronics for mobile communication), displays (thin film transistors, LEDs), projection (laser diodes) and general lighting (LEDs) are commonplace. Thus, fundamental research on semiconductors and semiconductor physics and its offspring in the form of devices has contributed largely to the development of modern civilization and culture.

1.1 Timetable and Key Achievements

In this section important milestones in semiconductor physics and technology are listed.

1782
A. Volta—coins the phrase 'semicoibente' (semi-insulating) which was translated then into English as 'semiconducting' [10].

M. Grundmann, *The Physics of Semiconductors*, Graduate Texts in Physics,
https://doi.org/10.1007/978-3-030-51569-0_1

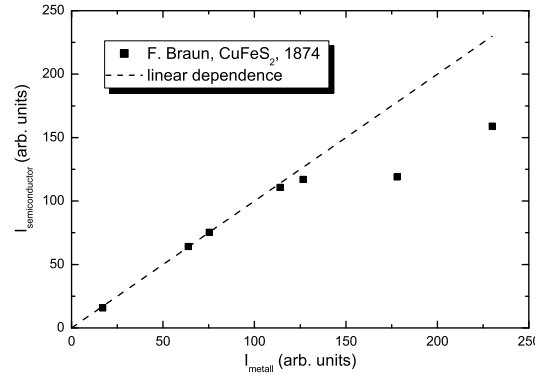

Fig. 1.1 Current through a silver–$CuFeS_2$–silver structure as a function of the current through the metal only, 1874. Data points are for different applied voltages. Experimental data from [24]

1821
T.J. Seebeck—discovery of thermopower (electrical phenomena upon temperature difference) in metals and PbS, FeS_2, $CuFeS_2$ [11, 12].

1833
M. Faraday—discovery of the temperature dependence of the conductivity of Ag_2S (sulphuret of silver, negative dR/dT) [13].

1839
A.E. Becquerel[1]—photoelectric effect (production of a photocurrent when electrodes covered by copper or silver halides salts (in an electrolyte) were illuminated by solar light) [14–17].

1834
J. Peltier—discovery of the Peltier effect (cooling by current) [18].

1873
W. Smith—discovery of photoconductivity in selenium [19, 20]. Early work on photoconductivity in Se is reviewed in [21, 22].

1874
F. Braun[2]—discovery of rectification in metal–sulfide semiconductor contacts [24], e.g. for $CuFeS_2$ and PbS. The current through a metal–semiconductor contact is nonlinear (as compared to that through a metal, Fig. 1.1), i.e. a deviation from Ohm's law. Braun's structure is similar to a MSM diode.

1876
W.G. Adams and R.E. Day—discovery of the photovoltaic effect in selenium [25].
W. Siemens—large response from selenium photoconductor [26], made by winding two thin platinum wires to the surface of a sheet of mica, and then covering the surface with a thin film of molten selenium. Resistance ratio between dark and illuminated by sunlight was larger than ten [26] and measured to 14.8 in [27].

1879
E.H. Hall—measurement of the transverse potential difference in a thin gold leaf on glass [28, 29]. Experiments were continued by his mentor H.A. Rowland [30]. A detailed account of the discovery of the Hall efect is given in [31, 32].

[1] This is Edmond Becquerel; his son Henri Becquerel received the Nobel Prize in Physics for the discovery of radioactivity.

[2] F. Braun made his discoveries on metal–semiconductor contacts in Leipzig while a teacher at the Thomasschule zu Leipzig [23]. He conducted his famous work on vacuum tubes later as a professor in Strasbourg, France.

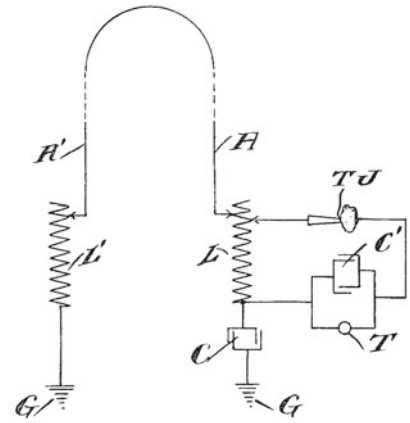

Fig. 1.2 Circuit diagram for a radio receiver with a point-contact diode (TJ). Adapted from [34]

1883
Ch. Fritts—first solar cell, based on an gold/selenium rectifier [27]. The efficiency was below 1%.

1901
J.C. Bose—point contact detector for electromagnetic waves based on galena (PbS) [33]. At the time, the term semiconductor was not introduced yet and Bose speaks about 'substances of a certain class (...) presenting a decreasing resistance to the passage of the electric current with an increasing impressed electromotive force'.

1906
G.W. Pickard—rectifier based on point contact (cat's whisker) diode on silicon [34–36]. Erroneously, the rectifying effect was attributed to a thermal effect, however, the drawing of the 'thermo-junction' (TJ in Fig. 1.2) developed into the circuit symbol for a diode (cmp. Fig. 21.63a).

1907
H.J. Round—discovery of electroluminescence investigating yellow and blue light emission from SiC [37].
K. Bädeker—preparation of metal (e.g. Cd, Cu) oxides and sulfides and also CuI from metal layers using a vapor phase transport method [38][3]. CuI is reported transparent ($\sim$ 200 nm thick films) with a specific resistivity of $\rho = 4.5 \times 10^{-2}\,\Omega\,\mathrm{cm}$, the first transparent conductor.[4] Also CdO (films of thickness 100–200 nm) is reported to be highly conductive, $\rho = 1.2 \times 10^{-3}\,\Omega\,\mathrm{cm}$, and orange-yellow in color, the first reported TCO (transparent conductive oxide).

1909
K. Bädeker—discovery of doping. Controlled variation of the conductivity of CuI by dipping into iodine solutions (e.g. in chloroform) of different concentrations [41].

1910
W.H. Eccles—negative differential resistance of contacts with galena (PbS), construction of crystal oscillators[5] [45].

[3]This work was conducted as Habilitation in the Physics Institute of Universität Leipzig. Bädeker became subsequently professor in Jena and fell in WW I. His scientific contribution to semiconductor physics is discussed in [39, 40]

[4]CuI is actually a p-type transparent conductor; at that time the positive sign of the Hall effect [41, 42] could not be interpreted as hole conduction yet.

[5]Historical remarks on Eccles' contributions to radio technology can be found in [43, 44]

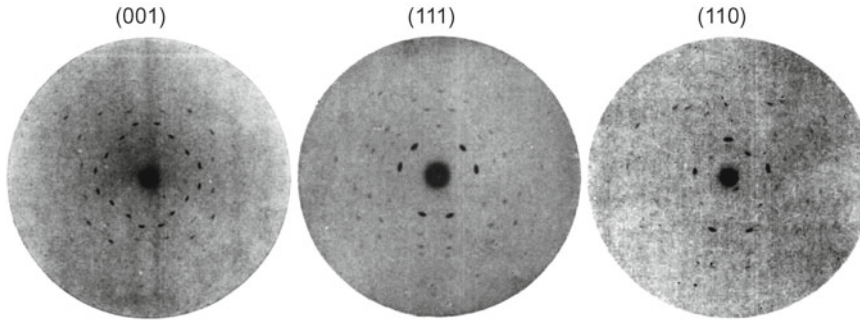

Fig. 1.3 Laue images of 'regular' (cubic) ZnS along three major crystallographic directions, directly visualizing their 4-, 3- and 2-fold symmetry. Adapted from [48]

Fig. 1.4 Sketch of a field-effect transistor, 1926. From [53]

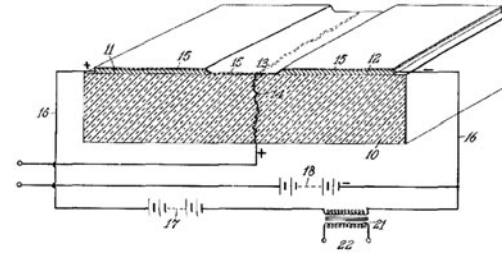

1911
The term 'Halbleiter' (semiconductor) is introduced for the first time by J. Weiss [46] and J. Königsberger and J. Weiss [47]. Königsberger preferred the term 'Variabler Leiter' (variable conductor).

1912
M. von Laue—X-ray diffraction of bulk crystals including ZnS (Fig. 1.3) [48, 49].

1925
J.E. Lilienfeld[6]—proposal of the metal-semiconductor field-effect transistor (MESFET) [53], with suggested copper sulfide thin film channel and aluminum gate.[7] (Fig. 1.4). Lilienfeld was also awarded patents for a depletion mode MOSFET [55] with proposed copper sulfide, copper oxide or lead oxide channel and current amplification with nppn- and pnnp-transistors [56]. Due to the lack of other publications of Lilienfeld on transistors, it is under discussion whether Lilienfeld just patented ideas or also build working devices with mounting evidence for the latter [51, 54, 57].

1927
A. Schleede, H. Buggisch—synthesis of pure, stoichiometric PbS, influence of sulphur excess and impurities [58].
A. Schleede, E. Körner—activation of luminescence of ZnS [59, 60].

[6] After obtaining his PhD in 1905 from the Friedrich-Wilhelms-Universität Berlin, Julius Edgar Lilienfeld joined the Physics Department of Universität Leipzig and worked on gas liquefaction and with Lord Zeppelin on hydrogen-filled blimps. In 1910 he became professor at the Universität Leipzig where he mainly researched on X-rays and vacuum tubes [50]. To the surprise of his colleagues he left in 1926 to join a US industrial laboratory [51, 52].

[7] In [51] it is suggested that the device works as a npn transistor, in [54] it is suggested to be a JFET.

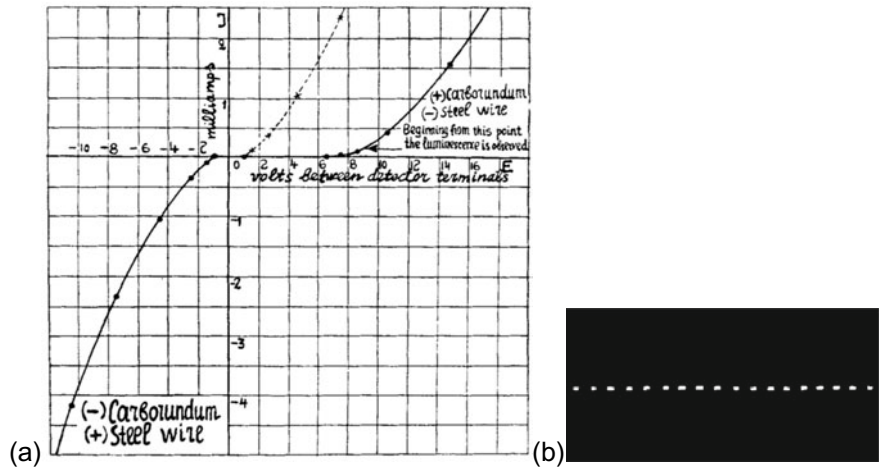

Fig. 1.5 **a** I–V characteristic of SiC/steel wire light emitting diode. The *dotted curve* is the flipped curve for negative voltage (3rd quadrant). **b** Recording of current modulated (at 500 Hz) LED on moving photographic plate. Adapted from [65]

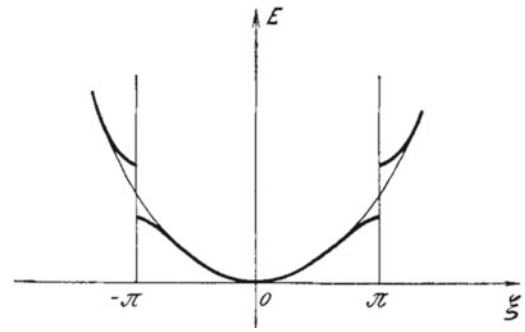

Fig. 1.6 First band structure calculation from Peierls ($\xi = k\,a$). Adapted from [69]

1928
F. Bloch—quantum mechanics of electrons in a crystal lattice, 'Bloch functions' [61].
O.V. Losev—description of the light emitting diode[8] (SiC) [65]; light emission was observed in forward direction and close to breakdown (Fig. 1.5a). Also current modulation of LED light output was reported (Fig. 1.5b) [65].

1929
R. Peierls—explanation of positive (anomalous) Hall effect with unoccupied electron states [66, 67].

1930
R. Peierls—first calculation of a band structure and band gap[9] (Fig. 1.6) [69].

1931
W. Heisenberg—theory of hole ('Löcher') states [70].
R. de L. Kronig and W.G. Penney—properties of periodic potentials in solids [71].

[8]The historic role of Losev regarding the invention of the LED and oscillators is discussed in [62–64].

[9]Peierls performed this work at suggestion of W. Pauli at ETH Zürich. The mathematical problem of Schrödinger's equation with a sinusoidal potential had been already treated by M.J.O Strutt in 1928 [68]

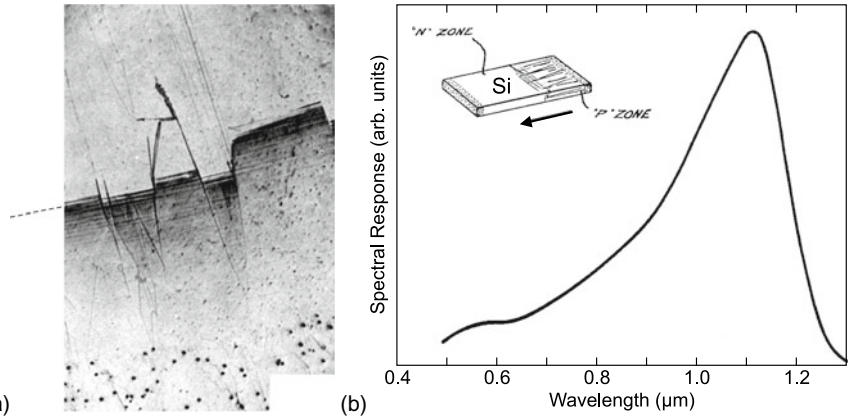

Fig. 1.7 **a** Optical image of directionally solidified silicon. The lower part contains predominantly boron, the upper part contains predominantly phosphorous. First the growth is porous and subsequently columnar. Adapted from [90]. **b** Spectral response of silicon pn-junction photoelement, 1940. The *inset* depicts schematically a Si slab with built-in pn-junction formed during directed solidification as shown in panel (**a**). The *arrow* denotes the direction of solidification (cmp. Fig. 4.6). Adapted from [89]

A.H. Wilson[10]—development of band-structure theory [74, 75].

1933
C. Wagner—excess ('Elektronenüberschuss-Leitung', n-type) and defect ('Elektronen-Defektleitung', p-type) conduction [76–79]. Anion deficiency in ZnO causes conducting behavior [80].

1934
C. Zener—Zener tunneling [81].

1936
J. Frenkel—description of excitons [82].

1938
B. Davydov—theoretical prediction of rectification at pn-junction [83] and in Cu_2O [84].
W. Schottky—theory of the boundary layer in metal–semiconductor contacts [85], being the basis for Schottky contacts and field-effect transistors.
N.F. Mott—metal–semiconductor rectifier theory [86, 87].
R. Hilsch and R.W. Pohl—three-electrode crystal (KBr) [88].

1940
R.S. Ohl—Silicon-based photoeffect (solar cell, Fig. 1.7) [89] from a pn-junction formed within a slab of polycrystalline Si fabricated with directed solidification due to different distribution coefficients of p- and n-dopants (boron and phosphorus, cmp. Fig. 4.6b) (J. Scaff and H. Theurer) [90, 91].

[10]Wilson was theoretical physicist in Cambridge, who spent a sabbatical with Heisenberg in Leipzig and applied the brand new field of quantum mechanics to issues of electrical conduction, first in metals and then in semiconductors. When he returned to Cambridge, Wilson urged that attention be paid to germanium but, as he expressed it long afterward, 'the silence was deafening' in response. He was told that devoting attention to semiconductors, those messy entities, was likely to blight his career among physicists. He ignored these warnings and in 1939 brought out his famous book 'Semiconductors and Metals' [72] which explained semiconductor properties, including the much-doubted phenomenon of intrinsic semiconductivity, in terms of electronic energy bands. His academic career seems indeed to have been blighted, because despite his great intellectual distinction, he was not promoted in Cambridge (he remained an assistant professor year after year) [73]. Compare the remark of W. Pauli (p. 179)

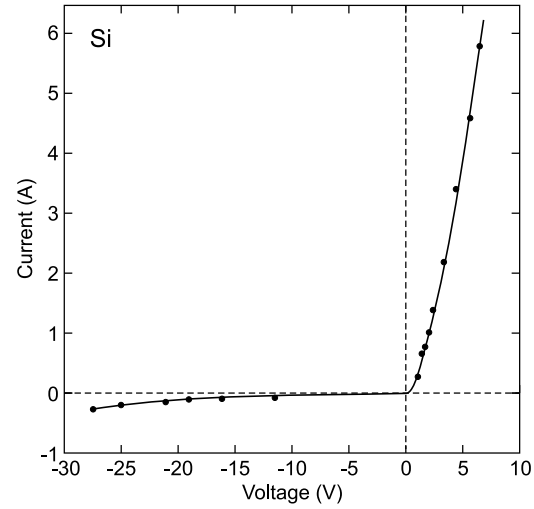

Fig. 1.8 Characteristics of a silicon rectifier, 1941. Adapted from [92]

1941
R.S. Ohl—Silicon rectifier with point contact [92, 93] (Fig. 1.8), building on work from G.W. Pickard (1906) and using metallurgically refined and intentionally doped silicon (J. Scaff and H. Theurer) [90].

1942
K. Clusius, E. Holz and H. Welker—rectification in germanium [94].

1945
H. Welker—patents for JFET and MESFET [95].

1947
W. Shockley, J. Bardeen and W. Brattain fabricate the first transistor in the AT&T Bell Laboratories, Holmdel, NJ in an effort to improve hearing aids [96].[11] Strictly speaking the structure was a point-contact transistor. A 50-μm wide slit was cut with a razor blade into gold foil over a plastic (insulating) triangle and pressed with a spring on n-type germanium (Fig. 1.9a) [97]. The surface region of the germanium is p-type due to surface states and represents an inversion layer. The two gold contacts form emitter and collector, the large-area back contact of the germanium the base contact [98]. For the first time, amplification was observed [99]. Later models use two close point contacts made from wires with their tips cut into wedge shape (Fig. 1.9b) [98].[12] More details about the history and development of the semiconductor transistor can be found in [100], written on the occasion of the 50th anniversary of its invention.

1948
W. Shockley—invention of the bipolar (junction) transistor [101].

1952
H. Welker—fabrication of III–V compound semiconductors[13] [104–107].

[11] Subsequently, AT&T, under pressure from the US Justice Department's antitrust division, licensed the transistor for $25,000. This action initiated the rise of companies like Texas Instruments, Sony and Fairchild.

[12] The setup of Fig. 1.9b represents a common base circuit. In a modern bipolar transistor, current amplification in this case is close to unity (Sect. 24.2.2). In the 1948 germanium transistor, the reversely biased collector contact is influenced by the emitter current such that current amplification $\partial I_C/\partial I_E$ for constant U_C was up to 2–3. Due to the collector voltage being much larger than the emitter voltage, a power gain of $\sim$ 125 was reported [98].

[13] An early concept for III–V semiconductors was developed in [102, 103].

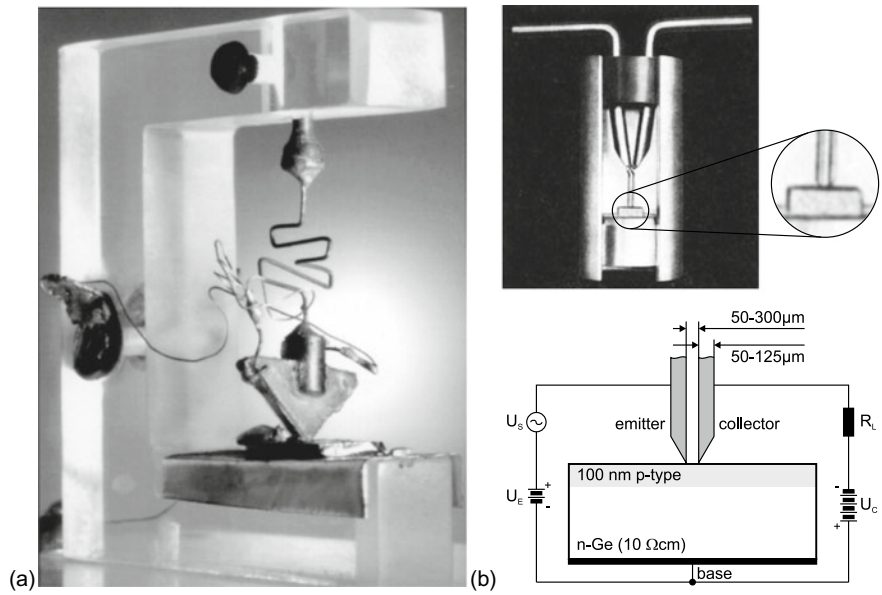

Fig. 1.9 **a** The first transistor, 1947 (length of side of wedge: 32 mm). **b** Cutaway model of a 1948 point contact transistor ('Type A') based on n-type bulk Ge ($n = 5 \times 10^{14}$ cm^{-3}) and common base circuit diagram. The surface region ($\sim$ 100 nm depth) of the Ge is p-type due to surface states and represents an inversion layer. The two wires are made from phosphor bronze. Adapted from [98]

W. Shockley—description of today's version of the (J)FET [108].

1953
G.C. Dacey and I.M. Ross—first realization of a JFET [109].
D.M. Chapin, C.S. Fuller and G.L. Pearson—invention of the silicon solar cell at Bell Laboratories [110]. A single 2 cm^2 photovoltaic cell from Si, Si:As with an ultrathin layer of Si:B, with about 6% efficiency generated 5 mW of electrical power.[14] Previously existing solar cells based on selenium had very low efficiency ($< 0.5\%$).

1958
J.S. Kilby made the first integrated circuit at Texas Instruments. The simple 1.3 MHz RC-oscillator consisted of one transistor, three resistors and a capacitor on a 11 $\times$ 1.7 mm^2 Ge platelet (Fig. 1.10a). J.S. Kilby filed in 1959 for a US patent for miniaturized electronic circuits [111]. At practically the same time R.N. Noyce from Fairchild Semiconductors, the predecessor of INTEL, invented the integrated circuit on silicon using planar technology [112]. A detailed and (very) critical view on the invention of the integrated circuit can be found in [113].
Figure 1.10b shows a flip-flop with four bipolar transistors and five resistors. Initially, the invention of the integrated circuit[15] met scepticism because of concerns regarding yield and the achievable quality of the transistors and the other components (such as resistors and capacitors).

[14] A solar cell with 1 W power cost $300 in 1956 ($3 in 2004). Initially, 'solar batteries' were only used for toys and were looking for an application. H. Ziegler proposed the use in satellites in the 'space race' of the late 1950s.

[15] The two patents led to a decade-long legal battle between Fairchild Semiconductors and Texas Instruments. Eventually, the US Court of Customs and Patent Appeals upheld R.N. Noyce's claims on interconnection techniques but gave J.S. Kilby and Texas Instruments credit for building the first working integrated circuit.

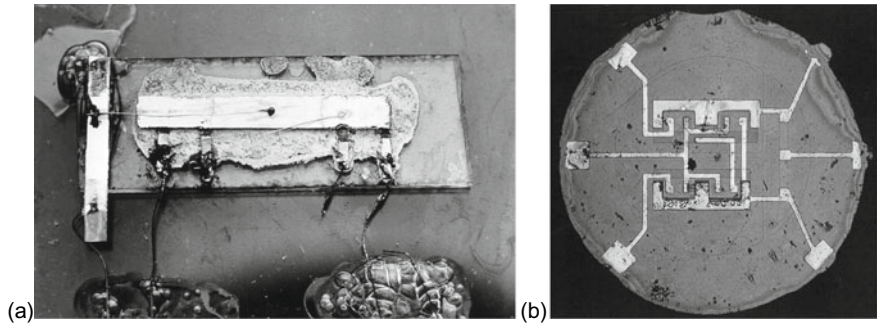

Fig. 1.10 **a** The first integrated circuit, 1958 (germanium, 11 × 1.7 mm^2). **b** The first planar integrated circuit, 1959 (silicon, diameter: 1.5 mm)

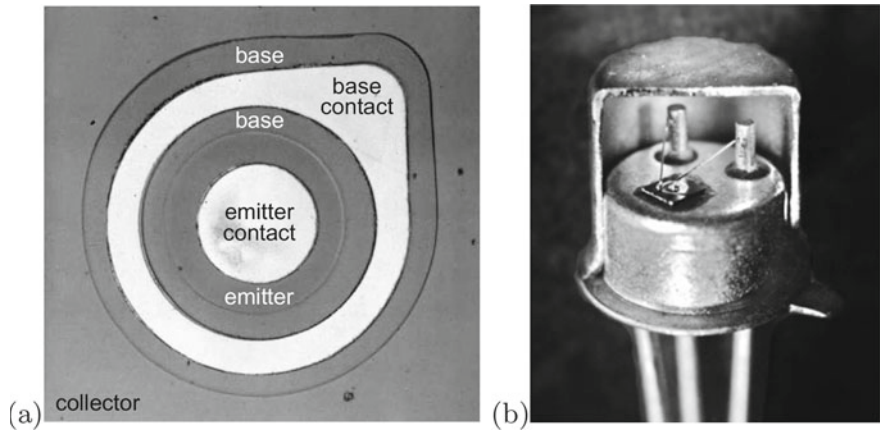

Fig. 1.11 (**a**) Optical image of planar pnp silicon transistor (2N1613 [120]), 1959. The contacts are Al surfaces (not bonded). (**b**) Housing of such transistor cut open

1959
J. Hoerni[16] and R. Noyce—first realization of a planar transistor (in silicon) (Fig. 1.11) [115–119].

1960
D. Kahng and M.M. Atalla—first realization of a MOSFET [121, 122].

1962
The first semiconductor laser on GaAs basis at 77 K at GE [123, 124] (Fig. 1.12) and at IBM [125] and MIT [126].
First visible laser diode [127].[17]

1963
Proposal of a double heterostructure laser (DH laser) by Zh.I. Alferov [130, 131] and H. Kroemer [132, 133].
J.B. Gunn—discovery of the Gunn effect, the spontaneous microwave oscillations in GaAs and InP at sufficiently large applied electric field (due to negative differential resistance) [134].

[16]The Swiss born Jean Hoerni also contributed $12 000 for the building of the first school in the Karakoram Mountain area in Pakistan and has continued to build schools in Pakistan and Afghanistan as described in [114].

[17]Remarks on the discovery and further development of the laser diode can be found in [128, 129].

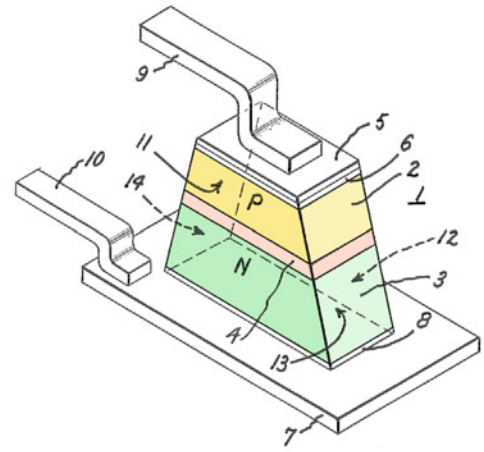

Fig. 1.12 Schematics of GaAs-based laser diode. The active layer is highlighted in *red*. Adapted from [124]

1966
C.A. Mead—proposal of the MESFET ('Schottky Barrier Gate FET') [135].

1967
Zh.I. Alferov—report of the first DH laser on the basis of Ga(As,P) at 77 K [136, 137].
W.W. Hooper and W.I. Lehrer—first realization of a MESFET [138].

1968
DH laser on the basis of GaAs/(Al,Ga)As at room temperature, independently developed by Zh.I. Alferov [139] and I. Hayashi [140].
GaP:N LEDs with yellow-green emission (550 nm) and 0.3% efficiency [141].

1968
SiC blue LED with efficiency of 0.005% [142].

1970
W.S. Boyle and G.E. Smith—invention of the charge coupled device (CCD) [143, 144].

1971
R.F. Kazarinov and R.A. Suris—proposal of the quantum cascade laser [145].

1975
R.S. Pengelly and J.A. Turner—first monolithic microwave integrated circuit (MMIC) (Fig. 1.13) [146]

1992
S. Nakamura—growth of high-quality group-III–nitride thin films [147], blue nitride heterostructure LED with efficiency exceeding 10% (1995) [148] (Fig. 1.14a). Later the white LED was built by combining a blue LED with yellow phosphors (Fig. 1.14b, c).

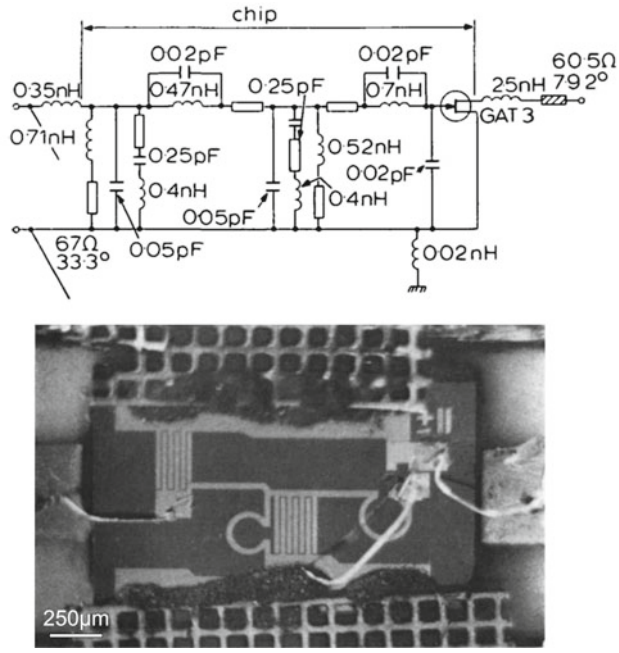

Fig. 1.13 Equivalent circuit and optical image of first monolithic microwave integrated circuit (exhibiting gain (4.5 ± 0.9 dB) in the frequency range 7.0–11.7 GHz). Adapted from [146]

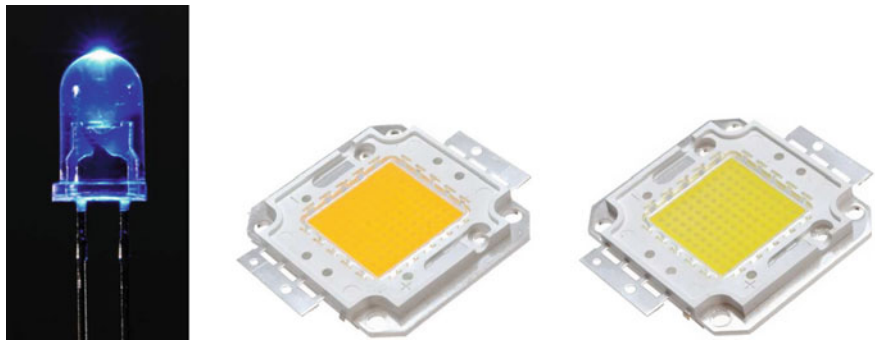

Fig. 1.14 **a** Blue LED (standard housing). 50 W, 4000 lm, **b** warm white and **c** cold white LED ($45 \times 45\,\text{mm}^2$)

1994

J. Faist and F. Capasso—quantum cascade laser [149].

N. Kirstaedter, N.N. Ledentsov, Zh.I. Alferov and D. Bimberg—quantum dot laser [150].

2004

H. Hosono and T. Kamiya—thin film transistor (TFT) from amorphous oxide semiconductor [151].

1.2 Nobel Prize Winners

Several Nobel Prizes[18] have been awarded for discoveries and inventions in the field of semiconductor physics (Fig. 1.15).

1909
Karl Ferdinand Braun
'in recognition of his contributions to the development of wireless telegraphy'

1914
Max von Laue 'for his discovery of the diffraction of X-rays by crystals'

1915
Sir William Henry Bragg
William Lawrence Bragg
'for their services in the analysis of crystal structure by means of X-rays'

1946
Percy Williams Bridgman
'for the invention of an apparatus to produce extremely high pressures, and for the discoveries he made therewith in the field of high pressure physics'

1953
William Bradford Shockley
John Bardeen
Walter Houser Brattain
'for their researches on semiconductors and their discovery of the transistor effect'

1973
Leo Esaki
'for his experimental discoveries regarding tunneling phenomena in semiconductors'

1985
Klaus von Klitzing
'for the discovery of the quantized Hall effect'

1998
Robert B. Laughlin
Horst L. Störmer
Daniel C. Tsui
'for their discovery of a new form of quantum fluid with fractionally charged excitations'

2000
Zhores I. Alferov
Herbert Kroemer
'for developing semiconductor heterostructures used in high-speed and optoelectronics'
Jack St. Clair Kilby
'for his part in the invention of the integrated circuit'

2009
Willard S. Boyle
George E. Smith
'for the invention of an imaging semiconductor circuit—the CCD sensor'

[18] www.nobel.se

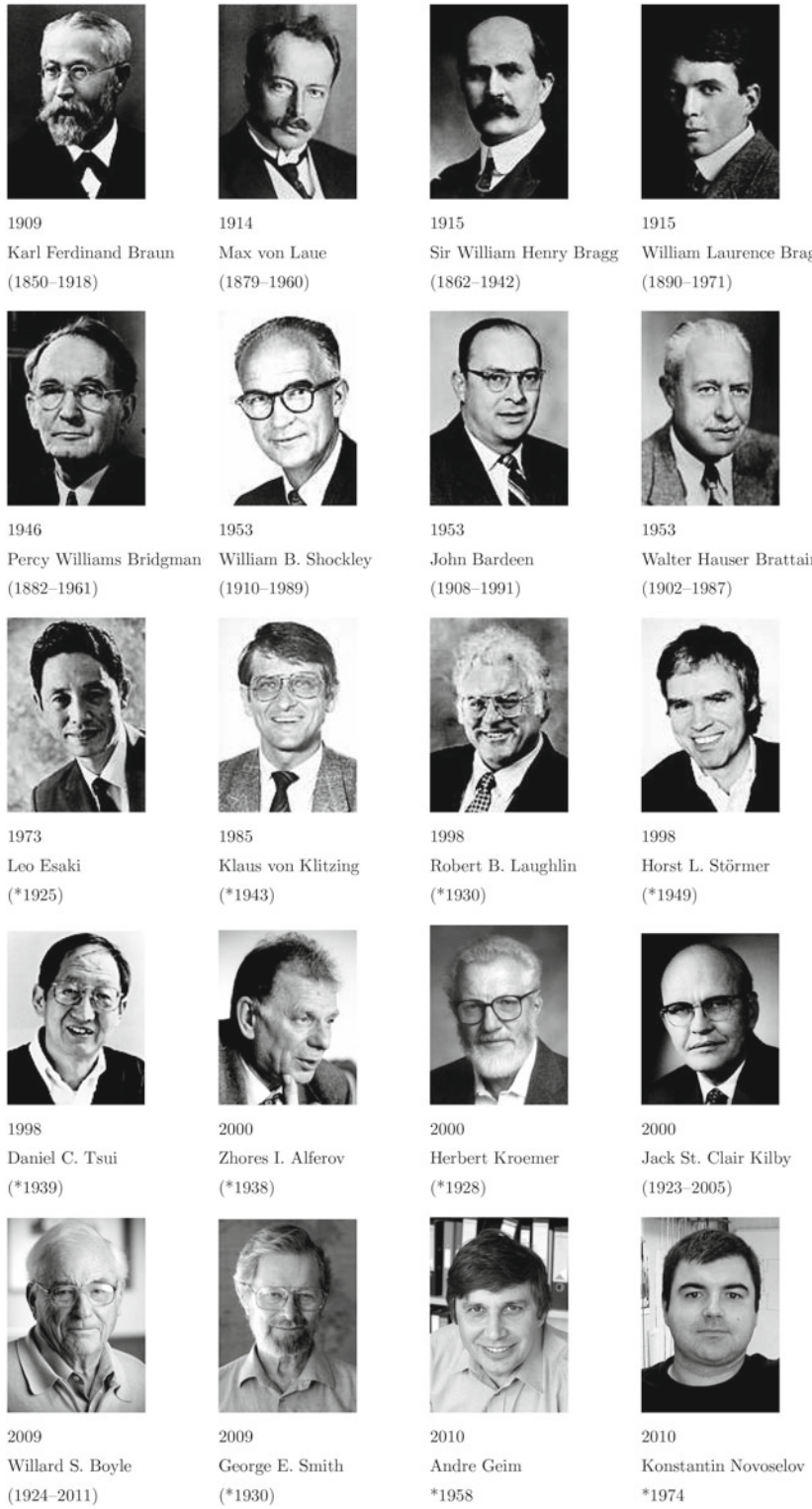

Fig. 1.15 Winners of Nobel Prize in Physics and year of award with great importance for semiconductor physics

Fig. 1.15 (continued)

2014
Isamu Akasaki
(*1929)

2014
Hiroshi Amano
(*1960)

2014
Shuji Nakamura
(*1954)

2010
Andre Geim
Konstantin Novoselov
'for groundbreaking experiments regarding the two-dimensional material graphene'

2014
Isamu Akasaki
Hiroshi Amano
Shuji Nakamura
'for the invention of efficient blue light-emitting diodes which has enabled bright and energy-saving white light sources'

1.3 General Information

In Fig. 1.16, the periodic table of elements is shown.
In Table 1.1 the physical properties of various semiconductors are summarized. Data on semiconductors can be found in [152–166].

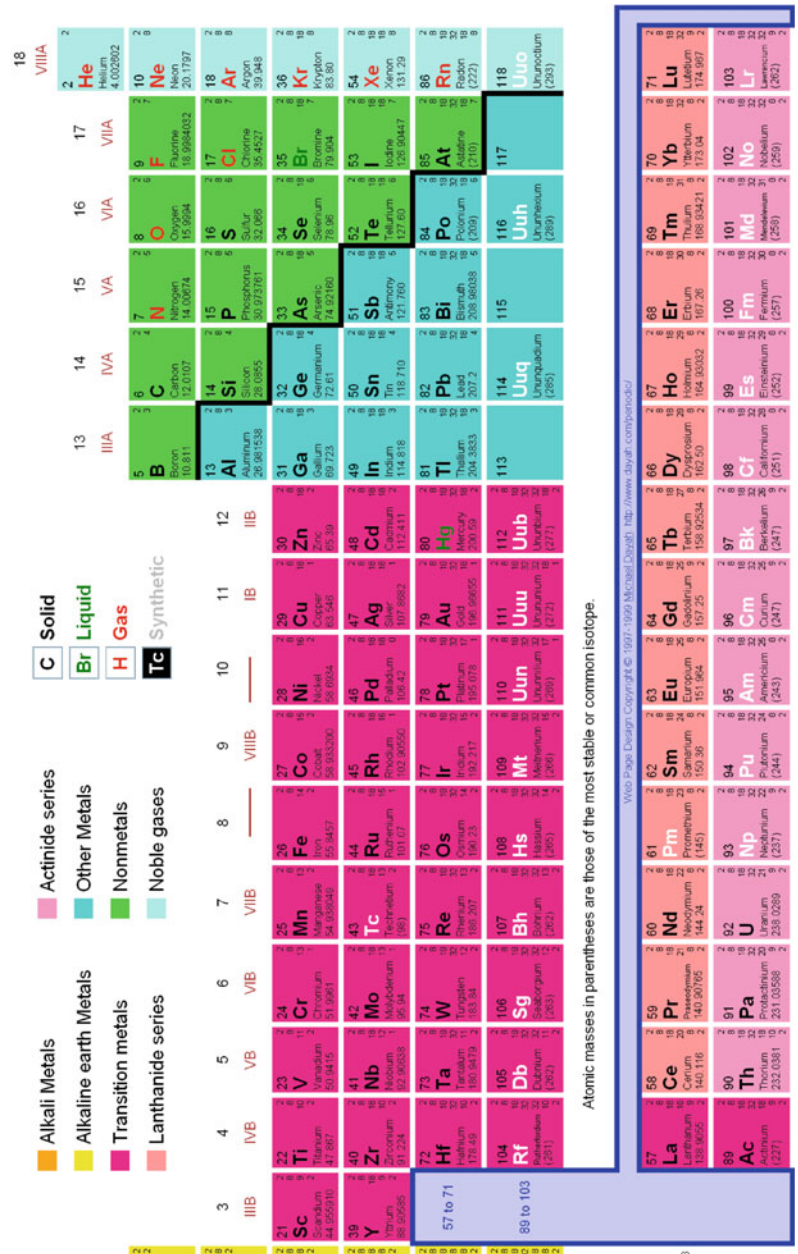

Fig. 1.16 Periodic table of elements. From [167]

Table 1.1 Physical properties of various (bulk) semiconductors at room temperature. 'S' denotes the crystal structure (d: diamond, w: wurtzite, zb: zincblende, ch: chalcopyrite, rs: rocksalt)

	S	a_0 (nm)	E_g (eV)	m_e^*	m_h^*	ϵ_0	n_r	μ_e (cm^2/Vs)	μ_h (cm^2/Vs)
C	d	0.3567	5.45 (Γ)			5.5	2.42	2200	1600
Si	d	0.5431	1.124 (X)	0.98 (m_l) 0.19 (m_t)	0.16 (m_{lh}) 0.5 (m_{hh})	11.7	3.44	1350	480
Ge	d	0.5658	0.67 (L)	1.58 (m_l) 0.08 (m_t)	0.04 (m_{lh}) 0.3 (m_{hh})	16.3	4.00	3900	1900
α-Sn	d	0.64892	0.08 (Γ)	0.02				2000	1000
3C-SiC	zb	0.436	2.4			9.7	2.7	1000	50
4H-SiC	w	0.3073 (a)	3.26			9.6	2.7		120
		1.005 (c)							
6H-SiC	w	0.30806 (a) 1.5117 (c)	3.101			10.2	2.7	1140	850
AlN	w	0.3111 (a) 0.4978 (c)	6.2			8.5	3.32		
AlP	zb	0.54625	2.43 (X)	0.13		9.8	3.0	80	
AlAs	zb	0.56605	2.16 (X)	0.5	0.49 (m_{lh}) 1.06 (m_{hh})	12		1000	80
AlSb	zb	0.61335	1.52 X)	0.11	0.39	11	3.4	200	300
GaN	w	0.3189 (a) 0.5185 (c)	3.4 (Γ)	0.2	0.8	12	2.4	1500	
GaP	zb	0.54506	2.26 (Γ)	0.13	0.67	10	3.37	300	150
GaAs	zb	0.56533	1.42 (Γ)	0.067	0.12 (m_{lh}) 0.5 (m_{hh})	12.5	3.4	8500	400
GaSb	zb	0.60954	0.72 (Γ)	0.045	0.39	15	3.9	5000	1000
InN	w	0.3533 (a)	0.69 (Γ)						
		0.5693 (c)							
InP	zb	0.58686	1.35 (Γ)	0.07	0.4	12.1	3.37	4000	600
InAs	zb	0.60584	0.36 (Γ)	0.028	0.33	12.5	3.42	22 600	200
InSb	zb	0.64788	0.18 (Γ)	0.013	0.18	18	3.75	100 000	1700
ZnO	w	0.325 (a)	3.4 (Γ)	0.24	0.59	6.5	2.2	220	
		0.5206 (c)							
ZnS	zb	0.54109	3.6 (Γ)	0.3		8.3	2.4	110	
ZnSe	zb	0.56686	2.58 (Γ)	0.17		8.1	2.89	600	
ZnTe	zb	0.61037	2.25 (Γ)	0.15		9.7	3.56		
CdO	rs	0.47	2.16						

(continued)

Table 1.1 (continued)

	S	a_0 (nm)	E_g (eV)	m_e^*	m_h^*	ϵ_0	n_r	μ_e (cm^2/Vs)	μ_h (cm^2/Vs)
CdS	w	0.416 (a) 0.6756 (c)	2.42 (Γ)	0.2	0.7	8.9	2.5	250	
CdSe	zb	0.650	1.73 (Γ)	0.13	0.4	10.6		650	
CdTe	zb	0.64816	1.50 (Γ)	0.11	0.35	10.9	2.75	1050	100
	S	a_0 (nm)	E_g (eV)	m_e^*	m_h^*	ϵ_0	n_r	μ_e (cm^2/Vs)	μ_h (cm^2/Vs)
MgO	rs	0.421	7.3						
HgS	zb	0.5852	2.0 (Γ)					50	
HgSe	zb	0.6084	−0.15 (Γ)	0.045		25		18 500	
HgTe	zb	0.64616	−0.15 (Γ)	0.029	0.3	20	3.7	22 000	100
PbS	rs	0.5936	0.37 (L)	0.1	0.1	170	3.7	500	600
PbSe	rs	0.6147	0.26 (L)	0.07 (m_{lh})	0.06 (m_{lh})	250		1800	930
				0.039 (m_{hh})	0.03 (m_{hh})				
PbTe	rs	0.645	0.29 (L)	0.24 (m_{lh}) 0.02 (m_{hh})	0.3 (m_{lh}) 0.02 (m_{hh})	412		1400	1100
$ZnSiP_2$	ch	0.54 (a)	2.96 (Γ)	0.07					
		1.0441 (c)							
$ZnGeP_2$	ch	0.5465 (a) 1.0771 (c)	2.34 (Γ)		0.5				
$ZnSnP_2$	ch	0.5651 (a) 1.1302 (c)	1.66 (Γ)						
$CuInS_2$	ch	0.523 (a) 1.113 (c)	1.53 (Γ)						
$CuGaS_2$	ch	0.5347 (a) 1.0474 (c)	2.5 (Γ)						
$CuInSe_2$	ch	0.5784 (a) 1.162 (c)	1.0 (Γ)						
$CuGaSe_2$	ch	0.5614 (a) 1.103 (c)	1.7 (Γ)						

Part I
Fundamentals

Chapter 2
Bonds

Protons give an atom its identity, electrons its personality.

B. Bryson [168]

Abstract A little bit of solid state physics... The schemes of covalent, ionic and mixed bonds are explained which are the basis for the atomic arrangement and crystal structures of semiconductors.

2.1 Introduction

The positively charged atomic nuclei and the electrons in the atomic shells of the atoms making up the semiconductor (or any other solid) are in a binding state. Several mechanisms can lead to such cohesiveness. First, we will discuss the homopolar, electron-pair or covalent bond, then the ionic bond and subsequently the mixed bond. We will only briefly touch on the metallic bond and the van-der-Waals bond. A classical book on bonds in semiconductors is [169, 170].

2.2 Covalent Bonds

Covalent bonds are formed due to quantum-mechanical forces. The prototype covalent bond is the bonding of the hydrogen molecule due to overlapping of the atomic shells. If several electron pairs are involved, directional bonds can be formed in various spatial directions, eventually making up a solid.

2.2.1 Electron-Pair Bond

The covalent bond of two hydrogen atoms in a H_2 molecule can lead to a reduction of the total energy of the system, compared to two single (distant) atoms (Fig. 2.1). For fermions (electrons have spin 1/2) the two-particle wavefunction of the two (indistinguishable) electrons A and B must be antisymmetric, i.e. $\Psi(A, B) = -\Psi(B, A)$ (Pauli principle). The wavefunction of each electron has degrees of freedom in real space ($\mathbf{r}$) and spin (σ), $\Psi(A) = \Psi_{\mathbf{r}}(A)\,\Psi_{\sigma}(A)$. The two-particle wavefunction

M. Grundmann, *The Physics of Semiconductors*, Graduate Texts in Physics,
https://doi.org/10.1007/978-3-030-51569-0_2

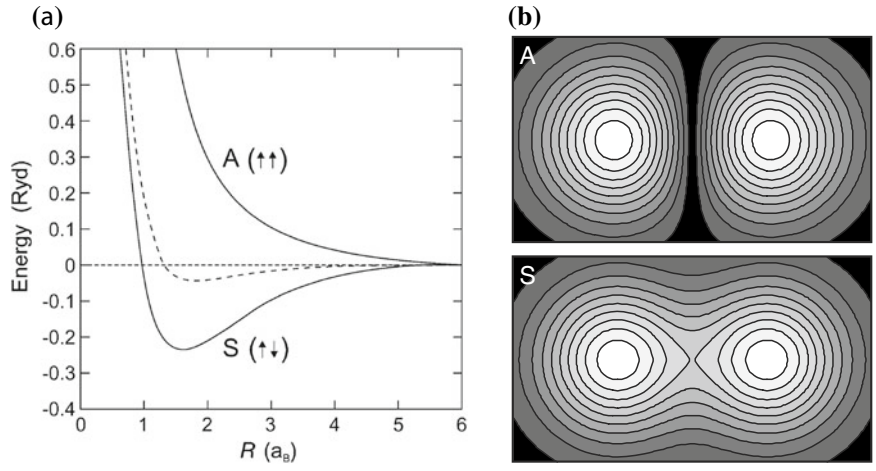

Fig. 2.1 Binding of the hydrogen molecule. **a** *Dashed line*: classical calculation (electrostatics), 'S', 'A': quantum-mechanical calculation taking into account Pauli's principle (S: symmetric orbital, antiparallel spins, A: antisymmetric orbital, parallel spins). The distance of the nuclei (protons) is given in units of the Bohr radius $a_B = 0.053\,\text{nm}$, the energy is given in Rydberg units (13.6 eV). **b** Schematic contour plots of the probability distribution ($\Psi^*\Psi$) for the S and A states

of the molecule is nonseparable and has the form $\Psi(A, B) = \Psi_{\mathbf{r}}(r_A, r_B)\,\Psi_\sigma(\sigma_A, \sigma_B)$. The binding state has a wavefunction with a symmetric orbital and antiparallel spins, i.e. $\Psi_{\mathbf{r}}(r_A, r_B) = \Psi_{\mathbf{r}}(r_B, r_A)$ and $\Psi_\sigma(\sigma_A, \sigma_B) = -\Psi_\sigma(\sigma_B, \sigma_A)$. The antisymmetric orbital with parallel spins is antibinding for all distances of the nuclei (protons).

2.2.2 sp^3 Bonds

Elements from group IV of the periodic system (C, Si, Ge, ...) have 4 electrons on the outer shell. Carbon has the electron configuration $1s^2 2s^2 2p^2$. For an octet configuration bonding to four other electrons would be optimal (Fig. 2.2). This occurs through the mechanism of sp^3 hybridization.[1] First, one electron of the ns^2np^2 configuration is brought into a p orbital, such that the outermost shell contains one s, p_x, p_y, and p_z orbital each (Fig. 2.3a–e). The energy necessary for this step is less than regained in the subsequent formation of the covalent bonds. The four orbitals can be reconfigured into four other wavefunctions, the sp^3 hybrids (Figs. 2.3f–i), i.e.

$$\Psi_1 = (\mathrm{s} + \mathrm{p}_x + \mathrm{p}_y + \mathrm{p}_z)/2 \tag{2.1a}$$
$$\Psi_2 = (\mathrm{s} + \mathrm{p}_x - \mathrm{p}_y - \mathrm{p}_z)/2 \tag{2.1b}$$
$$\Psi_3 = (\mathrm{s} - \mathrm{p}_x + \mathrm{p}_y - \mathrm{p}_z)/2 \tag{2.1c}$$
$$\Psi_4 = (\mathrm{s} - \mathrm{p}_x - \mathrm{p}_y + \mathrm{p}_z)/2\,. \tag{2.1d}$$

These orbitals have a directed form along tetrahedral directions. The binding energy (per atom) of the covalent bond is large, for H–H 4.5 eV, for C–C 3.6 eV, for Si–Si 1.8 eV, and for Ge–Ge 1.6 eV. Such energy is, for *neutral* atoms, comparable to the ionic bond, discussed in the next section.

[1] It is debated in femtosecond chemistry whether the bond *really* forms in this way. However, it is a picture of overwhelming simplicity.

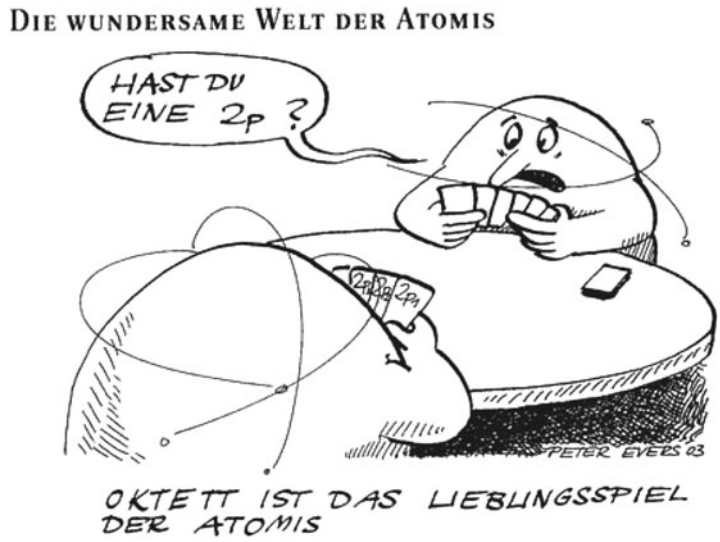

Fig. 2.2 Octet, the favorite card game of the 'Atomis' (trying to reach octet configuration in a bond by swapping wavefunctions). The bubble says: 'Do you have a 2p?'. Reprinted with permission from [171], ©2002 Wiley-VCH

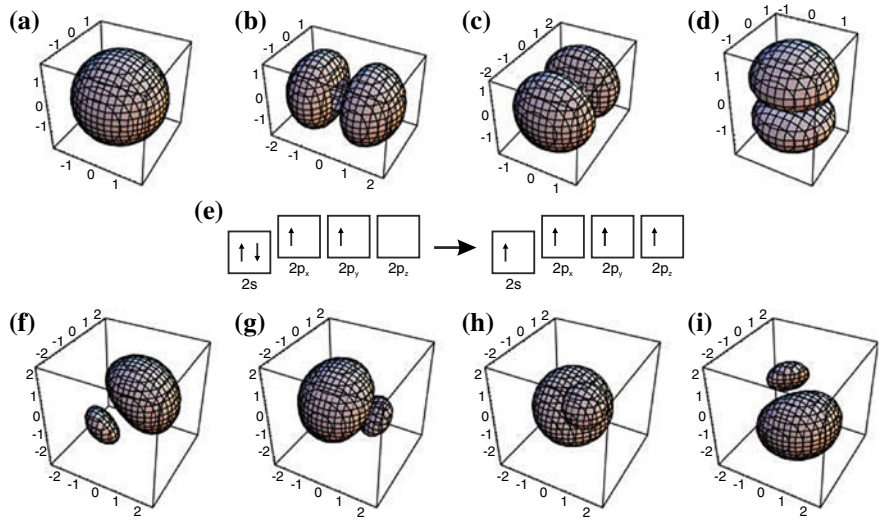

Fig. 2.3 **a** s orbital, **b**, **c**, **d** p_x, p_y and p_z orbital, **e** hybridization, **f**, **g**, **h**, **i** orbitals of the sp^3 hybridization: **f** $(s+p_x+p_y+p_z)/2$, **g** $(s+p_x-p_y-p_z)/2$, **h** $(s-p_x+p_y-p_z)/2$, **(i)** $(s-p_x-p_y+p_z)/2$

In Fig. 2.4a the energy of a crystal made up from silicon atoms is shown for various crystal structures[2] or phases (cf. Chap. 3). We note that the crystal energy of further silicon structures are discussed in [175]. The lattice constant with the lowest total energy determines the lattice spacing for each crystal structure. The thermodynamically stable configuration is the phase with the lowest overall energy for given external conditions.

The covalent bond of a group-IV atom to other group-IV atoms has a tetrahedral configuration with electron-pair bonds, similar to the hydrogen molecule bond. In Fig. 2.4b the energy states of the $n = 2$ shell for tetrahedrally bonded carbon (diamond, see Chap. 3.4.3) are shown as a function of

[2]Hexagonal diamond is wurtzite structure with identical atoms in the base.

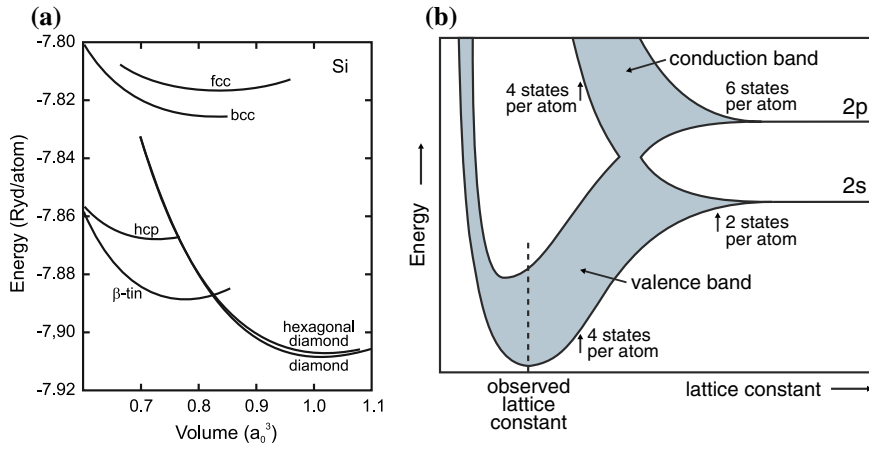

Fig. 2.4 **a** Energy per atom in silicon for various crystal structures. Adapted from [172]. **b** Electron energy levels in (diamond structure) carbon as a function of the distance of the atomic nuclei (schematic). Adapted from [173, 174]

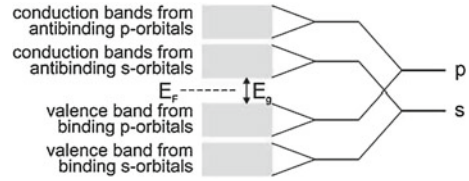

Fig. 2.5 Schematic of the origin of valence and conduction band from the atomic s and p orbitals. The band gap E_g and the position of the Fermi level E_F are indicated

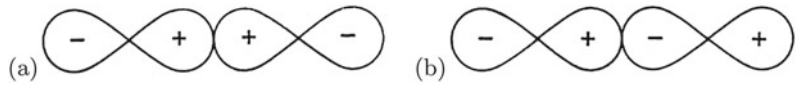

Fig. 2.6 Schematic representation of **a** bonding and **b** antibinding p orbitals. The signs denote the phase of the wavefunction

the distance from the nuclei. First, the energetically sharp states become a band due to the overlap and coupling of the atomic wavefunctions (cf. Sect. 6). The mixing of the states leads to the formation of the filled lower valence band (binding states) and the empty upper conduction band (antibinding states). This principle is valid for most semiconductors and is shown schematically also in Fig. 2.5. The configuration of bonding and antibinding p orbitals is depicted schematically in Fig. 2.6. The bonding and antibinding sp^3 orbitals are depicted in Figs. 2.7a, b and 2.13. We note that the energy of the crystal does not only depend on the distance from the nuclei but also on their geometric arrangement (crystal structure).

Per carbon atom there are (in the second shell) four electrons and four unoccupied states, altogether eight. These are redistributed into four states (filled) per atoms in the valence band and four states per atom (empty) in the conduction band. Between the top of the valence band and the bottom of the conduction band there is an energy gap, later called the *band gap* (cf. Chap. 6).

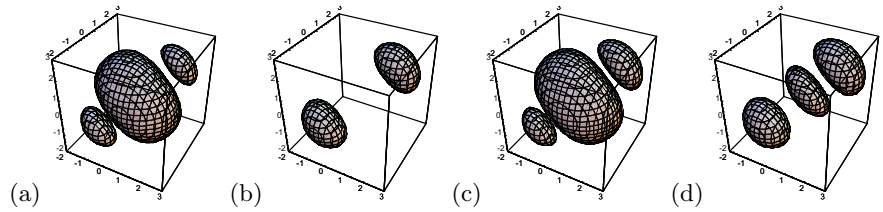

Fig. 2.7 Schematic representation of **a**, **c** bonding and **b**, **d** antibinding symmetric **a**, **b** and nonsymmetric **c**, **d** sp^3 orbitals

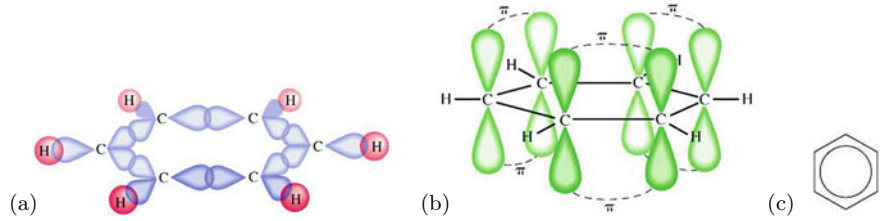

Fig. 2.8 Schematic representation of the **a** σ and **b** π bonds in benzene, **c** schematic symbol for benzene

2.2.3 sp^2 Bonds

Organic semiconductors (see Chap. 18) are made up from carbon compounds. While for inorganic semiconductors the covalent (or mixed, cf. Sect. 2.4) bond with sp^3 hybridization is important, the organic compounds are based on the sp^2 hybridization. This bonding mechanism, which is present in graphite, is stronger than the sp^3-bond present in diamond. The prototype organic molecule is the benzene ring[3] (C_6H_6), shown in Fig. 2.8. The benzene ring is the building block for small organic molecules and polymers.

In the benzene molecule neighboring carbon atoms are bonded within the ring plane via the binding σ states of the sp^2 orbitals (Fig. 2.8a). The wavefunctions (Fig. 2.9) are given by (2.2ac).

$$\Psi_1 = (\mathrm{s} + \sqrt{2}\,\mathrm{p}_x)/\sqrt{3} \tag{2.2a}$$

$$\Psi_2 = (\mathrm{s} - \sqrt{1/2}\,\mathrm{p}_x + \sqrt{3/2}\,\mathrm{p}_y)/\sqrt{3} \tag{2.2b}$$

$$\Psi_3 = (\mathrm{s} - \sqrt{1/2}\,\mathrm{p}_x - \sqrt{3/2}\,\mathrm{p}_y)/\sqrt{3}\,. \tag{2.2c}$$

The 'remaining' p_z orbitals do not directly take part in the binding (Fig. 2.8b) and form bonding (π, filled) and antibinding (π^*, empty) orbitals (see Fig. 2.10). The π and π^* states are delocalized over the ring. A more in-depth view considers the alternating 'staggered' spin configuration around the ring [177]. Between the highest populated molecular orbital (HOMO) and the lowest unoccupied molecular orbital (LUMO) is typically an energy gap (Fig. 2.11). The antibinding σ^* orbitals are energetically above the π^* states.

[3] Supposedly, the chemist Friedrich August Kekulé von Stadonitz had a dream about dancing carbon molecules and thus came up with the ring-like molecule structure [176].

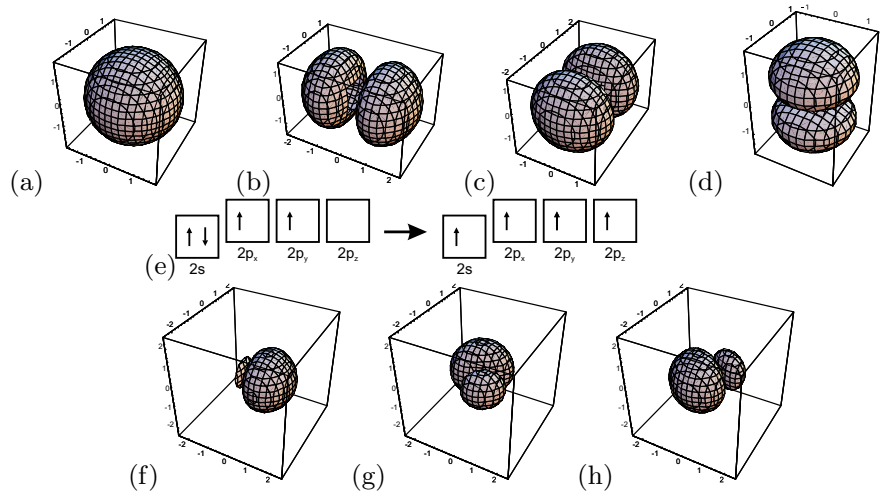

Fig. 2.9 **a** s orbital, **b**,**c**,**d** p_x, p_y and p_z orbital, **e** hybridization, **f**,**g**,**h** orbitals of the sp^2 hybridization: **f** $(s+\sqrt{2}\,p_x)/\sqrt{3}$, **g** $(s-\sqrt{1/2}\,p_x+\sqrt{3/2}\,p_y)/\sqrt{3}$, **h** $(s-\sqrt{1/2}\,p_x-\sqrt{3/2}\,p_y)/\sqrt{3}$

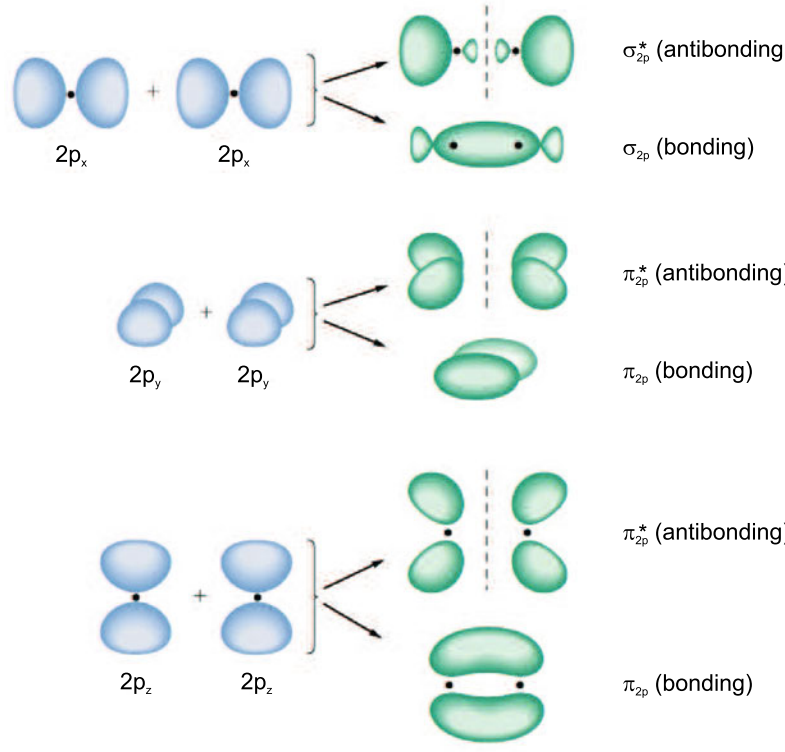

Fig. 2.10 Orbitals due to binding and antibinding configurations of various π orbitals

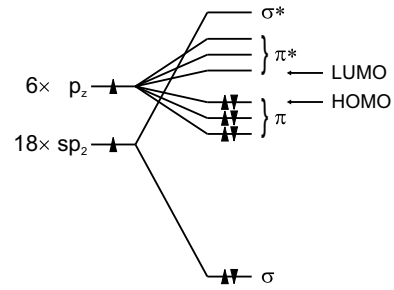

Fig. 2.11 Schematic energy terms of the benzene molecule

2.3 Ionic Bonds

Ionic crystals are made up from positively and negatively charged ions. The heteropolar or ionic bond is the consequence of the electrostatic attraction between the ions. However, the possibly repulsive character of next neighbors has to be considered.

For I–VII compounds, e.g. LiF or NaCl, the shells of the singly charged ions are complete: Li: $1s^2 2s^1 \rightarrow Li^+$: $1s^2$, F: $1s^2 2s^2 2p^5 \rightarrow F^-$: $1s^2 2s^2 2p^6$. Compared to ions in a gas, a Na–Cl pair in the crystal has a binding energy of 7.9 eV that mostly stems from the electrostatic energy (Madelung energy). Van-der-Waals forces (cf. Sect. 2.6) only contribute 1–2%. The ionization energy of Na is 5.14 eV, the electron affinity of Cl is 3.61 eV. Thus the energy of the NaCl pair in the solid is 6.4 (=7.9−5.1+3.6) eV smaller than in a gas of neutral atoms.

The interaction of two ions with distance vector $\mathbf{r}_{ij}$ is due to the Coulomb interaction

$$U_{ij}^{\mathrm{C}} = \frac{q_i\, q_j}{4\pi\epsilon_0}\,\frac{1}{r_{ij}} = \pm\frac{e^2}{4\pi\epsilon_0}\,\frac{1}{r_{ij}} \tag{2.3}$$

and a repulsive contribution due to the overlap of (complete) shells. This contribution is typically approximated by a radially symmetric core potential

$$U_{ij}^{\mathrm{core}} = \lambda\, \exp(-\lambda/\rho) \tag{2.4}$$

that only acts on next neighbors. λ describes the strength of this interaction and ρ parameterizes its range.

The distance of ions is denoted as $r_{ij} = p_{ij} R$, where R denotes the distance of next neighbors and the p_{ij} are suitable coefficients. The electrostatic interaction of an ion with *all* its neighbors is then written as

$$U_{ij}^{\mathrm{C}} = -\alpha\,\frac{e^2}{4\pi\epsilon_0}\,\frac{1}{R}\,, \tag{2.5}$$

where α is the Madelung constant. For an attractive interaction (as in a solid), α is positive. It is given (calculated for the i-th ion) as

$$\alpha = \sum_{ij}\frac{\pm 1}{p_{ij}}\,. \tag{2.6}$$

For a one-dimensional chain $\alpha = 2\ln 2$. For the rocksalt (NaCl) structure (cf. Sect. 3.4.1) it is $\alpha \approx 1.7476$, for the CsCl structure (see Sect. 3.4.2) it is $\alpha \approx 1.7627$, and for the zincblende structure (see Sect. 3.4.4) it is $\alpha \approx 1.6381$. This shows that ionic compounds prefer the NaCl or CsCl structure.

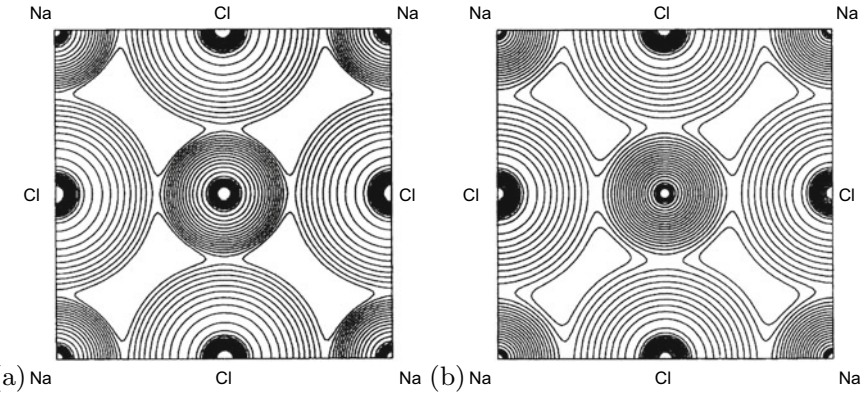

Fig. 2.12 **a** Experimental and **b** theoretical charge distribution in the (100) plane of NaCl. The lowest contour in the interstitial region corresponds to a charge density of 7 e/nm^3 and adjacent contours differ by $\sqrt{2}$. Differences are mainly due to the fact that the X-ray experiments have been made at room temperature. Adapted from [178]

The charge distribution for NaCl is shown in Fig. 2.12. For tetragonal and orthorhombic structures, the Madelung constant has been calculated in [179].

2.4 Mixed Bonds

The group-IV crystals are of perfectly covalent nature, the I–VII are almost exclusively ionically bonded. For III–V (e.g. GaAs, InP) and II–VI compounds (e.g. CdS, ZnO) we have a mixed case.

The (screened) Coulomb potentials of the A and B atoms (in the AB compound) shall be denoted V_A and V_B. The origin of the coordinate system is in the center of the A and B atom (i.e. for the zincblende structure (cf. Sect. 3.4.4) at $(1/8, 1/8, 1/8)a$. The valence electrons then see the potential

$$V_{\text{crystal}} = \sum_{\alpha} V_A(\mathbf{r} - \mathbf{r}_\alpha) + \sum_{\beta} V_B(\mathbf{r} - \mathbf{r}_\beta) \,, \tag{2.7}$$

where the sum α (β) runs over all A (B) atoms. This potential can be split into a symmetric (V_c, covalent) and an antisymmetric (V_i, ionic) part (2.8b), i.e. $V_{\text{crystal}} = V_\text{c} + V_\text{i}$

$$V_\text{c} = \frac{1}{2} \left\{ \sum_{\alpha} V_A(\mathbf{r} - \mathbf{r}_\alpha) + \sum_{\alpha} V_B(\mathbf{r} - \mathbf{r}_\alpha) + \sum_{\beta} V_B(\mathbf{r} - \mathbf{r}_\beta) + \sum_{\beta} V_A(\mathbf{r} - \mathbf{r}_\beta) \right\} \tag{2.8a}$$

$$V_\text{i} = \frac{1}{2} \left\{ \sum_{\alpha} V_A(\mathbf{r} - \mathbf{r}_\alpha) - \sum_{\alpha} V_B(\mathbf{r} - \mathbf{r}_\alpha) + \sum_{\beta} V_B(\mathbf{r} - \mathbf{r}_\beta) - \sum_{\beta} V_A(\mathbf{r} - \mathbf{r}_\beta) \right\} . \tag{2.8b}$$

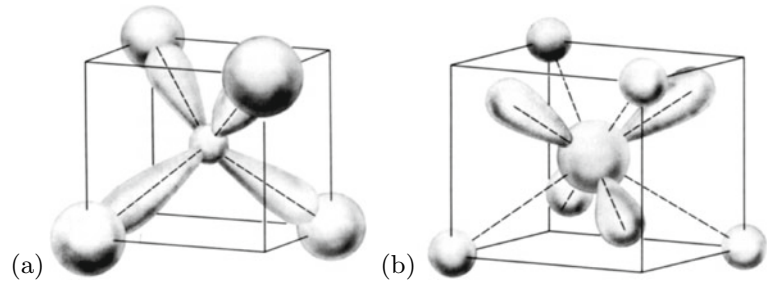

Fig. 2.13 Schematic representation of **a** bonding and **b** antibinding sp^3 orbitals. From [169]

For homopolar bonds $V_\mathrm{i} = 0$ and the splitting between bonding and antibinding states is E_h, which mainly depends on the bond length l_{AB} (and the related overlap of atomic wavefunctions). In a partially ionic bond the orbitals are not symmetric along A–B, but the center is shifted towards the more electronegative material (Figs. 2.7c, d and 2.13).

The band splitting[4] between the (highest) bonding and (lowest) antibinding state E_ba is then written as

$$E_\mathrm{ba} = E_\mathrm{h} + \mathrm{i}C \ , \tag{2.9}$$

where C denotes the band splitting due to the ionic part of the potential and depends only on $V_A - V_B$. C is proportional to the difference of the electronegativities X of the A and B atoms, $C(A, B) = 5.75(X_A - X_B)$. A material thus takes a point in the (E_h,C) plane (Fig. 2.14). The absolute value for the band splitting is given as $E_\mathrm{ba}^2 = E_\mathrm{h}^2 + C^2$.

The ionicity of the bond is described with the ionicity (after Phillips) f_i, defined as [181, 182]

$$f_\mathrm{i} = \frac{C^2}{E_h^2 + C^2} \ . \tag{2.10}$$

The covalent part is $1 - f_\mathrm{i}$. In Table 2.1 the ionicity is given for a number of binary compounds. The ionicity can also be interpreted as the angle $\tan(\phi) = C/E_h$ in the (E_h,C) diagram. The critical value of $f_\mathrm{i} = 0.785$ for the ionicity separates quite exactly (for about 70 compounds) the 4-fold (diamond, zincblende and wurtzite) from the 6-fold (rocksalt) coordinated substances ($f_\mathrm{i} = 0.785$ is indicated by a dashed line in Fig. 2.14).

For ionic compounds, an effective ionic charge e^* is defined connecting the displacement $\mathbf{u}$ of negative and positive ions and the resulting polarization $\mathbf{P} = (e^*/2a^3)\,\mathbf{u}$ [183]. Connected with the ionicity is the so-called s-parameter, describing the change of the charge upon change of bond length b from its equilibrium value b_0 [184]

$$e^*(b) = e^*(b_0) \left(\frac{b}{b_0}\right)^s \approx e_0^* \, (1 + s\,\epsilon) \ , \tag{2.11}$$

ϵ being the strain of the bond length, $b/b_0 = 1 + \epsilon$. It seems justified to assume that $e^*(b_0)$ is always positive at the metal atom in III–V and II–VI compounds. The relation of s with the ionicity f_i is shown in Fig. 2.15 for various compound semiconductors.

[4]This energy should not be confused with the *band gap* ΔE_cv, the energy separation of the highest valence-band state and the lowest conduction-band state. The energy splitting E_ba is the energy separation between the centers of the valence and conduction bands. Mostly, the term E_g is used for ΔE_cv.

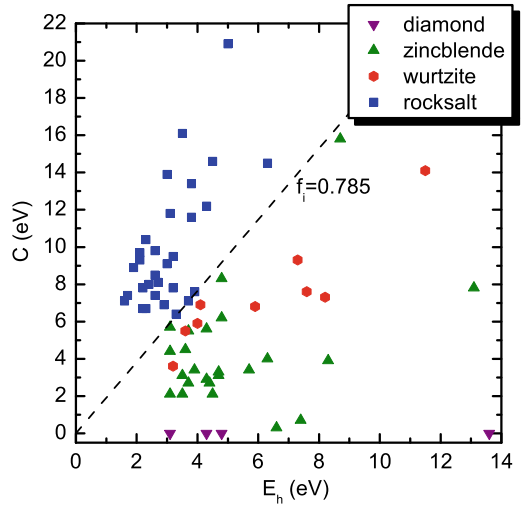

Fig. 2.14 Values of E_h and C for various $A^N B^{8-N}$ compounds. The *dashed line* $f_\mathrm{i} = 0.785$ separates 4-fold from 6-fold coordinated structures. Most data taken from [180]

Table 2.1 Ionicity f_i (2.10) for various binary compounds

C	0.0	AlAs	0.27	BeO	0.60	CuCl	0.75
Si	0.0	BeS	0.29	ZnTe	0.61	CuF	0.77
Ge	0.0	AlP	0.31	ZnO	0.62	AgI	0.77
Sn	0.0	GaAs	0.31	ZnS	0.62	MgS	0.79
BAs	0.002	InSb	0.32	ZnSe	0.63	MgSe	0.79
BP	0.006	GaP	0.33	HgTe	0.65	CdO	0.79
BeTe	0.17	InAs	0.36	HgSe	0.68	HgS	0.79
SiC	0.18	InP	0.42	CdS	0.69	MgO	0.84
AlSb	0.25	AlN	0.45	CuI	0.69	AgBr	0.85
BN	0.26	GaN	0.50	CdSe	0.70	LiF	0.92
GaSb	0.26	MgTe	0.55	CdTe	0.72	NaCl	0.94
BeSe	0.26	InN	0.58	CuBr	0.74	RbF	0.96

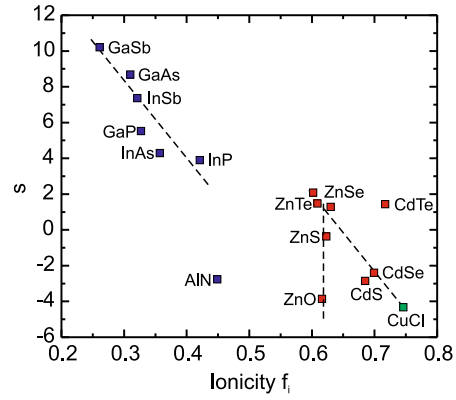

Fig. 2.15 s-Parameter as defined in (2.11) as a function of the ionicity f_i (2.10) for various compound semiconductors. *Dashed lines* are guides to the eye. Data from [185], value for CuCl from [184]

2.5 Metallic Bonding

In a metal, the positively charged atomic cores are embedded in a more or less homogeneous sea of electrons. The valence electrons of the atoms become the conduction electrons of the metal. These are freely moveable and at $T = 0\,\mathrm{K}$ there is no energy gap between filled and empty states. The bonding is mediated by the energy reduction for the conduction electrons in the periodic potential of the solid compared to free atoms. This will be clearer when the band structure is discussed (Chap. 6). In transition metals the overlap of inner shells (d or f) can also contribute to the bonding.

2.6 Van-der-Waals Bonds

The van-der-Waals bond is a dipole bond that leads to bonding in the noble-gas crystals (at low temperature). Ne, Ar, Kr and Xe crystallize in the densely packed fcc lattice (cf. Sect. 3.3.2.1). He^3 and He^4 represent an exception. They do not solidify at zero pressure at $T = 0\,K$ due to the large zero-point energy. This quantum-mechanical effect is especially strong for oscillators with small mass.

When two neutral atoms come near to each other (distance of the nuclei R), an attractive dipole–dipole interaction $-AR^{-6}$ arises (London interaction) the van-der-Waals interaction. The quantum-mechanical overlap of the (filled) shells leads to a strong repulsion $+BR^{-12}$. Altogether, a binding energy minimum results for the Lennard–Jones potential V_{LJ} (see Fig. 2.16)

$$V_{\mathrm{LJ}}(R) = -\frac{A}{R^6} + \frac{B}{R^{12}}\ . \tag{2.12}$$

The energy minimum $E_{\min} = -A^2/(2B)$ is at $R = (2B/A)^{1/6}$.

The origin of the attractive dipole–dipole interaction can be understood from a one-dimensional (1D) model as follows: Two atoms are modeled by their fixed positively charged nuclei in a distance R and their negatively charged electron shells that are polarizable, i.e. can be displaced along one direction x. Additionally, we assume (two identical) 1D harmonic oscillators for the electron motion at the positions 0 and R. Then, the Hamilton operator H_0 of the system without interaction (R is very large)

$$H_0 = \frac{1}{2m}\,p_1^2 + C\,x_1^2 + \frac{1}{2m}\,p_2^2 + C\,x_2^2\ . \tag{2.13}$$

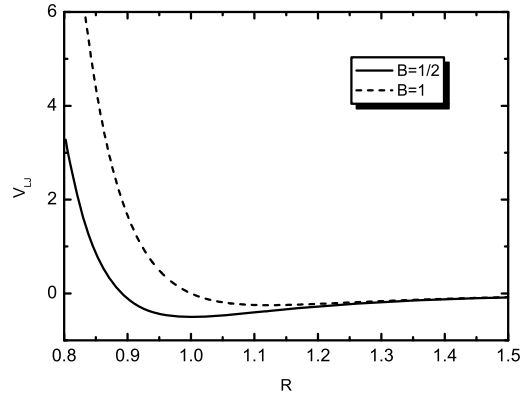

Fig. 2.16 Lennard–Jones potential (2.12) for $A = 1$ and two values of B

The indices 1 and 2 denote the two electrons of atoms. x_1 and x_2 are the displacements of the electrons. Both harmonic oscillators have a resonance frequency $\omega_0 = \sqrt{C/m}$, and the zero-point energy is $\hbar\omega_0/2$.

Taking into account the Coulomb interaction of the four charges, an additional term H_1 arises

$$H_1 = \frac{e^2}{R} + \frac{e^2}{R + x_1 + x_2} - \frac{e^2}{R + x_1} - \frac{e^2}{R - x_2} \approx -\frac{2e^2}{R^3}\, x_1\, x_2 \,. \tag{2.14}$$

The approximation is valid for small amplitudes $x_i \ll R$. A separation of variables can be achieved by transformation to the normal modes

$$x_s = \frac{x_1 + x_2}{\sqrt{2}}, x_a = \frac{x_1 - x_2}{\sqrt{2}} \,. \tag{2.15}$$

Then we find

$$\begin{aligned} H &= H_0 + H_1 \\ &= \left[\frac{1}{2m}\, p_s^2 + \frac{1}{2}\left(C - \frac{2e^2}{R^3}\right) x_s^2\right] + \left[\frac{1}{2m}\, p_a^2 + \frac{1}{2}\left(C - \frac{2e^2}{R^3}\right) x_a^2\right] \,. \end{aligned} \tag{2.16}$$

This equation is the Hamiltonian of two decoupled harmonic oscillators with the normal frequencies

$$\omega_\pm = \sqrt{\left(C \pm \frac{2e^2}{R^3}\right)/m} \approx \omega_0 \left[1 \pm \frac{1}{2}\left(\frac{2e^2}{C\, R^3}\right) - \frac{1}{8}\left(\frac{2e^2}{C\, R^3}\right)^2 + \ldots\right] \,. \tag{2.17}$$

The coupled system thus has a lower (zero-point) energy than the uncoupled. The energy difference per atom is (in lowest order) proportional to R^{-6}.

$$\Delta U = \hbar\omega_0 - \frac{1}{2}\left(\omega_+ - \omega_-\right) \approx -\hbar\omega_0\, \frac{1}{8}\left(\frac{2e^2}{C\, R^3}\right)^2 = -\frac{A}{R^6} \,. \tag{2.18}$$

The interaction is a true quantum-mechanical effect, i.e. the reduction of the zero-point energy of coupled oscillators.

2.7 Hamilton Operator of the Solid

The total energy of the solid, including kinetic and potential terms, is

$$\begin{aligned} H = &\sum_i \frac{\mathbf{p}_i^2}{2m_i} + \sum_j \frac{\mathbf{P}_j^2}{2M_j} \\ &+ \frac{1}{2}\sum_{j,j'} \frac{Z_j\, Z_{j'}\, e^2}{4\pi\epsilon_0\, |\mathbf{R}_j - \mathbf{R}_{j'}|} + \frac{1}{2}\sum_{i,i'} \frac{e^2}{4\pi\epsilon_0\, |\mathbf{r}_i - \mathbf{r}_{i'}|} \\ &- \sum_{i,j} \frac{Z_j\, e^2}{4\pi\epsilon_0\, |\mathbf{R}_j - \mathbf{r}_i|} \,, \end{aligned} \tag{2.19}$$

where $\mathbf{r}_i$ and $\mathbf{R}_i$ are the position operators and $\mathbf{p}_i$ and $\mathbf{P}_i$ are the momentum operators of the electrons and nuclei, respectively. The first term is the kinetic energy of the electrons, the second term is the kinetic energy of the nuclei. The third term is the electrostatic interaction of the nuclei, the fourth term is the electrostatic interaction of the electrons. In the third and fourth terms the summation over the same indices is left out. The fifth term is the electrostatic interactions of electrons and nuclei.

In the following, the usual approximations in order to treat (2.19) are discussed. First, the nuclei and the electrons tightly bound to the nuclei (inner shells) are united with ion cores. The remaining electrons are the valence electrons.

The next approximation is the Born–Oppenheimer (or adiabatic) approximation. Since the ion cores are much heavier than the electrons (factor $\approx 10^3$) they move much slower. The frequencies of the ion vibrations are typically in the region of several tens of meV (phonons, cf. Sect. 5.2), the energy to excite an electron is typically 1 eV. Thus, the electrons always 'see' the momentary position of the ions, the ions, however, 'see' the electron motions averaged over many periods. Thus, the Hamiltonian (2.19) is split into three parts:

$$H = H_{\text{ions}}(\mathbf{R}_j) + H_{\text{e}}(\mathbf{r}_i, \mathbf{R}_{j_0}) + H_{\text{e-ion}}(\mathbf{r}_i, \delta\mathbf{R}_j) \ . \tag{2.20}$$

The first term contains the ion cores with their potential and the time-averaged contribution of the electrons. The second term is the electron motion around the ion cores at their averaged positions $\mathbf{R}_{j_0}$. The third term is the Hamiltonian of the electron–phonon interaction that depends on the electron positions and the deviation of the ions from their average position $\delta\mathbf{R}_j = \mathbf{R}_j - \mathbf{R}_{j_0}$. The electron–phonon interaction is responsible for such effects as electrical resistance and superconductivity.

Chapter 3
Crystals

La science cristallographique ne consiste donc point à décrire scrupuleusement tous les accidens des formes cristallines; mais à spécifier, en décrivant ces formes, les rapports plus ou moins immédiats qu'elles ont entre elles.
Crystallographic science does not consist in the scrupulous description of all the accidental crystalline forms, but in specifying, by the description of these forms, the more or less close relationship they have with each other.

J.-B. Romé de l'Isle, 1783 [186]

Abstract A little bit of crystallography. The concepts of the direct and reciprocal lattice, point and space groups, unit and elementary cells and the Wigner- Seitz cell are laid out. The important crystal structures for semiconductors (diamond, sphalerite, wurtzite, chalcopyrite, ...) are discussed in some detail. Also alloys and ordering are covered.

3.1 Introduction

The economically most important semiconductors have a relatively simple atomic arrangement and are highly symmetric. The symmetry of the atomic arrangement is the basis for the classification of the various crystal structures. Using group theory [187], basic and important conclusions can be drawn about the physical properties of the crystal, such as its elastic and electronic properties. The presence of highly symmetric planes is obvious from the crystal shape of the minerals and their cleavage behavior.

Polycrystalline semiconductors consist of grains of finite size that are structurally perfect but have various orientations. The grain boundaries are a lattice defect (see also Sect. 4.4.3). Amorphous semiconductors are disordered on the atomic scale, see Sect. 3.3.7.

3.2 Crystal Structure

A crystal is built up by the (quasi-) infinite periodic repetition of identical building blocks. This translation lattice [188–190] is generated by the three fundamental *translation* vectors $\mathbf{a}_1$, $\mathbf{a}_2$ and $\mathbf{a}_3$. These three vectors may not lie in a common plane. The lattice (Fig. 3.1) is the set of all points $\mathbf{R}$

$$\mathbf{R} = n_1\,\mathbf{a}_1 + n_2\,\mathbf{a}_2 + n_3\,\mathbf{a}_3\ . \tag{3.1}$$

M. Grundmann, *The Physics of Semiconductors*, Graduate Texts in Physics,
https://doi.org/10.1007/978-3-030-51569-0_3

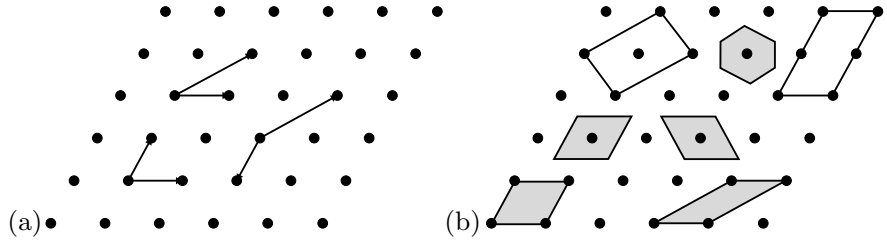

Fig. 3.1 **a** Two-dimensional lattice. It can be generated by various pairs of translation vectors. **b** Elementary cells of the lattice. Primitive elementary cells are shaded

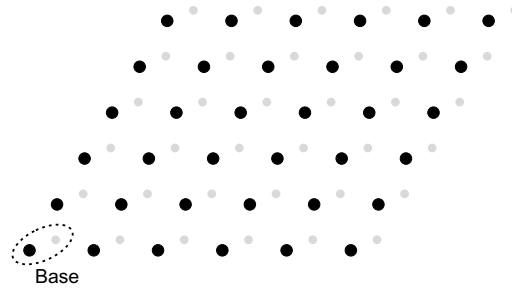

Fig. 3.2 Crystal structure, consisting of a lattice and a base

The crystal structure is made up by the lattice and the building block that is attached to each lattice point. This building block is called the *base* (Fig. 3.2). In the simplest case, e.g. for crystals like Cu, Fe or Al, this is just a single atom (monoatomic base). In the case of C (diamond), Si or Ge, it is a diatomic base with two identical atoms (e.g. Si–Si or Ge–Ge), in the case of zincblende compound semiconductors, such as GaAs or InP, it is a diatomic base with nonidentical atoms such as Ga–As or In–P. For wurtzite crystals such as GaN or ZnO the base has four atoms like Ga–N–Ga–N. There exist far more involved structures, e.g. $NaCd_2$ where the smallest cubic cell contains 1192 atoms. In protein crystals, the base of the lattice can contain 10,000 atoms.

In summary: Crystal structure = Lattice $\times$ Base.

3.3 Lattice

As described in Sect. 3.2 the lattice is spanned by three vectors $\mathbf{a}_i$. The lattice symmetry is decisive for the physical properties of the semiconductor. It is described by the appropriate groups of the symmetry operations.

3.3.1 2D Bravais Lattices

There are five two-dimensional (2D) Bravais lattices (Fig. 3.3) which are distinct and fill all (2D) space. These are very important for the description of symmetries at surfaces. The 2D Bravais lattices are the square, hexagonal, rectangular and centered-rectangular lattice.

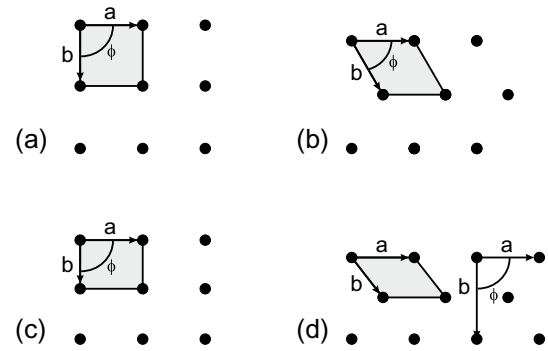

Fig. 3.3 The two-dimensional Bravais lattices with the primitive unit cells: **a** square lattice ($a = b$, $\phi = 90°$), **b** hexagonal lattice ($a = b$, $\phi = 60°$), **c** rectangular lattice ($a \neq b$, $\phi = 90°$), **d** centered-rectangular lattice ($a \neq b$, $\phi = 90°$, for the (nonprimitive) rectangular unit cell shown on the right)

3.3.2 3D Bravais Lattices

In three dimensions, the operations of the point group results in fourteen 3D Bravais lattices (Fig. 3.4), that are categorized into seven crystal classes (trigonal, monoclinic, rhombic, tetragonal, cubic, rhombohedral and hexagonal). These classes are discerned by the conditions for the lengths and the mutual angles of the vectors that span the lattice (Table 3.1). Some classes have several members. The cubic crystal can have a simple (sc), face-centered (fcc) or body-centered (bcc) lattice.

In the following, some of the most important lattices, in particular those most relevant to semiconductors, will be treated in some more detail.

3.3.2.1 Cubic fcc and bcc Lattices

The primitive translation vectors for the cubic face-centered (fcc) and the cubic body-centered (bcc) lattice are shown in Fig. 3.5 and Fig. 3.6, respectively. Many metals crystallize in these lattices, e.g. copper (fcc) and tungsten (bcc).

Table 3.1 Conditions for lengths and angles for the 7 crystal classes. Note that only the positive conditions are listed. The rhombohedral system is a special case of the trigonal class. Conditions for the trigonal and hexagonal classes are the same, however, trigonal symmetry includes a single C_3 or S_6 axis, while hexagonal symmetry includes a single C_6 or S_6^5 axis

System	#	Lattice symbol	Conditions for the usual unit cell
Triclinic	1		None
Monoclinic	2	s, c	$\alpha = \gamma = 90°$ or $\alpha = \beta = 90°$
Orthorhombic	4	s, c, bc, fc	$\alpha = \beta = \gamma = 90°$
Tetragonal	2	s, bc	$a = b$, $\alpha = \beta = \gamma = 90°$
Cubic	3	s, bc, fc	$a = b = c$, $\alpha = \beta = \gamma = 90°$
Trigonal	1		$a = b$, $\alpha = \beta = 90°$, $\gamma = 120°$
(Rhombohedral)	1		$a = b = c$, $\alpha = \beta = \gamma$
Hexagonal	1		$a = b$, $\alpha = \beta = 90°$, $\gamma = 120°$

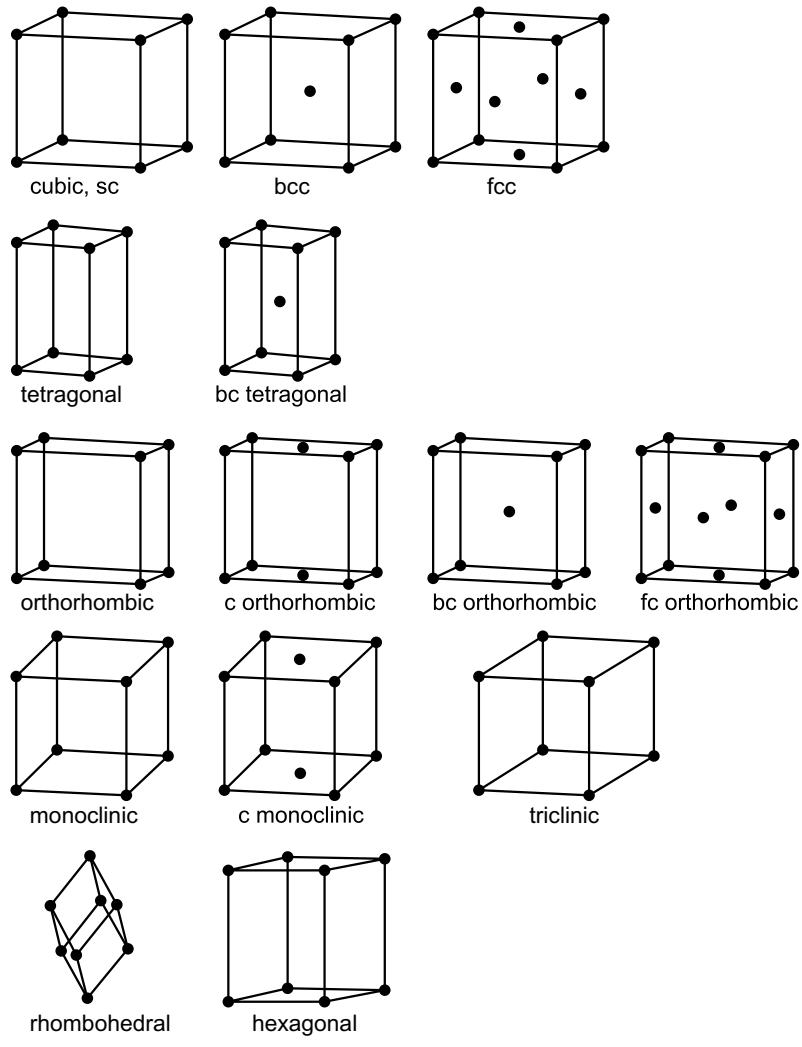

Fig. 3.4 The 14 three-dimensional Bravais lattices: cubic (sc: simple cubic, bcc: body-centered cubic, fcc: face-centered cubic), tetragonal (simple and body-centered), orthorhombic (simple, centered, body-centered and face-centered), monoclinic (simple and centered), triclinic, rhombohedral and hexagonal

In the fcc lattice, one lattice point sits in the center of each of the six faces of the usual cubic unit cell. The vectors spanning the primitive unit cell are

$$\mathbf{a}_1 = \frac{a}{2}\,(1,1,0)\,,\ \mathbf{a}_2 = \frac{a}{2}\,(0,1,1)\,,\ \mathbf{a}_3 = \frac{a}{2}\,(1,0,1)\ . \tag{3.2}$$

In the bcc lattice, one extra lattice point sits at the intersection of the three body diagonals at $(\mathbf{a}_1 + \mathbf{a}_2 + \mathbf{a}_3)/2$. The vectors spanning the primitive unit cell are

$$\mathbf{a}_1 = \frac{a}{2}\,(1,1,-1)\,,\ \mathbf{a}_2 = \frac{a}{2}\,(-1,1,1)\,,\ \mathbf{a}_3 = \frac{a}{2}\,(1,-1,1)\ . \tag{3.3}$$

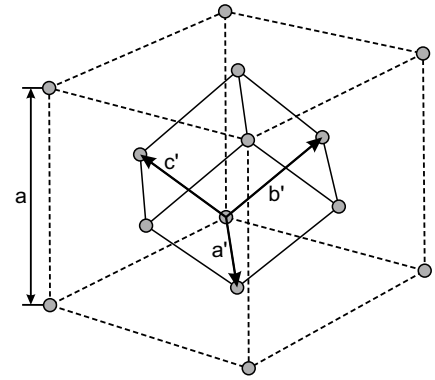

Fig. 3.5 Primitive translations of the fcc lattice. These vectors connect the origin with the face-center points. The primitive unit cell is the rhombohedron spanned by these vectors. The primitive translations $\mathbf{a}'$, $\mathbf{b}'$ and $\mathbf{c}'$ are given in (3.2). The angle between the vectors is 60°

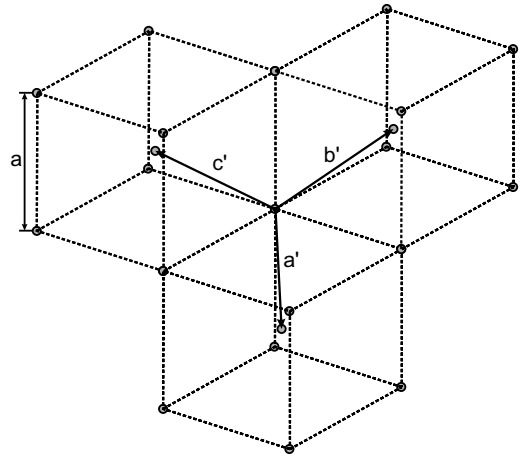

Fig. 3.6 Primitive translations of the bcc lattice. These vectors connect the origin with the lattice points in the cube centers. The primitive unit cell is the rhombohedron spanned by these vectors. The primitive translations $\mathbf{a}'$, $\mathbf{b}'$ and $\mathbf{c}'$ are given in (3.3). The angle between the vectors is $\approx 70.5°$

3.3.2.2 Hexagonally Close Packed Structure (hcp)

The 2D hexagonal Bravais lattice fills a plane with spheres (or circles) with maximum filling factor. There are two ways to fill space with spheres and highest filling factor. One is the fcc lattice, the other is the hexagonally close packed (hcp) structure.[1] Both fcc and hcp have a filling factor of 74%.

For the hcp, we start with a hexagonally arranged layer of spheres (A), see Fig. 3.7. Each sphere has six next-neighbor spheres. This could, e.g., be a plane in the fcc perpendicular to the body diagonal. the next plane B is put on top in such a way that each new sphere touches three spheres of the previous layer. The third plane can now be added in two different ways: If the spheres of the third layer are vertically on top of the spheres of layer A, a plane A' identical to A has been created that is shifted from A along the stacking direction (normally called the c-axis) by

$$c_{\mathrm{hcp}} = \sqrt{8/3}\, a \approx 1.633\, a \ . \tag{3.4}$$

The vectors spanning the primitive unit cell are

$$\mathbf{a}_1 = \frac{a}{2}\left(1, -\sqrt{3}, 0\right), \ \mathbf{a}_2 = \frac{a}{2}\left(1, \sqrt{3}, 0\right), \ \mathbf{a}_3 = c\ (0, 0, 1) \ . \tag{3.5}$$

[1] The hcp structure is not a Bravais lattice since the individual lattice sites are not completely equivalent.

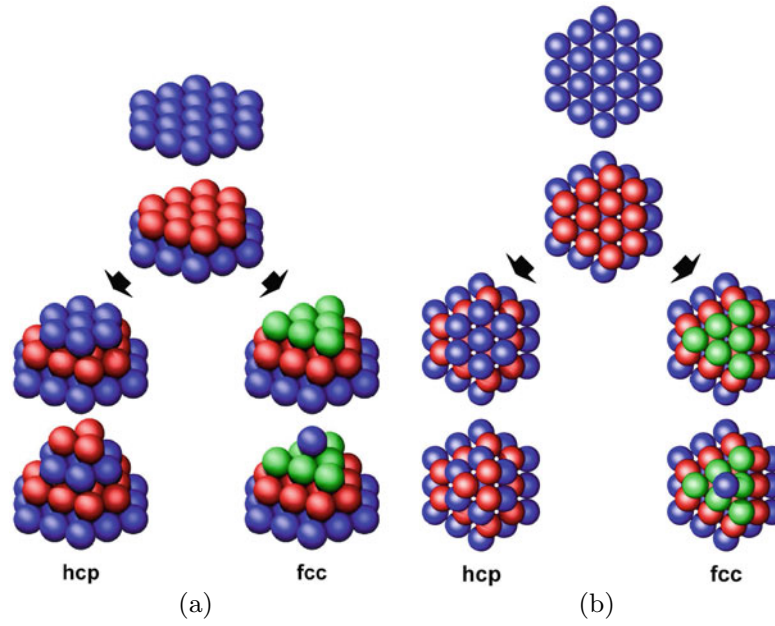

Fig. 3.7 Structure of the **a** hcp and **b** fcc lattice. For hcp the stacking (along the c-axis) is ABABAB. . ., for fcc (along the body diagonal) it is ABCABCABC. . .

The hcp stacking order is ABABAB. . . for hcp, the coordination number is 12. In the fcc structure, the third layer is put on the thus far unfilled positions and forms a new layer C. Only the forth layer is again identical to A and is shifted by

$$c_{\text{fcc}} = \sqrt{6}\, a \approx 2.45\, a \ . \tag{3.6}$$

The fcc stacking order is ABCABCABC. . .

In the hexagonal plane of the fcc lattice (which will later be called a {111} plane) the distance between lattice points is $a = a_0/\sqrt{2}$, where a_0 is the cubic lattice constant. Thus $c = \sqrt{3}\, a_0$, just what is expected for the body diagonal.

For real materials with hexagonal lattice the ratio c/a deviates from the ideal value given in (3.4). Helium comes very close to the ideal value, for Mg it is 1.623, for Zn 1.861. Many hcp metals exhibit a phase transition to fcc at higher temperatures.

3.3.3 Unit Cell

The choice of the vectors $\mathbf{a}_i$ making up the lattice is not unique (Fig. 3.1). The volume that is enclosed in the parallelepiped spanned by the vectors $\mathbf{a}_1$, $\mathbf{a}_2$ and $\mathbf{a}_3$ is called the *elementary cell*. A *primitive* elementary cell is an elementary cell with the smallest possible volume (Fig. 3.1b). In each primitive elementary cell there is exactly *one* lattice point. The coordination number is the number of next-neighbor lattice points. A primitive cubic (pc) lattice, e.g. has a coordination number of 6.

The typically chosen primitive elementary cell is the *Wigner–Seitz* (WS) cell that reflects the symmetry of the lattice best. The Wigner–Seitz cell around a lattice point $\mathbf{R_0}$ contains all points that are closer to this lattice point than to any other lattice point. Since all points fulfill such a condition for some lattice point $\mathbf{R_i}$, the Wigner–Seitz cells fill the volume completely. The boundary of the Wigner–Seitz cell is made up by points that have the same distance to $\mathbf{R_0}$ and some other lattice point(s). The

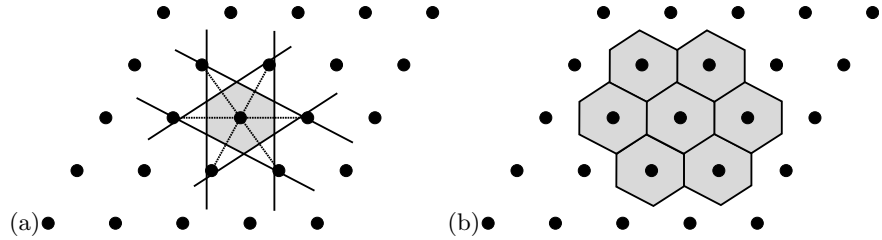

Fig. 3.8 **a** Construction of a two-dimensional Wigner–Seitz cell, **b** filling of space with WS cells

Wigner–Seitz cell around $\mathbf{R_0}$ is constructed by drawing lines from $\mathbf{R_0}$ to the next neighbors $\mathbf{R_j}$, taking the point at half distance and erecting a perpendicular plane at $(\mathbf{R_j} + \mathbf{R_0})/2$. The WS cell is the smallest polyhedron, circumscribed by these planes. A two-dimensional construction is shown in Fig. 3.8.

3.3.4 Point Group

Besides the translations there are other operations under which the lattice is invariant, i.e. the lattice is imaged into itself. These are:

Identity. The neutral element of any point group is the identity that does not change the crystal. It is denoted as 1 (E) in international (Schönfließ) notation.

Rotation. The rotation around an axis may have a rotation angle of 2π, $2\pi/2$, $2\pi/3$, $2\pi/4$ or $2\pi/6$ or their integer multiples. The axis is then called n = 1-, 2-, 3-, 4- or 6-fold, respectively[2], and denoted as n (international notation) or C_n (Schönfließ). Objects with C_n symmetry are depicted in Fig. 3.9.

Mirror operation with respect to a plane through a lattice point. Different mirror planes are discerned (Fig. 3.10) (after Schönfließ) σ_h: a mirror plane perpendicular to a rotational axis, σ_v: a mirror plane that contains a rotational axis, and σ_d: a mirror plane that contains a rotational axis and bisects the angle between two C_2 axes. The international notation is $\bar{2}$.

Inversion. All points around the inversion center $\mathbf{r}$ are replaced by $-\mathbf{r}$. The inversion is denoted $\bar{1}$ (i) in international (Schönfließ) notation.

Improper rotation. The improper rotation S_n is a rotation C_n followed immediately by the inversion operation i denoted as $\bar{n}$ in international notation. There are $\bar{3}$, $\bar{4}$ and $\bar{6}$ and their powers. Only the combined operation $\bar{n}$ is a symmetry operation, while the individual operations C_n and i alone are not symmetry operations. In the Schönfließ notation the improper rotation is defined as $S_n = \sigma_\mathrm{h} C_n$, with σ_h being a mirror operation with a plane perpendicular to the axis of the C_n rotation, denoted as S_n.

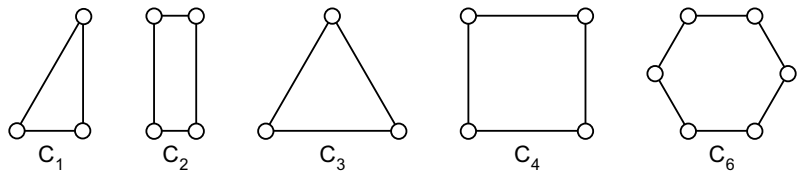

Fig. 3.9 Two-dimensional objects with perpendicular rotation axis C_n. Note that the circles do not exhibit σ_h symmetry with respect to the paper plane, i.e. they are different on the top and bottom side

[2] 5-fold periodic symmetry is geometrically impossible. However, *quasicrystals* with aperiodic five-fold symmetry exist [191, 192], some of them possibly being semiconducting [193, 194].

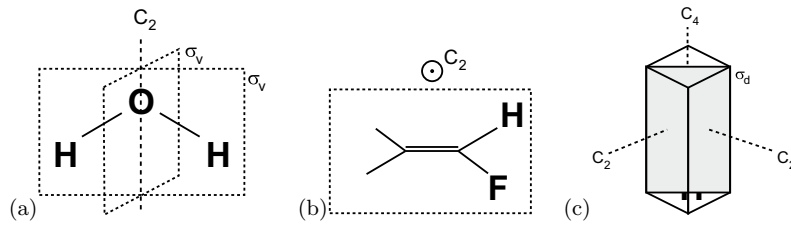

Fig. 3.10 Mirror planes: **a** σ_v (at H_2O molecule), **b** σ_h (at F_2H_2 molecule) and **c** σ_d

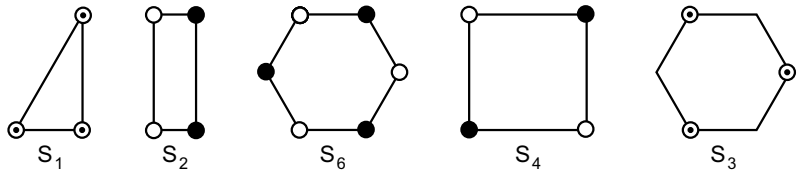

Fig. 3.11 Two-dimensional objects with perpendicular improper rotation axis S_n. Note that the white and black circles do not exhibit σ_h symmetry with respect to the paper plane, i.e. they are white on the top and black on the bottom. The circles with a dot in the center exhibit σ_h symmetry, i.e. they look the same from top and bottom

There are S_3, S_4 and S_6 and $\bar{3} = S_6^5$, $\bar{4} = S_4^3$ and $\bar{6} = S_3^5$. For successive applications, the S_n yield previously known operations, e.g. $S_4^2 = C_2$, $S_4^4 = E$, $S_6^2 = C_3$, $S_6^3 = i$, $S_3^2 = C_3^2$, $S_3^3 = \sigma_h$, $S_3^4 = C_3$, $S_3^6 = E$. We note that formally S_1 is the inversion i and S_2 is the mirror symmetry σ. Objects with S_n symmetry are schematically shown in Fig. 3.11.

These symmetry operations form 32 *point groups*. These groups are shown (with their different notations and elements) in Table B.2. The highest symmetry is the cubic symmetry $O_h = O \times i$. The tetraeder group T_d (methane molecule) is a subgroup of O_h, lacking the inversion operation.

Important for surface symmetries, there are ten two-dimensional point groups (Sect. 11.2 and Table B.1).

3.3.5 Space Group

The space group is formed by the combination of the elements of the point group with translations. The combination of a translation along a rotational axis with a rotation around this axis creates a screw axis n_m. In Fig. 3.12a, a so-called 4_1 screw axis is shown. The first index n indicates the rotation angle, i.e. $2\pi/n$, the second index indicates the translation, i.e. $c\,m/n$, c being the periodicity along the axis. There are eleven crystallographically allowed screw rotations.[3]

The combination of the mirror operation at a plane that contains a rotational axis with a translation along this axis creates a glide reflection (Fig. 3.12b). For an axial glide (or b-glide) the translation is parallel to the reflection plane. A diagonal glide (or d-glide) involves translation in two or three directions. A third type of glide is the diamond glide (or d-glide). There are 230 different space groups, listed in Appendix B. A detailed treatment can be found in [195].[4]

Important for surface symmetries, there are 17 two-dimensional space groups (Sect. 11.2).

[3] 2_1, 3_1, 3_2, 4_1, 4_2, 4_3, 6_1, 6_2, 6_3, 6_4, 6_5.

[4] One should in particular consider the pitfalls pointed out in Appendix 10 of this reference.

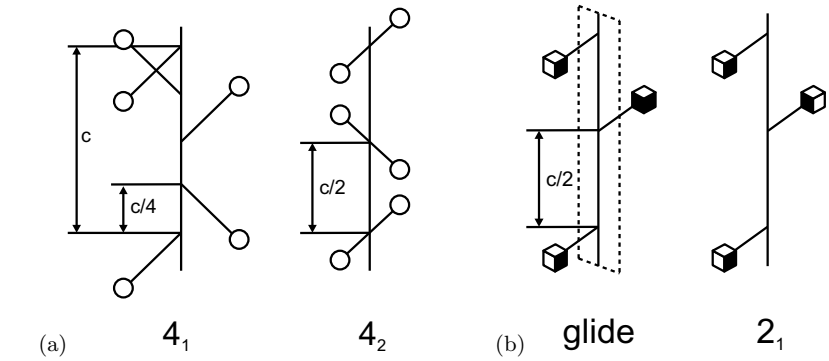

Fig. 3.12 **a** Schematic drawing of a 4_1 and 4_2 screw axis. **b** Schematic drawing of an axial glide reflection. The mirror plane is shown with dashed outline. Opposite faces of the cube have opposite color. For comparison a 2_1 screw axis is shown

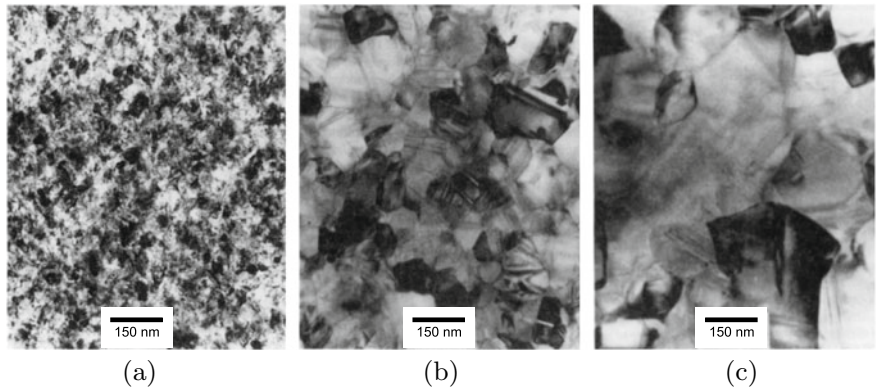

Fig. 3.13 Transmission electron micrographs of polycrystalline silicon (poly-Si). **a** As-deposited material from low-pressure chemical vapor deposition (LPCVD) at about 620 °C, grain size is about 30 nm. **b** After conventional processing (annealing at 1150 °C), average grain size is about 100 nm. **c** After annealing in HCl that provides enhanced point defect injection (and thus increased possibility to form larger grains), average grain size is about 250 nm. Adapted from [196]

3.3.6 Polycrystalline Semiconductors

A polycrystalline material consists of crystal grains that are randomly oriented with respect to each other. Between two grains a (large-angle) grain boundary (see also Sect. 4.4.3) exists. An important parameter is the grain size and its distribution. It can be influenced via processing steps such as annealing. Polycrystalline semiconductors are used in cheap, large-area applications such as solar cells (e.g. polysilicon, $CuInSe_2$) or thin-film transistors (poly-Si) or as n-conducting contact material in MOS diodes (poly-Si) as shown in Fig. 3.13 (see also Fig. 21.29). Polycrystalline material can be fabricated from amorphous material using annealing procedures as discussed in Sect. 24.6.1 for silicon.

3.3.7 Amorphous Semiconductors

An amorphous material lacks the long-range order of the direct lattice. It is disordered on the atomic scale. Historically, amorphous Se (a-Se) has been investigated first; since the 1950's amorphous chalco-

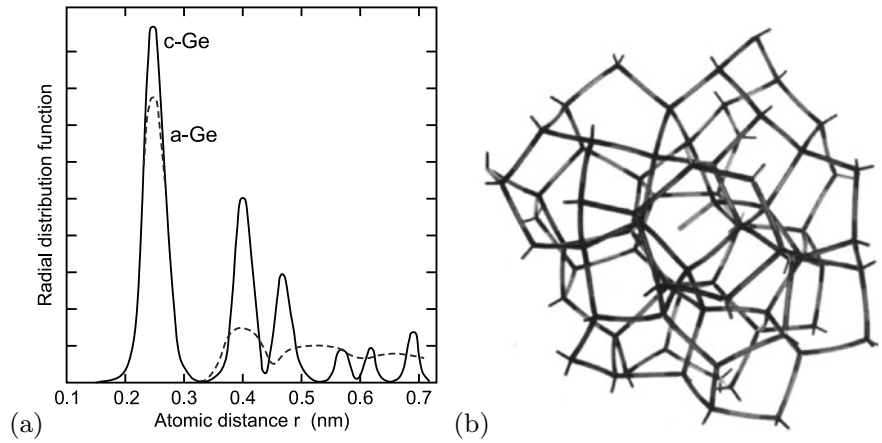

Fig. 3.14 **a** Radial atomic distribution functions of crystalline (c-Ge, *solid line*) and amorphous (a-Ge, *dashed line*) germanium, determined from EXAFS (extended X-ray absorption fine structure [201]). Adapted from [202]. **b** A continuous random network model of amorphous silicon containing a dangling bond in the center of the figure. Reprinted with permission from [203]

genides and a-Ge [197] and since the late 1960s a-Si [198] are researched. The field of amorphous oxides started in the mid 1950s with vanadate glasses [199] and is currently very active with mixed-metal-based oxides [200] (cmp. Chap. 20).

The local quantum mechanics provides almost rigorous requirements for the bond length to next neighbors. The constraints for the bond angle are less strict. Covalently bonded atoms arrange in an open network with the next-neighbor distance essentially preserved and correlations up to the third and fourth neighbors (Fig. 3.14a). The short-range order is responsible for the observation of semiconductor properties such as an optical absorption edge and also thermally activated conductivity. In Fig. 3.14b a model of a continuous random network (with a bond-angle distortion of less than about 20%) of a-Si is depicted. The diameter d_{SR} of the short-range order region is related to a disorder parameter α via [204]

$$d_{\mathrm{SR}} = \frac{a}{2\,\alpha}\ , \tag{3.7}$$

where a is the next-neighbor interatomic distance. For a diamond structure it is related to the lattice constant by $a = \sqrt{3}\,a_0/4$.

Typically, a significant number of dangling bonds exists. Bonds try to pair but if an odd number of broken bonds exists locally, an unsaturated, dangling bond remains. This configuration can be passivated by a hydrogen atom. Thus, the hydrogenation of amorphous semiconductors is very important, in particular for a-Si. A hydrogen atom can also break an overlong (and therefore weak) bond, saturate one side and eventually leave a dangling bond.

Amorphous material can be (re-)crystallized into crystalline, mostly polycrystalline material upon annealing. This is technologically very important for a-Si (see Sect. 24.6.1).

3.4 Important Crystal Structures

Now the crystal structures that are important for semiconductor physics will be discussed. These are mainly the rocksalt (PbS, CdO, ...), diamond (C, Si, Ge), zincblende (GaAs, InP, ...) and wurtzite (GaN, ZnO, ...) structures.

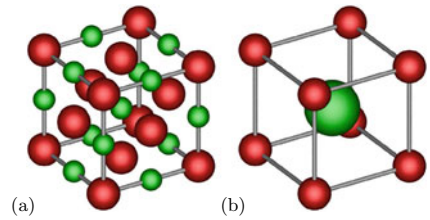

Fig. 3.15 **a** Rocksalt (NaCl) structure, **b** CsCl structure

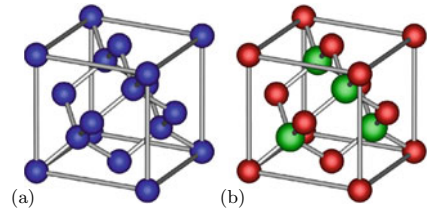

Fig. 3.16 **a** Diamond structure and **b** zincblende structure (*red spheres*: A atoms, *green spheres*: B atoms). The tetragonal bonds are indicated

3.4.1 Rocksalt Structure

The rocksalt (rs, NaCl, space group 225, $Fm\bar{3}m$) structure (Fig. 3.15a) consists of a fcc lattice with the period a and a diatomic base in which the Cl atom is positioned at (0,0,0) and the Na atom at (1/2,1/2,1/2)a with a distance $\sqrt{3}\,a/2$. Materials that crystallize (under normal conditions) in the rocksalt lattice are, e.g., KCl, KBr, PbS (galena), PbSe, PbTe, AgBr, MgO, CdO, MnO. AlN, GaN and InN undergo, under high pressure, a phase transition from the wurtzite into the rocksalt structure.

3.4.2 CsCl Structure

The CsCl structure (space group 221, $Pm\bar{3}m$) (Fig. 3.15b) consists of a simple cubic lattice. Similar as for the rocksalt structure, the base consists of different atoms at (0,0,0) and (1/2,1/2,1/2)a. Typical crystals with CsCl-structure are TlBr, TlI, CuZn (β-brass), AlNi.

3.4.3 Diamond Structure

The diamond structure (C, space group 227, $Fd\bar{3}m$) (Fig. 3.16a) has the fcc lattice. The base consists of two identical atoms at (0,0,0) and (1/4,1/4,1/4)a. Each atom has a tetrahedral configuration. The packing density is only about 0.34. The ABC-type stacking along the [111]-direction is visualized in Fig. 3.17a. The materials that crystallize in the diamond lattice are C, Ge, Si and α-Sn. Silicon as the most important semiconductor is particularly well researched [205].

The diamond structure (point group O_h) has an inversion center, located between the two atoms of the base, i.e. at (1/8,1/8,1/8)a. The radii of the wavefunctions for various group-IV elements increases with the order number (Table 3.2), and accordingly the lattice constant increases.

In Fig. 3.18a the unit cell with tetragonal symmetry of three places along the $\langle 111 \rangle$ direction is shown. In Fig. 3.18b the arrangement of atoms along $\langle 111 \rangle$ is depicted. The symmetry along this line is at least C_{3v}. At the atoms sites it is O_h. The bond center (BC) and the hexagonal (H) position are a center of inversion and have D_{3d} symmetry. The unoccupied 'T' positions have T_d symmetry. High-pressure phases of silicon are already found in indentation experiments [206].

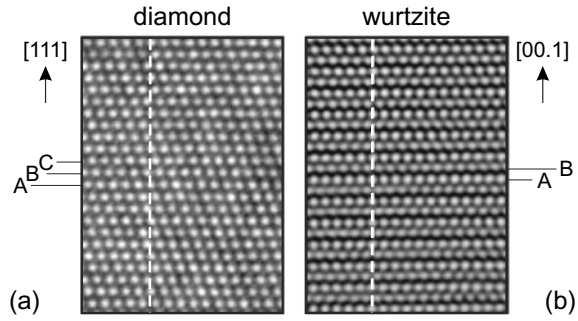

Fig. 3.17 HRTEM images of **a** diamond structure (Si, {110} cross section) and **b** wurtzite structure (GaN, ⟨10.0⟩ azimuth). The ABC and AB stacking is indicated

Table 3.2 Radii of the wavefunctions in the diamond structure, r_s and r_p are related to s^1p^3, r_d to $s^1p^2d^1$ and lattice constant a_0

	r_s (nm)	r_p (nm)	r_d (nm)	a_0 (nm)
C	0.121	0.121	0.851	0.3567
Si	0.175	0.213	0.489	0.5431
Ge	0.176	0.214	0.625	0.5646

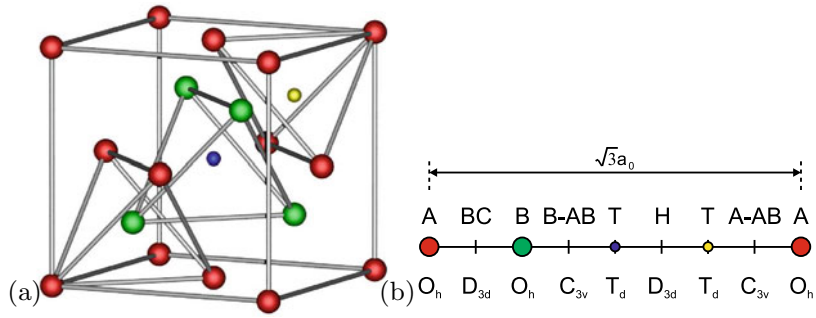

Fig. 3.18 **a** Unit cell of the zincblende structure with the indication of tetragonal symmetries. The position of the small *yellow* (*blue*) *sphere* is the tetrahedrally configured unoccupied positions of the A (B) sublattice, denoted with 'T' in part (**b**). **b** Line along [111] in the zincblende structure. The positions of the A and B atoms are denoted by *red* and *green circles* as labeled. Other positions are called the bond center ('BC'), antibonding ('AB') relative to A and B atoms ('A–AB', 'B–AB'), hexagonal ('H') and tetrahedral position ('T', *blue* and *yellow circles*)

We note that α-Sn has little current importance. The diamond structure α–Sn phase is stable below 13.2 °C. The addition of Ge inhibits the retransformation to metallic tin up to higher temperatures (e.g. 60 °C for 0.75 weight percent Ge). The properties of gray tin are reviewed in [207].

3.4.4 Zincblende Structure

The zincblende (sphalerite,[5] ZnS, space group 216, $F\bar{4}3m$) structure (Fig. 3.16b) has a fcc lattice with a diatomic base. The metal (A) atom is at (0, 0, 0) and the nonmetal (B) atom is at $(1/4, 1/4, 1/4)a$.

[5]Zincblende technically means the material ZnS which occurs in sphalerite (cubic) and wurtzite (hexagonal) phase. However, in the literature the term 'zincblende' for the sphalerite structure is common and used throughout this book.

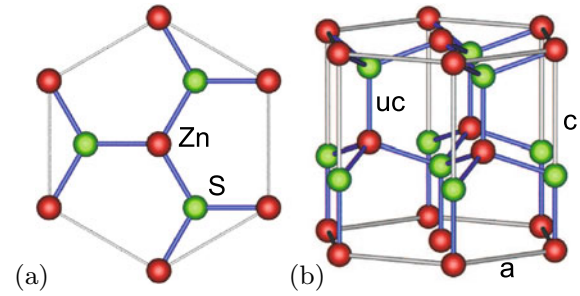

Fig. 3.19 **a** Top view (along the c-axis) and **b** side view of the wurtzite structure with the tetragonal bonds indicated. The top (bottom) surface of the depicted structure is termed the Zn-face, (00.1) (O-face, (00.$\bar{1}$))

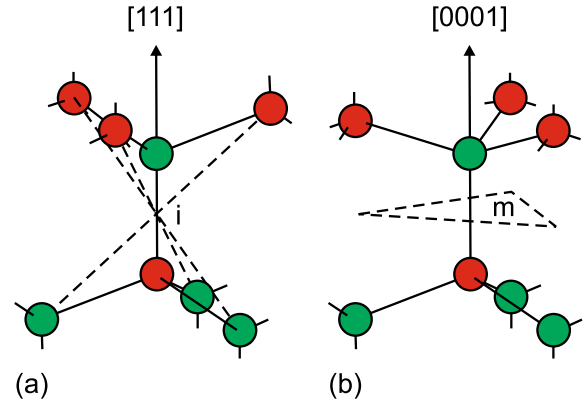

Fig. 3.20 Comparison of the tetragonal bonds in the **a** zincblende and **b** wurtzite structure (i: inversion center, m: symmetry plane)

Thus the cation and anion sublattices are shifted with respect to each other by a quarter of the body diagonal of the fcc lattice. The atoms are tetrahedrally coordinated, a Zn atom is bonded to four S atoms and vice versa. However, no inversion center is present any longer (point group T_d). In the zincblende structure the stacking order of diatomic planes along the body diagonal is aAbBcCaAbBcC...

Many important compound semiconductors, such as GaAs, InAs, AlAs, InP, GaP and their alloys (cf. Sect. 3.7), but also the II–VI compounds ZnS, ZnSe, ZnTe, HgTe and CdTe and halides, including AgI, CuF, CuCl, CuBr, and CuI, crystallize in the zincblende structure.

Four-fold coordinated materials (zincblende and wurtzite) typically undergo a phase transition into 6-fold coordinated structures upon hydrostatic pressure [208]. For GaAs under pressure see [209].

3.4.5 Wurtzite Structure

The wurtzite structure (ZnS, space group 186, P6$_3$mc) is also called the hexagonal ZnS structure (because ZnS has both modifications). It consists of a hexagonal lattice with a unit cell of four atoms (Fig. 3.19). Typically, it is thought of as a hcp structure with a diatomic base. The c/a ratio typically deviates from the ideal value $\zeta_0 = \sqrt{8/3} \approx 1.633$ (3.4) as listed in Table 3.3. The c-axis is a 6_3 screw axis.

The Zn atom is located at (0, 0, 0), the S atom at (0, 0, $\sqrt{3/8}$)a. This corresponds to a shift of $3/8\,c$ along the c-axis. This factor is called the cell-internal parameter u. For real wurtzite crystals u deviates from its ideal value $u_0 = 3/8 = 0.375$, e.g. for group-III nitrides $u > u_0$. The diatomic planes have a stacking order of aAbBaAbB... along the [00.1]-direction as visualized in Fig. 3.17b.

In Fig. 3.20 the different local structural environment of the atoms in the zincblende and wurtzite structure is shown.

Table 3.3 c/a ratio of various wurtzite semiconductors. Listed is $\xi = (c/a - \zeta_0)/\zeta_0$. Data based on [210]

Material	ξ (%)	Material	ξ(%)	Material	ξ (%)	Material	ξ (%)
AlN	−2.02	CdS	−0.61	CuBr	0.43	BeO	−0.61
GaN	−0.49	CdSe	−0.18	CuCl	0.55	ZnO	−1.9
InN	−1.35	CdTe	0.25	CuI	0.74	6H-SiC	0.49
ZnS	0.25	MgS	−0.80	AgI	0.12	BN	0.74
ZnSe	0.06	MgSe	−0.67	ZnTe	0.74	MgTe	−0.67

Many important semiconductors with large band gap crystallize in the wurtzite structure, such as GaN, AlN, InN, [211] ZnO, [212] SiC, [213], CdS und CdSe.

3.4.6 Chalcopyrite Structure

The chalcopyrite [214] (ABC_2, named after 'fool's gold' $CuFeS_2$, space group 122, $I\bar{4}2d$) structure is relevant for I–III–VI_2 (with chalcogenide anions) and II–IV–V_2 (with pnictide anions) semiconductors such as, e.g., (Cu,Ag)(Al,Ga,In)$(S,Se,Te)_2$ and (Mg,Zn,Cd)(Si,Ge,Sn)$(As,P,Sb)_2$.

In Fig. 3.21, the derivation of zincblende and chalcopyrite compounds is shown schematically, including the kesterite materials of type I_2-II-IV-VI_6.

In the chalcopyrite structure, a nonmetallic anion atom ('C') is tetrahedrally bonded to two different types of cation atoms ('A' and 'B') as shown in Fig. 3.22. The local surrounding of each anion is identical, two of both the A and B atoms. The structure is tetragonal. The aspect ratio $\eta = c/(2a)$ deviates from its ideal value 1; typically $\eta < 1$ [215, 216].

If the C atom is in the tetrahedral center of the two A and two B atoms, the bond lengths R_{AC} and R_{BC} of the A–C and B–C bonds, respectively, are equal. Since the ideal A–C and B–C bond lengths d_{AC} and d_{BC} are typically unequal, this structure is strained. The common atom C is therefore displaced

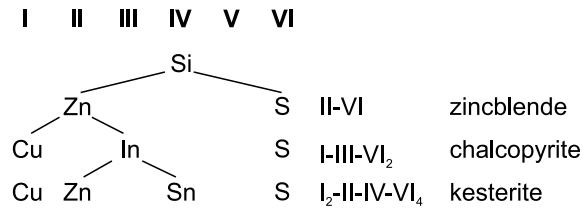

Fig. 3.21 Scheme of II–VI zincblende and related chalcopyrite and kesterite compounds

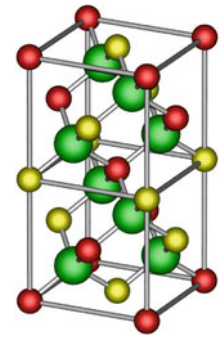

Fig. 3.22 Chalcopyrite structure, *red* and *yellow spheres* denote the metal species. The bigger *green spheres* represent the nonmetal anion

Table 3.4 Lattice nonideality parameters η and u (from (3.10)) of various chalcopyrite compounds and their experimentally observed disorder stability (+/− indicates compound with/without order–disorder (D–O) transition, respectively). Data from [216]

	η	u	D–O		η	u	D–O
$CuGaSe_2$	0.983	0.264	+	$ZnSiAs_2$	0.97	0.271	−
$CuInSe_2$	1.004	0.237	+	$ZnGeAs_2$	0.983	0.264	+
$AgGaSe_2$	0.897	0.287	−	$CdSiAs_2$	0.92	0.294	−
$AgInSe_2$	0.96	0.261	+	$CdGeAs_2$	0.943	0.287	
$CuGaS_2$	0.98	0.264		$ZnSiP_2$	0.967	0.272	−
$CuInS_2$	1.008	0.236	+	$ZnGeP_2$	0.98	0.264	+
$AgGaS_2$	0.895	0.288	−	$CdSiP_2$	0.92	0.296	−
$AgInS_2$	0.955	0.262		$CdGeP_2$	0.939	0.288	−

along [100] and [010] such that it is closer (if $d_{AC} < d_{BC}$) to the pair of A atoms and further away from the B atoms. The displacement parameter is

$$u = \frac{1}{4} + \frac{R_{AC}^2 - R_{BC}^2}{a^2} \tag{3.8}$$

and it deviates from the ideal value $u_0 = 1/4$ for the zincblende structure as listed in Table 3.4 for a number of chalcopyrite compounds. In the chalcopyrite structure

$$R_{AC} = a\sqrt{u^2 + \frac{1+\eta^2}{16}} \tag{3.9a}$$

$$R_{BC} = a\sqrt{\left(u - \frac{1}{2}\right)^2 + \frac{1+\eta^2}{16}}\,. \tag{3.9b}$$

The minimization of the microscopic strain yields (in first order) [217]

$$u \cong \frac{1}{4} + \frac{3}{8}\,\frac{d_{AC}^2 - d_{BC}^2}{d_{AC}^2 + d_{BC}^2}\,. \tag{3.10}$$

Compounds with $u > u_c$, $u_c = 0.265$ being a critical displacement parameter, (or $u < 1/2 - u_c = 0.235$) are stable with regard to cation disorder [216]. In Fig. 3.23 the correlation of the calculated value for u according to (3.10) and the experimental values is shown.

3.4.7 Spinel Structure

A large variety of ternary compounds of type $A^{II}B^{III}{}_2C^{VI}{}_4$ crystallize inb the cubic spinel structure (spinel, $MgAl_2O_4$, space group 227, Fd3m). Typical elements are A: Mg, Cr, Mn, Fe, Co, Ni, Cu, Zn, Cd, Sn, B: Al, Ga, In, Ti, V, Cr, Mn, Fe, Co, Rh, Ni, and C: O, S, Se, Te.

As an example $ZnGa_2O_4$ (zinc gallate) has received attention as interfacial layer in ZnO/GaAs epitaxy [218], luminescent material [219], and as ferromagnetic semiconductor [220]. Also the (unwanted) appearance of zinc gallate inclusions is in competition with the formation of highly doped wurtzite ZnO:Ga; in the (normal) spinel cubic structure of $ZnGa_2O_4$ the Zn^{2+} ions still occupy tetrahedral

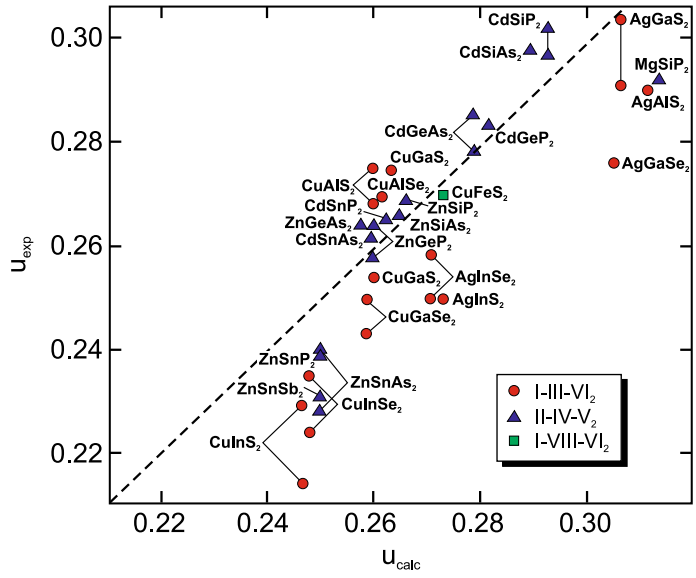

Fig. 3.23 Experimental values u_{exp} of the displacement parameter for various chalcopyrites vs. the calculated value u_{calc} according to (3.10). The *dashed line* indicates $u_{exp} = u_{calc}$. Adapted from [217]

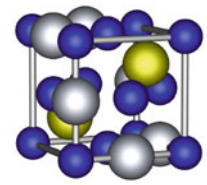

Fig. 3.24 Spinel AB_2C_4 crystal structure, the cations are depicted as *yellow* (A atoms) and *silver* (B atoms) *spheres*, the anions (C atoms) as *blue spheres*

sites, but the Ga^{3+} ions occupy octahedral sites instead of tetrahedral sites in doped wurtzite ZnO:Ga. (Sc,Al)MgO_4 (SCAM) is available as substrate material. Also $A^{VI}B^{II}{}_2C^{VI}{}_4$ compounds exist, e.g. GeB_2O_4 (with B=Mg, Fe, Co, Ni).

The anion atoms (C^{2-}) sit on a fcc lattice. The A atoms fill 1/8 of all tetraeder spaces and the B atoms fill half of all octaeder places (Fig. 3.24). Often the cations are charged A^{2+} and B^{3+}, e.g. in $ZnAl_2O_4$, $MgCr_2O_4$ or $ZnCo_2O_4$. Also A^{6+} and B^{1-} exists, e.g. in WNa_2O_4.

The cubic lattice constant is denoted as a. In real spinels, the anions deviate from the ideal fcc array which is accounted for by the parameter u, measuring the displacement of anions along the [111]-direction [221]; if the A-site cation is at (0,0,0), an anion is at (u, u, u). The cation-anion distances are given by [222]

$$R_{AC} = a\sqrt{3\,(u - 1/8)}\,, \tag{3.11a}$$

$$R_{BC} = a\sqrt{3\,u^2 - 2\,u - 3/8}\,. \tag{3.11b}$$

The ideal value is $u = 1/4$; examples are $u = 0.2624$ for $MgAl_2O_4$, $u = 0.2617$ for $ZnGa_2O_4$ and $u = 0.2409$ for $SiFe_2O_4$ [222].

In the inverted spinel structure, for $A^{II}B^{III}{}_2C^{VI}{}_4$ compounds, the cations are distributed like $B(AB)C_4$, i.e. the B cations occupy tetraeder and octaeder places, e.g. in $Mg^{2+}(Mg^{2+}Ti^{4+})O_4^{2-}$ or $Fe^{3+}(Ni^{2+}Fe^{3+})O_4^{2-}$. Examples are magnetite (Fe_3O_4), a material with high spin polarization, or $MgFe_2O_4$. Also $A^{VI}B^{II}{}_2C^{VI}{}_4$ compounds exist in this structure, e.g. SnB_2O_4 (with B = Mg, Mn, Co, Zn), TiB_2O_4 (with B = Mg, Mn, Fe, Co, Zn), and VB_2O_4 (with B = Mg, Co, Zn).

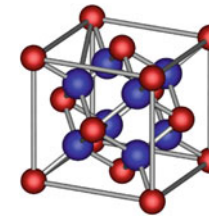

Fig. 3.25 Fluorite crystal structure, the cations are depicted as *red spheres*, the anions as *blue spheres*

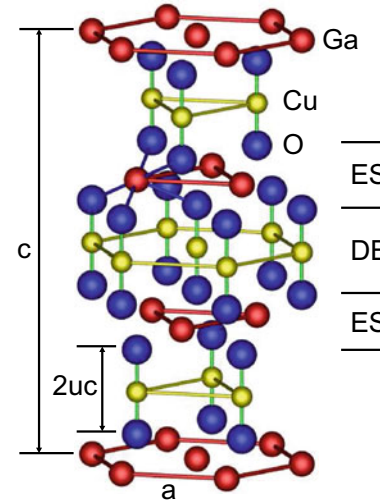

Fig. 3.26 Hexagonal unit cell of delafossite $CuGaO_2$. Oxygen atoms are bonded to the Cu in a dumbbell ('DB') configuration. In the edge-sharing ('ES') layer the Ga atoms are octahedrally configured as GaO_6

3.4.8 Fluorite Structure

Named after the minerale fluorite (CaF_2, space group 225, Fm3m), this structure for binary ionic compounds occurs when the cation valence is twice the anion valence, e.g. for (cubic) ZrO_2 (zirconia) or HfO_2. The lattice is fcc with a triatomic base. At (0,0,0) is the cation (e.g. Zr^{4+}), the anions (e.g. O^{2-}) are at $(1/4, 1/4, 1/4)\,a$ (as in the zincblende structure) and $(3/4, 3/4, 3/4)\,a$ (Fig. 3.25). The anion atom positions are on a simple cubic lattice with lattice constant $a/2$. Zirconia can crystallize in various phases [223], the most prominent being the monoclinic, tetragonal and cubic phases. The cubic phase can be extrinsically stabilized using yttrium [224, 225] (YSZ, yttria-stabilized zirconia). Hafnium oxide has the remarkable property that the HfO_2/Si interface is stable and allows the fabrication of transistor gate oxides with high dielectric constant (see Sect. 24.5.5).

3.4.9 Delafossite Structure

The I–III–O_2 materials crystallize in the trigonal delafossite ($CuFeO_2$, space group 166, $R\bar{3}m$) structure (Fig. 3.26). This structure is also called caswellsilverite ($NaCrS_2$). In Table 3.5 the lattice parameters of some delafossite compounds are given. The (Cu,Ag) (Al,Ga,In)O_2 materials are transparent conductive oxides (TCO). We note that Pt and Pd as group-I component create metal-like compounds because of the d^9 configuration as opposed to the d^{10} configuration of Cu and Ag.

3.4.10 Perovskite Structure

The perovskite structure for ABO_3 materials (calcium titanate, $CaTiO_3$, space group 62, Pnma) (Fig. 3.27) is relevant for ferroelectric semiconductors (cf. Sect. 16.3). It is cubic with the Ca (or Ba, Sr) ions (charge state 2+) on the corners of the cube, the O ions (2−) on the face centers and the Ti (4+) in the body center. The lattice is simple cubic, the base is Ca at (0,0,0), O at (1/2,1/2,0), (1/2,0,1/2) and (0,1/2,1/2) and Ti at (1/2,1/2,1/2). The ferroelectric polarization is typically evoked by a shift of the negatively and positively charged ions relative to each other. $LaAlO_3$ (lanthanium aluminate) is available as substrate material (space group 226, $Fm\bar{3}c$ [227]). Perovskites are also important for materials for high temperature superconductivity.

Another group of ABX_3 perovskites is formed by halogen atoms (Cl, Br, I) instead of oxygen on the X-site (in −1 charge state). The B-site (former Ti-position) is taken up by lead (Pb) or other elements of same +2 valence. The A-site (former Ba-position) is populated with an organic molecule (+1) such as CH_3NH_3 (methylammonium, or MA) [228] or $HC(NH_2)_2$ (formamidinium, or FA). In a purely inorganic version of such halogen perovskite, the A-site site is populated with Cs [229]. In order to avoid Pb, $CsSnX_3$ has been investigated. Various phases are observed next to the cubic phase (α-$CsPbI_3$) such as orthorhombic (δ-$CsPbBr_3$) or tetragonal [230]. Also, angular distortions of the PbX_6 octahedrons are common and depend on material composition (Fig. 3.28).

The phase stability depends on the octahedral factor $\mu = R_B/R_X$ and the tolerance factor t,

$$t = \frac{R_A + R_X}{\sqrt{2}(R_B + R_X)}\,, \tag{3.12}$$

with R_A, R_B and R_X denoting the radius of the A-site and B-site cation, and X-site anion, respectively. The stability of 138 different halide perovskites has been calculated in terms of μ and t [231] (Fig. 3.29) and stability criteria have been given. A stable cubic phase requires $0.44 < \mu < 0.9$ and $0.8 \leq t \leq 1$ [232].

Table 3.5 Lattice parameters a, c, and u of some delafossite compounds. Theoretical values are shown with asterisk. Data from [226]

	a (nm)	c (nm)	u (nm)
$CuAlO_2$	0.2858	1.6958	0.1099
$CuGaO_2$	0.2980	1.7100	0.1073*
$CuInO_2$	0.3292	1.7388	0.1056*

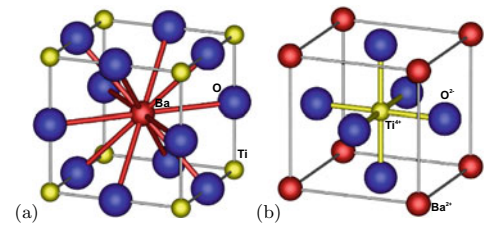

Fig. 3.27 Perovskite structure ($BaTiO_3$), **a** A cell with 12-fold (cuboctahedrally) configured Ba, **b** B cell with octahedrally configured Ti

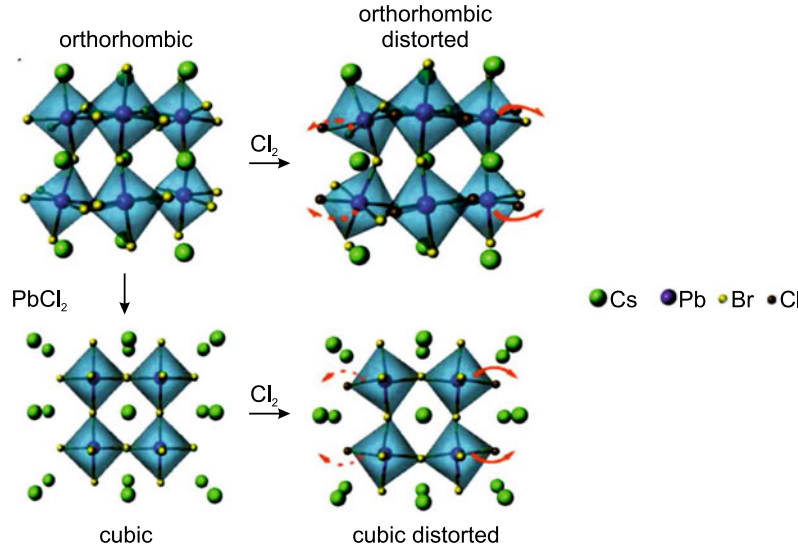

Fig. 3.28 Schematic molecular models of orthorhombic- and cubic-phase $CsPbBr_3$ perovskites with and without $PbCl_2$ and Cl_2 doping. Adapted from [232]

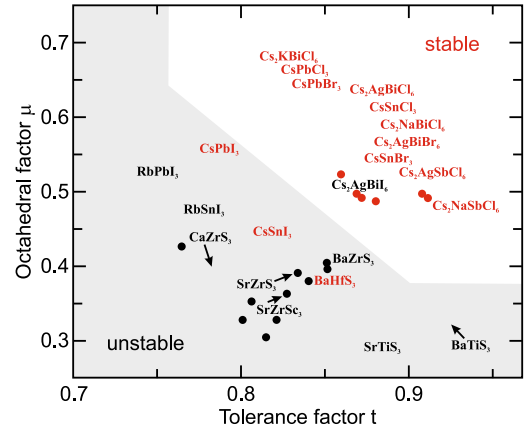

Fig. 3.29 Stability of ABX_3 halide perovskites in terms of octahedral factor μ and tolerance factor t. *Red* (*black*) dots indicate stable (unstable) compounds. The region of unstable materials is shown in *grey*. Adapted from [231]

3.4.11 NiAs Structure

The NiAs structure (space group 194, $P6_3/mmc$) (Fig. 3.30) is relevant for magnetic semiconductors, such as MnAs, and also occurs in the formation of Ni/GaAs Schottky contacts [233]. The structure is hexagonal. The arsenic atoms form a hcp structure and are trigonal prismatically configured with six nearest metal atoms. The metal atoms form hcp planes and fill all octahedral holes of the As lattice. For a cubic close packed, i.e. fcc, structure this would correspond to the rocksalt crystal. The stacking is ABACABAC... (A: Ni, B,C: As).

3.4.12 Further Structures

There are many other crystal structures that have relevance for semiconductor materials. Among them are the

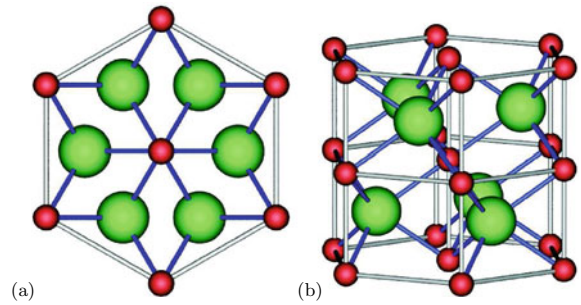

Fig. 3.30 NiAs structure, metal atoms: *dark grey*, chalcogenide atoms: *light grey*

- corundum structure (Al_2O_3, space group 167, $R\bar{3}c$) occurring, e.g., for sapphire substrates used in epitaxy or for gallium oxide α-Ga_2O_3 (Ga_2O_3 is a multiphase material [234, 235])
- bixbyite structure (In_2O_3, δ-Ga_2O_3, space group 206, $Ia\bar{3}$) (see Fig. 20.3)
- β-Ga_2O_3 monoclinic structure (space group 12, C2/m) [235]
- quartz (SiO_2) structures, α-quartz (space group 154, $P3_221$) and β-quartz (space group 180, $P6_222$)

Space does not permit to discuss these and other structures in more detail here. The reader should refer to textbooks on crystallography, e.g. [236–238], and space groups [195, 239]. A good source for information and images of crystal structures on the web is [240].

3.5 Polytypism and Polymorphism

In polytype materials, several stacking orders are possible. One of them represents the thermodynamic ground state but others have very similar energy. An example is GaN which has been extensively investigated in its (equilibrium) wurtzite and also in its (zincblende) cubic form. But not only hcp or fcc but many different sequences, such as, e.g., ACBCABAC as the smallest unit cell along the stacking direction, are possible. A typical example is SiC, for which besides hcp and fcc many other (>40) stacking sequences are known. The largest primitive unit cell of SiC [213] contains 594 layers. Some of the smaller polytypes are sketched in Fig. 3.31. In Fig. 3.32 cubic diamond crystallites and metastable hexagonal and orthorhombic phases (in silicon) are shown.

For the ternary alloy (cf. Sect. 3.7) $Zn_{1-x}Cd_xS$ the numbers n_h of diatomic layers with hexagonal stacking (AB) and n_c of layers with cubic stacking (ABC) have been investigated. CdS has wurtzite structure and ZnS mostly zincblende structure. The hexagonality index α as defined in (3.13) is shown in Fig. 3.33 for $Zn_{1-x}Cd_xS$

$$\alpha = \frac{n_h}{n_h + n_c} \,. \tag{3.13}$$

Some semiconductor materials possess several crystal phases (polymorphs) that can be readily prepared under various (non-equilibrium) conditions. Due to their different physical properties, eventually they can be employed for different device applications. GaN with its hexagonal and cubic phases can be counted as such material. A prominent example of a multi-phase semiconductor is Ga_2O_3 that exhibits, next to its monoclinic equilibrium structure, various other phases such as a rhombohedral (corundum, α-Ga_2O_3) and an orthorhombic (κ-Ga_2O_3) phase [244].

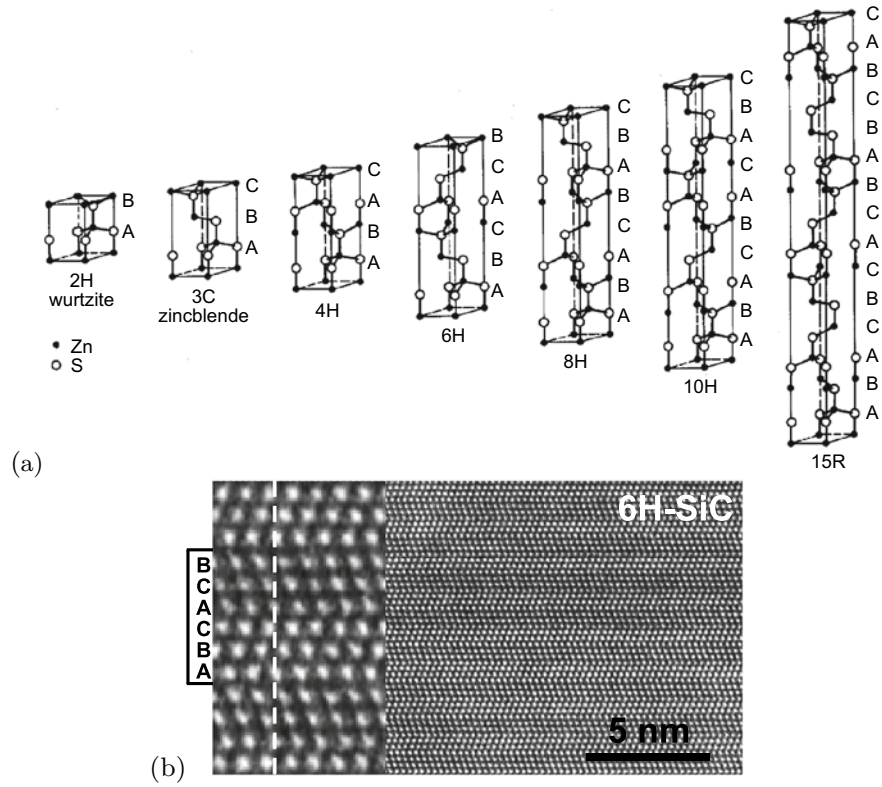

Fig. 3.31 **a** Polytypes of the zincblende and wurtzite lattice (found in SiC), the letters A, B and C denote the three possible positions of the diatomic layers (see Fig. 3.7). **b** High resolution TEM image of 6H-SiC. For the enlarged view on the left, the unit cell and the stacking sequence are indicated. Adapted from [241]

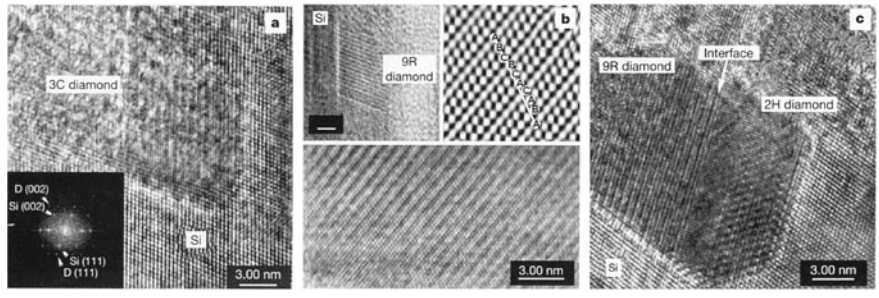

Fig. 3.32 Polytypes of diamond found in crystallites (metastable phases in silicon). **a** cubic type (3C) with stacking ABC, *inset* shows a diffractogram and the alignment of the C and Si lattice, **b** rhombohedral 9R crystallite with ABCBCACABA stacking, **c** 9R phase with interface to a hexagonal 2H (AB stacking) phase. Reprinted from [242] with permission, ©2001, Springer Nature

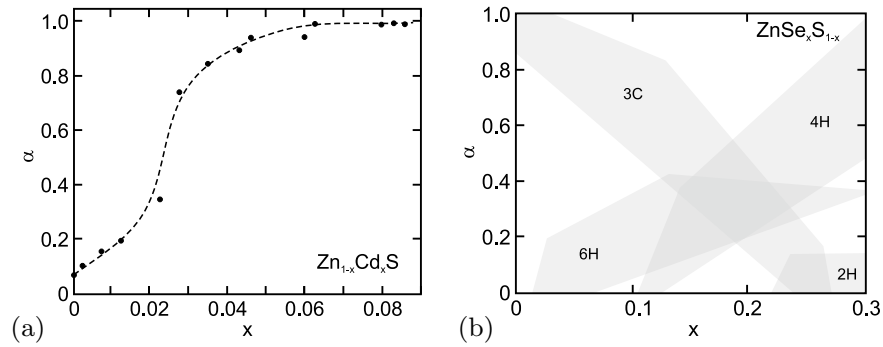

Fig. 3.33 **a** Hexagonality index α (3.13) of $Zn_{1-x}Cd_xS$ for various ternary compositions. *Dashed line* is a guide to the eye. **b** Regions of different polytypes in $ZnSe_xS_{1-x}$. Adapted from [243]

3.6 Reciprocal Lattice

The reciprocal lattice is of utmost importance for the description and investigation of periodic structures, in particular for X-ray diffraction [245], surface electron diffraction, phonon dispersion or scattering and the electronic band structure. It is the quasi-Fourier transformation of the crystal lattice. The crystal lattice is also called the *direct* lattice, in order to distinguish it from the *reciprocal* lattice.

3.6.1 Reciprocal Lattice Vectors

When $\mathcal{R}$ denotes the set of vectors of the direct lattice, the set $\mathcal{G}$ of the reciprocal lattice vectors is given by the condition[6]

$$\exp(\mathrm{i}\,\mathbf{G}\cdot\mathbf{R}) = 1 \tag{3.14}$$

for all $\mathbf{R} \in \mathcal{R}$ and $\mathbf{G} \in \mathcal{G}$. Therefore, for all vectors $\mathbf{r}$ and a reciprocal lattice vector $\mathbf{G}$

$$\exp(\mathrm{i}\,\mathbf{G}\cdot(\mathbf{r}+\mathbf{R})) = \exp(\mathrm{i}\,\mathbf{G}\cdot\mathbf{r}) \ . \tag{3.15}$$

Each Bravais lattice has a certain reciprocal lattice. The reciprocal lattice is also a Bravais lattice, since when $\mathbf{G}_1$ and $\mathbf{G}_2$ are two reciprocal lattice vectors, then this is obviously true also for $\mathbf{G}_1 + \mathbf{G}_2$. For the primitive translation vectors $\mathbf{a}_1$, $\mathbf{a}_2$ and $\mathbf{a}_3$ of the direct lattice, the vectors $\mathbf{b}_1$, $\mathbf{b}_2$ and $\mathbf{b}_3$ that span the reciprocal lattice are given directly for any lattice as

$$\mathbf{b}_1 = \frac{2\pi}{V_a}(\mathbf{a}_2 \times \mathbf{a}_3) \tag{3.16a}$$

$$\mathbf{b}_2 = \frac{2\pi}{V_a}(\mathbf{a}_3 \times \mathbf{a}_1) \tag{3.16b}$$

$$\mathbf{b}_3 = \frac{2\pi}{V_a}(\mathbf{a}_1 \times \mathbf{a}_2) \ , \tag{3.16c}$$

where $V_a = \mathbf{a}_1 \cdot (\mathbf{a}_2 \times \mathbf{a}_3)$ is the volume of the unit cell spanned by the vectors $\mathbf{a}_i$. The volume of the unit cell in reciprocal space is $V_a^* = (2\pi)^3 / V_a$.

[6] The dot product $\mathbf{a} \cdot \mathbf{b}$ of two vectors shall also be denoted as $\mathbf{ab}$.

The vectors $\mathbf{b}_i$ fulfill the conditions

$$\mathbf{a}_i \cdot \mathbf{b}_j = 2\pi\, \delta_{ij} \ . \tag{3.17}$$

Thus, it is clear that (3.14) is fulfilled. For an arbitrary reciprocal lattice vector $\mathbf{G} = k_1\mathbf{b}_1 + k_2\mathbf{b}_2 + k_3\mathbf{b}_3$ and a vector $\mathbf{R} = n_1\mathbf{a}_1 + n_2\mathbf{a}_2 + n_3\mathbf{a}_3$ in direct space we find

$$\mathbf{G} \cdot \mathbf{R} = 2\pi\ (n_1 k_1 + n_2 k_2 + n_3 k_3) \ . \tag{3.18}$$

The number in brackets is an integer. Additionally, we note that the reciprocal lattice of the reciprocal lattice is again the direct lattice. The reciprocal lattice of the fcc is bcc and vice versa. The reciprocal lattice of hcp is hcp (rotated by 30° with respect to the direct lattice).

For later, we note two important theorems. A (sufficiently well behaved) function $f(\mathbf{r})$ that is periodic with the lattice, i.e. $f(\mathbf{r}) = f(\mathbf{r}+\mathbf{R})$ can be expanded into a Fourier series with the reciprocal lattice vectors according to

$$f(\mathbf{r}) = \sum a_{\mathbf{G}}\ \exp(\mathrm{i}\,\mathbf{G}\cdot\mathbf{r}) \ , \tag{3.19}$$

where $a_{\mathbf{G}}$ denotes the Fourier component of the reciprocal lattice vector $\mathbf{G}$, $a_{\mathbf{G}} = \int_V f(\mathbf{r}) \exp(-\mathrm{i}\,\mathbf{G}\cdot\mathbf{r})\ \mathrm{d}^3\mathbf{r}$. If $f(\mathbf{r})$ is lattice periodic, the integral given in (3.20) is zero unless $\mathbf{G}$ is a reciprocal lattice vector.

$$\int_V f(\mathbf{r})\ \exp(-\mathrm{i}\,\mathbf{G}\cdot\mathbf{r})\ \mathrm{d}^3\mathbf{r} = \begin{cases} a_{\mathbf{G}} \\ 0, \mathbf{G} \notin \mathcal{G} \end{cases} \ . \tag{3.20}$$

3.6.2 Miller Indices

The Miller indices [246] form a triplet of integer numbers to denote directions and lattice planes in the crystal. A vector $\mathbf{R}$ in direct space is denoted with its components h, k, and l relative to the lattice vectors $\mathbf{a}_i$, i.e. $h = \mathbf{a}_1 \cdot \mathbf{R}$ and so forth. In order to arrive at the set of smallest possible integer numbers, the values possibly must be divided by a suitable fraction. Directions are denoted in square brackets $[hkl]$, and go into the direction of $h\mathbf{a_1} + k\mathbf{a_2} + l\mathbf{a_3}$. A set of crystallographically equivalent directions is denoted with $\langle hkl \rangle$. For negative indices, $[-1\,00]$ can also be written with a bar, $[\bar{1}00]$.

A lattice plane is the set of all lattice points in a plane spanned by two independent lattice vectors $\mathbf{R_1}$ and $\mathbf{R_2}$. Lattice planes are denoted as (hkl) with parentheses; a set of equivalent planes is denoted with curly brackets as $\{hkl\}$. The lattice points on that plane form a two-dimensional Bravais lattice. The entire lattice can be generated by shifting the lattice plane along its normal $\mathbf{n} = (\mathbf{R_1} \times \mathbf{R_2})/|\mathbf{R_1} \times \mathbf{R_2}|$. The plane belongs to the reciprocal lattice vector $\mathbf{G_n} = 2\pi\mathbf{n}/d$, d being the distance between planes.

This correspondence between reciprocal lattice vectors and sets of planes allows the orientation of planes to be described in a simple manner. The shortest reciprocal lattice vector perpendicular to the plane is used. The coordinates with respect to the primitive translation vectors of the reciprocal space $\mathbf{b}_i$ form a triplet of integer numbers and are called Miller indices of the plane, i.e. $\mathbf{G_n} = h\,\mathbf{b}_1 + k\,\mathbf{b}_2 + l\,\mathbf{b}_3$.

The plane described by $\mathbf{G_n}\cdot\mathbf{r} = A$ fulfills the condition for a suitable value of A. The plane intersects the axes $\mathbf{a}_i$ at the points $x_1\,\mathbf{a}_1$, $x_2\,\mathbf{a}_2$ and $x_3\,\mathbf{a}_3$. Thus we find $\mathbf{G_n}\, x_i\, \mathbf{a}_i = A$ for all i. From (3.18) follows $\mathbf{G_n} \cdot \mathbf{a}_1 = 2\pi\, h$, $\mathbf{G_n} \cdot \mathbf{a}_2 = 2\pi\, k$ and $\mathbf{G_n} \cdot \mathbf{a}_3 = 2\pi\, l$, where h, k and l are integers. The Miller indices (hkl) are thus proportional to the reciprocal values $1/x_i$ of the axis intersections of the plane with the lattice vectors of the direct lattice. An example is shown in Fig. 3.34.

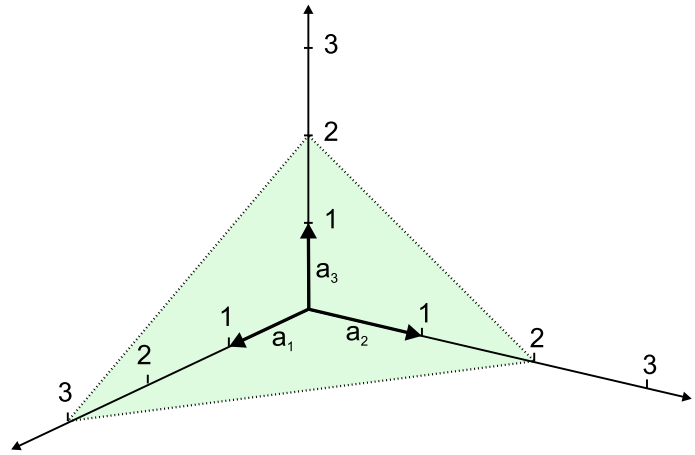

Fig. 3.34 The plane intersects the axes at 3, 2, and 2. The inverse of these numbers is 1/3, 1/2, and 1/2. The smallest integer numbers of this ratio form the Miller indices (233)

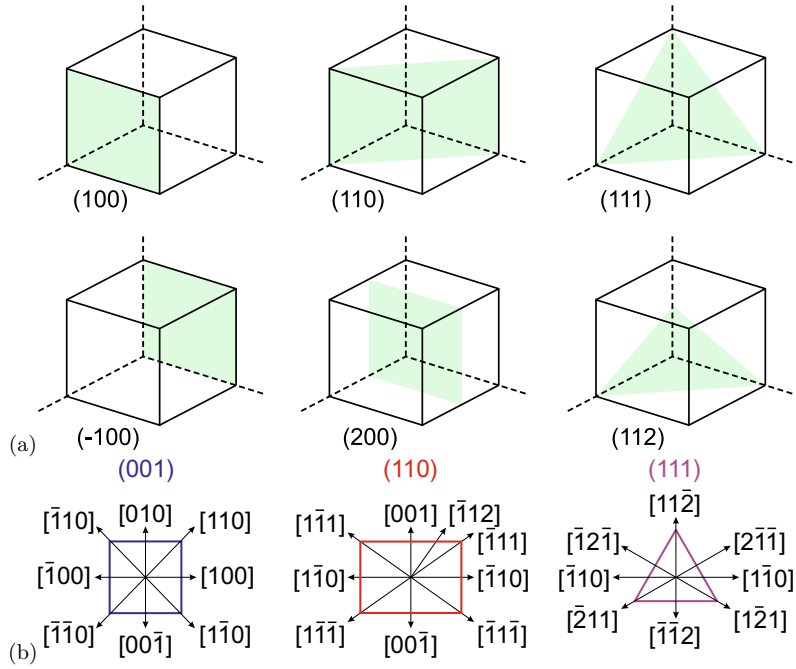

Fig. 3.35 **a** Miller indices of important planes for the simple cubic (and fcc, bcc) lattice. (**b**) Directions within three low index planes of cubic crystals

In a cubic lattice, the faces of the cubic unit cell are {001} and the planes perpendicular to the area (body) diagonals are {110} ({111}) (Fig. 3.35a). For example, in the simple cubic lattice (100), (010), (001), (−1 00), (0−1 0) are (00−1) equivalent and are denoted by {100}.

In the zincblende lattice, the {111} planes consist of diatomic planes with Zn and S atoms. It depends on the direction whether the metal or the nonmetal is on top. These two cases are denoted by A and B. We follow the convention that the (111) plane is (111)A and the metal is on top (as in Fig. 3.16b). For each change of sign the type changes from A to B and vice versa, e.g. (111)A, (1$\bar{1}$ 1)B and ($\bar{1}$ $\bar{1}$ $\bar{1}$)B. In Fig. 3.35b the in-plane directions for the (001), (110) and (111) planes are visualized.

We note that for orthogonal lattices, the (outward) normal direction of a plane (*hkl*) is the same direction as [*hkl*]. Caveat: in non-rectangular lattices this is not the case! This can be easily seen for a monoclinic lattice, depicted as example in Fig. 3.36.

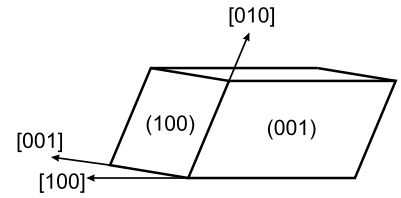

Fig. 3.36 Sketch of lattice directions and planes in a monoclinic lattice. The [100] direction and the normal of the (100) plane are not parallel

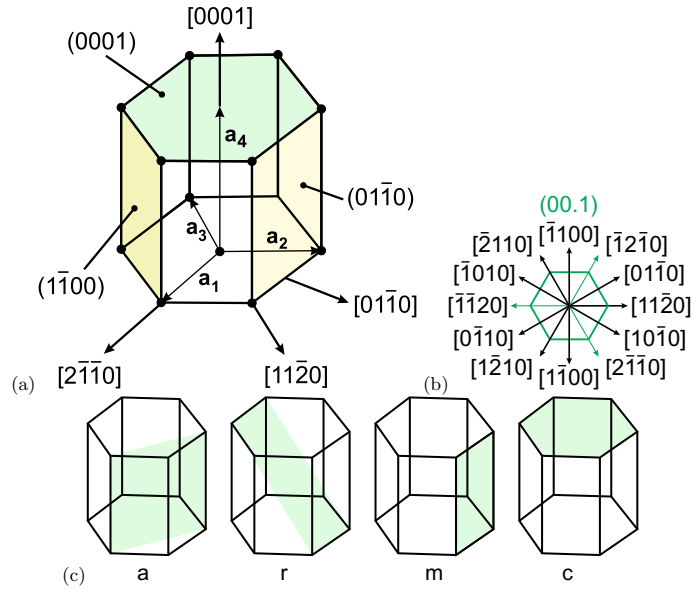

Fig. 3.37 (**a**, **b**) Miller indices for the wurtzite (or hcp) structure. (**c**) Orientation of the a-, r-, m-, and c-plane in the wurtzite structure

In the wurtzite lattice, the Miller indices are denoted as $[hklm]$ (Fig. 3.37). Within the (0001) plane three indices hkl are used that are related to the three vectors $\mathbf{a}_1$, $\mathbf{a}_2$ and $\mathbf{a}_3$ (see Fig. 3.37a) rotated with respect to each other by 120°. Of course, the four indices are not independent and $l = -(h + k)$. The third (redundant) index can be denoted as a dot. The c-axis [0001] is then denoted as [00.1]. Wurtzite (and trigonal, e.g. sapphire) substrates are available typically with (polished) a (11.0), m (01.0) and r (01.2), c (00.1) surfaces (Fig. 3.37b).

The distance of lattice planes $d = 2\pi/|\mathbf{G}|$ can be expressed via the Miller indices for cubic (3.21a), tetragonal (3.21b) and hexagonal (3.21c) crystals as

$$d^{\mathrm{c}}_{hkl} = \frac{a}{\sqrt{h^2 + k^2 + l^2}} \tag{3.21a}$$

$$d^{\mathrm{t}}_{hkl} = \frac{a}{\sqrt{h^2 + k^2 + l^2\,(a/c)^2}} \tag{3.21b}$$

$$d^{\mathrm{h}}_{hkl} = \frac{a}{\sqrt{4\,(h^2 + hk + k^2)/3 + l^2\,(a/c)^2}} \tag{3.21c}$$

Useful formulas for the angle θ between a $[hk.l]$-plane and the [00.1]-direction in the cubic, tetragonal and wurtzite structures are:

$$\cos\theta^{\mathrm{c}} = \frac{l}{\sqrt{h^2 + k^2 + l^2}} \tag{3.22a}$$

Table 3.6 High symmetry points and directions from Γ-point in the Brillouin zone of the fcc lattice

Point	$\mathbf{k}$ $(\frac{2\pi}{a})$	Direction	Multiplicity
Γ	(0, 0, 0)		1
X	(0, 1, 0)	Δ	6
K	3/4 (1, 1, 0)	Σ	12
L	1/2 (1, 1, 1)	Λ	8
W	(1, 1/2, 0)		24
U	(1, 1/4, 1/4)		24

Table 3.7 High symmetry points and directions from Γ-point in the Brillouin zone of the hcp lattice

Point	$\mathbf{k}$ (2π)	Direction	Multiplicity
Γ	(0, 0, 0)		1
A	$(0, 0, \frac{1}{2c})$	Δ	2
L	$(0, \frac{1}{\sqrt{3}a}, \frac{1}{2c})$		12
M	$(0, \frac{1}{\sqrt{3}a}, 0)$	Σ	6
H	$(-\frac{1}{3a}, \frac{1}{\sqrt{3}a}, \frac{1}{2c})$		12
K	$(-\frac{1}{3a}, \frac{1}{\sqrt{3}a}, 0)$	T	6

$$\cos\theta^{\mathrm{t}} = \frac{l}{\sqrt{l^2 + \frac{c^2}{a^2}(h^2 + k^2)}} \tag{3.22b}$$

$$\cos\theta^{\mathrm{h}} = \frac{l}{\sqrt{l^2 + \frac{4}{3}\frac{c^2}{a^2}(h^2 + h\,k + k^2)}}\,. \tag{3.22c}$$

3.6.3 Brillouin Zone

The Wigner–Seitz cell in reciprocal space is called the (first) Brillouin zone. In Fig. 3.38, the Brillouin zones for the most important lattices are shown. High symmetry points in the Brillouin zone are labeled with dedicated letters. The Γ point always denotes $\mathbf{k} = 0$ (zone center). High symmetry paths in the Brillouin zone are labeled with dedicated Greek symbols.

In the Brillouin zone of the fcc lattice (Si, Ge, GaAs, ...) the X point denotes the point at the zone boundary in ⟨001⟩-directions (at distance $2\,\pi/a$ from Γ), K for ⟨110⟩-directions (at distance $3\,\pi/\sqrt{2}\,a$ from Γ) and L for the ⟨111⟩-directions (at distance $\sqrt{3}\,\pi/a$ from Γ) (see Table 3.6). The straight paths from Γ to X, K, and L are denoted as Δ, Σ, and Λ, respectively. High symmetry points and directions of the Brillouin zone of the hcp lattice are given in Table 3.7.

3.7 Alloys

When different semiconductors are mixed various cases can occur:

- The semiconductors are not miscible and have a so-called miscibility gap. They will tend to form clusters that build up the crystal. The formation of defects is probable.

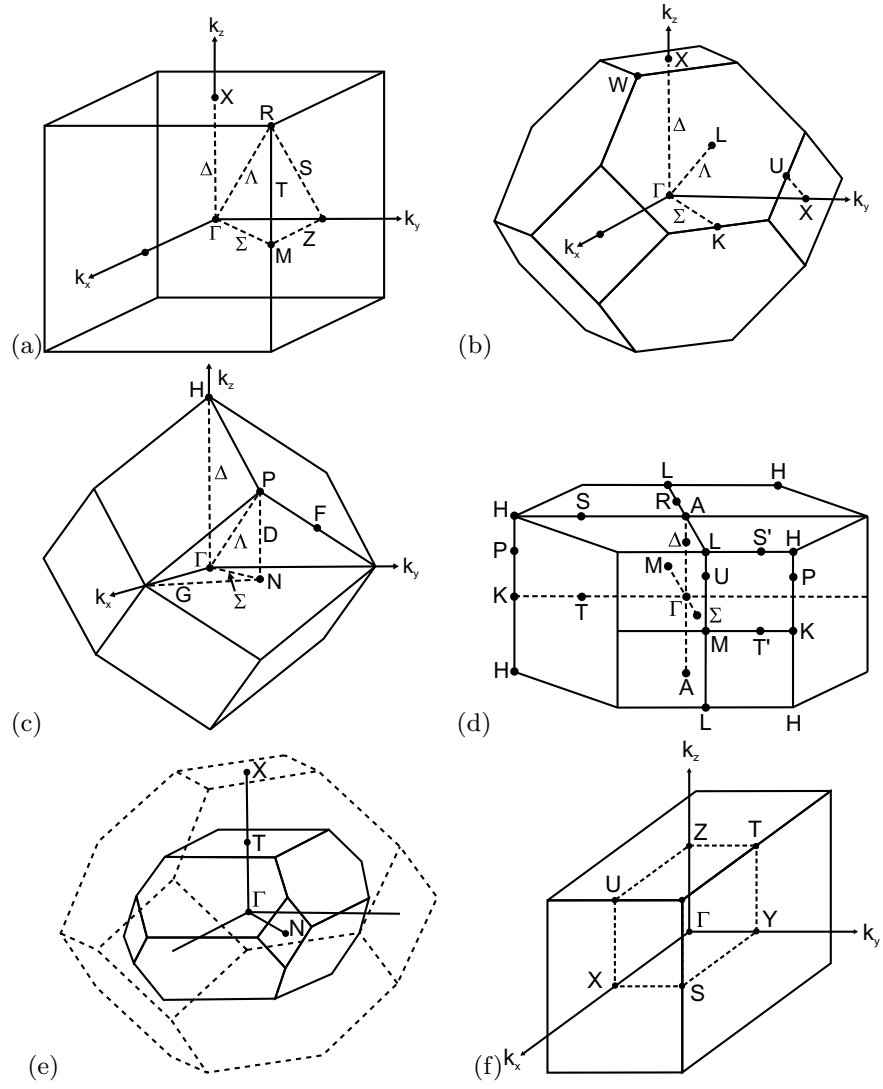

Fig. 3.38 Brillouin zones and special **k** points for the **a** primitive cubic (pc), (**b**) fcc, **c** bcc, and **d** hcp lattice. **e** Brillouin zone for chalcopyrite structure with fcc Brillouin zone shown as *dashed outline* **f** Brillouin zone for orthorhombic lattice with one quadrant shown with *dashed lines*

- They form an ordered (periodic) structure that is called a superlattice.
- They form a random alloy.

3.7.1 Random Alloys

Alloys for which the probability to find an atom at a given lattice site is given by the fraction of these atoms (i.e. the stoichiometry), independent of the surrounding, are called *random* alloys. Deviations from the random population of sites is termed *clustering*.

For a Ge_xSi_{1-x} alloy this means that any given atom site has the probability x to have a Ge atom and $1-x$ to have a Si atom. The probability p_n that a Si atom has n next-neighbor Ge atoms is

$$p_n = \binom{4}{n} x^n \, (1-x)^{4-n} \, , \tag{3.23}$$

and is depicted in Fig. 3.39 as a function of the alloy composition. The symmetry of the Si atom is listed in Table 3.8. If it is surrounded by four of the same atoms (either Ge or Si), the symmetry is T_d. If one atom is different from the other three next neighbors, the symmetry is reduced to C_{3v} since one bond is singled out. For two atoms each the symmetry is lowest (C_{2v}).

In an alloy from binary compound semiconductors such as $Al_xGa_{1-x}As$ the mixing of the Al and Ga metal atoms occurs only on the metal (fcc) sublattice. Each As atom is bonded to four metal atoms. The probability that it is surrounded by n Al atoms is given by (3.23). The local symmetry of the As atom is also given by Table 3.8. For $AlAs_xP_{1-x}$ the mixing occurs on the nonmetal (anion) sublattice. If the alloy contains three atom species it is called a *ternary* alloy. In Fig. 3.40 the $(1\bar{1}0)$ surface (UHV cleave) of an $In_{0.05}Ga_{0.95}As$ alloy is shown. Indium atoms in the first layer show up as brighter round dots [247]. Along the [001]-direction the positions are uncorrelated, along [110] an anti-correlation is

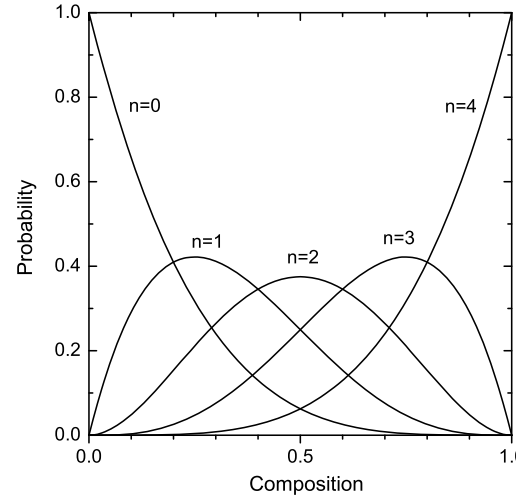

Fig. 3.39 Probability that a Si atom has n next-neighbor Ge atoms in a random Ge_xSi_{1-x} alloy

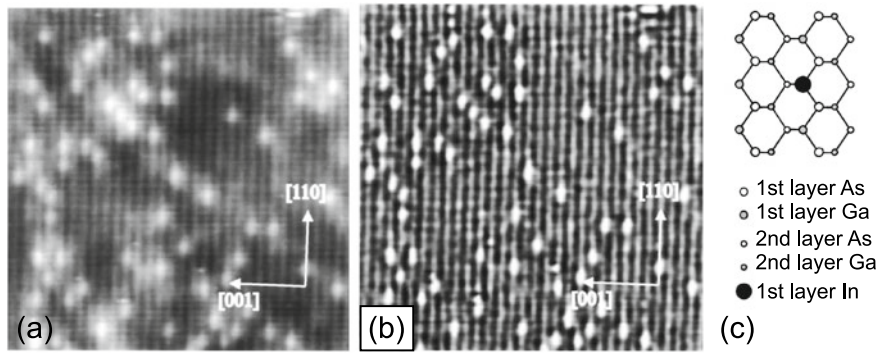

Fig. 3.40 **a** STM empty-state image ($17.5 \times 17.5\,nm^2$) of the $(1\bar{1}0)$ surface of an MBE-grown $In_{0.05}Ga_{0.95}As$ alloy on GaAs, **b** curvature-enhanced image. **c** Schematic atomic arrangement of the first and second atomic layer. Adapted from [248]

Table 3.8 Probability p_n (3.23) and symmetry of an A atom being surrounded by n B atoms in a tetrahedrally configured B_xA_{1-x} random alloy

n	p_n	Symmetry
0	x^4	T_d
1	$4\,x^3\,(1-x)$	C_{3v}
2	$6\,x^2\,(1-x)^2$	C_{2v}
3	$4\,x\,(1-x)^3$	C_{3v}
4	$(1-x)^4$	T_d

found, corresponding to an effective repulsive pair interaction energy of 0.1 eV for the nearest neighbor In–In pairs along the [110]-direction due to strain effects [248].

If the binary end components have different crystal structure, the alloy shows a transition (or compositional transition range) from one structure to the other at a particular concentration. An example is the alloy between wurtzite ZnO and rocksalt MgO. $Mg_xZn_{1-x}O$ alloy thin films exhibits wurtzite structure up to about $x = 0.5$ and rocksalt structure for $x > 0.6$ [249] (cmp. Fig. 3.43).

If the alloy contains four atom species it is called *quaternary*. A quaternary zincblende alloy can have the mixing of three atom species on one sublattice, such as $Al_xGa_yIn_{1-x-y}As$ or $GaAs_xP_ySb_{1-x-y}$ or the mixing of two atom species on both of the two sublattices, such as $In_xGa_{1-x}As_yN_{1-y}$.

The random placement of different atoms on the (sub)lattice in an alloy represents a perturbation of the ideal lattice and causes additional scattering (alloy scattering). In the context of cluster formation, the probability of an atom having a direct neighbor of the same kind on its sublattice is important. Given a $A_xB_{1-x}C$ alloy, the probability p_S to find a single A atom surrounded by B atoms is given by (3.24a). The probability p_{D^1} to find a cluster of two neighbored A atoms surrounded by B atoms is given by (3.24b).

$$p_S = (1-x)^{12} \tag{3.24a}$$

$$p_{D^1} = 12\,x\,(1-x)^{18}\ . \tag{3.24b}$$

These formulas are valid for fcc and hcp lattices. For larger clusters [250, 251], probabilities in fcc and hcp structures differ.

3.7.2 Phase Diagram

The mixture A_xB_{1-x} with average composition x between two materials A and B can result in a single phase (alloy), a two-phase system (phase separation) or a metastable system. The molar free enthalpy ΔG of the mixed system is approximated by

$$\Delta G = \Omega\,x\,(1-x) + kT\ [x\ \ln(x) + (1-x)\ \ln(1-x)]\ . \tag{3.25}$$

The first term on the right-hand side of (3.25) is the (regular solution) enthalpy of mixing with the interaction parameter Ω, which can depend on x. The second term is the ideal configurational entropy based on a random distribution of the atoms. The function is shown for various ratios of kT/Ω in Fig. 3.41a. In an equilibrium phase diagram (see Fig. 3.41b) the system is above the binodal curve in one phase (miscible). On the binodal line $T_b(x)$ in the (x, T) diagram the A- and B-rich disordered phases have equal chemical potentials, i.e. $\partial G/\partial x = 0$. For Ω independent of x the temperature T_b

is given by (3.26a). A critical point is at the maximum temperature T_{mg} and concentration x_{mg} of the miscibility gap. For Ω independent of x it is given by $T_{\mathrm{mg}} = \Omega/2$ and $x_{\mathrm{mg}} = 1/2$. In the region below the spinodal boundary, the system is immiscible and phases immediately segregate (by spinodal decomposition). On the spinodal line $T_{\mathrm{sp}}(x)$ the condition $\partial^2 G/\partial x^2 = 0$ is fulfilled. For Ω independent of x the temperature T_{sp} is given by (3.26b). The region between the binodal and spinodal curves is the metastable region, i.e. the system is stable to small fluctuations of concentration or temperature but not for larger ones.

$$kT_{\mathrm{b}}(x) = \Omega \frac{2x-1}{\ln(x) - \ln(1-x)} \tag{3.26a}$$

$$kT_{\mathrm{sp}}(x) = 2\Omega\, x\,(1-x)\ . \tag{3.26b}$$

In Fig. 3.42 calculated diagrams for GaAs-AlAs and GaAs-GaP [252] are shown. The arrows denote the critical point. These parameters and the interaction parameters for a number of ternary alloys are given in Table 3.9. For example, for $Al_xGa_{1-x}As$ complete miscibility is possible for typical growth temperatures (> 700 K), but for $In_xGa_{1-x}N$ the In solubility at a typical growth temperature of 1100 K is only 6% [253].

The alloy system (Al,Ga,In)(As,P,Sb) always crystallizes in the zincblende structure and (Al,Ga,In)N always in the wurtzite structure. If the binary end components of a ternary alloy have a *different* crystal structure things become more complicated and the crystal phase has to be determined experimentally (and modelled) for each composition. As an example the energy of the wurtzite, hexagonal and rocksalt

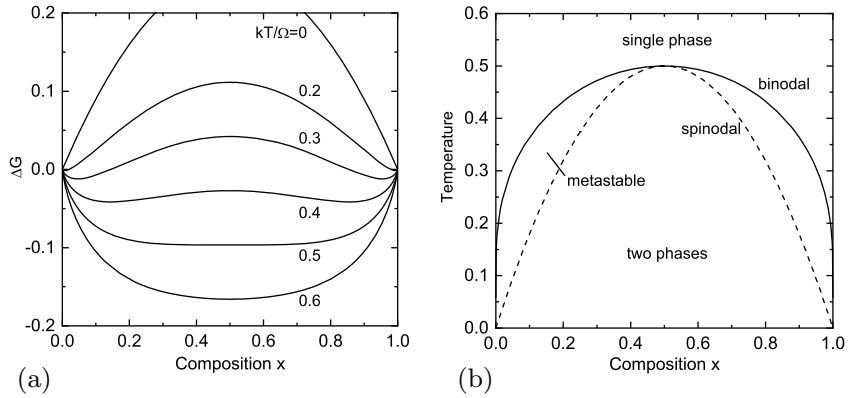

Fig. 3.41 **a** Free enthalpy ΔG of mixed binary system (3.25) in units of Ω for Ω =const. and various values of kT/Ω as labeled. **b** Schematic phase diagram for binary mixture. The temperature is given in units of Ω/k. The *solid* (*dashed*) line denotes the binodal (spinodal) line

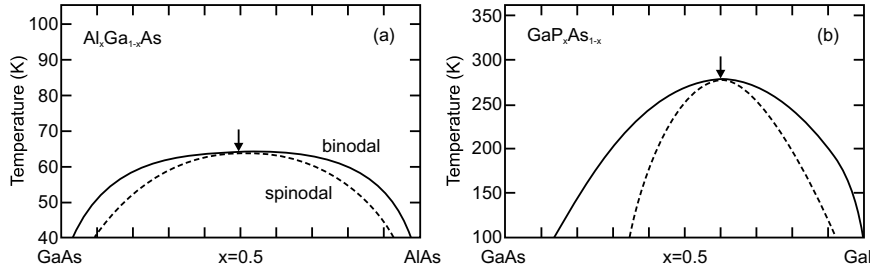

Fig. 3.42 Calculated phase diagrams for **a** $Al_xGa_{1-x}As$ and **b** GaP_xAs_{1-x}. The binodal (spinodal) curve is shown as *solid* (*dashed*) line. Adapted from [252]

Table 3.9 Calculated interaction parameter $\Omega(x)$ (at $T = 800$ K, 1 kcal/mol= 43.39 meV), miscibility-gap temperature T_{mg} and concentration x_{mg} for various ternary alloys. Data for (In,Ga)N from [253], other data from [252]

Alloy	T_{mg} (K)	x_{mg}	$\Omega(0)$ (kcal/mol)	$\Omega(0.5)$ (kcal/mol)	$\Omega(1)$ (kcal/mol)
$Al_xGa_{1-x}As$	64	0.51	0.30	0.30	0.30
GaP_xAs_{1-x}	277	0.603	0.53	0.86	1.07
$Ga_xIn_{1-x}P$	961	0.676	2.92	3.07	4.60
$GaSb_xAs_{1-x}$	1080	0.405	4.51	3.96	3.78
$Hg_xCd_{1-x}Te$	84	0.40	0.45	0.80	0.31
$Zn_xHg_{1-x}Te$	455	0.56	2.13	1.88	2.15
$Zn_xCd_{1-x}As$	605	0.623	2.24	2.29	2.87
$In_xGa_{1-x}N$	1505	0.50	6.32	5.98	5.63

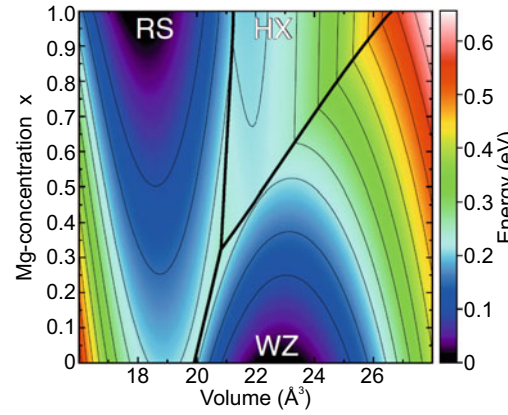

Fig. 3.43 Calculated energy vs. volume of the formula unit for $Mg_xZn_{1-x}O$ in the wurtzite (WZ), hexagonal (HX) and rocksalt phase (RS). The separations between the three phase are denoted by *straight bold lines*. Adapted from [254]

structure of $Mg_xZn_{1-x}O$ has been calculated [254] as depicted in Fig. 3.43 (cmp. Fig. 2.4 for silicon). The transition between wurtzite and rocksalt structure is predicted for $x = 0.33$.

3.7.3 Virtual Crystal Approximation

In the *virtual crystal approximation* (VCA) the disordered alloy AB_xC_{1-x} is replaced by an ordered binary compound AD with D being a 'pseudoatom' with properties that are configuration averaged over the properties of the B and C atoms, e.g. their masses or charges. Such an average is weighted with the ternary composition, e.g. the mass is $M_D = xM_B + (1-x)M_C$. For example, the A–D force constant would be taken as the weighted average over the A–B and A–C force constants.

3.7.4 Lattice Parameter

In the VCA for an alloy a new sort of effective atom is assumed that has an averaged bond length that depends linearly on the composition. Typically, Vegard's law (3.27), which predicts that the lattice constant of a ternary alloy $A_xB_{1-x}C$ depends linearly on the lattice constants of the binary alloys AC

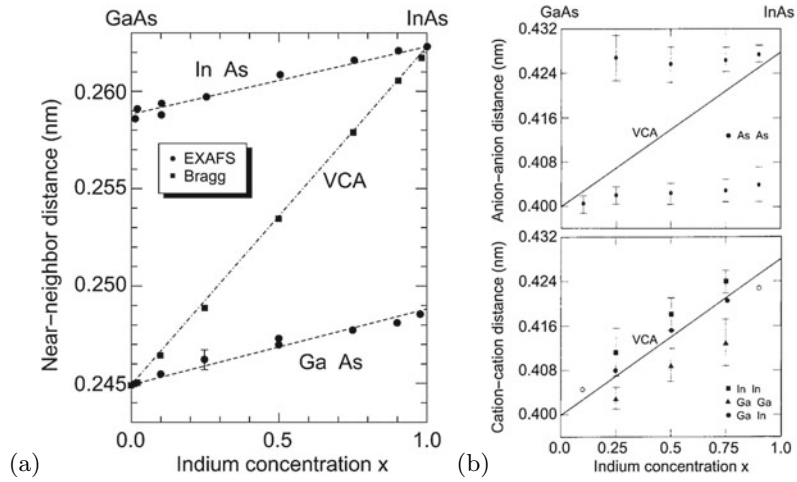

Fig. 3.44 **a** Near-neighbor distance ($\sqrt{3}\,a_0/4$) of $In_xGa_{1-x}As$ as measured by standard X-ray diffraction (Bragg reflection, *solid squares*) and VCA approximation (*dash-dotted line*). Near-neighbor Ga–As and In–As distances as determined by EXAFS (extended X-ray absorption fine structure, *solid squares*). *Dashed lines* are guides to the eye. Data from [255]. **b** Second-neighbor distances for $In_xGa_{1-x}As$ as determined from EXAFS, *top*: anion–anion distance (for As–As), *bottom*: cation–cation distance (for In–In, Ga–Ga, and Ga–In). *Solid lines* in both plots are the VCA ($a_0/\sqrt{2}$). Data from [256]

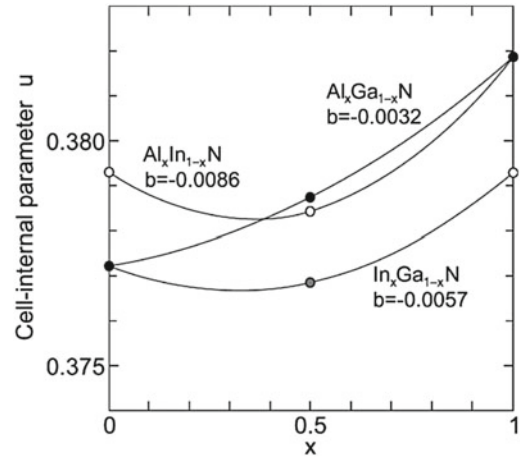

Fig. 3.45 Theoretical values ($T = 0\,K$) for the cell-internal parameter u as a function of the composition for group-III nitride alloys. The *solid lines* are quadratic curves (bowing parameter b is shown) through the points for $x = 0$, 0.5, and 1.0. Data from [257]

and BC, is indeed fulfilled

$$a_0(A_xB_{1-x}C) = a_0(BC) + x\,[a_0(AC) - a_0(BC)]\,. \tag{3.27}$$

In reality, the bond length of the AC and BC bonds changes rather little (Fig. 3.44a) such that the atoms in the alloy suffer a displacement from their average position and the lattice is deformed on the nanoscopic scale. In a lattice of the type $In_xGa_{1-x}As$ the anions suffer the largest displacement since their position adjusts to the local cation environment. For $In_xGa_{1-x}As$ a bimodal distribution, according to the As–Ga–As and As–In–As configurations, is observed (Fig. 3.44b). The cation–cation second-neighbor distances are fairly close to the VCA.

While the average lattice parameter in alloys changes linearly with composition, the cell-internal parameter u (for wurtzite structures, see Sect. 3.4.5) exhibits a nonlinear behavior as shown in Fig. 3.45.

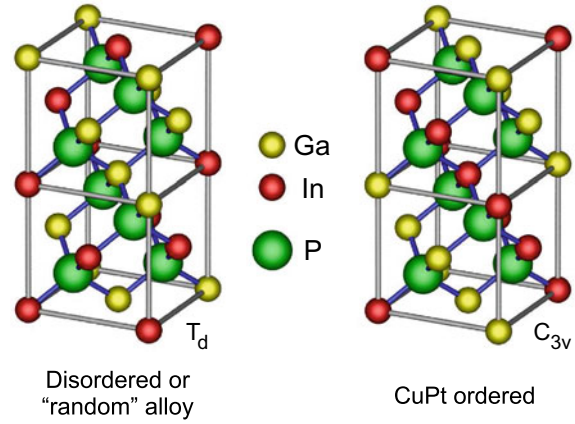

Fig. 3.46 CuPt-ordered ternary alloy $In_{0.5}Ga_{0.5}P$; the lattice symmetry is reduced from T_d to C_{3v}

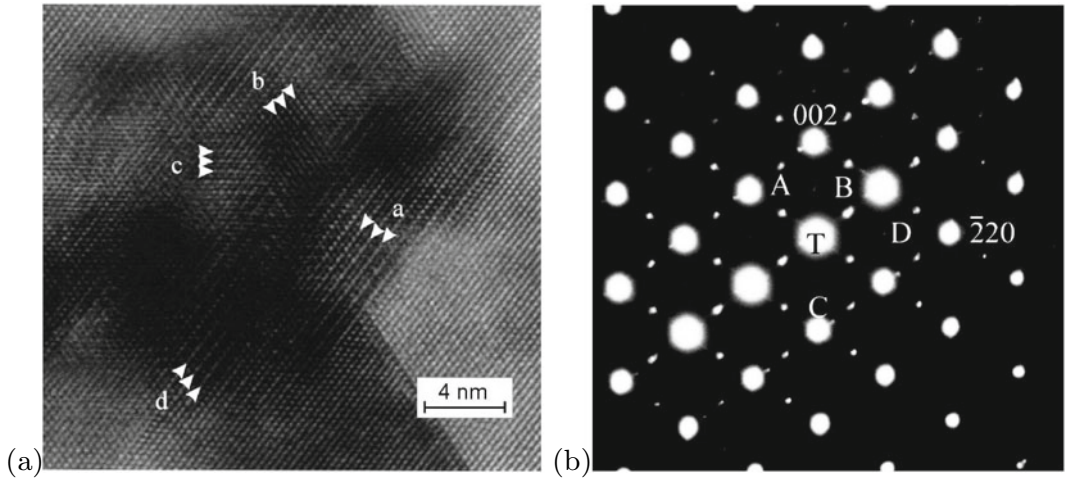

Fig. 3.47 (**a**) Cross-sectional transmission electron microscope image along the [110] zone axis of a $Cd_{0.68}Zn_{0.32}Te$ epilayer on GaAs showing ordered domains having a doublet periodicity on the {111} and {001} lattice planes. Two different {111} variants are labeled ‘a’ and ‘b’. The doublet periodicity in the [001] is seen in the ‘c’ region. (**b**) Selected-area diffraction pattern along the [110] zone. Strong peaks are fundamental peaks of the zincblende crystal, weak peaks are due to CuPt ordering, labeled A and B, and CuAu-I ordering, labeled C and D. The latter are the weakest due to a small volume fraction of CuAu-ordered domains. Adapted from [259]

Therefore physical properties connected to u, such as the spontaneous polarization, will exhibit a bowing.

3.7.5 Ordering

Some alloys have the tendency for the formation of a superstructure [258]. Growth kinetics at the surface can lead to specific adatom incorporation leading to ordering. For example, in $In_{0.5}Ga_{0.5}P$ the In and Ga atoms can be ordered in subsequent (111) planes (CuPt structure) instead of being randomly mixed (Fig. 3.46). This impacts fundamental properties such as the phonon spectrum or the band gap. CuPt ordering on (111) and $(\bar{1}\bar{1}1)$ planes is called $CuPt_A$, on $(\bar{1}11)$ and $(1\bar{1}1)$ planes $CuPt_B$ ordering. In

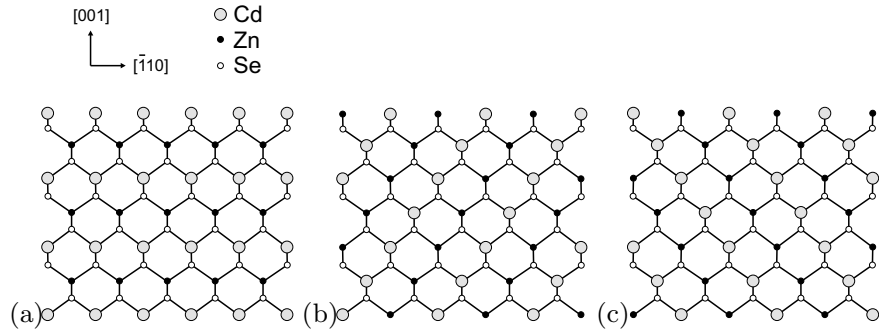

Fig. 3.48 Schematic diagrams of zincblende $Cd_xZn_{1-x}Te$ along [110] with (**a**) CuAu-I type ordering and (**b**, **c**) two types of the $CuPt_B$ type ordering. Doublet periodicity is along (**a**) [001] and [$\bar{1}$10], (**b**) [1$\bar{1}$1] and (**c**) [$\bar{1}$11]. Adapted from [259]

Fig. 3.47, a TEM image of a $Cd_{0.68}Zn_{0.32}Te$ epilayer is shown with simultaneous ordering in the CuPt structure (doublet periodicity along [1$\bar{1}$1] and [$\bar{1}$11]) and in the CuAu-I structure[7] (doublet periodicity along [001] and [$\bar{1}$10]).

[7]The CuAu-I structure has tetragonal symmetry. There exists also the CuAu-II structure that is orthorhombic.

Chapter 4
Structural Defects

Crystals are like people: it is the defects in them which tend to make them interesting!

C.J. Humphreys, 1979 [260]

Abstract No crystal is perfect. Various point defects and their thermodynamics, diffusion and distribution of defects are discussed. Also dislocations and extended defects such as cracks, stacking faults, grain boundaries and antiphase domains are covered.

4.1 Introduction

In an ideal lattice each atom is at its designated position. Deviations from the ideal structure are called defects. In the following, we will briefly discuss the most common defects. The electrical activity of defects will be discussed in Sects. 7.5 and 7.7. For the creation (formation) of a defect a certain free enthalpy $G_{\mathrm{D}}^{\mathrm{f}}$ is necessary. At thermodynamical equilibrium a (point) defect density $\propto \exp(-G_{\mathrm{D}}^{\mathrm{f}}/kT)$ will always be present (cf. Sect. 4.2.2).

Point defects (Sect. 4.2) are deviations from the ideal structure involving essentially only one lattice point. The formation energy for line defects (Sect. 4.3) or area defects (Sect. 4.4) scales with $N^{1/3}$ and $N^{2/3}$, respectively, N being the number of atoms in the crystal. Therefore, these defects are not expected in thermodynamic equilibrium. However, the path into thermodynamical equilibrium might be so slow that these defects are metastable and must be considered quasi-frozen. There may also exist metastable point defects. By annealing the crystal, the thermodynamic equilibrium concentration might be re-established. The unavoidable two-dimensional defect of the bulk structure is the surface, discussed in Chap. 11.

4.2 Point Defects

4.2.1 Point Defect Types

The simplest point defect is a vacancy V, a missing atom at a given atomic position. If an atom is at a position that does not belong to the crystal structure an interstitial I (or Frenkel defect) is formed.

M. Grundmann, *The Physics of Semiconductors*, Graduate Texts in Physics,
https://doi.org/10.1007/978-3-030-51569-0_4

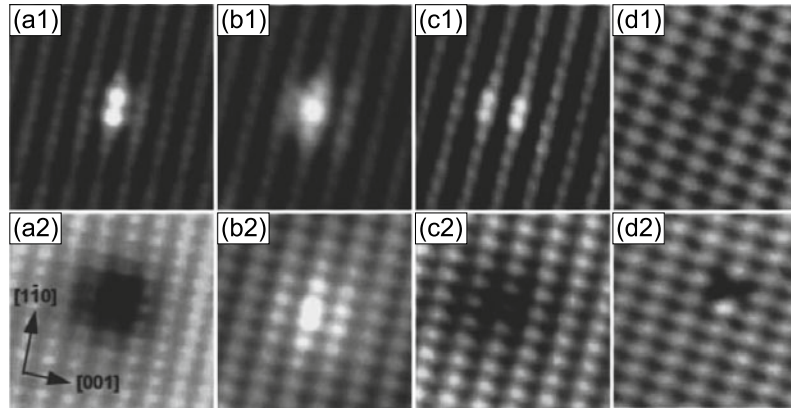

Fig. 4.1 Images of occupied (*upper frames*) and empty (*lower frames*) density of states of typical defects on Si-doped GaAs (110) surfaces. (**a1**, **a2**) show a Ga vacancy, (**b1**, **b2**) a Si_{Ga} donor, (**c1**, **c2**) a Si_{As} acceptor and (**d1**, **d2**) a Si_{Ga}–V_{Ga} complex. Adapted from [261]

Depending on the position of the interstitial different types are distinguished. An interstitial atom that has the same chemical species as the crystal is called 'self-interstitial'.

If an atom site is populated with an atom of different order number Z, an impurity is present. An impurity can also sit on interstitial position. If the number of valence electrons is the same as for the original (or correct) atom, then it is an isovalent impurity and quasi fits into the bonding scheme. If the valence is different, the impurity adds extra (negative or positive) charge to the crystal bonds, which is compensated by the extra, locally fixed charge in the nucleus. This mechanism will be discussed in detail in the context of doping (Chap. 7). If in an AB compound an A atom sits on the B site, the defect is called an antisite defect A_B.

A Ga vacancy, a silicon impurity atom on Ga- and As-site and a Si_{Ga}-vacancy complex at the (110) surface of Si doped GaAs are shown in Fig. 4.1 as observed with STM [261, 262]. Also antisite defects in GaAs can be observed with STM [263, 264].

A point defect is typically accompanied by a relaxation of the surrounding host atoms. As an example, we discuss the vacancy in Si (Fig. 4.2a). The missing atom leads to a lattice relaxation with the next neighbors moving some way into the void (Fig. 4.2b). The bond lengths of the next and second-next neighbor Si atoms around the neutral vacancy are shown in Fig. 4.2c. The lattice relaxation depends on the charge state of the point defect (Jahn–Teller effect) which is discussed in more detail in Sect. 7.7. In Fig. 4.2d the situation for the positively charged vacancy with one electron missing is shown. One of the two bonds is weakened since it lacks an electron. The distortion is therefore different from that for V^0. Also the (self-)interstitial is accompanied with a lattice relaxation as shown in Fig. 4.3 for a silicon interstitial at tetrahedral place. Self-interstitials in silicon and germanium are reviewed and compared in [265] for their various charge states.

4.2.2 Thermodynamics

For a given temperature, the free enthalpy G of a crystal (a closed system with regard to particle exchange)

$$G = H - TS \tag{4.1}$$

is minimum. H is the enthalpy and S the entropy. The enthalpy $H = E + pV$ is the thermodynamic potential for a system whose only external parameter is the volume V. It is used when the independent variables of the system are the entropy S and pressure p. The free enthalpy is used when the independent parameters are T and p. G_0 (H_0) is the free energy (enthalpy) of the perfect crystal. H^f is the formation

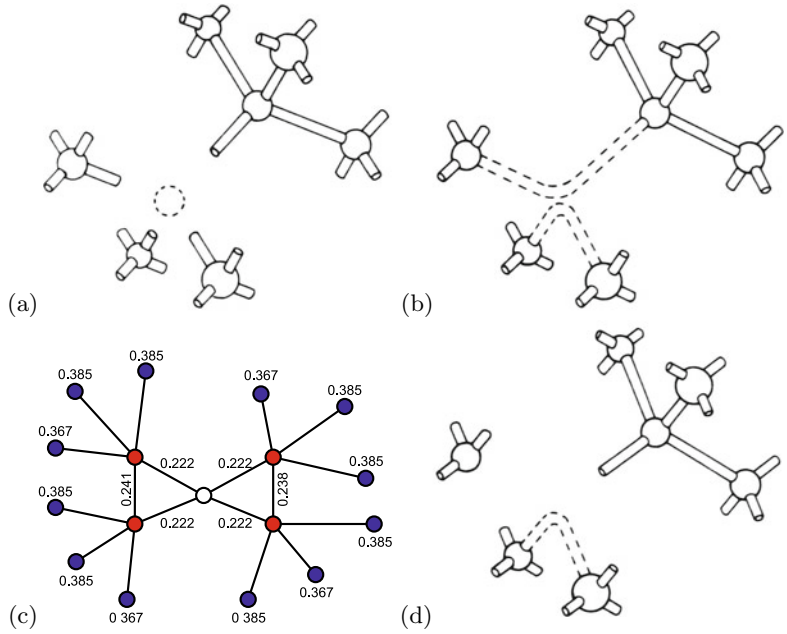

Fig. 4.2 (**a**) Schematic diamond lattice with vacancy, i.e. a missing Si atom without relaxation. (**b**) Si with neutral vacancy (V^0), lattice relaxation and formation of two new bonds. (**c**) Schematic diagram showing the (inward) relaxation of the neighbors around the neutral Si vacancy defect site (*empty circle*) calculated by an ab initio method. The distances of the outer shell of atoms (*red circles*) from the vacant site is labeled (in nm). The bond lengths of the two new bonds and the second-neighbor (*blue circles*) distance are also indicated. The bond length in bulk Si is 0.2352 nm, the second-neighbor distance 0.3840 nm. Adapted from [266]. (**d**) Si unit cell with positively charged vacancy (V^+). Parts (**a**, **b**, **d**) reprinted with permission from [267]

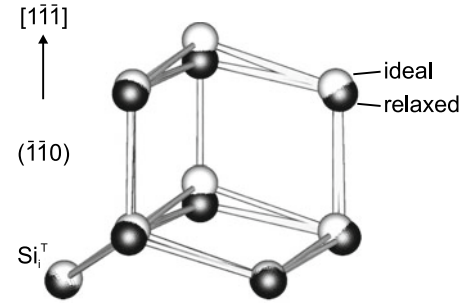

Fig. 4.3 Silicon tetrahedral interstitial Si_i^T and its next atoms in ideal (*white spheres*) and relaxed (*black spheres*) position. Adapted from [175]

enthalpy of an isolated defect. This could be, e.g., the enthalpy of a vacancy, created by bringing an atom from the (later) vacancy site to the surface, or an interstitial, created by bringing an atom from the surface to the interstitial site. In the limit that the n defects do not interact with each other, i.e. their concentration is sufficiently small, they can be considered independent and the enthalpy is given by

$$H = H_0 + n\,H^{\mathrm{f}}\ . \tag{4.2}$$

The increase of entropy due to increased disorder is split into the configurational disorder over the possible sites, denoted as S^{d}, and the formation entropy S_{f} due to localized vibrational modes. The total change ΔG of the free energy is

Table 4.1 Formation enthalpy H^{f} and entropy S^{f} of the interstitial (I) and vacancy (V) in Si and the Ga vacancy in GaAs. Data for Si from [268, 269], for GaAs from [270]

Material	Defect	H^{f} (eV)	S^{f} (k_{B})
Si	I	3.2	4.1
Si	V	2.8	~ 1
GaAs	V_{Ga}	3.2	9.6

$$\Delta G = G - G_0 = n\,(H^{\mathrm{f}} - T\,S^{\mathrm{f}}) - T\,S^{\mathrm{d}} = n\,G^{\mathrm{f}} - T\,S^{\mathrm{d}}\ , \tag{4.3}$$

where $G^{\mathrm{f}} = H^{\mathrm{f}} - T\,S^{\mathrm{f}}$ denotes the free enthalpy of formation of a single isolated defect. In Table 4.1 experimental values for the formation entropy and enthalpy are given for several defects. Surprisingly, despite their fundamental importance in semiconductor defect physics, these numbers are not very well known and disputed in the literature.

The defect concentration is obtained by minimizing ΔG, i.e.

$$\frac{\partial \Delta G}{\partial n} = G^{\mathrm{f}} - T\,\frac{\partial S^{\mathrm{d}}}{\partial n} = 0\ . \tag{4.4}$$

The entropy S^{d} due to disorder is given as

$$S^{\mathrm{d}} = k_{\mathrm{B}} \ln W\ , \tag{4.5}$$

where W is the complexion number, usually the number of distinguishable ways to distribute n defects on N lattice sites

$$W = \binom{N}{n} = \frac{N!}{n!\,(N-n)!}\ . \tag{4.6}$$

With Stirling's formula $\ln x! \approx x(\ln x - 1)$ for large x we obtain

$$\frac{\partial S^{\mathrm{d}}}{\partial n} = k_{\mathrm{B}}\left[\frac{N}{n}\,\ln\left(\frac{N}{N-n}\right) + \ln\left(\frac{N-n}{n}\right)\right]\ . \tag{4.7}$$

If $n \ll N$, $\partial N/\partial n = 0$ and the right side of (4.7) reduces to $k_{\mathrm{B}} \ln(N/n)$. The condition (4.4) reads $G^{\mathrm{f}} + k_{\mathrm{B}}T\ \ln(n/N)$, or

$$\frac{n}{N} = \exp\left(-\frac{G^{\mathrm{f}}}{kT}\right)\ . \tag{4.8}$$

In the case of several different defects i with a degeneracy Z_i, e.g. a spin degree of freedom or several equivalent configurations, (4.8) can be generalized to

$$\frac{n_i}{Z_i\,N} = \exp\left(-\frac{G_i^{\mathrm{f}}}{kT}\right)\ . \tag{4.9}$$

In [271] the equilibrium concentration of interstitials C_I^{eq} in silicon has been given as

$$C_I^{\mathrm{eq}} = \left(1.0 \times 10^{27}\,\mathrm{cm}^{-3}\right)\,\exp\left(-\frac{3.8\,\mathrm{eV}}{kT}\right)\ , \tag{4.10}$$

about $10^{14}\,\mathrm{cm}^{-3}$ at 1200 °C. The vacancy concentration has been investigated in [272]. Around a temperature of 1200 °C it is in the 10^{14}–$10^{15}\,\mathrm{cm}^{-3}$ range. Due to the reaction

$$0 \rightleftharpoons I + V \ , \tag{4.11}$$

a mass action law holds for the concentrations of interstitials and vacancies

$$C_I \, C_V = C_I^{\mathrm{eq}} \, C_V^{\mathrm{eq}} \ . \tag{4.12}$$

4.2.3 Diffusion

The diffusion of point defects is technologically very important, in particular for silicon as host material. Typically a dopant profile should be stable under following technological processing steps and also during device performance. Also defect annihilation is crucial after implantation processes. Diffusion of an interstitial I and a vacancy V to the same site is prerequisite for recombination of defects (so called *bulk process*) according to the scheme $I + V \rightarrow 0$. We note that the process $0 \rightarrow I + V$ is called *Frenkel pair process*.[1] Also the self-diffusion of silicon has been studied, e.g. using radioactively marked isotopes [271]. The diffusion of point defects including dopants in silicon has been reviewed in [273, 274]. Usually Fick's law is applied, stating how the flux J depends on the concentration gradient, for an interstitial it reads:

$$J_I = -D_I \, \nabla C_I \ , \tag{4.13}$$

D_I being the interstitial diffusion coefficient. For interstitials in Si it was found [271] that

$$D_I = 0.2 \, \exp\left(-\frac{1.2\,\mathrm{eV}}{kT}\right) \mathrm{cm}^2/\mathrm{s} \ . \tag{4.14}$$

The diffusion of neutral vacancies occurs with [275]

$$D_V = 0.0012 \, \exp\left(-\frac{0.45\,\mathrm{eV}}{kT}\right) \mathrm{cm}^2/\mathrm{s} \ . \tag{4.15}$$

The temperature dependent diffusion coefficients of point defects and dopants in silicon are shown in Fig. 4.4.

The self-diffusion coefficient of silicon has been determined from the annealing of isotope superlattices (Sect. 12.5) of sequence $^{28}\mathrm{Si}_n/^{30}\mathrm{Si}_n$, $n = 20$ to be [276]

$$D_{\mathrm{Si}}^{\mathrm{SD}} = \left[2175.4 \, \exp\left(-\frac{4.95\,\mathrm{eV}}{kT}\right) + 0.0023 \, \exp\left(-\frac{3.6\,\mathrm{eV}}{kT}\right)\right] \mathrm{cm}^2/\mathrm{s} \ , \tag{4.16}$$

the first (second) term being due to interstitial (vacancy) mechanism, dominant for temperatures larger (smaller) than 900 °C. The enthalpy in the exponent, e.g. $H_V = 3.6^{+0.3}_{-0.1}\,\mathrm{eV}$ [276], consists of the formation and migration enthalpies,

$$H_V = H_V^{\mathrm{f}} + H_V^{\mathrm{m}} \ . \tag{4.17}$$

[1] At higher temperatures a silicon atom can occasionally acquire sufficient energy from lattice vibrations to leave its lattice site and thus an interstitial and a vacancy are generated.

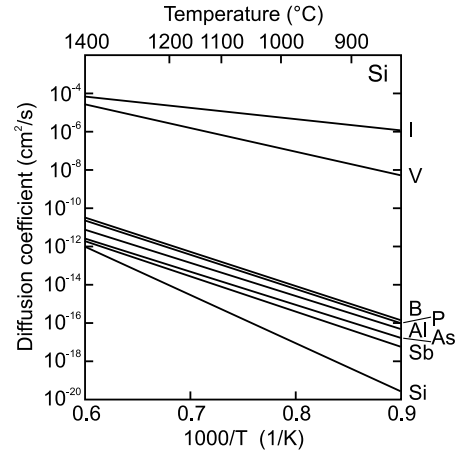

Fig. 4.4 The temperature dependent diffusion coefficient of Si interstitials I, vacancies V and various impurities in silicon. Also the self-diffusion coefficient, labeled with 'Si' is shown. Based on data from [273]

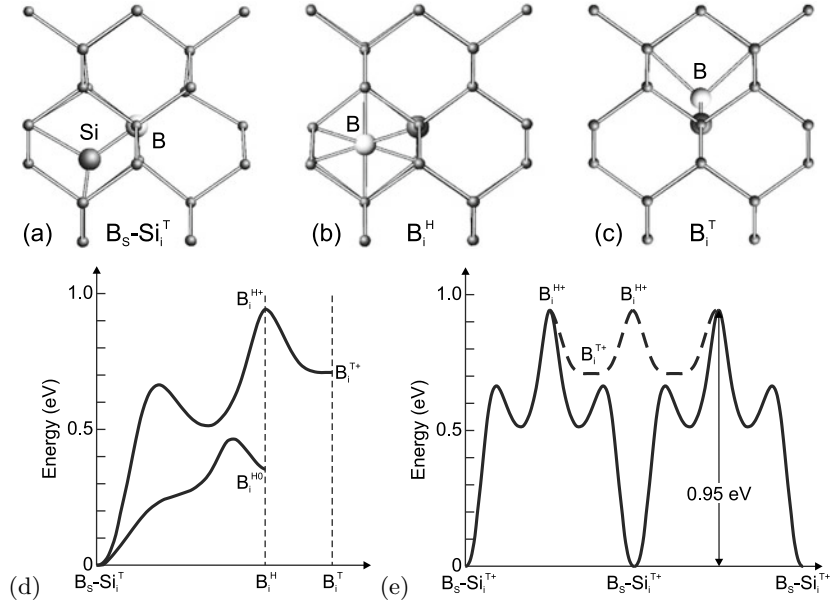

Fig. 4.5 Configurations of boron in Si: (**a**) Substitutional boron and Si self-interstitial at 'T' site (B_S–Si_i^T). Interstitial boron at (**b**) 'H' (B_i^H) and (**c**) 'T' site (B_i^T), each with the Si atoms on the Si lattice sites. The *large bright ball* represents the boron atom, *large* and *small dark balls* represent Si atoms. (**d**) Lowest energy barrier diffusion paths for positively charged and neutral B–Si states, total energy vs. configuration. (**e**) Two diffusion pathways for positively charged B–Si, kick-out (*dashed line*) and pair diffusion (*solid line*); the activation energy is labeled. Adapted from [279]

Using the experimental value $H_V^f = 2.8 \pm 0.3\,\text{eV}$ [269] from Table 4.1, for the migration enthalpy a value around $H_V^m \approx 0.8\,\text{eV}$ is obtained.

As an example for a dopant diffusion process that has been understood microscopically, we discuss here boron in silicon. In Fig. 4.5a the lowest-energy configuration of a boron-related defect in silicon is depicted, B_s–Si_i^T, i.e. boron on a substitutional site and a self-interstitial Si on the 'T' place with highest symmetry[2] (see Fig. 3.18). Due to its importance as an acceptor in Si, the configuration and diffusion

[2]The positive charge state is stable, the neutral charge state is metastable since the defect is a negative-U center (see Sect. 7.7.5).

of B in Si has found great interest [277–279]. The diffusion depends on the charge state of boron. The diffusion of positively charged boron has been suggested [279] to occur via the following route: The boron leaves its substitutional site and goes to the hexagonal site ('H') (Fig. 4.5b) with an activation energy of about 1 eV (Fig. 4.5d). It can then relax ($\sim$ 0.1 eV) without barrier to the tetrahedral 'T' position (Fig. 4.5c). The direct migration B_s–$Si_i^{T+} \rightarrow B_i^{T+}$ has a higher activation energy of 1.12 eV and is thus unlikely. The boron atom can then diffuse through the crystal by going from 'H' to 'T' to 'H' and so on (Fig. 4.5e). However, long-range diffusion seems to be not possible in this way because the kick-in mechanism will bring back the boron to its stable configuration. The pair diffusion mechanism for neutral boron B_s–$Si_i^T \rightarrow B_i^H \rightarrow B_s$–$Si_i^T$ via the hexagonal site has an activation energy of about 0.5 eV (Fig. 4.5d) while the path via B_i^T has a larger 0.9 eV barrier. The concentration dependence of the diffusion mechanism has been discussed in [280].

Similarly, indium diffusion in silicon has been investigated suggesting a minimum energy In_s–$Si_i^T \rightarrow In_i^T \rightarrow In_s$–$Si_i^T$ diffusion pathway via the tetrahedral site with 0.8 eV activation energy [281]. Microscopic modeling has been reported also for diffusion of phosphorus [282].

4.2.4 Dopant Distribution

The introduction of impurities into a semiconductor (or other materials such as glasses) is termed *doping*. The unavoidable incorporation of impurities in the nominally pure (nominally undoped) material is called *unintentional* doping and leads to a residual or background impurity concentration. Several methods are used for doping and the creation of particular doping profiles (in depth or lateral). All doping profiles underly subsequent diffusion of dopants (Sect. 4.2.3).

Various methods of doping are used. A straightforward method of doping is the incorporation during crystal growth or epitaxy. For semiconductor wafers a homogeneous doping concentration is targeted, both laterally and along the rod from which the wafer is cut (Sect. 12.2.2). When a crystal is grown from melt, containing a concentration c_0 of the impurity, the concentration in the solid is given by ('normal freezing' case [283–285])[3]

$$c(x) = c_0\, k\, (1-x)^{k-1}\ , \tag{4.18}$$

where $c(x)$ is the impurity concentration in the crystal at the freezing interface, x is the frozen melt fraction (ratio of solid mass to total mass, $0 \le x \le 1$). k is the *distribution coefficient* (or segregation coefficient) which is the fraction of impurities that is built into the crystal at the liquid–solid interface. Since the melt volume reduces during the solidification, the impurity concentration rises over time. For small distribution coefficients (4.18) can be approximated to

$$c(x) \approx c_0\, \frac{k}{1-x}\ , \tag{4.19}$$

An experimental example for Ge:In is shown in Fig. 4.6a.

In Table 4.2 the distribution coefficients for various impurities in Si, Ge and GaAs is given. The modification of distribution coefficients in SiGe alloys is discussed in [286]. Equilibrium values (k_{eq}) are obtained for 'slow' crystal growth. For finite growth rates, k becomes a function of the growth rate

[3] Mass preservation of the impurities can be written at any time $c_m(1-x)+\int_0^x c(x')\,dx' = c_0$, where c_m is the (remaining) concentration in the melt. At the beginning $c_m(0) = c_0$. At the interface $c(x) = k\, c_m(x)$. Putting this into the mass preservation, building $c'(x)$ and solving the resulting differential equation $c' = c(1-k)/(1-x)$ with $c(0) = k\, c_0$ leads to (4.18).

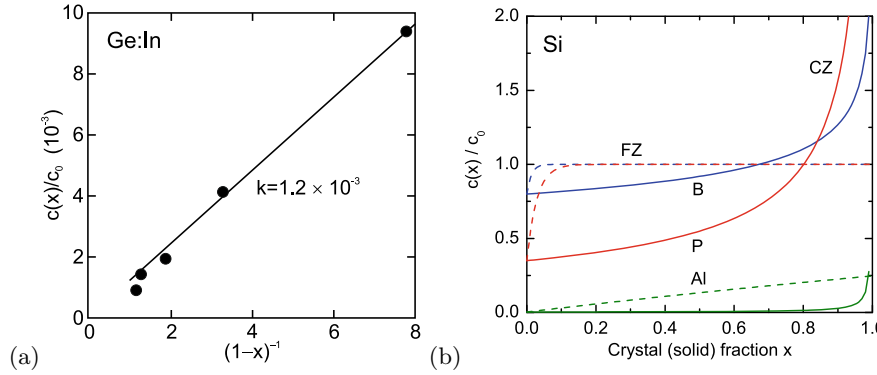

Fig. 4.6 (**a**) Relative concentration of indium along a CZ-grown germanium crystal. Absolute concentration is in the 10^{16} cm^{-3} range. *Solid line* follows (4.19) with $k = 1.2 \times 10^{-3}$. *Symbols* are experimental data from [288]. (**b**) Impurity distribution (relative concentration $c(x)/c_0$) for CZ (4.18) (*solid lines*) and FZ (4.20) (*dashed lines*, $z = 0.01$) silicon crystals for B (*blue*), P (*red*), and Al (*green*). Distribution coefficients have been taken from Table 4.2. Note crossing of B and P lines and possibly associated change from p-type to n-type (cmp. Fig. 1.7)

Table 4.2 Equilibrium distribution coefficients (at melting point) of various impurities in silicon, germanium and GaAs. Data for Si from [285, 287], for Ge from [164, 288–290] and for GaAs from [164]

Impurity	Si	Ge	GaAs
C	0.07	> 1.85	0.8
Si		5.5	0.1
Ge	0.33		0.03
N	7×10^{-4}		
O	≈ 1		0.3
B	0.8	12.2	
Al	2.8×10^{-3}	0.1	3
Ga	8×10^{-3}	0.087	
In	4×10^{-4}	1.2×10^{-3}	0.1
P	0.35	0.12	2
As	0.3	0.04	
Sb	0.023	3.3×10^{-3}	< 0.02
S	10^{-5}	$> 5 \times 10^{-5}$	0.3
Fe	6.4×10^{-6}	3×10^{-5}	2×10^{-3}
Ni	$\approx 3 \times 10^{-5}$	2.3×10^{-6}	6×10^{-4}
Cu	8×10^{-4}	1.3×10^{-5}	2×10^{-3}
Ag	$\approx 1 \times 10^{-6}$	10^{-4}	0.1
Au	2.5×10^{-5}	1.5×10^{-5}	
Zn	2.5×10^{-5}	6×10^{-4}	0.1

and is then called the *effective* distribution coefficient. For $k < 1$, $k_{\text{eff}} > k_{\text{eq}}$. k_{eff} approaches 1 for high growth rates, i.e. all impurities at the rapidly moving interface are incorporated.

Equation (4.18) applies to Czrochalski growth where the crystal is pulled out of the melt [291]. In float-zone (FZ) growth [291] a polycrystalline rod is transformed into a crystalline one while a

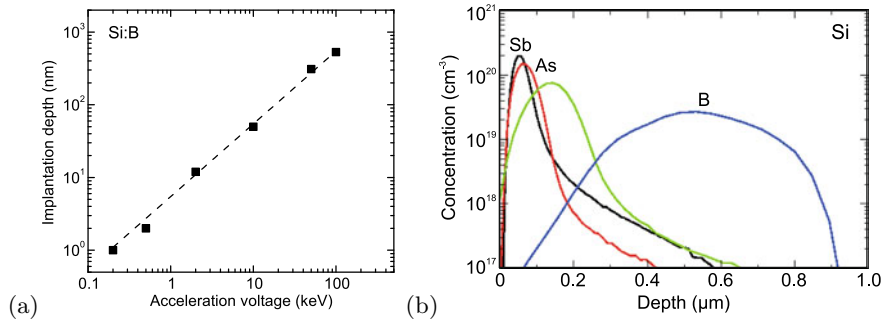

Fig. 4.7 (**a**) Depth of peak concentration of boron implanted in silicon for various acceleration voltages U. Data from various sources, for $U < 1$ keV from [299]. *Dashed line* is linear dependence. (**b**) Simulated depth profiles of impurity concentration for B, P, As, and Sb implanted into crystalline silicon with $U = 100$ keV and a dose of 10^{15} cm^{-2}. Adapted from [300]

RF-heated and liquid 'float' zone is moved through the crystal. In this case the impurity distribution is given by[4]

$$c(x) = c_0 \left[1 - (1-k)\, \exp\left(-\frac{k\, x}{z} \right) \right] , \tag{4.20}$$

where x is the ratio of the crystal mass to the total mass, i.e. crystal, liquid and feed rod. z is the relative mass of the (liquid) float zone, i.e. the ratio of liquid mass to the total mass. The impurity distribution for CZ and FZ crystals is compared in Fig. 4.6b. Obviously the FZ process can create much more homogeneous profiles.[5]

Using epitaxy arbitrary doping profiles along the growth directions can be created by varying the impurity supply during growth. Impurities can be introduced through the surface of the material by diffusion from a solid or gas phase. In ion implantation [292] the impurity atoms are accelerated towards the semiconductor and deposited with a certain depth profile due to multiple scattering and energy loss events, depending on the acceleration voltage (increasing deposition depth with increasing voltage, Fig. 4.7a) and ion mass (decreasing deposition depth with increasing mass, Fig. 4.7b). The depth profile is often investigated using secondary ion mass spectrometry (SIMS) [293, 294]. The profile also depends on the matrix material whose stopping power depends on its density and atomic mass. While an implantation depth of about 50 nm is reached for boron in silicon ($A \approx 28$) for 10 keV, 20 keV are necessary in germanium ($A \approx 72.6$) [295]. The mean path length[6] d_m depends also on the crystallographic direction (channeling effects, Fig. 4.8) [296]. A simulation of the interaction of ions and solids can be performed using the SRIM software [297, 298].

[4] When the float zone moves through the crystal, the change of mass of impurities $m_\mathrm{m} = c_\mathrm{m} z$ in the liquid is $m'_\mathrm{m} = c_0 - k c_\mathrm{m}$. The first term stems from the melting of the polycrystalline part, the second from the solidification of the crystal. Solving the resulting differential equation $c'_\mathrm{m} = (c_0 - k c_\mathrm{m})/z$ with $c_\mathrm{m}(0) = c_0$ and using $c(x) = k c_\mathrm{m}(x)$ yields (4.20).

[5] We note that during directed solidification of Si:(B,P) a pn-junction forms due to the different distribution coefficients of boron and phosphorus. This has been used in [89].

[6] The mean path length is the distance integrated along the ion trajectory until its direction deviates by more than 4 ° from the incident direction.

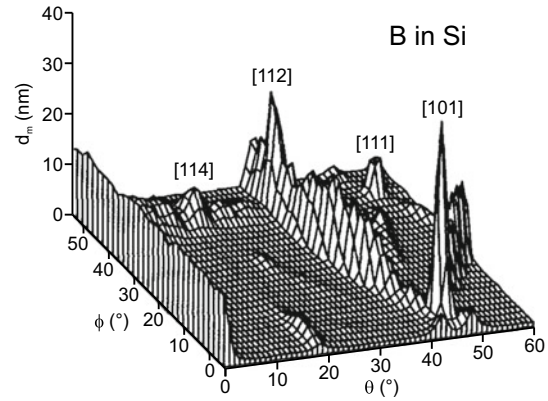

Fig. 4.8 Simulated mean path length as a function of implantation direction (azimuthal angle ϕ and polar angle θ) near [001] for 5 keV boron in silicon. The [001] channeling peak appears as a ridge at the left side of the plot ($\theta = 0$, any value of ϕ). Adapted from [296]

4.2.5 Large Concentration Effects

4.2.5.1 Lattice Constant

At high doping concentration, a noticeable effect on the lattice constant a_0 is found. For silicon the atom density[7] is $N_{Si} = 5 \times 10^{22}\,cm^{-3}$. A doping level of $N = 10^{19}\,cm^{-3}$ corresponds thus to a dopant fraction of 0.02%. Such crystal could also be considered a very dilute alloy. About each $(N_{Si}/N)^{1/3} \approx 17$-th atom in a given direction is a dopant.

The effect of high doping on the lattice constant is due to different ionic radius of the dopant and the hydrostatic deformation potential of the band edge occupied by the free carriers [301]. In a linear approach, the effect is summarized in the coefficient β via

$$\beta = \frac{1}{N} \frac{\Delta a_0}{a_0} \,. \tag{4.21}$$

The effect due to charge carriers on β is negative (positive) for p-doping (n-doping). Experimental data for Si, Ge, GaAs and GaP are compiled in [302, 303] and theoretically discussed. The effect is in the order of $\beta = \pm(1\text{–}10) \times 10^{-24}\,cm^3$. For example, in the case of Si:B, the shrinkage of the lattice constant is mostly due to the charge carrier effect, for Si:P both effects almost cancel. In [304] it is shown that boron incorporation in silicon changes the lattice constant in various directions quite differently, e.g. d_{333} is shrunk by 0.4% for a doping level of $10^{19}\,cm^{-3}$ while the {620} lattice constant remains constant.

4.2.5.2 Clustering

Point defects can cluster, i.e. several point defects aggregate at neighboring sites. An example the configuration of five nearby vacancies in silicon, the so-called V_5 cluster is shown in Fig. 4.9a. In [305] the ring-like hexavacancy in silicon is predicted a very stable defect. A large number of clustered vacancies is equivalent to a void. An example is depicted in Fig. 4.9b for an In_2O_3 crystal which has locally 'decomposed' into an indium particle and a void as revealed by TEM [306]. Also impurities can exhibit clustering.

[7] eight atoms per cubic unit cell of length $a_0 = 0.543\,nm$.

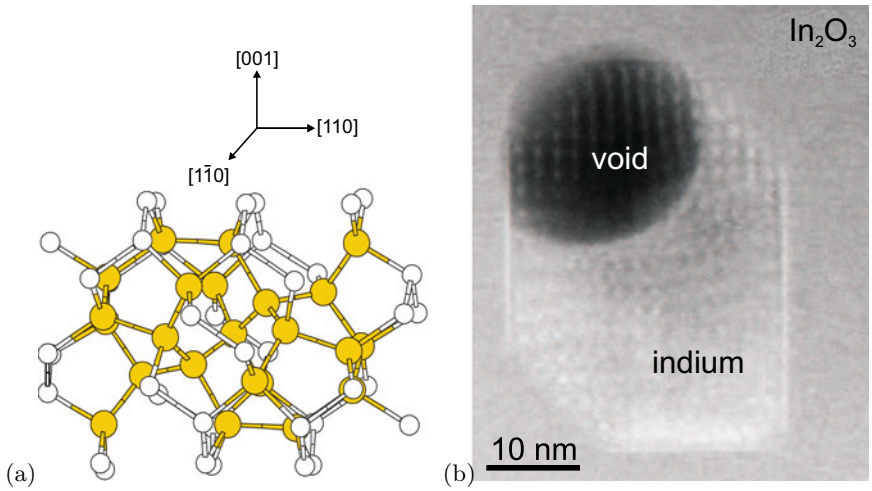

Fig. 4.9 (**a**) Predicted configuration of the V_5-cluster (five vacancies) in silicon. *Yellow spheres* indicate more distorted atoms than the rest of the lattice atoms (*white spheres*). Adapted from [307]. (**b**) Indium particle with adjacent void embedded in In_2O_3 (STEM image revealing Z-contrast in [001]). Adapted from [306]

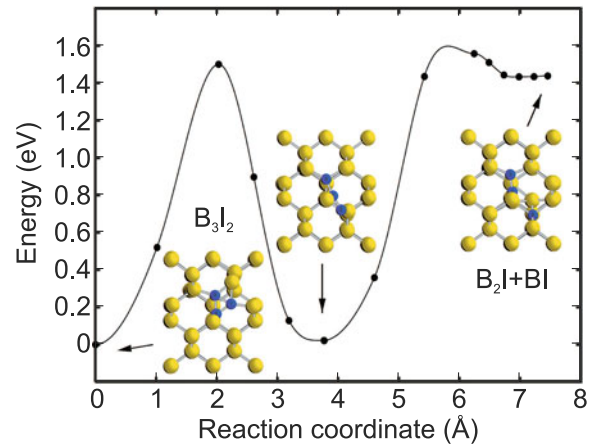

Fig. 4.10 Minimum energy path for the breakup of a B_3I_2 cluster into B_2I and BI. Silicon (boron) atoms are shown as *yellow* (*blue*) *spheres*. Adapted from [310]

Typically a random distribution of dopants in the host is assumed (cmp. Sect. 3.7.1 on random alloys). The introduction of several impurities can lead to pairing effects, e.g. described for Se and B, Ga, Al or In in silicon [308]. A high concentration of a single impurity makes the existence of clusters, i.e. two or more neighboring dopant atoms, more probable. This effect has been extensively studied for B in Si [309], showing that several boron atoms with interstitials I form thermodynamically stable clusters, e.g. B_3I_2. This cluster forms from B_2I and BI with only 0.2 eV activation barrier [310] as shown in Fig. 4.10. The formation is limited by diffusion of the smaller clusters to the same site. The number of free carriers (here holes) released from such cluster is smaller than the number of boron atoms since it forms a deep acceptor [309]. This autocompensation mechanism is thus limiting the maximum achievable free carrier concentration due to doping and is technologically unfavorable. Reactions between boron atoms and silicon self-interstitials often lead to boron clustering in the peak region of an implantation profile and require detailed optimization of the annealing process [311].

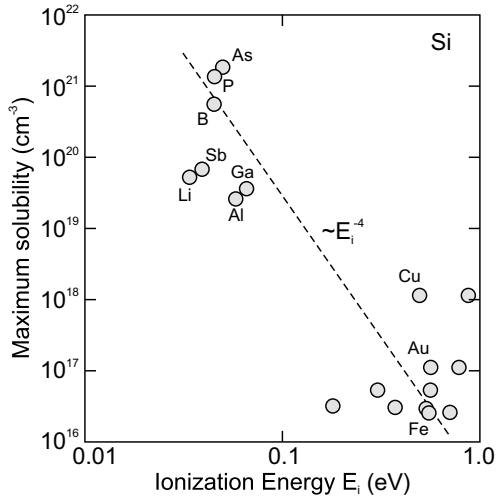

Fig. 4.11 Solubility limit for various impurities in silicon vs. their ionization energy. Adapted from [314]

Table 4.3 Maximum solubility N_s of some impurities in silicon. Data for B, P, As, Sb from [313], other data from [316]

Impurity	N_s ($10^{20}\,cm^{-3}$)
B	4
P	5
As	4
Sb	0.7
Al	0.13
Cu	1.4×10^{-2}
Au	1.2×10^{-3}
Fe	3×10^{-4}

4.2.5.3 Solubility Limit

The steady-state impurity solubility can be defined as the maximum concentration of impurity atoms in a crystal allowing thermodynamic balance between the crystal and another phase, e.g. a liquid phase, an extended defect or a precipitate. Precipitates are small inclusions of a second phase in a crystal, exhibiting a high concentration of 'gathered' impurities that cannot be solved in the crystal. Solubility limits for impurities in silicon have been first determined in [312] with a bulk of subsequent research [313] due to its practical relevance in device fabrication. The solubility limits for a few impurities in silicon are listed in Table 4.3. It is related to the ionization energy of the defect (cmp. Sect. 7.4) as shown in Fig. 4.11.

The temperature dependence of the solubility for a few dopants is depicted in Fig. 4.12a. The solubility depends also on the present strain [315]. The simple empirical relation $x_s = 0.1\,k$ (Fig. 4.12b) between the maximum molar solubility x_s and the distribution coefficient k in silicon and germanium has been pointed out in [316].

A typical example for the formation of precipitates is Fe in InP, used for compensation of shallow donors in order to produce semi-insulating material (Sect. 7.7.8). The solubility of Fe in InP is fairly low, about $10^{17}\,cm^{-3}$ at growth temperature [317]. In Fig. 4.13 a high-resolution TEM image of a precipitate in InP doped with $3 \times 10^{18}\,cm^{-3}$ Fe is shown. The precipitate exhibits a lattice constant

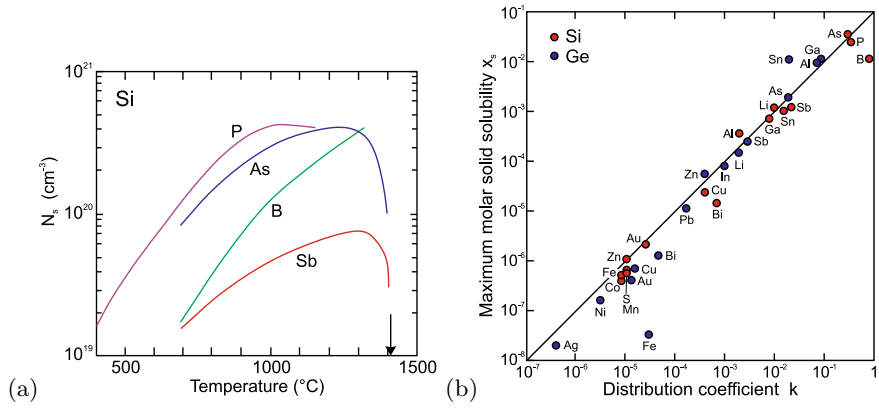

Fig. 4.12 **a** Steady-state solubility of impurities (P, As, B and Sb as labeled) in silicon. *Solid lines* are theoretical model matching various experimental data. *Arrow* denotes the melting point of silicon (1410 °). Adapted from [313]. **b** Maximum molar solid solubility x_s vs. the distribution coefficient for various impurities in crystalline silicon and germanium. *Solid line* follows $x_s = 0.1\,k$. Adapted from [316]

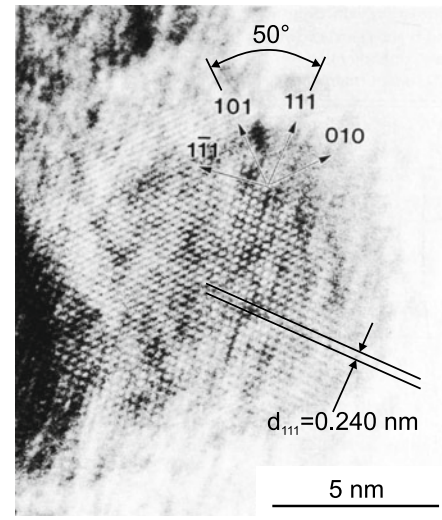

Fig. 4.13 High resolution TEM image of a FeP precipitate in iron-doped InP. Adapted from [318]

of $d_{111} = 0.240\,\text{nm}$ in [111]-direction, much different from that of InP ($d_{111}^{\text{InP}} = 0.339\,\text{nm}$). The angle between the [101] and [111] direction is 50° instead of 35° for InP. This is consistent with orthorhombic FeP [318]. Typically FeP and FeP_2 precipitates are found in highly Fe-doped InP [319].

4.3 Dislocations

Dislocations are line defects along which the crystal lattice is shifted by a certain amount. The vector along the dislocation line is called line vector **L**. A closed path around the dislocation core differs from that in an ideal crystal. The difference vector is called the Burger's vector **b**. Dislocations for which the Burger's vector is a vector of the lattice are called *full* dislocations. In contrast, dislocations with Burger's vectors that are not translation vectors of the lattice are called *partial* dislocations. The history of dislocation theory is described in [320].

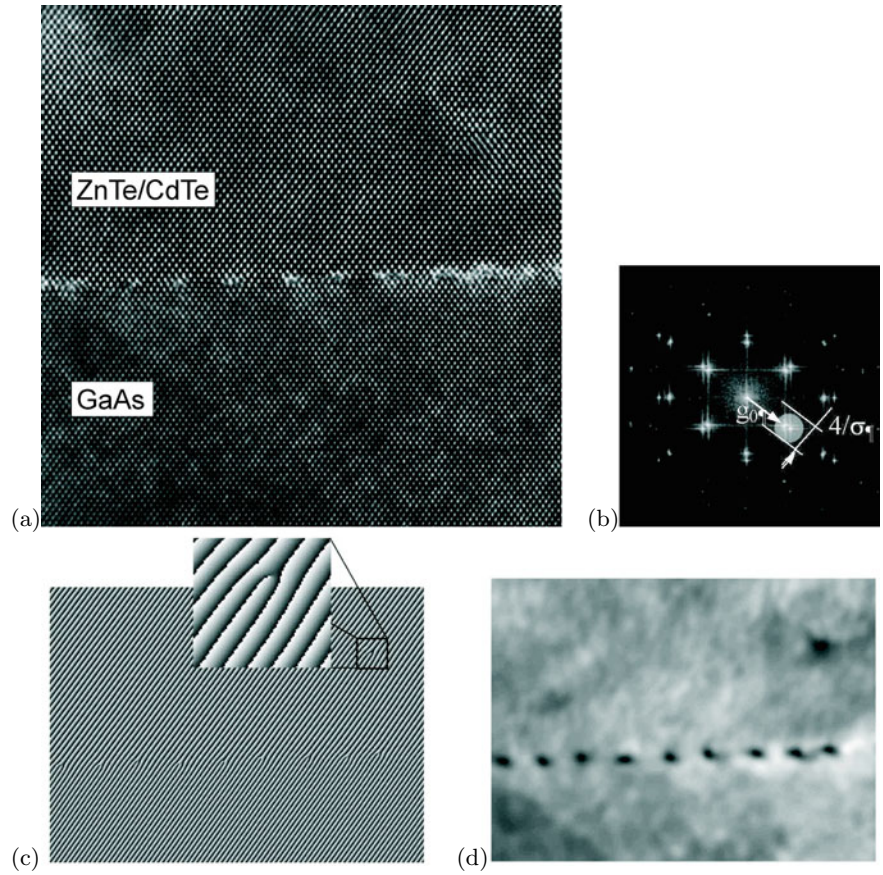

Fig. 4.14 **a** High-resolution transmission electron microscopy image (HRTEM) in the ⟨110⟩ projection of a network of misfit dislocations at a GaAs/CdTe/ZnTe interface. Substrate: GaAs (001), 2° off ⟨110⟩, ZnTe buffer layer is 2 monolayers thick. **b** Fourier transform with round mask around the (111) Bragg reflection. (**c**) Phase and **d** amplitude images for the mask from (**b**). From [321]

Since the energy of a dislocation is proportional to $\mathbf{b}^2$, only dislocations with the shortest Burger's vector are stable. The plane spanned by **L** and **b** is called the *glide* plane. In Fig. 4.14 a high-resolution image of the atoms around a dislocation and the phase and amplitude of the (111) reflection are shown. The phase corresponds to the atomic columns, the amplitude to the displacement of the atoms at the dislocation core (see also Fig. 4.14).

4.3.1 Dislocation Types

4.3.1.1 Edge Dislocations

For an *edge* dislocation (Fig. 4.15a) **b** and **L** are perpendicular to each other. An extra half-plane spanned by **L** and $\mathbf{b} \times \mathbf{L}$ is inserted.

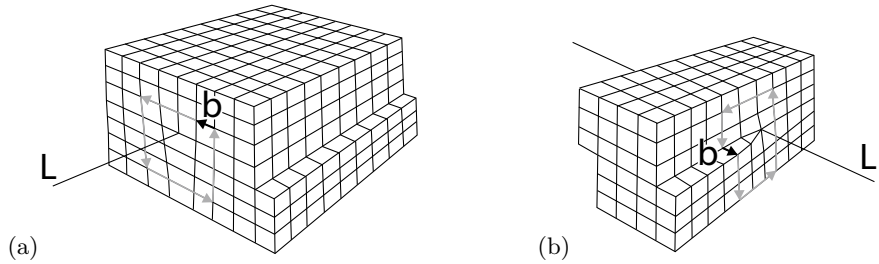

Fig. 4.15 Model of **a** an edge and **b** a screw dislocation. The line vector **L** and the Burger's vector **b** are indicated

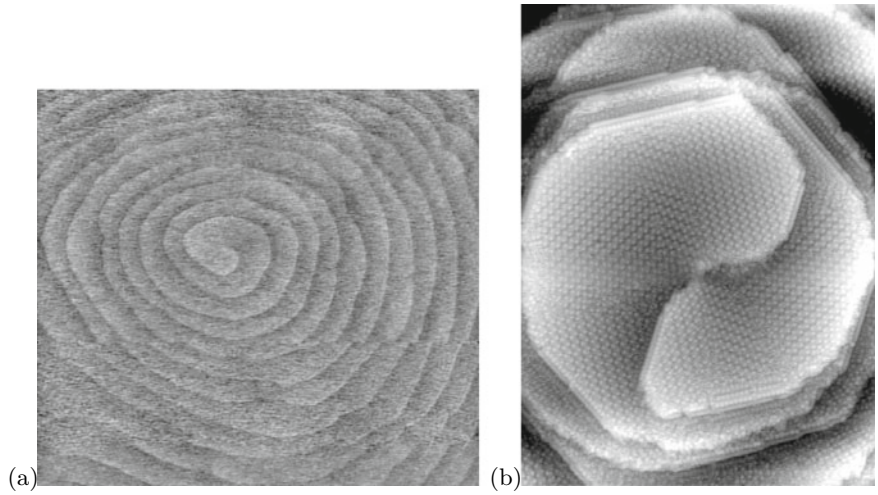

Fig. 4.16 **a** Atomic force microscopy image of growth spiral around a screw dislocation on a silicon surface; image width: 4 µm. (textbfb STM image (width: 75 nm) of a screw-type dislocation with a Burgers vector of [000-1] on the N-face of GaN. The reconstruction is c(6×12). The c(6×12) row directions correspond to $\langle \bar{1}100 \rangle$. Reprinted with permission from [322], ©1998 AVS

4.3.1.2 Screw Dislocations

For a *screw* dislocation (Fig. 4.15b) **b** and **L** are collinear. The solid has been cut along a half-plane up to the dislocation line, shifted along **L** by the amount **b** and reattached.

Around the intersection of a screw dislocation with a surface, the epitaxial growth occurs, typically in the form of a growth spiral that images the lattice planes around the defect.

4.3.1.3 60° Dislocations

The most important dislocations in the zincblende lattice (Fig. 4.17) have the line vector along $\langle 110 \rangle$. With the Burger's vector $a/2\,\langle 110 \rangle$ three different types of dislocations can be formed: edge, screw and 60° dislocations. The vicinity of the core of the latter is shown in more detail in Fig. 4.17d. We note that the atomistic structure of 60° dislocations is different for **L** along [110] and [−1 10]; depending on whether the cations or anions are in the core, they are labeled α or β dislocations.

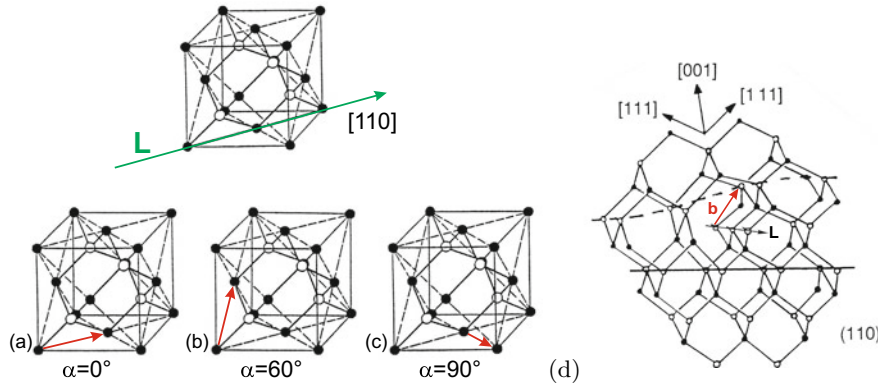

Fig. 4.17 Dislocations in the zincblende structure. The line vector is along [100]. The Burger's vector $a/2\,\langle 110\rangle$ can create an **a** edge dislocation, a **b** screw dislocation, and **c** a 60° dislocation. **d** Atomistic structure of a 60° dislocation

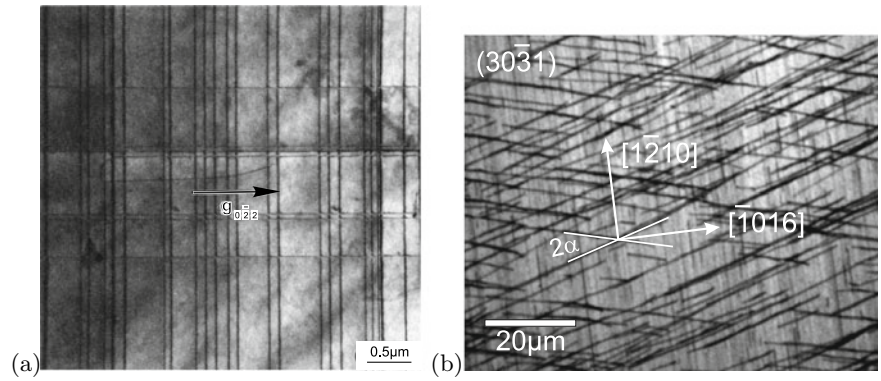

Fig. 4.18 **a** Plan-view transmission electron microscopy image of a network of ⟨110⟩ dislocation lines in (In,Ga)As on InP (001) with a lattice mismatch of about 0.1%. The TEM diffraction vector is $\mathbf{g} = [2\bar{2}0]$. Adapted from [323]. **b** Panchromatic cathodoluminescence image of partially relaxed $Al_{0.13}Ga_{0.87}N$ on $(30\bar{3}1)$ GaN heterostructure with in-plane directions indicated. Adapted from [324], reprinted under a Creative Commons Attribution (CC BY 3.0) unported licence

4.3.1.4 Misfit Dislocations

When materials with different lattice constants are grown on top of each other, the strain can plastically relax via the formation of misfit dislocations. A typical network of such dislocations is shown in Fig. 4.18a for (In,Ga)As on InP (001). Another example is given in Fig. 4.18b for the (Al,Ga)N/GaN system on a semipolar $(30\bar{3}1)$ lattice plane tilted to the c-axis. This leads to non-rectangular dislocation directions which are universal for dislocations from glide on a- and m-planes in heterostructures of trigonal and hexagonal materials [325] (Fig. 4.19).

4.3.1.5 Partial Dislocations

Partial dislocations, i.e. the Burger's vector is not a lattice vector, must necessarily border a two-dimensional defect, usually a stacking fault (Sect. 4.4.2). A typical partial dislocation in diamond or zincblende material is the Shockley partial dislocation (or just Shockley partial) with Burger's vector $b = (a_0/6)\,\langle 112\rangle$. Another important partial is the Frank partial with $b = (a_0/3)\,\langle 111\rangle$. A perfect

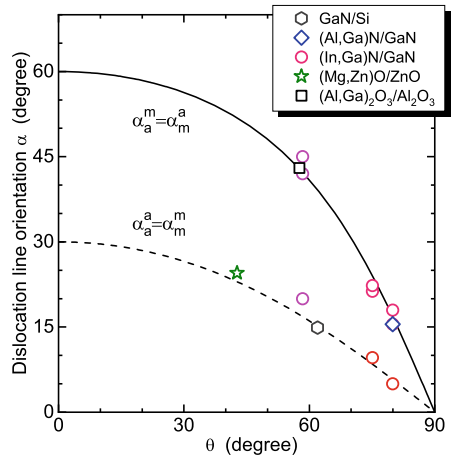

Fig. 4.19 Dislocation line orientation angle α (versus the projected c-axis direction) for the a-plane prismatic slip system for m-azimuth and vice versa (*solid line*) and the m-plane prismatic slip system for m-azimuth (and a/a) (*dashed line*) as a function of interface inclination angle θ. Experimental data from epitaxy on semipolar planes are shown for $(Al,Ga)_2O_3/Al_2O_3$ (square), (Al,Ga)N/GaN (diamond, cmp. Fig. 4.18b), (In,Ga)N/GaN (circles), GaN/Si (hexagon) and (Mg,Zn)O/ZnO (star). Adapted from [325, 326]

dislocation can be dissociated into two partials. This is energetically favorable. As an example we consider the reaction (Fig. 4.20a)

$$\frac{1}{2}\left[\bar{1}01\right] \rightarrow \frac{1}{6}\left[\bar{1}\bar{1}2\right] + \frac{1}{6}\left[\bar{2}11\right] . \tag{4.22}$$

The length of the full dislocation is $a_0/\sqrt{2}$. The length of the Shockley partial is $a_0/\sqrt{6}$. Thus the energy $E = G\,b^2$ of the full dislocation is $E_1 = Ga_0^2/2$ and the sum of the energies of the partials is smaller, $E_2 = 2Ga_0^2/6 = Ga_0^2/3$. In Fig. 4.20b a TEM image of a Ge/Si interface with a Shockley partial is shown.

4.3.2 *Visualization of Dislocations by Etching*

Defects can be made visible using etching techniques. This is particularly popular for finding dislocations. Many etches are anisotropic, i.e. the etch velocity varies for different crystal directions. As an example the result of etching a silicon sphere in molten KOH and a germanium sphere in a HNO_3/HF solution are shown in Fig. 4.21. The remaining bodies exhibit those planes with low etching velocity. The etch velocity of various etch solutions has been investigated in detail in particular for silicon (Fig. 4.22).

In a planar geometry, etch pits indicate the presence of dislocations, as shown in Fig. 4.23 for Ge of different orientation. The anisotropic etch prepares {111} planes. The dislocation core is at the intersection of the planes. In Fig. 4.24 hexagonal etch pits stretched along $[1\bar{1}0]$ are developed by molten KOH [330, 331]. The sides of the base are along [110], ⟨130⟩ and ⟨310⟩. The depth and width of the pits increases with increasing etching time. On the $(00\bar{1})$ surface, the orientation of the pits is rotated by 90° because of the polar [111]-axis of the zincblende structure [330]. Such etch pit develops

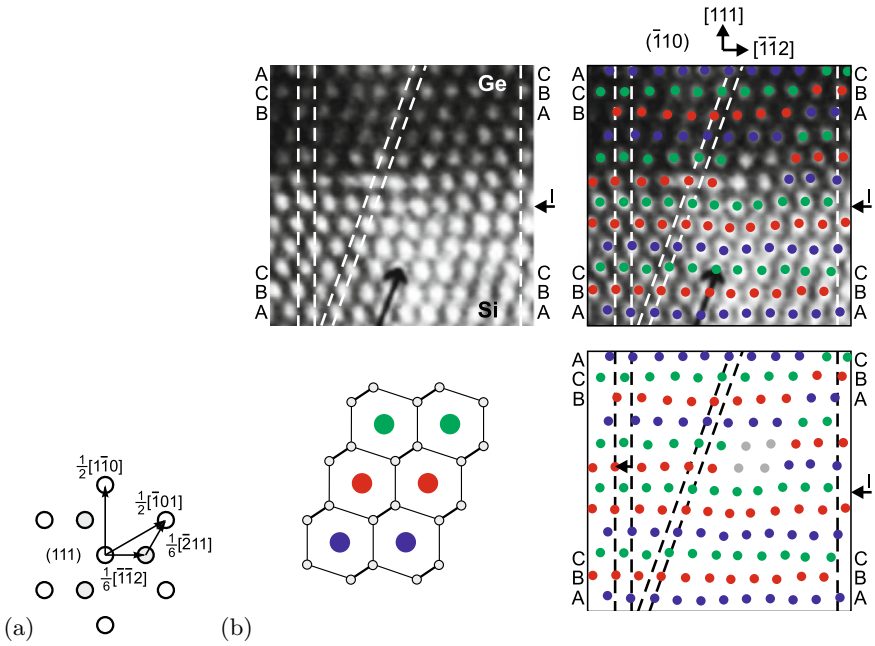

Fig. 4.20 **a** Graphical representation of the dislocation reaction of (4.22). **b** TEM image of the interface of a Ge/Si heterostructure with a $\left[\bar{2}11\right]/6$ Shockley partial dislocation. The image is overlayed with empty rod positions (as schematically shown in the *lower left* part of the figure) colored according to the stacking position (A: *blue*, B: *red*, C: *green*). The *arrows* labeled 'I' denote the position of the interface. Based on [327]

at a dislocation with Burger's vector $a/2\,[011]$ (inclined to the (001) surface) [332]. Other types of etch pits indicate dislocations with other Burger's vectors [332, 333]. Recipies how to wet chemically etch various semiconductors can be found in [328, 334–337]. Other etching techniques include dry processes such as plasma etching or reactive ion etching (RIE) [338–341].

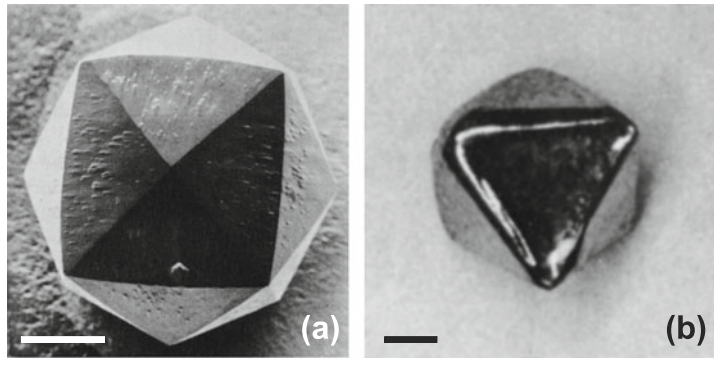

Fig. 4.21 **a** Resulting shape of Si sphere ('Lösungskörper') after 3 h at 100°C in molten KOH. **b** Resulting shape of Ge sphere after etching in HNO_3:HF:CH_3COOH, 35:30:35 weight percent. The octaedric form indicates {111} faces. Markers are 1 mm. Adapted from [328]

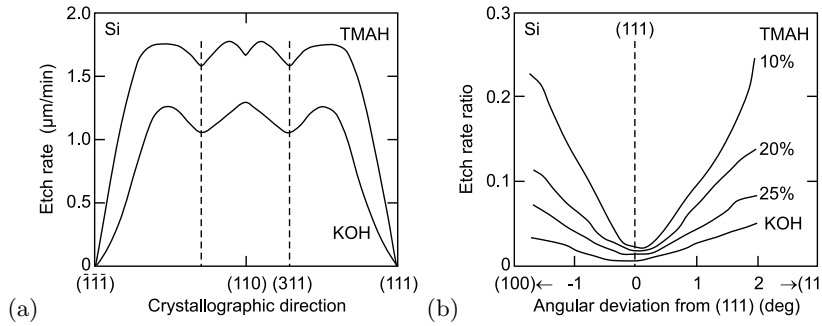

Fig. 4.22 **a** Etch rate of silicon for tetramethyl-ammonium-hydroxide (TMAH) water solution (25%) at 86°C and 40% KOH at 70 °C as a function of crystallographic direction. **b** Detail of the anisotropy around the (111) direction for TMAH solutions with three different concentrations and 40% KOH, all at 86 °C. Adapted from [329]

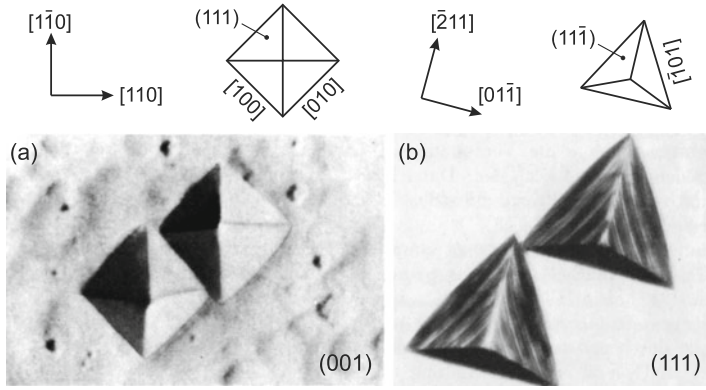

Fig. 4.23 Etch pits on germanium with (**a**) (001) and (**b**) (111) surface orientation. In both cases {111} facets are prepared by the etch. As etch in (**b**) a HNO_3/HF/CH_3COOH solution with $AgNO_3$ additive has been used. Width of the triangular etch pits is about 100 µm. Adapted from [334]

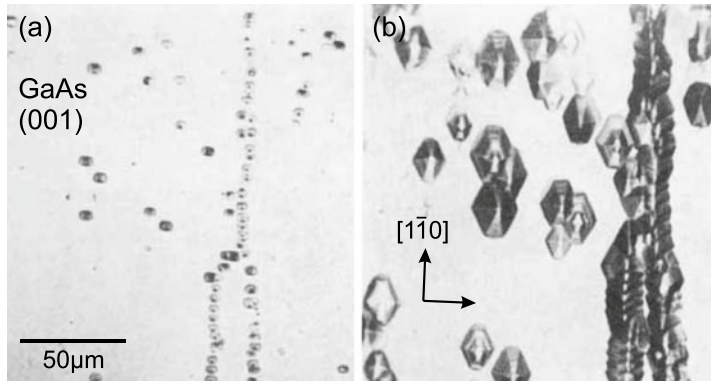

Fig. 4.24 Etch pits on GaAs (001) after **a** 3 min and **b** 10 min etch time in molten KOH at 300°C. Adapted from [330]

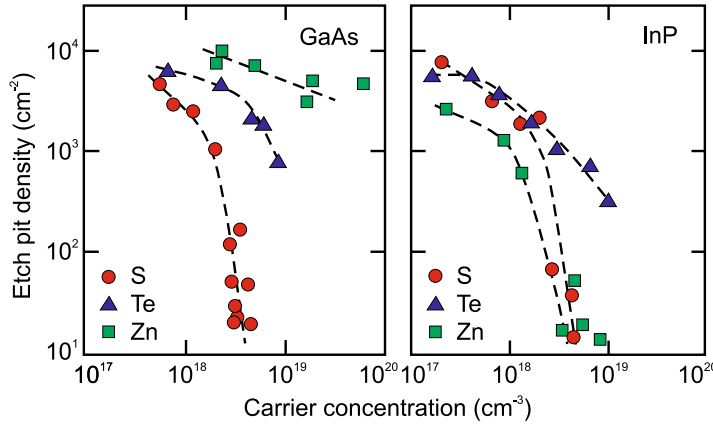

Fig. 4.25 Dislocation density (as revealed by etch pits) for GaAs and InP as a function of the carrier concentration for various concentrations of impurities (S, Te, and Zn). Adapted from [343]

4.3.3 Impurity Hardening

It has been found that the addition of impurities can lead to a substantial reduction of the dislocation density. This effect is known as impurity hardening and is caused by a hardening of the lattice due to an increase of the so-called critical resolved shear stress [342]. In Fig. 4.25 the dependence of the dislocation density in GaAs and InP is shown as a function of the carrier density that is induced by the incorporation of (electrically active) group-II or group-VI atoms (acceptors or donors, cf. Sect. 7.5). The high carrier concentration is unwanted when semi-insulating substrates (cf. Sect. 7.7.8) or low optical absorption (cf. Sect. 9.9.1) are needed. Thus the incorporation of isovalent impurities, such as In, Ga or Sb in GaAs and Sb, Ga or As in InP, has been investigated and found to be remarkably effective. Material containing such impurities in high concentration ($>10^{19}\,\mathrm{cm}^{-3}$) must be considered a low-concentration alloy. The lattice constant is thus slightly changed, which can cause problems in the subsequent (lattice-mismatched) epitaxy of pure layers.

4.4 Extended Defects

4.4.1 Micro-cracks

If the stress in a material becomes too big to be accommodated by dislocations, cracks may form to release strain energy.[8] In Fig. 4.26 an example is shown. In this case, micro-cracks have formed in a bulk mercury indium telluride crystal upon incorporation of residual stress and thermal stress during cooling of the material from growth temperature (about 1000 K) to room temperature. See also Fig. 12.19 for micro-cracks in an epitaxial layer.

[8] We note that in elasticity theory a *continuous* deformation is assumed. Obviously the separation (fracture) into two unstrained blocks is the lowest strain energy state of a stressed piece of material.

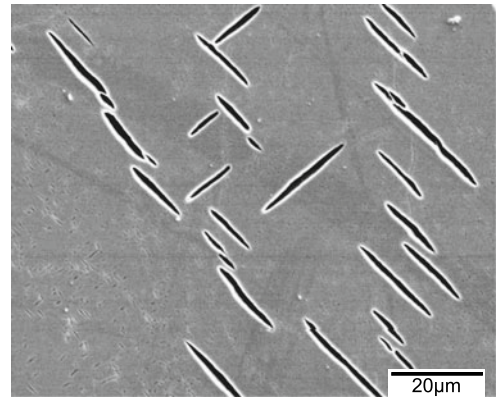

Fig. 4.26 Micro-cracks in a mercury indium telluride crystal. Adapted from [344]

4.4.2 Stacking Faults

The ideal stacking of (111) planes in the zincblende structure, ABCABC. . ., can be disturbed in various ways and creates area defects. If one plane is missing, i.e. the stacking is ABC*AC*ABC, an *intrinsic* stacking fault is present. If an additional plane is present, the defect is called an *extrinsic* stacking fault, i.e. ABCAB*A*CABC. An extended stacking fault in which the order of stacking is reversed is called a twin lamella, e.g. ABCABC*BAC B*ABCABC. If two regions have inverted stacking order they are called twins and their joint interface is called a twin boundary, e.g. . . .ABCABCAB*C*BACBACBA. . . (Fig. 4.29). The various types of stacking faults are shown in Fig. 4.27. In Fig. 4.28 a cross-sectional image of stacking faults in GaAs on Si is shown. They block each other and thus partially annihilate with increasing thickness.

A stacking fault is bounded by two partial dislocations (Sect. 4.3.1.5) formed by the dissociation of a perfect dislocation. A full (or *perfect*) dislocation with Burger's vector $a/2[110]$ in a III–V compound is dissociated into two Shockley partials according to (4.22) [348]. Since the dislocation energy is proportional to $|\mathbf{b}|^2$, the dissociation is energetically favored (see Sect. 4.3.1.5).

The stacking-fault energy in pure silicon is $\gamma = 47\,\mathrm{mJ\,m^{-2}}$ [349]. A similar value is found for Ge, $\gamma = 60\,\mathrm{mJ\,m^{-2}}$ [350] and undoped GaAs, $\gamma = 45\,\mathrm{mJ\,m^{-2}}$ [351]. In diamond a much larger value is found, $\gamma = 285\,\mathrm{mJ\,m^{-2}}$ [352]. Impurity incorporation typically reduces the stacking fault energy. The systematics of stacking fault energy for various III–V and II–VI compounds has been discussed [185, 353, 354]. It can be correlated with the s-parameter (2.11) as depicted in Fig. 4.30.

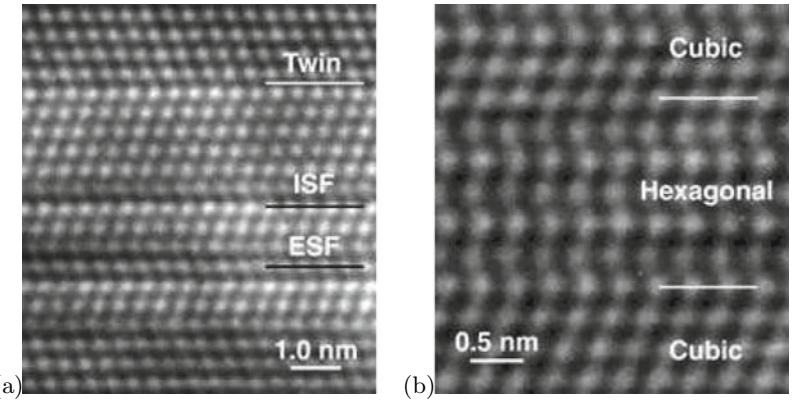

Fig. 4.27 HRTEM images of **a** thin-film silicon with intrinsic (labeled 'ISF') and extrinsic ('ESF') stacking faults and twin boundary ('Twin'). **b** Six monolayer thick hexagonal (wurtzite) CdTe layer in cubic (zincblende) CdTe. Stacking order (from bottom to top) is: ABCABABABABC. . . Reprinted with permission from [345]

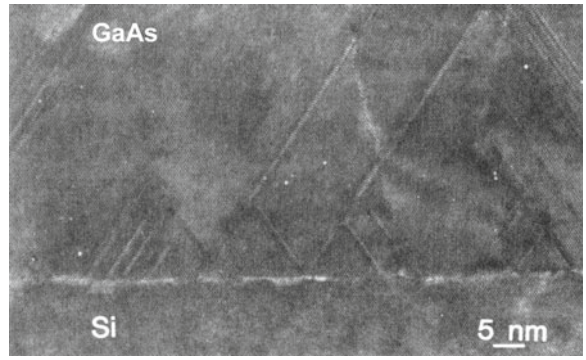

Fig. 4.28 Cross-sectional TEM image showing stacking faults in heteroepitaxial GaAs on Si. Adapted from [346]

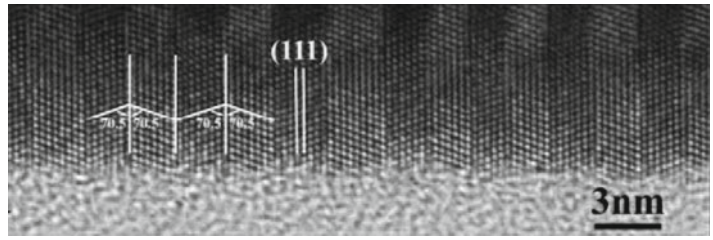

Fig. 4.29 High resolution TEM image of ZnS nanowire exhibiting periodical twin structures. Adapted from [347]

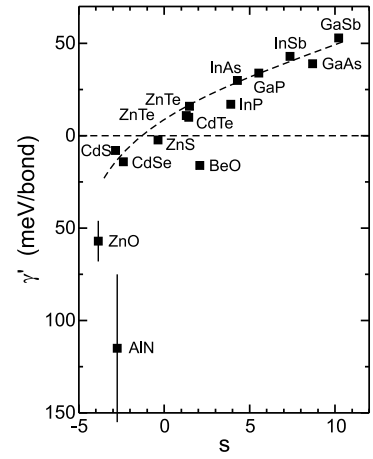

Fig. 4.30 Reduced stacking fault energy (stacking fault energy per bond) γ' for various compound semiconductors plotted as a function of the s-parameter. *Dashed line* is guide to the eye. Data from [185]

4.4.3 Grain Boundaries

The boundaries of crystal grains are called *grain boundaries*. They are defined by five parameters, three rotation angles (e.g. Euler angles) to describe how the orientation of grain II results from grain I and two parameters to define the boundary plane of the two grains in the coordinate system of reference grain I.

Such defects can have a large impact on the electric properties. They can collect point defects and impurities, act as barriers for transport (Sect. 8.3.8) or as carrier sinks due to (nonradiative) recombination. Details of their structure and properties can be found in [355, 356]. The two crystal grains meet each other with a relative tilt and/or twist. The situation is shown schematically in Fig. 4.31a for a small angle between the two crystals. A periodic pattern of dislocations forms at the interface that is called a small-angle grain boundary (SAGB) (Fig. 4.31b). In Fig. 4.32, experimental results for pure

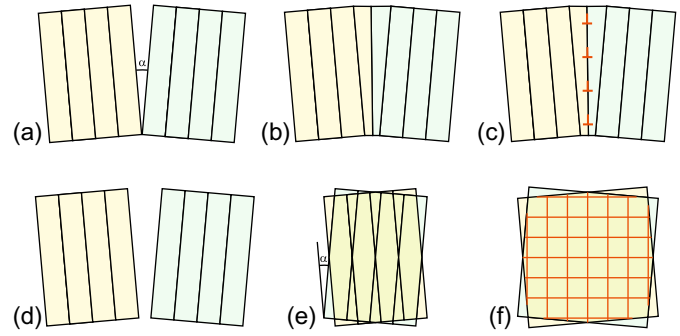

Fig. 4.31 Schemes of **a–c** pure tilt and **d–f** pure twist boundary, dislocation formation in (**c**) pure tilt and **f** twist boundaries

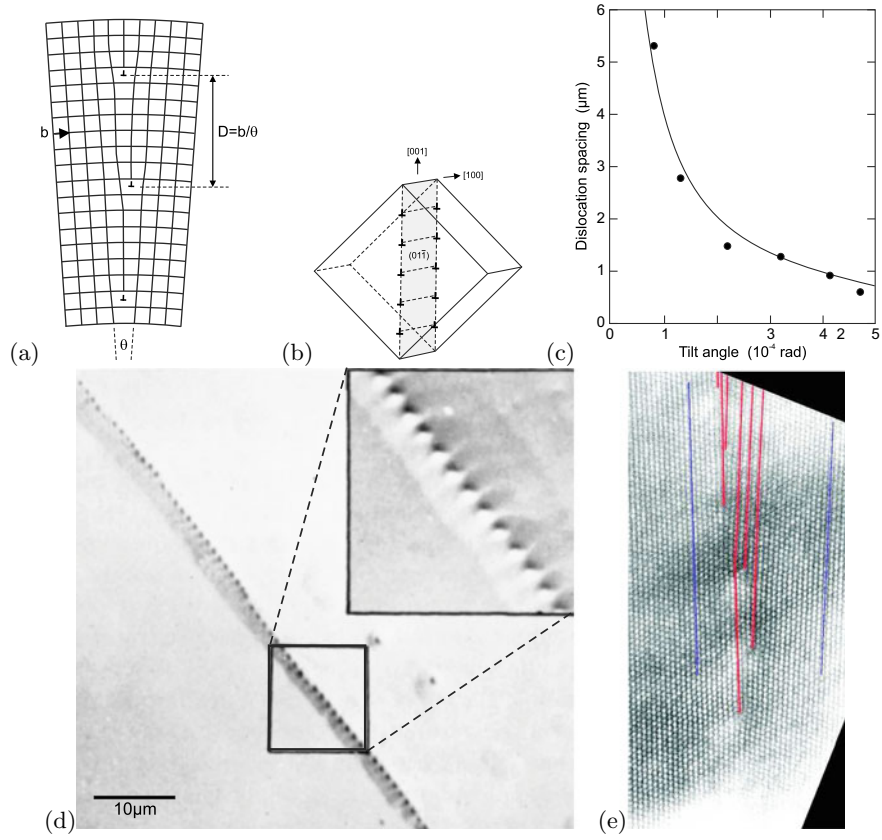

Fig. 4.32 **a** Scheme of a small-angle (pure tilt) grain boundary. **b** Model of edge dislocations in a {110} plane in Ge. **c** Relation of dislocation distance d and tilt angle θ for various small-angle grain boundaries in Ge. *Solid line* is relation $d = 4.0 \times 10^{-8}/\theta$. **d** Optical image of an etched (CP–4 etch) Ge sample with a small-angle grain boundary. Adapted from [359]. **e** HRTEM image of a small-angle grain boundary in Si with dislocations highlighted. From [360]

tilt SAGB are shown. The dislocation spacing is inversely proportional to the tilt angle θ. An image of a twist SAGB is shown in Fig. 4.33.

Special large angle boundaries possess (for a certain angle) a *coincident site lattice* (CSL). Some of these grain boundaries have a low energy and are thus commonly observed. The ratio of lattice points of the CSL and the lattice unit cell is an odd integer number n; the corresponding grain boundary is then labeled Σn. SAGB are also termed $\Sigma 1$. $\Sigma 3$ grain boundaries are always twin boundaries. An

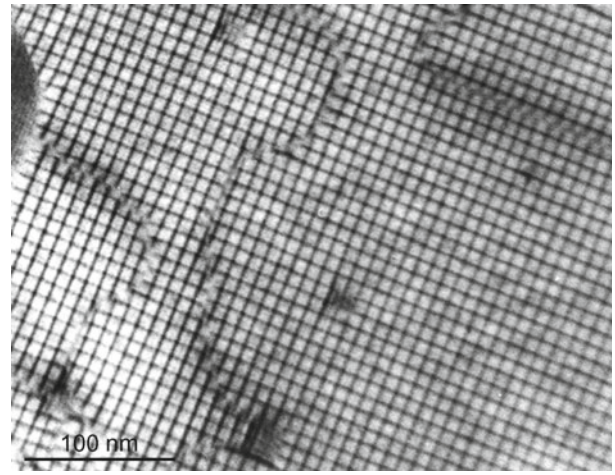

Fig. 4.33 Bright-field TEM image of pure twist boundary with network of pure twist dislocations fabricated by wafer bonding of two Si (001) surfaces with a relative twist. Adapted from [361]

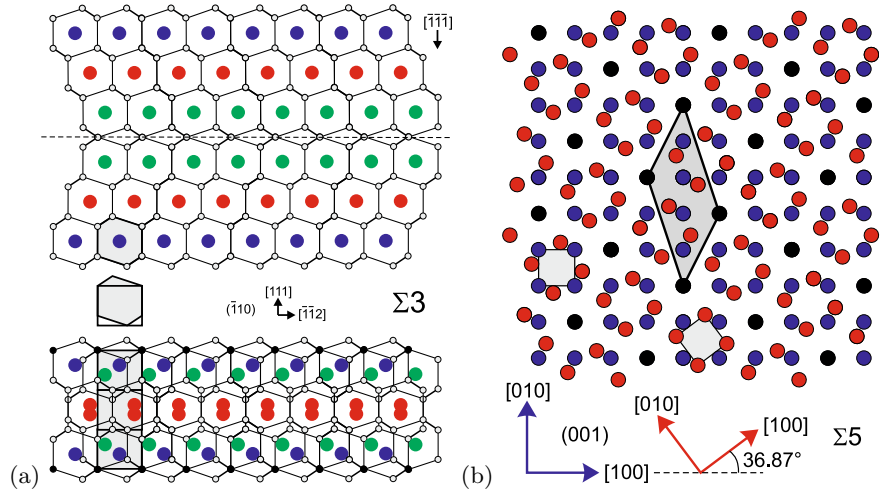

Fig. 4.34 **a** Schematic of Σ3 (111) twin boundary in a diamond or zincblende structure (cmp. Fig. 4.29). The grain boundary is marked by a *dashed line* shown in side-view. The hexagonal and rectangular *grey boxes* have the same area. The lattice points of the coincident site lattice (CSL) are shown with *black circles* in the lower part of the figure. The unit cell of the CSL has three times the volume of the unit cell of the fcc lattice. **b** Schematic of a Σ5 (001) grain boundary in a (simple) cubic crystal shown in plane-view. The *blue* and the *red* lattice are rotated by 36.86°, the lattice points of the CSL are shown in *black*. The unit cell of the CSL lattice (*dark grey*) has five times the volume of the cubic unit cell (*light grey*)

example with (111) grain boundary is schematically shown in an example in Fig. 4.34a. A Σ3 (twin) boundary in silicon with {112} grain boundary [357, 358] is depicted in Fig. 4.35 together with the atomic arrangement of the grain boundary itself. A Σ5 (001) grain boundary is schematically shown in Fig. 4.34b; the special angle is $\theta = \arctan 3/4 \approx 36.87°$.

Real grain boundaries may not be flat, contain impurities or precipitates and even consist of a thin amorphous layer.

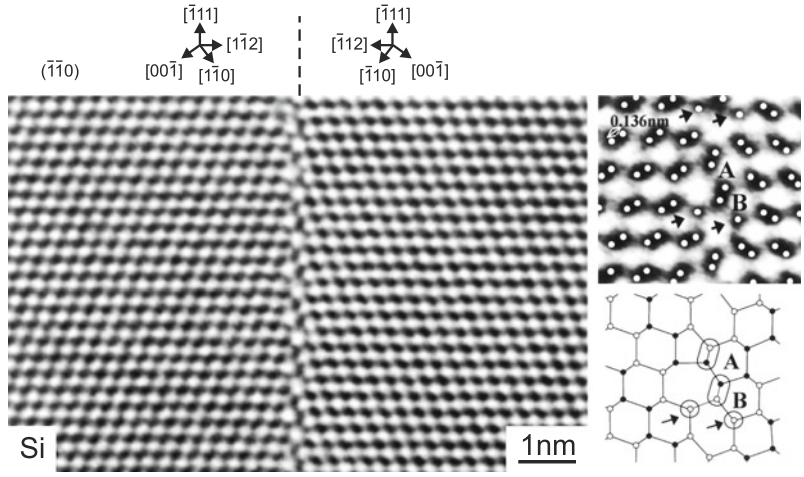

Fig. 4.35 TEM images in two magnifications of a Σ3 {112} boundary in silicon together with a schematic of the atomic arrangement. Adapted from [358]

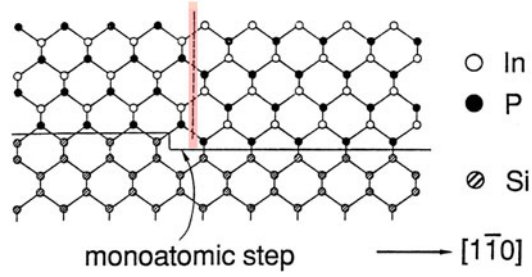

Fig. 4.36 Monoatomic step on the Si (001) surface and subsequent formation of an antiphase boundary in InP (zincblende)

4.4.4 Antiphase and Inversion Domains

Antiphase domains occur when one part of the crystal is shifted with respect to another by an antiphase vector **p**. This does not form a twin. If the polar direction changes between two domains they are called inversion domains.

In the zincblende structure the [110] and [$\bar{1}$10] directions are not equivalent. In one case there is a Zn-S lattice and in the other a S-Zn lattice. Both lattices vary by a 90° rotation or an inversion operation (which is not a symmetry operation of the zincblende crystal). If, e.g., a zincblende crystal is grown on a Si surface with monoatomic steps (Fig. 4.36, cmp. Fig. 11.6), adjoint regions have a different phase; they are called antiphase domains (APD). The antiphase vector is (0, 0, 1) $a_0/4$. At the boundaries a two-dimensional defect, an antiphase domain boundary, develops. The APD boundary contains bonds between identical atom species. In Fig. 4.37, intertwining APD boundaries are shown on the surface of InP layers on Si. The antiphase domains can be visualized with an anisotropic etch.

In Fig. 4.38a, inversion domains in iron-doped ZnO are shown. Between domains the direction of the *c*-axis is reversed. The iron is found preferentially in the inversion domain boundary (IDB) (Fig. 4.38b) and plays an important role in its formation [364, 365].

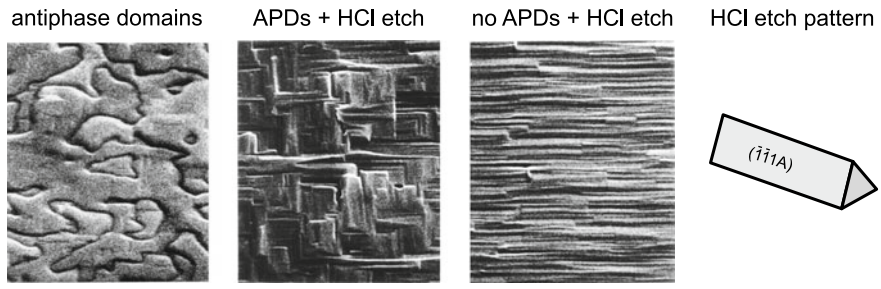

Fig. 4.37 Antiphase domains in InP on Si. HCl etchs InP anisotropically and prepares (111)A planes. The etch patterns of layers with (without) APDs are cross-hatched (linear). Adapted from [362]

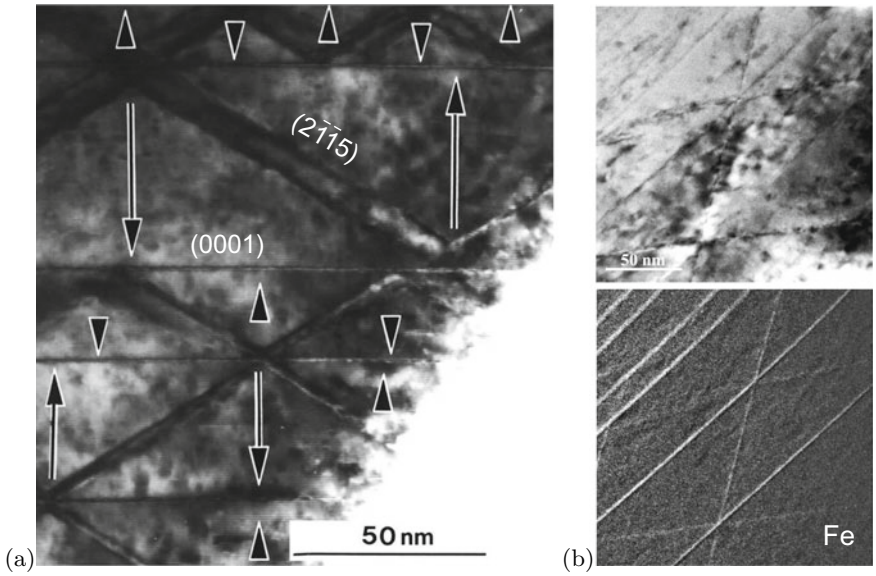

Fig. 4.38 Transmission electron microscopy of inversion domains in ZnO:Fe. **a** Inversion domains in iron-doped ZnO ($ZnO:Fe_2O_3$ = 100:1). *Arrows* denote the orientation of the *c*-axis in the respective domains. **b** *Top*: bright field TEM, *bottom* Fe distribution from energy-filtered image. Adapted from [363]

4.5 Disorder

Disorder is a general term for deviations from the ideal structure on a microscopic scale. Apart from the various structural defects discussed in the previous chapters, further examples of disorder are

- The presence of various isotopes of an element. This introduces disorder with regard to the mass of the atoms and impacts mostly phonon properties (see Fig. 8.28).
- The occupation of lattice sites in alloys (Sect. 3.7) ranging from a random alloy, clustering to (partially) ordered phases.
- The (unavoidable) thermal and zero-point motion of atoms around their equilibrium position.

Chapter 5
Mechanical Properties

If you want to find the secrets of the universe, think in terms of energy, frequency and vibration.

N. Tesla

Abstract Lattice vibrations and phonons are treated with one-dimensional models and examples for real phonon dispersions for several semiconductors including phonons in alloys and disordered materials are given. Then the theory of linear elasticity and its application to semiconductors with regard to epitaxial strain, substrate bending and sheet-scrolling is given. Finally plastic relaxation effects such as critical thickness and wafer breakage are discussed.

5.1 Introduction

The atoms making up the solid have an average position from which they can deviate since they are elastically bonded. The typical atomic interaction potential looks like the one shown in Fig. 2.1. The atoms thus perform a vibrational motion (including zero point fluctuations) and the solid is elastic. The potential is essentially asymmetric, being steeper for small distances due to quantum-mechanical overlap of orbitals. However, for small amplitudes around the minimum a harmonic oscillator can be assumed (harmonic approximation). Beyond the elastic regime, plastic deformation occurs such as generation of defects, e.g. dislocations. Eventually also the crystal can break.

5.2 Lattice Vibrations

In the following we will discuss the dispersion relations for lattice vibrations, i.e. the connection between the frequency ν (or energy $h\nu = \hbar\omega$) of the wave and its wavelength λ (or k-vector $k = 2\pi/\lambda$). Acoustic and optical vibrations are introduced in one-dimensional models. A detailed treatment of the physics of lattice vibrations is given in [366].

M. Grundmann, *The Physics of Semiconductors*, Graduate Texts in Physics,
https://doi.org/10.1007/978-3-030-51569-0_5

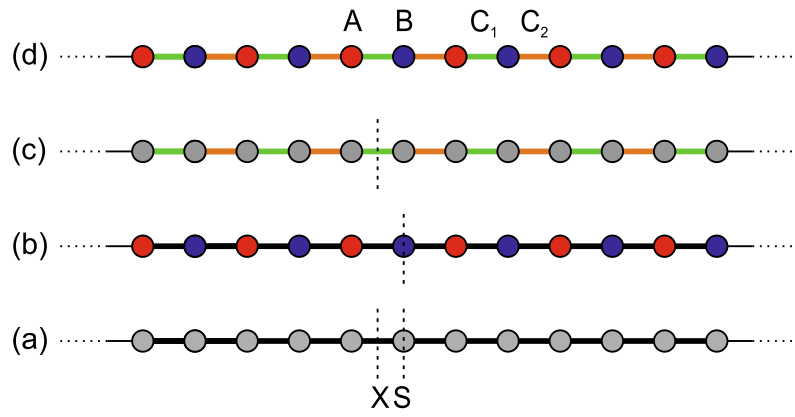

Fig. 5.1 Schematic linear chain models with **a** same masses and spring constants, **b** different masses and same spring constants, **c** same masses and different spring constants, **d** different masses and different spring constants. Mirror operation $\boldsymbol{X}$ ($\boldsymbol{S}$) exchanges the A–B atoms in the dimer (the spring constants)

5.2.1 Monoatomic Linear Chain

The essential physics of lattice vibrations can best be seen from a one-dimensional model that is called the linear chain model. The mechanical vibrations will also be called *phonons*, although technically this term is reserved for the quantized lattice vibrations resulting from the quantum-mechanical treatment.

In the monoatomic linear chain the atoms of mass M are positioned along a line (x-axis) with a period (lattice constant) a at the positions $x_{n_0} = na$. This represents a one-dimensional Bravais lattice. The Brillouin zone of this system is $[-\pi/a, \pi/a]$.

The atoms will interact with a harmonic potential, i.e. the energy is proportional to the displacement $u_n = x_n - x_{n_0}$ to the second power. This can be thought of as if the atoms are coupled by massless springs (Fig. 5.1a). The total (mechanical) energy of the system is then:

$$U = \frac{1}{2} C \sum_n (u_n - u_{n+1})^2 \,. \tag{5.1}$$

The model assumes that the mass points are connected via massless, ideal springs with a spring constant C. If $\phi(x)$ is the interaction energy between two atoms, C is given by $C = \phi''(a)$. Again, the harmonic approximation is only valid for small displacements, i.e. $u_n \ll a$. The displacement of the atoms can be along the chain (longitudinal wave) or perpendicular to the chain (transverse wave), see Fig. 5.2. We note that for these two types of waves the elastic constant C must not be the same.

When the sum in (5.1) has a finite number of terms ($n = 0, \ldots, N-1$), the boundary conditions have to be considered. There are typically two possibilities: The boundary atoms are fixed, i.e. $u_0 = u_{N-1} = 0$, the boundary conditions are periodic (Born–von Karman), i.e. $u_i = u_{N+i}$. If $N \gg 1$, the boundary conditions play no significant role anyway, thus those with the greatest ease for subsequent math are chosen. In solid-state physics typically periodic boundary conditions are used. Boundary phenomena, such as at surfaces, are then treated separately (see Sect. 11.6.1).

The equations of motion derived from (5.1) are

$$M\ddot{u}_n = F_n = -\frac{\partial U}{\partial u_n} = -C\,(2u_n - u_{n-1} - u_{n+1}) \,. \tag{5.2}$$

We solve for solutions that are periodic in time (harmonic waves), i.e. $u_n(x,t) = u_n \exp(-\mathrm{i}\,\omega t)$. Then the time derivative can be executed immediately as $\ddot{u}_n = -\omega^2 u_n$ and we obtain:

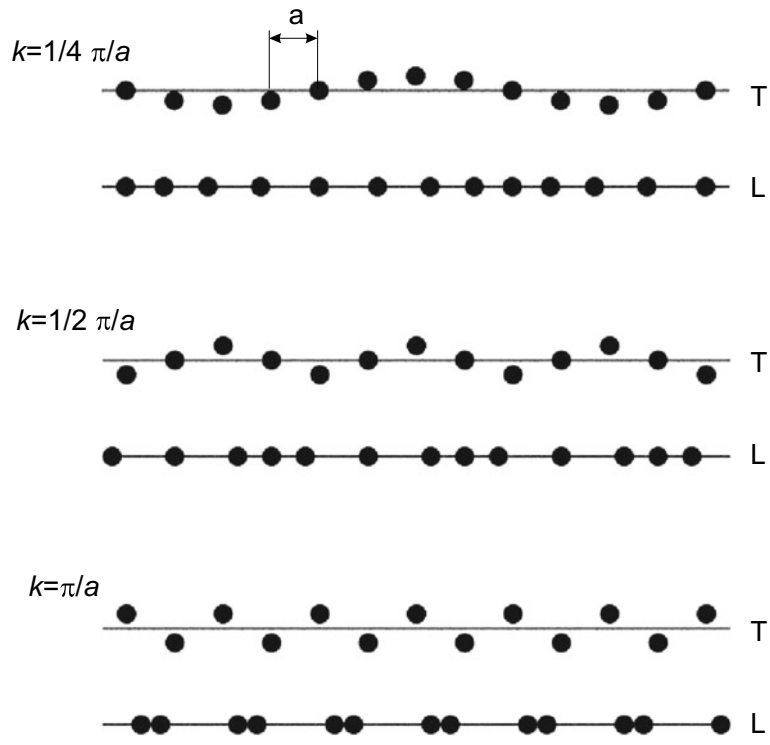

Fig. 5.2 Visualization of transverse ('T') and longitudinal ('L') waves in a linear monoatomic chain at different wavevectors

$$M\omega^2 u_n = C\,(2u_n - u_{n-1} - u_{n+1})\ . \tag{5.3}$$

If, also, the solution is periodic in space, i.e. is a (one-dimensional) plane wave, i.e. $u_n(x,t) = v_0 \exp(\mathrm{i}(kx - \omega t))$ with $x = n\,a$, we find from the periodic boundary condition $\exp(\mathrm{i}kNa) = 1$ and thus

$$k = \frac{2\,\pi}{a}\,\frac{n}{N},\ n \in \mathbf{N}\ . \tag{5.4}$$

It is important that, when k is altered by a reciprocal space vector, i.e. $k' = k + 2\pi n/a$, the displacements u_n are unaffected. This property means that there are only N values for k that generate independent solutions. These can be chosen as $k = -\pi/a, \ldots, \pi/a$, so that k lies in the Brillouin zone of the lattice (Fig. 5.3). Since the properties are periodic with the Brillouin zone, the k-values can be imagined being on a circle as visualized in Fig. 5.3; the angle $\phi = k\,a$ run from 0 to 2π or from $-\pi$ to $+\pi$ as you like.

In the Brillouin zone there is a total number of N k-values, i.e. one for each lattice point. The distance between adjacent k-values is

$$\frac{2\pi}{Na} = \frac{2\pi}{L}\ , \tag{5.5}$$

L being the lateral extension of the system.

The displacements at the lattice points n and $n + m$ are now related to each other via

$$\begin{aligned} u_{n+m} &= v_0\ \exp(\mathrm{i}k\,(n+m)\,a) \\ &= v_0\ \exp(\mathrm{i}kna)\ \exp(\mathrm{i}\,k\,m\,a) = \exp(\mathrm{i}\,k\,m\,a)\,u_n\ . \end{aligned} \tag{5.6}$$

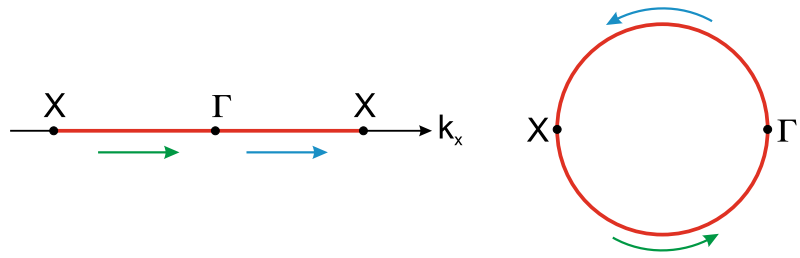

Fig. 5.3 Brillouin zone of a one-dimensional lattice from $-\pi/a$ to $+\pi/a$ and mapping to a circle with angles from $-\pi$ over 0 (at Γ) to $+\pi$

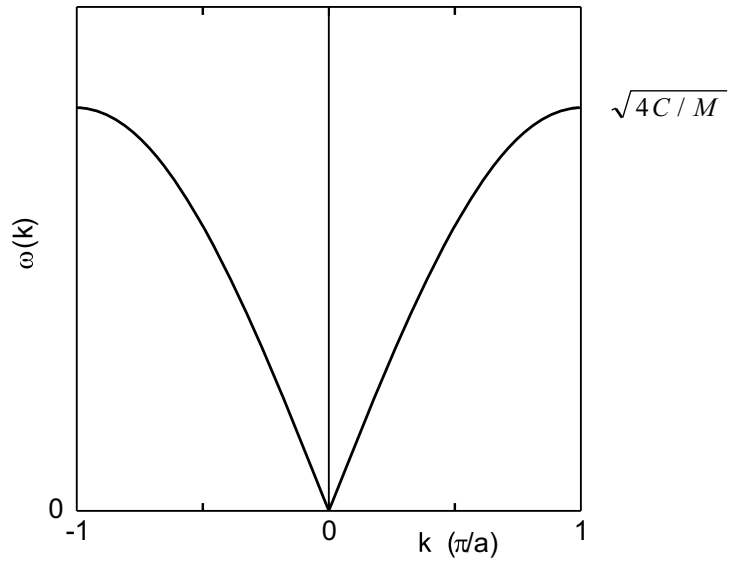

Fig. 5.4 Dispersion relation for a monoatomic linear chain

Thus, the equation of motion (5.3) reads

$$M\omega^2 u_n = C\left[2 - \exp(-\mathrm{i}\,k\,a) - \exp(\mathrm{i}\,k\,a)\right] u_n \,. \tag{5.7}$$

Using the identity $\exp(\mathrm{i}\,ka) + \exp(-\mathrm{i}\,ka) = 2\cos(k\,a)$, we find the dispersion relation of the monoatomic linear chain (Fig. 5.4):

$$\omega^2(k) = \frac{4C}{M}\,\frac{1-\cos(k\,a)}{2} = \frac{4C}{M}\,\sin^2\left(\frac{k\,a}{2}\right) \,. \tag{5.8}$$

The solutions describe plane waves that propagate in the crystal with a phase velocity $c = \omega/k$ and a group velocity $v_\mathrm{g} = \mathrm{d}\omega/\mathrm{d}k$,

$$v_\mathrm{g} = \pm\sqrt{\frac{4C}{M}}\,\frac{a}{2}\,\cos\left(\frac{|k|\,a}{2}\right) \,. \tag{5.9}$$

In the vicinity of the Γ point, i.e. $k \ll \pi/a$ the dispersion relation is linear in k

$$\omega(k) = a\sqrt{\frac{C}{M}}\,|k| \,. \tag{5.10}$$

We are used to such linear relations for sound (and also light) waves. The phase and group velocity are the same and do not depend on k. Thus, such solutions are called *acoustic*. The sound velocity of the medium ($v_g(k = 0)$ in (5.9)) is given by $v_s = a\sqrt{C/M}$.

It is characteristic of the non-continuous medium that for k approaching the boundary of the Brillouin zone, the behavior of the wave is altered. For $k = \pi/a$ the wavelength is just $\lambda = 2\pi/k = 2a$, and thus samples the granularity of the medium. The maximum phonon frequency ω_m is

$$\omega_m = \sqrt{\frac{4C}{M}} \,. \tag{5.11}$$

The group velocity is zero at the zone boundary, thus a standing wave is present.

Since the force constants of the longitudinal and transverse waves can be different, the dispersion relations are different. The transverse branch of the dispersion relation is two-fold degenerate when the two directions perpendicular to $\boldsymbol{k}$ are equivalent.

5.2.2 Diatomic Linear Chain

Now we consider the case that the system is made up from two different kinds of atoms (Fig. 5.5). This will be a model for semiconductors with a diatomic base, such as zincblende. We note that the diamond structure also needs to be modeled in this way, although both atoms in the base are the same.

The lattice will be the same and the lattice constant will be a. Alternating atoms of sort 1 and 2 with a relative distance of $a/2$ are on the chain. The displacements of the two atoms are labeled u_n^1 and u_n^2, both belonging to the lattice point n. The atoms have the masses M_1 and M_2. The force constants are C_1 (for the 1–2 bond within the base) and C_2 (for the 2–1 bond between different bases) (Fig. 5.1d).

The total energy of the system is then given as

$$U = \frac{1}{2} C_1 \sum_n \left(u_n^1 - u_n^2\right)^2 + \frac{1}{2} C_2 \sum_n \left(u_n^2 - u_{n+1}^1\right)^2 \,. \tag{5.12}$$

The equations of motion are

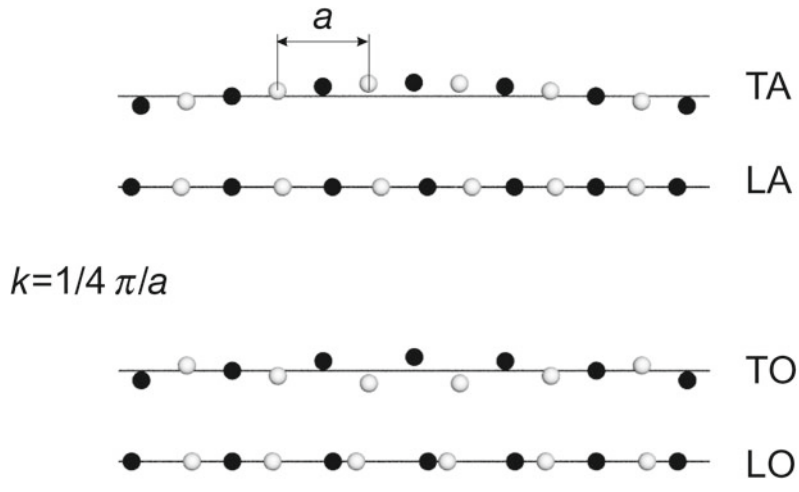

Fig. 5.5 Visualization of acoustic and optical waves in a diatomic linear chain

$$M_1\,\ddot{u}_n^1 = -C_1\left(u_n^1 - u_n^2\right) - C_2\left(u_n^1 - u_{n-1}^2\right) \tag{5.13a}$$
$$M_2\,\ddot{u}_n^2 = -C_1\left(u_n^2 - u_n^1\right) - C_2\left(u_n^2 - u_{n+1}^1\right)\ . \tag{5.13b}$$

With the plane-wave ansatz $u_n^1(x,t) = v_1 \exp(\mathrm{i}(kna - \omega t))$ and $u_n^2(x,t) = v_2 \exp(\mathrm{i}(kna - \omega t))$ and periodic boundary conditions we find

$$0 = -M_1\,\omega^2\,v_1 + C_1\,(v_1 - v_2) + C_2\,[v_1 - v_2\,\exp(-\mathrm{i}ka)] \tag{5.14a}$$
$$0 = -M_2\,\omega^2\,v_2 + C_1\,(v_2 - v_1) + C_2\,[v_2 - v_1\,\exp(\mathrm{i}ka)]\ . \tag{5.14b}$$

These equations for v_1 and v_2 can only be solved nontrivially if the determinant vanishes, i.e.

$$\begin{aligned} 0 &= \begin{vmatrix} M_1\,\omega^2 - (C_1 + C_2) & C_1 + \mathrm{e}^{-\mathrm{i}ka}\,C_2 \\ C_1 + \mathrm{e}^{\mathrm{i}ka}\,C_2 & M_2\,\omega^2 - (C_1 + C_2) \end{vmatrix} \\ &= M_1 M_2\,\omega^4 - (M_1 + M_2)(C_1 + C_2)\,\omega^2 + 2C_1C_2\,[1 - \cos(k\,a)]\ . \end{aligned} \tag{5.15}$$

Using the substitutions $C_+ = (C_1 + C_2)/2$, $C_\times = \sqrt{C_1\,C_2}$, the arithmetic and geometrical averages, and accordingly for M_+ and $M_\times$, the solution is

$$\omega_\pm^2(k) = \frac{\omega_{\max}^2}{2}\left[1 \pm \sqrt{1 - \gamma^2\,\sin^2(k\,a/2)}\right]\ , \tag{5.16}$$

with

$$0 < \gamma = \frac{C_\times\,M_\times}{C_+ M_+} \le 1\ , \tag{5.17}$$

and the maximum frequency $\omega_{\max}$ (for the upper branch ('+' sign in (5.16)) at the zone center ($k = 0$),

$$\omega_{\max} = \sqrt{\frac{4C_\times}{\gamma\,M_\times}} = 2\sqrt{\frac{C_+\,M_+}{M_\times^2}}\ . \tag{5.18}$$

The dispersion relation, as shown in Fig. 5.6, now has (for each longitudinal and transverse mode) two branches. The lower branch ('−' sign in (5.16)) is related to the acoustic mode; neighboring atoms have the same phase for $k = 0$ (Fig. 5.5). For the acoustic mode $\omega = 0$ at the Γ point and the frequency increases towards the zone boundary.

The upper branch is called the optical mode (since it can interact strongly with light, see Sect. 9.10) and neighboring atoms have opposite phase at $k = 0$. In the vicinity of the Γ point, the dispersion of optical phonons is parabolic with negative curvature:

$$\omega(k) \cong \omega_{\max}\left[1 - \frac{1}{2}\left(\frac{\gamma}{4}\right)^2 (k\,a)^2\right]\ . \tag{5.19}$$

Thus, four different vibrations exist that are labeled TA, LA, TO, and LO. Both the TA and TO branches are degenerate.

At the zone boundary (X point) a frequency gap exists (for $\gamma \neq 1$). The gap center is at

$$\overline{\omega_{\mathrm{X}}} = \frac{\omega_{\max}}{\sqrt{2}}\sqrt{\frac{1+\gamma}{2}}\ , \tag{5.20}$$

and the total width of the gap is

$$\Delta\omega_X = \omega_{\max}\sqrt{1-\gamma}\ . \tag{5.21}$$

The group velocity is zero for optical and acoustic phonons at $k = \pm\pi/a$ and for optical phonons at the Γ point.

Usually two special cases are treated explicitly: (i) atoms with equal mass ($M = M_1 = M_2$) and different force constants [367] or (ii) atoms with unequal mass and identical force constants $C = C_1 = C_2$ [368]. For the case $C_1 = C_2$ *and* $M_1 = M_2$, $\gamma = 1$ and thus $\Delta\omega_X = 0$. Then the dispersion relation is the same as for the monoatomic chain, except that the k space has been folded since the actual lattice constant is now $a/2$.

5.2.3 *Mode Patterns and Topological States*

First, we chose $M_1 = M_2$. In this case (Fig. 5.1c), $M_+ = M_\times = M$ and the dispersion relation is

$$\omega_\pm^2 = \frac{2C_+}{M}\left[1 \pm \sqrt{1 - \frac{C_\times^2}{C_+^2}\,\sin^2(k\,a/2)}\right]\ . \tag{5.22}$$

The frequencies for the lower (acoustic) and upper (optical) branch at the zone boundary $k = \pm\pi/a$ are

$$\omega_\pm^2(X) = \frac{C_1 + C_2 \pm |C_1 - C_2|}{M}\ , \tag{5.23}$$

or $\omega_-(X) = \sqrt{2\min(C_1, C_2)/M}$ and $\omega_+(X) = \sqrt{2\max(C_1, C_2)/M}$. The softer spring determines the top of the lower branch, the harder spring determines the bottom of the upper branch.

The eigenstates for the lower and upper branch (upper sign for the upper band) are given by (without the $\exp[\imath\,(k\,na - \omega\,t)]$ periodicity in time and space),

$$\boldsymbol{v}_\pm(k) = \begin{pmatrix} v_{\pm,1}(k) \\ v_{\pm,2}(k) \end{pmatrix} = \begin{pmatrix} 1 \\ \mp\frac{C_1 + C_2\,\exp(\imath\,k\,a)}{\sqrt{C_1^2 + C_2^2 + 2\,C_1\,C_2\,\cos k\,a}} \end{pmatrix}\ . \tag{5.24}$$

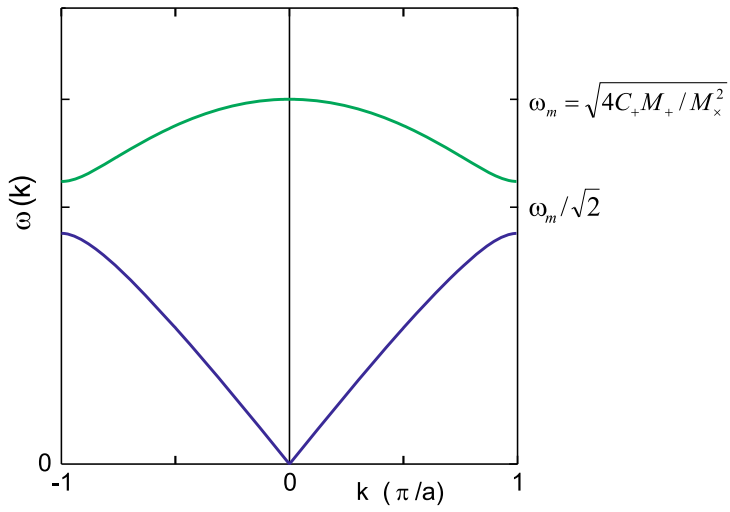

Fig. 5.6 Dispersion relation for a diatomic linear chain with acoustic (*blue*) and optical (*green*) branch

In the zone center, we find $v_{-,2}(\Gamma) = +v_{-,1}(\Gamma)$ in the lower branch and $v_{+,2}(\Gamma) = -v_{+,1}(\Gamma)$ in the upper branch. Thus the two atoms in the base oscillate in phase (out of phase) for long wavelengths in the acoustic (optical) branch as said before.

At the border of the Brillouin zone, $k = \pm\pi/a$ (and for $C_1 \neq C_2$),

$$v_{-,2}(X) = +v_{-,1}(X)\,\mathrm{sgn}(C_1 - C_2) \tag{5.25}$$

$$v_{+,2}(X) = -v_{+,1}(X)\,\mathrm{sgn}(C_1 - C_2)\ . \tag{5.26}$$

Now, the relative phase of the two atoms in the base depends on the ratio of $C_2/C_1 \gtrless 1$! For $C_1 > C_2$, the top of the acoustic branch has $v_{-,2}(X) = v_{-,1}(X)$ and thus the same as at the Γ-point, preserving the 'acoustic' nature of the band. For $C_2 > C_1$, however, $v_{-,2}(X) = -v_{-,1}(X)$ and thus out-of-phase, resembling an optical mode. For the upper branch the situation is vice versa.

The situation can be visualized by plotting the relative phase of v_2 and v_1, as expressed by

$$\delta\phi_{\pm}(k) = \arg\left[\frac{v_{\pm,2}(k)}{v_{\pm,1}(k)}\right]\ , \tag{5.27}$$

for the two cases $C_2/C_1 \gtrless 1$ (note that $|v_2| = 1$ for all cases) for the lower branch in Fig. 5.7. The dispersions for the two cases $C_2/C_1 \gtrless 1$ with the phase $\delta\phi_{\pm}$ depicted as color are compared in Fig. 5.8.

For all cases of $C_2/C_1 > 1$, $v_{\pm,2}(\pi/a) - v_{\pm,2}(-\pi/a) = 0$. For all cases of $C_2/C_1 < 1$, $v_{\pm,2}(\pi/a) - v_{\pm,2}(-\pi/a) = 2\,\pi$. Thus this number is a 'topological invariant' since it cannot be changed by smooth changes of the system, i.e. small and slow variations of C_1/C_2, unless one goes through the gapless state ($C_1/C_2 = 1$). The case $C_1 = C_2$, $\delta\phi_- = k\,a/2$ and $\delta\phi_+ = \pi + k\,a/2$ is shown as dotted lines in Fig. 5.7. It should be noted that the phase difference in (5.27) and the curves in Fig. 5.7 are independent of the mass ratio.

Generally, the symmetry of a mode $\boldsymbol{v}$ with respect to the operation $\boldsymbol{X}$ that exchanges A- and B-sites,

$$\boldsymbol{X}\,\boldsymbol{v} = \boldsymbol{X}\begin{pmatrix} v_1 \\ v_2 \end{pmatrix} = \begin{pmatrix} v_2 \\ v_1 \end{pmatrix} = \exp(\imath\,\delta\phi)\begin{pmatrix} v_1 \\ v_2 \end{pmatrix}\ , \tag{5.28}$$

can be expressed by the phase $\delta\phi$. $\boldsymbol{X}$ is a unitary transformation since $\boldsymbol{X}^{\mathrm{H}}\,\boldsymbol{X} = \mathbf{1}$. For a well defined parity-like symmetry, we demand $\boldsymbol{X}^2 = \mathbf{1}$; it is present for a phase factor of 1 ($\delta = 0$, positive

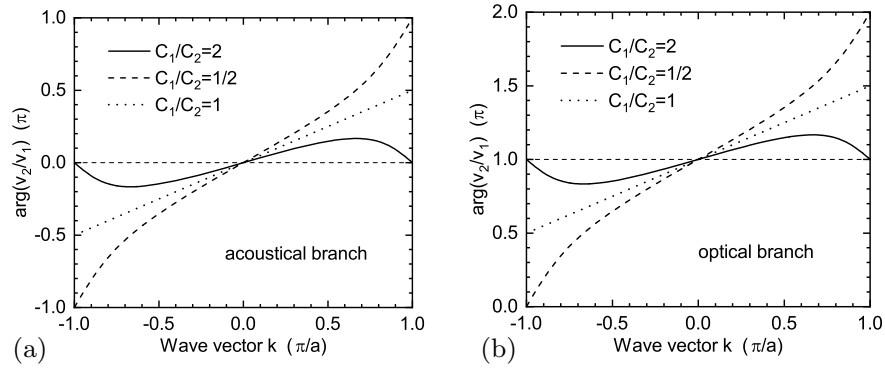

Fig. 5.7 Relative phase of the B-site to the A-site in the **a** lower (acoustic, $\delta\phi_-$) branch and **b** upper (optical, $\delta\phi_+$) branch, expressed by $\arg(v_2/v_1)$ from (5.27). The case $C_1/C_2 = 2$ is shown as *solid line*; the inverted case of $C_1/C/2 = 1/2$ is shown as *dashed line*. The case $C_1 = C_2$ is shown as *dotted lines*

parity) and a phase factor of -1 ($\delta = \pm\pi$, negative parity). In Fig. 5.8b, for the non-trivial phase, the parity changes twice within the Brillouin zone, while for the trivial case it does not. In view of later discussions of electronic band structure we remind the reader that electronic s-states (p-states) have positive (negative) parity.

The phase change summed up when going through the entire Brillouin zone must a multiple of $2\,\pi$ since the physical properties are periodic with the Brillouin zone. The property to calculate for obtaining a proper topological invariant here is the Berry phase [369, 370] γ_n for a branch n with the more general recipe,

$$\gamma_n = \imath \int_{\mathcal{C}} \boldsymbol{v}_{\boldsymbol{n}}^{*} \cdot \left(\frac{\partial}{\partial k} \boldsymbol{v}_{\boldsymbol{n}} \right) \mathrm{d}k \ , \tag{5.29}$$

where $\mathcal{C}$ is a closed loop in parameter space, here it is the integral over the entire Brillouin zone. The integrand is the one-dimensional equivalent to the 'Berry connection'.[1] For the diatomic linear chain, the integral yields

$$\gamma_{\pm} = \begin{cases} 0 & C_2 < C_1 \\ -\pi & C_2 = C_1 \\ -2\,\pi & C_2 > C_1 \end{cases} \ . \tag{5.30}$$

One should think also about the following: The situation for $C_2 > C_1$ means that the A–B inter-dimer spring constant is *larger* than the intra-dimer one. But our choice of unit cell is free and the situation can be thought of differently in terms of B–A dimers where then, for exactly the same physical situation, the inter-dimer spring constant (now C_1) is *smaller* than the intra-dimer one (C_2). Thus, the two bulk situations will not be much different per se and cannot be distinguished, in particular when the A- und B-sites are equivalent (here $M_1 = M_2$). However, when two media with different topology have an interface, edge states develop according to the bulk-boundary correspondence; this will be shown for the DLCM in Sect. 5.2.10.

In the case $C_1 = C_2$ (Fig. 5.1b), $C_+ = C_\times = C$ and the dispersion relation can be simplified to

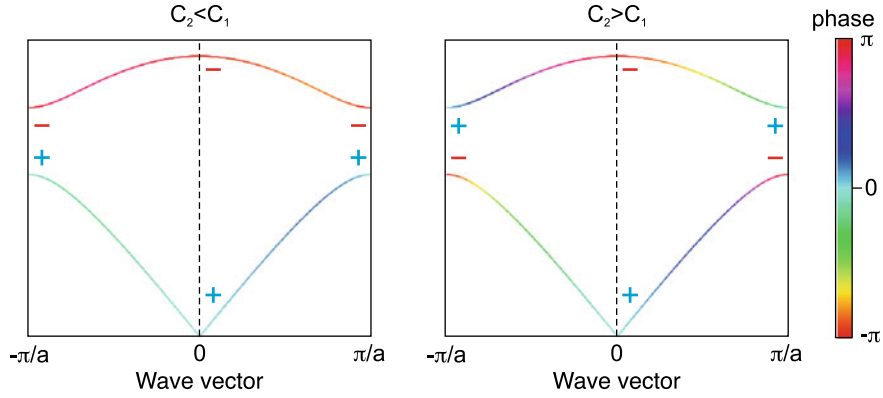

Fig. 5.8 Phonon dispersion with the phase of the wavefunction (relative phase between B- and A-sites) shown in false colors. *Left*: $C_1/C_2 = 2$, *right*: $C_1/C_2 = 1/2$. The parity symmetry of the mode with respect to exchange of A- and B-sites is indicated with '+' (in-phase) and '−' (out-of-phase)

[1] For higher dimensions, the integral over a closed path (or surface) can be replaced via Stokes' theorem with an area (or volume) integral of the Berry flux. Also it is invariant under a 'gauge transformation' where $\boldsymbol{v}_{\boldsymbol{n}}$ is replaced by $\exp(\mathrm{i}\,\theta)\,\boldsymbol{v}_{\boldsymbol{n}}$.

$$\omega_{\pm}^2 = \frac{2\,C\,M_+}{M_\times^2}\left[1 \pm \sqrt{1 - \frac{M_\times^2}{M_+^2}\,\sin^2(k\,a/2)}\right]. \tag{5.31}$$

At the zone boundary the frequencies for the acoustic and the optical branch are, assuming $M_2 < M_1$, $\omega_{X,1} = \sqrt{2C/M_1}$ with $v_2 = 0$ (oscillation of the larger mass) and $\omega_{X,2} = \sqrt{2C/M_2}$ with $v_1 = 0$ (oscillation of the smaller mass), respectively. In the vibrations at the X-point thus only one atom species oscillates, the other does not move. Close to the Γ point, the atoms are in phase in the acoustic branch with $v_2 = v_1$. For the optical branch, the frequency at the Γ point is given by $\omega = \sqrt{2C/M_\mathrm{r}}$ (with the reduced mass $M_\mathrm{r}^{-1} = M_1^{-1} + M_2^{-1} = 2M_+/M_\times^2$) and the amplitude ratio is given by the mass ratio: $v_2/v_1 = -M_1/M_2$, i.e. the atoms are out of phase and the heavier atom has the smaller amplitude.

It should be repeated that the relative phase of v_2 and v_1, as defined in (5.27), is the same for all masses (dotted line in Fig. 5.7). The situation $C_1 = C_2$ is therefore for all masses topologically the same as the gapless state and the gap has different character when due to different spring constants or due to different masses.

Finally, we consider the symmetry classification looking at Fig. 5.1 again. The monoatomic chain has two mirror-like symmetries, indicated by vertical dashed lines; it is symmetric with respect to exchange $\boldsymbol{X}$ of the A- and B-atoms and to the exchange $\boldsymbol{S}$ of the springs. The cases Fig. 5.1b, c preserve only one such symmetry while the general diatomic chain Fig. 5.1d preserves none of them individually but still possesses the so-called chiral symmetry which is the combination $\boldsymbol{X}\,\boldsymbol{S}$. In terms of the 'periodic system' of the CAZ classification of topological systems the diatomic linear chain is a BDI-type system [371] and the topological invariant is, derived from (5.30), an integer of the form, $\gamma/2\pi \in \mathbb{Z}$.

5.2.4 *Lattice Vibrations of a Three-Dimensional Crystal*

When calculations are executed for a three-dimensional crystal with a monoatomic base, there are $3N$ equations of motion. These are transformed to normal coordinates and represent 3 acoustic branches (1 LA phonon mode and 2 TA phonon modes) of the dispersion relation. In a crystal with a base with p

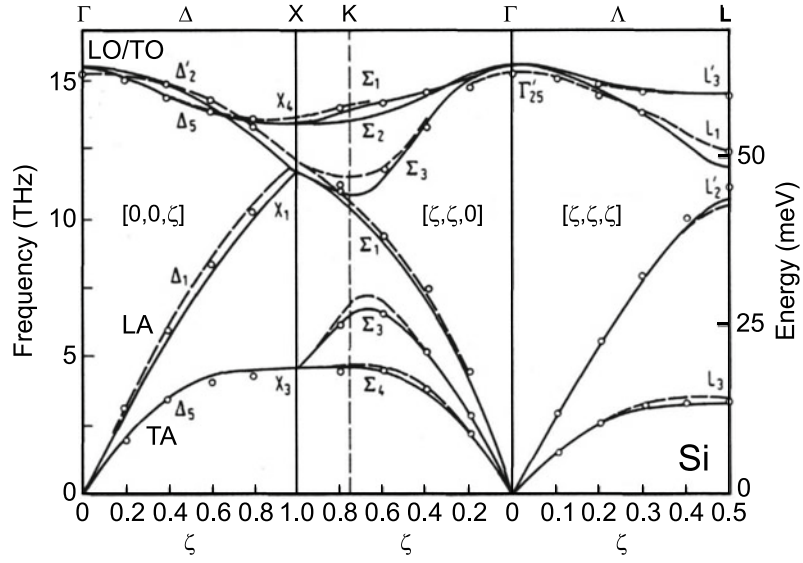

Fig. 5.9 Phonon dispersion in Si, experimental data and theory (*solid lines*: bond charge model, *dashed lines*: valence force field model). Adapted from [164]

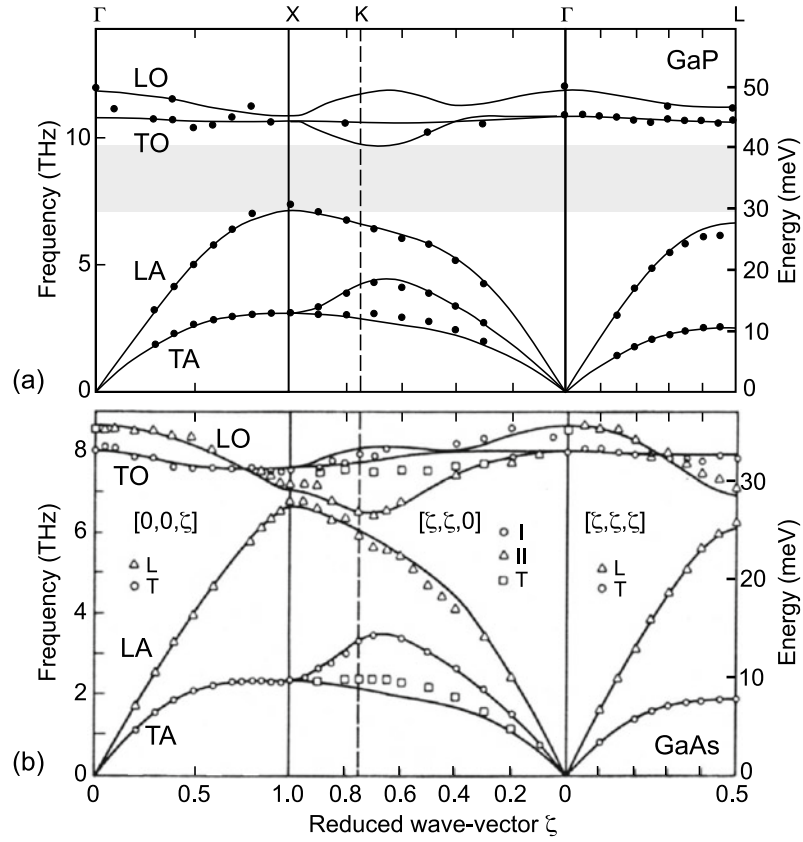

Fig. 5.10 Phonon dispersion in **a** GaP and **b** GaAs. Experimental data (*symbols*) and theory (*solid lines*, 14-parameter shell model). 'L' and 'T' refer to longitudinal and transverse modes, respectively. 'I' and 'II' (along $[\zeta, \zeta, 0]$) are modes whose polarization is in the $(1\bar{1}0)$ plane. The *grey area* in (**a**) denotes the gap between acoustical and optical states. **a** Adapted from [375], **b** Adapted from [373]

atoms, there are also 3 acoustic branches and $3(p-1)$ optical branches. For a diatomic base (as in the zincblende structure) there are 3 optical phonon branches (1 LO phonon mode and 2 TO phonon modes). The total number of modes is $3p$. The dispersion $\omega(\mathbf{k})$ now has to be calculated for all *directions* of $\mathbf{k}$.

In Figs. 5.9 and 5.10, the phonon dispersion in silicon, GaAs and GaP is shown along particular lines in the Brillouin zone (cf. Fig. 3.38). A detailed treatment can be found in [372]. The degeneracy of the LO and TO energies at the Γ point for the covalent group-IV semiconductor is lifted for the III–V semiconductors due to the ionic character of the bond and the macroscopic electric field connected with the long-wavelength LO phonon (see Sect. 9.5). Comparing GaAs [373] and GaP [374], the quite different mass of Ga- and P-atoms ($M_\times/M_+ \approx 0.92$) leads to the formation of a clear gap between the acoustic and optical branches, while for GaAs $M_\times/M_+ \approx 0.9994$ is close to 1 and no gap forms.

We note that the degeneracy of the TA phonon is lifted for propagation along the $\langle 110\rangle$ directions (Σ) because the two transverse directions $\langle 001\rangle$ and $\langle 1\bar{1}0\rangle$ are not equivalent.

In boron nitride the masses of the two constituents are so similar that no gap exists between acoustical and optical branches (Fig. 5.11). Also the density of states (averaged over the entire Brillouin zone) is depicted (see the next chapter).

The displacement of atoms is shown in Fig. 5.12 for the different phonon modes present in zincblende crystals. In Fig. 5.13 the optical phonon modes for wurtzite crystals are depicted. The E-modes with

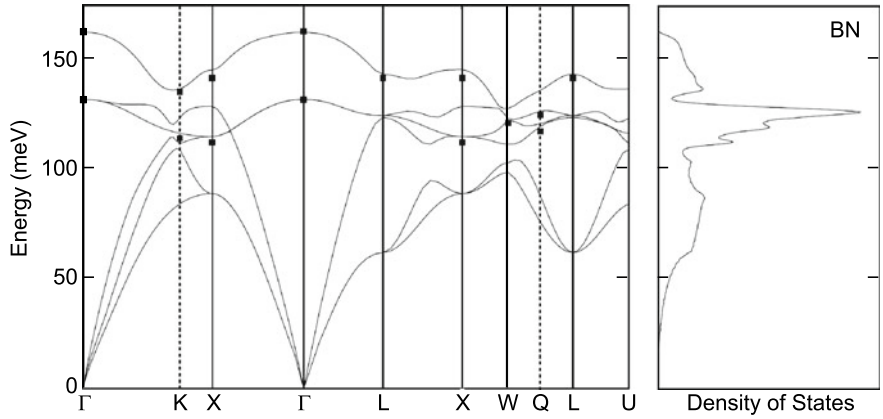

Fig. 5.11 Phonon dispersion in BN (*left panel*), experimental data (*symbols*) and theory (*solid lines*, first principles pseudopotential model). In the *right panel* the density of states is depicted. Adapted from [376]

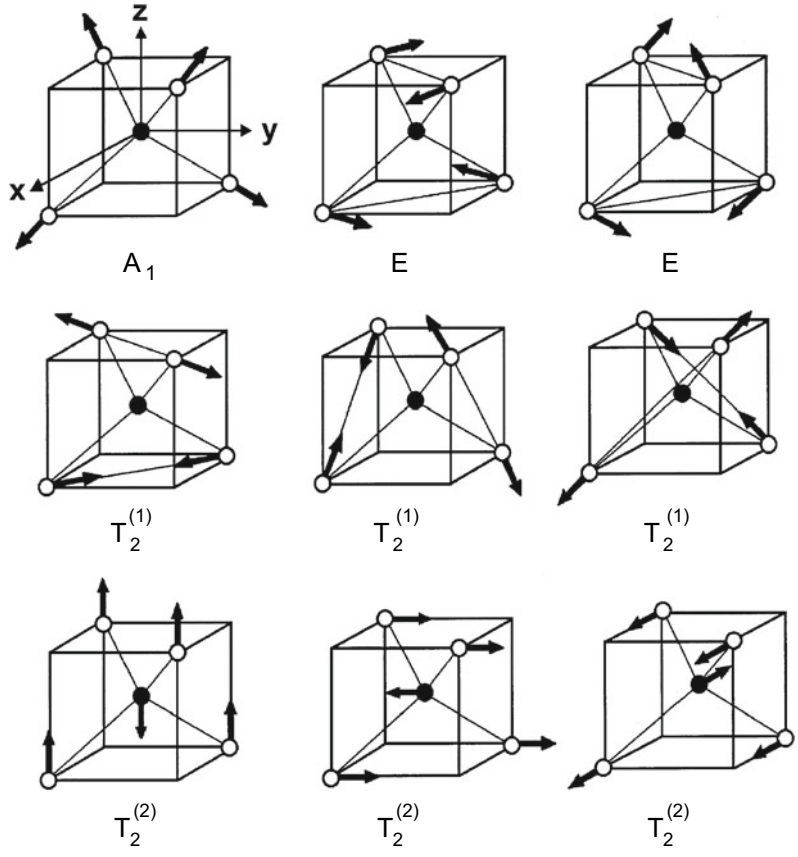

Fig. 5.12 Displacement of atoms for various phonon modes in zincblende crystals. Adapted from [377]

displacement perpendicular to the c-axis are double degenerate such that there are nine modes (the primitive unit cell has $p = 4$ atoms (Sect. 3.4.5)). The modes are labeled with their symmetry (in molecular notation) according to group theory (see remark in Sect. 6.2.5).

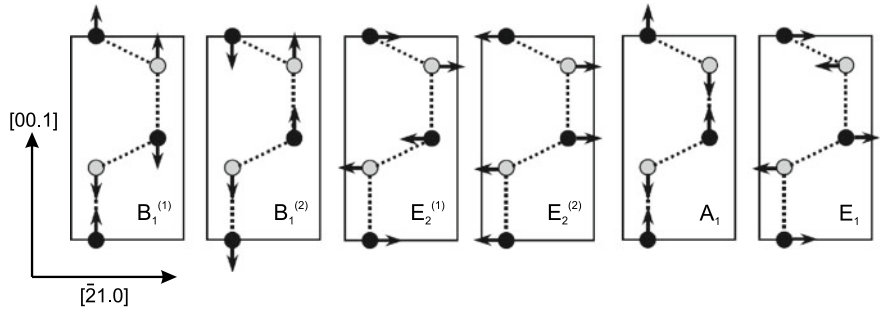

Fig. 5.13 Displacement of atoms for various phonon modes in wurtzite crystals. Adapted from [378]

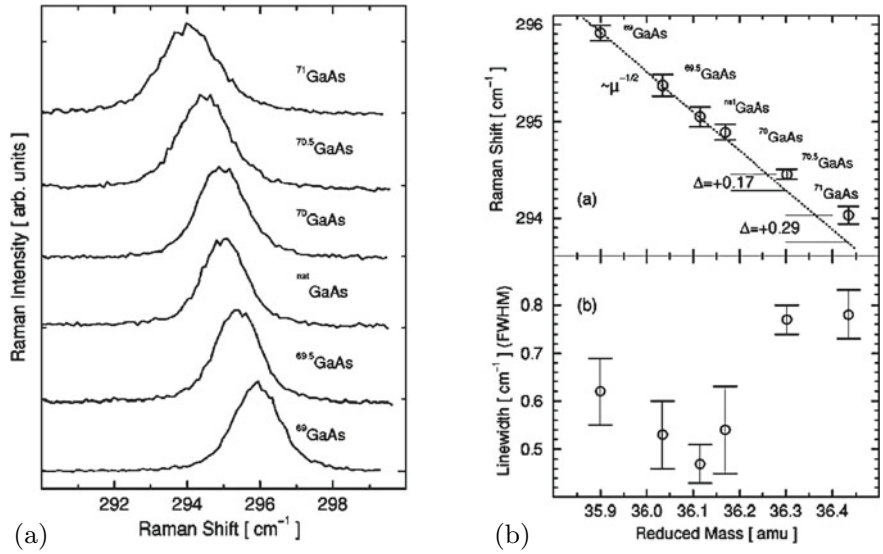

Fig. 5.14 **a** Raman spectra of GaAs with different isotope content as labeled. **b** Energy of optical phonons in GaAs with different isotope content [using the Raman spectra shown in (**a**)]. Reprinted with permission from [379], ©1999 APS

The dependence of the phonon frequency on the mass of the atoms ($\propto 1/\sqrt{M}$) can be demonstrated with the isotope effect, visualized for GaAs in Fig. 5.14. The dependence of the phonon frequencies on the stiffness of the spring can be seen from Fig. 5.15; the smaller lattice constant provides the stiffer spring.

5.2.5 *Density of States*

The *density of states* (DOS) tells how many of the total number of modes are in a given energy interval. The states are spaced equally in **k**-space but not on the energy scale (see also Sect. 6.13).

For the monoatomic linear chain model, the number of states $N(E')$ from $E = 0$ up to $E = \hbar\omega = E'(k')$ for the dispersion of the acoustic phonons (5.8) is given as

$$N(E') = k' \frac{N}{\pi/a} = \frac{L}{\pi} k' \,. \tag{5.32}$$

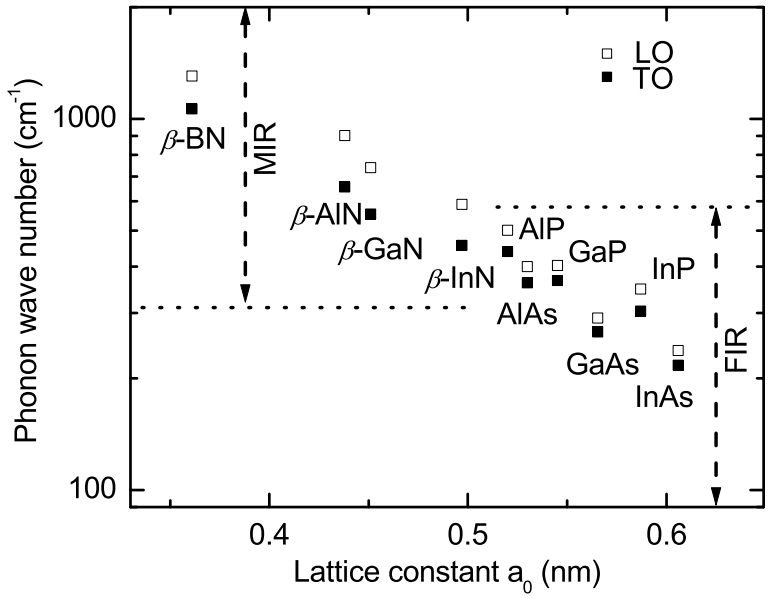

Fig. 5.15 Optical phonon frequencies (TO: *filled squares*, LO: *empty squares*) for a number of III–V compounds with different lattice constant a_0. 1 meV corresponds to 8.065 wave numbers (or cm^{-1}). Adapted from [380]

Using (5.8), we find for one polarization ($E_\mathrm{m} = \hbar\,\omega_\mathrm{m}$)

$$N(E) = \frac{2N}{\pi}\,\arcsin\left(\frac{E}{E_\mathrm{m}}\right)\,. \tag{5.33}$$

The DOS $D(E)$ is given by

$$D(E) = \frac{\mathrm{d}N(E)}{\mathrm{d}E} = \frac{2\,N}{\pi\;E_\mathrm{m}}\,\frac{1}{\sqrt{1-(E/E_\mathrm{m})^2}}\,. \tag{5.34}$$

Often the density of states is scaled by the (irrelevant) system size and given per atom (D/N) or per volume (D/L^3), per area (D/L^2) or per length (D/L) for three-, two- or one-dimensional systems, respectively.

In the diatomic linear chain model, additionally the optical phonons contribute to the density of states. In Fig. 5.16 the phonon density of states is shown for $\gamma = 0.9$ and for comparison for $\gamma = 1$ (gapless phonon dispersion). For small wavevector, the density of states is $4N/(\pi\;E_\mathrm{m})$.[2] Within the gap the density of states vanishes. At the edges of the band gap the density of states is enhanced. The total number of states for both dispersions is the same.

In a three-dimensional solid the total number of modes is $3\,p\,N$ ($N \gg 1$, p is the number of atoms in the base). Then (5.32) is modified to (for three degenerate polarizations)

$$N(E') = \frac{4\pi}{3}\,\frac{3}{(2\pi/L)^3}\,k'^3\,, \tag{5.35}$$

taking into account all states within a sphere in **k**-space of radius k'. Assuming a linear dispersion $\omega = v_\mathrm{s}\,k$ (for sufficiently small wave vector), we obtain

[2]The factor 2 compared to (5.34) stems from the folded Brillouin zone compared to the monoatomic chain model.

$$N(E) = \frac{V}{2\pi^2} \frac{E^3}{\hbar^3 v_s^3} \,. \tag{5.36}$$

Thus the density of states is approximately[3] proportional to E^2,

$$D(E) = \frac{3\,V}{2\pi^2} \frac{E^2}{\hbar^3 v_s^3} \,. \tag{5.37}$$

As realistic example for the phonon density of states, the DOS of bulk BN is depicted next to the dispersion in Fig. 5.11.

5.2.6 Phonons

Phonons are the quantized quasi-particles of the lattice vibrations (normal modes). The energy of a phonon can take the discrete values of a harmonic oscillator

$$E_{ph} = \left(n + \frac{1}{2}\right) \hbar\omega \,, \tag{5.38}$$

where n denotes the quantum number of the state, which corresponds to the number of energy quanta $\hbar\omega$ in the vibration. The amplitude of the vibration can be connected to n via the following discussion. For the classical oscillation $u = u_0 \exp \mathrm{i}(kx - \omega t)$ the space and time average for the kinetic energy yields

$$E_{\mathrm{kin}} = \frac{1}{2}\,\rho\, V \overline{\left(\frac{\partial u}{\partial t}\right)^2} = \frac{1}{8}\,\rho\, V\, \omega^2\, u_0^2 \,, \tag{5.39}$$

where ρ is the density and V the volume of the (homogeneous) solid. The energy of the oscillation is split in half between kinetic and potential energy. From $2E_{\mathrm{kin}} = E_{\mathrm{ph}}$ we find

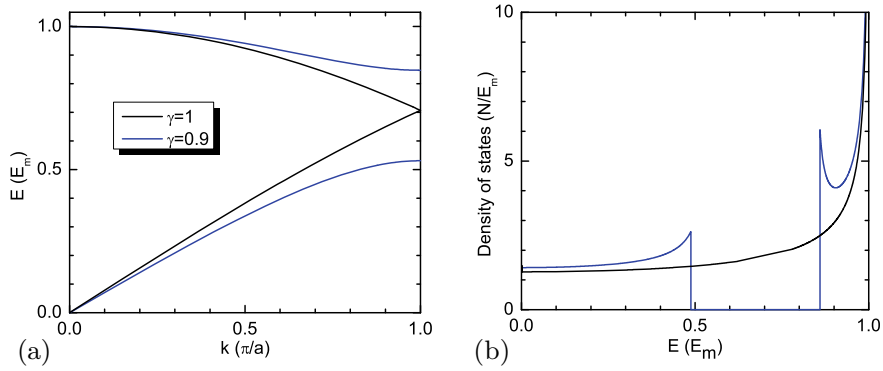

Fig. 5.16 **a** Phonon dispersion for the diatomic linear chain model for $\gamma = 1$ (*black line*) and $\gamma = 0.9$ (*blue lines*). **b** Corresponding density of states (in units of N/E_{m})

[3]This dependence is the base for Debye law for the T^3 temperature dependence of the heat capacity at low temperatures when only states with sufficiently small wave vector are thermally populated.

$$u_0^2 = \left(n + \frac{1}{2}\right) \frac{4\hbar}{\rho\, V\, \omega} \,. \tag{5.40}$$

The number of phonons with which a vibrational mode is populated is thus directly related to the classical amplitude square.

Phonons act with a momentum $\hbar\mathbf{k}$, the so-called crystal momentum. When phonons are created, destroyed or scattered the crystal momentum is conserved, except for an arbitrary reciprocal-space vector $\mathbf{G}$. Scattering with $\mathbf{G} = 0$ is called a *normal* process, otherwise (for $\mathbf{G} \neq 0$) it is called an *umklapp* process.

5.2.7 Localized Vibrational Modes

A defect in the crystal can induce localized vibrational modes (LVM). The defect can be a mass defect, i.e. one of the masses M is replaced by M_d, or the force constants in the neighborhood are modified to C_d. A detailed treatment can be found in [381]. LVM are discussed, e.g., in [382–384].

First we consider the LVM for the one-dimensional, monoatomic chain. If the mass at lattice point $i = 0$ is replaced by $M_\mathrm{d} = M + \Delta M$ ($\epsilon_\mathrm{M} = \Delta M/M$), the displacements are given by $u_i = AK^{|i|}$, A being an amplitude, with

$$K = -\frac{1 + \epsilon_\mathrm{M}}{1 - \epsilon_\mathrm{M}} \,, \tag{5.41}$$

and the defect phonon frequency ω_d is

$$\omega_\mathrm{d} = \omega_\mathrm{m} \sqrt{\frac{1}{1 - \epsilon_\mathrm{M}^2}} \,. \tag{5.42}$$

A real frequency is obtained for $|\epsilon_\mathrm{M}| < 1$. ω_d is then higher than the highest frequency of the bulk modes $\omega_\mathrm{m} = \sqrt{4C/M}$ (5.11). For $\epsilon_\mathrm{M} < 0$, i.e. the mass of the defect is smaller than the mass of the host atoms, K is negative and $|K| < 1$. Thus, the displacement can be written as

$$u_i \propto (-|K|)^{|i|} = (-1)^{|i|} \exp\left(+|i| \log|K|\right) \,. \tag{5.43}$$

The numerical value of the exponent is negative, thus the amplitude decreases exponentially from the defect and indeed makes a localized vibrational mode. For small mass $M_\mathrm{d} \ll M$ (5.42) yields approximately $\omega_\mathrm{d} = \sqrt{2C/M_\mathrm{d}}$. This approximation is the so-called one-oscillator model. Since typically the extension of the localized mode is only a few lattice constants, the picture of LVM remains correct for impurity concentrations up to $\sim 10^{18}$–$10^{20}\,\mathrm{cm}^{-3}$. For higher concentrations the concept of alloy modes has to be invoked (cf. Sect. 5.2.8).

For the case of group-III or -V substitutional impurities in group-IV semiconductors the change in force constants (treated below) can be neglected to some extent. For silicon ($M = 28$) and germanium ($M = 73$) the effect of various substitutions is shown in Fig. 5.17.

Now, additionally the force constants left and right of the defect are replaced by $C_\mathrm{d} = C + \Delta C$ ($\epsilon_\mathrm{C} = \Delta C/C$). The displacements are still given by $u_i = AK^{|i|}$, now with

$$K = -\frac{(1 + \epsilon_\mathrm{M})\,(1 + \epsilon_\mathrm{C})}{1 - \epsilon_\mathrm{M} - 2\epsilon_\mathrm{C}} \,. \tag{5.44}$$

An exponential decrease of the LVM amplitude occurs for negative K that is ensured for $\epsilon_M + 2\epsilon_C < 0$ (and $\epsilon_M > -1$ and $\epsilon_C > -1$). The defect frequency is given by

$$\omega_d = \omega_m \sqrt{\frac{(1+\epsilon_C)\,(2+\epsilon_C\,(3+\epsilon_M))}{2(1+\epsilon_M)\,(2\epsilon_C+1-\epsilon_M)}}\,. \tag{5.45}$$

We note that for $\epsilon_C = 0$ (5.41) and (5.42) are recovered.

For a given mass defect, the change of frequency with ΔC is (in linear order, i.e. for $\epsilon_C \ll 1$)

$$\frac{\partial\omega_d(\epsilon_M,\epsilon_C)}{\partial\epsilon_C} = \frac{1-4\,\epsilon_M-\epsilon_M^2}{4\,(1-\epsilon_M)\sqrt{1-\epsilon_M^2}}\,\epsilon_C\,. \tag{5.46}$$

The linear coefficient diverges for $\epsilon_M \to -1$. For ϵ_M between -0.968 and 0 the linear coefficient varies between 2 and 1/4. Therefore, a larger force constant ($\epsilon_C > 0$) increases the LVM frequency of the defect, as expected for a stiffer spring.

In a binary compound the situation is more complicated. We assume here that the force constants remain the same and only the mass of the substitution atom M_d is different from the host. The host has the atom masses M_1 and M_2 with $M_1 < M_2$. Substitution of the heavy atom with a lighter one creates a LVM above the optical branch for $M_d < M_2$. Additionally, a level in the gap between the optical and acoustic branch is induced. Such LVM is called a *gap mode*. Substitution of the lighter atom of the binary compound induces a LVM above the optical branch for $M_d < M_1$. A gap mode is induced for $M_d > M_1$. The situation for GaP is depicted in Fig. 5.18. LVM in GaAs have been reviewed in [382].

The energy position of a local vibrational mode is sensitive to the isotope mass of the surrounding atoms. In Fig. 5.19, a high-resolution ($0.03\,\mathrm{cm}^{-1}$) spectrum of the $^{12}C_{As}$ LVM in GaAs is shown together with a theoretical simulation. The various theoretical peak positions are given as vertical bars, their height indicating the oscillator strength. Five experimental peaks are obvious that are due to a total of nine different transitions. The C atom can experience five different

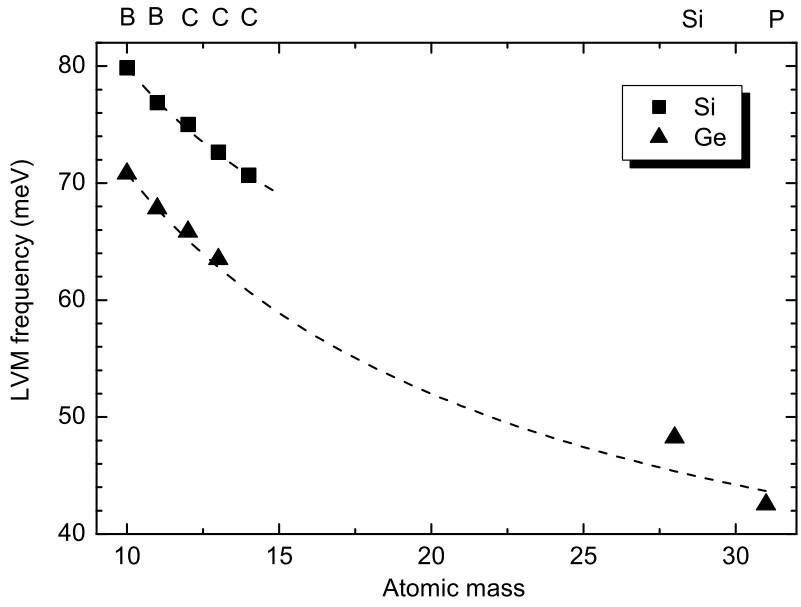

Fig. 5.17 Energy of local vibrational modes in Si and Ge. Experimental values at $T = 300\,\mathrm{K}$ (B in Ge: $T = 80\,\mathrm{K}$) taken from [381] and references therein and from [385] (C in Ge). The *dashed lines* are the mass dependence according to (5.42) scaled to the experimental frequency of the ^{10}B LVM

surroundings (see Table 3.8) with the four neighbors being ^{69}Ga or ^{71}Ga. The natural isotope mix is an 'alloy' $^{69}Ga_x{}^{71}Ga_{1-x}As$ with $x = 0.605$. The configurations with T_d symmetry contribute one peak each, the lowest (^{71}Ga surrounding) and highest (^{69}Ga surrounding) energy transitions. The configurations with C_{3v} and C_{2v} symmetry contribute each with 2 and 3 nondegenerate modes, respectively.

The vibrations of impurity complexes have been discussed in [387].

5.2.8 Phonons in Alloys

In an alloy of the type $AB_{1-x}C_x$, the phonon frequencies will depend qualitatively and quantitatively on the ternary composition [388]. For the binary end materials AB and AC clearly TO and LO frequencies exist. The simplest behavior of the alloy is the one-mode behavior (Fig. 5.20d) where the mode frequencies vary continuously (and approximately linearly) with the composition. The oscillator strength (LO–TO splitting, (9.86)) remains approximately constant. In many cases, the two-mode behavior is observed where the LO–TO gap closes (accompanied by decreasing oscillator strength) and a localized vibrational mode and a gap mode occur for the binary end materials (Fig. 5.20a). Also, a mixed-mode behavior (Fig. 5.20b, c) can occur.

The masses of the three constituent atoms will be M_A, M_B, and M_C. Without limiting the generality of our treatment, we assume $M_B < M_C$. From the considerations in Sect. 5.2.7 on LVM and gap modes, the condition

$$M_B < M_A, M_C \tag{5.47}$$

for two-mode behavior can be deduced. This ensures a LVM of atom B in the compound AC and a gap mode of atom C in the compound AB. However, it turns out that this condition is not sufficient, e.g. $Na_{1-x}K_xCl$ fulfills (5.47) but exhibits one-mode behavior. From a modified REI[4] model (for $\mathbf{k} \sim 0$ modes) it has been deduced that

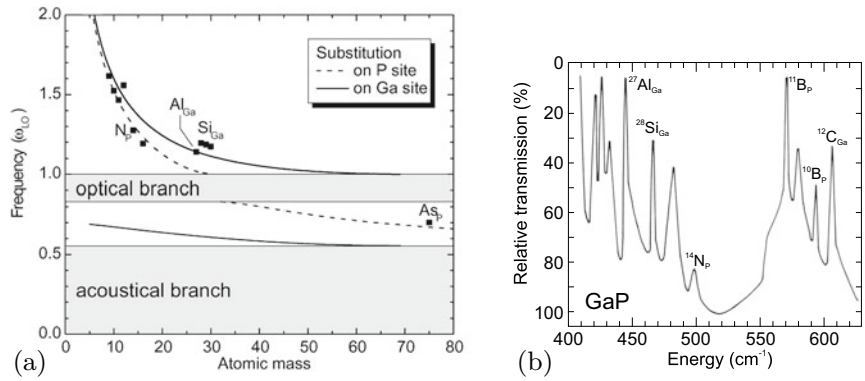

Fig. 5.18 **a** Numerical simulation of a linear chain model for GaP ($M_1 = 31$, $M_2 = 70$). Energy of local vibrational modes (*dashed* (*solid*) *line*): substitution on P (Ga) site) in units of the optical phonon frequency at Γ ($\hbar\omega_m = 45.4$ meV, cf. Fig. 5.10a). The *grey areas* indicate the acoustic and optical phonon bands. *Solid squares* are experimental data (from [381]), scaled to the theoretical curve for the $^{27}Al_{Ga}$ LVM frequency. **b** Differential transmission spectrum of GaP structure (nitrogen-doped layer on zinc-doped compensated substrate) against pure crystal ($T = 77$ K). Data from [386]

[4]Random element isodisplacement.

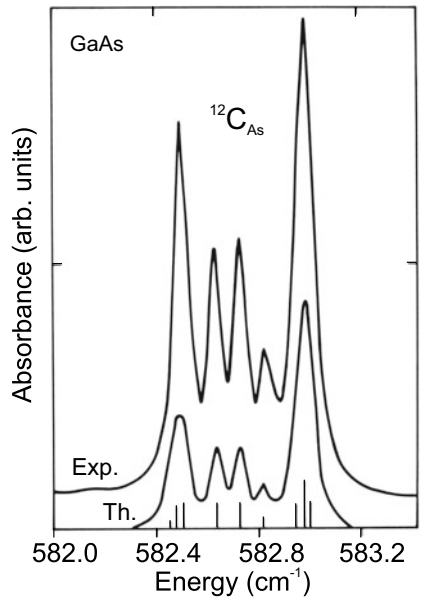

Fig. 5.19 Experimental (Exp., $T = 4.2$ K, resolution 0.03 cm^{-1}) and theoretical (Th., artificial Lorentzian broadening) infrared spectra of LVM of $^{12}C_{As}$ in GaAs. The positions and oscillator strengths of the theoretical transitions involving different configurations with ^{69}Ga and ^{71}Ga isotopes are shown as *vertical bars*. Data from [382]

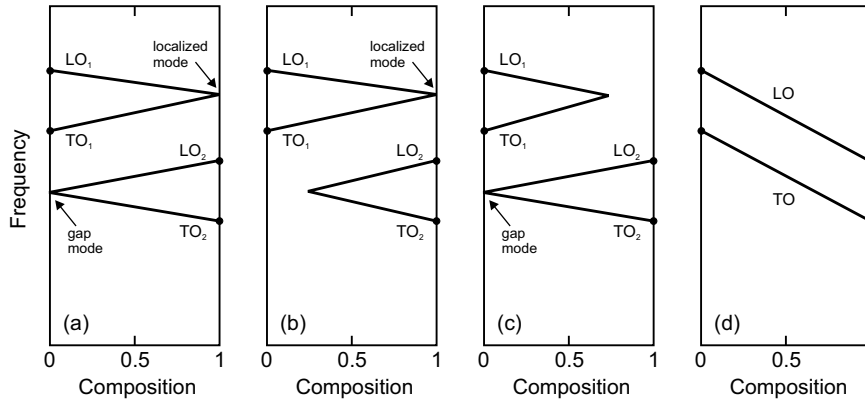

Fig. 5.20 Schematic behavior of phonon modes in an alloy. **a** Two-mode behavior with gap mode and localized mode, (**b**, **c**) mixed-mode behavior, **b** only localized mode allowed, **c** only gap mode allowed, **d** one-mode behavior with neither localized mode nor gap mode allowed

$$M_B < \mu_{AC} = \frac{M_A\, M_C}{M_A + M_C} < M_A, M_C \tag{5.48}$$

is a necessary and sufficient condition (unless the force constants between A–B and A–C are significantly different) for two-mode behavior [389]. A detailed discussion is given in [390]. Equation (5.48) is a stronger condition than the previous one (5.47). If (5.48) is not fulfilled the compound exhibits one-mode behavior. As an example, we show the mass relations for $CdS_{1-x}Se_x$ and $Cd_xZn_{1-x}S$ in Table 5.1 and the experimental phonon energies in Fig. 5.21. Also in Table 5.1 the masses for $GaP_{1-x}As_x$ ($GaAs_{1-x}Sb_x$) exhibiting two- (one-) mode behavior are shown.

Table 5.1 Atomic masses ($M_B < M_C$) of the constituents of various ternary compounds of type A(B,C), reduced mass μ_{AC} (5.48), fulfillment of the relation from (5.48) ('+': fulfilled, '−': not fulfilled) and experimental mode behavior ('2': two-mode, '1': one-mode)

Alloy	A	B	C	M_A	M_B	M_C	μ_{AC}	Rel.	Modes
$GaP_{1-x}As_x$	Ga	P	As	69.7	31.0	74.9	36.1	+	2
$GaAs_{1-x}Sb_x$	Ga	As	Sb	69.7	74.9	121.8	44.3	−	1
$CdS_{1-x}Se_x$	Cd	S	Se	112.4	32.1	79.0	46.4	+	2
$Cd_xZn_{1-x}S$	S	Zn	Cd	32.1	65.4	112.4	25.0	−	1
$Mg_xZn_{1-x}O$	O	Mg	Zn	16.0	24.3	65.4	12.9	−	1
$Al_xGa_{1-x}N$	N	Al	Ga	14.0	27.0	69.7	11.7	−	2(!)

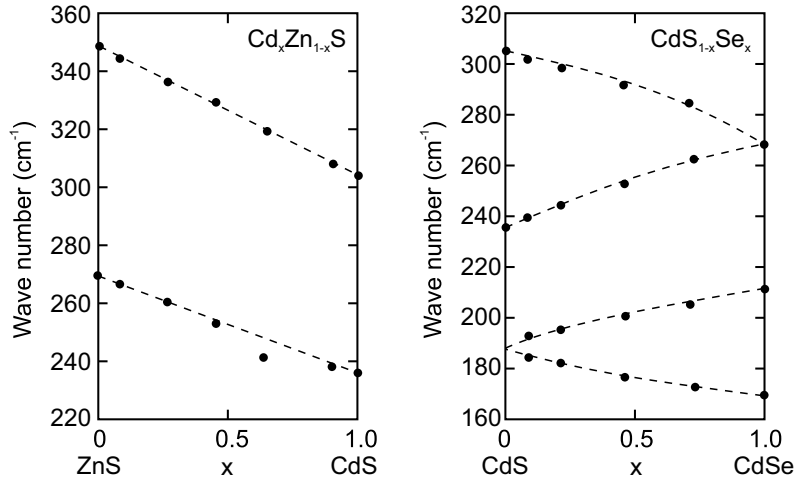

Fig. 5.21 Phonon energies of $Cd_xZn_{1-x}S$ and $CdS_{1-x}Se_x$ as a function of the ternary composition. Experimental data (*solid circles*) are from [389], *dashed lines* are guides to the eye

If the binary end components of a ternary alloy have different crystal structure, a transition between the two occurs which is reflected in the phonon structure (energies and mode symmetries). As an example, the optical phonon energies of $Mg_xZn_{1-x}O$ are depicted in Fig. 5.22 (cmp. Fig. 3.43).

An example for the variation of phonon oscillator strength (as defined in (9.86)) with alloy composition is depicted in Fig. 5.23 for (Al,Ga)N [392].[5]

5.2.9 Disorder

An example of local disorder are the localized vibrational modes due to a single defect. Here we consider in our one-dimensional model random fluctuations of the model parameters. To that avail we set up a numerical implementation of an one-dimensional chain with masses $M_1 = M_2 = 1$ and spring constants $C_1 \neq C_2$, here $C_2 = 2\,C_1$. Now each mass varies randomly by a factor with a

[5]The oscillator strengths f shown here have been calculated from the values S given in [392] divided by $\epsilon(\infty)$.

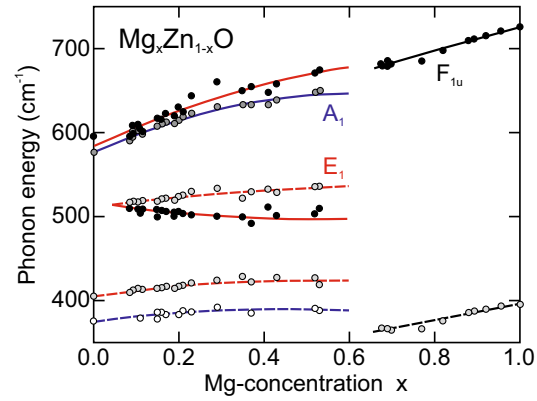

Fig. 5.22 LO (*solid lines*) and TO (*dashed lines*) phonon energies of $Mg_xZn_{1-x}O$ in the wurtzite structure (A_1 symmetry: *blue lines*, E_1 symmetry: *red lines*) and in the rocksalt phase (F_{1u} symmetry: *black lines*). Experimental data are shown as *symbols*. Adapted from data of [391]

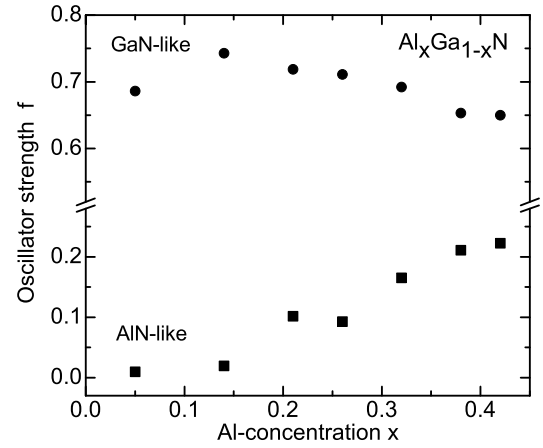

Fig. 5.23 Oscillator strength f (cf. (9.86)) of alloy phonons in (Al,Ga)N thin films on c-Al_2O_3. Based on data from [392]

statistical distribution of mean $\bar{M} = 1$ and a standard deviation[6] σ_M. The density of states is displayed for $\sigma_M/\bar{M} = 0.1$–0.5. The effects as shown in Fig. 5.24 are broadening of the peaks in the DOS, broadening of the band edges, the development of band tails into the gap and eventually a closing of the gap. This is a typical behavior that also exists for electronic states (cmp. Fig. 6.53).

5.2.10 *Topological Edge States of the Diatomic Linear Chain*

Here we treat a finite diatomic linear chain with N unit cells, i.e. A–B dimers. In case of periodic boundary conditions, the rightmost B-atom is 'connected' to the leftmost A-atom, but now we chose N to be finite.

The system of $2N$ equations of the type $\omega^2 u_n = (\partial U/\partial u_n)/M_n$ (like (5.13a) or (5.13b)) is written in matrix form and the eigenproblem $\boldsymbol{M} - \omega^2 \mathbf{1} = 0$ is solved numerically [393]. Also, we fix both ends, i.e. the displacements u_0^A and u_N^B are forced to be zero (Fig. 5.25). We set $M_1 = M_2$ and find two quite different situations for the cases (i) $C_1 > C_2$ and (ii) $C_1 < C_2$. Case (i) is similar to the bulk case

[6] In order to avoid negative values for the masses, not a normal or Gaussian distribution is used but the Gamma distribution with the parameters $G(1/\sigma^2, 1/\sigma^2)$.

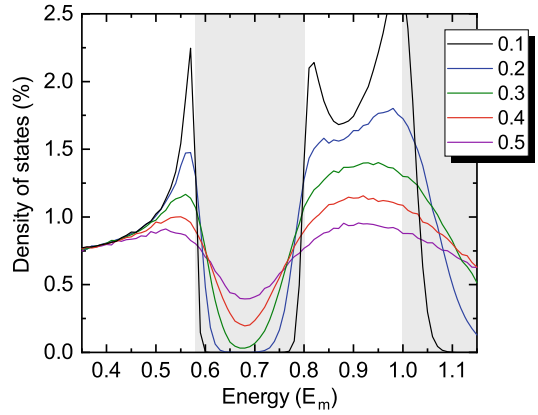

Fig. 5.24 Density of states versus energy (in units of maximum phonon energy $E_\mathrm{m} = \hbar\,\omega_\mathrm{max}$ according to (5.18)) for the diatomic linear chain model ($M_1 = M_2, C_2 = 2\,C_1$, 2^7 dimers, average over 2^{12} configurations) for various levels of random relative variations of the masses (*solid lines*). The forbidden energy ranges for the ideal chain are shown in *light grey*. The DOS has been normalized such that its integral over all energies is 1 (the energy bins have a width of 0.01 E_m)

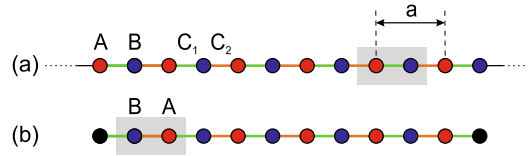

Fig. 5.25 **a** Diatomic linear chain model (DLCM) with A–B dimers (one unit cell shown in grey) in an infinite chain; A-sites (B-sites) are shown in *red* (*blue*); the connecting springs have force constants C_1 (*green*) and C_2 (*orange*), respectively. **b** DLCM with finite number of dimers (shown for $N = 6$) with both end sites fixed (shown in *black*). The movable sites now consist of B–A dimers (one unit cell shown in grey)

(i.e. for periodic boundary conditions) where a 'clean' gap is present; for $C_1 = C_2$ of course no gap appears. In case (ii), two states appear within the gap with energy $\omega_\mathrm{g} = \omega_\mathrm{max}/\sqrt{2}$. The eigenvalues of the problem are shown as a function of C_2/C_1 in Fig. 5.26a. The mode pattern for the two gap states are depicted in Fig. 5.27a (for $C_2/C_1 = 1/2$). All other states follow bulk like vibration patterns as expected from a vibrating string. For $M_1 = M_2$ the gap states are degenerate, otherwise split as shown in Fig. 5.26c. For the case of $C_2 > C_1$, the patterns for the highest mode of the lower band and the lowest mode of the top band are depicted in Fig. 5.27b; the are obviously bulk-like as all others and no localized states exist.

The appearance of end states in one of the cases is the expression of the fact that the two bulk band structures for $C_1 > C_2$ and $C_1 < C_2$ are *topologically* different[7] (cmp. Sect. 5.2.3). The general effect is the so-called 'bulk-boundary' correspondence where edge states appear at the interface between different topological phases (one of these phases can be the topologically trivial vacuum outside the solid). Such edge states are termed more precisely *end*-states for (quasi-) one-dimensional systems.

[7]Since the two outer atoms are fixed, the movable parts of the chain consists of B–A dimers (Fig. 5.25b), thus the topologically non-trivial case occurs here for $C_2 < C_1$.

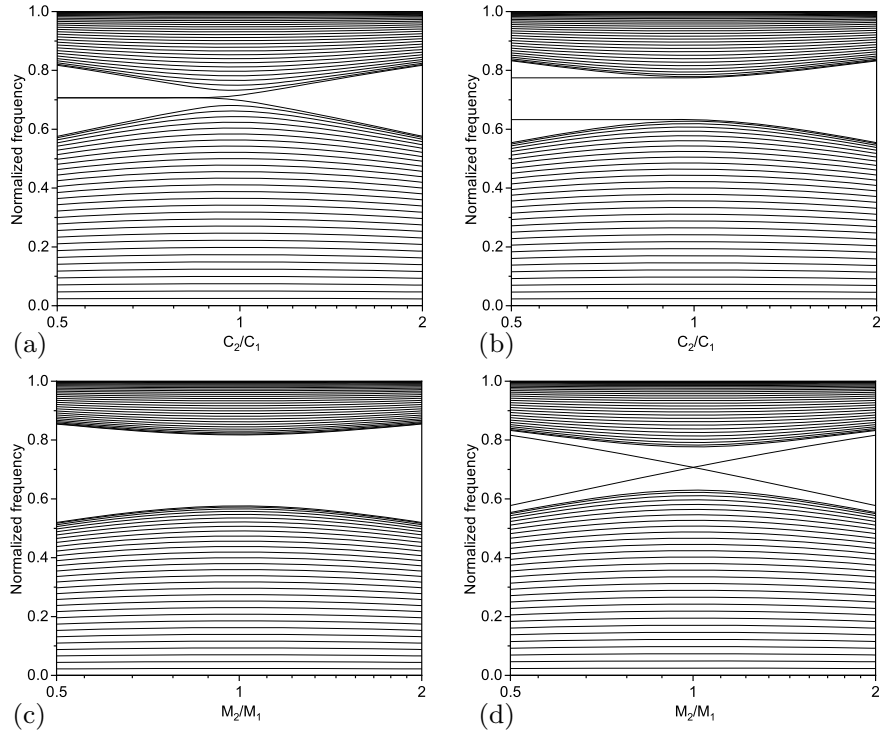

Fig. 5.26 **a** Eigenvalues of a diatomic chain with $N = 32$ unit cells (64 atoms) as a function of the ratio C_2/C_1 ($M_1 = M_2$). The frequency is normalized (to $\omega_{\max}$ from (5.18)). The abzissa is logarithmic. **b** Same calculation as for panel (**a**) but $M_1/M_2 = 1.5$ (would look the same for $M_2/M_1 = 1.5$). **c** Same calculation as for panel (**a**) but as a function of M_2/M_1 (for $C_2/C_1 = 2$). **d** Same calculation as for panel (**c**) but for $C_2/C_1 = 0.5$

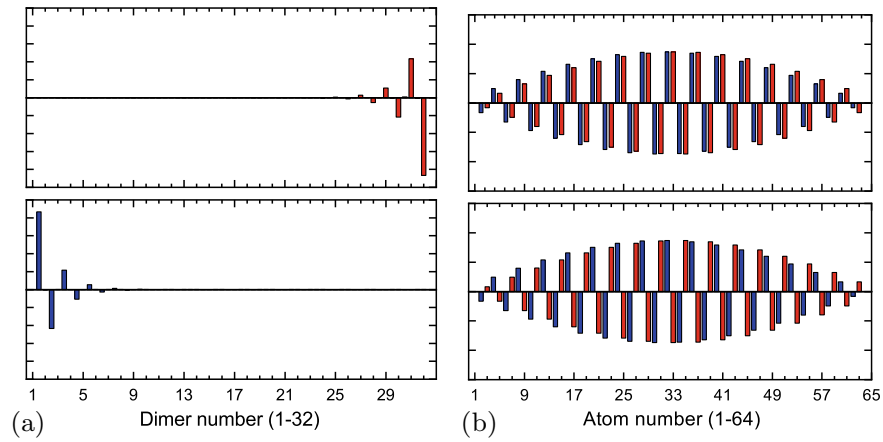

Fig. 5.27 Mode patterns for two states of the diatomic linear chain ($N = 32$ unit cells, $M_1 = M_2$) **a** within the gap for $C_2/C_1 = 1/2$ and **b** closest to the gap for $C_2/C_1 = 2$. The amplitudes of A-sites (B-sites) are shown in *red* (*blue*)

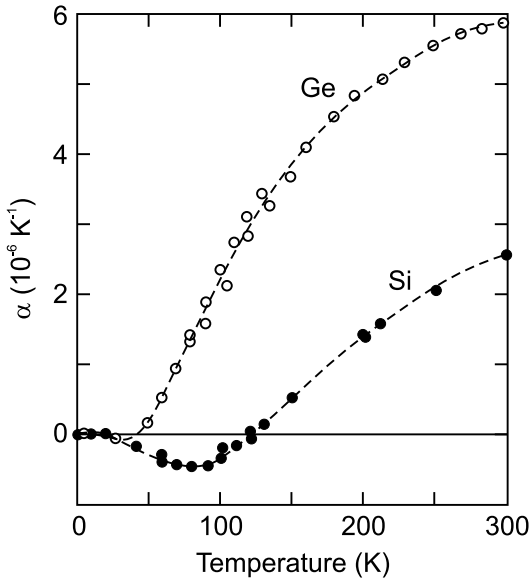

Fig. 5.28 Linear thermal expansion coefficient of silicon (*solid circles*) and germanium (*open circles*). Adapted from [394] based on experimental data from various sources. *Dashed lines* are guide to the eye

5.3 Elasticity

The elastic properties of the semiconductor are important if the semiconductor is subjected to external forces (pressure, temperature) or to lattice mismatch during heteroepitaxy.

5.3.1 Thermal Expansion

The lattice constant depends on temperature. The (linear) thermal expansion coefficient is defined as

$$\alpha(T_0) = \left.\frac{\partial a_0(T)}{\partial T}\right|_{T=T_0} \tag{5.49}$$

and is temperature dependent. The temperature dependence of α for silicon and germanium is shown in Fig. 5.28. α is approximately proportional to the heat capacity (C_V) except at low temperatures. The negative values are due to negative Grüneisen parameters [394]. These anharmonicity effects are discussed in detail in [366].

5.3.2 Stress–Strain Relation

In this section, we recall the classical theory of elasticity [395]. The solid is treated as a continuous medium (piecewise homogeneous) and the displacement vector is thus a continuous function $\mathbf{u}(\mathbf{r})$ of the spatial coordinates. When the spatial variation $\nabla\mathbf{u}$ of $\mathbf{u}$ is small, the elastic energy can be written as

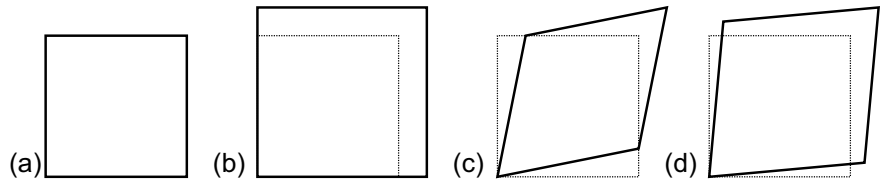

Fig. 5.29 Deformation of a square (**a**). (**b**) Pure hydrostatic deformation ($\epsilon_{xx} = \epsilon_{yy} = 0.2$, $\epsilon_{xy} = 0$), (**c**) pure shear deformation ($\epsilon_{xx} = \epsilon_{yy} = 0$, $\epsilon_{xy} = 0.2$), and (**d**) mixed deformation ($\epsilon_{xx} = \epsilon_{yy} = 0.1$, $\epsilon_{xy} = 0.1$)

$$U = \frac{1}{2} \int \frac{\partial u_l}{\partial x_k} C_{klmn} \frac{\partial u_n}{\partial x_m} \mathrm{d}^3\mathbf{r} \,, \tag{5.50}$$

where **C** is the (macroscopic) tensor of the elastic coefficients. 21 components of this tensor can be independent. For crystals with cubic symmetry the number of independent constants is reduced to 3. An exchange $k \leftrightarrow l$ and $m \leftrightarrow n$ does not matter, only six indices have to be considered (xx, yy, zz, yz, xz, and xy). The strain components ϵ_{ij} are symmetrized according to

$$\epsilon_{ij} = \frac{1}{2} \left(\frac{\partial u_j}{\partial x_i} + \frac{\partial u_i}{\partial x_j} \right) \,. \tag{5.51}$$

The strains ϵ_{xx} are along the main axes of the crystal as visualized in Fig. 5.29.

The stresses[8] σ_{kl} are then given by

$$\sigma_{kl} = C_{klmn}\, \epsilon_{mn} \,. \tag{5.52}$$

The inverse relation is mediated by the stiffness tensor **S**.

$$\epsilon_{kl} = S_{klmn}\, \sigma_{mn} \,. \tag{5.53}$$

Typically, the strain components e_{ij} or e_i are used with the convention $xx \to 1$, $yy \to 2$, $zz \to 3$, $yz \to 4$, $xz \to 5$, and $xy \to 6$ (Voigt notation):

$$e_{ij} = \epsilon_{ij}\,(2 - \delta_{ij}) \,. \tag{5.54}$$

Then, $\sigma_m = C_{mn} e_n$ with the C_{ij} being the elastic constants. The x, y, and z directions are the main axes of the cubic solid, i.e. the $\langle 100 \rangle$ directions.

For *zincblende* material, the stress–strain relation reads[9]

$$\begin{pmatrix} \sigma_1 \\ \sigma_2 \\ \sigma_3 \\ \sigma_4 \\ \sigma_5 \\ \sigma_6 \end{pmatrix} = \begin{pmatrix} C_{11} & C_{12} & C_{12} & 0 & 0 & 0 \\ C_{12} & C_{11} & C_{12} & 0 & 0 & 0 \\ C_{12} & C_{12} & C_{11} & 0 & 0 & 0 \\ 0 & 0 & 0 & C_{44} & 0 & 0 \\ 0 & 0 & 0 & 0 & C_{44} & 0 \\ 0 & 0 & 0 & 0 & 0 & C_{44} \end{pmatrix} \begin{pmatrix} e_1 \\ e_2 \\ e_3 \\ e_4 \\ e_5 \\ e_6 \end{pmatrix} \,. \tag{5.55}$$

Values of the compliances for several semiconductors are given in Table 5.2. The inverse relation is given by the matrix

[8] The stress is a force per unit area and has the dimensions of a pressure.

[9] $C_{11} = C_{1111}$, $C_{12} = C_{1122}$ and $C_{44} = C_{1212} = C_{1221} = C_{2121} = C_{2112}$.

Table 5.2 Elastic constants (in GPa) of some cubic semiconductors at room temperature. I_K refers to the Keating criterion (5.59)

Material	C_{11}	C_{12}	C_{44}	I_K
C	1076.4	125.2	577.4	1.005
Si	165.8	63.9	79.6	1.004
Ge	128.5	48.3	66.8	1.08
BN	820	190	480	1.11
GaAs	119	53.4	59.6	1.12
InAs	83.3	45.3	39.6	1.22
AlAs	120.5	46.86	59.4	1.03
ZnS	104.6	65.3	46.3	1.33
MgO	297	156	95.3	0.80

$$\begin{pmatrix} S_{11} & S_{12} & S_{12} & 0 & 0 & 0 \\ S_{12} & S_{11} & S_{12} & 0 & 0 & 0 \\ S_{12} & S_{12} & S_{11} & 0 & 0 & 0 \\ 0 & 0 & 0 & S_{44} & 0 & 0 \\ 0 & 0 & 0 & 0 & S_{44} & 0 \\ 0 & 0 & 0 & 0 & 0 & S_{44} \end{pmatrix} , \tag{5.56}$$

with the stiffness coefficients in this notation given by

$$S_{11} = \frac{C_{11} + C_{12}}{(C_{11} - C_{12})\,(C_{11} + 2C_{12})} \tag{5.57a}$$

$$S_{12} = \frac{C_{12}}{-C_{11}^2 - C_{11}C_{12} + 2C_{12}^2} \tag{5.57b}$$

$$S_{44} = \frac{1}{C_{44}} \, . \tag{5.57c}$$

We emphasize that in this convention (also called the *engineering* convention), e.g. $e_1 = \epsilon_{xx}$ and $e_4 = 2\,\epsilon_{yz}$. There is also another convention (the *physical* convention) without this factor of two; in this case the matrix in (5.55) contains the elements $2C_{44}$. We introduce

$$C_0 = 2\,C_{44} + C_{12} - C_{11} \, , \tag{5.58}$$

and note that $C_0 = 0$ for an isotropic material. The relation

$$I_K = \frac{2\,C_{44}\,(C_{11} + C_{12})}{(C_{11} - C_{12})\,(C_{11} + 3C_{12})} = 1 \tag{5.59}$$

known as the Keating criterion [396, 397], stems from the consideration of bending and stretching of the tetrahedral bonds in the valence force field (VFF) model. It is closely fulfilled (Table 5.2) for many tetrahedrally bonded semiconductors, in particular for the covalent ones. For MgO, the Keating criterion is not fulfilled because it has (six-fold coordinated) rocksalt structure and is thus not tetrahedrally bonded.

The Young's modulus Y,

$$\sigma_{\mathbf{nn}} = Y(\mathbf{n})\,\epsilon_{\mathbf{nn}} \, , \tag{5.60}$$

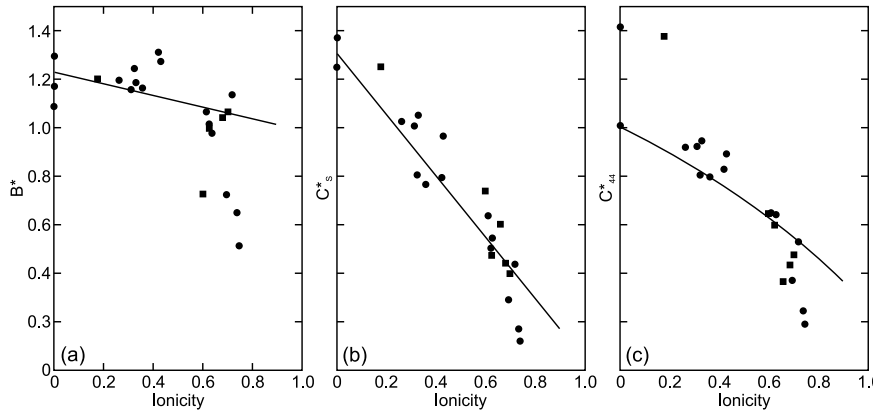

Fig. 5.30 Elastic constants as a function of ionicity for various semiconductors with diamond or zincblende (*circles*) and wurtzite (*squares*) structure. Constants are normalized by the modulus $C_0 = e^2/d^4$, d being the average nearest-neighbor distance. **a** Bulk modulus, $B^* = (C_{11} + 2C_{12})/(3C_0)$, (**b**, **c**) shear moduli, **b** $C_S^* = (C_{11} - C_{12})/C_0$, **c** $C_{44}^* = C_{44}/C_0$. *Solid lines* are a simple model as discussed in [402]. Adapted from [403]

generally depends on the normal direction **n** of a strain. It is equivalent to $1/S_{11}$ of (5.57a).

For *isotropic* material Y and the Poisson ratio ν are related to the elastic constants of cubic material by

$$Y = C_{11} - \frac{2\,C_{12}^2}{C_{11} + C_{12}} \tag{5.61a}$$

$$\nu = \frac{C_{12}}{C_{11} + C_{12}}\,. \tag{5.61b}$$

For isotropic materials also Lamé's constants λ and μ are used. They are given by[10] $C_{11} = \lambda + 2\mu$, $C_{12} = \lambda$ and $C_{44} = \mu$ (note that C_0 according to (5.58) is zero).

The bulk modulus B (inverse of the compressibility),

$$\frac{1}{B} = -\frac{1}{V}\,\frac{\partial V}{\partial p}\,, \tag{5.62}$$

for the zincblende crystal is given as

$$B = \frac{C_{11} + 2\,C_{12}}{3}\,. \tag{5.63}$$

We note that Y, ν and C_{ij} of typical materials are both positive. Materials with negative Poisson ratio are called *auxetic* [398–400]. Also materials with negative compressibility are possible [401].

Beyond the dependence of the elastic constants on the bond length (as materialized in the phonon frequencies in Fig. 5.15), they depend on the ionicity. In Fig. 5.30, the elastic constants of various zincblende semiconductors are shown as a function of the ionicity f_i. The values for the elastic constants are normalized by e^2/a^4, a being the average nearest-neighbor distance.

For *wurtzite* crystals, five elastic constant are necessary for the stress–strain relation that reads[11]

[10] For an isotropic material, $C_{ijkl} = \lambda\,\delta_{ij}\,\delta_{kl} + \mu\,(\delta_{ik}\,\delta_{jl} + \delta_{il}\,\delta_{jk})$.

[11] $(C_{11} - C_{12})/2 = C_{1212}$, $C_{44} = C_{1313} = C_{2323}$.

$$C_{ij} = \begin{pmatrix} C_{11} & C_{12} & C_{13} & 0 & 0 & 0 \\ C_{12} & C_{11} & C_{13} & 0 & 0 & 0 \\ C_{13} & C_{13} & C_{33} & 0 & 0 & 0 \\ 0 & 0 & 0 & C_{44} & 0 & 0 \\ 0 & 0 & 0 & 0 & C_{44} & 0 \\ 0 & 0 & 0 & 0 & 0 & \frac{1}{2}(C_{11} - C_{12}) \end{pmatrix} . \tag{5.64}$$

Experimental values for wurtzite materials are given in Table 5.3. The relation of the elastic tensor of wurtzite and zincblende materials, in particular viewed along the ⟨111⟩-direction has been discussed in [403, 404].

The bulk modulus of the wurtzite crystal is given by

$$B = \frac{(C_{11} + C_{12})\, C_{33} - 2\, C_{13}^2}{C_{11} + C_{12} + 2\, C_{33} - 4\, C_{13}} . \tag{5.65}$$

5.3.3 *Biaxial Stress*

In heteroepitaxy (cf. Sect. 12.2.6), a biaxial stress situation arises, i.e. layered material is compressed (or expanded in the case of tensile strain) in the interface plane and is expanded (compressed) in the perpendicular direction.[12] Here, we assume that the substrate is infinitely thick, i.e. that the interface remains planar. Substrate or wafer bending is discussed in Sect. 5.3.5.

The simplest case is epitaxy on the (001) surface, i.e. $e_1 = e_2 = \epsilon_\parallel$. The component e_3 is found from the condition $\sigma_3 = 0$ (no forces in the z direction). All shear strains are zero. For zincblende material it follows

$$\epsilon_\perp^{100} = e_3 = -\frac{C_{12}}{C_{11}} (e_1 + e_2) = -\frac{2\, C_{12}}{C_{11}} \epsilon_\parallel . \tag{5.66}$$

In Fig. 5.31 the ratio $\epsilon_\perp / \epsilon_\parallel$ is depicted for GaAs and various crystal orientations; the formulas for other orientations are more involved [409]:

$$\epsilon_\perp^{110} = -\frac{2C_{12} - C_0/2}{C_{11} + C_0/2} \epsilon_\parallel \tag{5.67}$$

$$\epsilon_\perp^{111} = -\frac{2C_{12} - 2C_0/3}{C_{11} + 2C_0/3} \epsilon_\parallel . \tag{5.68}$$

Table 5.3 Elastic constants (in GPa) of some wurtzite semiconductors

Material	C_{11}	C_{12}	C_{13}	C_{33}	C_{44}	Refs.
GaN	391	143	108	399	103	[405]
AlN	410	149	99	389	125	[406]
ZnS	124	60.2	45.5	140	28.6	[407]
ZnO	206	118	118	211	44	[408]

[12] In a large amount of literature and in previous editions of this book, this situation has been labelled 'biaxial *strain*'. However, there is in-plane *and* out-of-plane strain, thus the strain along all directions is non-zero. Since the out-of-plane stress is zero (for zero ambient pressure), it is actually a 'biaxial *stress*' situation.

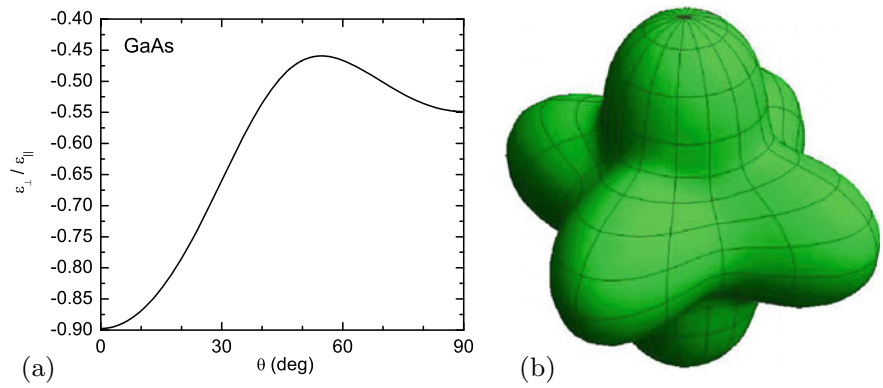

Fig. 5.31 Ratio $-\epsilon_\perp/\epsilon_\parallel$ for GaAs under symmetric biaxial stress. The angle θ denotes the surface normal in the $\langle 110\rangle$-azimuth ($\theta = 0$: [001], $\theta = 90°$: [110], the maximum of $\epsilon_\perp/\epsilon_\parallel$ is for [111]). (**b**) is a three-dimensional visualization

For wurtzite crystals and pseudomorphic growth along [00.1] the strain along the epitaxial direction (c-axis) is given by

$$\epsilon_\perp = -\frac{C_{13}}{C_{33}}\,(e_1 + e_2) = -\frac{2C_{13}}{C_{33}}\,\epsilon_\mathrm{a}\ , \tag{5.69}$$

where $\epsilon_\perp = \epsilon_\mathrm{c} = (c - c_0)/c_0$ and $\epsilon_\mathrm{a} = (a - a_0)/a_0$. For symmetric biaxial in-plane stress, the ratio $\epsilon_\perp/\epsilon_\parallel$ is shown in Fig. 5.32 for GaN and varying angle θ of the c-axis against the epitaxy direction. For the growth of wurtzite on wurtzite for $\theta \neq 0$, the epitaxial strain is actually *asymmetric* in the interface plane. For $\theta = 90°$, e.g. the epitaxy on m-plane substrate (cmp. Fig. 3.37) (c-axis lies in-plane), the in-plane strains are $e_1 = \epsilon_\mathrm{a}$ and $e_2 = \epsilon_\mathrm{c}$. For $\theta = 90°$, we find

$$\epsilon_\perp = -\frac{C_{12}\,\epsilon_\mathrm{a} + C_{13}\,\epsilon_\mathrm{c}}{C_{11}}\ . \tag{5.70}$$

The situation for pseudomorphic growth in the (Al,Ga,In)N system has been discussed for various interface orientations in [410] (cmp. also Fig. 16.14). The strains $\epsilon_\perp$ along the epitaxy direction and ϵ_c along the c-direction are depicted for $Al_{0.17}Ga_{0.83}N$/GaN and $Mg_{0.3}Ga_{0.7}O$/ZnO in Fig. 5.33. The different behavior of the nitride and the oxide system, e.g. regarding the sign change of ϵ_c, is due to the fact that ϵ_a is negative (positive) for $Al_xGa_{1-x}N$/GaN ($Mg_xGa_{1-x}O$/ZnO) ($\epsilon_\mathrm{c} < 0$ for both cases) [411].

We note that pseudomorphic growth and biaxial stress of rhombohedral/trigonal (e.g. Al_2O_3) and monoclinic (e.g. β-Ga_2O_3) thin films has been discussed as well [412–414]. A general treatment for all crystal symmetries and orientations has been provided in [415].

5.3.4 Three-Dimensional Stress

The strain distribution in two-dimensional or three-dimensional objects such as quantum wires and dots (see also Sect. 14) is more complicated.

A simple analytical solution for the problem of a strained inclusion is only possible for isotropic material parameters [416].

The solution for a sphere can be extended to yield the strain distribution of an inclusion of arbitrary shape. This scheme applies only for isotropic materials and identical elastic properties of the inclusion

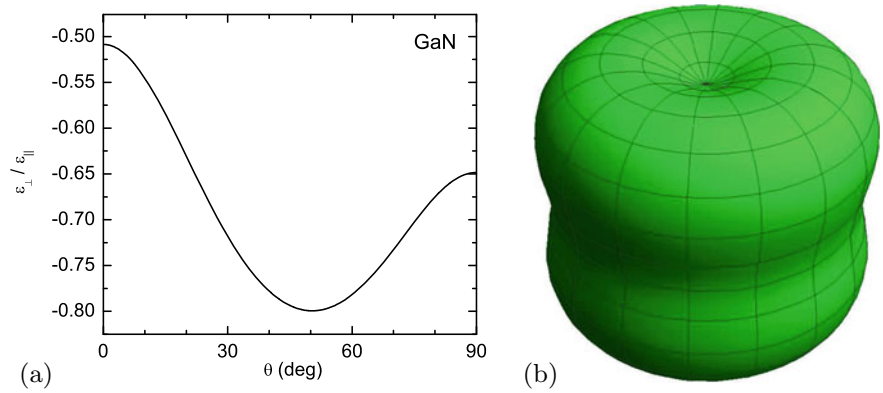

Fig. 5.32 Ratio $-\epsilon_\perp/\epsilon_\parallel$ for GaN under symmetric biaxial stress. In **a** θ denotes the angle of the c-axis with respect to the surface normal, **b** is a three-dimensional visualization, showing the in-plane isotropy

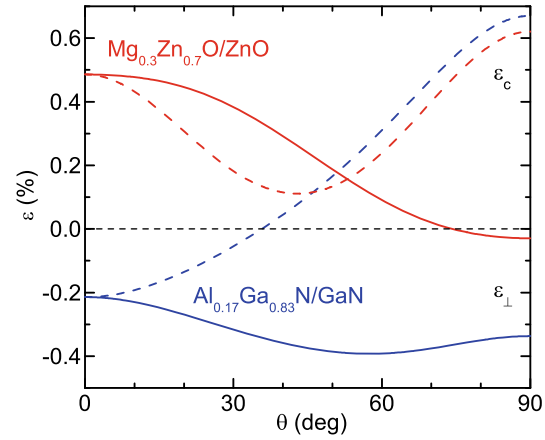

Fig. 5.33 Strains ϵ_c (*dashed lines*) and $\epsilon_\perp$ (*solid lines*) for $Al_{0.17}Ga_{0.83}N$/GaN (*blue*) and $Mg_{0.3}Ga_{0.7}O$/ZnO (*red*) as a function of the interface tilt angle θ with respect to [00.1]

and the surrounding matrix. The solution will be given in terms of a surface integral of the boundary of the inclusion, which is fairly easy to handle. Several disconnected inclusions can be treated by a sequence of surface integrals.

The strain distribution for the inner and outer parts of a sphere with radius ρ_0 is given (in spherical coordinates) by

$$\epsilon^{\text{in}}_{\rho\rho} = \frac{2}{3}\,\epsilon_0\,\frac{1-2\nu}{1-\nu} = \epsilon^{\text{in}}_{\theta\theta} = \epsilon^{\text{in}}_{\phi\phi} \tag{5.71}$$

$$\epsilon^{\text{out}}_{\rho\rho} = \frac{2}{3}\,\epsilon_0\,\frac{1+\nu}{1-\nu}\left(\frac{\rho_0}{\rho}\right)^3 = -2\epsilon^{\text{out}}_{\theta\theta} = -2\epsilon^{\text{out}}_{\phi\phi}\ , \tag{5.72}$$

where ρ denotes the radius, ν the Poisson ratio, and ϵ_0 the relative lattice mismatch of the inclusion and the matrix. The radial displacements are

$$u^{\text{in}}_\rho = \frac{2}{3}\,\epsilon_0\,\frac{1-2\nu}{1-\nu}\,\rho \tag{5.73}$$

$$u^{\text{out}}_\rho = \frac{2}{3}\,\epsilon_0\,\frac{1-2\nu}{1-\nu}\,\rho_0^3\,\frac{1}{\rho^2}\ . \tag{5.74}$$

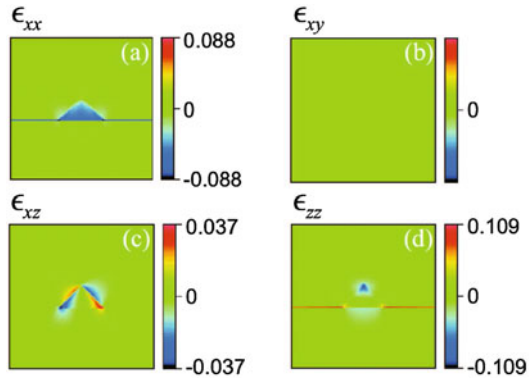

Fig. 5.34 Strain components in an InAs pyramid (quantum dot with {101} faces), embedded in GaAs. The cross section is through the center of the pyramid. The lattice mismatch between InAs and GaAs amounts to $\approx -7\%$. Reprinted with permission from [417], ©1995 APS

Dividing the displacement by the sphere's volume, we obtain the displacement per unit volume of the inclusion. From the displacement we can derive the stress σ_{ij}^0 per unit volume.

$$\sigma_{ii}^0 = \frac{1}{4\pi} \frac{Y\,\epsilon_0}{1-\nu} \frac{2x_i^2 - x_j - x_k}{\rho^5} \tag{5.75}$$

$$\sigma_{ij}^0 = \frac{3}{2} \frac{1}{4\pi} \frac{Y\,\epsilon_0}{1-\nu} \frac{x_i\,x_j}{\rho^5}\ , \tag{5.76}$$

where i, j and k are pairwise unequal indices. Due to the linear superposition of stresses, the stress distribution σ_{ij}^V for the arbitrary inclusion of volume V can be obtained by integrating over V

$$\sigma_{ij}^V = \int\limits_V \sigma_{ij}^0\,(\mathbf{r} - \mathbf{r_0})\,\mathrm{d}^3\mathbf{r}\ . \tag{5.77}$$

The strains can be calculated from the stresses.

When ϵ_0 is constant within V, the volume integral can be readily transformed into an integral over the surface ∂V of V using Gauss' theorem. With the 'vector potentials' $\mathbf{A}_{ij}$ we fulfill $\mathrm{div}\mathbf{A}_{ij} = \sigma_{ij}$.

$$\mathbf{A}_{ii} = -\frac{1}{4\pi} \frac{Y\,\epsilon_0}{1-\nu} \frac{x_i \mathbf{e}_i}{\rho^3} \tag{5.78}$$

$$\mathbf{A}_{ij} = -\frac{1}{2} \frac{1}{4\pi} \frac{Y\,\epsilon_0}{1-\nu} \frac{x_i\,\mathbf{e}_j + x_j\,\mathbf{e}_i}{\rho^3}\ . \tag{5.79}$$

Equation (5.79) is valid for the case $i \neq j$. $\mathbf{e}_i$ is the unit vector in the i-th direction. However, special care must be taken at the singularity $\mathbf{r} = \mathbf{r}_0$ if $\mathbf{r}_0$ lies within V because the stress within the 'δ-inclusion' is not singular (in contrast to the electrostatic analog of a δ-charge). Thus, we find

$$\sigma_{ij}^V(\mathbf{r}_0) = \oint\limits_{\partial V} \mathbf{A}_{ij}\,\mathrm{d}\mathbf{S} + \delta_{ij} \frac{Y\,\epsilon_0}{1-\nu} \int\limits_V \delta(\mathbf{r} - \mathbf{r_0})\,\mathrm{d}^3\mathbf{r}\ . \tag{5.80}$$

As an example, we show in Fig. 5.34 the numerically calculated strain components [417] (taking into account the different elastic properties of the dot and matrix materials) in the cross section of

a pyramidal InAs quantum dot in a GaAs matrix on top of a two-dimensional InAs layer. The strain component ϵ_{zz} is positive in the 2D layer, as expected from (5.66). However, in the pyramid ϵ_{zz} exhibits a complicated dependence and even takes negative values at the apex.

5.3.5 *Substrate Bending*

If a lattice-mismatched layer is pseudomorphically grown on top of a substrate it suffers biaxial strain. For finite substrate thickness part of the strain will relax via substrate bending. If the substrate is circular, a spherical cap is formed. If the lattice constant of the film is larger (smaller) than that of the substrate, the film is under compressive (tensile) strain and the curvature is convex (concave) with respect to the outward normal given by the growth direction (Fig. 5.35a). Substrate bending can also be induced by a mismatch of the thermal expansion coefficients $\alpha_{\rm th}^{\rm f}$ and $\alpha_{\rm th}^{\rm s}$ of the film and substrate, respectively. If a film/substrate system is flat at a given temperature, e.g. growth temperature, a decrease of temperature, e.g. during cooling, will lead to compressive (tensile) strain if $\alpha_{\rm th}^{\rm f}$ is smaller (larger) than $\alpha_{\rm th}^{\rm s}$.

In a curved structure, the lattice constant in the tangential direction increases from $a_{\rm i}^{\rm t}$ at the inner surface ($r = R = \kappa^{-1}$) to $a_{\rm u}^{\rm t}$ at the outer surface ($r = R + d$). Thus, the tangential lattice constant varies with the radial position

$$a^{\rm t}(r) = a_{\rm i}^{\rm t}\,(1 + r\,\kappa)\ , \tag{5.81}$$

where d is the layer thickness (Fig. 5.35b). Therefore $a_{\rm u} = a_{\rm i}(1 + d/R)$. We note that (5.81) holds in all layers of a heterostructure, i.e. the film *and* the substrate.

The lattice constant in the radial direction $a^{\rm r}$, however, depends on the lattice constant a_0 of the local material and is calculated from the biaxial strain condition, such as (5.66). The in-plane strain is $\epsilon_\parallel = (a^{\rm t} - a_0)/a_0$ (we assume a spherical cap with $\epsilon_\parallel = \epsilon_{\theta\theta} = \epsilon_{\phi\phi}$). For an isotropic material we find $a^{\rm r} = a_0\,(1 + \epsilon_\perp)$ with $\epsilon_\perp = -2\nu\epsilon_\parallel/(1 - \nu)$. The local strain energy density U is given by

$$U = \frac{Y}{1 - \nu}\,\epsilon_\parallel^2\ . \tag{5.82}$$

The total strain energy per unit area U' of a system of two layers with lattice constants a_1, a_2, Young's moduli Y_1, Y_2 and thickness d_1, d_2 (we assume the same Poisson constant ν in both layers) is

$$U' = \int_0^{d_1} U_1\,{\rm d}r + \int_{d_1}^{d_2} U_2\,{\rm d}r\ . \tag{5.83}$$

The total strain energy needs to be minimized with respect to $a_{\rm i}$ and R in order to find the equilibrium curvature κ. We find

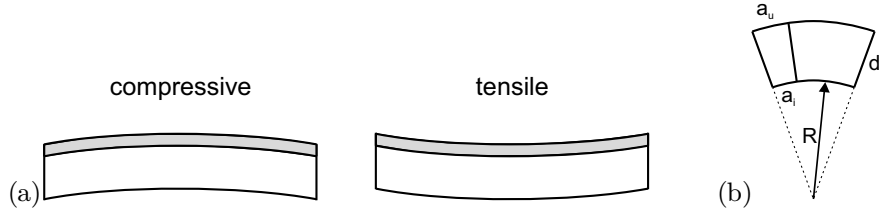

Fig. 5.35 **a** Schematic bending of a film/substrate system for compressive (left) and tensile (right) film strain. **b** Schematic deformation of curved film of thickness d. The lattice constants at the inner and outer surface are $a_{\rm i}$ and $a_{\rm u}$, respectively

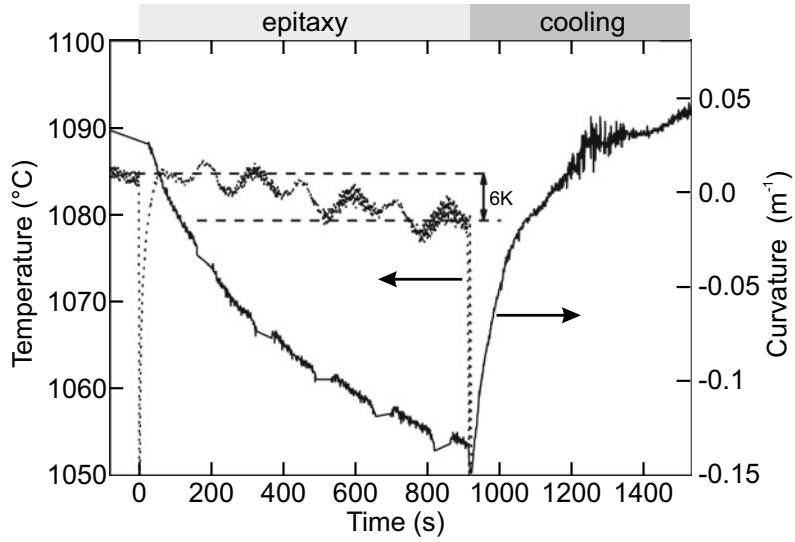

Fig. 5.36 Curvature of the middle of a Si wafer during GaN growth on an AlN interlayer grown at low temperatures on GaN and subsequent cooling. During growth the decrease in curvature indicates convex bowing due to compressive stress; during cooling the wafer flattens and becomes concave due to thermally induced tensile stress. Adapted from [422]

$$\kappa = \frac{6a_1a_2\,(a_2-a_1)\,d_1d_2\,(d_1+d_2)\,Y_1Y_2}{a_2^3\,d_1^4\,Y_1^2+\alpha\,Y_1Y_2+a_1^3\,d_2^4\,Y_2^4} \tag{5.84}$$
$$\alpha = a_1a_2\,d_1d_2\,\left[-a_2d_1(2d_1+3d_2)+a_1(6d_1^2+9d_1d_2+4d_2^2)\right]\,.$$

For $a_2 = a_1\,(1+\epsilon)$ we develop κ to first order of ϵ and find ($\chi = Y_2/Y_1$) [418, 419]

$$\kappa = \frac{6\chi\,d_1\,d_2\,(d_1+d_2)}{d_1^4+4\chi\,d_1^3\,d_2+6\chi\,d_1^2\,d_2^2+4\chi\,d_1\,d_2^3+\chi^2\,d_2^4}\,\epsilon\,. \tag{5.85}$$

In the case of a substrate (d_s) with a thin epitaxial layer ($d_f \ll d_s$), the radius of curvature is approximately (Stoney's formula [420])

$$\kappa = 6\,\epsilon\,\frac{d_f}{d_s^2}\,\frac{Y_f}{Y_s}\,. \tag{5.86}$$

Conversely, if the radius of curvature is measured [421], e.g. optically, the film curvature (and through models also the film strain) can be determined during epitaxy as depicted in Fig. 5.36.

5.3.6 Scrolling

In some cases cylindrically scrolled structures are important, e.g. for thin-film flexible electronics, nanotubes, nanoscrolls or nanohelixes. The scrolling of thin layers must be avoided by suitable strain management for thin layers that are lifted off from their substrate for transfer to another flat substrate. If the film remains attached to its substrate, a scroll can be fabricated as schematically shown in Fig. 5.37. Such structures were first reported in [423], a review can be found in [424]. The shape of such scroll is investigated in [425] without a priori assumptions on its shape.

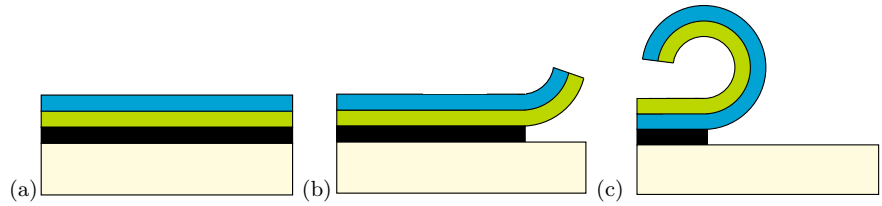

Fig. 5.37 Schematic representation of nanoscroll formation. **a** Strained heterostructure (*blue/green*) that is planar due to large substrate thickness, **b** starting removal of sacrificial layer (*black*), **c** release of thin film into nanoscroll geometry

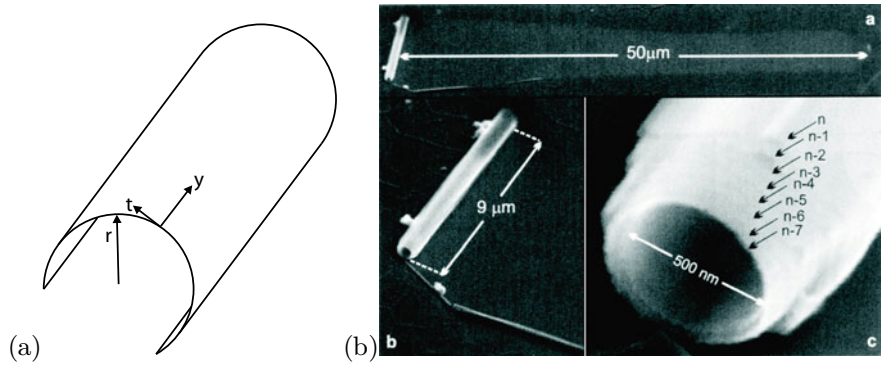

Fig. 5.38 **a** Schematic representation of a cylindrically rolled sheet with radial direction r, tangential direction t and direction along the cylinder axis y. **b** SEM images of multiwall (In,Ga)As/GaAs nanoscroll rolled up over about 50 µm. Part (**b**) from [426]

If bending strain occurs only in *one* of the tangential directions, the energy density is given by

$$U = \frac{Y}{2\,(1-\nu^2)}\,(\epsilon_t^2 + \epsilon_y^2 + 2\nu\,\epsilon_t\,\epsilon_y)\ , \tag{5.87}$$

where ϵ_y is the strain in the unbent direction (cylinder axis) as shown in Fig. 5.38a. For a strained heterostructure made up from two layers the curvature is given by (calculated analogous to (5.85), $\chi = Y_2/Y_1$ [419])

$$\kappa = \frac{6(1+\nu)\,\chi\,d_1\,d_2\,(d_1+d_2)}{d_1^4 + 4\chi\,d_1^3\,d_2 + 6\chi\,d_1^2\,d_2^2 + 4\chi\,d_1\,d_2^3 + \chi^2\,d_2^4}\,\epsilon\ , \tag{5.88}$$

which differs from (5.85) only by the factor $1+\nu$ in the nominator.

For cubic material and a (001) surface the energy is given as

$$U_{100} = \frac{C_{11}-C_{12}}{2C_{11}}\left[C_{11}\,(\epsilon_t^2 + \epsilon_y^2 + C_{12}\,(\epsilon_t+\epsilon_y)^2)\right] \tag{5.89}$$

for a scrolling direction along $\langle 100\rangle$. When the (001)-oriented film winds up along a direction $\langle hk0\rangle$ having an angle ϕ with the [100] direction ($\phi = 45°$ for $\langle 110\rangle$), the strain energy is given by (C_0 is given by (5.58))

$$U_\phi = U_{100} + C_0\left(\frac{\epsilon_t - \epsilon_y}{2}\right)^2 \sin^2(2\phi)\ . \tag{5.90}$$

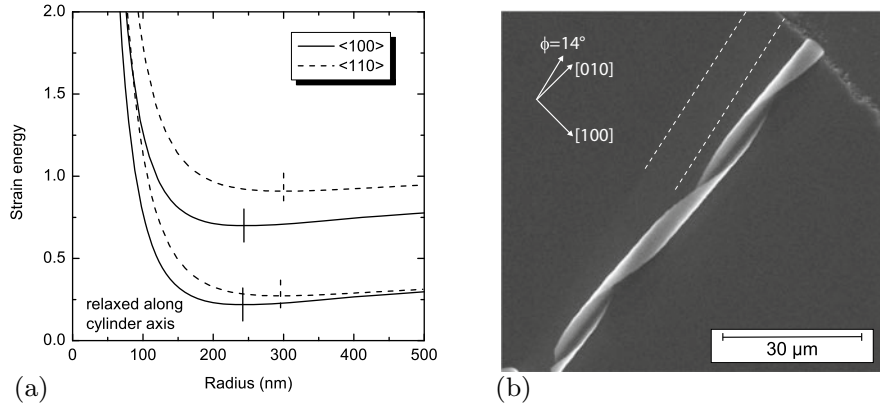

Fig. 5.39 **a** Strain energy (in units of the strain energy of the flat pseudomorphic layers) of a scroll of a 4-layer SiGe structure ($Si_{0.3}Ge_{0.7}$, $Si_{0.6}Ge_{0.4}$ and $Si_{0.8}Ge_{0.2}$, each 3 nm thick and a 1 nm Si cap) as a function of radius for winding directions along ⟨100⟩ and ⟨110⟩. *Top* (*bottom*) curves without (with complete) strain relaxation along the cylinder axis. *Vertical lines* indicate the positions of the respective energy minima [419]. **b** SEM image of curled (In, Ga)As/GaAs nanoscroll rolled $\phi = 14°$ off ⟨100⟩. The stripe from which the film was rolled off is indicated by *white dashed lines*. Part (**b**) from [429]

The strain energy versus bending radius ($= \kappa^{-1}$) is shown for a SiGe nanoscroll in Fig. 5.39. First, the relaxation along the cylinder axis plays a minor role. The smallest strain energy is reached for scrolling along ⟨100⟩, also yielding the smaller bending radius (larger curvature). Therefore, the film preferentially scrolls along ⟨100⟩. This explains the observed 'curl' behavior of scrolls winding up for $\phi \neq 0$ [423, 427] (Fig. 5.39b). The effect of surface strain needs to be included to yield improved quantitative agreement with experimental values of $\kappa(\epsilon, d)$ [428].

5.4 Plasticity

5.4.1 Critical Thickness

Strained epitaxial films are called pseudomorphic when they do not contain defects and the strain relaxes elastically, e.g. by tetragonal distortion. When the layer thickness increases, however, strain energy is accumulated that will lead at some point to plastic relaxation via the formation of defects. In many cases, a grid of misfit dislocations forms at the interface (Figs. 4.18 and 5.40).

In Fig. 5.41 the strain around misfit dislocations at a GaAs/CdTe heterointerface, as calculated from a TEM image (Fig. 4.14), is shown.

The average distance p of the dislocations is related to the misfit $f = (a_1 - a_2)/a_2$ and the edge component $b_\perp$ of the Burger's vector (for a 60° dislocation $b_\perp = a_0/\sqrt{8}$)

$$p = \frac{b_\perp}{f} \,. \tag{5.91}$$

Two mechanisms have been proposed for the formation of misfit dislocations (Fig. 5.42), the elongation of a grown-in threading dislocation [432, 433] and the nucleation and growth of dislocation half-loops [434]. For the modeling of such systems a mechanical approach based on the forces on dislocations [432] or an energy consideration based on the minimum strain energy necessary for defect formation

[434–437] can be followed. Both approaches have been shown to be equivalent [438] (if a periodic array of dislocations is considered). In [439] it was pointed out that the finite speed of plastic flow also has to be considered to explain experimental data. Temperature affects the observed critical thickness and a kinetic model is needed. Another way of introducing dislocations is the plastic relaxation at the edge of coherent strained islands (cmp. Fig. 14.37).

In the following, isotropic materials and identical elastic constants of substrate and thin film are assumed, following [438]. The interface plane is the (x,y)-plane, the growth direction is z. The energy E_d of a periodic dislocation array with period p and Burgers vector $\mathbf{b} = (b_1, b_2, b_3)$ is

$$
\begin{aligned}
E_\mathrm{d} &= \frac{Y}{8\pi\,(1-\nu^2)}\,\beta^2 \qquad (5.92)\\
\beta^2 &= \left[b_1^2 + (1-\nu)\,b_2^2 + b_3^2\right]\,\ln\left(\frac{p\,\left[1-\exp(-4\pi h/p)\right]}{2\pi\,q}\right)\\
&\quad + \left(b_1^2 - b_3^2\right)\,\frac{4\pi h}{p}\,\frac{\exp(-4\pi h/p)}{1-\exp(-4\pi h/p)}\\
&\quad - \frac{1}{2}\left(b_1^2 + b_3^2\right)\left(\frac{4\pi h}{p}\right)^2\,\frac{\exp(-4\pi h/p)}{\left[1-\exp(-4\pi h/p)\right]^2}\\
&\quad + b_3^2\,\frac{2\pi h}{p}\,\frac{\exp(-2\pi h/p)}{1-\exp(-2\pi h/p)}\,,
\end{aligned}
$$

where h is the film thickness and q denotes the cutoff length for the dislocation core, taken as $q = b$. The misfit strain including the relaxation due to dislocations with Burger's vectors $\mathbf{b}$ and $\hat{\mathbf{b}}$ in the two orthogonal interface $\langle 110\rangle$ directions $\mathbf{n}$ and $\hat{\mathbf{n}}$. We chose the coordinate system such that $\mathbf{n} = (1, 0, 0)$ and $\hat{\mathbf{n}} = (0, 1, 0)$ (the z direction remains). With respect to these axes the Burger's vectors are $\left(\pm\frac{1}{2}, \frac{1}{2}, \frac{1}{\sqrt{2}}\right) a_0/\sqrt{2}$. The misfit strain ϵ_{ij}^m is reduced due to the dislocation formation to the 'relaxed' misfit strain ϵ_{ij}^r with

$$
\epsilon_{ij}^\mathrm{r} = \epsilon_{ij}^\mathrm{m} + \frac{b_i\,n_j + b_j\,n_i}{2p} + \frac{\hat{b}_i\,\hat{n}_j + \hat{b}_j\,\hat{n}_i}{2p}\,, \qquad (5.93)
$$

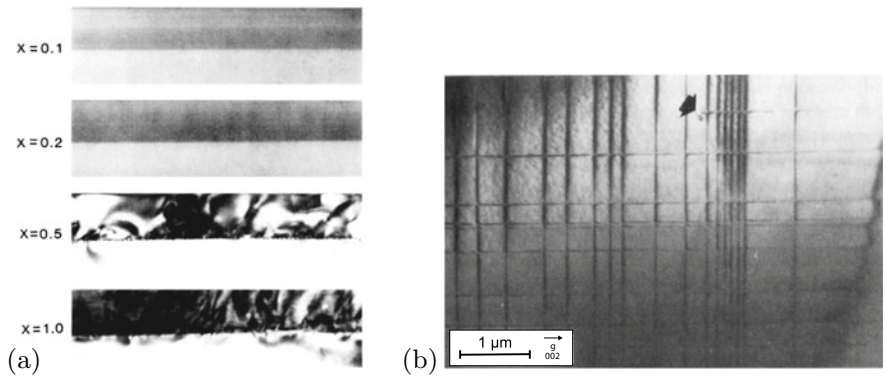

Fig. 5.40 **a** Series of cross-sectional TEM images of 100 nm thick Ge_xSi_{1-x} layers on Si(001) with different ternary compositions $x = 0.1$, 0.2, 0.5, and 1.0. The growth temperature was 550 °C. The transition from commensurate to incommensurate growth is obvious. Adapted from [430]. **b** Plan view $\langle 022\rangle$ TEM bright field image of a 250 nm $Ge_{0.15}Si_{0.85}$ layer on Si (001), annealed at about 700 °C. The arrow denotes the position of a dislocation loop. Reprinted with permission from [431], ©1989 AVS

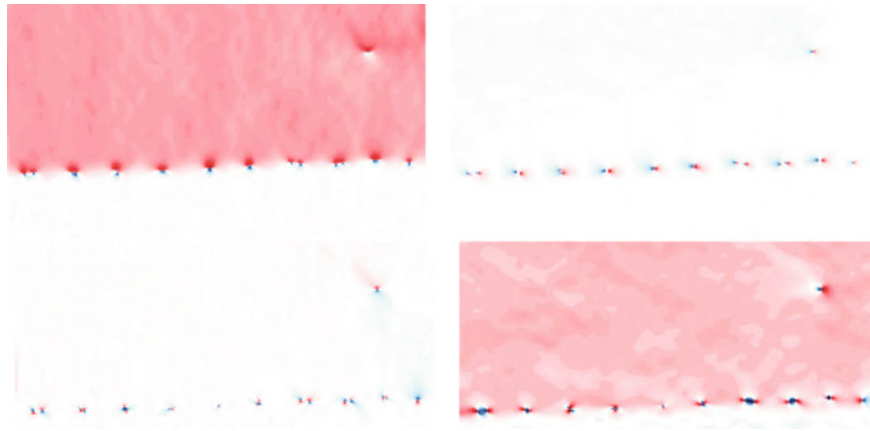

Fig. 5.41 Components $\begin{pmatrix} \epsilon_{xx} & \epsilon_{xz} \\ \epsilon_{zx} & \epsilon_{zz} \end{pmatrix}$ of the strain tensor (with respect to the GaAs lattice constant) of the dislocation array shown in Fig. 4.14, *red*/*blue*: positive/negative value, *white*: zero. From [321]

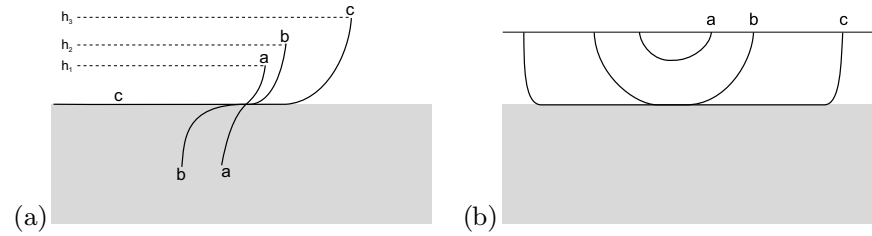

Fig. 5.42 Schematic formation of misfit dislocations by **a** elongation of a grown-in threading dislocation and **b** by the nucleation and growth of dislocation half-loops. **a** depicts a threading dislocation. Initially, for thickness h_1 the interface is coherent 'a', for larger thickness h_2 the interface is critical and the force of the interface on the dislocation is equal to the tension in the dislocation line, 'b'. For larger thickness, e.g. h_3, the dislocation line is elongated in the plane of the interface, 'c'. In **b** 'a' denotes a subcritical dislocation half-loop, 'b' depicts a half-loop being stable under the misfit stress and for 'c' the loop has grown under the misfit stress into a misfit dislocation line along the interface

with an associated stress σ_{ij}. The strain energy E_s of the layer due to the relaxed misfit is then

$$E_\mathrm{s} = \frac{1}{2}\, h\, \sigma_{ij}\, \epsilon^\mathrm{r}_{ij} \tag{5.94}$$

$$\lim_{p\to\infty} E_\mathrm{s} = 2h\, \frac{Y(1+\nu)}{1-\nu}\, f^2\ . \tag{5.95}$$

The total strain energy E is given by

$$pE = 2E_\mathrm{d} + 2E_\mathrm{c} + p\, E_\mathrm{s} \tag{5.96}$$

$$E_\infty = \lim_{p\to\infty} E\ , \tag{5.97}$$

with the core energy E_c of the dislocation that needs to be calculated with an atomistic model (not considered further here). This energy is shown in Fig. 5.43a for the material parameters of $Ge_{0.1}Si_{0.9}$/Si(001) (misfit -0.4%) for various layer thicknesses as a function of $1/p$. This plot looks similar to that for a first-order phase transition (with $1/p$ as the order parameter). For a certain critical thickness h_{c1} the

energy of the layer without any dislocation and the layer with a particular dislocation density p_1 are identical ($E - E_\infty = 0$) and additionally $\partial E/\partial p|_{p=p_1} = 0$. However, between $p \to \infty$ and $p = p_0$ there is an energy barrier. The critical thickness h_{c2} is reached when

$$\partial E/\partial p \mid_{p\to\infty} = 0 \,, \tag{5.98}$$

i.e. the energy decreases monotonically for increasing dislocation density up to the global energy minimum at a certain equilibrium dislocation spacing p_2. Equation (5.98) leads to the following implicit equation for the determination of h_{c2}:

$$h_{c2} = \frac{b\left[-16 + 3b^2 + 8\,(-4+\nu)\,\ln\left(2h_{c2}/q\right)\right]}{128\,f\pi\,(1+\nu)} \,, \tag{5.99}$$

with the length of the Burgers vector $b = a_0/\sqrt{2}$.

The theoretical dependence of h_{c2} for Ge_xSi_{1-x}/Si(001) with varying composition is shown in Fig. 5.43b together with experimental data. The critical thickness for a fairly high growth temperature is much closer to the energetic equilibrium than that deposited at lower temperature. This shows that there are kinetic limitations for the system to reach the mechanical equilibrium state. Also, the experimental determination of the critical thickness is affected by finite resolution for large dislocation spacing, leading generally to an overestimate of h_c.

In zincblende materials, two types of dislocations are possible, α and β, with Ga- and As-based cores, respectively. They have $[\bar{1}10]$ and $[110]$ line directions for a compressively strained interface. The α dislocation has the larger glide velocity. Therefore, strain relaxation can be anisotropic with regard to the $\langle 110\rangle$ directions for zincblende material, e.g. (In,Ga)As/GaAs [441, 442].

A more complicated relaxation situation is visualized in Fig. 4.18 for an $Al_{0.13}Ga_{0.87}N$/GaN heterostructure on $(30\bar{3}1)$ substrate. Below the critical thickness only threading dislocations stemming from the substrate are visible. Above the critical thickness, misfit dislocations have developed along three directions which related to the intersections of the basal c-plane (00.1) and two prismatic m-plane {10.1} glide systems with the $(30\bar{3}1)$ interface plane [324, 443]. We like to mention that cathodolumi-

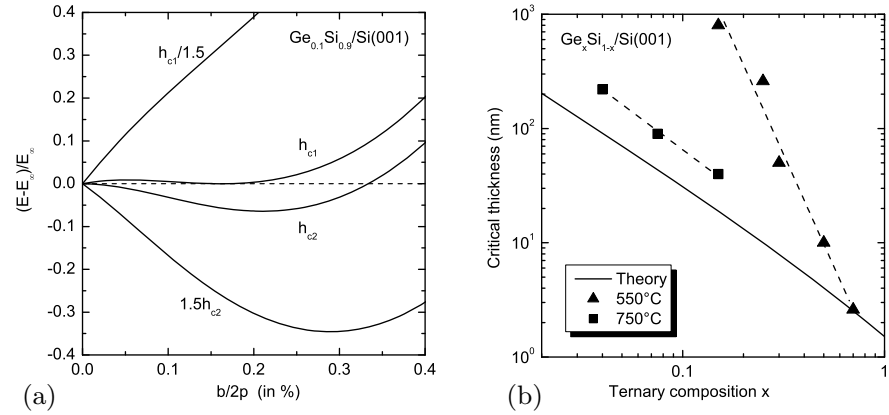

Fig. 5.43 **a** Theoretical calculation for the strain energy versus inverse dislocation density for various thicknesses of $Ge_{0.1}Si_{0.9}$ layers on Si (001). The ordinate is $b/2p$, $b/2$ being the edge component of the Burgers vector and p being the dislocation spacing. The abscissa is the strain energy E scaled with E_∞ (5.97). (**b**) Critical thickness for Ge_xSi_{1-x} layers on Si (001). The *solid line* is theory (h_{c2}) according to (5.99). Data points are from [440] (*squares*, growth temperature of 750 °C) and from [430] (*triangles* for growth temperature of 550 °C)

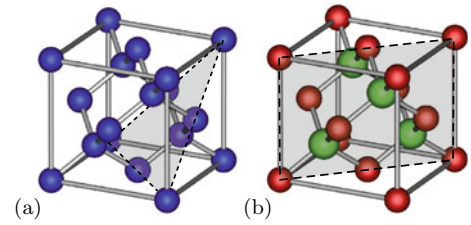

Fig. 5.44 Cleaving planes of the **a** diamond and **b** zincblende lattice

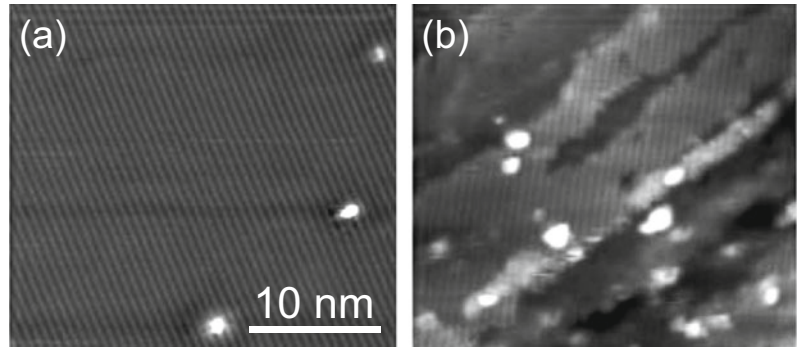

Fig. 5.45 Scanning tunneling microscopy images of a cleaved GaAs (110) surface with **a** good cleave and **b** bad cleave with defects dominating. Adapted from [446]

nescence (or X-ray imaging) offer a quite high sensitivity for plastic relaxation since a small number of dislocations can be detected in relatively large areas (while TEM finds defects but only within small areas and X-ray diffraction looks at large area but has only a low strain sensitivity).

5.4.2 Cleaving

The cleavage planes of the diamond structure are {111} planes (Fig. 5.44a). It is easiest to break the bonds connecting the double layers in the ⟨111⟩ directions.

The cleavage planes of the zincblende structure are {110} planes (Fig. 5.44b). Due to the ionic character, breaking the bonds connecting the double layers in the ⟨111⟩ directions would leave charged surfaces, which is energetically unfavorable. The {100} planes contain only one sort of atom and would also leave highly charged surfaces. The {110} planes contain equal amounts of A- and B-atoms and are neutral. Ideally, the cleaving plane is atomically flat (Fig. 5.45a) or exhibits large mono-atomically flat terraces. However, certain dopants in high concentrations, e.g. GaAs:Te, can induce a rough surface due to lattice distortion [444].

The natural cleavage planes of wurtzite (GaN) are $\{1\bar{1}.0\}$ (m-type) planes [445].

5.4.3 Wafer Breakage

The thickness and thus strength of wafers for semiconductor production (cmp. Sect. 12.2.2) is an important issue. The wafer should be as thin as possible for saving expensive materials but thick enough to avoid loss due to stress during handling, in particular during the later steps in a process since the value of a wafer increases with number of process steps it has undergone.

Reasons for wafer breakage is the mechanical handling (pick, place, transport) [447], stress loads due to processing (dielectrics, metals, asymmetric structures) and stress during processing for example due to thermal loads in annealing or deposition steps and cutting/dicing. The problem is less important in microelectronics but especially severe in photovoltaics (PV) industry, handling large total areas; on the other hand the profit loss per broken wafer is much higher in the microelectronics industry. An additional problem poses the grain structure of multicrystalline silicon wafers used for PV [448] and the effect of surface cracks and irregularities at wafer edges and corners. Just going from a wafer thickness of 270 µm to 250 µm can more than double the breakage rate at certain process steps [449]. The minimum strength of a wafer with surface cracks is about 100 MPa, while the strength of wafers with cracks at the edge can reach rather low values around 20 MPa. Also the careful shaping of the wafer edge is important to avoid breakage [450].

Chapter 6
Band Structure

Silicon is a metal.

A.H. Wilson, 1931 [74]

Abstract A treatment of electron states in one-dimensional potentials introduces into the concepts of band gap and effective mass. The band structures of various semiconductors are reviewed. The systematics of band gaps, symmetry considerations, band gaps in alloys, amorphous semiconductors and the effect of strain and temperature are discussed. Electron and hole dispersions are treated and the density of states in various dimensions is derived.

6.1 Introduction

Valence electrons that move in the crystals feel a periodic potential

$$U(\mathbf{r}) = U(\mathbf{r} + \mathbf{R}) \tag{6.1}$$

for all vectors $\mathbf{R}$ of the direct lattice. The potential[1] is due to the effect of the ion cores and all other electrons. Thus a serious many-body problem is present. In principle, the band structure can be calculated from the periodic arrangements of the atoms and their atomic order number. We note that for some problems, e.g. the design of optimal solar cells, a certain band structure is known to be ideal and a periodic atomic arrangement, i.e. a material, needs to be found that generates the optimal band structure. This problem is called the *inverse band structure problem*.

6.2 Electrons in a Periodic Potential

6.2.1 Bloch's Theorem

First, we will deduce some general conclusions about the structure of the solution as a consequence of the periodicity of the potential. We first investigate the solution of a Schrödinger equation of the type

[1] In this book the form of the potential will never be explicitly given.

M. Grundmann, *The Physics of Semiconductors*, Graduate Texts in Physics,
https://doi.org/10.1007/978-3-030-51569-0_6

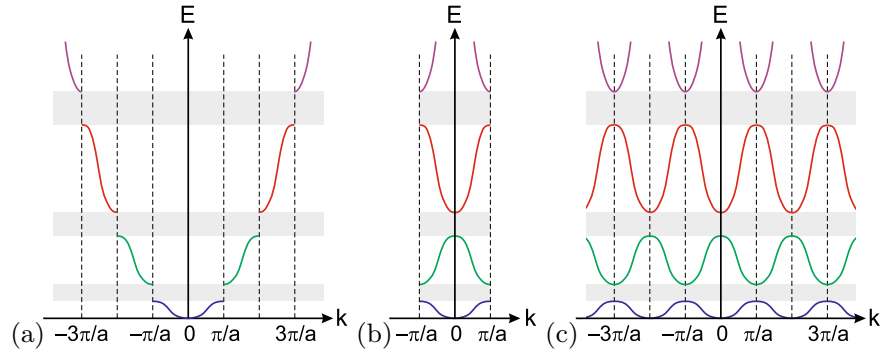

Fig. 6.1 Zone schemes for a band structure: **a** extended, **b** reduced and **c** repetitive zone scheme

$$H\,\Psi(\mathbf{r}) = \left[-\frac{\hbar^2}{2m}\nabla^2 + U(\mathbf{r})\right]\Psi(\mathbf{r}) = E\,\Psi(\mathbf{r}) \tag{6.2}$$

for an electron. U will be periodic with the lattice, i.e. it will obey (6.1).

Bloch's theorem says that the eigenstates Ψ of a one-particle Hamiltonian as in (6.2) can be written as the product of plane waves and a lattice-periodic function, i.e.

$$\Psi_{n\mathbf{k}}(\mathbf{r}) = A\,\exp(\mathrm{i}\,\mathbf{k}\,\mathbf{r})\,u_{n\mathbf{k}}(\mathbf{r})\ . \tag{6.3}$$

The normalization constant A is often omitted. If $u_{n\mathbf{k}}(\mathbf{r})$ is normalized, $A = 1/\sqrt{V}$, where V is the integration volume. The wavefunction is indexed with a quantum number n and the wavevector $\mathbf{k}$. The key is that the function $u_{n\mathbf{k}}(\mathbf{r})$, the so-called Bloch function, is periodic with the lattice, i.e.

$$u_{n\mathbf{k}}(\mathbf{r}) = u_{n\mathbf{k}}\,(\mathbf{r} + \mathbf{R}) \tag{6.4}$$

for all vectors $\mathbf{R}$ of the direct lattice. The proof is simple in one dimension and more involved in three dimensions with possibly degenerate wavefunctions, see [451].

If $E_{n\mathbf{k}}$ is an energy eigenvalue, then $E_{n\mathbf{k}+\mathbf{G}}$ is also an eigenvalue for all vectors $\mathbf{G}$ of the reciprocal lattice, i.e.

$$E_n(\mathbf{k}) = E_n\,(\mathbf{k} + \mathbf{G})\ . \tag{6.5}$$

Thus the energy values are periodic in reciprocal space. The proof is simple, since the wavefunction (for $\mathbf{k}+\mathbf{G}$) $\exp(\mathrm{i}(\mathbf{k}+\mathbf{G})\mathbf{r})u_{n(\mathbf{k}+\mathbf{G})}(\mathbf{r})$ is for $u_{n(\mathbf{k}+\mathbf{G})}(\mathbf{r}) = \exp(-\mathrm{i}\mathbf{G}\mathbf{r})u_{n\mathbf{k}}(\mathbf{r})$ obviously an eigenfunction to $\mathbf{k}$.

A band structure along one $\mathbf{k}$-direction can be displayed in various zone schemes as depicted in Fig. 6.1. The most frequently used scheme is the *reduced* zone scheme. In three dimensions, the band structure is typically shown along particular paths in the Brillouin zone, as depicted, e.g., in Fig. 6.2c.

6.2.2 Free-Electron Dispersion

If the entire wavefunction (from (6.3)) obeys the Schrödinger equation (6.2), the Bloch function $u_{n\mathbf{k}}$ fulfills the equation

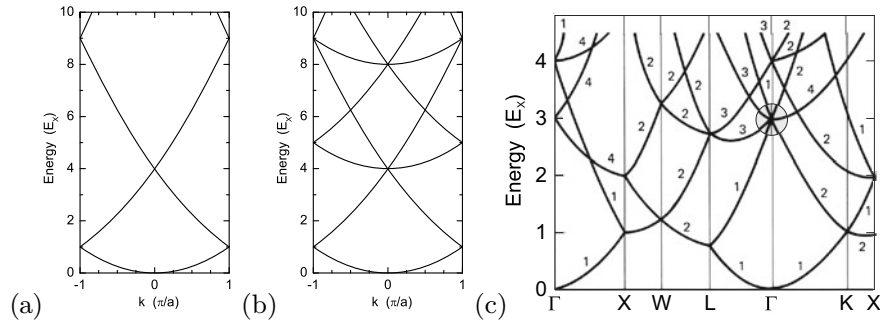

Fig. 6.2 Dispersion of free electrons (empty lattice calculation, $U = 0$, shown in the first Brillouin zone) in **a** a one-dimensional lattice ($\mathbf{G} = n\,2\pi/a$), **b** a simple cubic lattice ($\mathbf{G} = (h, k, l)\,2\pi/a$) and **c** in a fcc lattice. The energy is measured in units of the energy at the X-point, $E_X = (\hbar^2/2m)(\pi/a)^2$. The *shaded circle* in (**c**) represents the region where the band gap develops for finite periodic potential $U \neq 0$

$$\left[\frac{1}{2m}\,(\mathbf{p} + \hbar\,\mathbf{k})^2 + U(\mathbf{r})\right] u_{n\mathbf{k}}(\mathbf{r}) = E_{n\mathbf{k}}\,u_{n\mathbf{k}}(\mathbf{r})\ , \tag{6.6}$$

which is easy to see from $\mathbf{p} = -i\hbar\nabla$.

First, we discuss the simplest case of a periodic potential, $U \equiv 0$. This calculation is also called the *empty lattice* calculation. The solution of (6.6) is then just constant, i.e. $u_{\mathbf{k}} = c$ and $\Psi_{\mathbf{k}}(\mathbf{r}) = c\,\exp(\mathrm{i}\mathbf{k}\mathbf{r})$. The dispersion of the free electron is then given by

$$E(\mathbf{k}) = \frac{\hbar^2}{2m}\,\mathbf{k}^2\ , \tag{6.7}$$

where $\mathbf{k}$ is an arbitrary vector in the reciprocal space. $\mathbf{k}'$ is a vector from the Brillouin zone such that $\mathbf{k} = \mathbf{k}' + \mathbf{G}$ with a suitable reciprocal lattice vector $\mathbf{G}$. Because of (6.5) the dispersion relation can be written also as

$$E(\mathbf{k}) = \frac{\hbar^2}{2m}\,(\mathbf{k}' + \mathbf{G})^2\ , \tag{6.8}$$

where $\mathbf{k}'$ denotes a vector from the Brillouin zone. Thus, many branches of the dispersion relation arise from using various reciprocal lattice vectors in (6.8).

The resulting dispersion relation for the free electron is shown in Fig. 6.2a for a one-dimensional system ($\mathbf{k}'$ and $\mathbf{G}$ are parallel) and in Fig. 6.2b for the simple cubic lattice (in the so-called reduced zone scheme). In Fig. 6.2c, the (same) dispersion of the free electron is shown for the fcc lattice.

6.2.3 Non-Vanishing Potential

Now the effect of a non-vanishing periodic potential on electron motion will be discussed. A simple, analytically solvable model that visualizes the effect of a periodic potential on the dispersion relation of the electrons and the formation of a (one-dimensional) band structure with gaps is the Kronig-Penney model [71] which is discussed in the Appendix F.

6.2.3.1 General Wave Equation

In this section, we will discuss the solution of a general wave equation for electrons in a periodic potential. The solution is investigated particularly at the zone boundary. The potential U is periodic with the lattice (6.1). It can be represented as a Fourier series with the reciprocal lattice vectors (lattice vector expansion, cf. (3.19)):

$$U(\mathbf{r}) = \sum_{\mathbf{G}} U_{\mathbf{G}} \, \exp(\mathrm{i}\,\mathbf{G}\,\mathbf{r}) \ . \tag{6.9}$$

Since U is a real function, $U_{-\mathbf{G}} = U_{\mathbf{G}}^*$. The deeper reason for the success of such an approach is that for typical crystal potentials, the Fourier coefficients decrease rapidly with increasing $\mathbf{G}$, e.g. for the unscreened Coulomb potential $U_{\mathbf{G}} \propto 1/G^2$. The wavefunction is expressed as a Fourier series (or integral) over all allowed (Bloch) wavevectors $\mathbf{K}$,

$$\Psi(\mathbf{r}) = \sum_{\mathbf{K}} C_{\mathbf{K}} \, \exp(\mathrm{i}\,\mathbf{K}\,\mathbf{r}) \ . \tag{6.10}$$

The kinetic and potential energy terms in the Schrödinger equation (6.6) are

$$\nabla^2 \Psi = -\sum_{\mathbf{K}} \mathbf{K}^2 \, C_{\mathbf{K}} \, \exp(\mathrm{i}\,\mathbf{K}\,\mathbf{r}) \tag{6.11a}$$

$$U\Psi = \sum_{\mathbf{G}} \sum_{\mathbf{K}} U_{\mathbf{G}} \, C_{\mathbf{K}} \, \exp(\mathrm{i}\,(\mathbf{G}+\mathbf{K})\,\mathbf{r}) \ . \tag{6.11b}$$

With $\mathbf{K}' = \mathbf{K} + \mathbf{G}$, (6.11b) can be rewritten as

$$U\Psi = \sum_{\mathbf{G}} \sum_{\mathbf{K}'} U_{\mathbf{G}} \, C_{\mathbf{K}'-\mathbf{G}} \, \exp\left(\mathrm{i}\,\mathbf{K}'\,\mathbf{r}\right) \ . \tag{6.12}$$

Now, the Schrödinger equation can be written as an (infinite) system of algebraic equations:

$$(\lambda_{\mathbf{K}} - E)\, C_{\mathbf{K}} + \sum_{\mathbf{G}} U_{\mathbf{G}} \, C_{\mathbf{K}-\mathbf{G}} = 0 \ , \tag{6.13}$$

with $\lambda_{\mathbf{K}} = \hbar^2 \, \mathbf{K}^2/(2m)$.

6.2.3.2 Solution for One Fourier Coefficient

The simplest (non-trivial) potential energy has only one important Fourier coefficient $-U$ ($U > 0$) for the shortest reciprocal lattice vector $\mathbf{G}$. Also, we have $U_{-\mathbf{G}} = U_{\mathbf{G}}$. Thus, the (one-dimensional) potential has the form $U(x) = -2\,U\,\cos(Gx)$. Then the equation system (6.13) has only two equations for $C_{\mathbf{K}}$ and $C_{\mathbf{K}-\mathbf{G}}$, leading to the condition

$$\begin{vmatrix} \lambda_{\mathbf{K}} - E & -U \\ -U & \lambda_{\mathbf{K}-\mathbf{G}} - E \end{vmatrix} = 0 \ . \tag{6.14}$$

We find two solutions

$$E_{\pm} = \frac{\lambda_{\mathbf{K}} + \lambda_{\mathbf{K}-\mathbf{G}}}{2} \pm \sqrt{\left(\frac{\lambda_{\mathbf{K}} - \lambda_{\mathbf{K}-\mathbf{G}}}{2}\right)^2 + U^2} \ . \tag{6.15}$$

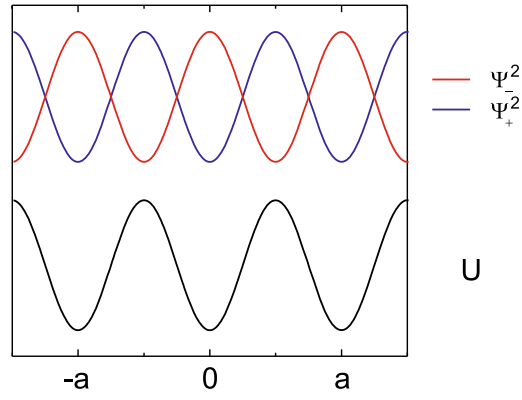

Fig. 6.3 Periodic potential U (one-dimensional cosine, *black*) and the squares of the wavefunctions Ψ_- (*red*) and Ψ_+ (*blue*) for the wavevector at the zone boundary, $K = G/2 = \pi/a$

6.2.3.3 Solution at the Zone Boundary

We consider the solution at the zone boundary, i.e. at $\mathbf{K} = \mathbf{G}/2$. The kinetic energy is then the same for $\mathbf{K} = \pm\mathbf{G}/2$, i.e. $\lambda_{\mathbf{K}} = \lambda_{\mathbf{K}-\mathbf{G}} = (\hbar^2/2m)\,(G^2/4) = \lambda$. The determinant (6.14) reads then

$$(\lambda - E)^2 - U^2 = 0\,. \tag{6.16}$$

Thus the energy values at the zone boundary are

$$E_\pm = \lambda \pm U = \frac{\hbar^2}{2m}\,\frac{G^2}{4} \pm U\,. \tag{6.17}$$

At the zone boundary, a splitting of the size $E_+ - E_- = 2U$ occurs. The center of the energy gap is given by the energy $\lambda_{\mathbf{K}}$ of the free-electron dispersion. The ratio of the coefficients is $C_{\mathbf{G}/2}/C_{-\mathbf{G}/2} = \mp 1$. The '$-$' solution of (6.17) (lower energy) is a standing cosine wave (Ψ_-), the '$+$' solution (Ψ_+) is a standing sine wave as visualized in Fig. 6.3. For the lower-energy (binding) state the electrons are localized at the potential minima, i.e. at the atoms, for the upper state (antibinding) the electrons are localized between the atoms. Both wavefunctions have the same periodicity since they belong to the same wavevector $\mathbf{K} = \mathbf{G}/2$. We note that the periodicity of Ψ is $2a$, while the periodicity of Ψ^2 is equal to the lattice constant a.

6.2.3.4 Gap States

For energies within the gap, solutions with a *complex* wavevector $K = G/2 + \mathrm{i}\,q$ exist. Solving (6.16) results (in terms of $q'^2 = (\hbar^2/2m)\,q^2$) to

$$E_\pm = \lambda - q'^2 \pm \sqrt{-4\,\lambda\,q'^2 + U^2}\,. \tag{6.18}$$

For energies $E = \lambda + \epsilon$ with $-U \le \epsilon \le U$, the complex part of the wavevector is given by

$$q'^2 = -(\epsilon + 2\lambda) + \sqrt{4\lambda\,(\epsilon + \lambda) + U^2}\,. \tag{6.19}$$

The maximum value of q is in the center of the band gap ($\epsilon = 0$); for $|U| \ll 2\,\lambda$, it is $q'^2_{\max} \approx U^2/(4\lambda)$. At the band edges ($\epsilon = \pm U$), $q = 0$. q is the characteristic length of an exponentially decaying wave

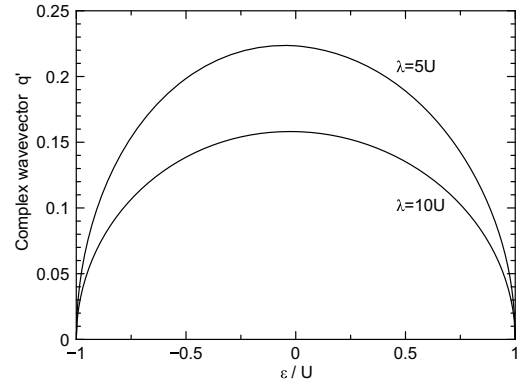

Fig. 6.4 Complex band structure $q'(\epsilon)$ according to (6.19) for two different values of λ/U

function. Such solutions occur at surfaces or interfaces. For larger band gaps, the localization length is smaller (larger q) (Fig. 6.4).

6.2.3.5 Solution in the Vicinity of the Zone Boundary

For $\mathbf{K}$ in the vicinity of the zone boundary the solutions (6.15) can be developed. Therefore, we use the (small) distance from the zone boundary $\widetilde{\mathbf{K}} = \mathbf{K} - \mathbf{G}/2$. With $\lambda = (\hbar^2/2m)\,(G^2/4)$ we rewrite still exactly (6.15):

$$E_{\pm}\left(\widetilde{\mathbf{K}}\right) = \frac{\hbar^2}{2m}\left(\frac{1}{4}\mathbf{G}^2 + \widetilde{\mathbf{K}}^2\right) \pm \left(4\lambda\,\frac{\hbar^2\widetilde{\mathbf{K}}^2}{2m} + U^2\right)^{1/2} . \tag{6.20}$$

For small $\widetilde{\mathbf{K}}$ with $\frac{\hbar^2\mathbf{G}\widetilde{\mathbf{K}}}{2m} \ll |U|$, the energy is then approximately given by

$$E_{\pm}\left(\widetilde{\mathbf{K}}\right) \cong \lambda \pm U + \frac{\hbar^2\widetilde{\mathbf{K}}^2}{2m}\left(1 \pm \frac{2\,\lambda}{U}\right) . \tag{6.21}$$

Thus the energy dispersion in the vicinity of the zone boundary is parabolic. The lower state has a negative curvature, the upper state a positive curvature. The curvature is

$$m^* = m\,\frac{1}{1 \pm 2\lambda/U} \approx \pm m\,\frac{U}{2\lambda} , \tag{6.22}$$

and will be later related to the *effective mass*. The approximation in (6.22) is valid for $|U| \ll 2\lambda$. We note that in our simple model m^* increases linearly with increasing band gap $2U$ (see Fig. 6.34 for experimental data).

6.2.4 Kramer's Degeneracy

$E_{\mathrm{n}}(\mathbf{k})$ is the dispersion in a band. The time-reversal symmetry (Kramer's degeneracy) implies

$$E_{\mathrm{n}\uparrow}(\mathbf{k}) = E_{\mathrm{n}\downarrow}(-\mathbf{k}) , \tag{6.23}$$

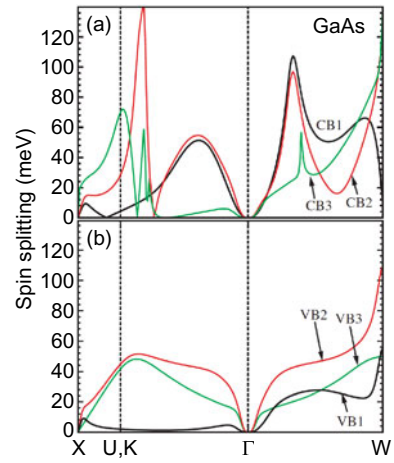

Fig. 6.5 Theoretical calculation of the spin splitting of **a** the three lowest conduction bands (CB1, CB2, and CB3) and **b** the top three valence bands (VB1, VB2, and VB3) of GaAs. Adapted from [453]

where the arrow refers to the direction of the electron spin. If the crystal is symmetric under inversion, we have additionally

$$E_{\mathrm{n}\uparrow}(\mathbf{k}) = E_{\mathrm{n}\uparrow}(-\mathbf{k}) \ . \tag{6.24}$$

With both time reversal and inversion symmetry the band structure fulfills

$$E_{\mathrm{n}\uparrow}(\mathbf{k}) = E_{\mathrm{n}\downarrow}(\mathbf{k}) \ . \tag{6.25}$$

The inversion symmetry is particularly important for the spin-orbit interaction. In the absence of inversion symmetry, e.g. in (non-centrosymmetric) zincblende crystals (Fig. 3.16b) or in heterostructures (Fig. 12.35b), a spin splitting, e.g. $E_{\mathrm{n}\uparrow}(\mathbf{k}) \neq E_{\mathrm{n}\downarrow}(\mathbf{k})$, is present. It can be thought of as provoked by an effective magnetic field. Bulk inversion asymmetry (BIA) leads to the Dresselhaus spin splitting [452, 453] that is shown in Fig. 6.5 for GaAs (cmp. Fig. 6.10a). The spin splitting due to structural inversion asymmetry (SIA) is described by the Bychkov-Rashba Hamiltonian [454, 455]. A review on these topics can be found in [456].

6.2.5 Symmetry Considerations

In general the symmetry of the lattice is a symmetry of the system's Hamiltonian and thus transfers into the electronic (and other) properties of the semiconductor. The means to formulate this mathematically is group theory and representation theory. At a given reciprocal lattice point, the wave function must fulfill the given spatial symmetry. Additional symmetry due to spin and spin-orbit interaction enters via the double-group scheme. This problem has been treated for the 32 point groups (cmp. Table B.2) in [457] and in [458] particularly for the pc, fcc, bcc and hcp lattices. A detailed treatment for the zincblende [459] and wurtzite [460] structures have been given. The most popular Hamiltonians are treated in [461].

The symmetry at particular points in direct or reciprocal space is denoted by the irreducible representations of the symmetry (point) group, e.g. by the Γ_i-symbols used in Figs. 6.9, 6.10 or also Fig. 6.44. As an example, base functions with the symmetry of the irreducible representations of tetraeder group $\mathrm{T_d}$ are listed in Table 6.1. With the knowledge of the wave functions at the points of high symmetry, it is possible to deduce the general nature of the energy bands in the vicinity of such symmetry points.

Table 6.1 Representations of the tetraeder group (zincblende structure) in molecular, BSW [462] and Koster [457] notation and (examples of) corresponding base functions (c.p.: cyclic permutations)

molecular	BSW	Koster	base functions
A_1	Γ_1	Γ_1	$x\,y\,z$, $x^2+y^2+z^2$
A_2	Γ_2	Γ_2	$x^4\,(y^2-z^2)$ + c.p.
E	Γ_{12}	Γ_3	$2\,z^2-(x^2+y^2)$, (x^2-y^2)
T_2	Γ_{15}	Γ_4	x, y, z, xy, xz, yz
T_1	Γ_{25}	Γ_5	$z\,(x^2-y^2)$ and c.p.

6.2.6 *Topological Considerations*

Starting with research on the quantum Hall effect and based on previous mathematical theorems, it has become clear that the band structure of 'insulators' has topological properties which in turn lead to a elegant classification of materials (and many effects/phases) [370, 463, 464]. In this context, the term 'insulator' means a material with gap between filled and empty states, i.e. semiconductors are exactly like this if the temperature is not too high (related to the gap divided by k_B). We recall the discussion of the diatomic linear chain in Sect. 5.2.3 where the bands turned out to have different topological properties depending on the ratio of sporing constants.

Topology is a branch of mathematics where objects that are related to each other by a smooth deformation are classified as the same. For example, a sphere and an ellipsoid are topologically the same. Also, a doughnut and a cup are the same since they have one hole. A quantity that is independent of such smooth transformations is termed 'topological invariant'. Such a number is the *genus* g of a surface that counts the number of holes. According to the Gauss-Bonnet theorem, the integral of the Gaussian curvature K over a closed surface S is given by

$$\int_S K \,\mathrm{d}A = 2\pi\,(2-2\,g)\;. \tag{6.26}$$

The Gaussian curvature $K = \kappa_1\,\kappa_2$ of a (differentiable) surface in 3D is the product of the principal curvatures κ_1 and κ_2 (maximum and minimum curvature of the curves from all normal planes that contain the normal vector intersecting with the surface). For a sphere of radius r, the Gaussian curvature is $1/r^2$ everywhere and the integral in (6.26) is $4\,\pi$, making $g = 0$. For a topologically different example we look at a torus (all points that have the fixed distance r from a circle of radius R, $r < R$). It is parametrized by

$$\boldsymbol{r} = R \begin{pmatrix} \cos\phi \\ \sin\phi \\ 0 \end{pmatrix} + r \begin{pmatrix} \cos\phi\,\cos\theta \\ \sin\phi\,\cos\theta \\ \sin\theta \end{pmatrix}\;, \tag{6.27}$$

with both the angles ϕ and θ running between 0 and $2\,\pi$. The principal curvature κ_1 along the θ-direction is $1/r$ (for all ϕ). The other principal curvature κ_2 in azimuthal (ϕ) direction changes sign with θ (positive outside, negative inside) and is also independent of ϕ. Its integral over the outer and inner part cancel exactly, thus the integral of $\kappa_1\,\kappa_2$ over the entire torus is zero and therefore $g = 1$.

Next, we connect the periodicity of the Brillouin zone in two dimensions with variables on a torus in 3D as shown in Fig. 6.6 (cmp. Fig. 5.3 for the 1D case). This concept can be generalized for a 3D band structure and a torus in four dimensions.

If a constant function $f = n\,a\,b/(2\,\pi)$ is integrated over the Brillouin zone (X is at $\pm\pi/a$, Y is at $\pm\pi/b$), the integral is

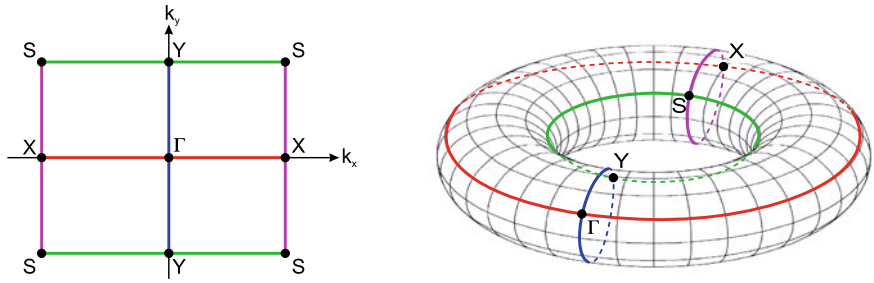

Fig. 6.6 Brillouin zone of a two-dimensional rectangular lattice and mapping to a torus

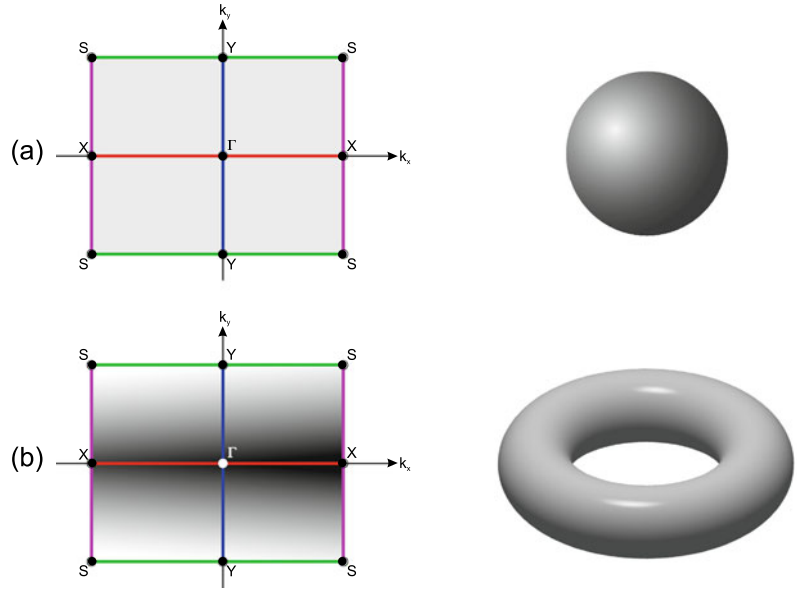

Fig. 6.7 Brillouin zone of a rectangular lattice with **a** a constant function and **b** a function that changes sign. On the right the topology of the situation is visualized

$$\frac{1}{2\pi}\int_{\mathrm{BZ}} f(\boldsymbol{k})\,\mathrm{d}^2\boldsymbol{k} = n\ . \tag{6.28}$$

If for example another function f that is independent of k_x and changes sign in k_y-direction with $\int f\,\mathrm{d}k_y = 0$, similar to the curvature of the torus, is integrated over the Brillouin zone, the results will be zero. This is schematically shown in Fig. 6.7 if the integrand is interpreted as curvature.

The generalization of the Berry phase [369] to Bloch states has been made in [465, 466]. For a two-dimensional system with Bloch bands and with Bloch functions $u_m(\boldsymbol{k})$ as in (6.3), the integrand leading to a topological invariant is given by the Berry connection (cmp. (5.29)) $\mathcal{A}_m = \langle u_m(\boldsymbol{k})|\imath\,\nabla_{\boldsymbol{k}}|u_m(\boldsymbol{k})\rangle$ and its Berry curvature or Berry flux in three-dimensional notation $\mathcal{F}_m = \nabla_{\boldsymbol{k}} \times \mathcal{A}_m$. The Chern number C_m for a band (separated by gaps from other bands), defined as integral over the Brillouin zone,

$$C_m = \frac{1}{2\pi}\int_{\mathrm{BZ}} \mathcal{F}_m\,\mathrm{d}^2\boldsymbol{k}\ , \tag{6.29}$$

takes only integer values and is a topological invariant. That means that small variations of the Hamilton operator behind the band structure do not change its value. In the case of degeneracies, still the sum of Chern numbers over all occupied bands, $n = \sum_m n_m$, is a topological invariant as long as the empty

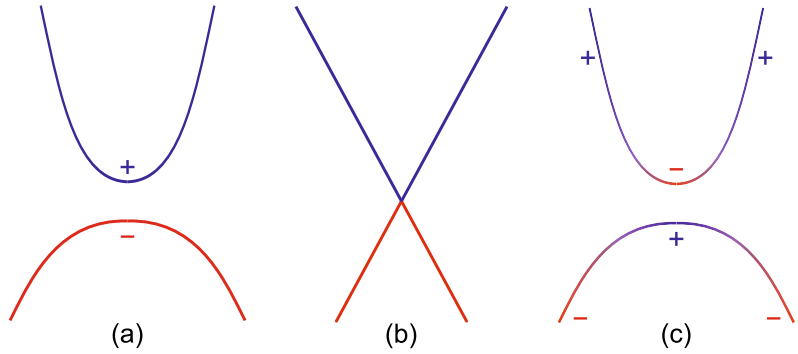

Fig. 6.8 Schematic band structures with (**a**) topologically trivial wave functions and **c** topologically non-trivial wave functions where within one band the character changes from s (*blue*, '+' for positive parity) to p (*red*, '−' for negative parity). In **b** the crossing point is visualized

states are separated by a gap. For a three-dimensional crystal and $\boldsymbol{k}$-space several topological invariants exist but a Chern number can be assigned to the Fermi surface or surface states (cmp. Sect. 11.6.3).

As an schematic example we show Fig. 6.8 for a topological trivial and non-trivial band structure. In the trivial bandstructure (as most semiconductors), the phase character of the wavefunction changes only little within the Brillouin zone, mostly p-type (negative parity) for the valence band and mostly s-type (positive parity) for the conduction band (Fig. 6.8a). In the topologically non-trivial bandstructure, band inversion takes place and the character of the wave function changes within a band (Fig. 6.8c). This sketch should be compared to Fig. 5.8 where a similar situation had been discussed for the lattice vibrations. An example for a semiconductor with band inversion is HgTe while CdTe or MnTe have trivial topology. Alloying leads at the transition from trivial to non-trivial (Fig. 6.8b) to zero-gap semiconductors (cf. Sect. 6.11).

6.3 Band Structures of Selected Semiconductors

In the following, the band structures of various important and prototype semiconductors are discussed. The band below the energy gap is called the valence band; the band above the gap is the conduction band. The band gap ΔE_{cv}, mostly denoted as E_{g}, is the energy separation between the highest valence-band state and the lowest conduction-band state. The maximum of the valence band is for most semiconductors at the Γ point.

6.3.1 Silicon

For silicon, an elemental semiconductor, (Fig. 6.9a) the minimum of the conduction band is located close to the X-point at $0.85\pi/a$ in the $\langle 100\rangle$ direction. Thus, it is not at the same point in **k** space as the top of the valence band. Such a band structure is called *indirect*. Since there are six equivalent $\langle 100\rangle$ directions, there are six equivalent minima of the conduction band.

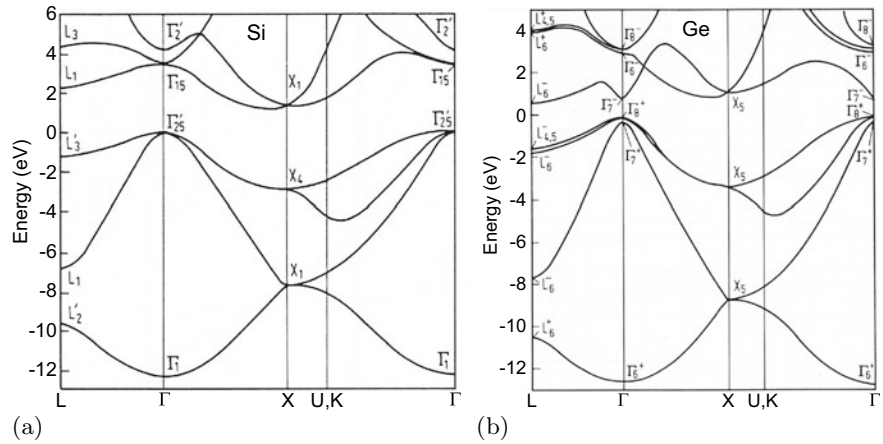

Fig. 6.9 Band structure of **a** silicon (indirect) and **b** germanium (indirect). In Si, the minima of the conduction band are in the ⟨100⟩ direction, for germanium in the ⟨111⟩ direction. Adapted from [164], based on [467]

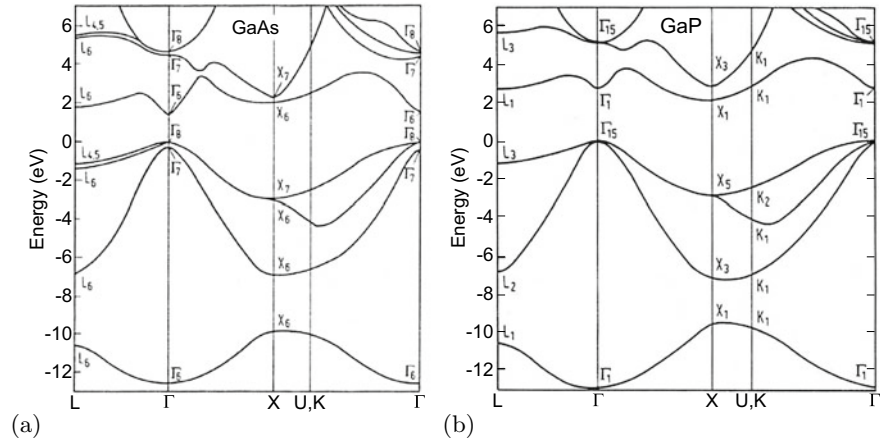

Fig. 6.10 Band structure of **a** GaAs (direct) and **b** GaP (indirect). For GaAs the minimum of the conduction band is at Γ, for GaP in the ⟨100⟩ direction. Adapted from [164], based on [467]

6.3.2 Germanium

Germanium, another elemental semiconductor, (Fig. 6.9b) also has an indirect band structure. The conduction minima are at the L point in the ⟨111⟩ direction. Due to symmetry there are eight equivalent conduction-band minima.

6.3.3 GaAs

GaAs (Fig. 6.10a) is a compound semiconductor with a *direct* band gap since the top of the valence band and the bottom of the conduction band are at the same position in **k** space (at the Γ-point). The next highest (local) minimum in the conduction band is close to the L point.

6.3.4 GaP

GaP (Fig. 6.10b) is an indirect compound semiconductor. The conduction-band minima are along the ⟨100⟩ directions.

6.3.5 GaN

GaN (Fig. 6.11) is a direct semiconductor that has wurtzite structure but can also occur in the metastable cubic (zincblende) phase.

6.3.6 Lead Salts

The band gap of PbS (Fig. 6.12), PbSe and PbTe is direct and located at the L point. The lead chalcogenide system shows the anomaly that with increasing atomic weight the band gap does not decrease monotonically. At 300 K, the band gaps are 0.41, 0.27 and 0.31 eV for PbS, PbSe and PbTe, respectively.

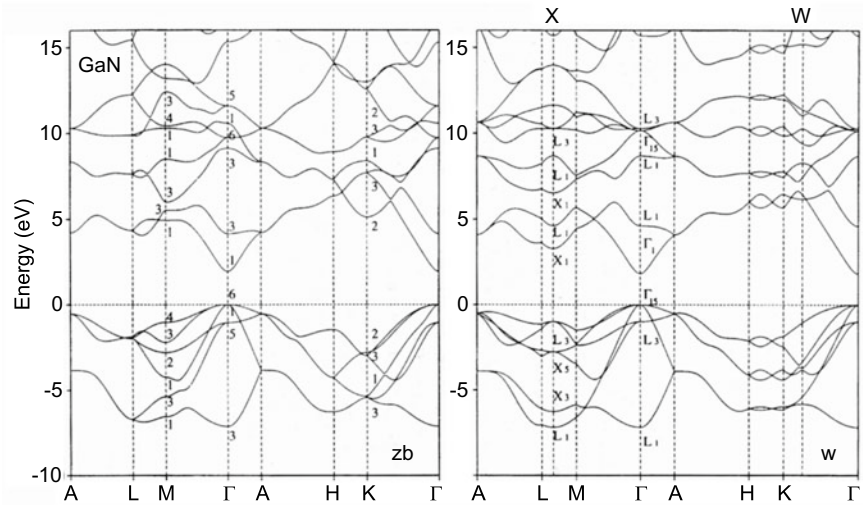

Fig. 6.11 Band structure of GaN (direct) in zincblende (zb) modification (*left*) and wurtzite (w) modification (*right*), both displayed in the wurtzite Brillouin zone to facilitate comparison

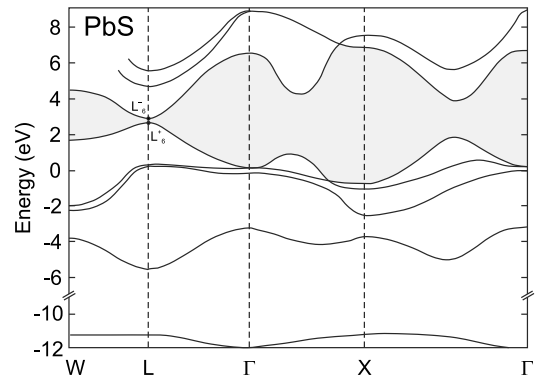

Fig. 6.12 Calculated band structure of PbS (direct). The energy gap is at the L point. The forbidden band is shown in *grey*. Adapted from [468]

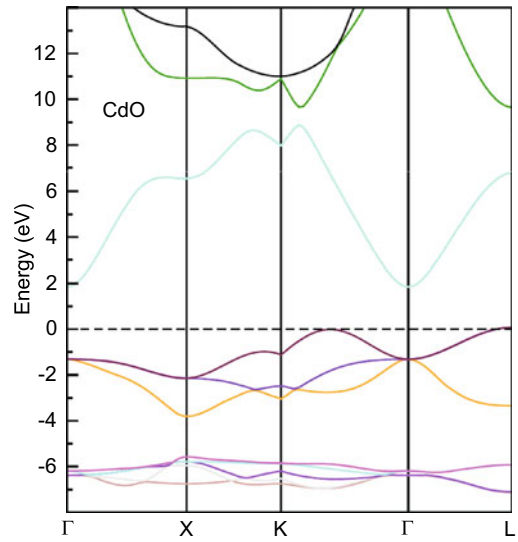

Fig. 6.13 Calculated indirect band structure of CdO. The top of the valence band is at $E = 0$. Adapted from [470]

6.3.7 MgO, ZnO, CdO

Cadmium oxide is a cubic semiconductor in the rocksalt structure. Due to symmetry considerations, coupling (repulsion) of oxygen 2p- and cadmium 3d-orbitals does not occur at the zone center in the rocksalt structure. Repulsion occurs though away from the Γ-point and therefore the valence band maximum is not located at the zone center (Fig. 6.13). Thus CdO is an indirect semiconductor. A similar effect would occur in rs-ZnO due to zinc 3d orbitals; however, ZnO has wurtzite structure for which p–d coupling at the Γ-point is allowed; thus ZnO is direct. In MgO, Mg of course only possesses populated s- and p-orbitals and no such repulsion is present; thus MgO even with its rocksalt structure is also direct [469].

6.3.8 Chalcopyrites

The experimental band gaps of a number of chalcopyrite semiconductors are listed in Table 6.2. The band structures of $CuAlS_2$, $CuAlSe_2$, and $CuGaSe_2$ are compared in Fig. 6.14.

In Fig. 6.15, the theoretical band structure of GaN and its closest related chalcopyrite $ZnGeN_2$ are compared, both shown in the chalcopyrite (orthorhombic) Brillouin zone. The band gap of $ZnGeN_2$ is smaller than that of GaN and the difference of 0.4 eV is fairly well reproduced by the calculation[2] (giving 0.5 eV).

[2]Due to the local density approximation (LDA) the absolute values of the band gaps are too small by about 1 eV.

Table 6.2 Band gaps of various chalcopyrite semiconductors

Material	E_g (eV)		E_g (eV)		E_g (eV)
$CuAlS_2$	3.5	$CuGaS_2$	2.5	$CuInS_2$	1.53
$CuAlSe_2$	2.71	$CuGaSe_2$	1.7	$CuInSe_2$	1.0
$CuAlTe_2$	2.06	$CuGaTe_2$	1.23	$CuInTe_2$	1.0–1.15
$AgAlS_2$	3.13	$AgGaS_2$	2.55	$AgInS_2$	1.87
$AgAlSe_2$	2.55	$AgGaSe_2$	1.83	$AgInSe_2$	1.24
$AgAlTe_2$	2.2	$AgGaTe_2$	1.1–1.3	$AgInTe_2$	1.0
$ZnSiP_2$	2.96	$ZnGeP_2$	2.34	$ZnSnP_2$	1.66
$ZnSiAs_2$	2.12	$ZnGeAs_2$	1.15	$ZnSnAs_2$	0.73
$CdSiP_2$	2.45	$CdGeP_2$	1.72	$CdSnP_2$	1.17
$CdSiAs_2$	1.55	$CdGeAs_2$	0.57	$CdSnAs_2$	0.26

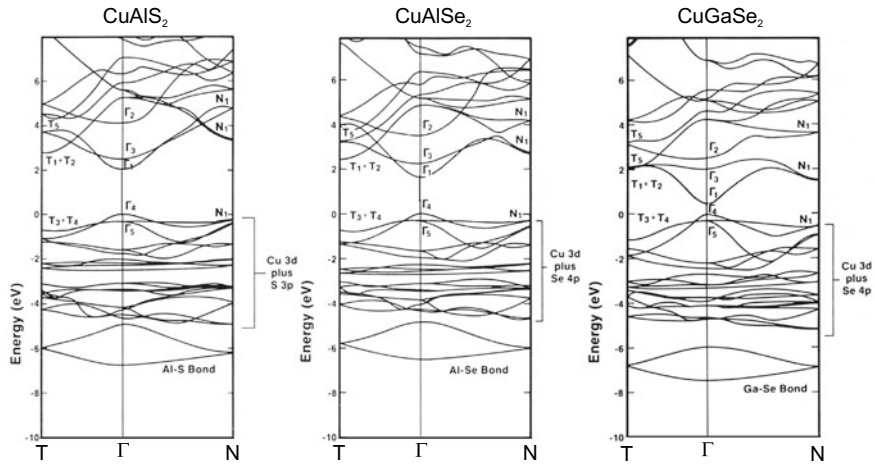

Fig. 6.14 Calculated band structures of $CuAlS_2$, $CuAlSe_2$, and $CuGaSe_2$. The absolute values of the gap energies are incorrect due to LDA calculation. Adapted from [471]

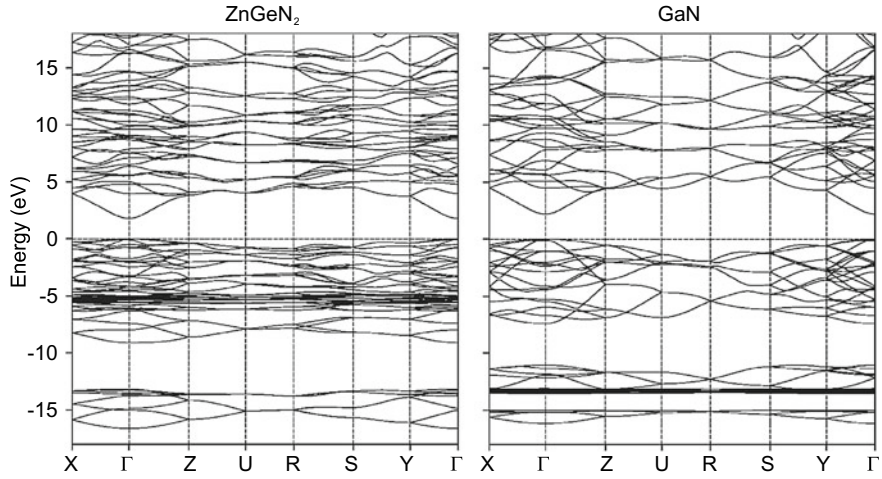

Fig. 6.15 Calculated (within LDA) band structures of $ZnGeN_2$ and its related III–V compound GaN, both displayed in the chalcopyrite (orthorhombic) Brillouin zone to facilitate comparison. Adapted from [472]

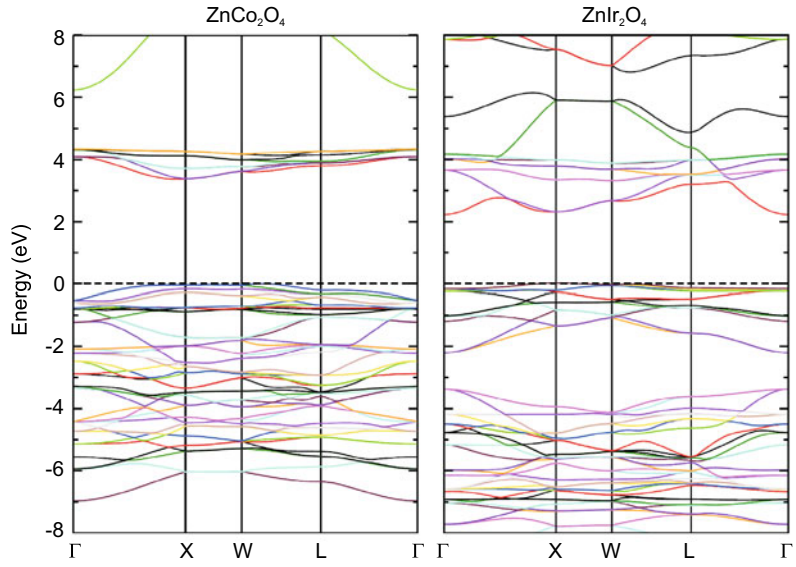

Fig. 6.16 Calculated band structures of $ZnCo_2O_4$ and $ZnIr_2O_4$. Adapted from [470]

6.3.9 Spinels

The band structure of spinels (in particular $CdIn_2S_4$) has been discussed in [473], the band structure of ZnM_2O_4 has been calculated in [470] for (M = Co, Rh, Ir) (Fig. 6.16) and in [474] for (M = Al, Ga, In).

6.3.10 Delafossites

In Fig. 6.17, the theoretical band structures of the delafossites $CuAlO_2$, $CuGaO_2$, and $CuInO_2$ are shown. The maximum of the valence band is not at Γ but near the F point. The direct band gap at Γ decreases for the sequence Al → Ga → In, similar to the trend for AlAs, GaAs and InAs. The direct band gap at F and L, causing the optical absorption edge, increases, however (experimental values are 3.5, 3.6, and 3.9 eV).

6.3.11 Perovskites

The calculated band structure of $BaTiO_3$ in the tetragonal phase is shown in Fig. 6.18. The minimum of the conduction band is at the Γ-point. The maximum of the valence band is not at the Γ-point but at the M point. The band gap of the LDA[3] calculation is too small (2.2 eV) compared to the experimental value ∼ 3.2 eV.

The band structure of the halide perovskites has been calculated for hybrid organic-inorganic compounds like $MAPbI_3$ and $FAPbI_3$ [476] and fully inorganic compounds $APbI_3$ (A = Li, Na, K, Rb, and Cs) [477]. Density of states and energy positions of (MA,FA,Cs)(Pb,Sn)$(Cl,Br,I)_3$ compounds are

[3]local density approximation.

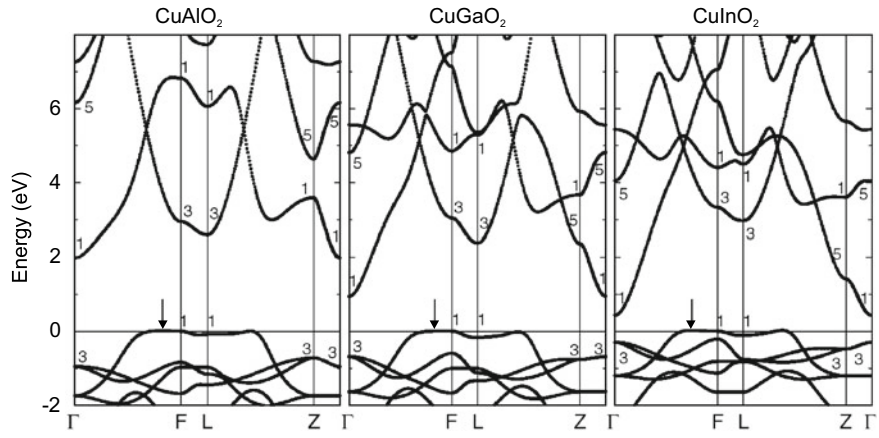

Fig. 6.17 Band structures of $CuAlO_2$, $CuGaO_2$, and $CuInO_2$, calculated with LDA (underestimating the absolute value of the band gaps). The *arrows* denote the maximum of the valence band that has been set to zero energy for each material. Adapted from [226]

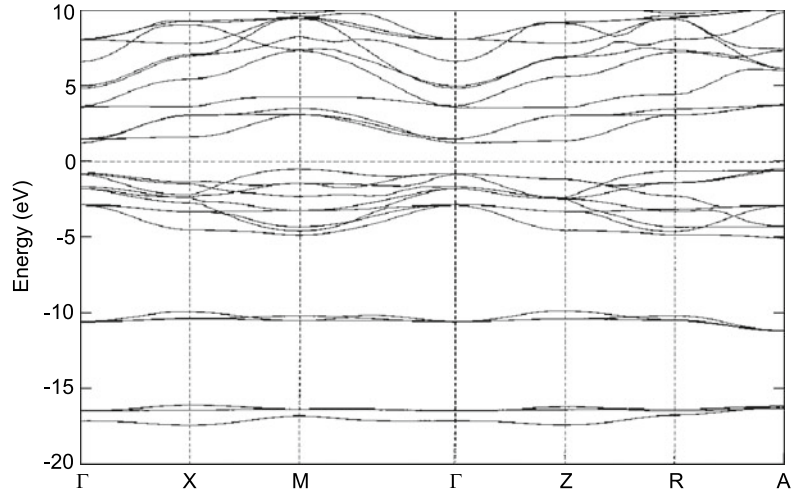

Fig. 6.18 Calculated energy band structure of $BaTiO_3$ along the major symmetry directions. The Fermi level (E_F) is set at zero energy. Adapted from [475]

discussed in [478]. The trends are summarized in Fig. 6.19. The band gap of halide perovskites can be varied across the visible range, e.g. within the $CsPb(Cl,Br,I)_3$ the system (Fig. 6.20).

6.4 Systematics of Semiconductor Band Gaps

The trends with regard to the size of the band gap for elemental, III–V and II–VI semiconductors can essentially be understood in terms of the bond strength and ionicity. In Fig. 6.21, the band gaps of many important semiconductors are shown as a function of the lattice constant. For elemental semiconductors, the band gap decreases with reduced bond strength, i.e. lattice constant (C→Si→Ge). A similar trend exists both for the III–V and the II–VI semiconductors.

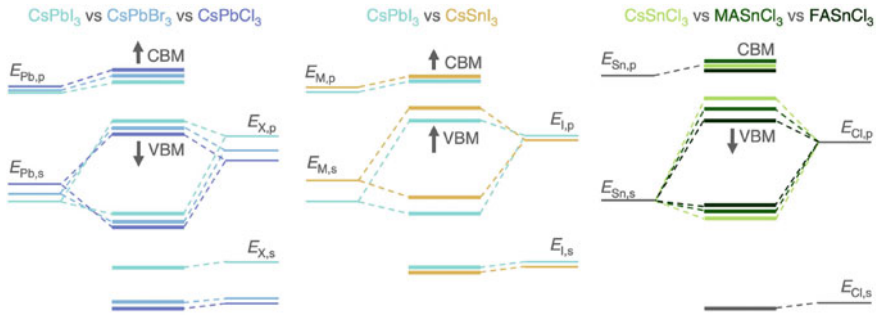

Fig. 6.19 Schematic energy levels in ABX_3 perovskites. Arrows indicate the shift of energy levels upon substitution of atoms or small organic molecules. Adapted from [478]

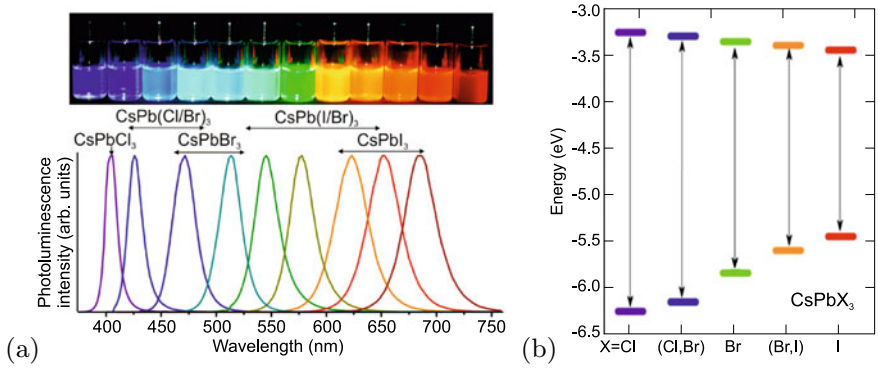

Fig. 6.20 **a** Photoluminescence of $CsPbX_3$ nanocrystals of halide perovskites with various anions (colloidal solutions in toluene under UV lamp ($\lambda = 365\,\text{nm}$)). Adapted from [479]. **b** Position of conduction and valence band edges of $CsPbX_3$ halide perovskites (relative to vacuum level at zero). Adapted from [480]

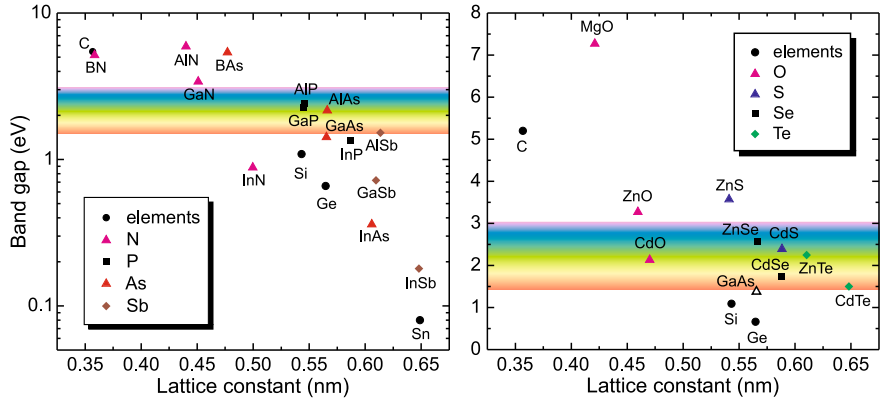

Fig. 6.21 Band gaps as a function of the lattice constant for various elemental, III–V and II–VI semiconductors. The lattice constant of wurtzite semiconductors has been recalculated for a cubic cell ($a^3_{\text{cubic}} = \sqrt{3}\,a^2\,c$)

For the same lattice constant, the band gap increases with increasing ionicity, i.e. IV–IV→ III–V→II–VI→I–VII. A typical example is the sequence Ge→ GaAs→ZnSe→ CuBr, for which all materials have almost the same lattice constant, and the band gaps increase 0.66 eV→1.42 eV→2.7 eV→ 2.91 eV.

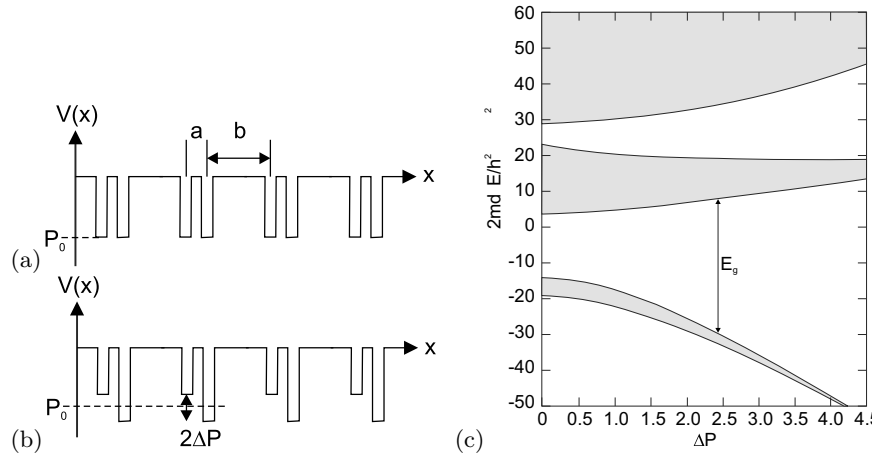

Fig. 6.22 Kronig-Penney model (along $\langle 111 \rangle$, $b/a = 3$) for a **a** IV–IV semiconductor and **b** for a III–V (or II–VI) semiconductor, **c** resulting band structure ($P_0 = -3$). d denotes the lattice constant ($d = b + a$). Adapted from [481]

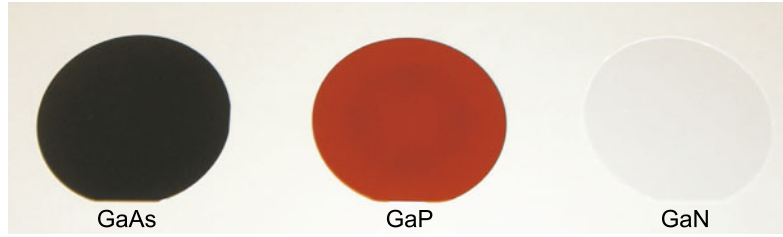

Fig. 6.23 Optical image of two inch wafers of GaAs (*left*), GaP (*center*) and ZnO (*right*). A GaN wafer would look like the ZnO wafer

This behavior can be understood within the framework of a modified Kronig-Penney model [481] (Appendix F). Double potential wells ($b/a = 3$) are chosen to mimic the diatomic planes along the $\langle 111 \rangle$ direction in the zincblende structure (Fig. 6.22a). The first investigation of such diatomic one-dimensional bandstructure was reported in [482]. Symmetric wells (depth P_0) are chosen to model covalent semiconductors and asymmetric wells with depths $P_0 \pm \Delta P$ to model partially ionic semiconductors. Results are shown in Fig. 6.22a for $P_0 = -3$. With increasing asymmetry, i.e. increasing ionicity, the band gap increases, mostly due to a downward shift of the valence band. The case of III–V (II–VI) semiconductors is reached for $\Delta P \approx 2$ (4). The calculation of effective masses in [481] is incorrect and has been rectified in [483]; the effective mass increases monotonically with ΔP.

In Fig. 6.23, the visual impression of 2" wafers of GaAs, GaP and GaN on white paper is shown. GaAs (and GaSb) is opaque since the band gap is below the visible spectral range. GaP has a band gap in the green and appears red, GaN has a band gap in the ultra-violet and thus appears transparent. As can be seen from Table 6.3, the anion sequence Sb, As, P, and N leads to smaller lattice constant and higher ionicity. A notable deviation from this rule is InN whose band gap (0.7 eV) is much smaller than that of InP [484].

6.5 Alloy Semiconductors

In alloy semiconductors [166], the size of the band gap and the character of the band gap will depend on the composition. The dependence of the band gap on the ternary composition is mostly nonlinear and can usually be expressed with a bowing parameter b that is mostly positive. For a compound $A_xB_{1-x}C$

Table 6.3 Comparison of band gap, lattice constant and ionicity of gallium–group V semiconductors for various anions. Lattice constant for GaN has been recalculated for a cubic cell

Anion	E_g (eV)	a_0 (nm)	f_i
N	3.4	0.45	0.50
P	2.26	0.545	0.33
As	1.42	0.565	0.31
Sb	0.72	0.61	0.26

the band gap is written as

$$E_g(A_xB_{1-x}C) = E_g(BC) + x\left[E_g(AC) - E_g(BC)\right] - b\,x\,(1-x)\ . \tag{6.30}$$

Even on the virtual crystal approximation (VCA) level (Sect. 3.7.3) a nonzero bowing parameter b is predicted. However, a more thorough analysis shows that the bowing cannot be treated adequately within VCA and is due to the combined effects of volume deformation of the band structure with the alloy lattice constant, charge exchange in the alloy with respect to the binary end components, a structural contribution due to the relaxation of the cation–anion bond lengths in the alloy and a small contribution due to disorder [485]. The discussion of Sect. 6.12.3 is related.

The Si_xGe_{1-x} alloy has diamond structure for all concentrations and the position of the conduction-band minimum in $\mathbf{k}$-space switches from L to X at about $x = 0.15$ (Fig. 6.24a). However, for all concentrations the band structure is indirect. The $In_xGa_{1-x}As$ alloy has zincblende structure for all compositions. The band gap is direct and decreases with a bowing parameter of $b = 0.6\,\text{eV}$ [486] (Fig. 6.24b). This means that for $x = 0.5$ the band gap is 0.15 eV smaller than expected from a linear interpolation between GaAs and InAs, as reported by various authors [487].

If one binary end component has a direct band structure and the other is indirect, a transition occurs from direct to indirect at a certain composition. An example is $Al_xGa_{1-x}As$ where GaAs is direct and AlAs is indirect. For all concentrations the crystal has zincblende structure. In Fig. 6.24c, the Γ, L and X conduction-band minima for ternary $Al_xGa_{1-x}As$ are shown. Up to an aluminum concentration of $x = 0.4$ the band structure is direct. Above this value the band structure is indirect with the conduction-band minimum being at the X-point. The particularity of $Al_xGa_{1-x}As$ is that its lattice constant is almost independent of x. For other alloys lattice match to GaAs or InP substrates is only obtained for specific compositions, as shown in Fig. 6.25. The band gap bowing in the group-III–nitride system has been discussed in [488].

If the two binary end components have different crystal structure, a phase transition occurs at a certain composition (range). An example is $Mg_xZn_{1-x}O$, where ZnO has wurtzite structure and MgO has rocksalt structure. The band gap is shown in Fig. 6.24d. In this case, each phase has its own bowing parameter.

All alloys of Fig. 6.24b–d have mixed cations. The band gap also varies upon anion substitution in a similar way as shown in Fig. 6.26 for ternary alloys with the cation Zn and the chalcogenides S, Se, Te and O.

6.6 Amorphous Semiconductors

Since the crystal lattice in an amorphous semiconductor is not periodic, the concept of $\mathbf{k}$-space and the related concepts such as band structure $E(\mathbf{k})$ break down at least partially. The density of states, however, remains a meaningful and useful quantity (Sect. 6.13.2).

In a perfectly crystalline semiconductor the eigenenergies of the states in the bands are real. An amorphous semiconductor can be modeled using a spectrum of complex energies [495]. In Fig. 6.27 the band structure of crystalline silicon is shown next to that calculated for amorphous silicon with $\alpha = 0.05$.

6.7 Temperature Dependence of the Band Gap

The band gap of a semiconductor typically decreases with increasing temperature. A direct visual impression can be obtained from the *same* LED chain at room temperature and dipped into liquid nitrogen (Fig. 6.28). Experimental data of band gap versus temperature are shown in Fig. 6.29 for bulk Si and ZnO.

The reasons for the temperature variation of the band gap are the change of electron–phonon interaction and the expansion of the lattice. The temperature coefficient may be written as

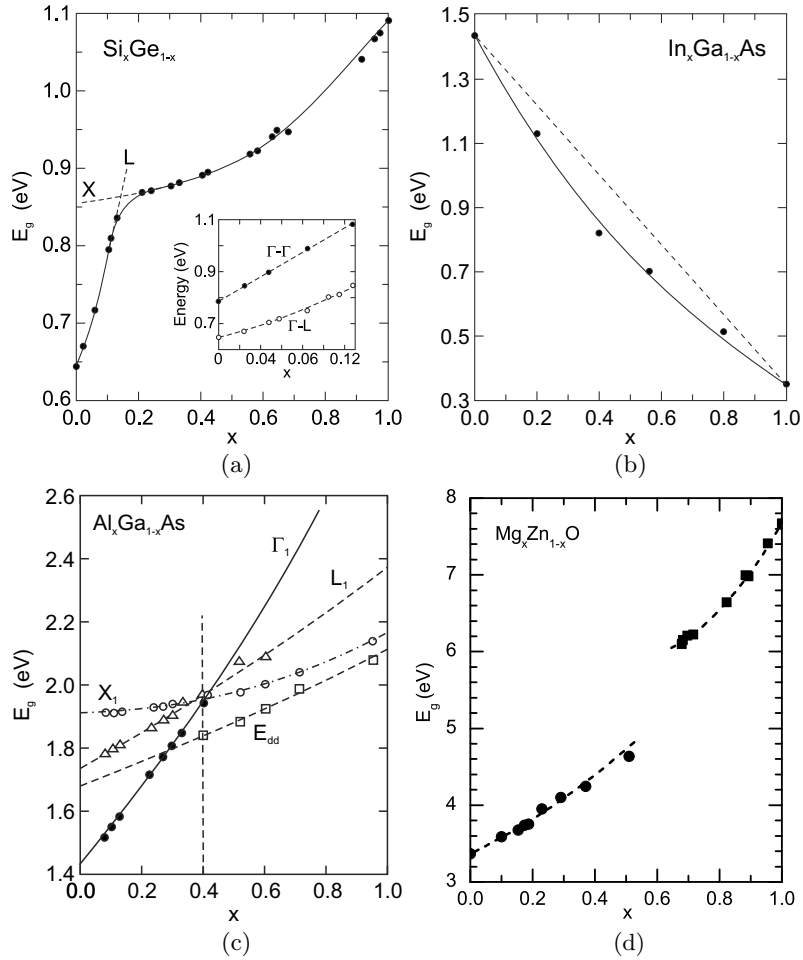

Fig. 6.24 **a** Band gap of Si_xGe_{1-x} alloy ($T = 296\,K$) with a change from the conduction-band minimum at L (Ge-rich) to X. The *inset* depicts the transition energy of the indirect (Γ–L) and direct (Γ–Γ) absorption edge for low Si content. Adapted from [489]. **b** Band gap (at room temperature) of $In_xGa_{1-x}As$. The *solid line* is an interpolation with bowing ($b = 0.6\,eV$) and the *dashed line* is the linear interpolation. Data from [486]. **c** Band gap (at room temperature) in the ternary system $Al_xGa_{1-x}As$. For $x < 0.4$ the alloy is a direct, for $x > 0.4$ an indirect, semiconductor. E_{dd} denotes the energy position of a deep donor (cf. Sect. 7.7.6). Adapted from [490]. **d** Band gap (at room temperature) in the ternary system $Mg_xZn_{1-x}O$. Data (from spectroscopic ellipsometry [491, 492]) are for hexagonal wurtzite phase (*circles*), and Mg-rich cubic rocksalt phase (*squares*). *Dashed lines* are fits to data with a different bowing parameter for each phase

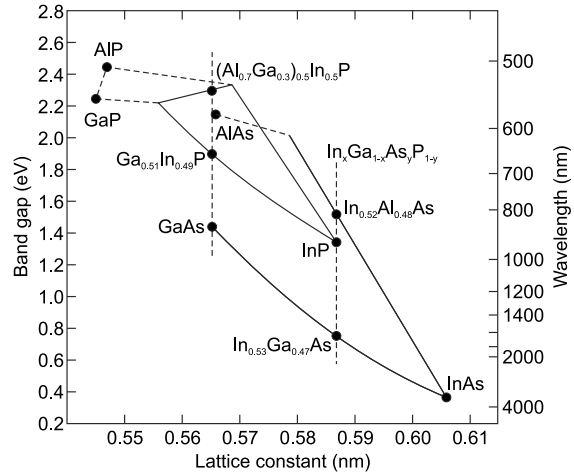

Fig. 6.25 Band gap versus lattice constant for $Ga_xIn_{1-x}P$ and $Al_xIn_{1-x}P$ (lattice matched to GaAs) as well as for $In_xAl_{1-x}As$ and $In_xGa_{1-x}As$ alloys (lattice matched to InP)

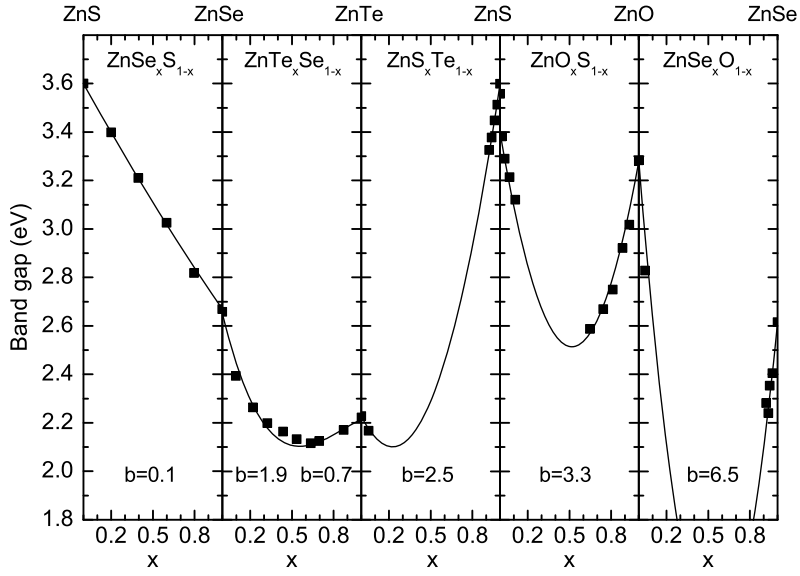

Fig. 6.26 Band gap of various Zn-based alloys with mixing in the anion sublattice. The *lines* are fits with (6.30), the bowing parameter b is labeled. Data for Zn(S,Se,Te) from [493], for Zn(O,Se/Te) from [494]

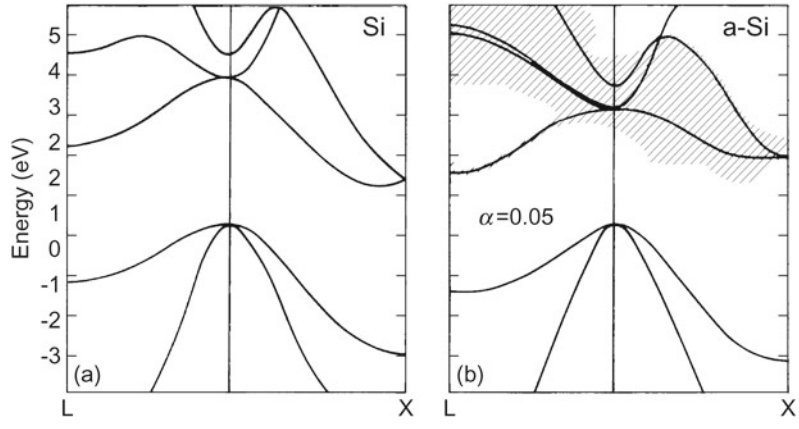

Fig. 6.27 **a** Calculated band structure of crystalline silicon. **b** Calculated band structure of amorphous silicon with $\alpha = 0.05$ (cf. (3.7)). The *solid lines* denote the real part of the energy, the *shaded areas* denote the regions with a width of twice the imaginary part of the energies centered around the real part. Adapted from [496]

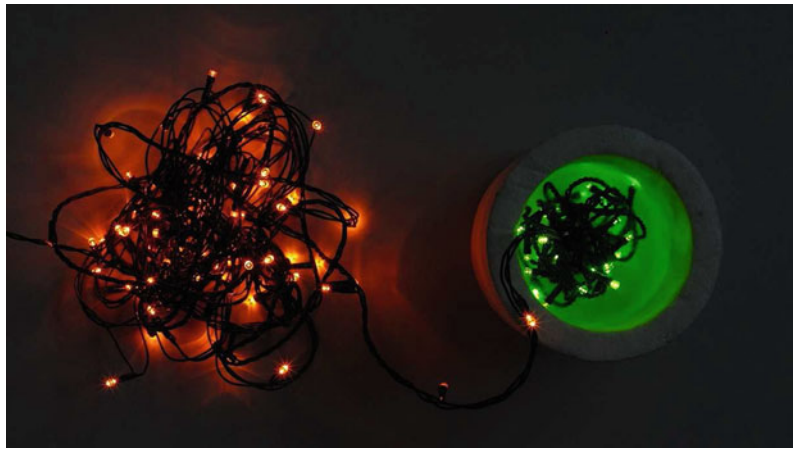

Fig. 6.28 LED chain with part at room temperature (left) and a part in a dewar filled with liquid nitrogen (right)

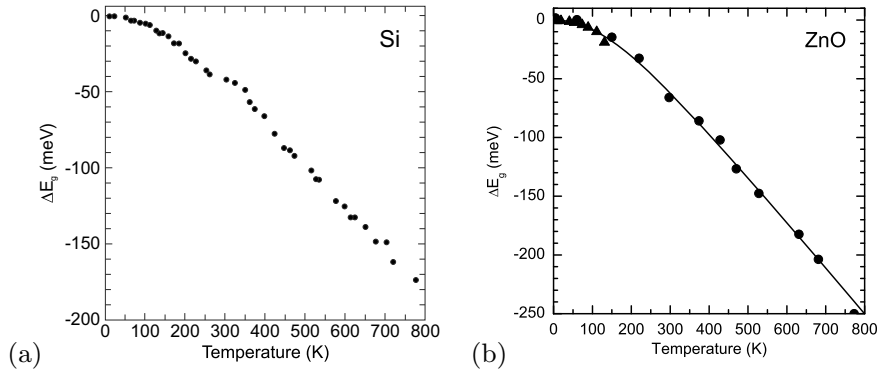

Fig. 6.29 Temperature dependence of the band gap of **a** Si (data from [498]) and **b** ZnO (experimental data from photoluminescence (*triangles*) and ellipsometry (*circles*)). The *solid lines* are fits with (6.34) and the parameters given in Table 6.4

$$\left(\frac{\partial E_g}{\partial T}\right)_p = \left(\frac{\partial E_g}{\partial T}\right)_V - \frac{\alpha}{\beta}\left(\frac{\partial E_g}{\partial p}\right)_T , \tag{6.31}$$

where α is the volume coefficient of thermal expansion and β is the volume compressibility. A recommendable discussion of the thermodynamic role of the band gap as chemical potential for the mass action law (7.12), entropy contributions and its temperature dependence can be found in [497].

An anomaly is present for the lead salts (PbS, PbSe, PbTe) for which the temperature coefficient is positive (Fig. 6.30a). Theoretical calculations [499] show that both terms in (6.31) are positive for the lead salts. The L_6^+ and L_6^- levels (see Fig. 6.12) shift as a function of temperature in such a way that their separation increases (Fig. 6.30b).

Also in copper and silver halides [500, 501] (Fig. 6.31a) and chalcopyrites [502] (Fig. 6.31b) the increase of band gap with increasing temperature has been found, sometimes only for a certain temperature range. This effect is attributed to the p-d electron hybridization in the valence band with Cu 3d electrons and to even stronger effect with Ag 4d electrons.

For many semiconductors the temperature dependence can be described with the empirical, three-parameter Varshni formula [503],

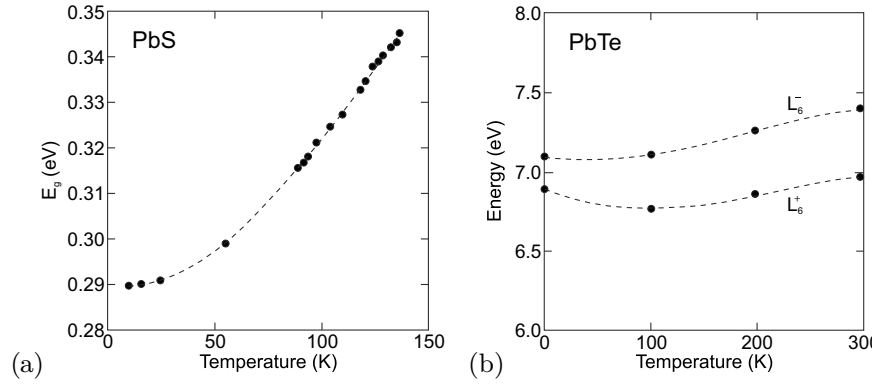

Fig. 6.30 **a** Band gap versus temperature for PbS. **b** Theoretical position of L_6^+ and L_6^- as a function of temperature for PbTe. Adapted from [468]

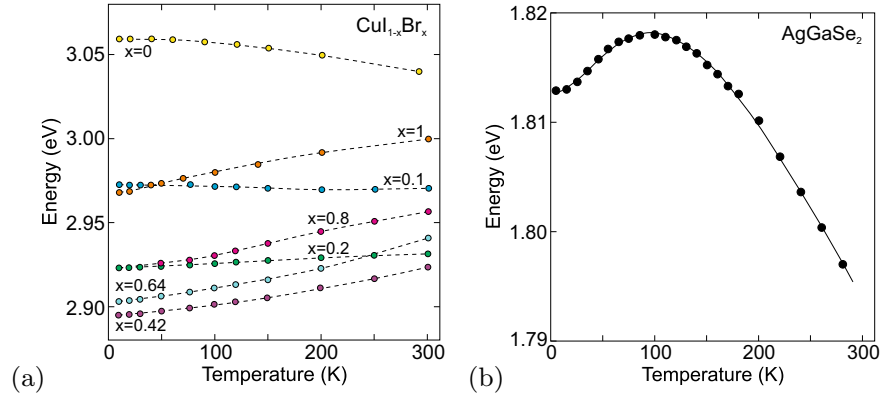

Fig. 6.31 **a** Band gap versus temperature for zincblende $CuI_{1-x}Br_x$ alloys with various compositions x (including binary CuI and CuBr) as labeled. *Dashed lines* are guide to the eye. Adapted from [500]. **b** Band gap vs. temperature for chalcopyrite $AgGaSe_2$. *Solid line* is fit with two-oscillator Bose-Einstein model. Adapted from [502]

$$E_g(T) = E_g(0) - \frac{\alpha\, T^2}{T + \beta}\,, \tag{6.32}$$

where $E_g(0)$ is the band gap at zero temperature. A more precise and physically motivated formula (based on a Bose-Einstein phonon model [504]) has been given in [505]

$$E_g(T) = E_g(0) - \frac{\alpha_B\, \Theta_B}{2}\left[\coth\left(\frac{\Theta_B}{2T}\right) - 1\right] = E_g(0) - \frac{\alpha_B\, \Theta_B}{\exp(\Theta_B/T) - 1}\,, \tag{6.33}$$

where α_B is a coupling constant and $k\Theta_B$ is a typical phonon energy; typical values are given in Table 6.4. This model reaches a better description of the fairly flat dependence at low temperatures.

The more elaborate model of [506] takes into account a more variable phonon dispersion, including optical phonons, and proposes the four-parameter formula

$$E_g(T) = E_g(0) - \alpha\,\Theta\left[\frac{1 - 3\,\Delta^2}{\exp\,(2/\gamma) - 1} + \frac{3\,\Delta^2}{2}\left(\sqrt[6]{1+\beta} - 1\right)\right] \tag{6.34}$$

Table 6.4 Parameters for the temperature dependence of the band gap according to 6.33 (Si, GaAs: [505], GaN: [507], ZnO: [508]) and (6.34) for various semiconductors

	α (10^{-4} eV/K)	Θ (K)	Δ	α_B (10^{-4} eV/K)	Θ_B (K)
Si	3.23	446	0.51	2.56	296
Ge	4.13	253	0.49		
GaAs	4.77	252	0.43	5.16	310
GaN	6.14	586	0.40	4.05	370
InP	3.96	274	0.48		
InAs	2.82	147	0.68		
ZnSe	5.00	218	0.36		
ZnO	3.8	659	0.54	5.9	616

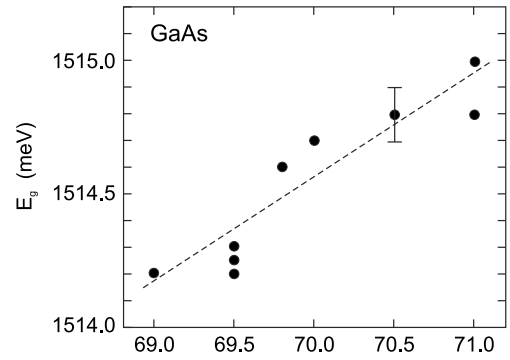

Fig. 6.32 Band gap of GaAs (at $T = 10\,\mathrm{K}$) as a function of the Ga isotope content. *Dashed line* is linear fit. Adapted from [509]

$$\beta = \frac{\pi^2}{3\,(1+\Delta^2)}\,\gamma^2 + \frac{3\Delta^2-1}{4}\,\gamma^3 + \frac{8}{3}\,\gamma^4 + \gamma^6$$
$$\gamma = 2\,T/\Theta\,,$$

where α is the high-temperature limiting magnitude of the slope (of the order of several 10^{-4} eV/K), Θ is an effective average phonon temperature and Δ is related to the phonon dispersion. Δ takes typically values between zero (Bose-Einstein model) and 3/4 [506].

6.8 Isotope Dependence of the Band Gap

The band edge slightly depends on the isotope composition of semiconductor, as shown for GaAs in Fig. 6.32. The effect is discussed in detail in [509].

6.9 Electron Dispersion

6.9.1 Equation of Electron Motion

The equation of motion for the electron in the band structure is no longer given by Netwon's law $\mathbf{F} = \mathrm{d}(m\mathbf{v})/\mathrm{d}t$ as in vacuum. Instead, the propagation of quantum-mechanical electron wave packets has to be considered. Their group velocity is given by ($v_g = \partial\omega/\partial k$)

$$\mathbf{v} = \frac{1}{\hbar} \nabla_{\mathbf{k}} E(\mathbf{k}) \ , \tag{6.35}$$

where $\nabla_{\mathbf{k}}$ is the gradient with respect to $\mathbf{k}$. Through the dispersion relation the influence of the crystal and its periodic potential on the motion enters the equation.

An electric field $\mathcal{E}$ acts on an electron during the time δt the work $\delta E = -e\mathcal{E} v_g \, \delta t$. This change in energy is related to a change in k via $\delta E = \mathrm{d}E/\mathrm{d}k \, \delta k = \hbar v_g \, \delta k$. Thus, we arrive at $\hbar \, \mathrm{d}k/\mathrm{d}t = -e\mathcal{E}$. For an external force we thus have

$$\hbar \frac{\mathrm{d}\mathbf{k}}{\mathrm{d}t} = -e \, \mathbf{E} = \mathbf{F} \ . \tag{6.36}$$

Thus, the crystal momentum $\mathbf{p} = \hbar\mathbf{k}$ takes the role of the momentum. A more rigorous derivation can be found in [451].

In the presence of a magnetic field $\mathbf{B}$ the equation of motion is

$$\hbar \frac{\mathrm{d}\mathbf{k}}{\mathrm{d}t} = -e \, \mathbf{v} \times \mathbf{B} = -\frac{e}{\hbar} (\nabla_{\mathbf{k}} E) \times \mathbf{B} \ . \tag{6.37}$$

The motion in a magnetic field is thus perpendicular to the gradient of the energy, i.e. the energy of the electron does not change. It oscillates therefore on a surface of constant energy perpendicular to $\mathbf{B}$.

6.9.2 *Effective Mass of Electrons*

From the free-electron dispersion $E = \hbar^2 k^2/(2m)$ the mass of the particle is inversely proportional to the curvature of the dispersion relation, i.e. $m = \hbar^2/(\mathrm{d}^2 E/\mathrm{d}k^2)$. This relation will now be generalized for arbitrary dispersion relations. The (inverse) tensor of the effective mass is defined as

$$(m^{*-1})_{ij} = \frac{1}{\hbar^2} \frac{\partial^2 E}{\partial k_i \, \partial k_j} \ . \tag{6.38}$$

The equation $\mathbf{F} = m^* \, \dot{\mathbf{v}}$ must be understood as a tensor equation, i.e. for the components of the force $F_i = m^*_{ij} \, a_j$. Force and acceleration must no longer be collinear. In order to find the acceleration from the force, the inverse of the effective-mass tensor must be used, $\mathbf{a} = (\mathbf{m}^*)^{-1} \, \mathbf{F}$.

In Fig. 6.33 the energy dispersion of the (lowest) conduction band in a typical semiconductor, the related electron velocity and the effective mass are shown schematically.

In (6.22) the ratio of the effective mass and the free-electron mass is of the order of $m^*/m \approx U/\lambda$, the ratio of the free particle energy and the band gap. For typical semiconductors, the width of the (valence) band is of the order of 20 eV, and the gap is about 0.2–2 eV. Thus, the effective mass is expected to be 10–100 times smaller than the free-electron mass. Additionally, the relation $m^* \propto E_\mathrm{g}$ is roughly fulfilled (Fig. 6.34).

From so-called $\mathbf{k} \cdot \mathbf{p}$ theory [510] (see Appendix H) the effective electron mass is predicted to be related to the momentum matrix element $\mathbf{p}_\mathrm{cv}$

$$\mathbf{p}_\mathrm{cv} = \langle c|\mathbf{p}|v\rangle = \int_{\Omega_0} u^*_{\mathrm{c},\mathbf{k}}(\mathbf{r}) \, \mathbf{p} \, u_{\mathrm{c},\mathbf{k}}(\mathbf{r}) \, \mathrm{d}^3\mathbf{r} \ , \tag{6.39}$$

with Ω_0 being the unit cell volume and the Bloch functions $|c\rangle$ and $|v\rangle$ of the conduction and valence band, respectively, given as

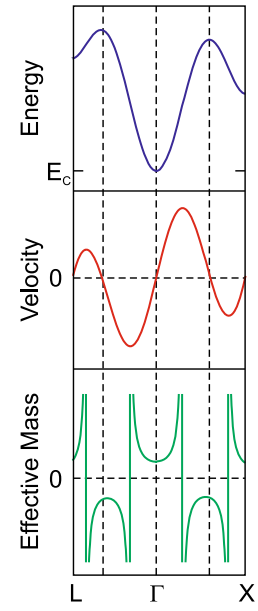

Fig. 6.33 Schematic diagram of the electron dispersion $E(\mathbf{k})$ in a typical semiconductor (*blue*) and corresponding carrier velocity ($\propto \partial E/\partial k$) (*red*) and effective mass ($\propto 1/(\partial^2 E/\partial k^2)$) (*green*)

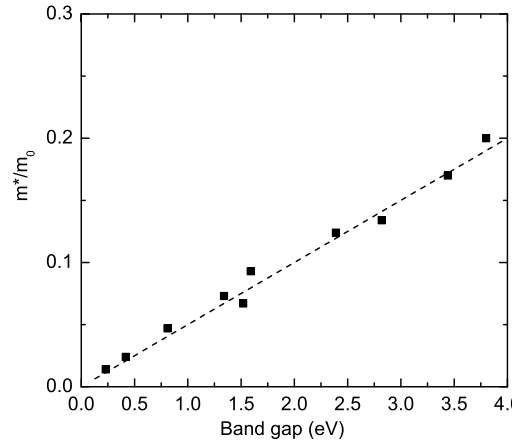

Fig. 6.34 Effective electron mass (in units of the free-electron mass m_0) as a function of the (low-temperature) band gap for several (direct band gap) semiconductors. The *dashed line* fulfills $m^*/m_0 = E_g/20\,\mathrm{eV}$

$$|c\rangle = u_{c,\mathbf{k}_c}(\mathbf{r})\ \exp(\mathrm{i}\,\mathbf{k}_c\mathbf{r}) \tag{6.40a}$$

$$|v\rangle = u_{v,\mathbf{k}_v}(\mathbf{r})\ \exp(\mathrm{i}\,\mathbf{k}_v\mathbf{r})\ . \tag{6.40b}$$

Typically, the $\mathbf{k}$-dependence of the matrix element is small and neglected. The momentum matrix element will also be important for optical transitions between the valence and conduction bands (Sect. 9.6). Other related quantities that are often used are the energy parameter E_P

$$E_P = \frac{2\,|\mathbf{p}_{cv}|^2}{m_0}\ , \tag{6.41}$$

and the bulk momentum matrix element M_b^2 that is given by

$$M_b^2 = \frac{1}{3}\,|\mathbf{p}_{cv}|^2 = \frac{m_0}{6}\,E_P\ . \tag{6.42}$$

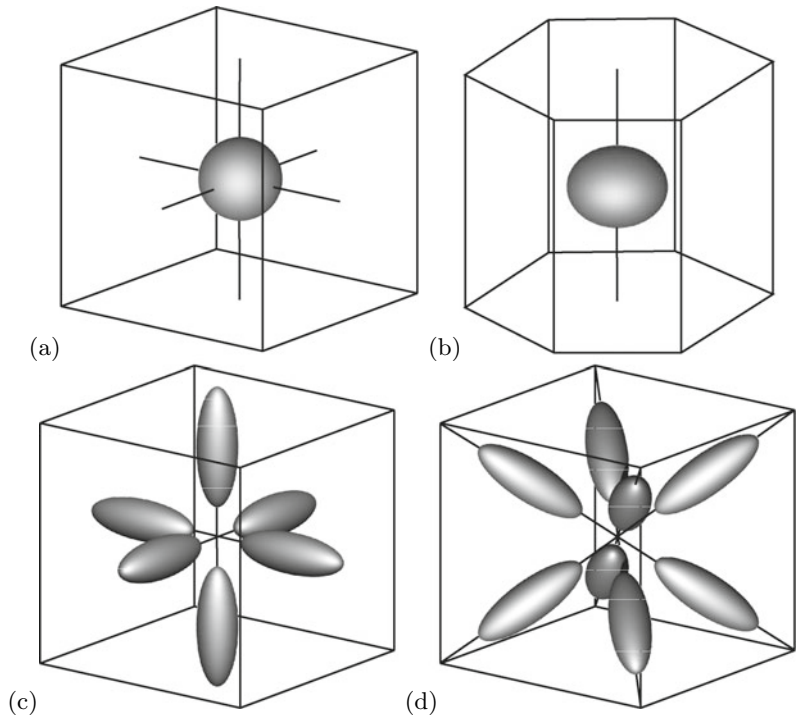

Fig. 6.35 Energy isosurfaces in **k**-space in the vicinity of the conduction-band minima for **a** GaAs with isotropic (spehrical) minimum at Γ-point, **b** ZnO with anisotropic (ellipsoidal) minimum at Γ-point (anisotropy exaggerated), **c** silicon with six equivalent anisotropic minima ($m_l/m_t = 5$ not to scale) along ⟨100⟩ and **d** germanium with eight equivalent anisotropic minima along ⟨111⟩. The cube indicates the ⟨100⟩ directions for the cubic materials. For the wurtzite material (part **b**) the vertical direction is along [00.1]

The electron mass is given by[4]

$$\frac{m_0}{m_e^*} = 1 + \frac{E_P}{3}\left(\frac{2}{E_g} + \frac{1}{E_g + \Delta_0}\right) = 1 + E_P \frac{E_g + 2\Delta_0/3}{E_g\left(E_g + \Delta_0\right)} \approx 1 + \frac{E_P}{E_g + \Delta_0/3} \approx \frac{E_P}{E_g} . \tag{6.43}$$

Comparison with the fit from Fig. 6.34 yields that E_P is similar for all semiconductors [511] and of the order of 20 eV (InAs: 22.2 eV, GaAs: 25.7 eV, InP: 20.4 eV, ZnSe: 23 eV, CdS: 21 eV).

In silicon there are six equivalent conduction-band minima. The surfaces of equal energy are schematically shown in Fig. 6.35c. The ellipsoids are extended along the ⟨100⟩ direction because the longitudinal mass (along the Δ path) is larger than the transverse mass in the two perpendicular directions (Table 6.5). For example, the dispersion relation in the vicinity of one of the minima is given as (k_x^0 denotes the position of one of the conduction-band minima close to a X-point)

$$E(\mathbf{k}) = \hbar^2 \left(\frac{(k_x - k_x^0)^2}{2\, m_l} + \frac{k_y^2 + k_z^2}{2\, m_t} \right) . \tag{6.44}$$

For germanium surfaces of constant energy around the eight conduction-band minima in the ⟨111⟩ directions are depicted in Fig. 6.35d. The longitudinal and the transverse masses are again different. For GaAs, the conduction-band dispersion around the Γ point is isotropic, thus the surface of constant energy is simply a sphere (Fig. 6.35a). In wurtzite semiconductors the conduction-band minimum is at the Γ-point. The mass along the c-axis is typically smaller than the mass within the (00.1) plane [512]

[4] Δ_0 is the spin-orbit splitting discussed in Sect. 6.10.2.

Table 6.5 Longitudinal direction of effective mass ellipsoid, longitudinal and transverse effective electron mass in several semiconductors. For the density of states mass $m_{d,e}$ see (6.72). Mass values in units of the free electron mass m_0

	Long. dir.	m_l	m_t	m_l/m_t	$m_{d,e}$	Ref.
C	⟨100⟩	1.4	0.36	3.9	1.9	[514]
Si	⟨100⟩	0.98	0.19	5.16	1.08	[515]
Ge	⟨111⟩	1.59	0.082	19.4	0.88	[515]
ZnO	[00.1]	0.21	0.25	0.88		[516]
CdS	[00.1]	0.15	0.17	0.9		[517]

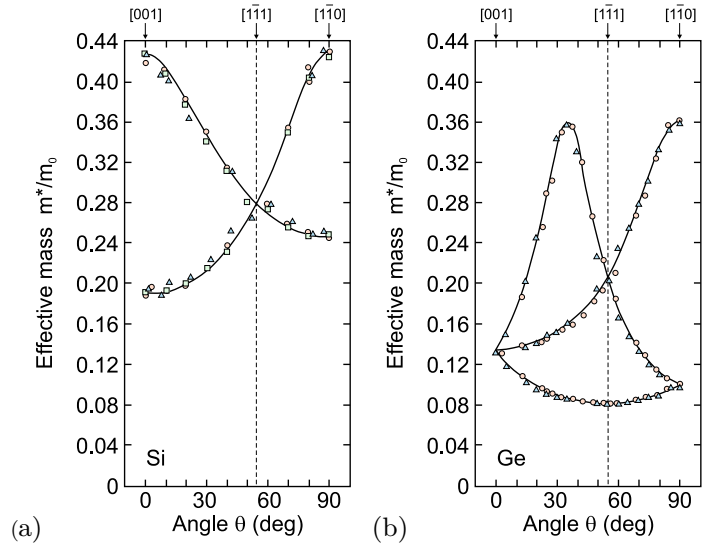

Fig. 6.36 Effective electron mass from cyclotron resonance experiments (at $T = 4\,\mathrm{K}$) on **a** Si and **b** Ge for the magnetic field in the (110) plane and various azimuthal directions θ. Experimental data (*symbols*) and fits (*solid lines*) using (6.45) with **a** $m_l = 0.98$, $m_t = 0.19$ and **b** $m_l = 1.58$, $m_t = 0.082$. Adapted from [515]

($m_l/m_t \approx 0.8$ for ZnO [513]), see Fig. 6.35b. In [512] also an anisotropy within the (00.1) plane is predicted.

The directional dependence of the mass can be measured with cyclotron resonance experiments with varying direction of the magnetic field. In Fig. 6.36, the field **B** is in the (110) plane with different azimuthal directions. When the (static) magnetic field makes an angle ϑ with the longitudinal axis of the energy surface, the effective mass is given as [518]

$$\frac{1}{m^*} = \sqrt{\frac{\cos^2\vartheta}{m_t^2} + \frac{\sin^2\vartheta}{m_t\, m_l}}\ . \tag{6.45}$$

6.9.3 Nonparabolicity of Electron Mass

The dispersion around the conduction-band minimum is only parabolic for small **k**. The further away the wavevector is from the extremum, the more the actual dispersion deviates from the ideal parabola (see, e.g., Fig. 6.10). This effect is termed *nonparabolicity*. Typically, the energy increases less quickly with k than in the parabolic model. This can be described in a so-called two-level model with the dispersion relation

$$\frac{\hbar^2 k^2}{2m_0^*} = E\left(1 + \frac{E}{E_0^*}\right) , \tag{6.46}$$

where $E_0^* > 0$ parameterizes the amount of nonparabolicity (a parabolic band corresponds to $E_0^* = \infty$). The nonparabolic dispersion for GaAs is shown in Fig. 6.37a. The curvature is reduced for larger $\mathbf{k}$ and thus the effective mass is energy dependent and increases with the energy. Equation (6.46) leads to the energy-dependent effective mass

$$m^*(E) = m_0^*\left(1 + \frac{2E}{E_0^*}\right) , \tag{6.47}$$

where m_0^* denotes here the effective mass at $\mathbf{k} = 0$. Theory and experimental data for the effective electron mass of GaAs are shown in Fig. 6.37b.

6.10 Holes

6.10.1 Hole Concept

Holes are missing electrons in an otherwise filled band. A Schrödinger-type wave-equation for holes (unoccupied electron states) was derived by Heisenberg [70] to interpret Hall effect data. The hole concept is useful to describe the properties of charge carriers at the top of the valence band. The hole is a new quasi-particle whose dispersion relation is schematically shown in Fig. 6.38 in relation to the dispersion of electrons in the valence band.

The wavevector of the hole (filled circle in Fig. 6.38) is related to that of the 'missing' electron (empty circle in Fig. 6.38) by $k_\mathrm{h} = -k_\mathrm{e}$. The energy is $E_\mathrm{h}(k_\mathrm{h}) = -E_\mathrm{e}(k_\mathrm{e})$, assuming that $E_\mathrm{V} = 0$, otherwise $E_\mathrm{h}(k_\mathrm{h}) = -E_\mathrm{e}(k_\mathrm{e}) + 2E_\mathrm{V}$. The hole energy is larger for holes that are further away from the top of the valence band, i.e. the lower the energy state of the missing electron. The velocity of the hole, $v_\mathrm{h} = \hbar^{-1}\,\mathrm{d}E_\mathrm{h}/\mathrm{d}k_\mathrm{h}$, is the same, $v_\mathrm{h} = v_\mathrm{e}$, and the charge is positive, $+e$. The effective mass of the

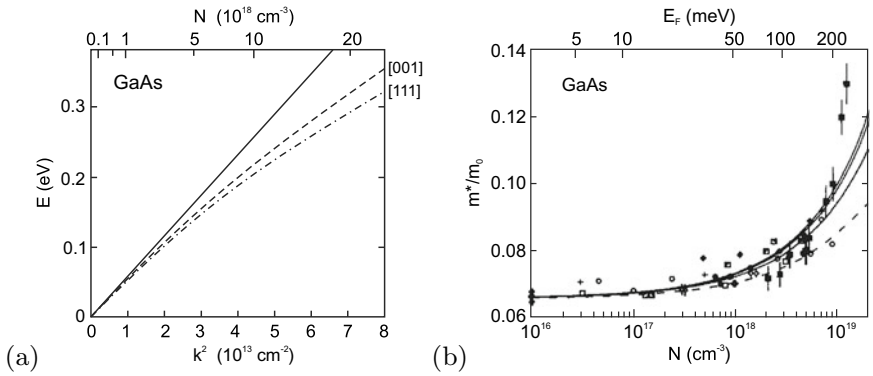

Fig. 6.37 **a** Dispersion relations for the conduction band of GaAs. The *solid line* is parabolic dispersion (constant effective mass). The *dashed* (*dash-dotted*) *line* denotes the dispersion for $\mathbf{k}$ along [001] ([111]) from a five-level $\mathbf{k}\cdot\mathbf{p}$ model (5LM). **b** Cyclotron resonance effective mass of electrons in GaAs as a function of the Fermi level (upper abscissa) and the corresponding electron concentration (lower abscissa). The *dashed line* is from a 2LM according to (6.47) with $E_0^* = 1.52\,\mathrm{eV}$. The *solid lines* are for a 5LM for the three principal directions of the magnetic field. The *symbols* represent experimental data from different sources. Data from [519]

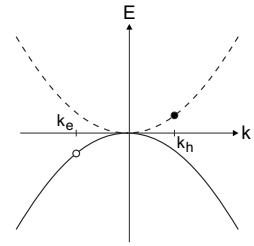

Fig. 6.38 Hole dispersion *dashed line* in relation to the electron dispersion in the valence band (*solid line*)

hole is positive at the top of the valence band, $m_h^* = -m_e^*$. Therefore, the drift velocities of an electron and hole are opposite to each other. The resulting current, however, is the same.

6.10.2 Hole Dispersion Relation

The valence band at the Γ-point is 3-fold degenerate. The band developed from the atomic (bonding) p states; the coupling of the spin $s = 1/2$ electrons with the orbital angular momentum $l = 1$ leads to a total angular momentum $j = 1/2$ and $j = 3/2$. The latter states are degenerate at Γ in zincblende bulk material and are called *heavy* holes (hh) for $m_j = \pm 3/2$ and *light* holes (lh) for $m_j = \pm 1/2$ due to their different dispersion (Fig. 6.39a). The two ($m_j = \pm/2$) states of the $j = 1/2$ state are split-off from these states by an energy Δ_0 due to spin-orbit interaction and are called *split-off* (s-o) holes. The spin-orbit interaction increases with increasing atomic order number Z of the anion since the electrons are located preferentially there (Fig. 6.40). A detailed discussion of the spin-orbit splitting in zincblende semiconductors is given in [520].

All three holes have different mass. In the vicinity of the Γ-point the dispersion for heavy and light holes can be described with (+:hh, −:lh)

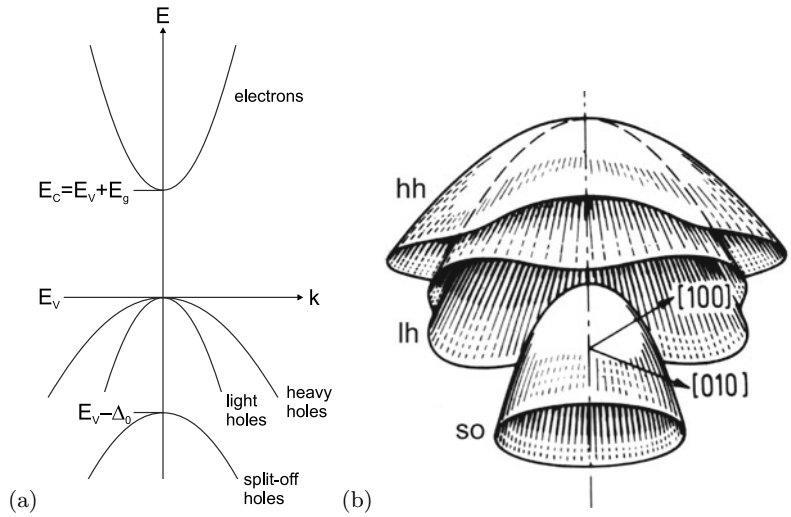

Fig. 6.39 **a** Simplified band structure with conduction band and three valence bands and (**b**) three-dimensional visualization (E versus (k_x, k_y)) of the valence bands of Ge (including warping). Part **b** from [521]

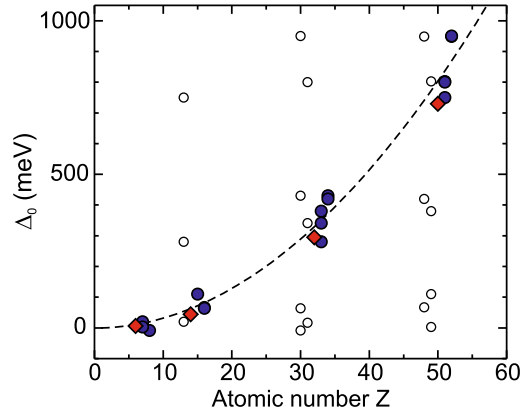

Fig. 6.40 Spin-orbit splitting Δ_0 for elemental (*diamonds*) and various III–V and II–VI (*circles*) semiconductors. The data are plotted as *empty* (*filled*) *circles* as a function of the cation (anion) order number. Obviously, Δ_0 correlates with the anion Z. The *dashed line* is proportional to Z^2

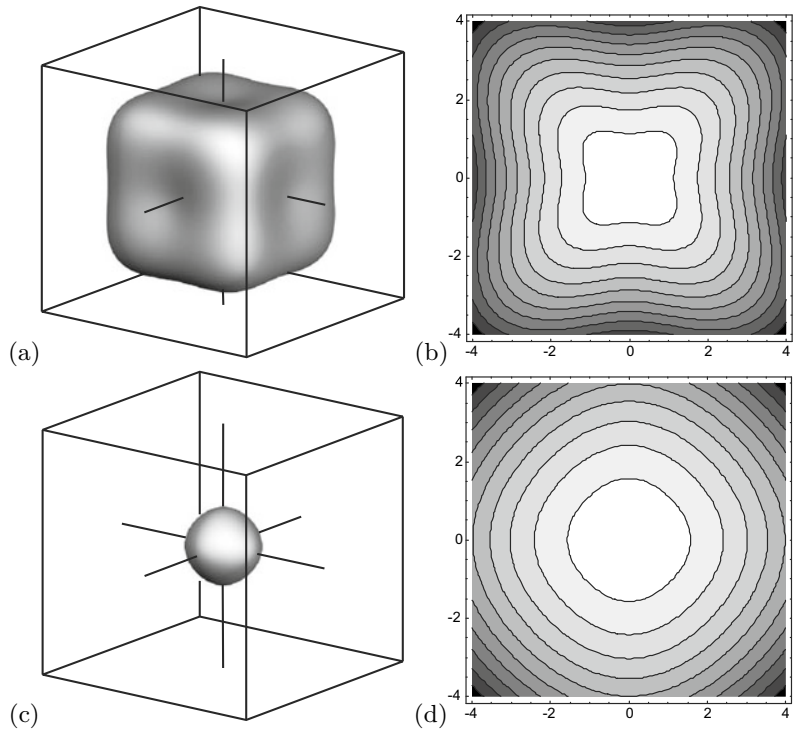

Fig. 6.41 Dispersion at the valence band edge of GaAs for **a**, **b** heavy holes and **c**,**d** light holes. **a**,**c** Constant energy surfaces and **b**,**d** isolines in the (k_x, k_y)-plane (**b** and **d** have different energy scales)

$$E(\mathbf{k}) = A\,k^2 \pm \sqrt{B^2\,k^4 + C^2\,\left(k_x^2\,k_y^2 + k_y^2\,k_z^2 + k_x^2\,k_z^2\right)}\,. \tag{6.48}$$

For heavy and light holes there is a dependence of the dispersion, i.e. the mass, in the (001) plane. This effect, sketched in Fig. 6.39b, is called *warping*. The warping at the GaAs valence-band edge is shown in Fig. 6.41. Equation (6.48) can also be expressed in terms of angular coordinates [522].

The s-o holes have the dispersion

$$E(\mathbf{k}) = -\Delta_0 + A\,k^2\,. \tag{6.49}$$

Table 6.6 Valence-band parameters (for (6.48)) A and B in units of $(\hbar^2/2m_0)$, C^2 in units of $(\hbar^2/2m_0)^2$, and Δ_0 in eV. From [164, 523, 524]

Material	A	B	C^2	Δ_0
C	−4.24	−1.64	9.5	0.006
Si	−4.28	−0.68	24	0.044
Ge	−13.38	−8.5	173	0.295
GaAs	−6.9	−4.4	43	0.341
InP	−5.15	−1.9	21	0.11
InAs	−20.4	−16.6	167	0.38
ZnSe	−2.75	−1.0	7.5	0.43

Values for A, B, C^2 and Δ_0 for a number of semiconductors are given in Table 6.6. The valence-band structure is often described with the Luttinger parameters γ_1, γ_2, and γ_3 that can be represented through A, B, and C via

$$\frac{\hbar^2}{2m_0}\,\gamma_1 = -\,A \tag{6.50a}$$

$$\frac{\hbar^2}{2m_0}\,\gamma_2 = -\,\frac{B}{2} \tag{6.50b}$$

$$\frac{\hbar^2}{2m_0}\,\gamma_3 = \frac{\sqrt{B^2 + C^2/3}}{2}\,. \tag{6.50c}$$

The mass of holes in various directions can be derived from (6.48). The mass along the [001] direction, i.e. $\hbar^2/(\partial^2 E(\mathbf{k})/\partial k_x^2)$ for $k_y = 0$ and $k_z = 0$, is

$$\frac{1}{m_{\mathrm{hh}}^{100}} = \frac{2}{\hbar^2}\,(A + B) \tag{6.51a}$$

$$\frac{1}{m_{\mathrm{lh}}^{100}} = \frac{2}{\hbar^2}\,(A - B)\,. \tag{6.51b}$$

The anisotropy of hole masses has been investigated with cyclotron resonance experiments (Fig. 6.42). For θ being the angle between the magnetic field and the [001] direction, the effective heavy hole (upper sign) and light hole (lower sign) mass in cubic semiconductors is given by [515]

$$m^* = \frac{\hbar^2}{2}\,\frac{1}{A \pm \sqrt{B^2 + C^2/4}} \times \left\{ \frac{C^2\,(1 - 3\cos^2\theta)^2}{64\sqrt{B^2 + C^2/4}\left[A \pm \sqrt{B^2 + C^2/4}\right]} + \ldots \right\}\,. \tag{6.52}$$

For $C^2 = 0$ the hole bands are isotropic, as is obvious from (6.48). In this case $\gamma_2 = \gamma_3$, the so-called spherical approximation. The average of the hole masses over all directions is

$$\frac{1}{m_{\mathrm{hh}}^{\mathrm{av}}} = \frac{2}{\hbar^2}\left(A + B\left[1 + \frac{2\,C^2}{15\,B^2}\right]\right) \tag{6.53a}$$

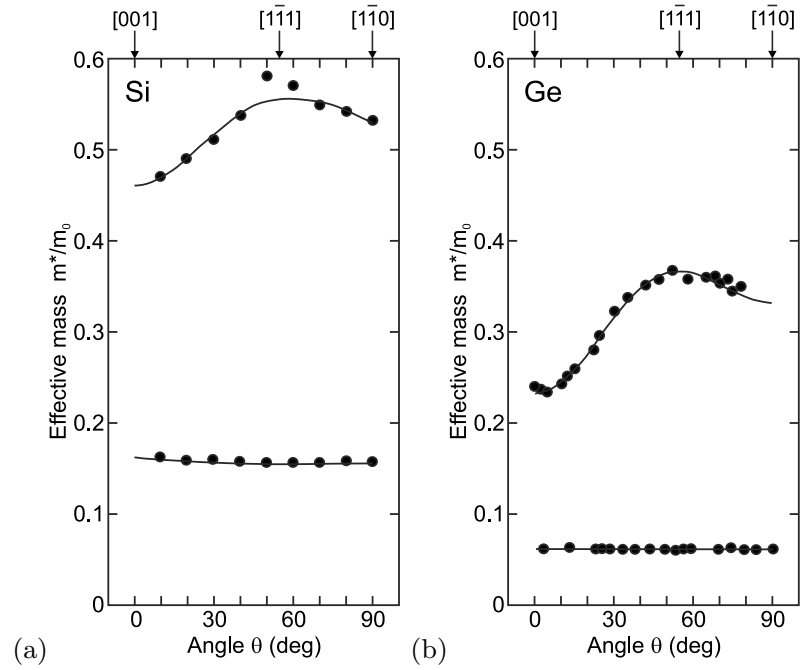

Fig. 6.42 Effective hole masses from cyclotron resonance experiments ($T = 4\,\mathrm{K}$) for heavy and light holes in **a** Si and **b** Ge for the magnetic field in the (110) plane and various azimuthal directions θ. Experimental data (*symbols*) and fits (*solid lines*) using (6.52). Adapted from [515]

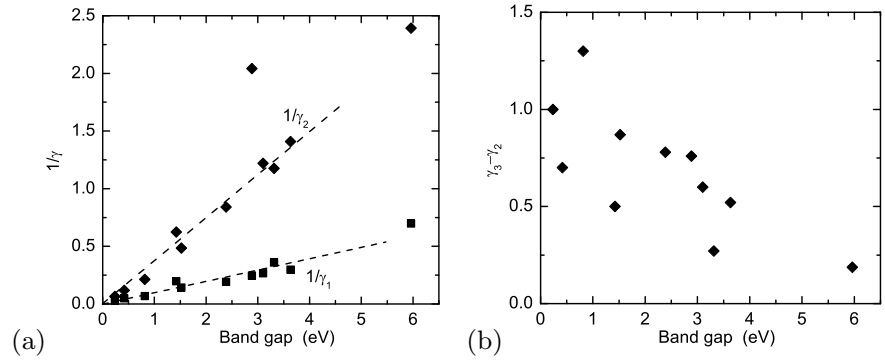

Fig. 6.43 Luttinger parameters for various III-V semiconductors versus their band gap. **a** Inverse values of γ_1 (*squares*) and γ_2 (*diamonds*). *Dashed lines* are guides to the eye. **b** $\gamma_3 - \gamma_2$ versus band gap

$$\frac{1}{m_{\mathrm{lh}}^{\mathrm{av}}} = \frac{2}{\hbar^2}\left(A - B\left[1 + \frac{2\,C^2}{15\,B^2}\right]\right) . \tag{6.53b}$$

Similar to the correlation of the electron mass with the band gap (Fig. 6.34), the Luttinger parameters are correlated with the band gap as shown in Fig. 6.43. The parameters $1/\gamma_1$ and $1/\gamma_2$ increase about linearly with E_g. The parameter $\gamma_3 - \gamma_2$, which is responsible for the valence band warping, decreases with increasing band gap.

6.10.3 Valence-Band Fine Structure

In Fig. 6.44, the schematic structure of the band edges for zincblende structure semiconductors is shown. The s-o holes in the zincblende structure are split-off due to the spin-orbit interaction Δ_{so}, the Γ_8 band is degenerate (heavy and light holes). Degeneracies for the holes are removed in the wurtzite and chalcopyrite structures by the additional crystal field splitting Δ_{cf} due to the anisotropy between the a- and c-axes. Typically, e.g. for CdS, the topmost valence band in the wurtzite structure has Γ_9 symmetry (allowed optical transitions only for $\mathbf{E} \perp \mathbf{c}$); an exception is ZnO for which the two upper bands are believed to be reversed. In the chalcopyrite structure optical transitions involving the Γ_6 band are only allowed for $\mathbf{E} \perp \mathbf{c}$. The three hole bands are usually labeled A, B, and C from the top of the valence band.

The energy positions of the three bands (with respect to the position of the Γ_{15} band) in the presence of spin-orbit interaction and crystal field splitting are given within the quasi-cubic approximation [525] by

$$E_1 = \frac{\Delta_{so} + \Delta_{cf}}{2} \tag{6.54a}$$

$$E_{2,3} = \pm \sqrt{\left(\frac{\Delta_{so} + \Delta_{cf}}{2}\right)^2 - \frac{2}{3}\,\Delta_{so}\,\Delta_{cf}}\,. \tag{6.54b}$$

In chalcopyrites the crystal field splitting is typically negative (Fig. 6.45). It is approximately linearly related to $1 - \eta$ (for $\eta = c/2a$ see Sect. 3.4.6).

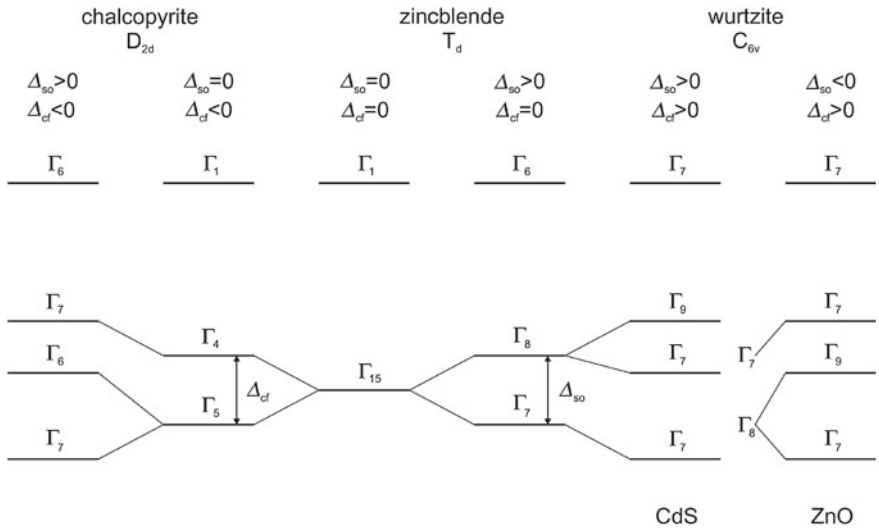

Fig. 6.44 Schematic band structure of zincblende and the valence-band splitting due to spin-orbit interaction Δ_{so} and crystal field splitting Δ_{cf} for chalcopyrites (typically $\Delta_{cf} < 0$, see Fig. 6.45) and wurtzites. For the wurtzites the situation is schematically shown for CdS ($\Delta_{so} = 67\,\text{meV}$, $\Delta_{cf} = 27\,\text{meV}$) (or GaN) and ZnO ($\Delta_{so} = -8.7\,\text{meV}$, $\Delta_{cf} = 41\,\text{meV}$)

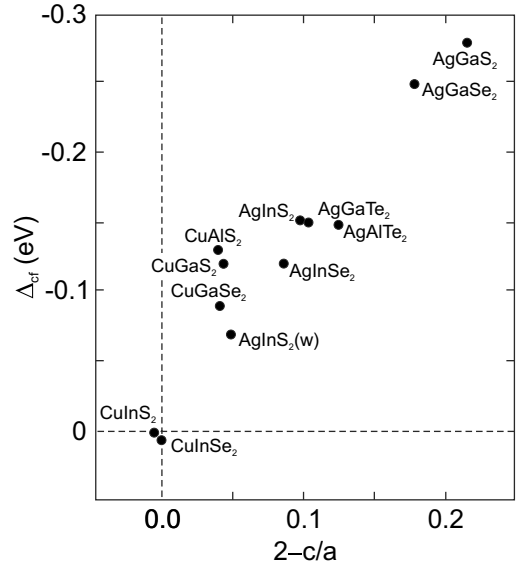

Fig. 6.45 Crystal field splitting Δ_{cf} for various chalcopyrite compounds versus the tetragonal distortion $2 - c/a = 2\,(1 - \eta)$. *Dash-dotted line* represents $\Delta_{cf} = 1.5\,b\,(2 - c/a)$ for $b = 1$ eV. Data from [526]

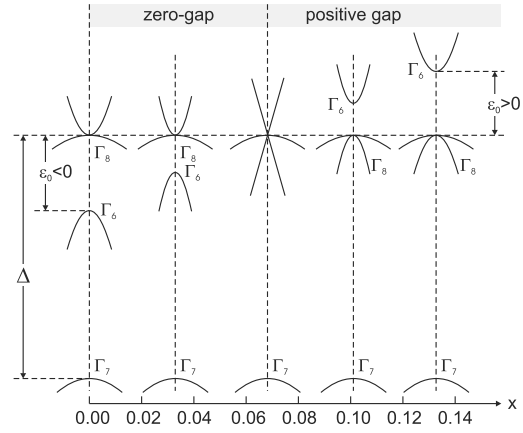

Fig. 6.46 Schematic band structure of zincblende with vanishing energy gap for the ternary compounds $Mn_xHg_{1-x}Te$. Note the linear dispersion for the zero-gap case at $x \approx 0.07$

6.11 Band Inversion

In certain compounds, typically mixing a semiconductor with a semimetal [527, 528], the band gap can shrink to zero (zero-gap semiconductor) and even become negative in the sense that the s-type Γ_6 symmetry (conduction) band is inverted below the Γ_8 (p-type) valence-band edge. HgTe is a classical example for such material as shown in Fig. 6.46, but similar effects are also present in other semiconductors, for example various chalcopyrites [529]. Remember that such band structures are topologically non-trivial (cf. Sect. 6.2.6).

For the zero-gap case, the dispersion of the two crossing bands is linear (like for graphene, cf. Sect. 13.1.2). The dielectric function of zero-gap semiconductors is discussed in [530].

For the $Cd_xHg_{1-x}Te$ system, around the zero-gap concentration of $x \approx 0.16$, the change from normal to inverted band structure will occur also as a function of temperature [531] as shown in Fig. 6.47. Such effect had been described already 50 years ago for (Pb,Sn)Te at the L-point (cf. Sect. 6.3.6) in [532].

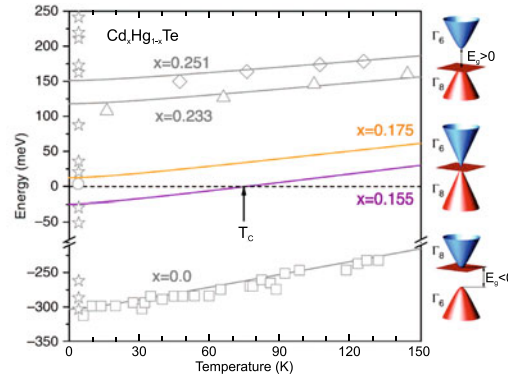

Fig. 6.47 Band gap of $Cd_xHg_{1-x}Te$ for various alloy compositions and temperatures. On the right, the schematic band structure of (Hg,Cd)Te with positive, zero and negative band gap is shown. Adapted from [531], reprinted under a Creative Commons Attribution (CC BY 4.0) licence

6.12 Strain Effects on the Band Structure

A mechanical strain (or equivalently stress) causes changes in the bond lengths. Accordingly, the band structure is affected. These effects have been exhaustively treated in [533, 534]. For small strain, typically $\epsilon \lesssim 0.01$ the shift of the band edges is linear with the strain, for large strain it becomes nonlinear [535]. Often homogeneous strain is assumed, the effect of inhomogeneous strain is discussed in [536].

6.12.1 Strain Effect on Band Edges

In a direct-gap zincblende material the position of the conduction-band edge is only affected by the hydrostatic component of the strain

$$E_C = E_C^0 + a_c \left(\epsilon_{xx} + \epsilon_{yy} + \epsilon_{zz}\right) = E_C^0 + a_c \,\mathrm{Tr}(\epsilon) \,, \tag{6.55}$$

where $a_c < 0$ is the conduction-band hydrostatic deformation potential and E_C^0 is the conduction-band edge of the unstrained material. Similarly, the valence-band edge is

$$E_V = E_V^0 + a_v \,\mathrm{Tr}(\epsilon) \,, \tag{6.56}$$

where $a_v > 0$ is the valence-band hydrostatic deformation potential. Therefore the band gap increases by

$$\Delta E_g = a \,\mathrm{Tr}(\epsilon) = a \left(\epsilon_{xx} + \epsilon_{yy} + \epsilon_{zz}\right) \,, \tag{6.57}$$

with $a = a_C - a_V$. Such linear behavior upon hydrostatic pressure has been found for many semiconductors and is shown in Fig. 6.48a for $Ga_{0.92}In_{0.08}As$. The anomaly for N-doping is discussed below in Sect. 6.12.3. In Fig. 6.49 the dependence of the direct and indirect gaps of GaAs is shown. The dependence of the direct gap on pressure is non-linear, that on the density is linear [537].

Biaxial and shear strains affect the valence bands and lead to shifts and splitting of the heavy and light holes at the Γ-point:

$$E_{v,hh/lh} = E_v^0 \pm E_{\epsilon\epsilon} \tag{6.58a}$$

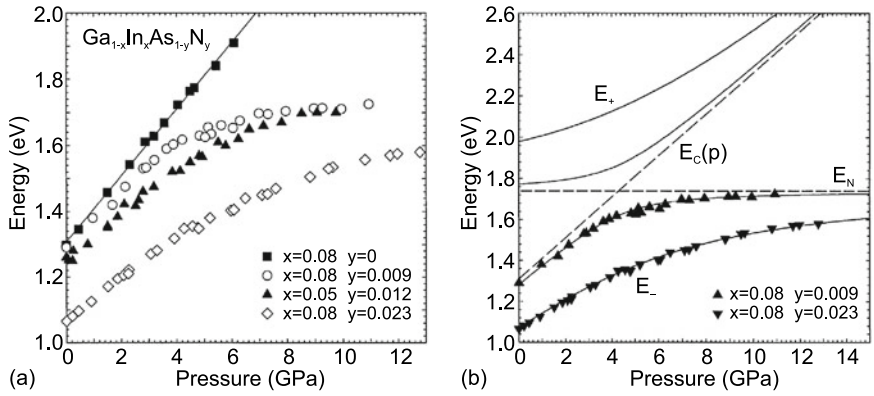

Fig. 6.48 **a** Dependence of the band gap of $Ga_{0.92}In_{0.08}As$ alloy (*squares*) and nitrogen-doped (Ga,In)As on (compressive) hydrostatic pressure, determined by photomodulated transmission at $T = 295\,\mathrm{K}$. **b** Pressure dependence of band gap for two (Ga,In)(As,N) samples together with model calculation (6.62). The coupling parameter is $V = 0.12\,\mathrm{eV}$ (0.4 eV) for a nitrogen content of 0.9% (2.3%). Adapted from [538]

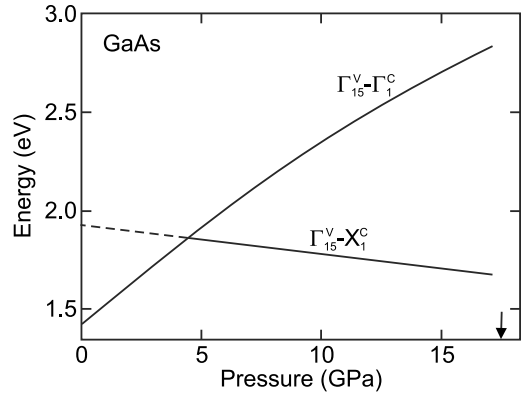

Fig. 6.49 Dependence of the direct Γ_{15}^{V}–Γ_{1}^{C} and indirect Γ_{15}^{V}–X_{1}^{C} band gap of GaAs ($T = 300\,\mathrm{K}$) on pressure. *Solid lines* are interpolations of experimental data, *dashed line* is extrapolation to $p = 0$. The crossing of the direct and indirect band gap occurs at 4.2 GPa. The *arrow* denotes the pressure of the phase transition from zincblende to an orthorhomic structure around 17 GPa. Adapted from [537]

$$E_{\epsilon\epsilon}^{2} = b^{2}/2\left[\left(\epsilon_{xx}-\epsilon_{yy}\right)^{2}+\left(\epsilon_{yy}-\epsilon_{zz}\right)^{2}+\left(\epsilon_{xx}-\epsilon_{zz}\right)^{2}\right] + d^{2}\left[\epsilon_{xy}^{2}+\epsilon_{yz}^{2}+\epsilon_{xz}^{2}\right],$$

where E_{v}^{0} denotes the bulk valence-band edge. b and d are the optical deformation potentials. For compressive strain the heavy-hole band is above the light-hole band. For tensile strain there is strong mixing of the bands (Fig. 6.50). In Table 6.7 the deformation potentials for some III–V semiconductors are listed. Typical values are in the eV regime.

In a wurtzite crystal, seven (or eight) deformation potentials are needed that are termed a (for the change of band gap with hydrostatic strain, again $a = a_C - a_V$) and D_1–D_6 (for the valence band structure) [539, 540].

In Si and Ge, three deformation potentials, termed a, b, d, are needed for the valence band and two for each conduction band minimum, Ξ_u and Ξ_d [541]. The energy position of the i-th conduction-band edge (with unit vector $\mathbf{a}_i$ pointing to the valley) is

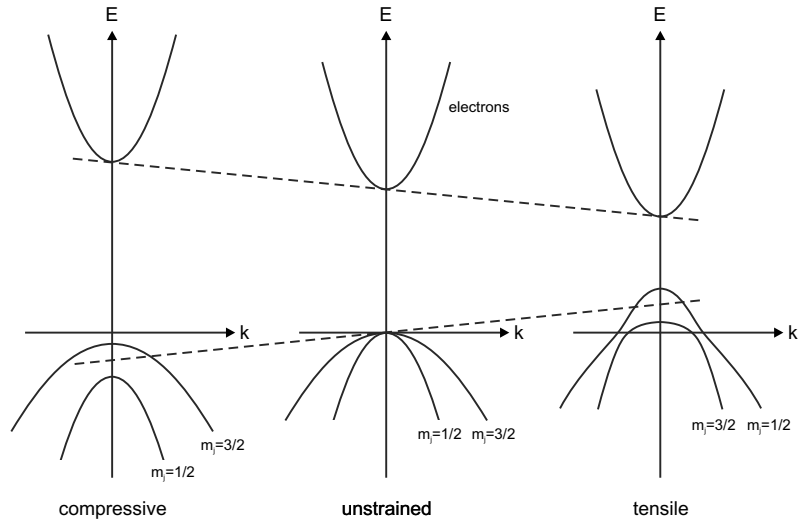

Fig. 6.50 Schematic band structure of GaAs in unstrained state (*center*) and under compressive and tensile biaxial strain as labeled. *Dashed lines* indicate shift of band edges due to hydrostatic part of strain

Table 6.7 Deformation potentials for some III–V semiconductors. All values in eV

Material	a	b	d
GaAs	−9.8	−1.7	−4.6
InAs	−6.0	−1.8	−3.6

Table 6.8 Deformation potentials for silicon and germanium. All values in eV from [542]

material	$\Xi_{\mathrm{d}}^{(\Delta)}$	$\Xi_{\mathrm{u}}^{(\Delta)}$	$\Xi_{\mathrm{d}}^{(\mathrm{L})}$	$\Xi_{\mathrm{u}}^{(\mathrm{L})}$	a	b	d
Si	1.1	10.5	−7.0	18.0	2.1	−2.33	−4.75
Ge	4.5	9.75	−4.43	16.8	2.0	−2.16	−6.06

$$E_{\mathrm{C},i} = E_{\mathrm{C},i}^{0} + \Xi_{\mathrm{d}}\,\mathrm{Tr}(\boldsymbol{\epsilon}) + \Xi_{\mathrm{u}}\,\mathbf{a}_i\,\boldsymbol{\epsilon}\,\mathbf{a}_i\ , \tag{6.59}$$

where $E_{\mathrm{C},i}^{0}$ denotes the energy of the unstrained conduction-band edge. The deformation potentials for Si and Ge are given in Table 6.8.

6.12.2 Strain Effect on Effective Masses

In the presence of strain the band edges are shifted (cf. Sect. 6.12). Since the electron mass is related to the band gap, it is expected that the mass will also be effected. In the presence of hydrostatic strain ϵ_{H} the electron mass is [543] (cf. to (6.43) for $\epsilon_{\mathrm{H}} \to 0$)

$$\frac{m_0}{m_{\mathrm{e}}^*} = 1 + \frac{E_{\mathrm{P}}}{E_{\mathrm{g}} + \Delta_0/3}\left[1 - \epsilon_{\mathrm{H}}\left(2 + \frac{3a}{E_{\mathrm{g}} + \Delta_0/3}\right)\right]\ , \tag{6.60}$$

with a being the hydrostatic deformation potential and $\epsilon_{\mathrm{H}} = \mathrm{Tr}(\epsilon)$. In [543], formulas are also given for biaxial and shear strain and also for hole masses. Since the effective mass enters the mobility, the electrical conductivity depends on the stress state of the semiconductor (piezoresistivity, see Sect. 8.3.14).

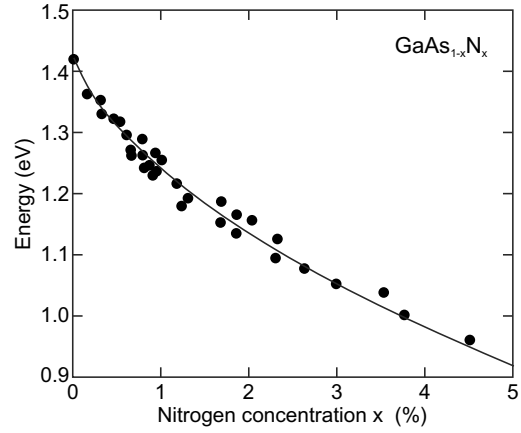

Fig. 6.51 Bandgap of $GaAs_{1-x}N_x$, experimental data from various sources (*symbols*) and model (*curve*) according to (6.62) with $V = V_0\sqrt{x}$ for $V_0 = 2.7\,\text{eV}$. Adapted from [545]

6.12.3 Interaction With a Localized Level

The normal dependence of the band gap on hydrostatic pressure is linear and given by (6.57). (Ga,In)As containing nitrogen exhibits a remarkable deviation from this behavior as shown in Fig. 6.48a. This is due to the interaction of the continuum states of the conduction band with the electron level of the isoelectronic nitrogen impurity (Sect. 7.7.9) E_N, being within the conduction band. For GaAs it is 0.2 eV above the conduction band edge E_C. This phenomenon has been investigated theoretically within microscopic detail [544]. Within a simple 'band anticrossing' two-level model, the coupling of the pressure-dependent conduction band edge E_C and the nitrogen level can be obtained from the Eigenwert equation

$$\begin{vmatrix} E - E_C & V \\ V & E - E_N \end{vmatrix} = 0\,, \tag{6.61}$$

V being the coupling constant. The determinant vanishes for

$$E_\pm = \frac{1}{2}\left(E_C + E_N \pm \sqrt{(E_C - E_N)^2 + 4V^2}\right)\,. \tag{6.62}$$

Here the weak pressure dependence of E_N is neglected for simplicity. This model can explain the pressure dependence of the band gap of (Ga,In)As:N fairly well [538] (Fig. 6.48b). The coupling parameter V is in the order of a few 0.1 eV for small nitrogen content. In photomodulated reflection also the E_+ levels can be observed [545]. The anti-crossing model can also model the dependence of the bandgap on the nitrogen concentration [545] (Fig. 6.51).

6.13 Density of States

6.13.1 General Band Structure

The dispersion relation yields how the energy of a (quasi-) particle depends on the **k** vector. Now we want to know how many states are at a given energy. This quantity is called the *density of states* (DOS) and is written as $D(E)$. It is defined in an infinitesimal sense such that the number of states between

E and $E + \delta E$ is $D(E)\delta E$. In the vicinity of the extrema of the band structure many states are at the same energy such that the density of states is high.

The dispersion relation of a band will be given as $E = E(\mathbf{k})$. If several bands overlap, the densities of state of all bands need to be summed up. The density of states at the energy $\tilde{E}$ for the given band is

$$D(\tilde{E})\,\mathrm{d}E = 2\int \frac{\mathrm{d}^3\mathbf{k}}{(2\pi/L)^3}\,\delta(\tilde{E} - E(\mathbf{k}))\,, \tag{6.63}$$

where, according to (5.5), $(2\pi/L)^3$ is the $\mathbf{k}$-space volume for one state. The factor 2 is for spin degeneracy. The integral runs over the entire $\mathbf{k}$-space and selects only those states that are at $\tilde{E}$. The volume integral can be converted to a surface integral over the isoenergy surface $S(\tilde{E})$ with $E(\mathbf{k}) = \tilde{E}$. The volume element $\mathrm{d}^3\mathbf{k}$ is written as $\mathrm{d}^2S\,\mathrm{d}\mathbf{k}_\perp$. The vector $\mathrm{d}\mathbf{k}_\perp$ is perpendicular to $S(\tilde{E})$ and proportional to $\nabla_\mathbf{k}E(\mathbf{k})$, i.e. $\mathrm{d}E = |\nabla_\mathbf{k}E(\mathbf{k})|\,\mathrm{d}\mathbf{k}_\perp$.

$$D(\tilde{E}) = 2\int_{S(\tilde{E})} \frac{\mathrm{d}^2S}{(2\pi/L)^3}\,\frac{1}{|\nabla_\mathbf{k}E(\mathbf{k})|}\,. \tag{6.64}$$

In this equation, the dispersion relation is explicitly contained. At band extrema the gradient diverges, however, in three dimensions the singularities are integrable and the density of states takes a finite value. The corresponding peak is named a van-Hove singularity. The concept of the density of states is valid for all possible dispersion relations, e.g. for electrons, phonons or photons.

The density of states for the silicon band structure (see Fig. 6.9a) is shown in Fig. 6.52.

6.13.2 Amorphous Semiconductors

If disorder is introduced, the density of states is modified as shown in Fig. 6.53 for amorphous germanium using a calculation with complex eigenenergies. The defects, as compared to the perfect lattice, introduced states in the band gap and generally wash out the sharp features from the crystalline DOS.

Several models exist for the defect level distributions within the band gap. The first model was the Mott model which has band tails at the valence and conduction band edges [547]. In the Cohen-Fritzsche-Ovshinsky (CFO) model [548], the band tails are more severe and overlap; the Fermi energy lies at the minimum of the density of states. In the Davis–Mott model [549] deep states were added in the gap and eventually the Marshall-Owen model [550] assumes band tails and donor- and acceptor-like deep states. The four models are schematically shown in Fig. 6.54. These model densities of states allow also the interpretation of carrier transport in amorphous semiconductors, taking into account localized and delocalized states (see Sect. 8.9).

The density of states for an amorphous semiconductor is best calculated from atomistic models, possibly averaging over many configurations. The typical features, compared to the clear band gap of a similar ordered material, are band tails due to disorder (cmp. Sect. 5.2.9) and deep levels within the gap due to specific atomic arrangements not present in ordered bulk. The most investigated system is amorphous silicon; in Fig. 6.55 a numerical calculation of the density of states is shown together with charge distribution of four states at selected energies [551]. The further the states are in the band tail, the stronger their localization is. The two most right states shown in Fig. 6.55 are not conducting.

As another example, simulations of $ZnSnO_3$ are shown in Fig. 6.56. The band tail between 0 and 0.5 eV is due to disorder of oxygen 2p orbitals [552]. At 0.9 eV a level due to under-coordinated oxygen appears. Deep levels are due to metal-metal bonds. Band tails due to chemically disordered oxygen have been experimentally observed for amorphous GIZO [553].

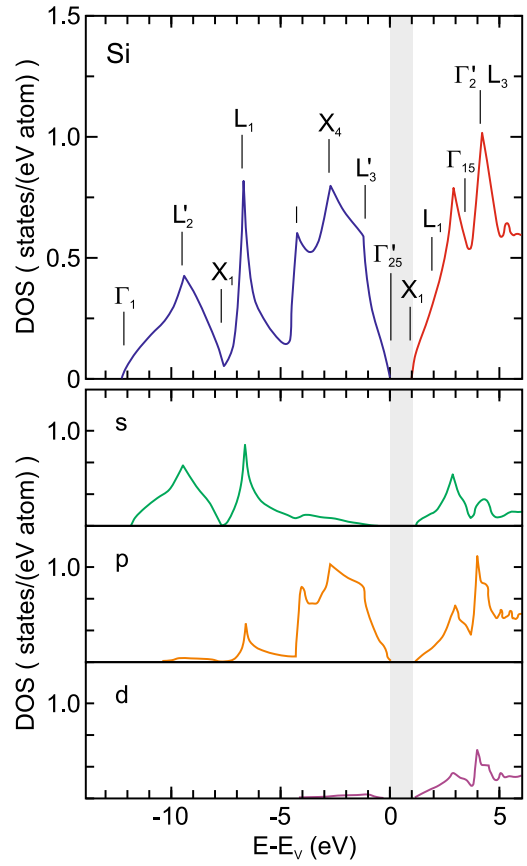

Fig. 6.52 Density of states in the silicon valence- (*blue*) and conduction-band (*red*) as obtained from theoretical calculation using empirical pseudopotentials. *Grey* regions denotes the band gap. Critical points (cf. Fig. 6.9a) are labeled. In the lower three graphs, the DOS is decomposed into contributions from different angular momentum states (s (*green*), p (*orange*) and d (*purple*)). *Top part* adapted from [546], *bottom part* adapted from [175]

6.13.3 *Free-Electron Gas*

In M dimensions, the energy states of a free-electron gas are given as

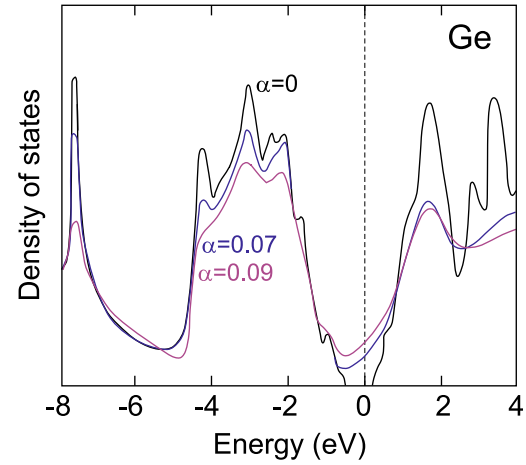

Fig. 6.53 Theoretical calculation for the density of states of amorphous Ge models as obtained for various degrees of disorder α (3.7). $\alpha = 0.09$ corresponds to a mean short-range order distance of about 2.4 lattice constants (cmp. Fig. 3.14b). Adapted from [204]

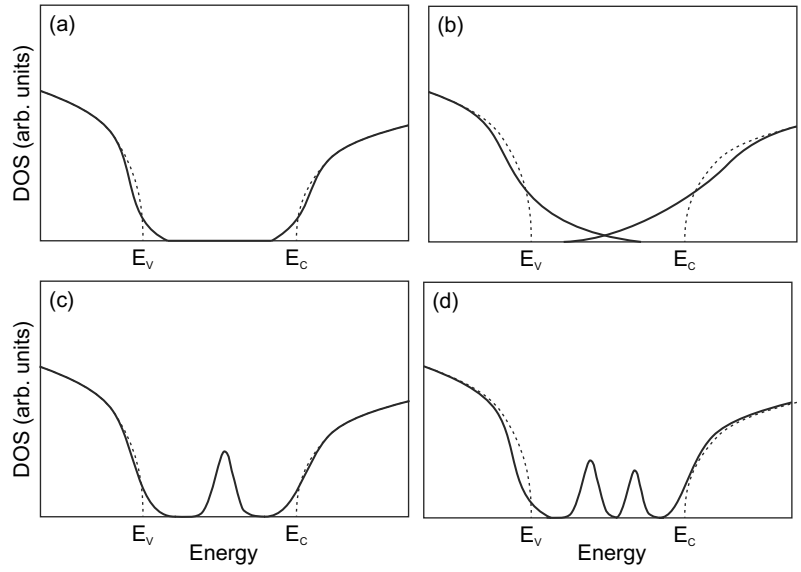

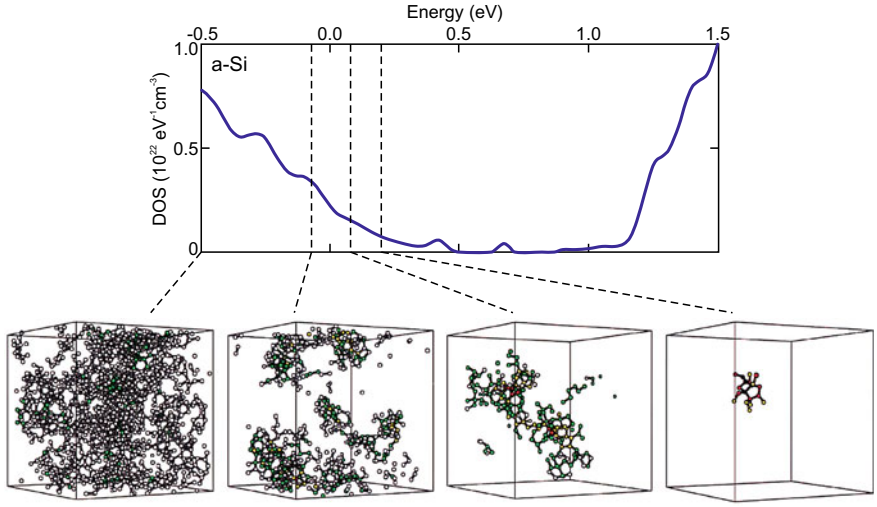

Fig. 6.54 Model density of states in amorphous semiconductors (*solid lines*) according to Mott [547], Cohen-Fritzsche-Ovshinsky [548], Davis–Mott [549] and Marshall–Owen [550]. *Dashed lines* represent the DOS of the same material without disorder

Fig. 6.55 Theoretical calculation of the density of electronic states of amorphous silicon. The charge distribution in four selected states at the indicated energies is shown, from right to left with decreasing localization. Adapted from [551]

$$E(\mathbf{k}) = \frac{\hbar^2}{2\,m^*} \sum_{i=1}^{M} k_i^2 \,. \tag{6.65}$$

The k_i can take the values $\pm\pi n/L$ (in the first Brillouin zone) with $n \leq N$, N being the number of unit cells in one dimension. These values are equidistant in $\mathbf{k}$-space. Each M-dimensional $\mathbf{k}$-point takes a volume of $(2\pi/L)^M$. The number of states $N(E_\mathrm{F})$ up to the energy $E_\mathrm{F} = \frac{\hbar^2}{2m} k_\mathrm{F}^2$ (later used as Fermi energy E_F and Fermi vector k_F) is

$$N(E_\mathrm{F}) = \frac{2}{(2\pi/L)^M} \int_{\mathbf{k}=0}^{|\mathbf{k}|=k_\mathrm{F}} \mathrm{d}^M k \,. \tag{6.66}$$

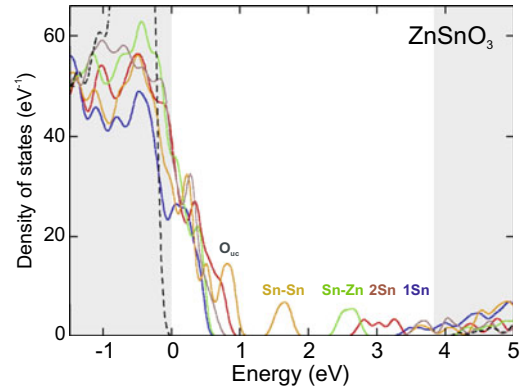

Fig. 6.56 Theoretical calculation for the density of states of crystalline (*dashed lines*, conduction and valence bands indicated by *greay areas*) and amorphous $ZnSnO_3$ with different configurations (*solid lines*). States due to under-coordinated oxygen (O_{uc}) and metal-metal bonds are labelled. Adapted from [552]

The factor 2 is for spin degeneracy, the integration runs over M dimensions. The density of states is the derivative

$$D(E) = \frac{\mathrm{d}N}{\mathrm{d}E} \,. \tag{6.67}$$

In the following, the density of states for $M = 3, 2, 1$ and zero dimensions is derived. A visualization is given in Fig. 14.1.

6.13.3.1 $M = 3$

This case relates to bulk material in which electrons are free to move in all three dimensions. Performing the integral (6.66) for $M = 3$ yields for an isotropic mass,

$$N^{3\mathrm{D}} = \frac{V}{3\pi^2}\, k_\mathrm{F}^3 = \frac{V}{3\pi^2}\left(\frac{2\,m\,E_\mathrm{F}}{\hbar^2}\right)^{3/2} \,. \tag{6.68}$$

Therefore, k_F and E_F are given by

$$k_\mathrm{F} = \left(\frac{3\pi^2\,N}{V}\right)^{1/3} \tag{6.69}$$

$$E_\mathrm{F} = \frac{\hbar^2}{2\,m^*}\left(\frac{3\pi^2\,N}{V}\right)^{2/3} \,, \tag{6.70}$$

and the density of states in three dimensions is

$$D^{3\mathrm{D}}(E) = \frac{V}{2\pi^2}\left(\frac{2\,m^*}{\hbar^2}\right)^{3/2}\sqrt{E} \,. \tag{6.71}$$

Mostly the density of states is used as density of states per volume, then the factor V in (6.71) is omitted.

If a conduction-band minimum is degenerate, a factor g_v (valley degeneracy) must be included in the density of states, i.e. $g_\mathrm{v} = 6$ for Si and $g_\mathrm{v} = 8$ for Ge ($g_\mathrm{v} = 1$ for GaAs). This factor is typically included in the mass used in (6.71) that then becomes the density of states mass $m_{\mathrm{d,e}}$. If the conduction-band minimum has cylindrical symmetry in **k**-space, such as for Si and Ge, the mass that has to be

used is

$$m_{\mathrm{d,e}} = g_{\mathrm{v}}^{2/3} \left(m_{\mathrm{t}}^2 m_{\mathrm{l}}\right)^{1/3} . \tag{6.72}$$

In the case of a degeneracy of the valence band, the states of several bands need to be summed. In bulk material, typically the heavy and light hole bands are degenerate at the Γ-point. If the split-off band is not populated because of insufficient temperature, the valence-band edge density of states is expressed by the density of states hole mass

$$m_{\mathrm{d,h}} = \left(m_{\mathrm{hh}}^{3/2} + m_{\mathrm{lh}}^{3/2}\right)^{2/3} . \tag{6.73}$$

The density of states (per volume) at the conduction and valence band edges are thus given by

$$D_{\mathrm{e}}^{\mathrm{3D}}(E) = \frac{1}{2\pi^2} \left(\frac{2\, m_{\mathrm{d,e}}}{\hbar^2}\right)^{3/2} \sqrt{E - E_{\mathrm{C}}} \, , \, E > E_{\mathrm{C}} \tag{6.74}$$

$$D_{\mathrm{h}}^{\mathrm{3D}}(E) = \frac{1}{2\pi^2} \left(\frac{2\, m_{\mathrm{d,h}}}{\hbar^2}\right)^{3/2} \sqrt{E_{\mathrm{V}} - E} \, , \, E < E_{\mathrm{V}} . \tag{6.75}$$

6.13.3.2 $M = 2$

This case is important for thin layers in which the electron motion is confined in one direction and free in a plane. Such structures are called quantum wells (see Sect. 12.3.2). We find for the 2D density of states (for each subband over which it is not summed here, including spin degeneracy)

$$N^{\mathrm{2D}} = \frac{A}{2\pi} k_{\mathrm{F}}^2 = \frac{A}{\pi} \frac{m^*}{\hbar^2} E \, , \tag{6.76}$$

where A is the area of the layer. The density of states is thus constant and given by

$$D^{\mathrm{2D}}(E) = \frac{A}{\pi} \frac{m^*}{\hbar^2} . \tag{6.77}$$

6.13.3.3 $M = 1$

The case $M = 1$ describes a quantum wire in which the electron motion is confined in two dimensions and free in only one dimension. For this case, we find for a wire of length L

$$N^{\mathrm{1D}} = \frac{2L}{\pi} k_{\mathrm{F}} = \frac{2L}{\pi} \left(\frac{2m^* E}{\hbar^2}\right)^{1/2} . \tag{6.78}$$

The density of states becomes singular at $E = 0$ and is given by (for one subband)

$$D^{\mathrm{1D}}(E) = \frac{L}{\pi} \left(\frac{2m^*}{\hbar^2}\right)^{1/2} \frac{1}{\sqrt{E}} . \tag{6.79}$$

6.13.3.4 $M = 0$

In this case electrons have no degrees of freedom, as, e.g., in a quantum dot (Sect. 14.4), and each state has a δ-like density of states at each of the quantized levels.

Chapter 7
Electronic Defect States

Über Halbleiter sollte man nicht arbeiten, das ist eine Schweinerei, wer weiß ob es überhaupt Halbleiter gibt.
One should not work on semiconductors. They are a mess. Who knows whether semiconductors even exist.

W. Pauli, 1931[554]

Abstract After the carrier statistics for intrinsic conduction and general doping principles, donors and acceptors, compensation and high doping effects are treated in detail. The concept of quasi-Fermi levels is introduced. Finally for deep levels and their thermodynamics general remarks and several examples are given.

7.1 Introduction

One cm^3 of a semiconductor contains about 5×10^{22} atoms. It is practically impossible to achieve perfect purity. Typical low concentrations of impurity atoms are in the $10^{12} - 10^{13}\,cm^{-3}$ regime. Such a concentration corresponds to a purity of 10^{-10}, corresponding to about one alien in the world's human population. In the beginning of semiconductor research the semiconductors were so impure that the actual semiconducting properties could only be used inefficiently. Nowadays, thanks to large improvements in high-purity chemistry, the most common semiconductors, in particular silicon, can be made so pure that the residual impurity concentration plays no role in the physical properties. However, the most important technological step for semiconductors is *doping*, the controlled incorporation of impurities, in order to manage the semiconductor's conductivity. Typical impurity concentrations used in doping are $10^{15} - 10^{20}\,cm^{-3}$. A milestone in the understanding of doping and the spreading of semiconductor technology was the 1950 textbook by Shockley [555].

7.2 Carrier Concentration

Generally, the density of electrons in the conduction band is given by

$$n = \int_{E_C}^{\infty} D_e(E)\, f_e(E)\, dE\ , \tag{7.1}$$

M. Grundmann, *The Physics of Semiconductors*, Graduate Texts in Physics,
https://doi.org/10.1007/978-3-030-51569-0_7

and accordingly the density of holes in the valence band is

$$p = \int_{-\infty}^{E_V} D_h(E)\, f_h(E)\, dE \,. \tag{7.2}$$

The energy of the top of the valence band is denoted by E_V, the bottom of the conduction band as E_C. We assume here parabolic band edges, i.e. effective masses m_h and m_e for holes and electrons, respectively. The density of states (per volume) in the conduction band D_e and valence bands D_h is given by (6.74) and (6.75).

The statistical distribution function for electrons is denoted by f_e is given in thermodynamical equilibrium by the Fermi-Dirac distribution, (E.22),

$$f_e(E) = \frac{1}{\exp\left(\frac{E-E_F}{kT}\right)+1} \,. \tag{7.3}$$

The distribution function for holes is $f_h = 1 - f_e$,

$$f_h(E) = 1 - \frac{1}{\exp\left(\frac{E-E_F}{kT}\right)+1} = \frac{1}{\exp\left(-\frac{E-E_F}{kT}\right)+1} \,. \tag{7.4}$$

If several hole bands (hh, lh, so) are considered, the same distribution is valid for all hole bands in thermal equilibrium.

If the Boltzmann distribution (E.23) is a good approximation, the carrier distribution is called *nondegenerate*. If the Fermi-Dirac distribution needs to be invoked, the carrier ensemble is called *degenerate*. If the Fermi level is within the band, the ensemble is highly degenerate.

If the Boltzmann approximation (E.23) cannot be applied, i.e. at high temperatures or for very small band gaps, the integral over Df cannot be analytically evaluated. In this case the Fermi integral is needed that is defined[1] as

$$F_n(x) = \frac{2}{\sqrt{\pi}} \int_0^\infty \frac{y^n}{1+\exp(y-x)}\, dy \,. \tag{7.5}$$

In the present case of bulk materials $n = 1/2$. For large negative argument, i.e. $x < 0$ and $|x| \gg 1$, $F_{1/2}(x) \approx \exp(x)$, which is the Boltzmann approximation. $F_{1/2}(0) = 0.765\ldots \approx 3/4$. For large argument, i.e. $x \gg 1$, $F_{1/2}(x) \approx (2/\sqrt{\pi})(2/3)x^{3/2}$. Such fairly simple approximations are plotted in Fig. 7.1 in comparison with the Fermi integral. For computations, analytical [556–559] or numerical approximations [560, 561] are used.

The derivative of the Fermi integral is given by $F_n'(x) = nF_{n-1}(x)$, $n > 0$. For $n = 0$, i.e. a two-dimensional system, the integral can be executed explicitly, $F_0(x) = (2/\sqrt{\pi}) \ln[1 + \exp(x)]$.

With the Fermi integral $F_{1/2}$ (7.10) and (7.11) the free-carrier densities can be written as

$$n = N_C\, F_{1/2}\left(\frac{E_F - E_C}{kT}\right) \tag{7.6}$$

$$p = N_V\, F_{1/2}\left(-\frac{E_F - E_V}{kT}\right) \,, \tag{7.7}$$

[1] Equation (7.5) is restricted to $n > -1$. A form without restriction is $\mathcal{F}_n(x) = \frac{1}{\Gamma(n+1)} \int_0^\infty \frac{y^n}{1+\exp(y-x)} dy$. The factor $2/\sqrt{\pi}$ is often omitted but must be then added explicitly in, e.g., (7.6).

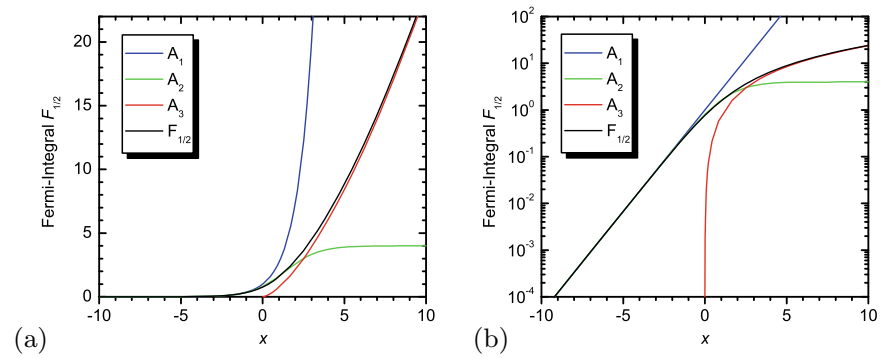

Fig. 7.1 Fermi integral $\hat{F}_{1/2} = (\sqrt{\pi}/2)F_{1/2}$ with approximations in three regions of the argument: $A_1(x) = (\sqrt{\pi}/2)\exp(x)$ for $x < 2$, $A_2(x) = (\sqrt{\pi}/2)(1/4 + \exp(-x))^{-1}$ for $-2 < x < 2$, $A_3(x) = 2/3x^{3/2}$ for $x > 2$. **a** linear, **b** semilogarithmic plot

Table 7.1 Band gap, intrinsic carrier concentration, conduction band and valence-band edge density of states at $T = 300\,\mathrm{K}$ for various semiconductors

	E_g (eV)	n_i (cm^{-3})	N_C (cm^{-3})	N_V (cm^{-3})
InSb	0.18	1.6×10^{16}		
InAs	0.36	8.6×10^{14}		
Ge	0.67	2.4×10^{13}	1.04×10^{19}	6.0×10^{18}
Si	1.124	1.0×10^{10}	7.28×10^{19}	1.05×10^{19}
GaAs	1.43	1.8×10^{6}	4.35×10^{17}	5.33×10^{18}
GaP	2.26	2.7×10^{0}		
GaN	3.3	$\ll 1$		

with

$$N_C = 2\left(\frac{m_e\, kT}{2\pi\,\hbar^2}\right)^{3/2} \tag{7.8}$$

$$N_V = 2\left(\frac{m_h\, kT}{2\pi\,\hbar^2}\right)^{3/2}, \tag{7.9}$$

where N_C (N_V) is called the conduction-band (valence-band) edge density of states. The masses in (7.8) and (7.9) are the density of states masses given in (6.72) and (6.73). Values of $N_{C,V}$ for Si, Ge and GaAs are given in Table 7.1.

Now, we assume that the Boltzmann approximation (E.23) can be used, i.e. the probability that a band state is populated is $\ll 1$. Then, the integral (7.1) can be executed analytically and the concentration n of electrons in the conduction band is given as

$$n = 2\left(\frac{m_e kT}{2\pi\hbar^2}\right)^{3/2} \exp\left(\frac{E_F - E_C}{kT}\right) = N_C \exp\left(\frac{E_F - E_C}{kT}\right). \tag{7.10}$$

For the Boltzmann approximation and a parabolic valence band, the density of holes is given by

$$p = 2\left(\frac{m_h kT}{2\pi\hbar^2}\right)^{3/2} \exp\left(-\frac{E_F - E_V}{kT}\right) = N_V \exp\left(-\frac{E_F - E_V}{kT}\right). \tag{7.11}$$

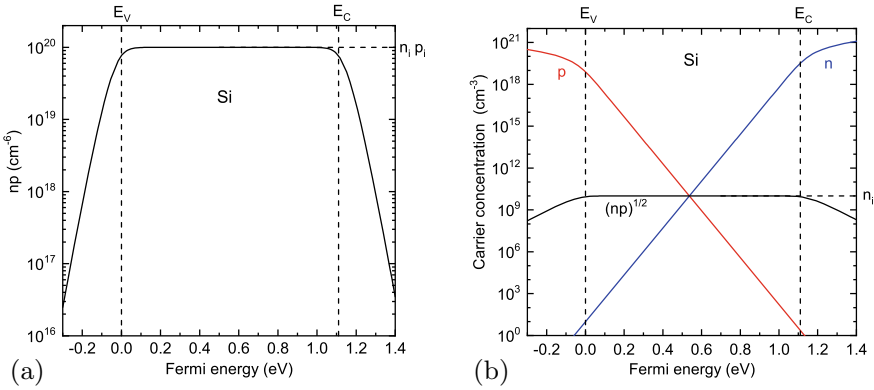

Fig. 7.2 **a** np for silicon at $T = 300\,\mathrm{K}$ as a function of the position of the Fermi level. The valence-band edge E_V is chosen as $E = 0$. np is constant for the range of Fermi energies given by (7.13) ($4kT \approx 0.1\,\mathrm{eV}$). **b** n, p and $\sqrt{np}$ as a function of the Fermi level

Within the Boltzmann approximation, the product of the electron and hole density is

$$\begin{aligned} n\,p &= N_\mathrm{V}\,N_\mathrm{C}\,\exp\left(-\frac{E_\mathrm{C}-E_\mathrm{V}}{kT}\right) = N_\mathrm{V}\,N_\mathrm{C}\,\exp\left(-\frac{E_\mathrm{g}}{kT}\right) \\ &= 4\left(\frac{kT}{2\pi\hbar^2}\right)^3 (m_{\mathrm{d,e}}\,m_{\mathrm{d,h}})^{3/2}\,\exp\left(-\frac{E_\mathrm{g}}{kT}\right)\,. \end{aligned} \tag{7.12}$$

Thus, the product $n\,p$ is *independent* of the position of the Fermi level, as long as the Boltzmann approximation is fulfilled. This is the case when the Fermi level lies within the band gap and it is sufficiently far away from the band edges, fulfilling about

$$E_\mathrm{V} + 4\,kT \;<\; E_\mathrm{F} \;<\; E_\mathrm{C} - 4\,kT\,. \tag{7.13}$$

The relation (7.12) is called the mass-action law.

In Fig. 7.2, the product np is shown for silicon over a wide range of Fermi energies. If E_F is within the band gap, np is essentially constant. If the Fermi level is in the valence or conduction band, np decreases exponentially.

7.3 Intrinsic Conduction

First, we consider the conductivity of the intrinsic, i.e. an ideally pure, semiconductor. At $T = 0$ all electrons are in the valence band, the conduction band is empty and thus the conductivity is zero (a completely filled band cannot conduct current). Only at finite temperatures the electrons have a finite probability to be in a conduction-band state and to contribute to the conductivity. Due to neutrality, the electron and hole concentrations in the intrinsic semiconductors are the same, i.e. each electron in the conduction band comes from the valence band,

$$-\,n + p = 0\,, \tag{7.14}$$

or $n_\mathrm{i} = p_\mathrm{i}$. Therefore

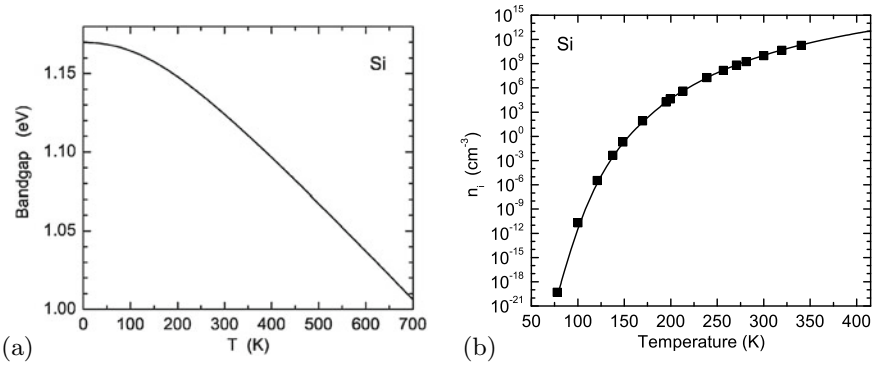

Fig. 7.3 **a** Band gap of silicon versus temperature. **b** Intrinsic carrier concentration of silicon versus temperature. *Solid line* is (7.17) using $E_g = 1.204\,\text{eV} - (2.73 \times 10^{-4}\,\text{eV/K})\,T$ [564], *symbols* are experimental data from [565]

$$n_i = p_i = \sqrt{N_V\,N_C}\,\exp\left(-\frac{E_g}{2kT}\right) \tag{7.15}$$
$$= 2\left(\frac{kT}{2\pi\hbar^2}\right)^{3/2}(m_e m_h)^{3/4}\,\exp\left(-\frac{E_g}{2kT}\right)\,.$$

The mass-action law

$$n\,p = n_i\,p_i = n_i^2 = p_i^2 \tag{7.16}$$

will be essential also for light and moderately doped semiconductors. The intrinsic carrier concentration is exponentially dependent on the band gap. Thus, in thermodynamic equilibrium intrinsic wide-gap semiconductors have much smaller electron concentrations than intrinsic small-gap semiconductors (see Table 7.1). The intrinsic carrier concentration of Si (in cm^{-3}) has been determined to be (within 1%, T in K)

$$n_i^{\text{Si}} = 1.640 \times 10^{15}\;T^{1.706}\,\exp\left(-\frac{E_g(T)}{2kT}\right) \tag{7.17}$$

for temperatures between 77 and 400 K [562, 563] (Fig. 7.3).

As we will see later in Part II, many semiconductor devices rely on regions of low conductivity (depletion layers) in which the carrier concentration is small. Since the carrier concentration cannot be smaller than the intrinsic concentration ($n + p \geq 2n_i$), an increase of temperature leads to increasing ohmic conduction in the depletion layers and thus to a reduction or failure of device performance. The small band gap of Ge leads to degradation of bipolar device performance already shortly above room temperature. For silicon, intrinsic conduction limits operation typically to temperatures below about 300 °C. For higher temperatures, as required for devices in harsh environments, such as close to motors or turbines, other semiconductors with wider band gaps need to be used, such as GaN, SiC or even diamond.

From the neutrality condition for the intrinsic semiconductor (7.14) and (7.10) and (7.11), the Fermi level of the intrinsic semiconductor can be determined as

$$E_F = E_i = \frac{E_V + E_C}{2} + \frac{kT}{2}\,\ln\left(\frac{N_V}{N_C}\right) = \frac{E_V + E_C}{2} + \frac{3}{4}\,kT\,\ln\left(\frac{m_h}{m_e}\right)\,. \tag{7.18}$$

Since the hole mass is perhaps a factor of ten larger than the electron mass, the second term has the order of kT. Thus, for typical semiconductors where $E_g \gg kT$, the intrinsic Fermi level, denoted by E_i, is close to the middle of the band gap, i.e. $E_i \approx (E_C + E_V)/2$.

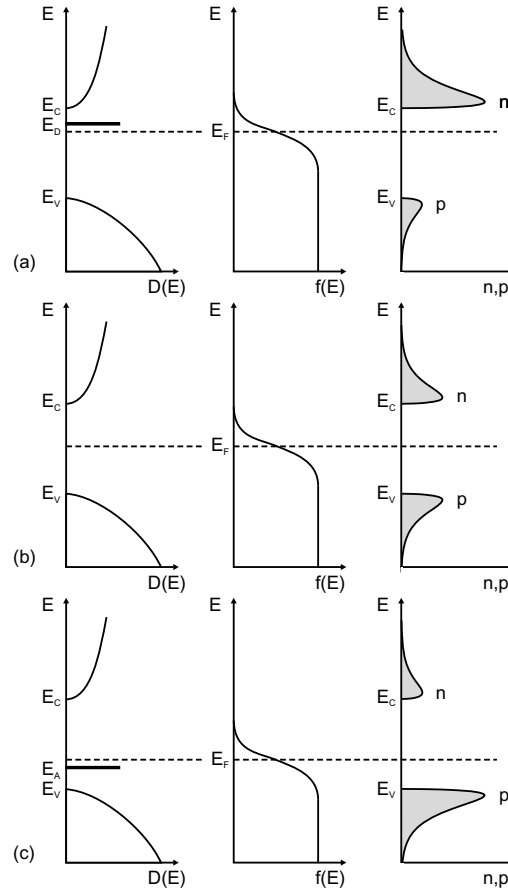

Fig. 7.4 Density of states (*left column*), Fermi distribution (*center column*) and carrier concentration (*right column*) for **a** n-type, **b** intrinsic and **c** p-type semiconductors in thermal equilibrium

The situation for an intrinsic semiconductor is schematically shown in Fig. 7.4b. In the following we will consider doping which can shift the Fermi level away from E_i. Within the Boltzmann approximation (also $n_\mathrm{i} = p_\mathrm{i}$),

$$n = n_\mathrm{i} \exp\left(\frac{E_\mathrm{F} - E_\mathrm{i}}{kT}\right) \tag{7.19}$$

$$p = p_\mathrm{i} \exp\left(-\frac{E_\mathrm{F} - E_\mathrm{i}}{kT}\right) . \tag{7.20}$$

7.4 Doping

7.4.1 Concept

The modification of the conductivity of a semiconductor using point defects is termed *doping*. In 1930 electrical conduction of semiconductors was attributed solely to impurities [566, 567]. However 'chemically pure' substances become conductive upon deviation from stoichiometry, e.g. historically

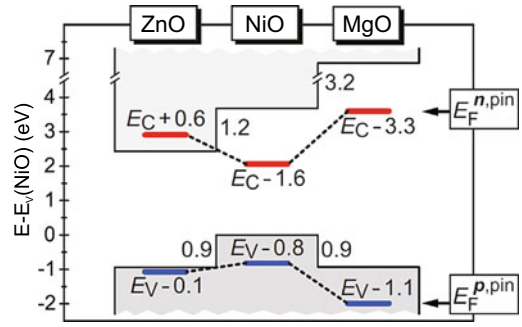

Fig. 7.5 Comparison of ZnO, NiO and MgO on a common energy scale, comparing conduction band and valence band edges and n-type (*red*) and p-type (*blue*) pinning energies (determined for metal-rich and oxygen-rich conditions, respectively). Adapted from [571]

found for changes in the anion concentration and conductivity in CuI [38] (p-type) and ZnO [80] (n-type). The modification of CuI by exposure to different partial pressure of iodine in organic solutions with different iodine concentration [41] and subsequently various concentrations of copper vacancies [568] can be considered the first doping of a semiconductor (1909).

The electronic levels of a defect or an impurity can exist within the forbidden gap of the bulk host material. These levels can lie close to the band edges or in the vicinity of the middle of the band gap. In a simplified approach, the first stem from *shallow* defects (Sect. 7.5), the latter from *deep* defects (Sect. 7.7).

7.4.2 Doping Principles

In [569] various doping principles are formulated. Essentially, the amount of impurities that lead to electrically active dopants is limited by the increasingly probable formation of compensating defects. In the case of donors, these are electron killers, e.g. n-type doping of Si:As is limited by the formation of V_{Si} [570]. In the case of acceptors, the compensating defects are hole killers. The so-called n-type *pinning energy* $E_F^{n,pin}$ is the Fermi level at which such killer defect (e.g. a cation vacancy) forms. When the Fermi level reaches the pinning energy, no further progress in n-type doping can be made, since the spontaneously generated electron killers will negate the introduced (impurity) donors. As a tendency, materials with low lying conduction band, i.e. large electron affinity (difference between vacuum level and conduction band) can be doped n-type. Similarly, p-type doping by acceptors, shifting the Fermi level towards the valence band, will meet at some point $E_F^{p,pin}$, called p-type pinning energy, when native hole killers, such as anion vacancies or cation interstitials form spontaneously. At this point, further p-type doping is no longer possible. p-type doping is facilitated by materials whose valance band maximum is close to the vacuum level [569].

A comparison of the wide gap materials ZnO, NiO and MgO is depicted in Fig. 7.5. The position of the pinning levels is marked on a common energy scale. From the position of $E_F^{n,pin}$ it can be understood, that ZnO can be highly n-doped while NiO and MgO cannot [571]. From $E_F^{p,pin}$, NiO can be doped p-type, while MgO cannot be doped at all.

For dopability, generally, it is also important that the ionized charges from impurities are free and thus contribute to the free charge carrier density and do not form localized states, e.g. due to polaronic effects (Sect. 8.7).

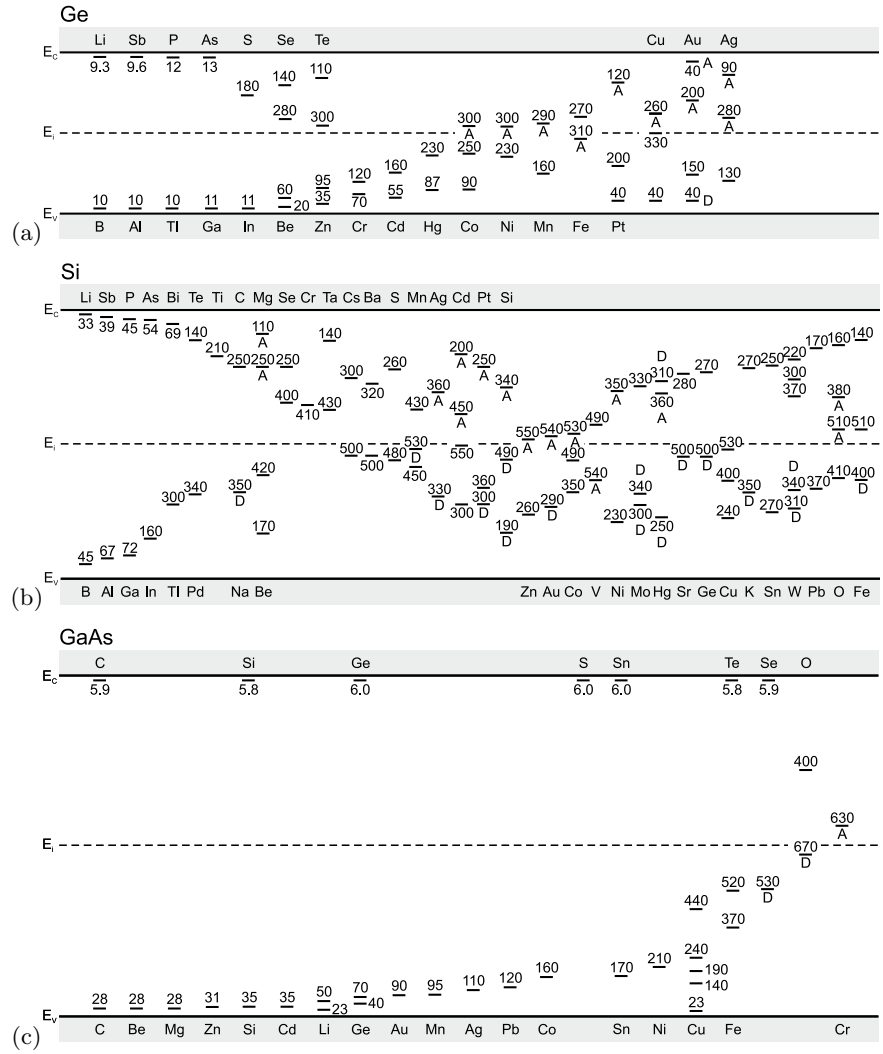

Fig. 7.6 Energetic position (ionization energy labeled in meV) of various impurities (A: acceptor, D: donor) in **a** Ge, **b** Si and **c** GaAs. Based on [574]

7.5 Shallow Defects

In Fig. 7.6, the positions of the energy levels of a variety of impurities are shown for Ge, Si and GaAs. An impurity for which the long-range Coulomb part of the ion-core potential determines the energetic level is termed a *shallow* impurity. The extension of the wavefunction is given by the Bohr radius. This situation is in contrast to a *deep* level where the short-range part of the potential determines the energy level. The extension of the wavefunction is then of the order of the lattice constant. A view on the history of the science of shallow impurity states is given in [572, 573].

We will consider first a group-IV semiconductor, Si, and (impurities) dopants from the groups III and V of the periodic system. When these are incorporated on a lattice site (with tetrahedral bonds), there is one electron too few (group III, e.g. B) or one electron too many (group V, e.g. As). The first case is called an *acceptor*, the latter a *donor*. The doping of III–V semiconductors is detailed in [575].

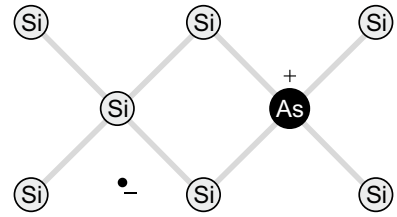

Fig. 7.7 Arsenic impurity in silicon. Arsenic donates one electron, and a fixed positive charge remains

7.5.1 Donors

Silicon doped with arsenic is denoted as Si:As. The situation is schematically shown in Fig. 7.7. The arsenic atom has, after satisfying the tetrahedral bonds, an extra electron. This electron is bound to the arsenic atom via the Coulomb interaction since the ion core is positively charged compared to the silicon cores. If the electron is ionized, a fixed positive charge remains at the As site.

Without being in the silicon matrix, an arsenic atom has an ionization energy of 9.81 eV. However, in the solid the Coulomb interaction is screened by the dielectric constant of the material, typically ϵ_r is of the order of 10 for typical semiconductors. Additionally, the mass is renormalized (effective mass) by the periodic potential to a value that is smaller than the free electron mass. Within effective-mass theory (Appendix I) the hydrogen problem is scaled with the (isotropic) effective mass m_e^* and the dielectric constant ϵ_r, the binding energy (ionization energy) E_D^b of the electron to the shallow donor is (relative to the continuum given by the conduction-band edge E_C)

$$E_D^b = \frac{m_e^*}{m_0} \frac{1}{\epsilon_r^2} \frac{m_0 e^4}{2 (4\pi\epsilon_0 \hbar)^2} . \tag{7.21}$$

The scaling with $1/\epsilon^2$ has been pointed out first in [576].

The absolute energy position of the level is $E_D = E_C - E_D^b$. The first factor in the right side of (7.21) is the ratio of effective and free-electron mass, typically 1/10, the second factor is typically 1/100. The third factor is the ionization energy of the hydrogen atom, i.e. the Rydberg energy of 13.6 eV. Thus, the binding energy in the solid is drastically reduced by a factor of about 10^{-3} to the 10 meV regime. The excited states of the hydrogen-like spectrum can also be investigated experimentally (Sect. 9.8).

The extension of the wavefunction of the electron bound to the fixed ion is given by the Bohr radius

$$a_D = \frac{m_0}{m_e^*} \epsilon_r a_B , \tag{7.22}$$

where $a_B = 0.053$ nm denotes the hydrogen Bohr radius. For GaAs $a_D = 10.3$ nm. A similar value has been determined for InP [577]. For semiconductors with a nonisotropic band minimum, such as Si, Ge or GaP, an 'elliptically deformed' hydrogen problem with the masses m_l and m_t has to be treated [578].

An impurity that fulfills (7.21) is called an *effective-mass* impurity. For GaAs, the effective-mass donor has a binding energy of 5.715 meV, which is closely fulfilled for several chemical species (Table 7.3). In GaP, experimental values deviate considerably from the effective-mass donor (59 meV). For silicon, considering the anisotropic tensor of the effective masses, the result for the effective-mass donor binding energy is 29 meV [578]. Some experimentally observed values are summarized in Table 7.2. Deviations from the effective-mass theory are due to modification of the potential in the immediate vicinity of the impurity atom and breakdown of the effective-mass formalism.

Different impurities can have quite similar binding energies. They can be distinguished, e.g., by electron spin resonance (ESR). At low temperatures the electron is localized on the impurity and the hyperfine interaction with the nucleus can be resolved in ESR. In Fig. 7.8 data are shown for As and P

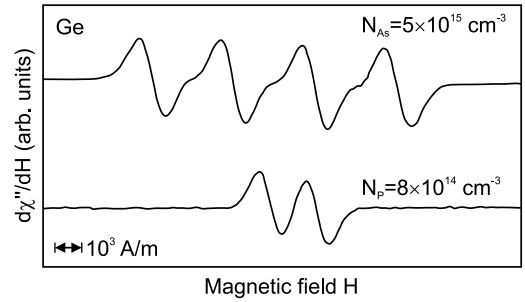

Fig. 7.8 Electron spin resonance signal from As and P in Ge with the magnetic field **H** parallel to [100], $T \approx 1.3\,\mathrm{K}$. Adapted from [579]

Table 7.2 Binding energies E_D^b of Li and group-V donors in elemental semiconductors. Data for carbon from [580]. All values in meV

	Li	N	P	As	Sb
C		1700	≈500		
Si	33		45	49	39
Ge	9.3		12.0	12.7	9.6

Table 7.3 Binding energies E_D^b of donors in GaAs (data from [581]), GaP (data from [582]) and GaN (low concentration limits, data from [583, 584]). All values in meV

	V site		III site	
GaAs	S	5.854	C	5.913
	Se	5.816	Si	5.801
	Te	5.786	Ge	5.937
GaP	O	897	Si	85
	S	107	Ge	204
	Se	105	Sn	72
	Te	93		
GaN	O	39	Si	22
			Ge	19

in germanium. The multiplets distinguish the nuclear spins $I = 3/2$ for arsenic (^{75}As) and $I = 1/2$ for phosphorus (^{31}P) [579].

The donors are typically distributed statistically (randomly) in the solid. Otherwise their distribution is called clustered. The concentration of donors is labeled N_D and usually given in cm^{-3}.

The concentration of donors populated with an electron (neutral donors) is denoted by N_D^0, the concentration of ionized donors (positively charged) is N_D^+. Other conventions in the literature label the concentrations N_1 and N_0, respectively:

$$N_1 = N_\mathrm{D}^0 = N_\mathrm{D}\, f_\mathrm{e}(E_\mathrm{D}) \tag{7.23a}$$

$$N_0 = N_\mathrm{D}^+ = N_\mathrm{D}\,(1 - f_\mathrm{e}(E_\mathrm{D}))\,, \tag{7.23b}$$

with $f_\mathrm{e}(E_\mathrm{D}) = [1 + \exp(E_\mathrm{D} - E_\mathrm{F})]^{-1}$. For the sum of these quantities the condition

$$N_\mathrm{D} = N_\mathrm{D}^+ + N_\mathrm{D}^0 \tag{7.24}$$

holds.

The ratio of the two concentrations is first given as (caveat: this formula will be modified below)

$$\frac{N_\mathrm{D}^0}{N_\mathrm{D}^+} = \frac{N_1}{N_0} = \frac{f}{1-f} = \exp\left(\frac{E_\mathrm{F}-E_\mathrm{D}}{kT}\right) . \tag{7.25}$$

Now, the degeneracy of the states has to be considered. The donor charged with one electron has a 2-fold degeneracy $g_1 = 2$ since the electron can take the spin up and down states. The degeneracy of the ionized (empty) donor is $g_0 = 1$. Additionally, we assume here that the donor cannot be charged with a second electron (cmp. Sect. 7.7.2). Due to Coulomb interaction, the energy level of the possible N_D^- state is in the conduction band. Otherwise, a multiply charged center would be present. We also do not consider excited states of N_D^0 that might be in the band gap as well. In the following, we will continue with $\hat{g}_\mathrm{D} = g_1/g_0 = 2$ as suggested in [585].[2] We note that the definition of the degeneracy factor for donors (and acceptors, see (7.38)) is not consistent in the literature as summarized in [586]. Considering now the degeneracy, (7.25) is modified to

$$\frac{N_\mathrm{D}^0}{N_\mathrm{D}^+} = \frac{N_1}{N_0} = \hat{g}_\mathrm{D} \exp\left(\frac{E_\mathrm{F}-E_\mathrm{D}}{kT}\right) . \tag{7.26}$$

This can be understood from thermodynamics (cf. Sect. 4.2.2), a rate analysis or simply the limit $T \to \infty$.

The probabilities f^1 and f^0 for a populated or empty donor, respectively, are

$$f^1 = \frac{N_1}{N_\mathrm{D}} = \frac{1}{\hat{g}_\mathrm{D}^{-1} \exp\left(\frac{E_\mathrm{D}-E_\mathrm{F}}{kT}\right) + 1} \tag{7.27a}$$

$$f^0 = \frac{N_0}{N_\mathrm{D}} = \frac{1}{\hat{g}_\mathrm{D} \exp\left(-\frac{E_\mathrm{D}-E_\mathrm{F}}{kT}\right) + 1} . \tag{7.27b}$$

First, we assume that no carriers in the conduction band stem from the valence band (no intrinsic conduction). This will be the case at sufficiently low temperatures when $N_\mathrm{D} \gg n_\mathrm{i}$. Then the number of electrons in the conduction band is equal to the number of ionized donors, i.e.

$$n = f^0 N_\mathrm{D} = N_0 = \frac{N_\mathrm{D}}{1 + \hat{g}_\mathrm{D} \exp\left(\frac{E_\mathrm{F}-E_\mathrm{D}}{kT}\right)} = \frac{1}{1+n/n_1} N_\mathrm{D} ,$$

with $n_1 = (N_\mathrm{C}/\hat{g}_\mathrm{D}) \exp(-E_\mathrm{D}^b/kT)$. The neutrality condition (its general from is given in equation (7.40)) is

$$-n + N_\mathrm{D}^+ = -n + N_0 = 0 , \tag{7.28}$$

leading to the equation (n is given by (7.10))

$$N_\mathrm{C} \exp\left(\frac{E_\mathrm{F}-E_\mathrm{C}}{kT}\right) - \frac{N_\mathrm{D}}{1 + \hat{g} \exp\left(\frac{E_\mathrm{F}-E_\mathrm{D}}{kT}\right)} = 0 . \tag{7.29}$$

Solving this equation will yield the Fermi level (as a function of temperature T, doping level E_D and doping concentration N_D).[3] The solution is

[2] We do not agree with the treatment of the conduction band valley degeneracy in [585] for the donor degeneracy factor for Ge and Si.

[3] As usual, the Fermi level is determined by the global charge neutrality, see also Sect. 4.2.2.

$$E_F = E_C - E_D^b + kT \ln\left(\frac{\left[1 + 4\hat{g}_D \frac{N_D}{N_C} \exp\left(\frac{E_D^b}{kT}\right)\right]^{1/2} - 1}{2\,\hat{g}_D}\right) . \tag{7.30}$$

For $T \to 0$ the Fermi level is, as expected, in the center between the populated and unpopulated states, i.e. at $E_F = E_C - E_D^b/2$. In Fig. 7.9a the position of the Fermi is shown for a donor with 45 meV binding energy in Si. For low temperatures the solution can be approximated as (dashed curve in Fig. 7.9b)

$$E_F \cong E_C - \frac{1}{2} E_D^b + \frac{1}{2} kT \ln\left(\frac{N_D}{\hat{g}_D N_C}\right) . \tag{7.31}$$

The freeze-out of carriers in n-type silicon has been discussed in detail in [587], taking into account the effects of the fine structure of the donor states. We note that the fairly high donor binding energy in silicon leads to freeze-out of carriers at about 40 K and is thus limiting for the low-temperature performance of devices. Ge has smaller donor ionization energies and subsequently a lower freeze-out temperature of 20 K. For n-type GaAs, conductivity is preserved down to even lower temperatures.

We note that the freeze-out of carriers involves the recombination of free electrons with the ionized donors. This aspect is considered in Sect. 10.9. Microscopically this process is equal to the emission of a (far infrared) photon [588, 589]. Similarly the release of an electron from the donor is due to the absorption of a photon.

For higher temperatures, when the electron density saturates towards N_D, the approximate solution is (dash-dotted curve in Fig. 7.9a)

$$E_F \cong E_C + kT \ln\left(\frac{N_D}{N_C}\right) . \tag{7.32}$$

The electron density n is given (still in the Boltzmann approximation) by

$$\begin{aligned} n &= N_C \exp\left(-\frac{E_D^b}{kT}\right) \frac{\left[1 + 4\,\hat{g}_D \frac{N_D}{N_C} \exp\left(\frac{E_D^b}{kT}\right)\right]^{1/2} - 1}{2\,\hat{g}_D} \\ &= \frac{2\,N_D}{1 + \left[1 + 4\,\hat{g}_D \frac{N_D}{N_C} \exp\left(\frac{E_D^b}{kT}\right)\right]^{1/2}} . \end{aligned} \tag{7.33}$$

The theoretical electron density as a function of temperature is shown in Fig. 7.9b. It fits very well to experimental data for arsenic doped germanium [594] as shown in Fig. 7.10 (Arrhenius plot, $\ln n$ vs. $1/T$).

For low temperatures, the solution (7.34) is close to

$$n \cong \sqrt{\frac{N_D N_C}{\hat{g}_D}} \exp\left(-\frac{E_D^b}{2kT}\right) = \sqrt{n_1\, N_D} . \tag{7.34}$$

For high temperatures, $n \cong N_D$. This regime is called *exhaustion* or *saturation* since all possible electrons have been ionized from their donors. We note that even in this case $np = n_i p_i$ holds, however, $n \gg p$.

While the characteristic energy for the ionization of electrons from donors is E_D^b, at high enough temperatures electrons are transferred also from the valence band into the conduction band. Thus, in order to make the above consideration valid for all temperatures, the intrinsic conduction also has to

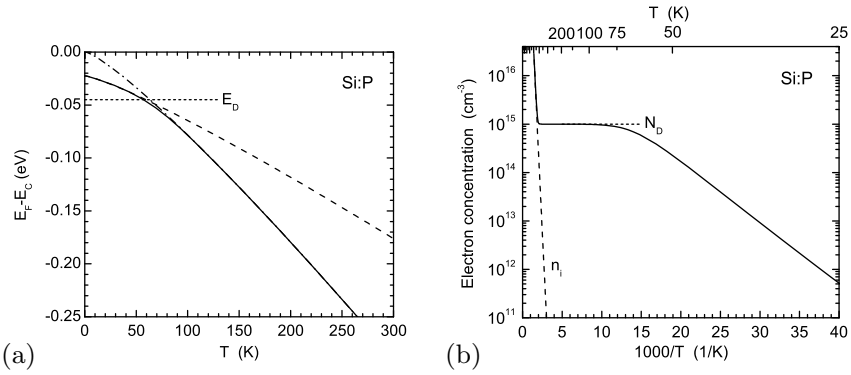

Fig. 7.9 **a** Position of the Fermi level in Si:P ($N_D = 10^{15}\,cm^{-3}$, $E_D^b = 45$ meV, no acceptors) as a function of temperature *without* consideration of intrinsic carriers. Zero energy refers to the (temperature-dependent, Table 6.4) conduction-band edge E_C with approximative solutions for low (*dashed line*, (7.31)) and high (*dash-dotted line*, (7.32)) temperatures. **b** Corresponding density of conduction-band electrons as a function of temperature

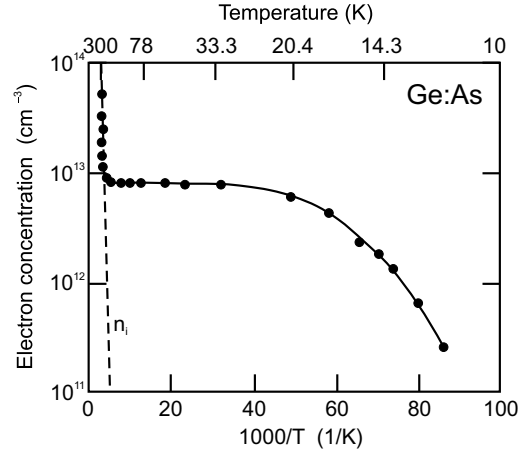

Fig. 7.10 Electron concentration as a function of temperature for a Ge:As sample with $N_D \approx 10^{13}\,cm^{-3}$. *Solid line* is fit to the data with a donor binding energy of 12.7 meV. Adapted from [594]

be considered. The neutrality condition (still in the absence of any acceptors) is

$$-n + p + N_D^+ = 0\,. \tag{7.35}$$

Using (7.10) and $p = n_i^2/n$, the equation reads:

$$N_C \exp\left(\frac{E_F - E_C}{kT}\right) - \frac{n_i^2}{N_C \exp(\frac{E_F - E_C}{kT})} - \frac{N_D}{1 + \hat{g}_D \exp(\frac{E_F - E_D}{kT})} = 0\,. \tag{7.36}$$

The solution can be given analytically but is more complicated[4]. The temperature-dependent position of the Fermi level is shown in Fig. 7.11.

The three important regimes are the intrinsic conduction at high temperatures when $n_i \gg N_D$, the exhaustion at intermediate temperatures when $n_i \ll N_D$ and $kT > E_D^b$, and finally the freeze-out regime for $kT \ll E_D^b$ at low temperatures when the electrons condense back into the donors. The three

[4]It is given in the third edition of this book.

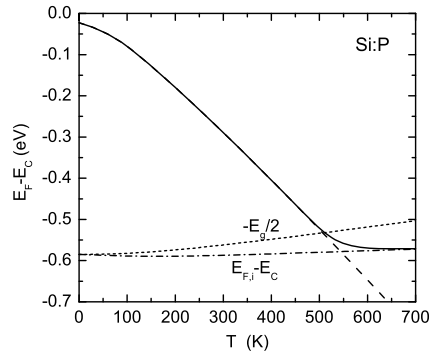

Fig. 7.11 Position of the Fermi level in Si:P ($N_D = 10^{15}\,\mathrm{cm}^{-3}$, $E_D^b = 45\,\mathrm{meV}$, no acceptors) as a function of temperature. The temperature dependence of the band gap (as given in Table 6.4) has been taken into account. Zero energy refers to the conduction-band edge for all temperatures. The *dotted curve* shows $E_g/2$. The *dashed* (*dash-dotted*) *line* shows the low- (high-) temperature limit according to (7.31) and (7.18), respectively. The corresponding electron concentration as a function of temperature is shown in Fig. 7.9b

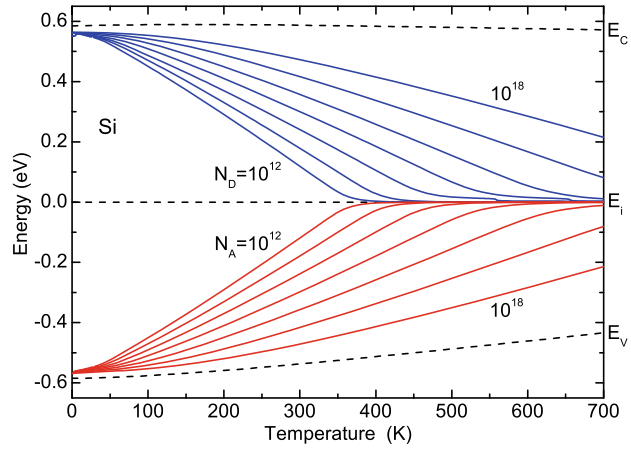

Fig. 7.12 Fermi level in silicon as a function of temperature for various doping levels (n-type (*blue lines*) and p-type (*red lines*)) of $10^{12}, 10^{13}, \ldots, 10^{18}\,\mathrm{cm}^{-3}$. The intrinsic Fermi level is chosen as zero energy for all temperatures. The (temperature-dependent) conduction and valence band edges are shown as *dashed lines*

regimes can be seen in the experimental data on carrier density of electrons in n-Ge (Fig. 7.10) and of holes in p-Ge (Fig. 7.15).

A similar plot as in Fig. 7.11 is shown in Fig. 7.12 but for different doping levels. With increasing temperature, the Fermi level shifts from close to the band edge towards the band center. At higher doping, this shift begins at higher temperatures.

The electronic states of individual donors can be directly visualized by scanning tunneling microscopy (STM) as shown in Fig. 7.13 for Si:P. For small negative bias, tunneling occurs through the charged dopant that is located within the first three monolayers. At high negative bias the large contribution from the filled valence band masks the effect of the donor. This image, however, shows that the contrast attributed to the dopant atom is not due to surface defects or absorbates.

7.5.2 Acceptors

A group-III atom in Si has one electron too few for the tetrahedral bond. Thus, it 'borrows' an electron from the electron gas (in the valence band) and thus leaves a missing electron (termed hole) in the

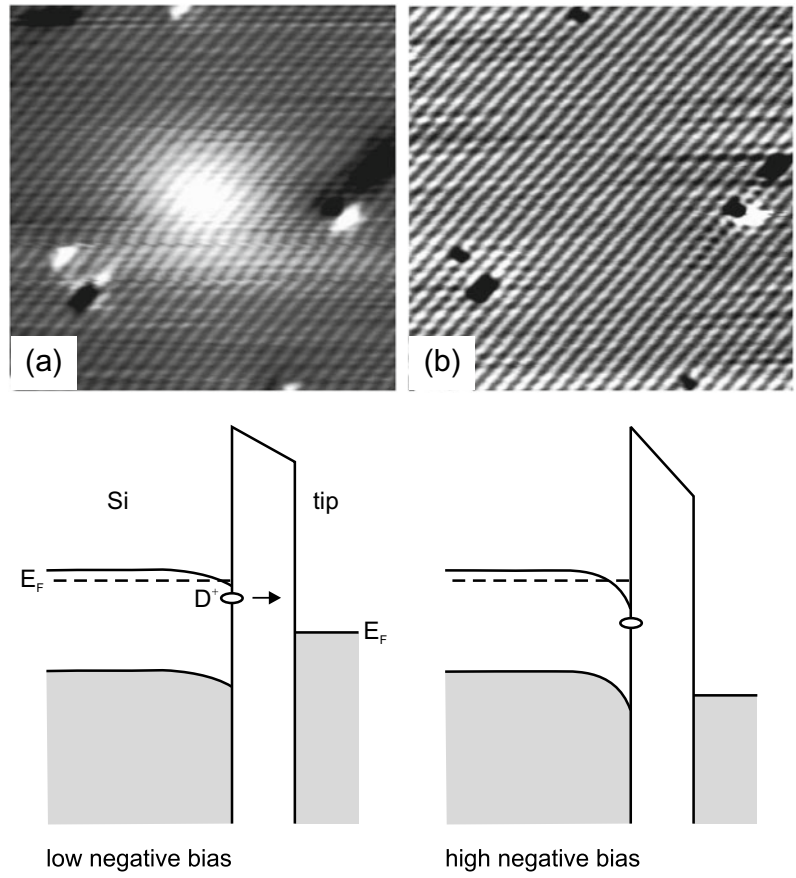

Fig. 7.13 Filled-state image of a phosphorus atom underneath a Si (001) surface at a tunneling current of 110 pA. The doping level is $5 \times 10^{17}\,\mathrm{cm}^{-3}$. **a** Sample bias -0.6 V, **b** sample bias -1.5 V between Si:P and tip. Image sizes are $22 \times 22\,\mathrm{nm}^2$. Reprinted with permission from [595], ©2004 APS. *Lower row* under parts **b**, **c**: Schematic band diagrams for the two bias situations

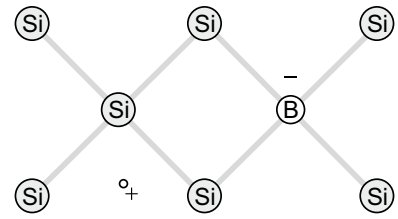

Fig. 7.14 Boron impurity in silicon. Boron accepts one electron and a fixed negative charge remains

valence band (Fig. 7.14). The energy level of the impurity is in the gap close to the valence-band edge. The latter consideration is made in the electron picture. In the hole picture, the acceptor ion has a hole and the hole ionizes (at sufficient temperature) into the valence band. After ionization the acceptor is charged negatively. Also, for this system a hydrogen-like situation arises that is, however, more complicated than for donors because of the degeneracy of the valence bands and their warping.

In Table 7.4 the acceptor binding energies E_{A}^b for group-III atoms in C, Ge and Si are listed. The absolute acceptor energy is given as $E_{\mathrm{A}} = E_{\mathrm{V}} + E_{\mathrm{A}}^b$. In Table 7.5 acceptor binding energies are listed for GaAs, GaP and GaN. While in GaAs some acceptors are close to the effective mass value of 27 meV, in GaP the deviation from the effective-mass value $\approx$50 meV is large.

When the conductivity is determined by holes or electrons, the material is called p-type or n-type, respectively. We note that some metals also show hole conduction (e.g. Al). However, for metals the

Table 7.4 Binding energies E_A^b of group-III acceptors in elemental semiconductors. Data for diamond from [596, 597]. All values in meV

	B	Al	Ga	In
C	369			
Si	45	57	65	16
Ge	10.4	10.2	10.8	11.2

Table 7.5 Binding energies E_A^b of acceptors in GaAs, GaP and GaN (low concentration values, data from [598, 599]). All values in meV

	V site		III site	
GaAs	C	27	Be	28
	Si	34.8	Mg	28.8
	Ge	40.4	Zn	30.7
	Sn	167	Cd	34.7
GaP	C	54	Be	57
	Si	210	Mg	60
	Ge	265	Zn	70
			Cd	102
GaN	C	230	Mg	220
	Si	224	Zn	340
			Cd	550

conductivity type is fixed, while the same semiconductor can be made n- or p-type with the appropriate doping.

The acceptor concentration is denoted by N_A. The concentration of neutral acceptors is N_A^0, the concentration of charged acceptors is N_A^-. Of course

$$N_A = N_A^0 + N_A^- \,. \tag{7.37}$$

The ratio of the degeneracy of the (singly) filled and empty acceptor level is $\hat{g}_A$. In Ge $\hat{g}_A = 4$ since the localized hole wave function may be formed in EMA with four Bloch wave functions (heavy and light holes) [600]. For Si with its small split-off energy (Table 6.6) $\hat{g}_A = 6$ according to [601]. For doubly ionized acceptors, e.g. Zn in Si and Ge (see Sect. 7.7.3), the more shallow level ($Zn^- \rightarrow Zn^0$) has $\hat{g}_A = 6/4 = 1.5$ in Ge [601]. A more general discussion of the degeneracy factor for multiply charged acceptors can be found in [585, 602]. Similar to the considerations for electrons and donors we have

$$\frac{N_A^0}{N_A^-} = \hat{g}_A \exp\left(-\frac{E_F - E_A}{kT}\right) \,. \tag{7.38}$$

The population of the acceptor levels is given by

$$N_A^- = \frac{N_A}{1 + \hat{g}_A \exp\left(-\frac{E_F - E_A}{kT}\right)} \,. \tag{7.39}$$

The formulas for the position of the Fermi level and the hole density are analogous to those obtained for electrons and donors and will not be explicitly given here. The analogue to Fig. 7.11b is shown for data on p-doped Ge [603, 604] in Fig. 7.15. The acceptor activation energy is 11 meV which could be

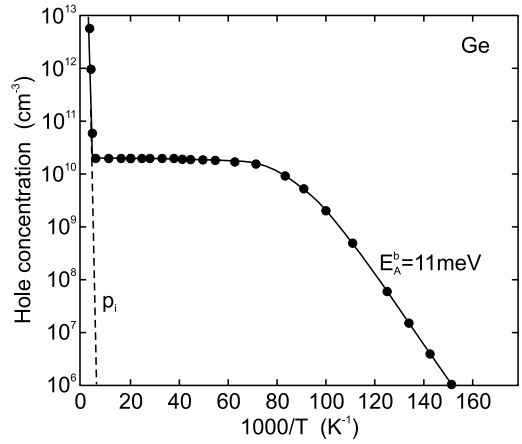

Fig. 7.15 Carrier concentration as a function of temperature for p-type Ge. The net shallow level concentration is $2 \times 10^{10}\,\mathrm{cm}^{-3}$. *Solid line* is fit to the data, the *dashed line* indicates the intrinsic hole concentration p_i. Adapted from [604]

due to various impurities (cf. Table 7.4). The different impurities (B, Al, Ga) can be distinguished by photothermal ionization spectroscopy [604] (cmp. Sect. 9.8).

In Fig. 7.12, the temperature dependence of the Fermi level is included for p-type Si. With increasing temperature the Fermi level shifts from the valence-band edge (For $T = 0$, $E_\mathrm{F} = E_\mathrm{V} + E_\mathrm{A}^b/2$) towards the middle of the band gap (intrinsic Fermi level).

Also, the wavefunction at acceptors can be imaged using scanning tunneling microscopy [605]. In [606] images of ionized and neutral Mn in GaAs have been reported (Fig. 7.16b). The tunneling I–V characteristics are shown in Fig. 7.16a. At negative bias, the acceptor is ionized and appears spherically symmetric due to the effect of the A^- ion Coulomb potential on the valence-band states. At intermediate positive voltages, tunneling is through the neutral state. The wavefunction of A^0 looks like a bow-tie due to the admixture of d-wavefunctions [607]. The Mn atom is presumably in the third subsurface atomic layer. At even higher positive bias the contrast due to the dopant is lost because the image is dominated by a large tunneling current from the tip to the empty conduction band.

7.5.3 Compensation

When donors *and* acceptors are simultaneously present, some of the impurities will compensate each other. Electrons from donors will recombine with holes on the acceptors. Depending on the quantitative situation the semiconductor can be n- or p-type. This situation can be invoked by intentional doping with donors or acceptors or by the unintentional background of donors (acceptors) in p-doped (n-doped) material. Also the formation of pairs, exhibiting a new defect level different from the single donor or single acceptor, has been described, e.g. for Se and B in silicon [308].

The charge-neutrality condition (now finally in its most general form) reads

$$-n + p - N_\mathrm{A}^- + N_\mathrm{D}^+ = 0\,. \tag{7.40}$$

We will now discuss the case of the presence of donors and acceptors, but limit ourselves to sufficiently low temperatures (or wide band gaps) such that the intrinsic carrier density can be neglected. We assume Boltzmann statistics and assume here $N_\mathrm{D} > N_\mathrm{A}$. Then it is a very good approximation to use $N_\mathrm{A}^- = N_\mathrm{A}$

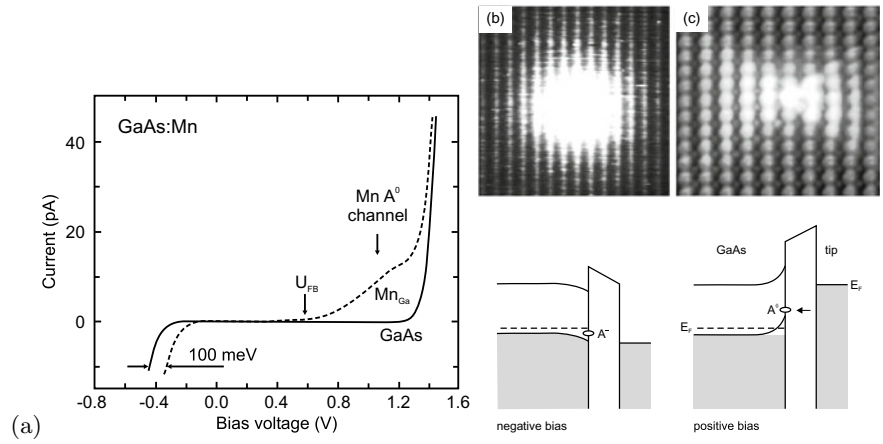

Fig. 7.16 **a** Tunneling I–V characteristic of GaAs:Mn sample. *Solid* (*dashed*) line is for pure GaAs (subsurface Mn on Ga site). U_{FB} denotes the simulated flat-band voltage. Adapted from [606]. (**b**, **c**) STM images of a Mn atom underneath a GaAs (110) surface. The doping level is $3 \times 10^{18}\,\mathrm{cm}^{-3}$. **b** Sample bias $-0.7\,\mathrm{V}$, **c** sample bias $+0.6\,\mathrm{V}$. Below the images are schematic band diagrams of GaAs:Mn and tip. Image sizes are **b** $8 \times 8\,\mathrm{nm}^2$ and **c** $5.6 \times 5\,\mathrm{nm}^2$. Reprinted with permission from [606], ©2004 APS. *Lower row* under parts **a**, **b**: Schematic band diagrams for the two bias situations

since there are enough electrons from the donors to recombine with (and thus compensate) all acceptors. Under the given assumptions regarding the temperature $p = 0$ and the material is n-type. Thus, in order to determine the position of the Fermi level, the charge-neutrality condition

$$n + N_{\mathrm{A}} - N_{\mathrm{D}}^{+} = 0 \tag{7.41}$$

must be solved (compare to (7.29))

$$N_{\mathrm{C}} \exp\left(\frac{E_{\mathrm{F}} - E_{\mathrm{C}}}{kT}\right) + N_{\mathrm{A}} - \frac{N_{\mathrm{D}}}{1 + \hat{g} \exp(\frac{E_{\mathrm{F}} - E_{\mathrm{D}}}{kT})} = 0\,. \tag{7.42}$$

We rewrite (7.41) and find $N_{\mathrm{D}} - N_{\mathrm{A}} - n = N_{\mathrm{D}}^{0} = N_{\mathrm{D}}^{+}\,\hat{g}_{\mathrm{D}} \exp\left(\frac{E_{\mathrm{F}} - E_{\mathrm{D}}}{kT}\right)$ using (7.26). Using again (7.41) and also (7.10), (7.42) can be written as

$$\frac{n\,(n + N_{\mathrm{A}})}{N_{\mathrm{D}} - N_{\mathrm{A}} - n} = \frac{N_{\mathrm{C}}}{\hat{g}_{\mathrm{D}}} \exp\left(-\frac{E_{\mathrm{D}}^{\mathrm{b}}}{kT}\right)\,, \tag{7.43}$$

a form given in [608]. Analogously for compensated p-type material

$$\frac{p\,(p + N_{\mathrm{D}})}{N_{\mathrm{A}} - N_{\mathrm{D}} - p} = \frac{N_{\mathrm{V}}}{\hat{g}_{\mathrm{A}}} \exp\left(-\frac{E_{\mathrm{A}}^{\mathrm{b}}}{kT}\right) \tag{7.44}$$

holds.

The solution of (7.42) is

$$E_{\mathrm{F}} = E_{\mathrm{C}} - E_{\mathrm{D}}^{b} + kT \ln\left(\frac{\left[\alpha^2 + 4\hat{g}_{\mathrm{D}} \frac{N_{\mathrm{D}} - N_{\mathrm{A}}}{N_{\mathrm{C}}} \exp\left(\frac{E_{\mathrm{D}}^{b}}{kT}\right)\right]^{1/2} - \alpha}{2\,\hat{g}_{\mathrm{D}}}\right)\,, \tag{7.45}$$

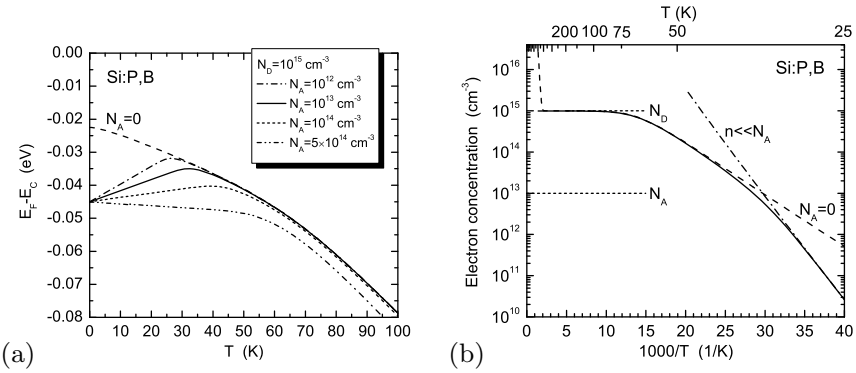

Fig. 7.17 **a** Position of Fermi level in partially compensated Si:P,B ($N_D = 10^{15}\,cm^{-3}$, $E_D^b = 45\,meV$, $E_A^b = 45\,meV$, *solid line*: $N_A = 10^{13}\,cm^{-3}$, *dashed line*: $N_A = 0$, *dash-dotted line*: $N_A = 10^{12}\,cm^{-3}$, *short-dashed line*: $N_A = 10^{14}\,cm^{-3}$, *dash-double dotted line*: $N_A = 5 \times 10^{14}\,cm^{-3}$) as a function of temperature. **b** Corresponding electron concentration for $N_A = 10^{13}\,cm^{-3}$ as a function of temperature (neglecting intrinsic carriers), *dashed line* for $N_A = 0$ according to (7.34), *dash-dotted line* approximation for $n \ll N_A$ as in (7.49)

with

$$\alpha = 1 + \hat{g}_D \frac{N_A}{N_C} \exp\left(\frac{E_D^b}{kT}\right) = 1 + \frac{N_A}{\beta} \tag{7.46a}$$

$$\beta = \frac{N_C}{\hat{g}_D} \exp\left(-\frac{E_D^b}{kT}\right) . \tag{7.46b}$$

The carrier density is best obtained from (7.43),

$$2\,n = \sqrt{(N_A - \beta)^2 + 4\,N_D\,\beta} - (N_A + \beta) . \tag{7.47}$$

For $N_A = 0$ we have $\alpha = 1$ and (7.30) is reproduced, as expected. For $T = 0$ (and $N_A \neq 0$) the Fermi energy lies at $E_F = E_D$ since the donor level is *partially* filled ($N_D^0 = N_D - N_A$). For low temperatures the Fermi level is approximated by

$$E_F \cong E_C - E_D^b + kT\,\ln\left(\frac{N_D/N_A - 1}{\hat{g}_D}\right) . \tag{7.48}$$

The corresponding carrier density at low temperatures is

$$n = \frac{N_C}{\hat{g}_D} \exp\left(-\frac{E_D^b}{kT}\right)\left(\frac{N_D}{N_A} - 1\right) . \tag{7.49}$$

For higher temperatures (7.34) holds approximately for $n > N_A$; the slope is now given by $E_D^b/2$ as in the uncompensated case (Fig. 7.17b). For sufficiently high temperatures in the exhaustion regime (but still $n_i < n$) the electron density is given by

$$n \cong N_D - N_A . \tag{7.50}$$

At even higher temperatures the electron density will be determined by the intrinsic carrier concentration. Only in this case $p \neq 0$!

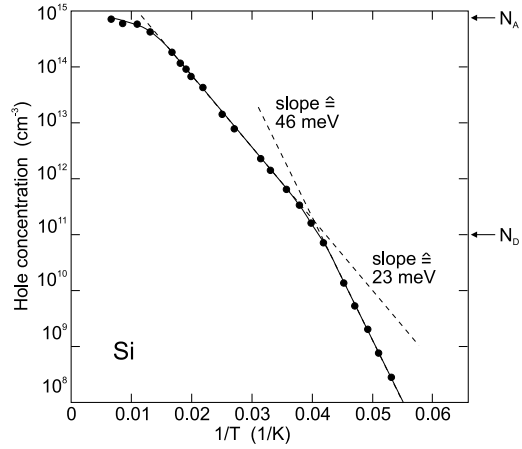

Fig. 7.18 Hole density in p-type silicon ($N_A = 7.4 \times 10^{14}\,\mathrm{cm}^{-3}$, $E_A^b = 46\,\mathrm{meV}$ (probably boron) and partial compensation with $N_D = 1.0 \times 10^{11}\,\mathrm{cm}^{-3}$). Adapted from [609]

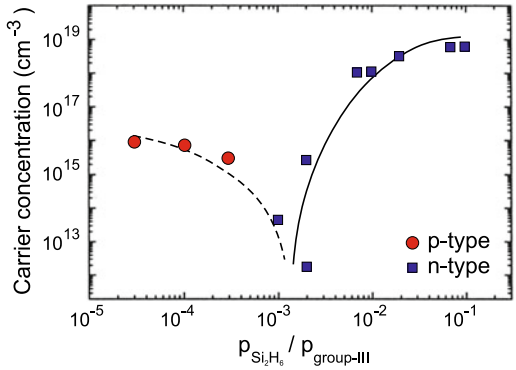

Fig. 7.19 Carrier concentration and conductivity type (*red circles*: p, *blue squares*: n) for MOVPE-grown $In_xGa_{1-x}As_{1-y}N_y$ layers on GaAs (001) (layer thickness $\approx 1\,\mu\mathrm{m}$, $x \approx 5\%$, $y \approx 1.6\%$) doped with different amounts of silicon. The ordinate is the ratio of the partial pressures of disilane and the group-III precursors (TMIn and TMGa) in the gas phase entering the MOVPE reactor. *Lines* are guides to the eye. Experimental data from [610]

An experimental example is shown in Fig. 7.18 for partially compensated p-Si (with $N_D \ll N_A$). The change of slope around $p \approx N_D$ is obvious.

If donors are added to a p-type semiconductor, first the semiconductor remains p-conducting as long as $N_D \ll N_A$. If the donor concentration becomes larger than the acceptor concentration, the conductivity type switches from p- to n-conduction. If the impurities are exhausted at room temperature, the lowest carrier concentration is reached for $N_D = N_A$. Such a scenario is shown for p-type $In_xGa_{1-x}As_{1-y}N_y$ doped with various concentrations of Si in Fig. 7.19. At high Si incorporation, the number of charge carriers saturates due to autocompensation (see Sect. 7.5.5) and the formation of Si precipitates. Since the ionization energies of donors and acceptors are typically different, the situation for $N_D \approx N_A$ needs, in general, to be investigated carefully and will depend on the temperature.

7.5.4 Multiple Impurities

If more than one donor species is present, (7.42) can be generalized, e.g. for the case of two donors D1 and D2 in the presence of compensating acceptors,

$$n + N_A - \frac{N_{D1}}{1 + \hat{g}_1 \exp(\frac{E_F - E_{D1}}{kT})} - \frac{N_{D2}}{1 + \hat{g}_2 \exp(\frac{E_F - E_{D2}}{kT})} = 0 \,. \tag{7.51}$$

This case is treated in [611]. Simple high and low temperature approximations can be found where the trap with the larger and smaller activation energy, respectively, dominates. The case for multiple acceptors (and compensating donors) is treated analogously. As detailed in [612], the function $\mathrm{d}n/\mathrm{d}E_F$ has a maximum at the donor level position; this can be used to visualize the contribution of several donors (with sufficiently different binding energies) from $n(T)$ as measured by Hall effect (Fig. 7.20).

7.5.5 Amphoteric Impurities

If an impurity atom can act as a donor and acceptor it is called amphoteric. This can occur if the impurity has several levels in the band gap (such as Au in Ge or Si). In this case, the nature of the impurity depends on the position of the Fermi level. Another possibility is the incorporation on different lattice sites. For example, carbon in GaAs is a donor if incorporated on the Ga-site. On the As-site carbon acts as an acceptor.

Thus, e.g., crystal growth kinetics can determine the conductivity type. In Fig. 7.21 the conductivity due to carbon background is shown for GaAs grown using MOVPE under various growth conditions. At high (low) arsine partial pressure incorporation of carbon on As-sites is less (more) probable, thus the conductivity is n-type (p-type). Also, growth on different surfaces can evoke different impurity incorporation, e.g., n-type on (001) GaAs and p-type on (311)A GaAs, since the latter is Ga-stabilized.

The charge density at an impurity nucleus can be investigated via the isomer shift as determined by Mössbauer spectroscopy [614, 615]. The incorporation of the isotope ^{119}Sn can be controlled in III-V compounds to be on cation or anion site as donor or acceptor, respectively. This is accomplished by introducing ^{119}In or ^{119}Sb on group-III and group-V site, respectively, both decaying into ^{119}Sn

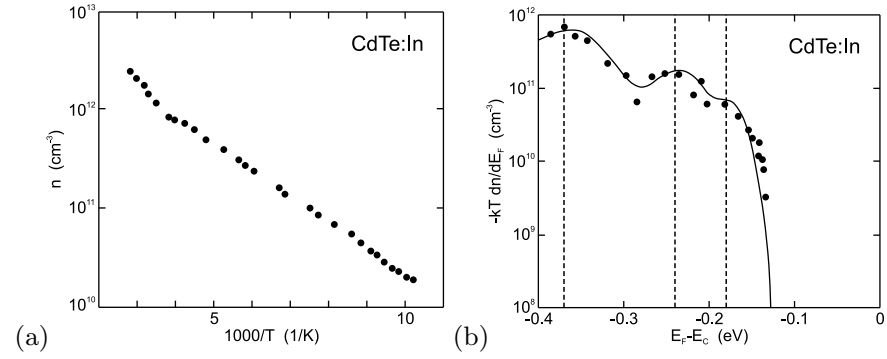

Fig. 7.20 **a** Electron concentration versus temperature as determined from Hall effect for a CdTe sample doped with indium. **b** $-kT\,\mathrm{d}n/\mathrm{d}E_F$, as determined from the experimental Hall data (*symbols*). The *solid line* is theory for three donor levels ($E_{D1} = E_C - 0.37\,\mathrm{eV}$, $N_{D1} = 2.5\times10^{12}\,\mathrm{cm}^{-3}$; $E_{D2} = E_C - 0.24\,\mathrm{eV}$, $N_{D2} = 7.0\times10^{11}\,\mathrm{cm}^{-3}$; $E_{D3} = E_C - 0.18\,\mathrm{eV}$, $N_{D3} = 2.5\times10^{11}\,\mathrm{cm}^{-3}$) whose energy positions are indicated by *dashed lines*. Adapted from [612]

without leaving their lattice site. The isomer shifts of ^{119}Sn in various III-V compounds are shown in Fig. 7.22. In [615] it is concluded from these data that the tin donor is formed by a positive tin ion and the electron charge transfer to its neighboring (group-V) atoms is rather small. For tin as an acceptor, for the present conditions an ionized, i.e. negatively charged acceptor, the isomer shift follows closely the trend from substitution in group-IV semiconductors. Therefore four electrons form the tetrahedral bond, while the extra electron is located rather at the (positively charged) group-III next neighbors and not in the impurity cell. The difference to the point charge Coulomb distribution is called central-cell correction.

Deviation from the ideal stoichiometry introduces point defects that can be electrically active and change conductivity type and carrier concentration. In the case of $CuInSe_2$, excess Cu could go on interstitial positions or promote selenium vacancies, both leading to n-type behavior. This material is particularly sensitive to deviations from ideal stoichiometry for both Cu/In ratio (Fig. 7.23) and Se deficiency [616].

7.5.6 *Autodoping*

If intrinsic defects such as vacancies or interstitials, possibly as a result of non-stoichiometry, or anti-site defects cause electronic levels relevant for conductivity one speaks of autodoping. An example is the role of A-B antisites in AB_2O_4 spinels (Sect. 3.4.7). In the perfect crystal the A (B) atoms occupy tetraeder (octaeder) places. Typical charges are A^{2+} and B^{3+}. Thus (without charge transfer) the A

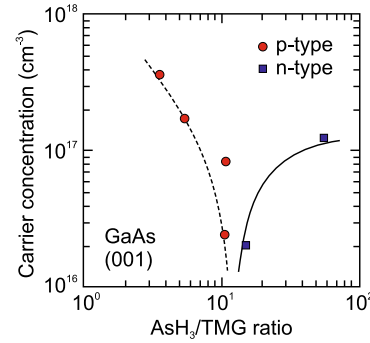

Fig. 7.21 Background doping of GaAs due to carbon in MOVPE for different ratios of the partial pressures of AsH_3 and TMG (trimethylgallium). The conductivity type (*blue squares*: n-type, *red circles*: p-type) depends on the incorporation of C from CH_3 radicals on Ga- or As-site. *Lines* are guides to the eye. Experimental data from [613]

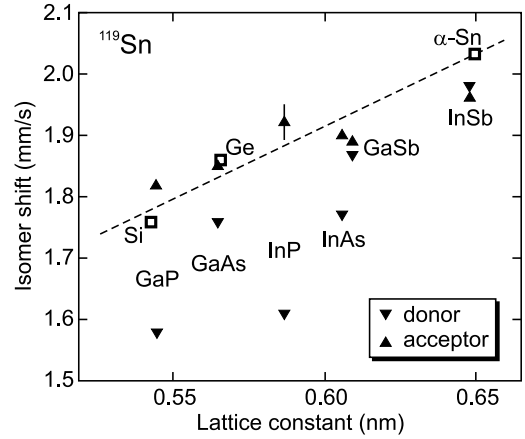

Fig. 7.22 Isomer shift (relative to $CaSnO_3$) of ^{119}Sn in various group-IV and III-V compound semiconductors as labeled. *Dashed line* is trend from isoelectronic substitution. Experimental data from [615]

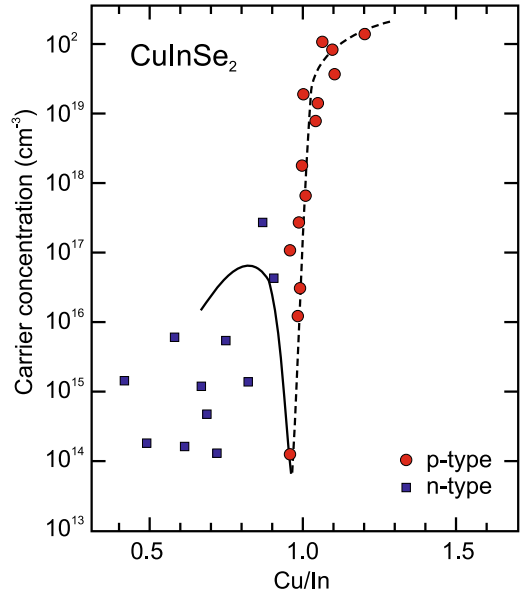

Fig. 7.23 Carrier concentration and conductivity type (*blue squares*: n-type, *red circles*: p-type) as a function of stoichiometry for $CuInSe_2$ thin films. *Lines* are guides to the eye. Experimental data from [616]

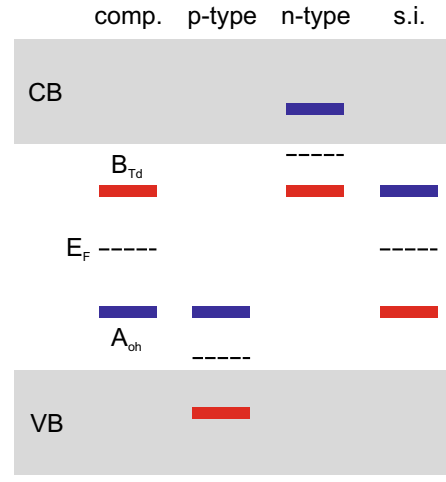

Fig. 7.24 Schematic position of electronic levels of A_B (*blue*, 0/− transition level) and B_A (*red*, +/0 transition level) defects in AB_2O_4 spinels and resulting material properties (compensated, n- or p-type or semi-insulating). After [617]

atom on octaeder site (A_{Oh}) acts like a donor and the B atom on a tetraeder site (B_{Td}) as an acceptor. Such defects have been classified in [617] as being able to create compensated, semi-insulating, n-type or p-type material depending on the defect formation energies and the position of the electronic levels of the A_B and B_A defects in the band gap (Fig. 7.24). An example for a p-type spinel oxide is $ZnCo_2O_4$ [618].

7.5.7 High Doping

For low doping concentrations, the impurity atoms can be considered to be decoupled. At low temperature, only hopping from one impurity to the next is possible due to thermal emission or tunneling and the semiconductor becomes an insulator.

With increasing concentration, the distance between impurities decreases and their wavefunctions can overlap. Then, an impurity band develops (Fig. 7.25). A periodic arrangement of impurity atoms would result in well-defined band edges as found in the Kronig-Penney model. Since the impurity atoms are randomly distributed, the band edges exhibit tails. For high doping, the impurity band overlaps with the conduction band. In the case of compensation, the impurity band is not completely filled and contains (a new type of) holes. In this case, conduction can take place within the impurity band even at low temperature, making the semiconductor a metal. This metal–insulator transition has been discussed by Mott [619]. Examples for highly doped semiconductors are transparent conductive oxides (Sect. 20), the contact layer for an ohmic contact (Sect. 21.2.6) or the active layers in a tunneling diode (Sect. 21.5.9). The physics, properties and preparation of highly doped semiconductors are treated in detail in [620].

The formation of the impurity band leads to a reduction of the impurity ionization energy as known from (7.21). Typical results are shown in Fig. 7.26a for n-type Ge [594] and Fig. 7.26b for p-type ZnTe [621]. At the critical doping concentration of $N_c = 1.5 \times 10^{17}$, the activation energy for the carrier concentration disappears. Similar effects have been observed for Si [622] and GaAs [623]. The freeze-out of the carrier concentration (see Fig. 7.9) disappears as shown in Fig. 7.27. Critical doping concentrations are listed in Table 7.6. The decrease of the ionization energy E^b (donor or acceptor) follows the dependence [594, 622]

$$E^b = E_0^b - \alpha\, N_i^{1/3} = E_0^b \left[1 - \left(\frac{N_i}{N_c}\right)^{1/3}\right] , \tag{7.52}$$

where N_i is the concentration of ionized dopants. A refined theory, considering screening, shift and tails of the conduction band and most importantly broadening of the donor level has been presented in [624].

The critical density can be estimated from the Mott criterion when the distance of the impurities becomes comparable to their Bohr radius (7.22)

$$2a_D = \frac{3}{2\pi}\, N_c^{1/3} . \tag{7.53}$$

The pre-factor $3/(2\pi)$ stems from the random distribution of impurities and disappears for a periodic arrangement. The Mott criterion is (rewriting (7.53))

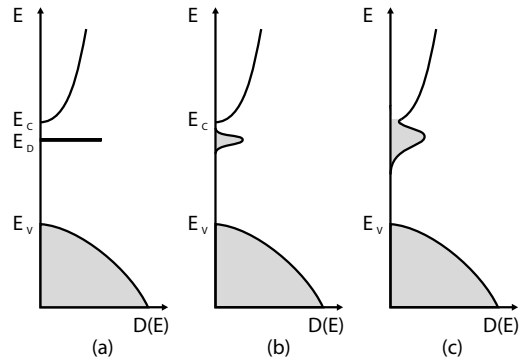

Fig. 7.25 Principle of the formation of a (donor) impurity band. **a** Small doping concentration and sharply defined impurity state at E_D, **b** increasing doping and development of an impurity band that **c** widens further and eventually overlaps with the conduction band for high impurity concentration. The *shaded areas* indicate populated states at $T = 0\,K$

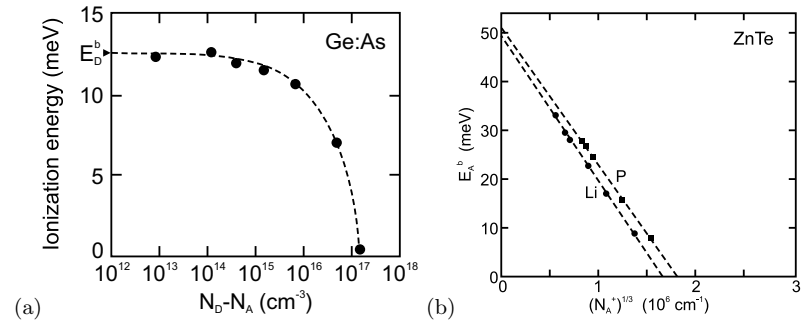

Fig. 7.26 **a** Donor ionization energy in n-type Ge for various doping concentrations. *Dashed line* is a guide to the eye. The arrow labeled E_D^b denotes the low-concentration limit (cf. Table 7.2). Experimental data from [594]. **b** Acceptor ionization energy for ZnTe:Li and ZnTe:P as a function of the third root of the ionized acceptor concentration. Data from [621]

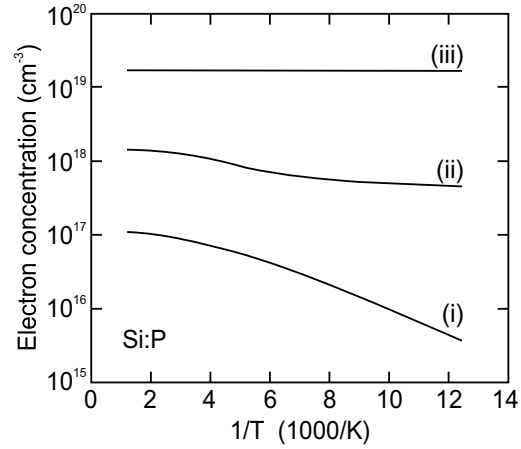

Fig. 7.27 Electron concentration versus inverse temperature for Si:P for three different doping concentrations ((i): $1.2 \times 10^{17}\,\mathrm{cm}^{-3}$, (ii): $1.25 \times 10^{18}\,\mathrm{cm}^{-3}$, (iii): $1.8 \times 10^{19}\,\mathrm{cm}^{-3}$). Experimental data from [622]

$$a_D\, N_c^{1/3} \approx 0.24\ . \tag{7.54}$$

For GaAs with $a_D = 10.3\,\mathrm{nm}$, the criterion yields $N_c = 1.2 \times 10^{16}\,\mathrm{cm}^{-3}$, in agreement with experiment.

The achievable maximum concentration of electrically active dopants is limited by the concentration dependence of the diffusion coefficient, Coulomb repulsion, autocompensation and the solubility limit [575]. In Table 7.7 the maximum carrier concentrations for GaAs with various dopants are listed.

As an example we show the Ga-doping of epitaxial ZnO layers on sapphire in Fig. 7.28. Under slightly Zn-rich (O-polar) conditions the growth mode is two-dimensional and the carrier concentration increases linearly with the Ga concentration, $n \approx c_{Ga}$, up to high values in the $10^{20}\,\mathrm{cm}^{-3}$ range [630]. For O-rich (Zn-polar) conditions the growth mode changes to three-dimensional growth and the activation ratio of Ga donors becomes low [631]. Above a gallium content of 2%, the octahedral coordination of gallium and thus the partial segregation into a parasitic $ZnGa_2O_4$ spinel phase is observed for [Ga] = 4% [632].

The doping of semiconductors beyond the solubility limit is termed 'hyperdoping'. It involves non-equilibrium preparation methods [637, 638].

Table 7.6 Critical doping concentration for various semiconductors (at room temperature)

Material	Type	N_c (cm^{-3})	References
C:B	p	2×10^{20}	[597]
Ge:As	n	1.5×10^{17}	[594]
Si:P	n	1.3×10^{18}	[622]
Si:B	p	6.2×10^{18}	[622]
GaAs	n	1.0×10^{16}	[623]
GaP:Si	n	6×10^{19}	[625]
GaP:Zn	p	2×10^{19}	[626]
GaN:Si	n	2×10^{18}	[627]
GaN:Mg	p	4×10^{20}	[598]
$Al_{0.23}Ga_{0.77}N$:Si	n	3.5×10^{18}	[628]
ZnTe:Li	p	4×10^{18}	[621]
ZnTe:P	p	6×10^{18}	[621]
ZnO:Al	n	8×10^{18}	[629]

Table 7.7 Maximum electrically active doping concentration for GaAs

Material	Type	N_c (cm^{-3})	References
GaAs:Te	n	2.6×10^{19}	[633]
GaAs:Si	n	1.8×10^{19}	[634]
GaAs:C	p	1.5×10^{21}	[635]
GaAs:Be	p	2×10^{20}	[636]

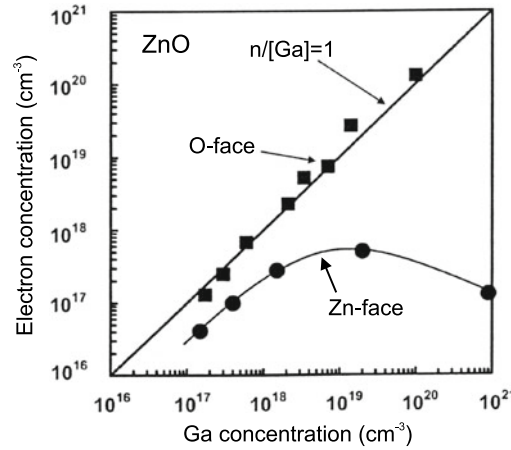

Fig. 7.28 Electron concentration as a function of gallium concentration in MBE grown ZnO:Ga on sapphire for the two different polarities. Adapted from [630, 631]

7.6 Quasi-fermi Levels

The carrier concentrations were given by (7.6) and (7.7). So far, we have only considered semiconductors in thermodynamic equilibrium for which $np = n_i^2$. In a nonequilibrium situation, e.g. for external excitation or carrier injection in a diode, the electron and hole densities can each take arbitrary values, in principle. In particular, np will no longer be equal to n_i^2 and there is no Fermi level constant throughout the structure. In this case, however, quasi-Fermi levels F_n and F_p for electrons and holes, respectively, are defined via

$$n(\mathbf{r}) = N_{\mathrm{C}}\, F_{1/2}\left(\frac{F_{\mathrm{n}}(\mathbf{r}) - E_{\mathrm{C}}}{kT}\right) \tag{7.55a}$$

$$p(\mathbf{r}) = N_{\mathrm{V}}\, F_{1/2}\left(-\frac{F_{\mathrm{p}}(\mathbf{r}) - E_{\mathrm{V}}}{kT}\right) . \tag{7.55b}$$

A quasi-Fermi level is sometimes called imref[5] and can also be denoted as $E_{\mathrm{F_n}}$ or $E_{\mathrm{F_p}}$. We emphasize that the quasi-Fermi levels are *only* a means to describe the local carrier density in a logarithmical way. The quasi-Fermi levels can be obtained from the density via

$$F_{\mathrm{n}} = E_{\mathrm{C}} + kT\, \ln\left(\frac{n}{N_{\mathrm{C}}}\right) \tag{7.56a}$$

$$F_{\mathrm{p}} = E_{\mathrm{V}} - kT\, \ln\left(\frac{p}{N_{\mathrm{V}}}\right) . \tag{7.56b}$$

The quasi-Fermi levels do not imply that the carrier distribution is actually a Fermi distribution. This is generally no longer the case in thermodynamical nonequilibrium. However, in 'well-behaved' cases the carrier distribution in nonequilibrium can be approximated locally as a Fermi distribution using a local quasi-Fermi level and a local temperature, i.e.

$$f_{\mathrm{e}}(\mathbf{r}, E) \cong \frac{1}{\exp\left(\frac{E - F_{\mathrm{n}}(\mathbf{r})}{kT(\mathbf{r})}\right) + 1} . \tag{7.57}$$

Using the quasi-Fermi levels, np is given by

$$n(\mathbf{r})\, p(\mathbf{r}) = n_{\mathrm{i}}^2\, \exp\left(\frac{F_{\mathrm{n}}(\mathbf{r}) - F_{\mathrm{p}}(\mathbf{r})}{kT}\right) . \tag{7.58}$$

We note that for an inhomogeneous semiconductor or a heterostructure (cf. Chap. 12), n_{i} may also depend on the spatial position. In the case of thermodynamic equilibrium the difference of the quasi-Fermi levels is zero, i.e. $F_{\mathrm{n}} - F_{\mathrm{p}} = 0$ and $F_{\mathrm{n}} = F_{\mathrm{p}} = E_{\mathrm{F}}$.

7.7 Deep Levels

For deep levels the short-range part of the potential determines the energy level. The long-range Coulomb part will only lead to a correction. The term 'deep level' implies that the level is within the band gap and far from the band edges. However, some deep levels (in the sense of the potential being determined by the ion core) have energy levels close to the band edges or even within a band. Details can be found in [267, 639–642].

The wavefunction is strongly localized. Thus, it cannot be composed of Bloch functions, as has been done for the shallow levels for the effective-mass impurity. The localization in **r** space leads to a delocalization in **k** space. Examples are Si:S, Si:Cu or InP:Fe, GaP:N, ZnTe:O. Deep levels can also be due to intrinsic defects such as vacancies or antisite defects.

Due to the larger distance to the band edges, deep levels are not efficient at providing free electrons or holes. Quite the opposite, they rather capture free carriers and thus lead to a reduction of conductivity.

[5] W. Shockley had asked E. Fermi for permission to use his name reversed. Fermi was not too enthusiastic but granted permission.

Centers that can capture electrons *and* holes lead to nonradiative recombination of electrons through the deep level into the valence band (see also Chap. 10). This can be useful for the fabrication of semi-insulating layers with low carrier concentration and fast time response of, e.g., switches and photodetectors.

While the electronic properties of deep levels can be readily characterized, the microscopic origin is not immediately apparent. Next to theoretical modeling of defects and correlation with experimental results, paramagnetic hyperfine interactions have proven useful to identify the microscopic nature of various defects [643].

7.7.1 Charge States

The deep level can have different charge states depending on the occupancy with electrons. The energy position within the gap varies with the charge state due to the Coulomb interaction. Also, the lattice relaxation around the defect depends on the charge state and modifies the energy level.

The localized charge q_d at the defect is the integral over the change $\Delta\rho$ of the charge density compared to the perfect crystal over a sufficiently large volume V_∞ around the defect

$$q_\mathrm{d} = \int\limits_{V_\infty} \Delta\rho(\mathbf{r})\,\mathrm{d}^3\mathbf{r} = \frac{n\,e}{\epsilon_\mathrm{r}}\,. \tag{7.59}$$

In semiconductors, the charge $q_\mathrm{d}\epsilon_\mathrm{r}$ is an integer multiple of the elementary charge. The defect is said to be in the nth charge state. Each charge state has a certain stable atomic configuration $\mathbf{R}_n$. Each charge state has a ground state and excited states that can each have different stable atomic configurations.

Now, we discuss how the concentration of the various charge states depends on the position of the Fermi level. The overall constraint of global charge neutrality determines the chemical potential of the electron, i.e. the Fermi level in Fermi–Dirac statistics. We use the approximation that the concentration of defects is so small that the mutual interaction of defects becomes negligible.

As an example, we treat the possible reaction $V^0 \rightleftharpoons V^+ + e^-$, where V^0 denotes a neutral vacancy and V^+ is a positively charged vacancy, created by the ionization of an electron from the vacancy into the conduction band. The free energy G depends on the numbers n_0 of neutral and n_+ of positively charged vacancies. The minimum condition is met by

$$\mathrm{d}G = \frac{\partial G}{\partial n_0}\,\mathrm{d}n_0 + \frac{\partial G}{\partial n_+}\,\mathrm{d}n_+ = 0\,. \tag{7.60}$$

The neutrality constraint is $\mathrm{d}n_0 + \mathrm{d}n_+ = 0$ and therefore the minimum condition reads

$$\frac{\partial G}{\partial n_0} = \frac{\partial G}{\partial n_+}\,. \tag{7.61}$$

For noninteracting defects and using (4.9) we write

$$\frac{\partial G}{\partial n_0} = G^\mathrm{f}(V^0) + kT\,\ln\left(\frac{n_0}{N_0}\right) \tag{7.62a}$$

$$\frac{\partial G}{\partial n_+} = \frac{\partial G(V^+)}{\partial n_+} + \frac{\partial G(e^-)}{\partial n_+} = G^\mathrm{f}_{V^+} + kT\,\ln\left(\frac{n_+}{N_+}\right) + \mu_{\mathrm{e}^-}\,, \tag{7.62b}$$

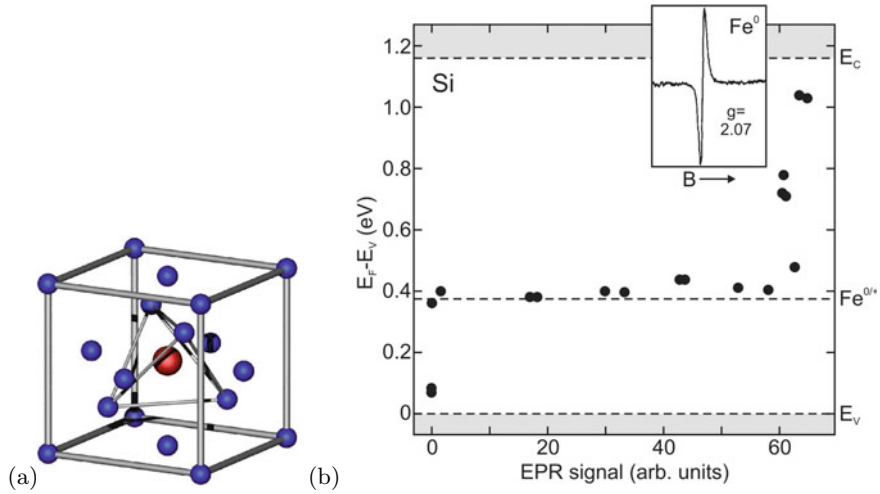

Fig. 7.29 **a** Silicon cubic unit cell with an interstitial iron atom (*red*) at tetrahedral site. **b** EPR intensity (at $T = 95\,\mathrm{K}$ from interstitial iron in neutral state, Fe^0 with $S = 1$) versus Fermi level position for iron-doped silicon with varying Fermi level due to different amounts of shallow impurity levels from to Al, B and P as labeled. The *shaded areas* indicate the valence and conduction band. The *dashed line* at $E_t = E_V + 0.375\,\mathrm{eV}$ indicates the trap level. The *inset* shows a typical EPR spectrum of Fe^0. Adapted from [649], *inset* adapted from [650]

where $N_0 = NZ_0$ and $N_+ = NZ_+$ are the number of available sites, given by the number N of atomic sites and including possible internal degeneracies Z_0 and Z_+, respectively. Degeneracy factors of deep levels are not a simple subject [601] and , e.g., the degeneracy factors of Au donor and acceptor levels in Si are under discussion [644–646]. G_f denotes the free enthalpy of formation of the respective defect, as in (4.3). We have written the free enthalpy of the separated pair V^+ and e^- as the sum $G(V^+) + G(e^-)$. $\mu_{e^-} = \partial G(e^-)/\partial n_+$ is (by definition) the chemical potential of the electron, i.e. the Fermi energy E_F of Fermi–Dirac statistics.[6] From (7.62a,b) we find for the ratio of the concentrations of defects $c_0 = n_0/N$ and $c_+ = n_+/N$

$$\frac{c_0}{c_+} = \frac{Z_+}{Z_0}\,\exp\left(-\frac{G^f_{V^+} - G^f_{V^0} + E_F}{kT}\right) = \frac{Z_+}{Z_0}\,\exp\left(\frac{E_t(V^0) - E_F}{kT}\right)\,, \tag{7.63}$$

where the trap level energy (for the particular charge transition), $E_t(V^0) = G^f_{V^0} - G^f_{V^+}$, is the free enthalpy of ionization of V^0. We note that c_0 can be obtained from (4.9) and E_F is determined by the charge-neutrality condition.

As example experimental data on the charge transition $Fe^0 \rightleftharpoons Fe^+ + e^-$ of interstitial iron (in tetrahedral position, Fig. 7.29a, cmp. Fig. 3.18) in silicon is shown. The concentration of Fe^0 is tracked via the EPR signal from the neutral $S = 1$ state[7] with g-factor $g = 2.07$ [647]. For n-type samples the iron is in neutral state and the maximum EPR signal is found. For strongly p-type samples, the Fermi energy is below the trap level and all iron is in Fe^+ state, yielding no EPR signal at the given g-factor. From the investigation of various silicon samples with different doping levels and consequently

[6]The chemical potential in a one-component system is $\mu = \partial G/\partial n = G/n$. In a multicomponent system it is, for the ith component, $\mu_i = \partial G/\partial n_i \neq G/n_i$.

[7]The electron configuration is $3d^8$ with two paramagnetic electrons. Under uniaxial stress along [100] the EPR line splits into a doublet [647]. Further details can be found in [648].

Table 7.8 Binding energies (to conduction band) of double donor chalcogenide impurities in Si and Ge. All energies in meV, data from [651, 652]

Host	State	S	Se	Te
Si	D^0	318	307	199
	D^+	612	589	411
Ge	D^0	280	268	93
	D^+	590	512	330

different position of the Fermi level, the trap (deep donor) energy is found to be $E_V + 0.375\,\text{eV}$ as indicated in Fig. 7.29b.

7.7.2 Double Donors

An impurity that has two extra electrons available after bonding in the matrix may give rise to a double donor. Typical examples are substitutional chalcogenide atoms (S, Se or Te) in silicon [651] and germanium [652], interstitial impurities such as Mg_i in Si [653], or group-V atoms on a group-III site in a III–V compound (antisite defect), such as P_{Ga} in GaP [654] or As_{Ga} in GaAs [655].

The double donor is electronically similar to a helium atom. Due to the repulsive Coulomb interaction of the two electrons on the neutral double donor, the (single) ionization energy E_1 (also often labeled $E(0, 1)$ or $E(0, +)$) of D^0 is smaller than that of D^+ (E_2, also labeled $E(1, 2)$ or $E(+, ++)$). For He and He^+ the ratio of ionization energies is 0.45; for chalcogenides in Si and Ge similar ratios have mostly been found (Table 7.8).

The carrier statistics and the degeneracy factors for a double donor have been discussed in [585, 656]. Typically, the degeneracy factor for the ionization of the double donor $D^0 \rightarrow D^+$ is $\hat{g}_D = g_2/g_1 = 1/2$ and for the ionization $D^+ \rightarrow D^{++}$ is $\hat{g}_D = g_1/g_0 = 2/1 = 2$.

For the probabilities to find a neutral, single and double ionized donor we find following the treatment in [656]

$$d^0 = \frac{N_D^0}{N_D} = \frac{\exp\frac{2E_F}{kT}}{\exp\frac{E_1+E_2}{kT} + \exp\frac{2E_F}{kT} + 2\exp\frac{E_1+E_F}{kT}} \tag{7.64a}$$

$$d^+ = \frac{N_D^+}{N_D} = \frac{\exp\frac{E_1+E_2}{kT}}{\exp\frac{E_1+E_2}{kT} + \exp\frac{2E_F}{kT} + 2\exp\frac{E_1+E_F}{kT}} \tag{7.64b}$$

$$d^{++} = \frac{N_D^{++}}{N_D} = \frac{2\exp\frac{E_1+E_F}{kT}}{\exp\frac{E_1+E_2}{kT} + \exp\frac{2E_F}{kT} + 2\exp\frac{E_1+E_F}{kT}} \tag{7.64c}$$

The probabilities are depicted in Fig. 7.30a. The maximum of d^+ is at the energy $(E_1 + E_2)/2$. Its value is

$$d^+\left(\frac{E_1+E_2}{2}\right) = \frac{1}{1+\exp\left(-\frac{E_1-E_2}{2kT}\right)} \tag{7.65}$$

and reaches a value close to one for $(E_1 - E_2)/kT \gg 1$. In Fig. 7.30b the number of electrons per donor $\tilde{n} = (N_D^+ + 2\,N_D^{++})/N_D$ is shown as a function of the Fermi level; at $(E_1 + E_2)/2$, exactly $\tilde{n} = 1$. In Fig. 7.31 the temperature dependent electron concentration in Si:Te is depicted. Up to 570 K the single ionization is visible (other shallow impurities present in the sample in lower concentrations $< 10^{14}\,\text{cm}^{-3}$

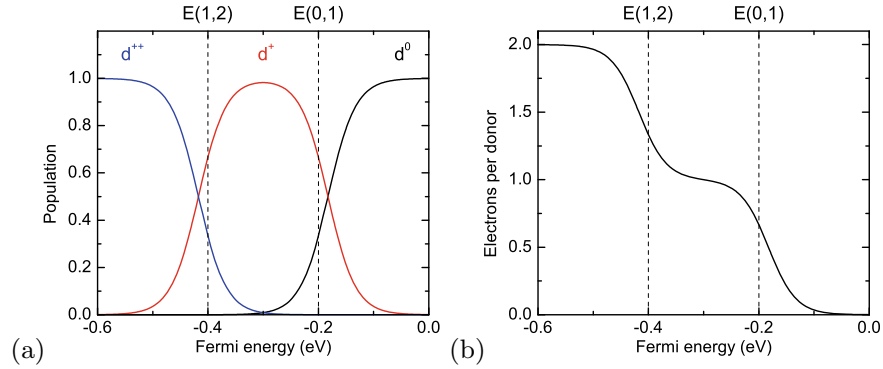

Fig. 7.30 **a** Population of states of a double donor (neutral: *black*, single ionized: *red*, double ionized: *blue*) according to (7.64a–c) as a function of the Fermi level. The ionization energies have been chosen as $E_1 = -0.2\,\mathrm{eV}$ and $E_2 = -0.4\,\mathrm{eV}$ and are indicated by *dashed lines* ($kT = 25\,\mathrm{meV}$); these energies are similar to Si:Te (cmp. Table 7.8). The conduction band edge is taken as zero energy. **b** depicts the according number of electrons $\tilde{n}$ ionized from the donor

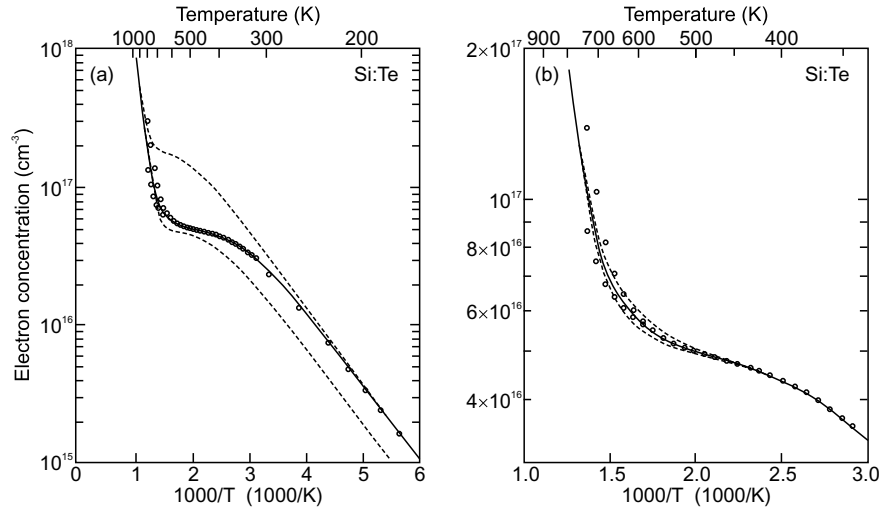

Fig. 7.31 Temperature dependent electron concentration (from Hall data) for Si:Te. **a** Experimental data and fit with double donor model using $N_{\mathrm{Te}} = 5 \times 10^{16}\,\mathrm{cm}^{-3}$, $E_1 = 200\,\mathrm{meV}$ and $E_2 = 440\,\mathrm{meV}$ (*solid line*). Single donor models would fail ($N_{\mathrm{Te}} = 5 \times 10^{16}\,\mathrm{cm}^{-3}$ and $N_{\mathrm{Te}} = 2 \times 10^{17}\,\mathrm{cm}^{-3}$, *dashed lines*). **b** Second ionization step in more detail with fits using different values for E_2; the *solid line* is for $E_2 = 440\,\mathrm{meV}$, the other *dashed lines* for $E_2 = 420$ and $460\,\mathrm{meV}$. Adapted from [657]

play no role). From the fit $E_1 = 200 \pm 2.7\,\mathrm{meV}$ is determined [657]. Single donor models would fail. The second ionization step is somewhat masked by the onset of intrinsic conduction. According to (7.15), the slope of n_i is $E_g/2 \approx 500\,\mathrm{meV}$ which is similar to $E_2 \approx 440\,\mathrm{meV}$.

7.7.3 Double Acceptors

In analogy to double donor defects, double acceptors can introduce up to two holes into the valence band. A typical example is Zn in silicon [658], exhibiting its 'normal' acceptor level ($\mathrm{Zn}^0/\mathrm{Zn}^-$) at $E_V + 0.31\,\mathrm{eV}$. In moderately n-doped silicon another level ($\mathrm{Zn}^-/\mathrm{Zn}^{2-}$) is observed at $E_C - 0.55\,\mathrm{eV}$,

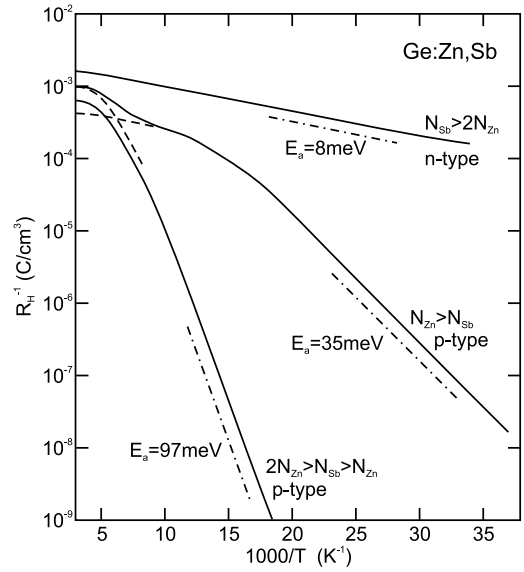

Fig. 7.32 Inverse (absolute) Hall coefficient (cmp. Sect. 15.2.1) R_H^{-1}, i.e. charge concentration, for three Ge:Zn samples with different degree of compensation with Sb donors as labeled. The *dash-dotted lines* indicate typical slopes. The *dashed lines* sketch the $Zn^0 \rightarrow Zn^-$ and the $Zn^- \rightarrow Zn^{--}$ processes. Adapted from [659]

when the n-doping is sufficient to partially compensate the Zn and supply one electron for each Zn atom but not two ($2N_{Zn} > N_D > N_{Zn}$). A similar situation has been observed for Zn in germanium, exhibiting the levels $E_V + 0.03\,eV$ and $E_V + 0.09\,eV$ [659]. In Fig. 7.32 three different Ge:Zn samples are compared. If the additional Sb donor concentration ($N_D \approx 3.4 \times 10^{16}\,cm^{-3}$) is larger than $2N_{Zn}$ ($N_{Zn} \approx 1.2 \times 10^{16}\,cm^{-3}$), the sample is n-type (upper curve). The slope is similar to the Ge:Sb donor binding energy (Table 7.2). If compensation with donors is weak ($N_{Zn} > N_D$, middle curve) first the shallow donor level with 0.03 eV activation energy is activated and subsequently the deeper one with 0.09 eV activation energy, creating p-conduction with a saturated hole density of $p \approx 2N_A - N_D > N_{Zn}$ (negative Hall coefficient). The two individual activation processes are sketched as dashed lines in Fig. 7.32. If the Sb concentration is larger than N_{Zn} but smaller than $2N_{Zn}$, the shallow acceptor level is filled with electrons, leaving still the only partially filled deeper acceptor level available for ionization (lower curve). In this case the sample is still p-type, but the saturation hole density is $p \approx 2N_A - N_D < N_{Zn}$. The degeneracy factors for Zn in Si and Ge have been discussed in [601].

7.7.4 Jahn–Teller Effect

The lattice relaxation can reduce the symmetry of the defect. Many defects, such as a vacancy, a tetrahedral interstitial or an impurity, occupy initially tetrahedral sites in the zincblende structure. The lattice relaxation reduces the symmetry, e.g. to tetragonal or trigonal, and therefore causes initially degenerate levels to split. Such splitting is called the static Jahn–Teller effect [639, 660]. The energy change in terms of the atomic displacement Q can be denoted (using perturbation theory for the simplest, nondegenerate case) as $-I\,Q$ ($I > 0$). Including the elastic contribution with a force constant C, the energy of a configuration Q is

$$E = -I\,Q + \frac{1}{2}\,C\,Q^2\,. \tag{7.66}$$

The stable configuration Q_{min}, for which the energy is minimal (E_{min}), is therefore given by

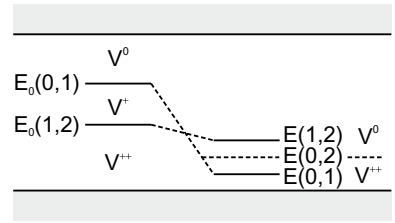

Fig. 7.33 Charge states of the vacancy in silicon. *Left*: level scheme without lattice relaxation, *right*: level scheme including the Jahn–Teller effect. For a Fermi level below (above) $E(0, 2)$ the charge state V^{++} (V^0) is dominant

$$Q_{\min} = \frac{I}{C} \tag{7.67a}$$

$$E_{\min} = -\frac{I^2}{2C} \,. \tag{7.67b}$$

Several equivalent lattice relaxations may exist, e.g. a 3-fold minimum for remaining C_{3v} symmetry. The energy barrier between them has a finite height. Therefore, e.g. at sufficient temperature, the defect can switch between different configurations and eventually again becomes isotropic (dynamic Jahn–Teller effect). The experimental observation depends on the relation between the characteristic time of the experiment and the reorientation time constant of the defect.

7.7.5 *Negative-U Center*

We explain the principle of a so-called negative-U center [661] for the Si vacancy [662] (cf. Fig. 4.2). It was first proposed by Anderson to explain the properties of amorphous chalcogenide glasses [663]. Many defects in semiconductors exhibit negative-U behavior, e.g. also the boron interstitial in Si [662, 664]. Coulomb energy and the Jahn–Teller effect compete for the position of the occupancy level for different charge states. U refers to the additional energy upon charging of the defect with an additional electron. The Coulomb repulsion of electrons leads to an *increase* of the energy, i.e. positive U, which has been calculated to be 0.25 eV for the Si vacancy [665] for all charge states. The occupation level (cf. Sect. 4.2.2) $E_0(1, 2)$ (the index 0 indicates effects only due to many-electron Coulomb interaction), separating the domination of V^{++} and V^+ (Fig. 7.33) is 0.32 eV above the valance-band edge. Therefore, the occupation level $E_0(0, 1)$ is expected to lie at about 0.57 eV about E_V.

The Jahn–Teller effect may lead to a splitting of the otherwise 4-fold degenerate states of the vacancy. A detailed experimental study using hyperfine interactions can be found in [666]. The schematic level diagram for the Jahn–Teller splitting is shown in Fig. 7.34. The V^{++} state (A_1 is always populated

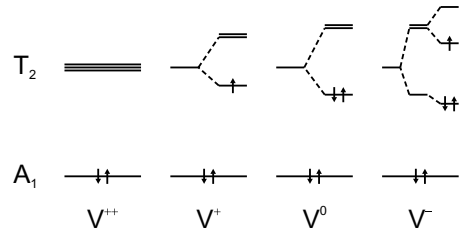

Fig. 7.34 Jahn–Teller splitting for different charge states of the vacancy. A_1 and T_2 refer to irreducible representations of the T_d point symmetry group. A_1 is nondegenerate and therefore does not exhibit a Jahn–Teller effect. T_2 is triply degenerate. The arrows represent electrons and their spin orientation

with two electrons) is resonant with the valence band. The T_2 state lies in the band gap. When the Jahn–Teller effect (now on the T_2 state) is included, the energies of the different charge states depend on the configuration coordinate (a mostly tetragonal distortion in the case of the Si vacancy).

$$E_{V^0} = E(0, Q) = E(0, Q = 0) - 2IQ + \frac{1}{2}CQ^2 \tag{7.68a}$$

$$E_{V^+} = E(1, Q) = E(1, Q = 0) - IQ + \frac{1}{2}CQ^2 \tag{7.68b}$$

$$E_{V^{++}} = E(2, Q) = E(2, Q = 0) + \frac{1}{2}CQ^2 \,. \tag{7.68c}$$

For the $n = 2$ state the T_2 gap state is empty and thus no degeneracy and Jahn–Teller term arises. For $n = 1$ there is a linear Jahn–Teller term. The occupation with two electrons (V^0) causes an approximately twice as large Jahn–Teller splitting for the $n = 0$ state. The force constant is assumed to be independent of the charge state. The energies for the minimum configurations $Q^n_{\min}$ are therefore

$$E(0, Q^0_{\min}) = E(0, Q = 0) - 4\,\frac{I^2}{2C} \tag{7.69a}$$

$$E(1, Q^1_{\min}) = E(1, Q = 0) - \frac{I^2}{2C} \tag{7.69b}$$

$$E(2, Q^2_{\min}) = E(2, Q = 0) \,. \tag{7.69c}$$

The Jahn–Teller energy $E_{\mathrm{JT}} = I^2/2C$ lowers the position of the occupancy levels E_0 calculated with Coulomb terms only. The occupancy levels *including* the Jahn–Teller contribution are therefore given as

$$E(1, 2) = E_0(1, 2) - E_{\mathrm{JT}} \tag{7.70a}$$

$$E(0, 1) = E_0(0, 1) - 3\,E_{\mathrm{JT}} \,. \tag{7.70b}$$

For the vacancy in silicon the Jahn–Teller energy E_{JT} is about 0.19 eV. Thus the $E(1, 2)$ level is lowered from 0.32 eV to 0.13 eV. The E(0,1) occupancy level, however, is reduced from 0.57 eV to 0.05 eV [662, 667] (see Fig. 7.33). The occupancy level $E(0, 2)$ is in the middle between $E(0, 1)$ and $E(1, 2)$ ($E(0, 2) = (E(0, 1) + E(1, 2))/2$) and indicated in Fig. 7.35a. At this energy, $c(V^0) = c(V^{++})$ and the value of $c(V^+)$ is small ($\approx \exp \frac{E_1 - E_2}{2kT}$) since $E(0, 1) < E(1, 2)$ (cmp. (7.65)).

The relative concentrations of the three charge states are determined by (7.63) (degeneracy and entropy terms have been neglected)

$$\frac{c(V^{++})}{c(V^+)} = \exp\left(\frac{E(1, 2) - E_{\mathrm{F}}}{kT}\right) \tag{7.71a}$$

$$\frac{c(V^+)}{c(V^0)} = \exp\left(\frac{E(0, 1) - E_{\mathrm{F}}}{kT}\right) \,. \tag{7.71b}$$

They are depicted in Fig. 7.35a in a plot related to Fig. 7.30a. Therefore, V^{++} dominates if $E_{\mathrm{F}} < E(0, 1)$ and V^0 dominates for $E_{\mathrm{F}} > E(1, 2)$. In the intermediate range $E(0, 1) < E_{\mathrm{F}} < E(1, 2)$ we know from (7.71a, b) that V^+ is dominated by V^0 and V^{++}. However, at this point it is not clear whether V^{++} or V^0 dominates overall. The ratio of the concentrations of V^{++} and V^0 is given by

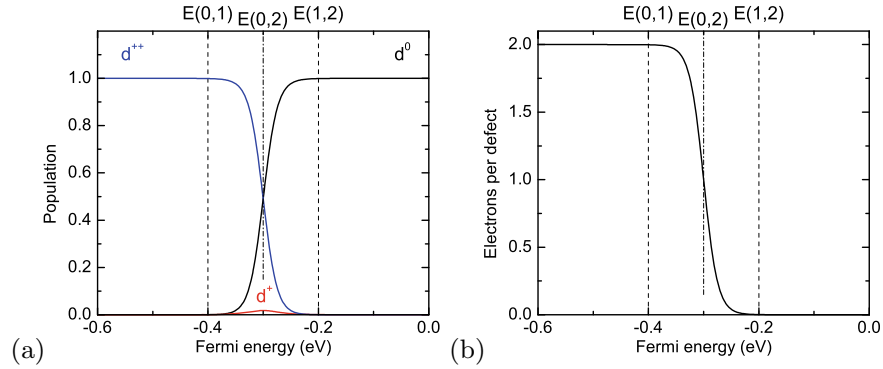

Fig. 7.35 **a** Population of states of a negative-U defect (neutral: *black*, single ionized: *red*, double ionized: *blue*) according to (7.64a–c) as a function of the Fermi level. The ionization energies have been chosen as $E_1 = -0.4\,\mathrm{eV}$ and $E_2 = -0.2\,\mathrm{eV}$ (cmp. Fig. 7.30) and are indicated by *dashed lines* ($kT = 25\,\mathrm{meV}$). The occupancy level $E(0, 2)$ is indicated with a *dash-dotted line*. The conduction band edge is taken as zero energy. **b** depicts the according number of electrons ionized from the defect

$$\frac{c(V^{++})}{c(V^0)} = \exp\left(\frac{E(1,2) + E(0,1) - 2E_\mathrm{F}}{kT}\right) = e^2 \exp\left(\frac{E(0,2) - E_\mathrm{F}}{kT}\right) . \tag{7.72}$$

The occupancy level $E(0, 2)$ is thus again given as

$$E(0,2) = \frac{E(0,1) + E(1,2)}{2} , \tag{7.73}$$

and is shown in Fig. 7.33. V^{++} dominates if $E_\mathrm{F} < E(0, 2)$ and V^0 dominates for $E_\mathrm{F} > E(0, 2)$. V^+ is, for no position of the Fermi level, the dominating charge state of the Si vacancy. We note that for n-doped Si the V^- and V^{--} can also be populated. The population of the V^0 state with an extra electron introduces another Jahn–Teller splitting (Fig. 7.34) that has trigonal symmetry.

Generally, the Jahn–Teller effect can make the addition of an electron cause an effectively negative charging energy; in this case the center is termed a negative-U center. We note that the single vacancy in germanium is not a negative-U center due to smaller Jahn–Teller distortion and smaller electron-lattice coupling [668].

7.7.6 DX Center

The DX center is a deep level that was first investigated for n-doped (e.g. Si-doped) $\mathrm{Al}_x\mathrm{Ga}_{1-x}\mathrm{As}$. It dominates the transport properties of the alloy for $x > 0.22$. For smaller Al concentrations and GaAs the DX level lies in the conduction band. DX-type deep levels have also been found for other alloys and dopants, e.g. GaAsP:S.

It is experimentally found that the capture process of electrons into the DX center is thermally activated. The capture energy E_c depends on the AlAs mole fraction (Fig. 7.36). The (average) barrier for electron capture has a minimum of 0.21 eV for $x \approx 0.35$, near the crossover point between direct and indirect band gap (cf. Fig. 6.24). For lower Al concentrations, the capture barrier increases to 0.4 eV for $x = 0.27$; for $x > 0.35$ the capture barrier increases to about 0.3 eV for x around 0.7 [669]. The barrier for thermally releasing carriers from the DX center has been determined to be about 0.43 eV, independent of the Al mole fraction [669].

Carriers can be removed from the DX center by optical absorption of photons with energy larger than about 1.2 eV. If carriers are removed by optical excitation at low temperatures the (re-)capture is so slow ($\sigma < 10^{-30}\,\mathrm{cm}^2$) that the carriers remain in the conduction band and cause persistent photoconductivity (PPC). The PPC is only reduced upon increasing the sample temperature. The concentration of the DX center is about the same as the net doping concentration.

The properties of the DX center are reviewed in [670, 671]. So far, no definite microscopic model of the DX center has been agreed on. Lang [672] proposed that the DX center involves a donor and an unknown defect (probably a vacancy). It probably involves large lattice relaxation as in the configuration coordinates model of Fig. 7.37 where the donor binding energy E_D^b with respect to the conduction-band minimum, the barrier for electron capture E_c, the barrier for electron emission E_e and the optical ionization energy E_o are labeled. The donor binding energy is measured with Hall effect (cf. Sect. 15.2.1) at temperatures sufficient to overcome the capture and emission barriers, the emission barrier is measured with deep level transient spectroscopy (DLTS). The capture barrier manifests itself in PPC experiments. We note that the DX center is related to the L-conduction band. For small Al mole fraction, the DX level is degenerate with the Γ-related conduction band (see Fig. 7.37b).

Theoretical models and experimental evidence hint at a vacancy-interstitial model for the Si-DX center [673]. The donor (Si) is displaced along the ⟨111⟩ direction from the Ga substitution site. The displacement is predicted to be 0.117 nm and the distorted geometry can be viewed as a Ga vacancy and a Si interstitial. The charge state of the (filled) DX center is proposed to be a two-electron negative-U state.

7.7.7 EL2 Defect

The EL2 defect is a deep donor in GaAs. It is not related to impurities but occurs for intrinsic material, in particular grown under As-rich conditions. It has physical properties similar to the DX center. The bleaching of absorption due to EL2, i.e. the optical removal of electrons from the defect at low temperatures, is shown in Fig. 7.38. The microscopic model [674] describes the EL2 defect as an arsenic antisite defect, i.e. an arsenic atom on a Ga site, $\mathrm{As_{Ga}}$. In the charged state the arsenic atom is displaced from the lattice position and a complex of a Ga vacancy (symmetry T_{3d}) and an interstitial As (symmetry C_{3v}) with 0.14 nm displacement along ⟨111⟩ forms ($\mathrm{V_{Ga}}$-$\mathrm{As_i}$). The charged state is filled with two electrons.

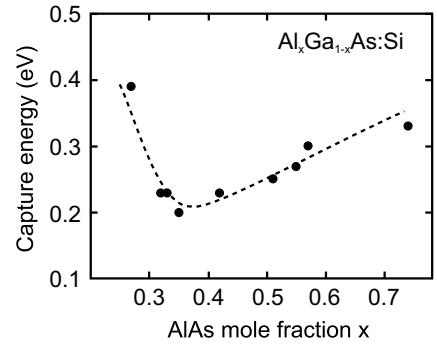

Fig. 7.36 Energy barrier for electron capture E_c at the Si-DX center in $\mathrm{Al}_x\mathrm{Ga}_{1-x}\mathrm{As}$ for various compositions. Experimental data from [669]

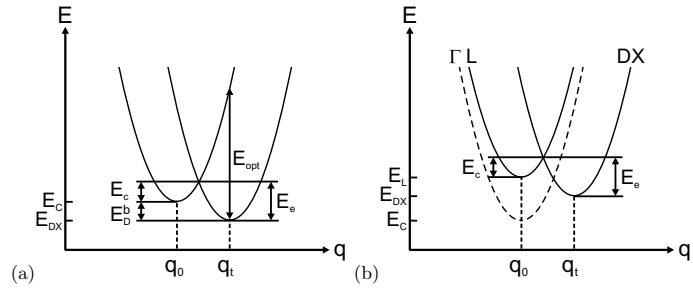

Fig. 7.37 **a** Schematic configuration coordinate diagram for the DX level with large lattice relaxation. q_0 is the configuration of the empty defect, q_t is the configuration of the filled defect. The donor binding energy E_D^b, the barrier for electron capture E_c, the barrier for electron emission E_e and the optical ionization energy E_o are labeled. E_C denotes the conduction-band edge. We note that in (Al,Ga)As the DX level is associated with the L conduction band (see Fig. 6.24). **b** Schematic configuration coordinate diagram for the DX level in $Al_{0.14}Ga_{0.86}As$ with the DX level being degenerate with the (Γ-related) conduction band

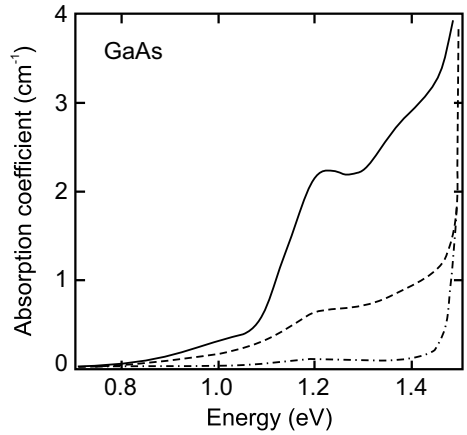

Fig. 7.38 Absorption spectrum of GaAs at low temperatures ($T = 10\,\mathrm{K}$) when cooled in the dark (*solid line*). The *dashed* (*dash-dotted*) *line* is the absorption after illuminating the sample for 1 min (10 min) with white light, leading to quenching of the EL2-related absorption. Adapted from [675]

7.7.8 Semi-insulating Semiconductors

Semiconductors with high resistivity (10^7–$10^9\,\Omega\,\mathrm{cm}$) are called semi-insulating ('s.i.' or 'si'). Semi-insulating substrates are needed for high-speed devices. The high resistivity should stem from a small free-carrier density at finite temperature and not from a small mobility due to poor crystal quality. For sufficiently wide band gap, the intrinsic carrier concentration is small and such pure material is semi-insulating, e.g. GaAs with $n_i = 1.47 \times 10^6\,\mathrm{cm}^{-3}$ and $5.05 \times 10^8\,\Omega\,\mathrm{cm}$ [676]. Since shallow impurities are hard to avoid, another route is used technologically. Impurities that form deep levels are incorporated in the semiconductor in order to compensate free carriers. For example, a deep acceptor compensates all electrons if $N_A > N_D$. Since the acceptor is deep ($E_A^b \gg kT$), it does not release holes for reasonable temperatures. Examples of suitable impurities for compensation of electrons are Si:Au [677], GaAs:Cr [678] and InP:Fe [679]. A deep donor, e.g. InP:Cr [680], is necessary to compensate p-type conductivity.

Figure 7.39a shows the terms of Fe in InP [681, 682]. An overview of transition metals in III–V semiconductors can be found in [683]. The electron configuration of neutral Fe atoms is $3d^6 4s^2$ (cf.

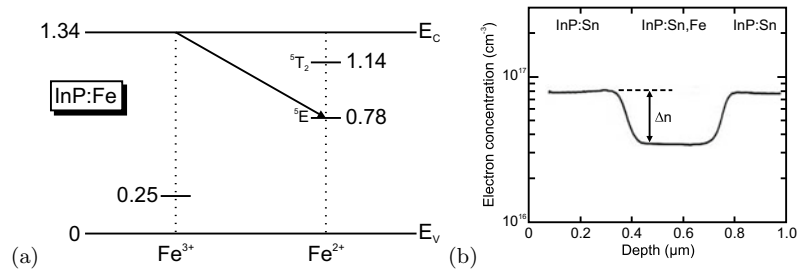

Fig. 7.39 **a** Schematic band diagram of InP with levels of Fe impurities in the 3+ and 2+ charge states at low temperature. All energies are given in eV. The *arrow* denotes capture of an electron (from the conduction band or a shallow donor) on the deep acceptor. Compare this figure also with Figs. 9.36 and 10.25. **b** Depth profile of electron concentration in an InP:Sn/InP:Sn,Fe/InP:Sn structure. The change $\Delta n \approx 4.5 \times 10^{16}\,\mathrm{cm}^{-3}$ of electron concentration is due to the compensation by Fe and corresponds to the chemical iron concentration determined by SIMS, $[\mathrm{Fe}] = 4.9 \times 10^{19}\,\mathrm{cm}^{-3}$. Part **b** adapted from [688]

Table 17.2). The Fe is incorporated on the In site and thus has a Fe^{3+} state as a neutral acceptor (A^0). The Fe^{3+} state has the electron configuration $3d^5$. The arrow in Fig. 7.39a represents the capture of an electron from the conduction band or from a shallow donor. The charge state of the Fe becomes Fe^{2+} (charged acceptor, A^-) with the electron configuration $3d^6$. The cubic crystal field (T_d symmetry) splits this ^{5}D Fe state[8] into two terms [684] that exhibit further fine structure [682]. The large thermal activation energy of 0.64 eV found in the Hall effect on semi-insulating InP:Fe [679] corresponds to the energy separation of the ^{5}E level and the conduction band.

The maximum electron concentration that can be compensated in this way is limited by the solubility of Fe in InP [685], about $1 \times 10^{17}\,\mathrm{cm}^3$. Higher Fe incorporation leads to the formation of Fe (or FeP) precipitates and degrades the crystal quality. Only a fraction of the incorporated Fe may then be electrically active and contribute to the compensation. The maximum electrically active Fe concentration is found to be $5\text{–}6 \times 10^{16}\,\mathrm{cm}^{-3}$ [686]. The compensation can be directly visualized via the depth profile of the electron concentration in a n-si-n structure (Fig. 7.39b). The poor thermal stability of Fe, i.e. high diffusion coefficient, has evoked proposals for more stable dopants such as InP:Ru [687].

7.7.9 Isoelectronic Impurities

Isoelectronic impurities, generally represent a deep level with a short range potential. The isoelectronic trap introduces a bound state for an electron or a hole. Once a carrier has been captured, the defect becomes charged. The other carrier type is then easily trapped, forming a bound exciton (Sect. 10.3.2). The theory of isoelectronic impurities is outlined in [689]. A detailed theoretical treatment of N in GaAs and GaP is given in [544].

In GaP:N, an electron is spatially localized on the N impurity. Most of the wave function is at the X-point. The nitrogen-bound electron level in GaP (A_1 symmetry) is close to the conduction band edge and within the band gap. Important for the energy position is the lattice relaxation, leading to an inward relaxation of the surrounding Ga atoms (Fig. 7.41). Due to the spatial localization of the wave function it is delocalized in k-space (Fig. 7.40a) and obtains a sizeable component at the Γ-point, facilitating zero-phonon absorption from the valence band. This effect is present only when the lattice relaxation around the impurity is considered; without relaxation the Γ-component is zero, with relaxation about 1% [544]. The Γ-component of the wave-function is larger for localization at an isoelectronic impurity

[8] The notation is ^{2S+1}J (multiplicity), with S being the total spin and J being the total angular momentum.

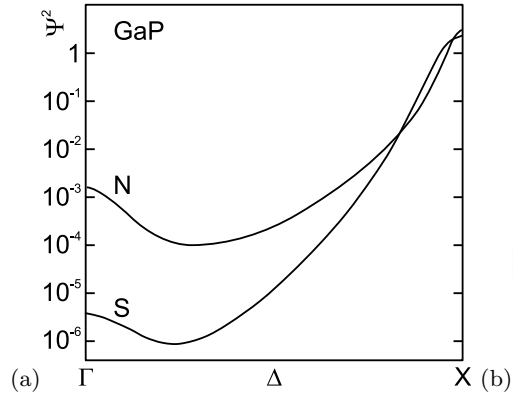

Fig. 7.40 **a** Model calculation of the wave-vector dependence of the probability density of an electron bound to a 10 meV deep isoelectronic trap (N) and to a 100 meV deep shallow donor (S) in GaP. Adapted from [690]. **b** Wavefunction (isosurface at 20% of maximum) of isolated nitrogen (N) and neighboring N–N pair (NN_1) in GaP. Adapted from [544]

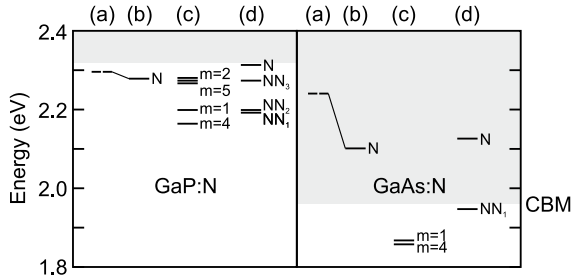

Fig. 7.41 Energy levels of nitrogen impurity states in GaP (*left*) and GaAs (*right*). The energy scale is relative to the bulk GaP valence band maximum, the conduction band minima (CBM) are thus shown relative to the vacuum level. The conduction band is shown in *grey*. For both materials, (a) denotes the isolated N impurity level calculated *without* lattice relaxation (*dashed line*), and (b) *with* lattice relaxation. (c) denotes the position of N–N pair levels, *m* denoting the neighbor. (d) shows selected experimental data. NN_1 denotes the direct neighbor NN-pair. The other NN_n follow the usual nomenclature as in [694]. Data taken from [544]

than at a shallow donor such as sulfur [690]. This way a large oscillator strength for optical transitions occurs (Sects. 9.7.9, 10.3.2). The wavefunction of an isolated single N impurity and a neighboring N–N pair (NN_1) in GaP are shown in Fig. 7.40b.

Isolated nitrogen impurities in (unstrained) GaAs introduce states only within the conduction band (Fig. 7.41). The reason is that the GaAs conduction band edge is further from the vacuum level than that of GaP (see Fig. 12.21). Only the NN_1 and NN_4 pair levels are theoretically expected to be within the GaAs band gap. The index denotes the *n*th neighbor position. The NN_1 level has been experimentally observed [691, 692]. The isolated nitrogen impurity level is forced into the GaAs band gap upon hydrostatic pressure [692, 693] (Fig. 7.42). Further levels deeper within the band gap are due to clusters containing more than two nitrogen atoms.

7.7.10 Surface States

The investigation of (semiconductor) surfaces is a large field with sophisticated methods that allow real-space imaging with atomic resolution by scanning probe microscopy and highly depth resolved electronic studies. The surface represents first of all a break in the periodic crystal potential and thus a defect of the bulk crystal. The unsatisfied bonds partly rearrange, e.g. by building dimers, forming a surface reconstruction or remain as dangling bonds. The surface exhibits a surface density of states.

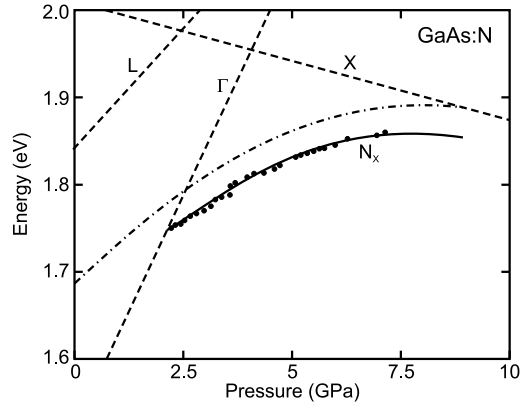

Fig. 7.42 Pressure dependence of the energy of excitons bound to isolated nitrogen impurities in GaAs (*circles*), measured from the top of the GaAs valence band. The *dashed lines* are the pressure dependent GaAs bulk band gaps (cmp. Fig. 6.49). The *solid* (*dash-dotted*) *line* is a theoretical model for the nitrogen-bound exciton (electron) level. Adapted from [693]

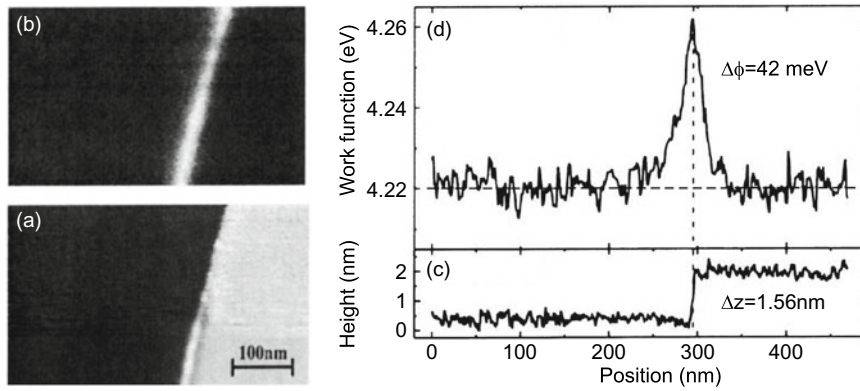

Fig. 7.43 Image of **a** topography ($\Delta z = 2.8\,\text{nm}$) and **b** work function ($\Delta\phi = 4.21$–$4.26\,\text{eV}$) of a surface step along [111] on a n-GaP(110) surface cleaved in UHV. Adapted from [696]. **c** and **d** show the corresponding linescans. Adapted from [696]

Such states can lie in the band gap and capture electrons, leading to recombination and a depletion layer. For a brief introduction on semiconductor surface physics see Chap. 11; for more details we refer to [695].

As an example of the formation of electronic states at surface defects we show in Fig. 7.43 the comparison of topography and work function (measured by Kelvin probe force microscopy [696]) at a surface step on a GaP(110) surface that has been prepared by cleaving in-situ in ultrahigh vacuum (UHV). The depletion-type band bending of the surface is about 0.4 eV. The further increase of the position of the vacuum level at the step edge shows the presence of trap states in the band gap causing the conduction band to bend upwards (cf. Sect. 21.2.1). Modeling of the effect shows that the charge density at the surface is $6 \times 10^{11}\,\text{cm}^{-2}$ and at the step edge $1.2 \times 10^{6}\,\text{cm}^{-1}$.

7.8 The Charge Neutrality Level

The charge neutrality level (CNL) of a semiconductor is defined as the maximum occupied surface state energy at a neutral surface. In this case it is identical with the Fermi level (which renders the surface without a net charge). The CNL is also termed Fermi level stabilization energy [700] or 'branch point energy' [697] and marks the energy at which the character of intrinsic defects changes from predominantly donor-like (below CNL) to predominantly acceptor-like (above CNL). If Fermi level in the bulk and CNL deviate, surface charges appear; when the Fermi level is above (below) the charge neutrality level, the surface is negatively (positively) charged. Whether this means a depletion or accumulation layer depends on the conductivity type of the semiconductor. Band bending and space charge regions are discussed in more detail further below (Sect. 12.3.4, Sect. 21.2.1). The position of the CNL can be calculated from the Brillouin zone average of the conduction-to-valence band difference [698, 699].

Experimentally, the Fermi level will be established at the CNL when a lot of deep defects are introduced, e.g. by irradiation. For many semiconductors, the CNL is close to the middle of the band gap (Si, GaAs). Notable exceptions are e.g. InAs or In_2O_3 with a CNL within the conduction band leading to n-type surface conduction.

7.9 Hydrogen in Semiconductors

The role of hydrogen in semiconductors was first recognized in studies of ZnO [701]. It is now clear that hydrogen plays an important role in the passivation of defects. As a 'small' atom, it can attach easily to dangling bonds and form an electron-pair bond. Thus, surfaces, grain boundaries, dislocations and shallow (donor and acceptor) and deep impurity levels become passivated. A good overview and many details of the physics and technological use of hydrogen in semiconductors can be found in [702, 703]. The hydrogen must be typically introduced as atomic species into semiconductors, e.g. from a plasma in the vicinity of the surface or by ion irradiation.

With regard to silicon it is important to note that the Si–H bond is stronger than the Si–Si bond. Thus a silicon surface under atomic hydrogen exhibits Si–H termination rather than Si–Si dimers [704]. Due to the stronger bond, the hydrogenation leads to an increase of the silicon band gap, which can be used for surface passivation [705], leading to reduced reverse diode current.

The hydrogen concentration in amorphous Si (a-Si) can be as high as 50% [706]. Electronic grade a-Si contains typically 10–30 atomic% hydrogen and is thus rather a silicon–hydrogen alloy.

Hydrogen in crystalline silicon occupies the bond-center interstitial position (see Fig. 3.18b) as shown in Fig. 7.44a. The complexes formed by hydrogen with shallow acceptors and donors have been studied in detail. It is now generally accepted that for acceptors (e.g. boron) in silicon the hydrogen is located close to the bond-center position of the Si–B pair (BM, bond minimum) as sketched in Fig. 7.45a. The boron atom forms an electron-pair bond with three silicon atoms of the tetrahedra, the fourth silicon bonds to the hydrogen atom. The complex therefore no longer acts as an acceptor. The silicon atoms and the acceptor relax their positions. The adiabatic potential energy surface of hydrogen in Si:B is shown in Fig. 7.44b. The hydrogen can sit on four equivalent sites (BM) along the ⟨111⟩ directions of the initial B–Si_4 tetrahedron. This reduces the symmetry, e.g. of H–B vibrations [708]. The energetic barrier for the hydrogen orientation has been determined to be 0.2 eV theoretically [707] for a hydrogen motion along the path BM–C–BM in Fig. 7.44b. Stress (along [100] and [112]) reduces the symmetry and leads to splitting of the local vibrational modes, now showing axial symmetry [709]. However, this preferential orientation disappears with an activation energy of 0.19 eV, close to the theoretical value.

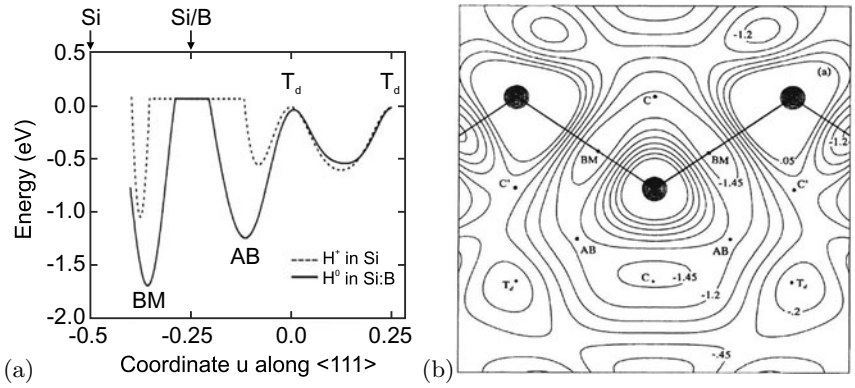

Fig. 7.44 **a** Energy for positions u of the hydrogen atom along the $\langle 111 \rangle$ direction for H^+ in pure Si (Si atom at $u = -0.25$) and neutral hydrogen (B atom at $u = -0.25$). u is measured in units of $\sqrt{3}a_0$. For all positions of the hydrogen atom the positions of the other atoms have been relaxed in the calculation. Data from [707]. **b** Adiabatic potential energy in the (110) plane for hydrogen in Si:B. 'BM' denotes the bond minimum site (high valence electron density), C and C' are equivalent for pure Si. Reprinted with permission from [707], ©1989 APS

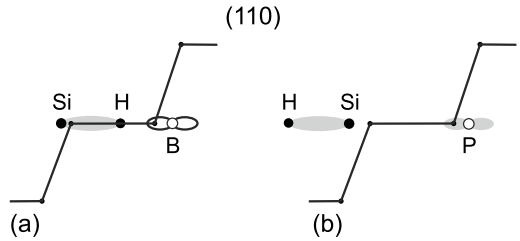

Fig. 7.45 Schematic model for hydrogen in silicon forming a complex with **a** a shallow acceptor (boron, empty orbital) and **b** a shallow donor (phosphorus, double-filled orbital)

Hydrogen has experimentally been found to also passivate shallow donors. The microscopic configuration is sketched in Fig. 7.45b. The hydrogen atom sits on the Si–AB (antibonding) position and forms an electron-pair bond with the silicon atom. The donor, e.g. phosphorus, is left with a double-filled p-orbital (lone pair) whose level is in the valence band and thus no longer contributes to conductivity.

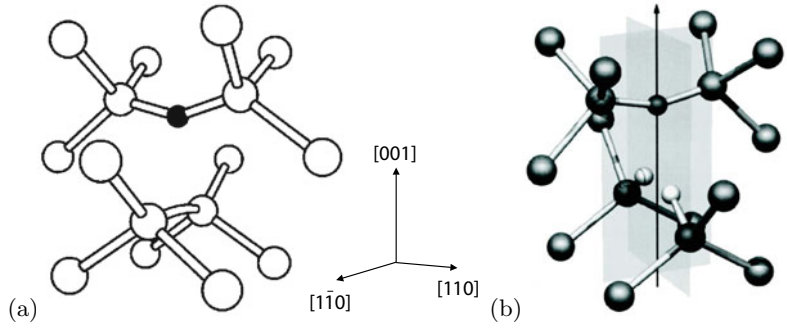

Fig. 7.46 **a** Structure of the V–O complex (A center) in silicon. The *black sphere* represents the oxygen atom. Reprinted with permission from [710], ©2004 APS. **b** Calculated ground-state structure for the V–O–H_2 center in silicon. Oxygen is over the C_2 axis, and the two *white* spheres represent hydrogen. Reprinted with permission from [711], ©2000 APS

Molecular hydrogen can passivate the so-called A center in Si, an oxygen–vacancy complex [711]. The atomistic configuration of the V–O–H_2 complex is shown in Fig. 7.46. The deep double donor S in Si with a level at 0.3 eV below the conduction-band edge can also be passivated by two hydrogen atoms [712].

Chapter 8
Transport

Um über den Temperaturverlauf des Widerstandes Rechenschaft geben zu können, müssen andere Abweichungen von der strengen Periodizität entscheidend sein, nämlich diejenigen, welche von den thermischen Eigenschwingungen des Kristalls herrühren.
In order to be able to account for the temperature dependence of the resistivity, other deviations from the strict periodicity must be decisive, namely those which result from the thermal vibrations of the crystal.

F. Bloch, 1928 [61]

Abstract The physics of transport in semiconductors is treated foremost for charge transport. Band transport and scattering, mobility, low field and high field effects as well as polarons and hopping transport are covered. A short section mentions ionic transport before heat conduction and coupled heat and charge transport including thermopower and Peltier effect are discussed.

8.1 Introduction

Charge and heat energy can be transported through the semiconductor in the presence of appropriate (generalized) forces. Such a force can be an electric field or a temperature gradient. Both transport phenomena are coupled since electrons transport energy and charge simultaneously through the crystal. First, we will treat the charge transport as a consequence of a gradient in the Fermi level, then the heat transport upon a temperature gradient and finally the coupled system, i.e. the Peltier and Seebeck effects. Detailed treatments of carrier transport can be found in [713, 714].

Practically all important semiconductor devices are based on the transport of charge, such as diode, transistor, photodetector, solar cell and laser.

Carriers move in the semiconductor driven by a gradient in the Fermi energy. We distinguish

- drift, as a consequence of an electric field $\mathbf{E}$,
- diffusion, as a consequence of a concentration gradient ∇n or ∇p.

In inhomogeneous semiconductors for which the position of the band edges is a function of position, another force occurs. This will not be treated here, since later (cf. Chap. 12) it will be included as an additional, internal electric field.

M. Grundmann, *The Physics of Semiconductors*, Graduate Texts in Physics,
https://doi.org/10.1007/978-3-030-51569-0_8

In Sects. 8.2–8.5 we treat band conductivity, i.e. the transport of charge carriers in extended states, the conduction and valence bands characterized by an effective mass. Conductivity is then determined by the carrier concentration (free electrons and holes) and scattering mechanisms (mobility). In disordered semiconductors such as amorphous material, the charge transport due to *hopping* between localized states close to the Fermi level dominates the conductivity which is discussed in Sect. 8.8.

Many semiconductor properties, such as the carrier concentration and the band gap, depend on the temperature. Thus, device properties will also depend on temperature. During operation of a device typically heat is generated, e.g. by Joule heating due to finite resistivity. This heat leads to an increase of the device temperature that subsequently alters the device performance, mostly for the worse. Ultimately, the device can be destroyed. Thus cooling of the device, in particular of the active area of the device, is essential. Mostly the thermal management of device heating limits the achievable performance (and lifetime) of the device. In high-power devices quite high energy densities can occur, e.g. the facet of a high-power semiconductor laser has to withstand an energy density beyond $10\,\mathrm{MW\,cm^{-2}}$.

8.2 Conductivity

Under the influence of an electric field the electrons accelerate according to (cf. (6.36))

$$\mathbf{F} = m^* \frac{\mathrm{d}\mathbf{v}}{\mathrm{d}t} = \hbar \frac{\mathrm{d}\mathbf{k}}{\mathrm{d}t} = q\,\mathbf{E} = -e\,\mathbf{E}\,. \tag{8.1}$$

In the following, q denotes a general charge, while e is the (positive) elementary charge. We also consider an isotropic effective mass m^* at first. After the time δt the $\mathbf{k}$ vector of all conduction electrons (and the center of the Fermi sphere) has been shifted by $\delta\mathbf{k}$

$$\delta\mathbf{k} = -\frac{e\,\mathbf{E}}{\hbar}\,\delta t\,. \tag{8.2}$$

In the absence of scattering processes this goes on further (similar to an electron in vacuum). This regime is called *ballistic* transport. In a (periodic) band structure, the electron will perform a closed cycle as indicated in Fig. 8.1. Such motion is called a Bloch oscillation. However, in a bulk crystal the period T of such an oscillation $eET/\hbar = 2\pi/a_0$ is of the order of 10^{-10} s for $E = 10^4$ V/cm. This time is much longer than a typical scattering time of 10^{-14} s. Thus, in bulk material the Bloch electron cannot reach the zone boundary. However, in artificial superlattices (cf. Chap. 12) with larger periodicity ($\approx$10 nm), high electric fields ($\approx 10^6$ V/cm) and high quality (reduced collision time) such motion is possible. We note that in the absence of scattering, electrons also perform a periodic oscillation in a magnetic field (cyclotron motion).

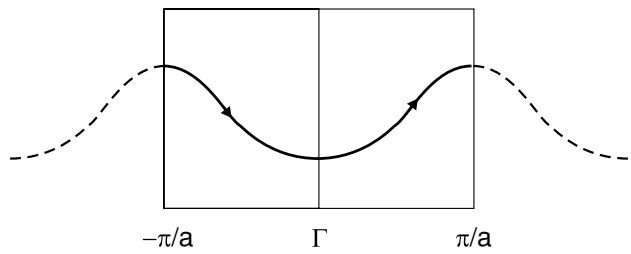

Fig. 8.1 Schematic representation of a Bloch oscillation

In a real semiconductor, at finite temperatures, impurities, phonons and defects (finally also the surface) will contribute to scattering. In the relaxation-time approximation it is assumed that the probability for a scattering event, similar to friction, is proportional to the (average) carrier velocity. The average relaxation time τ is introduced via an additional term $\dot{\mathbf{v}} = -\mathbf{v}/\tau$ that sums up all scattering events.[1] Thus, the maximum velocity that can be reached in a static electric field is given by (steady-state velocity)

$$\mathbf{v} = -\frac{e\,\mathbf{E}\,\tau}{m^*} \,. \tag{8.3}$$

The current density per unit area is then linear in the field, i.e. fulfills Ohm's law

$$\mathbf{j} = n\,q\,\mathbf{v} = \frac{n\,e^2\,\mathbf{E}\,\tau}{m^*} = \sigma\,\mathbf{E} \,. \tag{8.4}$$

The conductivity σ in the relaxation-time approximation is given by

$$\sigma = \frac{1}{\rho} = \frac{n\,e^2\,\tau}{m^*} \,. \tag{8.5}$$

In the case of a cylindrically symmetric mass such as for electrons in silicon or germanium, for the effective mass in (8.5) the effective conductivity mass must be used,

$$\frac{1}{m^*_\sigma} = \frac{1}{3}\left(\frac{2}{m_\mathrm{t}} + \frac{1}{m_\mathrm{l}}\right) \,. \tag{8.6}$$

The specific resistivity is the inverse of the conductivity. Metals have a high conductivity (see Table 8.1), e.g. for Cu at room temperature $\sigma = 5.8 \times 10^5\,\Omega^{-1}\,\mathrm{cm}^{-1}$. At low temperatures (4 K) the conductivity is even a factor of 10^5 higher. The mean free path $d = \tau v_\mathrm{F}$ is

$$d = \frac{\sigma\,m^* v_\mathrm{F}}{n\,e^2} \,, \tag{8.7}$$

v_F being the Fermi velocity ($E_\mathrm{F} = m^* v_\mathrm{F}^2/2$). For copper, $d = 3\,\mathrm{mm}$ at low temperature (and thus susceptible to the sample geometry) while at room temperature the mean free path is only about 40 nm. However, this becomes an issue when the metal line width and height of interconnects in integrated circuits approaches this length scale [715] (see Sect. 24.5.5).

In semiconductors, the carrier concentration depends strongly on the temperature. At zero temperature the conductivity is zero. Also, the scattering processes and thus the relaxation time constant exhibit a temperature dependence. The conductivity spans a large range from insulating to almost metallic conduction (see Table 8.1).

8.3 Low-Field Transport

First we consider only *small* electric fields. The real meaning of this will only become clear in Sect. 8.4 on high-field transport. In the low-field regime the velocity is proportional to the electric field.

[1] Going beyond the relaxation time approximation is discussed in Appendix J.

Table 8.1 Conductivity at room temperature for various metals, semiconductors, insulators and liquids

Material	σ ($\Omega^{-1}\,\mathrm{cm}^{-1}$)
Ag	6.25×10^5
Al	3.6×10^5
Au	4.35×10^5
Cu	5.62×10^5
Fe	1.1×10^5
Pt	1.02×10^5
Ge pure ($N_\mathrm{D} \sim 10^{13}\,\mathrm{cm}^{-3}$)	10^{-2}
Ge ($N_\mathrm{D} \sim 10^{15}\,\mathrm{cm}^{-3}$)	1
Ge ($N_\mathrm{D} \sim 10^{17}\,\mathrm{cm}^{-3}$)	2×10^1
Ge ($N_\mathrm{D} \sim 10^{18}\,\mathrm{cm}^{-3}$)	2×10^2
Si pure	4.5×10^{-6}
Si:As ($N_\mathrm{D} \sim 3 \times 10^{19}\,\mathrm{cm}^{-3}$)	4×10^2
Si:B ($N_\mathrm{A} \sim 1.5 \times 10^{19}\,\mathrm{cm}^{-3}$)	1.2×10^2
GaAs pure	1.4×10^{-7}
ZnO:Al (highly doped)	$\approx 1 \times 10^4$
Pentacene	10^{-8}–10^{-4}
SiO_2	$\approx 10^{-15}$
Al_2O_3	$\approx 10^{-16}$
H_2O pure	4×10^{-8}
Hexane	$\approx 10^{-18}$

8.3.1 Mobility

The mobility is defined (scalar terms) as

$$\mu = \frac{v}{E} \,. \tag{8.8}$$

By definition, it is a negative number for electrons and positive for holes. However, the numerical value is usually given as a positive number for both carrier types. In an intrinsic semiconductor the mobility is determined by scattering with phonons. Further scattering is introduced by impurities, defects or alloy disorder. The conductivity is (8.4)

$$\sigma = q\, n\, \mu \tag{8.9}$$

for each carrier type. Using (8.5) the mobility in the relaxation time approximation is

$$\mu = \frac{q\,\tau}{m^*} \,. \tag{8.10}$$

In the presence of both electrons and holes,

$$\sigma = \sigma_\mathrm{e} + \sigma_\mathrm{h} = -e\, n\, \mu_\mathrm{n} + e\, p\, \mu_\mathrm{p} \,, \tag{8.11}$$

where μ_n and μ_p are the mobilities for electrons and holes, respectively. These are given by $\mu_\mathrm{n} = -e\,\tau_\mathrm{n}/m_\mathrm{e}^*$ and $\mu_\mathrm{p} = e\,\tau_\mathrm{p}/m_\mathrm{h}^*$.

As the unit for mobility, usually $\mathrm{cm}^2/\mathrm{Vs}$ is used. While Cu at room temperature has a mobility of $35\,\mathrm{cm}^2/\mathrm{Vs}$, semiconductors can have much higher values. In two-dimensional electron gases (cf.

Table 8.2 Mobilities of electrons and holes at room temperature for various semiconductors

Material	$-\mu_n$ (cm^2/Vs)	μ_p (cm^2/Vs)
Si	1300	500
Ge	4500	3500
GaAs	8800	400
GaN	300	180
InSb	77 000	750
InAs	33 000	460
InP	4600	150
ZnO	230	8

Chap. 12), the mobility can reach several 10^7 cm^2/Vs at low temperature (Fig. 12.37). In bulk semiconductors with small band gap, a high electron mobility is caused by its small effective mass. Some typical values are given in Table 8.2.

8.3.2 Microscopic Scattering Processes

The relaxation time constant summarizes all scattering mechanisms. If the relaxation times τ_i of various processes are independent, the Matthiesen rule can be used to obtain the mobility ($\mu_i = q\,\tau_i/m^*$)

$$\frac{1}{\mu} = \sum_i \frac{1}{\mu_i} \,. \tag{8.12}$$

A more detailed book keeping is provided within the framework of the Boltzmann transport theory (Appendix J).

The various scattering mechanisms have quite different temperature dependences such that the mobility is a rather complicated function of temperature. In [716] the mechanisms determining the low and high-field transport properties of (cubic) semiconductors are reviewed. A schematic overview of the various carrier scattering processes discussed in the following is shown in Fig. 8.2.

8.3.3 Ionized Impurity Scattering

Theoretically, this problem is treated similar to Rutherford scattering. A screened Coulomb potential is assumed, as the scattering potential

$$V(r) = -\frac{Z\,e}{4\pi\epsilon_0\epsilon_r}\,\frac{1}{r}\,\exp\left(-\frac{r}{l_D}\right) \,, \tag{8.13}$$

where l_D is the screening length. The problem has been treated classically by Conwell and Weisskopf [717] and quantum mechanically by Brooks [718] and Herring. An expression for the mobility that encompasses the Conwell–Weisskopf and Brooks–Herring results is derived in [719]. Further details are given in [720, 721]. For the mobility it is found that

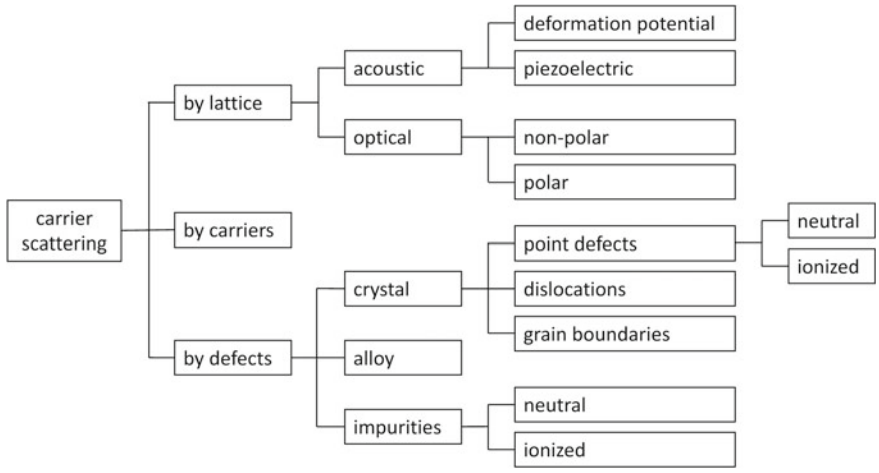

Fig. 8.2 Scheme of microscopic carrier scattering mechanisms

$$\mu_{\text{ion.imp.}} = \frac{2^{7/2}(4\pi\epsilon_0\epsilon_\text{r})^2}{\pi^{3/2}\,Z^2\,e^3\,\sqrt{m^*}}\,\frac{(kT)^{3/2}}{N_\text{ion}}\,\frac{1}{\ln(1+b)-1/(1+1/b)}\,, \tag{8.14}$$

with $b = 4(k/l_\text{D})^2 = 8\,m^*E\,(l_\text{D}/\hbar)^2$. In the Thomas-Fermi screening model

$$l_\text{D}^2 = 4\pi\,\frac{e^2}{\epsilon_0\epsilon_\text{r}}\,N(E_\text{F}) = \left(\frac{3}{\pi}\right)^{1/3}\frac{4\,m^*e^2}{\epsilon_0\epsilon_\text{r}\hbar^2}\,n^{1/3}\,. \tag{8.15}$$

The formula (8.14) is valid only for $b \gg 1$, i.e. small carrier densities. A similar formula from [720] is

$$\mu_{\text{ion.imp.}} = \frac{128\sqrt{2\pi}\,(\epsilon_0\epsilon_\text{r})^2\,(kT)^{3/2}}{m^{*1/2}\,Z^2\,N_\text{ion}\,e^3}\left[\ln\frac{24\,m^*\,\epsilon_0\epsilon_\text{r}\,(kT)^2}{n\,e^2\,\hbar^2}\right]^{-1}\,. \tag{8.16}$$

For large ionized impurity (and carrier) density ($b \ll 1$), the mobility is given by [555]

$$\mu_{\text{ion.imp.}} = \frac{4\,e}{3^{1/3}\,\pi^{2/3}\,h}\,n^{-2/3}\,, \tag{8.17}$$

the value of the pre-factor being about $3 \times 10^{14}\,(\text{Vs})^{-1}$.

The scattering time depends like $\tau \propto (E/kT)^s$ on the kinetic energy; for moderate or weak scattering $s = 3/2$, for very strong scattering, $s = -1/2$ [714].

For typical substitutional impurities, the charge of the scattering center is $|Z| = 1$; in oxides, oxygen vacancies may have $Z = 2$. At high impurity densities, impurity clusters may form with $|Z| > 1$; this will have a strong influence on the scattering rate since it proportional to Z^2. The decrease of mobility for $N_\text{D} > 10^{20}\,\text{cm}^{-3}$ (Fig. 8.3a) is attributed to such effect which can be described with an effective impurity clustering charge Z_D (Fig. 8.3b) [722, 723].

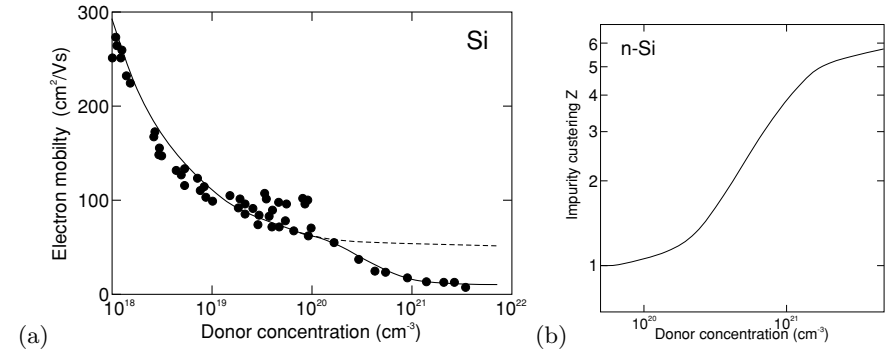

Fig. 8.3 **a** Electron mobility in highly doped silicon. Experimental data (*symbols*) from various sources and modeling with ionized impurity scattering with (*solid line*) and without (*dashed line*) considering impurity clustering. **b** Effective impurity cluster charge Z_D. Adapted from [722]

8.3.4 Deformation Potential Scattering

Acoustic phonons with small wavevector, i.e. a wavelength large compared to the unit cell, can have TA or LA character. The TA phonons represent a shear wave (with zero divergence), the LA phonons are a compression wave (with zero rotation). The LA is a plane wave of displacement $\delta\mathbf{R}$ parallel to the k-vector $\mathbf{q}$,

$$\delta\mathbf{R} = \mathbf{A}\ \sin\left(\mathbf{q}\cdot\mathbf{R} - \omega t\right)\ . \tag{8.18}$$

The strain tensor is given by

$$\epsilon_{ij} = \frac{1}{2}\left(\mathbf{q}_i\,\mathbf{A}_j + \mathbf{q}_j\,\mathbf{A}_i\right)\cos\left(\mathbf{q}\,\mathbf{R} - \omega t\right)\ . \tag{8.19}$$

It has a diagonal form $\epsilon_{ij} = \mathbf{q}_i\mathbf{A}_j$ for $\mathbf{q}$ and $\omega \to 0$. Therefore, the LA phonon creates an oscillatory volume dilatation (and compression) with amplitude $\mathbf{q}\cdot\mathbf{A}$. This volume modulation affects the position of the band edges. For the conduction-band edge the energy change is related to the volume change by the hydrostatic deformation potential $E_{\text{ac.def.}} = V\partial E_C/\partial V$. Since the modulation is small compared to the energy of the charge carriers, it is mostly an elastic scattering process. The Hamilton operator for the LA scattering is

$$\hat{H} = E_{\text{ac.def.}}\,(\mathbf{q}\cdot\mathbf{A})\ . \tag{8.20}$$

The size of the LA amplitude is given by the number of phonons in the mode that is given by the Bose–Einstein distribution, $N_{\text{ph}}(\hbar\omega) = [\exp(\frac{\hbar\omega}{kT})]^{-1}$. The mobility due to acoustic deformation potential scattering is found to be

$$\mu_{\text{ac.def.}} = \frac{2\sqrt{2\pi}\,e\,\hbar^4\,c_1}{3\,m^{*5/2}\,E_{\text{ac.def.}}^2}\,(kT)^{-3/2}\ , \tag{8.21}$$

where $c_1 = \rho c_s^{\text{LA}}$, ρ being the density and c_s being the sound velocity. The scattering time increases like $\tau \propto E^{-1/2}$ with the kinetic energy [714].

The acoustical deformation potential scattering is important at high temperatures. It is dominating in nonpolar semiconductors (Ge, Si) at high temperatures (typically at and above room temperature).

8.3.5 Piezoelectric Potential Scattering

In piezoelectric crystals (see Sect. 16.4), i.e. crystals that show an electric polarization upon strain, certain acoustic phonons lead to piezoelectric fields. In GaAs, with ⟨111⟩ being the piezoelectric directions, this is the case for shear waves. In strongly ionic crystals, e.g. II–VI semiconductors, the piezoelectric scattering can be stronger than the deformation potential scattering. The mobility due to piezoelectric potential scattering is

$$\mu_{\text{pz.el.}} = \frac{16\sqrt{2\pi}}{3} \frac{\hbar\,\epsilon_0\epsilon_\text{r}}{m^{*3/2}\,e\,K^2}\,(kT)^{-1/2}\ , \tag{8.22}$$

with $K = \frac{e_\text{p}^2/c_\text{l}}{\epsilon_0\epsilon_\text{r}+e_\text{p}^2/c_\text{l}}$, e_p being the piezoelectric coefficient.

8.3.6 Polar Optical Scattering

LO phonons are connected with an electric field antiparallel to the displacement (9.29). In the scattering mechanism the absorbed or emitted phonon energy $\hbar\omega_0$ is comparable to the thermal energy of the carriers. Therefore, the scattering is inelastic and the relaxation-time approximation does not work. The general transport theory is complicated. If the temperature is low compared to the Debye temperature, $T \ll \Theta_\text{D}$

$$\mu_{\text{pol.opt.}} = \frac{e}{2\,m^*\,\alpha\,\omega_0}\,\exp\left(\frac{\Theta_\text{D}}{T}\right)\ , \tag{8.23}$$

where $\alpha = \frac{1}{137}\sqrt{\frac{m^*c^2}{2k\Theta_\text{D}}}\left(\frac{1}{\epsilon(\infty)} - \frac{1}{\epsilon(0)}\right)$ is the dimensionless polar constant.

8.3.7 Dislocation Scattering

Dislocations can contain charge centers and thus act as scattering centers citeyou. This has been first demonstrated for n-Ge crystals that have been deformed [725, 726]. The deformation has introduced acceptor-type defects reducing the mobility in particular at low temperatures (similar to ionized impurity scattering). The mobility due to dislocation scattering in an n-type semiconductor is given by [727, 728]

$$\mu_{\text{disl.}} = \frac{30\sqrt{2\pi}\,\epsilon^2\,d^2\,(kT)^{3/2}}{N_\text{disl}\,e^3\,f^2\,L_\text{D}\,\sqrt{m^*}} \propto \frac{\sqrt{n}}{N_\text{disl}}\,T\ , \tag{8.24}$$

d being the average distance of acceptor centers along the dislocation line, f their occupation rate, N_disl the area density of dislocations and $L_\text{D} = (\epsilon kT/(e^2n))^{1/2}$ the Debye screening length. The relation $\mu \propto \sqrt{n}/N_\text{disl}$ has been confirmed for various n-type GaN samples [729].

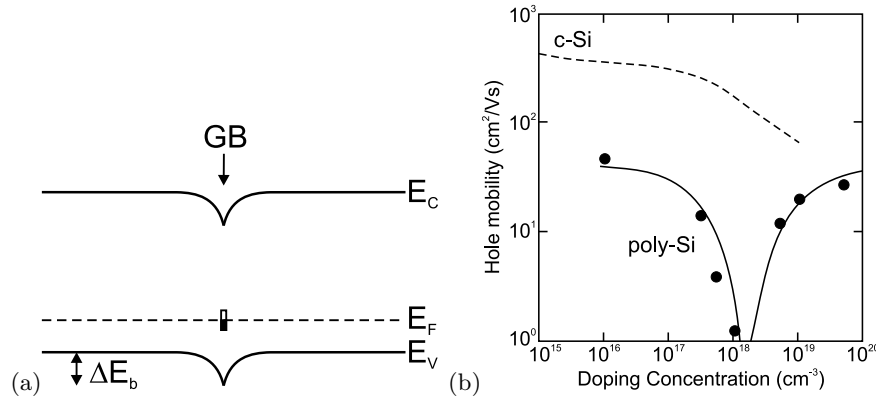

Fig. 8.4 **a** Electronic barrier (ΔE_b) for (hole) transport at a grain boundary (GB). **b** Average hole mobility in polysilicon, experimental data (*symbols*) and theoretical model (*solid line*). The dependence for monocrystalline silicon is shown for comparison as *dashed line*. Adapted from [730]

8.3.8 Grain Boundary Scattering

The lowering of mobility due to transport across grain boundaries is an important effect in polycrystalline materials, such as poly-silicon for solar cells or thin film transistors [730–733]. Grain boundaries contain electronic traps whose filling depends on the doping of the bulk of the grains. Charges will be trapped in the grain boundaries and a depletion layer will be created.[2] At low doping the grains are fully depleted and all free carriers are trapped in the grain boundaries. This means low conductivity, however, no electronic barrier to transport exists. At intermediate doping, traps are partially filled and the partial depletion of the grain leads to the creation of an electronic barrier ΔE_b (Fig. 8.4a) hindering transport since it must be overcome via thermionic emission. At high doping the traps are completely filled and the barrier vanishes again. Accordingly the mobility goes through a minimum as a function of the doping concentration (Fig. 8.4b) [730]. In [734] these data have been modeled with a 20 nm grain size, the value found in [730] from TEM analysis.

The expression for the limitation of the mobility due to scattering at grain boundaries is given by [733, 735]

$$\mu_\mathrm{GB} = \frac{e\,L_\mathrm{G}}{\sqrt{8m^*\pi k}}\,T^{-1/2}\,\exp\left(-\frac{\Delta E_\mathrm{b}}{kT}\right)\,, \tag{8.25}$$

where L_G is the grain size.

8.3.9 Alloy Scattering

The random population of lattice sites represents disorder from a perfectly periodic lattice. The charge carrier mobility in an alloy $\mathrm{A}_x\mathrm{B}_{1-x}$ due to scattering in this potential is proportional to the alloy scattering potential ΔU [590],

$$\mu_\mathrm{alloy} = \frac{2\,e\,\hbar}{3\pi\,m^*\,\Omega\,x\,(1-x)\,(\Delta U)^2}\,\frac{kT}{n}\,\left[1+\exp(E_\mathrm{F}/kT)\right]\,, \tag{8.26}$$

[2] The following arguments may only be followed once the concept of depletion layers and band bending is understood, see Sect. 21.2.1.

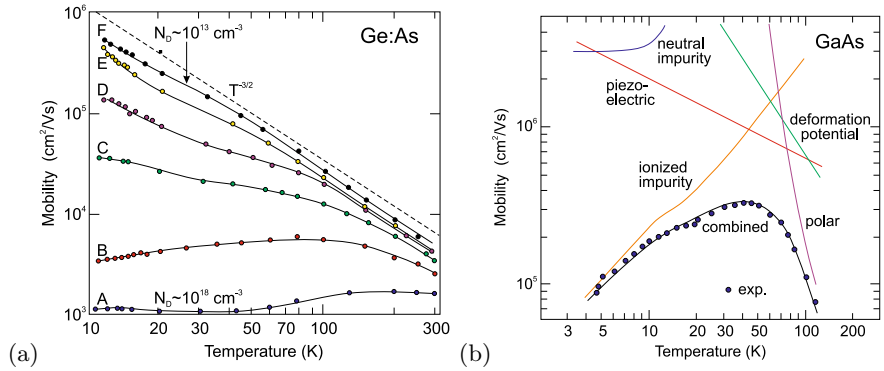

Fig. 8.5 **a** Temperature dependence of the electron mobility in n-doped Ge (for various doping levels from $N_D \approx 10^{18}$ for sample A to 10^{13} cm^{-3} for sample F in steps of a factor of ten). *Dashed line* indicates $T^{-3/2}$ dependence of deformation potential scattering, *solid lines* are guides to the eye. Adapted from [594]. **b** $\mu_n(T)$ for n-type GaAs ($N_D \approx 5 \times 10^{13}$ cm^{-3}, $N_A \approx 2 \times 10^{13}$ cm^{-3}). *Solid lines* are theoretical mobilities for various scattering mechanisms and combined mobility according to (8.12). Adapted from [736]

$\Omega(x)$ being the volume of the unit cell over which the alloy-scattering potential is effective. Such effect is present in any alloy such as $In_xGa_{1-x}As$ [591] of $Al_xGa_{1-x}N$ [592]. For the latter material, see also the following section.

8.3.10 Dipole Scattering

In alloys of *polar* semiconductors (Chap. 16), i.e. lower-symmetric (non-cubic) semiconductors with an electric polarization, the additional potential due to the random variation of the polarization introduces an additional scattering mechanism, the so-called dipole scattering [592]. Dipole scattering originally has been studied in the context of scattering in highly compensated semiconductors due to ionized donor-acceptor pairs [593].

8.3.11 Temperature Dependence

The sum of all scattering processes leads to a fairly complicated temperature dependence of the mobility $\mu(T)$. In covalent semiconductors (Si, Ge) the most important processes are the ionized impurity scattering ($\mu \propto T^{3/2}$) at low temperatures and the deformation potential scattering ($\mu \propto T^{-3/2}$) at high temperatures (Fig. 8.5a). In polar crystals (e.g. GaAs) at high temperatures the polar optical scattering is dominant (Fig. 8.5b).

In Fig. 8.6 the electron mobility of bulk and thin-film ZnO is compared. Since ZnO is polar the mobility at room temperature is limited by polar optical phonon scattering. In the thin film, grain-boundary scattering (Sect. 8.3.8) additionally occurs and limits the mobility.

In Fig. 8.7 the temperature dependence of the mobility is depicted for an alloy of polar semiconductors, namely $Al_{0.25}Ga_{0.75}N$. The contributions of alloy scattering and dipole scattering determine the mobility [592].

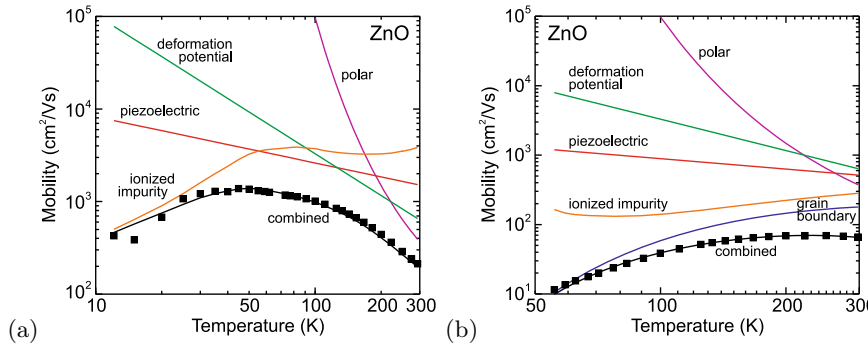

Fig. 8.6 Temperature dependence of the electron mobility in n-type **a** bulk ZnO and **b** a PLD-grown ZnO thin film on sapphire. In the latter, grain-boundary scattering is limiting the mobility. *Squares* are experimental data, *solid lines* are theoretical mobilities for various scattering mechanisms and combined mobility according to (8.12). Experimental data from [737]

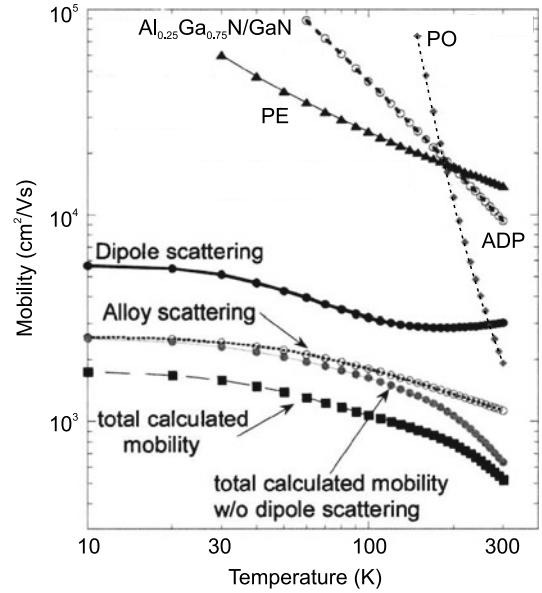

Fig. 8.7 Calculated temperature dependence of the electron mobility in n-type $Al_{0.25}Ga_{0.75}N$, ($N_D = 5 \times 10^{17}\,cm^{-3}$). PO: polar optic scattering, PE: piezoelectric scattering, ADP: acoustic deformation potential scattering. Adapted from [592]

Since the carrier concentration increases with increasing temperature and the mobility decreases, the conductivity has a maximum, typically around 70 K (see Fig. 8.8). At very high temperature, when intrinsic conduction starts, σ shows a strong increase due to the increase in n.

At low temperature, the disorder due to doping (random positions of the impurity atoms) leads to a temperature driven metal–insulator transition as depicted in Fig. 8.21.

8.3.12 Doping Dependence

The mobility decreases with increasing dopant concentration as already shown in Figs. 8.3 and 8.5a. In Fig. 8.9a the low doping limit is due to deformation potential scattering; the decrease with doping is due

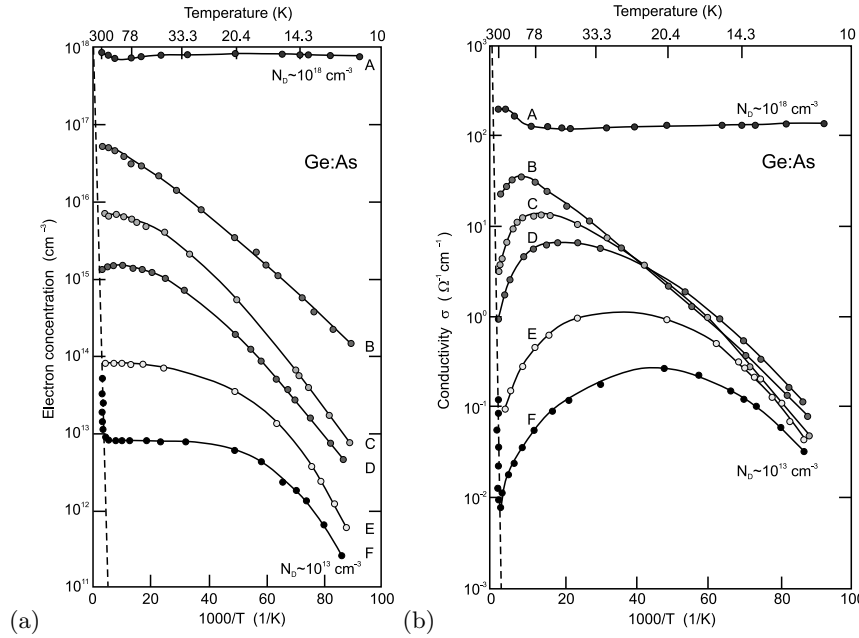

Fig. 8.8 **a** Carrier concentration and **b** conductivity of n-type Ge as a function of temperature. The doping level varies from $N_D \approx 10^{13}$ to 10^{18} (samples A–F as in Fig. 8.5a where the mobility of the same samples is shown). The *dashed lines* are for intrinsic Ge. The *solid lines* are guides to the eye. Adapted from [594]

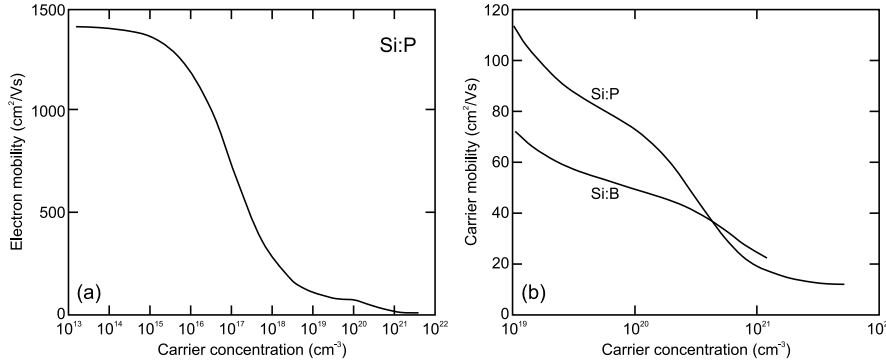

Fig. 8.9 **a** Electron mobility in Si:P at room temperature over a wide range of carrier concentrations. **b** Electron mobility in Si:P and hole mobility in Si:B for various high carrier concentrations. Adapted from [739]

to ionized impurity scattering. At high doping level, it becomes more important at room temperature than (acoustical or optical) phonon scattering [738]. The mobility of carriers in n- and p-type silicon with very high carrier concentrations is depicted in Fig. 8.9b.

Thus, for bulk material high carrier density and high mobility are contrary targets and cannot be achieved simultaneously. A solution will be provided with the concept of *modulation* doping where the dopants and the (two-dimensional) carrier gas will be spatially separated in a heterostructure (cf. Sect. 12.3.4).

At high doping, the substitutional character of the impurities may be lost and secondary phases can arise, e.g. as observed for highly doped ZnO:Ga, exhibiting octahedral coordination of gallium

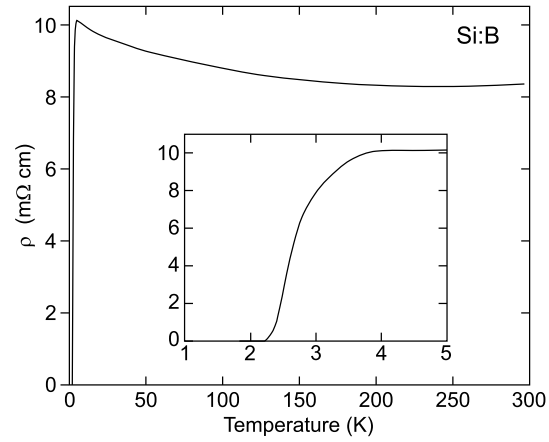

Fig. 8.10 Conductivity of B-doped diamond as a function of temperature. Adapted from [746]

in a parasitic $ZnGa_2O_4$ spinel phase for [Ga]=4% [632]. The onset of such segregation phenomena is accompanied with the decrease of mobility and conductivity.

8.3.13 Superconductivity

It has been found that highly doped semiconductors do not only behave like metals in the sense that the carrier concentration is largely independent of temperature but that they can also exhibit superconductivity. Theoretical and early experimental investigations suggested the possibility of such behavior [740–743] even when the electron concentration is much smaller than one per atom. Experimentally, robust superconductivity in semiconductors has been found more recently for a number of semiconductors [744, 745], namely boron-doped diamond (C:B) [746] (Fig. 8.10), Si:B [747] and Ge:Ga [748]. The preparation of superconducting semiconductors with critical temperature above 1 K typically involves hyperdoping with impurity concentrations of several atomic percent. The detailed physics of these materials, such as the superconductor type (type-II behavior was found for C:B) or the electron coupling mechanism (generally, phonon-assisted pairing is assumed), are still under debate.

Another type of superconducting semiconductor structure are twisted monolayers in Van-der-Waals heterostructures for particular values of twist angle and carrier concentration (cf. Sect. 13.3).

8.3.14 Piezoresistivity

The dependence of resistivity on stress or strain is known as piezoresistive effect, first described in [749]. It is a consequence of the modification of the band structure upon stress and the change of effective masses (Sect. 6.12.2). In a cubic material, the resistivity ρ_i for transport in cartesian direction i changes compared to the unstrained state in a phenomenological description according to

$$\frac{\Delta\rho_i}{\rho_i} = \pi_{ij}\,\sigma_j \ , \tag{8.27}$$

where $\boldsymbol{\pi}$ is the piezoresistivity tensor (8.28) and the σ_j form the six-component stress tensor (5.55),

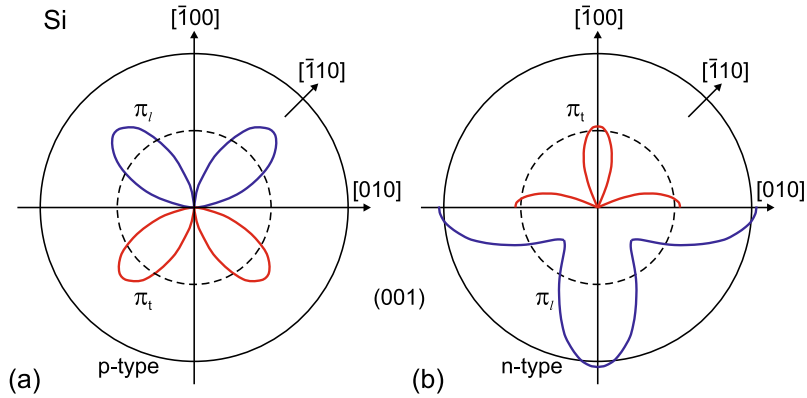

Fig. 8.11 Piezoresistive coefficient for current parallel (perpendicular) to the stress π_l as *blue lines* (π_t, *red lines*) for uniaxially stressed Si (001) at room temperature, **a** for p-type Si, **b** for n-type Si. The *upper* (*lower*) halves of the graphs show positive (negative) values of the piezoresistive coefficient, i.e. resistivity increases (decreases) with tensile stress. The *solid circle* indicates the value of $|\pi| = 10^{-9}\,\mathrm{Pa}^{-1}$, the *dashed circle* half that value. Adapted from [752]

Table 8.3 Piezoresistivity coefficients (in $10^{-11}\,\mathrm{Pa}^{-1}$) for Si, Ge and GaAs at room temperature

Material	ρ (Ω cm)	π_{11}	π_{12}	π_{44}	References
p-Si	7.8	6.6	−1.1	138.1	[749]
n-Si	11.7	−102.2	53.4	−13.6	[749]
p-Ge (Ge:Ga)	15.0	−10.6	5.0	98.6	[749]
n-Ge (Ge:As)	9.9	−4.7	−5.0	−137.9	[749]
p-GaAs	$\sim 10^{-3}$	−12.0	−0.6	46	[753]
n-GaAs	$\sim 10^{-3}$	−3.2	−5.4	−2.5	[753, 754]

$$\boldsymbol{\pi} = \begin{pmatrix} \pi_{11} & \pi_{12} & \pi_{12} & 0 & 0 & 0 \\ \pi_{12} & \pi_{11} & \pi_{12} & 0 & 0 & 0 \\ \pi_{12} & \pi_{12} & \pi_{11} & 0 & 0 & 0 \\ 0 & 0 & 0 & \pi_{44} & 0 & 0 \\ 0 & 0 & 0 & 0 & \pi_{44} & 0 \\ 0 & 0 & 0 & 0 & 0 & \pi_{44} \end{pmatrix} . \tag{8.28}$$

Values for the piezoelectric coefficients are given in Table 8.3 for Si, Ge and GaAs.

The piezoelectric effect has been discussed in detail [750] and modeled for p-type Si [751]. We shall only give a simple example which is particularly relevant for advanced CMOS design (Sect. 24.5.5); the directional dependence of the piezoresistive coefficient of silicon is shown for uniaxial stress within in the (001) plane in Fig. 8.11. Uniaxial tensile stress increases hole resistivity along ⟨110⟩ stress directions, compressive stress thus increases hole conductivity.

8.4 High-Field Transport

In the case of small electric fields the scattering events are elastic. The drift velocity is linearly proportional to the electric field. The average thermal energy is close to its thermal value $3kT/2$ and the carriers are close to their band edges (Fig. 8.12a). The scattering efficiency, however, is reduced

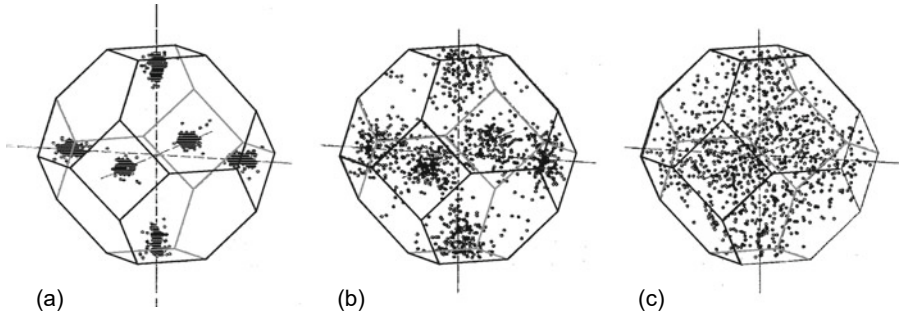

Fig. 8.12 Distribution of electrons in silicon in momentum space (cmp. Fig. 6.35c) for electric fields of **a** 10 kV/cm, **b** 10^2 kV/cm and **c** 10^3 kV/cm. Adapted from [756]

already at moderate fields. Then, the electron temperature [755] becomes larger than the lattice temperature. With increasing electrical field the carriers can gain more and more energy and will on average populate higher states, assuming a non-Boltzmann (and non-Fermi) statistical distribution [756]. The electron distribution in **k**-space is depicted for silicon for three different electric fields in Fig. 8.12b,c. Hot carriers suffer additional scattering processes that are discussed in the following, namely optical phonon emission, intervalley scattering and impact ionization.

8.4.1 Drift-Saturation Velocity

If the carrier energy is large enough it can transfer energy to the lattice by the emission of an optical phonon. This mechanism is very efficient and limits the maximum drift velocity. Such behavior is non-ohmic. The limiting value for the drift velocity is termed the *drift-saturation velocity*. It is given by [757]

$$v_\mathrm{s} = \sqrt{\frac{8}{3\pi}} \sqrt{\frac{\hbar\omega_\mathrm{LO}}{m^*}} \,. \tag{8.29}$$

This relation can be obtained from an energy-balance consideration. The energy gain per unit time in the electric field is equal to the energy loss by the emission of an optical phonon.

$$q\,\mathbf{v}\cdot\mathbf{E} = \frac{\hbar\omega_\mathrm{LO}}{\tau} \,, \tag{8.30}$$

where τ is the typical relaxation time constant for LO phonon emission. Together with (8.3) we find (8.30) except for the pre-factor, which is close to 1. The exact pre-factor results from a quantum-mechanical treatment. For Ge the drift-saturation velocity at room temperature is 6×10^6 cm/s, for Si it is 1×10^7 cm/s (Fig. 8.13a). The carrier velocity also depends on the crystallographic direction [758].

8.4.2 Negative Differential Resistivity

In GaAs, the initially linear regime (constant mobility) saturates at a maximum drift velocity of about 2×10^7 cm/s for about 3 kV/cm; for higher fields, a reduction in drift velocity (with increasing field!) is present (1.2×10^7 cm/s at 10 kV/cm, 0.6×10^7 cm/s at 200 kV/cm), as shown in Fig. 8.13a. This

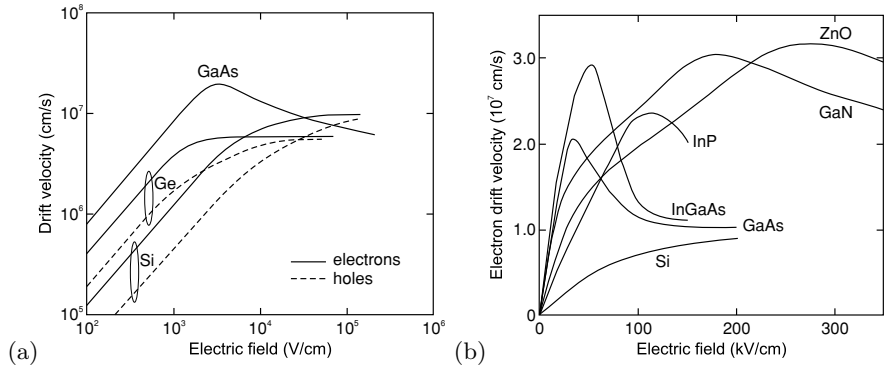

Fig. 8.13 Drift velocity at room temperature as a function of applied electric field for **a** high-purity Si, Ge, and GaAs on a double-logarithmic plot and **b** on linear plots for Si [759], Ge [760], GaAs [676], InP [761], (In, Ga)As [762], GaN and ZnO [763]

Table 8.4 Material parameters for multi-valley bandstructure of GaAs and InP. ΔE denotes the energetic separation of the two lowest valleys of the conduction band, E_{thr} the threshold field for NDR and v_{P} the peak velocity (at E_{thr}). Most values from [766]

Material					Lower valley (Γ)		Upper valley (L)	
	E_{g} (eV)	ΔE (eV)	E_{thr} (kV/cm)	v_{P} (10^7 cm/s)	m^* (m_0)	μ_{n} (cm^2/Vs)	m^* (m_0)	μ_{n} (cm^2/Vs)
GaAs	1.42	0.36	3.2	2.2	0.068	≈8000	1.2	≈180
InP	1.35	0.53	10.5	2.5	0.08	≈5000	0.9	≈100

regime, above the threshold field of $E_{\mathrm{thr}} = 3.2\,\mathrm{kV/cm}$ in GaAs, is called *negative differential resistivity* (NDR) and was predicted in [764]. This phenomenon can be used in microwave oscillators, e.g. the Gunn element (Sect. 21.5.11).

The effect occurs in a multi-valley band structure (see Fig. 8.14, for values cf. Table 8.4), e.g. in GaAs or InP, when the carrier energy is high enough to scatter (Fig. 8.14c,d) from the Γ minimum (small mass and high mobility) into the L valley (large mass and low mobility) [765].

The temperature dependence of the saturation velocity is shown in Fig. 8.15. With increasing temperature the saturation velocity decreases since the coupling with the lattice becomes stronger.

8.4.3 Velocity Overshoot

When the electric field is switched on, the carriers are at first in the Γ minimum (Fig. 8.14a). Only after a few scattering processes are they scattered into the L minimum. This means that in the first moments transport occurs with the higher mobility of the lowest minimum (Fig. 8.14e). The velocity is then larger than the (steady-state) saturation velocity in a dc field. This phenomenon is called *velocity overshoot* and is a purely dynamic effect (Fig. 8.16). Velocity overshoot in GaN is discussed in [769]. It is an important effect in small transistors.

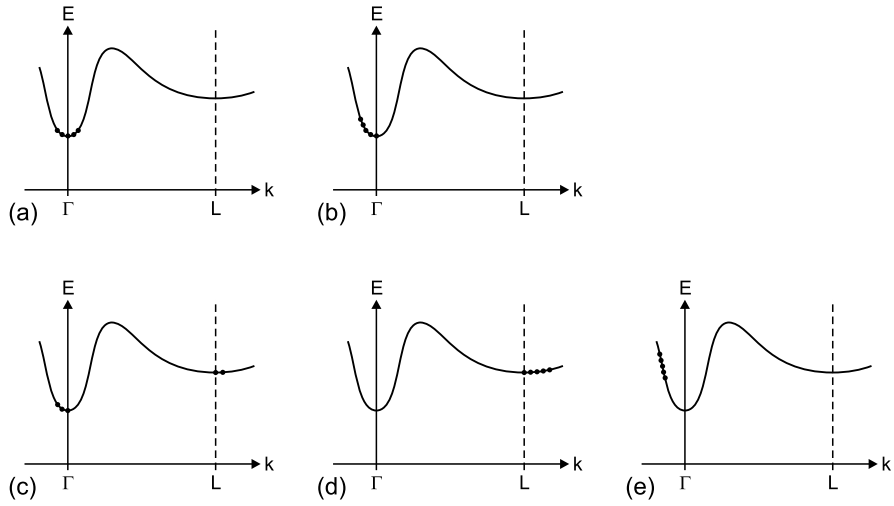

Fig. 8.14 Charge-carrier distribution in a multi-valley band structure (e.g. GaAs, InP) for **a** zero, **b** small ($E < E_a$), **c** intermediate and **d** large ($E > E_b$) field strength. The situation shown in **e** is reached temporarily during velocity overshoot (see also Fig. 8.16)

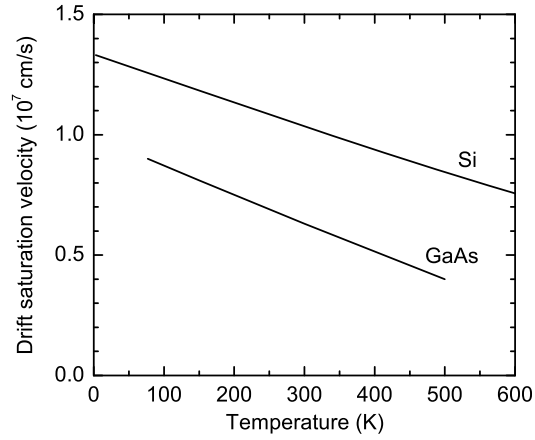

Fig. 8.15 Temperature dependence of the saturation velocity for Si (following $v_s = v_{s_0}(1 + 0.8\exp(T/600\,K))^{-1}$ with $v_{s_0} = 2.4 \times 10^7$ cm/s from [759]) and GaAs [676, 767, 768]

8.4.4 Impact Ionization

If the energy gain in the field is large enough to generate an electron–hole pair, the phenomenon of impact ionization occurs. The kinetic energy is $\propto v^2$. Momentum and energy conservation apply. Thus, at small energies (close to the threshold for impact ionization) the vectors are short and collinear to fulfill momentum conservation. At higher energy, larger angles between the velocity vectors of the impact partners can also occur. If the process is started by an electron (Fig. 8.17a) the threshold energy is given by [770]

$$E_e^{thr} = \left(1 + \frac{m_e}{m_e + m_{hh}}\right) E_g \,. \tag{8.31}$$

If the process starts with a heavy hole, the threshold [770],

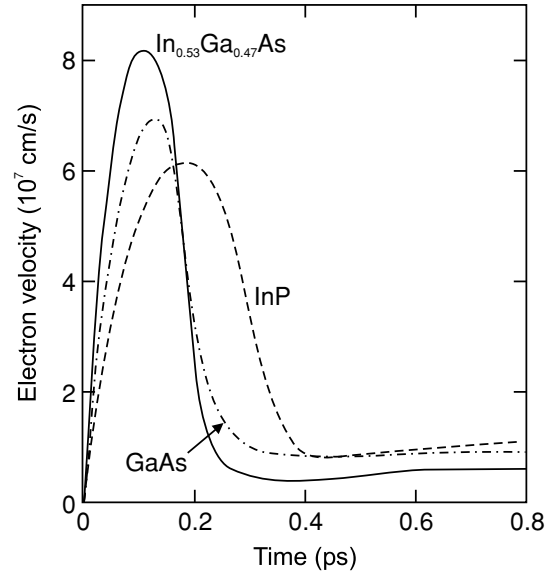

Fig. 8.16 Time dependence of the electron velocity at room temperature upon a step-like electric field (40 kV/cm) for GaAs (*dash-dotted line*), InP (*dashed line*) and $In_{0.53}Ga_{0.47}As$ (*solid line*)

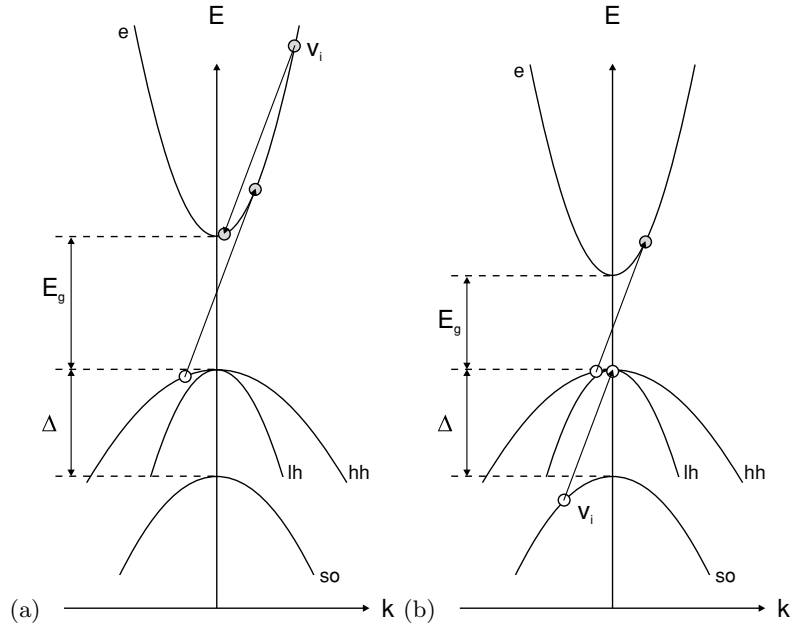

Fig. 8.17 Electron and hole transitions for impact ionization close to the threshold energy. Ionization is triggered by **a** an electron and **b** a split-off hole of velocity v_i

$$E_{hh}^{thr} = \left(1 + \frac{m_{hh}}{m_e + m_{hh}}\right) E_g \,, \tag{8.32}$$

is larger because of the larger hole mass.

The threshold for impact ionization triggered by a split-off hole (shown schematically in Fig. 8.17b) is [771]

$$E_h^{thr} = \left(1 + \frac{m_{so}\,(1 - \Delta_0/E_g)}{2\,m_{hh} + m_e - m_{so}}\right) E_g \,. \tag{8.33}$$

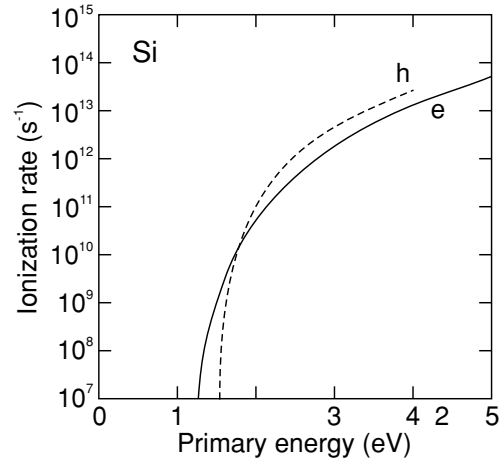

Fig. 8.18 Impact ionization rate as a function of primary carrier energy for electrons (*solid line*) and holes (*dashed line*) in silicon at room temperature. The curves are fit to results from a Monte-Carlo simulation. Adapted from [772, 773]

Thus so-holes have typically the smaller threshold.[3] At energies where impact ionization occurs, non-parabolicities are typically important, thus (8.31)–(8.33) are only indicative. The threshold behavior and the dependence of the scattering rate as a function of the primary carrier energy in Si, calculated considering the detailed band structure, is shown in Fig. 8.18.

The generation rate G of electron–hole pairs during impact ionization is given by

$$G = \alpha_\mathrm{n}\, n\, v_\mathrm{n} + \alpha_\mathrm{p}\, p\, v_\mathrm{p}\ , \tag{8.34}$$

where α_n is the electron ionization coefficient. It describes the generation of electron–hole pairs per incoming electron per unit length. α_p denotes the hole ionization coefficient. The coefficients depend strongly on the applied electric field. They are shown in Fig. 8.19. They also depend on the crystallographic direction.

The impact ionization initiated by electrons and holes in silicon has been calculated considering the full band structure using a Monte Carlo technique in [772] and [773], respectively. In both cases the impact ionization rate is anisotropic for excess energies smaller than 3 eV and become isotropic above. The average energies at the moment of generation of secondary generated carriers depends linearly on the primary electron or hole energy.

The energy dependence of the electron initiated impact ionization rate has been calculated for GaAs, GaN and ZnS considering details and anisotropy of the band structure in [774]. The rates averaged over the Brillouin zone are compared in Fig. 8.20. Because of the large band gap of GaN, impact ionization can only be generated by electrons in higher conduction bands. The sharp increase of ionization rate for GaN around 5.75 eV correlates with a large valence band DOS from hole states at the zone boundary.

8.5 High-Frequency Transport

The above consideration pertained to dc (or slowly varying) fields. Now, we consider an ac field. It accelerates the carriers but at the same time the dissipative force in the relaxation-time approximation is present, i.e. (for electrons)

$$m^*\dot{\mathbf{v}} = -e\,\mathbf{E} - m^*\,\frac{\mathbf{v}}{\tau}\ . \tag{8.35}$$

[3] Assuming $m_\mathrm{so} = m_\mathrm{e}$, $m_\mathrm{e} \ll m_\mathrm{hh}$ and $\Delta_0 \ll E_\mathrm{g}$, $E_\mathrm{so}^\mathrm{thr}/E_\mathrm{e}^\mathrm{thr} \approx 1 - (m_\mathrm{e}/m_\mathrm{hh})(1 + \Delta/E_\mathrm{g})/2 < 1$.

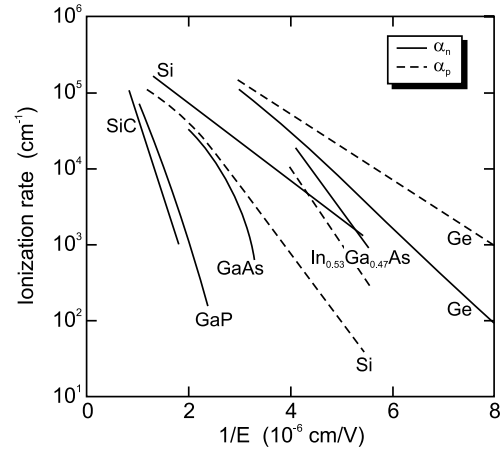

Fig. 8.19 Impact ionization rates for electrons and holes as a function of the inverse electric field for Si, Ge and other compound semiconductors at 300 K. Adapted from [574]

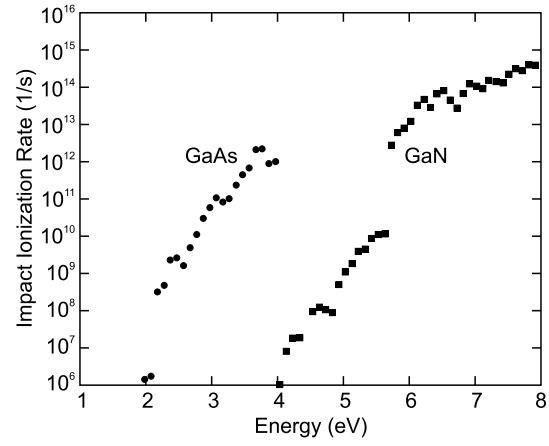

Fig. 8.20 Averaged rates for electron initiated impact ionization in GaAs (*circles*) and GaN (*squares*). Adapted from [774]

For a harmonic field $E \propto \exp(-\mathrm{i}\omega t)$ the complex conductivity ($\mathbf{j} = \sigma\mathbf{E} = nq\mathbf{v}$) is

$$\sigma = \frac{n\,e^2\,\tau}{m^*}\,\frac{1}{1-\mathrm{i}\,\omega\tau} = \frac{n\,e^2}{m^*}\,\frac{\mathrm{i}}{\omega+\mathrm{i}\gamma}\,, \tag{8.36}$$

with $\gamma = 1/\tau$ being the damping constant. Splitting into real and imaginary parts yields

$$\sigma = \frac{n\,e^2\,\tau}{m^*}\left(\frac{1}{1+\omega^2\tau^2} + \mathrm{i}\,\frac{\omega\tau}{1+\omega^2\tau^2}\right)\,. \tag{8.37}$$

For small frequencies ($\omega \to 0$) the dc conductivity from (8.5) is recovered, i.e. $\sigma = ne^2\tau/m^*$. For high frequencies ($\omega\tau \gg 1$)

$$\sigma = \frac{n\,e^2\,\tau}{m^*}\left(\frac{1}{\omega^2\tau^2} + \mathrm{i}\,\frac{1}{\omega\tau}\right)\,. \tag{8.38}$$

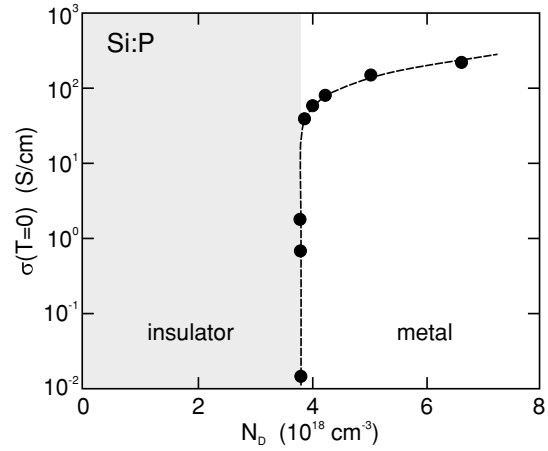

Fig. 8.21 Zero temperature conductivity of Si:P for various (donor) doping concentrations. Experimental data (*symbols*) and guide to the eye (*dashed line*). Adapted from [781]

8.6 Impurity Band Transport

In Sect. 7.5.7, the formation of an impurity band in the presence of high doping and overlap of impurity wave functions was discussed. The hopping (tunneling) transport of carriers from impurity to impurity leads to an additional transport channel termed 'impurity band conduction'[775–777]. The phenomenon has been found for many doped semiconductors, among them more recently GaAs:Mn [778] or Ga_2O_3:Sn [779] where at low temperatures a constant carrier concentration is attributed to the impurity band conduction effect.

The random distribution of dopants essentially makes a doped semiconductor a disordered system. The physics of electronic states in disordered systems has been reviewed in [780]. A metal–insulator transition is observed at a certain value of doping ($N_P = 3.8 \times 10^{18}\,\mathrm{cm}^{-3}$), as shown in Fig. 8.21 for Si:P [781]. For a certain value of disorder all states become localized (Anderson localization [782, 783], cmp. Sect. 8.9).

8.7 Polarons

In an ionic lattice, the electron polarizes the ions and causes a change of their equilibrium position. Depending on the severity of this effect, the lattice polarization leads to a modification of carrier (electron or hole) mass during band transport (Sect. 8.7.1) (*large* polarons) or the lattice deformation is so strong that it leads to carrier localization on the length scale of the lattice constant. Such self-trapped carriers are termed *small* polarons and discusssed in Sect. 8.7.1. Reviews are given in [784, 785].

8.7.1 Large Polarons

When the electron moves through the ionic crystal and must drag an ion displacement with it, the effective electron mass changes to the 'polaron mass' m_p,[4]

[4]For the calculation, many-particle theory and techniques are needed; the best solution is still given by Feynman's path integral calculation [786–788].

Table 8.5 Fröhlich coupling constant α for various semiconductors. Data from [165]

GaSb	GaAs	GaP	GaN	InSb	InAs	InP	InN
0.025	0.068	0.201	0.48	0.022	0.045	0.15	0.24
3C-SiC	ZnO	ZnS	ZnSe	ZnTe	CdS	CdSe	CdTe
0.26	1.19	0.63	0.43	0.33	0.51	0.46	0.35

$$m_\mathrm{p} = m^* \left(1 + \frac{\alpha}{6} + 0.025\,\alpha^2 + \cdots\right) , \tag{8.39}$$

for $\alpha \leq 1$, with m^* being the band mass as defined in Sect. 6.9.2 and α the Fröhlich coupling constant[5]

$$\alpha = \frac{1}{2}\,\frac{e^2}{\hbar}\sqrt{\frac{2\,m^*}{\hbar\omega_\mathrm{LO}}}\left(\frac{1}{\epsilon_\infty} - \frac{1}{\epsilon_0}\right) . \tag{8.40}$$

This process it called the *polaronic* effect and requires additional energy [786, 789]. Often, the polaron mass is given as $m_\mathrm{p} = m^*/(1 - \alpha/6)$ which is the result of perturbation theory [789] and an approximation to (8.39) for small α.

For large coupling parameter, $\alpha \gg 1$, the polaron mass is given by [787]

$$m_\mathrm{p} = m^*\,\frac{16}{81\,\pi^4}\,\alpha^4 . \tag{8.41}$$

The energy of the electron is lowered due to the interaction with the lattice. The energy E_0 for $k = 0$ is given, relative to the uncoupled case, by

$$E_0 = -\left(\alpha + 0.0098\,\alpha^2 + \cdots\right)\hbar\omega_0 , \quad \alpha \leq 1 \tag{8.42a}$$

$$E_0 = -\left(2.83 + 0.106\,\alpha^2\right)\hbar\omega_0 , \quad \alpha \gg 1 \tag{8.42b}$$

Numerical results are reported in [790].

Polarons in semiconductors are typically 'large' or Fröhlich-type polarons, i.e. the coupling constant is small (Table 8.5). The dressing with phonons (as the ion displacement is called in a quantum-mechanical picture) is then only a perturbative effect and the number of phonons per electron ($\approx\alpha/2$) is small. If α becomes large ($\alpha > 1$, $\alpha \sim 6$), as is the case for strongly ionic crystals such as alkali halides, the polaron becomes localized by the electron–phonon interaction[6] and hopping occurs infrequently from site to site.

8.7.2 Small Polarons

In a polaron, the charge carrier (electron or hole) sits in a potential well resulting from the ionic displacements it created. In some materials, the shape and strength of this potential well is such that the charge is confined to a volume of approximately one unit cell or less. In this case, the polaron is

[5] This constant is part of the matrix element in the Hamiltonian of the electron–phonon interaction and is related to the electric field created by LO phonons, as given in (9.29).

[6] One can think about it in the way that the electron strongly polarizes the lattice and digs itself a potential hole out of which it can no longer move.

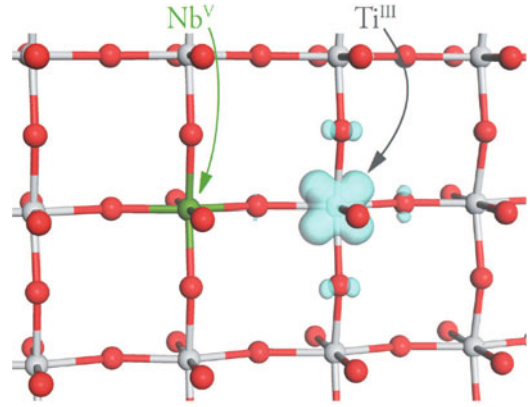

Fig. 8.22 Hole from Nb acceptor localized on Ti site (small polaron) in rutile TiO_2. Adapted from [793]

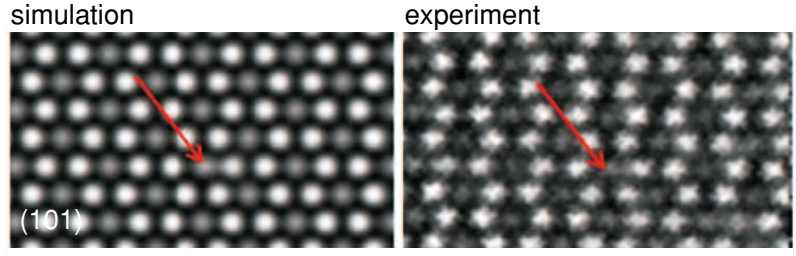

Fig. 8.23 Simulated and experimental TEM images of β-Ga_2O_3 in (101) projection. The *arrow* denotes the position of a polaron. Adapted from [792]

called a small polaron. An example of a hole polaron in rutile TiO_2:Nb is depicted in Fig. 8.22. In oxides often the hole from an acceptor is bound to oxygen, e.g. in $BaTiO_3$:Na, as reviewed in [791]. In Fig. 8.23 the lattice relaxation due to a hole bound to oxygen in the monoclinc unit cell of β-Ga_2O_3 is depicted directly using aberration corrected TEM. The bonding of the hole to the oxygen atom breaks the bond to a Ga atom which moves by 0.1 nm from its equilibrium position [792].

A proper theoretical analysis of a small polaron requires ab initio techniques that account for the motion of each atom in the few unit cells nearest the electron.[7]

The transport of small polarons occurs generally via thermally-activated hopping (cmp. Sect. 8.8). Under certain conditions the following mobilities for drift and Hall effect have been given [784]:

$$\mu_\mathrm{d} \propto T^{-1} \exp(-W/(2kT)) \,, \tag{8.43}$$

$$\mu_\mathrm{H} \propto T^{-1/2} \exp(-W/(6kT)) \,, \tag{8.44}$$

W being the polaron binding energy. Generally, materials with small polaron transport exhibit high carrier density, often due to structural defects, and low mobility.

8.8 Hopping Transport

Disordered solids such as amorphous semiconductors, films containing quantum dots or material with many defects are characterized by a large density of localized states which can form band tails or a large density of states within the band gap. Hopping conduction is the tunneling between localized states and has been treated with various models [795–797].

[7] This paragraph has been taken from the concise tutorial by S.J.F. Byrnes [794].

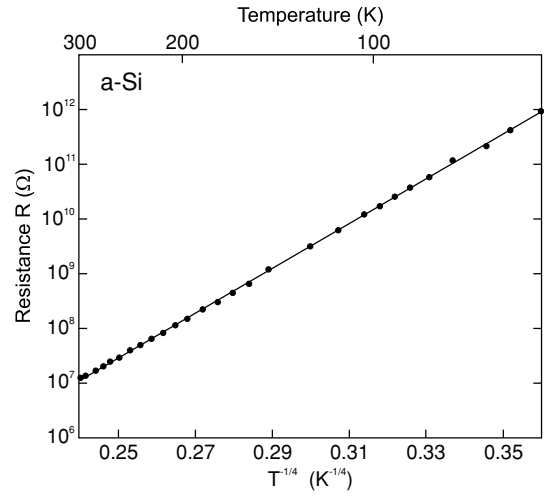

Fig. 8.24 Temperature dependence of the planar resistance for Si films deposited at room temperature. *Solid line* is linear fit with $T_0 = 8 \times 10^7$ K according to (8.45) ($s = 1/4$). Adapted from [798]

A commonly observed phenomenon is the variable range hopping with a conductivity given by

$$\sigma = \sigma_0 \exp\left(-(T_0/T)^s\right) \tag{8.45}$$

with $s = 1/4$. Such law is fulfilled for amorphous silicon (Fig. 8.24). Mott has derived [799] the exponent $s = 1/4$ using the following argument: The probability p to hop from one localized site to another is proportional to

$$p \propto \exp(-2\alpha R - W/kT) \; . \tag{8.46}$$

The first term stems from the probability to find the electron within radius R from its initial site, α being the decay constant of its wave function, $\Psi(r) \propto \exp(-\alpha r)$. The second term is the Boltzmann factor for bridging the energy mismatch W between localized states with a phonon-assisted process, assuming a low temperature limit ($kT \ll W$). There is a trade-off between hopping to levels closer in energy but spatially further away (on average), preferred at low temperature and the hopping to energy levels with larger W but spatially closer at higher temperatures. Thus the hopping range changes with temperature, giving the mechanism its name.

$D(E_\mathrm{F})$ shall be the (constant) density of localized states around the Fermi level. Within a radius R, there is on average one state of energy between 0 and $W(R)$ when (for three-dimensional bulk material)

$$W(R) = \frac{1}{D(E_\mathrm{F})\,(4\pi/3)\,R^3} \; . \tag{8.47}$$

Substituting (8.47) in (8.45) and searching for the maximum yields the most probable hopping distance

$$R \approx (\alpha\, kT\, D(E_\mathrm{F}))^{-1/4} \; , \tag{8.48}$$

showing again, the varying range of hopping with temperature. Thus we find for T_0 in (8.45),

$$T_0 \approx \frac{\alpha^3}{k\, D(E_\mathrm{F})} \; . \tag{8.49}$$

Other types of hopping mechanisms are the Efros–Shklovskii variable range hopping ($s = 1/2$), emerging for an energy dependent density of states $D(E) \propto (E - E_\mathrm{F})^2$ due to Coulomb interaction between hopping sites [800], or the next neighbor hopping ($s = 1$).

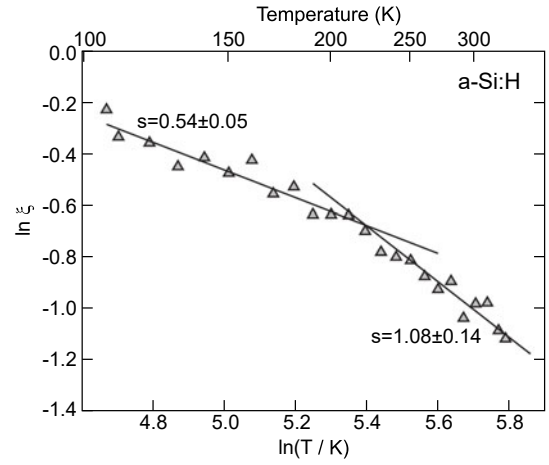

Fig. 8.25 Temperature dependence of conductivity of a hydrogenated amorphous Si thin film, plotted as $\ln \xi$ vs. $\ln T$ (8.50). *Solid lines* are linear fits for constant s according to (8.50) as labelled. Adapted from [801]

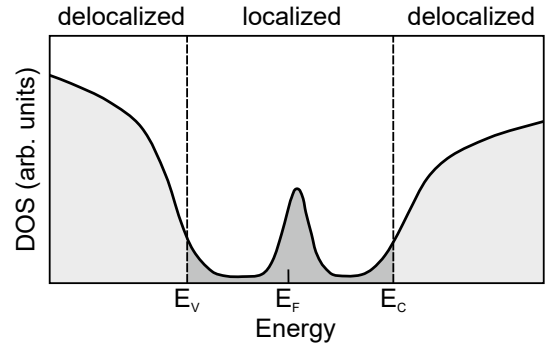

Fig. 8.26 Schematic density of states of amorphous semiconductor with band tails and deep levels. The localized (delocalized) states are shown in *dark* (*light*) *grey*. The mobility edges for electrons and holes are indicated by *dashed lines*

From (8.45) one can rewrite for $\xi = \mathrm{d}(\ln \sigma(T))/\mathrm{d} \ln T$,

$$\ln \xi = \ln s + s \ln T_0 - s \ln T \ . \tag{8.50}$$

Thus in a plot of $\ln \xi$ vs. $\ln T$, the exponent s can be determined from the slope. As can be seen in Fig. 8.25, for the conductivity of a hydrogenated amorphous silicon thin film the transition of hopping mechanism from Efros–Shklovskii variable range hopping ($s \approx 1/2$) to next neighbor hopping ($s \approx 1$) takes place around $T = 220\,\mathrm{K}$, as discussed in detail in [801].

8.9 Transport in Amorphous Semiconductors

Many models have been presented for the carrier transport in amorphous semiconductors [203]. The most important concept is that of a *mobility edge*, an energy separating localized from delocalized states [547, 548, 802]. This is schematically depicted in Fig. 8.26. The carrier transport between localized states is mediated via tunneling (hopping) which has been described in the previous section (Sect. 8.8). The localization of carriers in random lattices has been treated by Anderson [782] and reviewed in [780]. If the degree of disorder surpasses a certain value, diffusion is suppressed (at $T = 0$) and conductivity vanishes altogether (Anderson metal–insulator transition).

The transport in delocalized states is similar to band transport. The conductivity (for electrons) is given as

$$\sigma = -e \int_{E_C}^{\infty} D_e(E)\, \mu_e(E)\, f_e(E)\, \mathrm{d}E \ . \tag{8.51}$$

If the Fermi energy is close to the middle of the gap, pinned to deep states, the Fermi-Dirac distribution can be replaced by the Boltzmann factor. Assuming a constant density of states and mobility for the delocalized states,

$$\sigma = -e\, D_e(E_C)\, \mu_e(E_C)\, kT\, \exp\left(\frac{E_C - E_F}{kT}\right) \ . \tag{8.52}$$

Charge carriers from localized states in the tails can be thermally excited into delocalized states and contribute to conductivity (thermally activated hopping). The mobility then contains an exponential thermal activation term [203].

8.10 Ionic Transport

Ionic transport is the movement of ions upon application of a voltage. Here, we discuss only solid electrolytes. The transport can include the motion of one or several of the constituents of the lattice and the transport of other ions (e.g. hydrogen ions (protons), oxygen ions) through the crystal. Related to this is the diffusive ionic movement of impurities or defects through the crystal (cmp. Sect. 4.2.3). Ionic conduction of the lattice constituents under dc voltage will eventually destroy the crystal.

In typical semiconductors like silicon or gallium arsenide, the conductivity is entirely due to electronic conduction. A typical solid electrolyte is zirconia (ZrO_2) doped with yttria, so-called yttria-stabilized zirconia (YSZ) that takes on a cubic fluorite lattice (see Sect. 3.4.8). It can conduct oxygen ions via the mobility of oxygen vacancies for use in solid-oxide fuel cells (SOFC) [803]. The conductivity is about 0.01 S/cm at a temperature around 1000 K, almost entirely due to ionic transport. Doping with calcium oxide results in an oxygen conductor that is used in oxygen sensors in automobiles (lambda sensor). The ionic conductivity can be significantly increased, compared to bulk material, along interfaces [804, 805].

Other typical solid electrolytes are copper iodide (CuI) [568] and also AgI. In the high temperature cubic phase (α-polymorph), the iodide ions form a fairly rigid cubic framework and the metal ions are mobile; the copper diffusion pathways have been discussed [806, 807]. The temperature dependence of conductivity of CuI is shown in Fig. 8.27.

8.11 Diffusion

A gradient of a particle concentration n leads to a particle current proportional to $-\nabla n$. This diffusion law (Fick's law) corresponds microscopically to a random walk. The gradients of the semiconductor carrier densities ∇n or ∇p thus lead to electron and hole currents, respectively:

$$\mathbf{j}_n = e D_n \nabla n \tag{8.53a}$$

$$\mathbf{j}_p = -e D_p \nabla p \ . \tag{8.53b}$$

The coefficients D_n and D_p are called the electron and hole diffusion coefficient, respectively. Thus the total electron and hole currents in the presence of an electric field $\mathbf{E}$ and diffusion are

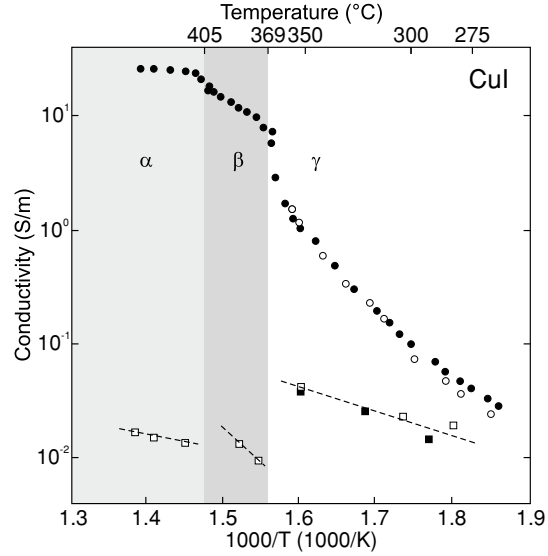

Fig. 8.27 Total (*circles*) and electronic (*squares*) conductivity of CuI coexisting with copper. *Filled* (*empty*) symbols refer to polycrystalline (single crystal) samples. The different structural phases (α (cubic), β (wurtzite), γ (zincblende)) are indicated by shaded areas as labeled. *Dashed lines* are guides to the eye. Adapted from [808]

$$\mathbf{j}_\mathrm{n} = -e\mu_\mathrm{n} n\,\mathbf{E} + eD_\mathrm{n}\,\nabla n \tag{8.54a}$$

$$\mathbf{j}_\mathrm{p} = e\mu_\mathrm{p} p\,\mathbf{E} - eD_\mathrm{p}\,\nabla p\ . \tag{8.54b}$$

This relation can also be deduced more generally from the gradient of the Fermi level as

$$\mathbf{j}_\mathrm{n} = -e\mu_\mathrm{n} n\,\mathbf{E} - n\mu_\mathrm{n}\,\nabla E_\mathrm{F} \tag{8.55a}$$

$$\mathbf{j}_\mathrm{p} = e\mu_\mathrm{p} p\,\mathbf{E} - p\mu_\mathrm{p}\,\nabla E_\mathrm{F}\ . \tag{8.55b}$$

Using (7.6) and (7.7) for the concentrations (valid also in the case of degeneracy) and using $\mathrm{d}F_j(x)/\mathrm{d}x = F_{j-1}(x)$ we obtain

$$\mathbf{j}_\mathrm{n} = -e\mu_\mathrm{n} n\,\mathbf{E} - kT\mu_\mathrm{n}\frac{F_{1/2}(\eta)}{F_{-1/2}(\eta)}\,\nabla n \tag{8.56a}$$

$$\mathbf{j}_\mathrm{p} = e\mu_\mathrm{p} p\,\mathbf{E} - kT\mu_\mathrm{p}\frac{F_{1/2}(\zeta)}{F_{-1/2}(\zeta)}\,\nabla p\ , \tag{8.56b}$$

with $\eta = (E_\mathrm{F} - E_\mathrm{C})/kT$ and $\zeta = -(E_\mathrm{F} - E_\mathrm{V})/kT$. If the pre-factor of the density gradient is identified as the diffusion coefficient we find the (generalized) so-called 'Einstein relations' ($\beta = e/(kT)$) [608, 809]:

$$D_\mathrm{n} = -\beta^{-1}\mu_\mathrm{n}\frac{F_{1/2}(\eta)}{F_{-1/2}(\eta)} \tag{8.57a}$$

$$D_\mathrm{p} = \beta^{-1}\mu_\mathrm{p}\frac{F_{1/2}(\zeta)}{F_{-1/2}(\zeta)}\ . \tag{8.57b}$$

The effect of non-parabolicity has been included in [810].

Useful analytical approximations have been discussed in [811]. We note that, e.g., (8.57a) can also be written as [812, 813]

$$D_\mathrm{n} = -\beta^{-1}\mu_\mathrm{n}\, n\,\frac{\partial\eta}{\partial n}\ . \tag{8.58}$$

In the case of nondegeneracy, i.e. when the Fermi level is within the band gap and not closer than about $4kT$ to the band edges, $\eta = \ln(n/N_\mathrm{C})$. Then $\partial\eta/\partial n = 1/n$, and the equation simplifies to $D = (kT/q)\mu$, i.e. the 'regular' Einstein-relations,

$$D_\mathrm{n} = -\beta^{-1}\mu_\mathrm{n} \tag{8.59a}$$
$$D_\mathrm{p} = \beta^{-1}\mu_\mathrm{p}\ . \tag{8.59b}$$

In this case, (8.54a,b) read

$$\mathbf{j}_\mathrm{n} = -e\mu_\mathrm{n} n\,\mathbf{E} - kT\mu_n\,\nabla n \tag{8.60a}$$
$$\mathbf{j}_\mathrm{p} = e\mu_\mathrm{p} p\,\mathbf{E} - kT\mu_p\,\nabla p\ . \tag{8.60b}$$

We recall that both diffusion coefficients are positive numbers, since μ_n is negative. Generally, the diffusion coefficient depends on the density. A Taylor series of the Fermi integral yields

$$D_\mathrm{n} = -\beta^{-1}\mu_\mathrm{n}\left[1 + 0.35355\left(\frac{n}{N_\mathrm{C}}\right) - 9.9\times10^{-3}\left(\frac{n}{N_\mathrm{C}}\right)^2 + \cdots\right]\ . \tag{8.61}$$

8.12 Continuity Equation

The balance equation for the charge is called the continuity equation. The temporal change of the charge in a volume element is given by the divergence of the current and any source (generation rate G), e.g. an external excitation, or drain (recombination rate U). Details about recombination mechanisms are discussed in Chap. 10. Thus, we have

$$\frac{\partial n}{\partial t} = G_\mathrm{n} - U_\mathrm{n} - \frac{1}{q}\,\nabla\cdot\mathbf{j}_\mathrm{n} = G_\mathrm{n} - U_\mathrm{n} + \frac{1}{e}\,\nabla\cdot\mathbf{j}_\mathrm{n} \tag{8.62a}$$
$$\frac{\partial p}{\partial t} = G_\mathrm{p} - U_\mathrm{p} - \frac{1}{e}\,\nabla\cdot\mathbf{j}_\mathrm{p}\ . \tag{8.62b}$$

In the case of nondegeneracy we find, using (8.54ab)

$$\frac{\partial n}{\partial t} = G_\mathrm{n} - U_\mathrm{n} - \mu_\mathrm{n} n\,\nabla\cdot\mathbf{E} - \mu_\mathrm{n}\,\mathbf{E}\,\nabla n + D_\mathrm{n}\Delta n \tag{8.63a}$$
$$\frac{\partial p}{\partial t} = G_\mathrm{p} - U_\mathrm{p} - \mu_\mathrm{p} p\,\nabla\cdot\mathbf{E} - \mu_\mathrm{p}\,\mathbf{E}\,\nabla p + D_\mathrm{p}\Delta p\ . \tag{8.63b}$$

In the case of zero electric field these read

$$\frac{\partial n}{\partial t} = G_\mathrm{n} - U_\mathrm{n} + D_\mathrm{n}\Delta n \tag{8.64a}$$
$$\frac{\partial p}{\partial t} = G_\mathrm{p} - U_\mathrm{p} + D_\mathrm{p}\Delta p\ , \tag{8.64b}$$

and if the stationary case also applies:

$$D_{\mathrm{n}}\Delta n = -G_{\mathrm{n}} + U_{\mathrm{n}} \tag{8.65a}$$
$$D_{\mathrm{p}}\Delta p = -G_{\mathrm{p}} + U_{\mathrm{p}} \,. \tag{8.65b}$$

8.13 Heat Conduction

We consider here the heat transport [814] due to a temperature gradient. The heat flow $\mathbf{q}$, i.e. energy per unit area per time in the direction $\hat{\mathbf{q}}$, is proportional to the local gradient of temperature. The proportionality constant κ is called, heat conductivity,

$$\mathbf{q} = -\kappa\,\nabla T \,. \tag{8.66}$$

In crystals, the heat conductivity can depend on the direction and thus κ is generally a tensor of rank 2. In the following, κ will be considered as a scalar quantity. The quite generally valid Wiedemann–Franz law connects the thermal and electrical conductivities

$$\kappa = \frac{\pi^2}{3}\left(\frac{k}{e}\right)^2 T\sigma \,. \tag{8.67}$$

The balance (continuity) equation for the heat energy Q is

$$\nabla\cdot\mathbf{q} = -\frac{\partial Q}{\partial t} = -\rho\,C\,\frac{\partial T}{\partial t} + A \,, \tag{8.68}$$

where ρ denotes the density of the solid and C the heat capacity. A denotes a source or drain of heat, e.g. an external excitation. Combining (8.66) and (8.68), we obtain the equation for heat conductivity

$$\Delta T = \frac{\rho\,C}{\kappa}\,\frac{\partial T}{\partial t} - \frac{A}{\kappa} \,, \tag{8.69}$$

which simply reads $\Delta T = 0$ for a stationary situation without sources.

The random mixture of various atoms in natural elements represents a perturbation of the perfectly periodic lattice. Since the mass of the nuclei varies, in particular lattice vibrations will be perturbed. Thus we expect an effect on the heat conductivity. In Fig. 8.28, the thermal conductivity of crystals from natural Ge and enriched ^{74}Ge are compared [815], the latter having, as expected, the higher heat conductivity, i.e. less scattering. The T^3-dependence of the heat conductivity at low temperature has been attributed to scattering of phonons at the sample boundary [816]. The thermal conductivity of isotopically pure ^{28}Si thin films has been measured to be 60% greater than natural silicon at room temperature and at least 40% greater at 100°C, a typical chip operating temperature [817, 818].

8.14 Coupled Heat and Charge Transport

The standard effect of coupled charge and heat transport is that a current heats its conductor via Joule heating. However, more intricate use of thermoelectric effects can also be employed to cool certain areas of a device. For further details see [819, 820].

For the analysis of coupled charge and heat transport we first sum the electric field and the concentration gradient to a new field $\hat{\mathbf{E}} = \mathbf{E} + \nabla E_{\mathrm{F}}/e$. Then, the heat flow and charge current are

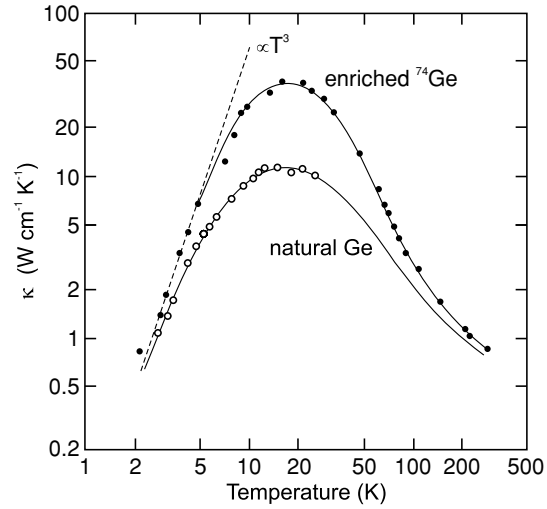

Fig. 8.28 Thermal conductivity of Ge vs. temperature. The enriched Ge consists of 96% ^{74}Ge while the natural isotope mix is 20% ^{70}Ge, 27% ^{72}Ge, 8% ^{73}Ge, 27% ^{74}Ge and 8% ^{76}Ge. The *dashed line* shows a $\kappa \propto T^3$ dependence at low temperatures. Adapted from [815]

$$\mathbf{j} = \sigma \hat{\mathbf{E}} + L \nabla T \tag{8.70}$$

$$\mathbf{q} = M \hat{\mathbf{E}} + N \nabla T \ , \tag{8.71}$$

where $\hat{\mathbf{E}}$ and ∇T are the stimulators for the currents. From the experimental point of view there is interest to express the equations in $\mathbf{j}$ and ∇T since these quantities are measurable. With new coefficients they read

$$\hat{\mathbf{E}} = \rho \mathbf{j} + S \nabla T \tag{8.72}$$

$$\mathbf{q} = \Pi \mathbf{j} - \kappa \nabla T \ , \tag{8.73}$$

where ρ, S and Π are the specific resistance, thermoelectric power and Peltier coefficient (transported energy per unit charge), respectively. The relations with the coefficients σ, L, M, and N are given by

$$\rho = \frac{1}{\sigma} \tag{8.74a}$$

$$S = -\frac{L}{\sigma} \tag{8.74b}$$

$$\Pi = \frac{M}{\sigma} \tag{8.74c}$$

$$\kappa = \frac{ML}{\sigma} - N \ . \tag{8.74d}$$

8.14.1 Thermopower and Seebeck Effect

A semiconductor shall have two ends at different temperatures T_2 and T_1 and a temperature gradient in between in an open circuit, i.e. $\mathbf{j} = 0$. Then a field $\hat{\mathbf{E}} = S \nabla T$ and a voltage $U = S/(T_2 - T_1)$ will arise. This effect is called the thermoelectric or Seebeck effect. S is termed the Seebeck coefficient or the *thermoelectric power*, often also denoted as Q in the literature. The voltage can be measured and used to determine the temperature at one end if the temperature at the other end is known, forming

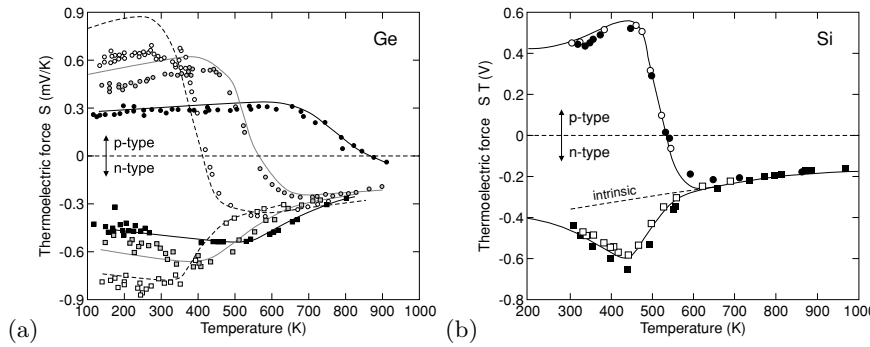

Fig. 8.29 **a** Seebeck coefficient S for n- and p-doped germanium. Experimental data (*symbols*) and theory (*lines*). $N_A - N_D$ is $5.7 \times 10^{15}\,\mathrm{cm}^{-3}$ (*white circles*), $1.7 \times 10^{17}\,\mathrm{cm}^{-3}$ (*grey*) and $7.2 \times 10^{18}\,\mathrm{cm}^{-3}$ (*black*); $N_D - N_A$ is $3.3 \times 10^{15}\,\mathrm{cm}^{-3}$ (*white squares*), $1.1 \times 10^{17}\,\mathrm{cm}^{-3}$ (*grey*) and $6.2 \times 10^{17}\,\mathrm{cm}^{-3}$ (*black*). Adapted from [821]. **b** Thermoelectric force Π of lowly doped n- and p-silicon as a function of temperature. *Solid line* is from simple model calculation and *symbols* represent data from silicon samples with the approximate doping of *circles*: $1 \times 10^{15}\,\mathrm{cm}^{-3}$ B, $2 \times 10^{14}\,\mathrm{cm}^{-3}$ donors, *squares*: $4 \times 10^{14}\,\mathrm{cm}^{-3}$ P, $9 \times 10^{13}\,\mathrm{cm}^{-3}$ acceptors. Adapted from [822]

a thermometer. The Seebeck coefficient is positive if the electric field is in the same direction as the temperature gradient.

A famous relation from irreversible thermodynamics connects it to the Peltier coefficient via

$$S = \frac{\Pi}{T} \,. \tag{8.75}$$

The Seebeck coefficient is related to the energy transport by charge carriers. The heat (energy) flow is obviously from the hot to the cold end (assuming here $T_2 > T_1$), so is the flow of charge carriers. In a simple picture, if the energy is carried by (hot) holes, the current (by definition the direction of positive charge carriers) is from the hot to the cold end ($2 \to 1$); if the energy flow is carried by electrons, the current flows from the cold to the hot end ($1 \to 2$). Accordingly, energy transport by electrons and holes gives rise to different signs of the thermoelectric coefficient (Fig. 8.29). If the cold (unheated) substrate is grounded, the sign of the voltage at a hot solder tip pressed (carefully) on the surface of the semiconductor yields the conductivity type, n-type (p-type) for a negative (positive) voltage.

However, the semiconductor should not be heated so strongly that intrinsic conduction arises. In this case the conductivity and the thermoelectric power is determined by the carrier type with the higher mobility; typically, and for the case of silicon shown in Fig. 8.29, these are the electrons thus yielding a negative Seebeck coefficient in the intrinsic regime.

For band conduction the thermopower (J.29) is given for electrons (S_n) and holes (S_p) by [823] (for a derivation see Appendix J.4)

$$S_n = -\frac{k}{e}\left(\frac{E_C - E_F}{kT} + A_C\right) \tag{8.76a}$$

$$S_p = \frac{k}{e}\left(\frac{E_F - E_V}{kT} + A_V\right) \,, \tag{8.76b}$$

where A_i are constants (J.31a) depending on the energy dependence of the density of states and the mobility. The sign of the thermopower tells whether conduction takes place above (negative sign) or below (positive sign) the Fermi level.

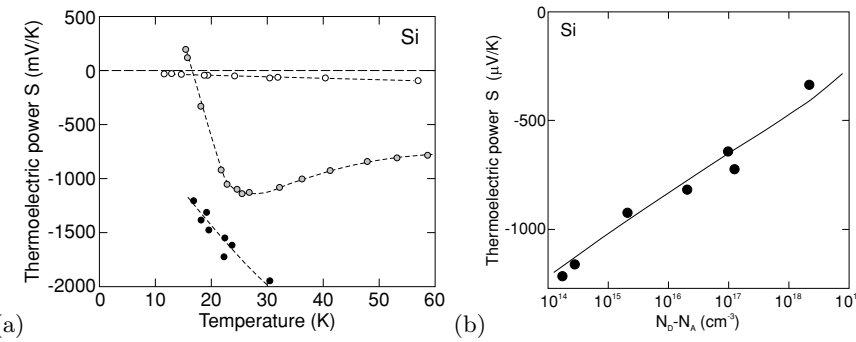

Fig. 8.30 **a** Thermoelectric power S of highly doped n-type silicon as a function of temperature. *Circles* are experimental data and *dashed lines* guides to the eye. The approximate doping of the samples is *white*: $2.7 \times 10^{19}\,\mathrm{cm}^{-3}$ As, *grey*: $2.2 \times 10^{18}\,\mathrm{cm}^{-3}$ As, *black*: $1.1 \times 10^{18}\,\mathrm{cm}^{-3}$ As and $1.0 \times 10^{18}\,\mathrm{cm}^{-3}$ B with $N_\mathrm{D} - N_\mathrm{D} = 1.25 \times 10^{17}\,\mathrm{cm}^{-3}$ at room temperature. Adapted from [822]. **b** Thermopower of doped n-type silicon at room temperature as a function of doping concentration. Experimental data (*symbols*) from [822] and theory (*solid line*) from [824]

If the Fermi level is fixed and both electrons and holes contribute (two-band conduction), the thermopower is (evaluating (J.32), $b = \sigma_n/\sigma_p$ and the gap center energy $E_\mathrm{M} = (E_\mathrm{C} - E_\mathrm{V})/2$)

$$S = \frac{k}{e}\left(\frac{1-b}{1+b}\,\frac{E_\mathrm{g}}{2\,kT} + \frac{E_\mathrm{F} - E_\mathrm{M}}{kT} + \frac{A_\mathrm{V} - b\,A_\mathrm{C}}{1+b}\right) . \tag{8.77}$$

In the case of intrinsic conduction from (7.18) $E_\mathrm{F} - E_\mathrm{M} = (kT/2)\ln(N_\mathrm{V}/N_\mathrm{C})$.

The thermoelectric power from some highly doped n-type silicon samples is depicted in Fig. 8.30a. At low temperature the (low) conductivity is due to conduction in a donor impurity band (cmp. Sect. 7.5.7). At high compensation of about 90% (grey data points in Fig. 8.30a), the band is only 10% filled and acts like a valence band with positive thermopower at sufficiently low temperature when the free carrier density is small. Without compensation, the thermopower remains negative since the almost completely filled impurity band acts conduction band like. The dependence of thermopower on doping has been simulated in [824] (Fig. 8.30); the decrease with increasing doping is mostly attributed to the reduced mobility due to ionized impurity scattering. The increase of thermopower at low temperatures is due to the *phonon-drag* effect which is discussed for the samples from [822] in [825].

As a figure of merit for the production of thermoelectric power the ZT-value is used, $ZT = \sigma\, S^2\, T/\kappa$.

8.14.2 Peltier Effect

In a semiconductor with a temperature difference at its ends a current flow will be allowed now (short circuit). The current leads via the charge transport also to a heat (or energy) transport. This effect is called the Peltier effect. The Peltier coefficient is negative (positive) for electrons (holes). The total amount of energy P that is transported consists of the generation term and the loss due to transport:

$$P = \mathbf{j}\cdot\hat{\mathbf{E}} - \nabla\cdot\mathbf{q}\ . \tag{8.78}$$

With (8.72) and (8.73) we find

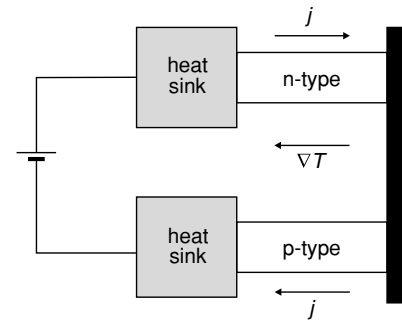

Fig. 8.31 Schematic Peltier cooler. The heat sinks (*grey*) and the cold junction (*black*) on the left are metals that make ohmic contacts with the semiconductors. The current flow is such that electrons move through the n-type semiconductor from right to left

$$P = \frac{\mathbf{j}\cdot\mathbf{j}}{\sigma} + S\,\mathbf{j}\cdot\nabla T - \Pi\,\nabla\cdot\mathbf{q} + \kappa\,\Delta T\ . \tag{8.79}$$

The first term is Joule heating, the second term is Thomson heating. The third exists only when carriers are generated or when they recombine. The fourth term is the heat conduction. In the Thomson term $S\,\mathbf{j}\cdot\nabla T$ heat is generated in an n-type semiconductor if $\mathbf{j}$ and ∇T are in the same direction. This means that electrons that move from the hotter to the colder part transfer energy to the lattice. The effect can be used to construct a thermoelectric cooler, as shown in Fig. 8.31, that generates a temperature difference due to a current flow. For optimal performance σ should be large to prevent excess Joule heating and κ should be small such that the generated temperature difference is not rapidly equalized.

Chapter 9
Optical Properties

Do not Bodies and Light act mutually upon one another.

Sir I. Newton, 1704 [826]

Abstract After introduction of the complex dielectric function, reflection, diffraction are briefly discussed. The focus lies on absorption mechanisms; several transition types (direct and indirect band-band transitions, impurity-related transitions, lattice absorption) are discussed including the effects of excitons, polaritons and high carrier density. Also the various effects of the presence of free carriers are given.

9.1 Spectral Regions and Overview

The interaction of semiconductors with light is of decisive importance for photonic and optoelectronic devices as well as for the characterization of semiconductor properties. When light hits a semiconductor, reflection, transmission and absorption are considered, as for any dielectric material. The response of the semiconductor largely depends on the photon energy (or wavelength) of the light and various processes contribute to the dielectric function.

An overview of the electromagnetic spectrum in the optical range is given in Table 9.1. The energy and wavelength of a photon are related by[1] $E = h\nu = hc/\lambda$, i.e.

$$E\ [\mathrm{eV}] = \frac{1240}{\lambda\ [\mathrm{nm}]}\ . \tag{9.1}$$

In the infrared regime, energy is often measured in wave numbers (cm^{-1}) for which the conversion $1\,\mathrm{meV} = 8.056\,\mathrm{cm}^{-1}$ holds.

[1] The more exact numerical value in (9.1) is 1239.84.

M. Grundmann, *The Physics of Semiconductors*, Graduate Texts in Physics,
https://doi.org/10.1007/978-3-030-51569-0_9

Table 9.1 Spectral ranges with relevance to semiconductor optical properties

Range		Wavelengths	Energies
Deep ultraviolet	DUV	<250 nm	>5 eV
Ultraviolet	UV	250–400 nm	3–5 eV
Visible	VIS	400–800 nm	1.6–3 eV
Near infrared	NIR	800 nm–2 μm	0.6–1.6 eV
Mid-infrared	MIR	2–20 μm	60 meV–0.6 eV
Far infrared	FIR	20–80 μm	1.6–60 meV
THz region	THz	>80 μm	<1.6 meV

9.2 Complex Dielectric Function

The dielectric function (DF) ϵ fulfills the relation between the displacement field **D**, the polarization **P** and the electric field **E**,

$$\mathbf{D} = \epsilon_0 \mathbf{E} + \mathbf{P} = \epsilon_0 \epsilon \mathbf{E} , \tag{9.2}$$

and is generally a tensor of rank 2 since **D** and **E** must not be collinear. For cubic materials, the DF is isotropic and can be described with a (complex) scalar ϵ. Less symmetric crystals are optically anisotropic and the DF must be used in tensor form. Also, external fields can induce optical anisotropy in an otherwise isotropic material as discussed in Sect. 15.2.2 for magnetic fields or has been observed for mechanical strain fields. The general form of the dielectric function tensor for various crystal symmetries is compiled in Table 9.2.

In most cases in the following, ϵ will be used as scalar (isotropic case). The dielectric function is frequency dependent $\epsilon(\omega)$ due to the various oscillators playing a role and decreases (non-monotonically) from its static value (for $\omega = 0$) to 1 for $\omega \to \infty$. Major influence on the DF stems from (optical)

Table 9.2 General form of the tensor form of the dielectric function for the seven crystallographic systems

Crystal system	Optical symmetry	ϵ	Examples
Cubic	Isotropic	$\begin{pmatrix} a & 0 & 0 \\ 0 & a & 0 \\ 0 & 0 & a \end{pmatrix}$	Si, GaAs, MgO, ZnSe, CuI
tetragonal hexagonal trigonal	uniaxial	$\begin{pmatrix} a & 0 & 0 \\ 0 & a & 0 \\ 0 & 0 & c \end{pmatrix}$	$CuGaSe_2$, GaN, ZnO, Bi_2Se_3
orthorhombic	biaxial	$\begin{pmatrix} a & 0 & 0 \\ 0 & b & 0 \\ 0 & 0 & c \end{pmatrix}$	κ-Ga_2O_3, Sb_2Se_3
monoclinic	biaxial	$\begin{pmatrix} a & 0 & d \\ 0 & b & 0 \\ d & 0 & c \end{pmatrix}$	β-Ga_2O_3, anthracene
triclinic	biaxial	$\begin{pmatrix} a & d & e \\ d & b & f \\ e & f & c \end{pmatrix}$	$K_2Cr_2O_7$, tetracene

lattice vibrations (Sect. 9.5) and transitions within the electronic band structure (Sect. 9.6). In some cases also its **k**-dependence is important, known as 'spatial dispersion' (cmp. Sect. 9.7.8).

An optic axis in the transparency regime (all tensor elements of $\boldsymbol{\epsilon} \in \mathbb{R}$) is the direction in which the speed of light or the index of refraction is independent of polarization. Uniaxial (biaxial) materials have one (two) of such axes. The anisotropy of the index of refraction and its polarization dependence must be taken into account when light propagation is considered in birefringent semiconductors, e.g. for Raman spectroscopy [827], unless the propagation is along an optic axis.

The dielectric function is generally complex and written as (scalar)

$$\epsilon = \epsilon' + \mathrm{i}\,\epsilon'' = \epsilon_1 + \mathrm{i}\,\epsilon_2 \ . \tag{9.3}$$

The real (ϵ' or ϵ_1) and imaginary (ϵ'' or ϵ_2) part of the dielectric function are related to each other via the Kramers-Kronig relations (Appendix C).

The complex index of refraction n^* is

$$n^* = \sqrt{\epsilon} = n_\mathrm{r} + \mathrm{i}\,\kappa \ . \tag{9.4}$$

From $n^{*2} = \epsilon$ follows

$$\epsilon' = n_\mathrm{r}^2 - \kappa^2 \tag{9.5}$$

$$\epsilon'' = 2\,n_\mathrm{r}\,\kappa \ . \tag{9.6}$$

From $\epsilon\,\bar{\epsilon} = (n_\mathrm{r}^2 + \kappa^2)^2$ and (9.5) follows

$$n_\mathrm{r}^2 = \frac{\epsilon' + \sqrt{\epsilon'^{\,2} + \epsilon''^{\,2}}}{2} \tag{9.7}$$

$$\kappa = \frac{\epsilon''}{2\,n_\mathrm{r}} \ . \tag{9.8}$$

The real part of the complex index of refraction n_r is responsible for the dispersion, the imaginary part κ is named extinction coefficient and is related to the absorption coefficient for a plane wave (damping of the intensity $\propto \mathbf{E}^2$) by

$$\alpha = 2\,\frac{\omega}{c}\,\kappa = \frac{4\pi}{\lambda}\,\kappa = 2\,k\,\kappa \ . \tag{9.9}$$

Here, k and λ denote the respective values in vacuum. Through the Kramers-Kronig relations (Appendix C), *birefringence*, i.e. the orientational dependence of the index of refraction, is thus automatically related to *dichroism*, i.e. the orientational dependence of the absorption coefficient.

As an example, in Fig. 9.1 the dielectric function of GaAs is shown in the vicinity of the band edge and above. Since GaAs is cubic, the dielectric function at each photon energy can represented by a single complex number. The tensor character of the dielectric function is demonstrated in Fig. 9.2a where the four independent tensor elements for (monoclinic) β-Ga_2O_3 are depicted [828]. The contributions of various dipole oscillators (strength and orientation) to the dielectric function can be analyzed from these data [829].

In the absorption regime, for biaxial crystals the two optic axes split into four singular optic axes [830] as visualized for β-Ga_2O_3 in Fig. 9.2b [831]. It should be noted that optical activity [832] is not considered in the following.

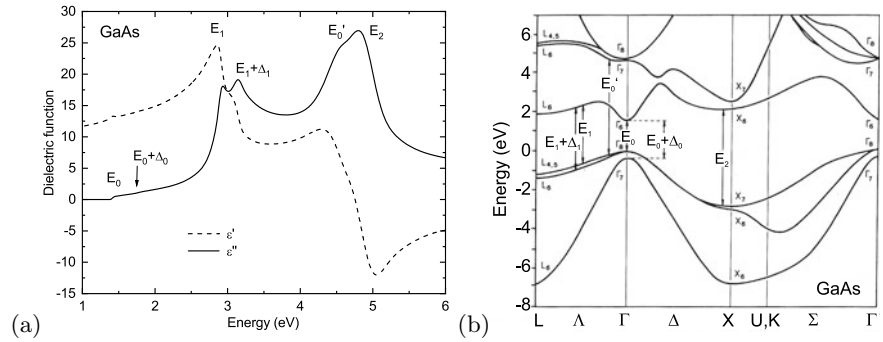

Fig. 9.1 **a** Complex dielectric function of GaAs at room temperature *dashed* (*solid*) *line*: real (imaginary) part of dielectric constant. Peak labels relate to transitions shown in part **b**. **b** Band structure of GaAs with fundamental band gap transition (E_0) and higher transitions ($E_0 + \Delta_0$, E_1, $E_1 + \Delta_1$, E_0', and E_2) as indicated

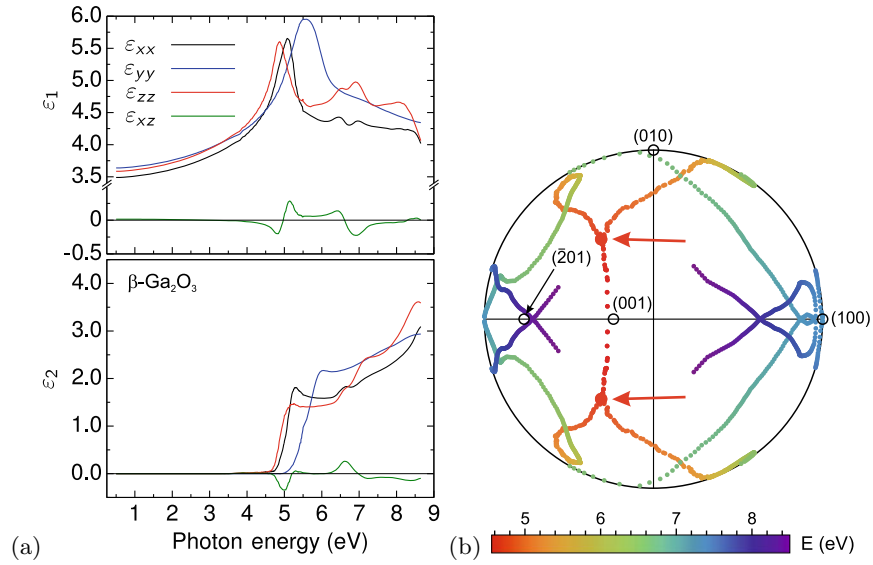

Fig. 9.2 **a** Experimental (generalized spectroscopic ellipsometry) tensor elements of the complex dielectric function of β-Ga_2O_3 at room temperature. Adapted from [828]. **b** Stereographic projection of the angular orientation of the optic and singular optic axes of β-Ga_2O_3. Some crystallographic orientations are indicated. The *color* refers to the photon energy. The splitting of the two optic axes into four singular optic axes at the onset of absorption is denoted by two *red arrows*. Adapted from [831]

9.3 Reflection and Diffraction

From Maxwell's equations and the boundary conditions at a planar interface between two media with different index of refraction for the components of the electric and magnetic fields the laws for reflection and diffraction are derived. We denote the index of refraction as n and also n_r in the following. The interface between two media with refractive indices n_1 and n_2 is depicted in Fig. 9.3. In the following we assume first that no absorption occurs.

Snell's law [833] for the angle of diffraction is

$$n_1 \sin\phi = n_2 \sin\psi \,. \tag{9.10}$$

When the wave enters the denser medium, it is diffracted towards the normal. If the wave propagates into the less-dense medium (reversely to the situation shown in Fig. 9.3), a diffracted wave occurs only up to a critical angle of incidence

$$\sin \phi_{\mathrm{TR}} = \frac{n_2}{n_1} \,. \tag{9.11}$$

For larger angles of incidence, total internal reflection occurs and the wave remains in the denser medium. Thus, the angle in (9.11) is called the critical angle for total reflection. For GaAs and air the critical angle is rather small, $\phi_{\mathrm{TR}} = 17.4°$.

The reflectance depends on the polarization (Fresnel formulas [834]). The index 'p' ('s') denotes parallel polarized/TM (perpendicular polarized/TE) waves.

$$R_{\mathrm{p}} = \left(\frac{\tan(\phi - \psi)}{\tan(\phi + \psi)} \right)^2 \tag{9.12}$$

$$R_{\mathrm{s}} = \left(\frac{\sin(\phi - \psi)}{\sin(\phi + \psi)} \right)^2 \,. \tag{9.13}$$

The situation for GaAs and air is shown for both polarization directions and unpolarized radiation in Fig. 9.4 for a wave going into and out of the GaAs.

When the reflected and the diffracted wave are perpendicular to each other, the reflectance of the p-polarized wave is zero. This angle is the Brewster angle ϕ_{B},

$$\tan \phi_{\mathrm{B}} = \frac{n_2}{n_1} \,. \tag{9.14}$$

If a wave has vertical incidence from vacuum on a medium with index of refraction n_{r}, the reflectance is given (both polarizations are degenerate) as

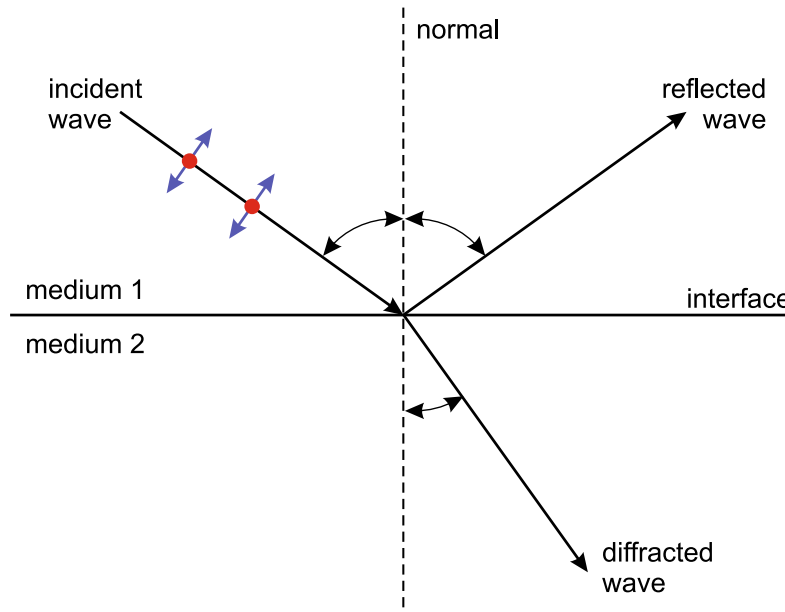

Fig. 9.3 Reflection and diffraction of an electromagnetic wave at the transition between medium '1' and '2', $n_2 > n_1$. The polarization plane is defined by the surface normal and the k-vector of the light (plane of incidence). The parallel ('p') polarized wave (TM-wave, electric field vector oscillates in the plane) is shown as '↔'; perpendicular ('s') polarization (TE-wave, electric field vector is perpendicular to plane) is depicted as '·'

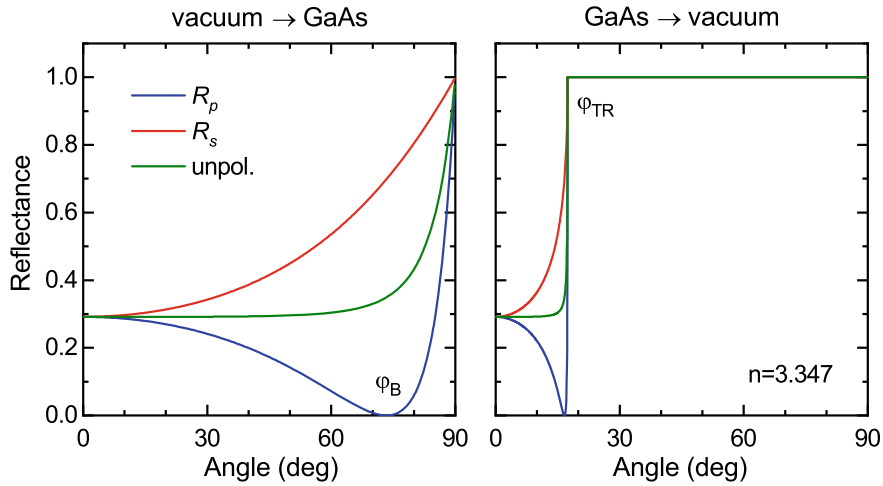

Fig. 9.4 Reflectance of the GaAs/vacuum interface (close to the band gap, $n_r = 3.347$) for radiation from vacuum/air (*left panel*) and from the GaAs (*right panel*), respectively, as a function of incidence angle and polarization

$$R = \left(\frac{n_r - 1}{n_r + 1}\right)^2 . \tag{9.15}$$

For GaAs, the reflectance for vertical incidence is 29.2%.

9.4 Absorption

In the absorption process, energy is transferred from the electromagnetic field to the semiconductor. In the case of a linear absorption process, when the probability of light absorption is proportional to the incoming intensity, the decrease of intensity in the absorbing medium is exponential (Lambert–Beer's law [835, 836]),[2]

$$I(x) = I(0)\ \exp(-\alpha\, x)\ . \tag{9.16}$$

The quantity α is the *absorption coefficient*, its reverse the absorption depth.

The spectral dependence $\alpha(E)$, the absorption spectrum, contains the information of the possible absorption processes, their energy, momentum and angular momentum selection rules, and their oscillator strength.

In Fig. 9.5 a schematic absorption spectrum of a semiconductor is depicted. The transition of electrons from the valence to the conduction band begins at the band gap energy. The band gaps of Si, Ge, GaAs, InP, InAs, InSb are in the IR, those of AlAs, GaP, AlP, InN in the VIS, those of GaN and ZnO in the UV, MgO and AlN are in the deep UV. The Coulomb correlation of electrons and holes leads to the formation of excitons that leads to absorption below the band gap. The typical exction binding energy is in the range of 1–100 meV (see Fig. 9.19). Optical transitions from valence-band electrons into donors and from electrons on acceptors into the conduction band lead to band–impurity absorption. In the region from 10–100 meV the interaction with lattice vibrations (phonons) leads to absorption if the phonons are infrared active. Further in the FIR lie transitions from impurities to the

[2] In [836], the absorption coefficient μ was defined via $I(d)/I(0) = \mu^d$, i.e. $\mu = \exp -\alpha$.

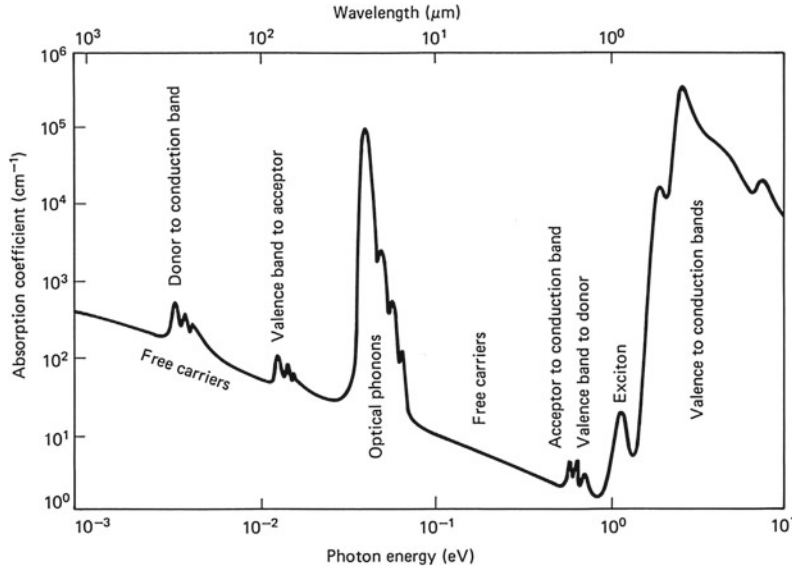

Fig. 9.5 Schematic absorption spectrum of a typical semiconductor. From [837]

closest band edge (donor to conduction and acceptor to valence band). A continuous background is due to free-carrier absorption.

If absorption is considered, the reflectance (9.15) needs to be modified. Using the complex index of refraction $n^* = n_\mathrm{r} + \mathrm{i}\kappa$, it is given as

$$R = \left|\frac{n^* - 1}{n^* + 1}\right|^2 = \frac{(n_\mathrm{r} - 1)^2 + \kappa^2}{(n_\mathrm{r} + 1)^2 + \kappa^2} \,. \tag{9.17}$$

9.5 Dielectric Function due to Optical Phonons

In this section, the dielectric function around the resonance energy of optical phonons is developed. Adjacent atoms oscillate with opposite phase in an optical phonon. If the bond has (partial) ionic character, this leads to a time-dependent polarization and subsequently to a macroscopic electric field. This additional field will influence the phonon frequencies obtained from a purely mechanical approach. We consider in the following the case $\mathbf{k} \approx 0$. The phonon frequency for TO and LO vibrations is given by

$$\omega_0 = \sqrt{\frac{2\,C}{M_\mathrm{r}}} \,, \tag{9.18}$$

where M_r is the reduced mass of the two different atoms (cf. Sect. 5.2.2). $\mathbf{u}$ is the relative displacement $\mathbf{u}_1 - \mathbf{u}_2$ of the two atoms in a diatomic base. When the interaction with the electric field $\mathbf{E}$ (which will be calculated self-consistently in the following) is considered, the Hamiltonian for the long-wavelength limit is given by [838]:

$$\hat{H}(\mathbf{p}, \mathbf{u}) = \frac{1}{2}\left(\frac{1}{M_\mathrm{r}}\,\mathbf{p}^2 + b_{11}\,\mathbf{u}^2 + 2b_{12}\,\mathbf{u}\cdot\mathbf{E} + b_{22}\,\mathbf{E}^2\right) \,. \tag{9.19}$$

The first term is the kinetic energy ($\mathbf{p}$ stands for the momentum of the relative motion of the atoms 1 and 2 in the base, $\mathbf{p} = M_\mathrm{r}\dot{\mathbf{u}}$), the second the potential energy, the third the dipole interaction and the fourth the electric-field energy. The equation of motion for a plane wave $\mathbf{u} = \mathbf{u}_0 \exp[-\mathrm{i}(\omega t - \mathbf{k}\cdot\mathbf{r})]$ ($\ddot{\mathbf{u}} = -\omega^2\mathbf{u}$) yields

$$M_\mathrm{r}\,\omega^2\,\mathbf{u} = b_{11}\,\mathbf{u} + b_{12}\,\mathbf{E}\ . \tag{9.20}$$

Thus, the electric field is

$$\mathbf{E} = (\omega^2 - \omega_\mathrm{TO}^2)\,\frac{M_\mathrm{r}}{b_{12}}\,\mathbf{u}\ . \tag{9.21}$$

Here, the substitution $\omega_\mathrm{TO}^2 = b_{11}/M_\mathrm{r}$ was introduced that is consistent with (9.18) and $b_{11} = 2C$. ω_TO represents the mechanical oscillation frequency of the atoms undisturbed by any electromagnetic effects. Already now the important point is visible. If ω approaches ω_TO, the system plus electric field oscillates with the frequency it has without an electric field. Therefore the electric field must be zero. Since the polarization $\mathbf{P} = (\epsilon - 1)\epsilon_0\mathbf{E}$ is finite, the dielectric constant ϵ thus diverges.

The polarization is

$$\mathbf{P} = -\nabla_\mathbf{E}\hat{H} = -\,(b_{12}\,\mathbf{u} + b_{22}\,\mathbf{E})\ . \tag{9.22}$$

The displacement field is

$$\mathbf{D} = \epsilon_0\,\mathbf{E} + \mathbf{P} = \epsilon_0\,\mathbf{E} - \left(b_{22} - \frac{b_{12}^2/M_\mathrm{r}}{\omega_\mathrm{TO}^2 - \omega^2}\right)\mathbf{E} = \epsilon_0\,\epsilon(\omega)\,\mathbf{E}\ . \tag{9.23}$$

Therefore, the dielectric function is

$$\epsilon(\omega) = \epsilon(\infty) + \frac{\epsilon(0) - \epsilon(\infty)}{1 - (\omega/\omega_\mathrm{TO})^2}\ . \tag{9.24}$$

Here, $\epsilon(\infty) = 1 - b_{22}/\epsilon_0$ is the high-frequency dielectric constant and $\epsilon(0) = \epsilon(\infty) + b_{12}^2/(b_{11}\epsilon_0)$ the static dielectric constant. The relation (9.24) is shown in Fig. 9.6.

From the Maxwell equation $\nabla\cdot\mathbf{D} = 0$ for zero free charge we obtain the relation

$$\epsilon_0\,\epsilon(\omega)\,\nabla\cdot\mathbf{E} = 0\ . \tag{9.25}$$

Thus, either $\epsilon(\omega) = 0$ or $\nabla\cdot\mathbf{E} = 0$, i.e. $\mathbf{u}$ is perpendicular to $\mathbf{k}$. In the latter case we have a TO phonon and, neglecting retardation effects, using $\nabla\times\mathbf{E} = 0$ we find $\mathbf{E} = 0$ and therefore $\omega = \omega_\mathrm{TO}$, justifying our notation. In the case of $\epsilon(\omega) = 0$, we call the related frequency ω_LO and find the so-called Lyddane–Sachs–Teller (LST) relation [839]

$$\frac{\omega_\mathrm{LO}^2}{\omega_\mathrm{TO}^2} = \frac{\epsilon(0)}{\epsilon(\infty)}\ . \tag{9.26}$$

This relation holds reasonably well for optically isotropic, heteropolar materials with two atoms in the basis, such as NaI and also GaAs. Since at high frequencies, i.e. $\omega \gg \omega_\mathrm{TO}$, only the individual atoms can be polarized, while for low frequencies the atoms can also be polarized against each other, $\epsilon(0) > \epsilon(\infty)$ and therefore also $\omega_\mathrm{LO} > \omega_\mathrm{TO}$. For GaAs, the quotient of the two phonon energies is 1.07. Using the LST relation (9.26), we can write for the dielectric function

$$\epsilon(\omega) = \epsilon(\infty)\left(\frac{\omega_\mathrm{LO}^2 - \omega^2}{\omega_\mathrm{TO}^2 - \omega^2}\right)\ . \tag{9.27}$$

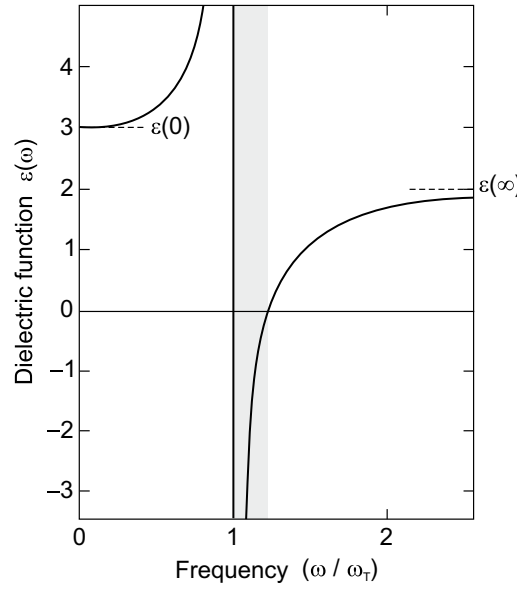

Fig. 9.6 Dielectric function according to (9.24) with $\epsilon(0) = 3$ and $\epsilon(\infty) = 2$ (without damping). *Grey area* denotes the region of negative ϵ

The (long-wavelength) TO-phonon does not create a long-range electric field. Using $\nabla \cdot \mathbf{D} = 0$ and (9.23) and looking at the longitudinal fields, we have

$$\epsilon_0 \, \mathbf{E} = b_{12} \, \mathbf{u} + b_{22} \, \mathbf{E} \, . \tag{9.28}$$

This can be rewritten as

$$\mathbf{E} = -\,\omega_{\mathrm{LO}} \sqrt{\frac{M_{\mathrm{r}}}{\epsilon_0}} \sqrt{\frac{1}{\epsilon(\infty)} - \frac{1}{\epsilon(0)}} \; \mathbf{u} \propto -\mathbf{u} \, . \tag{9.29}$$

The (long-wavelength) LO-phonon thus creates a long-range electric field acting *against* the ion displacement and represents an additional restoring force; this is consistent with the fact that $\omega_{\mathrm{LO}} > \omega_{\mathrm{TO}}$.

9.6 Electron–Photon Interaction

The absorption process within the band structure is quantum mechanically described by the coupling of electrons and photons. The process is described with time-dependent perturbation theory. If $\boldsymbol{H}_{\mathbf{em}}$ is the perturbation operator (electromagnetic field), the transition probability per time w_{fi} for electrons from (unperturbed) state 'i' (initial) to state 'f' (final) is given (with certain approximations) by Fermi's golden rule

$$w_{\mathrm{fi}}(\hbar\omega) = \frac{2\pi}{\hbar} \left| H'_{\mathrm{fi}} \right|^2 \delta(E_{\mathrm{f}} - E_{\mathrm{i}} - \hbar\omega) \, , \tag{9.30}$$

where $\hbar\omega$ is the photon energy, E_{i} (E_{f}) is the energy of the initial (final) state. H'_{fi} is the matrix element

$$H'_{\mathrm{fi}} = \left\langle \Psi_{\mathrm{f}} \left| \boldsymbol{H}' \right| \Psi_{\mathrm{i}} \right\rangle \, , \tag{9.31}$$

where Ψ_{i} (Ψ_{f}) are the wavefunctions of the unperturbed initial (final) state.

$\mathbf{A}$ is the vector potential for the electromagnetic field, i.e. $\mathbf{E} = -\dot{\mathbf{A}}$, $\mu\mathbf{H} = \nabla \times \mathbf{A}$, $\nabla \cdot \mathbf{A} = 0$ (Coulomb gauge). The Hamiltonian of an electron in the electromagnetic field is

$$\boldsymbol{H} = \frac{1}{2m} \left(\hbar\mathbf{k} - q\mathbf{A}\right)^2 \ . \tag{9.32}$$

When terms in $\mathbf{A}^2$ are neglected (i.e. two-photon processes), the perturbation Hamiltonian is thus

$$\boldsymbol{H}_{\mathbf{em}} = -\frac{q}{m}\,\mathbf{A}\,\mathbf{p} = \frac{\mathrm{i}\,\hbar q}{m}\,\mathbf{A}\cdot\nabla \approx q\,\mathbf{r}\cdot\mathbf{E}\ . \tag{9.33}$$

The latter approximation is valid for small wavevectors of the electromagnetic wave and is termed the *electric dipole approximation*.

In order to calculate the dielectric function of the semiconductor from its band structure we assume that $\mathbf{A}$ is weak and we can apply (9.30). The transition probability R for the photon absorption rate at photon energy $\hbar\omega$ is then given by[3]

$$R(\hbar\omega) = \frac{2\pi}{\hbar} \int\limits_{\mathbf{k}_\mathrm{c}} \int\limits_{\mathbf{k}_\mathrm{v}} |\langle c|\boldsymbol{H}_{\mathbf{em}}|v\rangle|^2\, \delta\left(E_\mathrm{c}(\mathbf{k}_\mathrm{c}) - E_\mathrm{v}(\mathbf{k}_\mathrm{v}) - \hbar\omega\right) \mathrm{d}^3\mathbf{k}_\mathrm{c}\, \mathrm{d}^3\mathbf{k}_\mathrm{v}\ , \tag{9.34}$$

with the Bloch functions $|c\rangle$ and $|v\rangle$ of the conduction and valence band, respectively, as given in (6.40b).

The vector potential is written as $\mathbf{A} = A\hat{\mathbf{e}}$ with a unit vector $\hat{\mathbf{e}}$ parallel to $\mathbf{A}$. The amplitude is connected to the electric-field amplitude E via

$$A = -\frac{E}{2\,\omega} \left[\exp\left(\mathrm{i}(\mathbf{qr} - \omega t)\right) + \exp\left(-\mathrm{i}(\mathbf{qr} - \omega t)\right)\right] \ . \tag{9.35}$$

In the electric-dipole approximation the momentum conservation $\mathbf{q} + \mathbf{k}_\mathrm{v} = \mathbf{k}_\mathrm{c}$, $\mathbf{q}$ being the momentum of the light wave is approximated by $\mathbf{k}_\mathrm{v} = \mathbf{k}_\mathrm{c}$. The matrix element is then given by

$$|\langle c|\boldsymbol{H}_{\mathbf{em}}|v\rangle|^2 = \frac{e^2\,|A|^2}{m^2} \left|\langle c|\hat{\mathbf{e}}\cdot\mathbf{p}|v\rangle\right|^2 \ , \tag{9.36}$$

with

$$\langle c\left|\hat{\mathbf{e}}\cdot\mathbf{p}|v\rangle\right|^2 = \frac{1}{3}\,|\mathbf{p}_\mathrm{cv}|^2 = M_\mathrm{b}^2\ , \tag{9.37}$$

and the momentum matrix element $\mathbf{p}_\mathrm{cv}$ given in (6.39). A $\mathbf{k}$-independent matrix element $|\mathbf{p}_\mathrm{cv}|^2$ is often used as an approximation. In Fig. 9.7 the matrix elements for valence to conduction band transitions in GaN are shown as a function of $\mathbf{k}$.

In terms of the electric-field amplitude $E(\omega)$ the transition probability is

$$R(\hbar\omega) = \frac{2\pi}{\hbar} \left(\frac{e}{m\,\omega}\right)^2 \left|\frac{E(\omega)}{2}\right|^2 |\mathbf{p}_\mathrm{cv}|^2 \int\limits_{\mathbf{k}} \delta\left(E_\mathrm{c}(\mathbf{k}) - E_\mathrm{v}(\mathbf{k}) - \hbar\omega\right)\, \mathrm{d}^3\mathbf{k}\ . \tag{9.38}$$

If the integration over $\mathbf{k}$ is restricted to those values allowed in unit volume, the power that is lost from the field in unit volume is given by $R\,\hbar\omega$, leaving a $1/E$ factor. The dielectric function $\epsilon = \epsilon' + \mathrm{i}\epsilon''$ is

[3] Here we assume that the valence-band states are filled and the conduction-band states are empty. If the conduction-band states are filled and the valence-band states are empty, the rate is that of stimulated emission.

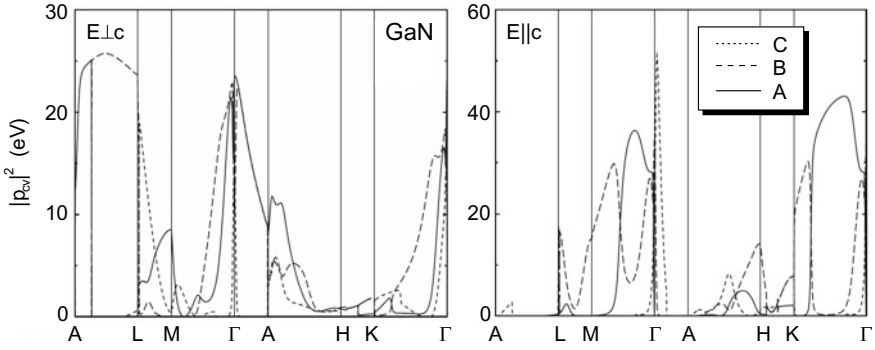

Fig. 9.7 Theoretical momentum matrix elements $|p_{cv}|^2$ along high-symmetry directions in the Brillouin zone (see Fig. 3.38d) for transitions between valence and conduction bands in GaN and light polarized perpendicular (*left panel*) and parallel (*right panel*) to the c-axis. The transitions are A: Γ_9(A)→ Γ_{7c}, B: Γ_7(B)→ Γ_{7c}, C: Γ_7(C)→ Γ_{7c} (see Fig. 6.44). Adapted from [840]

given by

$$\epsilon'' = \frac{1}{4\pi\epsilon_0}\left(\frac{2\pi\, e}{m\,\omega}\right)^2 |\mathbf{p}_{cv}|^2 \int_{\mathbf{k}} \delta\left(E_c(\mathbf{k}) - E_v(\mathbf{k}) - \hbar\omega\right)\, \mathrm{d}^3\mathbf{k} \tag{9.39a}$$

$$\epsilon' = 1 + \int_{\mathbf{k}} \frac{e^2}{\epsilon_0\, m\, \omega_{cv}^2}\, \frac{2\,|\mathbf{p}_{cv}|^2}{m\,\hbar\omega_{cv}}\, \frac{1}{1-\omega^2/\omega_{cv}^2}\, \mathrm{d}^3\mathbf{k}\,, \tag{9.39b}$$

with $\hbar\omega_{cv} = E_c(\mathbf{k}) - E_v(\mathbf{k})$. Equation (9.39b) has been obtained via the Kramers–Kronig relations[4] (see Appendix C).

Comparison with (D.7) yields that the oscillator strength of the band–band absorption is given by

$$f = \frac{e^2}{\epsilon_0\, m\, \omega_{cv}^2}\, \frac{2\,|\mathbf{p}_{cv}|^2}{m\,\hbar\omega_{cv}} = \frac{e^2}{\epsilon_0\, m\, \omega_{cv}^2}\, N_{cv}\,, \tag{9.40}$$

with the classical 'number' of oscillators with the frequency ω_{cv},

$$N_{cv} = \frac{2\,|\mathbf{p}_{cv}|^2}{m\,\hbar\omega_{cv}}\,. \tag{9.41}$$

9.7 Band–Band Transitions

9.7.1 Joint Density of States

The strength of an allowed optical transitions between valence and conduction bands is proportional to the joint density of states (JDOS) $D_j(E_{cv})$ (cf. (6.63), (6.64) and (9.39a))

[4]The real and imaginary parts of the dielectric function are generally related to each other via the Kramers–Kronig relations.

Table 9.3 Functional dependence of the joint density of states for critical points in 3, 2 and 1 dimensions. E_0 denotes the energy (band separation) at the critical point, C stands for a constant value. The type of critical point is given (min.: minimum, saddle: saddle point, max.: maximum)

Dim.	Label	Type	D_j for $E < E_0$	D_j for $E > E_0$
3D	M_0	min.	0	$\sqrt{E - E_0}$
	M_1	saddle	$C - \sqrt{E_0 - E}$	C
	M_2	saddle	C	$C - \sqrt{E - E_0}$
	M_3	max.	$\sqrt{E_0 - E}$	0
2D	M_0	min.	0	C
	M_1	saddle	$-\ln(E_0 - E)$	$-\ln(E - E_0)$
	M_2	max.	C	0
1D	M_0	min.	0	$\sqrt{E - E_0}$
	M_1	max.	$\sqrt{E_0 - E}$	0

$$D_j(E_{cv}) = 2 \int\limits_{S(\tilde{E})} \frac{d^2S}{(2\pi/L)^3} \frac{1}{|\nabla_{\mathbf{k}} E_{cv}|} , \tag{9.42}$$

where E_{cv} is an abbreviation for $E_c(\mathbf{k}) - E_v(\mathbf{k})$ and d^2S is a surface element of the constant energy surface with $\tilde{E} = E_{cv}$. The spin is assumed to generate doubly degenerate bands and accounts for the pre-factor 2. Singularities of the JDOS (*van-Hove singularities* or *critical points*) appear where $\nabla_{\mathbf{k}} E_{cv}$ vanishes. This occurs when the gradient for both bands is zero or when both bands are parallel. The latter generates particularly large JDOS because the condition is valid at many points in $\mathbf{k}$-space.

Generally, the (three-dimensional) energy dispersion $E(\mathbf{k})$ around a three-dimensional critical point (here developed at $\mathbf{k} = 0$) can be written as

$$E(\mathbf{k}) = E(0) + \frac{\hbar^2 k_x^2}{2m_x} + \frac{\hbar^2 k_y^2}{2m_y} + \frac{\hbar^2 k_z^2}{2m_z} . \tag{9.43}$$

The singularities are classified as M_0, M_1, M_2 and M_3 with the index being the number of masses m_i in (9.43) that are negative. M_0 (M_3) describes a minimum (maximum) of the band separation. M_1 and M_2 are saddle points. For a two-dimensional $\mathbf{k}$-space there exist M_0, M_1 and M_2 points (minimum, saddle point and maximum, respectively). For a one-dimensional $\mathbf{k}$-space, there exist M_0 and M_1 points (minimum and maximum, respectively). The functional dependence of the JDOS at the critical points is summarized in Table 9.3. The resulting shape of the dielectric function is visualized in Fig. 9.8.

9.7.2 Direct Transitions

Transitions between states at the band edges at the Γ point are possible (Fig. 9.9). The $\mathbf{k}$ conservation requires (almost) vertical transitions in the $E(\mathbf{k})$ diagram because the length of the light $\mathbf{k}$ vector, $k = 2\pi/\lambda$, is much smaller than the size of the Brillouin zone $|k| \leq \pi/a_0$. The ratio of the lengths of the $\mathbf{k}$ vectors is of the order a_0/λ and typically about 10^{-3} for NIR wavelengths.

For isotropic parabolic bands the band-band transition energy versus wavevector relation is

$$E_{cv}(k) = E_g + \frac{\hbar^2}{2} \left(\frac{1}{m_e^*} + \frac{1}{m_h^*} \right) k^2 . \tag{9.44}$$

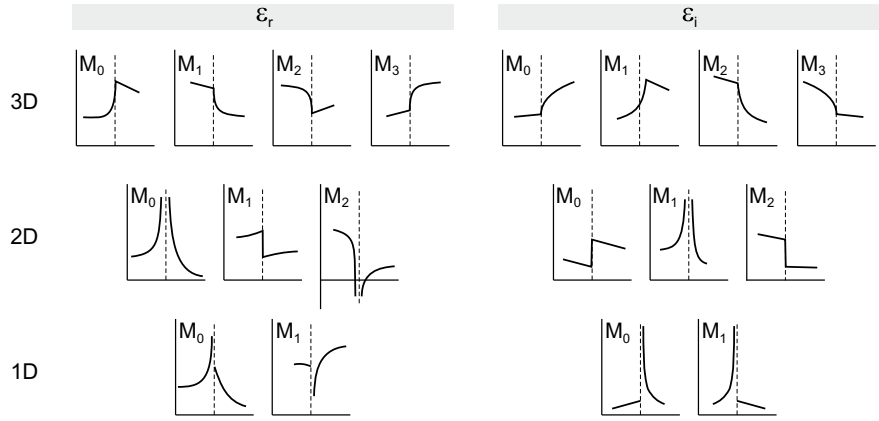

Fig. 9.8 Shape of the real (*left panel*) and imaginary (*right panel*) parts of the dielectric function in the vicinity of critical points in 3, 2 and 1 dimensions (for labels see Table 9.3). The *dashed line* in each graph indicates the energy position of the critical point E_0. Adapted from [841]

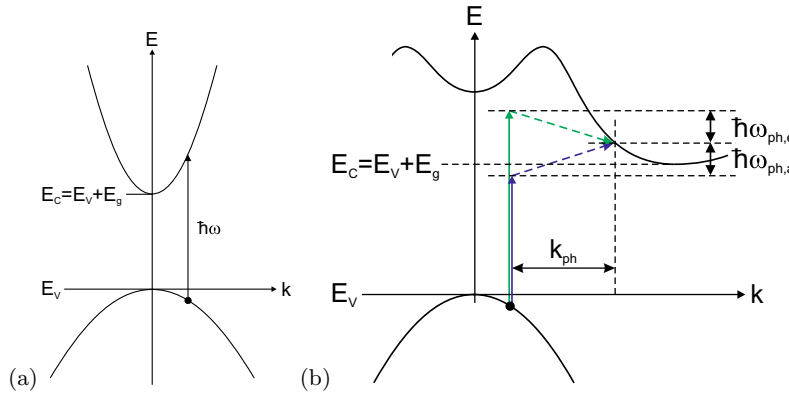

Fig. 9.9 **a** Direct optical transition and **b** indirect optical transitions between valence and conduction bands. The indirect transition involves a phonon with energy $\hbar\omega_{\mathrm{ph}}$ (index *a*: phonon absorption, *e*: phonon emission) and wavevector k_{ph}

When the energy dependence of the matrix element is neglected, the absorption coefficient is determined by the corresponding square-root joint density of states (M_0 critical point):

$$\alpha(E) \propto \frac{\sqrt{E - E_{\mathrm{g}}}}{E} \approx \propto \sqrt{E - E_{\mathrm{g}}}\,. \tag{9.45}$$

The approximation is valid if the considered energy interval, e.g. around a band edge, is small.

Absorption spectra of $(\mathrm{In}_x\mathrm{Ga}_{1-x})_2\mathrm{O}_3$ alloy thin films at room temperature are shown in Fig. 9.10a. The α^2 versus photon energy so-called Tauc plot shows a linear dependence with broadening and additional states at the band edge due to disorder effects. The extrapolation of the linear part yields the absorption edge (Fig. 9.10b).

Absorption spectra of GaAs are shown in Fig. 9.11a for photon energies close to the band gap at various temperatures. The rapid increase, typical for direct semiconductors, is obvious. In particular at low temperatures, however, the absorption lineshape close to the band gap is dominated by an excitonic feature, discussed in Sect. 9.7.6.

Due to the increasing density of states, the absorption increases with the photon energy (Fig. 9.11c). At 1.85 eV there is a step in the absorption spectrum of GaAs due to the beginning of the contribution of transitions between the s-o hole band and the conduction band (see $E_0 + \Delta_0$ transition in Fig. 9.1b).

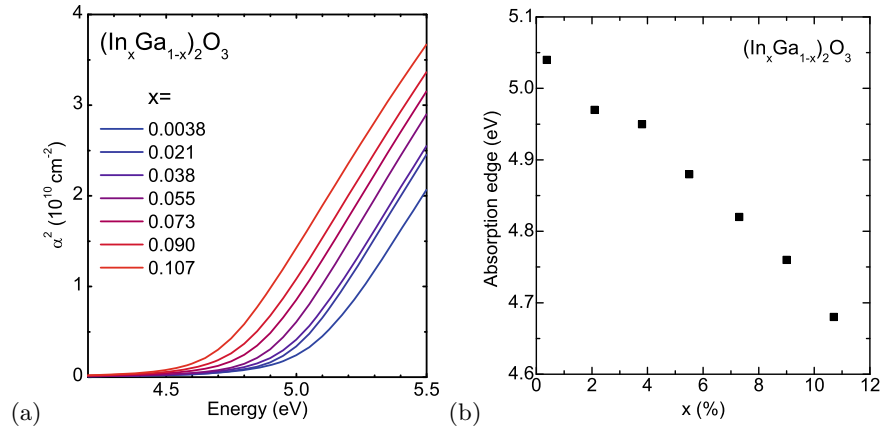

Fig. 9.10 **a** Absorption spectra of $(In_xGa_{1-x})_2O_3$ alloy thin films on Al_2O_3, plotted as α^2 versus photon energy. **b** Band edge determined from extrapolation of linear parts

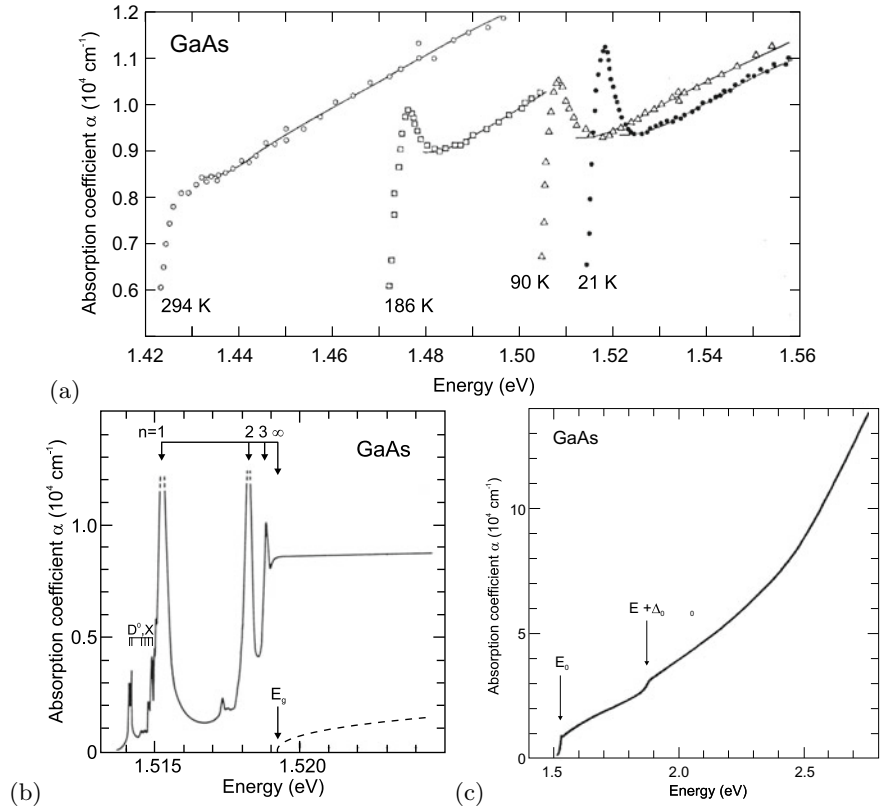

Fig. 9.11 **a** Absorption of GaAs close to the band gap at different temperatures. Adapted from [842]. **b** High-resolution absorption spectrum of highly pure GaAs at $T = 1.2$ K in the exciton region. *Dashed line* is theory without excitonic correlation. Adapted from [843]. **c** Absorption spectrum of GaAs at $T = 21$ K in the vicinity of the band gap. Adapted from [842]

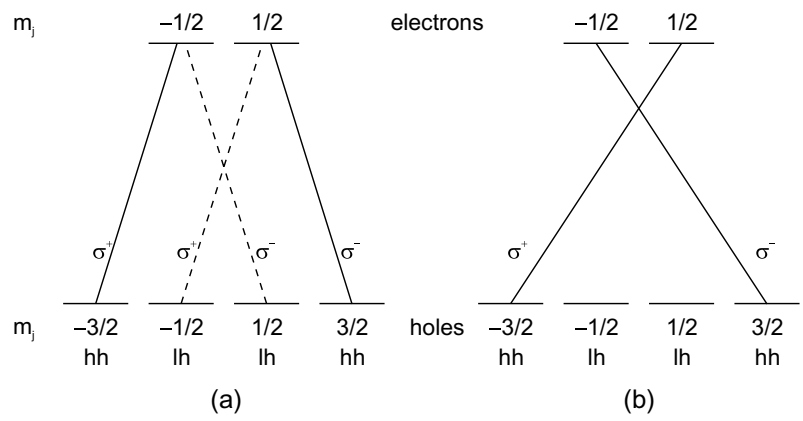

Fig. 9.12 Optical selection rules for band–band transitions in bulk material for **a** single photon transitions and **b** two-photon transitions (with photon energy equal to half the transition energy)

When bands run in parallel, i.e. with the same separation, in the $E(\mathbf{k})$ diagram, the absorption processes accumulate at the same transition energy. In this way peaks at higher energy in the complex part of the dielectric function and in the absorption spectrum due to the E_1 or E_0' transitions originate as shown in Fig. 9.1.

The selection rules for transitions from valence to conduction band must take into account the angular momentum and spin states of the wavefunctions. The optical transitions for circularly polarized light are shown in Fig. 9.12a, fulfilling the selection rule $\Delta m_j = \pm 1$. A lifting of the energetic degeneracies of these states occurs, e.g. by magnetic fields (cmp. Fig. 15.12) or spatial confinement (cmp. Fig. 12.30). For two-photon absorption (Chap. 9.7.14), the selection rule is $\Delta m_j = \pm 2$ as shown in Fig. 9.12b [844].

We note that in some materials the direct transition between certain bands is forbidden. An example is SnO_2 where the direct transition from the topmost valence band into the lowest conduction band (at Γ) is forbidden (cmp. Fig. 9.48). If the matrix element increases linearly with $E - E_g$, the absorption coefficient varies like

$$\alpha(E) \propto (E - E_g)^{3/2} \,. \tag{9.46}$$

9.7.3 Indirect Transitions

In an indirect band structure the missing **k** difference (across the Brillouin zone) between valence- and conduction-band state needs to be provided by a second quantum. A phonon can provide the necessary momentum and additionally contributes a small amount of energy $\hbar\omega_{ph}$. There are several steps in the absorption spectrum due to various involved phonons (or combinations of them). At low temperature ($T = 1.6\,\mathrm{K}$, Fig. 9.13) phonons can only be generated and the absorption starts at energies *above* the band gap. At higher temperatures (typically above 40 K [845], Fig. 9.13), acoustical phonons assisting the optical absorption transition can also be absorbed from the crystal; in this case due to energy conservation the absorption starts already at an energy $E_g - \hbar\omega_{ph}$ *below* the band gap. At even higher temperatures ($> 200\,\mathrm{K}$, Fig. 9.13), also optical phonons can be absorbed.

The perturbation calculation yields an absorption coefficient with a quadratic dependence on energy (9.47a) [846]. Essentially, for the absorption into a specific (empty) conduction band state (with square-root density of states) various initial (filled) valence band states (also with square-root density of states) are possible, making the probability depend on the product of the DOS and thus on the energy to the first power. Integrating over all energy states with energy separation $E \pm \hbar\omega_{ph}$, yields an E^2-dependence.[5]

[5] A flat optical phonon dispersion is assumed.

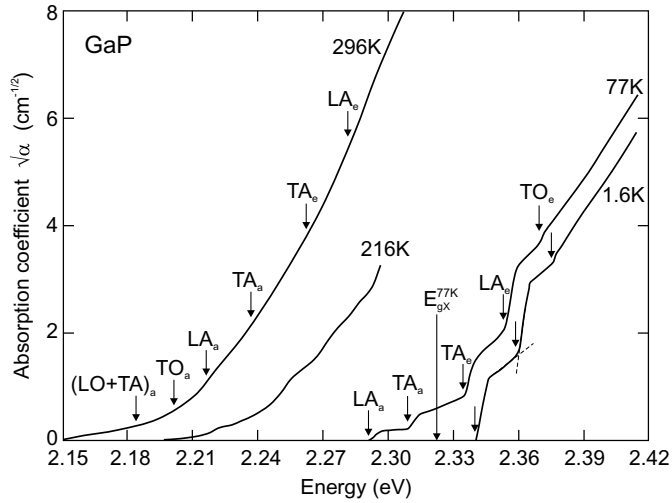

Fig. 9.13 Absorption edge of GaP ($\sqrt{\alpha}$ versus E) at various temperatures. The index 'e' ('a') indicates phonon emission (absorption) during the optical absorption process. The theoretical excitonic gap (E_{gX}) at $T = 77\,\mathrm{K}$ is indicated. Adapted from [845]

Considering the temperature dependent population of the phonon density of states (Bose statistics, (E.3)) the absorption coefficients for transitions with phonon emission (α_e) and phonon absorption (α_a) are:

$$\alpha_e(E) \propto \frac{(E - (E_g + \hbar\omega_{ph}))^2}{1 - \exp(-\hbar\omega_{ph}/kT)} \tag{9.47a}$$

$$\alpha_a(E) \propto \frac{(E - (E_g - \hbar\omega_{ph}))^2}{\exp(\hbar\omega_{ph}/kT) - 1}\,. \tag{9.47b}$$

The two-particle process is less probable than the direct absorption that only involves one photon. The strength of indirect absorption close to the band gap is about 10^{-3} smaller than for the direct transition.

An 11-parameter formula based on terms like (9.47a) can describe the room temperature absorption spectrum of silicon in the visible with a precision of a few percent [847].

The absorption spectra close to the absorption edge are shown for GaP (Fig. 9.13) and Si (Fig. 9.14a). According to (9.47a), the plot of $\sqrt{\alpha}$ versus energy (Macfarlane–Roberts plot [848]) yields a straight line beyond the spectral region of phonon effects. The complicated form close to the (indirect) gap energy is due to the contribution of different phonons. The phonon energies found to contribute to the silicon absorption edge [849] agree with the TA and TO energy at the X minimum [850] (Fig. 9.14b). Also multiple phonons can contribute (Fig. 9.13). The momentum conservation can also be achieved by impurity scattering or electron-electron scattering [851].

We note also that the indirect semiconductors have an optical transition between Γ valence- and conduction-band states. However, this transition is at higher energies than the fundamental band gap, e.g. for Si ($E_g = 1.12\,\mathrm{eV}$) at 3.4 eV (see Fig. 6.9a). In Fig. 9.15, the absorption scheme for indirect and direct absorption processes starting with an electron at the top of the valence band is shown together with an experimental absorption spectrum for Ge with the direct transition ($\Gamma_8 \rightarrow \Gamma_7$) at 0.89 eV, 0.136 eV above the fundamental band gap.

In Fig. 9.16, the absorption edge of $BaTiO_3$ is shown. An indirect transition with an increase of (weak) absorption $\propto E^2$ and an indirect gap of $E_i = 2.66\,\mathrm{eV}$ and a direct transition with an increase of (strong) absorption $\propto E^{1/2}$ and a direct gap of $E_d = 3.05\,\mathrm{eV}$ are observed. These transitions could be due to holes at the M (indirect gap) and Γ (direct gap) points (cf. Sect. 6.3.11), respectively.

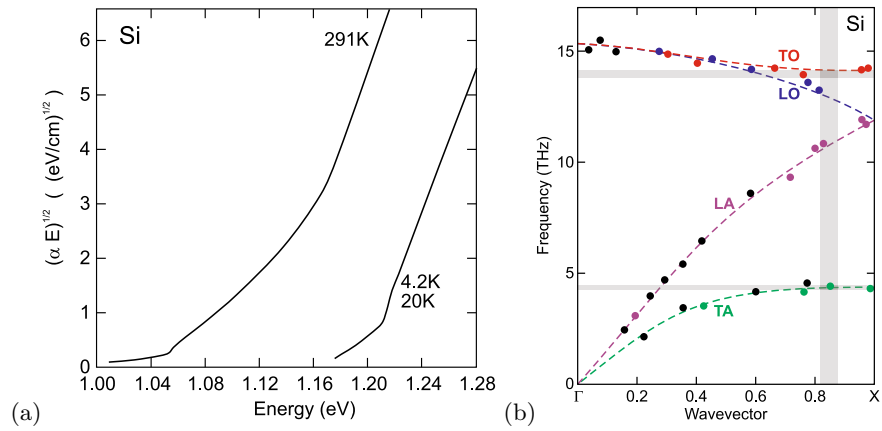

Fig. 9.14 **a** Absorption edge of Si at two different temperatures. Adapted from [849]. **b** Phonon energies in silicon along [001] obtained from neutron scattering (*black*: unidentified, *green*: TA, *purple*: LA, *blue*: LO, *red*: TO). The *vertical grey bar* indicates the position of the conduction band minimum, the *horizontal grey bars* the energies of the phonons observed at the indirect optical absorption edge. The *dark grey* overlap areas indicate that TO and TA phonons contribute. Adapted from [850]

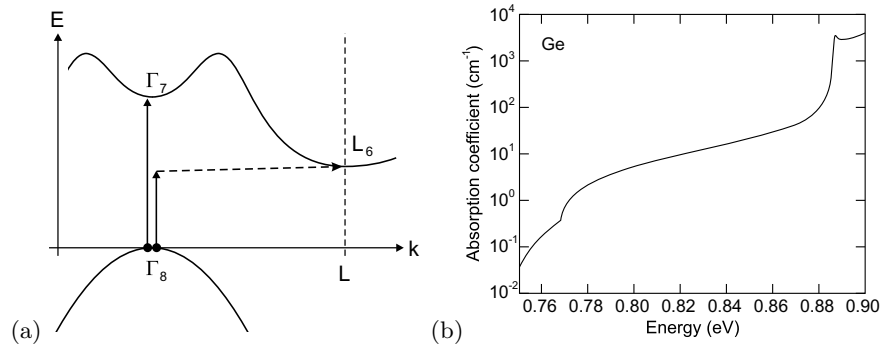

Fig. 9.15 **a** Scheme of indirect and direct optical transitions starting at the top of the valence band in Ge. Vertical *solid lines* represent the involved photon, the horizontal *dashed line* the involved phonon. **b** Experimental absorption spectrum of Ge ($T = 20\,\mathrm{K}$). Adapted from [849]

9.7.4 Urbach Tail

Instead of the ideal $(E - E_\mathrm{g})^{1/2}$ dependence of the direct band-edge absorption, often an exponential tail is observed (see Fig. 9.17). This tail is called the Urbach tail [853] and follows the functional dependence (for $E < E_\mathrm{g}$)

$$\alpha(E) \propto \exp\left(\frac{E - E_\mathrm{g}}{E_0}\right) , \tag{9.48}$$

where E_0 is the characteristic width of the absorption edge, the so-called Urbach parameter.

The Urbach tail is attributed to transitions between band tails below the band edges. Such tails can originate from disorder of the perfect crystal, e.g. from defects or doping, and the fluctuation of electronic energy bands due to lattice vibrations. The temperature dependence of the Urbach parameter E_0 is thus related to that of the band gap as discussed in [854, 855].

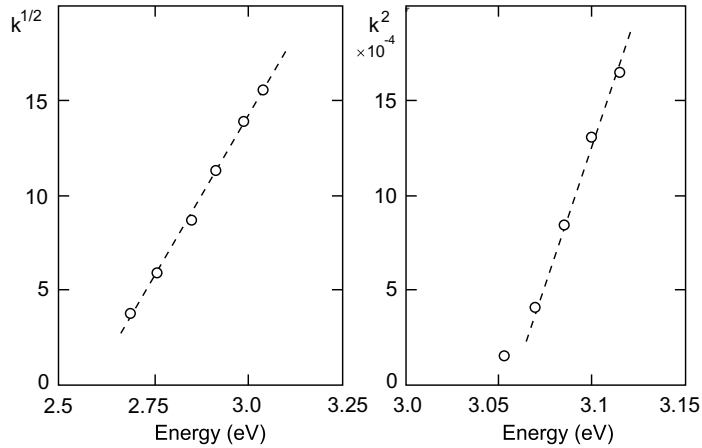

Fig. 9.16 Absorption of $BaTiO_3$ at room temperature. Experimental data (*circles*) from [852] with fits (*dashed lines*) $\propto E^2$ and $\propto E^{1/2}$, respectively

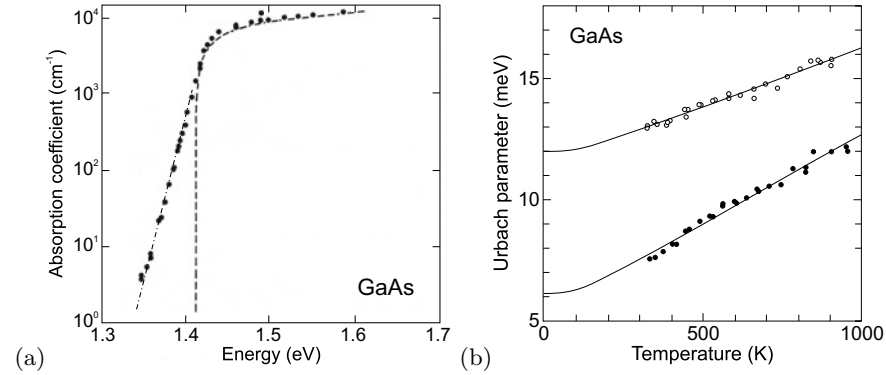

Fig. 9.17 **a** Experimental absorption spectrum (*circles*) of GaAs at room temperature on a semilogarithmic plot. The exponential tail below the band gap is called the Urbach tail (the *dash-dotted* line corresponds to $E_0 = 10.3\,\text{meV}$ in (9.48)). The *dashed line* is the theoretical dependence from (9.45). Adapted from [856]. **b** Temperature dependence of Urbach parameter E_0 for two GaAs samples. Experimental data for undoped (*solid circles*) and Si-doped ($n = 2 \times 10^{18}\,\text{cm}^{-3}$, *empty circles*) GaAs and theoretical fits (*solid lines*) with one-phonon model. Adapted from [854]

9.7.5 Amorphous Semiconductors

The sharp features in the dielectric function due to critical points in the band structure of crystalline semiconductors are washed out in amorphous material. As an example the spectra of the imaginary part of the dielectric function for crystalline (trigonal) and amorphous selenium are shown in Fig. 9.18.

9.7.6 Excitons

An electron in the conduction band and a hole in the valence band form a hydrogen-like state due to the mutual Coulomb interaction. Such a state is called an exciton. The center-of-mass motion is separated and has a dispersion $E = \frac{\hbar^2}{2M}\mathbf{K}^2$, where $M = m_\text{e} + m_\text{h}$ is the total mass and $\hbar\mathbf{K}$ is the center-of-mass

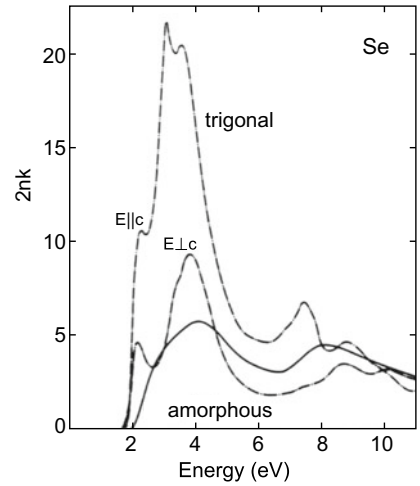

Fig. 9.18 Imaginary part of the dielectric function of amorphous (*solid line*) and crystalline (trigonal) selenium (*dash-dotted lines* for two different polarization directions). From [857]

Table 9.4 Exciton (E_X^b) and biexciton (E_{XX}^b, see Sect. 9.7.10) binding energies in various bulk semiconductors. Values for 10 nm GaAs/15 nm $Al_{0.3}Ga_{0.7}As$ quantum well (QW) are taken from [861]

Material	E_X^b (meV)	E_{XX}^b (meV)	E_{XX}^b/E_X^b
GaAs	4.2		
GaAs QW	9.2	2.0	0.22
ZnSe	17	3.5	0.21
GaN	25	5.6	0.22
CdS	27	5.4	0.20
ZnS	37	8.0	0.22
ZnO	59	15	0.25

momentum

$$\mathbf{K} = \mathbf{k}_e + \mathbf{k}_h \ . \tag{9.49}$$

The relative motion yields hydrogen-like quantized states $E_n \propto n^{-2} (n \geq 1)$:

$$E_X^n = -\frac{m_r^*}{m_0} \frac{1}{\epsilon_r^2} \frac{m_0 e^4}{2(4\pi\epsilon_0\hbar)^2} \frac{1}{n^2} \ , \tag{9.50}$$

where m_r^* denotes the reduced effective mass $m_r^{*-1} = m_e^{*-1} + m_h^{*-1}$. The third factor is the atomic Rydberg energy (13.6 eV). The exciton binding energy $E_X^b = -E_X^1$ is scaled by $(m^*/m_0)\,\epsilon_r^{-2} \approx 10^{-3}$. A more detailed theory of excitons beyond the simple hydrogen model presented here, taking into account the valence-band structure, can be found in [858] for direct and [859] for indirect cubic and in [860] for wurtzite semiconductors. The exciton binding energies for various semiconductors are listed in Table 9.4 and shown in Fig. 9.19a versus the band gap.

The radius of the exciton is

$$r_X^n = n^2 \frac{m_0}{m_r^*} \epsilon_r \, a_B \ , \tag{9.51}$$

where $a_B = 0.053$ nm denotes the hydrogen Bohr radius.[6] The Bohr radius of the exciton is $a_X = r_X^1$ (14.6 nm for GaAs, $\sim$ 2 nm for ZnO). The exciton moves with the center-of-mass **K**-vector through

[6] Cf. (7.22); an electron bound to a donor can be considered as an exciton with an infinite hole mass.

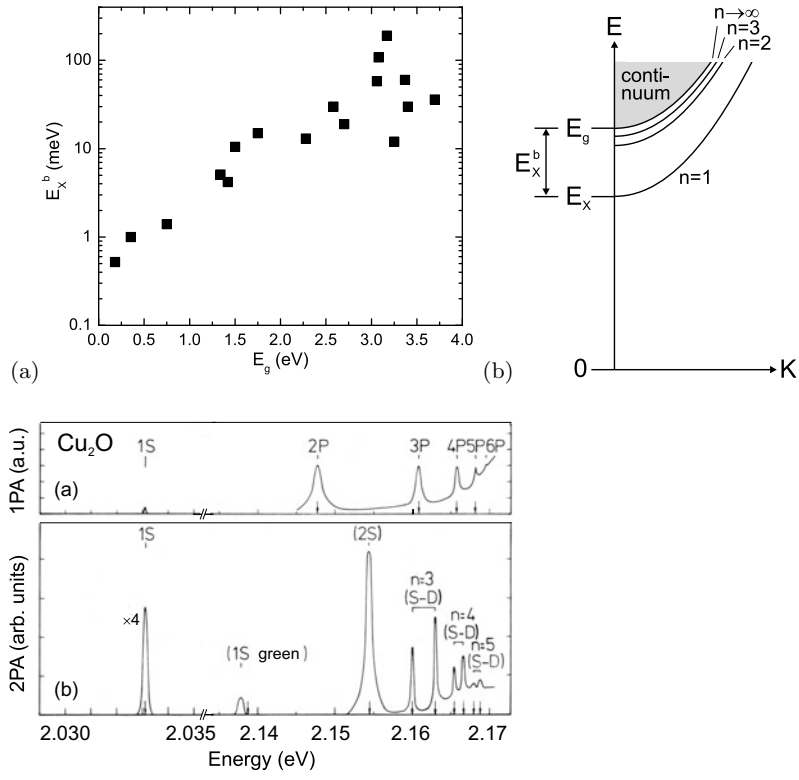

Fig. 9.19 **a** Exciton binding energy versus band gap for various semiconductors. **b** Schematic dispersion of excitonic levels. The K-vector refers to the center-of-mass motion

Fig. 9.20 One-photon (*top*) and two-photon (*bottom*) absorption spectra of Cu_2O at $T = 4.2$ K. *Arrows* denote theoretical peak positions. Adapted from [864]

the crystal. The complete dispersion is (see Fig. 9.19b)

$$E = E_g + E_X^n + \frac{\hbar^2}{2M}\,\mathbf{K}^2\,. \tag{9.52}$$

The oscillator strength of the exciton states decays $\propto n^{-3}$. The absorption due to excitons is visible in Fig. 9.11a for GaAs at low temperatures. If inhomogeneities are present, typically only the $n = 1$ transition is seen. However, under special conditions also higher transitions of the exciton Rydberg series are seen (e.g. $n = 2$ and 3 in Fig. 9.11b).

The exciton concept was introduced first for absorption in Cu_2O [862]. The $J = 1/2$ absorption spectrum ('yellow series') is shown in Fig. 9.20. In this particular material both the valence and conduction bands have s character, thus the 1s transition of the exciton is forbidden and the np transitions are observed in normal (one-photon) absorption. With two-photon absorption also the s (and d) transitions can be excited. On a piece of natural Cu_2O, the Rydberg series has been measured up to $n = 25$ [863] (Fig. 9.21a). The peak energy and the oscillator strength follow the n^{-2} ($E_X^b = 92$ meV, $E_g = 2.17208$ eV) and n^{-3} laws, respectively, expected from a hydrogen model (Fig. 9.21b). The deviation from the n^{-3}-dependence for the oscillator strength at large n is due to interaction effects of excitons with large radius at finite exciton density.

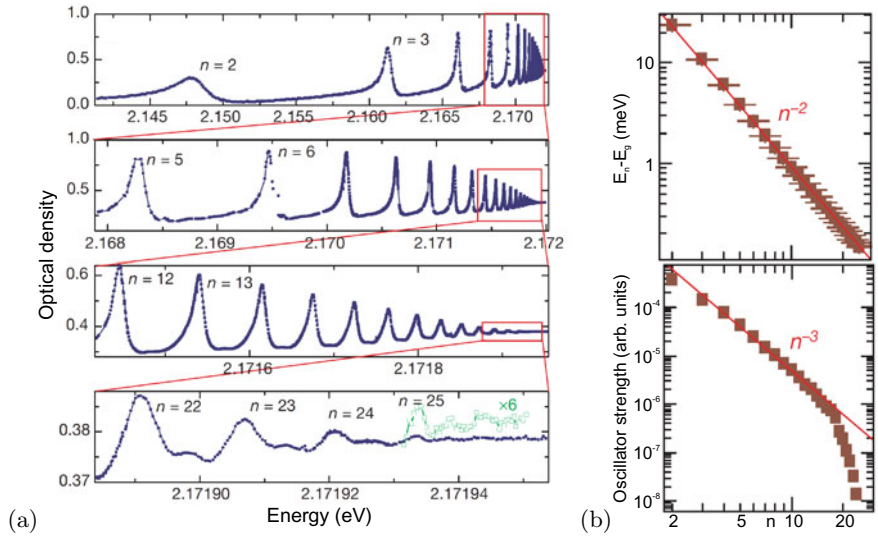

Fig. 9.21 (One photon) Absorption spectrum of Cu_2O (thickness 34 µm) at $T = 1.2$ K with transitions labelled $n = 2 \ldots 25$. Adapted from [863]

The scattering (unbound) states of the exciton [865] for $E > E_g$ contribute to absorption above the band gap. The factor by which the absorption spectrum is changed is called the Sommerfeld factor. For bulk material it is

$$S(\eta) = \eta \frac{\exp(\eta)}{\sinh(\eta)} , \tag{9.53}$$

with $\eta = \pi[E_X^b/(E - E_g)]^{1/2}$. The change of the absorption spectrum due to the Coulomb correlation is shown in Fig. 9.22. There is a continuous absorption between the bound and unbound states. At the band gap there is a finite absorption ($S(E \to E_g) \to \infty$). The detail to which exciton peaks can be resolved depends on the spectral broadening.

In Fig. 9.23 the energy separations of the A-, B-, and C-excitons in GaN are shown [540]. Thus, the ordering of the valence bands depends on the strain state of the semiconductor.

9.7.7 *Phonon Broadening*

The scattering with phonons and the related dephasing leads to homogeneous broadening Γ_{hom} of absorption (and recombination) lines. Acoustic and optical phonons contribute to the broadening according to the dependence [867]

$$\Gamma_{hom}(T) = \Gamma_0 + \gamma_{AC}\, T + \gamma_{LO} \frac{1}{\exp(\hbar\omega_{LO}/kT) - 1} , \tag{9.54}$$

where $\hbar\omega_{LO}$ is the optical phonon energy and the last factor is the Bose function (E.24). Γ_0 is a temperature-independent contribution, $\Gamma_0 = \Gamma(T = 0)$. The increasing broadening with increasing temperature is obvious, e.g., in absorption spectra (Fig. 9.24a). In Fig. 9.24b experimental data for GaAs, ZnSe and GaN are assembled. The data have been fitted with (9.54); the resulting phonon

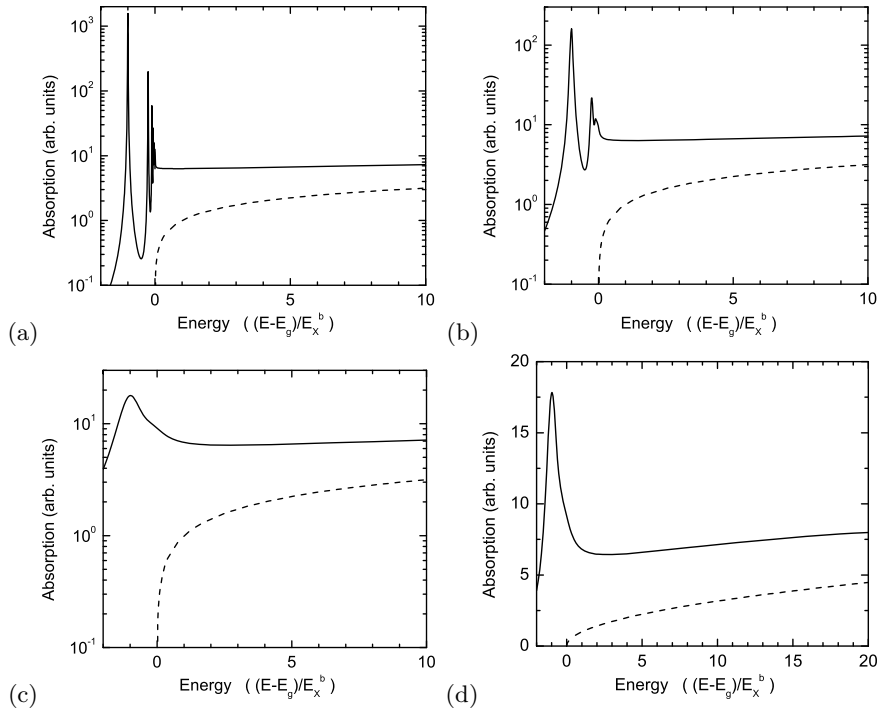

Fig. 9.22 Modification of the absorption edge of a direct transition by excitonic effects for different spectral (Lorentzian) broadening ($\propto (E^2 + \Gamma^2/4)^{-1}$), **a** $\Gamma = 0.01 E_{\mathrm{X}}^{\mathrm{b}}$, **b** $\Gamma = 0.1 E_{\mathrm{X}}^{\mathrm{b}}$, **c** $\Gamma = E_{\mathrm{X}}^{\mathrm{b}}$. **d** is **c** in linear scale. *Dashed lines* are electron–hole plasma absorption according to (9.45)

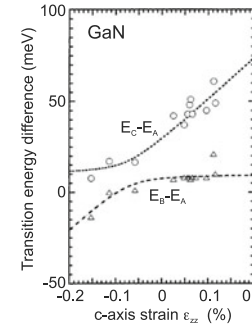

Fig. 9.23 Theoretical dependency (*lines*) for the the differences of the C-line and A-line as well as B-line and A-line exciton transition energies in GaN as a function of the *c*-axis strain. *Symbols* are experimental data from [866]. Adapted from [540]

broadening parameters are listed in Table 9.5.[7] The optical transitions in polar semiconductors exhibit stronger coupling to optical phonons. The phonon coupling parameters from different measurements on GaN are discussed and compared in [870].

[7] Such parameter can be directly determined from spectroscopic broadening (as in [868]) or a time-resolved measurement of the decay of the coherent polarization (four-wave mixing) as in [869]. In the latter, the decay constant of the dephasing T_2 is related to the decay constant τ of the FWM-signal by $T_2 = 2\tau$ for homogeneous broadening. The Fourier transform of $\exp -t/(2\tau)$ is a Lorentzian of the type $\propto ((E - E_0)^2 + \Gamma^2/4)^{-1}$ with $\Gamma = 1/\tau$ being the FWHM.

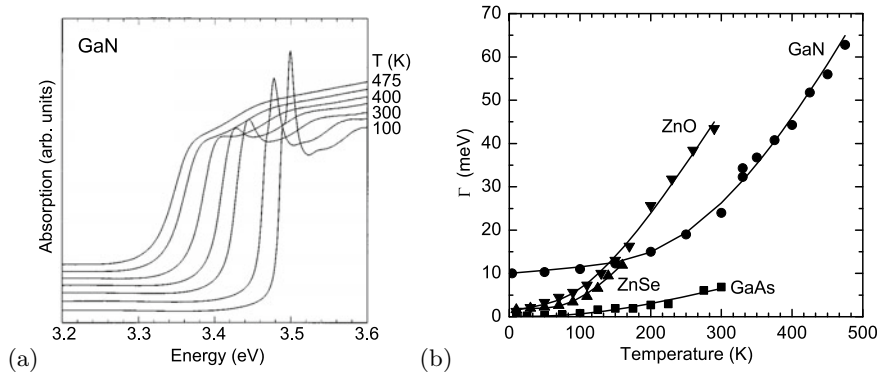

Fig. 9.24 **a** Absorption spectra of GaN bulk (0.38 µm thick epilayer on sapphire) for various temperatures $T = 100$, 200, 300, 350, 400, 450, and 475 K. Adapted from [868] **b** Homogeneous broadening as a function of temperature, *symbols* are experimental data, *solid lines* are fits, rf. Table 9.5

Table 9.5 Phonon broadening parameters (FWHM) of various bulk semiconductors. Values from fits with (9.54) to experimental data for GaAs [871], ZnSe [869], GaN [868], ZnO [872] (phonon energy fitted) as shown in Fig. 9.25b

Material	$\hbar\omega_{LO}$ (meV)	Γ_0 (meV)	γ_{AC} (µeV/K)	γ_{LO} (meV)
GaAs	36.8	0	4 ± 2	16.8 ± 2
ZnSe	30.5	1.9	0 ± 7	84 ± 8
GaN	92	10	15 ± 4	408 ± 30
ZnO	33	1.2	32 ± 26	96 ± 24

9.7.8 Exciton Polariton

Electrons and holes are particles with spin 1/2. Thus, the exciton can form states with total spin $S = 0$ (para-exciton, singlet) and $S = 1$ (ortho-exciton, triplet). The exchange interaction leads to a splitting of these states, the singlet being the energetically higher. The singlet state splits into the longitudinal and transverse exciton with respect to the orientation of the polarization carried by the Bloch functions and the center-of-mass motion **K** of the exciton. Dipole transitions are only possible for singlet excitons (bright excitons). The triplet excitons couple only weakly to the electromagnetic field and are thus also called dark excitons.

The coupling of these states to the electromagnetic field creates new quasi-particles, the exciton polaritons [873, 874]. The dielectric function of the exciton (with background dielectric constant ϵ_b) is

$$\epsilon(\omega) = \epsilon_b \left[1 + \frac{\beta}{1 - (\omega^2/\omega_X)^2}\right] \cong \epsilon_b \left[1 + \frac{\beta}{1 - (\omega^2/\omega_T)^2 + \hbar K^2/(M\,\omega_T)}\right] , \tag{9.55}$$

where β is the oscillator strength and the energy is $\hbar\omega_X = \hbar\omega_T + \hbar^2 K^2/2M$. $\hbar\omega_T$ is the energy of the transverse exciton at $K = 0$. With this dispersion the wave dispersion must be fulfilled, i.e.

$$c^2 k^2 = \omega^2 \epsilon(\omega) , \tag{9.56}$$

where k is the k-vector of the light that needs to be $k = K$ due to momentum conservation. The dependence of the dielectric function on k is called *spatial dispersion* [875]. Generally, up to terms in k^2 it is written as

Table 9.6 Exciton energy (low temperature), LT splitting and exciton polariton oscillator strength for various semiconductors. Values for ZnO from [878], values for GaAs from [879], all other values from [880]

		CdS A	CdS B	ZnO A	ZnO B	ZnSe	GaN A	GaN B	GaAs
$\hbar\omega_T$	(eV)	2.5528	2.5681	3.3776	3.3856	2.8019	3.4771	3.4816	1.5153
Δ_{LT}	(meV)	2.2	1.4	1.45	5	1.45	1.06	0.94	0.08
β	(10^{-3})	1.7	1.1	0.9	3.0	1.0	0.6	0.5	0.11

$$\epsilon(\omega) = \epsilon_b \left[1 + \frac{\beta}{1 - (\omega^2/\omega_0)^2 + D\,k^2} \right] . \tag{9.57}$$

The term k^2 with curvature D (for the exciton polariton $D = \hbar/(M\,\omega_T)$) plays a role in particular when $\omega_T^2 - \omega^2 = 0$. For $\mathbf{k} \neq 0$ even a cubic material is anisotropic. The dimensionless curvature $\hat{D} = Dk'^2$ should fulfill $\hat{D} = \hbar/(Mc) \ll 1$ in order to make k^4 terms unimportant. For exciton polaritons[8] typically $\hat{D} = \hbar\omega_T/(m\,c^2) \approx 2 \times 10^{-5}$ for $\hbar\omega_T = 1\,\text{eV}$ and $m^* = 0.1$.

From (9.56) together with (9.57) two solutions result:

$$\begin{aligned} 2\omega^2 &= c^2k^2 + (1 + \beta + Dk^2)\,\omega_0^2 \\ &\pm \left[-4c^2k^2(1 + Dk^2)\,\omega_0^2 + (c^2k^2 + (1 + \beta + Dk^2)\,\omega_0^2)^2 \right]^{1/2} . \end{aligned} \tag{9.58}$$

The two branches are shown schematically in Fig. 9.25a. Depending on the k value they have a photonic (linear dispersion) or excitonic (quadratic dispersion) character. The anticrossing behavior at $k' \approx \omega_T/c$ (for $\hbar\omega_T = 1\,\text{eV}$, $k' \approx 0.5 \times 10^{-5}\,\text{cm}^{-1}$) creates a bottleneck region in the lower polariton branch. This name stems from the small emission rate of acoustic phonons (i.e. cooling) in that region, as predicted in [876] and experimentally found, e.g. in CdS [877]. The polaritons decay into a photon when they hit the surface. The effect of the oscillator strength of the dispersion is shown in Fig. 9.26 for two-exciton resonance. In the case of several excitons (9.57) reads

$$\epsilon(\omega) = \epsilon_b \left[1 + \sum_{i=1}^{n} \frac{\beta_i}{1 - (\omega^2/\omega_{0,i})^2 + D_i\,k^2} \right] . \tag{9.59}$$

For $k = 0$ either $\omega = 0$ (lower polariton branch) or $\epsilon(\omega_L) = 0$. For the latter we find from (9.57)

$$\omega_L = \sqrt{1 + \beta}\,\omega_T . \tag{9.60}$$

Therefore, the energy splitting ΔE_{LT}, mostly denoted as Δ_{LT}, between the L- and T-exciton energy given by

$$\Delta E_{LT} = \hbar(\omega_L - \omega_T) = \left[\sqrt{1 + \beta} - 1 \right] \hbar\omega_T \approx \beta\,\hbar\omega_T/2 \tag{9.61}$$

is proportional to the exciton oscillator strength (for experimental values see Table 9.6). We note that if (D.9) is used for the dielectric function, β in (9.61) needs to be replaced by β/ϵ_b.

The effect of spatial dispersion on the reflection at the fundamental exciton resonance is depicted in Fig. 9.25b. For non-normal incidence an additional feature due to the longitudinal wave is observed for p-polarization [875]. For a detailed discussion additional effects due to anisotropy in wurtzite crystals,

[8] The dependence of the optical-phonon energies on k is typically too small to make spatial dispersion effects important. According to (5.19) $\hat{D} = -(a_0\omega_{TO}/4c)^2 \approx 4 \times 10^{-11}$ for typical material parameters (lattice constant $a_0 = 0.5\,\text{nm}$, TO phonon frequency $\omega_{TO} = 15\,\text{THz}$).

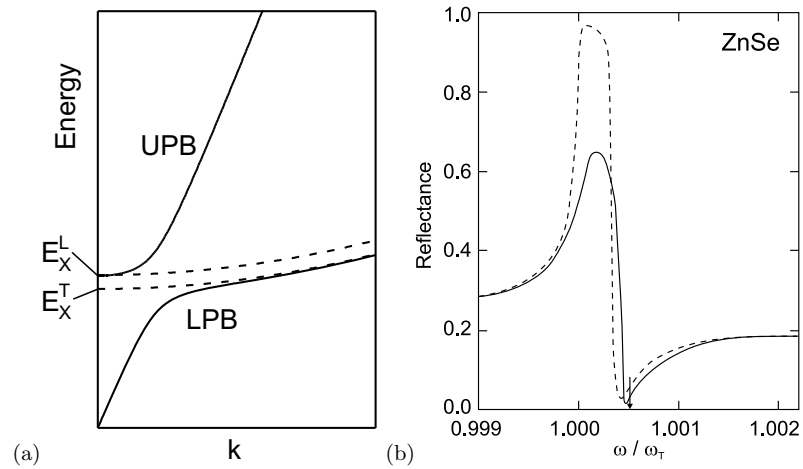

Fig. 9.25 **a** Schematic dispersion of exciton polaritons. The lower polariton branch ('LPB') is at small k photon-like, at large k exciton-like. The upper branch ('UPB') is exciton-like at small k and photon-like at larger k. The limit of the UPB for $k \to 0$ is the energy of the longitudinal exciton. The *dashed lines* represent the pure exciton dispersions. **b** Theoretical effect of spatial dispersion on the reflectance at the fundamental exciton resonance at normal incidence for ZnSe material parameters ($\hbar\omega_T$ =2.8 eV, $\beta = 1.0 \times 10^{-3}$ and a background dielectric constant of $\epsilon_b = 8.1$, damping was set to $\Gamma = 10^{-5}\omega_T$). The arrow denotes the position of ω_L. The *solid* (*dashed*) *line* is with (without) spatial dispersion for $\hat{D} = 0.6 \times 10^{-5}$ ($\hat{D} = 0$). Data from [875]

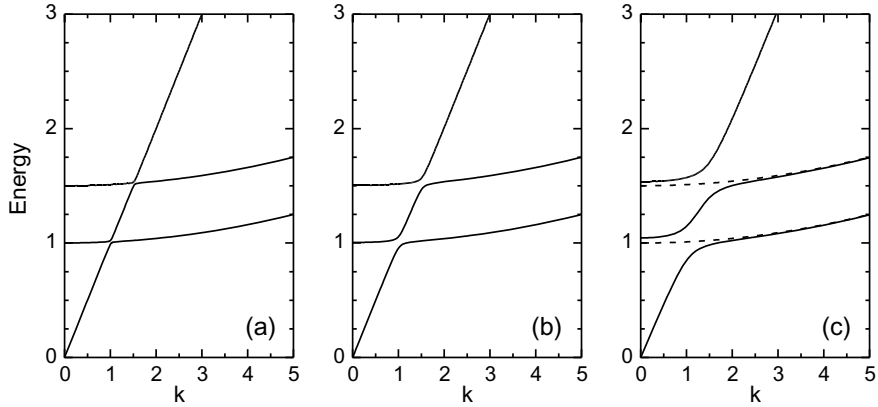

Fig. 9.26 Schematic polariton dispersion for a two-exciton resonance (curvature of exciton dispersion greatly exaggerated, $\hat{D} = 10^{-2}$) at $\omega_{T,1} = 1$ and $\omega_{T,2} = 1.5$ for three different oscillator strengths **a** $f = 10^{-3}$, **b** $f = 10^{-2}$, **c** $f = 10^{-1}$. The *dashed lines* in **c** represent the pure exciton dispersions

an exciton free layer at the semiconductor surface, additional boundary conditions and damping need to be considered [881, 882]. The polariton dispersions of ZnO and GaN are shown in Fig. 9.27.

9.7.9 Bound-Exciton Absorption

Excitons can localize at impurities or inhomogeneities. Such excitons are called *bound excitons*. Here, the absorption due to such complexes is discussed. The recombination is discussed in Sect. 10.3.2.

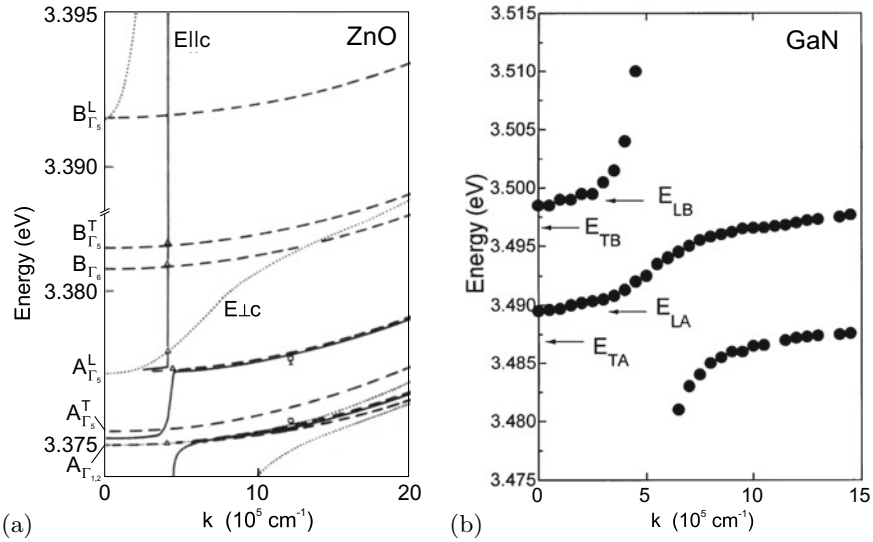

Fig. 9.27 **a** Exciton polariton dispersion ($\mathbf{k} \perp c$) of ZnO with experimental data ($T = 1.8\,\mathrm{K}$). *Solid* (*dotted*) *lines* are for polaritons with $\mathbf{E} \parallel c$ ($\mathbf{E} \perp c$). The *dashed lines* refer to excitons. Adapted from [883]. **b** Exciton polariton dispersion ($T = 2\,\mathrm{K}$) in GaN (on sapphire) for $\mathbf{E} \perp c$. Adapted from [884]

Table 9.7 Index of nitrogen pairs NN_n and energy separation ΔE of bound-exciton transitions from the free-exciton line for $n = 1 \ldots 10$ and the 'A' line

n	1	2	3	4	5	6	7	8	9	10	∞ (A)
ΔE (meV)	143	138	64	39	31	25	22	20	18	17	11

In GaP:N excitons are bound to isoelectronic N impurities (substituting P), resulting in the 'A' line at 2.3171 eV (at $T = 4.2\,\mathrm{K}$).[9] The absorption due to A excitons is well resolved in the spectrum of Fig. 9.28b. At sufficiently high nitrogen doping, there exist nitrogen pairs, i.e. a complex where a nitrogen impurity has a second nitrogen impurity in the vicinity. The pairs are labeled NN_n. It was believed that the second nitrogen atom is in the nth shell around the first one. However, the proper level asignment is probably different in the view of modern theory [544]. Also clusters with more than two nitrogen atoms may exist. NN_1 is a prominent level and relates to a N–Ga–N complex having 12 equivalent sites for the second N atom on the next neighbor anion site. The transitions due to excitons bound to NN_n, as shown in Fig. 9.28a, give a series of lines (see Table 9.7) that fulfill $\lim_{n\to\infty} \mathrm{NN}_n = \mathrm{A}$. Although GaP has an indirect band structure, the absorption coefficient of N-related transitions is large, about $10^5\,\mathrm{cm}^{-1}$ for a nitrogen doping level of $10^{19}\,\mathrm{cm}^{-3}$.[10] This is due to the fact that the electron spatially localized at the nitrogen isoelectronic trap (Sect. 7.7.9) has a sizeable $k = 0$-component of its wave-function (Fig. 7.40), leading to a large transition probability for Γ-point holes with an oscillator strength of 0.09 [885].

[9] The A line is due to excitons with $J = 1$, resulting of coupling of the electron spin 1/2 with the hole angular momentum of 3/2. The B-line is a dipole forbidden line due to 'dark' excitons with $J = 2$.

[10] Also the recombination (Sect. 10.3.2) is efficient and allows green GaP:N and yellow GaAsP:N light emitting diodes.

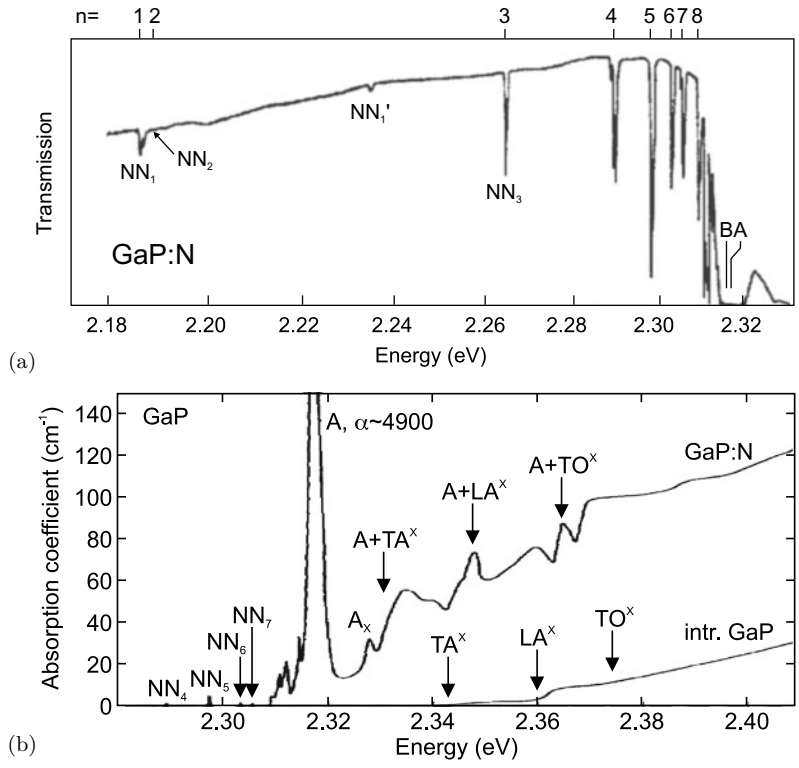

Fig. 9.28 **a** Transmission spectrum of GaP:N with a nitrogen concentration of about $10^{19}\,\mathrm{cm}^{-3}$ at 1.6 K (thickness: 1.1 mm). n is indicated for the first eight transitions due to excitons bound to nitrogen pairs. NN_n' indicate phonon replica. The 'A' line denotes the position of the transition due to excitons bound to a single nitrogen atom (observable for samples with low N doping). The 'B' line is forbidden and due to the $J = 2$ exciton. Adapted from [694]. **b** Absorption spectra of N-doped ($N_N = 7 \times 10^{18}\,\mathrm{cm}^{-3}$) and intrinsic GaP ($T = 2\,\mathrm{K}$). Adapted from [690]

9.7.10 Biexcitons

Similar to two hydrogen atoms forming a hydrogen molecule, two excitons can also form a bound complex, the biexciton involving two electrons and two holes. The biexciton binding energy is defined as

$$E_{XX}^{b} = 2\,E_X - E_{XX}\ . \tag{9.62}$$

Biexcitons are binding in bulk material. Accordingly, the biexciton recombination or absorption occurs at lower energy than that of the exciton. Values of the biexciton binding energy are listed in Table 9.4 for various semiconductors. The ratio of biexciton and exciton binding energies is fairly constant about 0.2. In semiconductors with small exciton binding energy, such as GaAs, biexcitons are hard to observe in bulk material but show up in heterostructures that provide additional carrier confinement (see also Sect. 14.4.4). While the exciton density increases linearly with external excitation, the density of biexcitons increases quadratically.

9.7.11 Trions

The complexes 'eeh' and 'ehh' are called trions. Also, the notation X^- and X^+ is common. X^- is typically stable in bulk material but hard to observe. In quantum wells or dots, trions are easier to observe. In quantum dots excitons with higher charge, e.g. X^{2-}, have also been observed (see Fig. 14.45).

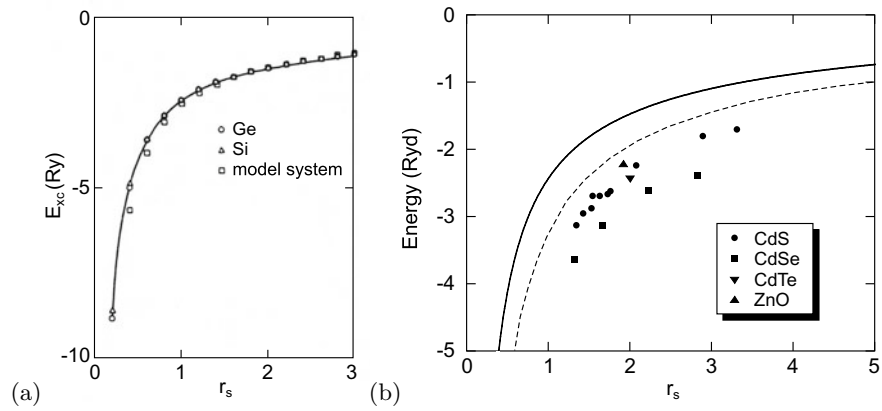

Fig. 9.29 **a** Theoretical exchange and correlation energies in units of the exciton Rydberg energy as a function of the dimensionless variable r_s for Ge, Si and a model system (with one isotropic conduction and valence band each). The *solid line* is a fit according to (9.64). Adapted from [886]. **b** Band gap renormalization in terms of the excitonic Rydberg for various II–VI semiconductors. *Solid line* is the relation according to (9.64), *dashed line* is the dependence predicted in [887] for $T = 30\,\mathrm{K}$. Data are compiled in [888]

9.7.12 Band Gap Renormalization

The band structure theory has been developed so far for small carrier densities. If the carrier density is large the interaction of free carriers has to be considered. The first step was exciton formation. However, at high temperatures (ionization) and at large carrier density (screening) the exciton is not stable. Exchange and correlation energy leads to a decrease of the optical absorption edge that is called *band gap renormalization* (BGR).

An effect due to significant carrier density is to be expected when the density is of the order of the exciton volume, i.e. $n \sim a_B^{-3}$. For $a_B \sim 15\,\mathrm{nm}$ (GaAs) this means $n \sim 3\times10^{17}\mathrm{cm}^{-3}$. The dimensionless radius r_s is defined via

$$\frac{4\pi}{3} r_s^3 = \frac{1}{n\, a_B^3} \,. \tag{9.63}$$

The sum of exchange and correlation energies E_{xc} is found to be mostly independent of material parameters [886] (Fig. 9.29a) and follows the form

$$E_{xc} = \frac{a + b\, r_s}{c + d\, r_s + r_s^2} \,, \tag{9.64}$$

with $a = -4.8316$, $b = -5.0879$, $c = 0.0152$ and $d = 3.0426$. Thus the density dependence of the band gap at small carrier density is $\propto n^{1/3}$. Experimental data for a number of II–VI semiconductors roughly follow such a dependence (Fig. 9.29b).

In Fig. 9.30, a theoretical calculation of the absorption spectrum of bulk GaAs for various carrier densities (n=p) [889] is shown. With increasing density, the excitonic resonance broadens and vanishes. The shape approaches the electron–hole plasma shape. The absorption edge shifts to smaller energies. At high carrier density, the absorption becomes negative in a spectral range before absorption sets in. In this spectral region, the material exhibits gain and an incoming light wave is amplified (cmp. Sect. 10.2.6).

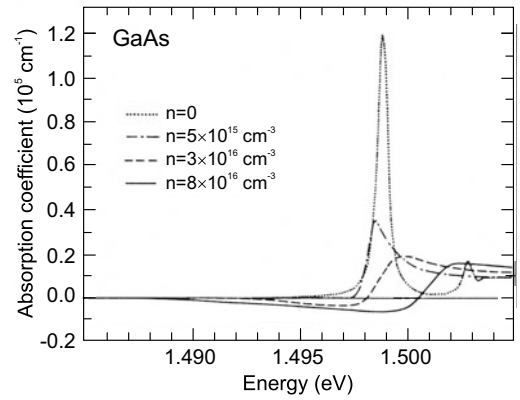

Fig. 9.30 Absorption of GaAs (low temperature, $T = 10\,\mathrm{K}$) as a function of the electron–hole density n (theory). Adapted from [889]

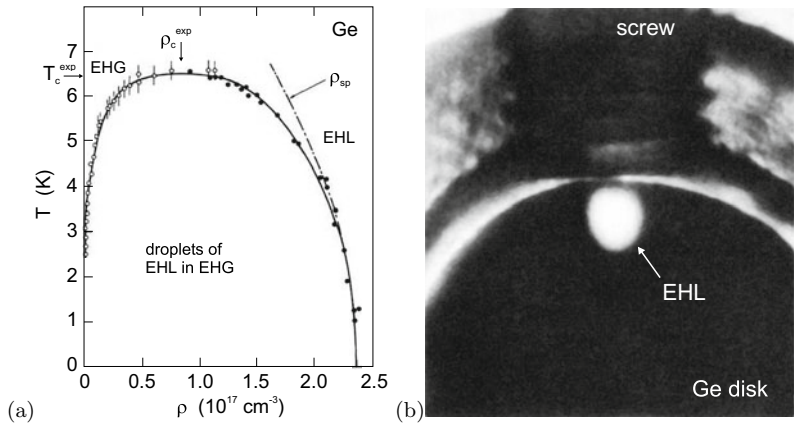

Fig. 9.31 **a** Temperature–density phase diagram of electrons and holes in Ge. The regions of electron–hole gas (EHG) and liquid (EHL) and the droplet phase are labeled. *Solid line* is theoretical calculation, *symbols* are experimental data from [892]. The *dash-dotted line* denoted ρ_{sp} is the experimentally obtained temperature dependence of the liquid density due to single-particle excitations. $\rho_{\mathrm{c}}^{\mathrm{exp}}$ and $T_{\mathrm{c}}^{\mathrm{exp}}$ denote the experimental critical density and temperature, respectively. Adapted from [893]. **b** Photographic image of radiative recombination (at 1.75 μm wavelength) from a 300-μm diameter droplet of electron–hole liquid (EHL) in a stressed (001) Ge disk (diameter 4 mm, thickness 1.8 mm) at $T = 2\,\mathrm{K}$. The stress is applied from the top by a nylon screw along a ⟨110⟩ direction. Adapted from [894], reprinted with permission, ©1977 APS

9.7.13 Electron–Hole Droplets

At low temperature and high density, electron–hole pairs in Ge and Si can undergo a phase transition into a liquid state. This electron–hole liquid (EHL) was suggested in [890] and is a Fermi liquid exhibiting the high conductivity of a metal and the surface and density of a liquid. The condensation is due to exchange interaction and correlation. The formation is fostered by the band structure of Ge [891] and the long lifetime of carriers in the indirect band structure. In unstressed Ge typically a cloud of electron–hole droplets with diameter in the μm range exists. The phase diagram is shown in Fig. 9.31a. In suitably stressed Ge electron–hole droplets with several hundred μm diameter form around the point of maximum shear strain in inhomogeneously strained crystals, as shown in Fig. 9.31b. The pair density in such a liquid is of the order of $10^{17}\,\mathrm{cm}^{-3}$.

We note that the metallic EHL state hinders observation of the Bose–Einstein condensation (BEC) of (bosonic) excitons. The light-exciton mass offers a high condensation temperature in the 1 K range

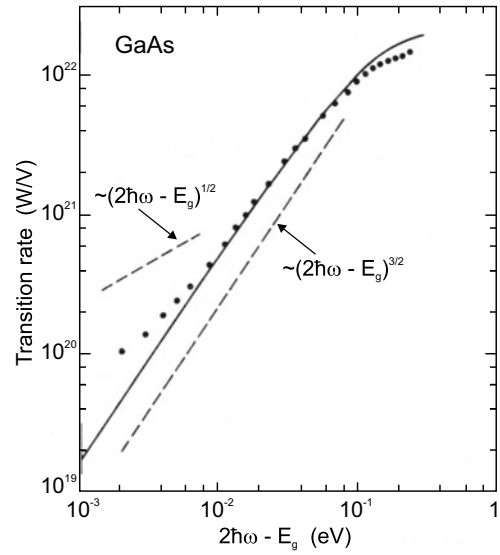

Fig. 9.32 Experimental two-photon absorption spectrum of GaAs ($T = 4\,\mathrm{K}$) (*dots*) plotted as a function of the difference of the double-photon energy $2\hbar\omega$ from the GaAs band edge E_g. The *solid line* is a theoretical calculation, the *dashed lines* represent slopes with exponent 1/2 and 3/2, respectively. Adapted from [901]

(compared to the mK range for atoms). Recent experiments with spatially indirect excitons in coupled quantum wells lead towards BEC [895, 896]. A sufficiently long lifetime ensures cooling of the excitons close to the lattice temperature. Another potential candidate for BEC are long-living excitons (ms-range) in Cu_2O [897]. The condensation of polaritons (cf. Sect. 9.7.8) in microcavities to well-defined regions of **k**-space has been discussed in [898] and compared to bosonic condensation in bulk.

9.7.14 Two-Photon Absorption

So far, only absorption processes that involve one photon have been considered. The attenuation of the intensity I of a light beam (of frequency ω_0) along the z direction can be written as

$$\frac{\mathrm{d}I}{\mathrm{d}z} = -\alpha\, I - \beta\, I^2 \,, \tag{9.65}$$

where α is due to the (linear) absorption coefficient (and possibly scattering) and β is the two-photon absorption coefficient. A two-photon process can occur in two steps, e.g. via a midgap level, which is not considered any further here. Here, we consider two-photon absorption (TPA) via the population of a state at $2\hbar\omega_0$ higher energy than the initial state with a nonlinear optical process. The TPA coefficient is related to the nonlinear third-order electric dipole susceptibility tensor [899] χ_{ijkl}. Within the two-band approximation theory predicts [900]

$$\beta \propto \left(2\,\hbar\omega_0 - E_\mathrm{g}\right)^{3/2} \,. \tag{9.66}$$

The exponent 3/2 is indeed found experimentally, as shown in Fig. 9.32 for GaAs. The strength of absorption depends on the relative orientation of the light polarization with respect to the main crystallographic directions, e.g. TPA for polarization along $\langle 110\rangle$ is about 20% larger than for the $\langle 100\rangle$ orientation.

9.8 Impurity Absorption

9.8.1 Shallow Levels

For charge carriers bound to shallow impurities long range Coulomb forces are most important and they exhibit a hydrogen-like term scheme

$$E_n = \frac{m^*}{m_0}\frac{1}{\epsilon_r^2}\frac{1}{n^2} \times 13.6\,\mathrm{eV}\ , \tag{9.67}$$

with the ionization limit E_∞ being the conduction (valence) band edge for donors (acceptors), respectively. They can be excited by light to the nearest band edge. Such absorption is typically in the FIR region and can be used for photodetectors in this wavelength regime. The optical absorption cross section of impurity absorption can be related to the carrier capture cross section [588, 589].

The actual transition energies can deviate from (9.67) due to deviation of the potential close to the impurity from the pure Coulomb potential. Such an effect is known as the chemical shift or central cell correction (cf. Sect. 7.5.5) and is characteristic of the particular impurity. In GaAs such shifts are small ($\sim$100 μeV) [902].

The term scheme for P in Si is shown in Fig. 9.33a. The ground state (1s) is split because of a reduction of the tetrahedral symmetry due to intervalley coupling. The anisotropic mass at the X-valley in Si

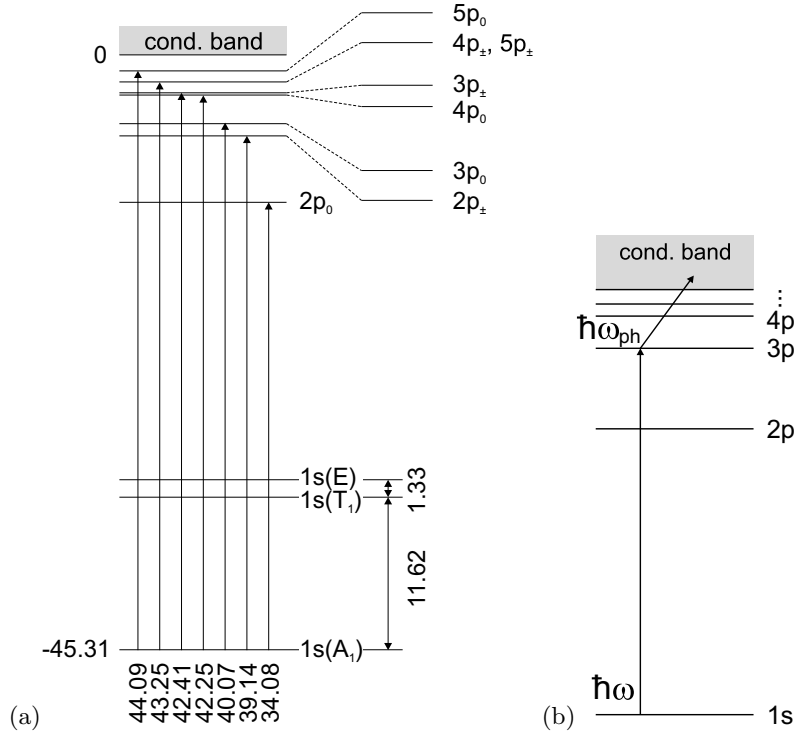

Fig. 9.33 **a** Term scheme of phosphorus donor in silicon, all energies in meV. After [903]. **b** Schematic sequence for photothermal ionization, here absorption of a photon with $\hbar\omega = E_{3p} - E_{1s}$ and subsequent absorption of a phonon with energy $\hbar\omega_{ph} \geq E_\infty - E_{3p}$

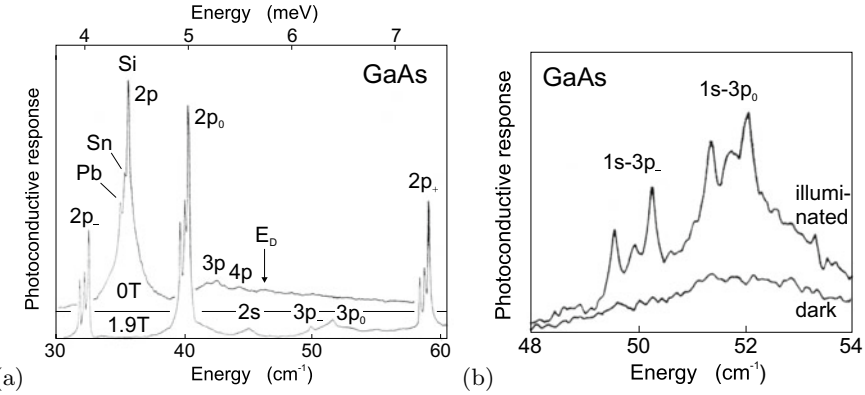

Fig. 9.34 **a** Far-infrared photoconductivity response (Lyman-type s→p series) of not intentionally doped GaAs with residual donors Pb, Sn, and Si, $N_A = 2.6 \times 10^{13}\,cm^{-3}$, $N_D - N_A = 8 \times 10^{12}\,cm^{-3}$. The *upper* (*lower*) curve is for a magnetic field of 0 (1.9) T. Measurement temperature is 4.2 K. **b** Photoconductive response of a (different) GaAs sample with the same impurities ($N_D = 1 \times 10^{13}\,cm^{-3}$) with (*upper curve*) and without (*lower curve*) illumination with above-bandgap light ($B = 1.9\,T$, $T = 4.2\,K$). Adapted from [905]

causes the p states (and states with higher orbital angular momentum) to split into p_0 and $p_\pm$ states. Such an effect is absent in a direct semiconductor with an isotropic conduction-band minimum such as GaAs (Fig. 9.34). Optical transitions between the 1s and various p states can be directly observed in absorption, e.g. for Si:P in [904]. These transitions are also observed in photoconductivity because the missing energy to the ionization into the continuum is supplied by a phonon at finite temperature (photothermal ionization) (Fig. 9.33b) [903]. The splitting of the 2p transition in Fig. 9.34a is the chemical shift due to different donors incorporated in the GaAs (Si, Sn, and Pb). Peak broadening is mostly due to Stark broadening due to neighboring charged impurities. The application of a magnetic field induces Zeeman-like splittings and increases the sharpness of the peaks. The peak width can be

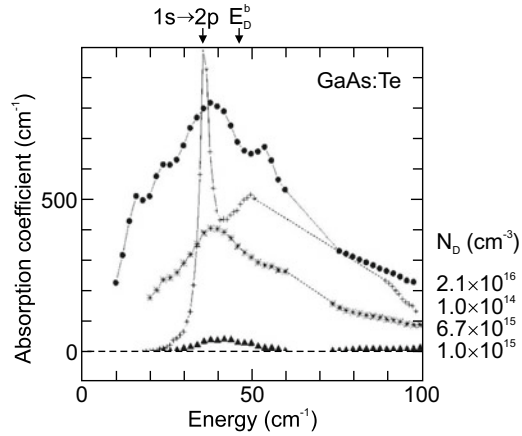

Fig. 9.35 Low-temperature ($T = 1.35\,K$) absorption spectra of highly doped n-type GaAs:Te with doping concentrations as labeled (*circles*: $N_D = 2.1 \times 10^{16}\,cm^{-3}$, *stars*: 6.7×10^{14}, *triangles*: 1.0×10^{15}). A sharp photoconductivity spectrum (in arbitrary units) from low-doped GaAs:Te (*crosses*, $N_D = 1.0 \times 10^{14}\,cm^{-3}$) is shown for comparison (cf. Fig. 9.34a). The energy of the 1s→2p transition and the donor binding energy (onset of continuum absorption) are indicated. Adapted from [906]

further increased by illuminating the sample with light having a higher energy than the band gap. The additional charge carriers neutralize charged impurities and allow higher resolution (Fig. 9.34b).

In Fig. 9.35 absorption spectra of highly doped n-type GaAs are shown. For doping concentrations larger than the critical concentration of $\sim 1 \times 10^{16}\,\mathrm{cm}^{-3}$ (cf. Table 7.6) significant broadening is observed due to the formation of an impurity band.

9.8.2 Deep Levels

The absorption of deep levels is typically in the infrared. In Fig. 9.36a the possible optical absorption processes involving the Fe levels in InP (cf. Sect. 7.7.8) during the charge transfer $Fe^{3+} \rightarrow Fe^{2+}$ are shown. These transitions and their fine structure (Fig. 9.36b) have been observed in calorimetric absorption spectroscopy (CAS) experiments [682].

In Fig. 9.37 photoproductivity of Si:Mg is shown. The sharp peaks are due to transitions of interstitial, singly ionized Mg, Mg_i^+ [907]. Mg in Si is a double donor [653] (see Sect. 7.7.2). Above the ionization limit of about 256 meV, the peaks are replicated, shifted by the LO phonon energy of 59.1 meV. However, now they rather appear as dips. This behavior is typical for a discrete state interacting with a continuum, also called Fano resonance[908, 909] with its characteristic lineshape, going *below* the continuum level.

The absorption spectra due to various deep acceptors in GaAs are compared in Fig. 9.38. The density of states in the band increases with k (proportional to $\sqrt{E - E_c}$). The carrier on the impurity is strongly localized and described with a wave packet centered around Γ, its k-components decreasing with increasing k. Thus the maximum absorption will be at an intermediate k-value and an associated energy larger than the ionization energy E_i (lowest transition to continuum at for $k = 0$). The lineshapes in Fig. 9.38 fit to a model with a δ-potential (zero range model, neglecting long range Coulomb terms) [910] with maximum absorption close to 2 E_i,

$$\alpha(E) \propto \frac{E_i^{1/2}\,(E - E_i)^{3/2}}{E^3} \,. \tag{9.68}$$

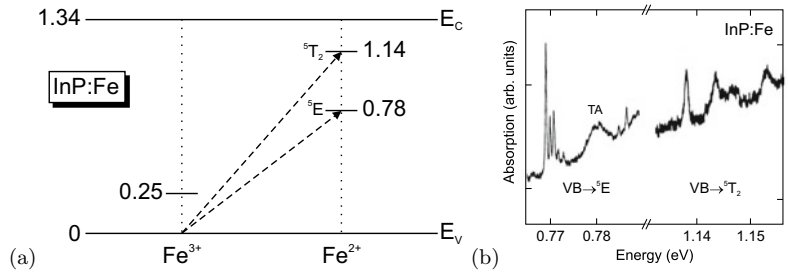

Fig. 9.36 **a** Schematic band diagram of InP with levels of Fe impurities in the 3+ and 2+ charge states at low temperature. All energies are given in eV. The *arrows* denote the optical transition of a valence-band electron to the Fe center, $Fe^{3+} + \hbar\omega \rightarrow Fe^{2+} + h$. **b** Calorimetric absorption spectra (at $T = 1.3\,\mathrm{K}$) of InP:Fe, [Fe]=$5 \times 10^{16}\,\mathrm{cm}^{-3}$. Part **b** Adapted from [682]

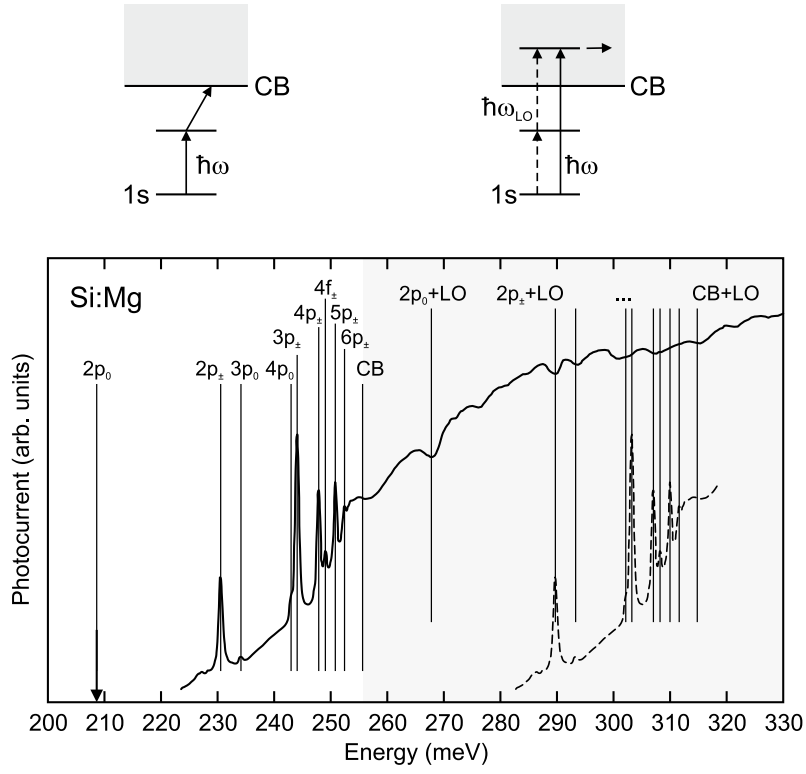

Fig. 9.37 Photocurrent spectrum of Si:Mg. Transitions are due to Mg_i^+ from its 1s state to excited states as labeled and indicated by *vertical lines*. CB denotes the conduction band edge (ionization limit). Above the CB edge (*shaded area*) phonon-assisted absorption occurs (Fano resonances). For comparison the absorption spectrum below CB is shown shifted by the phonon energy (*dashed line*). Above the plot, the transition mechanisms (photothermal ionization and Fano resonance) are schematically shown. Adapted from [907]

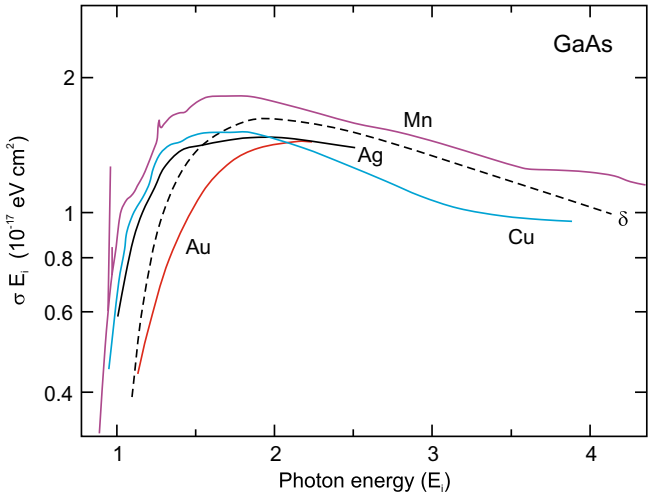

Fig. 9.38 Absorption spectra ($\sigma = \alpha/p$) due to various deep impurities in GaAs as labeled. The *dashed line* is a theoretical lineshape assuming a hole bound to a δ-potential. The energy axis is scaled by the ionization energy. The kink for Mn at 3.5 $E_i \approx 450$ meV is due to the onset of absorption into the split-off valence band. Adapted from [314]

9.9 Absorption in the Presence of Free Charge Carriers

In the presence of charge carriers, various absorption processes can occur. First, the dissipative motion of carriers leads to infrared absorption, termed the free carrier absorption (Sect. 9.9.1). Filling of a band with carriers leads to a shift of the band-band absorption edge, the Burstein-Moss shift (Sect. 9.9.2). Besides the free-carrier absorption, free carriers present in the semiconductor can lead to further absorption processes with transition energies below the band gap. These processes are due to transitions within the band structure and can be

- inter-valence band transitions of holes (Sect. 9.9.3),
- phonon-assisted inter-valley transitions of electrons (Sect. 9.9.4),
- phonon-assisted intra-band transitions of electrons (Sect. 9.9.5).

9.9.1 Absorption Coefficient, Plasma Frequency

The absorption due to free carriers in the infrared spectral range (away from phonon resonances) can be described with the Drude model [911].

A time-dependent electric field accelerates the charge carriers within a band. The excess energy is subsequently transferred to the lattice via scattering with phonons. A review of the effect of free carriers on optical properties can be found in [912]. In the relaxation-time approximation energy is relaxed with a time constant τ. Thus energy is absorbed from the electromagnetic wave and dissipated. Effectively, this process represents an intra-band excitation.

The complex conductivity (8.37) is given by

$$\sigma^* = \sigma_\mathrm{r} + \mathrm{i}\sigma_\mathrm{i} = \frac{n\,e^2\,\tau}{m^*}\left(\frac{1}{1+\omega^2\tau^2} + \mathrm{i}\frac{\omega\tau}{1+\omega^2\tau^2}\right) . \tag{9.69}$$

We note that a static magnetic field introduces birefringence as discussed in more detail in Sect. 15.2.2. The wave equation for the electric field is

$$\nabla^2\mathbf{E} = \epsilon_\mathrm{r}\,\epsilon_0\,\mu_0\,\ddot{\mathbf{E}} + \sigma^*\,\mu_0\,\dot{\mathbf{E}} . \tag{9.70}$$

For a plane wave $\propto \exp[\mathrm{i}(\mathbf{kr} - \omega t)]$ the wavevector obeys

$$k = \frac{\omega}{c}\sqrt{\epsilon_\mathrm{r} + \mathrm{i}\,\frac{\sigma^*}{\epsilon_0\,\omega}} , \tag{9.71}$$

where $c = (\epsilon_0\mu_0)^{-1/2}$ is the velocity of light in vacuum, ϵ_r is the background dielectric constant (for large ω).

The part ϵ_FC of the dielectric function due to free carriers is

$$\epsilon_\mathrm{FC} = \frac{\mathrm{i}}{\epsilon_0\,\omega}\,\sigma^* . \tag{9.72}$$

The complex index of refraction is

$$n^* = n_\mathrm{r} + \mathrm{i}\,\kappa = \sqrt{\epsilon_\mathrm{r} + \mathrm{i}\frac{\sigma^*}{\epsilon_0\,\omega}} . \tag{9.73}$$

Taking the square of this equation yields

$$n_r^2 - \kappa^2 = \epsilon_r + i\,\frac{\sigma_i}{\epsilon_0\,\omega} = \epsilon_r - \frac{n\,e^2}{\epsilon_0\,m^*}\,\frac{\tau^2}{1+\omega^2\tau^2} \tag{9.74a}$$

$$2\,n_r\,\kappa = \frac{\sigma_r}{\epsilon_0\omega} = \frac{n\,e^2}{\epsilon_0\,\omega\,m^*}\,\frac{\tau}{1+\omega^2\tau^2}\,. \tag{9.74b}$$

The absorption coefficient is related to κ by (9.9). For the case of higher frequencies, i.e. $\omega\tau \gg 1$, the absorption is

$$\alpha = \frac{n\,e^2}{\epsilon_0\,c\,n_r\,m^*\,\tau}\,\frac{1}{\omega^2} \propto \lambda^2\,. \tag{9.75}$$

The absorption decreases with increasing frequency like ω^{-r}. The classical Drude treatment as followed here results in an exponent of $r = 2$. This is the case for neutral impurity scattering and also for small frequencies $\hbar\omega \ll E_F$. A more detailed discussion of the energy dependence of free-carrier absorption can be found in [913]. Other exponents have been derived for scattering by acoustical phonons ($r = 3/2$), LO phonons ($r = 5/2$) and ionized impurities ($r = 7/2$). More detailed quantum mechanical treatments of free-carrier absorption in the presence of impurities and phonons can be found in [914–916].

For semiconductors free-carrier absorption is particularly important in the mid- and far-infrared regions when carriers are present due to doping or thermal excitation. In Fig. 9.39a absorption spectra of n-type Ge for various doping concentrations are shown. The absorption coefficient in the transparency regime varies proportionally to λ^2 as predicted in (9.75). In Fig. 9.39a, the absorption can be seen to rise for photon energy above 0.7 eV due to absorption in the band structure. Electrons are excited from the valence band across the fundamental band gap into the conduction band (cmp. Sect. 9.7.3), which is an indirect transition in Ge.

In Fig. 9.39b the absorption coefficient due to free carrier absorption at fixed wavelength is shown as a function of dopant concentration.[11] The slope is slightly overlinear, indicating a weak dependence $\tau(n)$. A sub-linear relation has been found for heavily p-doped GaAs [917].

The index of refraction is given by (also for $\omega\tau \gg 1$)

$$\begin{aligned} n_r^2 &= \epsilon_r - \frac{ne^2}{\epsilon_0 m^*\omega^2} + \kappa^2 = \epsilon_r\left[1 - \left(\frac{\omega_p}{\omega}\right)^2\right] + \frac{\epsilon_r^2}{4n_r^2}\left(\frac{\omega_p}{\omega}\right)^4 \frac{1}{\omega^2\tau^2} \\ &\approx \epsilon_r\left[1 - \left(\frac{\omega_p}{\omega}\right)^2\right], \end{aligned} \tag{9.76}$$

where

$$\omega_p = \sqrt{\frac{n\,e^2}{\epsilon_r\,\epsilon_0\,m^*}} \tag{9.77}$$

is the plasma frequency. The approximation is valid for small absorption and when $(\omega\tau)^{-2}$ can be neglected. A graphical representation is given in Fig. 9.40a. For coupling to electromagnetic waves (still $\omega\tau \gg 1$)

$$\epsilon(\omega) = \epsilon_r\left[1 - \left(\frac{\omega_p}{\omega}\right)^2\right] = \frac{c^2\,k^2}{\omega^2} \tag{9.78}$$

must be fulfilled. It follows that the dispersion relation in the presence of free carriers (Fig. 9.40b) is

[11] Even at low temperature, $n \approx N_D$ since $N_D \gg N_c$ (cf. [594] and Sect. 7.5.7).

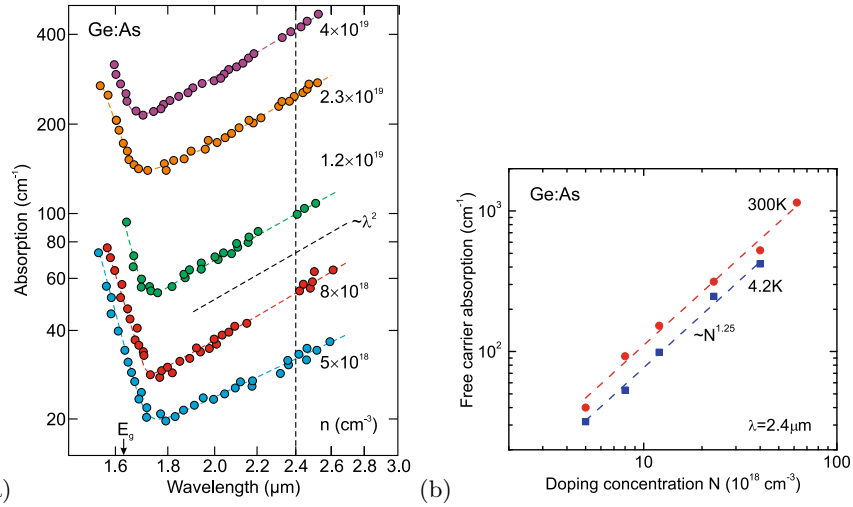

Fig. 9.39 **a** Optical absorption spectra (at $T = 4.2\,\mathrm{K}$) of n-type Ge for various As dopant concentrations as labeled. The *arrow* denotes the band edge of undoped Ge, the *vertical dashed line* the energy for which the free-carrier absorption is measured in part **b**. The inclined *dashed line* visualizes the slope $\propto \lambda^2$. *Curved dashed lines* are guides to the eye. Adapted from [851]. **b** Free-carrier absorption at $\lambda = 2.4\,\mu\mathrm{m}$ as determined from part **a** of the figure (*blue squares*) as a function of As dopant concentration. Additionally data at 300 K (*red circles*) from the same samples are included [851]. The *dashed lines* visualizes the slope $\propto N_\mathrm{D}^{1.25}$

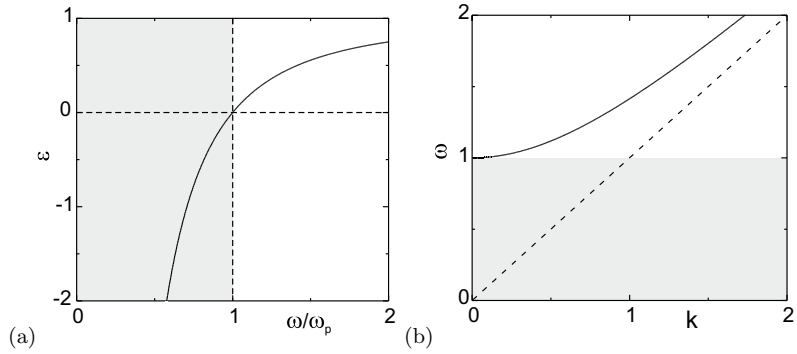

Fig. 9.40 **a** Dielectric constant for plasmon oscillations. *Shaded area* represents region of attenuation (negative ϵ). **b** Dispersion relation (k in units of ω_p/c, ω in units of ω_p) in the presence of free carriers (9.79, for $\epsilon_\mathrm{r} = 1$). *Shaded area* represents forbidden frequency range for propagating solutions. *Dashed line* is photon dispersion $\omega = ck$

$$\omega^2 = \omega_\mathrm{p}^2 + \frac{c^2 k^2}{\epsilon_\mathrm{r}} \,. \tag{9.79}$$

For $\omega > \omega_\mathrm{p}$, $\epsilon > 0$, thus waves can propagate. For $\omega < \omega_\mathrm{p}$, however, the dielectric constant is negative, i.e. $\epsilon < 0$. For such frequencies waves are exponentially damped and cannot propagate or penetrate a layer. This effect can be used in a plasmon waveguide or in metamaterials (cf. Sect. 19.1.10). The expected dependence of the plasmon wavelength on the carrier density $\lambda_\mathrm{p} = 2\pi c/\omega_\mathrm{p} \propto n^{-1/2}$ is depicted in Fig. 9.41 for GaAs. For semiconductors the plasmon frequency is in the mid-or far-infrared spectral region.[12]

[12]The much higher free-electron density in metals shifts the plasma frequency to the UV, explaining the reflectivity of metals in the visible and their UV transparency.

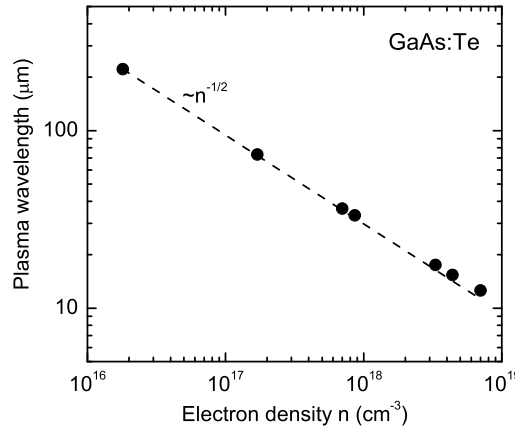

Fig. 9.41 Plasma wavelength λ_p for n-type GaAs with various electron concentrations due to different doping levels. *Filled circles*: experimental values, *dashed line*: $n^{-1/2}$ dependence; the deviation is due to nonparabolicity of the electron mass (cf. Fig. 9.53b). Data from [918]

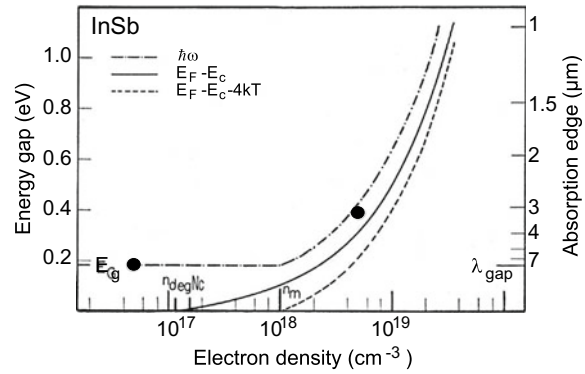

Fig. 9.42 Burstein–Moss effect at InSb ($E_g = 0.18\,\text{eV}$) at room temperature. Theoretical dependence and data points for intrinsic InSb and $5 \times 10^{18}\,\text{cm}^{-3}$ n-type. Data from [919]

9.9.2 *Burstein–Moss Shift*

In the discussion so far it has been assumed that all target states in the conduction band are empty. In the presence of free carriers the absorption is modified by the

- change of the distribution function
- many-body effects (band gap renormalization).

The latter is discussed in the next section. For a degenerate electron distribution all states close to the conduction-band edge are populated. Thus a transition from the valence band cannot take place into such states. This shift of the absorption edge to higher energies is called the Burstein–Moss shift [919, 920]. Originally, the Burstein–Moss shift was evoked to explain the absorption shift in InSb with varying carrier concentration (Fig. 9.42).

k-conserving optical transitions between parabolic hole and electron bands have the dependence

$$E = E_g + \frac{\hbar^2 k^2}{2\,m_e} + \frac{\hbar^2 k^2}{2\,m_h} = E_g + \frac{\hbar^2 k^2}{2\,m_r}\,, \tag{9.80}$$

where m_r is the reduced mass of electron and hole. About $4kT$ below the Fermi level all levels in the conduction band are populated (Fig. 9.43). Thus the k value at which the absorption starts is given as

$$\hat{k} = \sqrt{\frac{2\,m_e}{\hbar^2}\,(E_F - E_C - 4kT)}\,. \tag{9.81}$$

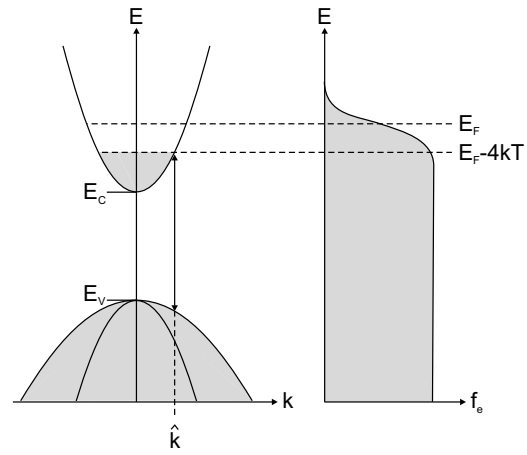

Fig. 9.43 Principle of Burstein–Moss shift. *Left panel*: Schematic band structure with completely filled electron states shown in *grey*. The k-vector for the lowest photon energy optical absorption process is indicated as $\hat{k}$. *Right panel*: Electron distribution function for a degenerate electron gas with Fermi level in the conduction band

Besides the energy shift in the conduction band, the corresponding energy shift in the valence band $\hbar\hat{k}^2/(2m_\mathrm{h})$ must be considered. Thus, the Burstein–Moss shift of the absorption edge is

$$\Delta E = \hbar\omega - E_\mathrm{g} = (E_\mathrm{F} - 4kT - E_\mathrm{C})\left(1 + \frac{m_\mathrm{e}}{m_\mathrm{h}}\right) . \tag{9.82}$$

The relation between n and the Fermi level is given by (7.6). If $E_\mathrm{F} - E_\mathrm{C} \gg kT$ the Fermi integral can be approximated by $\frac{2}{\sqrt{\pi}}\frac{2}{3}\left(\frac{E_\mathrm{F}-E_\mathrm{C}}{kT}\right)^{3/2}$. Using (7.8) for N_C, the Burstein–Moss shift can be written for this case as

$$\Delta E = n^{2/3}\,\frac{h^2}{8\,m_\mathrm{e}}\left(\frac{3}{\pi}\right)^{2/3}\left(1 + \frac{m_\mathrm{e}}{m_\mathrm{h}}\right) \approx 0.97\,\frac{h^2}{8\,m_\mathrm{r}}\,n^{2/3} . \tag{9.83}$$

The $n^{2/3}$ dependence of the energy shift is found, e.g., for CdO[13] with different carrier concentrations (due to different deposition temperature, no intentional doping) [921] and depicted in Fig. 9.44a. Similar behavior is found for ITO (indium-tin-oxide) thin films, deposited at different sputtering conditions, leading to different carrier concentrations (9.44b).

9.9.3 Inter-Valenceband Transitions

Transitions within the valence band can occur between three bands, i.e. lh→hh, so→hh, and so→lh, as schematically depicted in Fig. 9.45. Theoretical treatments have been given in [923, 924]. For GaAs, such intravalence-band absorption occurs at photon energies close to Δ_0 as shown in Fig. 9.46a for p-type GaAs:Zn [925]. For p-type GaSb, the absorption coefficient below the fundamental band gap is found almost entirely due to inter-valence band transitions, as shown in Fig. 9.46b for a hole concentration of $p = 3.2 \times 10^{16}\,\mathrm{cm}^{-3}$ [926].

[13] CdO is an indirect semiconductor, the optical band gap is the energy of the direct transition at the Γ-point, typically obtained from extrapolation in the α^2 versus energy plot. The indirect transitions involve holes from other points in the Brillouin zone (cmp. Fig. 6.13).

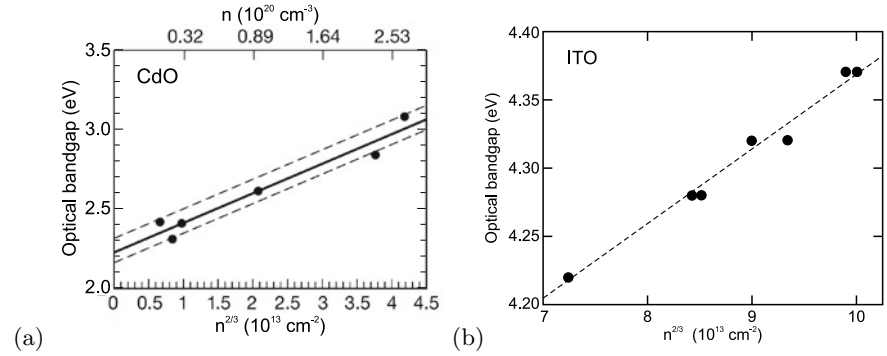

Fig. 9.44 **a** Burstein–Moss effect in CdO. The linear fit is for $E_g = 2.22(8)\,\text{eV}$ and $m_r = 0.113(11)\,m_e$. The *dashed lines* indicate the confidence interval of $\pm 0.08\,\text{eV}$. Adapted from [921]. **b** Burstein–Moss effect in ITO (indium-tin-oxide) versus the 'optical' carrier density determined from the position of the plasma edge. The *dashed line* is guide to the eye. Data from [922]

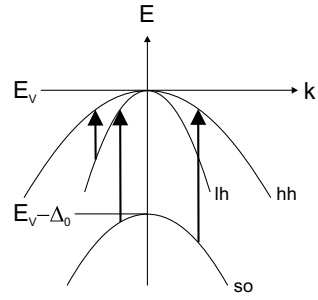

Fig. 9.45 Schematic optical transitions within the valence band

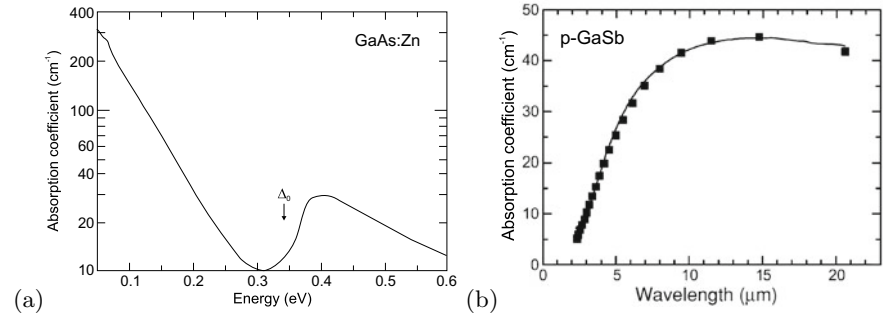

Fig. 9.46 **a** Optical absorption spectrum of GaAs:Zn with $p = 2.7 \times 10^{17}\,\text{cm}^{-3}$ at $T = 84\,\text{K}$. The absorption above the split-off energy Δ_0 is due to the hh/lh $\rightarrow$ s-o process. Adapted from [925]. **a** Optical absorption coefficient of GaSb with $p = 3.2 \times 10^{16}\,\text{cm}^{-3}$. Experimental data (*solid line*) and calculation of inter-valence band contribution (*squares*). The free carrier contribution is less than $5\,\text{cm}^{-1}$ in the considered spectral range. Adapted from [926]

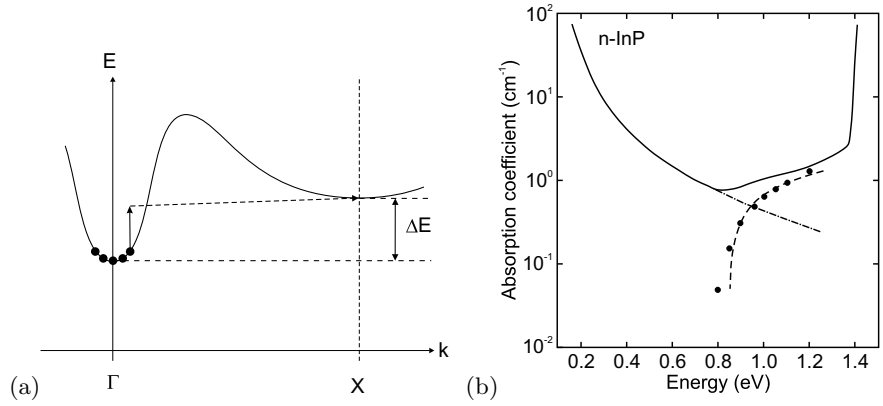

Fig. 9.47 **a** Schematic of inter-valley conduction band transitions involving a photon (*solid line arrow*) and a phonon (*dashed line arrow*). **b** Optical absorption coefficient of InP with $n = 1.65 \times 10^{18}\,\mathrm{cm}^{-3}$. Experimental data (*solid line*) and calculation of inter-valley band contribution (*dashed line*). The extrapolated free carrier contribution is shown as *dash-dotted line* and the difference of experimental absorption and extrapolated free carrier contribution as *circles*. Adapted from [927]

9.9.4 Inter-Valley Transitions

Electrons at the conduction band minimum can undergo optical transitions to the same band at a different point of the Brillouin zone. Such intervalley transition, as sketched in Fig. 9.47a, is phonon-assisted to fulfill momentum conservation and occurs around the energy difference ΔE between the two valleys (cmp. Table 8.4).

For InP with an electron concentration of $n = 1.65 \times 10^{18}\,\mathrm{cm}^{-3}$, below the fundamental band edge at 1.4 eV, an additional contribution starting around 0.8–0.9 eV is found besides the free carrier absorption (Fig. 9.47b) [927]. Taking into account the filling of the bottom of the conduction band, an energy separation for the two valleys of $\Delta E = 0.90 \pm 0.02\,\mathrm{eV}$ was found for various values of the electron concentrations. This energy corresponds to the energy difference of conduction band minima at Γ and X in InP. The lineshape of this absorption processes can be modeled and fits well the difference of measured absorption and extrapolated free-carrier absorption spectra. Transitions to the lower minimum at L ($\Delta E = 0.6\,\mathrm{eV}$) are not observed, possibly masked by the free-carrier absorption.

9.9.5 Intra-Band Transitions

Phonon-assisted transitions within the lowest conduction band (not to a different valley), as indicated schematically in Fig. 9.48a for the SnO_2 band structure [928], can cause absorption at photon energies below the fundamental absorption edge. Actually in SnO_2, the optical transition across the fundamental band gap is only weakly dipole-allowed and leads to small absorption coefficient below $100\,\mathrm{cm}^{-1}$ directly above the fundamental band gap of about 3.6 eV. The strong dipole-allowed transition with absorption coefficient around $10^5\,\mathrm{cm}^{-1}$ begins at about 4.3 eV and stems from electrons in a lower valence band [929]. The free-carrier absorption due to transitions within the lowest conduction band are calculated to dominate below 2.8 eV (Fig. 9.48b) and thus can also impact transparency in the visible spectral range. The calculated slope is close to $\alpha \propto \lambda^3$ (cmp. (9.75)), expected from the linear dispersion of the conduction band away from the Γ-point [928]. A similar effect with the contribution

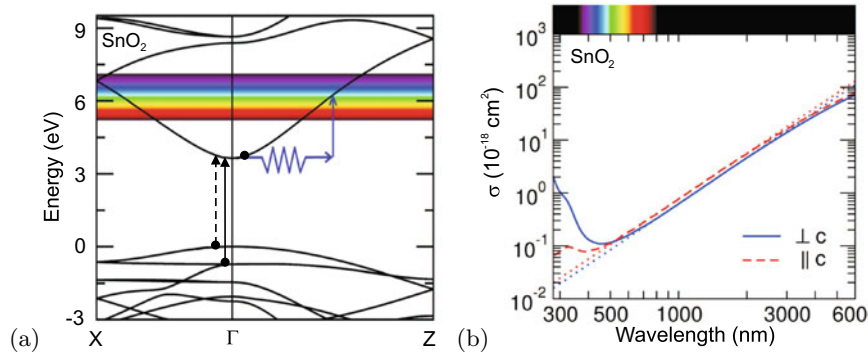

Fig. 9.48 **a** Band structure of SnO_2 and indirect intra-band absorption process; the transition from the topmost valence band (*dashed arrow*) is forbidden. **b** Calculated free-carrier absorption($\sigma = \alpha/n$) for SnO_2. The *solid* and *dashed lines* are results including phonon-assisted transitions for two light polarizations. The *dotted lines* are fits of the Drude model to the infrared regime. Adapted from [928]

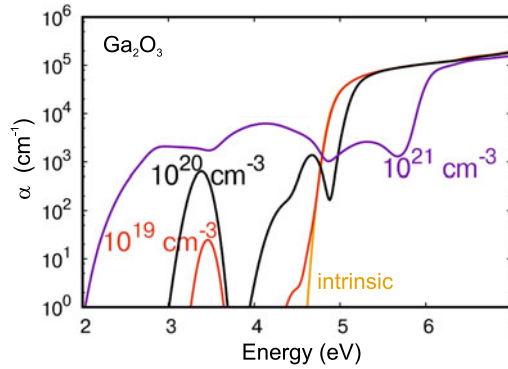

Fig. 9.49 Calculated room temperature absorption coefficient Ga_2O_3 as a function of energy (for light polarized along the z direction) for undoped/intrinsic material and three different electron concentrations as labelled. Adapted from [930]

of inter-band and intra-band transitions leading to absorption within the band gap transparency regime has been calculated for Ga_2O_3 as shown in Fig. 9.49 for various doping levels [930].

9.10 Lattice Absorption

Due to the lack of a dipole moment of the optical phonons, no first order interaction of optical phonons and (infrared) light exists in the diamond structure for Si and Ge due to crystal structure symmetry [931]. However, higher order processes contribute to lattice absorption in these materials [932, 933]. E.g., two-photon bands are due to a dipole moment that is of second order in the nuclear displacement. Strong absorption effects are present for compound semiconductors. A review can be found in [934].

9.10.1 Dielectric Constant

The (relative) dielectric constant (with damping parameter Γ) in the vicinity of the optical phonon energies is given by (cf. (9.27))

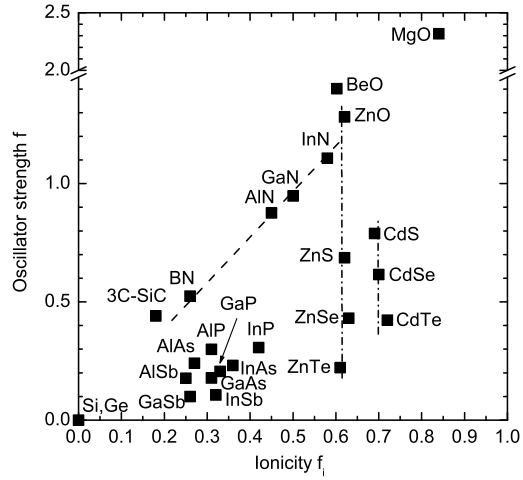

Fig. 9.50 Lattice absorption oscillator strength f from (9.86) for various elemental, III–V and II–VI semiconductors as a function of their ionicity f_i (cf. Table 2.1). *Dashed line* is linear dependence on ionicity for similar (reduced) mass, *dash-dotted lines* are guides to the eye for similar ionicity and varying mass

$$\epsilon(\omega) = \epsilon(\infty)\left(\frac{\omega_{\mathrm{TO}}^2 - \omega^2 - \mathrm{i}\omega\Gamma}{\omega_{\mathrm{TO}}^2 - \omega^2 - \mathrm{i}\omega\Gamma}\right) . \tag{9.84}$$

The dispersion relation (without damping) can be rewritten as

$$\epsilon(\omega) = \epsilon(\infty) + \frac{\epsilon(0) - \epsilon(\infty)}{1 - (\omega/\omega_{\mathrm{TO}})^2} = \epsilon(\infty)\left[1 + \frac{f}{1 - (\omega/\omega_{\mathrm{TO}})^2}\right] . \tag{9.85}$$

Thus the dimensionless oscillator strength (compare with (D.10)) is $f = (\epsilon(0)/\epsilon(\infty) - 1$. With the LST relation (9.26) the oscillator strength is

$$f = \frac{\epsilon(0) - \epsilon(\infty)}{\epsilon(\infty)} = \frac{\omega_{\mathrm{LO}}^2 - \omega_{\mathrm{TO}}^2}{\omega_{\mathrm{TO}}^2} \approx 2\,\frac{\omega_{\mathrm{LO}} - \omega_{\mathrm{TO}}}{\omega_{\mathrm{TO}}} , \tag{9.86}$$

and thus proportional to the splitting $\Delta_{\mathrm{LT}} = \omega_{\mathrm{LO}} - \omega_{\mathrm{TO}}$ between the longitudinal and transverse optical phonon frequency. The approximation in (9.86) is valid for $\Delta_{\mathrm{LT}} \ll \omega_{\mathrm{TO}}$.

The oscillator strength increases with the ionicity, i.e. the electronegativity difference of the atoms in the base (Fig. 9.50). Additionally, the oscillator strength depends on the reduced mass and the high-frequency polarizability; this can be seen, e.g., for the series of the Zn compounds that all have similar ionicity. For the series of the nitrides, the mass effect is small since the reduced mass is dominated by the light N mass. We refer to Fig. 5.23 for the change of phonon oscillator strength in an (Al,Ga)N alloy.

9.10.2 Reststrahlenbande

The absorption of electromagnetic radiation by optical phonons is governed by the dielectric function that has been derived in (9.84). For small damping, i.e. $\Gamma \ll \Delta_{\mathrm{LT}}$, the dielectric constant is negative between ω_{TO} and ω_{LO}. From $\epsilon_{\mathrm{r}} = n_{\mathrm{r}}^2 - \kappa^2$ it follows that κ^2 is much larger than n_{r}^2. Therefore,

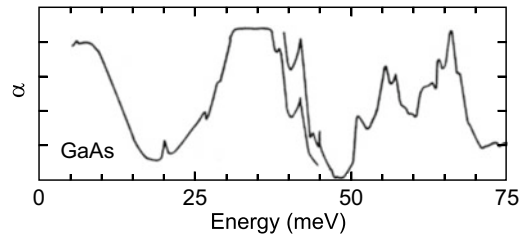

Fig. 9.51 Far-infrared absorption (linear scale) of GaAs. In the region around 35 meV is the reststrahlenbande with high absorption due to optical phonons. The sharp little peak at 45 meV is a LVM, probably from Al_{Ga}. Adapted from [935]

the reflectance (9.17) will be close to 1. This energy range is the so-called *reststrahlenbande*. This term stems from multiple reflections in this wavelength regime that suppresses neighboring spectral regions and thus achieves a certain monochromatization in the far-infrared spectral region. Within the semiconductor the absorption is large in the reststrahlenbande (Fig. 9.51).

9.10.3 Polaritons

The coupled propagation of phonons and electromagnetic radiation is (without phonon damping) related to the dielectric function given in (9.27),

$$\epsilon(\omega) = \epsilon(\infty)\left(\frac{\omega_{\mathrm{LO}}^2 - \omega^2}{\omega_{\mathrm{TO}}^2 - \omega^2}\right) = \frac{c^2\,k^2}{\omega^2}\ . \tag{9.87}$$

There are two branches of propagating waves (real k):

$$\omega^2 = \frac{1}{2}\left(\omega_{\mathrm{LO}}^2 + \frac{c^2k^2}{\epsilon(\infty)}\right) \pm \sqrt{\frac{1}{4}\left(\omega_{\mathrm{LO}}^2 + \frac{c^2k^2}{\epsilon(\infty)}\right)^2 - \left(\frac{c^2k^2\omega_{\mathrm{TO}}^2}{\epsilon(\infty)}\right)^2}\ . \tag{9.88}$$

For $k = 0$ we find the solutions $\omega = \omega_{\mathrm{LO}}$ and $\omega = k\,c/\sqrt{\epsilon(0)}$. For large k we find $\omega = \omega_{\mathrm{TO}}$ and $\omega = k\,c/\sqrt{\epsilon(\infty)}$. These solutions are shown in Fig. 9.52. Both branches have a phonon- and a photon-like part. The coupled state between the phonon and the photon field is called the (phonon-) polariton.

In the interval $[\omega_{\mathrm{TO}}, \omega_{\mathrm{LO}}]$ the wavevector is purely imaginary, i.e. $k = \mathrm{i}\tilde{k}$ with real $\tilde{k}$. For this case there is only one solution that is also depicted in Fig. 9.52,

$$\omega^2 = \frac{1}{2}\left(\omega_{\mathrm{LO}}^2 + \frac{c^2\tilde{k}^2}{\epsilon(\infty)}\right) + \sqrt{\frac{1}{4}\left(\omega_{\mathrm{LO}}^2 + \frac{c^2\tilde{k}^2}{\epsilon(\infty)}\right)^2 + \left(\frac{c^2\tilde{k}^2\omega_{\mathrm{TO}}^2}{\epsilon(\infty)}\right)^2}\ . \tag{9.89}$$

9.10.4 Phonon–Plasmon Coupling

The coupling of phonons and plasmons in the spectral region of the reststrahlenbande leads to the development of two new branches, the longitudinal phonon plasmon modes (LPP+ and LPP−), in the

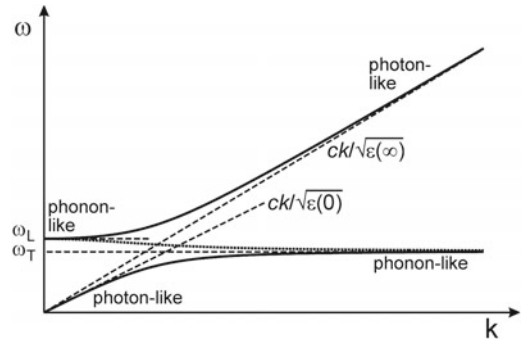

Fig. 9.52 Dispersion of the polariton. The *dotted line* displays the dispersion for a purely imaginary wavevector with the absolute value k

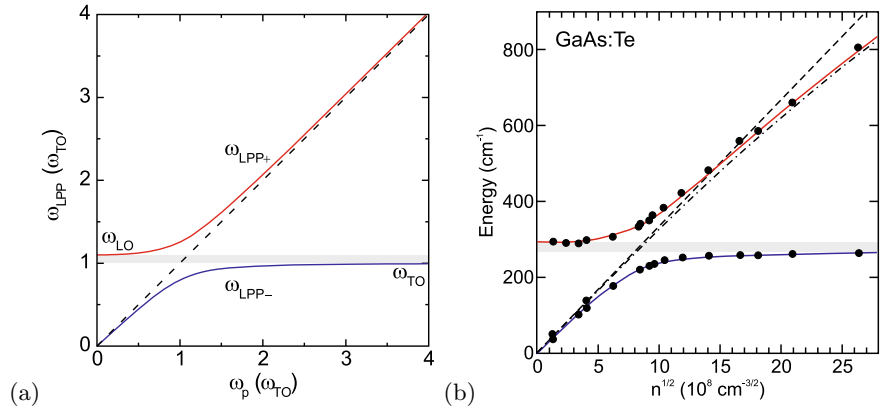

Fig. 9.53 **a** Frequency of the coupled longitudinal-phonon plasmon (LPP) modes (lower (upper) polariton branch in *blue* (*red*)) as a function of the plasma frequency. *Dashed line* shows uncoupled plasmon frequency ($\omega = \omega_p$), *grey area* indicates spectral region between TO and LO modes. **b** Experimental data on the polariton energies in n-type GaAs with different carrier concentration $\omega_p \propto \sqrt{n\,m^*}$ (9.77). *Dashed* (*dash-dotted*) *line* is plasmon frequency ω_p without (with) consideration of conduction band non-parabolicity (cf. Fig. 6.37b). Data from [918, 936]

common dispersion. The dielectric function is

$$\epsilon(\omega) = \epsilon(\infty)\left(1 + \frac{\omega_{LO}^2 - \omega^2}{\omega_{TO}^2 - \omega^2} - \frac{\omega_p^2}{\omega^2}\right) . \tag{9.90}$$

For $\epsilon(\omega) = 0$ for $k = 0$ (coupling to photons) the two solutions ω_{LPP+} and ω_{LPP-} do not cross as a function of ω_p (Fig. 9.53),

$$\omega_{LPP\pm} = \frac{1}{2}\left[\omega_{LO}^2 + \omega_p^2 \pm \sqrt{(\omega_{LO}^2 + \omega_p^2)^2 - 4\,\omega_{TO}^2\,\omega_p^2}\right] . \tag{9.91}$$

For small plasma frequencies $\omega_{LPP+} = \omega_{LO}$, i.e. the optical phonons couple to the electromagnetic field without change. Also $\omega_{LPP-} = \omega_p$. For large carrier density, i.e. $\omega_p \gg \omega_{LO}$, we find $\omega_{LPP-} = \omega_{TO}$ and $\omega_{LPP+} = \omega_p$. Thus, the carriers have effectively screened the electric field of the phonon that had led to the increase of the TO to the LO frequency.

Chapter 10
Recombination

Les hommes discutent, la nature agit.
Men argue, nature acts.

Voltaire

Abstract The various mechanisms and statistics of carrier recombination in semiconductors including band-band, excitonic, band-impurity (Shockley-Read-Hall kinetics) and Auger recombination are explained. Also recombination at extended defects and surfaces is treated. Using the diffusion-recombination theory, the one-dimensional carrier profiles for typical situations in experiments and devices are derived.

10.1 Introduction

In thermodynamic nonequilibrium excess charges can be present in the semiconductor. They can be created by carrier injection through contacts, an electron beam or the absorption of light with wavelength smaller than the band gap. After the external excitation is turned off, the semiconductor will return to the equilibrium state. The relaxation of carriers into energetically lower states (and energy release) is called recombination. The term stems from the electron recombining with the hole created after absorption of a photon. However, there are other recombination mechanisms. A dedicated textbook is [937].

In the simplest picture an excitation generates carriers with a rate G (carriers per unit volume and unit time). In the steady state (after all turn-on effects) a constant excess charge n carrier density is present. Then the generation exactly compensates the recombination processes. The principle of detailed balance even says that each microscopic process is balanced by its reverse process. If the time constant of the latter is τ, n is given by $n = G\,\tau$. This follows from the steady-state solution $\dot{n} = 0$ of

$$\frac{\mathrm{d}n}{\mathrm{d}t} = G - \frac{n}{\tau}\,. \tag{10.1}$$

In the literature two limiting cases have been discussed, the *relaxation* and the *lifetime* semiconductor, depending on the relation of two time constants. The one time constant τ_0 is the relaxation time constant due to recombination as discussed in the following. The smaller τ_0 is, the faster excited electrons and holes recombine and 'disappear'. Fast lifetimes are typically present in direct semiconductors (compared to indirect ones), semiconductors with high defect density and amorphous semiconductors.

M. Grundmann, *The Physics of Semiconductors*, Graduate Texts in Physics,
https://doi.org/10.1007/978-3-030-51569-0_10

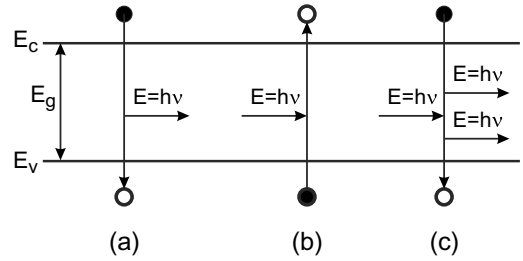

Fig. 10.1 Processes of band–band recombination: **a** spontaneous emission, **b** absorption and **c** stimulated emission. A *full* (*empty*) *circle* represents an occupied (unoccupied) electron state

The other time constant is $\tau_D = \epsilon/\sigma$, the dielectric relaxation time; it describes the transport of carriers due to mobility (and diffusion). Large dielectric relaxation times are present in semiconductors with high mobility (low defect density, small carrier mass), small τ_D typically for hopping conduction. The relaxation case is given for $\tau_0 \ll \tau_D$; carriers will recombine quickly and it is hard to build up non-equilibrium carriers and separate them with an applied electric field. In the recombination case $\tau_D \ll \tau_0$, non-equilibrium carriers can assume non-uniform distributions and an applied electrical field generates separate quasi-Fermi levels for electrons and holes.[1] (cmp. Sect. 7.6).

10.2 Band–Band Recombination

The band–band recombination is the relaxation from an electron in the conduction band into the valence (the empty state there is the hole). In a direct semiconductor, electrons can make an optical transition between the bottom of the conduction band to the top of the valence band. In an indirect semiconductor, this process is only possible with the assistance of a phonon and is thus much less probable.

10.2.1 Spontaneous Emission

We consider the spontaneous recombination of an electron of energy E_e and a hole of energy E_h (Fig. 10.1a). $C(E_e, E_h)$ is a constant proportional to the matrix element of the optical transition (cf. Sect. 9.6). The spontaneous recombination rate r_{sp} at photon energy $E \geq E_C - E_V = E_g$ is (assuming energy conservation, i.e. $E = E_e - E_h$, but without k-conservation in a dense plasma [938]),

$$\begin{aligned} r_{sp}(E) &= \int_{E_C}^{\infty} \mathrm{d}E_e \int_{-\infty}^{E_V} \mathrm{d}E_h \; C(E_e, E_h) \times \\ &\quad D_e(E_e)\, f_e(E_e)\, D_h(E_h)\, f_h(E_h)\, \delta(E - E_e + E_h) \\ &= \int_{E_C}^{E+E_V} \mathrm{d}E_e \; C(E_e, E_e - E) \times \\ &\quad D_e(E_e)\, f_e(E_e)\, D_h(E_e - E)\, f_h(E_e - E)\ , \end{aligned} \tag{10.2}$$

where f_h denotes the hole occupation $f_h = 1 - f_e$.

[1] In the relaxation case, the separation of quasi-Fermi levels is $\ll kT$.

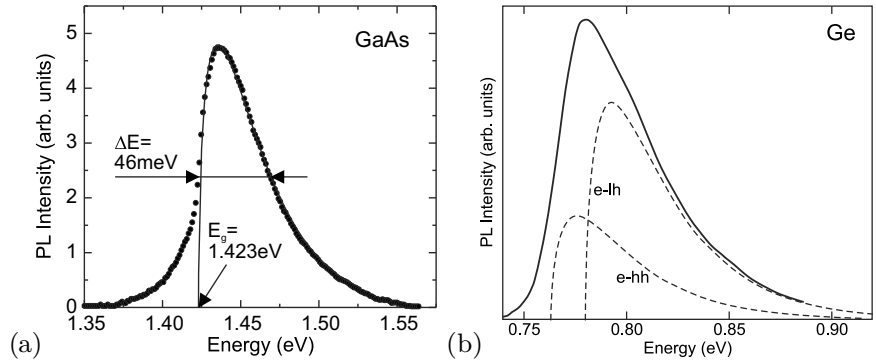

Fig. 10.2 **a** Photoluminescence spectrum of an undoped LPE-grown epitaxial GaAs layer at room temperature and low cw ($\lambda = 647\,\text{nm}$) excitation density ($10\,\text{W/cm}^2$). The *solid line* is a lineshape fit with (10.3) and $E_\text{g} = 1.423\,\text{eV}$ and $T = 293\,\text{K}$. (**b**) Room temperature, direct (e_Γ–h_Γ) recombination from heavily n-doped ($10^{19}\,\text{cm}^{-3}$) germanium ($1\,\mu\text{m}$ thick Ge layer on silicon (001)) with biaxial (thermal) tensile strain. The strain-split valence band edge (Fig. 6.50) causes the e–hh and e–lh transitions (individual contributions with lineshape according to (10.3) shown as *dashed lines*) to occur at different energies. Adapted from [939]

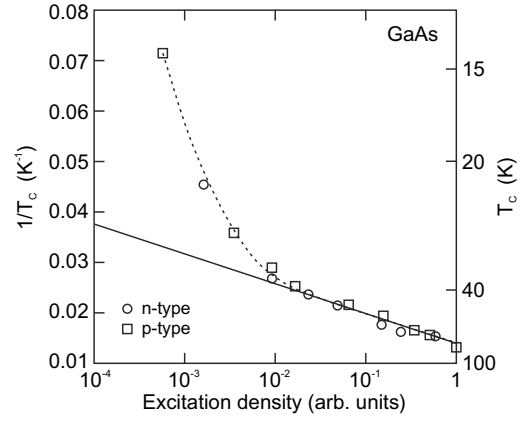

Fig. 10.3 Carrier temperature T_C in GaAs as a function of excitation density at a lattice temperature of 1.6 K. The *dashed line* is guide to the eye, the *solid line* corresponds to an activation energy of 33 meV, similar to the GaAs optical phonon energy. Adapted from [940]

The lineshape of the band–band recombination with k-conservation[2] is proportional to the joint density of states (9.42) and the Fermi distribution function. At small excitation and at low doping it can be approximated by the Boltzmann distribution function and the lineshape is given as

$$I(E) \propto \sqrt{E - E_\text{g}}\, \exp\left(-\frac{E}{kT}\right) . \tag{10.3}$$

An experimental spectrum is shown in Fig. 10.2 together with a fit according to (10.3). The expected FWHM of the peak is $1.7954\,kT$, which is about 46 meV at $T = 300\,\text{K}$. At low sample temperature, the temperature of the carrier gas is typically higher than the lattice temperature, depending on the cooling mechanisms (carrier–carrier scattering, optical phonon emission, acoustic phonon emission, recombination, ...) and the excitation rate. The carrier temperature in GaAs, determined from the Boltzmann tail of spontaneous emission (photoluminescence) is depicted in Fig. 10.3 as a function of excitation density; clearly it increases with increasing excitation.

The recombination rate in indirect semiconductors is small since the transition is phonon-assisted. For silicon, an internal quantum efficiency in the 10^{-6}-range has been reported [941]. For germanium,

[2]Excitonic effects are neglected here, e.g. for temperatures $kT \gg E_\text{X}^\text{b}$. Such effects are discussed in Sect. 10.3.

the direct transition is energetically fairly close to the fundamental, indirect L–Γ band edge transition (Fig. 9.15). The energy difference can be reduced from its bulk value of 136 meV by tensile strain. Additionally, the direct transition can be favored by heavily n-doping and filling the L conduction band minimum states (see Sect. 9.9.2). In this case, direct recombination from the conduction band Γ-minimum can be observed [939] and the effective energy difference has been lowered to about 100 meV.

10.2.2 Absorption

A similar consideration is made for the absorption process (Fig. 10.1b). An electron is transferred upon light absorption from a valence-band state (occupied) to a conduction-band state that must be empty. The coefficient is B_1. Also, the process is proportional to the light intensity, represented by the density of occupied photon states $N_{\mathrm{ph}}(E)$,

$$r_{\mathrm{abs}}(E) = \int_{E_{\mathrm{C}}}^{E+E_{\mathrm{V}}} \mathrm{d}E_{\mathrm{e}}\; B_1(E_{\mathrm{e}}, E_{\mathrm{e}} - E) \times D_{\mathrm{e}}(E_{\mathrm{e}})\,(1 - f_{\mathrm{e}}(E_{\mathrm{e}}))\, D_{\mathrm{h}}(E_{\mathrm{e}} - E)\,(1 - f_{\mathrm{h}}(E_{\mathrm{e}} - E))\, N_{\mathrm{ph}}(E)\ . \tag{10.4}$$

10.2.3 Stimulated Emission

In this case, an incoming photon 'triggers' the transition of an electron in the conduction band into an empty state in the valence band. The emitted photon is in phase with the initial photon (Fig. 10.1c). The rate is (with coefficient B_2):

$$r_{\mathrm{st}}(E) = \int_{E_{\mathrm{C}}}^{E+E_{\mathrm{V}}} \mathrm{d}E_{\mathrm{e}}\; B_2(E_{\mathrm{e}}, E_{\mathrm{e}} - E) \times D_{\mathrm{e}}(E_{\mathrm{e}})\, f_{\mathrm{n}}(E_{\mathrm{e}})\, D_{\mathrm{h}}(E_{\mathrm{e}} - E)\, f_{\mathrm{h}}(E_{\mathrm{e}} - E)\, N_{\mathrm{ph}}(E)\ . \tag{10.5}$$

The photon density N_{ph} at a given energy is given by Planck's law and the Bose–Einstein distribution (Appendix E)

$$N_{\mathrm{ph}}(E) = N_0 \frac{1}{\exp\left(E/kT\right) - 1}\ . \tag{10.6}$$

The pre-factor is the density of states of the electromagnetic field[3] $N_0(E) = 8\,\pi\,E^2\,(n_{\mathrm{r}}/hc)^3$.

10.2.4 Net Recombination Rate

In thermodynamical equilibrium the rates fulfill

[3] The total number of photon states in vacuum between the frequencies zero and ν is $N(\nu) = 8\pi\nu^3/(3c^3)$. With $\nu = E/h$ and $N_0 = \mathrm{d}N(E)/\mathrm{d}E$ and considering $c \to c/n_{\mathrm{r}}$ we obtain the given value for N_0.

$$r_{\mathrm{sp}}(E) + r_{\mathrm{st}}(E) = r_{\mathrm{abs}}(E) \ . \tag{10.7}$$

Since for absorption and stimulated emission the same quantum-mechanical matrix element is responsible, $B_1 = B_2$. If the population functions are Fermi-Dirac distributions with quasi-Fermi levels F_{n} and F_{p} (Sect. 7.6), the detailed balance (10.7) yields

$$C(E_1, E_2) = B_1(E_1, E_2)\, N_{\mathrm{ph}} \left[\exp\left(\frac{E - (F_{\mathrm{n}} - F_{\mathrm{p}})}{kT} \right) - 1 \right] . \tag{10.8}$$

In thermodynamic equilibrium, i.e. $F_{\mathrm{n}} = F_{\mathrm{p}}$,

$$C(E_1, E_2) = N_0\, B_1(E_1, E_2) = B \ . \tag{10.9}$$

If the constant B, the bimolecular recombination coefficient, is independent of the energy E, the integration for the net bimolecular recombination rate r_{B} can be executed analytically and we find

$$\begin{aligned} r_{\mathrm{B}} &= \int_{E_{\mathrm{g}}}^{\infty} \left[r_{\mathrm{sp}}(E) + r_{\mathrm{st}}(E) - r_{\mathrm{abs}}(E) \right] \mathrm{d}E \\ &= B\, n\, p \left[1 - \exp\left(-\frac{F_{\mathrm{n}} - F_{\mathrm{p}}}{kT} \right) \right] . \end{aligned} \tag{10.10}$$

In thermodynamic equilibrium, of course, $r_{\mathrm{B}} = 0$. The recombination rate Bnp is then equal to the thermal generation rate G_{th}

$$G_{\mathrm{th}} = B\, n_0\, p_0 \ . \tag{10.11}$$

The bimolecular recombination rate typically used in Shockley–Read–Hall (SRH) [942, 943] kinetics is

$$r_{\mathrm{B}} = B\, (n\, p - n_0\, p_0) \ . \tag{10.12}$$

Values for the coefficient B are given in Table 10.1. In the case of carrier injection, np is larger than in thermodynamical equilibrium, i.e. $n\, p > n_0\, p_0$, and the recombination rate is positive, i.e. light is emitted. If the carrier density is smaller than in thermodynamical equilibrium, e.g.. in a depletion region, absorption is larger than emission. This effect is also known as 'negative luminescence' [944] and plays a role particularly at elevated temperatures and in the infrared spectral region.

Table 10.1 Bimolecular recombination coefficient at room temperature for a number of semiconductors. Data for GaN from [945], Si from [946], SiC from [947], other values from [948]

Material	B (cm^3/s)
GaN	1.1×10^{-8}
GaAs	1.0×10^{-10}
AlAs	7.5×10^{-11}
InP	6.0×10^{-11}
InAs	2.1×10^{-11}
4H-SiC	1.5×10^{-12}
Si	1.1×10^{-14}
GaP	3.0×10^{-15}

10.2.5 Recombination Dynamics

The carrier densities n and p, are decomposed into the densities n_0 and p_0 in thermodynamic equilibrium and the excess-carrier densities δn and δp, respectively

$$n = n_0 + \delta n \tag{10.13a}$$
$$p = p_0 + \delta p \ . \tag{10.13b}$$

Here, only neutral excitations are considered, i.e. $\delta n = \delta p$. Obviously the time derivative fulfills $\frac{\partial n}{\partial t} = \frac{\partial \delta n}{\partial t}$, and correspondingly for the hole density. The equation for the dynamics

$$\dot{n} = \dot{p} = -Bnp + G_{\text{th}} = -B\,(n\,p - n_0\,p_0) = -B\,(n\,p - n_{\text{i}}^2) \tag{10.14}$$

can be written as

$$\frac{\partial\,\delta p}{\partial t} = -B\ (n_0\,\delta p + p_0\,\delta n + \delta n\,\delta p)\ . \tag{10.15}$$

The general solution of (10.15) is given by

$$\delta p(t) = \frac{(n_0 + p_0)\,\delta p(0)}{[n_0 + p_0 + \delta p(0)]\,\exp\left[B\,t\,(n_0 + p_0)\right] - \delta p(0)}\ . \tag{10.16}$$

In the following, we discuss some approximate solutions of (10.15). First, we treat the case of a small (neutral) excitation, i.e. $\delta n = \delta p \ll n_0,\, p_0$. The dynamic equation is in this case

$$\frac{\partial\,\delta p}{\partial t} = -B\,(n_0 + p_0)\,\delta p\ . \tag{10.17}$$

Then the decay of the excess-carrier density is exponential with a time constant (lifetime) τ given by

$$\tau = \frac{1}{B\,(n_0 + p_0)}\ . \tag{10.18}$$

In an n-type semiconductor additionally $n_0 \gg p_0$, and thus the minority carrier lifetime τ_p is

$$\tau_p = \frac{1}{B\,n_0}\ . \tag{10.19}$$

If the nonequilibrium carrier densities are large, i.e. $n \approx p \gg n_0,\, p_0$, e.g. for strong injection, the kinetics obeys

$$\frac{\partial\,\delta p}{\partial t} = -B\,(\delta p)^2\ , \tag{10.20}$$

and the transient has the form

$$\delta p(t) = \frac{\delta p(0)}{1 + B\,t\,\delta p(0)}\ , \tag{10.21}$$

where $\delta p(0)$ is the excess hole density at time $t = 0$. Such a decay is called *hyperbolic* and the recombination is bimolecular. The exponential decay time is formally $\tau^{-1} = B\delta p(t)$ and is thus time and density dependent. A detailed discussion of minority carrier lifetime is given in [949].

10.2.6 Lasing

The net rate for stimulated emission and absorption is

$$r_{\mathrm{st}}(E) - r_{\mathrm{abs}}(E) = \left[1 - \exp\left(\frac{E - (F_{\mathrm{n}} - F_{\mathrm{p}})}{kT}\right)\right] \times \int_{E_{\mathrm{C}}}^{E+E_{\mathrm{V}}} \mathrm{d}E_{\mathrm{e}}\, B\, D_{\mathrm{e}}(E_{\mathrm{e}})\, f_{\mathrm{e}}(E_{\mathrm{e}})\, D_{\mathrm{h}}(E_{\mathrm{e}} - E)\, f_{\mathrm{h}}(E_{\mathrm{e}} - E)\, N_{\mathrm{ph}}(E)\ . \tag{10.22}$$

The net rate at photon energy $E = \hbar\omega$ is only larger than zero (i.e. dominating stimulated emission) when

$$F_{\mathrm{n}} - F_{\mathrm{p}} > E \geq E_{\mathrm{g}}\ . \tag{10.23}$$

When the difference of the quasi-Fermi levels is larger than the band gap, the carrier population is inverted, i.e. close to the band edges the conduction-band states are more strongly populated with electrons than the valence-band states, as shown in Fig. 10.4. An incoming optical wave of energy E will then be net amplified by stimulated emission. Equation (10.23) is also called the thermodynamic laser condition. We note that lasing requires further conditions as discussed in Sect. 23.4.

10.3 Exciton Recombination

10.3.1 Free Excitons

The observation of free-excitons is limited for semiconductors with a small exciton binding energies (such as in GaAs) to low temperatures. However, for large exciton binding energy, recombination from free-excitons is observed even at room temperature, as shown in Fig. 10.5 for ZnO.

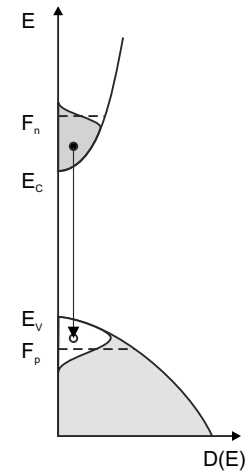

Fig. 10.4 Charge-carrier distribution during inversion, necessary for lasing. *Shaded areas* are populated with electrons. A stimulated transition between an electron and a hole is indicated

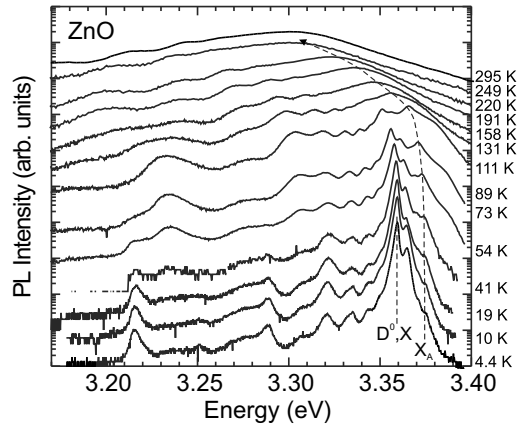

Fig. 10.5 Temperature-dependent luminescence spectra of a ZnO thin film (on sapphire). At low temperatures, the spectra are dominated by donor-bound exciton transitions (Al^0,X)). The *vertical dashed line* indicates the low-temperature position of the donor-bound exciton transition (D^0,X). The *curved dashed line* visualizes the energy position of the free-exciton transition (X_A) that becomes dominant at room temperature

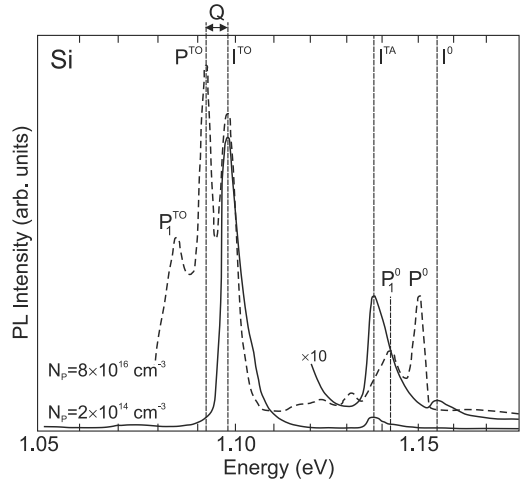

Fig. 10.6 Low temperature recombination spectra from silicon with low (*solid lines*) and sizeable (*dashed line*) phosphorus dopant concentration. Spectrum for $N_P = 2 \times 10^{14}\,cm^{-3}$ ($N_P = 8 \times 10^{16}\,cm^{-3}$) taken at 26 K (15 K). Transitions in pure Si are label with 'I', transitions involving P donors are labeled with 'P'. Q indicates the dissociation energy of the bound exciton. Adapted from [950]

A low temperature recombination spectrum of silicon is shown in Fig. 10.6. In pure silicon, phonon-assisted exciton recombination (cmp. Sect. 10.4) is observed involving acoustic (I^{TA}) and optical (I^{TO}) phonons. The weakly observed no-phonon line (I^0) is forbidden in perfect Si.

10.3.2 Bound Excitons

Excitons can localize at impurities, defects or other potential fluctuations and subsequently recombine [951, 952]. Excitons can be bound to neutral or ionized donors and acceptors impurities [953]. Also

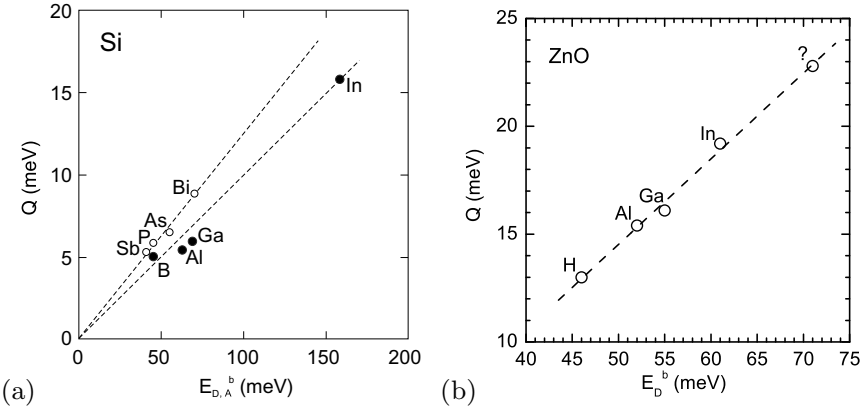

Fig. 10.7 Energy Q required to remove an exciton from a neutral impurity (10.24) as a function of the ionization energy E_D^b (*open circles*) or E_A^b (*solid circles*) of the involved impurity in (**a**) silicon (experimental data from [965]) and (**b**) ZnO (experimental data from [966])

they can be bound to isoelectronic impurities, the most prominent example being N in GaP [954] (cmp. Sect. 9.7.9) or isoelectronic clusters [955]. The recombination of excitons localized in quantum wells (Sect. 12.4) and quantum dots (Sect. 14.4.4) is discussed later.

The transition energy $\hbar\omega$ of an exciton bound to a neutral impurity is

$$\hbar\omega = E_g - E_X{}^b - Q \,, \tag{10.24}$$

where Q is the binding (or localization) energy of the exciton to the impurity. The binding energy of an exciton to an ionized impurity is denoted with Q^*. A transition involving an exciton bound to a neutral donor is denoted (D^0,X); correspondingly (D^+,X), also denoted as (h,D^0), and (A^0,X). Values for donor-bound excitons in various semiconductors are listed in Table 10.2. The (D^0,X) complex is stable for $0 < \sigma = m_e^*/m_h^* < 0.43$ according to [956]. The (D^+,X) peak can occur on the low- or high-energy side of the (D^0,X) recombination. Whether $Q^* < Q$ or $Q^* > Q$ depends on σ being smaller or larger than 0.2, respectively [956], and is fulfilled for many semiconductors, e.g. GaAs, GaN, CdS, and ZnSe.

Recombination in silicon due to excitons involving phosphorus donors is depicted in Fig. 10.6. The (D^0,X) transition in Si:P is labeled 'P^0' ($Q = 6$ meV). Other P-related transitions are discussed in [950]. In Si, the binding energy to the impurity is about one tenth of the binding energy of the impurity (Haynes's rule [951, 965]), i.e. Q/E_D^b and $Q/E_A^b \approx 0.1$ (Fig. 10.7a). In GaP the approximate relations $Q = 0.26E_D^b - 7$ meV and $Q = 0.056E_A^b + 3$ meV have been found [954]. For donors in ZnO, the relation $Q = 0.365E_D^b - 3.8$ meV holds (Fig. 10.7b) [966]. In Fig. 10.8, the recombination spectrum of GaAs:C is shown that exhibits recombination from excitons bound to the acceptor (carbon) and shallow donors. The exciton is more strongly bound to an ionized donor (D^+) than to a neutral donor.

Varying the concentration of a specific impurity and observing the corresponding change in the intensity of the (D^0,X) transition allows to identify the chemical species to which the exciton is bound. This can be achieved via the comparison of different samples or more elegantly by introducing radioactive isotopes. This is shown in Fig. 10.9 for In in ZnO; the ($^{111}In^0$,X) transition disappears with the characteristic time constant close to that (97 h) of the nuclear decay of ^{111}In into stable ^{111}Cd. However, in such experiments it should be considered that the decay product and accompanying high-energy radiation can create new electronic and structural defects, respectively.

The peak labeled (D^0,X)$_{2s}$ in Fig. 10.8 is called a two-electron satellite (TES) [968]. High-resolution spectra of the TES in GaAs [581, 969] are shown in Fig. 10.10a. The TES recombination is a (D^0,X)

Table 10.2 Localization energy Q (Q^*) of excitons on selected impurities (ionized impurities, D^+ or A^-, respectively) in various semiconductors. σ is the ratio of effective electron and hole (polaron) masses. EMD: effective mass donor

host	donor	Q (meV)	Q^* (meV)	Q^*/Q	σ	Ref.
GaAs	EMD	0.88	1.8	2.0	0.28	[957]
	Zn	8.1	31.1	3.8		
GaN	EMD	6.8	11.2	1.6	0.36	[959]
	Mg	20				
AlN	Si	16				[960]
	Mg	40				
CdS	EMD	6.6	3.8	0.6	0.17	[961]
ZnSe	Al	4.9	5.4	1.1	0.27	[962, 963]
	Ga	5.1	6.6	1.3		
	In	5.4	7.5	1.4		
ZnO	Al	15.5	3.4	0.21	0.3	[964]
	Ga	16.1	4.1	0.25		
	In	19.2	8.5	0.44		

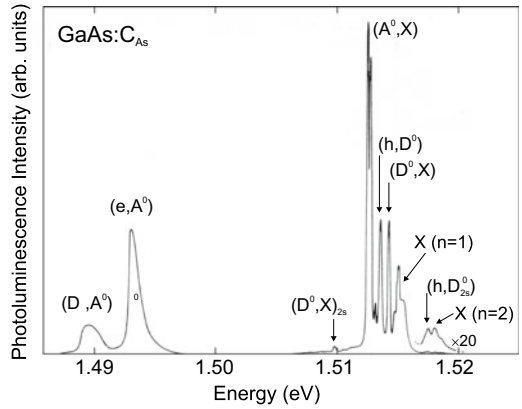

Fig. 10.8 Photoluminescence spectrum ($T = 2\,\mathrm{K}$, $D = 10\,\mathrm{mW\,cm^{-2}}$) of GaAs:$C_{As}$ ($N_A = 10^{14}\,\mathrm{cm^{-3}}$) with donor- and acceptor-related bound-exciton recombination around 1.512 eV, (e,A^0), (h,D^0) and (D^0,A^0) pair and free-exciton recombination. Adapted from [957]

recombination that leaves the donor in an excited state as schematically shown in Fig. 10.10b. Therefore a hydrogen-like series with $n = 2, 3, \ldots$ is observed with energies

$$E^n_{\mathrm{TES}} = E_{(\mathrm{D^0,X})} - E^{\mathrm{b}}_{\mathrm{D}} \left(1 - \frac{1}{n^2}\right) . \tag{10.25}$$

The effect of isotope disorder on the sharpness and splitting of impurity states has been investigated in [970, 971]. The recombination of excitons bound to Al, Ga and In in natural silicon (92.23% ^{28}Si, 4.67% ^{29}Si, 3.10% ^{30}Si) is split into three lines due to the valley-orbit splitting [972] of electron states at the band minimum (Fig. 10.11). Each of these (A^0,X) lines is split by $0.01\,\mathrm{cm^{-1}}$ for Si:Al due to a symmetry reduction of the 4-fold degenerate A^0 ground state, as observed in the presence of applied axial strain or an electric field. The comparison to spectra from enriched ^{28}Si shows that the observed splitting without external perturbation is due to isotope disorder that causes random strains and splits the A^0 ground state into two doublets [971] (Fig. 10.11). Similarly, the (unsplit) phosphorus-induced

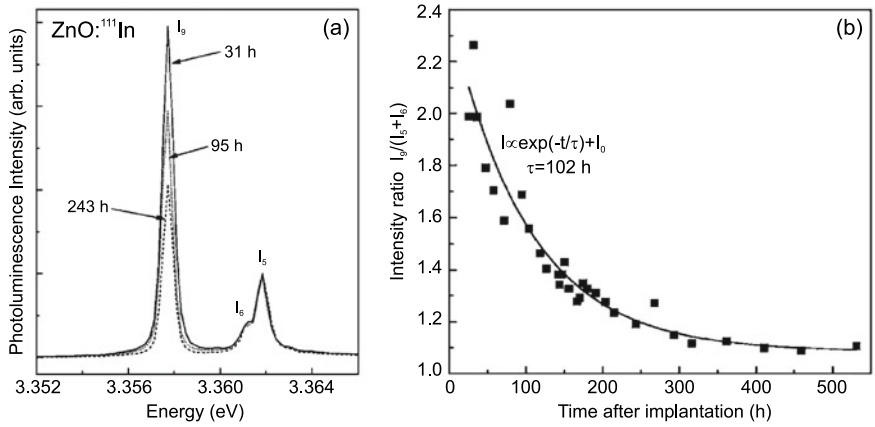

Fig. 10.9 **a** Low-temperature photoluminescence spectrum of ZnO implanted with ^{111}In featuring the so-called I_9-line. Spectra are recorded at various times after implantation as labeled. **b** Intensity of I_9-line as a function of time. Adapted from [967]

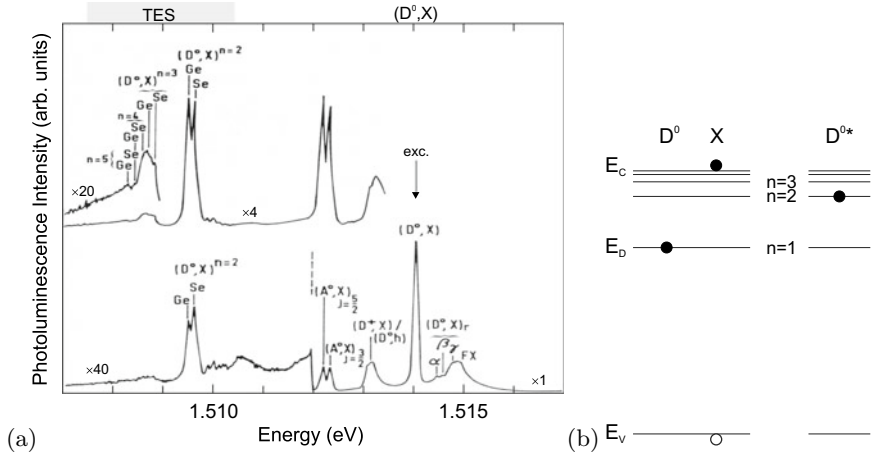

Fig. 10.10 **a** Photoluminescence spectrum ($T = 1.5$ K, $D = 50\,\mathrm{mW\,cm^{-2}}$) of high-purity GaAs with two donors (Ge and Se/Sn). The lower spectrum has been excited 6 meV above the band gap, the upper spectrum has been resonantly excited with the laser set to the (D^0,X) transition and exhibits $n = 2, 3, 4$, and 5 TES transitions. α,β,γ denote excited (hole rotational) states of the (D^0,X) complex. Adapted from [969]. **b** Schematic representation of the $n = 2$ TES process, *left*: initial, *right*: final state

(D^0,X) transition in enriched Si is found to be much sharper ($< 40\,\mu$eV) than in natural Si (330 μeV) [970]. At higher resolution, a hyperfine splitting of 485 neV due to the ^{31}P nuclear spin $I = 1/2$ ($2 \times 10^{12}\,\mathrm{cm^{-3}}$) in isotopically pure (99.991%) ^{28}Si ($I = 0$) is observed for the (P^0,X) recombination [973]. In a magnetic field, the Zeeman-split lines have a FWHM of about 150 neV.

In Fig. 10.12 the recombination of excitons bound to the N isoelectronic impurity in lowly doped GaP is shown. The efficient recombination of nitrogen-bound electrons with holes at the Γ point is due to the wave-function component of the localized electron at $k = 0$ [690] (Fig. 7.40). The decay time of the A exciton is about 40 ns [974] and thus larger than the typical lifetime of excitons in direct semiconductors (ns-range). The forbidden B exciton has a much longer lifetime of 4 μs [974].

In the case of In in GaAs it has been found that down to the regime of $N_{\mathrm{In}} < 10^{19}\,\mathrm{cm^{-3}}$ the indium does not act as a substitutional isoelectronic impurity but still fully participates in the composition

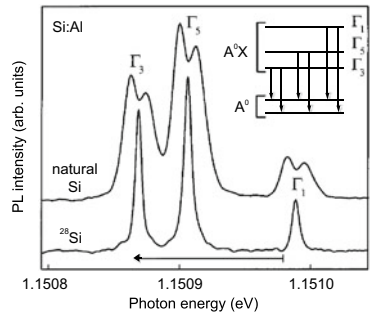

Fig. 10.11 High-resolution photoluminescence (PL) spectra of (A^0,X) recombination in natural and ^{28}Si-enriched silicon doped with aluminum ($T = 1.8$ K). The ^{28}Si PL spectrum is shifted up in energy by 0.114 meV, as indicated by the arrow, to compensate for the shift in band gap. The *inset* shows a level scheme for the recombination in natural silicon. Adapted from [971], reprinted with permission, ©(2002) APS

Fig. 10.12 Photoluminescence spectrum ($T = 4.2$ K) of GaP:N ($N_N \approx 5 \times 10^{16}$ cm^{-3}). The A exciton is bound to an isolated nitrogen impurity, cmp. to Fig. 9.28. Adapted from [690]

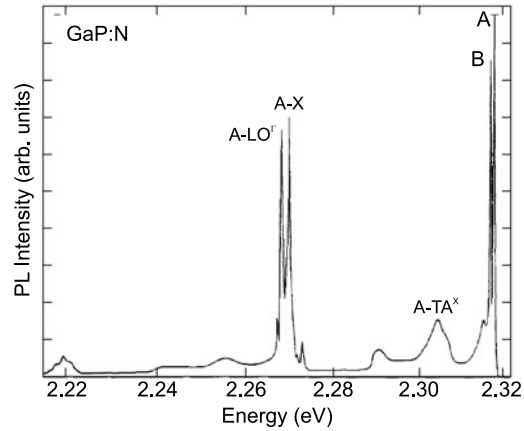

Fig. 10.13 Spectral position of neutral donor- and acceptor-bound exciton photoluminescence transition ($T = 2$ K) in GaAs doped with different amounts of indium relative to the donor-bound exciton luminescence in pure GaAs (1.5146 eV). Adapted from [975]

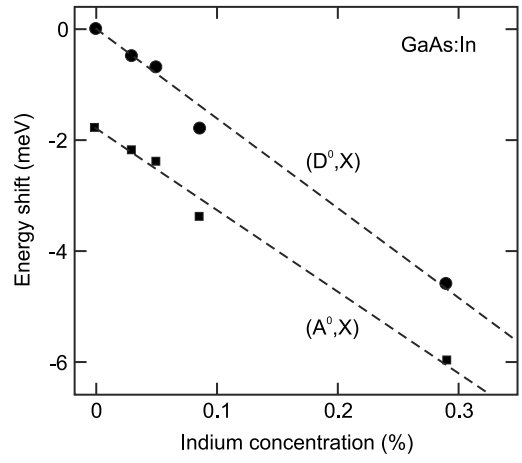

of a pseudo-binary system (Sect. 6.5). Recombination from excitons bound to single indium atoms or In–In pairs could not be found. The energy shift of donor- and acceptor-bound excitons in the dilute limit (Fig. 10.13) follows the band-gap dependence established for larger indium concentrations. The non-occurrence of localization effects is attributed to the small effective electron mass in InAs [544].

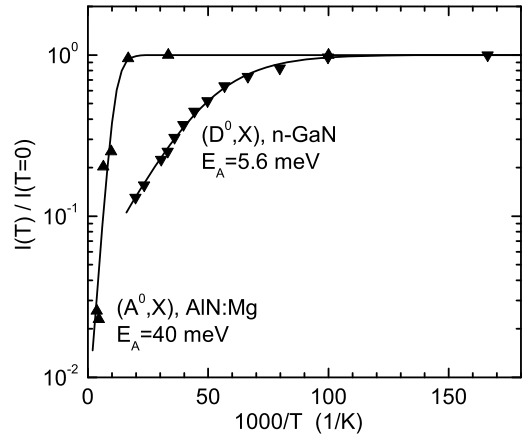

Fig. 10.14 (Temperature dependent PL intensity of (D^0,X) in GaN and (A0,X) in AlN:Mg recombination. *Solid lines* are fits with (10.26). Data from [960, 978]

The luminescence intensity $I(T)$ of bound exciton lines is quenched with increasing temperature due to ionization of the excitons from the impurities. The temperature dependence can be modeled using the relation [976]

$$\frac{I(T)}{I(T=0)} = \frac{1}{1 + C\ \exp(-E_A/kT)}\ , \tag{10.26}$$

E_A being the thermal activation energy and C a pre-factor. Often the activation energy is found equal to the localization energy, $E_A = Q$ (Fig. 10.14, cmp. Table 10.2). If several processes contribute, additional exponential terms can be added with further activation energies. For acceptor-bound excitons in GaAs two processes are found to contribute, the ionization from the impurity into a free exciton ($E_A^1 \approx Q$) and into an electron-hole pair ($E_A^2 \approx Q + E_X^b$) [976]. In [977] the model is refined by considering the temperature dependence of the parameter C due to the ionization of the impurity itself.

So far *single* excitons bound to a center have been discussed. Also bound exciton *complexes* [979] containing up to six excitons have been observed at sufficient excitation density, e.g. for substitutional boron [980] or phosphorus [981] and interstitial Li [982] in silicon. In a multi-valley semiconductor several electrons are available to form bound excitons which follow approximately a shell model and exhibit further fine structure.

10.3.3 Alloy Broadening

The bound-exciton recombination peak in a binary compound is spectrally fairly sharp (Sect. 10.3.2), even in the presence of isotope disorder (Fig. 10.11). In an alloy (see Sect. 3.7), the random distribution of atoms (with different atomic order number Z) causes a significant broadening effect of the luminescence (and absorption) line, the so-called *alloy broadening* [983, 984]. As an example, we treat $Al_xGa_{1-x}As$. The exciton samples, at different positions of the lattice, different coordinations of Ga and Al atoms. If the experiment averages over these configurations, an inhomogeneously broadened line is observed.

The cation concentration c_c for the zincblende lattice is given as $c_c = 4/a_0^3$, for the wurtzite lattice as $c_c = 4/(\sqrt{3}\,a^2 c)$. For example, $c_c = 2.2 \times 10^{22}\,\mathrm{cm}^{-3}$ for $Al_xGa_{1-x}As$ in the entire composition range $0 \le x \le 1$ since the lattice constant does not vary significantly, and $c_c = 4.2 \times 10^{22}\,\mathrm{cm}^{-3}$ for wurtzite $Mg_xZn_{1-x}O$ [985]. In a random alloy, the probability $p(N)$ to find exactly N Ga atoms in a given volume V (with a total of $c_c V$ cations) is given by the binomial distribution

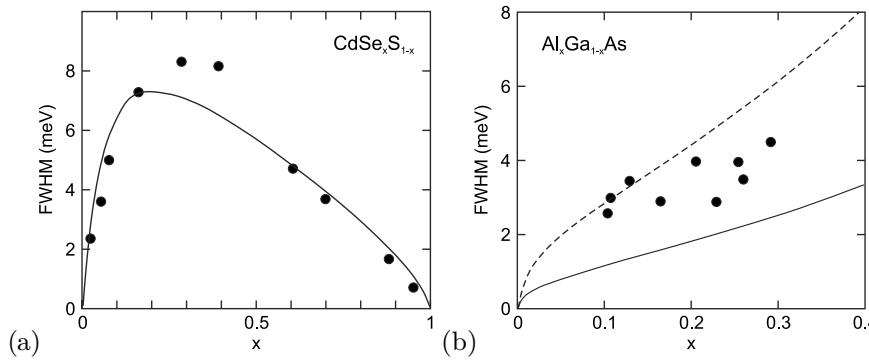

Fig. 10.15 **a** Spectral width of the photoluminescence from CdS_xSe_{1-x} alloys. *Solid line* is theory according to (10.30). Adapted from [983]. (**b**) Spectral width of the bound exciton recombination in $Al_xGa_{1-x}As$ with various Al content within the direct-bandgap regime. *Solid line* is (10.30) with (10.28), *dashed line* with pre-factor $4\pi/3$ instead of $10\,\pi$. Adapted from [987]

$$p(N) = \binom{c_c\,V}{N} x^N\,(1-x)^{c_c V - N}\ . \tag{10.27}$$

The sampling volume for a luminescence event is the exciton volume (cf. (9.51)) that is given for the free-exciton (in 1s hydrogen state) as [983, 986]

$$V_{ex} = 10\,\pi\,a_X^3 = 10\,\pi\,\left(\frac{m_0}{m_r^*}\,\epsilon_s\,a_B\right)^3\ . \tag{10.28}$$

One should note that due to the variation of the involved material parameters V_{ex} depends itself on x. In GaAs there are about 1.2×10^6 cations in the exciton volume. In $Al_xGa_{1-x}As$, there are on average $x c_c V_{ex}$ Al atoms in the exciton volume. The fluctuation is given by the standard deviation of the binomial distribution [986]

$$\sigma_x^2 = \frac{x\,(1-x)}{c_c\,V_{ex}}\ . \tag{10.29}$$

The corresponding energetic broadening (full width at half-maximum) of the spectral line is given by $\Delta_E = 2.36\,\sigma$ with

$$\sigma = \frac{\partial E_g}{\partial x}\,\sigma_x = \frac{\partial E_g}{\partial x}\,\sqrt{\frac{x\,(1-x)}{c_c V_{ex}}}\ . \tag{10.30}$$

We note that instead of the quantum mechanically correct factor $10\,\pi$ [983, 986], often the factor $4\pi/3$ [984] is used, resulting in larger theoretical broadening.

Experimental data for Cd_xSe_{1-x} in Fig. 10.15a are consistent with (10.30). The theoretical dependence (10.30) is shown in Fig. 10.15b also for $Al_xGa_{1-x}As$ together with experimental data and found to disagree [987]. Since the exciton volume is much smaller (cf. Sect. 9.7.6) than in $Al_xGa_{1-x}As$, alloy broadening in $Mg_xZn_{1-x}O$ is much larger for a given for given x.

The spectral broadening due to alloy disorder masks the fine structure of recombination lines near the band edge present for binary semiconductors. Often for all temperatures only a single recombination line appears for alloys. Spectra for three different $Mg_xZn_{1-x}O$ alloys are shown in Fig. 10.16a. The increasing inhomogeneous broadening is obvious, causing a single peak for $x > 0.03$. The temperature dependence of the peak positions is shown in Fig. 10.17 for the same samples. For $x = 0.005$ the bound exciton (Al-donor) (D^0,X) and free exciton (X_A) recombination lines can still be resolved despite

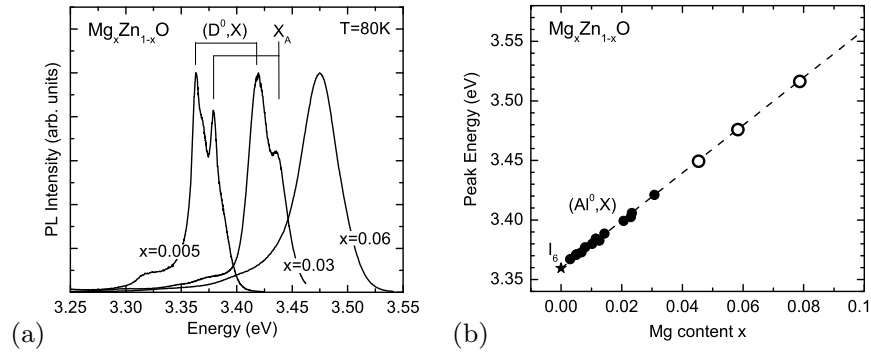

Fig. 10.16 **a** Photoluminescence spectra ($T = 80$ K, scaled) of three $Mg_xZn_{1-x}O$ alloy layers on sapphire with three different Mg-contents, $x = 0.005$, $x = 0.03$, and $x = 0.06$ as labeled. The energy positions of (D^0,X) and X_A peaks are marked. Adapted from [977]. **b** Peak energy of the photoluminescence spectrum ($T = 2$ K) of ZnO (I_6-line, *star*) and various $Mg_xZn_{1-x}O$ alloys (*circles*). For $x \leq 0.03$ (*filled circles*) the (D^0,X) recombination peak (Al donor) can be spectrally separated from the free exciton (X_A) recombination. For the samples with higher Mg content (*empty circles*) a single recombination peak is present at all temperatures. The *dashed line* is a linear least square fit for the alloys with $0 \leq x \leq 0.03$, showing that also for $x > 0.03$ the low temperature recombination peak is due to donor-bound excitons. Adapted from [988]

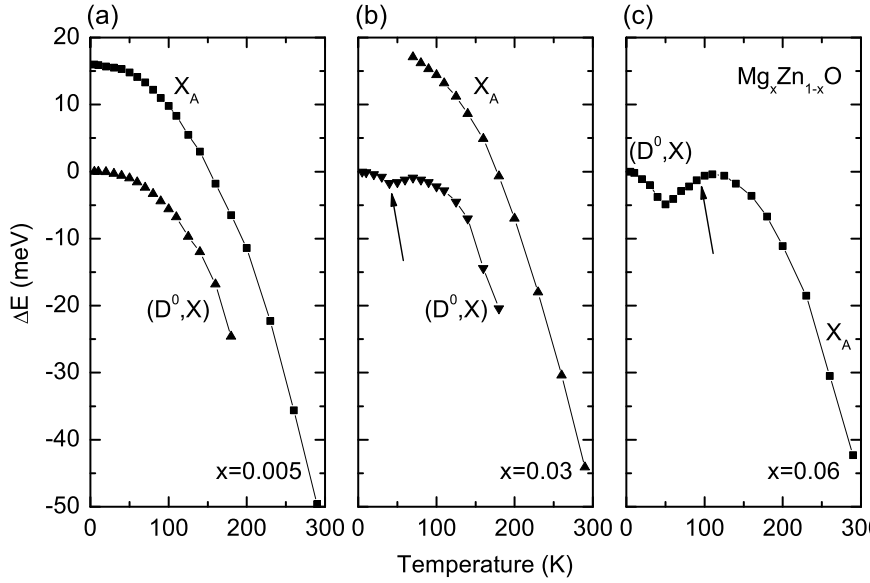

Fig. 10.17 Temperature dependence of the shift of energy position of (D^0,X) and X_A photoluminescence peak in $Mg_xZn_{1-x}O$ alloys with three different Mg-contents, (**a**) $x = 0.005$, (**b**) $x = 0.03$, (**c**) $x = 0.06$. The energy positions are given relative to the low temperature position of the respective (D^0,X) peaks. Adapted from [977]

the inhomogeneous broadening of $\sigma = 2.6$ meV. At low temperature the luminescence intensity is dominated by (D^0,X) recombination, at room temperature by free exciton (X_A) recombination. Both peaks are present at low temperatures and exhibit a red-shift with increasing temperatures due to the shrinking of the band gap (Fig. 10.17a). The (D^0,X) peak vanishes at about 180 K due to ionization of the excitons from the donors ($Q \approx 15$ meV, similar as in pure ZnO).

For larger Mg-content of $x = 0.03$ the two peaks can still mostly be separated ($\sigma = 6.0$ meV). The (D^0,X) energy position shows a small dip (about 2 meV) due to exciton localization in the alloy

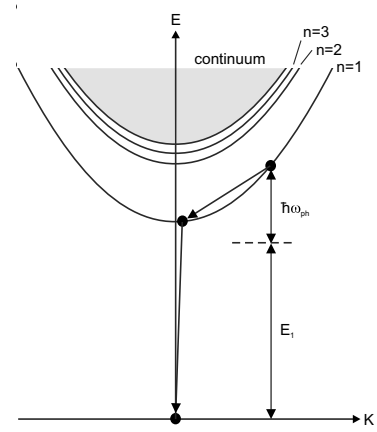

Fig. 10.18 Schematic representation of 1 LO exciton scattering of an exciton at $\mathbf{K} \neq 0$ to an intermediate state with $\mathbf{K} \approx 0$ and subsequent radiative decay. $\hbar\omega$ represents the phonon energy and E_1 the energy of the emitted photon

disorder potential (arrow in Fig. 10.17b). At low temperatures excitons are frozen in local potential minima and have a non-thermal (non-Boltzmann) population. With increasing temperature they can overcome energy barriers and thermalize, leading to a shift of the recombination peak to lower energies. Further increase of temperature populates higher levels and leads to a shift of the recombination peak to higher energies. Superimposed is the red-shift due to the band gap shrinkage. This so-called "S"-shape effect of $E(T)$ is discussed in Sect. 12.4 in detail with regard to exciton localization in a quantum well disorder potential.

For $x = 0.06$ only a single photoluminescence peak is observed for the alloy ($\sigma = 8.5$ meV). The (D^0,X) peak is the dominant for the $Mg_xZn_{1-x}O$ alloys at low temperatures even in the presence of large alloy broadening (Fig. 10.16(b)). The peak changes its nature from (D^0,X) at low temperatures to X_A at room temperature. In between, first exciton thermalization (red-shift) in the disorder potential and subsequently exciton ionization from the donors (blue-shift, arrow in Fig. 10.17c) are observed [977]. Such exciton ionization from impurities has also been observed for (Al,Ga)N:Si [628, 989].

10.4 Phonon Replica

The momentum selection rule for free-exciton recombination allows only excitons with $\mathbf{K} \approx 0$ (for $\mathbf{K}$, cf. (9.49)) to recombine. The fine structure of this recombination is connected to polariton effects (cf. Sect. 9.7.8). Excitons with large $\mathbf{K}$ can recombine if a phonon or several phonons are involved [990] that provide the necessary momentum $\mathbf{q} = \mathbf{K}_1 - \mathbf{K}_2$, with $\mathbf{K}_1$ ($\mathbf{K}_2$) being the wavevector of the initial (intermediate) exciton state (Fig. 10.18). A so-called *zero-phonon* line at energy E_0 is then accompanied by *phonon replica* below E_0 at integer multiples (at low temperature) of the (LO) phonon energy $\hbar\omega_{\mathrm{ph}}$

$$E_n = E_0 - n\,\hbar\omega_{\mathrm{ph}}\ . \tag{10.31}$$

Phonon replicas have been observed in many polar semiconductors such as CdS [991] and ZnSe [992]. A sequence of such phonon replica, as observed in GaN [993], is depicted in Fig. 10.19a.

The lineshape of the n-th phonon-assisted line is proportional to the exciton population at a given excess energy, which is proportional to the density of states and the Boltzmann distribution function [994]

$$I_n(E_{\mathrm{ex}}) \propto \sqrt{E_{\mathrm{ex}}}\,\exp\left(-\frac{E_{\mathrm{ex}}}{kT}\right) w_n(E_{\mathrm{ex}})\ . \tag{10.32}$$

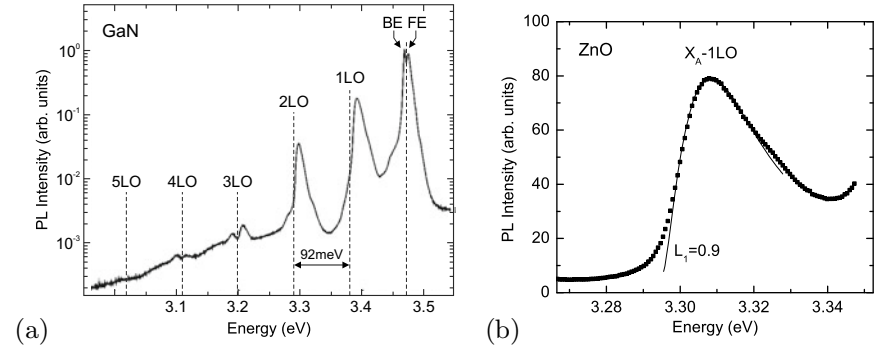

Fig. 10.19 **a** Photoluminescence spectrum of GaN (grown on SiC substrate) at $T = 50\,\mathrm{K}$. In addition to emission from free (FE) and bound (BE) excitons several phonon replica (labeled as 1LO–5LO) are observed. *Vertical dashed lines* indicate energy positions of multiple LO-phonon energies ($\hbar\omega_{\mathrm{LO}} = 92\,\mathrm{meV}$) below the FE peak. Adapted from [993]. **b** Photoluminescence spectrum of 1 LO phonon-assisted recombination peak at $T = 103\,\mathrm{K}$ (from the data of Fig. 10.5). Data points (*dots*) and lineshape fit (*solid line*) according to (10.32) with the parameters $L_1 = 0.9$ and $E_1 = 3.2955\,\mathrm{eV}$ (and background)

Here, E_{ex} represents the exciton kinetic energy. The factor $w_n(E_{\mathrm{ex}})$ accounts for the $\mathbf{q}$-dependence of the matrix element. It is typically expressed as

$$w_n(E_{\mathrm{ex}}) \propto E_{\mathrm{ex}}^{L_n} \,. \tag{10.33}$$

Accordingly, as temperature dependent refinement of (10.31), the energy separation ΔE_n of the energy of the peak maximum of phonon replica from E_0 is given by

$$\Delta E_n = E_n - E_0 = -n\,\hbar\omega_{\mathrm{ph}} + \left(L_n + \frac{1}{2}\right) kT \,. \tag{10.34}$$

It is found theoretically that $L_1 = 1$ and $L_2 = 0$ [994]. These relations are approximately fulfilled for GaN [995]. A lineshape fit for the 1 LO phonon-assisted transition in ZnO is shown in Fig. 10.19b.

In Fig. 10.20a the 'green band' emission of ZnO is shown as presented in [996]. This band is mostly attributed to a Cu impurity; recently, evidence has grown from isotope decay and annealing studies that it is related to the zinc vacancy [997] (Fig. 10.20b). The zero phonon line is followed by many replica with a maximum at about 6 LO phonons. The intensity I_N of the N-th replica is given by [998, 999]

$$I_N \propto \exp(-S)\,\frac{S^N}{N!} \,, \tag{10.35}$$

where S is the so-called Huang–Rhys parameter. In [997], a coupling parameter of $S = 6.9$ has been determined.

Equation (10.35) is obtained from the consideration of transitions in the configuration diagram [998, 1000] (Fig. 10.21), using the Born–Oppenheimer approximation. Here the electronic wavefunctions are separated from the vibrational wavefunctions, leading to the Franck–Condon principle, that optical transitions occur with the positions of the nuclei fixed and thus vertical in the configuration diagram Fig. 10.21. Assuming low temperatures, only the lowest state is (partially) occupied. The Huang–Rhys parameter, the average number of phonons involved in the transition, is related to the displacement $\delta q = q_1 - q_0$ of the two configurations

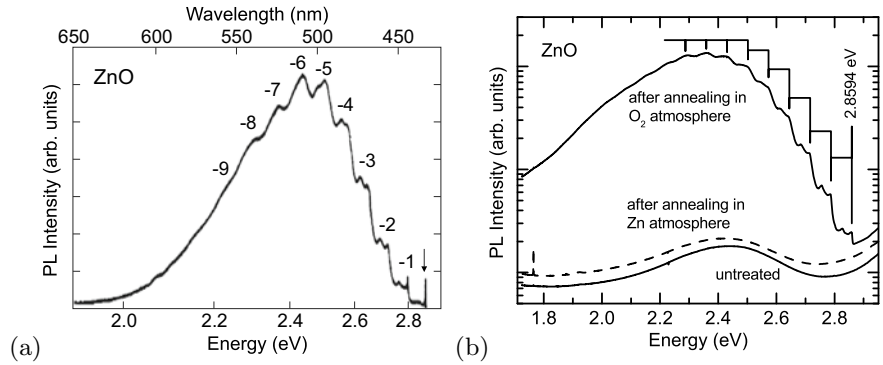

Fig. 10.20 **a** Luminescence spectrum of ZnO in the visible. The *arrow* denotes the zero-phonon line at 2.8590 eV. The numbers of the phonon replica are labeled. Adapted from [996]. **b** Luminescence spectra (*solid lines*) of a ZnO bulk crystal before ('untreated') and after annealing in O_2 atmosphere at $T = 1073$ K. After annealing in Zn atmosphere at the same temperature, the green band disappears again (*dashed line*). From [997]

$$S = \frac{C\,\delta q^2}{2\,\hbar\omega_{\rm ph}}\,, \tag{10.36}$$

where C is the 'spring constant' of the parabola, $C = \mathrm{d}^2E/\mathrm{d}q^2$.

For small $S \ll 1$, we are in the weak coupling regime and the zero-phonon line is the strongest. In the strong coupling regime, $S > 1$, the maximum is (red-) shifted from the zero-phonon line. We note that in absorption, phonon replica occur on the high-energy side of the zero-phonon absorption. For large S the peak intensities are close to a Gaussian. The correspondence of emission and absorption is nicely seen for excitons on isoelectronic oxygen traps in ZnTe [1001]. The oxygen is on substitutional Te site. Up to seven phonon replica are visible in Fig. 10.22 around the zero-phonon or A-line with a

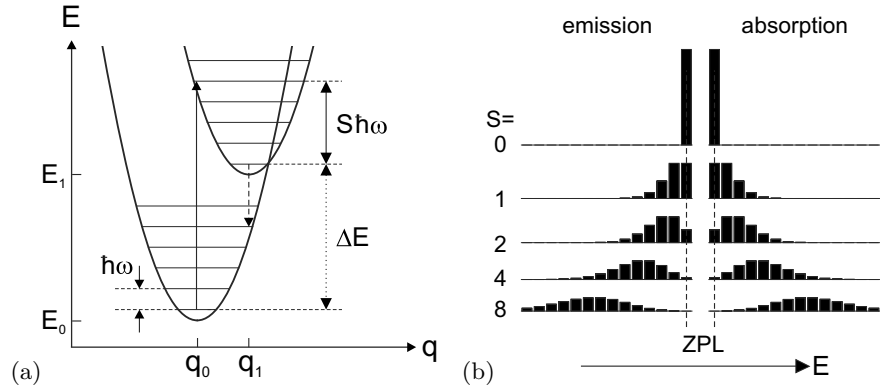

Fig. 10.21 **a** Configuration diagram of two states that differ in their configuration coordinate by $\delta q = q_1 - q_0$. Both are coupled to phonons of energy $\hbar\omega$. The absorption maximum (*solid vertical line*) and emission maximum (*dashed vertical line*) are shifted with respect to the zero-phonon line (*dotted vertical line*) with energy $E_1 - E_0$. The Huang–Rhys parameter is $S \sim 4$. (**b**) Intensity of zero-phonon line ('ZPL') and phonon replica (10.35) for emission and absorption processes with different values of the Huang–Rhys parameter S as labeled

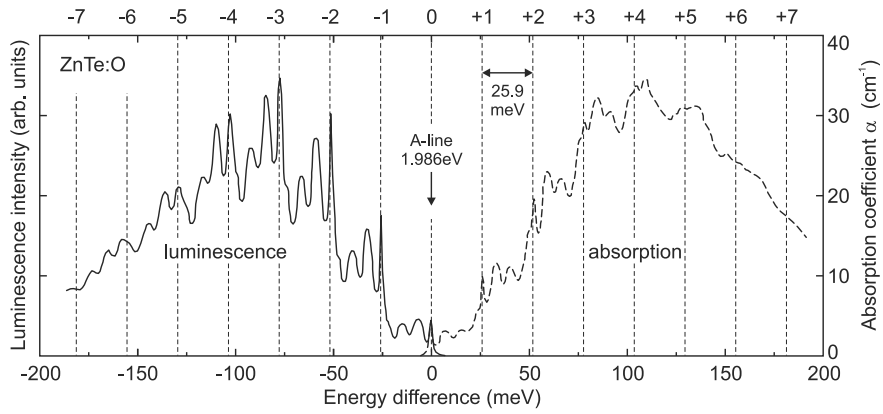

Fig. 10.22 Photoluminescence (*solid line*) and absorption (*dashed line*) spectra of excitons bound to substitutional oxygen in ZnTe at $T = 20\,\mathrm{K}$. The energy position is relative to the A-line at 1.9860 eV. The *vertical dashed lines* have a separation of 25.9 meV. Adapted from [1001]

separation of about 26 meV, the optical phonon energy in ZnTe. The Huang-Rhys parameter is about 3–4. Other peaks are due to acoustic phonons.

10.5 Self-Absorption

Luminescence that is emitted within the semiconductor can be (re-)absorbed before it may reach the surface and can leave the crystal. This effect is called self-absorption. It is particularly strong for radiation with an energy where the absorption $\alpha(\hbar\omega)$ is high, i.e. above the band gap of a direct semiconductor. Similarly to the penetration depth $1/\alpha$ for radiation entering the crystal, emission approximately occurs only from a layer of such thickness. For typical values of α in the range of $10^5\,\mathrm{cm}^{-1}$, the 'skin' of the semiconductor that emits light with energy above the band gap is 100 nm. For light at the low energy side of the band gap or with energy within the band gap (deep levels), the emission depth can be much larger.

After re-absorption, the energy has another chance to relax non-radiatively, thus reducing the quantum efficiency. Alternatively it can be reemitted, either at the same energy or at a lower energy. Possibly several re-absorption processes occur before a photon eventually leaves the semiconductor ('photon recycling'). Such processes are important in LED structures where photon extraction has to be optimized (Sect. 23.3.4). Emission on phonon replica (Sect. 10.4) is red-shifted from the energy range of strong absorption and thus suffers no (or only little) self-absorption. This can be seen from the spectrum of a thick ZnO crystal excited homogeneously (via two-photon absorption with a red Ruby laser), Fig. 10.23. The zero phonon line (at E_X), originating from the $\approx$100 nm skin of the samples and being by far the strongest in thin films (Fig. 10.5), is practically absent and emission on the phonon replica collected from the entire volume dominates the spectrum.

10.6 Donor–Acceptor Pair Transitions

Optical transitions can occur between neutral donors and acceptors. The (spatially indirect) donor–acceptor pair (DAP) recombination is present in (partially) compensated semiconductors and follows

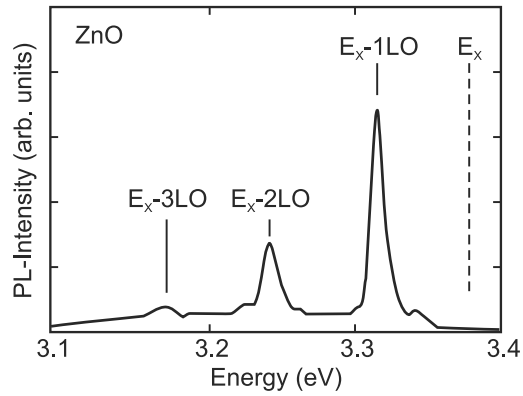

Fig. 10.23 Photoluminescence spectrum (at $T = 55\,\mathrm{K}$) from bulk ZnO excited homogeneously via two-photon excitation by a Q-switched ruby laser (pulse width 40 ns). Adapted from [1002]

the scheme $D^0A^0 \rightarrow D^+A^-eh \rightarrow D^+A^- + \gamma$, where γ is a photon with the energy $\hbar\omega$. The energy of the emitted photon is given by

$$\hbar\omega = E_\mathrm{g} - E_\mathrm{D}^\mathrm{b} - E_\mathrm{A}^\mathrm{b} + \frac{1}{4\pi\epsilon_0}\frac{e^2}{\epsilon_\mathrm{r} R}\,, \tag{10.37}$$

where R is the distance between the donor and the acceptor for a specific pair. Since R is discrete, the DAP recombination spectrum consists of several discrete lines. If the donor and acceptor occupy the same sublattice, e.g.. O and C both substituting P sites in GaP, the spatial distance of the donor and acceptor is $R(n) = a_0\sqrt{n/2}$, where a_0 is the lattice constant and n is an integer. However, for certain 'magic' numbers $n = 14, 30, 46, \ldots$ no lattice points exist and therefore the corresponding lines are missing (labeled 'G' in Fig. 10.24). No such gaps exist in DA spectra where donors and acceptors occupy different sublattices, e.g. GaP:O,Zn (see also Fig. 10.24). In this case, the spatial separation is given by $R(n) = a_0\sqrt{n/2 - 5/16}$. If significant broadening is present, the lines are washed out and a donor–acceptor pair band forms.

10.7 Inner-Impurity Recombination

The transitions of electrons between different states of an impurity level can be nonradiative or radiative. As an example, the radiative transition of electrons in the Fe^{2+} state in InP $^5T_2 \rightarrow {}^5E$ (Fig. 10.25) and its fine structure were observed first in [1005] at around 0.35 eV.

Certain defects, also termed 'color centers', have been investigated towards their ability to act as efficient single photon source. If a single defect is optically excited, it can emit a photon. However, it cannot be excited further. Also, it cannot emit another photon before it has been excited again. This can be measured through the correlation function for the time difference of emitted photons going to zero for zero time difference. A popular example of such center is the NV center in diamond, the complex of a vacancy and a nitrogen impurity [1006, 1007]. The emission rate saturates at about 2×10^5 photons/s (pick up with microscope objective). The sensitivity of the spectrum to magnetic fields makes the NV center a nanoscopic magnetic field sensor [1008]. Also the spins on the center are fairly isolated and can be manipulated coherently.

10.8 Auger Recombination

In competition with the radiative, bimolecular recombination is the Auger recombination (Fig. 10.26). In the Auger process, the energy that is released during the recombination of an electron and hole is

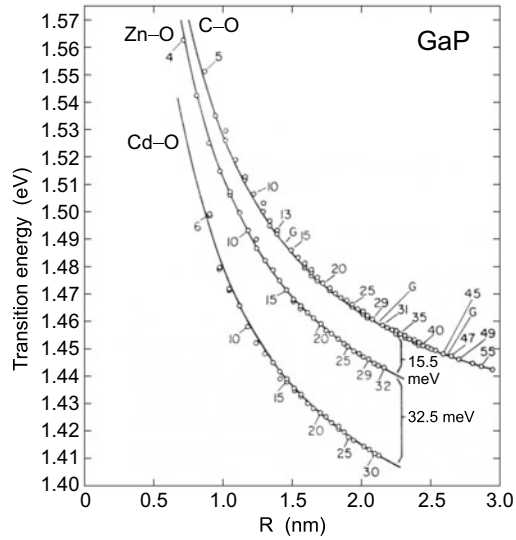

Fig. 10.24 Transition energies in GaP ($T = 1.6\,\mathrm{K}$) of the donor–acceptor recombination involving the deep oxygen donor and C, Zn, and Cd acceptors, respectively. The lines follow (10.37) for $E_g^{\mathrm{GaP}} = 2.339\,\mathrm{eV}$, $\epsilon_r = 11.1$ and $(E_D^b)_O = 893\,\mathrm{meV}$, $(E_A^b)_C = 48.5\,\mathrm{meV}$, $(E_A^b)_{Zn} = 64\,\mathrm{meV}$, and $(E_A^b)_{Cd} = 96.5\,\mathrm{meV}$. Predicted missing modes for GaP:C,O are labeled with 'G'. Adapted from [1003]

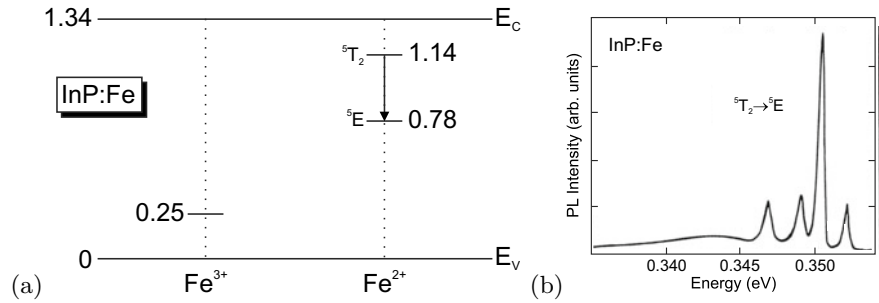

Fig. 10.25 **a** Schematic band diagram of InP with levels of Fe impurities in the 3+ and 2+ charge states at low temperature. All energies are given in eV. The *arrow* denotes the optical transition from an excited Fe^{2+} state to the Fe^{2+} ground state. (**b**) Photoluminescence spectrum (at $T = 4.2\,\mathrm{K}$) of InP:Fe sample with [Fe]=$5 \times 10^{16}\,\mathrm{cm}^{-3}$. Part (**b**) adapted from [1004]

not emitted with a photon but, instead, transferred to a third particle. This can be an electron (eeh, Fig. 10.26a) or a hole (hhe, Fig. 10.26b). The energy is eventually transferred nonradiatively from the hot third carrier via phonon emission to the lattice. The probability for such process is $\propto n^2 p$ if two electrons are involved and $\propto np^2$ if two holes are involved. The Auger process is a three-particle process and becomes likely for high carrier density, either through doping, in the presence of many excess carriers, or in semiconductors with small band gap. Auger recombination is the inverse of the impact ionization (cf. Sect. 8.4.4). Phonon-assisted Auger recombination relaxes the momentum conservation rule for the involved charge carriers at the cost of an additional particle being involved in the scattering process. It has been pointed out that this process is dominating in bulk material [1010, 1011] and quantum wells [1012].

In thermodynamic equilibrium the rates for Auger recombination and thermal Auger generation must be equal, thus

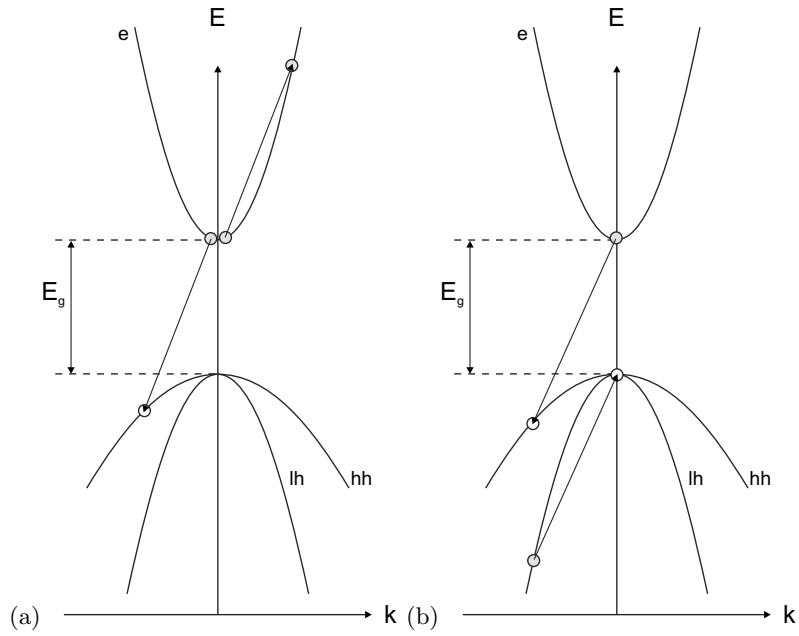

Fig. 10.26 Schematic representation of Auger recombination. An electron recombines with a hole and transfers the energy to **a** another electron in the conduction band, **b** another electron in the valence band

Table 10.3 Auger recombination coefficients for some semiconductors. Data for InSb from [1013], SiC from [947], others from [948]

material	C_n (cm^6/s)	C_p (cm^6/s)
4H-SiC	5×10^{-31}	2×10^{-31}
Si, Ge	2.8×10^{-31}	9.9×10^{-32}
GaAs, InP	5.0×10^{-30}	3.0×10^{-30}
InSb	1.2×10^{-26}	

$$G_{\text{th}} = C_n\, n_0^2\, p_0 + C_p\, n_0\, p_0^2\,, \tag{10.38}$$

where C_n and C_p denote the Auger recombination coefficients. The equation for the dynamics in the presence of excess carriers (if solely Auger recombination is present) is given as

$$\frac{\partial\, \delta n}{\partial t} = G_{\text{th}} - R = -C_n\,(n^2\, p - n_0^2\, p_0) - C_p\,(n\, p^2 - n_0\, p_0^2)\,. \tag{10.39}$$

The Auger recombination rate typically used in SRH kinetics is

$$r_{\text{Auger}} = (C_n\, n + C_p\, p)\,(np - n_0 p_0)\,. \tag{10.40}$$

Typical values for the Auger recombination coefficients are given in Table 10.3.

In Fig. 10.27a the electron lifetime in heavily p-doped (In,Ga)As (lattice matched to InP) is shown [1014]. It follows $\tau_n^{-1} = C_p\, N_A^2$ as expected from (10.39) for p-type material. The Auger process in silicon has been discussed in detail [1015]. In Fig. 10.27b experimental data for n-type and p-type Si are summarized. Auger theory can predict the lifetimes in n-type material. The predicted rate in p-type material is too small, thus a phonon-assisted process is evoked [1015].

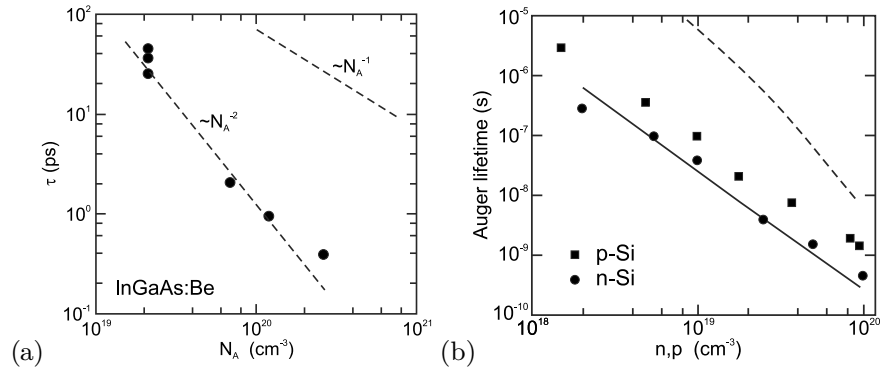

Fig. 10.27 **a** Experimental values of the electron lifetime in heavily p-doped (In,Ga)As on InP at room temperature. The *dashed lines* show dependencies of Auger ($\propto N_A^{-2}$, $C_p = 8.1 \times 10^{-29}\,\mathrm{cm}^{-6}\,\mathrm{s}^{-1}$) and band-band recombination ($\propto N_A^{-1}$, $B = 1.43 \times 10^{-10}\,\mathrm{cm}^{-3}\,\mathrm{s}^{-1}$). Adapted from [1014]. (**b**) Experimental Auger lifetimes in p-type (*squares*) and n-type (*circles*) silicon at 300 K. The *dashed* (*solid*) *line* is theory for p-type (n-type) material. Adapted from [1015]

10.9 Band–Impurity Recombination

A very important recombination process is the capture of carriers by impurities. This process is in competition with all other recombination processes, e.g. the radiative recombination and the Auger mechanism. The band–impurity recombination is the inverse process to the carrier release from impurities and intimately related to carriers statistics (Chap. 7). It is particularly important at low carrier densities, for high dopant concentration and in indirect semiconductors since for these the bimolecular recombination is slow. This process is generally considered to be non-radiative since no photons close to the band edge are emitted.[4]

10.9.1 Shockley–Read–Hall Kinetics

The theory of capture on and recombination involving impurities is called Shockley–Read–Hall (SRH) kinetics [942]. An example of radiative band–impurity recombination (of the type shown in Fig. 10.28a) is shown in Fig. 10.8 for the (e,A^0) recombination at the carbon acceptor in GaAs.

We consider electron traps [1016] (see Fig. 10.28) with a concentration N_t with an energy level E_t. In thermodynamic equilibrium they have an electron population

$$f_t^0 = \frac{1}{\exp\left(\frac{E_t - E_F}{kT}\right) + 1}\,, \tag{10.41}$$

where f_t is the nonequilibrium population of the trap. Then the capture rate r_c is proportional to the unoccupied traps and the electron concentration, $r_c \propto nN_t(1 - f_t)$. The proportionality factor has the form $v_{th}\sigma_n$, where v_{th} is the thermal velocity $v_{th} = \sqrt{3kT/m^*} \approx 10^7$ cm/s and σ_n is the capture cross section that is of atomic scale, typically $\sim 10^{-15}\mathrm{cm}^2$. The capture cross section can be related to the optical absorption cross section [588, 589].

In order to make the following calculation more transparent, we put the effective-mass ratio $\sqrt{m_0/m^*}$ into σ in the following and thus have the same thermal velocity $v_{th} = \sqrt{3kT/m_0}$ for electrons and

[4] Depending on the energetic depth of the trap, mid or far infrared photons can be emitted.

holes. The capture rate of electrons is

$$r_c = v_{th}\,\sigma_n\,n\,N_t\,(1 - f_t)\ . \tag{10.42}$$

The emission rate from filled traps is

$$g_c = e_n\,N_t\,f_t\ , \tag{10.43}$$

where e_n denotes the emission probability. In a similar way, the emission and capture rates for holes can be written:

$$r_v = v_{th}\,\sigma_p\,p\,N_t\,f_t \tag{10.44}$$

$$g_v = e_p\,N_t\,(1 - f_t)\ . \tag{10.45}$$

In thermodynamical equilibrium, capture and generation rates are equal, i.e. $r_c = g_c$ and $r_v = g_v$. Thus, the emission probability is

$$e_n = v_{th}\,\sigma_n\,n_0\,\frac{1 - f_t^0}{f_t^0}\ . \tag{10.46}$$

Using $\frac{1-f_t^0}{f_t^0} = \exp\left(\frac{E_t - E_F}{kT}\right)$, (7.10) and (7.11) the emission probabilities can be written as

$$e_n = v_{th}\,\sigma_n\,n_t \tag{10.47}$$

$$e_p = v_{th}\,\sigma_p\,p_t\ , \tag{10.48}$$

with

$$n_t = N_C\,\exp\left(\frac{E_t - E_C}{kT}\right) \tag{10.49}$$

$$p_t = N_V\,\exp\left(-\frac{E_t - E_V}{kT}\right)\ . \tag{10.50}$$

We note that $n_t\,p_t = n_0\,p_0$ (cf. (7.15)).

The temperature dependence of the thermal velocity is $\propto T^{1/2}$, the temperature dependence of the band-edge density of states is $\propto T^{3/2}$ (7.8) and (7.9). Thus, the temperature dependence of the emission

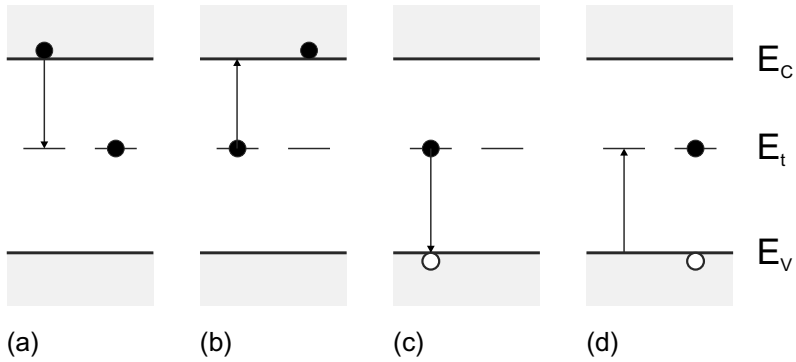

Fig. 10.28 Band-to-impurity processes at an impurity with one level (*left*: initial, *right*: final state in each part): **a** electron capture (from conduction band), **b** electron emission (into conduction band), **c** hole capture (from valence band), **d** hole emission (into valence band). The *arrows* indicate the transition of the electron

rate e_n is (apart from the exponential term) $\propto T^2$ if σ is temperature independent. Charge conservation requires in nonequilibrium (and of course in equilibrium) $r_c - r_v = g_c - g_v$. From this we obtain the population of the trap in nonequilibrium:

$$f_t = \frac{\sigma_n\, n + \sigma_p\, p_t}{\sigma_n\,(n + n_t) + \sigma_p\,(p + p_t)} \,. \tag{10.51}$$

The recombination rate r_{b-i} of the band–impurity recombination is then

$$\begin{aligned} r_{b-i} = -\frac{\partial \delta n}{\partial t} &= r_c - g_c \\ &= \frac{\sigma_n\, \sigma_p\, v_{th}\, N_t}{\sigma_n\,(n + n_t) + \sigma_p\,(p + p_t)}\ (n\, p - n_0\, p_0) \,. \end{aligned} \tag{10.52}$$

Using the 'lifetimes'

$$\tau_{n_0} = (\sigma_n\, v_{th}\, N_t)^{-1} \tag{10.53}$$

$$\tau_{p_0} = (\sigma_p\, v_{th}\, N_t)^{-1} \,, \tag{10.54}$$

this is typically written as

$$r_{b-i} = \frac{1}{\tau_{p_0}\,(n + n_t) + \tau_{n_0}\,(p + p_t)}\ (n\, p - n_0\, p_0) \,. \tag{10.55}$$

For an n-type semiconductor the Fermi level is above E_t and the traps are mostly full. Thus hole capture is the dominating process. The equation for the dynamics simplifies to

$$\frac{\partial \delta p}{\partial t} = -\frac{p - p_0}{\tau_{p_0}} \,. \tag{10.56}$$

Thus, an exponential decay with minority-carrier lifetime τ_{p_0} (or τ_{n_0} for p-type material) occurs.

A recombination center is most effective when it is close to the middle of the band gap (midgap level). The condition $\partial r_{b-i}/\partial E_t = 0$ leads to the trap energy E_t^{max} with the maximum recombination rate being located at

$$E_t^{max} = \frac{E_C + E_V}{2} - kT\ \ln\left(\frac{\sigma_n\, N_C}{\sigma_p\, N_V}\right) \,. \tag{10.57}$$

The curvature $\partial^2 r_{b-i}/\partial E_t^2$ at E_t^{max} is proportional to $-(np - n_0 p_0)$ and thus indeed is negative in the presence of excess carriers. However, the maximum can be fairly broad.

The SRH kinetic presented here is valid for low densities of recombination centers. A more detailed discussion and a more general model can be found in [1018].

A typical example for a recombination center is gold in silicon. The minority carrier lifetime decreases from 2×10^{-7} s to 2×10^{-10} s upon increase of the Au concentration from 10^{14} to 10^{17} cm^{-3}. The incorporation of recombination centers is an important measure for the design of high-frequency devices [1019]. Due to importance in silicon technology the recombination properties of many metals in silicon have been investigated, in particular Fe-contamination and the role of FeB-complexes [1020–1022].

A reduction in minority-carrier lifetime can also be achieved by irradiation with high-energy particles and the subsequent generation of point defects with energy levels at midgap.

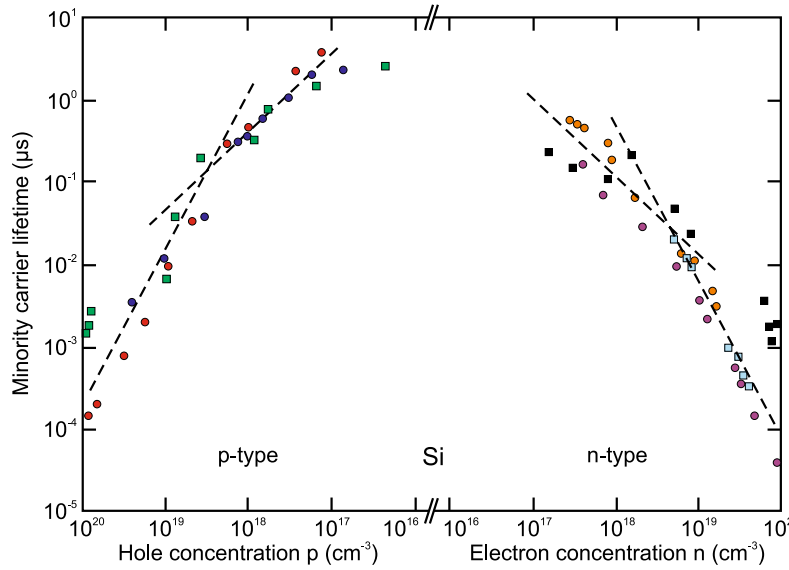

Fig. 10.29 Minority carrier lifetime at room temperature as a function of majority carrier concentration in n-type and p-type silicon. The *dashed lines* have the slopes N^{-1} and N^{-2}. Data from [1024]

In Fig. 10.29 various data on minority carrier lifetime in silicon are compiled. Over some doping range, a dependence of the lifetime $\propto N^{-1}$ as in (10.54) prevails. For doping beyond the $10^{19}\,\mathrm{cm}^{-3}$ range, Auger recombination (Sect. 10.8) with $\tau \propto N^{-2}$ is dominant. A more detailed discussion can be found in [1023, 1024]. Generally the lifetimes are temperature dependent [1025] as expected from (10.52).

10.9.2 Multilevel Traps

Traps with multiple levels in the band gap have generally similar but more complicated dynamics as compared to single-level traps. Lifetimes are an average over negatively and positively charged states of the trap.

10.10 ABC Model

Summarizing the results on band-impurity recombination (Sect. 10.9), bimolecular recombination (Sect. 10.2) and Auger recombination (Sect. 10.8), the total recombination rate R can be written simplified as

$$R = A\,n + B\,n^2 + C\,n^3\ , \tag{10.58}$$

where A is the coefficient for the band-impurity recombination, B the bimolecular recombination coefficient and C the Auger recombination coefficient; n denotes the carrier density. This model is known as the 'ABC' model. It can be refined separating effects of electrons and holes and including higher terms. Often such model is used to investigate recombination in devices as a function of injection, e.g. [1026, 1027].

The internal radiative quantum efficiency η_{int} is given by ratio of the radiative recombination rate and the total recombination rate,

$$\eta_{\text{int}} = \frac{B\,n^2}{A\,n + B\,n^2 + C\,n^3} = \frac{B\,n}{A + B\,n + C\,n^2}\ . \tag{10.59}$$

10.11 Field Effect

The emission of electrons from a trap is thermally activated with an ionization energy $E_\text{i} = E_\text{C} - E_\text{t}$. If the trap is in a strong electric field E, the emission probability can change. An acceptor-like trap after removal of the electron is neutral and its potential is short range. A donor has a long-range Coulomb potential after ionization. In an electric field, these potentials are modified as visualized in Fig. 10.30. Various additional processes can now occur.

10.11.1 Thermally Activated Emission

For the δ-like potential the ionization energy remains unchanged. For the Coulomb potential the barrier in the field direction is lowered by

$$\Delta E_\text{i} = e\sqrt{\frac{e}{\pi\,\epsilon_0\,\epsilon_r}}\sqrt{E}\ . \tag{10.60}$$

The emission rate e_n is increased in the field by $\exp(\Delta E_\text{i}/kT)$. This effect is called the Poole–Frenkel effect [1028] and can be quite important. For silicon and $E = 2 \times 10^5$ V/cm and $\Delta E_\text{i} = 100$ meV a 50-fold increase of the emission rate at room temperature is expected. As an example the Poole–Frenkel effect for the electron emission from (neutral) interstitial boron in silicon ($\text{B}_\text{i}^0 \rightarrow \text{B}_\text{i}^+ + e^-$) is shown in Fig. 10.31, following the enhancement of $e_\text{n} \propto \exp(\sqrt{E})$. The extrapolation to $E = 0$ agrees with the EPR result [275, 1029].[5]

10.11.2 Direct Tunneling

Carriers can tunnel from the trap level through the barrier in the field direction into the conduction band. This process is temperature independent. The transmission factor of a barrier is (in WKB approximation) proportional to $\exp[-(2/\hbar)\int\sqrt{2m\,[V(x) - E]}\,\text{d}E]$. The emission probability for a triangular

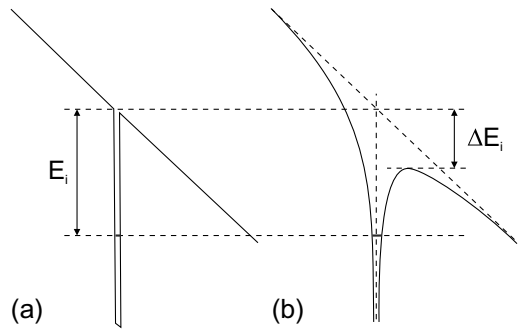

Fig. 10.30 Field effect at **a** a δ-like potential and **b** a Coulomb potential

[5] The slope of the line in Fig. 10.31 is slightly smaller than expected from (10.60).

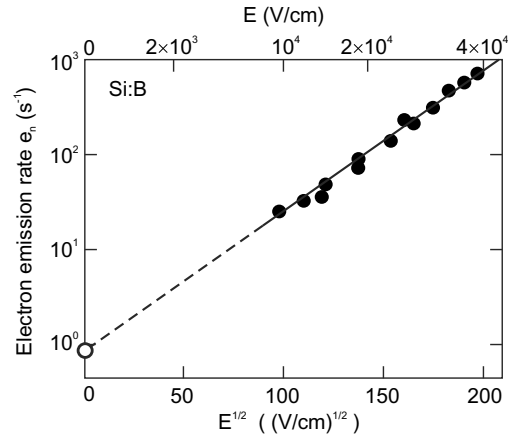

Fig. 10.31 Field effect for electron emission from interstitial boron in silicon ($T = 65\,\mathrm{K}$). The *filled circles* represent experimental data from DLTS, the data point marked with an *empty circle* is from EPR (zero field). The *line* is a linear fit and extrapolation. Adapted from [1029]

barrier is then

$$e_\mathrm{n} = \frac{e\,E}{4\sqrt{2m^*E_\mathrm{i}}}\,\exp\left(-\frac{4\sqrt{2m^*}\,E_\mathrm{i}^{3/2}}{3\,e\,\hbar\,E}\right)\,. \tag{10.61}$$

In the case of a Coulomb-like potential the argument of the exponent in (10.61) needs to be multiplied by a factor $1-(\Delta E_\mathrm{i}/E_\mathrm{i})^{5/3}$ with ΔE_i from (10.60).

10.11.3 Assisted Tunneling

In a thermally assisted tunneling process the electron on the trap level is first excited to a virtual level $E_\mathrm{t}+E_\mathrm{ph}$ by phonon absorption and then tunnels out of the trap (photon-assisted tunneling). From the energetically higher level the tunneling rate is higher. The probability is proportional to $\exp(E_\mathrm{ph}/kT)$. The additional energy can also be supplied by a photon (photon-assisted tunneling).

10.12 Recombination at Extended Defects

10.12.1 Surfaces

A surface (cmp. Chap. 11) is typically a source of recombination, e.g. through midgap levels induced by the break of crystal symmetry. The recombination at surfaces is modeled as a recombination current

$$j_\mathrm{s} = -e\,S\,(n_\mathrm{s}-n_0)\,, \tag{10.62}$$

where n_s is the carrier density at the surface and S is the so-called *surface recombination velocity*.

The surface recombination velocity for GaAs is shown in Fig. 10.32. For InP, if the surface Fermi level is pinned close to midgap, the surface recombination velocity increases from $\sim 5\times10^3\,\mathrm{cm/s}$ for a doping level of $n\sim 3\times10^{15}\,\mathrm{cm^{-3}}$ to $\sim 10^6\,\mathrm{cm/s}$ for a doping level of $n\sim 3\times10^{18}\,\mathrm{cm^{-3}}$ [1030]. For Si, the surface recombination rate depends on the treatment of the surface and lies in the range

between 1–10^4 cm/s [1031, 1032]. The Si-SiO_2 interface can exhibit $S \leq 0.5$ cm/s. Time-resolved measurements and detailed modeling for Si have been reported in [1033].

The recombination velocity at surfaces can be reduced using suitable passivation schemes. Typically inert layers or chemical treatments are used. Surface passivation can be accomplished in two fundamentally different ways: Either the surface defect states themselves are removed or an internal electrical field is established that screens excess charge carriers from the surface defects. Sulfur chemistry is a popular treatment of GaAs surfaces. A review of the passivation schemes for III–V semiconductors can be found in [1035].

10.12.2 Grain Boundaries

Grain boundaries can be a source of non-radiative recombination. This is technologically important for solar cells made from polycrystalline silicon (cf. Sect. 22.4.6). The grain boundary can be understood as an inner surface in the crystal. Modeling of recombination at a grain boundary can be done using an interface recombination velocity [1036, 1037] or considering deep traps [1038]. The minority carrier lifetime decreases with decreasing grain boundary area A (Fig. 10.33a). The carrier loss at a grain boundary can be imaged directly via the efficiency of the collection of an electron beam induced current (EBIC) as shown in Fig. 10.33b. The minority carrier lifetime is only unaffected when the average distance to a grain boundary is much larger than the minority carrier diffusion length, $\sqrt{A} \gg L_D$, otherwise the entire grain volume is subject to non-radiative recombination.

The recombination velocity at grain boundaries can be reduced, similar to that at surfaces, using suitable passivation schemes. A famous one is the chlorine treatment of polycrystalline CdTe used in thin film solar cells [1041].

10.12.3 Dislocations

Also dislocations typically act as recombination centers, sometimes called carrier sinks. In Fig. 10.34 it can be seen that the minority carrier lifetime depends on the dislocation density n_d and follows a $\tau^{-1} \propto n_d$ law, as if each dislocation is a recombination center [1042]. The non-radiative recombination

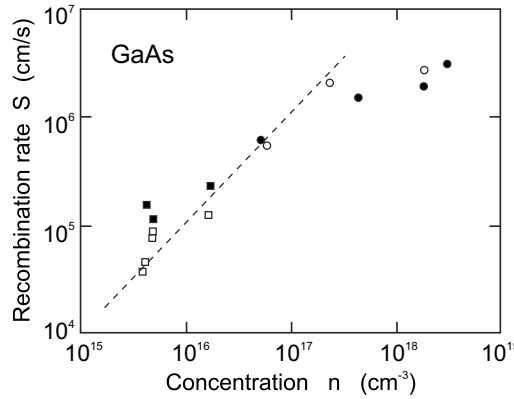

Fig. 10.32 Surface recombination velocity for GaAs as a function of n-type doping concentration. Different experimental points correspond to different surface treatment methods. *Dashed line* is a guide to the eye. Experimental data from [1034]

makes dislocations appear as 'dark line defects' in luminescence imaging [1043]. In [1044] also the decrease of carrier lifetime around (misfit) dislocations has been imaged. The effect of dislocations on the radiative recombination efficiency depends on the diffusion length [1044].

10.13 Excess-Carrier Profiles

In this section, some typical excess-carrier profiles (in one-dimensional geometry) are discussed that arise from certain excitation conditions. The excess-carrier density Δp (here holes in an n-type semiconductor, i.e. $\Delta p = p_{\mathrm{n}} - p_{\mathrm{n_0}}$) is determined by the diffusion equation (cf. (8.65a))

$$D_{\mathrm{p}} \frac{\partial^2 \Delta p}{\partial x^2} = -G(x) + \frac{\Delta p}{\tau_{\mathrm{p}}} \,. \tag{10.63}$$

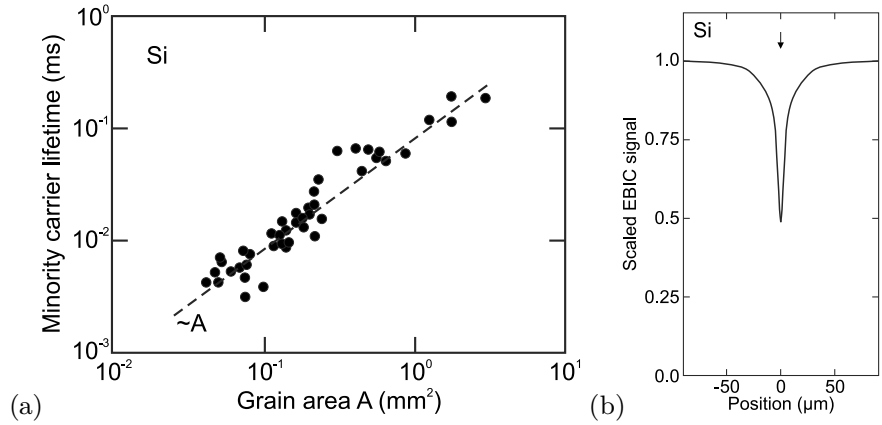

Fig. 10.33 **a** Minority carrier lifetime in (p-type) silicon as a function of grain boundary size. The *dashed line* has the slope $\propto A$. Data from [1039]. **b** Linescan of the electron beam induced current (EBIC) perpendicular to a single grain boundary in silicon. The arrow denotes the position of the grain boundary. Compiled from [1040]

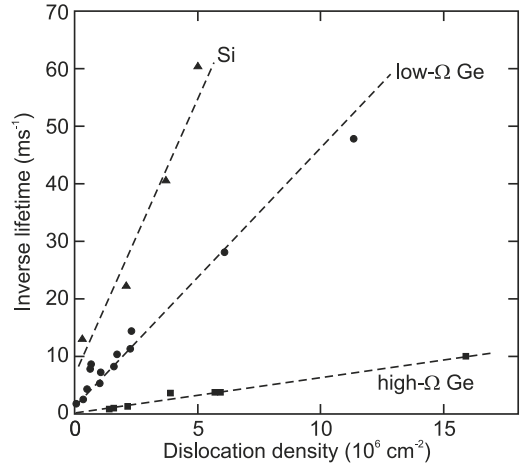

Fig. 10.34 Inverse minority carrier lifetime in n-type silicon (40 Ω cm), low resistivity Ge (3–5 Ω cm) and high resistivity Ge (30–40 Ω cm). Data from [1042]

10.13.1 Generation at Surface

First, the generation of excess carriers in a semi-infinite piece of semiconductor shall occur only at the surface at $x = 0$ (strong absorption limit). The generation is zero everywhere else and the excitation is incorporated via the boundary condition $\Delta p(x = 0) = \Delta p_0$. The general solution for the homogeneous equation (10.63), i.e. $G = 0$, is

$$\Delta p(x) = C_1 \exp\left(-\frac{x}{L_\mathrm{p}}\right) + C_2 \exp\left(\frac{x}{L_\mathrm{p}}\right) , \tag{10.64}$$

with the diffusion length $L_\mathrm{p} = \sqrt{D_\mathrm{p}\tau_\mathrm{p}}$. Taking the boundary condition $\Delta p(x \to \infty) = 0$ the solution is ($C_2 = 0$)

$$\Delta p(x) = \Delta p_0 \exp\left(-\frac{x}{L_\mathrm{p}}\right) . \tag{10.65}$$

In order to connect Δp_0 with the total generation rate per unit area G_tot, we calculate

$$G_\mathrm{tot} = \int_0^\infty \frac{\Delta p(x)}{\tau_\mathrm{p}}\,\mathrm{d}x = \Delta p_0 \frac{L_\mathrm{p}}{\tau_\mathrm{p}} = \Delta p_0 \sqrt{\frac{D_\mathrm{p}}{\tau_\mathrm{p}}} . \tag{10.66}$$

If a slab of finite thickness d is considered, the boundary condition on the back surface comes into play. Assuming a contact that extracts all excess charge carriers, $\Delta p(d) = 0$. In conjunction with (10.64), we find

$$\begin{aligned}\Delta p(x) = \frac{\Delta p_0}{2} \Bigg[&\left(1 + \coth\left(\frac{d}{L_\mathrm{p}}\right)\right) \exp\left(-\frac{x}{L_\mathrm{p}}\right) \\ &+ \left(1 - \coth\left(\frac{d}{L_\mathrm{p}}\right)\right) \exp\left(\frac{x}{L_\mathrm{p}}\right)\Bigg] ,\end{aligned} \tag{10.67}$$

with

$$G_\mathrm{tot} = \int_0^d \frac{\Delta p(x)}{\tau_\mathrm{p}}\,\mathrm{d}x = \Delta p_0 \frac{L_\mathrm{p}}{\tau_\mathrm{p}} \tanh\left(\frac{d}{2\,L_\mathrm{p}}\right) . \tag{10.68}$$

Generally, the excited electrons and holes diffuse into the bulk at different speed due to their different diffusion length (or mobility). As consequence, a spatial separation of electrons and hole densities occurs which leads to an electric field, the Dember field [1045–1047]. The illuminated surface becomes positive compared to the dark case since $D_\mathrm{n} > D_\mathrm{p}$. A treatment of the non-neutral diffusion situation is given in [1048]. As shown in Fig. 10.35, the non-equal electron and hole densities create locally a non-zero charge density $\delta\rho$ and an associated potential $\delta\phi$; for a silicon material parameters ($n_\mathrm{i} = 10^{10}\,\mathrm{cm}^{-3}$), the Dember voltage is calculated as $V_\mathrm{Dem} = \delta\phi(0) = 1.84\,\mathrm{meV}$ for a generation rate of $G = 2 \times 10^{10}/(\mathrm{cm}^2\,\mathrm{s})$. Extensions of the theory have been given considering traps [1049] and the effect of finite sample thickness and surface recombination [1050] (under certain conditions, the sign of the field can be reverse).

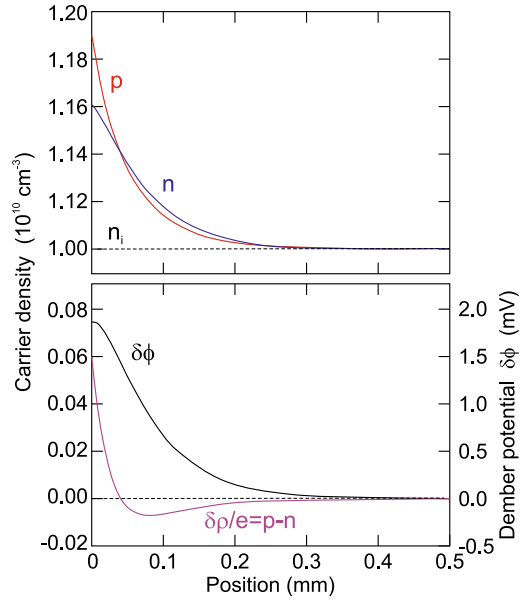

Fig. 10.35 Charge carrier density profiles (in a semi-infinite slab) for electrons and holes as well as their difference $p - n = \delta\rho/e$, as well as the associated Dember potential $\delta\phi$. The ratio of electron and hole mobility in this model calculation (using silicon material parameters) was 5. Adapted from [1048]

10.13.2 Generation in the Bulk

Now, a generation rate following (9.16), realistic for photodiodes and solar cells, is considered,

$$G(x) = G_0 \, \exp\left(-\alpha\, x\right) \ , \tag{10.69}$$

i.e. due to light absorption with the (wavelength-dependent) absorption coefficient α. The total generation rate is

$$G_{\text{tot}} = \int_0^\infty G(x)\, \mathrm{d}x = \frac{G_0}{\alpha} \ . \tag{10.70}$$

The total generation rate is equal to the number of photons per second Φ_0 that enter the semiconductor.

The solution of (10.63) is the sum of the homogeneous solution (10.64) and a particular solution that is given by

$$\Delta p(x) = C \, \exp\left(-\alpha\, x\right) \ . \tag{10.71}$$

The constant C is determined to be

$$C = \frac{G_0\, \tau_\text{p}}{1 - \alpha^2\, L_\text{p}^2} \ . \tag{10.72}$$

Therefore, the solution is

$$\Delta p(x) = C_1 \exp\left(-\frac{x}{L_\text{p}}\right) + C_2 \exp\left(\frac{x}{L_\text{p}}\right) + \frac{G_0\, \tau_\text{p}}{1 - \alpha^2\, L_\text{p}^2} \, \exp\left(-\alpha\, x\right) \ . \tag{10.73}$$

Using again $\Delta p(x \to \infty) = 0$ (leading to $C_2 = 0$) and a recombination velocity S at the front surface, i.e.

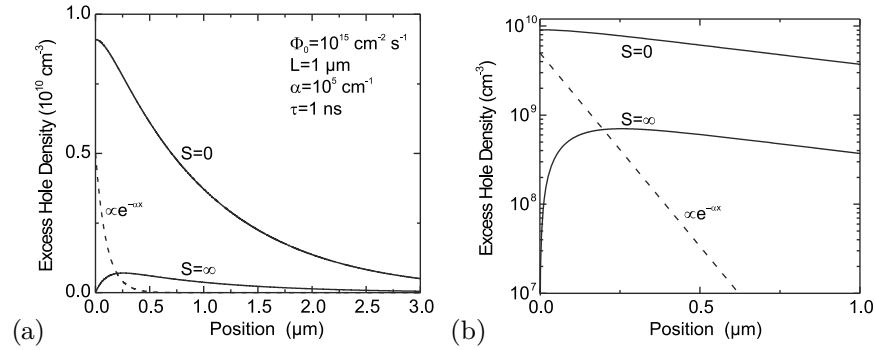

Fig. 10.36 Excess carrier density profile (10.75) in **a** linear and **b** semi-logarithmic plot for $S = 0$ and $S = \infty$. Other parameters are given in panel (**a**)

$$-e\,S\,\Delta p_0 = -e\,D_\mathrm{p}\,\left.\frac{\partial \Delta p}{\partial x}\right|_{x=0} . \tag{10.74}$$

The solution is given as

$$\Delta p(x) = \frac{G_0\,\tau_\mathrm{p}}{1-\alpha^2\,L_\mathrm{p}^2}\left[\exp\left(-\alpha\,x\right) - \frac{S+\alpha\,D_\mathrm{p}}{S+D_\mathrm{p}/L_\mathrm{p}}\,\exp\left(-\frac{x}{L_\mathrm{p}}\right)\right] . \tag{10.75}$$

For vanishing surface recombination, $S = 0$, the solution is (Fig. 10.36)

$$\Delta p(x) = \frac{G_0\,\tau_\mathrm{p}}{1-\alpha^2\,L_\mathrm{p}^2}\left[\exp\left(-\alpha\,x\right) - \alpha\,L_\mathrm{p}\,\exp\left(-\frac{x}{L_\mathrm{p}}\right)\right] . \tag{10.76}$$

For $\alpha L_\mathrm{p} \gg 1$, (10.65) is recovered. This dependence is the excess-carrier profile if the absorption is strong, which is a tendency for short wavelengths. The current at the surface, $j(x=0) \propto \nabla\Delta p$, is zero.

In the case of very strong surface recombination, $S \to \infty$, (10.75) becomes

$$\Delta p(x) = \frac{G_0\,\tau_\mathrm{p}}{1-\alpha^2\,L_\mathrm{p}^2}\left[\exp\left(-\alpha\,x\right) - \exp\left(-\frac{x}{L_\mathrm{p}}\right)\right] , \tag{10.77}$$

with $\Delta p(0) = 0$ (Fig. 10.36). The current at the surface is ($D_\mathrm{p}\,\tau_\mathrm{p} = L_\mathrm{p}^2$)

$$j(x=0) = -e\,D\,\left.\frac{\partial \Delta p}{\partial x}\right|_{x=0} = -e\,\frac{G_0\,L_\mathrm{p}}{1+\alpha\,L_\mathrm{p}} = -e\,\Phi_0\,\frac{\alpha\,L_\mathrm{p}}{1+\alpha\,L_\mathrm{p}} . \tag{10.78}$$

Part II
Selected Topics

Chapter 11
Surfaces

Gott schuf das Volumen, der Teufel die Oberfläche.
God created the bulk; surfaces were made by the devil.

attributed to W. Pauli

Abstract The specifics of semiconductors surfaces, their symmetry, equilibrium crystal shape, reconstructions, steps and faceting are summarized, being important for epitaxy. Physical surface properties such as vibrational and electronic states are discussed.

11.1 Introduction

Obviously every crystal has a surface all around it, connecting it to the surrounding world. This represents a brutal perturbation of the bulk periodicity with the consequence of a whole new world of physics at the surface. With regard to semiconductor technology, the surface properties are of large importance in a number of instances:

- The crystal growth of semiconductors always occurs at a surface. This subject will be discussed in Chap. 12.
- The surface is subject to interaction with the chemistry of the surrounding atmosphere. This is of essential importance for catalysis, e.g., oxidation of CO at noble metals or photocatalytic water splitting, e.g., using TiO_2, into oxygen and hydrogen [1051, 1052]. Photocatalysis is briefly discussed in Sect. 22.1. The interaction and reaction with the surrounding atmosphere can lead modifications of the semiconductor such as change of conductivity, e.g.., in SnO_2, which can be used in the construction of gas detectors [1053–1055].
- Surface passivation and barriers, e.g., using photoresist, silicon oxides or nitrides, are often necessary in practical devices in order to avoid surface recombination (Sect. 10.12.1) or the interaction with atmospheric oxygen or water.

But surface physics is interesting in its own right, investigating the properties of a complex mostly two-dimensional system. 'Pure' surfaces are studied using crystals cleaved in ultra-high vacuum or carefully prepared atomically clean surfaces. A special case are two-dimensional materials, also termed atomic sheets, such as graphene; these will be discussed in Sect. 13.1.

At the surface the atoms rearrange, compared to their bulk positions, vertically and laterally, also forming new bonds (surface reconstructions). The mechanical properties (surface phonons) and elec-

M. Grundmann, *The Physics of Semiconductors*, Graduate Texts in Physics,
https://doi.org/10.1007/978-3-030-51569-0_11

tronic properties (surface states) are different from the bulk modes. Detailed treatments of surface physics and its experimental methods can be found in [695, 1056–1058].

11.2 Surface Crystallography

The surface symmetry, i.e. the two-dimensional spatial periodicity of the constituent atoms, is described with the ten two-dimensional point groups (Table B.1). The point symmetries are 1-, 2-, 3-, 4-, and 6-fold rotational symmetry (Fig. 3.9) with or without mirror plane(s). The two-dimensional point symmetries of popular substrate orientations are compiled in Table 11.1; the different symmetry of the first layer and the half-space are notable. The combination of five 2D Bravais lattices (cmp. Sect. 3.3.1) with the 10 2D point groups leads to the 17 two-dimensional space groups (wallpaper groups) [1059].

For the treatment of surface in reciprocal space, the three-dimensional $\mathbf{k}$-vector is split into the two-dimensional component $\mathbf{k}_{||}$ parallel and the one-dimensional component $\mathbf{k}_{\perp}$ perpendicular to the surface,

$$\mathbf{k} = \mathbf{k}_{||} + \mathbf{k}_{\perp} \ . \tag{11.1}$$

The three most important Brillouin zones in two-dimensional $\mathbf{k}$-space are depicted in Fig. 11.1. Often the special points of the 2D Brillouin zones are denoted with a bar over the letter.

Table 11.1 Two-dimensional point symmetries of common substrates with ideal low-index surfaces

Crystal	Surface	1st layer	1st & 2nd layers	Half space
Rocksalt	(001)	4 mm	4 mm	4 mm
	(110)	2 mm	2 mm	2 mm
	(111)	6 mm	3 m	3 m
Diamond	(001)	4 mm	2 mm	2 mm
	(110)	2 mm	2 mm	2 mm
	(111)	6 mm	3 m	3 m
Zincblende	(001)	4 mm	2 mm	2 mm
	(110)	1 m	1 m	1 m
	(111)	6 mm	3 m	3 m
Wurtzite	(00.1)	6 mm	3 m	3 m
	(10.1)	2 mm	2 mm	1 m
	(11.0)	2 mm	2 mm	1 m

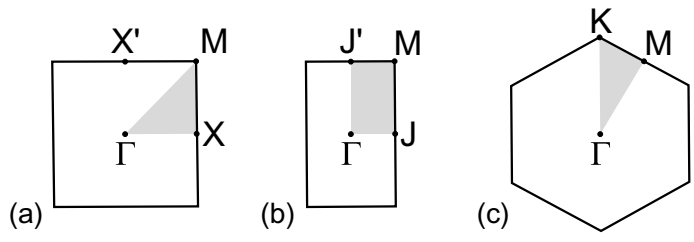

Fig. 11.1 Two-dimensional Brillouin zones for **a** square, **b** rectangular and **c** hexagonal surface symmetry. Special points are labelled and the *grey areas* indicate the smallest irreducible area

11.3 Surface Energy

The surface energy, more precisely the surface energy per area γ, is related to the work that is necessary to split a crystal in two parts. Such process will leave broken ('dangling') bonds. This energy will depend on the crystal orientation as is already clear from the fact that there are easy cleaving planes (Sect. 5.4.2). The surface energy will also depend on the surface reconstruction (see Sect. 11.4), i.e. the rearrangement of surface bonds and atoms. Generally, the reduction of the number of dangling bonds on a surface lowers its energy, while the distortion of bonds increases its energy.

The anisotropy of the surface energy for a given orientation hkl, $\gamma(hkl)$, determines the equilibrium crystal shape (ECS) at a given temperature (below melting temperature). The crystallite is assumed to be of at least mesoscopic size such that energy effects due to edges and apexes can be neglected compared to the surface energy terms. As an example theoretically calculated surface energy values for covalent semiconductors are listed in Table 11.2. The equilibrium shape of silicon has been observed for µm-sized bulbs as shown in Fig. 11.2a for $T = 1323\,K$; the experimental anisotropy of surface energy of silicon is shown in Fig. 11.2b.

11.4 Surface Reconstruction

When in a *Gedankenexperiment* the bulk crystal is split such that a surface with defined orientation develops, many bonds are cut. These dangling bonds can be saturated with other atoms such as hydrogen. In particular under vacuum conditions, the dangling bonds will rearrange and form new

Table 11.2 Surface energy (in J/m^2) for various C, Si and Ge surfaces. Data from [1060]

Material	{111}	{110}	{100}	{311}
C	8.12	7.48	9.72	8.34
Si	1.82	2.04	2.39	2.12
Ge	1.32	1.51	1.71	1.61

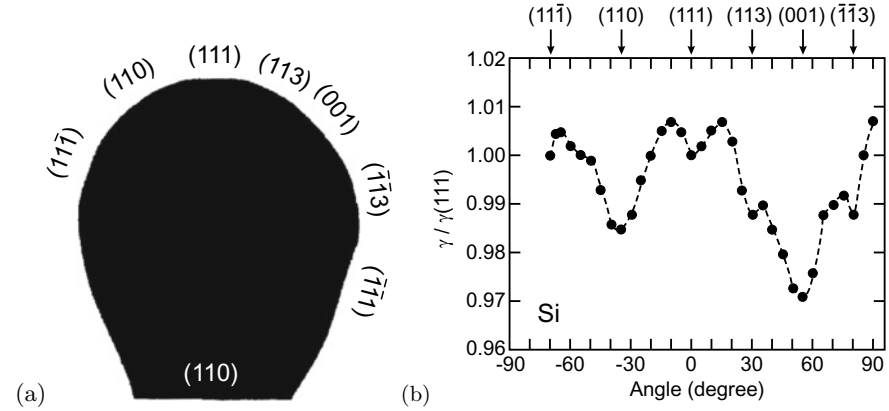

Fig. 11.2 **a** Equilibrium crystal shape (cross section in ⟨110⟩ azimuth) of 1.06 µm diameter Si bulb at $T = 1323$ K with facet orientations as labelled. **a** Anisotropy of surface energy (relative to $\gamma(111)$) for Si, the *dashed line* is guide to the eye. Adapted from [1061]

bonds such as dimers along the surface, lowering the total energy. This surface reconstruction displays two-dimensional periodicity of a surface unit cell.

Since the forces from the split-away half-space are missing, the atomic planes will rearrange vertically[1] and the surface-near layers will exhibit slightly different lattice spacing than in bulk. In [1062] the surface reconstructions of many semiconductors are reviewed. In Fig. 11.3a the rearrangement of surface atoms on GaAs(110) is depicted as an example. The anion is moved up, the cation moved down, preserving the bond length, rotating the bond by about $\gamma = 30°$ for various III–V semiconductors [1063] (Fig. 11.3b). The height difference of the top anion and cation Δ_1 scales with the bulk lattice constant (Fig. 11.3c). The details are specific to materials and orientations.

Different reconstructions occur for different thermodynamical conditions, some of them being metastable, as depicted for GaAs(100) in Fig. 11.4. Several different surface reconstructions can also be present simultaneously at a surface within different domains.

The stable reconstruction of the Si(111) surface is the somewhat complicated 7×7 reconstruction which is schematically depicted in Fig. 11.5a as proposed in [1066] ('DAS' dimer-adatom-stacking fault model'). A STM image of this surface has been reported first in [1067] and is depicted in Fig. 11.5b. Details of this surface are also recently a subject of interest [1068].

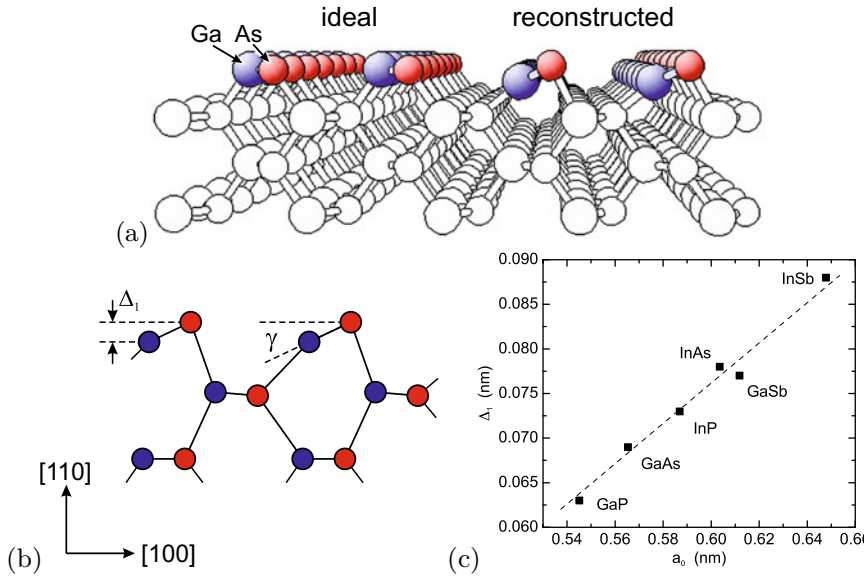

Fig. 11.3 **a** Schematic drawing of the GaAs(110) surface after cutting bonds ('ideal') and actual atomic rearrangement with asymmetric dimer in the reconstructed state. Adapted from [1064]. **b** Schematic of the III–V (110) surface relaxation (*red circles*: anions, *blue circles*: cations) with bond rotation ω and atom shift Δ. **c** Experimental values for he relaxation Δ_1 as shown in panel (**b**) for various semiconductors vs. their bulk lattice constant a_0; *dashed line* is straight line as guide to the eye. Data from [1063]

[1] Typically the distance between the first and second layer is reduced, and the distance between the second and third layer a little bit increased.

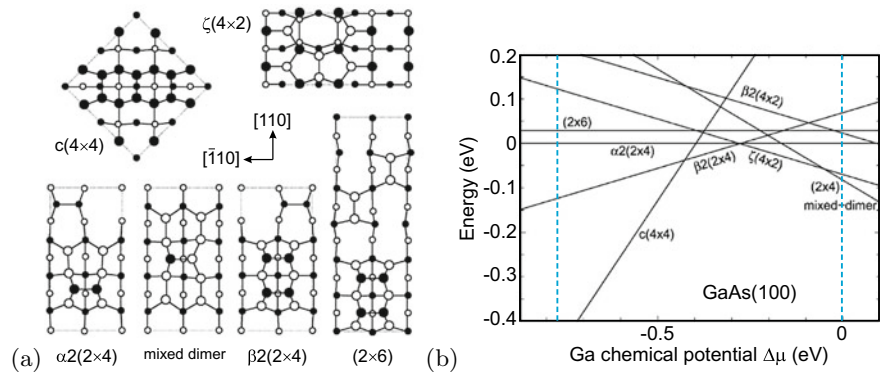

Fig. 11.4 **a** Various reconstructions of the GaAs(100) surface. *Filled* (*empty*) *circles* represent As (Ga) atoms. Atom positions in the top two atomic layers are indicated by *larger symbols*. **b** The relative formation energy per (1×1) unit cell of various reconstructions as a function of the Ga chemical potential. *Vertical dashed lines* mark the approximate anion- and cation-rich limits of the thermodynamically allowed range of $\Delta\mu$. Adapted from [1065]

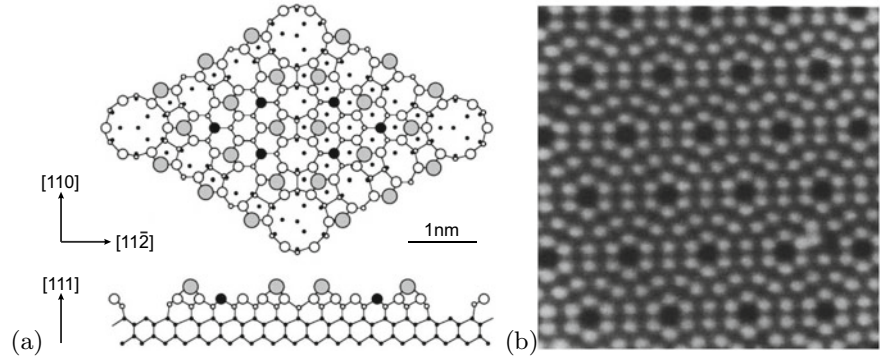

Fig. 11.5 **a** Schematic drawing of the 7×7 reconstruction of Si(111) surface. The *large grey circles* represent adatoms, the *small balck circles* rest atoms. Adapted from [1066] **b** STM image (empty states) of such surface. Adapted from [1067]

11.5 Surface Morphology

The surface reconstruction is related to the local atomic arrangement of the surface atoms. On larger length scales, surfaces can exhibit roughness in general and various specific morphologies, among them steps, step bunches, facets, hillocks or pits. When atomically flat terraces are separated by steps of equal heights, the surface is termed *vicinal*. The step height can be an atomic monolayer or more. The step edges can be straight, smoothly curved or rugged, depending on the formation energy of kinks. If the substrate surface is inclined by a small 'off-cut' angle θ with respect to a low index plane, for a step height h the average terrace width L is given by

$$L = \frac{h}{\tan\theta} \approx \frac{h}{\theta} \,. \tag{11.2}$$

The Si(001) surface (under certain conditions) exhibits monoatomic steps between the A-type 1×2 and B-type 2×1 terraces [1069]; clearly also the step edges between A–B and B–A are quite different, one being much rougher than the other (Fig. 11.6). The surface is thus a two domain surface, the symmetry of both A- and B-type terraces being 2 mm, rotated by 90° against each other.

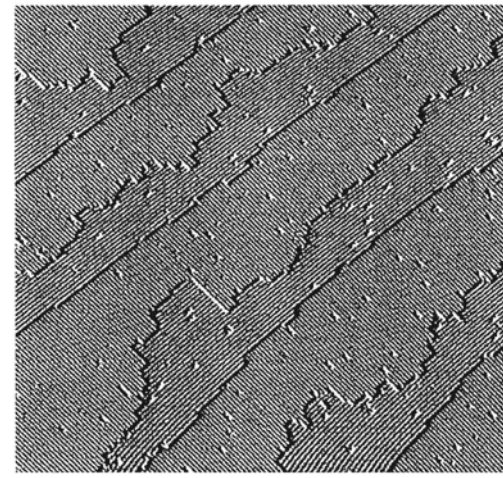

Fig. 11.6 STM image of Si(001) surface with an off-cut $\theta = 0.5°$. Adapted from [1069]

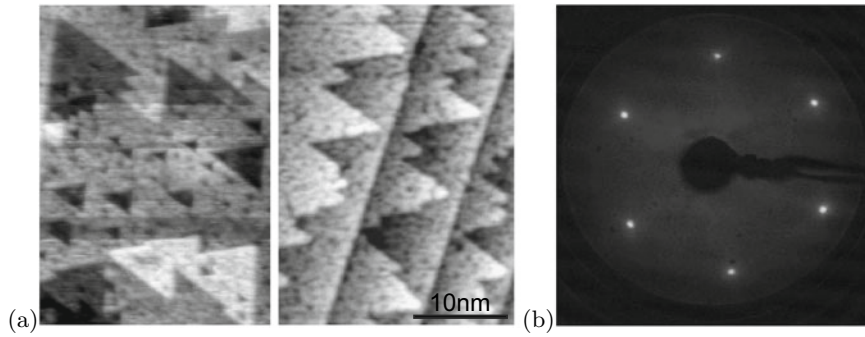

Fig. 11.7 **a** STM images a ZnO(00.1) O-terminated surface, left (right) panel with zero (about 1.3°) off-cut, exhibiting monolayer step heights of 0.27 nm. **a** LEED pattern of such surface (recorded at 70 eV). Adapted from [1070]

A similar example is the Zn(00.1) surface. The found step height of the monoatomic steps is 0.27 nm and corresponds $c/2$ [1070]. The terrace width is about 12 nm (Fig. 11.7a), yielding an off-cut (11.2) of about 1.3°. The surface pattern shows triangular features in two orientations, rotated by 60°. The $3m$ symmetry of the surface, although the first monolayer has 6 m point symmetry (Table 11.1), occurs in two domains rotated against each other by 60°. The LEED pattern from each individual terrace is expected to have three-fold symmetry; the mixed character of the surface yields a six-fold pattern (Fig. 11.7b).

Steps can gather and form step bunches with a height much larger than a monolayer (Fig. 11.8). Faceting of higher index planes occurs when it is energetically favorable to form alternating facets of low energy low index planes, for example Si(223) exhibits periodic ridges with (111) and (113) facets [1071]. The faceting of a surface close to (113), exhibiting smooth (113) and rough (114) planes, is depicted in Fig. 11.9.

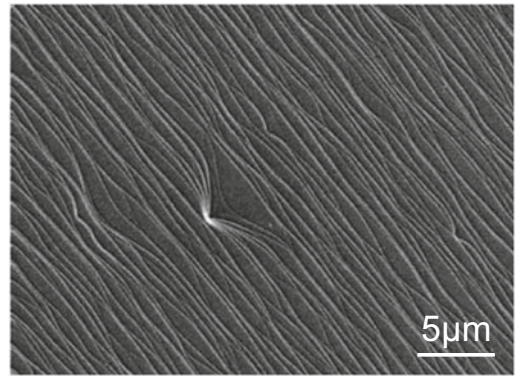

Fig. 11.8 SEM image of the surface of a 4H–SiC layer on [00.1]-oriented substrate with 8° misorientation towards [11.0]. Adapted from [1072]

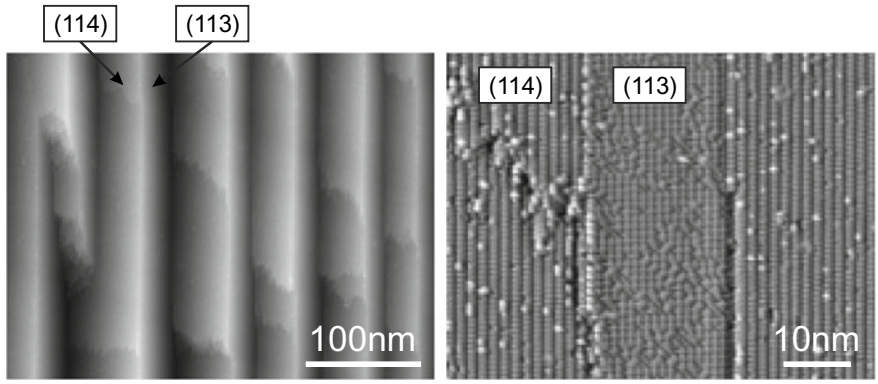

Fig. 11.9 STM images of a silicon surface close to (113), 21.5° from (001) towards (111), i.e. (113)-3.7°. Adapted from [1073]

11.6 Surface Physical Properties

11.6.1 Surface Phonons

As a model for surface vibrational states, the diatomic one-dimensional chain model discussed in Sect. 5.2.2 can be modified to allow for a different surface spring constant C_s instead of C_1 or C_2. Such model can be solved numerically for finite chain length. The bulk dispersion is found with an extra mode in the gap or above the maximum frequency for a range of values of C_s as depicted in Fig. 11.10. When the spring constant of the surface atom is smaller than the larger of the two spring constants C_1 and C_2 (in our model calculation $C_2 > C_1$), a state in the gap forms; for a surface spring constant larger than C_2, first the surface vibration lies within the optical bulk band and then forms a state above the maximum optical frequency ω_m, given by (5.18).[2]

In order to display the dispersion of surface states together with the bulk band structure, the latter is projected to the surface $\mathbf{k}_{||}$-vector: $E_n(\mathbf{k})$ is considered as $E_{n,\mathbf{k}_\perp}(\mathbf{k}_{||}) = E_\nu(\mathbf{k}_{||})$, where $\nu = n$, $\mathbf{k}_\perp$ is a new, continuous index. In the plot of E_n^{surf} vs. $\mathbf{k}_{||}$, for each value of $\mathbf{k}_{||}$ a *range* of energies reflects the

[2]The appearance of states within the gap and above ω_m resembles that of localized vibrational modes of substitutional masses (Sect. 5.2.7).

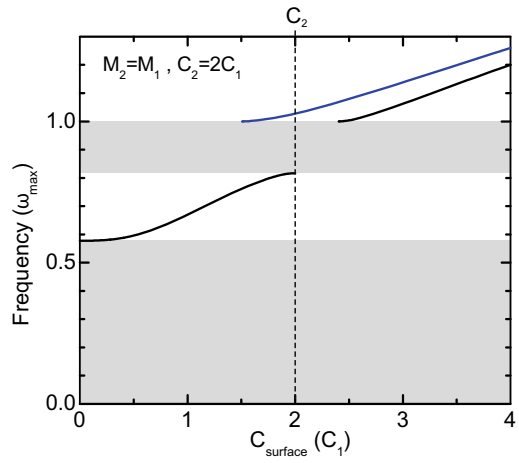

Fig. 11.10 One-dimensional model calculation of surface vibrational state frequency (in units of the maximum bulk optical phonon frequency ω_m) as a function of the spring constant $C_{surface}$ of the surface atom replacing C_1 (*blue curve*) or C_2 (*black curves*). As model parameters we use equal masses and $C_2 = 2\,C_1$ ($\gamma = 0.943$ from (5.17)). The *grey areas* represent the energy range of the acoustic and optical phonon bulk bands

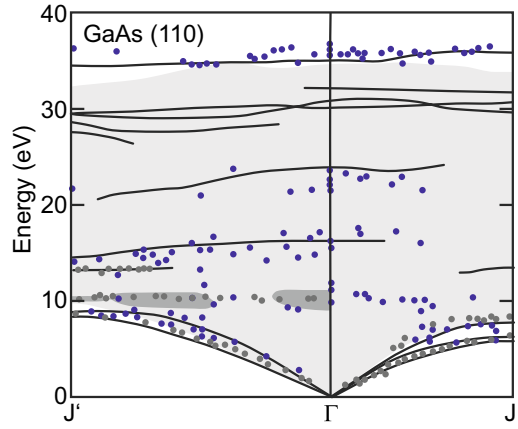

Fig. 11.11 Surface phonon dispersion for GaAs(110) (*solid lines*) with the surface projected bulk band structure (*light grey area*). The *symboles* are experimental data from two different methods. The *dark grey areas* at about 10 meV indicate regions where the A_1-peak is present in the calculated scattering cross-section. Adapted from [1063]

bulk band structure (Fig. 11.11). This concept pertains to phonon dispersion as well as to electronic states.

11.6.2 Surface Plasmons

Free-carrier oscillations in the bulk had been discussed in Sect. 9.9.1. A surface plasmon is the quantum of a surface-bound plasma oscillation. Such effect has been discussed in [1074] and reviewed in [1075, 1076]. A metal (or conductive semiconductor) with dielectric constant according to (9.77) $\epsilon_1 = \epsilon_m = \epsilon_r\,(\omega_p/\omega)^2$ and a dielectric (or vacuum) with $\epsilon_2 = \epsilon_d$ are assumed (Fig. 11.12).

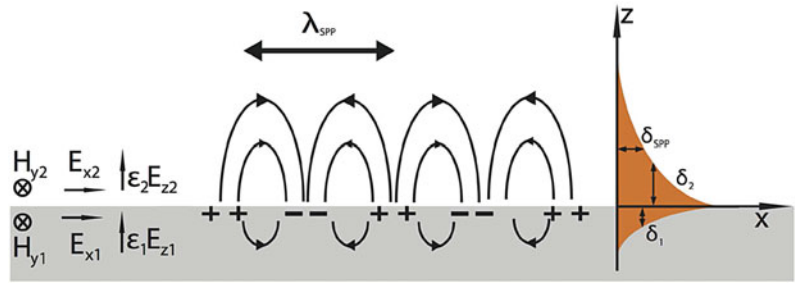

Fig. 11.12 Sketc.h of surface plasmon field distribution. Adapted from [1077]

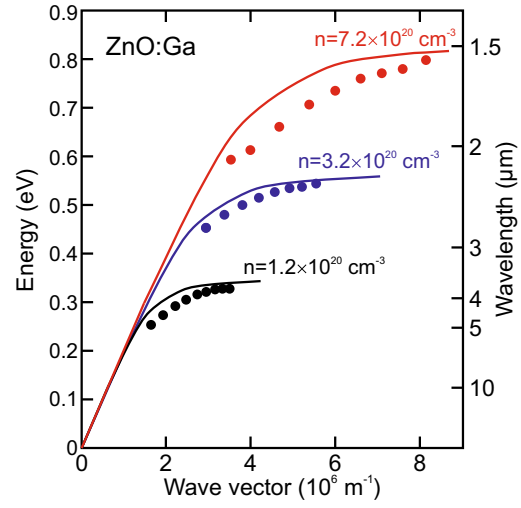

Fig. 11.13 Surface plasmon polariton dispersion for ZnO:Ga/air for three different carrier concentrations as labelled, experimental data (*symbols*) and theory (*lines*). Adapted from [1078]

The surface plasmon (polariton) (SPP) is a wave localized at the surface with evanescent parts into the metal and the dielectric. The dispersion of the surface plasmon (polariton) is given by

$$k_{\mathrm{SPP}} = \frac{\omega}{c}\sqrt{\frac{\epsilon_1\,\epsilon_2}{\epsilon_1+\epsilon_2}}\,. \tag{11.3}$$

For large k, the limiting frequency is the SPP frequency (from $\epsilon_1 = \epsilon_2$)

$$\omega_{\mathrm{SPP}} = \frac{\omega_{\mathrm{p}}}{\sqrt{1+\epsilon_{\mathrm{d}}/\epsilon_{\mathrm{r}}}} < \omega_{\mathrm{p}}\,, \tag{11.4}$$

which is smaller than the plasma frequency. For a metal against vacuum, $\omega_{\mathrm{SPP}} = \omega_{\mathrm{p}}/\sqrt{2}$. The SPP dispersion for a ZnO:Ga/air interface is depicted in Fig. 11.13 for three different doping concentrations.

11.6.3 Electronic Surface States

The bulk band structure is given by the energy eigenvalues $E_n(\mathbf{k})$. The surface adds its own states $E_n^{\mathrm{surf}}(\mathbf{k}_{||})$, many of them in the gap. The calculation of gap states has been already briefly discussed in Sect. 6.2.3. The nature of bulk states is oscillatory in the bulk and exponentially decaying in the outside (Fig. 11.14a), the nature of surface states is localized at the surface and decaying both towards

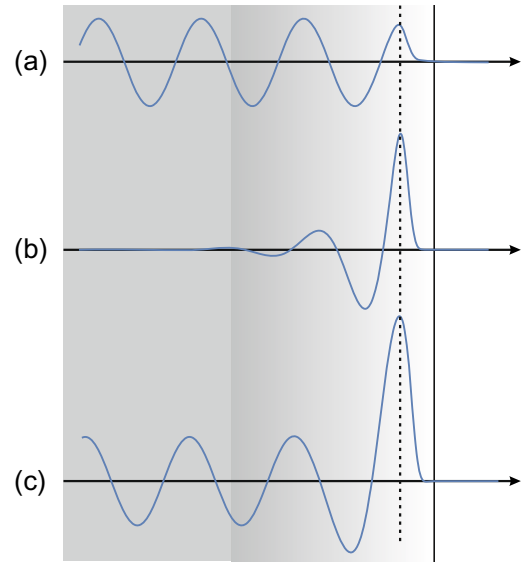

Fig. 11.14 Schematic wavefunction versus coordinate for **a** bulk state in the vicinity of the surface (its position indicated by the *vertical dashed line*), **b** surface state and **c** surface resonance state

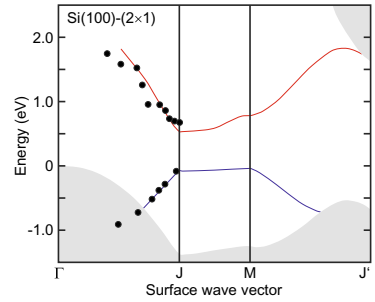

Fig. 11.15 Surface band structure of Si(100)-(2 × 1), *lines* denote a theoretical quasi-particle calculation, *symbols* represent experimental data. The *grey areas* indicate the projected bulk band structure. Adapted from [1079]

the bulk and the outside (Fig. 11.14b). A third type of states is a *surface resonance* which is oscillatory in the bulk and has enhanced probability at the surface, of course also decaying towards the outside (Fig. 11.14c); such states are surface related but energetically degenerate with states of the bulk band structure.

Surface states for Si(100) in 2 × 1 reconstruction are shown in Fig. 11.15. The surface bands arise from (filled and unfilled) π- and π^*-orbitals from the dangling bonds on the threefold-coordinated surface atoms [1079]. A calculation for the ideal (unreconstructed) (100), (110) and (111) surfaces of Si, Ge and GaAs can be found in [1080]. Further work on silicon surface states (clean and with adsorbates) is compiled in [1081].

For a conventional insulating material (with gap) the states of conduction and valence band have defined s- and p-type symmetry (cmp. Fig. 2.5) and the surface states can be populated with spin up and down electrons as is schematically drawn in Fig. 11.16a. Such 'normal' surface states are thus not spin-polarized. This has been shown, e.g., for the well-known surface states of Si(111)-(7 × 7) [1082] in [1083].

In a so-called *topological insulator* [464], a band inversion is present (cf. Sect. 6.2.6). In HgTe-like materials, s- and p-type bands are inverted at the Γ point (cmp. Sect. 6.11). In layered (orthorhombic) Bi_2Se_3-like tri-chalcogenide materials two p_z-orbitals with opposite parity are inverted at the Γ point. Reasons for the band inversion are spin-orbit interaction but also scalar relativistic effects and lattice distortions [1084]. The spin-orbit interaction is responsible for opening a gap; the associated surface

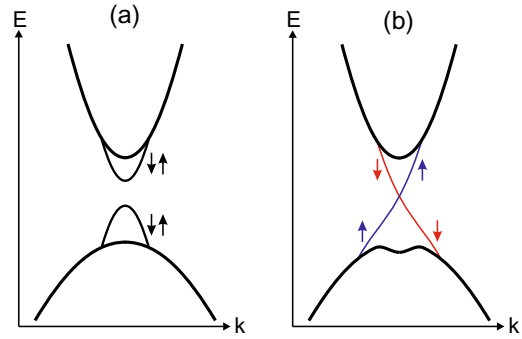

Fig. 11.16 **a** 'Normal' band structure with surface states, the valence band states are antisymmetric ('–') from p-states, the conduction band states are symmetric ('+') from s-states. The *arrows* denote the electron spin orientation of the states. **b** 'Topological' band structure with surface states crossing the gap and electrons in the two surface states having unique spin orientations

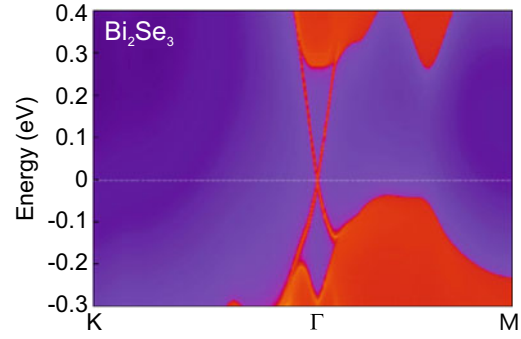

Fig. 11.17 Density of states for Bi_2Se_3 (111) surface. Adapted from [1086]

states cross the band gap (Fig. 11.16b) and are spin-polarized (Fig. 11.16c) [1085, 1086]. A review of various systems is given in [463]. Charge transport in such spin-polarized surface states suffers no scattering (thus these states are called 'topologically protected') unless by a center that breaks time reversal symmetry (magnetic impurity). The more or less linear dispersion of these states forms a 'Dirac cone' (cmp. Sect. 13.1.2 for the band structure of graphene with six Dirac cones) (Fig. 11.17).

Topological surface states have been observed in various systems [463]. As an example we show data on bulk Bi_2Se_3 [1087] for which the surface states are found to cross the band gap (Fig. 11.18a) and spin-polarized measurements (Fig. 11.18b) show a strong spin polarization (about 50%) of the two branches. Another situation where topological edge states appear is the interface between two semiconductors with bands of different topology, such as HgTe and CdTe (cf. Sect. 6.11).

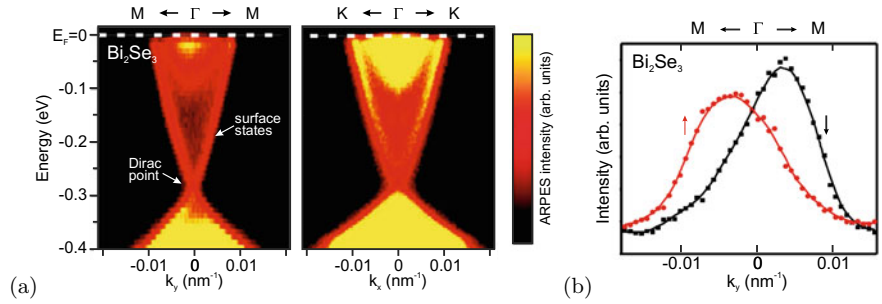

Fig. 11.18 **a** Angle-resolved photoemission spectra from Bi_2Se_3 (111) surface along two different **k**-space directions. The Fermi level is at energy zero. The *blue dashed line* indicates the angular scan displayed in panel (**b**). **b** Spin-polarized momentum distribution curve at a binding energy of -140 meV, measured along the k_y-direction. Adapted from [1088]

Chapter 12
Heterostructures

The interface is the device.

H. Kroemer [133]

Abstract Heterostructures are the most important basis for modern devices and are covered regarding various aspects including heteroepitaxy on planar and patterned substrates, surfactants, heterostructure band lineup as well as energy levels and recombination in planar confined systems (quantum wells and two-dimensional electron gases).

12.1 Introduction

Heterostructures consist of (at least two) different materials. The geometry of the interfaces between the two materials can be complicated. The simplest case is a planar interface, i.e., a layered system. A metal–semiconductor junction is generally a heterostructure. However, we will use the term mostly for structures of various semiconductors. Most of the heterostructures discussed here are epitaxial, i.e., fabricated by the successive epitaxy of the various layers on a substrate. Another method to fabricate heterostructures of different (and dissimilar) materials is wafer bonding that is briefly discussed in Sect. 12.6.

Many modern semiconductor devices rely on heterostructures, such as the heterobipolar transistor (HBT), the high electron mobility transistor (HEMT), lasers and nowadays also light-emitting diodes. Shockley had already considered heterostructures in his 1951 patent for pn-junctions. For the development and the realization of heterostructures H. Kroemer and Zh.I. Alferov were awarded the 2000 Physics Nobel Prize. The properties of charge carriers in layers that are part of heterostructures can be quite different from those in bulk material, e.g., extremely high mobility, high radiative recombination efficiency or novel states of matter, as revealed in the quantum Hall effects.

M. Grundmann, *The Physics of Semiconductors*, Graduate Texts in Physics,
https://doi.org/10.1007/978-3-030-51569-0_12

12.2 Heteroepitaxy

12.2.1 Growth Methods

Since the thickness of layers in the active part of heterostructures has to be controlled to monolayer precision and the thickness of layers can go down to the single monolayer range, special growth methods have been developed [1089–1091]. Among these molecular beam epitaxy (MBE [1092]), chemical vapor deposition (CVD [1093, 1094]) and metalorganic vapor phase epitaxy (MOVPE [1095]) are the most common for Si, Ge, III–V and II–VI semiconductors. Thin films for many materials can also be fabricated by atomic layer deposition (ALD [1096, 1097]). In particular oxide semiconductors (and superconductors) are also fabricated with pulsed laser deposition (PLD [1098]). Liquid phase epitaxy (LPE [1099]) used to be very important for the fabrication of LEDs but has lost its role largely to MOVPE.

MBE is performed in an ultrahigh vacuum (UHV) chamber, pumped by getter pumps and cryo-shrouds. The source materials are evaporated from effusion cells and directed towards the heated substrate. If the source materials are supplied as a gas stream, the method is called gas-source MBE (GSMBE). If metalorganic compounds are used as precursors, the method is denoted as MOMBE. The atoms impinge on the substrate with thermal energy and are first physisorbed. After diffusion on the surface they either desorb or they are chemisorbed, i.e., incorporated into the crystal. In order to obtain high spatial homogeneity of material properties such as composition, thickness and doping, the substrate is rotated during deposition.

During CVD and MOVPE the heated substrate is in a gaseous environment. The transport gas is typically H_2, N_2 or O_2. Precursor materials are hydrides such as silane, germane, arsine or phosphine (SiH_4, GeH_4, AsH_3, PH_3) and (for MOVPE) metalorganic compounds, such as, e.g., trimethylgallium (TMG). Due to the toxicity of the hydrides, alternative, i.e., less-toxic and less-volatile compounds are used, such as TBAs ($(CH_3)_3CAsH_2$). The crystal growth occurs after pyrolysis and catalysis of the compounds close to or on the substrate surface. All remaining C and H atoms (and whatever else that is not incorporated into the crystal) leave the reactor and are neutralized and stopped in a scrubber. In ALD alternating injections of molecular precursors and purge cycles build up the thin film atomic layer by atomic layer; this method is particularly advantageous for achieving conformal coatings.

In-situ monitoring is of importance to obtain information about the growth process while it is underway. Using the information in a feedback loop it is possible to achieve in-situ control of the process, e.g., for precise determination of growth rates or layer thickness. Techniques are RHEED (reflection high-energy electron diffraction) [1100] (only for UHV systems) and RAS (reflection anisotropy spectroscopy) [1101, 1102].

12.2.2 Substrates

Thin-film epitaxy is mostly performed on wafers, i.e., thin circular slices of substrate material. The most common substrate materials are Si (currently up to 400 mm diameter [1103, 1104]), Ge (also up to 300 mm [1105]), GaAs (up to 6 inch), InP (up to 4 inch) and sapphire (up to 6 inch). Typical wafer thickness is 300–500 µm. Also, very thin, flexible Si wafers (8–10 µm) have been developed [1106]. A wafer is cut from a large single cylindrical crystal that is fabricated with suitable growth techniques such as Czochralski (CZ) growth [1107, 1108] modified by Teal and Little [1109–1111]. In CZ growth the crystal, starting with a small seed crystal, is pulled out of a melt of previously polycrystalline, pure or doped material. All dislocations stop in the narrow neck between the seed and the main body of the cylinder. The diameter of the crystal is controlled by the pulling rate (matching the crystallization

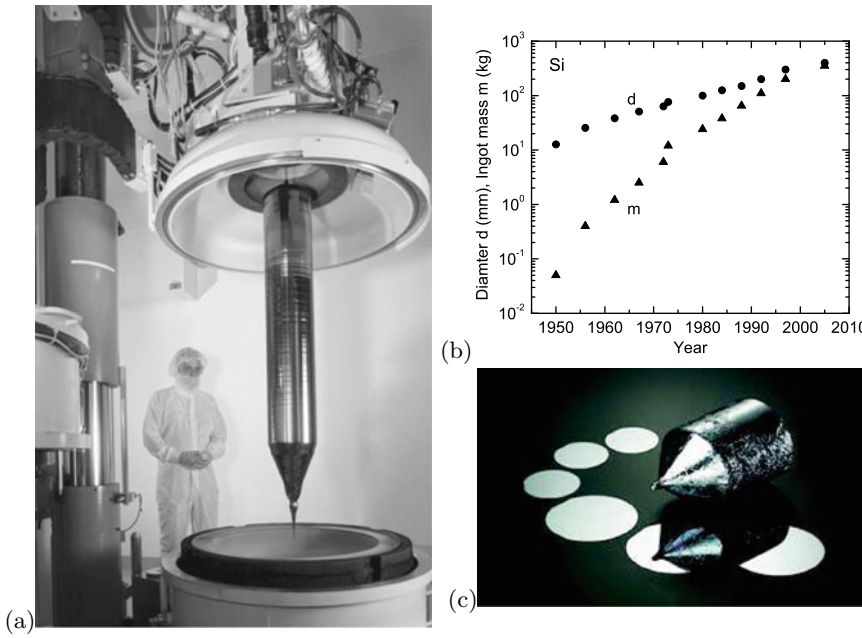

Fig. 12.1 **a** Silicon single crystal for 300-mm diameter wafers after opening of the crucible. From [1114] with permission. **b** Historic development (first year of larger production) of silicon wafer diameter and ingot mass. Data from [1104]. **c** GaAs single crystal (boule) for 4-inch wafers and some cut and polished wafers

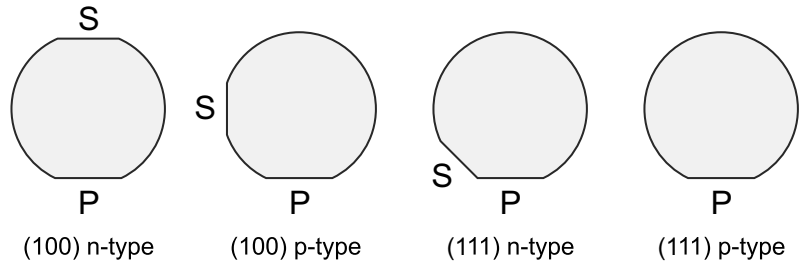

Fig. 12.2 Schematic semiconductor wafer geometry for various orientations and doping with the primary (P) and secondary (S) flats indicated

speed of the material) and the heating power. For the growth of III–V compound semiconductors, liquid encapsulated CZ (LEC) growth has been developed to counteract the high volatility of the group-V component. During LEC growth the melt is completely covered with molten boric oxide (B_2O_3). The keys to optimization of the crystal growth process are numerical modeling and computer control. In Fig. 12.1a,c a large CZ silicon crystal and a smaller LEC GaAs crystal (boule) are shown. Over time wafer size and ingot mass have increased remarkably (Fig. 12.1b). For details on other important fabrication methods for bulk crystals, including float-zone (FZ [291, 1112]) or vertical gradient freeze (VGF), we refer to the literature [1113]. Significant expertise is necessary for cutting, grinding and polishing (lapping) wafers for epitaxy.

For semiconductors, the wafer is marked with *flats* to indicate orientation and doping. In Fig. 12.2 the standard flats are shown for (100)- and (111)-oriented material. The primary (major) flat (OF, orientation flat) defines the crystallographic orientation[1] is longer than the secondary (minor) flat which defines the conductivity type (IF, identification flat). For a 4-inch (100 mm) diameter wafer the OF is 32 and the IF 12 mm long. The front surface, on which the epitaxy is performed, typically undergoes

[1] In the 'US' flat definition, the primary flat is the $(01\bar{1})$ surface, in the 'EJ' definition, the primary flat is $(0\bar{1}\bar{1})$.

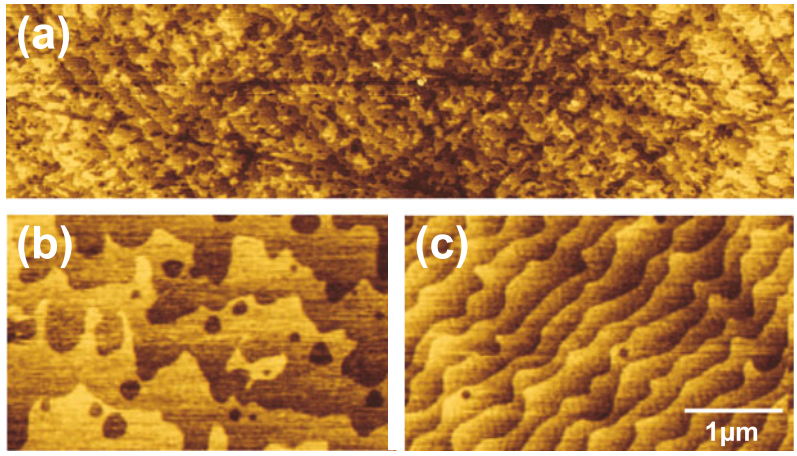

Fig. 12.3 **a** AFM images of an as-received ZnO wafer, exhibiting small terraces and nm deep scratches from polishing. (**b**, **c**) Two ZnO $(000\bar{1})$ wafers with vicinal surfaces after thermal treatment (1000 °C for 2 h in O_2), exhibiting atomically flat terraces with $c/2$ monoatomic step heights. Two different substrates with different off-cut (misorientation direction and angle) are shown. Adapted from [1122]

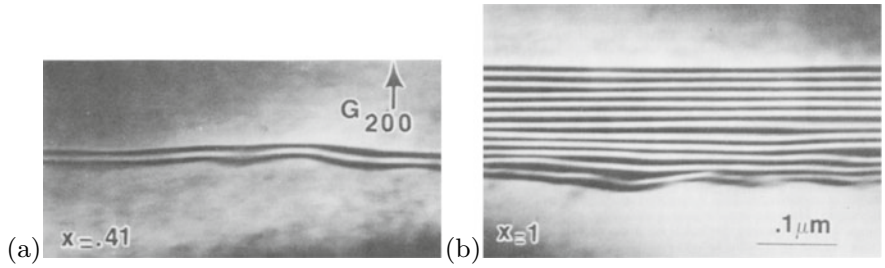

Fig. 12.4 Cross-sectional TEM of MBE-grown $Al_xGa_{1-x}As$/GaAs heterostructures for (**a**) $x = 0.41$ and (**b**) $x = 1.0$. Using an AlAs/GaAs superlattice an excellent flattening of substrate roughness is achieved. From [1123]

an elaborate cleaning and polishing process. Silicon processes [1115, 1116] are based on the RCA cleaning procedure [1117] and the related Shiraki etch [1118] and can achieve clean, atomically flat surfaces [1119]. III-V semiconductors are typically prepared using a polishing etch [1120, 1121], often solutions containing bromine. It is possible to create compound semiconductor surfaces that exhibit large, essentially monoatomically flat terraces between individual surface steps. Polishing or other surface damage can also be removed prior to epitaxy with thermal (Fig. 12.3) or ion beam treatments.

One prerequisite for making high-quality heterostructures with thin layers is a flat surface. Even if the polished substrate is not perfect, flat interfaces can be achieved with the growth of appropriate superlattice buffer layers (Fig. 12.4). Roughness can exist on all length scales and is typically investigated using atomic force microscopy scans.

High throughput demands and the advent of multi-wafer reactors make prior cleaning and etching procedures tedious. For this purpose, substrates for well-developed material systems are offered 'epiready'. Epiready wafers are often covered with a very thin protective film that can be released using a thermal treatment at or below typical growth temperature in the growth reactor immediately prior to epitaxy. The protective film separates the polished semiconductor wafer from the ambient. Examples are a few monolayers of arsenic on GaAs or two monolayers GaN on SiC. However, the suitability of a purchased substrate may depend on the duration and conditions of its storage.

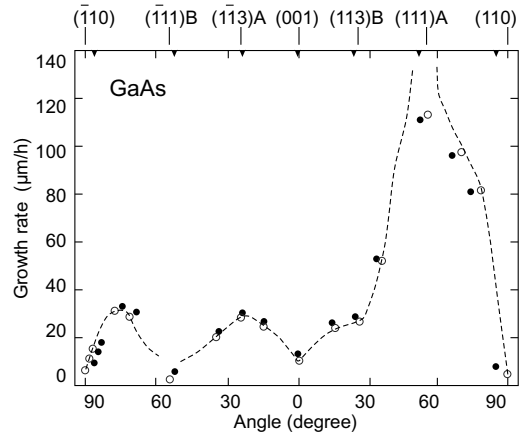

Fig. 12.5 Growth rate of GaAs in vapor phase transport at 725° as a function of crystal orientation. The *dashed line* is guide to the eye. Adapted from [1128]

A special case is the use of *curved* substrates which allow the study of growth on different crystal orientations in a continuous fashion. Such experiments have been performed using cylindrical substrates [1124] and hemispherical crystals. For the latter homoepitaxy has been reported for Si [1125, 1126], SiC [1127] or GaAs [1128]. Also heteroepitaxy has been investigated, for example for GaP and GaAs on Ge [1129] (cmp. Fig. 12.12). Using such curved substrates, the growth rate can be determined as a function of crystal orientation as shown for GaAs (on GaAs) in Fig. 12.5; large differences are found for (111)A and (111)B surfaces. For growth of silicon the variations with angle are much smaller in the range of 10% [1124].

12.2.3 Growth Modes

The growth of a material A on a material B can occur via three fundamental growth modes (Fig. 12.6), the layer-by-layer or Frank-van der Merwe (FvdM) growth mode [435], the island or Volmer-Weber (VW) growth mode [1130] and the Stranski-Krastanow (SK) growth mode [1131, 1132]. In [1132] the possibility of island formation on an initially flat heteroepitaxial surface was proposed for the growth of lattice-*matched* ionic crystals that have different charges. The term SK growth is now typically used in lattice-*mismatched* heteroepitaxy for the island formation (and related relaxation of strain energy, cmp. Fig. 14.37) on an initially two-dimensional layer (wetting layer).[2] Also growth of islands *relaxed* by misfit dislocations in strained heteroepitaxy has been termed SK growth [1133].

The growth mode is determined by the relation of the free energies (per area) of the surface σ_s, interface σ_i and film σ_f. Wetting of the substrate and growth of a coherent film (FvdM-growth) occurs for

$$\sigma_s > \sigma_i + \sigma_f \ . \tag{12.1}$$

If the inequality has the opposite sign, Volmer-Weber or Stranski-Krastanow growth occurs. Additionally the strain energy of the film must be considered. The SK growth generally occurs when there is wetting of the substrate but layer strain is unfavorable and leads to islanding.

Layer-by-layer growth typically involves nucleation of two-dimensional islands and 'filling' of the remaining monolayer before the next one is started. Another growth mode resulting in smooth

[2] This is the growth mode of self-assembled epitaxial quantum dots as discussed in Sect. 14.4.3.

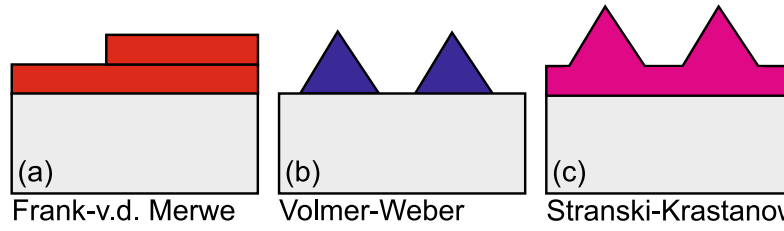

Fig. 12.6 Schematic of the three different fundamental epitaxial growth modes

epitaxial layers is step-flow growth where adatoms are incorporated mainly at step edges. A more detailed discusion can be found in [1134]. Further details on crystal growth can be found in [1135].

The nucleation and the initial film growth are important and determine the film quality. Several techniques have been developed to overcome common problems. A typical strategy is the growth of a low-temperature nucleation layer.

12.2.4 Heterosubstrates

If homosubstrates are not available or very expensive, semiconductors are grown on dissimilar substrates, e.g., (Al,Ga)N and ZnO on sapphire (Al_2O_3) or SiC.[3] In Fig. 12.7 the interface region of hexagonal AlN on 6H-SiC (cmp. Fig. 3.31b) is shown. The change of crystallographic phase is obvious; the perfect atomic arrangement justifies the term 'epitaxy', literally meaning 'order on top'.

In many cases, the integration of III–V- or II–VI-based semiconductors for optoelectronic applications on silicon for electronic devices is desirable, such as GaAs/Si, InP/Si, GaN/Si or the growth on economic substrates is attractive such as GaN/Al_2O_3 and ZnO/Al_2O_3. For all such combinations the epitaxial relationship, i.e., the alignment of the crystallographic directions of both materials, which can have different space groups, has to be considered. Some examples for epitaxial relationships are given in Table 12.1. The epitaxial relation is determined by the energetically favorite formation of the interface and the early stages of growth.

In Fig. 12.8, X-ray diffraction data are shown from a ZnO layer on *c*-oriented sapphire. The hexagonal ZnO lattice is rotated by 30° with respect to the trigonal sapphire lattice. In the case of growth of ZnO on Si(111) an amorphous SiO_2 layer can form at the interface such that the crystallographic information of the substrate is lost. The ZnO grains exhibit random in-plane orientation (Fig. 12.9).

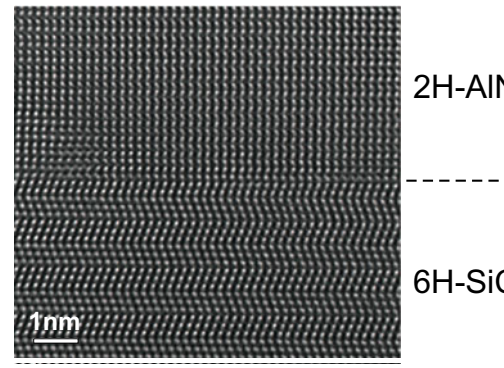

Fig. 12.7 HRTEM cross section of the interface region of MOVPE grown hexagonal AlN on 6H-SiC substrate. Adapted from [1137]

[3] For ZnO, homosubstrates have recently been produced with 3-inch diameter [1136].

Table 12.1 Epitaxial relationship for various film/substrate combinations, ZnO (or GaN) on *c*-, *a*- and *r*-sapphire and Si(111)

ZnO	Al_2O_3 [00.1]	ZnO	Al_2O_3 [11.0]	ZnO	Al_2O_3 [$\bar{1}$0.2]	ZnO/GaN	Si [111]
[00.1]	[00.1]	[00.1]	[11.0]	[11.0]	[$\bar{1}$0.2]	[00.1]	[111]
[11.0]	[01.0]	[11.0]	[00.1]	[00.1]	[0$\bar{1}$.1]	—/[2$\bar{1}$.0]	[$\bar{1}$10]

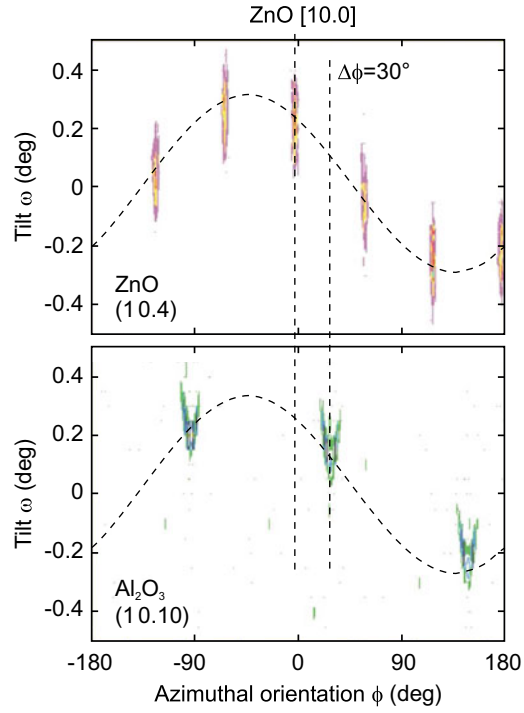

Fig. 12.8 X-ray diffraction intensity from the asymmetric ZnO (10.4) (*upper panel*) and the sapphire (10.10) (*lower panel*) reflections as a function of the azimuthal sample orientation (rotation angle ϕ around the [00.1] axis). The peaks appear at different tilt angles ω due to an overall tilt of the mounted sample (*dashed sinusoidal lines*). The ZnO [00.1] axis is not tilted with respect to the sapphire [00.1] direction

If substrate and epilayer have different space groups, the formation of domains can occur [1139]. The two-dimensional symmetries of various substrates are listed in Table 11.1. The group theoretical minimum number of domains N_{RD} in dependence of the two-dimensional symmetries of substrate and epilayer with rotational symmetries C_n and C_m, respectively, is given by [1140]

$$N_{RD} = \frac{\mathrm{lcm}(n, m)}{m} , \tag{12.2}$$

where lcm denotes the least common multiple. The values are listed in Table 12.2 and visualized in Fig. 12.10.

If the main symmetry axes of substrate and epilayer are not aligned, mirror domains appear. An example is the growth of GaN(00.1) on Ge(111), for which it has been reported that the major symmetry directions do not align exactly. There is a 4° in-plane rotation of the lattices with respect to the usual [11.0] ∥ [1$\bar{1}$0] in-plane relationship [1141] (cmp. the exact alignment for GaN/Si(111) in Table 12.1). Due to 3 m mirror symmetry of the substrate, the misaligment is equivalent for clockwise and counter-clockwise rotation. Therefore two domains with an angle of 8° occur (Fig. 12.11).

Another well-known domain effect in heteroepitaxy is the occurence of antiphase domains of zincblende semiconductors (e.g., GaAs, GaP, InP, ...) grown on Si(001) with monoatomic steps;

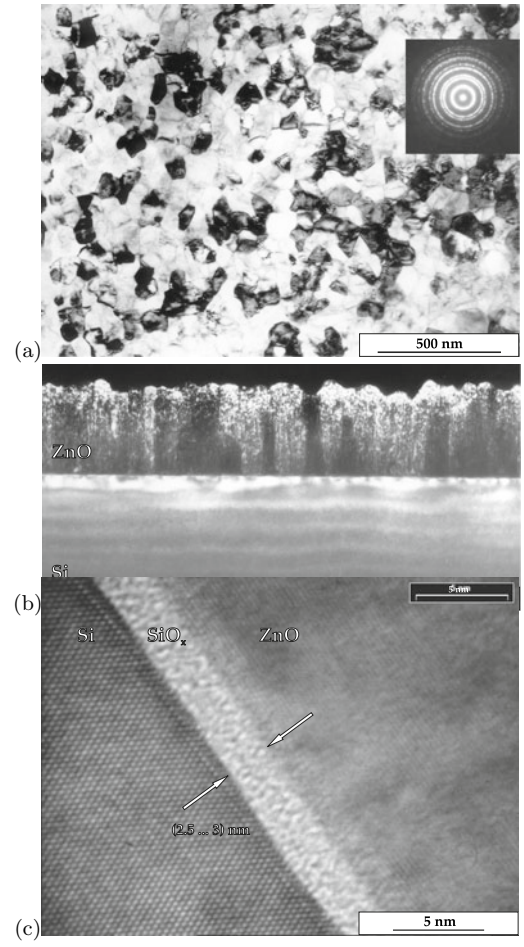

Fig. 12.9 **a** Plan-view TEM image (*inset*: electron diffraction diagram averaged over several grains) of ZnO on Si(111). **b** Cross-sectional TEM of the same sample. **c** High-resolution cross-sectional image of the ZnO/SiO_2/Si interface region. Adapted from [1138]

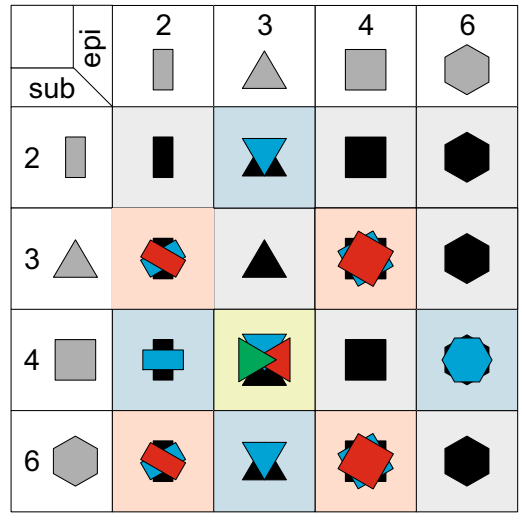

Fig. 12.10 Visualization of the minimum number of rotational domains for different substrate and epilayer symmetries according to Table 12.2

Table 12.2 Number of rotational (or mirror) domains N_{RD} for all 2D point groups of substrate (G_S) (rows) and epilayer (G_E) (columns). When two numbers are given ($x|y$), the first (second) number represents the number of domains if mirror symmetry planes of substrate and epilayer align (misalign)

$G_S \backslash G_E$	1	m	2	$2mm$	3	$3m$	4	4 mm	6	6 mm
1	1	1	1	1	1	1	1	1	1	1
m	2	1|2	2	1|2	2	1|2	2	1|2	2	1|2
2	2	2	1	1	2	2	1	1	1	1
2 mm	4	2|4	2	1|2	4	2|4	2	1|2	2	1|2
3	3	3	3	3	1	1	3	3	1	1
3 m	6	3|6	6	3|6	2	1|2	6	3|6	2	1|2
4	4	4	2	2	4	4	1	1	2	2
4 mm	8	4|8	4	2|4	8	4|8	2	1|2	4	2|4
6	6	6	3	3	2	2	3	3	1	1
6 mm	12	6|12	6	3|6	4	2|4	6	3|6	2	1|2

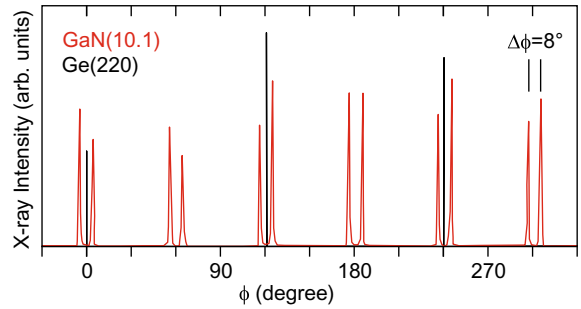

Fig. 12.11 X-ray diffraction ϕ-scans of GaN(00.1)/Ge(111). Adapted from [1141]

such surface actually exhibits two kind of terraces (1×2 and 2×1 reconstructions) and is thus itself not homogeneous. The formation of antiphase domains can be avoided by using an off-cut of the surface against the (001)-planes promoting double-atomic steps [1142]. In Fig. 12.12a the growth of GaP on a Ge hemisphere with [111]-pole is depicted; spherical triangles meeting at the ⟨100⟩ poles can be seen. In a similar experiment GaAs was grown in a spherical depression in Ge(001) (Fig. 12.12b), allowing a more detailed look at the [001]-pole. Close to the it, within an approximately square area, antiphase domains (cmp. Sect. 4.4.4) form. Along the connection lines between different ⟨001⟩-poles, an antiphase domain boundary forms, microscopially broken up into domains [1129].

Details of the initial deposition steps can determine the orientation in polar materials. GaN directly grown on c-Al_2O_3 grows with N-face orientation (see Fig. 3.19). The high surface mobility of Ga allows nitrogen to take its preferred position in the first atomic layer. Even under Ga-rich conditions the N atoms can kick-off the Ga from its favorite site on the surface. If an AlN buffer is used the strong bond between Al and oxygen leads to an Al atomic layer at the interface and subsequent GaN grows with a Ga-face [1143]. Also for the epitaxy of ZnO on on c-Al_2O_3 the polarity of the epilayer can be controlled, e.g., via the details of an MgO buffer layer [1144].

12.2.5 Patterned Substrates

Using patterning of the substrate certain growth modes and crystallographic directions of the growth front can be evoked.

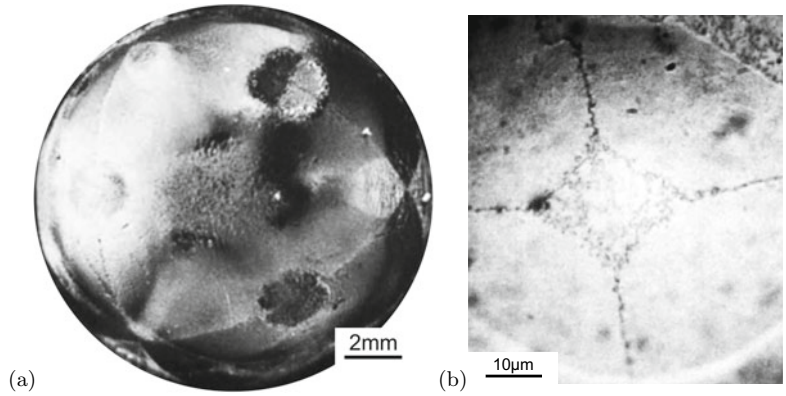

Fig. 12.12 The morphology of **a** GaP grown on a Ge hemisphere with [111]-pole and **b** GaAs grown in a Ge(001) spherical depression. Adapted from [1129]

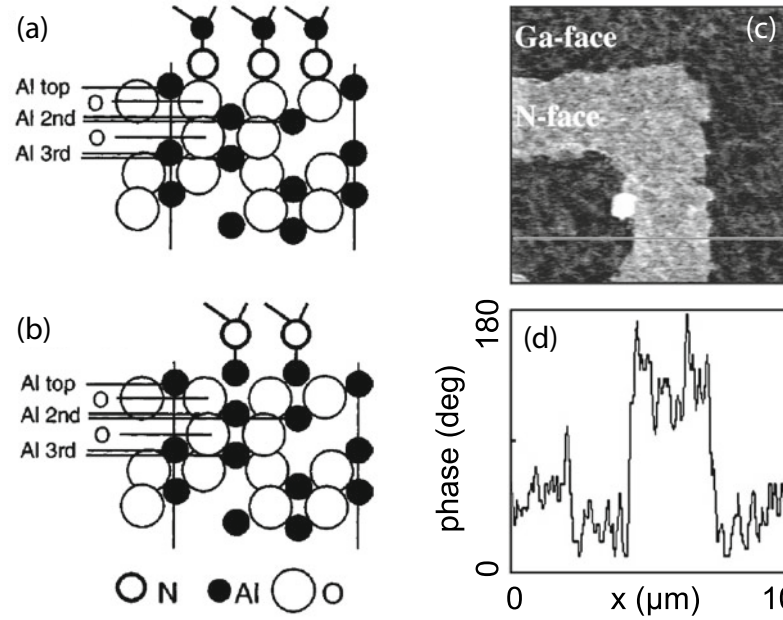

Fig. 12.13 Side view of the heterointerfaces between AlN and *c*-oriented sapphire with nitrogen (**a**) and Al (**b**) being the first layer. Adapted from [1143]. **c** Phase image of piezoresponse force microscopy (PFM) of lateral polarity GaN heterostructure and **d** linescan of phase signal along *white line* in part (**c**). Adapted from [1146], part (**c**) reprinted with permission, ©2002 AIP

Returning to the discussion of [00.1] or [00.$\bar{1}$] growth of wurtzites, on a sapphire substrate with lateral AlN patterns, laterally orientation-modulated GaN can be grown (Fig. 12.13). At the juncture of the phases an inversion domain boundary forms [1145].

The defect density can be reduced in parts of the structure using pendeo-epitaxy [1147] or epitaxial lateral overgrowth (ELO) [1148]. The defects thread only from the limited contact area of the layer with the substrate and the part of the layer away from the mask ('wing') is free of defects (Fig. 12.14).

While the patterning of a mask may be cumbersome and require interruption of growth, the in-situ deposition of a random SiN mask with small holes has been found beneficial in the epitaxy of GaN [1149]. GaN islands nucleate selectively in the mask openings (Fig. 12.15a). The nucleation and subsequent coalescence of islands (Fig. 12.15b) leads to defect annihilation and eventually again to a flat film (Fig. 12.15c). The reduction of defect density is evident (Fig. 12.15d) and leads to improved optical properties [1150].

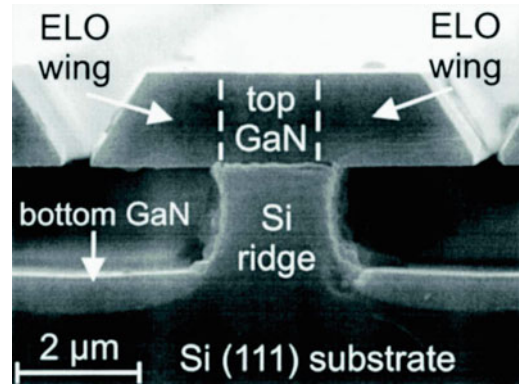

Fig. 12.14 SEM cross-sectional image of GaN grown on a structured Si(111) substrate. The laterally grown wings extend about 2.5 µm over the grooves. The thickness of the GaN layer is 0.5 µm on the bottom of the grooves, while it is 1.4 µm on top of the ridges. Reprinted with permission from [1148], ©2001 AIP

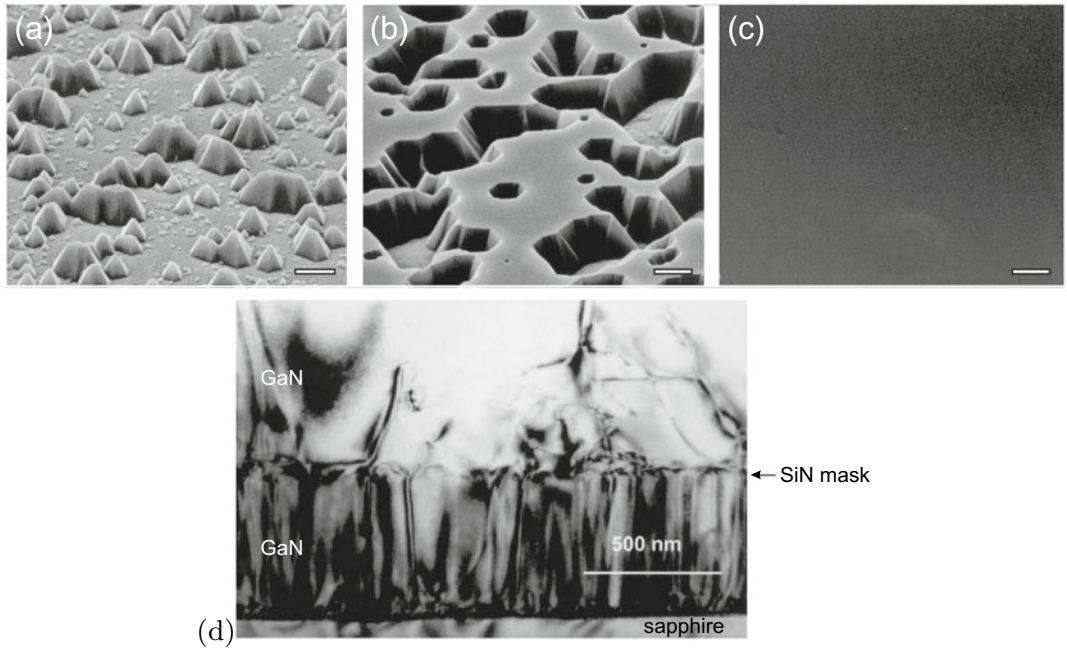

Fig. 12.15 SEM images of GaN **a** growing through the openings of a random SiN mask, **b** laterally overgrowing the mask and coalescing and **c** eventually forming a flat film. Bar widths are 2 µm, 1 µm and 10 µm. **d** Cross-section TEM image. Adapted from [1149]

Using patterned substrates with stripe-like mesas and promoting the growth on a sidewall of the mesa, the direction of GaN growth front can be steered into a semipolar direction (cmp. Sect. 16.4.3). The r-plane sapphire substrate with etched mesa stripes oriented along the [11.0] direction exposes [00.1]-oriented sidewall facets on which the GaN grows along its *c*-axis; The angle of 57.6° between the r- and the c-planes of sapphire is very close to the angle (3.22c) of 58.4° between the GaN semipolar (11.2) and the (00.1) plane. The flat growth front represents a (11.2) facet [1151] (Fig. 12.16). After coalescence of grains from various mesas, a flat (11.2) surface arises, allowing the reduction of various defects including basal stacking faults [1152, 1153].

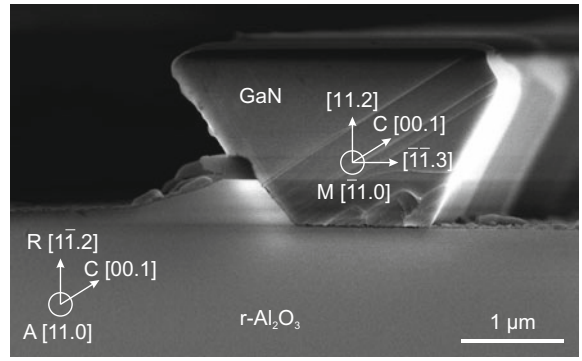

Fig. 12.16 SEM cross-sectional image of MOVPE GaN grown on patterned r-sapphire exposing a (11.2) growth front. Based on SEM image courtesy of F. Tendille

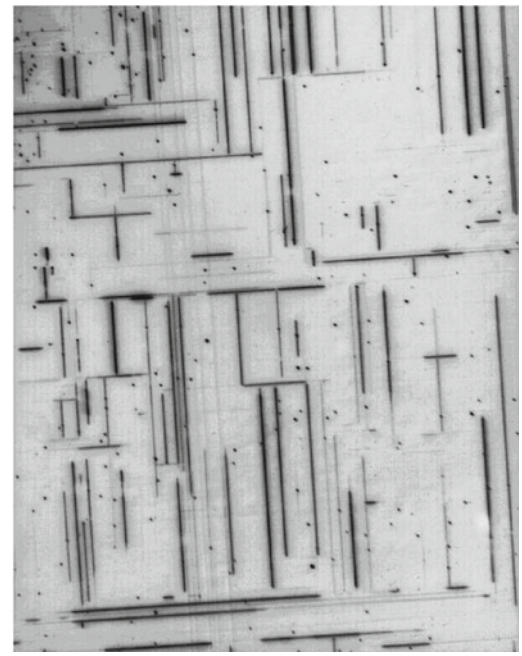

Fig. 12.17 Optical image of the surface of a supercritical, plastically relaxed $In_xGa_{1-x}As$ film on GaAs. Image width is about 1 mm. The cross-hatch pattern is due to misfit dislocations along [110] and [1$\bar{1}$0]. A pseudomorphic layer would exhibit no contrast under the given conditions

12.2.6 Pseudomorphic Structures

Heterostructures can generally be made from any sequence of materials. However a mismatch in lattice constant (or a different crystal structure) leads to strains and stresses that are of the order of 10^3 atmos for strains of 1% ($\sigma \sim C\epsilon$, $C \approx 5 \times 10^{10}$ Pa) as discussed in Sect. 5.3.3. The total strain energy is $\propto C\epsilon^2$. Above a critical thickness $h_c \propto \epsilon^{-1}$ (cf. Sect. 5.4.1) defects, e.g., misfit dislocations (relaxing strain with their edge components), are generated (Sect. 12.2.7). There are a number of semiconductor combinations that are lattice matched and thus can be grown with arbitrary thickness. $Al_xGa_{1-x}As$ is closely lattice matched to GaAs for all Al concentrations. See Fig. 6.25 for lattice-matched pairs, e.g., $In_{0.53}Ga_{0.47}As$/InP. Often, thin layers of lattice-mismatched materials with thickness smaller than the critical thickness are used.

For many device applications the ability to grow pseudomorphic layers thicker than the critical layer thickness would be beneficial. The use of compliant substrates was proposed in [1154] to meet this demand. A recent review on compliant substrate technologies can be found in [445]. Schemes

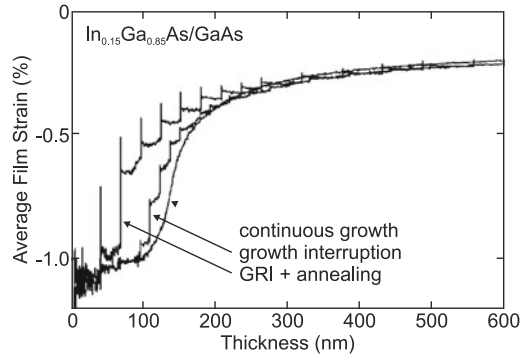

Fig. 12.18 Average film strain (measured in-situ via substrate curvature) of $In_{0.15}Ga_{0.85}As/GaAs$ grown at 450 °C as a function of film thickness (determined from growth time × deposition rate). Relaxation for three different growth modes are shown (as labeled): continuous growth, employment of several growth interruptions (GRI) and GRI with annealing step (to 550°). Adapted from [1155]

to accommodate part of the mismatch strain in the substrate include the use of cantilevered membranes, silicon-on-insulator, twist bonding, glass bonding or trenched substrates. In this sense also nanowhiskers (Sect. 14.2.3) represent a compliant substrate, enabling the growth of coherent (laterally confined) layers thicker than the critical thickness of a 2D layer (cmp. Fig. 14.8).

12.2.7 Plastic Relaxation

Above the critical thickness, a film will relax plastically by forming defects, often misfit dislocations. A cross-hatch pattern at the surface due to misfit dislocations is shown in Fig. 12.17 (cf. also Sect. 4.3.1.4).

The strain relaxation in mismatched heteroepitaxy can be determined experimentally via the wafer curvature of the heterostructure (Sect. 5.3.5). Data for the thickness dependent relaxation $\epsilon(d)$ of $In_{0.15}Ga_{0.85}As$ on GaAs (mismatch $\approx 1\%$) are shown in Fig. 12.18. Growth interruptions lead to larger relaxation at smaller thickness. Therefore relaxation at early times or small thickness (above h_c) is kinetically hindered, i.e., the available dislocation density and glide velocity are not sufficient to relieve the strain. At large thickness the strain does not go to zero (saturation regime) and the film remains in a metastable, incompletely relaxed state as discussed in more detail in [1155].

An extreme case of plastic relaxation is cracking (Sect. 4.4.1) which can occur for example in thick films during cooling due to the mismatch of the thermal expansion coefficients of substrate and epilayer (Fig. 12.19). Such cracking can be avoided by the introduction of suitable stress-relaxing layers and growth on predefined mesas [1156, 1157].

12.2.8 Surfactants

The condition (12.1) allows layer-by-layer growth (cf. Sect. 12.2.3), i.e., the substrate surface free energy is higher than the than the total of interface and film surface free energy. This makes wetting energetically favorable. For two elements A and B, one of them must have the lower surface free energy. If A can be grown on B in Frank-van der Merwe (or Stranski-Krastanow) growth mode, then (12.1) does not hold for B on A and the growth will occur in Volmer-Weber mode, i.e., with islands.

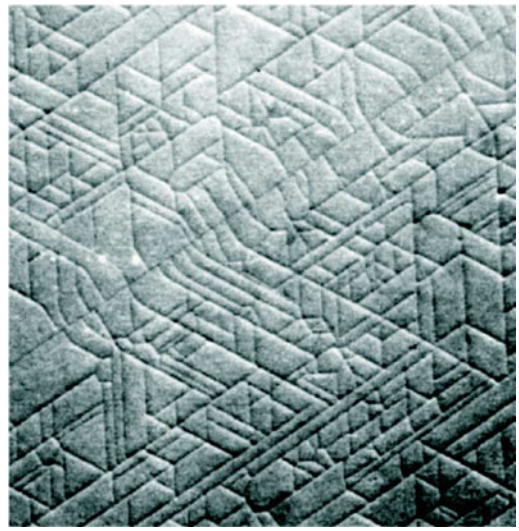

Fig. 12.19 $1 \times 1\,\mathrm{mm}^2$ top view with a differential interference contrast microscope of a $1.3\,\mu\mathrm{m}$ thick GaN layer grown on Si(111). Reproduced with permission from [1156], ©2000 IPAP

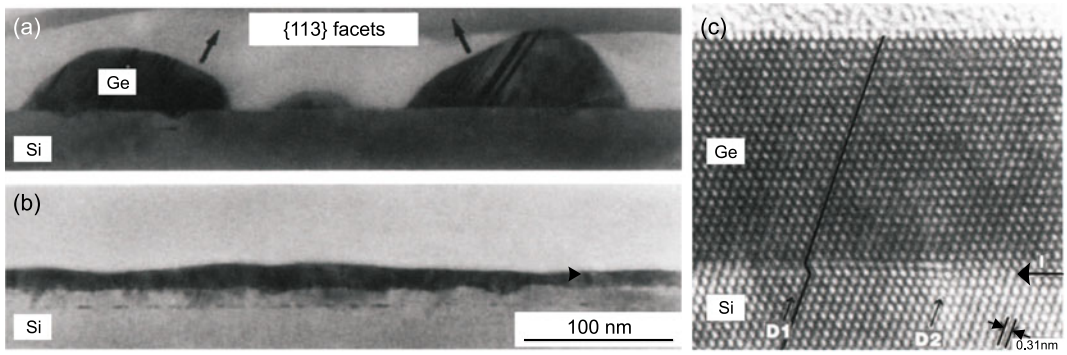

Fig. 12.20 **a**, **b** 10 nm thick Ge layer on Si (100) deposited at room temperature with MBE and annealed up to 770 °C without (**a**) and with (**b**) Sb surfactant. Adapted from [1165]. **c** Cross-section TEM image of a heterostructure of 70 monolayers germanium on Si (111), grown by MBE with Sb surfactant. The *horizontal arrow* labeled 'I' denotes the position of the interface. The *arrows* labeled 'D1' and 'D2' denote the positions of partial dislocations (cmp. Fig. 4.20). Adapted from [327]

This is a serious problem for the growth of embedded layers of the type A–B–A. If the embedded film grows well, the capping does not and vice versa.

In the case of Ge on Si, Ge has the lower surface free energy than Si. Ge grows on Si in Stranski-Krastanow mode [1158] (Fig. 12.20a). Si grows both on Ge(001) and Ge/Si(001) in a Volmer-Weber mode [1159] causing severe problems for the fabrication of Si/Ge/Si quantum wells or superlattices. A substantial modification of growth mode can be achieved by using a third element C as a capping layer, saturating surface bonds. It lowers the surface free energy of both materials A and B, thus favoring wetting of the substrate. Such element C is called *surfactant* (surface-active species) [1160, 1161]. Typical examples are As [1160] or Sb [327] on Si and Ge (Fig. 12.20b). Also the surfactant modifies defect nucleation and can lead to defect-free epitaxial Ge/Si layers (Fig. 12.20c). Surfactants have also been described for the growth of compound semiconductors, e.g., In [1162] or Sb [1163, 1164] for GaAs.

12.3 Energy Levels in Heterostructures

12.3.1 Band Lineup in Heterostructures

In heterostructures, semiconductors with different band gaps are combined. The relative position of conduction and valence band (band alignment) is determined by the electron affinities χ as shown in Fig. 12.21. For a semiconductor, the electron affinity is the (positive) energy difference between vacuum level and conduction band edge. It can lead to different types of heterostructures. Early perspectives of semiconductor heterostructures are discussed in [1166]. The band alignment can be estimated from the position of the branch point energies (Sect. 7.8) of the two constituents [699] but additional interface dipoles may have to be considered.

In Fig. 12.22, the band alignment for type-I, type-II and type-III heterostructures are shown. In the type-I structure (straddled band lineup) the lower conduction-band edge and the higher valence-band edge are both in the material with smaller band gap. Thus, electrons and holes will localize there. In the type-II structure a staggered lineup is present and electrons and holes will localize in different materials. In the type-III structure, also termed 'broken gap' structure, the conduction band of one material is below the valence band of the other material. The technologically most relevant are type-I structures. The design of heterostructures to fulfill a certain device functionality or to have certain physical properties is called 'band gap engineering'.

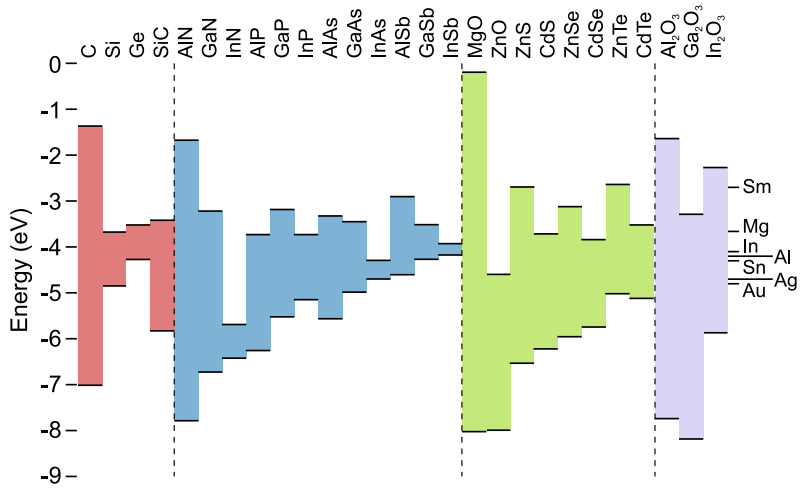

Fig. 12.21 Position of conduction and valence-band edges for a variety of semiconductors (relative to a common vacuum level at $E = 0\,\text{eV}$). Based on values from [1167], and from Al_2O_3 (on InP) [1168], InN on diamond [1169], InN on MgO [1170], Ga_2O_3 on GaN from [1171], and In_2O_3 on Si from [1172, 1173]. On the right hand side, the work functions of several metals are shown for comparison

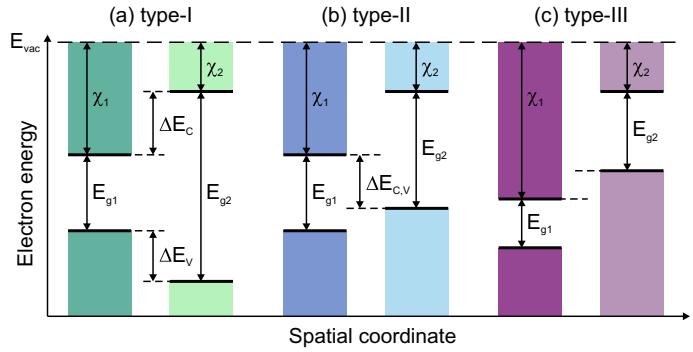

Fig. 12.22 Position of band edges (band alignment) in **a** type-I, **b** type-II and **c** type-III heterostructure

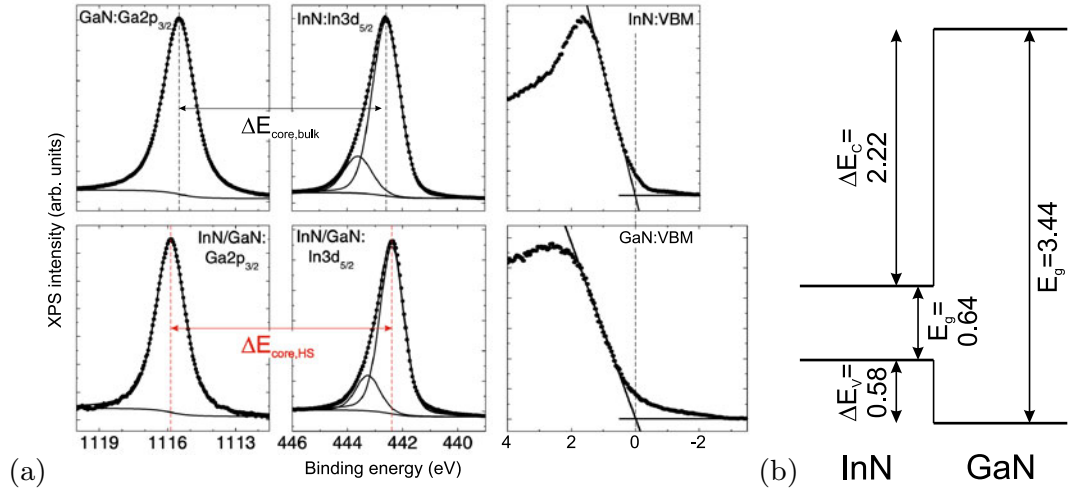

Fig. 12.23 **a** XPS measurements of InN and GaN and a InN/GaN heterostructure. The vertical dashed lines indicate the core level positions in the bulk (black) and the heterostructure (red). The valence band offset is given by $\Delta E_V = \Delta E_{core,HS} - \Delta E_{core,bulk}$ (when E_V is set to zero for both the bulk materials). **b** Schematic band lineup of the type-I InN/GaN heterojunction (all energies in eV). Adapted from [1174]

In a type-I heterostructure, the conduction- and valence-band discontinuities are given, respectively, by

$$\Delta E_C = \chi_1 - \chi_2 \tag{12.3a}$$

$$\Delta E_V = (\chi_1 + E_{g_1}) - (\chi_2 + E_{g_2}) \, . \tag{12.3b}$$

Experimentally, the valence band offset can be determined using X-ray photoelectron spectroscopy (XPS) probing the filled states; together with the band gap then also the conduction band offsets are obtained. As example, in Fig. 12.23a the binding energies of an indium and a gallium core level are shown with the valence band edges of InN and GaN, respectively, set to zero energy. Both core levels are then also investigated in a 5 nm InN on GaN heterostructure (the InN layer is sufficiently thin to allow photoelectrons to escape from the GaN underneath). The sum of the shifts represents the valence band offset ($\Delta E_V = 0.58(8)$ eV from the analysis of several core levels [1174]). Together with the band gaps, the conduction band offset results in $\Delta E_V = 2.22$ eV as schematically depicted in Fig. 12.23b.

Depending on the layer sequence of high- and low-bandgap materials various configurations, as shown in Fig. 12.24 have obtained special names, such as single heterointerface, quantum well (QW), multiple quantum well (MQW), superlattice (SL). In the extreme case the layer is only one monolayer thick (Fig. 12.25) and the concept of layer and interface blurs. Such atomically precise layer sequences are mastered nowadays for a variety of material systems such as (Al,Ga)As/GaAs/InAs, InP/(In,Ga)As, Si/SiGe, ZnO/(Mg,Zn)O and also $BaTiO_3/SrTiO_3$.

The abruptness of interfaces is determined by the epitaxial machine through the switching precision of the incoming material flux and fundamentally limited by segregation phenomena which can be modeled with a segregation coefficient [1175] (cmp. Sect. 4.2.4). As shown in Fig. 12.25c, In has the tendency to be carried into the following GaAs layer. A quantitative evaluation is possible using aberration-corrected scanning transmission electron microscopy [1176].

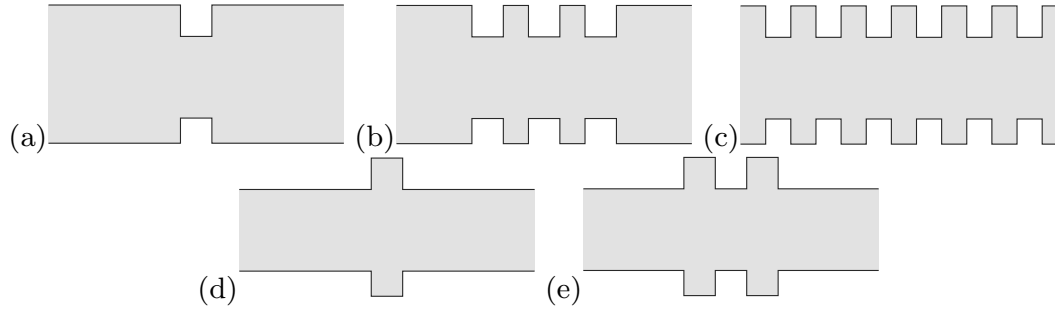

Fig. 12.24 Heterostructures with different layer sequences (band gap engineering). **a** quantum well (QW), **b** multiple quantum well (MQW), **c** superlattice (SL), **d** single-barrier tunneling structure, **e** double-barrier tunneling structure

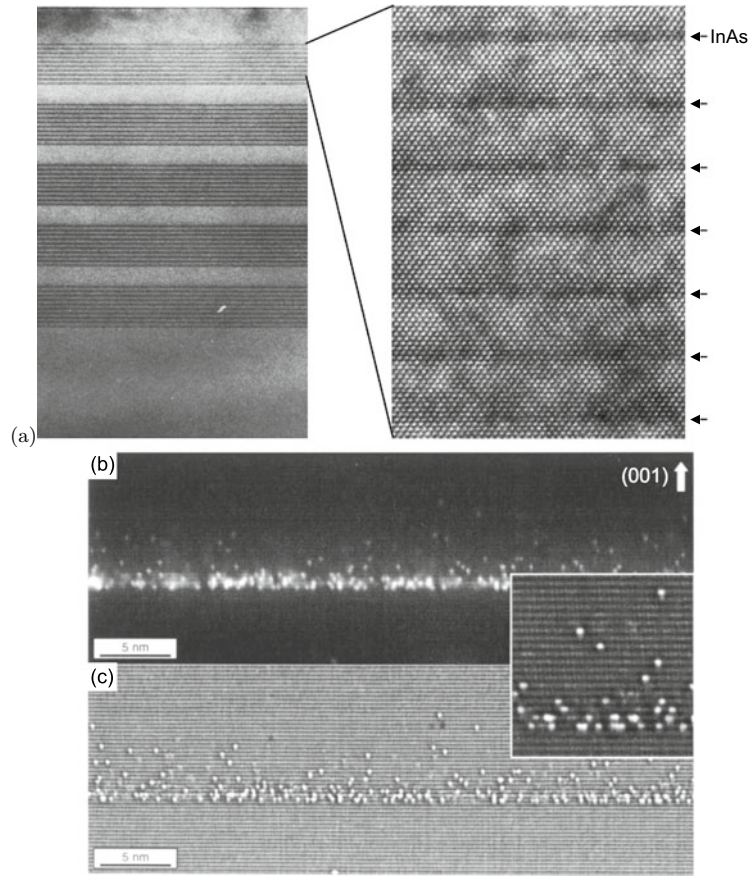

Fig. 12.25 Ultrathin heterostructures: **a** Cross-sectional TEM of a MOVPE-grown short-period superlattice (SPS) of InAs layers in $GaAs_{1-x}N_x$). In high resolution (*right image*), the individual rows of atoms can be seen. From [1177]. **b**, **c** Cross-section STM image of 2 ML InAs on GaAs; the segregation of In into the top layer is visible atom by atom. Adapted from [1178]

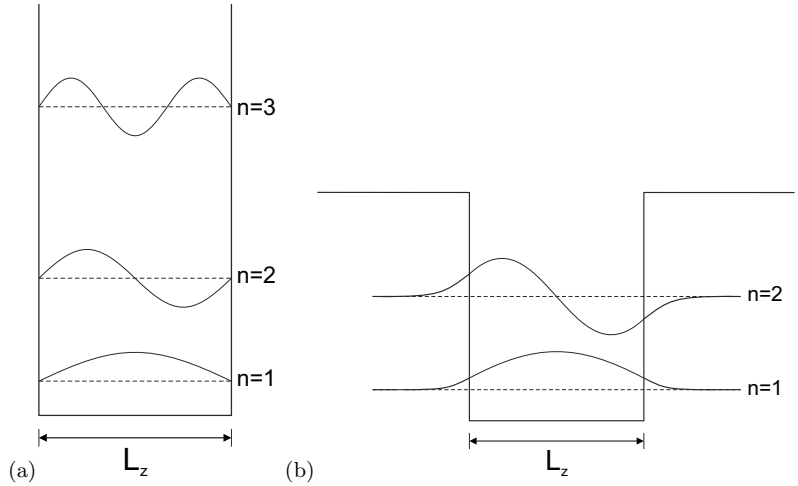

Fig. 12.26 Schematic energy levels and wavefunctions in a potential well with **a** infinite barriers, and **b** finite barrier height

12.3.2 Quantum Wells

The energy in a single quantum well of thickness L_z (along the growth direction z) can be calculated with the quantum-mechanical particle-in-a-box model. In the envelope function approximation (Appendix I) the wavefunction is written as a product of the Bloch function and the envelope function $\chi(z)$.

$$\Psi^{\mathrm{A,B}}(\mathbf{r}) = \exp(\mathrm{i}\,\mathbf{k}_\perp\,\mathbf{r})\; u_{n\mathbf{k}}(\mathbf{r})\,\chi_n(z)\;, \tag{12.4}$$

where 'A' and 'B' denote the two different materials. The envelope function χ fulfills, approximately, the one-dimensional Schrödinger-type equation,

$$\left[-\frac{\hbar^2}{2m^*}\frac{\partial^2}{\partial z^2} + V_\mathrm{c}(z)\right]\chi_n(z) = E_n\,\chi_n(z)\;, \tag{12.5}$$

where m^* denotes the effective mass. V_c is the confinement potential determined by the band discontinuities. Typically, $V_\mathrm{c} = 0$ in the well and $V_0 > 0$ outside in the barrier. E_n are the resulting energy values of the quantized levels. In the case of infinite barriers ($V_0 \to \infty$, Fig. 12.26a) the boundary conditions $\chi(0) = \chi(L_z) = 0$ yield

$$E_n = \frac{\hbar^2}{2m^*}\left(\frac{n\,\pi}{L_z}\right)^2 \tag{12.6}$$

$$\chi_n(z) = A_n\,\sin\left(\frac{n\,\pi}{L_z}\,z\right)\;, \tag{12.7}$$

where E_n is called the confinement energy.

For finite barrier height V_0 (Fig. 12.26b) the calculation leads to a transcendental equation. The wavefunction tunnels into the barrier. While for infinite barrier height the lowest level diverges for $L_z \to 0$, for finite barrier height $E_1 \to V_0$. A complication arises from the different effective mass in the well and barrier material. This is taken into account by forcing the continuity of χ and χ'/m^* across the interfaces[4] ('BenDaniel-Duke' boundary conditions [1180]). The Schrödinger equation and

[4]The kinetic energy term in (12.5) is written as $\frac{\hbar^2}{2}\frac{\partial}{\partial z}\frac{1}{m^*(z)}\frac{\partial \chi}{\partial z}$ for varying mass across the structure [1179].

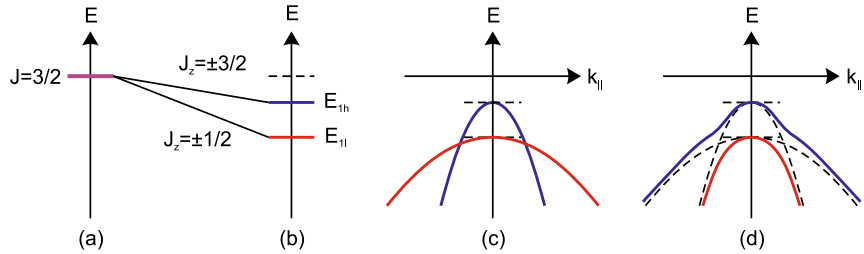

Fig. 12.27 Schematic representation of the development of hole levels in a quantum well: **a** degenerate bulk levels at Γ, **b** splitting at the subband edge (due to different quantized values of k_z), **c** in-plane dispersion (mass reversal), **d** anticrossing behavior. Based on [1123]

(semi-)analytical solutions for special and numerical methods for arbitrary potential distributions are discussed in [1181]. The application of $\mathbf{k} \cdot \mathbf{p}$ theory (Appendix H) to heterostructures is discussed in [1182].

The motion of carriers in the plane is still free and has a two-dimensional dispersion. Thus, each quantized level contributes $m^*/(\pi\hbar^2)$ to the density of states at each subband edge E_n.

For holes, the situation is a little more complicated than for electrons (Fig. 12.27). First, the degeneracy of heavy and light holes is lifted since their mass enters the confinement energy. The effective hole masses along the z direction, i.e., those that enter (12.5), are

$$\frac{1}{m^z_{\mathrm{hh}}} = \gamma_1 - 2\,\gamma_2 \tag{12.8a}$$

$$\frac{1}{m^z_{\mathrm{lh}}} = \gamma_1 + 2\,\gamma_2\,. \tag{12.8b}$$

The light holes have the higher quantization energy. The angular momentum is quantized along the z direction. The transverse masses for the dispersion in the interface plane are

$$\frac{1}{m^{xy}_{\mathrm{hh}}} = \gamma_1 + \gamma_2 \tag{12.9a}$$

$$\frac{1}{m^{xy}_{\mathrm{lh}}} = \gamma_1 - \gamma_2\,. \tag{12.9b}$$

Now the heavy hole, i.e., the $J_z = \pm\frac{3}{2}$ state, has the smaller mass and the light hole ($J_z = \pm\frac{1}{2}$) the larger (Fig. 12.27c). However, this consideration is only an approximation since the lifting of degeneracy and the dispersion have to be treated on the same level. Higher terms of the perturbation calculation lead to band mixing and remove the band crossing that seems to originate from the situation at the Γ point. In reality, the bands show anticrossing behavior and are strongly deformed. The hole dispersion in a superlattice and the anticrossing behavior is shown in Fig. 12.28.

Experimentally observed transition energies in quantum wells of varying thickness are shown in Fig. 12.29 and are in good agreement with the theoretical calculation. We note that for infinite barriers optical transitions are only allowed between confined electron and hole states with the same quantum number n. For finite barriers this selection rule becomes relaxed, and other transitions become partially allowed, e.g., e_1–hh_3. The optical matrix element from the Bloch part of the wavefunction, which was isotropic for (cubic) bulk material (9.37), is anisotropic for quantum wells. TE (TM) polarization is defined with the electromagnetic field in (perpendicular to) the plane of the quantum well (Fig. 12.30a). At the subband edge, i.e., for in-plane wavevector $k_{||} = 0$ the matrix elements for the various polariza-

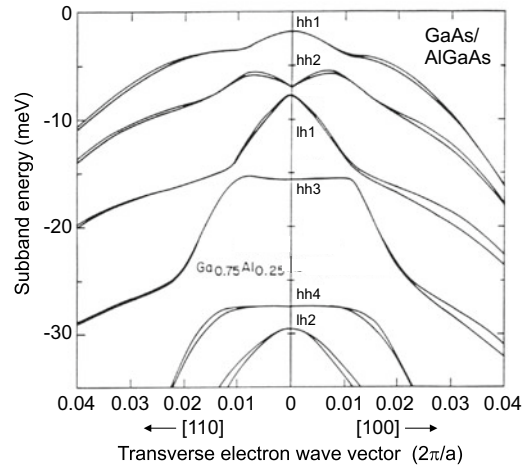

Fig. 12.28 Hole dispersion in a 68-ML GaAs/71 ML $Al_{0.25}Ga_{0.75}As$ superlattice (numerical calculation). The double curves originate from a lifting of time-reversal symmetry at $\mathbf{k} \neq 0$. Reprinted with permission from [1183], ©1985 APS

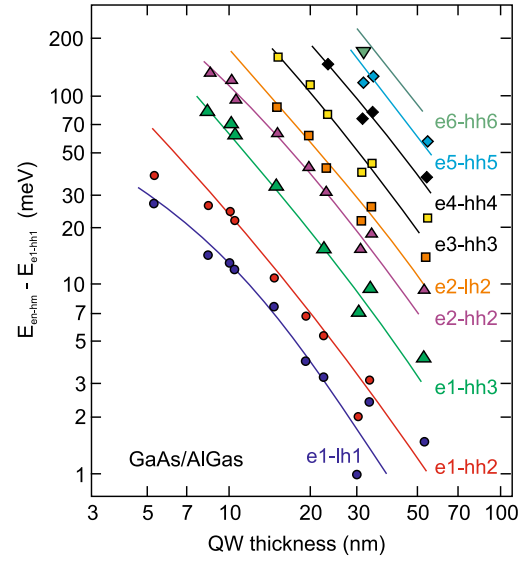

Fig. 12.29 Observed electron–hole transitions (energy difference to the first e–h transition from excitation spectroscopy) in GaAs/(Al,Ga)As quantum wells of varying thickness. *Symbols* are experimental data, *solid lines* are theoretical model. Data from [1184]

tions and propagation directions are given in Table 12.3. The matrix elements averaged over all in-plane directions for TE-polarization are $3/2M_b^2$ ($1/2M_b^2$) for the electron to heavy (light) hole transition. For TM polarization the values are 0 and $2M_b^2$, respectively [1185]. The optical selection rules are shown in Fig. 12.30 (see Fig. 9.12 for bulk material). For propagation along the quantum-well plane, the ratio between the strength of the TE polarized e–hh and e–lh transitions is 3:1.

The confinement potential squeezes charge carriers bound to impurities closer to the ion. Therefore, the binding energy increases as shown in Fig. 12.31. This behavior can be modeled theoretically with good precision. It makes a difference whether the impurity is located at the center or the interface of the quantum well.

The confinement potential also squeezes electrons and holes in the exciton closer together and thus increases their Coulomb interaction. The binding energy of the quantum-well exciton is thus larger than in bulk material and depends on the well width (Fig. 12.32). In the simple hydrogen-like model with infinite barriers the exciton binding energy is 4 times the bulk binding energy in the limit $L_z \to 0$.

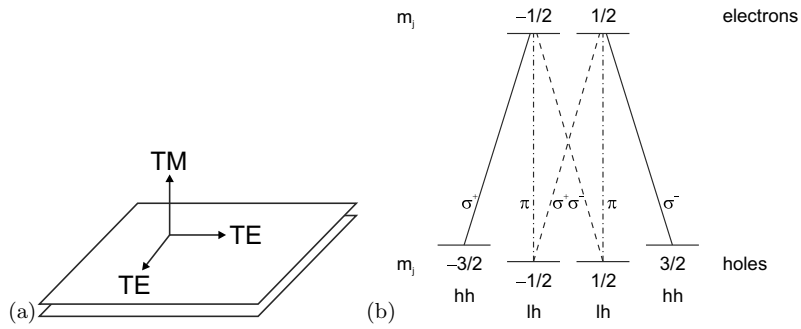

Fig. 12.30 **a** Directions of electric-field vector relative to the quantum-well plane for TE and TM polarization. **b** Optical selection rules for band–band transitions in a quantum well. If the (in-plane averaged) relative strength of the e–hh transitions (*solid lines*) is 1, the relative strength of the TE-polarized e–lh transitions (*dashed lines*) is 1/3 and that of the TM-polarized e–lh transitions (*dash-dotted lines*) is 4/3

Table 12.3 Squared momentum matrix elements $|\langle c|\hat{\mathbf{e}}\cdot\mathbf{p}|v\rangle|^2$ in a quantum well for various propagation directions in units of M_b^2. The quantum-well normal is along **z**

	Propagation	$\hat{\mathbf{e}}_x$ (TE)	$\hat{\mathbf{e}}_y$ (TE)	$\hat{\mathbf{e}}_z$ (TM)
e–hh	**x**	–	1/2	0
	y	1/2	–	0
	z	1/2	1/2	–
e–lh	**x**	–	1/6	2/3
	y	1/6	–	2/3
	z	1/6	1/6	–
e–so	**x**	–	1/3	1/3
	y	1/3	–	1/3
	z	1/3	1/3	–

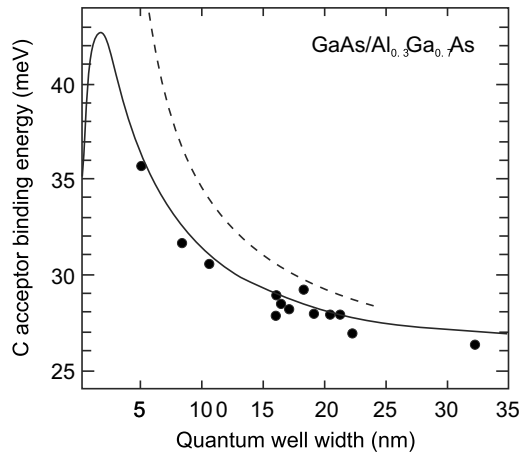

Fig. 12.31 Experimental values for the acceptor binding energy in $GaAs/Al_{0.3}Ga_{0.7}As$ quantum wells (*solid circles*) from [1186] as a function of well width. *Solid line* is theory (variational calculation) for the well-center acceptor including top four valence bands and finite barriers, *dashed line* is hydrogen-like model with infinite barrier height. Adapted from [1187]

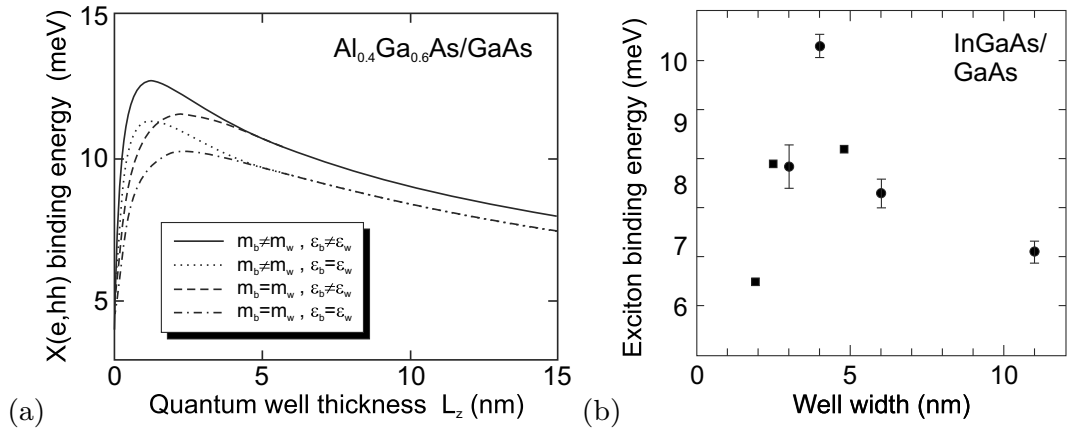

Fig. 12.32 **a** Theoretical (variational) calculation (*solid line*) of the heavy-hole exciton binding energy versus QW thickness in a GaAs/$Al_{0.4}Ga_{0.6}As$ quantum well (using also different approximations, *other lines*). Adapted from [1188]. **b** Experimental exciton binding energy in $In_xGa_{1-x}As$/GaAs quantum wells of different thickness. *Circles*: data and error bars from [1189], x unspecified, *squares*: data from [1190], $x = 0.18$

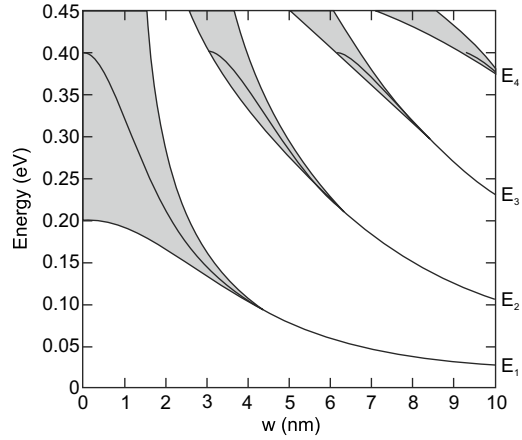

Fig. 12.33 Band structure of a superlattice with a potential depth of 0.4 eV and well and barrier width w ($L_{QW} = L_{barr}$). Adapted from [1191]

In a realistic calculation the effect of different dielectric constants in the well and barrier (image charge effect) need to be considered.

12.3.3 Superlattices

In a superlattice, the barrier thickness is so small that carriers can tunnel in neighboring wells or, in other terms, that there exists a significant wavefunction overlap between adjacent wells. This leads to a band structure (Fig. 12.33), similar to the Kronig-Penney model (Appendix F). For the superlattice the bands are called minibands, the gaps are called minigaps. The density of states does not make a step at the subband edge but follows an arccos function. The modification of the density of states, as seen in the absorption spectrum, are shown in Fig. 12.34 for 1, 2, 3 and 10 coupled wells.

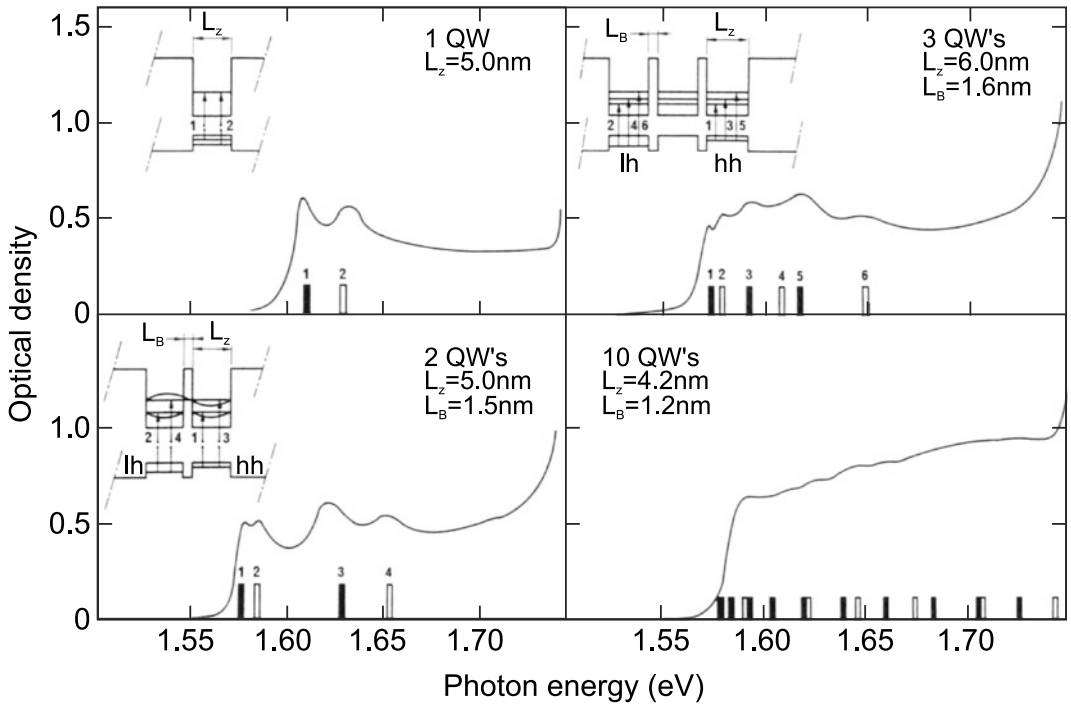

Fig. 12.34 Absorption spectra of a single, double, triple and ten coupled quantum wells. Theoretically predicted transitions with heavy (light) holes are labeled with *filled* (*empty*) *bars* at their respective transition energies. Adapted from [1192]

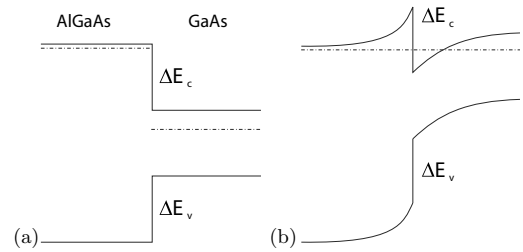

Fig. 12.35 Schematic formation of a triangular potential well in a n-(Al,Ga)As/n-GaAs heterostructure, **a** before and **b** after equilibration of Fermi levels

12.3.4 Heterointerface Between Doped Materials

We consider a single heterointerface between n-doped materials. As an example we take n-(Al,Ga)As/n-GaAs (Fig. 12.35). First, we consider the materials without contact, forming a type-I structure. In thermodynamic equilibrium the system must have a constant Fermi level. Thus, charge is transferred from the region close to the interface from (Al,Ga)As to GaAs. This results in the formation of a triangular potential well in the GaAs close to the interface. A two-dimensional electron gas (2DEG) forms in this potential well (Fig. 12.36). The charge transfer in thermodynamic equilibrium adjusts the band bending and the charge density (quantized levels in the well) in such a way that they are self-consistent. The Poisson equation and the Schrödinger equation are simultaneously fulfilled. Numerically, both equations are iteratively solved and the solution is altered until it is self-consistent, i.e., it fulfills both equations.

If the region of the 2DEG is not doped, the electron gas exists without any dopant atoms and ionized impurity scattering no longer exists. This concept is called *modulation doping*. Mobilities up to $3.1 \times 10^7\,\mathrm{cm}^2/\mathrm{Vs}$ have been realized (Fig. 12.37). The theoretical limits of mobility in a 2DEG at modulation-doped (Al,Ga)As/GaAs heterointerfaces are discussed in detail in [1194].

12.3.5 Heterointerface Between Semiconductors with Band Structures of Different Topology

Let us remember the situation of the topological linear chain developing end states when sandwiched between trivial material (cf. Sect. 5.2.10). Also surface states develop between a material with non-trivial topological band structure and vacuum (which is trivial) (cf. Sect. 11.6.3). These effects are expression of the bulk-boundary correspondence, which says that at the interface of topologically different materials, edge states develop.

If now a semiconductor heterointerface is made up from two topologically differnt materials, a conductive interface channel is expected. This effect has been found for the HgTe/CdTe system where HgTe represents the non-trivial material with inverted band structure. (cf. Sect. 6.11). A quantum well structure was proposed where HgTe is sandwiched between layers of $\mathrm{Hg}_x\mathrm{Cd}_{1-x}\mathrm{Te}$ [1196]. Taking the electron and hole quantization effects into account, normal band order is present for thickness of the HgTe layer up to a critical thickness of $d_\mathrm{c} = 6.35\,\mathrm{nm}$ (for $x = 0.32$) and the sample should be insulating. For thicker QWs, the two-dimensional bands invert and edge states arise. The quantized electrical conductance due to the edge states was indeed found and measured [1197, 1198].

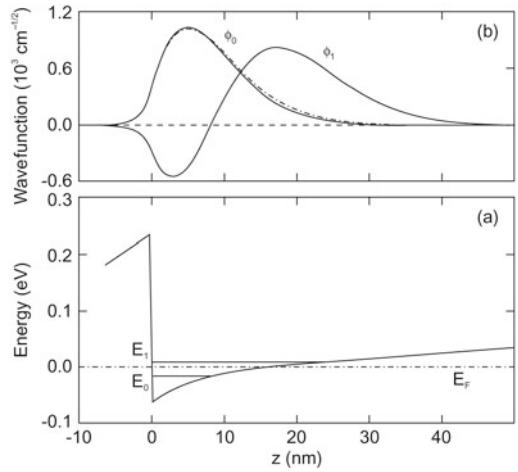

Fig. 12.36 **a** Conduction-band edge at a GaAs/$\mathrm{Al}_{0.3}\mathrm{Ga}_{0.7}\mathrm{As}$ heterointerface ($T = 0\,\mathrm{K}$) with two confined states at E_0 and E_1 marked with *solid horizontal lines*. In the GaAs channel there are $5 \times 10^{11}\,\mathrm{cm}^{-2}$ electrons. The barrier height is 300 meV, $N_\mathrm{D}^\mathrm{GaAs} = 3 \times 10^{14}\,\mathrm{cm}^{-3}$. The position of the Fermi level E_F is at $E = 0$ and indicated with a *dash-dotted line*. **b** Envelope wavefunctions ϕ_0 and ϕ_1 of the two confined states, *dash-dotted line*: calculation without exchange and correlation for state at E_0. Adapted from [1193]

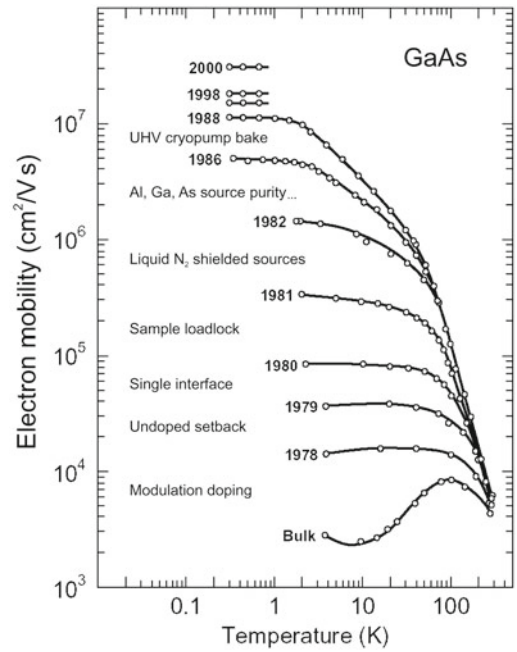

Fig. 12.37 Progress in the achievement of high electron mobility in GaAs, annotated with the technical innovation responsible for the improvement. Adapted from [1195], reprinted with permission, ©2003 Elsevier B.V

12.4 Recombination in Quantum Wells

12.4.1 Thickness Dependence

The energy of exciton recombination in quantum wells is blue-shifted with respect to that in bulk material due to the quantum-confinement energies of electrons and holes (Fig. 12.38). The electron–hole recombination lineshape in quantum wells is given by the product of the joint density of states and the Boltzmann function (when Boltzmann statistics apply). The JDOS is given by a step function (Heavyside function $H(E)$).

$$I(E) \propto H(E - E_{11}) \exp\left(-\frac{E}{kT}\right) , \tag{12.10}$$

where $E_{11} = E_g + E_{e1} + E_{h1}$ represents the energy of the E1–H1 subband edge as shown in Fig. 12.38. An experimental spectrum (Fig. 12.40a) shows that excitonic effects influence the recombination lineshape in a GaAs quantum well even at room temperature [1199].

The recombination decay constant of excitons decreases with decreasing well width, partly due to the increase of exciton binding energy as discussed in [1200].

12.4.2 Broadening Effects

Many-Body Effects

At high carrier densities when the electron (quasi-) Fermi level is above the electron subband edge, the spectrum broadens and reflects the Fermi–Dirac distribution (Fig. 12.40b). At low temperatures

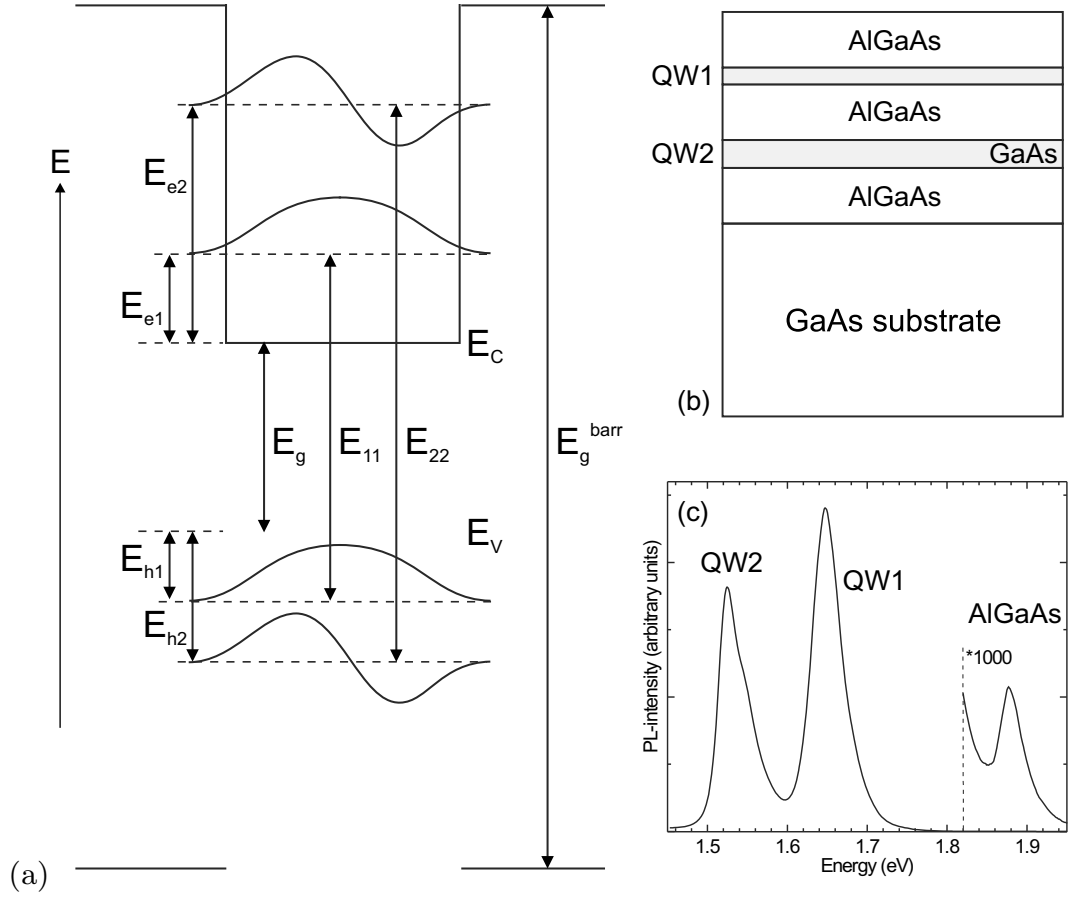

Fig. 12.38 **a** Schematic energy diagram of a quantum well with confined electron (e1, e2) and hole (h1, h2) states and recombination between them at energies E_{11} and E_{22}. **b** Schematic sample structure with two GaAs/$Al_xGa_{1-x}As$ quantum wells with thicknesses 3 nm and 6 nm. **c** Photoluminescence spectrum ($T = 300$ K) of the structure from part (**b**). A small amount of barrier luminescence appears at 1.88 eV, according to $x = 0.37$ (cf. Fig. 6.24c)

a many-body effect, multiple electron–hole scattering with electrons at the Fermi edge, leads to an additional peak, termed *Fermi-edge singularity* that is discussed in [1201].

Homogeneous Broadening

The temperature dependence of the homogeneous broadening of quantum well luminescence has been investigated in [1202]. It follows the dependence of the broadening known from bulk material (Sect. 9.7.7) with similar values for the LO broadening parameter. In Fig. 12.39a the reflectance spectra for different temperatures of a 17 nm GaAs/$Al_{0.3}Ga_{0.7}As$ QW are shown. The optical phonon broadening parameter for various well widths is shown in Fig. 12.39b and coincides with the bulk value.

The homogeneous broadening leads to excitons with in-plane center-of-mass wave-vector $\mathbf{K} \neq 0$ being allowed to recombine radiatively. This leads to a linear increase of exciton lifetime as demonstrated for GaAs quantum wells up to 50 K in [1200]. In [1203] all exciton wave-vectors within the light cone are considered, explaining the linear increase of exciton lifetime in (non-polar) ZnO quantum wells up to room temperature.

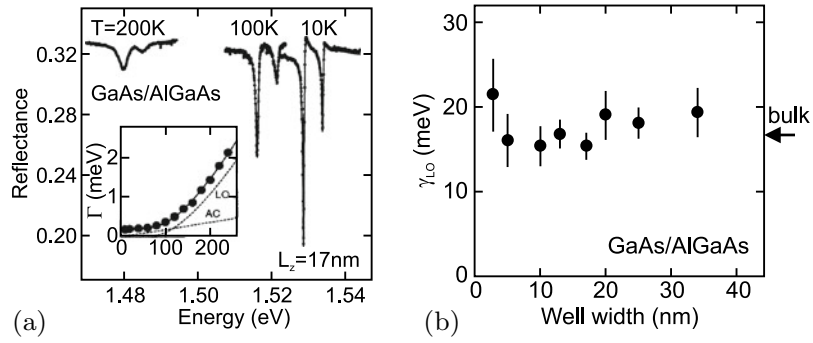

Fig. 12.39 **a** Reflectance spectra at various temperatures from a 17 nm thick GaAs/$Al_{0.3}Ga_{0.7}As$ quantum well. The *inset* shows the temperature dependence of the homogeneous linewidth. **b** LO phonon broadening parameter (FWHM) for various quantum well widths. Adapted from [1202]

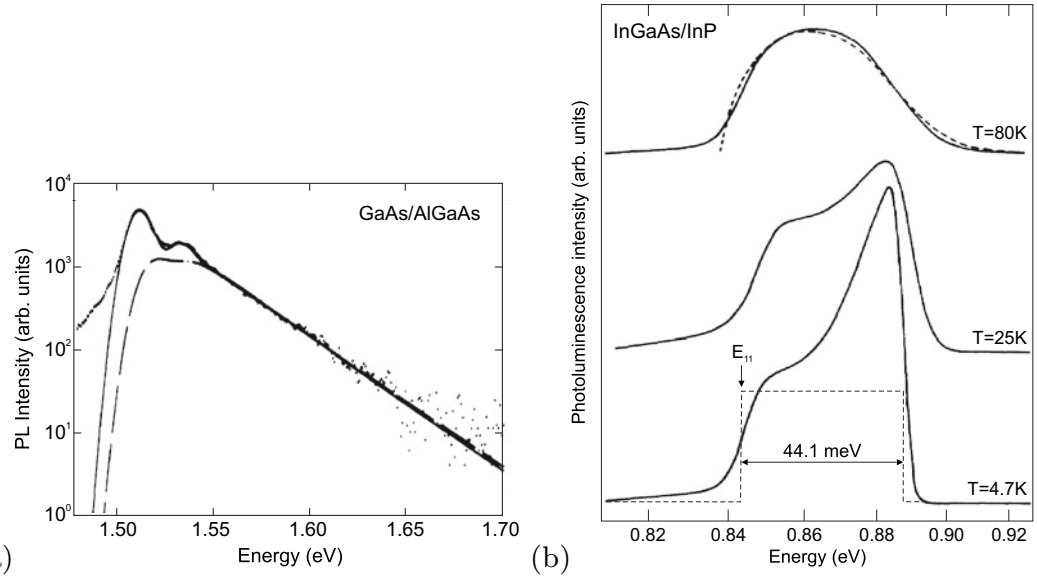

Fig. 12.40 **a** Photoluminescence spectrum of a 5-nm GaAs/(Al,Ga)As quantum well at $T = 300\,\mathrm{K}$. The *solid* (*dashed*) line is fit with (without) excitonic effects. The two peaks are due to transitions involving heavy and light holes. Adapted from [1199]. **b** Photoluminescence spectra at three different temperatures as labeled of a 10-nm modulation-doped (In, Ga)As/InP quantum well with an electron sheet density $n_s = 9.1 \times 10^{11}\,\mathrm{cm}^{-2}$. The electron quasi-Fermi level is $F_n - (E_C + E_{e1}) = 44.1\,\mathrm{meV}$ from the subband edge. The *dashed line* in the $T = 80\,\mathrm{K}$ spectrum is the lineshape from JDOS and a Fermi–Dirac distribution without enhancement at the Fermi edge. Adapted from [1201]

Inhomogeneous Broadening

Inhomogeneous broadening affects the recombination lineshape. Since the interfaces of the QW are not ideally flat, the exciton averages over different quantum-well thicknesses within its volume. Also, e.g., for the GaAs/(Al,Ga)As system, the wavefunction in the (binary) quantum well tunnels into the barrier, the amount depending on the QW width, and there 'sees' the alloy broadening (see Sect. 10.3.3). The problem of exciton dynamics in a potential with random fluctuations has been treated in detail [1204, 1205].

A simplified picture is as follows: At low temperatures the excitons populate preferentially the potential minima. A simple lineshape[5] of the QW absorption or joint density of states is given by a step function (cf. Table 9.3) at the QW band edge E_0. The inhomogeneous broadening has a Gaussian

[5] neglecting excitonic enhancement.

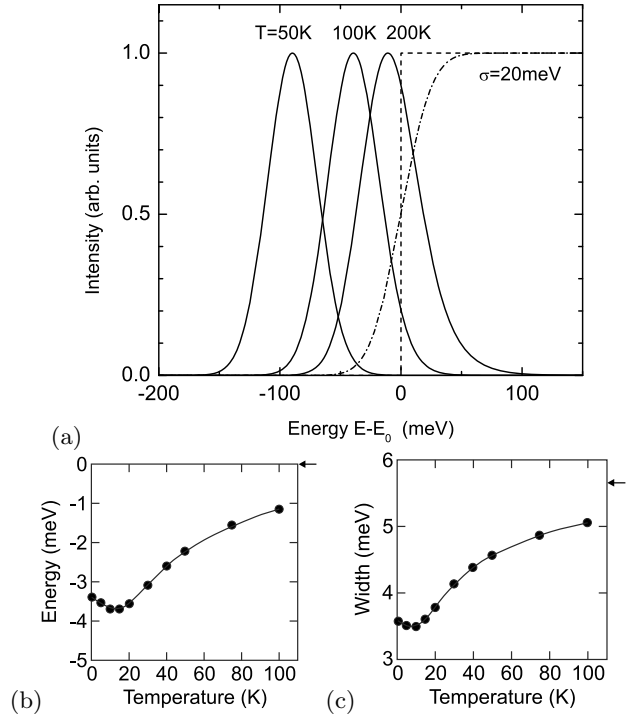

Fig. 12.41 a Recombination spectra (*solid lines*, scaled to same height) of a model quantum well for different temperatures as labeled and complete thermalization, *dashed* (*dash-dotted*) *line* is unperturbed (inhomogeneously broadened by $\sigma = 20\,\mathrm{meV}$) shape of the QW absorption edge. The energy scale is relative to the energy position of the unperturbed QW absorption edge at E_0. **b** Theoretical energy position and **c** linewidth of exciton recombination from a model disordered quantum well. The high-temperature limits are marked by *arrows*. Parts (**b**, **c**) adapted from [1204]

probability distribution $p(\delta E) \propto \exp[-(\delta E)^2/2\sigma^2)]$ with δE being the deviation from the QW band edge $\delta E = E - E_0$. The resulting lineshape is given by the convolution of the Gaussian with the unperturbed absorption spectrum yielding an error-function-like spectrum[6] as shown in Fig. 12.41a.

For complete thermalization the level population is given by the Boltzmann function. The recombination spectrum is given by the product of the absorption spectrum (or JDOS) and the Boltzmann function. It is (red-) shifted with respect to E_0 by about[7]

$$\Delta E(T) = -\frac{\sigma^2}{kT} = \gamma(T)\, kT \ . \tag{12.11}$$

This shift between emission and absorption is also called the Stokes shift.

Within their lifetime, limited at least by radiative recombination, the excitons are typically unable to reach the energy position required by the Boltzmann function, but only a local minimum. Thus, their thermalization may be incomplete due to insufficient lateral diffusion. This effect is particularly important at low temperatures when thermal emission into adjacent deeper potential minima is suppressed. In this case, the red-shift is smaller than expected from (12.11). A numerical simulation [1204] yields such behavior of the energy position of the recombination line as shown in Fig. 12.41b. Simultaneously, the width of the recombination spectrum also exhibits a minimum (Fig. 12.41c). These findings are in agreement with experiments [1206, 1207]. An analytical model for temperature dependent exciton localization in the presence of disorder has been given in [1208], yielding a value $0 \le \gamma \le \gamma_0 = (\sigma/kT)^2$ in (12.11).

[6] The error function is defined as $\mathrm{erf}(x) = (2/\sqrt{\pi}) \int_0^z \exp -t^2 \, \mathrm{d}t$.

[7] Formula (12.11) is exact for the product of a Gaussian and the Boltzmann function.

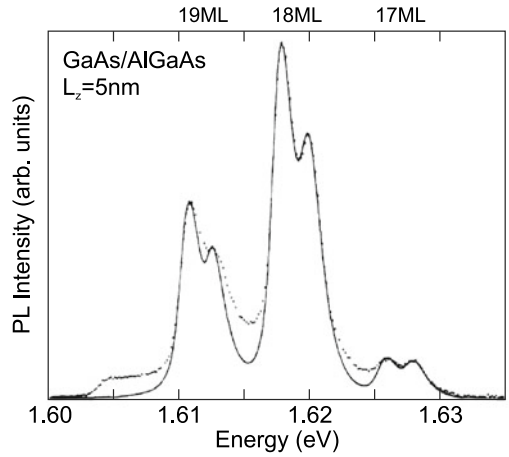

Fig. 12.42 Photoluminescence spectrum ($T = 2\,\mathrm{K}$) (*dots*) of GaAs/ (Al,Ga)As quantum well grown by MBE with 120 s growth interruptions. Recombination is due to excitons in islands of 19, 18, and 17 monolayers ($a_0/2$) height. The *solid line* is a lineshape fit including lifetime broadening ($\Gamma = 1.34\,\mathrm{meV}$) and residual inhomogeneous broadening ($\sigma = 0.04\,\mathrm{meV}$) due to (Al,Ga)As barrier alloy fluctuations. Note that the energy separation of the peaks is much larger than kT. The peak doublet structure is discussed in [1199]. Adapted from [1199]

A potential fluctuation can localize an exciton laterally at low temperatures [1199] and behave like a quantum dot (cf. Sect. 14.4). Localized and delocalized excitons are separated by a boundary called the mobility edge [1209]. The transition between the two regimes is a Mott transition [1210].

Monolayer Growth Islands

Under certain growth conditions, quantum wells with piecewise very flat interfaces can be fabricated. The thickness difference between such regions (with lateral extension in the μm range) is an integer monolayer. Accordingly, the recombination spectrum yields several, typically two or three, discrete lines (Fig. 12.42).

12.4.3 Quantum Confined Stark Effect

The quantum confined Stark effect (QCSE, Sect. 15.1.2) in quantum wells shifts energy levels when electric fields are present along the width of the quantum well. A strong effect exists for pyro- and piezoelectric material combinations such as *c*-axis oriented (In,Ga)N/(Al,Ga)N [1211, 1212] or (Cd,Zn)O/(Mg,Zn)O [1213, 1214] quantum wells due to the built-in electric field (cf. Sect. 16.2). The QCSE induced red-shift is larger in thicker quantum wells and goes beyond the bulk band gap of the quantum well material (Fig. 12.43b). Also the wavefunction overlap is reduced with increasing well width, leading to an increase of the radiative recombination lifetime as shown in Fig. 12.43. The pyroelectric field and the related modification of lifetime are absent in quantum wells grown on non-polar directions such as [11.0] (Fig. 12.43a).

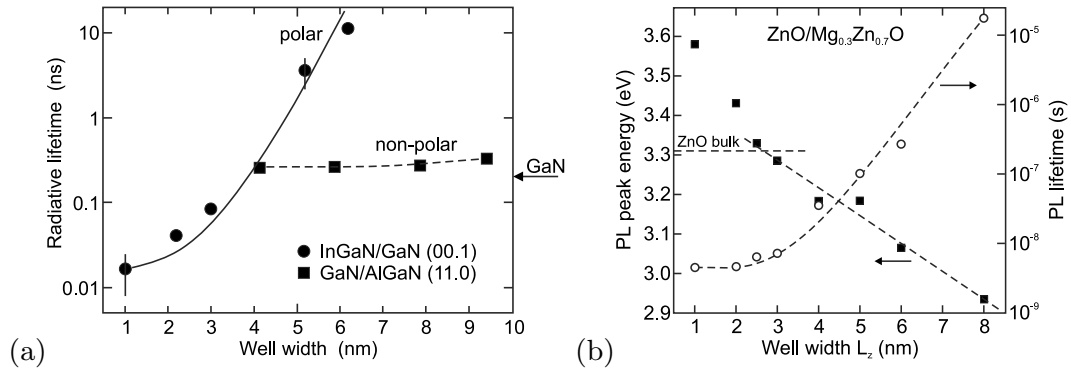

Fig. 12.43 **a** Radiative lifetime of electron-hole pairs in polar [00.1]-oriented $In_{0.2}Ga_{0.8}$ N/GaN (*circles*) and non-polar [11.0]-oriented GaN/$Al_{0.2}Ga_{0.8}$N (*squares*) quantum wells of varying thickness. Experimental data are shown in *symbols*. The *solid line* is the (scaled) theoretical dependence of the electron-hole overlap for (In,Ga)N/GaN QWs. The *dashed line* is guide to the eye. The *arrow* denotes the recombination time constant in bulk GaN. Adapted from [1215, 1216]. **b** Low temperature PL peak recombination energy (*solid squares*) for ZnO/$Mg_{0.3}Zn_{0.7}O$ quantum wells for various well widths L_z (barrier width $L_B = 5$ nm). *Dashed line* indicates dependence for internal field of 0.9 MV/cm, *horizontal dashed line* indicates recombination energy in ZnO bulk. Carrier lifetime determined from PL (*circles*), *dashed line* is guide to the eye. Adapted from [1214]

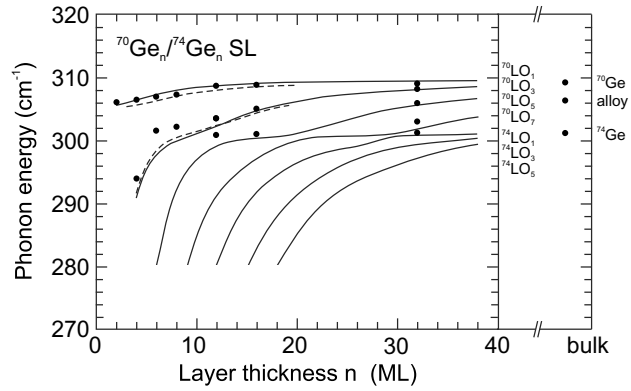

Fig. 12.44 Measured (*full circles*) and theoretical (*solid lines*) confined LO phonon energies in $^{70}Ge_n/^{74}Ge_n$ superlattices versus the layer thickness (number of monolayers) n. The *dashed lines* represent a calculation that considers intermixing at the interfaces. On the right, the energies of bulk modes for isotopically pure ^{70}Ge and ^{74}Ge are shown together with that of an $^{70}Ge_{0.5}{}^{70}Ge_{0.5}$ alloy. Adapted from [1217]

12.5 Isotope Superlattices

A special type of heterostructure is the modulation of the isotope content. The first kind of heterostructures made like this were $^{70}Ge_n/^{74}Ge_n$ symmetric superlattices [1217]. Figure 12.44 shows phonon energies determined from Raman spectroscopy for various layer numbers n. The modes are classified by $^{70}LO_m$ and $^{74}LO_m$ denoting the material in which the amplitude is maximal and m being the number of maxima in that medium.[8] Such modes are visualized in Fig. 12.45a for a $^{69}GaP_{16}/^{71}GaP_{16}$ superlattice. Theoretical mode energies as a function of the superlattice period are shown in Fig. 12.45b.

[8] Only modes with odd m are Raman-active.

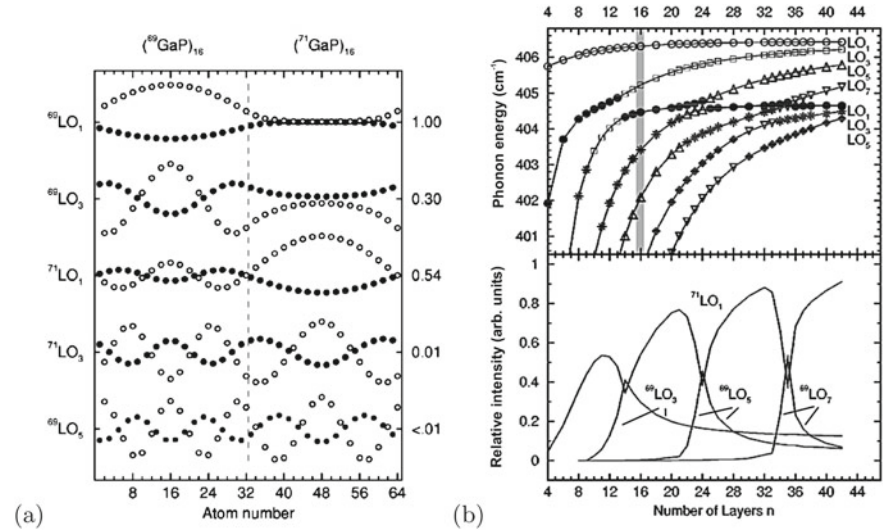

Fig. 12.45 **a** Atomic displacements [Ga (*filled dots*) and P (*open circles*)] of odd-index LO modes in a $^{69}Ga_{16}P/^{71}Ga_{16}P$ superlattice unit cell. These modes have even parity with respect to midlayer planes, which are at atom numbers 16 and 48 in this example. The labels on the left identify the predominant character of the mode, those on the right give the relative Raman intensities with respect to that of the $^{69}LO_1$ mode. The tick marks on the vertical axis indicate zero displacement of the respective mode. **b** *Upper panel*: Energies and characters of odd-index LO phonon modes in GaP isotope SLs as calculated within the planar bond charge model for the case of ideal interfaces. $^{69}LO_m$ modes are shown as *open symbols*; $^{71}LO_m$ modes as *full symbols*. The *shaded area* marks $n = 16$ for which the atomic displacements of the modes are shown in part (**a**). *Lower panel*: Calculated intensities of the modes relative to that of the $^{69}LO_1$ phonon mode. Adapted from [379], reprinted with permission, ©1999 APS

12.6 Wafer Bonding

Wafer bonding is a fairly recently developed method to join different and dissimilar materials. Two wafers of the respective materials are put together face to face and are adequately fused. The idea is to not only 'glue' the wafers together with a sticky (and compliant) organic material, but to form strong atomic bonds between the two materials with possibly a perfect interface. In some cases, the interface needs to allow charge-carrier transport through it. Less stringent conditions need to be met for photon transport.

Mechanical deficiencies such as surface roughness, dust particles and the like must be avoided in the wafer-bonding process since they result in voids. Several methods have been developed for bonding various materials [1220–1222]. Such processes are successful for large substrate sizes. With proper processing, ideal interfaces can be created, as shown in Fig. 12.46. Such structures, if made between a p-doped and a n-doped semiconductor, show diode characteristics.

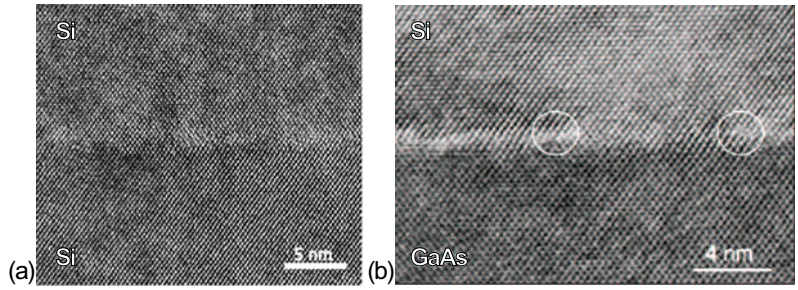

Fig. 12.46 High-resolution TEM images of wafer-bonded **a** Si–Si and **b** GaAs–Si interfaces. *White circles* indicate the position of misfit dislocations. Part (**a**) reprinted from [1218], ©2003, with permission from Elsevier. Part (**b**) reprinted with permission from [1219], ©1998 AIP

Chapter 13
Two-Dimensional Semiconductors

Introducing a new experimental system is generally more rewarding than trying to find new phenomena within crowded areas. [...] Of course, the fantastic results one originally hopes for are unlikely to materialise, but, in the process of studying any new system, something original inevitably shows up.

A.K. Geim, 2010 [1223]

Abstract 2D materials or atomic sheets are materials without a bulk. They offer unique physics and properties, but also challenges in preparation and stability. Stacking of such 2D materials in van-der-Waals heterostructures extends the possibilities.

2D materials are the ultimate thickness limit for semiconductors. While the thickness of quantum wells can be controlled to the sub-atomic average thickness, they are still impacted by the roughness or undulation of the underlying substrate. 2D materials are more like free two-dimensional molecules with giant lateral extension and a vertical structure well defined by atomic bonding. Paper collections and textbooks are available for this topic, e.g. [1224–1226].

13.1 Graphene and Related Materials

Graphene, its name proposed in [1227], is the ultimately thin material, a single sheet of carbon atoms in honeycomb arrangement; this is *not* a hexagonal (cf. Fig. 3.3b) but a trigonal lattice with a two-atom basis (Fig. 13.1). Graphene possesses unique physical properties such as a linear dispersion around the Fermi energy, making it a solid-state analogue to ultra-relativistic physics [1228]. Graphene does not possess a band gap in its ideal form. An account of the history of graphene research, starting in 1840, is given in [1229].

Many applications for graphene and graphene-based composites have been envisioned in electronics such as superior conductor or transistor material [1230, 1231] as well as applications in energy, biomedical, membranes and sensors [1232, 1233], but the current industrial use is still rather limited. Here, we introduce 'flat' graphene while quasi one-dimensional nanotubes based on graphene are treated in Sect. 14.3.

M. Grundmann, *The Physics of Semiconductors*, Graduate Texts in Physics,
https://doi.org/10.1007/978-3-030-51569-0_13

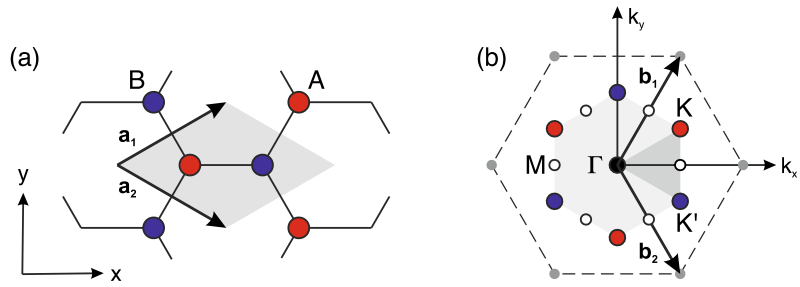

Fig. 13.1 Unit cell of A–B compound honeycomb lattice in **a** real space and **b** reciprocal space. The irreducible part of the Brillouin zone is shown in dark grey

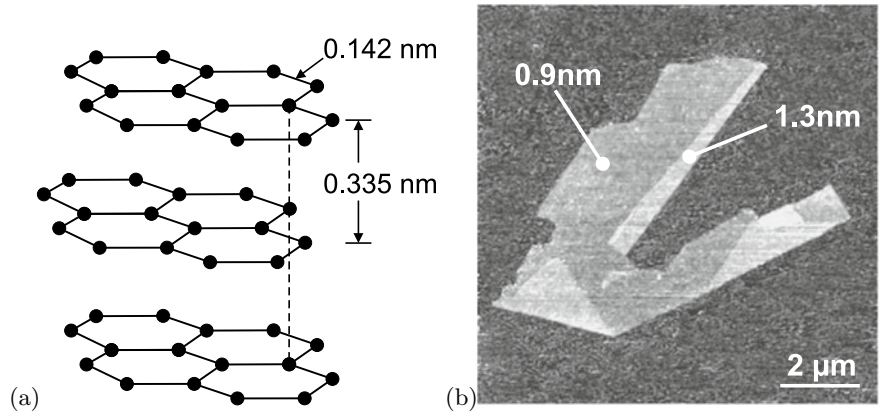

Fig. 13.2 **a** Schematic layer structure of graphite with bond length and layer distance labelled. **b** AFM image of graphene on oxidized silicon. The height of two areas relative to the background is labelled. Adapted from [1240]

13.1.1 Structural Properties

The carbon bond length in graphene is $d_{\mathrm{C-C}} = 0.142\,\mathrm{nm}$ (cmp. Table 13.1). Due to instabilities [1234, 1235], freely suspended graphene layers are not perfectly flat but exhibit corrugations [1236]. Graphene can be prepared from graphite via micromechanical cleavage, i.e. mechanical exfoliation (repeated peeling) of small mesas of highly oriented pyrolytic graphite [1237, 1238]. Epitaxial growth on SiC [1239] and the growth on copper in large sheets [1232] have been reported.

Graphite is a stacked arrangement of such graphene sheets (Fig. 13.2a) held together by van-der-Waals forces (cmp. Sect. 13.3) as shown in Fig. 13.2b. The carbon atoms bond via sp^2 hybridization. Organic molecules such as, e.g., anthracene or coronene (Fig. 18.1) can be understood as molecular-size pieces of such two-dimensional graphene sheet with hydrogen saturating the outside, broken bonds. Single layer graphene sheets (SLG) and few-layer graphene (FLG) sheets must distinguished since for the latter the exact stacking arrangement and vertical coupling effects play a role. Ideally, such two-dimensional crystal is infinitely extended, e.g. for band structure calculations. Of course real crystals always have a (quasi-) one-dimensional boundary which is topologically a line or very thin sidewall. Various defects have been studied in graphene. The vacancy is discussed in [1241] and exhibits a magnetic moment of $2\mu_{\mathrm{B}}$.

The unit cells in real and reciprocal space are shown in Fig. 13.1. The lattice vectors are $\boldsymbol{a}_{1,2} = a/2(3, \pm\sqrt{3})$ (Fig. 13.1a). The reciprocal lattice vectors are $\boldsymbol{b}_{1,2} = 2\pi/(3a)(1, \pm\sqrt{3})$, where $a = d_{\mathrm{C-C}}$. The Brillouin zone (Fig. 13.1b) has two triples of K-points that are labeled K and K' (or K+

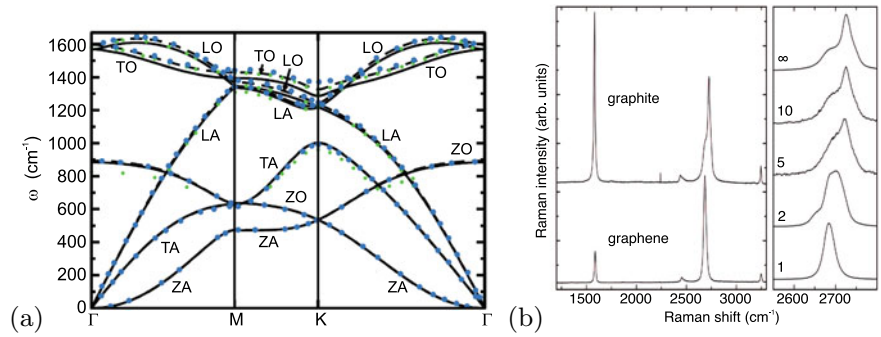

Fig. 13.3 **a** Phonon dispersion in graphene (cmp. Fig. 13.1b). *Symbols* are experimental data from various methods. *Dashed lines* is DFT-LDA theory, *solid lines* GGA. Adapted from [1244], reprinted with permission, ©2004 Elsevier Ltd. **b** Comparison of graphite and graphene Raman spectra (excited at 514 nm). In the right panel the number of monolayers in FLG is labeled (1: graphene, ∞: graphite). Adapted from [1245], reprinted with permission, ©2006 APS

and K−) at $\boldsymbol{K}$, $\boldsymbol{K'} = 2\pi/(3a)\,(1, \pm 1/\sqrt{3})$. When the A- and B-sites are identical, as for graphene, the difference between K- and K'-points is often subtle and a Γ–M–K Brillouin zone is sufficient.

Mechanical properties of graphene are discussed in [1242, 1243]; it has exceptional strength (Young's modulus in the range of 1 TPa). The breaking stress 200 times greater than steel, with a 2D tensile stress of 42 N/m, corresponding to a strain of 25%. The phonon dispersion of graphene is shown in Fig. 13.3a. For the ZA and ZO modes, the displacement is perpendicular to the graphene plane (out-of plane modes). In Fig. 13.3b the Raman spectra of graphite and graphene are compared. The peak (termed 'G') at about 1580 cm^{-1} ist due to the zone center mode. The peak at about 2680 cm^{-1} (termed '2D') is due to two phonons (double resonance) with opposite momentum in the highest optical branch near the K-point. It splits into four peaks for bilayer graphene due to changes in the electronic band structure [1245].

13.1.2 Band Structures

The band structure of graphene from first principles [1246] is depicted in Fig. 13.4a. Graphene is a zero-gap semiconductor (cf. Fig. 6.46) which shows a linear photon-like spectrum,

$$E = \hbar k\, v_\mathrm{F}\ , \tag{13.1}$$

around the Fermi energy at the K-point (Fig. 13.4b). Such point is also called 'Dirac' point.

The important bands close to the Fermi level stem from the (out-of-plane) π-orbitals while the (in-plane) chemical bonds are sp^2-type (Sect. 2.2.3). The linear dispersion around the K-point is similar to that of relativistic particles without rest mass. The electrons in graphene are of course not really massless, their velocity (6.35) being $v_\mathrm{F} \approx 10^6$ m/s, about 300 times smaller than the speed of light [1248, 1249].

In the simplest tight-binding approximation (cf. Appendix G), considering the coupling of the carbon (out-of-plane) p_z-orbitals with three nearest neighbors, the band structure is given as [1250, 1251] (cf. (G.23)

$$E(\mathbf{k}) = \pm t \sqrt{1 + 4\cos\left(3\frac{a\,k_x}{2}\right)\cos\left(\frac{\sqrt{3}\,a\,k_y}{2}\right) + 4\cos^2\left(\frac{\sqrt{3}\,a\,k_y}{2}\right)}\ , \tag{13.2}$$

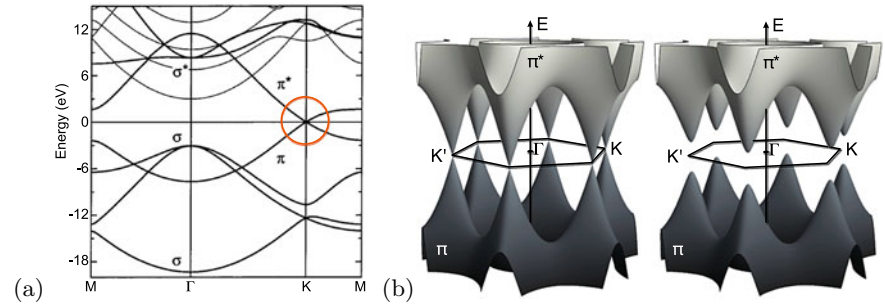

Fig. 13.4 **a** Band structure of graphene from first principles (zero energy refers to the intrinsic Fermi level). The *circle* focusses on the linear band crossing at the Fermi level. Adapted from [1247], reprinted with permission, ©2004 WILEY-VCH. **b** Three-dimensional representation $E(k_x, k_y)$ of the π-bands of graphene (*left*) and of graphene-like material with gap (*right*)

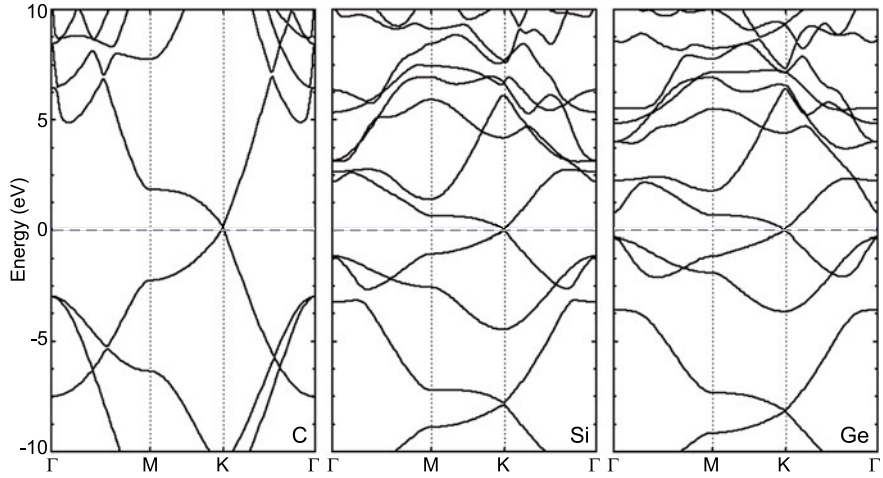

Fig. 13.5 Band structure of graphene, silicene and germanene as labeled. Adapted from [1255], reprinted with permission, ©2014 RSC

where $t \approx 2.8\,\text{eV}$ is the next-neighbor hopping energy (cf. Fig. G.1). More elaborate tight-binding schemes have been reported [1252, 1365]. The second next-neighbor energy t' is about a factor of 10–100 smaller; a tight-binding fit to cyclotron resonance experiments finds $t' = 0.1\,\text{eV}$ [1253]. The two-dimensional band structure is visualized in Fig. 13.4b. Such band structure has been directly confirmed experimentally [1254] as shown in Fig. 13.6a–e. The distortion of the band structure with increasing electron concentration (Fig. 13.6e–h) from the conical bands is due to strong electron-electron, electron-phonon, and electron-plasmon coupling effects [1254].

The band structures of atomic sheets of C, Si and Ge are compared in Fig. 13.5. The bands cross for all three materials at the K-point while the band gap at the zone center decreases with increases order number. Any kind of asymmetry between the A- and B-sites, as might occur for example on certain corrugated substrates, will introduce a band gap at the Dirac points (Fig. 13.4b).

The band structure of FLG has been theoretically analyzed in [1256, 1257]. For bilayers experimental data on the band structure can be found in [1258]. Subtle differences exist for different stacking orders of the graphene sheets (see below, Sect. 13.3). Bulk graphite shows a semi-metallic behavior with a band overlap of about 41 meV. For more than ten graphene layers the difference with the band overlap in bulk graphite is less than 10%.

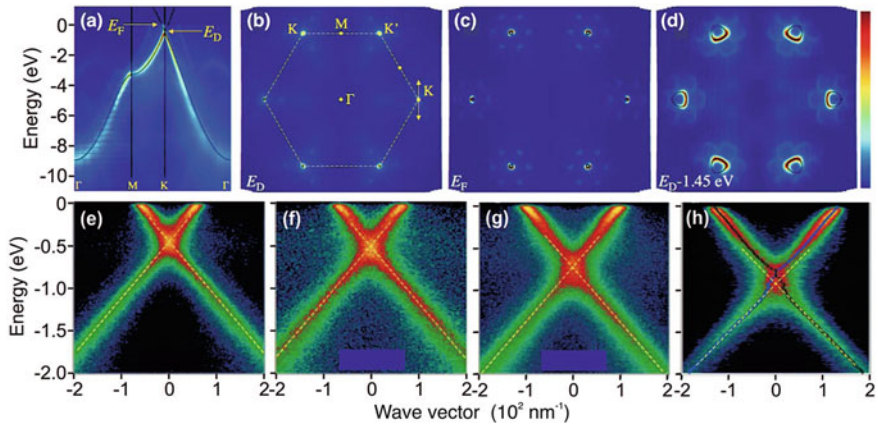

Fig. 13.6 Experimental bandstructure of graphene (on (0001) 6H-SiC) as determined from ARPES. **a** Energy distribution of states as a function of momentum along principal directions in the Brillouin zone. The single-orbital tight-binding model (13.2) with $T = 2.82\,\mathrm{eV}$ is shown as *solid lines*. The Fermi level is shifted by 0.435 eV due to doping. **b** Constant energy map of the states at binding energy corresponding to the Dirac energy E_D; the boundary of the Brillouin Zone boundary is superimposed as *dashed line*. The arrow at the K-point indicates the directions over which the data in (**e**–**h**) were acquired. **c**, **d** Constant energy maps at the Fermi energy $E_\mathrm{F} = E_\mathrm{D} + 0.45\,\mathrm{eV}$ and $E_\mathrm{D} - 1.5\,\mathrm{eV}$, respectively. **e**–**h** Experimental energy bands along the line through the K-point parallel to Γ–M direction as indicated in (**b**). The *dashed lines* are an extrapolation of the lower bands below the Dirac crossing energy, which are observed not to pass through the upper bands (above E_D), suggesting the kinked shape of the bands around E_D. The sheet electron density is $n_\mathrm{S} = 1.1$, 1.5, 3.7, and $5.6 \times 10^{13}\,\mathrm{cm}^{-2}$ for (**e**)–(**h**), respectively, due to increased doping upon potassium adsorption. Adapted from [1254], reprinted with permission, ©2006, Springer Nature

13.1.3 Electrical Properties

The Shubnikov-de Haas (SdH) oscillations from a graphene sheet exhibit a behavior [1249]

$$\frac{1}{\Delta B} = \frac{4e}{h}\frac{1}{n_\mathrm{S}}\,, \tag{13.3}$$

which corresponds to (15.39) for a two-dimensional electron system and a spin- and valley-degeneracy[1] of both two. The cyclotron mass has been determined from the temperature dependence of the SdH oscillations to be proportional[2] to $\sqrt{n}$ (Fig. 13.7). The cyclotron mass is generally related [1259] to the area $S(E) = \pi k^2$ in k-space of the orbits at the Fermi energy via

$$m_\mathrm{c} = \frac{\hbar^2}{2\pi}\frac{\partial S(E)}{\partial E} \tag{13.4}$$

With the linear dispersion (13.1) we can write (13.4) as

$$m_\mathrm{c} = \frac{\hbar^2}{2\pi}\frac{2\pi E}{\hbar^2 v_\mathrm{F}^2} = \frac{E}{v_\mathrm{F}^2}\,. \tag{13.5}$$

For the linear energy dispersion (13.1) the number of states up to energy E_F is (with a degeneracy of 4)

[1] Each of the six valleys at the K-points is shared by three Brillouin zones; keep in mind that the K- and K'-points are not equivalent.

[2] In a parabolic dispersion as in (15.38), the cyclotron mass is independent of n.

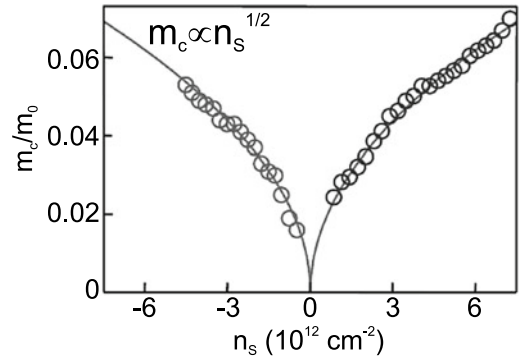

Fig. 13.7 Cyclotron mass in graphene as a function of the sheet electron concentration n_S (negative values relate to hole concentration, $E_F < E_D$). Adapted from [1249]

$$N(E_F) = 4\,\frac{\pi\,k_F^2}{(2\pi/L)^2} = A\,\frac{4\pi\,E_F^2}{h^2\,v_F^2}\,, \tag{13.6}$$

where A is the system area. Therefore we have (at low temperature) with (13.5)

$$n_S = \frac{4\pi}{h^2}\,\frac{E_F^2}{v_F^2} \propto m_c^2\,, \tag{13.7}$$

as determined experimentally. Therefore the behavior of the SdH oscillations confirms the linear dispersion relation. The experimental value for the velocity is $v_F \approx 10^6$ m/s. From (13.7) the density of states (per area and energy) around the Dirac point increases linearly with energy,

$$D(E) = \frac{8\pi}{h^2\,v_F^2}\,E\,. \tag{13.8}$$

The carrier density in a graphene sheet can be controlled via the field effect. The graphene is positioned on an insulator/semiconductor structure, typically SiO_2/Si (cf. Sect. 21.3). The carrier density is then related to the applied (gate) voltage V_g via (21.93) and (21.95), i.e.

$$n_S = \frac{\epsilon_i\,V_g}{e\,d}\,, \tag{13.9}$$

where d is the thickness of the insulator and ϵ_i its dielectric constant. By applying positive (negative) bias electron (holes) can be induced in the sheet. The electron and hole densities depend on the Fermi energies[3]

$$n_S = \frac{8\pi}{h^2\,v_F^2}\int_{E_D}^{\infty}\frac{E - E_D}{1 + \exp\left[(E - E_F)/kT\right]}\,\mathrm{d}E \tag{13.10a}$$

$$p_S = \frac{8\pi}{h^2\,v_F^2}\int_{-\infty}^{E_D}\frac{-(E - E_D)}{1 + \exp\left[-(E - E_F)/kT\right]}\,\mathrm{d}E \tag{13.10b}$$

as visualized in Fig. 13.8. These relations cannot be inverted to obtain $E_F(n, p)$ analytically. The total charge carrier density is $\rho_S = e(p_S - n_S)$.

The Hall effect (Fig. 13.9) shows the expected ambipolar dependence according to (15.16) which takes the form

[3]Here we assume the linear dispersion for all thermally populated states.

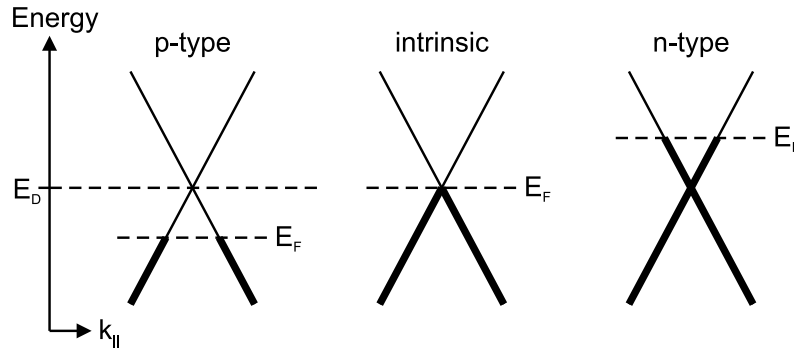

Fig. 13.8 Band structure of graphene with various positions of the Fermi energy E_F in relation to the Dirac energy E_D. States occupied with electrons are shown with in *bold*

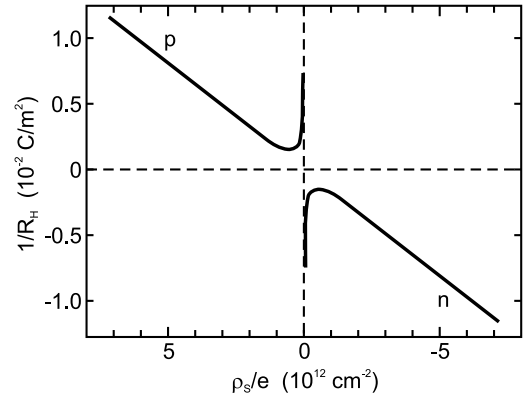

Fig. 13.9 Hall coefficient ($T = 10\,\mathrm{K}$) for a graphene sheet as a function of the free carrier sheet density $\rho_S/e = p_S - n_S$ (positive values indicate p-type). Data shown as *solid lines* from [1249]

$$R_H = \frac{1}{e}\,\frac{p_S - n_S}{(n_S + p_S)^2} \tag{13.11}$$

for equal electron and hole mobilities.[4]

From Hall effect measurements the mobility has been determined to be about $10^4\,\mathrm{cm}^2/\mathrm{Vs}$, independent of temperature between 10 and 100 K, and the same for electrons and holes. This value, however, is much smaller than the in-plane mobility of about $10^6\,\mathrm{cm}^2/\mathrm{Vs}$ at 4.2 K in high quality samples of highly ordered pyrolithic graphite (HOPG) [1260]. In suspended graphene a mobility of $2.3 \times 10^5\,\mathrm{cm}^2/\mathrm{Vs}$ has been found, limited by finite sample size [1261]. Thus in graphene layers on a solid surface extrinsic effects such as charge traps, interfacial phonons, ripples or fabrication residue seem to limit the carrier mobility.

The QHE has been observed in graphene [1249], reportedly up at room temperature [1262]. The plateaus $(4e^2/h)(n + 1/2)$ correspond to unusual half-integer filling, the first plateau occurring at $2e^2/h$, as has been also suggested from theory, and related to the 'pseudospin'. Another consequence of the Dirac-like behavior of the fermions in graphene is the presence of finite maximum resistivity $\rho_{max} = h/4e^2 = 6.45\,\mathrm{k\Omega}$ even at low temperature and $E_F = E_D$. It is due to the fact that localization effects, leading to insulating behavior, are strongly suppressed. Then each carrier keeps a mean free path in the order of its Fermi wavelength.

The Klein paradox [1263, 1264], the efficient tunneling of Dirac particles through high and thick barriers seems accessible in transport experiments with graphene [1265].

[4] Including sign, $\mu_h = -\mu_e$. For $T = 0$ and $E_F = E_D$, $n_S = p_S = 0$ and thus $1/R_H$ should be zero. For finite temperatures there is always $n_S > 0$ and $p_S > 0$, even for $E_F = E_D$. Thus $1/R_H \propto 1/(p_S - n_S)$ diverges at $\rho_S = e(p_S - n_S) = 0$ with a change of sign.

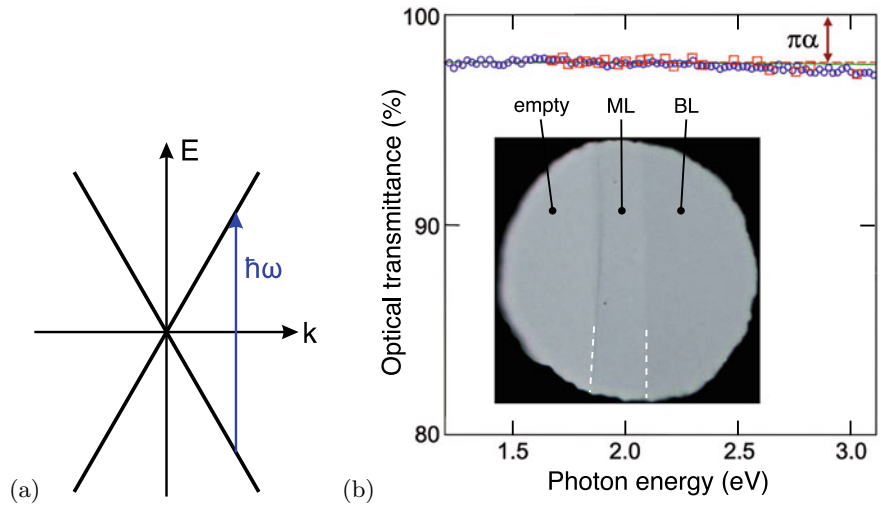

Fig. 13.10 **a** Scheme for interband absorption in the graphene band structure around one of the Dirac points. **b** Transmission spectrum of graphene, measured using standard spectroscopy for a uniform membrane that completely covered a 30 μm aperture (*blue circles*) and measured using an optical microscope (*red squares*). The inset shows a 50 μm aperture partly covered with monolayer (ML) and bilayer (BL) graphene as labeled (*white dashed lines* highlight the borders). Adapted from [1266]

13.1.4 Optical Properties

The transmission of graphene has been investigated in [1266] over apertures and in [1267] on SiO_2 substrate. The band-band absorption process is schematically shown in Fig. 13.10a. A theoretical analysis of this process yields an absorbance of $\pi\,\alpha \approx 0.023$, $\alpha = e^2/(\hbar\, c)$ being the fine structure constant [1266, 1268]. Effects due to next-to-nearest neighbors are not present theoretically [1269]. This universal number is found in the experimental spectrum in the visible spectral range as shown in Fig. 13.10b. In order to exhibit this value, half the photon energy may not be too large because the band structure will deviate from the linear dependence due to the triangular warping and nonlinearities (cf. Appendix G.3.2 and remember $t \approx 2.8\,\text{eV}$). In the infrared regime, deviations are due to state blocking due to finite temperature and non-zero Fermi level relative to the Dirac point and due to intraband transitions [1267]. For FLG, the transmission decreases stepwise; the step sequence deviates from $\pi\alpha$ due to inter-layer effects [1270].

13.2 Two-Dimensional Compound Semiconductors

Two-dimensional crystals have been reported also for compound semiconductor materials such as BN, MoS_2, $NbSe_2$, $Bi_2Sr_2CaCu_2O_x$ [1238] or ZnO [1271] and in particular transition metal dichalcogenides (TMDC) of the type MX_2, where M represents a transition metal atom and X a chalcogen atom forming the $(W,Mo)(S,Se,Te)_2$ system [1272, 1273]. But many other materials also form atomically thin sheets [1225, 1255, 1274]. The main difference to graphene is that they form a band gap. A few physical properties are listed in Table 13.1.

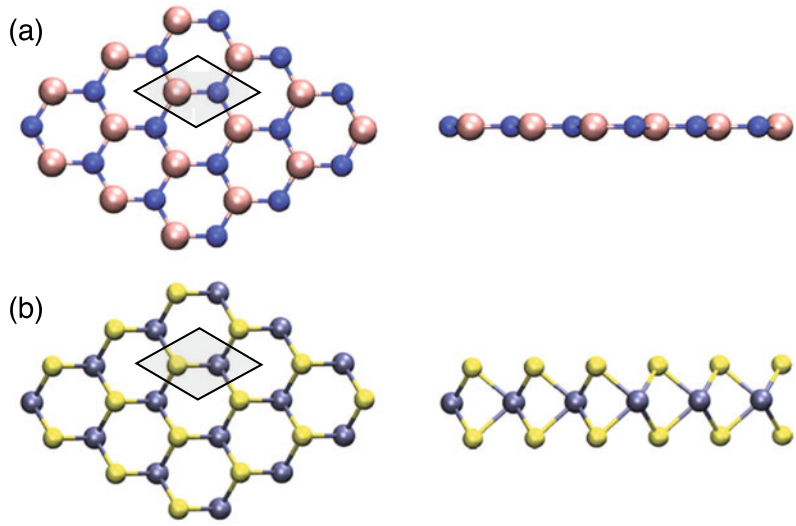

Fig. 13.11 Crystal structure of two 2D materials of **a** hexagonal BN-type and **b** MX_2-type transition metal dichalcogenides. The unit cell is indicated. *Left*: Bird's eye view on the plane and *right*: side view. The greyed area denotes an elementary cell. Adapted from [1255], reprinted with permission, ©2014 RSC

Table 13.1 Properties of various two-dimensional (monolayer) semiconductors, in-plane nearest neighbor distance d_{A-B}, vertical distance of anions d_{X-X} for MX_2-type TMDC, band gap E_g, exciton binding energy E_X^b (exfoliated on silica) and spin-splitting Δ_{SOC} in conduction and valence band

material	C	BN	MoS_2	$MoSe_2$	WS_2	WSe_2
d_{A-B} (nm)	0.142	0.144	0.184	0.192	0.184	0.192
d_{X-X} (nm)			0.317	0.334	0.314	0.334
E_g (eV)	0	7.3	2.15	2.18	2.41	2.2
E_X^b (eV)		2.2	0.31	0.5	0.32	0.5
$\Delta_{SOC,CB}$ (meV)	0		-3	-21	29	36
$\Delta_{SOC,VB}$ (meV)	0		148	184	430	466

13.2.1 Structural Properties

Various two-dimensional configurations are known, the two most prominent that are typical for BN (1H, hexagonal) and for TMDC (2H, trigonal prismatic, ABA-stacking) respectively, are shown in Fig. 13.11. A plane-view TEM of the 2H structure of MoS_2 is depicted in Fig. 13.12 [1275]. Other configurations of the TMDC such as an ABC-like stacking (1T, distorted octahedral) are possible [1276]. A variation are Janus TMDC of MXY type where the bottom and top layer consist of different anions [1277]. Two-dimensional alloys can be formed by mixing cations [1279] or anions [1283] (or both). As example, a STEM image of a $Mo_{0.47}W_{0.53}S_2$ monolayer is shown in Fig. 13.12b which shows the distribution of W and Mo atoms.

Various defects have been investigated for compound 2D semiconductors. For the vacancies in BN we refer to [1284]. Single sulphur vacancies in MoS_2 are investigated in [1278]. Various antisite defects in MoS_2 have been identified [1280] (Fig. 13.13). Also extended defects such as dislocations [1275], grain boundaries [1281] or rotational stacking faults [1282] have been observed.

The phonon spectra of graphene, BN- and BC_2N-sheets are compared in Fig. 13.14. The spectrum of BC_2N is similar to the superposition of the C and BN spectra [1285]. The Raman peaks from MoS_2 show discrete peak energies for thickness of 1–5 or 6 monolayers and then merge closely to the bulk

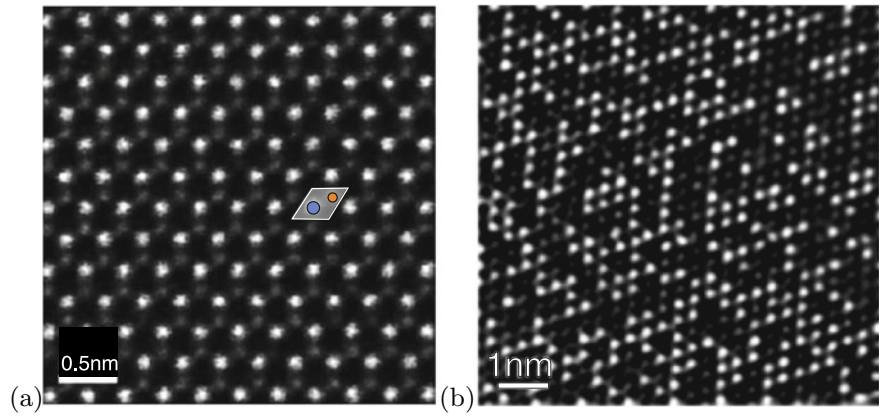

Fig. 13.12 **a** STEM-ADF image of a MoS_2 monolayer; a unit cell with Mo (S) atom shown in *blue* (*orange*) is overlaid (cf. Fig. 13.1a). Reprinted (with adaptation) with permission from [1275]. ©2013 American Chemical Society. **b** STEM image (Fourier filtered) of a $Mo_{0.47}W_{0.53}S_2$ monolayer. The bright (dark) spots relate to W (Mo) atoms. Reprinted (with adaptation) with permission from [1279], ©2013 ACS

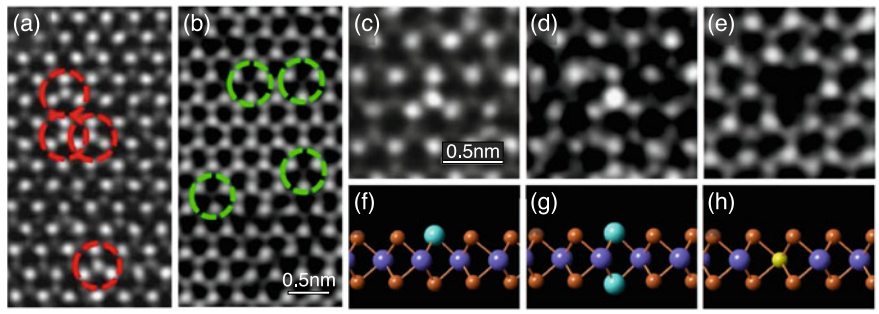

Fig. 13.13 Various point defects (vacancies and antisites) in MoS_2 monolayer as revealed by TEM (**a**)–(**e**) together with atomic models (**f**)–(**h**). **a** S vacancy (V_S), **b** S divacancy (V_{S2}), **c** Mo on S site (Mo_S), **d** 2 Mo on 2 S sites ($Mo2_{S2}$), **e** S on Mo site (S_{Mo}). Adapted from [1280], reprinted under Creative Commons Attribute (CC BY 4.0) license

values [1286, 1287]. The dispersion of 2D MoS_2 [1288] (Fig. 13.15) is quite similar to that of bulk material [1287, 1289]. Of course, due to the mass difference between Mo and S, a clear gap exists between acoustic and optical phonons (which is absent for graphene, cmp. Fig. 13.3a).

13.2.2 Band Structures

The band structure of a h-BN monolayer has been calculated to be indirect [1290]. In Fig. 13.16, the band structure for a typical TMDC is depicted for a monolayer, a bilayer and bulk material. The latter features an indirect band structure with the valence band maximum at the Γ-point and the conduction band minimum about half the way to the K-point. Similar band structures are found for multi-layers down to 2. However, for a single layer the band gap is direct at the K-points. The possible optical transitions are indicated in Fig. 13.16 as arrows. For the single layer, the direct transition has a lower energy than the indirect one; in a bilayer it is vice versa. Generally, the band gap increases with decreasing number of layers; this can be understood by thinking about the slab being a quantum well surrounded by a vacuum 'barrier'.

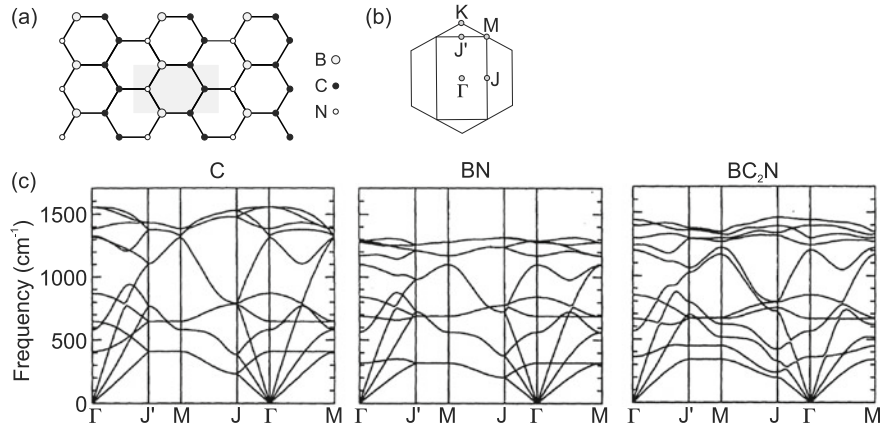

Fig. 13.14 **a** Crystal structure of BC_2N with unit cell indicated. **b** Brillouin zone of BC_2N (*rectangle*) and C, BN (*hexagon*, cmp. Fig. 13.1b). **c** Phonon dispersion of graphene (C) and BN- and BC_2N-sheets. Adapted from [1285]

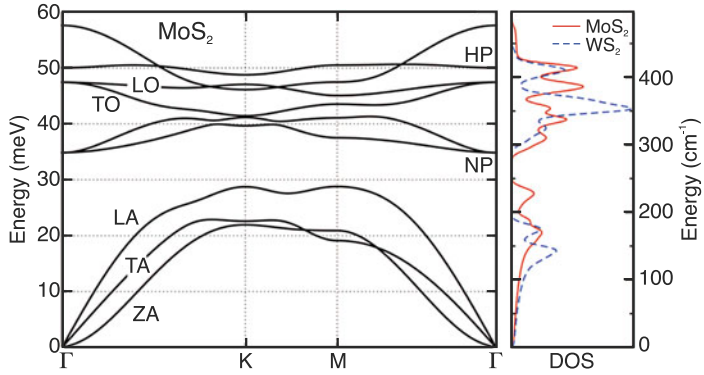

Fig. 13.15 Phonon dispersion of MoS_2 monolayer. ZA: out-of plane acoustic mode, NP: non-polar optical modes, HP: homopolar modes. On the right, the phonon density of states (DOS) is shown for Mo_2 (*red solid line*) and for WS_2 (*blue dashed line*) in comparison. Dispersion adapted from [1288], DOS adapted from [1287]

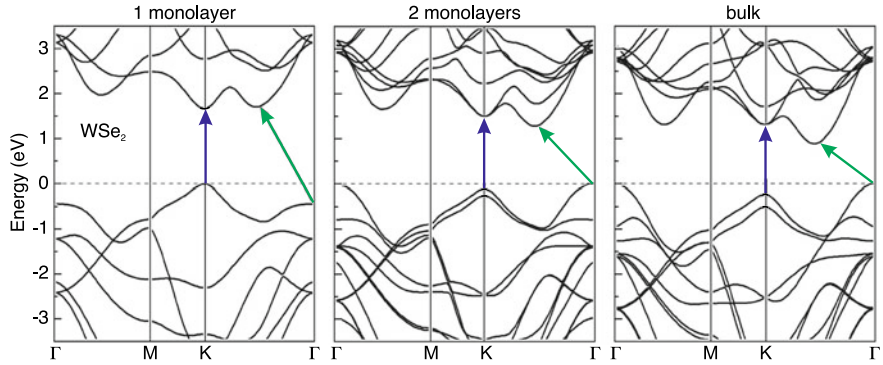

Fig. 13.16 Band structure of monolayer, bilayer and bulk WSe_2. The *blue* (*green*) *arrows* indicate the direct (indirect) band-band transitions. Based on [1272]

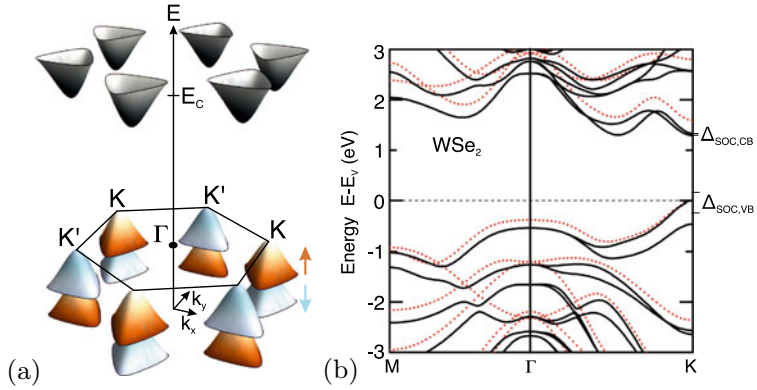

Fig. 13.17 **a** Schematic three-dimensional view of (unsplit) conduction band minima (*grey*) and spin-split valence band maxima with opposite (*red*: up, *blue*: down) spin orientation. **b** Relativistic band structure of 2H-WSe_2 (*red dots* show band structure without inclusion of spin-orbit splitting) with spin-splittings of conduction and valence band indicated. Adapted from [1296], reprinted with permission, ©2011 APS

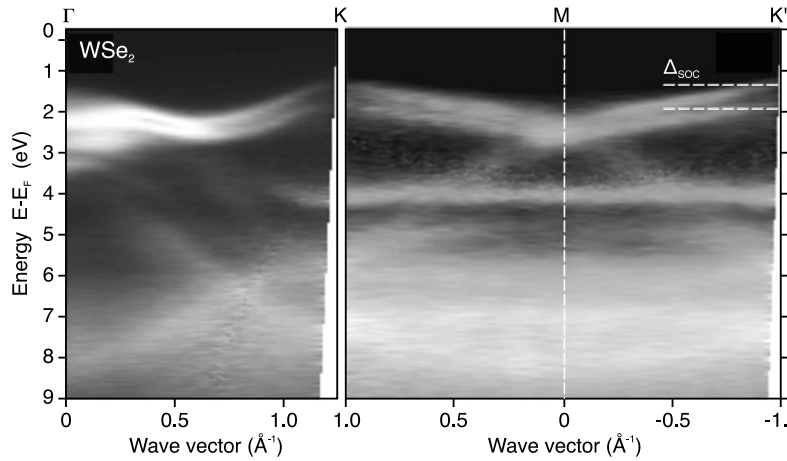

Fig. 13.18 ARPES measurement of the band structure of monolayer WSe_2. The *horizontal dashed white lines* indicate the spin-orbit splitting $\Delta_{SOC} = 513(10)$ meV of the top of the valence band. Adapted from [1297], reprinted with permission, ©2015 IOP Publishing

The lack of inversion symmetry results in a splitting of the electronic bands due to spin-orbit interaction. This effect is particularly strong in the valence band. Splitting energies Δ_{SOC} from fully relativistic calculations have been predicted for various 2H-MX_2 systems [1292, 1293, 1296], ranging between about 150 meV (MoS_2) and 500 meV (WTe_2). For WSe_2, an experimental value of about 500 meV has been found [1297] (Fig. 13.18). For the same materials, the spin-splitting in the conduction band[5] is an order of magnitude smaller in the range of 3–50 meV [1292, 1293]. Because of time reversal symmetry, the spin-splitting (cf. Sect. 6.2.4) of the bands at K and K' has opposite sign as visualized in Fig. 13.17a; this property is termed 'spin-valley coupling'.

[5]The splitting is negative (positive) for MoX_2 (WX_2) compounds, i.e. the lowest conduction band at the K-point is spin up (down) [1292, 1294]; the valence band maximum at K is spin up for all cases.

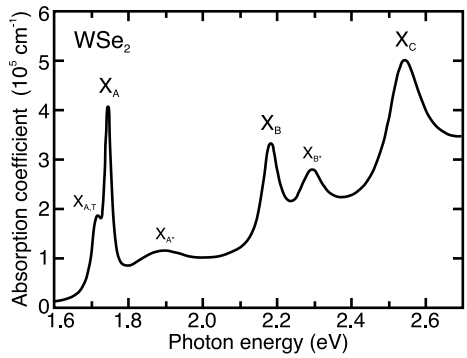

Fig. 13.19 Absorption spectrum of WSe_2 monolayer (derived from reflectance spectrum). $X_{A,B}$ (X_{A,B^*}) denote the ground state (excited states) of the A- and B-exciton, respectively. $X_{A,T}$ at the low energy side denotes a trion. X_C denotes a further transition discussed further in [1299]. Based on data from [1298]

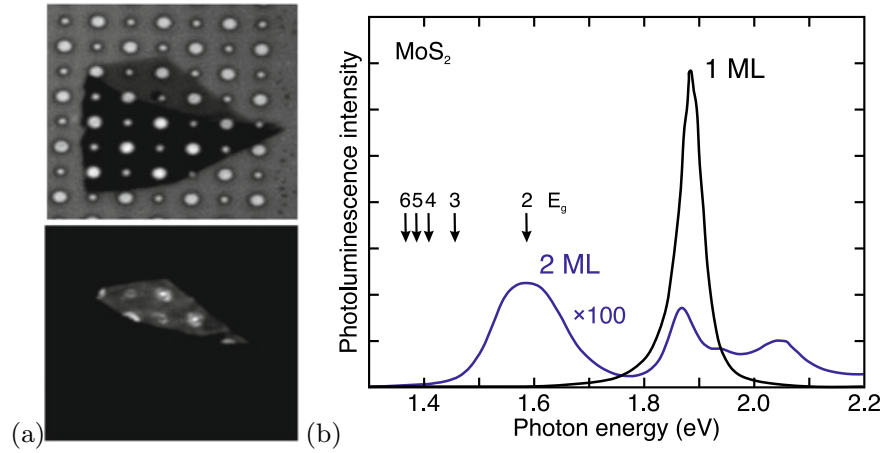

Fig. 13.20 **a** *Top*: Optical image of MoS_2 crystal on a silicon substrate with 1.0 and 1.5 μm diameter holes. *Bottom*: Photoluminescence intensity image of the same sample. The freely suspended parts of the single layer exhibit the highest intensity. **b** Photoluminescence spectra (excited at 532 nm) detected from regions with monolayers and bilayers, respectively. The arrows denote the positions of the (indirect) transitions for 2–6 layers. Adapted from [1291]

13.2.3 Optical Properties and Valley Polarization

The absorption spectrum of a WSe_2 monolayer is shown in Fig. 13.19 as reported in [1298]; various excitonic transitions are labeled that are discussed further below. The A- and B-excitons are formed from the upper and lower state of the spin-split valence band, respectively.

The direct-to-indirect transition of the band structure for monolayer and multiplayer TMDC can be directly observed from the photoluminescence. For MoS_2, the single layer exhibits a 2–3 orders of magnitude higher luminescence intensity (Fig. 13.20a) than any multilayer sample since no phonons are needed for the optical band-band transition. The direct transition is at about 1.9 eV; the indirect band gap decreases monotonously and discretely from about 1.6 eV for a bilayer, via that of 3, 4, 5 or 6 layers (Fig. 13.20b) to that of bulk material ($E_g \approx 1.3$ eV) [1291].

The K- and K'-point pseudo-spin together with the spin-orbit interaction leads to spin-polarized bands as shown schematically in Fig. 13.22a. If excited with polarized light, optical absorption occurs between bands of the same spin orientation. In the absence of any inter-valley scattering, optical

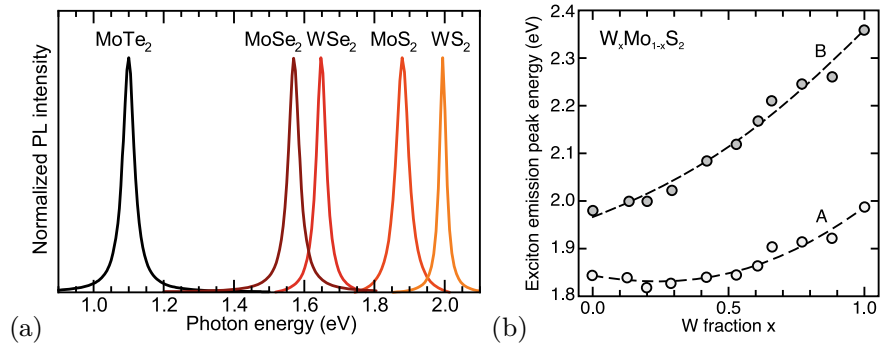

Fig. 13.21 **a** Photoluminescence spectra (at room temperature) of MoS_2, WS_2, $MoSe_2$, WSe_2, and $MoTe_2$ monolayers as labeled. From [1300], with permission. **b** Transition energies of A and B excitons in $W_xMo_{1-x}S_2$ alloy monolayers as a function of composition (spectra were excited at 514.5 nm for x =0-0.61 and at 457.9 nm for x =0.66-1). The *dashed lines* are fits with bowing parameters $b_A = 0.25(4)$ eV and $b_B = 0.19(6)$ eV. Based on data from [1279]

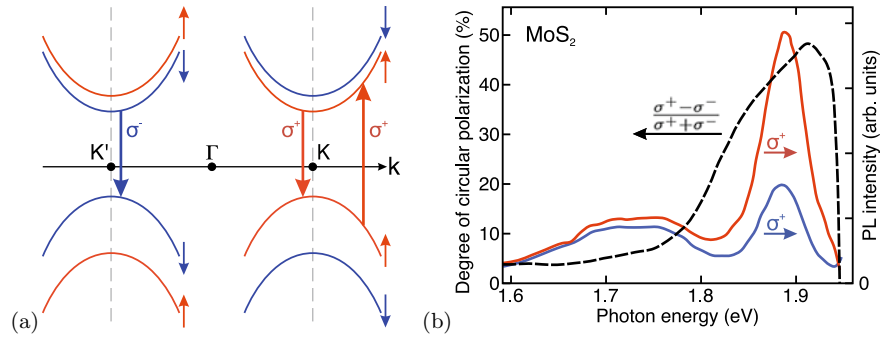

Fig. 13.22 **a** Schematic band structure of MoS_2 monolayer around the K- and K'-point with spin-splitting (band order according to [1294]). Circularly polarized absorption and recombination processes are shown. **b** Circularly polarized detected photoluminescence ($T = 83$ K) from MoS_2 monolayer (*red*: σ^+, *blue*: σ^-) after excitation with σ^+-polarized light at 1.96 eV (at the right end of the energy scale). The degree of circular polarization, $(\sigma^+ - \sigma^-)/(\sigma^+ + \sigma^-)$ is depicted as black curve with the left-hand scale. Adapted from data in [1302]

transitions are expected with a high degree of circular polarization [1301], leading to large dichroism effects (without magnetic ions). However, a maximum degree of circular polarization of about 50% was found in [1302] for MoS_2 excited with circularly polarized light (Fig. 13.22b). The inter-valley dynamics reducing the polarization effects depends on the time scales of scattering and recombination which both can be in the range of several ps [1303]. The two oppositely polarized peaks in Fig. 13.22b have the same peak energy as expected from time-reversal symmetry; a magnetic field perpendicular to the layer will lift this degeneracy and introduce a K-K' splitting (valley Zeeman effect) [1304, 1305] (Fig. 13.21).

13.2.4 Excitons

The properties of excitons are particular in 2D materials. The purely two-dimensional hydrogen problem [1306, 1307] leads to a series of bound states $E = -R/(n - 1/2)^2$, where R denotes the Rydberg energy and $n = 1, 2, \ldots$ as usual. However, for the excitons in 2D material, the case of a stepwise changing dielectric constant ϵ, leading to image charge effects, as known from quantum well het-

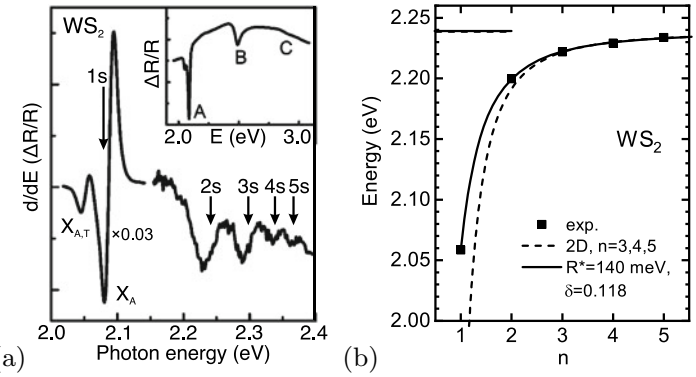

Fig. 13.23 **a** Differential reflection contrast spectrum of WS_2 monolayer (*inset*: reflection contrast). X_A denotes the A-exciton, $X_{A,T}$ at the low energy side the trion. Based on data from [1311]. **b** Experimental transition energies (*circles*) for WS_2 from magneto-optical data [1313] (cf. Fig. 15.13) with fits using the modified hydrogen model $\propto 1/(n+\delta)^2$ (*solid line*) and a 2D hydrogen model with constant dielectric function fitted to the $n = 3, 4, 5$ levels (both theories displayed for continuous n). The (very similar) band gap $E_g = 2.239\,\text{eV}$ for the two models is shown as *lines* on the left

erostructures [1188] (cmp. Sect. 12.3.2), must be considered. The thin slab is surrounded by vacuum which gives a huge contrast in ϵ. Even when packed, as often done in experiments, between other layers such as h-BN ($\epsilon \approx 4.5$) or on a substrate, the contrast in dielectric constant is very large.[6]

This problem has been treated theoretically first in [1308, 1309] and recently rigorously in [1310]. The exciton binding energy is typically increased by this effect to several 100 meV. Also, the strongly anisotropic dielectric surrounding affects different quantum states differently, leading to non-hydrogenic terms in the exciton spectrum [1311] (Fig. 13.23). Schematics of the field lines for the 1s- and 2s-states are depicted in Fig. 13.24c, motivating that the anisotropic dielectric environment acts differently on these states. The higher the quantum number n is, the lower is the average dielectric constant 'seen' by the 2D-exciton. In the example of excitons in WS_2, the effective dielectric constant changes from about 5 for the 1s state to 2.5 for the 2s state to values close to 1 for the higher states [1311].

In [1312] it has been discussed that the exciton level can be well described by the formula $E_n = E_g - R^*/(n-\delta)^2$, with δ being a fitting parameter. Such parameter δ is known as 'quantum defect' in the description of alkali spectra [1314]. For WSe_2 (embedded between h-BN layers), $E_g = 1.873\,\text{eV}$, $R^* = 140.5\,\text{meV}$ and $\delta = 0.083$ has been found [1312]. The data from [1313] for WS_2 (also sandwiched between slabs of exfoliated hexagonal h-BN) can be fitted with $E_g = 2.239\,\text{eV}$, $R^* = 140.4\,\text{meV}$ and $\delta = 0.118$ (Fig. 13.23b).

The calculated plane-view of the electron wave function of the exciton ground state (A-exciton) in a MoS_2 monolayer is depicted in Fig. 13.24a; the contributions to the exciton wave packet stem, from around the K-points as shown in Fig. 13.24b [1299]. Magneto-optical spectroscopy of 2D excitons and the Zeeman splittings and diamagnetic shifts up to the $5s$ state in WS_2 and $Mo(S,Se,Te)_2$ monolayers are reported in [1313] and (on Si/SiO_2 substrate) [1315]; the g-factor (cf. Sect. 15.2) of the exciton is very close to $4\,\mu_B$ (cf. Fig. 15.13d), a fact that is under theoretical consideration [1316]. Charged excitons have been discussed in [1317, 1318]. The influence of various surrounding media to the TMDC on the dielectric screening has been investigated theoretically [1319] and experimentally [1320].

[6] In QW heterostructures, the differences in ϵ are typically around 1 or smaller [1188].

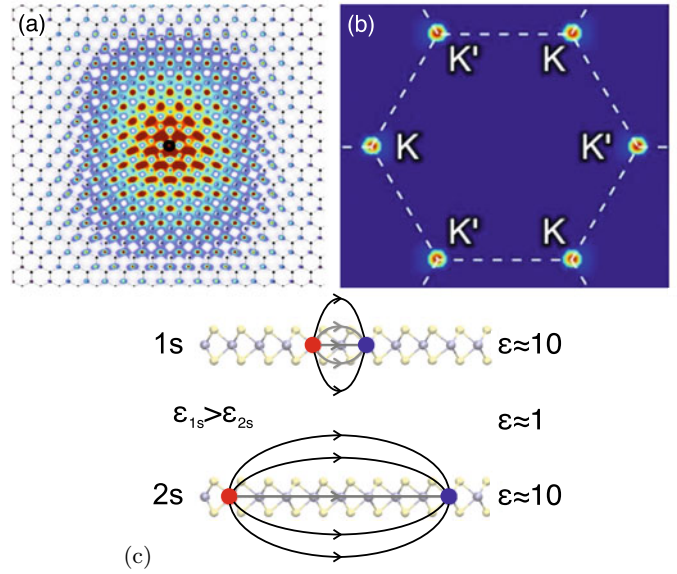

Fig. 13.24 Plane-view of the electron wave function of the exciton ground state in MoS_2 monolayer in **a** real space and **b** $\boldsymbol{k}$-space. Adapted from [1299], reprinted with permission, ©2013 APS. **c** Schematic 1s and 2s exciton wave functions with different sensing of the low-ϵ environment

13.3 Van-der-Waals Heterostructures

Let's recall that graphite is a stacked arrangement of graphene layers. It is called the 'Bernal'-phase or -stacking and relates to the AB- or 2H-stacking like in a hcp crystal (Fig. 13.25a). Other meta-stable arrangements are the AA'-stackings (twisted bilayer graphene), in which the crystallographic axes of the two layers have an arbitrary angle ϑ between zero and 30° as depicted in Fig. 13.25b); the stacking vor $\vartheta = 0$ is also termed AA. Electronic properties depend on the twist angle [1321]. A refined theory considering the super-periodicities (moiré pattern) of interlayer hopping potential has been reported in [1322, 1323]. The different stackings can be distinguished, e.g., in infrared spectroscopic imaging [1324].

As an extension of this concept, van-der-Waals heterostructures been conceived [1326, 1327] which consist of vertically stacked atomic sheets of various 2D materials, a kind of molecular LEGO™ (Fig. 13.26a). Virtually any combination is possible for various electronic, sprintronic and photonic applications [1329, 1330]. An advantage is the well controlled tunneling effect by the present exact layer thicknesses in the device.

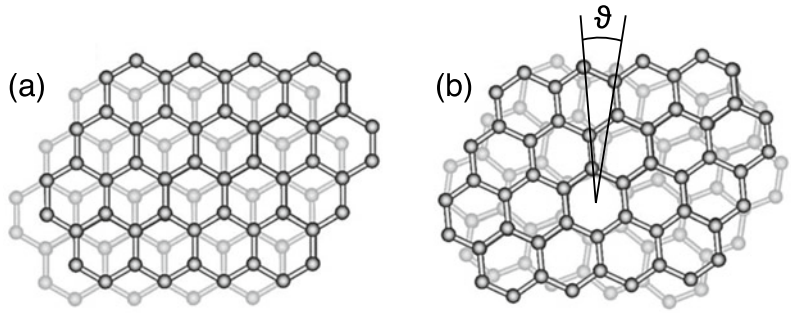

Fig. 13.25 Vertical stacking phases of graphene in **a** AB-type, Bernal-stacking and **b** AA'-type, non-Bernal stacking. The rotation angle ϑ is indicated. Adapted from [1325]

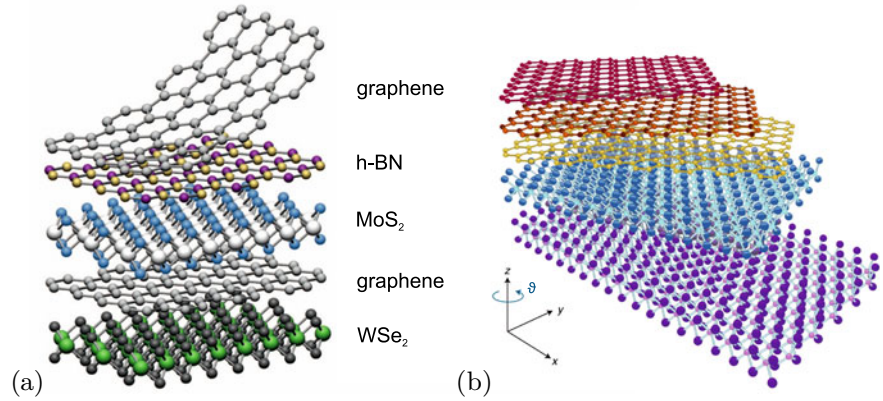

Fig. 13.26 **a** Example of van-der-Waals heterostructure from various 2D materials as proposed in [1326]. Reprinted with permission, ©2013, Springer Nature. **b** Van-der-Waals heterostructure with twisted layers. Adapted from [1328], reprinted with permission, ©2018, Springer Nature

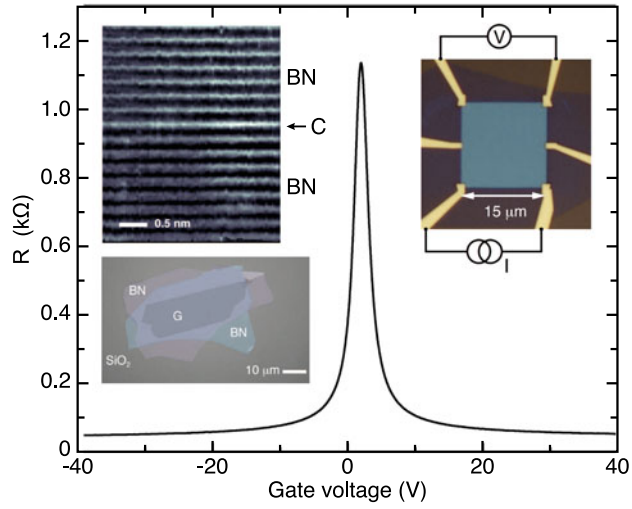

Fig. 13.27 Resistance of BN-graphene-BN van-der-Waals heterostructure (insets show optical image and cross section TEM as well as the device and its schematic measurement scheme). Adapted from [1331]

The field effect for a graphene layer between BN flakes is shown in Fig. 13.27. The measured mobility (at room temperature) is in the range of $10^5\,\mathrm{cm}^2/\mathrm{Vs}$ for a 2D carrier density below $1 \times 10^{12}\,\mathrm{cm}^{-2}$ and thus larger than values achieved for InSb or InAs [1331]. Van-der-Waals heterostructures of boron nitride and graphene are reviewed in [1332].

The effect of surrounding media via the modified dielectric screening on excitons has been mentioned already above [1319, 1320]. Encapsulation by h-BN monolayers can enhance the luminescence yield and reduce the recombination time constant of a TMDC monolayer, as demonstrated in [1334] for a three monolayer h-BN/WS_2/h-BN heterostructure.

Generally, in van-der-Waals heterostructures, the weak interlayer bonding allows a new degree of freedom, the twist angle ϑ (cf. Fig. 13.25b for twist of two graphene layers) between two 2D crystals (Fig. 13.26b). The situation is similar to the twist boundary between two grains (Sect. 4.4.3). This rotation causes the formation of moiré patterns that are directly observable in STM images as depicted in Fig. 13.28. The physical properties of the heterostructure can drastically depend on the twist angle [1335]. A prominent consequence is the periodic modification of the energy landscape for

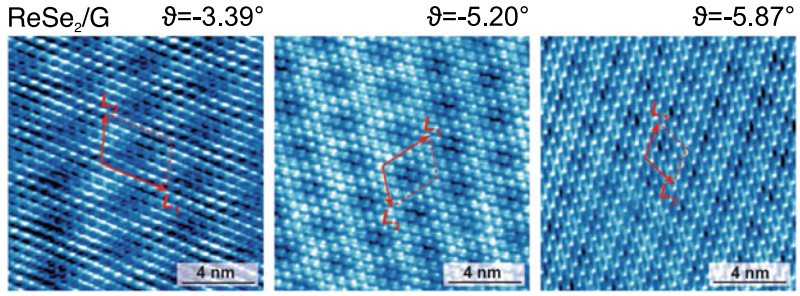

Fig. 13.28 STM images of $ReSe_2$ monolayers on graphene. The twist angle ϑ (cmp. Fig. 13.26b), as deducted from comparison with theoretical calculations, is indicated. The *red arrows* indicate the moiré pattern's periodicity. Adapted from [1333], reprinted unter Creative Commons Attribute (CC BY-NC 4.0) license

excitons leading to localization and modification of spectra [1336]. A particularly intriguing effect is the occurrence of superconductivity with a critical temperature of up to 1.7 K for a graphene bilayer with the 'magic' twist angle of $\vartheta \approx 1.1°$ and specific (gate-controlled) carrier densities in the range of $(1–2)\times 10^{12}\,\mathrm{cm}^{-2}$ [1337].

Chapter 14
Nanostructures

The principles of physics, as far as I can see, do not speak against the possibility of maneuvering things atom by atom.

R.P. Feynman, 1959 [1338]

Abstract One-dimensional nanostructures (quantum wires) and zero-dimensional ones (quantum dots) are discussed with regard to their various fabrication methods and the tunable physical properties in such systems. Main effects covered are the modified density of states, confined energy levels, (envelope) wave-function symmetry and the resulting novel electrical and optical properties.

14.1 Introduction

When the structural size of functional elements enters the size range of the de Broglie matter wavelength, the electronic and optical properties are dominated by quantum-mechanical effects. The most drastic impact can be seen from the density of states (Fig. 14.1). The quantization in a potential is ruled by the Schrödinger equation with appropriate boundary conditions. These are simplest if an infinite potential is assumed. For finite potentials, the wavefunction leaks out into the barrier. Besides making the calculation more complicated (and more realistic), this allows electronic coupling of nanostructures. Via the Coulomb interaction, a coupling is even given if there is no wavefunction overlap. In the following, we will discuss some of the fabrication techniques and properties of quantum wires (QWR) and quantum dots (QD). In particular for the latter, several textbooks can also be consulted [1339, 1340].

14.2 Quantum Wires

14.2.1 V-Groove Quantum Wires

Quantum wires with high optical quality, i.e. high recombination efficiency and well-defined spectra, can be obtained by employing epitaxial growth on corrugated substrates. The technique is shown schematically in Fig. 14.2. A V-groove is etched, using, e.g., an anisotropic wet chemical etch, into a GaAs substrate. The groove direction is along $[1\bar{1}0]$. Even when the etched pattern is not very sharp on the bottom, subsequent growth of AlGaAs sharpens the apex to a self-limited radius ρ_l of the order

M. Grundmann, *The Physics of Semiconductors*, Graduate Texts in Physics,
https://doi.org/10.1007/978-3-030-51569-0_14

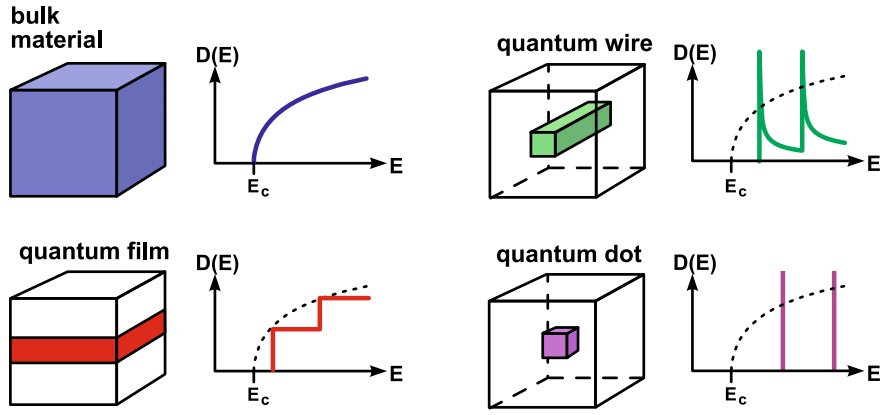

Fig. 14.1 Schematic geometry and density of states for 3D, 2D, 1D and 0D electronic systems

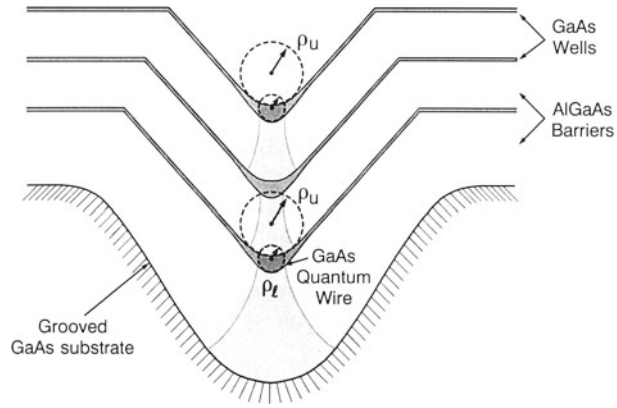

Fig. 14.2 Schematic cross section of a GaAs/AlGaAs heterostructure grown on a channeled substrate, illustrating the concept of self-ordered quantum-wire fabrication. Adapted from [1341], reprinted with permission, ©1992, Elsevier Ltd

of 10 nm. The side facets of the groove are {111}A. Subsequent deposition of GaAs leads to a larger upper radius $\rho_u > \rho_l$ of the heterostructure. The GaAs QWR formed in the bottom of the groove is thus crescent-shaped as shown in Fig. 14.3a. A thin GaAs layer also forms on the side facets (sidewall quantum well) and on the top of the ridges. Subsequent growth of AlGaAs leads to a resharpening of the V-groove to the initial, self-limited value ρ_l. The complete resharpening after a sufficiently thick AlGaAs layer allows vertical stacking of crescent-shaped QWRs of virtually identical size and shape, as shown in Fig. 14.3b. In this sense, the self-limiting reduction of the radius of curvature and its recovery during barrier-layer growth leads to self-ordering of QWR arrays whose structural parameters are determined solely by growth parameters. The lateral pitch of such wires can be down to 240 nm.

To directly visualize the lateral modulation of the band gap, a lateral cathodoluminescence (CL) linescan perpendicular across the wire is displayed in Fig. 14.4. In Fig. 14.4a, the secondary electron (SE) image of the sample from Fig. 14.3a is shown in plan view. The top ridge is visible in the upper and lower parts of the figure, while in the middle the sidewalls with the QWR in the center are apparent. In Fig. 14.4b, the CL spectrum along a linescan perpendicular to the wire (as indicated by the white line in Fig. 14.4a) is displayed. The x-axis is now the emission wavelength, while the y-axis is the lateral position along the linescan. The CL intensity is given on a logarithmic scale to display the full dynamic range. The top QW shows almost no variation in band gap energy ($\lambda = 725$ nm); only directly at the edge close to the sidewall does a second peak at lower energy ($\lambda = 745$ nm) appear, indicating a thicker region there. The sidewall QW exhibits a recombination wavelength of 700 nm at the edge to the top QW, which gradually increases to about 730 nm at the center of the V-groove. This directly

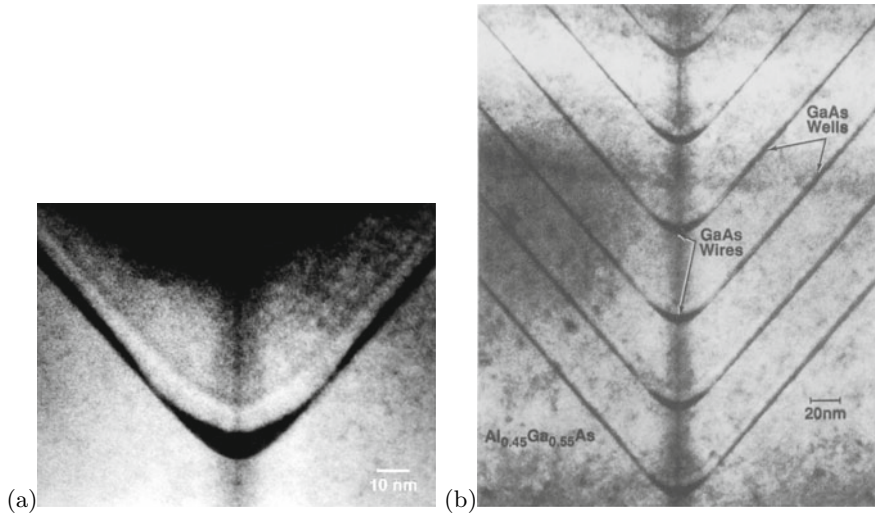

Fig. 14.3 **a** Transmission electron microscopy cross-sectional image of a crescent-shaped single GaAs/AlGaAs quantum wire. From [1342], reprinted with permission, ©1994 IOP. (**b**) TEM cross-sectional image of a vertical stack of identical GaAs/AlGaAs crescent-shaped QWRs. From [1341], reprinted with permission, ©1992, Elsevier Ltd

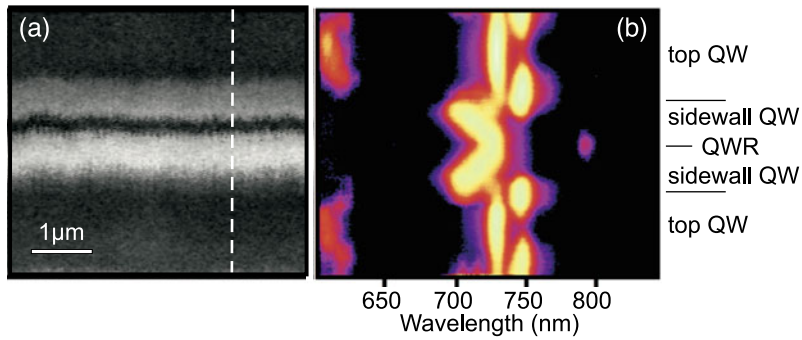

Fig. 14.4 **a** Plan-view SE image of single QWR, showing top and sidewall with QWR in the center. The *white dashed line* indicates the position of the linescan on which the CL spectra linescan **b** has been taken at $T = 5\,\mathrm{K}$. The CL intensity is given on a logarithmic false color scale to display the full dynamic range as a function of wavelength and position. Adapted from [1342], reprinted with permission, ©1994 IOP

visualizes a linear tapering of the sidewall QW from about 2.1 nm thickness at the edge to 3 nm in the center. The QWR luminescence itself appears at about 800 nm.

After fast capture from the barrier into the QWs and, to a much smaller extent corresponding to its smaller volume, into the QWR, excess carriers will diffuse into the QWR via the adjacent sidewall QW and the vertical QW. The tapering of the sidewall QW induces an additional drift current.

14.2.2 Cleaved-Edge Overgrowth Quantum Wires

Another method to create quantum wires of high structural perfection is cleaved-edge overgrowth (CEO) [1343], shown schematically in Fig. 14.5. First, a layered structure is grown (single or multiple quantum wells or superlattice). Then, a {110} facet is fabricated by cleaving (in vacuum) and epitaxy

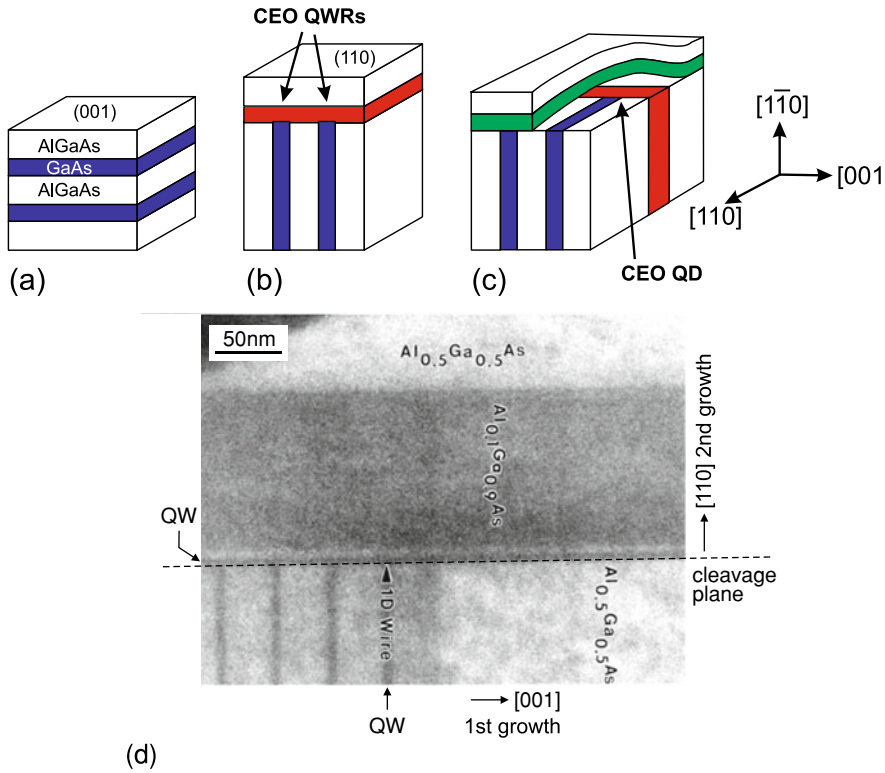

Fig. 14.5 Principle of CEO quantum wires and 2-fold CEO quantum dots. Part (**a**) depicts a layered structure (quantum wells or superlattice, *blue*), (**b**) describes the growth on the cleaved facet used for fabrication of quantum wires. In (**c**) a second cleave and growth on top of the plane allows the fabrication of quantum dots. From [1344]. (**d**) Cross-sectional TEM image of CEO GaAs/AlGaAs quantum wires. Two quantum wells (QW) and the QWR at their junction are labeled. The first epitaxy was from left to right. The second epitaxy step was on top of the cleavage plane (*dashed line*) in the upward direction. Adapted from [1345], reprinted with permission, ©1997 APS

is continued on the cleaved facet. At the junctures of the {110} layer and the original quantum wells QWRs form. Due to their cross-sectional form they are also called *T-shaped* QWRs. A second cleave and another growth step allow fabrication of CEO quantum dots [1344, 1345] (Fig. 14.5c).

14.2.3 Nanowhiskers

Whiskers are primarily known as thin metal spikes and have been investigated in detail [1346]. Semiconductor whiskers can be considered as (fairly short) quantum wires. They have been reported for a number of materials, such as Si, GaAs, InP and ZnO [1347]. A field of ZnO whiskers is shown in Fig. 14.6. If heterostructures are incorporated along the whisker axis [1348], quantum dots or tunneling barriers can be created (Fig. 14.7a). The growth mode relies often a VLS (vapor-liquid-solid) mechanism in which the wire materials are first incorporated into a liquid catalyzer (most often gold) drop at the tip and then used to build up the nanocrystal. In [1349], the layer-by-layer growth of a GaAs nanowire via this mechanism has been observed in-situ by TEM (Fig. 14.7b) and is also available as an impressive video. Another nanowire growth mechanism is the VSS (vapor-solid-solid) mechanism that works without liquid drop on top of the wire.

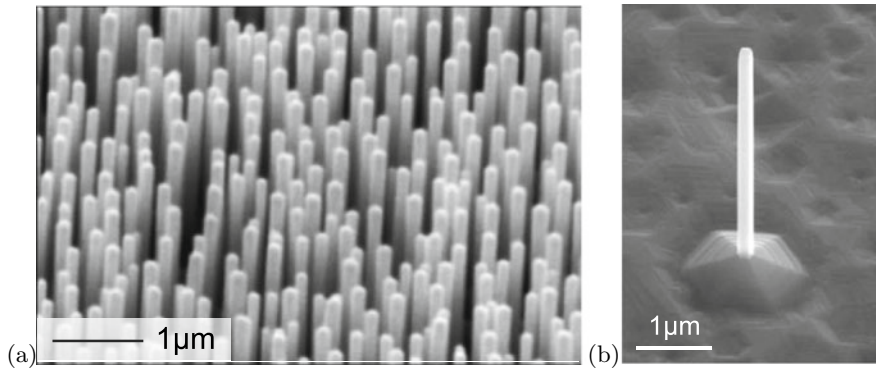

Fig. 14.6 **a** Array of ZnO nanowhiskers on sapphire, fabricated using thermal evaporation. Adapted from [1353]. **b** Single, free-standing ZnO nanowire fabricated using PLD. Adapted from [1354]

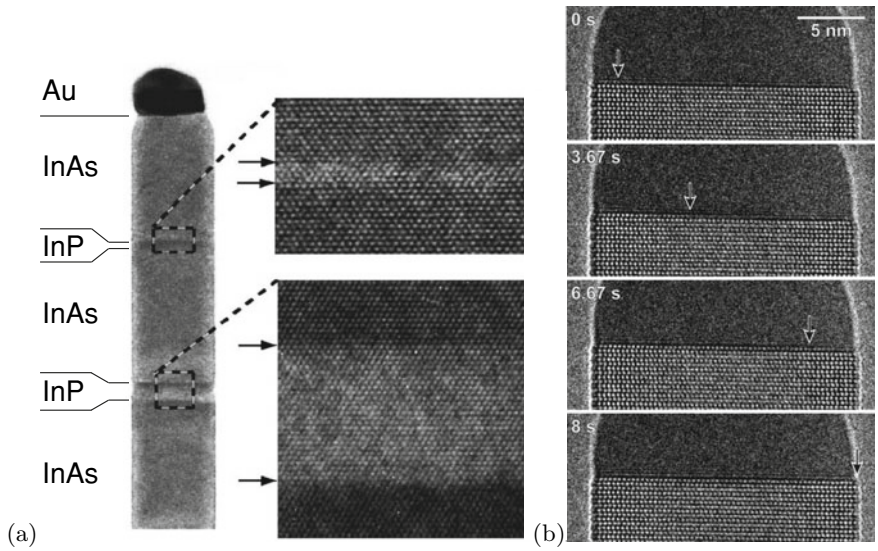

Fig. 14.7 **a** TEM image of a part of an InAs whisker 40 nm in diameter that contains InP barriers. The zooms show sharp interfaces. On top of the whisker is a gold droplet from the so-called vapor–liquid–solid growth mechanism. The whisker axis is [001], the viewing direction is [110]. Adapted from [1348], reprinted with permission, ©2002 AIP. **b** Subsequent growth stages of the tip of a GaAs nanowire with Au cap; times at which (in-situ) TEM image has been taken are labelled. The *arrows* indicate the position of the growth front. Adapted from [1349], reprinted with permission, ©2018 APS

Such nanocrystals can also act as a nanolaser [1350, 1351]. In ZnO nanowhiskers the conversion of mechanical energy into electrical energy has been demonstrated [1352] based on the piezoelectric effect (Sect. 16.4).

The critical thickness h_c in nanowire heterostructure is strongly modified from the 2D situation (Sect. 5.4.1). Based on the strain distribution of a misfitted slab in a cylindrical wire [1355] the dependence of critical thickness on the nanowhisker radius r was developed [1356, 1357]. For given misfit ϵ there is a critical radius r_c for which h_c is infinite for $r < r_c$ (Fig. 14.8).

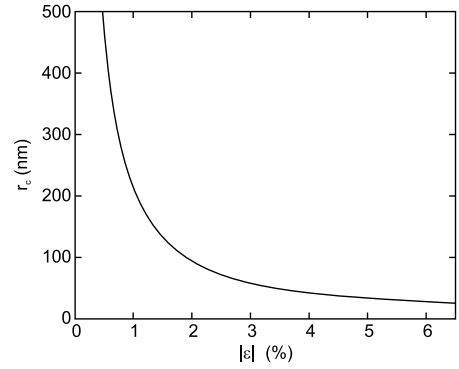

Fig. 14.8 Critical radius r_c above which an infinitely thick layer with misfit ϵ grows coherently on a cylindrical nanowire (relaxation by 60° dislocations, $b = 0.4$ nm, $\nu = 1/3$). Adapted from [1357]

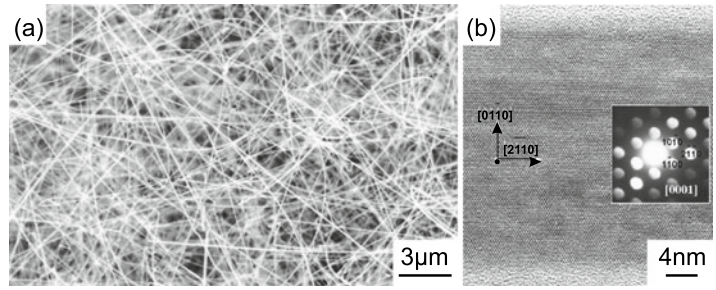

Fig. 14.9 **a** SEM image of an ensemble of ZnO nanobelts. **b** HRTEM image of a single ZnO nanobelt, viewing direction is [00.1]. The *inset* shows the diffraction pattern. Adapted from [1358], reprinted with permission, ©2004 AIP

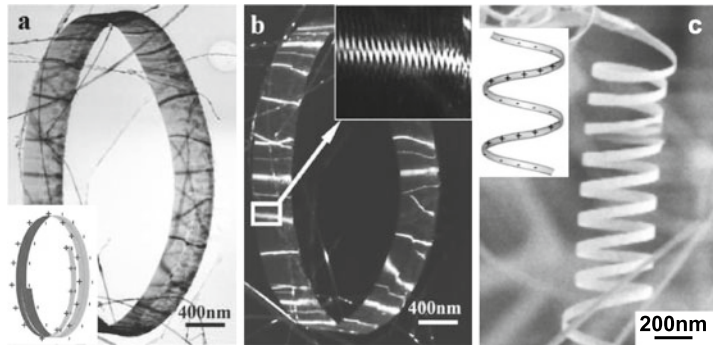

Fig. 14.10 **a** Bright field and **b** dark field TEM image of a ZnO nanoring formed by the 'slinky'-like growth of a nanobelt. **c** SEM image of an open ZnO nanospiral. The *insets* in (**a**, **c**) show schematically the surface charge distribution. Adapted from [1359], ©2006 IOP

14.2.4 Nanobelts

A number of belt-shaped nanostructures has been reported [1347]. These are wire-like, i.e. very long in one dimension. The cross-section is rectangular with a high aspect ratio. In Fig. 14.9a ZnO nanobelts are shown. The wire direction is $[2\bar{1}.0]$. The large surface is (00.1), the thickness of the belt extends in [01.0]-direction. High resolution transmission microscopy (Fig. 14.9b) shows that these structures are defect-free. The pyroelectric charges on the ZnO (0001) surfaces (Sect. 16.2) lead to the formation of open (Fig. 14.10c) spirals. Closed spirals (Fig. 14.10a) occur if the short dimension is along [00.1] and alternating charges become compensated in a 'slinky'-like ring (Fig. 14.10b).

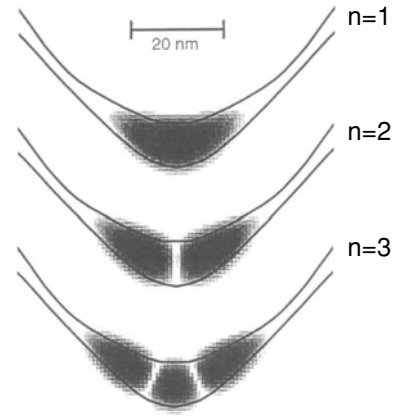

Fig. 14.11 Electron wavefunctions ($|\Psi|^2$ on logarithmic grey scale) for the first three confined levels for the QWR of Fig. 14.3a. From [1342]

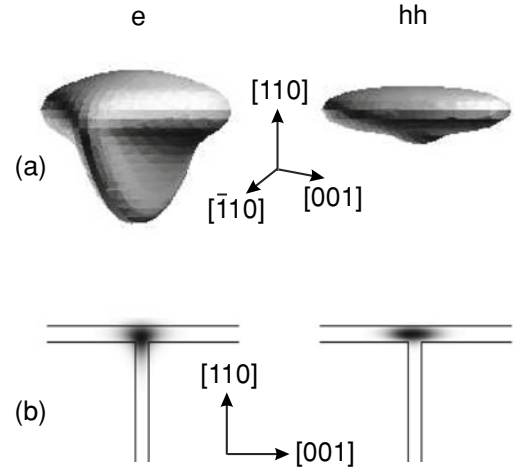

Fig. 14.12 **a** Three-dimensional view of the electron and (heavy) hole part of the excitonic wavefunction in a 4 nm × 5 nm T-shaped $In_{0.2}Ga_{0.8}As/GaAs$ QWR. The orbitals correspond to 70% probability inside. **b** Cross section through the electron and hole orbitals in their center along the wire direction. Reprinted with permission from [1361], ©1998 APS

14.2.5 Quantization in Two-Dimensional Potential Wells

The motion of carriers along the quantum wire is free. In the cross-sectional plane the wavefunction is confined in two dimensions. The simplest case is for constant cross section along the wire. However, generally the cross section along the wire may change and therefore induce a potential variation along the wire. Such potential variation will impact the carrier motion along the longitudinal direction. Also, a twist of the wire along its axis is possible.

In Fig. 14.11, the electron wavefunctions in a V-groove GaAs/AlGaAs QWR are shown. Further properties of V-groove QWRs have been reviewed in [1360]. In Fig. 14.12, the excitonic electron and hole wavefunctions are shown for a (strained) T-shaped QWR.

In Fig. 14.13a the atomic structure of a very thin ZnO nanowhisker with a cross-section consisting of seven hexagonal unit cells is shown. The theoretical one-dimensional band structure [1362] is shown in Fig. 14.13b together with the charge density of the lowest conduction band state (LUMO) and the highest valence band state (HOMO). The band gap is generally too small because of the LDA method used.[1] In [1362] also the properties of nanowires with various diameters are compared. The HOMO at Γ lies only 80 meV above the top of valence band of bulk ZnO, and its position changes little with

[1] The LDA in [1362] yields $E_g = 0.63$ eV for the bulk ZnO band gap; its experimental value is 3.4 eV.

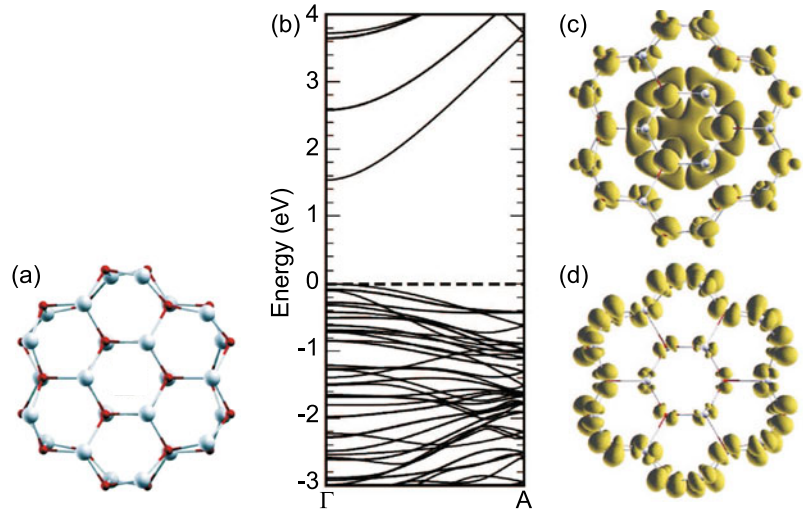

Fig. 14.13 **a** Atomic arrangement of a 1 nm wide ZnO nanowire. **b** Theoretical band structure and charge density of the **c** lowest conduction band and **d** highest valence band state. Adapted from [1362], reprinted with permission, ©2006 AIP

the wire diameter. It is mainly composed by surface oxygen 2p like dangling bonds (Fig. 14.13d). The LUMO (Fig. 14.13c) is delocalized in the whole nanowire, indicating that it is a bulk state. The delocalized distribution is also responsible for the large dispersion of the LUMO from Γ to A. The energy of the LUMO increases substantially with decreasing diameter due to the radial confinement.

14.3 Carbon Nanotubes

14.3.1 Structure

A carbon nanotube (CNT) is a part of a graphene sheet (cf. Sect. 13.1) rolled up to form a cylinder. CNTs were first described as multi-walled nanotubes by Iijima [1363] in 1991 (Fig. 14.14b) and in their single-walled form (Fig. 14.14a) in 1993 [1364]. Reviews can be found in [1247, 1365].

The chirality and diameter of a nanotube are uniquely described by the chiral vector

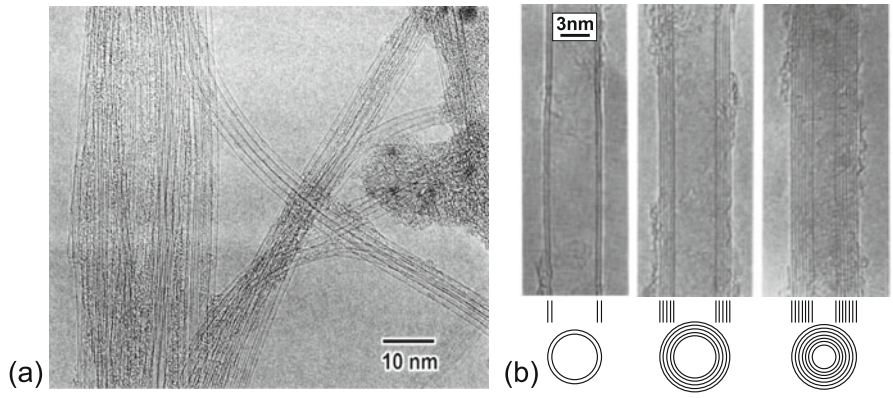

Fig. 14.14 **a** TEM image of single-walled carbon nanotubes (SWNT). **b** TEM images of various multi-walled carbon nanotubes (MWNT). Adapted from [1363], reprinted with permission, ©1991, SpringerNature

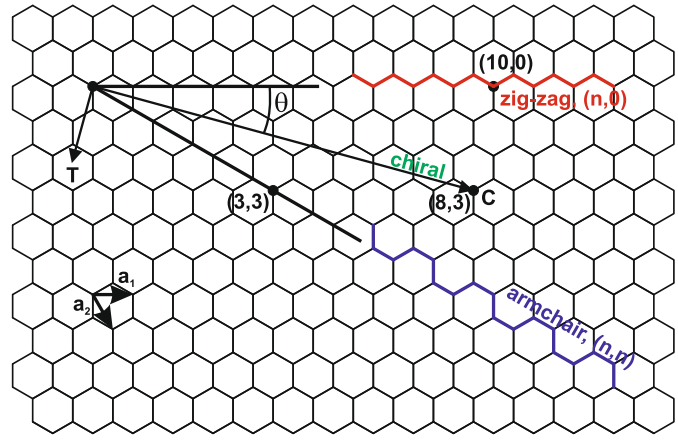

Fig. 14.15 Schematic atomic arrangement in graphene; the C–C bond length is $d_{C-C} = 0.142\,\text{nm}$. Several vectors for making carbon nanotubes (cf. Sect. 14.3) are shown

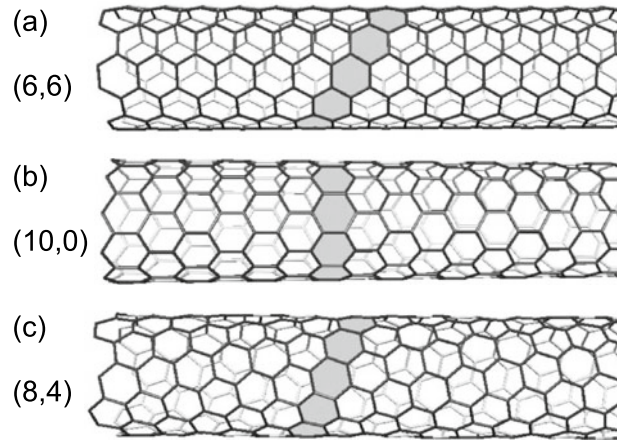

Fig. 14.16 Structure of different types of carbon nanotubes that have similiar diameter of 0.8 nm. **a** Armchair (6, 6), **b** zigzag (8, 0) and **c** chiral symmetry. Adapted from [1247]

$$\mathbf{c}_\text{h} = n_1\,\mathbf{a}_1 + n_2\,\mathbf{a}_2 \equiv (n_1, n_2)\ , \tag{14.1}$$

where $\mathbf{a}_1$ and $\mathbf{a}_2$ are the unit vectors of the graphene sheet. The chiral vector denotes two crystallographic equivalent sites which are brought together along the circumference of the nanotube. The possible vectors are visualized in Fig. 14.15 for $-30° \le \theta \le 0°$. The fiber diameter is given by

$$d = \frac{|\mathbf{c}_\text{h}|}{\pi} = \frac{a}{\pi}\left(n_1^2 + n_1\,n_2 + n_2^2\right)\ , \tag{14.2}$$

with the graphene lattice constant $a = \sqrt{3}\,d_{C-C} = 0.246\,\text{nm}$. Ab-initio calculations show that the diameter becomes a function of the chiral angle below 0.8 nm; deviations from (14.2) are below 2% for tube diameters $d > 0.5\,\text{nm}$ [1366]. The $(n, 0)$ tubes ($\theta = 0$) are termed 'zig-zag' and an example is depicted in Fig. 14.16b. Nanotubes with $\theta = \pm\pi/6$, i.e. of the (n, n) (and $(2n, -n)$) type, are called 'armchair'. All others are termed 'chiral'.

The extension along the wire axis is large compared to the diameter. The tip of a nanotube is part of a buckminster-fullerene type molecule (Fig. 14.17). When the nanotube if formed by rolling a single sheet of graphene (SLG), a single-walled nanotube (SWNT) is formed. A FLG sheet creates a multi-walled nanotube (MWNT). For small number of layers they are called double-walled, triple-walled and so forth.

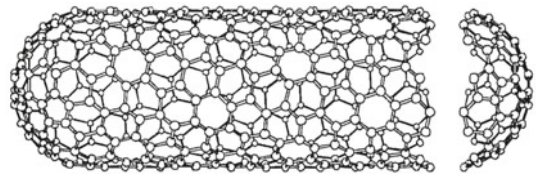

Fig. 14.17 A chiral nanotube (chiral vector is (10, 5), $\theta = -19.11°$) with hemispherical caps at both ends based on an icosahedral C_{140} fullerene. The tube diameter is 1.036 nm. Adapted from [1367]

The mechanical strength of carbon nanotubes is very large. For SWNT Young's moduli of 10^3 GPa have been found experimentally [1368] in agreement with theoretical predictions [1369].

14.3.2 Band Structure

In carbon nanotubes there is some mixing of the $\pi(2p_z)$ and $\sigma(2s \text{ and } 2p_z)$ carbon orbitals due to the radial curvature. This mixing is, however, small and can be neglected near the Fermi level [1370]. The band structure of a nanotube is mainly determined by zone-folding of the graphene band structure. The vector along the (infinitely extended) wire k_z is continuous. The vector $k_\perp$ around the nanotube is discrete with the periodic boundary condition

$$\mathbf{c}_\mathrm{h} \cdot \mathbf{g}_\perp = 2\pi\, m \ , \tag{14.3}$$

where m is an integer. The distance of allowed $k_\perp$-values is (5.5)

$$\Delta k_\perp = \frac{2\pi}{\pi\, d} = \frac{2}{d} \ . \tag{14.4}$$

The character of the nanotube band structure depends on how the allowed k-values lie relative to the graphene Brillouin zone and its band structure. This is visualized in Fig. 14.18. For the case of an armchair tube (n, n), as shown in Fig. 14.18a, the K-point of the graphene band structure always lies on an allowed k-point. Therefore, the nanotube is metallic, i.e. zero-gap, as seen in the bandstructure in Fig. 14.18b. The Dirac point is between Γ and X. For a zig-zag nanotube, the k-space is shown in Fig. 14.18c for a (6, 0) nanotube. The corresponding band structure for a (6, 0) nanotube is also metallic (Fig. 14.18d) with the Dirac point at the Γ point.

In Fig. 14.19c the band structure of another metallic (12, 0) zig-zag nanotube is shown. However, only for (3 m, 0) the K-point is on an allowed state and thus the tube metallic. For the other cases, as shown for the k-space of a (8, 0) nanotube in Fig. 14.19b, this is not the case. The corresponding band structure (Fig. 14.19c for (13, 0)) has a gap and thus the nanotube is a semiconductor. Generally, the condition for a nanotube to be metallic is with an integer m

$$n_1 - n_2 = 3\, m \ . \tag{14.5}$$

There are two semiconducting 'branches' with $\nu = (n_1 - n_2) \bmod 3 = \pm 1$. The tubes with $\nu = +1$ have a small band gap, those with $\nu = -1$ have a larger band gap.

The density of states is a series of one-dimensional DOS, proportional to $\sqrt{E}$ (6.79). It is compared in Fig. 14.20 for a metallic and a semiconducting nanotube. Within 1 eV from the Fermi energy the DOS can be expressed in an universal term [1373].

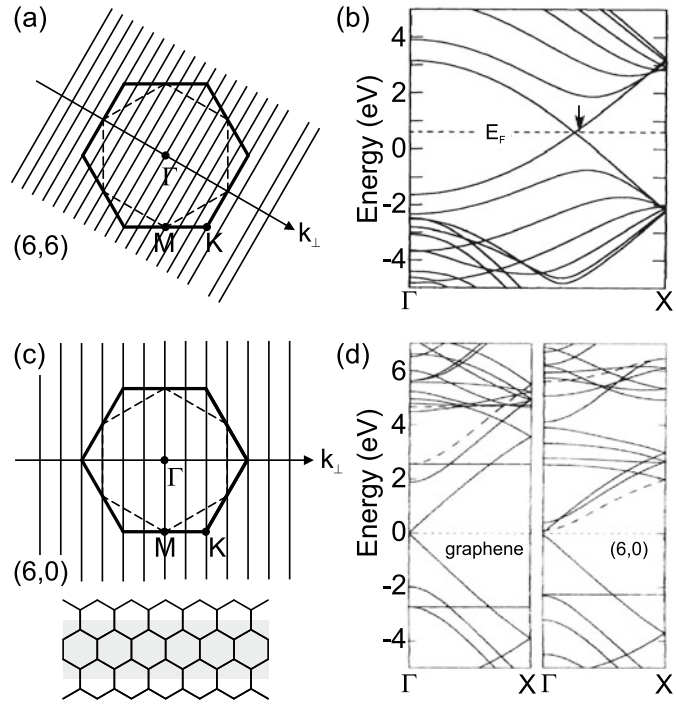

Fig. 14.18 **a** Brillouin zone of the graphene lattice (*bold* line) and allowed k-values for a (6, 6) armchair nanotube. **b** Band structure of a (6, 6) carbon nanotube. Adapted from [1371]. **c** Brillouin zone of the graphene lattice (*bold* line) and allowed k-values for a (6, 0) zig-zag carbon nanotube. In the *lower part* the real space structure is visualized. (**d**) Band structure of graphene (*left*) and a (6, 6) nanotube (*right*). Adapted from [1372]

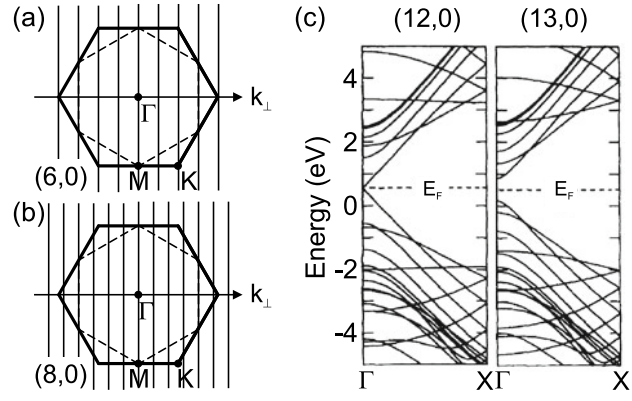

Fig. 14.19 **a**, **b** Brillouin zone of the graphene lattice (*bold* line) and allowed k-values for a (**a**) (6, 0) and a (**b**) (8, 0) zig-zag nanotube. **c** Band structures of a (12,0) metallic and (13, 0) semiconducting armchair carbon nanotube. Adapted from [1371]

14.3.3 Optical Properties

Optical transitions occur with high probability between the van-Hove singularities of the DOS. The theoretical absorption spectrum of a (10, 0) nanotube is shown in Fig. 14.21.

In an ensemble of nanotubes various types and sizes occur. The transition energies of all possible nanotubes sorted by diameter are assembled in the Kataura plot (Fig. 14.22a). Experimental data are shwon in Fig. 14.22b. The two branches of semiconducting nanotubes $\nu = \pm 1$ yield different transition energies. The overall dependence of the transition energy follows a $1/d$-law.

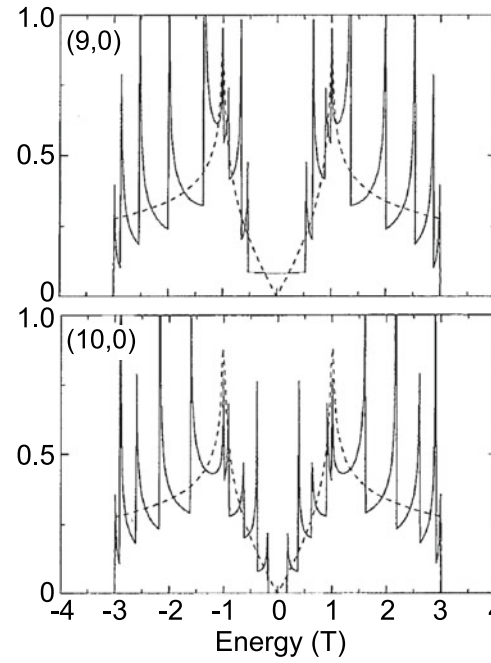

Fig. 14.20 Density of states for a (9, 0) metallic and (10, 0) semiconducting zig-zag carbon nanotube within the tight-binding approximation (13.2). The energy scale is given in units of the tight-binding parameter $T \approx 3\,\text{eV}$. The *dashed lines* are the DOS of graphene. Adapted from [1367]

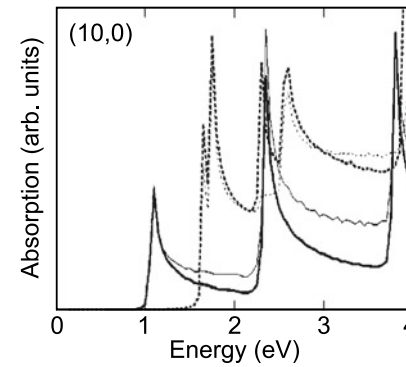

Fig. 14.21 Calculated absorption spectra for a (semiconducting) (10, 0) carbon nanotube for parallel (*solid line*) and perpendicular (*dotted line*) polarization. The *thick* (*thin*) lines are calculated with (without) the matrix element included. Adapted from [1374]

14.3.4 Other Anorganic Nanotubes

Structures similar to carbon nanotubes have been reported for BN [1378, 1379]. A boron nitride nanotube is a cylindrically rolled part of a BN sheet. BN tubes are always semiconducting (Fig. 14.23) and have a band gap beyond 5 eV similar to hexagonal BN which is mostly independent on chirality and diameter [1380]. Thus, while carbon nanotubes appear black since they absorb within 0–4 eV, BN is transparent (or white if scattering). For high energies larger than 10 eV C and BN tubes are quite similar since they are isoelectronic and the high-lying unoccupied states are less sensitive to the difference in the nuclear charges than the states at and below the Fermi energy [1381].

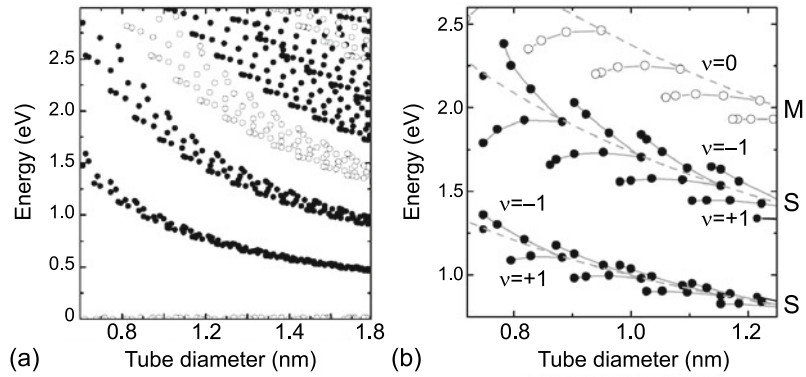

Fig. 14.22 **a** Theoretical transition energies of semiconducting (*filled symbols*) and metallic (*open symbols*) carbon nanotubes as a function of tube diameter (Kataura plot). Energies are calculated from van-Hove singularities in the JDOS within the third-order tight-binding approximation [1252]. **b** Experimental Kataura plot for the first two semiconducting (S, *closed symbols*) and the first metallic (M, *open symbols*) transition. *Dashed lines* connect the (near-to) armchair tubes; *full lines* connect tubes in a branch, $\nu = (n_1 - n_2) \bmod 3$. Data from photoluminescence [1375] and resonant Raman scattering [1376]. Adapted from [1377]

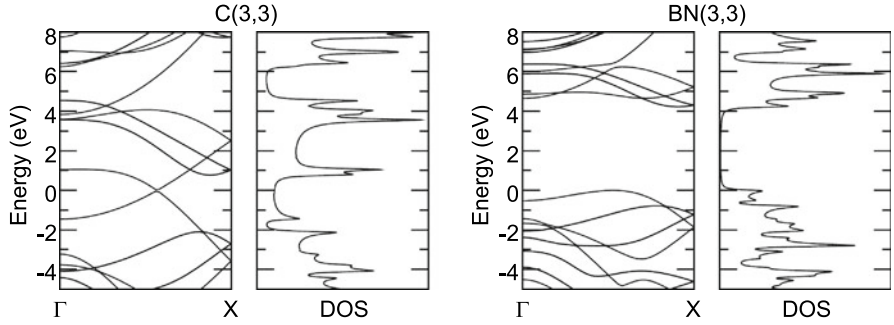

Fig. 14.23 Band structure and density of states (DOS) of C(3,3) and BN(3,3) nanotubes, calculated with DFT-LDA. Adapted from [1381]

14.4 Quantum Dots

14.4.1 Quantization in Three-Dimensional Potential Wells

The solutions for the d-dimensional ($d = 1$, 2, or 3) harmonic oscillator, i.e. the eigenenergies for the Hamiltonian

$$\hat{H} = \frac{\mathbf{p}^2}{2m} + \sum_{i=1}^{d} \frac{1}{2}\, m\, \omega_0^2\, x_i^2 \tag{14.6}$$

are given by

$$E_n = \left(n + \frac{d}{2}\right) \hbar\omega_0 \ , \tag{14.7}$$

with $n = 0, 1, 2, \ldots$. More detailed treatments can be found in quantum-mechanics textbooks.

Next, we discuss the problem of a particle in a centrosymmetric finite potential well with different masses m_1 in the dot and m_2 in the barrier. The Hamiltonian and the potential are given by

$$\hat{H} = \nabla \frac{\hbar^2}{2m} \nabla + V(r) \tag{14.8}$$

$$V(r) = \begin{cases} -V_0 \ , r \leq R_0 \\ 0 \quad , r > R_0 \end{cases} . \tag{14.9}$$

The wavefunction can be separated into radial and angular components $\Psi(\mathbf{r}) = R_{nlm}(r)\ Y_{lm}(\theta, \phi)$, where Y_{lm} are the spherical harmonic functions. For the ground state ($n = 1$) the angular momentum l is zero and the solution for the wavefunction (being regular at $r = 0$) is given by

$$R(r) = \begin{cases} \frac{\sin(k\,r)}{k\,r} & , r \leq R_0 \\ \frac{\sin(k\,R_0)}{k\,R_0}\ \exp\left(-\kappa\ (r - R_0)\right) & , r > R_0 \end{cases} \tag{14.10a}$$

$$k^2 = \frac{2\,m_1\,(V_0 + E)}{\hbar^2} \tag{14.10b}$$

$$\kappa^2 = -\frac{2\,m_2\,E}{\hbar^2} \ . \tag{14.10c}$$

From the boundary conditions that both $R(r)$ and $\frac{1}{m}\frac{\partial R(r)}{\partial r}$ are continuous across the interface at $r = R_0$, the transcendental equation

$$k\,R_0\ \cot\left(k\,R_0\right) = 1 - \frac{m_1}{m_2}\,(1 + \kappa\,R_0) \tag{14.11}$$

is obtained. From this formula the energy of the single particle ground state in a spherical quantum dot can be determined. For a given radius, the potential needs a certain strength $V_{0,\min}$ to confine at least one bound state; this condition can be written as

$$V_{0,\min} = \frac{\pi^2\,\hbar^2}{8\,m^*\,R_0^2} \tag{14.12}$$

for $m_1 = m_2 = m^*$. For a general angular momentum l, the wavefunctions are given by spherical Bessel functions j_l in the dot and spherical Hankel functions h_l in the barrier. Also, the transcendental equation for the energy of the first excited level can be given:

$$k\,R_0\ \cot\left(k\,R_0\right) = 1 + \frac{k^2\,R_0^2}{\frac{m_1}{m_2}\,\frac{2+2\kappa\,R_0+\kappa^2\,R_0^2}{1+\kappa\,R_0} - 2} \ . \tag{14.13}$$

In the case of infinite barriers ($V_0 \to \infty$), the wavefunction vanishes outside the dot and is given by (normalized)

$$R_{nml}(r) = \sqrt{\frac{2}{R_0^3}}\ \frac{j_l(k_{nl}\,r)}{j_{l+1}(k_{nl}\,R_0)} \ , \tag{14.14}$$

where k_{nl} is the n-th zero of the Bessel function j_l, e.g. $k_{n0} = n\pi$. With two-digit precision the lowest levels are determined by

k_{nl}	$l = 0$	$l = 1$	$l = 2$	$l = 3$	$l = 4$	$l = 5$
$n = 0$	3.14	4.49	5.76	6.99	8.18	9.36
$n = 1$	6.28	7.73	9.10	10.42		
$n = 2$	9.42					

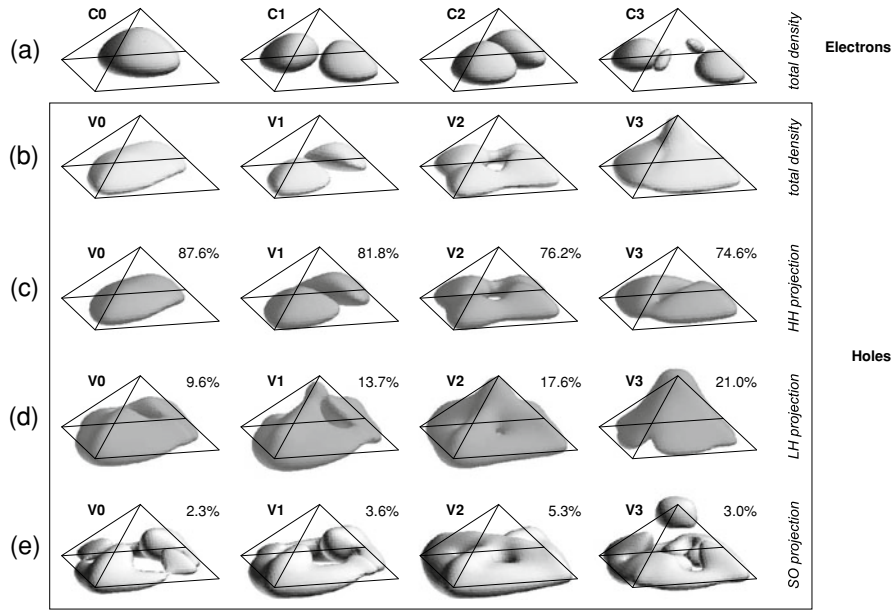

Fig. 14.24 Isosurface plots (25% of maximum value) of the total probability densities **a**, **b** and valence-band projections (**c**)–(**e**) of bound electron (**a**) and hole (**b**)–(**e**) states in a model pyramidal InAs/GaAs quantum dot with base length $b = 11.3\,\text{nm}$. The percentages are the integrals of the projections to the bulk heavy, light and split-off hole bands, respectively, and the isosurfaces show the corresponding projection shapes. For each valence-band state the difference from 100% is the integral $\int_{-\infty}^{\infty} |\psi_{s\uparrow}|^2 + |\psi_{s\downarrow}|^2 \mathrm{d}^3\mathbf{r}$ of the s-type (conduction band) Bloch function projection (not shown). Reprinted with permission from [1385], ©2002, Springer

The $(2l+1)$ degenerate energy levels E_{nl} are ($V_0 = \infty$, $m = m_1$):

$$E_{nl} = \frac{\hbar^2}{2m} k_{nl}^2 \frac{1}{R_0^2} \,. \tag{14.15}$$

The 1s, 1p, and 1d states have smaller eigenenergies than the 2s state.

A particularly simple solution is given for a cubic quantum dot of side length a_0 and infinite potential barriers. One finds the levels $E_{n_x n_y n_z}$:

$$E_{n_x n_y n_z} = \frac{\hbar^2}{2m} \left(n_x^2 + n_y^2 + n_z^2\right) \frac{\pi^2}{a_0^2} \,, \tag{14.16}$$

with $n_x, n_y, n_z = 1, 2, \ldots$. For a sphere, the separation between the ground and first excited state is $E_1 - E_0 \approx E_0$, for a cube and a two-dimensional harmonic oscillator it is exactly E_0. For a three-dimensional harmonic oscillator this quantity is $E_1 - E_0 = 2E_0/3$.

For realistic quantum dots a full three-dimensional simulation of strain, piezoelectric fields and the quantum-mechanical confinement must be performed [1382, 1383]. In Fig. 14.24, the lowest four electron and hole wavefunctions in a pyramidal InAs/GaAs quantum dot (for the strain distribution see Fig. 5.34 and for the piezoelectric fields see Fig. 16.16) are shown. The figure shows that the lowest hole states have dominantly heavy-hole character and contain admixtures of the other hole bands. The wavefunction in such quantum dots can be imaged using scanning tunneling microscopy [1384].

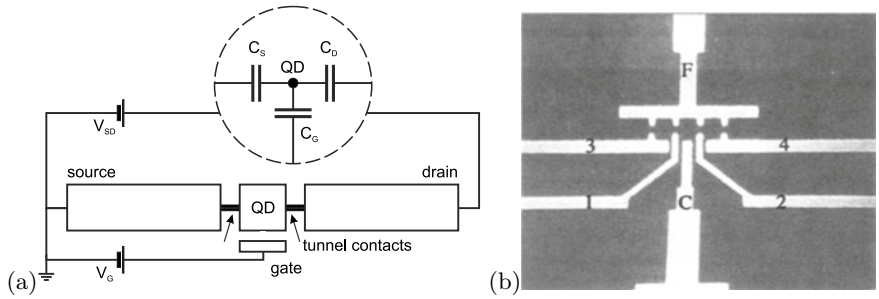

Fig. 14.25 **a** Schematic drawing of a quantum dot (QD) with tunnel contacts and gate electrode. The *inset* depicts an equivalent circuit with capacitances. **b** Realization with an in-plane gate structure. The distance between 'F' and 'C' (gate electrode) is 1 μm. Electron transport occurs from a 2DEG between 3/F to 4/F through the quantum points contacts 1/3 and 2/4. Part (**b**) from [1386], reprinted with permission, ©1991, Springer Nature

14.4.2 Electrical and Transport Properties

The classical electrostatic energy of a quantum dot with capacitance C_G that is capacitively coupled to a gate (Fig. 14.25) at a bias voltage V_G is given by

$$E = \frac{Q^2}{2C_G} - Q\,\alpha\,V_G\,, \tag{14.17}$$

where α is a dimensionless factor relating the gate voltage to the potential of the island and Q is the charge of the island.

Mathematically, minimum energy is reached for a charge $Q_{min} = \alpha\,C_G\,V_G$. However, the charge has to be an integer multiple of e, i.e. $Q = N\,e$. If V_g has a value, such that $Q_{min}/e = N_{min}$ is an integer, the charge cannot fluctuate as long as the temperature is low enough, i.e.

$$kT \ll \frac{e^2}{2\,C_G}\,. \tag{14.18}$$

Tunneling into or out of the dot is suppressed by the Coulomb barrier $e^2/2C_G$, and the conductance is very low. Analogously, the differential capacitance is small. This effect is called *Coulomb blockade*. Peaks in the tunneling current (Fig. 14.26b), conductivity (Fig. 14.26a) and the capacitance occur, when the gate voltage is such that the energies for N and $N+1$ electrons are degenerate, i.e. $N_{min} = N + \frac{1}{2}$. The expected level spacing is

$$e\,\alpha\,\Delta V_G = \frac{e^2}{C_G} + \Delta\epsilon_N\,, \tag{14.19}$$

where $\Delta\epsilon_N$ denotes the change in lateral (kinetic) quantization energy for the added electron. e^2/C will be called the charging energy in the following.

A variation of the source–drain voltage (for a given gate voltage) leads to a so-called Coulomb staircase since more and more channels of conductivity contribute to the current through the device (Fig. 14.27). In Fig. 14.28 the tunneling current is shown as a function of the potential of a dot, formed by gates on a WSe_2 flake [1388], and the source-drain voltage. The iso-current lines form so-called 'Coulomb blockade diamonds'.

The charge Q on the QD is determined by the charges on the gate, source and drain capacities, $Q = Q_G - Q_S + Q_D$. Together with $Q_S = C_S\,V_S$, $Q_D = C_D\,V_D$ and $V_{SD} = V_S + V_D$ and $Q_G =$

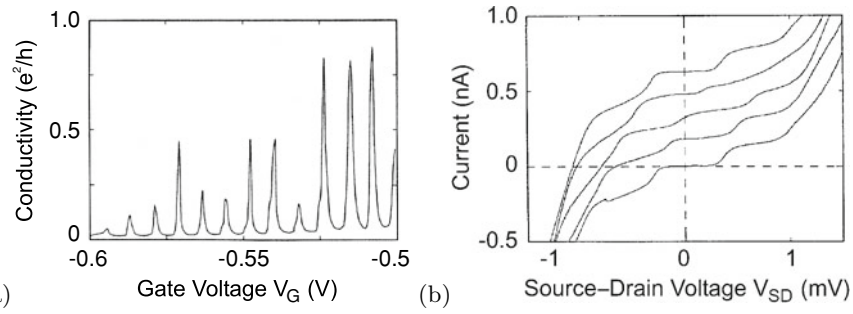

Fig. 14.26 **a** Conductivity (Coulomb oscillations) and **b** current–voltage diagram at different gate voltages (Coulomb staircase, shifted vertically for better readability) of a tunnel junction with a quantum dot as in Fig. 14.25. Adapted from [1386], reprinted with permission, ©1991, SpringerNature

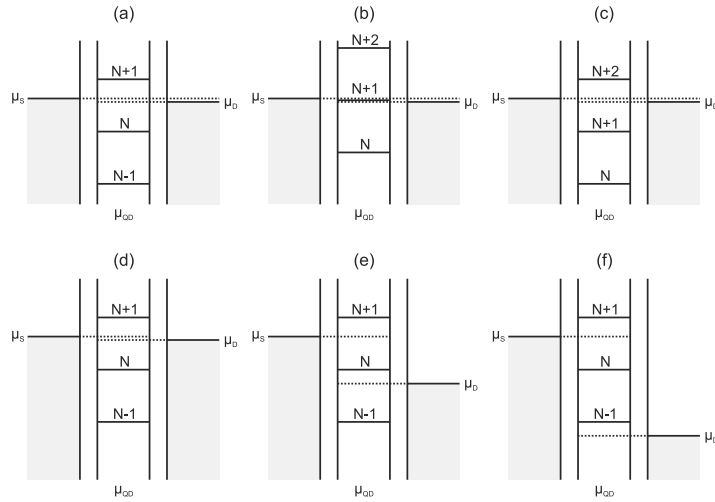

Fig. 14.27 Chemical potentials of source and drain and of a quantum dot in between them. **a**, **b**, and **c** show the sequence for a variation of the gate voltage and visualize the origin of the Coulomb oscillations (see Fig. 14.26a). **d**, **e** and **f** visualize a variation of the source–drain voltage and the origin of the Coulomb staircase (cf. Fig. 14.26b)

$C_G\,(V_G - V_S)$, we find ($C_\Sigma = C_G + C_S + C_D$),

$$V_S = \frac{1}{C_\Sigma}\,(Q + C_G\,V_G + C_D\,V_{SD}) \tag{14.20}$$

$$V_D = \frac{1}{C_\Sigma}\,(-Q - C_G\,V_G + (C_\Sigma - C_D)\,V_{SD})\ . \tag{14.21}$$

Now, if for a given pair of (V_G, V_{SD}) in a diagram like Fig. 14.28b the current is Coulomb-blocked and low, then it is for all voltages with the same charge Q on the dot and either the same V_S or V_D. The derivatives of (14.20) and (14.21) yield the slopes $\partial V_{SD}/\partial V_G = \gamma_1 = -C_G/C_D$ and $\gamma_2 = +C_G/(C_G + C_S)$, respectively, that defined the borders of the diamond in the schematic stability diagram as depicted in Fig. 14.29. We note that such analysis is allowed when $|V_S|, |V_D| \ll e/2C_\Sigma$ and the quantum dot circuit can be treated as a system of capacitors (inset in Fig. 14.25a). Changing Q to $Q - e$ requires V_G to increase by e/C_G for the same $V_{S,D}$, yielding the periodicity of the stability diagram.

Single electron tunneling (SET) circuits [1387] are investigated with respect to metrology for a novel ampere standard [1389].

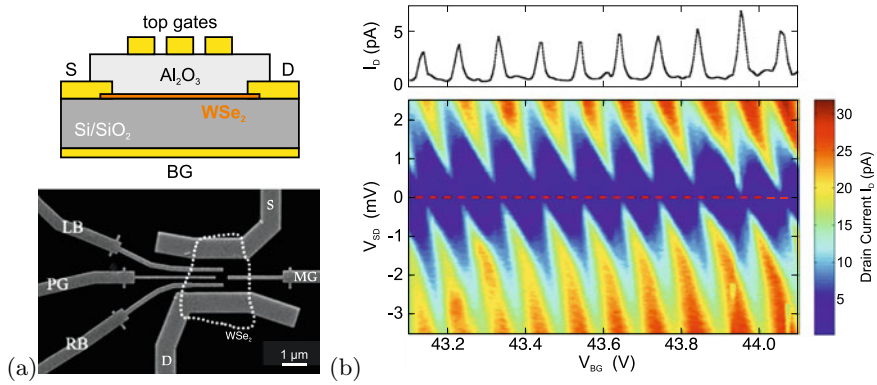

Fig. 14.28 **a** *Top*: Sketch of WSe_2 flake with gate structure, defining a lateral quantum dot. *Bottom*: SEM image of the structure. The outline of the WSe_2 flake (thickness 4.5 nm) is indicated as *dotted line*. BG: back gate, PG: plunger gate. **b** Current (in false colors) as a function of the back gate voltage V_{BG} and the source-drain voltage V_{SD} ($T = 240$ mK). On the top is a current trace as a function of V_G (for $V_{SD} = 0$, along the *red dashed line* in the diagram). SEM image in panel (**a**) and panel (**b**) adapted from [1388] with permission from RSC

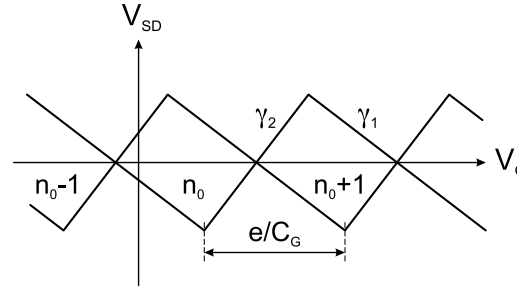

Fig. 14.29 Schematic Coulomb diamond stability diagram. The slopes γ_1 and γ_2 are discussed in the text. The periodicity in the gate voltage is given by e/C_G. The charge on the dot is $Q = (-e)\,n$

A lot of research so far has been done on lithographically defined systems where the lateral quantization energies are small and smaller than the Coulomb charging energy. In this case, periodic oscillations are observed, especially for large N. A deviation from periodic oscillations for small N and a characteristic shell structure (at $N = 2, 6, 12$) consistent with a harmonic oscillator model ($\hbar\omega_0 \approx 3$ meV) has been reported for ≈500-nm diameter mesas (Fig. 14.30b,c). In this structure, a small mesa has been etched and contacted (top contact, substrate back contact and side gate). The quantum dot consists of a 12-nm $In_{0.05}Ga_{0.95}As$ quantum well that is laterally constricted by the 500-nm mesa and vertically confined due to 9- and 7.5-nm thick $Al_{0.22}Ga_{0.68}As$ barriers (Fig. 14.30a). By tuning the gate voltage, the number of electrons can be varied within 0 and 40. Measurements are typically carried out at a sample temperature of 50 mK.

In the sample shown in Fig. 14.31, self-assembled QDs are positioned in the channel under a split-gate structure. In a suitable structure, tunneling through a single QD is resolved.

In small self-assembled quantum dots single-particle level separations can be larger than or similar to the Coulomb charging energy. Classically, the capacitance for a metal sphere of radius R_0 is given as

$$C_0 = 4\pi\,\epsilon_0\,\epsilon_r\,R_0\ , \tag{14.22}$$

e.g.. $C_0 \approx 6$ aF for $R_0 = 4$ nm in GaAs, resulting in a charging energy of 26 meV. Quantum mechanically, the charging energy is given in first-order perturbation theory by

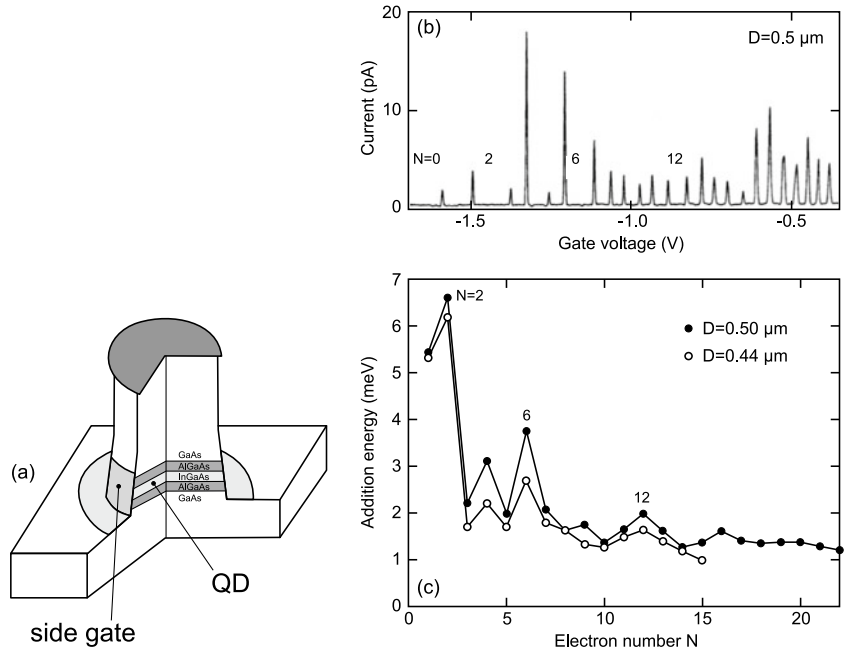

Fig. 14.30 **a** Schematic sample geometry for side-gated $In_{0.05}Ga_{0.95}As/Al_{0.22}Ga_{0.68}As$ disk-shaped quantum dot. **b** Coulomb oscillations in the current versus gate voltage at $B = 0\,\mathrm{T}$ observed for a $D = 0.5\,\mu\mathrm{m}$ disk-shaped dot. **c** Addition energy versus electron number for two different dots with $D = 0.50$ and $0.44\,\mu\mathrm{m}$. Adapted from [1391]

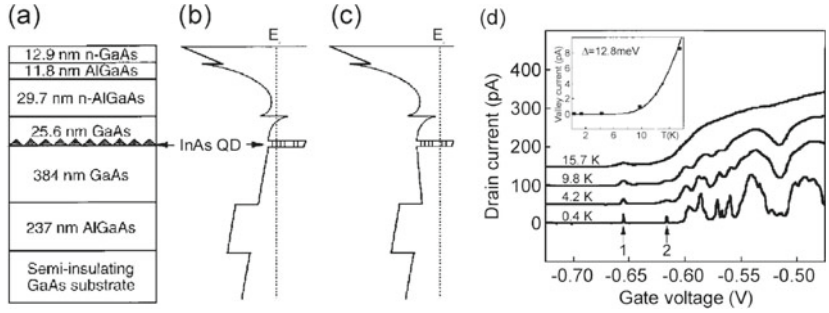

Fig. 14.31 **a** Schematic layer sequence of epitaxial structure comprising a n-AlGaAs/GaAs heterointerface with a two-dimensional electron gas and a layer of InAs/GaAs quantum dots. **b** and **c** are corresponding band diagrams with no gate bias and gate voltage below the critical value, respectively. **d** Experimental dependence of drain current on gate voltage in a split-gate structure at a drain source voltage of $10\,\mu\mathrm{V}$. *Inset*: Dependence of valley current on temperature (*squares*) with theoretical fit. Reprinted with permission from [1392], ©1997 AIP

$$E_{21} = \langle 00|W_{ee}|00\rangle = \iint \Psi_0^2(\mathbf{r}_e^1)\, W_{ee}(\mathbf{r}_e^1, \mathbf{r}_e^2)\, \Psi_0^2(\mathbf{r}_e^2)\, \mathrm{d}^3\mathbf{r}_e^1\, \mathrm{d}^3\mathbf{r}_e^2\,, \tag{14.23}$$

where W_{ee} denotes the Coulomb interaction of the two electrons and Ψ_0 the ground state (single particle) electron wavefunction. The matrix element gives an upper bound for the charging energy since the wavefunctions will rearrange to lower their overlap and the repulsive Coulomb interaction. For lens-shaped InAs/GaAs quantum dots with radius 25 nm a charging energy of about 30 meV has been predicted.

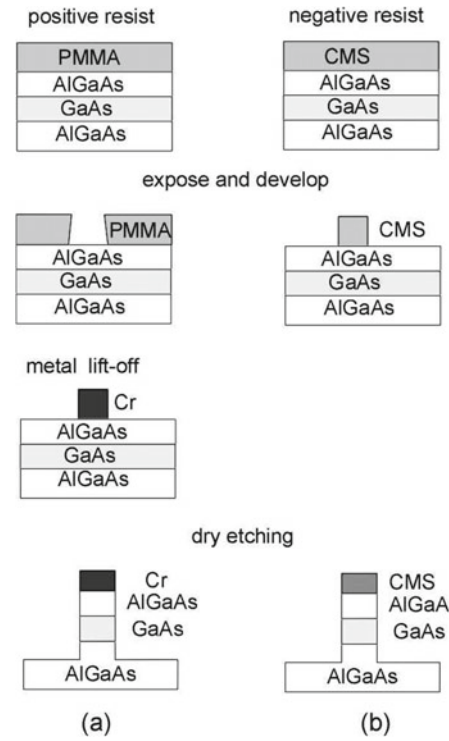

Fig. 14.32 Lithography and etching techniques for the fabrication of semiconductor structures

14.4.3 Self-Assembled Preparation

The preparation methods for QDs split into top-down (lithography and etching) and bottom-up (self-assembly) methods. The latter achieve typically smaller sizes and require less effort (at least concerning the machinery).

Artificial Patterning

Using artificial patterning, based on lithography and etching (Fig. 14.32), quantum dots of arbitrary shape can be made (Fig. 14.33). Due to defects introduced by high-energy ions during reactive ion etching the quantum efficiency of such structures is very low when they are very small. Using wet-chemical etching techniques the damage can be significantly lowered but not completely avoided. Since the QDs have to compete with other structures that can be made structurally perfect, this is not acceptable.

Template Growth

Template growth is another technique for the formation of nanostructures. Here, a mesoscopic structure is fabricated by conventional means. The nanostructure is created using size-reduction mechanisms, e.g., faceting, (Fig. 14.34). This method can potentially suffer from low template density, irregularities of the template, and problems of reproducibility.

Colloids

Another successful route to nanocrystals is the doping of glasses with subsequent annealing (color filters). When nanocrystals are prepared in a sol-gel process, the nanoparticles are present as a colloid in wet solution. With the help of suitable stabilizing agents they are prevented from sticking to each other

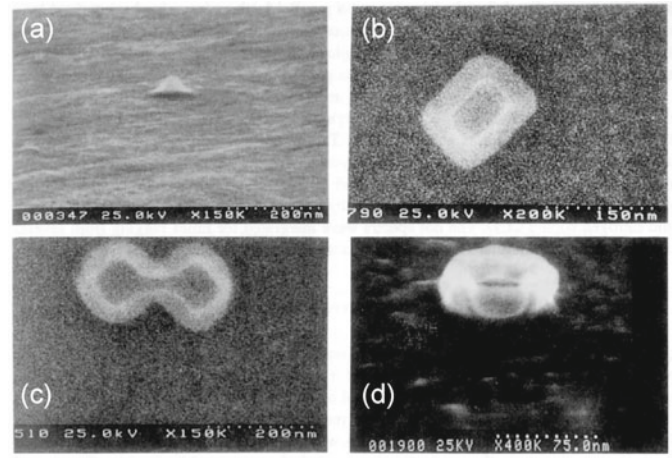

Fig. 14.33 Quantum dots of various shapes created by lithography and etching techniques. From [1393]

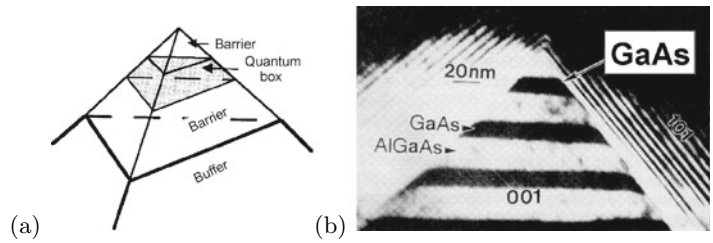

Fig. 14.34 **a** Schematic representation of growth on top of a predefined template, **b** cross-sectional TEM of quantum dot formation at the apex. Reprinted with permission from [1394], ©1992 MRS

and can be handled in ensembles and also individually. Such nanocrystals have been synthesized and investigated in particular for II–VI (Fig. 14.35a) and halide perovskite (Fig. 14.35b) semiconductors.

Mismatched Epitaxy

The self-assembly (or self-organization) relies on strained heterostructures that achieve energy minimization by island growth on a wetting layer (Stranski-Krastanow growth mode, see Sect. 12.2.3 and [1339]). Additional ordering mechanisms [1397, 1398] lead to ensembles that are homogeneous in size[2] [1399] and shape [1400] (Fig. 14.36).

When a thin layer of a semiconductor is grown on top of a flat substrate with different lattice constant, the layer suffers a tetragonal distortion (Sect. 5.3.3). Strain can only relax along the growth direction (Fig. 14.37). If the strain energy is too large (highly strained layer or large thickness), plastic relaxation via dislocation formation occurs. If there is island geometry, strain can relax in all three directions and about 50% more strain energy can relax, thus making this type of relaxation energetically favorable. When the island is embedded in the host matrix, the strain energy is similar to the 2D case and the matrix becomes strained (metastable state).

When such QD layers are vertically stacked, the individual quantum dots grow on top of each other (Fig. 14.38) if the separation is not too large (Fig. 14.40). This effect is due to the effect of the underlying QD. In the case of InAs/GaAs (compressive strain), the buried QD stretches the surface above it (tensile surface strain). Thus, atoms impinging in the next QD layer find a smaller strain right on top of the buried QDs. In STM images of the cross section through (XSTM) such a stack (Fig. 14.39) individual indium atoms are visible and the shape can be analyzed in detail [1402].

[2]The ordering in size is remarkable. Typically Ostwald ripening (due to the Gibbs-Thomson effect; smaller droplets have larger vapor pressure and dissolve, larger droplets accordingly grow) occurs in an ensemble of droplets or nuclei. In the case of strained QDs, surface energy terms stabilize a certain QD size.

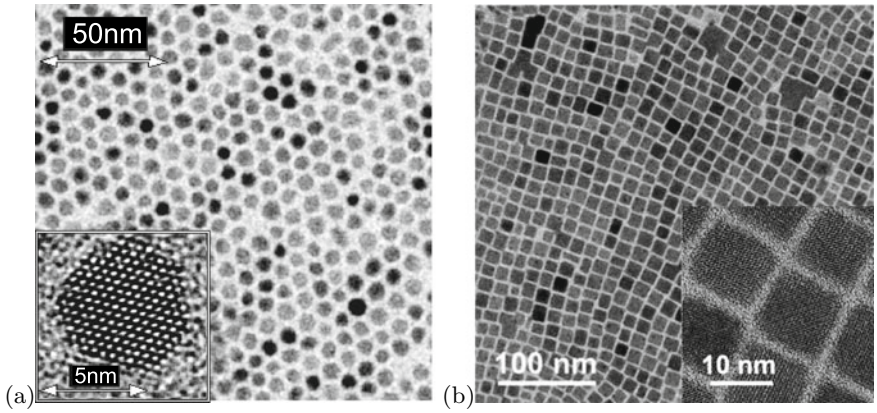

Fig. 14.35 **a** CdSe colloidal (hexagonal) nanoparticles. From [1395]. **b** $CsPbBr_3$ perovskite (cubic) colloidal nanocrystals. Adapted from [1396] under Creative Commons Attribution (CC BY 4.0) license

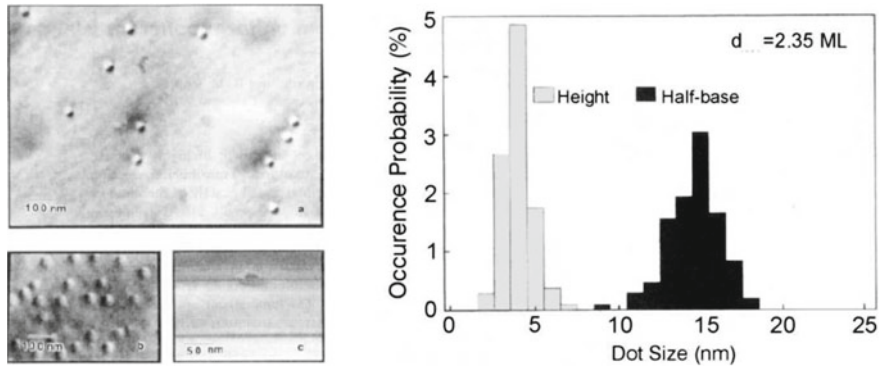

Fig. 14.36 Self-organized formation of InGaAs/GaAs quantum dots during epitaxy. *Left*: Plan-view and cross-sectional transmission electron micrographs. *Right*: Histogram of vertical and lateral size of the quantum dots. Reprinted with permission from [1401], ©1993 AIP

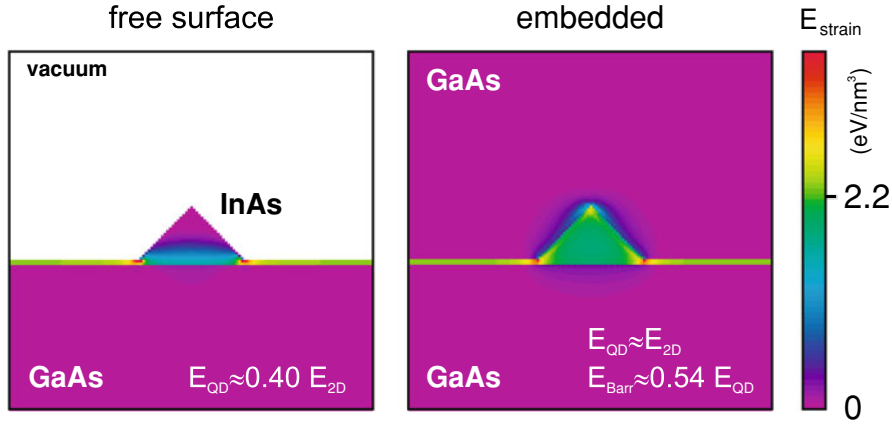

Fig. 14.37 Distribution of strain energy for (*left*) uncapped island and (*right*) island embedded in host matrix. Numerical values are for InAs/GaAs

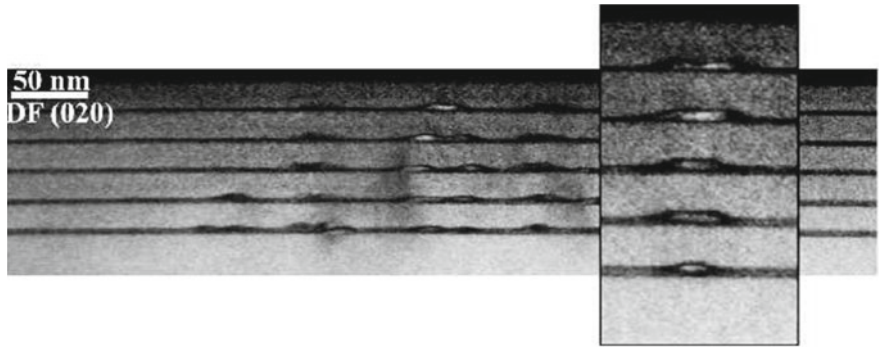

Fig. 14.38 Cross-sectional TEM image of a stack of five layers of quantum dots. Due to strain effects, vertical arrangement is achieved

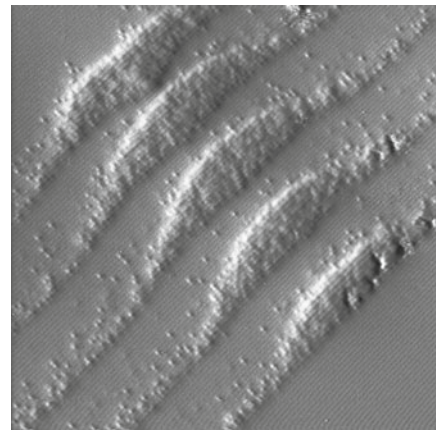

Fig. 14.39 Cross-sectional STM image of a stack of five InAs quantum dots in a GaAs matrix. Individual In atoms can be observed in-between the wetting layers and the quantum dots. Each quantum dot layer was formed by growing 2.4 ML of InAs. The intended distance between the quantum dot layers was 10 nm. Image size is $55 \times 55\,\mathrm{nm}^2$. Reprinted with permission from [1402], ©2003 AIP

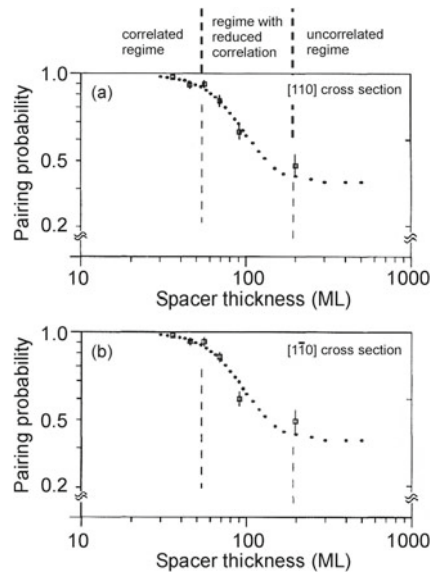

Fig. 14.40 Experimentally observed pairing probability in MBE-grown stacks of InAs/GaAs quantum dots as a function of the spacer-layer thickness. Data are taken from (**a**) (110) and (**b**) (1–10) cross-sectional TEM images. The *filled circles* are fit to data from theory of correlated island formation under strain fields. Reprinted with permission from [1403], ©1995 APS

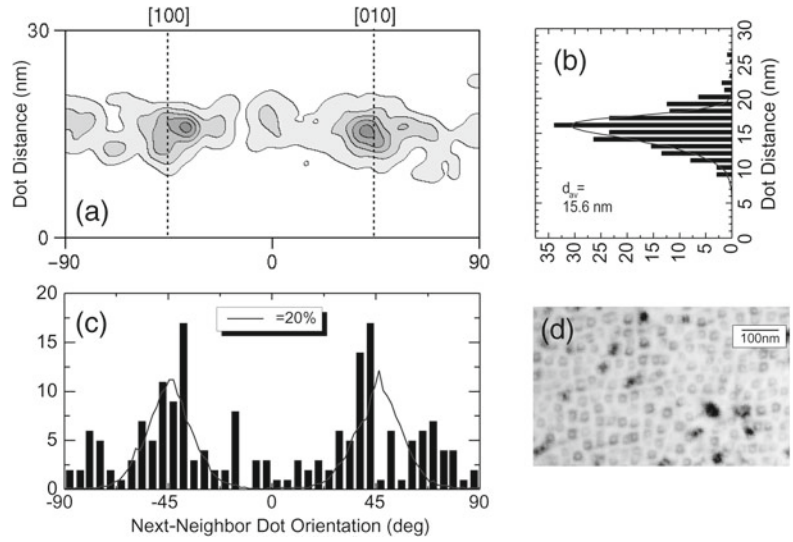

Fig. 14.41 Lateral ordering of QD array. **d** Plan-view TEM of QD array on which the statistical evaluation is based. **a** Two-dimensional histogram of QDs as a function of the nearest-neighbor distance and direction, (**b**, **c**) projections of part (**a**). *Solid lines* in (**b**) and (**c**) are theory for square array with $\sigma = 20\%$ deviation from ideal position. Adapted from [1339, 1397]

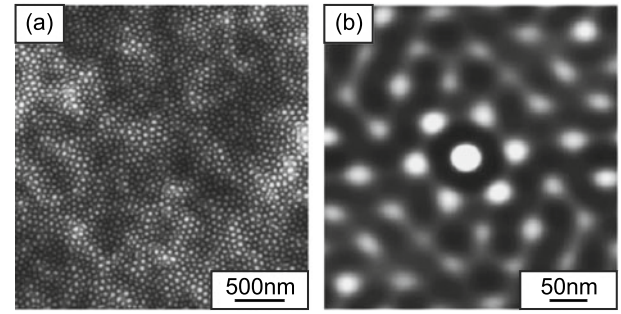

Fig. 14.42 **a** AFM image of a Si (001) substrate after 960 min of ion sputtering (1.2 keV Ar^+, normal incidence). **b** Two-dimensional autocorrelation function from a $400 \times 400\,nm^2$ area of image in part (**a**). Adapted from [1406] with permission, ©2001 AIP

The vertical arrangement can lead to further ordering since a homogenization in lateral position takes place. If two QDs in the first layers are very close, their strain fields overlap and the second layer 'sees' only one QD.

The lateral (in-plane) ordering of the QDs with respect to each other occurs in square or hexagonal patterns and is mediated via strain interaction through the substrate. The interaction energy is fairly small, leading only to short-range in-plane order [1397] as shown in Fig. 14.41. The in-plane ordering can be improved up to the point that regular one- or two-dimensional arrays form or individual quantum dots are placed on designated positions using directed self-assembly [1339]. Among others, dislocation networks buried under the growth surface of the nanostructure, surface patterning and modification have been used to direct the QD positioning.

Ion-Beam Erosion

During the erosion of a surface with low-energy ion beam sputtering ordered patterns of dots appear [1404–1407]. Isotropic [1408] and hexagonal [1404, 1406] (Fig. 14.42) near-range ordering has been observed. The pattern formation mechanism is based on the morphology-dependent sputter yield and further mechanisms of mass redistribution [1409]. Also linear patterns have been reported [1410].

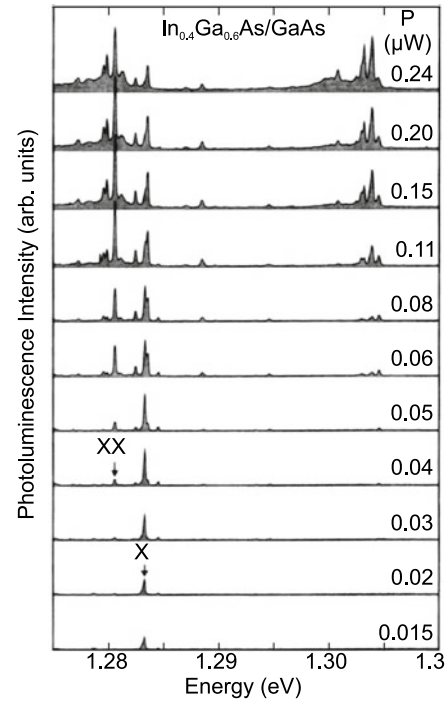

Fig. 14.43 Optical emission spectra ($T = 2.3\,\mathrm{K}$) of a single InGaAs/GaAs quantum dot at different laser excitation levels P as labeled. The single exciton (X) and biexciton (XX) lines are indicated. Adapted from [1411]

14.4.4 Optical Properties

The optical properties of QDs are related to their electronic density of states. In particular, optical transitions are allowed only at discrete energies due to the zero-dimensional density of states.

Photoluminescence from a single QD is shown in Fig. 14.43. The δ-like sharp transition is strictly true only in the limit of small carrier numbers ($\ll 1$ exciton per dot on average) since otherwise many-body effects come into play that can encompass recombination from charged excitons or multiexcitons. At very low excitation density the recombination spectrum consists only of the one-exciton (X) line. With increasing excitation density small satellites on either side of the X-line develop that are attributed to charged excitons (trions) X^+ and X^-. On the low-energy side, the biexciton (XX) appears. Eventually, the excited states are populated and a multitude of states contribute with rich fine structure. In bulk material the biexciton (Sect. 9.7.10) is typically a bound state, i.e. its recombination energy E_{XX} is lower than that of the exciton E_X. A similar situation is present in Fig. 14.43. It was pointed out in [1412] that in QDs the biexciton recombination energy can also be *larger* than the exciton recombination energy. In [1413] the modification of the QD confinement potential of InAs/GaAs QDs by annealing was reported. The exciton binding energy (E_X-E_{XX}) is tuned from positive ('normal') to negative values upon annealing (Fig. 14.44).

The charging state of the exciton can be controlled in a field-effect structure. The recombination energy is modified due to Coulomb and exchange effects with the additional carriers. In charge-tunable quantum dots [1414] and rings [1415] exciton emission has been observed in dependence of the number of additional electrons. The electron population can be controlled in a Schottky-diode-like structure through the manipulation of the Fermi level with the bias voltage. At high negative bias all charge carriers tunnel out of the ring and no exciton emission is observed. A variation of the bias then leads to an average population with $N = 1, 2, 3, \ldots$ electrons. The recombination of additional laser-excited

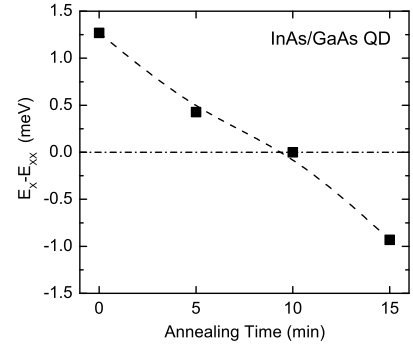

Fig. 14.44 Biexciton binding energy determined for a single InAs/GaAs quantum dot for various annealing times. Data from [1413]

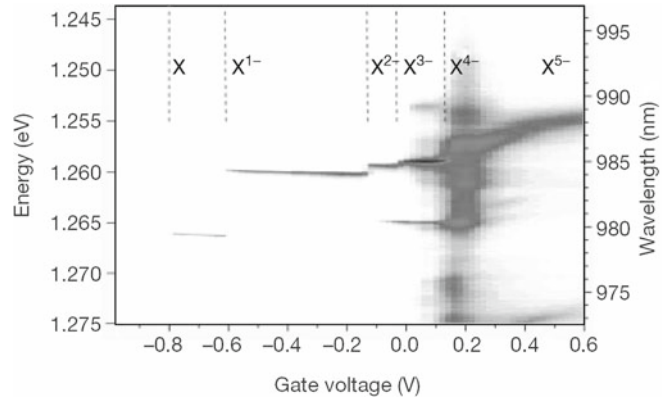

Fig. 14.45 Luminescence of charged excitons from a single quantum ring at $T = 4.2\,\mathrm{K}$ versus the bias voltage with which the number of electrons in the quantum dot N is tuned from zero to $N > 3$. Adapted from [1415], reprinted with permission, ©2000, Springer Nature

excitons depends (due to the Coulomb interaction) on the number of the electrons present (Fig. 14.45). The singly negatively charged exciton X^- is also called a trion.

The interaction of a spin with an exciton in a CdTe quantum dot has been observed in [1416]. If the CdTe quantum dot is pure, a single line arises. If the dot contains a single Mn atom, the exchange interaction of the exciton with the Mn $S = 5/2$ spin leads to a six-fold splitting of the exciton line (Fig. 14.46. In an external magnetic field a splitting into a total of twelve lines due to Zeeman effect at the Mn spin is observed.

In a QD ensemble, optical transitions are inhomogeneously broadened due to fluctuations in the QD size and the size dependence of the confinement energies (Fig. 14.47). Interband transitions involving electrons and holes suffer from the variation of the electron and hole energies:

$$\sigma_E \propto \left(\left| \frac{\partial E_\mathrm{e}}{\partial L} \right| + \left| \frac{\partial E_\mathrm{h}}{\partial L} \right| \right) \delta L \ . \tag{14.24}$$

A typical relative size inhomogeneity of σ_L/L of 7% leads to several tens of meV broadening. Additional to broadening due to different sizes fluctuations of the quantum dot shape can also play a role. The confinement effect leads to an increase of the recombination energy with decreasing quantum-dot size. This effect is nicely demonstrated with colloidal quantum dots of different size as shown in Fig. 14.48.

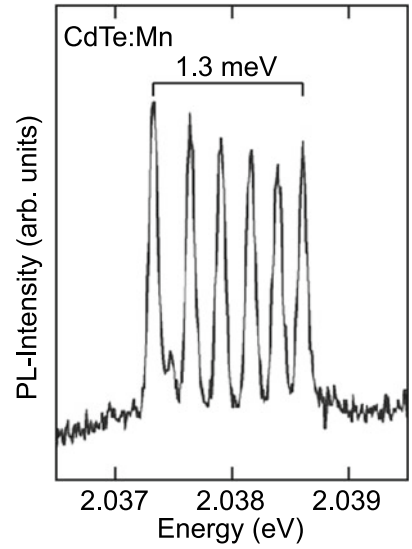

Fig. 14.46 Photoluminescence spectrum of a single CdTe/ZnSe quantum dot containing a single Mn atom ($T = 5\,\mathrm{K}$). Adapted from [1416], reprinted with permission, ©2004 APS

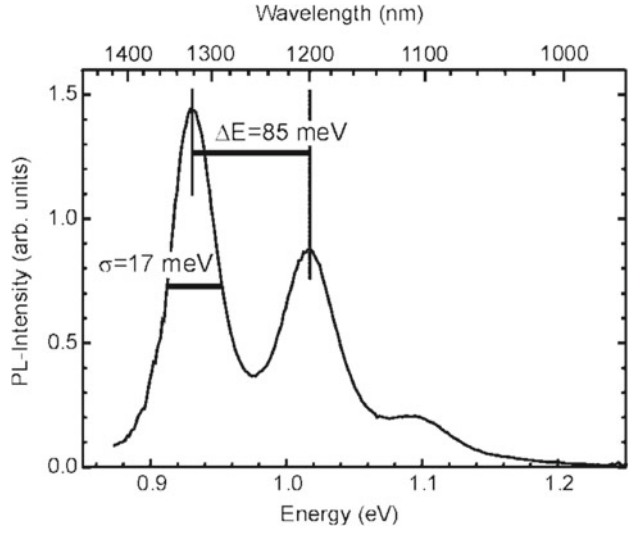

Fig. 14.47 Ensemble photoluminescence spectrum ($T = 293\,\mathrm{K}$, excitation density $500\,\mathrm{W/cm^2}$) of InAs/GaAs QDs

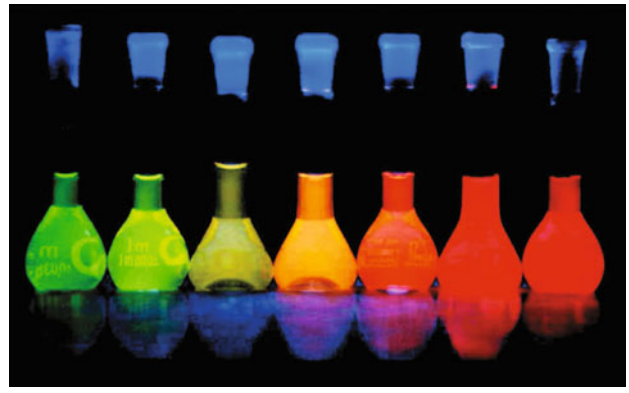

Fig. 14.48 Luminescence (under UV excitation) from flasks of colloidal CdTe quantum dots with increasing size (from left to right). From [1395]

Chapter 15
External Fields

Abstract The effects of external electric and magnetic fields on the electronic and optical properties of bulk materials and quantum wells are discussed including the Stark effect and quantum-confined Stark effect, the Hall effect and Quantized Hall Effects. The energy levels of the solid and its optical and electronic properties depend on external electric and magnetic fields. In high magnetic fields and at low temperatures the quantum Hall effects give evidence for new states of matter in many-body systems.

15.1 Electric Fields

15.1.1 Bulk Material

The center-of-mass motion of the exciton is not influenced by a homogeneous electric field. The Hamilton operator for the relative motion of an electron-hole pair of reduced mass μ along z in the presence of an electric field E along the z direction is

$$\hat{H} = -\frac{\hbar^2}{2\mu}\,\Delta - e\,E\,z\;. \tag{15.1}$$

Here, the Coulomb interaction, leading to the formation of bound exciton states, is neglected. In the plane perpendicular to the field (here the z direction) the solutions for the relative motion are just plane waves.

In the electric field the bands are tilted (Fig. 15.1), i.e. there is no longer an overall band gap. Accordingly, the wavefunctions are modified and have exponential tails in the energy gap.

After separation of the motion in the (x,y) plane the Schrödinger equation for the motion in the z direction is

$$\left(-\frac{\hbar^2}{2\mu}\,\frac{\mathrm{d}^2}{\mathrm{d}z^2} - e\,E\,z - E_z\right)\phi(z) = 0\;, \tag{15.2}$$

which is of the type

$$\frac{\mathrm{d}^2 f(\xi)}{\mathrm{d}\xi^2} - \xi\, f(\xi) = 0\;, \tag{15.3}$$

M. Grundmann, *The Physics of Semiconductors*, Graduate Texts in Physics,
https://doi.org/10.1007/978-3-030-51569-0_15

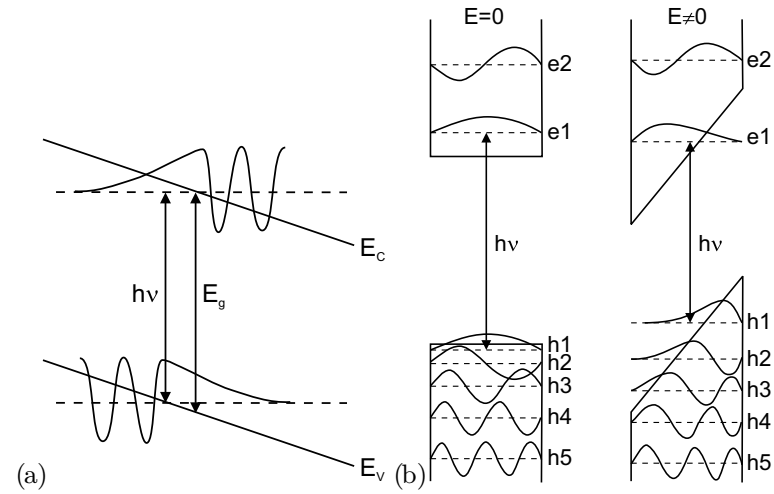

Fig. 15.1 Impact of an electric field on **a** bulk material (tilt of bands) and **b** a quantum well (quantum confined Stark effect, QCSE)

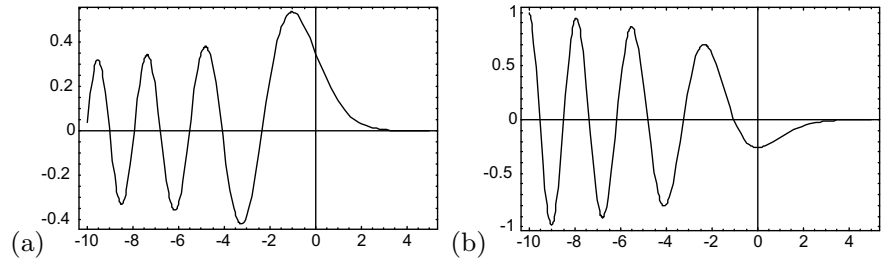

Fig. 15.2 **a** Airy function Ai(x), **b** Ai'(x)

with $\xi = \frac{E_z}{\Theta} - z\left(\frac{2\mu}{\hbar^2}\, e\, E\right)^{1/3}$ and the optoelectronic energy $\Theta = \left(\frac{e^2 E^2 \hbar^2}{2\mu}\right)^{1/3}$. The solution of (15.3) is given by the Airy function Ai (cf. Fig. 15.2):

$$\phi_{E_z}(\xi) = \frac{\sqrt{e\,E}}{\Theta}\, Ai(\xi)\ . \tag{15.4}$$

The pre-factor guaranties the orthonormality (with regard to the E_z). The absorption spectrum is then given by

$$\alpha(\omega, E) \propto \frac{1}{\omega}\sqrt{\Theta}\,\pi\left[Ai'^2(\eta) - \eta\, Ai^2(\eta)\right]\ , \tag{15.5}$$

with $\eta = (E_\mathrm{g} - E)/\Theta$ and $Ai'(x) = \mathrm{d}Ai(x)/\mathrm{d}x$.

Optical transitions below the band gap become possible that are photon-assisted tunneling processes. The below-bandgap transitions have the form of an exponential tail. Additionally, oscillations develop above the band gap, the so-called Franz-Keldysh oscillations (FKO) [1417, 1418] (Fig. 15.3a).

The absorption spectrum scales with the optoelectronic energy Θ. The energy position of the FKO peaks E_n is periodic with ($\nu \sim 0.5$)

$$\left(E_n - E_\mathrm{g}\right)^{3/2} \propto (n - \nu)\, E\, \sqrt{\mu}\ . \tag{15.6}$$

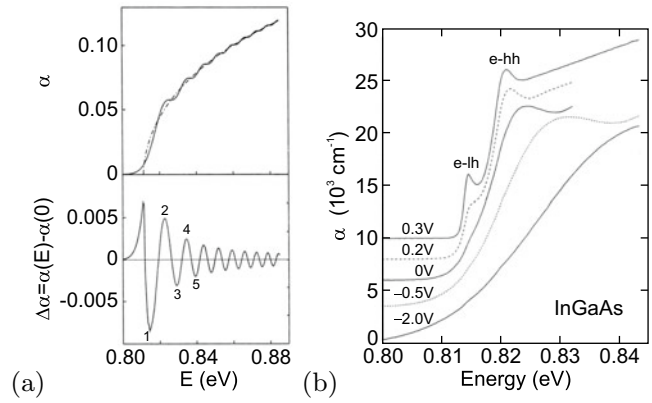

Fig. 15.3 **a** Theoretical absorption (*top panel*) with (*solid line*) and without (*dash-dotted line*) electric field for a volume semiconductor (without Coulomb interaction) and theoretical change of absorption (*bottom panel*). **b** Experimental absorption spectra of (In,Ga)As on InP at $T = 15\,\mathrm{K}$ for various applied voltages as labeled. Adapted from [1421]

A more detailed theory including interband coupling and excitonic effects can be found in [1419]. The effect is best determined with modulation spectroscopy can measuring the difference of absorption with and without field [1420] since it exhibits more defined features (Fig. 15.3a, lower panel).

A nonperiodicity can indicate a nonparabolicity of the mass. Also, the contributions of heavy and light holes merge. For a given mass the electric field strength can be determined. Well-pronounced oscillations are only present for homogeneous fields.

Experimental spectra show additionally the peaks due to excitonic correlation (Fig. 15.3b) at low field strength. At higher fields the FKO evolve and the amplitude of the excitonic peaks decreases because the excitons are ionized in the field.

15.1.2 Quantum Wells

In a quantum well an electric field along the confinement direction (z direction) causes electrons and holes to shift their mean position to opposite interfaces (Fig. 15.1b). However, excitons are not ionized due to the electric field. With increasing field (for both field directions) the energy position of the absorption edge and the recombination energy is reduced. This is the quantum confined Stark effect (QCSE). Corresponding experimental data are shown in Fig. 15.4i–v. The shift depends quadratically on the electric field since the exciton has no permanent dipole moment (mirror symmetry of the quantum well). Thus, only the second-order Stark effect is present (as for the hydrogen atom) in which the field first induces a dipole $\mathbf{p} = \alpha\mathbf{E}$. This dipole interacts with the field with an energy $E = -\mathbf{p}\cdot\mathbf{E} = -\alpha\mathbf{E}^2$. The carrier separation in opposite sides of the quantum well (Fig. 15.4b) leads to a reduced overlap of the electron and hole wavefunctions and subsequently to an increased recombination lifetime (see Fig. 12.43).

If the field is within the quantum-well interface plane, the field leads to the ionization of excitons without shift of the energy position. The loss of the excitonic peak is visualized in the spectra in Fig. 15.4a–c.

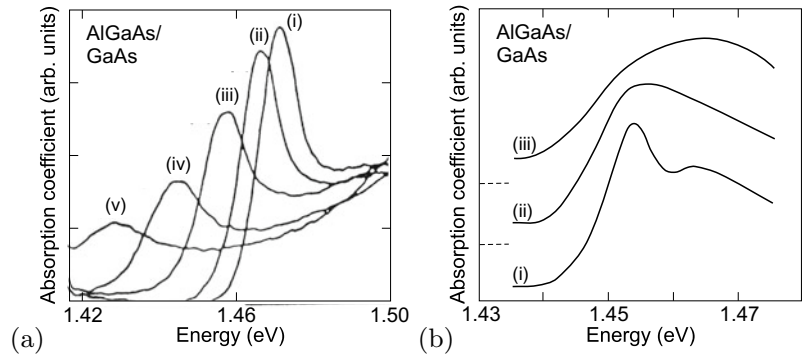

Fig. 15.4 Impact of electric fields on the absorption spectrum of $n \times$ (9.5 nm GaAs/9.8 nm $Al_{0.32}Ga_{0.68}As$) multiple quantum well structures. **a** Electric field along the [001] growth direction ($n = 50$), (**i**)–(**v**) $E = 0$, 0.6, 1.1, 1.5, and 2×10^5 V/cm. **b** Electric field within the interface plane (n = 60), (**i**, **ii**, **iii**) $E = 0$, 1.1, and 2×10^5 V/cm. Adapted from [1422]

15.2 Magnetic Fields

In magnetic fields, electrons (or holes) perform a cyclotron motion with frequency $\omega_c = eB/m^*$, i.e. a motion perpendicular to the magnetic field on a line of constant energy in **k**-space. This line is the intersection of a plane perpendicular to the magnetic field and the respective isoenergy surface in **k**-space. For semiconductors with anisotropic mass, such as Si and Ge, the quantum theory of cyclotron resonance has been given in [1423]. The physics of semiconductors in magnetic fields is covered in detail in [1424].

The ballistic cyclotron motion can only occur between two scattering events. Thus, a significantly long path along the cyclotron trajectory (classically speaking) and the connected magnetotransport properties are only possible when

- $\omega_c \tau \gg 1$, i.e. when the average scattering time τ is sufficiently large. This requires high mobility.
- the magnetic field is sufficiently strong and the temperature sufficiently low, i.e. $\hbar\omega_c \gg kT$, such that thermal excitations do not scatter electrons between different Landau levels.
- the cyclotron path is free of geometric obstructions.

An external magnetic field also produces a Zeeman-like splitting of the spin states. For the electron, the energy splitting ΔE is given by

$$\Delta E = g_e^* \, \mu_B \, B \, , \tag{15.7}$$

where B is the magnetic-field amplitude and g_e^* the (effective) electron g-factor. This value differs from the free-electron value in vacuum of $g_e = 2.0023$ due to the presence of spin-orbit interaction (see Sect. 15.2.3). Values for g_e^* at low carrier density and low temperatures are 2 for Si, 1.2 for InP and ZnSe, -1.65 for CdTe, -0.44 for GaAs, -15 in InAs, and -50 for InSb. In [1425] the temperature dependence of g_e^* in GaAs, InP and CdTe is also measured and discussed. The electron g-factor increases in thin GaAs/(Al,Ga)As quantum wells [1426].

15.2.1 Classical Hall Effect

An electrical current along the x (longitudinal) direction in a perpendicular magnetic field $\mathbf{B} = (0, 0, B)$ along z causes an electric field E_y along the transverse (y) direction (Fig. 15.5). The charge accumu-

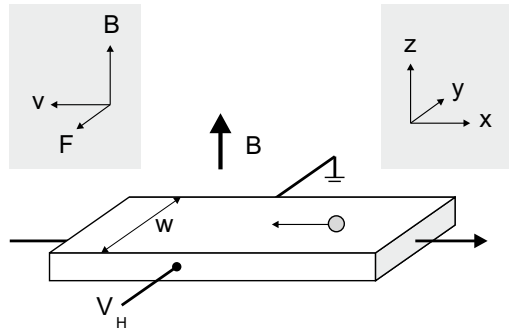

Fig. 15.5 Scheme of the Hall-effect geometry. The movement of one electron in the longitudinal electric current I is shown schematically. The coordinate system (x, y, z) and the directions of the magnetic field **B**, the drift velocity of an electron **v** and the resulting Lorentz force **F** are given. The transverse field E_y is given by V_H/w

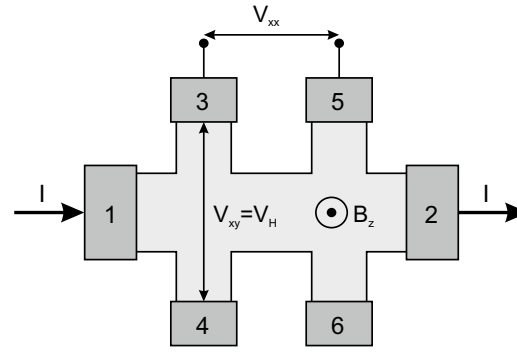

Fig. 15.6 Hallbar geometry. The current I is driven by a source from contact 1 to 2. The Hall voltage is measured between contacts 3 and 4, the longitudinal voltage between 3 and 5

lation is due to the Lorentz force. The related transverse voltage is called the Hall voltage and the resistivity $\rho_{xy} = E_y/j_x$ the Hall resistivity [28, 31, 32]. Many aspects of the Hall effect are discussed in [1427]. For thin-film samples typically Hall bars [1428] (see Fig. 15.6 and also Fig. 15.19, for a reasonable measurement of the Hall voltage the ratio of length and width of the Hall bar should be at least 3) or the van-der-Pauw geometry (Fig. 15.7) and method are used [1429–1431].

For band transport in the relaxation time approximation (Chap. 8.2), the steady-state equation of motion is (in the vicinity of an isotropic extremum)

$$m^* \frac{\mathbf{v}}{\tau} = q\ (\mathbf{E} + \mathbf{v} \times \mathbf{B})\ . \tag{15.8}$$

We note that this equation of motion is also valid for holes, given the convention of Sect. 6.10.1, i.e. positive effective mass and charge. With the cyclotron frequency $\omega_c = qB/m^*$ the conductivity tensor is ($\mathbf{j} = qn\mathbf{v} = \boldsymbol{\sigma}\,\mathbf{E}$)

$$\boldsymbol{\sigma} = \begin{pmatrix} \sigma_{xx} & \sigma_{xy} & 0 \\ \sigma_{yx} & \sigma_{yy} & 0 \\ 0 & 0 & \sigma_{zz} \end{pmatrix} \tag{15.9a}$$

$$\sigma_{xx} = \sigma_{yy} = \sigma_0 \frac{1}{1 + \omega_c^2 \tau^2} = \sigma_0 \frac{1}{1 + \mu^2 B^2} \tag{15.9b}$$

$$\sigma_{xy} = -\sigma_{yx} = \sigma_0 \frac{\omega_c \tau}{1 + \omega_c^2 \tau^2} = \sigma_0 \frac{\mu B}{1 + \mu^2 B^2} \tag{15.9c}$$

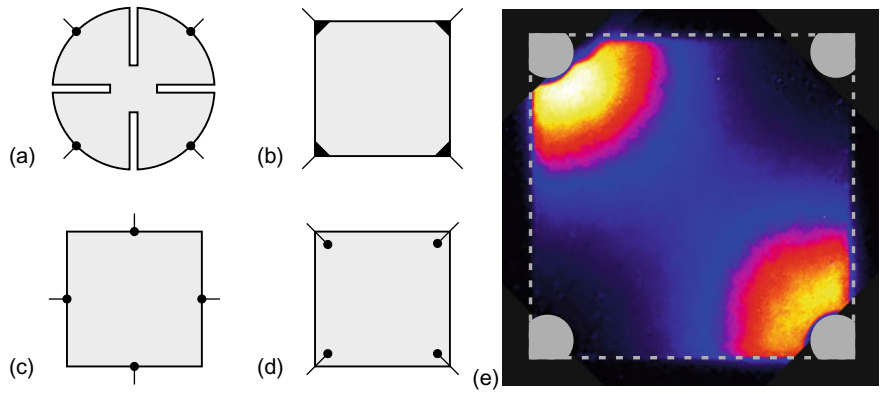

Fig. 15.7 **a**–**d** Geometry for van-der-Pauw Hall measurements. **a** Best geometry (cloverleaf), **b** acceptable square geometry with small contacts on the corners, **c**,**d** not recommended geometries with contacts on the edge centers or inside the square, respectively. **e** Current distribution, as visualized by lock-in thermography [1432], in epitaxial ZnO layer on sapphire with Hall geometry as in part **b**. *Grey dashed line* indicates the outline of the $10 \times 10\,\mathrm{mm}^2$ substrate, *grey areas* indicate gold ohmic contacts

$$\sigma_{zz} = \sigma_0 = \frac{q^2\, n\, \tau}{m^*} = q\, n\, \mu \ . \tag{15.9d}$$

Perpendicular to the magnetic field, the conductivity (σ_{zz}) is given by (8.5). If only one type of carrier (charge q, density n) is considered, the condition $j_y = 0$ leads to $E_y = \mu B\, E_x$ and $j_x = \sigma_0\, E_x$. The Hall coefficient is defined as $R_\mathrm{H} = E_y/(j_x\, B)$ or more precisely as

$$R_\mathrm{H} = \frac{\rho_{xy}}{B} \ , \tag{15.10}$$

where the resistivity tensor $\boldsymbol{\rho}$ is the inverse of the conductivity tensor $\boldsymbol{\sigma}$,

$$\boldsymbol{\rho} = \boldsymbol{\sigma}^{-1} = \begin{pmatrix} \rho_{xx} & \rho_{xy} & 0 \\ \rho_{yx} & \rho_{yy} & 0 \\ 0 & 0 & \rho_{zz} \end{pmatrix} \tag{15.11a}$$

$$\rho_{xx} = \rho_{yy} = \frac{\sigma_{xx}}{\sigma_{xx}^2 + \sigma_{xy}^2} \tag{15.11b}$$

$$\rho_{xy} = -\rho_{yx} = \frac{\sigma_{xy}}{\sigma_{xx}^2 + \sigma_{xy}^2} \tag{15.11c}$$

$$\rho_{zz} = \frac{1}{\sigma_{zz}} = \frac{1}{\sigma_0} \ . \tag{15.11d}$$

For a single type of carriers, the Hall coefficient is therefore given by

$$R_\mathrm{H} = \frac{\mu}{\sigma_0} = \frac{1}{q\, n} \ . \tag{15.12}$$

It is negative (positive) for electron (hole) conduction. We note that electrons and holes are deflected in the *same* y-direction by the magnetic field and collect at the same electrode. Thus the Hall effect

allows the determination of the carrier type and the carrier density.[1]

If both types of carriers are present simultaneously, the conductivity (two-band conduction) is given by the sum of electron and hole conductivity (8.11),

$$\boldsymbol{\sigma} = \boldsymbol{\sigma}_\mathrm{e} + \boldsymbol{\sigma}_\mathrm{h} \,. \tag{15.13}$$

The Hall constant (15.10) is then

$$R_\mathrm{H} = \frac{1}{e} \, \frac{-n\,\mu_\mathrm{e}^2\,(1+\mu_\mathrm{h}^2\,B^2) + p\,\mu_\mathrm{h}^2\,(1+\mu_\mathrm{e}^2\,B^2)}{n^2\,\mu_\mathrm{e}^2\,(1+\mu_\mathrm{h}^2\,B^2) - 2\,n\,p\,\mu_\mathrm{e}\,\mu_\mathrm{h}\,(1+\mu_\mathrm{e}\,\mu_\mathrm{h}\,B^2) + p^2\,\mu_\mathrm{h}^2\,(1+\mu_\mathrm{e}^2\,B^2)} \,. \tag{15.14}$$

Under the assumption of small magnetic fields,[2] i.e. $\mu B \ll 1$, the Hall coefficient is

$$R_\mathrm{H} = \frac{1}{e} \left[\frac{-n\,\mu_\mathrm{e}^2 + p\,\mu_\mathrm{h}^2}{(-n\,\mu_\mathrm{e} + p\,\mu_\mathrm{h})^2} + \frac{n\,p\,(-n+p)\,\mu_\mathrm{e}^2\,\mu_\mathrm{h}^2\,(\mu_\mathrm{e}-\mu_\mathrm{h})^2}{(-n\,\mu_\mathrm{e} + p\,\mu_\mathrm{h})^4}\,B^2 + \ldots \right] . \tag{15.15}$$

For small magnetic field this can be written as

$$R_\mathrm{H} = \frac{1}{e} \, \frac{p - n\,\beta^2}{(p - n\,\beta)^2} \,, \tag{15.16}$$

with $\beta = \mu_\mathrm{e}/\mu_\mathrm{h} < 0$. For large magnetic fields, i.e. $\mu B \gg 1$, the Hall coefficient is given by

$$R_\mathrm{H} = \frac{1}{e} \, \frac{1}{p-n} \,. \tag{15.17}$$

In Fig. 15.8, the absolute value of the Hall coefficient for InSb samples with different doping concentrations is shown. The p-doped samples exhibit a reverse of the sign of the Hall coefficient upon increase of temperature when intrinsic electrons contribute to the conductivity. The zero in R_H occurs for $n = p\,\mu_\mathrm{h}^2/\mu_\mathrm{e}^2 = n_\mathrm{i}/|\beta|$. For high temperatures, the Hall coefficient for n- *and* p-doped samples is dominated by the electrons that have much higher mobility (Table 8.2).

The simultaneous conduction in a band and an impurity band (cmp. Sect. 8.6) has been separated with a suitable model assuming two conduction channels for holes [1434] (Fig. 15.9).

In (15.8) an isotropic mass was considered. For semiconductors with multiple valleys and anisotropic extrema, in particular the conduction bands of Si and Ge (cf. Sect. 6.9.2), the Hall coefficient has been derived in [1435, 1436]. With $K = m_\mathrm{l}/m_\mathrm{t}$ being the mass anisotropy (cmp. Table 6.5), the Hall coefficient (15.12) changes to,

$$R_\mathrm{H} = \frac{1}{q\,n} \, \frac{3\,K\,(K+2)}{(2K+1)^2} \,. \tag{15.18}$$

In the derivation of the (unipolar) Hall coefficient we had assumed that all carriers involved in the transport have the same properties, in particular that they are subject to the same scattering time. This assumption is generally not the case (cmp. Chap. J) and we need to operate with the ensemble average of the discussed quantities. The ensemble average of an energy-dependent quantity $\zeta(E)$ over the

[1] Using the Hall effect, the net *free* charge carrier concentration is determined. We note that the concentration of *fixed* charges in semiconductors can be investigated by depletion layer spectroscopy (Sect. 21.2.4).

[2] We note that for a mobility of $10^4\,\mathrm{cm}^2/\mathrm{Vs}$, μ^{-1} is a field of $B = 1\,\mathrm{T}$.

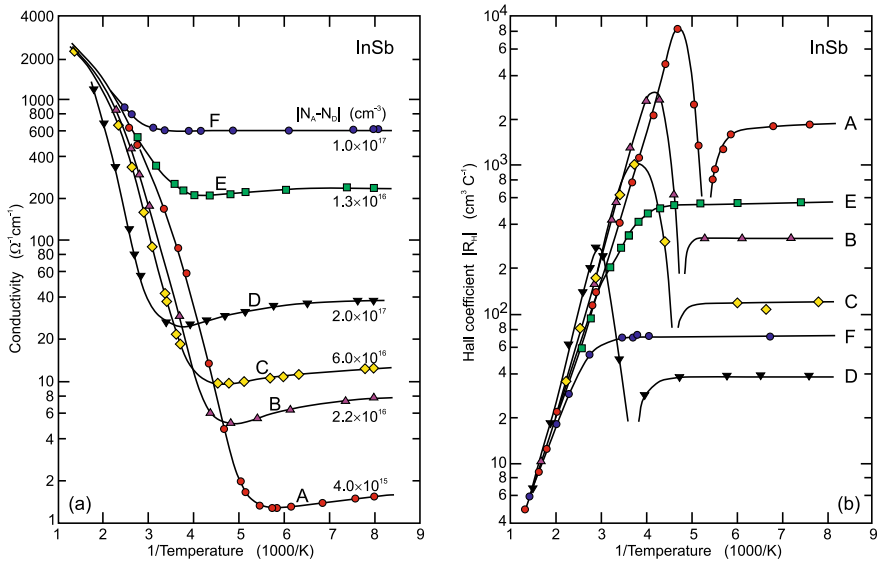

Fig. 15.8 **a** Conductivity and **b** absolute value of the Hall coefficient versus inverse temperature for four p-doped (A–D) and two n-doped (E, F) InSb samples. The doping levels are given in (**a**). Adapted from [1433]

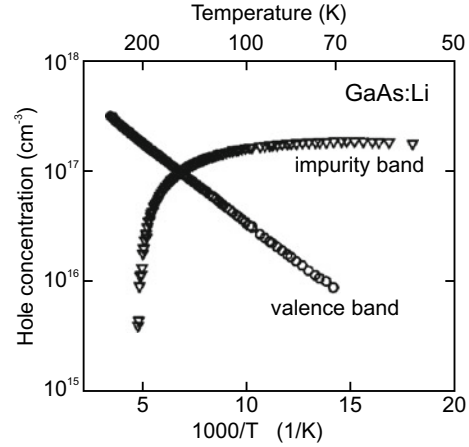

Fig. 15.9 Carrier densities in valence band (*circles*) and impurity band (*triangles*) from evaluating the Hall effect on GaAs doped with lithium (and annealed) taking into account two conduction channels. Adapted from [1434]

(electron) distribution function $f(E)$ is denoted as $\langle\zeta\rangle$ and is given as[3]

$$\langle\zeta\rangle = \frac{\int \zeta(e)\, f(E)\, \mathrm{d}E}{\int f(E)\, \mathrm{d}E} \,. \tag{15.19}$$

In particular, the average $\langle\tau\rangle^2$ is now different from $\langle\tau^2\rangle$. Considering the equation $\langle\mathbf{j}\rangle = \langle\boldsymbol{\sigma}\rangle\,\mathbf{E}$ for the ensemble-averaged current density we find (for one type of carrier, cf. (15.12))

[3]For this consideration it is assumed that the energy dependence is the decisive one. Generally, averaging may have to be performed over other degrees of freedom as well, such as the spin or, in the case of anisotropic bands, the orbital direction.

$$R_{\mathrm{H}} = \frac{1}{q\,n}\,r_{\mathrm{H}}\ , \tag{15.20}$$

with the so-called *Hall factor* r_{H} given by

$$\begin{aligned} r_{\mathrm{H}} &= \frac{\gamma}{\alpha^2 + \omega_{\mathrm{c}}^2\,\gamma^2}\ , \\ \alpha &= \left\langle \frac{\tau}{1+\omega_{\mathrm{c}}^2\,\tau^2} \right\rangle\ , \quad \gamma = \left\langle \frac{\tau^2}{1+\omega_{\mathrm{c}}^2\,\tau^2} \right\rangle\ . \end{aligned} \tag{15.21}$$

The Hall factor depends on the scattering mechanisms and is of the order of 1. For large magnetic fields the Hall factor approaches 1. For small magnetic fields we have

$$R_{\mathrm{H}} = \frac{1}{q\,n}\,\frac{\langle\tau^2\rangle}{\langle\tau\rangle^2}\ . \tag{15.22}$$

The mobility calculated from (cf. (15.9d)) $\sigma_0 R_{\mathrm{H}}$ is called the *Hall mobility* μ_{H} and is related to the mobility via

$$\mu_{\mathrm{H}} = r_{\mathrm{H}}\,\mu\ . \tag{15.23}$$

It is assumed so far that the free carrier density and mobility are homogeneous within the volume of current transport. Multi-layer models can be fitted to experimental Hall data in order to account for different conduction channels in different layered parts of the sample [1437]. E.g., in a two-layer model, contributions from bulk and surface/interface conduction can be separated [1438–1440].

The magnetic field dependence of $\boldsymbol{\sigma}$ can be used in a general case to separate contributions of carriers with different density and mobility (including its sign) without assumptions and obtain the mobility spectrum $s(\mu)$ (MSA, mobility spectral analysis),

$$\sigma_{xx} = \int_{-\infty}^{\infty} s(\mu)\,\frac{1}{1+\mu^2 B^2}\,\mathrm{d}\mu \tag{15.24a}$$

$$\sigma_{xy} = \int_{-\infty}^{\infty} s(\mu)\,\frac{\mu B}{1+\mu^2 B^2}\,\mathrm{d}\mu\ , \tag{15.24b}$$

as a generalization of (15.13), (15.9b) and (15.9c) [1441–1443]. Examples are the separation of electron conductivity in (GaAs-) Γ- and (InAs-) X-Minima in a GaAs/(Al,Ga)As/InAs double quantum well structures [1441] (Fig. 15.10a), substrate and 2DEG electron conductivity in (Al,Ga)N/GaN heterostructures [1444], and electrons and holes in an InAs/GaSb quantum well [1442] (Fig. 15.10b).

In the case of hopping conduction (Chap. 8.8), the theory of Hall effect is more involved [1445, 1446]. If carriers are transported by hopping, generally, they may not be free to move as expected by (15.8) in response to the applied magnetic field and the Lorentz force. A Hall effect occurs only at the junction of *three* (or more) hopping sites [1445]. The sign of the experimentally determined Hall coefficient is often opposite to the one expected from the carrier type according to (15.12), e.g., as studied in a-Si [1447, 1448]. The *sign anomaly* depends on intricacies such as the local site geometry and interference processes taking place among bonding and antibonding orbitals of various numbers as summarized in [1449].

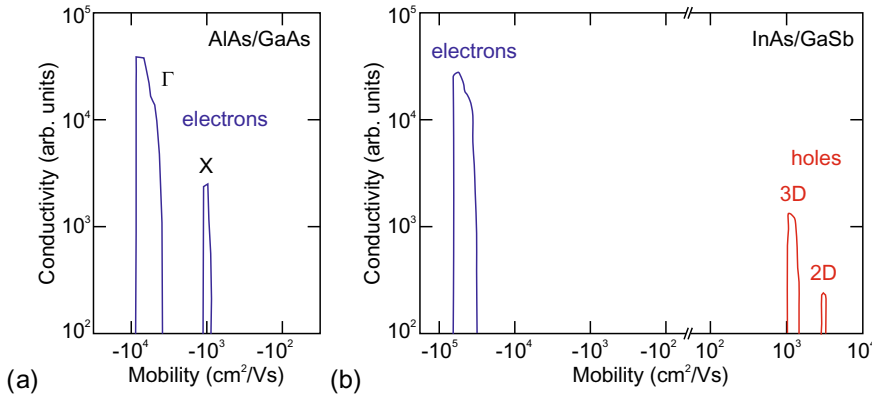

Fig. 15.10 **a** Mobility spectrum of GaAs/(Al,Ga)As/InAs double quantum well structure. Adapted from [1441]. **b** Mobility spectrum of InAs/GaSb quantum well structure. Adapted from [1442]

15.2.2 Free-Carrier Absorption

The absorption of free carriers was treated in Sect. 9.9.1 without the presence of a static magnetic field. Solving (15.8) for a static magnetic field $\mathbf{B} = \mu_0 \mathbf{H}$ with $\mathbf{H} = H\,(h_x, h_y, h_z)$ and a harmonic electric field $\mathbf{E} \propto \exp(-\mathrm{i}\omega t)$ yields for the dielectric tensor (cf. (9.72))

$$\boldsymbol{\epsilon} = \frac{\mathrm{i}}{\epsilon_0\,\omega}\,\boldsymbol{\sigma}\ , \tag{15.25}$$

and by comparing to $\mathbf{j} = \boldsymbol{\sigma}\,\mathbf{E} = q\,n\,\mathbf{v}$,

$$\boldsymbol{\epsilon}(\omega) = -\omega_\mathrm{p}^{*2}\left[(\omega^2 + \mathrm{i}\,\omega\,\gamma)\,\mathbf{1} - \mathrm{i}\,\omega_\mathrm{c}^2\begin{pmatrix} 0 & -h_z & h_y \\ h_z & 0 & -h_x \\ -h_y & h_x & 0 \end{pmatrix}\right]^{-1}\ , \tag{15.26}$$

where $\mathbf{1}$ denotes the (3 by 3) unity matrix and $\gamma = 1/\tau = q/(m^*\mu)$ is the damping parameter with μ representing the optical carrier mobility (in the non-isotropic case a tensor $\boldsymbol{\gamma}$ needs to be used). The (unscreened) plasma frequency is given by (cmp. (9.77))

$$\omega_\mathrm{p}^* = \sqrt{n\,\frac{e^2}{\epsilon_0\,m^*}}\ . \tag{15.27}$$

The free-carrier cyclotron frequency is

$$\omega_\mathrm{c} = e\,\frac{\mu_0\,H}{m^*}\ . \tag{15.28}$$

If the effective mass is treated as a tensor, $1/m^*$ is replaced by $\mathbf{m}^{*-1}$ in (15.27) and (15.28). For zero magnetic field the classical Drude theory for one carrier species is recovered (cf. (9.74a))

$$\epsilon(\omega) = -\frac{\omega_\mathrm{p}^{*2}}{\omega\,(\omega + \mathrm{i}\gamma)}\ . \tag{15.29}$$

With the magnetic field perpendicular to the sample surface, i.e. $\mathbf{B} = \mu_0\,(0, 0, H)$ the magneto-optic dielectric tensor simplifies to (cf. (15.9d))

$$\epsilon(\omega) = -\frac{\omega_\mathrm{p}^{*2}}{\omega^2}\begin{pmatrix} \tilde{\epsilon}_{xx} & \mathrm{i}\tilde{\epsilon}_{xy} & 0 \\ -\mathrm{i}\tilde{\epsilon}_{xy} & \tilde{\epsilon}_{xx} & 0 \\ 0 & 0 & \tilde{\epsilon}_{zz} \end{pmatrix} \tag{15.30a}$$

$$\tilde{\epsilon}_{xx} = \frac{1 + \mathrm{i}\gamma/\omega}{(1 + \mathrm{i}\gamma/\omega)^2 - (\omega_\mathrm{c}/\omega)^2} \tag{15.30b}$$

$$\tilde{\epsilon}_{zz} = \frac{1}{(1 + \mathrm{i}\gamma/\omega)} \tag{15.30c}$$

$$\tilde{\epsilon}_{xy} = \frac{\omega_\mathrm{c}/\omega}{(1 + \mathrm{i}\gamma/\omega)^2 - (\omega_\mathrm{c}/\omega)^2}\,. \tag{15.30d}$$

The in-plane component ϵ_{xx} provides information about ω_p^* and γ, i.e. two of the three parameters n, μ and m^* are known. Additionally, the antisymmetric tensor component ϵ_{xy} is linear in the cyclotron frequency and provides q/m^*. This subtle but finite birefringence depends on the strength (and orientation) of the magnetic field and can be experimentally determined in the infrared using magneto-ellipsometry [1450, 1451]. Such 'optical Hall effect' experiment allows the determination of the carrier density n, the mobility μ, the carrier mass[4] m^* and the sign of the carrier charge $\mathrm{sgn}(q)$ with optical means. The electrical Hall effect (Sect. 15.2.1) can reveal n, μ and $\mathrm{sgn}(q)$ but cannot reveal the carrier mass.

15.2.3 Energy Levels in Bulk Crystals

In a 3D electron gas (the magnetic field is along z, i.e. $\mathbf{B} = B\,(0, 0, 1)$) the motion in the (x, y) plane is described by Landau levels. Quantum mechanically they correspond to levels of a harmonic oscillator. The magnetic field has no impact on the motion of electrons along z, such that in this direction a free dispersion relation $\propto k_z^2$ is present. The energy levels are given as

$$E_{nk_z} = \left(n + \frac{1}{2}\right)\hbar\omega_\mathrm{c} + \frac{\hbar^2}{2m}\,k_z^2\,. \tag{15.31}$$

Thus, the states are on concentric cylinders in $\mathbf{k}$-space (Fig. 15.11a). The populated states of the 3D electron gas (at 0 K) lie within the Fermi vector of length k_F. For the 3D system the density of states at the Fermi energy is a square root function of the Fermi energy (6.71). In the presence of a magnetic field the density of states diverges every time that a new cylinder (with a one-dimensional density of states, (6.79)) touches the Fermi surface at E_F. In real systems, the divergence will be smoothed, however, a pronounced peak or the periodic nature of the density of states is often preserved.

The period is given by the number n_m of cyclotron orbits (Landau levels) within the Fermi surface.

$$\left(n_\mathrm{m} + \frac{1}{2}\right)\hbar\omega_\mathrm{c} = E_\mathrm{F}\,. \tag{15.32}$$

If the number of carriers is constant, the density of states at the Fermi energy at varying magnetic field varies periodically with $1/B$. From the conditions $(n_\mathrm{m} + \frac{1}{2})\hbar e B_1/m = E_\mathrm{F}$ and $(n_\mathrm{m} + 1 + \frac{1}{2})\hbar e B_2/m = E_\mathrm{F}$ with $1/B_2 = 1/B_1 + 1/\Delta B$ we find,

[4] We note that mobility and effective mass defined and measured in this way may be referred to as 'optical'. Other definitions and approaches to the mobility or effective mass may give different results.

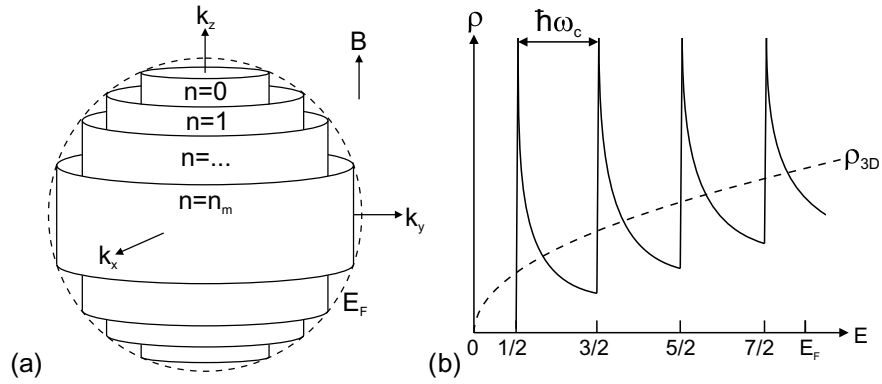

Fig. 15.11 3D electron gas in an external magnetic field. **a** Allowed states in **k**-space for magnetic field along the z direction. **b** Density of states (DOS) ρ versus energy (in units of $\hbar\omega_c$). *Dashed line* is three-dimensional DOS without magnetic field. Based on [1123]

$$\frac{1}{\Delta B} = \frac{e\,\hbar}{m^*\,E_\mathrm{F}}\ . \tag{15.33}$$

This periodicity is used to determine experimentally, e.g., the properties of the Fermi surface in metals using the Shubnikov-de Haas oscillations (of the magnetoresistance) or the de Haas-van Alphén effect (oscillation of the magnetic susceptibility).

Equation (15.31) needs to be extended to account for the splitting (15.7) of the Landau level due to the electron spin. According to [1452], the electron Landau level energy can be written as

$$E_n = \left(n + \frac{1}{2}\right)\frac{\hbar\,e\,B}{m^*(E)} \pm g_\mathrm{e}^*(E)\,\mu_\mathrm{B}\,B\ , \tag{15.34}$$

with energy dependent effective mass and g-factor

$$\frac{1}{m^*(E)} = \frac{1}{m^*(0)}\,\frac{E_\mathrm{g}\,(E_\mathrm{g}+\Delta_0)}{3E_\mathrm{g}+2\Delta_0}\left(\frac{2}{E+E_\mathrm{g}} + \frac{1}{E+E_\mathrm{g}+\Delta_0}\right) \tag{15.35a}$$

$$g_\mathrm{e}^*(E) = g_\mathrm{e}^*(0)\,\frac{E_\mathrm{g}(E_\mathrm{g}+\Delta_0)}{\Delta_0}\left(\frac{1}{E+E_\mathrm{g}} - \frac{1}{E+E_\mathrm{g}+\Delta_0}\right) \tag{15.35b}$$

The band edge value $m^*(0)$ of the effective mass is given by (6.43) and that of the g-factor by

$$g_\mathrm{e}^*(0) = 2\left[1 - \frac{2\,\Delta_0}{3\,E_\mathrm{g}\,(E_\mathrm{g}+\Delta_0)}\,E_\mathrm{P}\right]\ . \tag{15.36}$$

For large spin-orbit splitting, the value of the g-factor deviates strongly from 2 and becomes negative.

15.2.4 Magnetic Field Effect on Impurities

The Zeeman effect is the magnetic field dependence (and the lifting of degeneracies) of spectral lines. For semiconductor physics this is a tool to investigate properties of defect related states with sufficiently sharp spectral features. As example we refer to the investigation of the Si:P donor system

(cmp. Fig. 9.33) and its linear and quadratic Zeeman effect [1453] as visualized in Fig. 15.12. The difference in transition energies for lines 4 and 1 depends linearly on the magnetic field and is equal to the electron spin splitting. The quadratic Zeeman effect is also termed 'diamagnetic shift' and allows a determination of the wavefunction size. In the present case, the electron Bohr radius at the neutral phosphorus donor in Si was found to be $a_D = 1.33(5)$ nm (cmp. (7.22)) [1453].

15.2.5 Magnetic Field Effect on Excitons

The effect of an magnetic field on excitons is similar to that on the wave function at an impurity, except that the electron and hole are effected simultaneously. The effect is two-fold: The Zeeman-like effect on the spin states leads to a splitting of the exciton lines which become circularly polarized; for 'weak' fields the splitting is linear with the field. Additionally, the magnetic field leads to a reduction of exciton size leading to a quadratic shift of the line center to larger energies, the so-called diamagnetic shift. Calculations for various confinement geometries have been given in [1454]. The change of exciton size leads also to modification of localization effects in disordered quantum wells [1455]. As example the magnetic field dependence of quasi two-dimensional excitons in a WS_2 monolayer is shown in Fig. 15.13 (cf. Sect. 13.2.4).

15.2.6 Energy Levels in a 2DEG

In a 2D electron gas (2DEG), e.g., in a quantum well or a potential well at a modulation-doped heterointerface, a free motion in z is not possible and k_z is quantized. The energy levels (for each 2D subband) are only given by the cyclotron energy (Fig. 15.14a). The density of states is a sequence of δ-like peaks (Fig. 15.14b). Each peak contributes (degeneracy $\hat{g}$ of a Landau level) a total number of

$$\hat{g} = \frac{e\,B}{h} \tag{15.37}$$

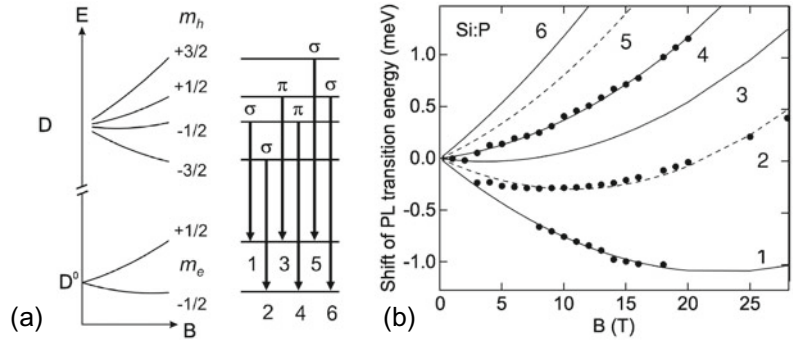

Fig. 15.12 **a** Schematic level scheme and transitions (and their polarization) of donor bound excitons at Si:P. **b** Experimental magnetic field dependent shift of photoluminescence transition energies (from about $E = 1.150$ eV at $B = 0$ T) (*symbols*) together with fits for heavy (*dashed lines*) and light (*solid lines*) hole transitions. Adapted from [1453]

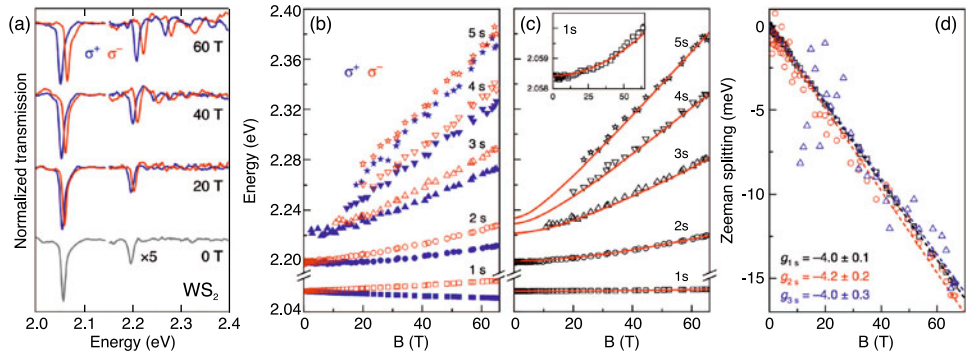

Fig. 15.13 Magnetic field effect on excitons in WS_2 monolayer. **a** Normalized transmission spectra. **b** Energy position of $E_{\sigma+}$ and $E_{\sigma-}$ of (circularly polarized) spectral lines of the 1–5 s exciton lines. **c** Calculated energy $(E_{\sigma+} + E_{\sigma-})/2$, showing the diamagnetic shift. *Solid lines* are model calculation with reduced exciton mass $m_r^* = 0.175$ (and further parameters), **d** Zeeman splitting $E_{\sigma+} - E_{\sigma-}$ of the 1–3 s states together with linear fits (*dashed line*), g-factors are around 4, as labelled. Adapted from [1313], reprinted under Creative Commons Attribute (CC BY 4.0) license

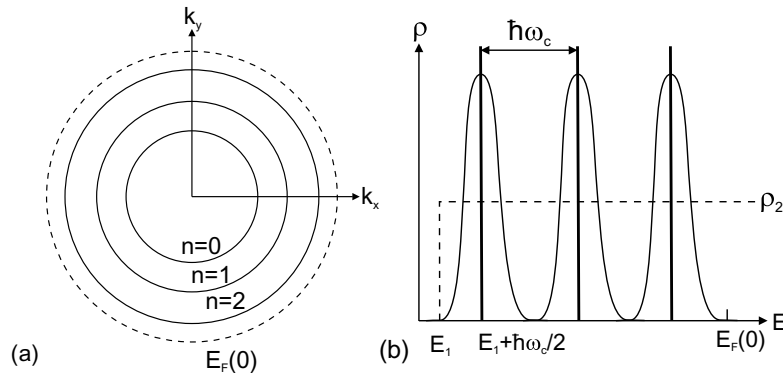

Fig. 15.14 2D electron gas in an external magnetic field. **a** Allowed states in **k**-space. **b** Density of states (DOS) ρ versus energy. *Dashed line* is two-dimensional DOS without magnetic field. *Thick vertical lines*: δ-like DOS without broadening, *curves*: broadened DOS. Based on [1123]

states (per unit area without spin degeneracy and without the degeneracy of the band extremum). In reality, disorder effects lead to an inhomogeneous broadening of these peaks. The states in the tails of the peaks correspond to states that are localized in real space.

Also, in a 2D system several physical properties exhibit an oscillatory behavior as a function of Fermi level, i.e. with varying electron number, and as a function of the magnetic field at fixed Fermi energy, i.e. at fixed electron number (Fig. 15.15).

15.2.7 Shubnikov-De Haas Oscillations

From the 2D density of states (per unit area including spin degeneracy) $D^{2D}(E) = m^*/\pi\hbar^2$ the sheet density of electrons n_s can be expressed as a function of the Fermi level (at $T = 0\,\mathrm{K}$ without spin degeneracy)

$$n_s = \frac{m^*}{2\pi\,\hbar^2}\,E_F\ . \tag{15.38}$$

Using (15.33) we thus find (without spin degeneracy, without valley degeneracy), that the period of $1/B$ is $\propto n_s$:

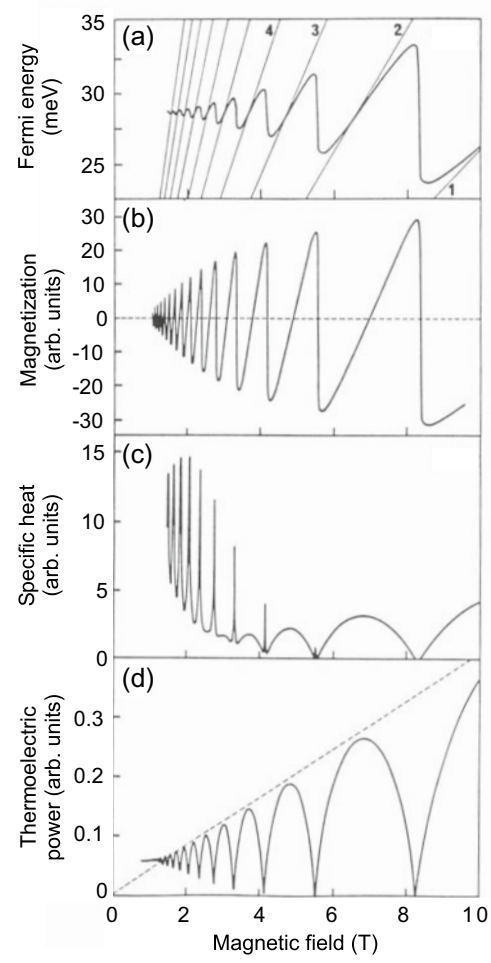

Fig. 15.15 Oscillatory (theory, $T = 6\,\mathrm{K}$) behavior of a 2DEG (GaAs/(Al,Ga)As) in a magnetic field: **a** Fermi level, **b** magnetization, **c** specific heat, **d** thermoelectric power. A Gaussian broadening of 0.5 meV was assumed. Adapted from [1123, 1456]

$$\frac{1}{\Delta B} = \frac{e}{h}\,\frac{1}{n_\mathrm{s}}\,. \tag{15.39}$$

The carrier density of a 2DEG can therefore be determined from the oscillations of magnetoresistance, and is proportional to the density of states at the Fermi level (Shubnikov-de Haas effect). A corresponding measurement with varying field and fixed electron density is shown in Fig. 15.16. The periodicity with $1/B$ is obvious. Since only the component of the magnetic field perpendicular to the layer affects the (x, y) motion of the carriers, no effect is observed for the magnetic field parallel to the layer.

In another experiment the carrier density was varied at constant field (Fig. 15.17). The electron density in an inversion layer in p-type silicon is (linearly) varied with the gate voltage of a MOS (metal-oxide-semiconductor) structure (inset in Fig. 15.17, for MOS diodes cf. Sect. 24.5). In this experiment, the Fermi level was shifted through the Landau levels. The equidistant peaks show that indeed each Landau level contributes the same number of states.

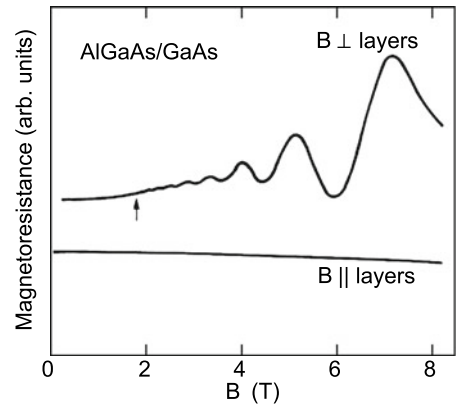

Fig. 15.16 Shubnikov-de Haas oscillations at a modulation-doped (Al,Ga)As/GaAs heterostructure with a 2DEG, $n = 1.7 \times 10^{17}\,\mathrm{cm}^{-2}$ and $\mu = 11\,400\,\mathrm{cm}^2/\mathrm{Vs}$. Data from [1457]

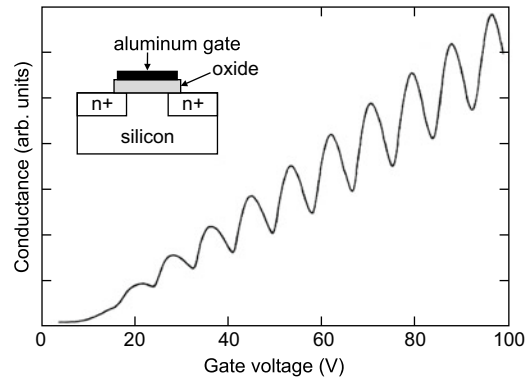

Fig. 15.17 Shubnikov-de Haas oscillations of a 2DEG at the (100) surface of p-type silicon ($100\,\Omega\,\mathrm{cm}$) at a magnetic field of $B = 3.3\,\mathrm{T}$ and $T = 1.34\,\mathrm{K}$. The *inset* shows schematically the contact geometry. Data from [1458]

15.2.8 Quantum Hall Effect

In high magnetic fields, at low temperatures and for high-mobility, 2D electron gases exhibit a deviation from the classical behavior. We recall that the classical Hall effect (i.e. considering the Lorentz force, classical Drude theory), the generation of a field E_y perpendicular to a current flow j_x (cf. Sect. 15.2.1), was described with the conductivity tensor σ (here, for the (x, y)-plane only)

$$\sigma = \frac{\sigma_0}{1 + \omega_c^2 \tau^2} \begin{pmatrix} 1 & \omega_c \tau \\ -\omega_c \tau & 1 \end{pmatrix} \tag{15.40a}$$

$$\sigma_{xx} = \sigma_0 \frac{1}{1 + \omega_c^2 \tau^2} \to 0 \tag{15.40b}$$

$$\sigma_{xy} = \sigma_0 \frac{\omega_c \tau}{1 + \omega_c^2 \tau^2} \to \frac{n\,e}{B}\,, \tag{15.40c}$$

where σ_0 is the zero-field conductivity $\sigma_0 = ne^2\tau/m^*$ (8.5). The arrows denote the limit for $\omega_c\tau \to \infty$, i.e. large fields. The resistivity tensor $\rho = \sigma^{-1}$ is given by

$$\rho = \begin{pmatrix} \rho_{xx} & \rho_{xy} \\ -\rho_{xy} & \rho_{xx} \end{pmatrix} \tag{15.41a}$$

$$\rho_{xx} = \frac{\sigma_{xx}}{\sigma_{xx}^2 + \sigma_{xy}^2} \to 0 \tag{15.41b}$$

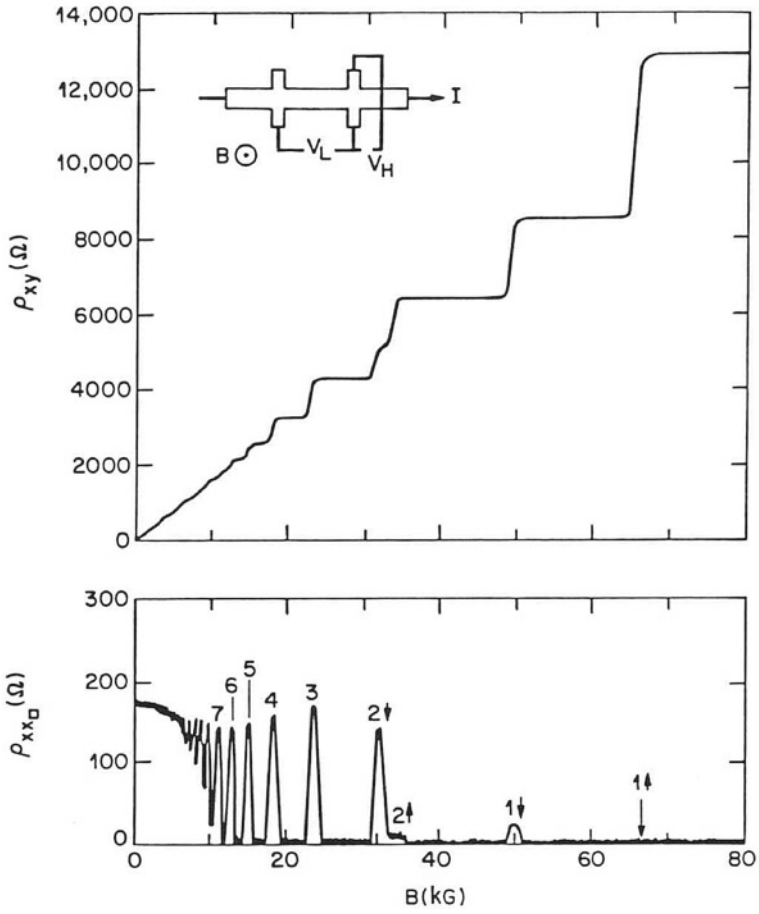

Fig. 15.18 Hall resistivity ρ_{xy} and longitudinal resistivity ρ_{xx} for a modulation-doped GaAs/(Al,Ga)As heterostructure ($n = 4 \times 10^{11}\,\mathrm{cm}^{-2}$, $\mu = 8.6 \times 10^4\,\mathrm{cm}^2/\mathrm{Vs}$) at 50 mK as a function of magnetic field (10 kG=1 T). The numbers refer to the quantum number and spin polarization of the Landau level involved. The inset shows schematically the Hall bar geometry, V_L (V_H) denotes the longitudinal (Hall) voltage drop. Reprinted with permission from [1459], ©1982 APS

$$\rho_{xy} = \frac{-\sigma_{xy}}{\sigma_{xx}^2 + \sigma_{xy}^2} \to -\frac{B}{n\,e}\,. \tag{15.41c}$$

15.2.8.1 Integer QHE

Experiments yield strong deviations from the linear behavior of the transverse resistivity $\rho_{xy} \propto B$ (15.41c) for large magnetic fields at low temperatures for samples with high carrier mobility, i.e. $\omega_\mathrm{c}\tau \gg 1$ (Fig. 15.18). In Fig. 15.19a, b, Hall bars are shown for 2DEGs in silicon metal-oxide-semiconductor field-effect transistor (Si-MOSFET) electron inversion layers and at GaAs/(Al,Ga)As heterostructures, respectively.

The Hall resistivity exhibits extended Hall plateaus with resistivity values that are given by

$$\frac{1}{\rho_{xy}} = \nu\,\frac{e^2}{h}\,, \tag{15.42}$$

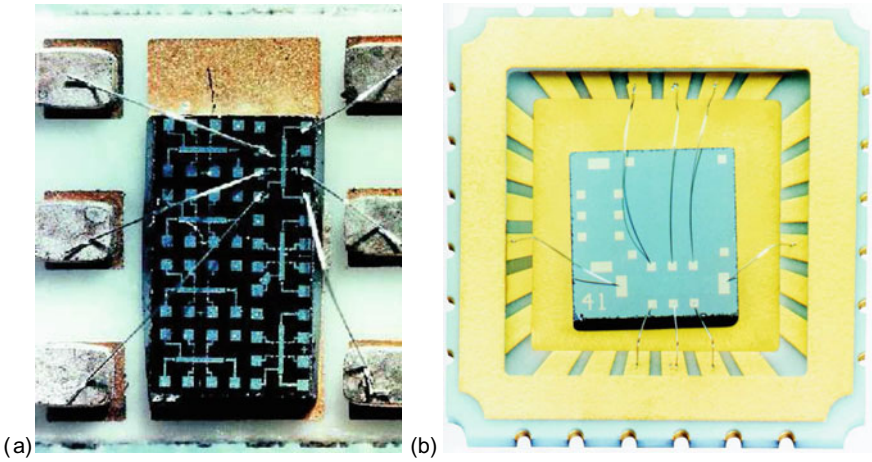

Fig. 15.19 **a** Silicon MOS (metal-oxide-semiconductor) structure of K. v. Klitzing's et al. original experiments. **b** GaAs/(Al,Ga)As heterostructure sample grown with molecular beam epitaxy for QHE measurements, chip carrier and bond wires. Reprinted with permission from [1460]

with $\nu \in \mathbb{N}$, i.e. integer fractions of the quantized resistance $\rho_0 = h/e^2 = 25812.807\ldots\,\Omega$, which is also called the von-Klitzing constant. In Fig. 15.18, a spin splitting is seen for the $n = 1$ Landau level (and a small one for the $n = 2$). We note that the topmost Hall plateau is due to the completely filled $n = 0$ Landau level; the resistance is $\rho_0/2$ due to the spin degeneracy of 2.

The integer quantum Hall effect, first reported in [1461, 1462], and the value for ρ_0 are found for a wide variety of samples and conditions regarding sample temperature, electron density or mobility of the 2DEG and the materials of the heterostructure. Besides the Hall effect in Si-based structures and record mobility (Al,Ga)As/GaAs heterostructures (cf. Fig. 12.37), also (Mg,Zn)O/ZnO heterostructures exhibit the effect [1463, 1464] in the same fashion.

Within the plateau, the resistivity is well defined within 10^{-7} or better up to the 10^{-9} regime. A precise determination allows for a new normal for the unit Ohm [1389, 1465], being two orders of magnitude more precise than the realization in the SI system, and an independent value for the fine-structure constant $\alpha = (e^2/h)/(2\,c\,\epsilon_0)$. At the same time, the longitudinal resistivity, starting from the classical value for small magnetic fields, exhibits oscillations and eventually it is close to zero for the plateaus in ρ_{xy}. For ρ_{xx} values of $10^{-10}\,\Omega/\square$ have been measured, which corresponds to $10^{-16}\,\Omega$/cm for bulk material, a value three orders of magnitude smaller than for any non-superconductor.

The interpretation of the quantum Hall effect(s) is discussed in [1466] among many other treatises. The simplest explanation is that the conductivity is zero when a Landau level is completely filled and the next is completely empty, i.e. the Fermi level lies between them. The temperature is small, i.e. $kT \ll \hbar\omega_c$, such that no scattering between Landau levels can occur. Thus no current, similar to a completely filled valence band, can flow. The sheet carrier density n_s is given by counting the i filled Landau levels (degeneracy according to (15.37)) as

$$n_s = i\,\frac{e\,B}{h}\,. \tag{15.43}$$

In the transverse direction energy dissipation takes place and the Hall resistivity $\rho_{xy} = B/(n_s e)$ takes the (scattering-free) values given in (15.42).

However, this argument is too simple as it will not explain the extension of the plateaus. As soon as the system has one electron more or less, the Fermi energy will (for a system with δ-like density of

states) be located in the upper or lower Landau level, respectively. Then, the longitudinal conductivity should no longer be zero and the Hall resistivity deviates from the integer fraction of ρ_0. In general, a single particle picture is insufficient to model the IQHE.

The accepted model for the explanation of the QHE, supported now with plenty of experimental evidence, is the edge state model where quantized one-dimensional conductivity of edge channels, i.e. the presence of conductive channels along the sample boundaries, is evoked [1475].

The most fundamental arguments for the origin of the IQHE come from gauge invariance and the presence of a macroscopic quantum state of electrons and magnetic flux quanta [1468]. This model holds as long as there are any extended states at all in the inhomogeneously broadened density of states (Landau levels) (Fig. 15.14). These edge states arise from the fact that the quantum Hall state has another topology than the (topologically trivial) surrounding [463, 1469, 1470]. Each plateau corresponds to a distinct topological phase characterized by a Chern number (cmp. (6.29)) related to the 'Hofstadter butterfly' [1471, 1472] (cf. Sect. G.3.1).

It is remarkable that the classical Hall effect is based on homogeneous conduction for a proper evaluation (cf. Fig. 15.7e), while the quantum Hall effect involves electrical transport only along the edges. A detailed microscopic picture of the edge channels is also of interest. Due to depletion at the boundary of the sample, the density of the 2DEG varies at the edge of the sample and 'incompressible' stripes develop for which $\partial\mu/\partial n_s \to \infty$. When the filling factor is far from an integer, the Hall voltage is found to vary linearly across the conductive channel and the current is thus homogeneous over the sample (Fig. 15.20d). In the Hall plateau, the Hall voltage is flat in the center of the channel and exhibits drops at the edges, indicating that the current flows along the boundary of the sample (edge current) [1473] in agreement with predictions from [1476]. Although the current pattern changes with varying magnetic field, the Hall resistivity remains at its quantized value.

In graphene, the IQHE plateaus take on the resistance values [1249, 1477],

$$\frac{1}{\rho_{xy}} = \pm 4 \left(n + \frac{1}{2} \right) \frac{e^2}{h} , \tag{15.44}$$

with $n \in \mathbb{N}_0$. This new 'half integer' quantization condition can be translated into the quantized filling factor $\nu = \pm 4\,(n + 1/2)$ in the usual QHE formalism of (15.42). The condition (15.44) is due to the different nature of Landau levels for a linear dispersion (Dirac spectrum) [1478]. The $+/-$-sign denotes the QHE for electrons and holes, respectively. The factor $g = 4$ stems from the degeneracy of the Landau levels, accounting for spin degeneracy (when the Landau level separation is much larger than the Zeeman spin splitting) and for the sublattice degeneracy. The two $n = 0$ Hall plateaus have even been observed (for $B = 45\,\mathrm{T}$) at room temperature [1479].

15.2.8.2 Fractional QHE

For very low temperatures and in the extreme quantum limit, novel effects are observed when the kinetic energy of the electrons is smaller than their Coulomb interaction. New quantum Hall plateaus are observed at various fractional filling factors $\nu = p/q$. We note that the effects of the fractional quantum Hall effect (FQHE) in Fig. 15.21 mostly arise for magnetic fields beyond the $n = 1$ IQHE plateau. The filling factor $\nu = n/(eB/h)$ is now interpreted as the number of electrons per magnetic flux quantum $\phi_0 = h/e$.

The effects of the FQHE cannot be explained by single-electron physics. The plateaus at fractional fillings ν occur when the Fermi energy lies within a highly degenerate Landau (or spin) level and imply the presence of energy gaps due to many-particle interaction and the result of correlated 2D electron motion in the magnetic field.

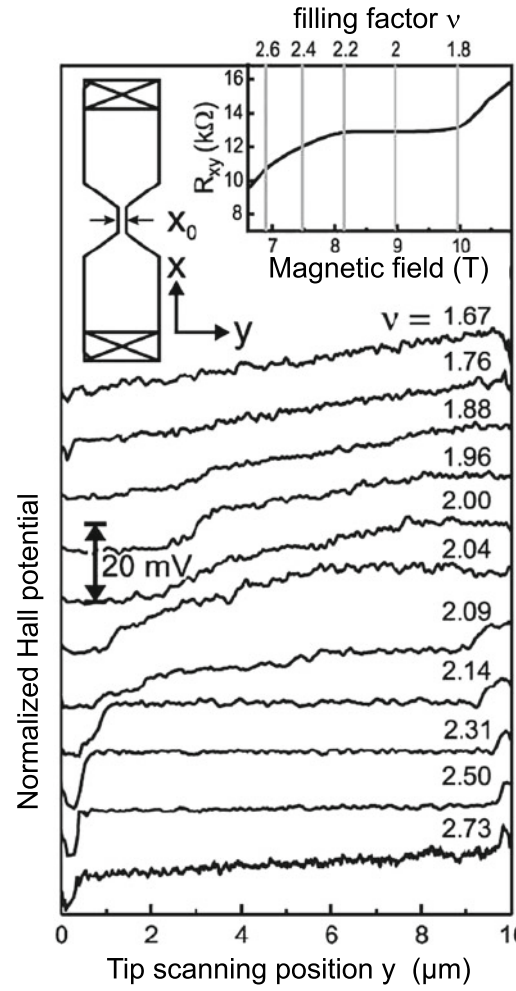

Fig. 15.20 Normalized Hall potential profile for different magnetic fields around filling factor $\nu = 2$. The overall voltage drop corresponds to 20 mV. The *insets* show the sample geometry and transport data. The 2DEG is from a GaAs/$Al_{0.33}Ga_{0.67}$As modulation-doped heterostructure, $n_s = 4.3 \times 10^{11}\,\mathrm{cm}^{-2}$, $\mu = 5 \times 10^5\,\mathrm{cm}^2/\mathrm{Vs}$, $T = 1.4\,\mathrm{K}$. Adapted from [1473]

A decisive role is played by the magnetic flux quanta. The presence of the magnetic field requires the many-electron wavefunction to assume as many zeros per unit area as there are flux quanta penetrating it. The decay of the wavefunction has a length scale of the magnetic length $l_0 = \sqrt{\hbar/(eB)}$. Since the magnetic field implies a 2π phase shift around the zero, such an object is also termed a *vortex*, being the embodiment of the magnetic flux quanta in the electron system. Such a vortex represents a charge deficit (compared to a homogeneous charge distribution) and thus electrons and vortices attract each other. If a vortex and an electron are placed onto each other, considerable Coulomb energy is gained. At $\nu = 1/3$, there are three times more vortices than there are electrons, each vortex representing a charge deficit of $1/3\,e$. Such a system is described with many-particle wavefunctions, such as the Laughlin theory for $\nu = 1/q$ [1468] and novel quasi-particles called *composite fermions* [1481, 1482] for other fractional fillings. For further reading we refer readers to [1483] and references therein.

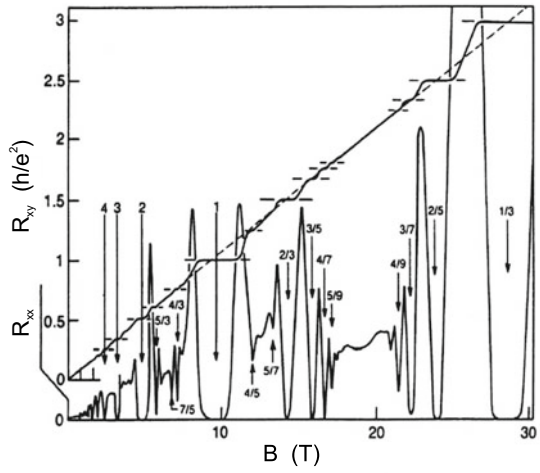

Fig. 15.21 Hall resistance R_{xy} and magnetoresistance R_{xx} of a two-dimensional electron system (GaAs/(Al,Ga)As heterostructure) of density $n = 2.33 \times 10^{11}\,\mathrm{cm}^{-2}$ at a temperature of 85 mK, versus magnetic field B. Numbers identify the filling factor ν, which indicates the degree to which the sequence of Landau levels is filled with electrons. Plateaus are due to the integral ($\nu = i$) quantum Hall effect (IQHE) and fractional ($\nu = p/q$) quantum Hall effect (FQHE). Adapted from [1480], reprinted with permission, ©1990 AAAS

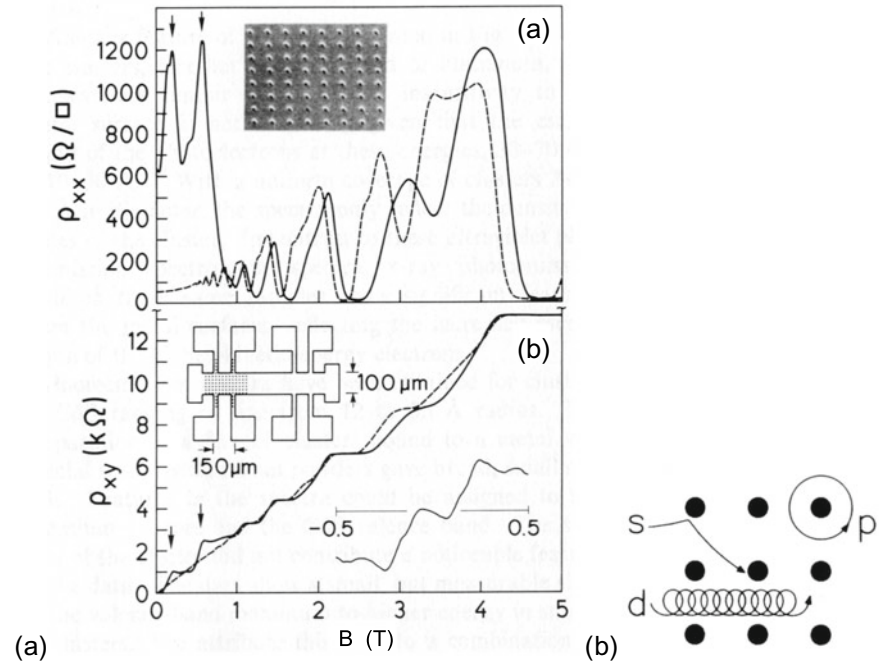

Fig. 15.22 Weiss oscillations: **a** magnetoresistance and **b** Hall resistance of an antidot lattice (*inset* in (**a**)) with pattern (*solid lines*) and without pattern (*dashed lines*) at $T = 1.5\,\mathrm{K}$. **b** Schematic of the different orbits: ('p': pinned, 'd': drifting, 's': scattered). Reprinted with permission from [1484], ©1991 APS

15.2.8.3 Weiss Oscillations

In Fig. 15.22, measurements are shown for a Hall bar in which an array of antidots (in which no conduction is possible) has been introduced by dry etc.hing. The antidot size is 50 nm (plus depletion layer) and the period is 300 nm. These obstructions for the cyclotron motion lead to a modification of the magnetotransport properties.

Before etc.hing of the antidot array the 2DEG has a mean free path length of 5–10 μm at 4 K for the mobility of $\approx 10^6\,\mathrm{cm}^2/\mathrm{Vs}$. At low magnetic fields there is a strong deviation of the Hall resistivity from the straight line to which the QHE levels converge. Similarly, ρ_{xx} shows a strong effect as well.

These effects are related to commensurability effects between the antidot lattice and the cyclotron resonance path. When the cyclotron orbit is equal to the lattice period, electrons can fulfill a circular motion around one antidot (pinned orbit, Fig. 15.22b) that leads to a reduction of conductivity. At high fields, drifting orbits for which the cyclotron orbit is much smaller than the lattice period occur. At small fields, scattering orbits also contribute for which the cyclotron radius is large and the electron has antidots from time to time. Resonances in the Hall resistivity have been found due to pinned orbits enclosing 1, 2, 4, 9 or 21 antidots.

Chapter 16
Polarized Semiconductors

Abstract In this chapter semiconductors with a spontaneous polarization and ferroelectric semiconductors are discussed. Also the effect of piezoelectricity is treated in some detail for zincblende and wurtzite materials.

16.1 Introduction

Semiconductors can have an electric polarization. Such polarization can be induced by an external electric field (Fig. 16.1a). This phenomenon, i.e. that the semiconductor is dielectric, has been discussed already in Chap. 9. In this chapter, we discuss pyroelectricity, i.e. a spontaneous polarization without an external field (Fig. 16.1b), ferroelectricity,[1] i.e. pyroelectricity with a hysteresis (Fig. 16.1c) and piezoelectricity, i.e. a polarization due to external stress.

16.2 Spontaneous Polarization

The reason for a spontaneous polarization $P_{\rm sp}$ (without external electric field) is the static, relative shift of positive and negative charges in the unit cell. For a slab of semiconductor material (thus ignoring depolarization effects present in other geometries), the polarization causes polarization charges located at the upper and lower surfaces (Fig. 16.2a). The polarization vector $\mathbf{P}$ points from the negative to the positive charge. The electric field due to the polarization charges has the opposite direction. In the absence of free charges, the Maxwell equation $\nabla \cdot \mathbf{D} = 0$ yields for piecewise constant fields at a planar interface (Fig. 16.2b) $(\mathbf{D}_2 - \mathbf{D}_1) \cdot \mathbf{n}_{12} = 0$ where $\mathbf{n}_{12}$ is the surface normal pointing from medium 1 to medium 2. Therefore, the polarization charge $\sigma_{\rm P} = \epsilon_0 \nabla \cdot \mathbf{E}$ is given by

$$\sigma_{\rm P} = -(\mathbf{P}_2 - \mathbf{P}_1) \cdot \mathbf{n}_{12} \,. \tag{16.1}$$

Polarization charges develop at interfaces where the polarization is discontinuous, e.g. an interface between two semiconductors with different spontaneous polarization. Vacuum (at a surface) represents a special case with $\mathbf{P} = 0$.

[1] Ferromagnetic semiconductors are discussed in Chap. 17. We note that there exist so called *multiferroic* materials that possess more than one ferroic property [1485, 1486].

M. Grundmann, *The Physics of Semiconductors*, Graduate Texts in Physics,
https://doi.org/10.1007/978-3-030-51569-0_16

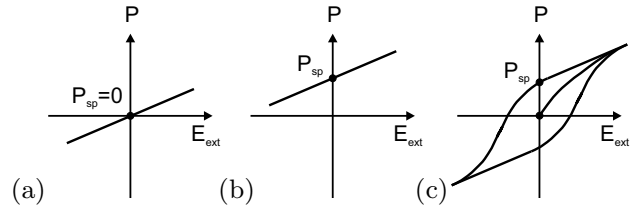

Fig. 16.1 Schematic representation of the polarization versus external electric field dependence for **a** dielectric, **b** pyroelectric and **c** ferroelectric semiconductors

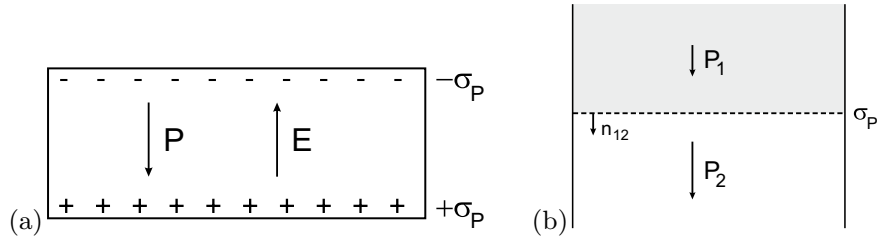

Fig. 16.2 **a** Surface polarization charges σ_P on a slab of semiconductor material with polarization. The electric field is given by $\mathbf{E} = -\mathbf{P}/\epsilon_0$. **b** Polarization charge σ_P at an interface between two semiconductors with different polarization. In the depicted situation σ is negative

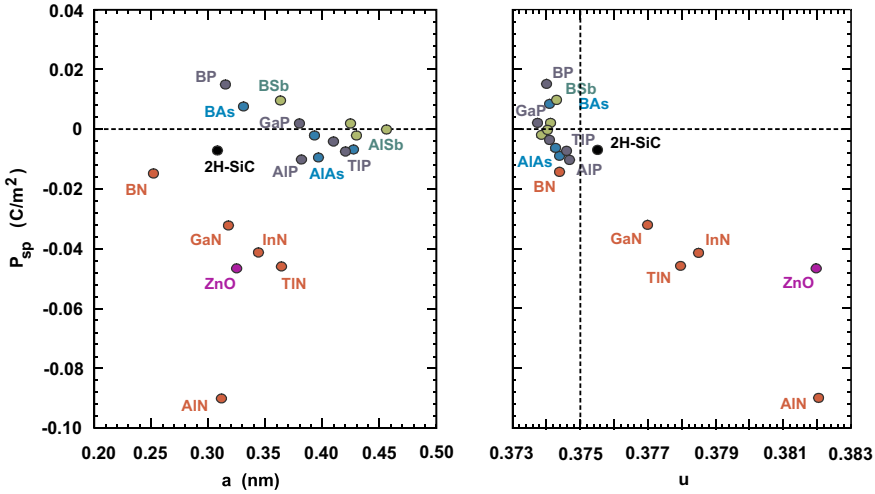

Fig. 16.3 Spontaneous polarization P_{sp} for various semiconductors as a function of the lattice constant a (left) and the cell-internal parameter u (right). Based on [1487]

For cubic zincblende structure semiconductors, P_{sp} is typically fairly small. The anisotropy of the wurtzite structure allows for sizeable effects (Fig. 16.3). The main cause is the nonideality of the cell-internal parameter u (cf. Sect. 3.4.5).

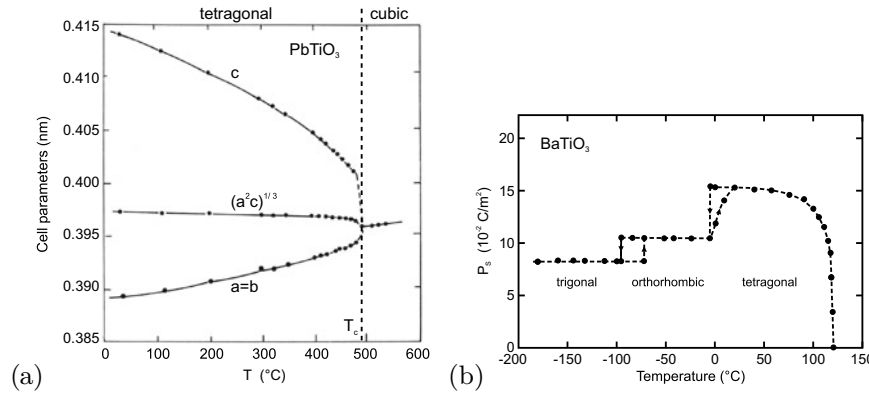

Fig. 16.4 **a** Cell parameters of $PbTiO_3$ as a function of temperature. Adapted from [1493]. **b** Phase transitions of $BaTiO_3$ as a function of temperature. The spontaneous polarization P_S points along ⟨100⟩, ⟨110⟩ and ⟨111⟩ in the tetragonal (C_{4v}), orthorhombic (C_{2v}) and trigonal (C_{3v}, rhombohedral) phase, respectively. Adapted from [1494]

16.3 Ferroelectricity

Ferroelectric semiconductors exhibit a spontaneous polarization in the ferroelectric phase and zero spontaneous polarization in the paraelectric phase. As a function of temperature, the ferroelectric material undergoes a phase transition from the high-temperature paraelectric phase into the ferroelectric phase. There can be further phase transitions between different ferroelectric phases that differ in the direction of the polarization. The literature until 1980 is summarized in [1488]. A more recent treatment can be found in [1489, 1490].

$PbTiO_3$ has perovskite structure (cf. Sect. 3.4.10). It exhibits a phase transition at $T_C = 490\,°C$ from the cubic into the (ferroelectric) tetragonal phase as shown in Fig. 16.4a. Mostly the cell symmetry changes, while the cell volume remains almost constant. A more complicated situation arises for $BaTiO_3$. At 120 °C the transition into the ferroelectric phase occurs (Fig. 16.4b) that is tetragonal with the polarization in the [100] direction. At −5 °C and −90 °C transitions occur into an orthorhombic and a rhombohedral (trigonal) phase, respectively. The largest polarization is caused by a displacement of the negatively (O) and positively (Ba, Ti) charged ions of the unit cell by $\delta \approx 0.02\,nm$ (Fig. 16.5). Such an origin of the spontaneous polarization is called a *displacement* transition.[2]

16.3.1 Materials

A large class of ferroelectric semiconductors are of the type ABO_3, where A stands for a cation with larger ionic radius and B for an anion with smaller ionic radius. Many ferroelectrics have perovskite ($CaTiO_3$) structure. They are $A^{2+}B^{4+}O_3^{2-}$, e.g. (Ba,Ca,Sr) (Zi,Zr)O_3 or $A^{1+}B^{5+}O_3^{2-}$, e.g. (Li,Na,K) (Nb,Ta)O_3. Ferroelectrics can also be alloyed. Alloying in the B component yields, e.g. $PbTi_xZr_{1-x}O_3$ also called PZT. PZT is widely used for piezoelectric actuators. Also, alloying in the A component is possible, e.g. $Ba_xSr_{1-x}TiO_3$.

[2]The widely accepted model for such ferroelectric is that the basic displacement occurs into the ⟨111⟩-direction at low temperature. The three higher symmetry phases at higher temperature are the result of 2 (orthorhombic), 4 (tetragonal) or 8 (cubic) allowed ⟨111⟩ orientations which make the macroscopically averaged polarization appear in ⟨110⟩- or ⟨100⟩-direction or vanishing altogether, respectively [1491, 1492].

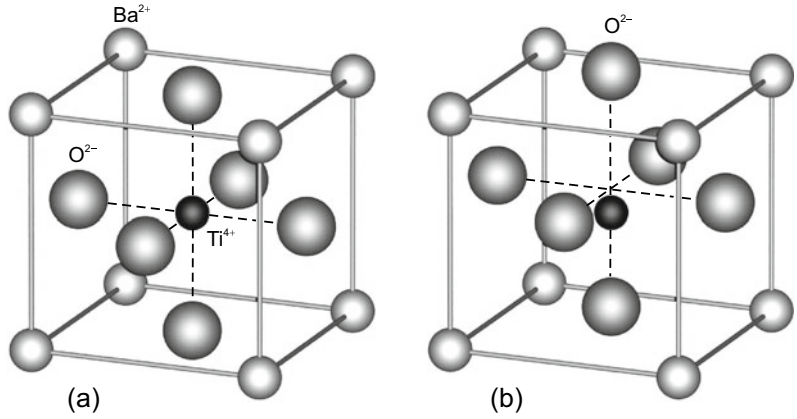

Fig. 16.5 **a** Crystal structure of $BaTiO_3$ (see Fig. 3.27). **b** Schematic tetragonal deformation below the Curie temperature, generating a dipole moment

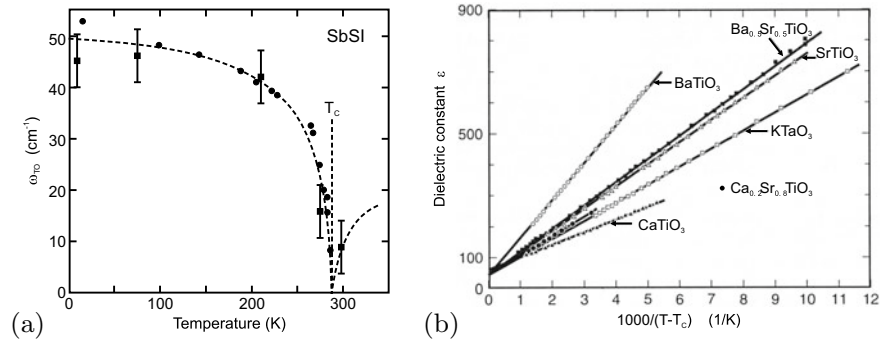

Fig. 16.6 **a** Decrease of the transverse phonon mode of SbSI close to the Curie temperature of $T_C = 288\,K$. The *dashed curved line* represents a $|T - T_C|^{1/2}$ dependence. Adapted from [1495]. **b** Dielectric constant of various perovskites versus $1/(T - T_C)$ in the paraelectric phase ($T > T_C$). Adapted from [1496]

Another class of ferroelectrics are $A^VB^{VI}C^{VII}$ compounds, such as SbSI, SbSBr, SbSeI, BiSBr. These materials have a width of the forbidden band in the $\sim 2\,eV$ range. A further class of ferroelectric semiconductors are $A_2^VB_3^{VI}$ compounds, such as Sb_2S_3.

16.3.2 Soft Phonon Mode

The finite displacement of the sublattices in the ferroelectric means that the related lattice vibration has no restoring force. The displacement is, however, finite due to higher-order terms (anharmonicity). Thus, for $T \to T_C$ $\omega_{TO} \to 0$. Such a mode is called a *soft phonon mode*. The decrease of the phonon frequency is shown in Fig. 16.6a for SbSI.

From the LST relation (9.26), it follows that the static dielectric function must increase strongly. The increase is $\propto (T - T_C)^{-1}$ (Fig. 16.6b).

16.3.3 Phase Transition

In the case of ferroelectrics, the order parameter for the Ginzburg–Landau theory of phase transitions is the spontaneous polarization P. The free energy F of the ferroelectric crystal is written in terms of the free energy of the paraelectric phase F_0 and is expanded in powers of P (here up to P^6) as

$$F = F_0 + \frac{1}{2}\alpha P^2 + \frac{1}{4}\beta P^4 + \frac{1}{6}\gamma P^6 . \tag{16.2}$$

In this equation, we have neglected effects due to charge carriers, an external electric field or external stresses and we assume homogeneous polarization. In order to obtain a phase transition, it has to be assumed that α has a zero at a certain temperature T_C and we assume (expanding only to the linear term)

$$\alpha = \alpha_0 (T - T_C) . \tag{16.3}$$

16.3.3.1 Second-Order Phase Transition

For modeling a second-order phase transition, we set $\gamma = 0$. Thus, the free energy has the form (Fig. 16.7a)

$$F = F_0 + \frac{1}{2}\alpha P^2 + \frac{1}{4}\beta P^4 . \tag{16.4}$$

The equilibrium condition with regard to the free energy yields a minimum for

$$\frac{\partial F}{\partial P} = \alpha P + \beta P^3 = 0 \tag{16.5a}$$

$$\frac{\partial^2 F}{\partial P^2} = \alpha + 3\beta P^2 > 0 . \tag{16.5b}$$

Equation (16.5a) yields two solutions. $P = 0$ corresponds to the paraelectric phase. $P^2 = -\alpha/\beta$ is the spontaneous polarization in the ferroelectric phase. The condition from (16.5b) yields that $\alpha > 0$ in the paraelectric phase, while $\alpha < 0$ in the ferroelectric phase. Also, $\beta > 0$ below the Curie temperature (β is assumed to be temperature independent in the following). Using (16.3), the polarization is given as (Fig. 16.7b)

$$P^2 = \frac{\alpha_0}{\beta}(T - T_C) . \tag{16.6}$$

Therefore, the entropy $S = -\frac{\partial F}{\partial T}$ and the discontinuity ΔC_p of the heat capacity $C_p = T\left(\frac{\partial S}{\partial T}\right)_p$ at the Curie point T_C are given by

$$S = S_0 + \frac{\alpha_0^2}{\beta}(T - T_C) \tag{16.7a}$$

$$\Delta C_p = \frac{\alpha_0^2}{\beta} T_C , \tag{16.7b}$$

with $S_0 = -\frac{\partial F_0}{\partial T}$ being the entropy of the paraelectric phase. This behavior is in accordance with a second-order phase transition with vanishing latent heat (continuous entropy) and a discontinuity of the heat capacity. The dielectric function in the paraelectric phase is $\propto 1/\alpha$ and in the ferroelectric phase $\propto -1/\alpha$. The latter relation is usually written as the Curie–Weiss law

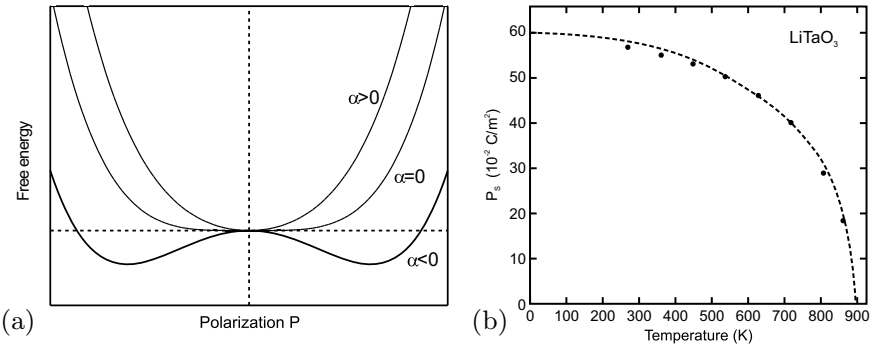

Fig. 16.7 **a** Schematic plot of the free energy versus spontaneous polarization for a second-order phase transition. $\alpha > 0$ ($\alpha < 0$) corresponds to the paraelectric (ferroelectric) phase. **b** Spontaneous polarization of $LiTaO_3$ as a function of temperature exhibiting a second-order phase transition. The *dashed line* is theory with suitable parameters. Adapted from [1497]

$$\epsilon = \frac{C}{T - T_C} \,. \tag{16.8}$$

16.3.3.2 First-Order Phase Transition

When the P^6 term is included in (16.2) ($\gamma \neq 0$), a first-order phase transition is modeled. However, in order to obtain something new, compared to the previous consideration, now $\beta < 0$ (and $\gamma > 0$) is necessary. The dependence of the free energy on P is schematically shown in Fig. 16.8a for various values of α. The condition $\frac{\partial F}{\partial P} = 0$ yields

$$\alpha\, P + \beta\, P^3 + \gamma\, P^5 = 0 \,, \tag{16.9}$$

with the solutions $P = 0$ and

$$P^2 = -\frac{\beta}{2\gamma}\left(1 + \sqrt{1 - \frac{4\,\alpha\,\gamma}{\beta^2}}\right) \,. \tag{16.10}$$

For a certain value of α, i.e. at a certain temperature $T = T_1$, the free energy is zero for $P = 0$ *and* also for another value $P = P_0$ (second curve from the top in Fig. 16.8a). From the condition

$$\frac{1}{2}\,\alpha(T_1)\,P_0^2 + \frac{1}{4}\,\beta\,P_0^4 + \frac{1}{6}\,\gamma\,P_0^6 = 0 \,, \tag{16.11}$$

the values for P_0 and α at the transition temperature $T = T_1$ are given by

$$P_0^2 = = -\frac{3}{4}\,\frac{\beta}{\gamma} \tag{16.12a}$$

$$\alpha(T_1) = \frac{3}{16}\,\frac{\beta^2}{\gamma} > 0 \,. \tag{16.12b}$$

The schematic dependence of P at the phase transition temperature T_1 is depicted in Fig. 16.8b.

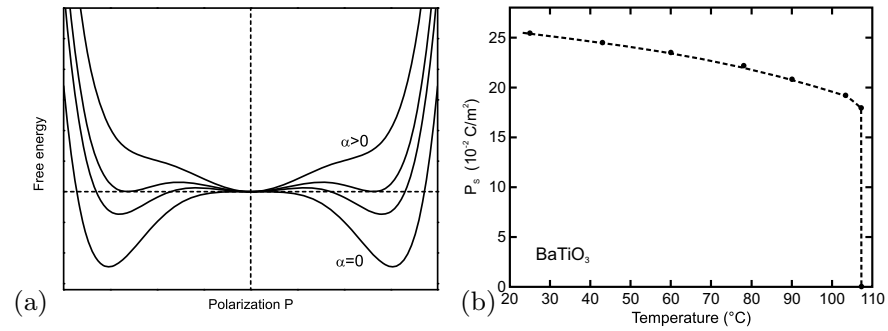

Fig. 16.8 **a** Schematic plot of the free energy versus spontaneous polarization for a first-order phase transition. The lowest curve is for $\alpha = 0$, the others are for $\alpha > 0$. **b** Spontaneous polarization in $BaTiO_3$ as a function of temperature exhibiting a first-order phase transition. The *dashed line* is a guide to the eye. Adapted from [1498]

For $T \leq T_1$ the absolute minimum of the free energy is reached for finite polarization $P > P_0$. However, between $F(P = 0)$ and the minimum of the free energy an energy barrier (second lowest curve in Fig. 16.8) is present for T close to T_1. The energy barrier disappears at the Curie–Weiss temperature T_0. At the phase transition temperature, the entropy has a discontinuity

$$\Delta S = \alpha_0 \, P_0^2 \, , \tag{16.13}$$

that corresponds to a latent heat $\Delta Q = T \Delta S$. Another property of the first-order phase transition is the occurrence of hysteresis in the temperature interval between T_1 and T_0

$$\Delta T \approx T_1 - T_0 = \frac{1}{4\alpha_0} \frac{\beta^2}{\gamma} \, , \tag{16.14}$$

in which an energy barrier is present to hinder the phase transition. For decreasing temperature, the system tends to remain in the paraelectric phase. For increasing temperature, the system tends to remain in the ferroelectric phase. Such behavior is observed for $BaTiO_3$, as shown in Fig. 16.4b.

16.3.4 Domains

Similar to ferromagnets, ferroelectrics form domains with different polarization directions in order to minimize the total energy by minimizing the field energy outside the crystal. The polarization can have different orientations, 6 directions for P along $\langle 100 \rangle$ (tetragonal phase), 12 directions for P along $\langle 110 \rangle$ (orthorhombic phase) and 8 directions for P along $\langle 111 \rangle$ (rhombohedral phase). In Fig. 16.9, such domains are visualized for $BaTiO_3$. Due to the restricted geometry, domain formation in thin films is different from that in bulk material.

Domains can also be artificially created by so-called poling. The ferroelectric semiconductor is heated to the paraelectric phase. With electrodes, appropriate electric fields are applied and the material is cooled. The polarization is then frozen in the ferroelectric phase. The domains of a periodically poled structure in $LiNbO_3$ (PPLN) are shown in Fig. 16.10b. The nonlinear optical properties in such structures can be used for efficient second harmonic generation (SHG).

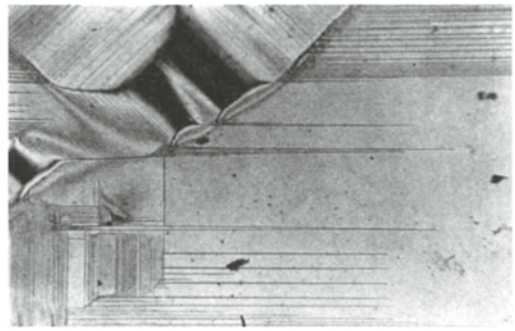

Fig. 16.9 Ferroelectric domains in a $BaTiO_3$ single crystal visualized by birefringence contrast. Reprinted with permission from [1499], ©1949 APS

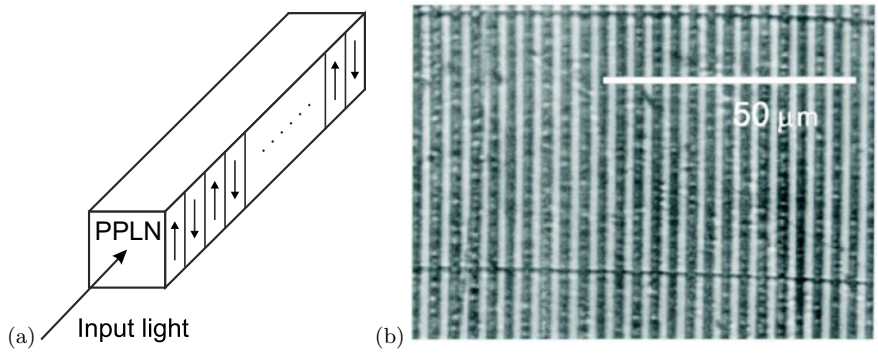

Fig. 16.10 **a** Scheme of PPLN (perodically poled lithium niobate), *arrows* denote the direction of spontaneous polarization. **b** Polarization microscopy image (vertical stripes are domains, horizontal dark lines are scratches)

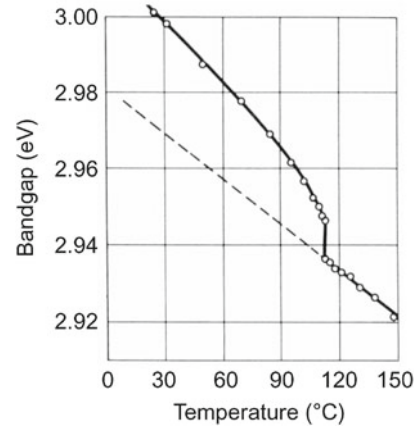

Fig. 16.11 Temperature dependence of the band gap in $BaTiO_3$ (for polarized light with $\mathbf{E} \perp c$). Experimental data from [1500]

16.3.5 Optical Properties

The first-order phase transition of $BaTiO_3$ manifests itself also in a discontinuity of the band gap (Fig. 16.11). The coefficient $\partial E_g/\partial T$ for the temperature dependence of the band gap is also different in the para- and ferroelectric phases.

Table 16.1 Piezoelectric coefficients (in $\mathrm{C\,m^{-2}}$) for various zincblende and wurtzite semiconductors. Data from [165, 1501, 1504], for zb-ZnO from [1505], for zb-GaN from [1506]

Zincblende				Wurtzite			
III–V	e_{14}	II–VI	e_{14}		e_{33}	e_{31}	e_{15}
InSb	−0.123	CdTe	0.054	CdSe	0.347	−0.16	−0.138
InAs	−0.078	ZnSe	0.049	CdS	0.385	−0.262	−0.183
GaSb	−0.218	ZnS	0.254	ZnS	0.265	−0.238	−0.118
GaAs	−0.277	ZnO	0.69	ZnO	0.89	−0.51	−0.45
AlSb	−0.118	GaN	0.375	GaN	0.73	−0.49	−0.3
				AlN	1.46	−0.60	−0.48
				BeO	0.02	−0.02	

16.4 Piezoelectricity

16.4.1 Piezoelectric Effect

External stress causes atoms in the unit cell to shift with respect to each other. In certain directions, such a shift can lead to a polarization. Generally, all ferroelectric materials are piezoelectric. However, there are piezoelectric materials that are not ferroelectric, e.g. quartz, GaAs and GaN. Piezoelectricity can occur only when no center of inversion is present. Thus, e.g., GaAs is piezoelectric along ⟨111⟩, but Si is not. Also, the cubic perovskite structure (in the paraelectric phase) is not piezoelectric. Generally, the piezoelectric polarization is related to the strains via the tensor e_{ijk} of the piezoelectric modules[3]

$$P_i = e_{ijk}\,\epsilon_{jk}\ . \tag{16.15}$$

16.4.2 Zincblende Crystals

In zincblende semiconductors, the polarization (with respect to $x = [100]$, $y = [010]$, $z = [001]$) is due to shear strains only and is given as

$$\mathbf{P}_{\mathrm{pe}} = 2\,e_{14}\begin{pmatrix}\epsilon_{yz}\\ \epsilon_{xz}\\ \epsilon_{xy}\end{pmatrix}\ . \tag{16.16}$$

The values of e_{14} for various zincblende compound semiconductors are listed in Table 16.1. We note that the sign of e_{14} reverses from negative in cubic III–V to positive in cubic II–VI semiconductors. This non-trivial behavior involves strain effects on ionic and electronic polarization and ionicity as discussed in [184, 1501]. The coefficient e_{33}, the equivalent to e_{14} in wurtzite semiconductors (see below), is positive for III–V and II-VI semiconductors.

The strain in pseudomorphic heterostructures (cf. Sect. 5.3.3) can cause piezoelectric polarization in a piezoelectric semiconductor. In zincblende, the main effect is expected when the growth direction is along [111] and the strain has a purely shear character. In this case, the polarization is in the [111] direction, i.e. perpendicular to the interface ($P_\perp$). For the [001] growth direction, no piezoelectric

[3] Another formulation is used with parameters d_{ijk} and $P_i = d_{ijk}\,\sigma_{jk}$.

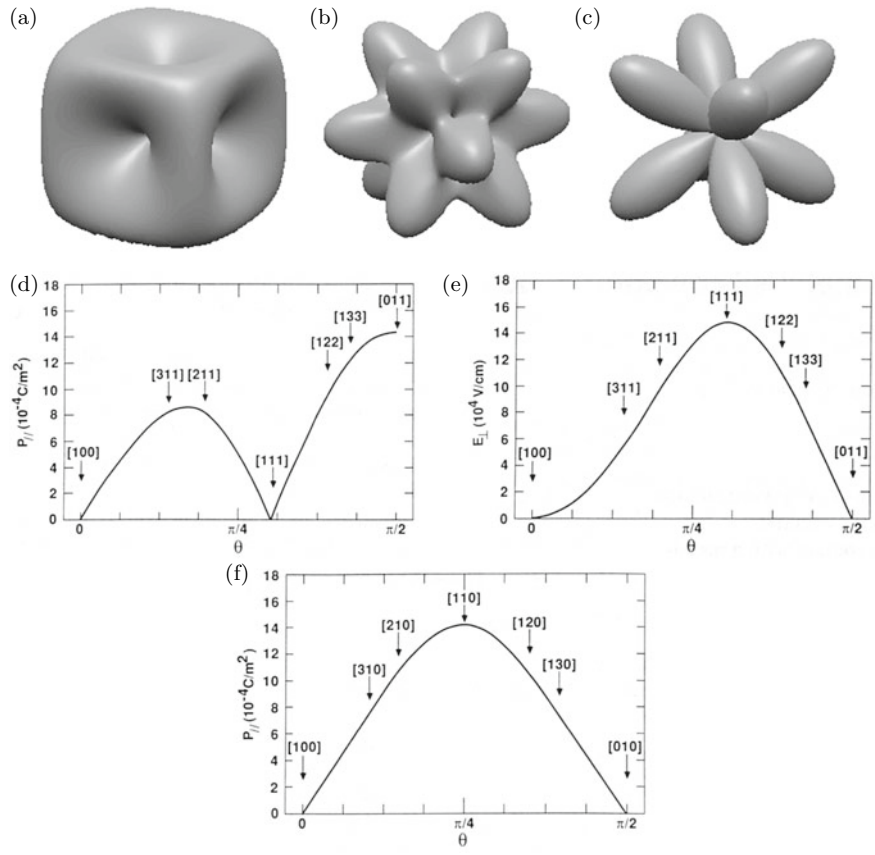

Fig. 16.12 Three-dimensional view of the **a** total, **b** longitudinal and **c** transverse polarization in uniaxially compressed GaAs. Adapted from [1502]. **d** Transverse polarization $P_\parallel$ (parallel to the interface) and **e** longitudinal electric field $E_\perp$ (perpendicular to the interface) in the InGaAs layer of a GaAs/$In_{0.2}Ga_{0.8}As$ superlattice with joint in-plane lattice constant (obtained from energy minimization, 1.4% lattice mismatch, the InGaAs is under compressive and the GaAs under tensile strain). The layer thicknesses of the GaAs and InGaAs layers are identical. The quantities are shown for various orientations of the growth direction. The vector of the growth direction varies in the (01–1) plane ($\phi = \pi/4$) with polar angle θ reaching from [100] (0°) over [111] to [011] (90°). Image (**f**) depicts the transverse polarization $P_\parallel$ ($P_\perp = 0$ in this geometry) for growth directions in the (001) plane ($\phi = 0$). Parts **d**–**f** reprinted with permission from [1503], ©1988 AIP

polarization is expected. For the [110] growth direction, the polarization is found to be parallel to the interface ($P_\parallel$). The situation is shown for various orientations of the growth direction in Fig. 16.12.

16.4.3 Wurtzite Crystals

In wurtzite crystals, the piezoelectric polarization (with respect to $x = [2\text{–}1.0]$, $y = [01.0]$, $z = [00.1]$) is given by[4]

[4]In Voigt notation, $P_x = e_{15}\, e_5$, $P_y = e_{15}\, e_4$

$$\mathbf{P}_{\rm pe} = \begin{pmatrix} 2\,e_{15}\,\epsilon_{xz} \\ 2\,e_{15}\,\epsilon_{yz} \\ e_{31}\,(\epsilon_{xx}+\epsilon_{yy}) + e_{33}\,\epsilon_{zz} \end{pmatrix} . \tag{16.17}$$

Values for the piezoelectric coefficients of several wurtzite semiconductors[5] are listed in Table 16.1.

The polarization (along c) for biaxial strain in heteroepitaxy (5.69) on the [00.1] surface is

$$P_{\rm pe} = 2\,\epsilon_{\parallel}\left(e_{31} - \frac{C_{13}}{C_{33}}\,e_{33}\right) , \tag{16.18}$$

where $\epsilon_{\parallel} = (a - a_0)/a_0$ is the in-plane strain. The dependence of the magnitude for GaN on the in-plane strain is shown in Fig. 16.13 together with the polarization for uniaxial stress along [00.1] and hydrostatic strain. In the latter two cases, the polarization is smaller.

The difference of spontaneous polarization of the constituent materials in heterostructures and piezoelectric effects in strained quantum wells lead to quantum confined Stark effect (QCSE, Sect. 15.1.2). The spatial separation of electrons and holes leads to a larger radiative lifetime (Fig. 12.43) and thus reduced radiative recombination rate in the presence of nonradiative channels, an effect unwanted in light emitting diodes. In particular nitride based LEDs grown along the c-direction are prone to this effect. Therefore growth on nonpolar surfaces such as $(1\bar{1}00)$ (m-plane) and $(11\bar{2}0)$ (a-plane) has been investigated [1509, 1510]. However, crystal quality for these growth planes seems limited.

An alternative route are 'semipolar' planes, e.g. $(10\bar{1}\bar{1})$ or $(11\bar{2}\bar{2})$ [1511], with at least reduced polarization effects. The $(11\bar{2}2)$-plane is tilted about 58° (for GaN) from the c-axis, close to the theoretically predicted zero of the internal electric field for InGaN/GaN quantum wells [1512] (Fig. 16.14). Promising experimental results have been published on semipolar growth, especially for InGaN/GaN on $(11\bar{2}\bar{2})$-oriented GaN substrates [1513].

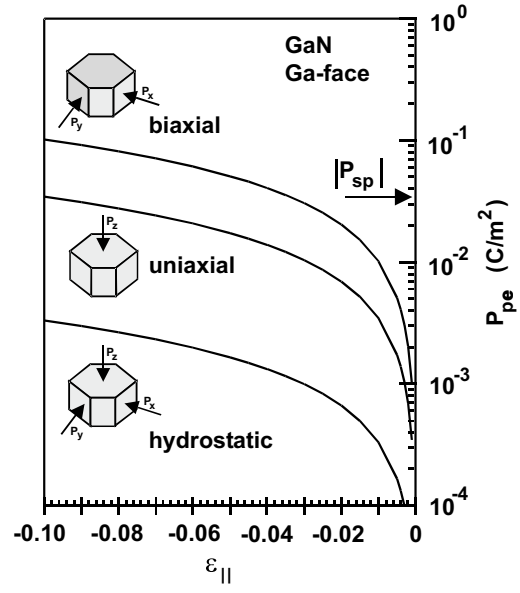

Fig. 16.13 Piezoelectric polarization $P_{\rm pe}$ in GaN (Ga-face) versus in-plane strain $\epsilon_{\parallel} = (a - a_0)/a_0$ for biaxial, uniaxial and hydrostatic strain. The value of the spontaneous polarization $P_{\rm sp}$ is indicated by an *arrow*. From [1508]

[5] If e_{14} for a zincblende material is transformed to a coordinate system along [111], the wurtzite-like piezoelectric constants are $e_{33} = 2\,e_{14}/\sqrt{3}$ and $e_{31} = -e_{14}/\sqrt{3}$ [1507].

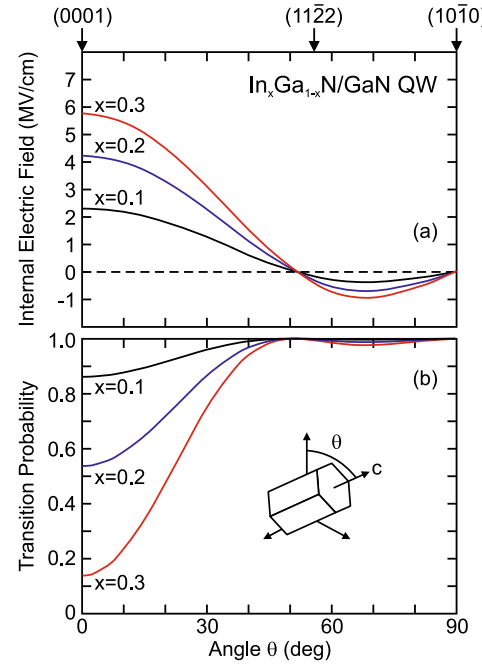

Fig. 16.14 **a** Internal electric field and **b** transition probability for electron-hole pairs in pseudomorphic $In_xGa_{1-x}N$/GaN quantum well ($L_w = 3$ nm) for three different indium contents x as labeled. θ denotes the angle between the c-axis and the normal of the interface plane (see *inset*). Based on [1512]

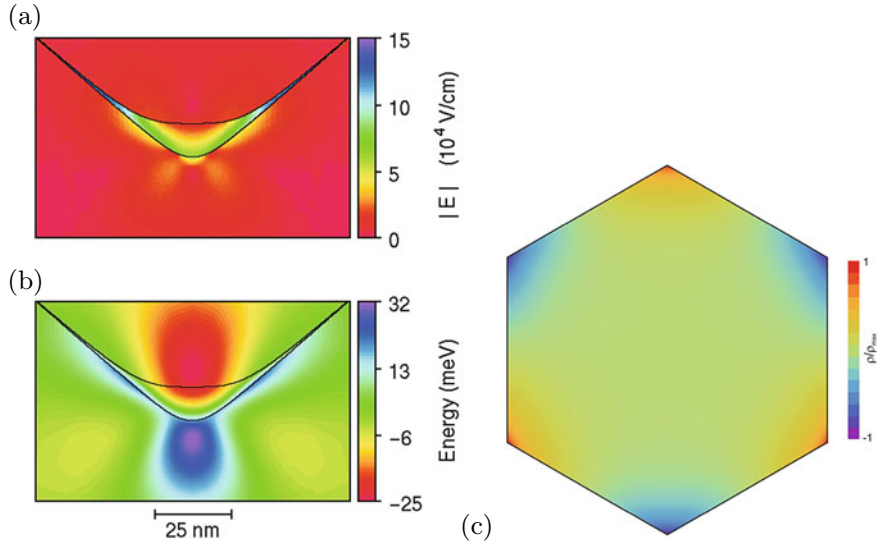

Fig. 16.15 **a** Electric field and **b** additional confinement potential for electrons due to piezoelectric charges for a strained $In_{0.2}Ga_{0.8}As$/GaAs quantum wire. Adapted from [1502]. **c** Piezoelectric charge density in a (111)-oriented GaAs wire with hexagonal cross section. Adapted from [1514]

16.4.4 Piezoelectric Effects in Nanostructures

The strain distribution around zincblende strained quantum wires [1502], (111)-oriented wires under torsion [1514] and epitaxial (embedded) quantum dots [417] contains shear components and thus generates piezoelectric fields. In Fig. 16.15a,b, the electric field and potential due to the piezoelec-

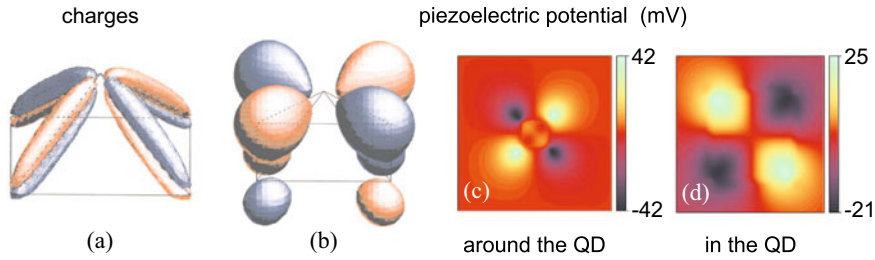

Fig. 16.16 **a** Piezoelectric charges and **b–d** resulting Coulomb potential for InAs/GaAs quantum dot with base length $b = 12$ nm. **a** Isosurfaces corresponding to volume charges $\pm 0.3\,\mathrm{e\,nm^{-3}}$. **b** Isosurfaces for the Coulomb potential at ± 30 meV. **c**,**d** Cross section through the Coulomb potential somewhat above the wetting layer in two different magnifications, **d** is a zoom into (**c**). The InAs/GaAs interface is visible in **d** due to the image charge effect. Parts **a** and **b** reprinted with permission from [417], ©1995 APS

tric charges are shown for a strained $In_{0.2}Ga_{0.8}As/GaAs$ quantum wire. In Fig. 16.15c the three-fold symmetric piezoelectric charge density within the cross-section of a (111)-oriented GaAs wire under torsion (due to second order piezoelectricity) is depicted.

In Fig. 16.16, the piezoelectric charges and potential are shown for the quantum dot from Fig. 5.34. The piezoelectric potential has quadrupole character and thus reduces the symmetry of the QD (to C_{2v}) [417].[6] Piezoelectric effects are particularly important in wurtzite nanostructures [1515].

[6]The strain distribution has C_{2v} symmetry for a square-based pyramid for zincblende materials. The energy levels and wavefunctions are more strongly impacted by the piezoelectric effects than by the strain asymmetry [1382, 1383].

Chapter 17
Magnetic Semiconductors

Abstract Materials and properties of two types of semiconductors with spontaneous magnetization or ferromagnetic and paramagnetic properties are explained: Compound materials and diluted magnetic semiconductors. A short introduction to semiconductor spintronics covers the concepts of spin transistor and spin LED.

17.1 Introduction

Magnetic semiconductors exhibit spontaneous magnetic order. Even ferromagnetism, important for spin polarization, as needed in spinelectronics (also called *spintronics*), can occur below the Curie temperature that is characteristic of the material. Magnetic semiconductors can be binary compounds such as EuTe (antiferromagnetic) or EuS (ferromagnetic). Another class of magnetic semiconductors contains paramagnetic ions in doping concentration (typically $< 10^{21}\,\mathrm{cm}^{-1}$) or alloy concentration x (typically $x \geq 0.1\%$). Such materials are termed *diluted magnetic semiconductors* (DMS). The incorporation of the magnetic atoms leads first to conventional alloy effects, such as the modification of the lattice constant, the carrier concentration or the band gap. The status of the field up to the mid-1980s can be found in [1516, 1517], mostly focused on II–VI DMS. A review of work on III–V based materials for spintronics, mostly GaAs:Mn, can be found in [1518]. A 2003 review of wide band gap ferromagnetic semiconductors is given in [1519], a 2014 review of Mn-containing DMS in [1520].

17.2 Magnetic Semiconductors

In a magnetic semiconductor, one sublattice is populated with paramagnetic ions. The first two ferromagnetic semiconductors discovered were $CrBr_3$ [1521] in 1960 and EuO [1522] one year later. Europium monoxide has an ionic $Eu^{2+}O^{2-}$ character, such that the electronic configuration of europium is $[Xe]4f^7 5d^0 6s^0$ and that of oxygen is $1s^2 2s^2 2p^6$. Some properties of europium chalcogenides [1523] are summarized in Table 17.1.

EuO can be modeled as a Heisenberg ferromagnet with dominant nearest- and next-nearest Eu–Eu interactions [1524]. The Heisenberg exchange parameters J_1 and J_2 for these four compounds are shown in Fig. 17.1. In the nearest-neighbor interaction J_1 a 4f electron is excited to the 5d band, experiences an exchange interaction with the 4f spin on a nearest neighbor and returns to the initial state. This mechanism generally leads to ferromagnetic exchange. The next-nearest-neighbor interaction J_2 is weakly ferromagnetic (EuO) or antiferromagnetic (EuS, EuSe, EuTe). In the superexchange process,

M. Grundmann, *The Physics of Semiconductors*, Graduate Texts in Physics,
https://doi.org/10.1007/978-3-030-51569-0_17

Table 17.1 Material properties of Eu chalcogenides. 'FM' ('AF') denotes ferromagnetic (antiferromagnetic) order. T_C (T_N) denotes the Curie (Néel) temperature. Data collected in [1525]

Material	E_g (eV)	Magnetic order	T_C, T_N (K)
EuO	1.12	FM	69.3
EuS	1.65	FM	16.6
EuSe	1.8	AF	4.6
		FM	2.8
EuTe	2.00	AF	9.6

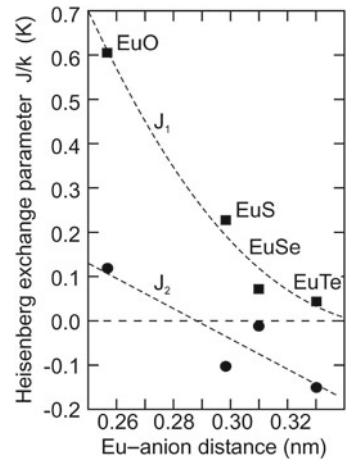

Fig. 17.1 Heisenberg nearest (J_1, *squares*) and next-nearest (J_2, *circles*) exchange parameters (in units of $J_{1,2}/k_B$) for the Eu chalcogenides versus the Eu–anion distance. *Dashed lines* are guides to the eye. Experimental data from [1525]

Table 17.2 3d, 4d and 5d transition metals and their electron configurations. Note that Hf^{72} has an incompletely filled 4f-shell with $4f^{14}$

Sc^{21}	Ti^{22}	V^{23}	Cr^{24}	Mn^{25}	Fe^{26}	Co^{27}	Ni^{28}	Cu^{29}	Zn^{30}
3d	$3d^2$	$3d^3$	$3d^4$	$3d^5$	$3d^6$	$3d^7$	$3d^8$	$3d^9$	$3d^{10}$
$4s^2$	$4s^2$	$4s^2$	4s	$4s^2$	$4s^2$	$4s^2$	$4s^2$	4s	$4s^2$
Y^{39}	Zr^{40}	Nb^{41}	Mo^{42}	Tc^{43}	Ru^{44}	Rh^{45}	Pd^{46}	Ag^{47}	Cd^{48}
4d	$4d^2$	$4d^3$	$4d^4$	$4d^5$	$4d^6$	$4d^7$	$4d^8$	$4d^9$	$4d^{10}$
$5s^2$	$5s^2$	5s	5s	5s	5s	5s	–	5s	$5s^2$
La^{57}	Hf^{72}	Ta^{73}	W^{74}	Re^{75}	Os^{76}	Ir^{77}	Pt^{78}	Au^{79}	Hg^{80}
5d	$5d^2$	$5d^3$	$5d^4$	$5d^5$	$5d^6$	$5d^7$	$5d^8$	$5d^9$	$5d^{10}$
$6s^2$	$6s^2$	$6s^2$	$6s^2$	$6s^2$	$6s^2$	$6s^2$	6s	6s	$6s^2$

electrons are transferred from the anionic p states to the 5d states of the Eu^{2+} cations, resulting in an antiferromagnetic coupling.

17.3 Diluted Magnetic Semiconductors

In Table 17.2, the transition metals and their electron configurations are summarized. The 3d transition metals are typically used for magnetic impurities in DMS due to their partially filled 3d shell. Due to Hund's rule, the spins on the 3d shell are filled in parallel for the first five electrons up to half filling (in

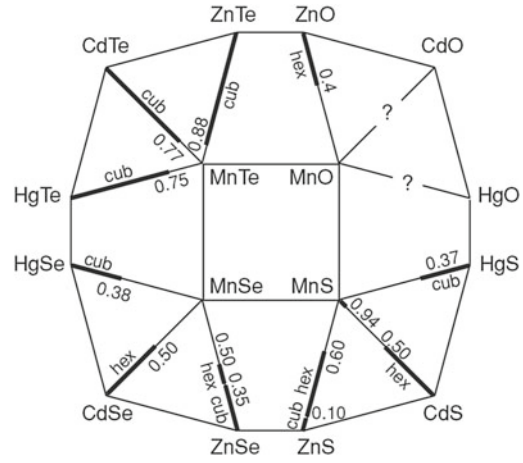

Fig. 17.2 Diagrammatic overview of $A^{II}_{1-x}Mn_xB^{VI}$ alloys and their crystal structures. The *bold lines* indicate ranges of the molar fraction x for which homogeneous crystal phases form. 'Hex' and 'Cub' indicate wurtzite and zincblende, respectively. From [1526]

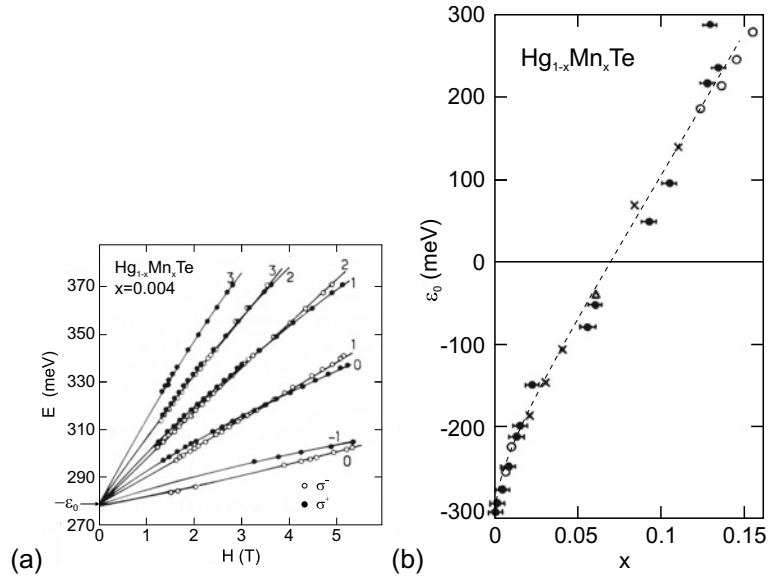

Fig. 17.3 **a** Energies of $\Gamma_6 \rightarrow \Gamma_8$ transitions versus magnetic field for $Hg_{0.996}Mn_{0.004}Te$ at $T = 2\,K$. *Symbols* are experimental values for two polarization directions as indicated. Numbers denote quantum numbers of transitions. *Solid lines* are theoretical fits. **b** Interaction gap versus Mn concentration for $Hg_{1-x}Mn_xTe$ at $T = 4.2\,K$. Various *symbols* represent data from different authors and methods. *Dashed line* is a guide to the eye. Adapted from [1528]

order to allow the electrons to get out of their way in real space). Thus, the atoms have a sizeable spin and a magnetic moment. The spin of Mn is $S = 5/2$. Most transition metals have a $4s^2$ configuration that makes them isovalent in II–VI compounds. We note that Zn has a complete 3d shell and thus no net spin. In Fig. 17.2, an overview of the crystallographic properties is given for Mn-alloyed II–(Se, S, Te, O) based DMS [1526] (DMS with Se, S, and Te have been discussed in [1527]).

As an example, the properties of $Hg_{1-x}Mn_xTe$ are discussed. This alloy is semiconducting (positive band gap ϵ_0) for $x > 0.075$ and a zero-gap material (negative interaction gap ϵ_0) for smaller Mn concentration (cf. Fig. 6.46). The transitions between the Γ_6 and Γ_8 bands can be determined with magnetoabsorption spectra in the infrared [1528]. In Fig. 17.3a, the magnetic field dependence of transition energies between different Landau levels is shown that can be extrapolated to yield the interaction gap. The interaction gap is shown in Fig. 17.3b as a function of the Mn concentration.

For small Mn concentrations, the DMS behaves like a paramagnetic material. For larger concentrations, the Mn atoms have increasing probability to be directly neighbored by another Mn atom and suffer superexchange interaction (cf. (3.24b)). At a certain critical concentration x_c, the cluster size

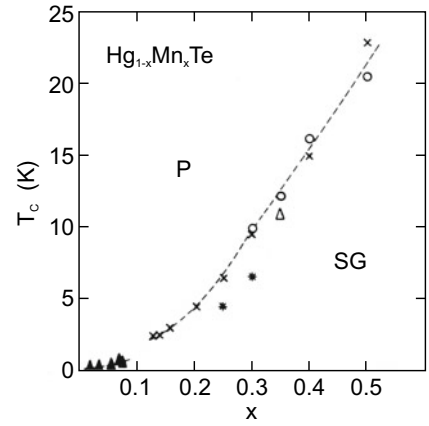

Fig. 17.4 Magnetic phase diagram of $Hg_{1-x}Mn_xTe$, 'P' ('SG') denotes the paramagnetic (spin glass) phase. Various *symbols* represent data from different authors and methods. *Dashed line* is a guide to the eye. Adapted from [1528]

becomes comparable with the size of the sample. If interaction up to the first, second or third neighbor are taken into account for a fcc lattice, the critical concentrations are given by $x_c = 0.195$, 0.136, and 0.061, respectively [1529]. The nearest-neighbor interaction between Mn atoms in such DMS as (Zn, Cd, Hg) Mn(S, Se, Te) was found to be antiferromagnetic,[1] i.e. neighboring spins are aligned antiparallel. Due to frustration of antiferromagnetic long-range order on a fcc lattice, an antiferromagnetic spin glass forms. The transition temperature T_C between the paramagnetic and spin-glass phases of $Hg_{1-x}Mn_xTe$ is shown in Fig. 17.4.

In III–V compounds, the 3d transition metals represent an acceptor if incorporated on the site of the group-III element as, e.g., in the much investigated compound $Ga_{1-x}Mn_xAs$. This material will be used in the following to discuss some properties of magnetic semiconductors. It seems currently well understood and has a fairly high Curie temperature of $T_C \approx 160$ K. Ferromagnetism in a diluted magnetic semiconductor is believed to be caused by indirect exchange through itinerant charge carriers. The ferromagnetic coupling can be invoked by the Ruderman–Kittel–Kasuya–Yoshida (RKKY) interaction, i.e. the spins of the paramagnetic ions are aligned via interaction with the free carriers in the semiconductor. A related concept is the double exchange[2] [1530–1532] in which carriers move in a narrow Mn-derived d-band (for d-wave character see Fig. 7.16c). Such a mechanism was first invoked for PbSnMnTe [1533]. Later, ferromagnetism was discovered in InMnAs [1534] and GaMnAs [1535]. In (In,Ga)MnAs a Mn ion (spin up) spin polarizes the surrounding hole gas (spin down), which has been supplied from the Mn acceptors. This mechanism lowers the energy of the coupled system. The interaction

$$H = -\beta\, N_0\, x\, S\, s \tag{17.1}$$

between the Mn d-shell electrons ($S = 5/2$) and the p-like free holes ($s = 1/2$) is facilitated by p–d hybridization of the Mn states. N_0 denotes the concentration of cation sites in the $A_{1-x}Mn_xB$ alloys. The coupling via electrons is much weaker (coupling coefficient α). The holes interact with the next Mn ion and polarize it (spin up), thus leading to ferromagnetic order. The ferromagnetic properties are evident from the hysteresis shown in Fig. 17.6a. Without the carrier gas such interaction is not present and the material is only paramagnetic. Theoretical results for the Curie temperature of various p-type semiconductors are shown in Fig. 17.5. Generally, the quest for higher Curie temperatures (well above room temperature) is underway and wide band gap materials such as GaN or ZnO doped with transition metals have shown some encouraging results. Mn-substituted chalcopyrite semiconductors

[1] Such superexchange leads to antiferromagnetic interaction if the bond angle is 'close' to 180°.

[2] This model is also called the Zener model.

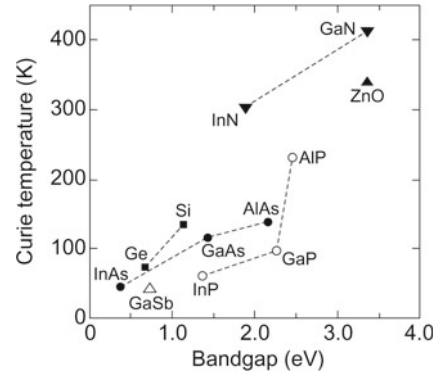

Fig. 17.5 Computed values of the Curie temperature T_C for various p-type semiconductors plotted versus the band gap (*dashed lines* are guides to the eye). All materials contain 5% Mn on the cation sublattice and a hole concentration of $p = 3.5 \times 10^{20}\,\mathrm{cm}^{-3}$. Values for T_C taken from [1532]

are analyzed theoretically in [1536] and are predicted to exhibit less-stable ferromagnetism than III–V semiconductors of comparable band gap.

The carrier density and thus magnetic properties in a DMS can be controlled in a space-charge region (cf. Sect. 21.2.2) as demonstrated in [1537]. In Fig. 17.6, results are shown for hydrogen- (deuterium-) passivated GaMnAs that exhibits ferromagnetism as 'as-grown' thin film. The deuterium is incorporated in similar concentration as the Mn, assumes a back-bond position (forming a H–As–Mn complex) and compensates the hole gas from the Mn (cf. Sect. 7.9). The low-temperature conductivity drops nine orders of magnitude [1538]. Such material displays only paramagnetic behavior. An optimal Mn concentration for ferromagnetic $Ga_{1-x}Mn_xAs$ is around $x = 0.05$. For smaller Mn concentrations, the hole density is too small and the Curie temperature drops; for larger Mn concentrations, the structural properties of the alloy degrade (phase separation into GaAs and MnAs.[3]).

Magnetic hysteresis has been found in nearly compensated Mn-doped ZnO [1539, 1540] (Fig. 17.7). Such material is interesting due to its small spin-orbit coupling. The exchange mechanism is under debate.

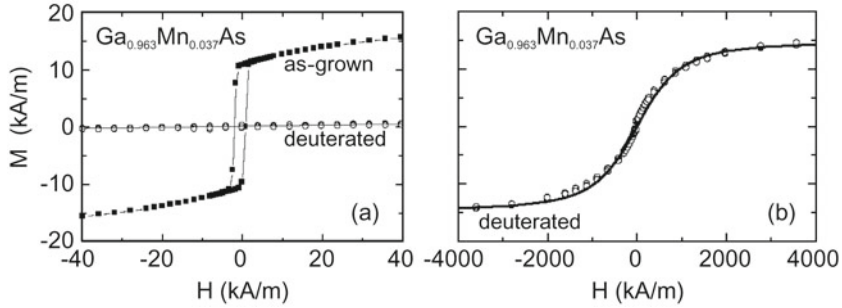

Fig. 17.6 Magnetization M versus magnetic field H for $Ga_{0.963}Mn_{0.037}As$ at low temperature. **a** Comparison of as-grown (*full squares*) and deuterated (*open circles*) thin film with magnetic field in the layer plane at $T = 20\,\mathrm{K}$. **b** Magnetization of the deuterated sample at $T = 2\,\mathrm{K}$ for larger magnetic fields. *Solid line* is Brillouin function for $g = 2$ and $S = 5/2$. Adapted from [1538]

[3] MnAs is a ferromagnetic metal. MnAs clusters can be a problem since they create ferromagnetic properties but not in the way the DMS is supposed to work.

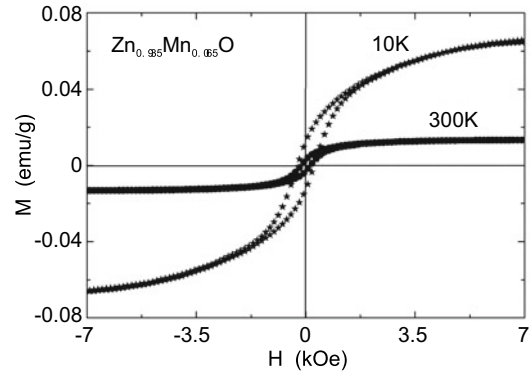

Fig. 17.7 Magnetization M versus magnetic field H for $Zn_{0.935}Mn_{0.065}O$ thin film at $T = 10$ and 300 K. A hysteresis is obvious for both temperatures

17.4 Spintronics

Spintronics (as opposed to electronics) is an emerging field that uses the electron *spin* rather than its *charge* for transport, processing and storage of information. Prototype devices are the spin transistor and the spin LED. A crucial point is spin injection, i.e. the creation of (highly) spin-polarized currents. It remains to be seen whether spintronics can be developed to its theoretically envisioned potential and will play a commercially important role in the course of microelectronics. The spin degree of freedom also promises potential for quantum information processing due to its weak coupling to charge and phonons and the resulting long dephasing time.

It shall be mentioned here that the magnetization alters also the 'classical' transport properties of the semiconductor. The Hall effect is modified strongly and reflects the magnetic hysteresis, also termed *anomalous* Hall effect (AHE).[4] This effect was already discovered by Hall in 1881 for Ni and Co [1541]; a review of the AHE can be found in [1542]. Also the optical excitation of spin-polarized carriers in non-magnetic materials causes AHE [1543]. For a magnetic material with topological band structure, the internal field can be sufficient to evoke the QHE [1544]; this quantum anomalous Hall effect (QAHE) has been reported for $(Bi,Sb)_2Te_3$:Cr [1545] and $MnBi_2Te_4$ [1546].

17.4.1 Spin Transistor

In this device (for regular transistors cf. Chap. 24), spin-polarized electrons are injected from contact 1, transported through a channel and detected in contact 2. During the transport, the spin rotates (optimally by π) such that the electrons cannot enter contact 2 that has the same magnetization as contact 1 (Fig. 17.8). The spin rotation is caused by spin-orbit interaction due to the electric field under the gate contact. This effect is called the Rashba effect and is purely relativistic [1547]. As channel material, a semiconductor with strong spin-orbit coupling such as InAs or (In,Ga)Sb is preferable. However, the use of narrow-gap semiconductors and the increase of spin scattering at elevated temperatures [1548] make the realization of such a transistor at room temperature difficult.

[4] This use of the term 'anomalous' should be distinguished from the historical use of 'anomalous' Hall effect for the sign reversal of the Hall voltage for hole conductors.

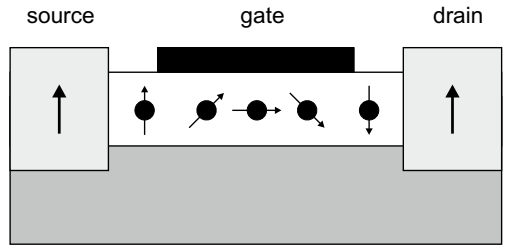

Fig. 17.8 Scheme of spin transistor after the proposal of [1549]. Source and drain are ferromagnets with their magnetization shown schematically as arrows. The channel under the gate transports electrons whose spin rotates in the electric field under the gate

17.4.2 Spin LED

In a spin LED (for LEDs see Sect. 23.3), the injection of spin-polarized carriers into the active layer leads to circularly polarized luminescence. The spin alignment can be achieved with semimagnetic semiconductors grown on top of the active layer or via spin injection from a ferromagnetic metal into the semiconductor (for metal–semiconductor junctions cf. Sect. 21.2). In Fig. 17.9a, a Fe/AlGaAs interface is shown.

Ideally, the spin-polarized electrons from the ferromagnetic metal tunnel into the semiconductor and transfer to the recombination region. Subsequently, the emission is circularly polarized (Fig. 12.30b). The degree of circular polarization is

$$P_\sigma = \frac{I_{\sigma+} - I_{\sigma-}}{I_{\sigma+} + I_{\sigma-}} , \tag{17.2}$$

with $I_{\sigma\pm}$ being the intensity of the respective polarization. The degree of polarization depends on the magnetization of the metal. For the saturation magnetization of Fe, the maximum polarization is about

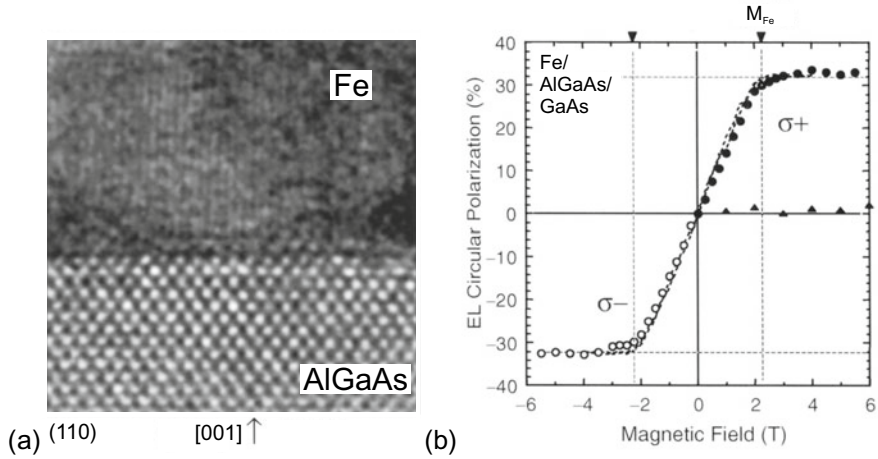

Fig. 17.9 **a** Transmission electron microscopy image of the (110) cross section of the Fe/AlGaAs interface of a spin LED. The *vertical lines* in Fe are the (110) planes with 0.203 nm distance. **b** Magnetic-field dependence of the circular polarization ratio P_σ at $T = 4.5\,\mathrm{K}$ (17.2) (*filled* and *empty* circles) and the out-of-plane component of the Fe-film magnetization (*dashed line*, scaled to the maximum of P_σ). Reproduced from [1551] by permission of the MRS Bulletin

30% at $T = 4.5\,\mathrm{K}$ (Fig. 17.9b) [1550]. The interface and its structural nonideality of the interface presumably prevent the spin injection from being 100% efficient [1551]. Recently, close to pure (95%) circular polarization has been obtained from a (Al,Ga)As/GaAs-based stripe-laser-like (edge emitting) structure with Fe/crystalline AlO_x spin-tunnel barrier [1552].

Chapter 18
Organic Semiconductors

Abstract An introduction to organic semiconductors, based on the sp^2 bonding scheme is given, covering small organic molecules and polymers. Their electronic structure, doping schemes, as well as their particular transport and optical properties are covered.

18.1 Introduction

Organic semiconductors are based on carbon compounds. The main structural difference from inorganic semiconductors is the bond based on sp^2 hybridization (cf. Sect. 2.2.3) as present in benzene (and graphite). Diamond, although consisting of 100% carbon, is not considered an organic semiconductor. We note that carbon can form further interesting structures based on sp^2 bonds, such as carbon nanotubes (Sect. 14.3), (single or few layer) graphene sheets (Sect. 13.1) rolled up to form cylinders, or fullerenes, e.g. soccer-ball-like molecules such as C_{60}.

In the 1980 Handbook on Semiconductors only a good ten pages were devoted to organic semiconductors [1553]. Now several textbooks are available [1554, 1555] for a much more detailed treatment than given here.

18.2 Materials

18.2.1 Small Organic Molecules, Polymers

The prototype organic molecule is the benzene molecule with its ring-like structure (Fig. 2.8).

There is a large number of organic, semiconducting molecules that differs by the number of benzene rings (Fig. 18.1), the substitution of carbon atoms by nitrogen or sulfur (Fig. 18.2a, b), the polymerization (Fig. 18.2c) or the substitution of hydrogen atoms by side groups (Fig. 18.2d). Since PPV is insoluble, typically derivatives such as MEH-PPV[1] [1557] that are soluble in organic solvents are used. Compared to benzene, the substitution of one carbon atom by nitrogen (pyridine) represents doping with one electron. In Fig. 18.3, the most important building blocks of organic molecules are shown.

[1] 2-ethoxy,5-(2'-ethyl-hexyloxy)-1,4-phenylene vinylene.

M. Grundmann, *The Physics of Semiconductors*, Graduate Texts in Physics,
https://doi.org/10.1007/978-3-030-51569-0_18

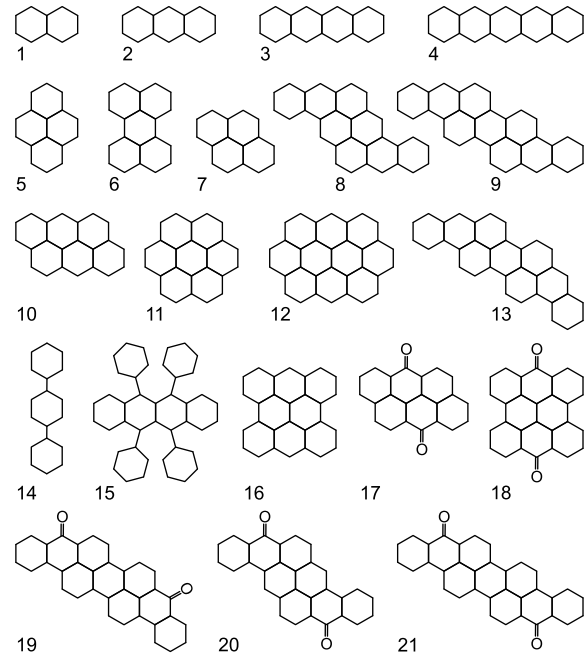

Fig. 18.1 Various organic compounds: 1: naphtalene, 2: anthracene, 3: tetracene, 4: pentacene, 5: pyrene, 6: perylene, 7: chrysene, 8: pyranthrene, 9: isoviolanthrene, 10: anthanthrene, 11: coronene, 12: ovalene, 13: violanthrene, 14: p-terphenyl, 15: rubrene, 16: m-dinaphthanthrene, 17: anthanthrone, 18: m-dinaphthanthrone, 19: violanthrone, 20: pyranthrone, 21: isoviolanthrone

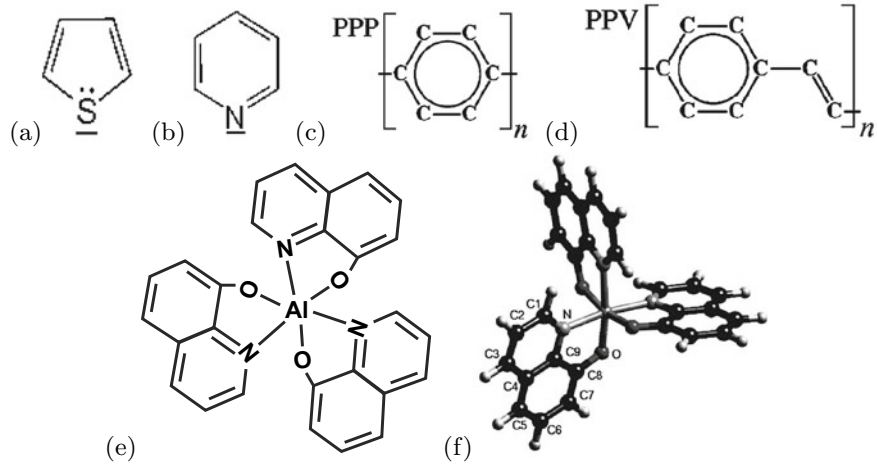

Fig. 18.2 Organic compounds: **a** thiophene, **b** pyridine, **c** poly-(p-phenyl), **d** poly-(p-phenylvinyl), **e** Alq_3 (tris-(8-hydroxyquinolate)-aluminum) and **f** a three-dimensional view of the Alq_3 molecule. Part (**f**) reprinted with permission from [1556], ©1998 AIP

18.2.2 Organic Semiconductor Crystals

Small organic molecules can crystallize into solids, so-called *organic molecular crystals* (OMC), due to van-der-Waals interaction. In Fig. 18.4a, the monoclinic unit cell of an anthracene crystal [1558] is shown as an example. Also tetracene and pentacene (Fig. 18.4b) have this layered 'herringbone' structure. A comparison of the unit cells of oligoacene crystals is given in Table 18.1.

Crystal growth of single crystal OMC is achieved with a variety of methods, among them sublimation, Bridgman- and Czochralski-type methods [1560, 1561], vapor phase growth [1562, 1563]

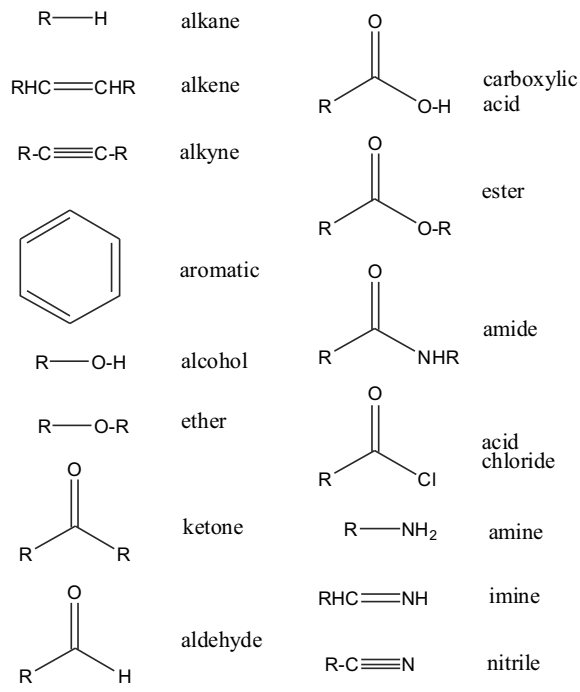

Fig. 18.3 Building blocks of organic molecules, 'R'=alkyl group, i.e. CH_3 (methyl-), CH_3CH_2 (buthyl-), . . .

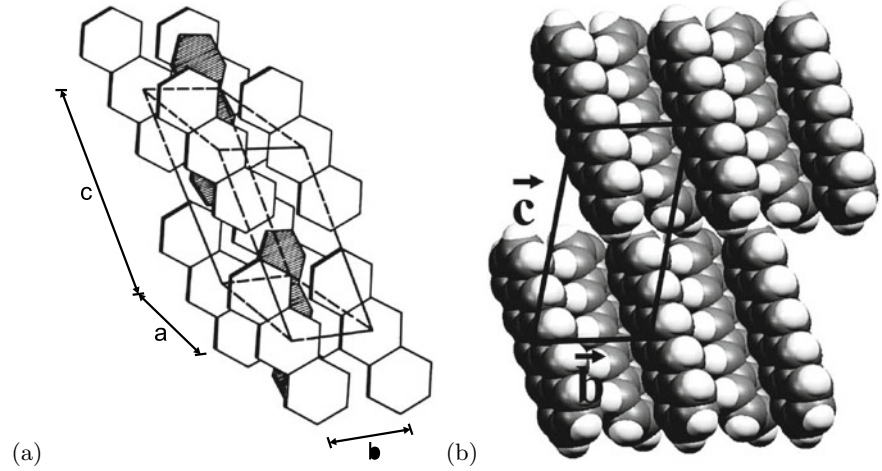

Fig. 18.4 **a** Monoclinic unit cell (for size see Table 18.1) of anthracene crystal. **b** Two herringbone layers of pentacene in a projection onto the bc plane of the triclinic unit cell. Adapted from [1566]

or from solution [1564, 1565]. Single organic molecular crystals exhibit intrinsic material properties. The practical use of organic semiconductors involves thin films, e.g. in LEDs (OLED, Sect. 23.3.7) and transistors (OFET, Sect. 24.6.4). Thin films of organic molecules are typically disordered and their performance parameters are inferior to that of OMCs.

Table 18.1 Properties of oligoacene crystals. Melting point and unit cell parameters. Data from [1559]

Property	Naphtalene	Anthracene	Tetracene	Pentacene
Melting point (°C)	80	217	357	> 300 °C
Crystal system	Monoclinic	Monoclinic	Triclinic	Triclinic
a (nm)	0.824	0.856	0.798	0.793
b (nm)	0.600	0.604	0.614	0.614
c (nm)	0.866	1.116	1.357	1.603
α (°)	90	90	101.3	101.9
β (°)	122.9	124.7	113.2	112.6
γ (°)	90	90	87.5	85.8

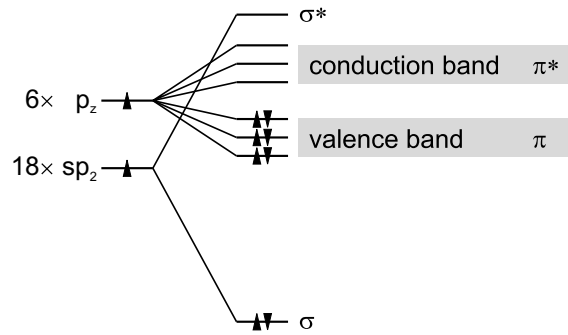

Fig. 18.5 Schematic band structure of a polymer originating from the states of the benzene molecule (see Fig. 2.11)

18.3 Electronic Structure

The p_z orbitals in benzene are partially filled and there is an energy gap between HOMO and LUMO (Fig. 2.11). A similar consideration is valid for polymers. The coupling of orbitals along the polymer chain leads to broadening of the π and π^* states into a (filled) valence and an (empty) conduction band, respectively (Fig. 18.5).

The HOMO and LUMO positions of various organic semiconductors are shown in Fig. 18.6 relativ to the vacuum level (cmp. Fig. 12.21 for inorganic semiconductors). The HOMO is also known as *ionization energy* (IE), the LUMO as *electron affinity* (EA). With layered organic semiconductors heterostructures can be built, e.g. to design recombination pathways (recombination layer, electron blocking layers (EBL) and hole blocking layers (HBL)). For electron injection and electron extraction (hole injection) contacts, metals with appropriate work function (in connection with a possible interface dipole layer) have to be used. More details on injection and extraction contacts to organic semiconductors are discussed in Sect. 21.2.7.

18.4 Doping

The doping of organic semiconductors can be achieved by

- partial oxidation or reduction of the organic molecule,
- substitution of atoms in the organic molecule,
- mixing of the matrix with 'dopant' molecules.

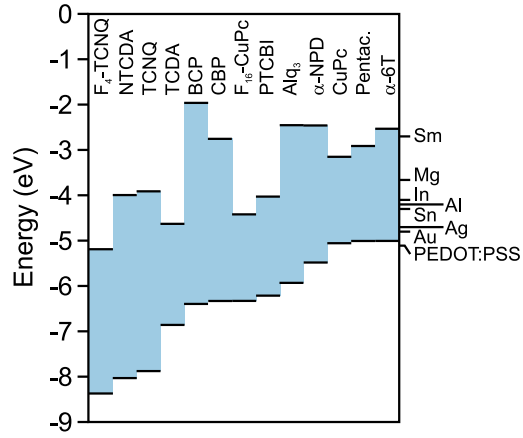

Fig. 18.6 Position of HOMO and LUMO for a variety of organic semiconductors (relative to a common vacuum level at $E = 0\,\mathrm{eV}$). Based on values from [1567]. On the right hand side the work functions of several metals are shown for comparison

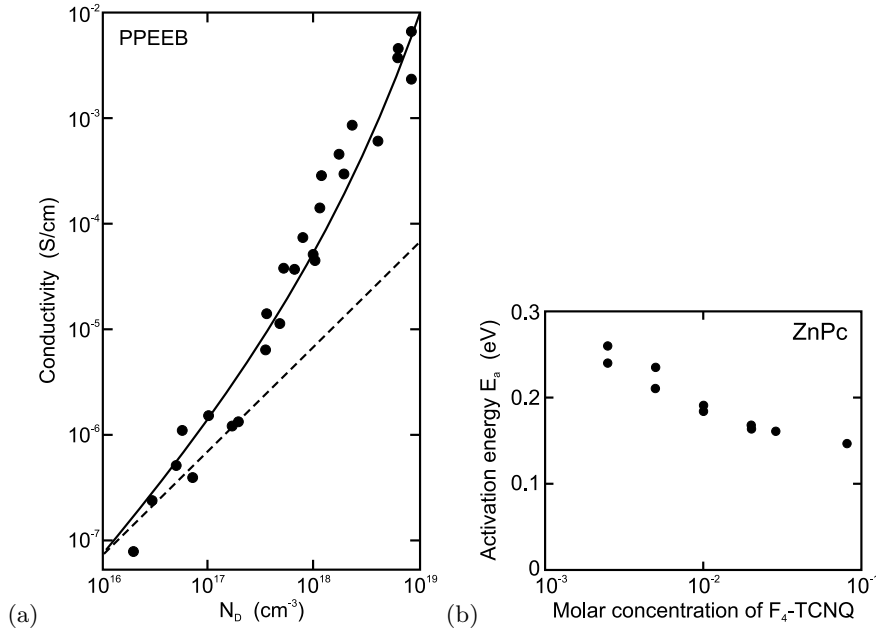

Fig. 18.7 **a** Conductivity (at 0.9 V/μm) versus dopant concentration N_D for PPEEB films. Experimental data (*circles*) and fit (*solid line*) according to (18.1) with activation energy $E_{\mathrm{a},0} = 0.23\,\mathrm{eV}$ and $\beta = 6.5 \times 10^{-8}\,\mathrm{eV\,cm}$ ($\mu = 0.2\,\mathrm{cm^2/Vs}$). *Dashed line* denotes linear relation between conductivity and N_D. Adapted from [1571]. **b** Thermal activation energy E_a of carriers (holes) in ZnPc:F_4-TCNQ as a function of the molar dopant concentration. Adapted from [1568]

The systematic shift of the Fermi level with dopant concentration has been reported in [1568]. Typically, the conductivity increases superlinearly with the doping concentration (Fig. 18.7a), an effect discussed in detail in [1569]. While the mobility remains constant, the thermal activation energy E_a for carriers decreases with increasing doping (Fig. 18.7b) due to electrostatic interaction [594, 1570], an effect already discussed in Sect. 7.5.7. The activation energy in the dilute limit $E_{\mathrm{a},0}$ is modified to (cmp. (7.52))

$$E_\mathrm{a} = E_{\mathrm{a},0} - \beta\, N_\mathrm{D}^{1/3}\ . \tag{18.1}$$

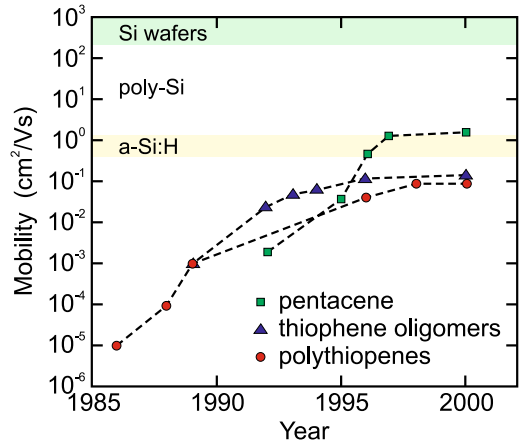

Fig. 18.8 Historic development of the experimentally achieved mobility of organic semiconductors at room temperature

18.5 Transport Properties

Transport in organic semiconductors is characterized by

- strong polaronic effects,
- hopping conduction,
- low mobility, low drift saturation velocity.

The interaction of charges with lattice deformations leads to the formation of polarons [1572]. In organic materials these are often 'small', i.e. the extension of the deformation is on atomic scale. Such self-trapping of charges reduces their mobility. Two charges can share the same deformation (bipolaron) or oppositely charged polarons can attract (similar to an exciton). If these charges are on the same (neighboring) polymer chain, the polaron is called intrachain (interchain).

The conductivity within a molecule, e.g. a long polymer chain, and the conductivity between different molecules have to be distinguished. The conduction between different molecules occurs via *hopping*. Typically, the conductivity is thermally activated according to

$$\sigma = \sigma_0 \exp\left(-\frac{E_\mathrm{a}}{kT}\right) , \tag{18.2}$$

where E_a is an energy of the order of 1 eV. Such activation also pertains to the mobility alone, e.g. $E_\mathrm{a} = 0.48\,\mathrm{eV}$ for PPV [1573].

The maximum low-field mobility of many crystalline organic semiconductors at room temperature is around $1\,\mathrm{cm}^2/\mathrm{Vs}$ with a weak temperature dependence [1574]. Such mobility is much smaller than that of crystalline silicon and rather comparable to that of amorphous silicon. Improved purity and handling of organic semiconductors has allowed to achieve intrinsic material properties (Fig. 18.8). The mobility increases at low temperatures, e.g. below 100 K in naphtalene [1575]. This has been attributed to the freeze-out of phonons and the transition from hopping to band transport.

The drift velocity at higher fields shows saturation but the values, even at low temperature, are much smaller than in silicon (Fig. 18.9). An analytical model for the described main features of transport in organic semiconductors has been given in [1576].

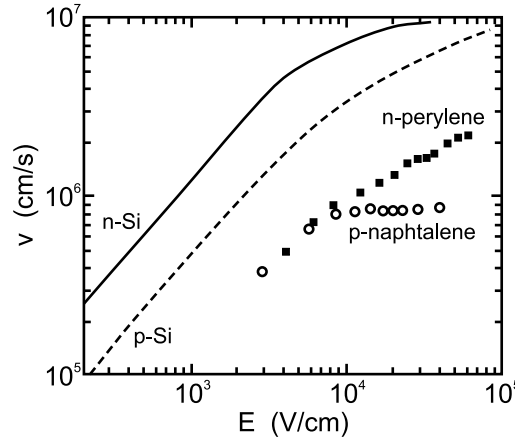

Fig. 18.9 Carrier velocity in ultrapure and highly perfect single crystals of (n-conducting) perylene at $T = 30\,\mathrm{K}$ and (p-conducting) naphtalene at $T = 4.3\,\mathrm{K}$. For comparison electron (hole) velocity in silicon at room temperature is shown as *solid* (*dashed*) line. Adapted from [1561]

18.6 Optical Properties

Organic molecules can emit light efficiently and are thus useful for light emitters. For the photo-physics of organic materials it is essential to recall the molecular physics of singlet and triplet states. In the singlet (triplet) state, the total spin quantum number of the unpaired electrons is $S = 0$ ($S = 1$). A simple energy scheme includes a ground state S_0 and excited singlet (S_1) and triplet (T_1) states. The recombination transition $S_1 \rightarrow S_0$ is allowed and its lifetime short. Such luminescence is termend 'fluorescence'. Recombination from the triplet state is forbidden or at least very slow ('phosphorescence').

As an example for a small organic molecule, the fluorescence lifetime of Alq_3 is about 12 ns [1577]. The triplet lifetime is in the 10 µs range [1578]. Luminescence and absorption spectra of Alq_3 are shown in Fig. 18.10. The luminescence peak is redshifted with respect to the absorption edge due to the Frank-Condon principle (Fig. 10.21). The density of excited (empty) states of the Alq_3 molecule is shown in Fig. 18.11 together with the orbitals associated with the four prominent states. The lowest orbital is the LUMO and leads to the visible luminescence of the Alq_3 in the red.

In Fig. 18.12, the photoluminescence (PL) and absorption of a polymer, poly-thiophene are shown. The recombination is below the band gap of 2.1–2.3 eV on an excitonic level at 1.95 eV. There are

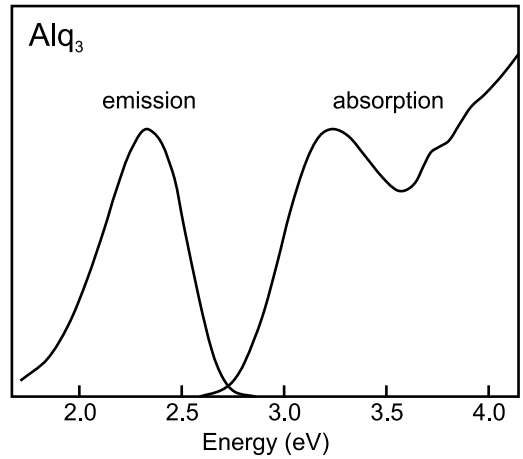

Fig. 18.10 Luminescence and absorption spectra of Alq_3 (vapor-deposited 150 nm thin film on a quartz substrate) at room temperature. Adapted from [1579]

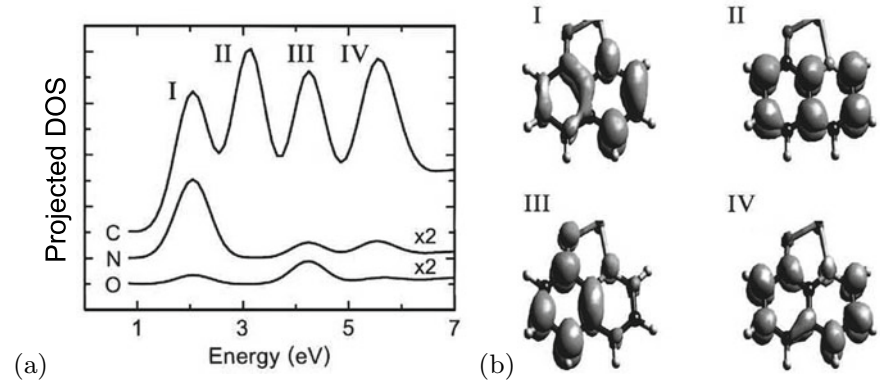

Fig. 18.11 **a** Projected density of states (for C, N, and O) of excited states in an Alq_3 molecule. The origin of the energy axis is the HOMO level. **b** Orbitals for the four states labeled I–IV in (**a**). Reprinted with permission from [1556], ©1998 AIP

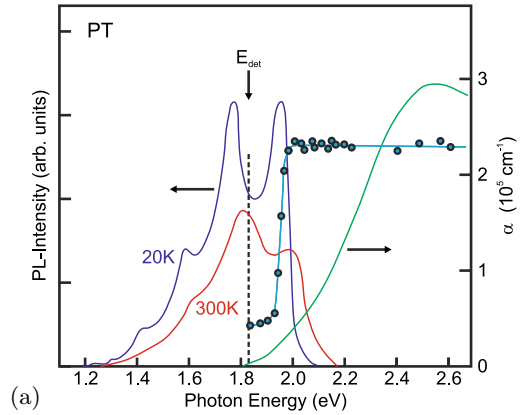

Fig. 18.12 Photoluminescence (PL) spectra at $T = 20$ and 300 K and absorption spectrum (*green line*) of poly-thiophene. The *vertical dashed line* denotes the detection energy ($E_{det} = 1.83$ eV) of the PL excitation (PLE) spectrum (*blue circles*) ($T = 20$ K). Adapted from [1580]

several phonon replica whose separation of 180 meV corresponds to the C–C stretching mode. The PL excitation (PLE) spectrum of poly-thiophene demonstrates that the PL at 1.83 eV can be excited via the exciton level.

The theoretical band structure of poly-thiophene is shown in Fig. 18.13a. The Brillouin zone is one-dimensional. The situation I corresponds to a single molecular chain, the situation II pertains to the chain embedded in a medium with a dielectric constant $\epsilon = 3$. The predicted band gaps are 3.6 eV and 2.5 eV, respectively. The exciton binding energy is about 0.5 eV. The exciton is a Frenkel exciton that has a small extension and is localized. The high binding energy is favorable for radiative recombination since the exciton is stable at room temperature. For photovoltaic applications, it is unfavorable since it has to be overcome in order to separate electrons and holes (after absorption). Generally, intrachain excitons (as here) and interchain excitons, where electron and the hole are localized on different chains, are distinguished.

Collection of carriers in the 'dark' triplet state poses a problem limiting the quantum efficiency to 25% in a simple model [1582]. Harvesting luminescence from *all* exciton states would yield significantly higher efficiencies than is possible in purely fluorescent materials (or devices).

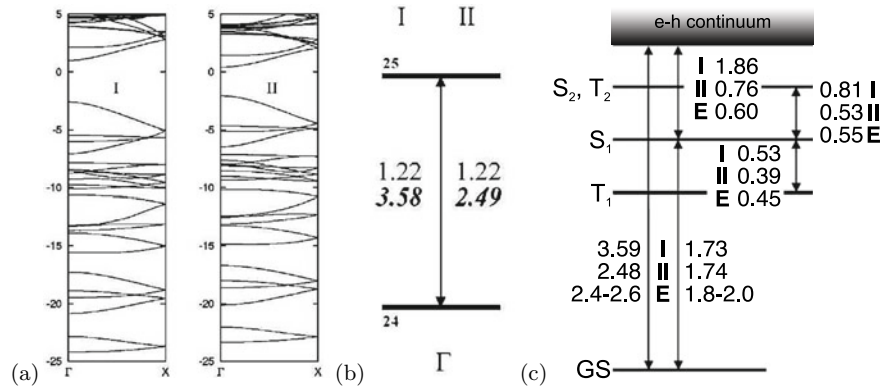

Fig. 18.13 **a** Band structure of poly-thiophene ('I': naked chain, 'II': chain in a dielectric medium ($\epsilon = 3$)), **b** single-particle energies and band gap, **c** exciton levels ('E': experimental values). Reprinted with permission from [1581], ©2002 APS

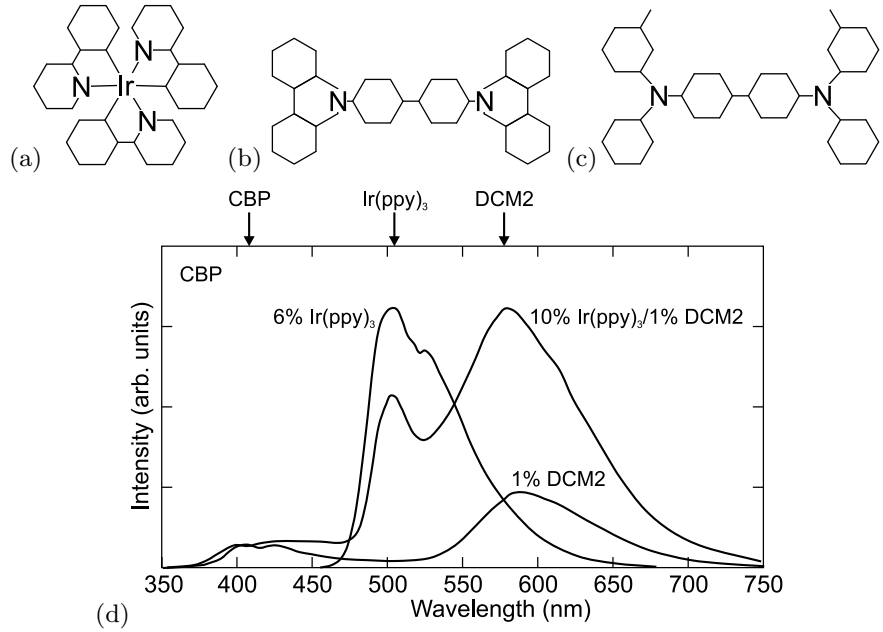

Fig. 18.14 Molecular structure of **a** $Ir(ppy)_3$, **b** CBP and **c** TDP (see text). **d** Electroluminescence spectra (at room temperature) of CBP:6% $Ir(ppy)_3$, CBP:10% $Ir(ppy)_3$/1%DCM2 and CBP:2%DCM2. Based on data from [1585, 1586]

A successful route is the use of a phosphorescent guest material. Radiative transitions from triplet states become partially allowed when the excited singlet and triplet states are mixed. This is typically achieved in metalorganic molecules with heavy metal atoms, providing large spin-orbit interaction effects [1583, 1584]. Most prominently Ru-, Pt- and Ir-containing compounds are used, e.g. *fac* tris(2-phenylpyridine) iridium [$Ir(ppy)_3$] in 4,4'-N,N'-dicarbazole-biphenyl [CBP] (Fig. 18.14a,b) [1585]. The luminescence spectrum of $Ir(ppy)_3$ is shown in Fig. 18.14d. The radiative decay constant of the $Ir(ppy)_3$ triplet state is about 800 ns and observable if energy transfer from the host triplet state is exotherm ($\Delta G = G_G - G_H < 0$ [1578], see Fig. 18.15a) and fast. This is the case for CBP:$Ir(ppy)_3$ (Fig. 18.15b), $\Delta G \approx -0.2$ eV. Actually, reverse transfer from $Ir(ppy)_3$ to CBP seems responsible for some loss in luminescence efficiency and the decrease in phosphorescent lifetime from 800 ns to 400 ns.

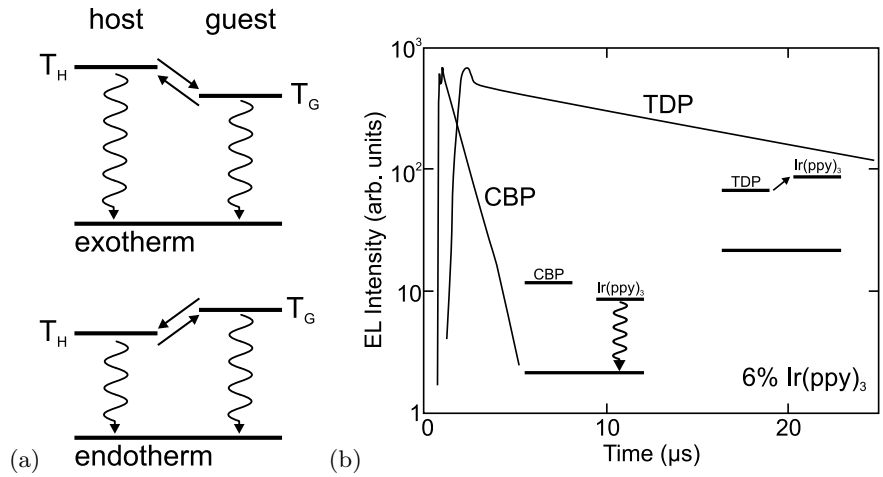

Fig. 18.15 **a** Schematic term diagram of host (T_H) and guest (T_G) triplet states. *Straight arrows* denote energy transfer between triplet states, *wiggly arrows* denote radiative transitions to the (singlet) ground state. **b** Electroluminescence transients (at room temperature, detected in the range 500–560 nm [cmp. Fig. 18.14b]) of CBP:6% $Ir(ppy)_3$ ($\tau \approx 1\,\mu s$) and TDP:6% $Ir(ppy)_3$ ($\tau \approx 15\,\mu s$). *Insets*: term schemes with arrow denoting the rate limiting step. Based on data from [1578]

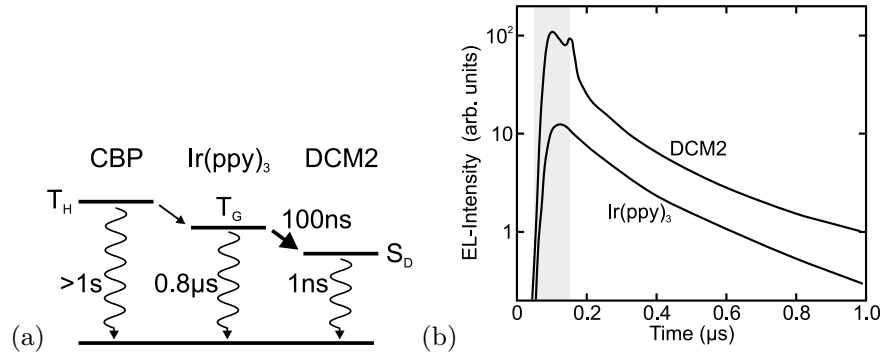

Fig. 18.16 **a** Schematic term scheme of CBP:$Ir(ppy)_3$/DCM2 and energy transfer and recombination paths (cmp. spectrum in Fig. 18.14). The rate constants are shown for various processes, the rate limiting step is shown with a *bold arrow*. **b** Electroluminescence transients after 100 ns excitation pulse (*grey area*) of $Ir(ppy)_3$ and DCM2 luminescence from CBP:10% $Ir(ppy)_3$/1% DCM2. Based on data from [1586]

In the case of N,N'-diphenyl-N,N'-bis(3-methylphenyl)-[1,1'-biphenyl]-4,4'-diamine [TDP] (Fig. 18.14c) host, the triplet energy transfer to the phosphorent $Ir(ppy)_3$ guest is endotherm ($\Delta G \approx +0.1$ eV) and represents the rate limiting step [1578]. In this case the recombination of $Ir(ppy)_3$ has a decay constant of about 15 µs (Fig. 18.15b). The thermal activation character is confirmed by even longer decay times at low temperatures ($\tau \approx 80\,\mu s$ at $T = 200$ K) [1578]. Endothermic transfer allows to pump a blue guest phosphor without a blue host material.

Further, subsequent Förster energy transfer [1587] from the guest triplet state to a fast and efficient singlet state (S_D) of a fluorescent dye is possible, e.g. from CBP:$Ir(ppy)_3$ to DCM2 [1586]. The transient lifetime of pure DCM2 is about 1 ns. In a mixture of CBP:10% $Ir(ppy)_3$/1% DCM2 the luminescence of DCM2 appears with the same 100 ns decay constant as that of $Ir(ppy)_3$ (Fig. 18.16b). This decay constant (rate limiting step, see Fig. 18.16a) corresponds to the energy transfer depleting the triplet state of $Ir(ppy)_3$ to DCM2 and is much faster than the pure $Ir(ppy)_3$ radiative lifetime.

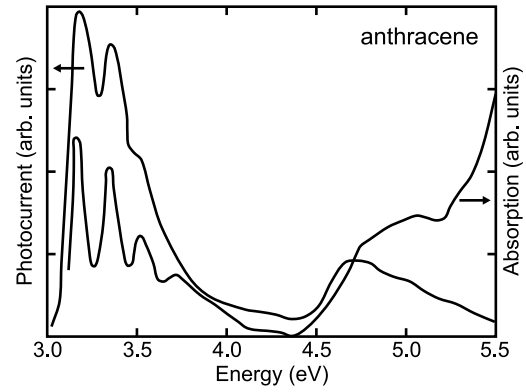

Fig. 18.17 Photoconductivity and absorption spectrum of anthracene

The photoconductivity of organic semiconductors is typically related to their absorption spectrum as shown for anthracene in Fig. 18.17.

Chapter 19
Dielectric Structures

Abstract Dielectric structures, in particular periodic dielectric structures are treated. A general one-dimensional model is developed describing Bragg mirrors. Examples for photonic band gap materials in one, two and three dimensions are given. Different types of dielectric cavities and microscopic resonators including Fabry-Pérot and whispering gallery resonators are treated. Quantum electrodynamic physical effects from light matter coupling such as Purcell effect and strong coupling are treated.

19.1 Photonic Band Gap Materials

Layered structures of dielectric materials with different index of refraction are used as optical elements such as filters or reflection and anti-reflection coatings [1588]. In this section we discuss the use of such concepts in one-, two- and three-dimensional photonic band gap materials.

19.1.1 Introduction

A structure with a so-called *photonic* band gap (PBG) exhibits an energy range (color range) in which photons cannot propagate in any direction. In the photonic band gap, there are no optical modes, no spontaneous emission and no vacuum (zero-field) fluctuations. We recollect that spontaneous emission is not a necessary occurrence: Looking at Fermi's golden rule (9.30) for the transition probability integrated over all final states

$$w(E) = \frac{2\pi}{\hbar} |M|^2 \rho_{\mathrm{f}}(E) \ , \tag{19.1}$$

we see that the decay rate depends on the density ρ_{f} of final states at energy E. In the case of spontaneous emission, this is the (vacuum) density D_{em} of electromagnetic modes (per energy per volume) that varies $\propto \omega^2$:

$$D_{\mathrm{em}}(E) = \frac{8\pi}{(hc)^3} E^2 \ . \tag{19.2}$$

In a homogeneous optical medium c must be replaced with c/n (cmp. Sect. 10.2.3).

If the band gap of a PBG is tuned to the electronic gap of a semiconductor, the spontaneous emission, and also induced emission, can be suppressed. Thus, one mode has to be left by 'doping' the structure. In this mode all emission will disappear and an efficient single-mode (monochromatic) LED or 'zero-threshold' laser could be built. A schematic comparison of the band structure of electrons and photons is given in Fig. 19.1.

M. Grundmann, *The Physics of Semiconductors*, Graduate Texts in Physics,
https://doi.org/10.1007/978-3-030-51569-0_19

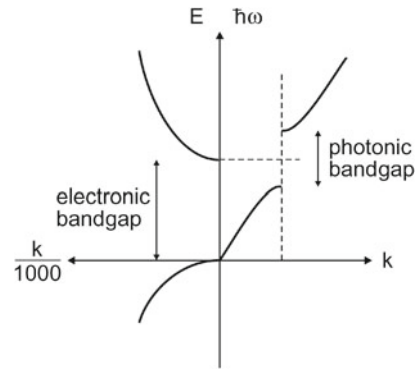

Fig. 19.1 *Right*: electromagnetic dispersion with a forbidden gap at the wavevector of the periodicity. *Left*: Electron-wave dispersion typical of a direct-gap semiconductor. When the photonic band gap straddles the electronic band gap, electron–hole recombination into photons is inhibited since the photons have no place to go (zero final density of states)

19.1.2 General 1D Scattering Theory

The formation of a photonic band gap in a one-dimensional dielectric can be calculated to a large extent analytically and thus with direct insight. Let $n(x)$ be the spatially varying index of refraction (no losses or nonlinear optical effects). The one-dimensional wave equation (Helmholtz equation) reads for the electric field E

$$\frac{\partial^2 E(x)}{\partial x^2} + n^2(x)\,\frac{\omega^2}{c^2}\,E(x) = 0\ . \tag{19.3}$$

A comparison with a one-dimensional Schrödinger equation

$$\frac{\partial^2 \Psi(x)}{\partial x^2} + \frac{2m}{\hbar^2}\,[E - V(x)]\,\Psi(x) = 0 \tag{19.4}$$

shows that the Helmholtz equation corresponds to the quantum-mechanical wave equation of zero external potential V and a spatially modulated mass, i.e. a case that is usually not considered.

Let us consider now the amplitude a_k of the k eigenvector. The eigenvalue is then ω_k. The one-dimensional mode density $\rho(\omega)$ (per energy and per unit length) is

$$\rho(\omega) = \frac{\mathrm{d}k}{\mathrm{d}\omega}\ , \tag{19.5}$$

which is the inverse of the group velocity.

We follow one-dimensional scattering theory as presented in [1589]. At this point we do not rely on any specific form of $n(x)$ (Fig. 19.2a). The (complex) transmission coefficient t for any index structure is

$$t = x + \mathrm{i}y = \sqrt{T}\,\exp(\mathrm{i}\phi)\ , \tag{19.6}$$

where $\tan\phi = y/x$. ϕ is the total phase accumulated during propagation through the structure. It can be written as the product of the physical thickness of the structure d and the effective wave number k. Hence we have the dispersion relation

$$\frac{\mathrm{d}}{\mathrm{d}\omega}\tan(k\,d) = \frac{\mathrm{d}}{\mathrm{d}\omega}\left(\frac{y}{x}\right)\ . \tag{19.7}$$

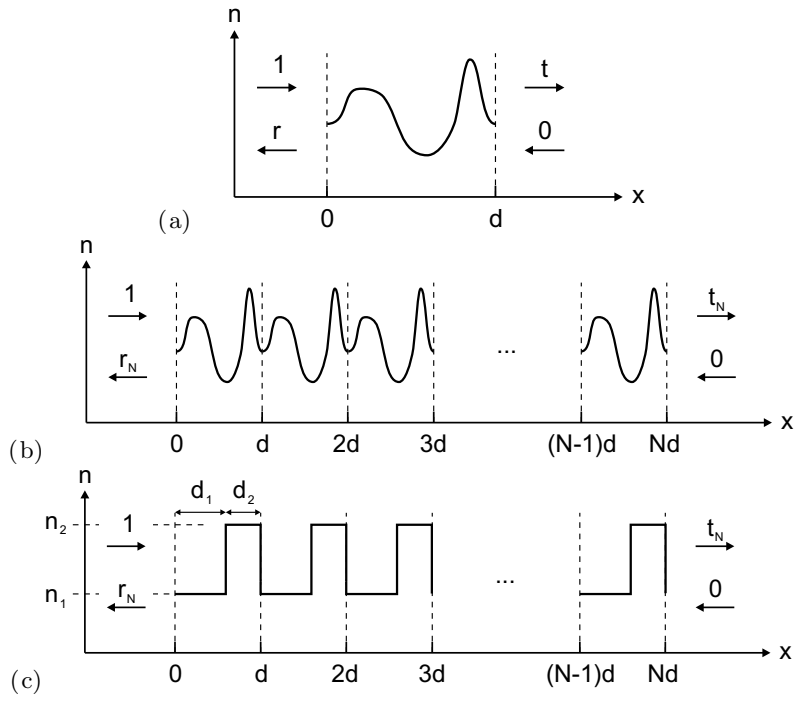

Fig. 19.2 1D scattering problem: **a** General scattering of an index of refraction distribution, **b** N-period stack, **c** two-layer (quarter-wave) stack

Evaluating the derivative we find

$$\frac{d}{\cos^2(k\,d)}\,\frac{\mathrm{d}k}{\mathrm{d}\omega} = \frac{y'x - x'y}{x^2}\ , \tag{19.8}$$

where the prime denotes derivation with respect to ω. Using the relation $\cos^2\theta = (1+\tan^2\theta)^{-1}$, we obtain the general expression

$$\rho(\omega) = \frac{\mathrm{d}k}{\mathrm{d}\omega} = \frac{1}{d}\,\frac{y'x - x'y}{x^2+y^2}\ . \tag{19.9}$$

19.1.3 Transmission of an N-Period Potential

Now, the behavior of N periods of a given index distribution $n(x)$ within a thickness d of one period (Fig. 19.2b) is investigated. The scattering matrix $\mathbf{M}$ connects the intensity at $x = 0$ with that at $x = d$. We use the column vector $\mathbf{u} = (u^+, u^-)^{\mathrm{T}}$ containing the right- and left-going waves (labeled '+' and '−', respectively), $u^{\pm} = f^{\pm}\exp(\pm \mathrm{i}k\,x)$,

$$\mathbf{u}(0) = \mathbf{M}\,\mathbf{u}(d)\ . \tag{19.10}$$

Using the boundary conditions $\mathbf{u}(0) = (1, r)$ and $\mathbf{u}(d) = (t, 0)$, we find that $\mathbf{M}$ has the structure

$$\mathbf{M} = \begin{pmatrix} 1/t & r^*/t^* \\ r/t & 1/t^* \end{pmatrix}\ . \tag{19.11}$$

The conservation of energy requires that $\det \mathbf{M} = (1 - R)/T = 1$. The eigenvalue equation for $\mathbf{M}$ is

$$\mu^2 - 2\mu \,\mathrm{Re}(1/t) + 1 = 0 \,. \tag{19.12}$$

The two eigenvalues $\mu^{\pm}$ are related by $\mu^+\mu^- = \det \mathbf{M} = 1$. If we consider an infinite, periodic structure, we know from Bloch's theorem (cf. Sect. 6.2.1) that the eigenvector varies between unit cells only via a phase factor, i.e. $|\mu| = 1$. Therefore, the eigenvalues can be written as

$$\mu^{\pm} = \exp(\pm \mathrm{i}\beta) \,, \tag{19.13}$$

where β corresponds to the Bloch phase of a hypothetical infinite periodic structure. This phase β should not be confused with ϕ defined earlier, which is associated with the unit cell transmission. We find the condition

$$\mathrm{Re}(1/t) = \cos\beta \tag{19.14}$$

for the Bloch phase. Since every matrix obeys its own eigenvalue equation, we have also ($\mathbf{1}$ being the unity matrix)

$$\mathbf{M}^2 - 2\,\mathbf{M}\cos\beta + \mathbf{1} = 0 \,. \tag{19.15}$$

By induction one can show that the N-period case has the scattering matrix

$$\mathbf{M}^N = \mathbf{M}\,\frac{\sin(N\,\beta)}{\sin\beta} - \mathbf{1}\,\frac{\sin((N-1)\,\beta)}{\sin\beta} \,. \tag{19.16}$$

The solution for the finite period case can be written in terms of the Bloch phase of the infinite potential. The transmission and reflection of the N-period system are given by

$$\frac{1}{t_n} = \frac{1}{t}\,\frac{\sin(N\,\beta)}{\sin\beta} - \frac{\sin((N-1)\,\beta)}{\sin\beta} \tag{19.17a}$$

$$\frac{r_n}{t_n} = \frac{r}{t}\,\frac{\sin(N\,\beta)}{\sin\beta} \,. \tag{19.17b}$$

The transmission of intensity can be written as ($T = t^*t$)

$$\frac{1}{T_N} = 1 + \frac{\sin^2(N\,\beta)}{\sin^2\beta}\left(\frac{1}{T} - 1\right) \,. \tag{19.18}$$

Again, up to this point no specific distribution of the index of refraction within the unit cell has been specified.

From (19.17a), a general formula for the mode density $\rho_N(\omega)$ of the N-stack can be obtained as [1589]

$$\rho_N = \frac{1}{N\,d}\,\frac{\frac{\sin(2N\beta)}{2\sin\beta}\left(\eta' + \frac{\eta\,\xi\,\xi'}{1-\xi^2}\right) - \frac{N\,\eta\,\xi'}{1-\xi^2}}{\cos^2(N\beta) + \eta^2\left(\frac{\sin(N\beta)}{\sin\beta}\right)^2} \,, \tag{19.19}$$

where $\xi = x/T = \cos\beta$ and $\eta = y/T$.

19.1.4 The Quarter-Wave Stack

A quarter-wave stack, also known as a Bragg mirror, exhibits a one-dimensional photonic band gap. One period consists of two regions with thickness and index of refraction (d_1, n_1) and (d_2, n_2), respectively (Fig. 19.2c). In the quarter-wave stack each region has an optical thickness of $\lambda/4$ (the wave accumulates in each region a phase of $\pi/2$) for a particular wavelength λ_0 or (midgap) frequency ω_0. Thus, the condition reads

$$n_1 d_1 = n_2 d_2 = \frac{\lambda_0}{4} = \frac{\pi}{2} \frac{c}{\omega_0} . \tag{19.20}$$

Using the Fresnel formulas, the transmission of an arbitrary two-layer cell is

$$t = \frac{T_{12} \exp(\mathrm{i}\,(p+q))}{1 + R_{12} \exp(2\mathrm{i}\,q)} , \tag{19.21}$$

where $p = n_1 d_1 \omega/c$ and $q = n_2 d_2 \omega/c$ are the phases accumulated in the two layers, respectively. The values of T_{12} and R_{12} are given as

$$T_{12} = \frac{4\, n_1\, n_2}{(n_1 + n_2)^2} \tag{19.22}$$

$$R_{12} = \frac{(n_1 - n_2)^2}{(n_1 + n_2)^2} . \tag{19.23}$$

For the quarter-wave stack ($p = q = \pi/2$), we obtain for (19.21)

$$t = \frac{T_{12} \exp(\mathrm{i}\pi\, \tilde{\omega})}{1 + R_{12} \exp(\mathrm{i}\pi\, \tilde{\omega})} , \tag{19.24}$$

where $\tilde{\omega} = \omega/\omega_0$ is the frequency scaled to the midgap value.

The transmission of a single two-layer cell is

$$T = \frac{T_{12}^2}{1 - 2\, R_{12} \cos(\pi\, \tilde{\omega}) + R_{12}^2} , \tag{19.25}$$

and the Bloch phase is given by

$$\cos\beta = \xi = \frac{\cos(\pi\, \tilde{\omega}) - R_{12}}{T_{12}} \tag{19.26}$$

$$\eta = \frac{\sin(\pi\, \tilde{\omega})}{T_{12}} . \tag{19.27}$$

For the N-period quarter-wave stack the transmission is given by

$$T_N = \frac{1 + \cos\beta}{1 + \cos\beta + 2\,(R_{12}/T_{12})\, \sin^2(N\,\beta)} . \tag{19.28}$$

A band gap forms. Within the band gap, the density of modes is lowered, at the edges it is enhanced (Figs. 19.3 and 19.4). The transmission at midgap decreases $\propto (n_i/n_j)^{2N}$, where $n_i < n_j$.

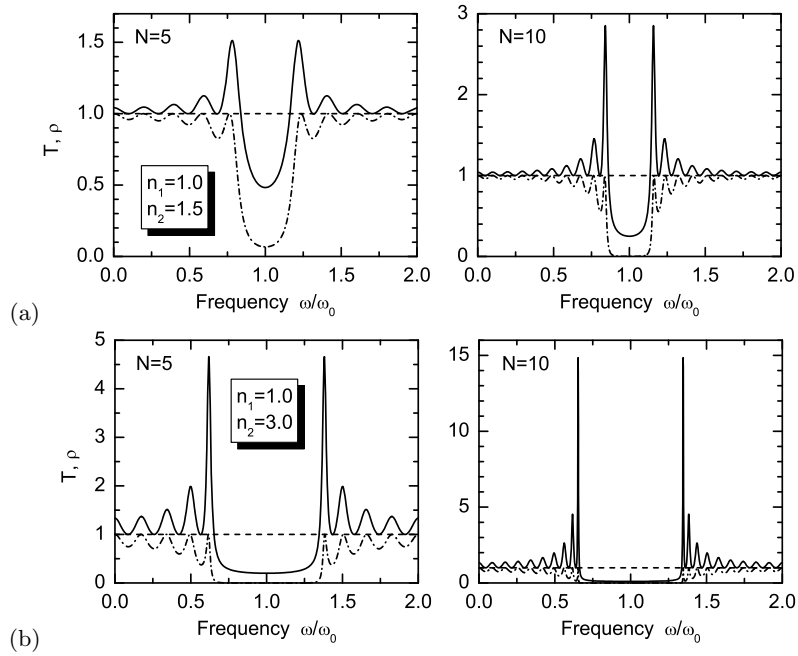

Fig. 19.3 Quarter-wave stack with indices of refraction **a** $n_1, n_2 = 1.0, 1.5$ and **b** 1.0, 3.0. *Solid lines*: dimensionless density of modes ρ_N (19.19), *dashed lines*: transmission T_N (19.28) for two different numbers of pairs $N = 5$ (*left panels*) and 10 (*right panels*) versus the dimensionless frequency $\tilde{\omega}$

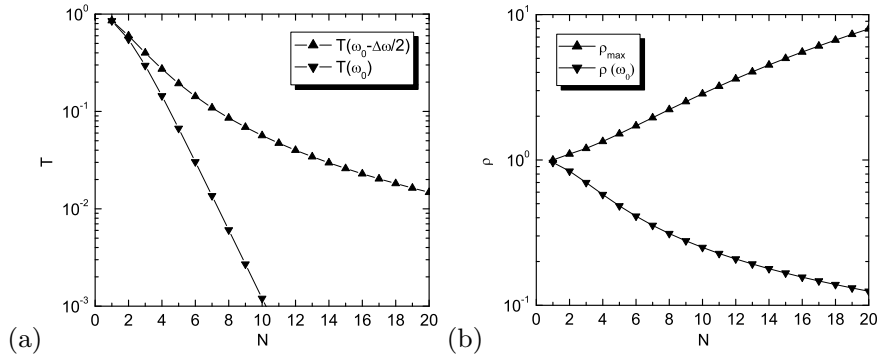

Fig. 19.4 Quarter-wave stack with indices of refraction $n_1, n_2 = 1.0, 1.5$: **a** Transmission T_N at midgap ($\tilde{\omega} = 1$, *down triangles*) and at the band edge ($\tilde{\omega} = 1 - \Delta\tilde{\omega}/2$, *up triangles*) versus number of pairs N. **b** Dimensionless density of modes ρ_N at maximum near the band edge and at midgap versus number of pairs N

In the limit of large N the complete width $\Delta\tilde{\omega}$ of the band gap is implicitly given by

$$\cos\left(\frac{\pi}{2}\,\Delta\tilde{\omega}\right) = 1 - 2\left(\frac{n_1 - n_2}{n_1 + n_2}\right)^2 . \tag{19.29}$$

If $|n_1 - n_2| \ll n_1 + n_2$, we find

$$\Delta\tilde{\omega} \approx \frac{4}{\pi}\,\frac{|n_1 - n_2|}{n_1 + n_2} . \tag{19.30}$$

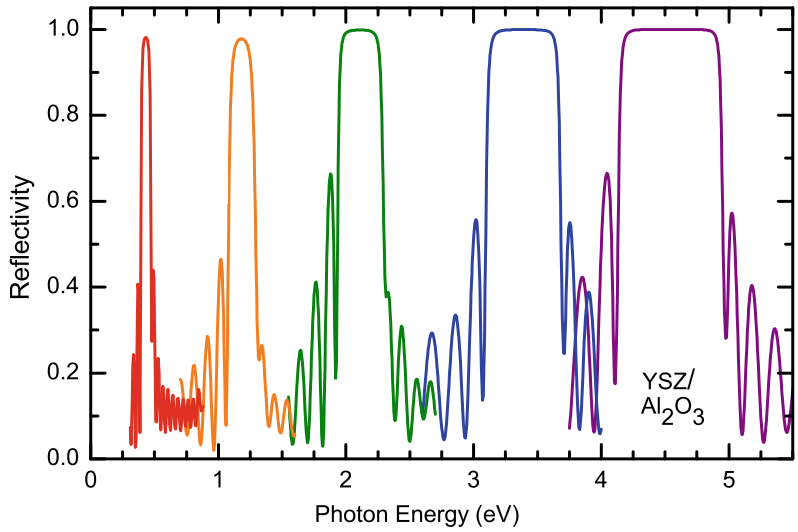

Fig. 19.5 Reflectance of various Bragg mirrors from YSZ/Al_2O_3 grown by pulsed laser deposition on sapphire. The different layer thicknesses result in the design energies 0.43 eV ($N = 10.5$, $R_{max} = 0.9812$, *red*), 1.19 eV ($N = 10.5$, $R_{max} = 0.9779$, *orange*), 2.11 eV ($N = 15.5$, $R_{max} = 0.99953$, *green*), 3.39 eV ($N = 15.5$, $R_{max} = 0.99946$, *blue*) and 4.54 eV ($N = 15.5$, $R_{max} = 0.99989$, *purple*)

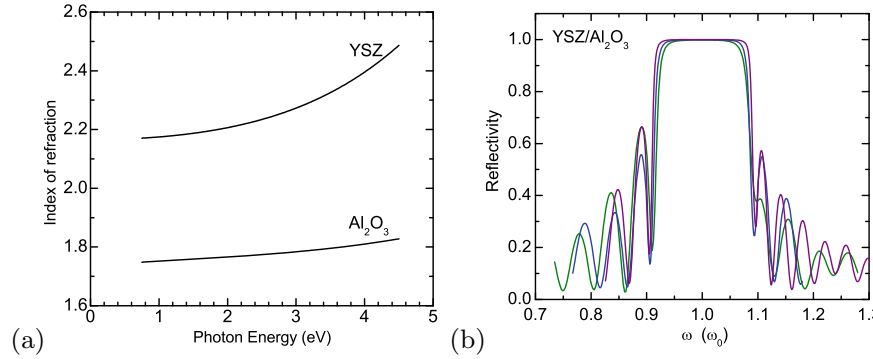

Fig. 19.6 **a** Index of refraction of YSZ and Al_2O_3 as a function of photon energy. **b** Reflectance spectra of the 2.11 eV (*green*), 3.39 eV (*blue*) and 4.54 eV (*purple*) Bragg mirrors of Fig. 19.5 replotted as a function of the scaled frequency $\tilde{\omega} = \omega/\omega_0$

The principle of the quarter-wave stack is scalable to frequencies other than visible light.[1] In Fig. 19.5 the reflectance of various quarter-wave stacks from yttria-stabilized zirconia (YSZ [1590], high index material, Fig. 19.6a) and Al_2O_3 are shown [1591]. The different design wavelengths have been achieved solely by varying the layer thicknesses.

In Fig. 19.6b the three Bragg mirrors from Fig. 19.5 with $N = 15.5$ pairs are replotted in relative frequency units $\tilde{\omega}$. The spectra look very similar; subtle differences in the width of the reflectance band are due to slightly larger index contrast at higher design energy (cmp. Fig. 19.6a). The width of the gap is approximately $\Delta\tilde{\omega} \approx 0.18$ in agreement with (19.30).

As further example, a Mo/Si Bragg mirror with a period of 6.7 nm is shown in Fig. 19.7. Such a mirror works in the extreme UV and is used for soft X-ray optics, possibly in advanced lithography

[1] This is a general property of Maxwell's equations which do not contain a specific length scale.

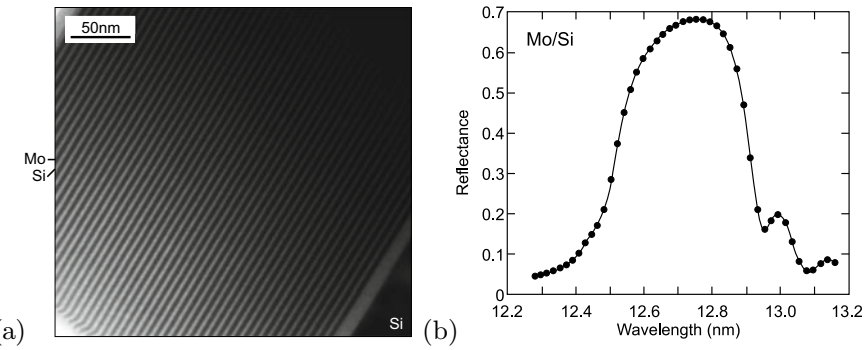

Fig. 19.7 **a** Cross-sectional TEM of Mo/Si superlattice with 2.7 nm Mo (*dark*) and 4.0 nm Si (*bright*) layers on Si(001) substrate. From [1592]. **b** Reflection spectrum for a SL with nominal period of 6.5 nm and 88.5° angle of incidence. Data points are shown as *circles*, the *solid line* is a fit with a period of 6.45 nm. Adapted from [1593]

systems. Dielectric thin films can also be designed for anti-reflection coatings, edge filters or pass and stop band filters as detailed in [1588].

19.1.5 Formation of a 3D Band Structure

For other applications, e.g. waveguides with minimized footprint, 3D (or at least 2D) photonic band gap structures are needed. Details can be found in dedicated textbooks [1594–1596]. In [1597] planar, cylindrical and spherical Bragg mirrors are discussed.

Since we want a photonic band gap that is present for *all* directions of propagation, a Brillouin zone with a shape close to a sphere is preferable. Then, the main directions are at similar k-values (Fig. 19.8). One of the best suited is the fcc lattice. Since the L-point is centered at ≈14% lower frequency than the X-point, the forbidden gaps for different directions must be, however, sufficiently wide to create a forbidden frequency band overlapping at all points along the surface of the Brillouin zone. For example, the bcc lattice has a Brillouin zone that is less symmetric than that of the fcc lattice (see Fig. 3.38) and thus is less suited for the creation of an omnidirectional photonic band gap. However, the photonic

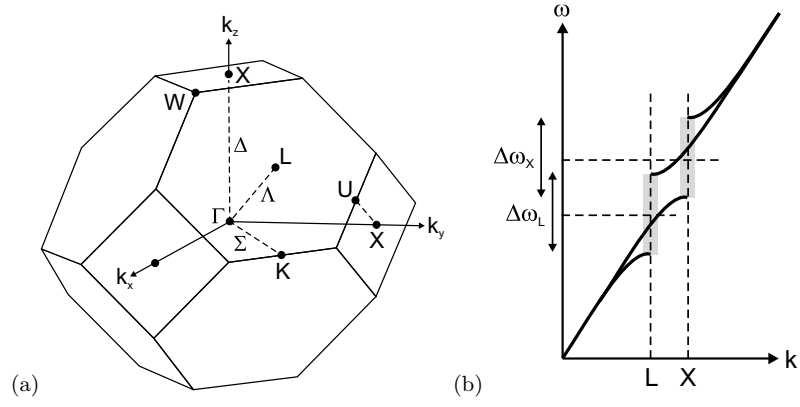

Fig. 19.8 **a** The Brillouin zone of the fcc lattice. **b** Schematic forbidden gaps at the L- and X-points

Table 19.1 Various photonic band gap structures and some of their properties. The band gap is between the n-th and $(n+1)$th band, $\Delta\tilde{\omega}$ is given for air/silicon ($\epsilon \approx 12$)

Name	Crystal type	n	$\Delta\tilde{\omega}$ (%)	Refs.
Diamond	diamond	2	29	[1598]
Yablonovite	fcc	2	19	[1602]
Woodpile	fc tetragonal	2	20	[1603]
Spirals	sc	4	17	[1604]
Square-spirals	tetragonal	4	24	[1599]
Layered 3D	bc orthorhombic	4	23	[1605]
Inverted scaffold	sc	5	7	[1606]
Inverse opal	fcc	8	4.25	[1607]
Inverse hcp	hcp	16	2.8	[1608]

band gap must not arise above the first band, relaxing problems due to asymmetry of the Brillouin zone (cf. Table 19.1).

Maxwell's equations (zero charge density) for monochromatic waves $\propto \exp(\mathrm{i}\omega t)$ (and isotropic dielectric function)

$$\nabla \cdot \mathbf{D} = 0 \tag{19.31}$$

$$\nabla \times \mathbf{E} = \mathrm{i}\,\frac{\mu\,\omega}{c}\,\mathbf{H} \tag{19.32}$$

$$\nabla \times \mathbf{H} = \mathrm{i}\,\frac{\omega}{c}\,\mathbf{D} \tag{19.33}$$

$$\nabla(\mu\,\mathbf{H}) = 0\,, \tag{19.34}$$

together with $\mathbf{D}(\mathbf{r}) = \epsilon(\mathbf{r})\,\mathbf{E}(\mathbf{r})$ and $\mu = 1$ they are combined into the wave equation

$$\nabla \times \left[\epsilon^{-1}(\omega, \mathbf{r})\,\nabla \times \mathbf{H}(\mathbf{r})\right] + \frac{\omega^2}{c^2}\,\mathbf{H}(\mathbf{r}) = 0\,. \tag{19.35}$$

This equation is numerically solved for planar waves with wavevector $\mathbf{k}$.

In the following, results are shown for various structures. In a fcc lattice of air spheres in a dielectric medium with $n = 3.6$ (a typical semiconductor), no band gap can be achieved (Fig. 19.9a), only a pseudogap (Fig. 19.9b) appears.

In a diamond lattice (imagine as two fcc lattices shifted by $1/4\ \langle 111\rangle$), a complete photonic band gap is possible [1598] (Fig. 19.10). Recently, a periodic array of spirals (Fig. 19.11) has been predicted to exhibit a large photonic band gap [1599]. Glancing-angle deposition [1600] (GLAD) is a way to realize such structures. Another method to fabricate structures with arbitrary geometry within a material is two-photon lithography or two-photon holography. Another path to PBG structures are so-called inverted opals. First, a close-packed structure of spheres, e.g. monodisperse silica spheres, is fabricated by sedimentation or self-assembly. The gaps are filled with a high-index medium and the template is subsequently removed, e.g. by etching or dissolving. The resulting structure is shown in Fig. 19.12a. Such a structure has a photonic band gap (Fig. 19.12b) if the refractive index is sufficiently high (> 2.85) [1601]. The band gap in this case is between the 4th and 5th band. Table 19.1 offers a compilation of various PBG structures and their properties.

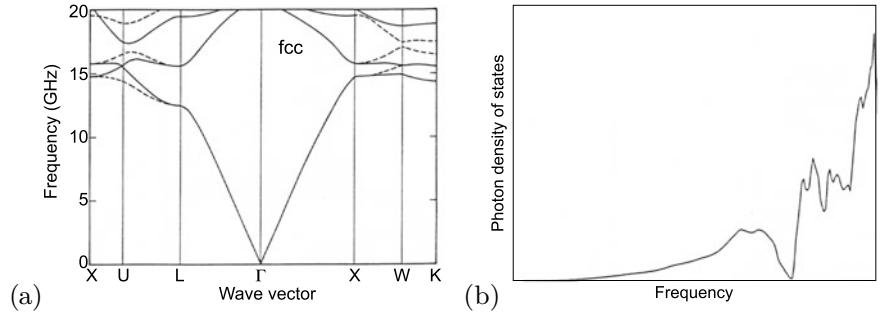

Fig. 19.9 **a** Calculated photonic band gap structure of a fcc dielectric structure composed of air spheres in a dielectric background of refractive index $n = 3.5$. The filling ratio is 86% air and 14% dielectric material. *Dotted* and *solid lines* represent coupling to s- and p-polarized light, respectively. **b** Density of states for the band structure of part (**a**). Reprinted from [1598] with permission, ©1990 APS

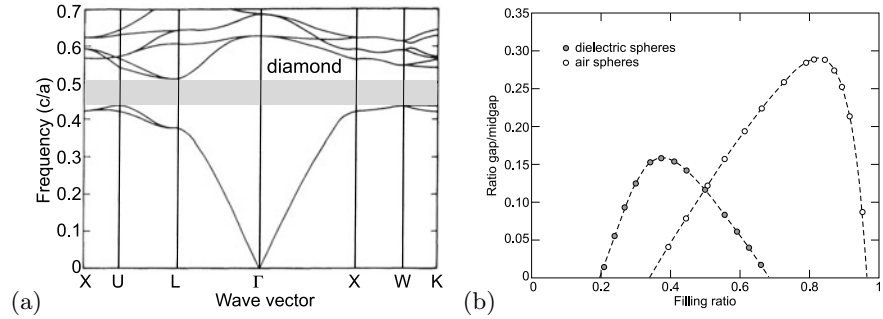

Fig. 19.10 **a** Calculated photonic band structure for a diamond dielectric structure consisting of overlapping air spheres in a dielectric material with $n = 3.6$. Filling ratio of air is 81%. The frequency is given in units of c/a, a being the cubic lattice constant of the diamond lattice and c being the velocity of light. The gap is indicated as *grayed rectangle*. **b** Gap-to-midgap frequency ratio for the diamond structure as a function of filling ratio for dielectric spheres $n = 3.6$ in air (*solid circles*) and air spheres in dielectric n (*open circles*). Optimal case: air spheres with 82% filling ratio. Adapted from [1598], reprinted with permission, ©1990 APS

19.1.6 Disorder

A real photonic band gap structure deviates from the ideal, perfectly periodic system by slight variations of the position and possibly also the size of the dielectric 'atoms'. This is schematically shown in Fig. 19.13a. The difference between the real and ideal structure is a (bipolar) spatial distribution of $\Delta\epsilon(\mathbf{r})$ which acts as a source of scattering and hence exponential attenuation of coherent beams propagating through photonic crystals over lengths l, named the '(extinction) mean free path'. After propagating over such distance l, a light beam is converted to a diffuse glow that corrupts the functionality of any photonic integrated circuit. Experimentally for opals a mean free path consistent with 5% fabrication accuracy has been found (Fig. 19.13b). For such disorder and a lattice constant $a \approx \lambda$, the mean free path is about only 10 wavelengths, $l \approx 10\lambda$.

19.1.7 Defect Modes

Similar to a perfect periodic atomic arrangement leading to the formation of the electronic band structure, a perfectly periodic dielectric structure leads to the photonic band structure. As we know

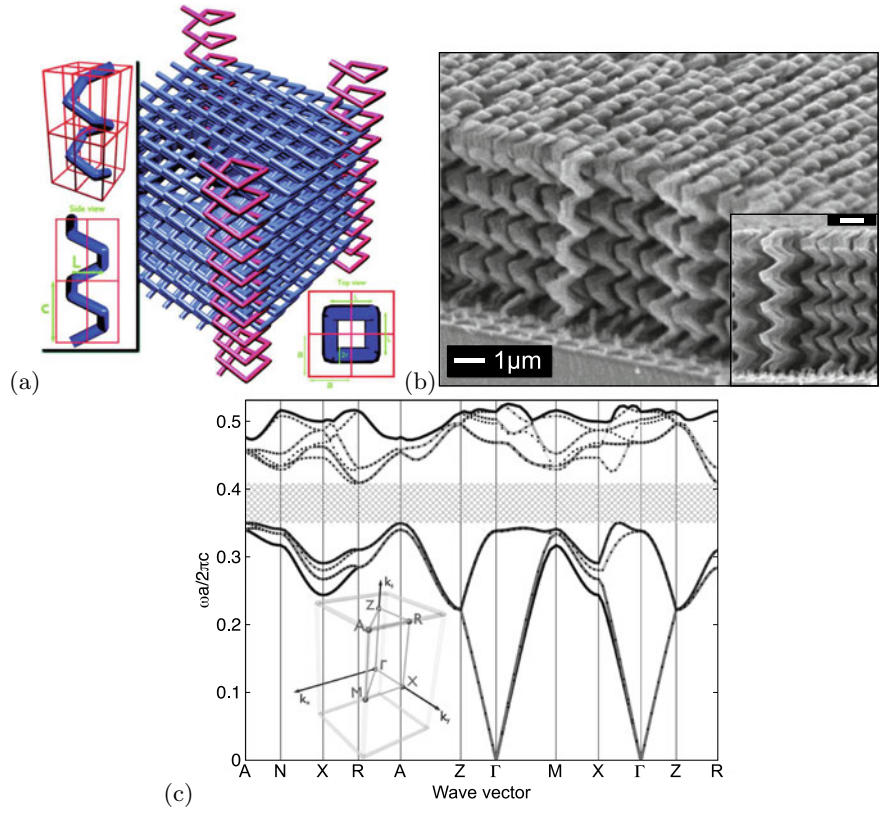

Fig. 19.11 **a** Tetragonal square-spiral photonic crystal. The crystal shown here has a solid filling fraction of 30%. For clarity, spirals at the corners of the crystal are highlighted with a different shade and height. The tetragonal lattice is characterized by lattice constants a and b. The geometry of the square spiral is illustrated in the *insets* and is characterized by its width, L, cylinder radius, r, and pitch, c. The *top left inset* shows a single spiral coiling around four unit cells. **b** Oblique and edge views of a tetragonal square spiral structure grown using the GLAD (glancing-angle deposition) process. Both markers are 1 μm. **c** Band structure for the direct structure crystal characterized by $[L,C,r]$=[1.6,1.2,0.14] and a spiral filling factor of 30%. The lengths are given in units of a, the lattice constant. The width of the PBG is 15.2% relative to the center frequency for background dielectric constant of 1 and spiral material dielectric constant of 11.9. The positions of high-symmetry points of the BZ are illustrated in the *inset*. Panel (**a**) reprinted and panel (**c**) adapted and reprinted from [1599], with permission, ©2001 AAAS. Panel (**b**) reprinted from [1600] with permission, ©2002 ACS

from semiconductor physics, much of the interesting physics and numerous applications lie in defect modes, i.e. localized electronic states due to doping and recombination at such centers. The equivalent in PBG structures are point defects (one unit missing) or line defects (a line of units, straight, bend or with sharp angles, missing). Such defects create localized states, i.e. regions for light localization. In the case of line defects we deal with waveguides that can be conveniently designed and could help to reduce the size of photonic and optoelectronic integrated circuits.

1D Model

We revisit our 1D scattering theory and create now a 'defect'. A simple defect is the change of the width of the center n_2-region in a quarter-wave stack. For the numerical example, we choose $N = 11$, $n_1 = 1, n_2 = 2$.

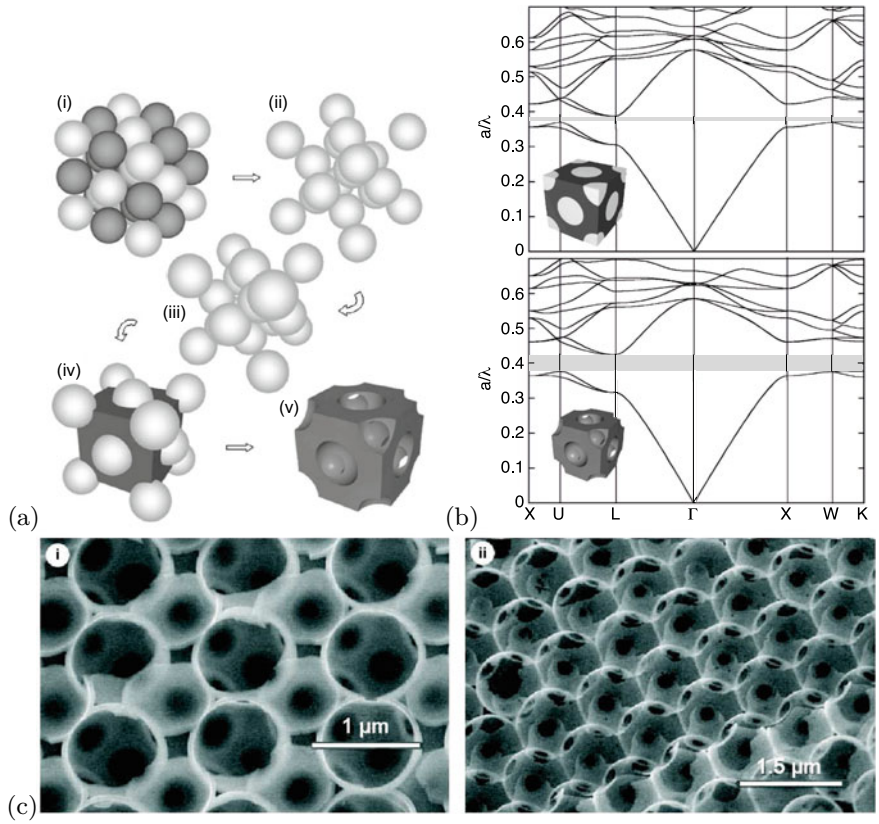

Fig. 19.12 **a** Cartoon showing, in five steps, the fabrication of an inverse diamond structure with a full photonic band gap. First, (i) a mixed body-centered cubic lattice is assembled (ii) after which the latex sublattice is removed; (iii) then the structure is sintered to a filling fraction of ∼50% after that (iv) silicon or germanium infiltration takes place and finally (v) silica elimination. **b** Photonic band diagrams of (upper panel) a silicon/silica composite diamond opal and (lower panel) made of air spheres in silicon resulting from the removal of the silica spheres from the former. The filling fraction for silicon is 50%. The inset shows the corresponding real space structures. Adapted from [1609], reprinted with permission, ©2001 AIP. **c** SEM images of internal facets of silicon inverse opal: (i) (110) facet, (ii) (111) facet. Adapted from [1610], reprinted with permission, ©2000, Springer Nature

In Fig. 19.14, the transmission curves are shown for the undisturbed quarter-wave stack and the microcavity with $n_2\, d_2^{\text{center}} = 2\lambda_0/4 = \lambda_0/2$. A highly transmissive mode at $\omega = \omega_0$ arises that is quite sharp with $\Delta\omega = 3 \times 10^{-4}$. Thus, the quality factor Q, also called the Q-factor or finesse,

$$Q = \frac{\omega_0}{\Delta\omega}\,, \tag{19.36}$$

with ω_0 being the resonance frequency and $\Delta\omega$ being the linewidth, is 3.3×10^3 in this case.

If the thickness is varied (Fig. 19.15), the mode shifts away from the center. A similar scenario arises for higher-order $n_l/2$-cavities, e.g. $n_2 d_2^{\text{center}} = 4\lambda_0/4 = \lambda_0$ (Fig. 19.16).

2D or 3D Defect Modes

An example of 2D waveguiding is shown in Fig. 19.17. Point defects can be used for high-finesse wavelength filtering. Emitters surrounded by a photonic band gap material with a defect mode can emit into the defect mode only, leading to spectrally filtered, highly directional emission.

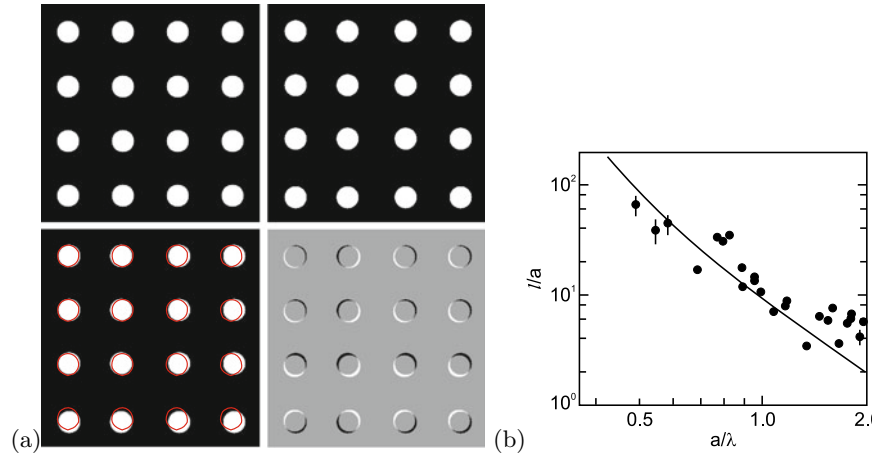

Fig. 19.13 **a** Schematic photonic band gap structure with perfect (*upper left*) and disordered (*upper right*) periodicity. In the *lower left* panel the disordered structure is overlayed with the ideal structure (*red circles*). In the *lower right* panel, the difference between ideal and disordered structure is shown. **b** Optical mean free path in an opal photonic band gap structure for various lattice constants. *Solid line* is theory for 5% fabrication accuracy. Adapted from [1611], reprinted with permission, ©2005 APS

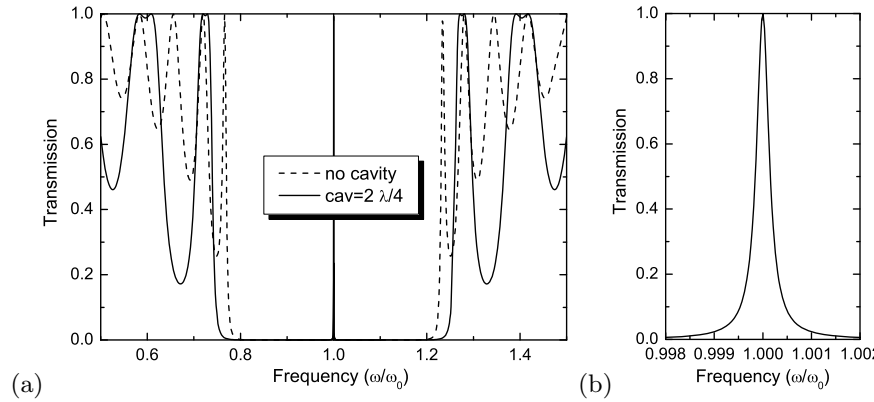

Fig. 19.14 Defect mode in 1D photonic band gap: **a** Transmission of $N = 11$ quarter-wave stack exhibiting a photonic band gap ($n_1 = 1, n_2 = 2$) (*dashed line*) and of microcavity (*solid line*) with center n_2-region of width $\lambda_0/2$ (instead of $\lambda_0/4$). **b** Relative width of mode is about 3×10^{-4}

19.1.8 Topological Photonic Band Structures

A review of two-dimensional topological photonics can be found in [1613]. The idea of topologically non-trivial 2D photonic band structures has been put forward in [1614] theoretically, employing a Faraday-effect medium breaking time-reversal symmetry. The system is a two-dimensional photonic crystals with an external magnetic field perpendicular to the plane of light propagation. A hexagonal array of dielectric cylindrical rods is modeled. The degeneracy of the Dirac points (at the K-points) is lifted by introducing the Faraday medium outside the rods. The bands close to the gap obtain non-zero Chern numbers $C_n = \pm 1$ (breaking inversion symmetry only creates a gap but does not lead to non-zero Chern number). Reversal of the magnetic field inverts the bands to $C_n = \mp 1$. The Berry curvature of the photonic bands plays a role analogous to that of the magnetic field in the QHE. The calculations show the existence of unidirectionally propagating photonic edge states between media with up and

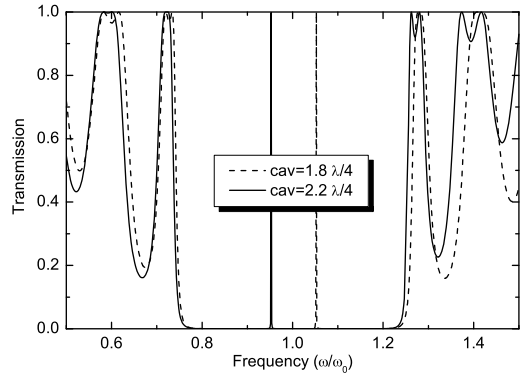

Fig. 19.15 Transmission of $N = 11$ quarter-wave stack ($n_1 = 1$, $n_2 = 2$) with center n_2-region of widths $1.8\,\lambda_0/4$ (*dashed line*) and $2.2\,\lambda_0/4$ (*solid line*)

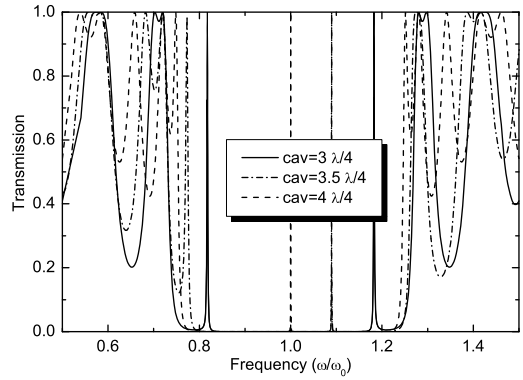

Fig. 19.16 Transmission of $N = 11$ quarter-wave stack ($n_1 = 1, n_2 = 2$) with center n_2-regions of widths $3\,\lambda_0/4$ (*solid line*), $3.5\,\lambda_0/4$ (*dash-dotted line*) and $4\,\lambda_0/4$ (*dashed line*)

down magnetic fields. An experimental system similar to this is based on yttrium iron garnet (YIG) as gyrotropic material for breaking time reversal symmetry and exhibits topological edge modes [1615].

A non-magnetic version which is much more desirable in terms of fabrication and choice of materials is based on the idea of the Haldane model put forward in [1616]. A next-nearest neighbor coupling t' in the honeycomb lattice is considered and produces topological states if the phase ϕ' of the (complex) hopping parameter t' is not zero or π. Further theoretical considerations and modeling of such non-magnetic, fully dielectric topological resonators were reported in [1617, 1618]. Such resonators have been realized and investigated in [1619]. The system consists of a square lattice of ring resonators, which are coupled to each other through link rings. These intermediary links are spatially shifted with respect to the ring resonators, to introduce an asymmetric set of hopping phases controlling whether the structure results in topologically trivial $\phi' = 0$ or non-trivial $\phi' = \pi/2$ situation. Lasing in edge modes and light transport at the circumference of a 10×10 field of resonators have been demonstrated [1619].

A similar concept, also playing with the different hopping parameters to create topologically trivial and non-trivial two-dimensional photonic band structures has been reported in [1620] (Fig. 19.18). The dipole (odd parity) and quadrupole (even parity) character of the states changes (does not change) within a band for the topologically non-trivial (trivial) parts. The optically pumped laser emission stems from the topologically non-trivial 2D bulk area [1620]. This is attributed to the fact that the band-inversion around the Γ point leads to a topology-induced mode selection with lower threshold,

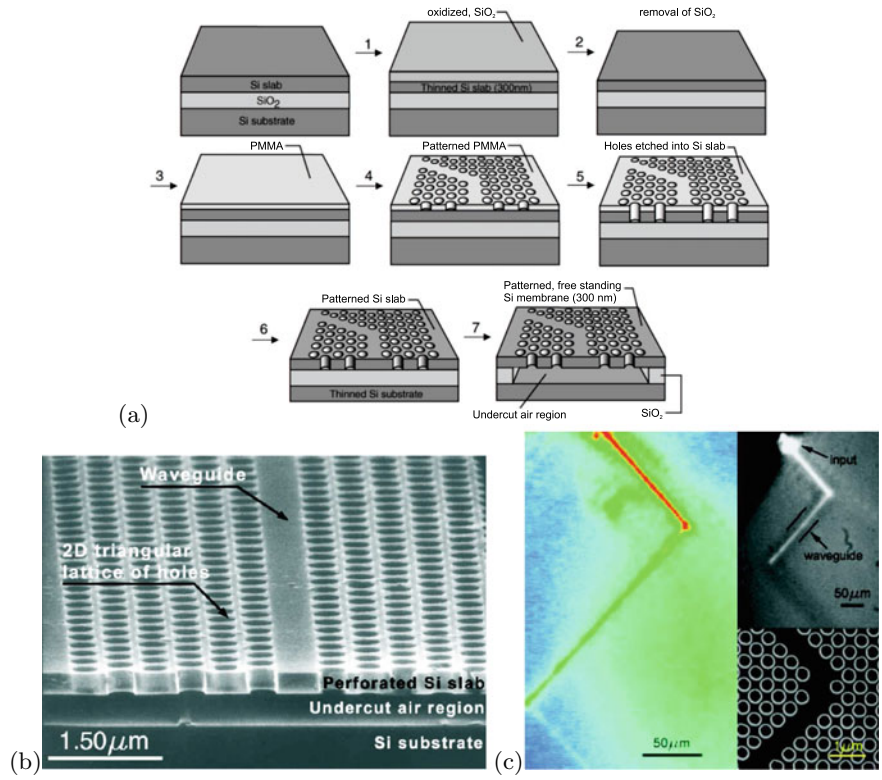

Fig. 19.17 2D photonic band gap waveguide structure. **a** Fabrication principle, **b** SEM image of the structure, **c** light guiding at a 90° bend. Reprinted with permission from [1612], ©2000 AIP

due to limitation of the number of cavity modes with efficient confinement; also the mode closer to the band edge has a higher quality factor.

19.1.9 Coupling to an Electronic Resonance

In a vertical-cavity surface-emitting laser (cf. Sect. 23.4.14), an optical defect mode in a 1D dielectric structure is coupled to an electronic excitation, such as an exciton in a quantum well or dot. In the simplest picture, the oscillator must emit its radiation into the cavity mode since other modes do not exist in the Bragg band. Thus, the emission energy is given and fixed by the cavity mode. However, the photon mode (field oscillator) and the electronic oscillator form a coupled system that generally must be described using quantum electrodynamics. Energy is periodically exchanged between the two oscillators with the Rabi frequency. An analogous phenomenon is investigated in the field of atom–cavity interactions. A necessary condition for the observation of such an oscillation is that the radiation energy remains long enough in the cavity that can be expressed as [1621, 1622] (cf. (19.42))

$$\alpha\, d \gg 1 - R \approx \pi/Q \;, \tag{19.37}$$

where α is the absorption coefficient of the electronic transition, d is the length of the absorbing medium, R is the reflectance of the cavity mirror and Q is the finesse of the cavity given in (19.36).

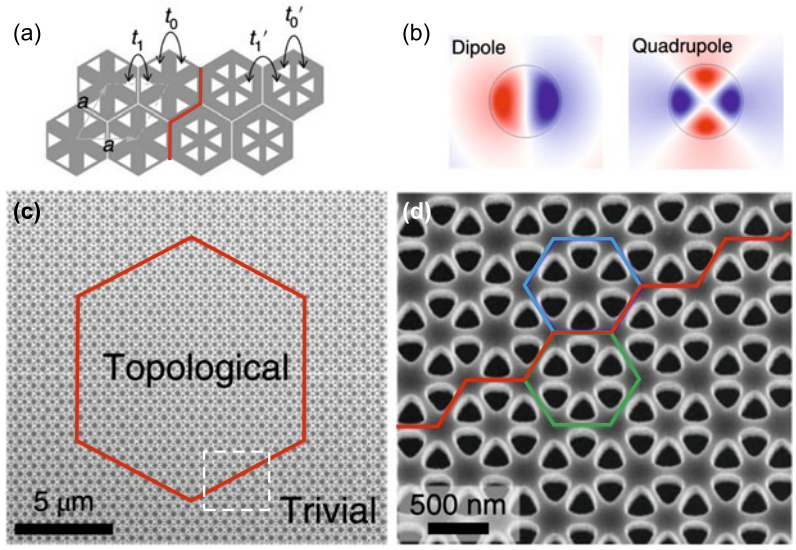

Fig. 19.18 **a** Schematic different hopping parameters for hexagonal dielectric structures with different aspect ratios of medium and air. The boundary between the two parts is highlighted in *red*. **b** Visualization of the odd (even) parity dipole (quadrupole) mode. **c** SEM image of the structure with the boundary between topologically trivial and non-trivial parts highlighted in *red*. A magnified view of the area indicated with the *dashed white rectangle* is depicted in panel **d**. A topologically trivial (non-trivial) hexagon is highlighted in *green* (*blue*). Adapted from [1620]

This situation is called the *strong coupling* regime since it leads to anticrossing behavior of the cavity mode and electronic resonance. In the *weak coupling* regime for small absorption, the resonances cross (within their linewidth). For resonance, the emission intensity of the oscillator into the cavity mode is enhanced and its lifetime is reduced (Purcell effect, cf. Sect. 19.2.2).

The transmission T of a Fabry–Perot cavity with two (equal and lossless) mirrors of transmission $T_\mathrm{m} = 1 - R_\mathrm{m}$ is given by

$$T(\omega) = \frac{T_\mathrm{m}^2 \, \exp\left(-2\,L\,\alpha(\omega)\right)}{|1 - R_\mathrm{m} \, \exp\left(\mathrm{i}\,2\,n^*\,L\,\omega/c\right)|^2} \,, \tag{19.38}$$

with the complex index of refraction $n^* = n_\mathrm{r} + \mathrm{i}\kappa = \sqrt{\epsilon}$ and $\alpha = 2\omega\kappa/c$ (cf. (9.9)). For an empty cavity, i.e. a (small) background absorption α_B and a background index of refraction $n_\mathrm{r} = n_\mathrm{B}$, the resonances occur when the phase shift $2n_\mathrm{B}L\omega/c$ is an integer multiple of 2π, i.e. for

$$\omega_\mathrm{m} = m \, \frac{\pi \, c}{n_\mathrm{B} \, L} \,, \tag{19.39}$$

with $m \geq 1$ being a natural number. In the vicinity of the resonance, i.e. for $\omega = \omega_\mathrm{m} + \delta\omega$, we can expand $\exp(2n_\mathrm{B}L\omega/c) \approx 1 + \mathrm{i}2n_\mathrm{B}L\delta\omega/c$ and obtain from (19.38) a Lorentzian for the transmission

$$T(\omega) \approx \frac{T_\mathrm{m}^2 \exp\left(-2L\alpha(\omega)\right)}{|1 - R_\mathrm{m}(1 + \mathrm{i}2n_\mathrm{B}L\,\delta\omega/c)|^2} = \frac{(T_\mathrm{m}/R_\mathrm{m})^2 \exp\left(2L\alpha(\omega)\right)}{(\delta\omega)^2 + \gamma_\mathrm{c}^2} \,. \tag{19.40}$$

The frequency width (HWHM) γ_c of the empty-cavity resonance is given by

$$\gamma_\mathrm{c} = \frac{1 - R'}{R'} \, \frac{c}{2\,n_\mathrm{B}\,L} \,, \tag{19.41}$$

where $R' = R_\mathrm{m} \exp(-2L\alpha)$. Thus, the decay rate (photon loss from the cavity) is proportional to $T_\mathrm{m} + \alpha_\mathrm{B} L$ if both terms are small. The quality factor of the cavity resonance m is given by

$$Q = \frac{\omega_\mathrm{m}}{2\,\gamma_\mathrm{c}} \approx \frac{m\,\pi}{1-R} \,. \tag{19.42}$$

Now, the electronic resonance is put into the cavity leading to a change in the dielectric function to (cf. (D.11))

$$\epsilon = n_\mathrm{B}^2 \left[1 + \frac{f}{1 - (\omega^2 + \mathrm{i}\omega\Gamma)/\omega_0^2} \right] \,, \tag{19.43}$$

where the index of refraction due to the electronic resonance is given by $n(\omega) = \sqrt{\epsilon}$ and (D.13a,b). For resonance of the cavity mode and the electronic oscillator, i.e. $\omega_\mathrm{m} = \omega_0$, the solution for the cavity resonance condition $2n_\mathrm{r}\omega L/c = m2\pi$ is obtained, using (19.39), from

$$n_\mathrm{r}(\omega) = m\,\frac{\pi\,c}{\omega\,L} = n_\mathrm{B}\,\frac{\omega_\mathrm{m}}{\omega} \,. \tag{19.44}$$

A graphical solution (Fig. 19.19a) yields three intersections of the left and right hands of (19.44). The very high absorption at the central solution ($\omega = \omega_0$) results in very low transmission. The other two solutions[2] yield the frequencies of the coupled normal mode peaks. For $f \ll 1$, we use (D.13a) in (19.44) and find for the splitting $\pm\Omega_0/2$ of the two modes

$$\Omega_0^2 = f\,\omega_0^2 - \Gamma^2 \,. \tag{19.45}$$

This frequency is called the Rabi frequency. If the dielectric function of the oscillator is put into (19.38), the splitting is found to be

$$\Omega_0^2 = f\,\omega_0^2 - (\Gamma - \gamma_\mathrm{c})^2 \,. \tag{19.46}$$

A splitting will only be observable if $\Omega_0 \gg \Gamma, \gamma_\mathrm{c}$. If the two resonances ω_c and ω_0 are detuned by $\Delta = \omega_\mathrm{c} - \omega_0$, the splitting Ω of the transmission peaks shows the typical anticrossing behavior of two coupled oscillators

$$\Omega^2 = \Omega_0^2 + \Delta^2 \,. \tag{19.47}$$

In the experiment, typically the electronic resonance remains fixed at ω_0 and the cavity resonance is detuned by variation of the cavity length across the wafer (Fig. 19.19b).

A detailed theory of cavity polaritons is given in [1623]. The nonlinear optics of normal mode coupling in semiconductor microcavities is reviewed in [1624].

The in-plane dispersion of the cavity polaritons depends on the coupling strength. First, the photon dispersion is given by

$$E_\mathrm{ph}(\mathbf{k}) = \hbar\,\omega = \hbar\,c\,k = \hbar\,c\,\left(k_\parallel^2 + k_z^2\right)^{1/2} \,, \tag{19.48}$$

where $k_\parallel$ is the in-plane k-vector and k_z is given by the resonance condition, $k_z = \omega_m/c$ with (19.39),

$$k_z = m\,\frac{\pi}{n_\mathrm{B}\,L} \,. \tag{19.49}$$

Thus the dispersion relation is no longer linear as for freely propagating light.

[2] These solutions only occur for sufficient oscillator strength $f > (\Gamma/\omega_0)^2$, i.e. in the strong coupling regime where $\Omega_0^2 > 0$. The absorption coefficient at ω_0 must be larger than $\Gamma n_\infty/c$.

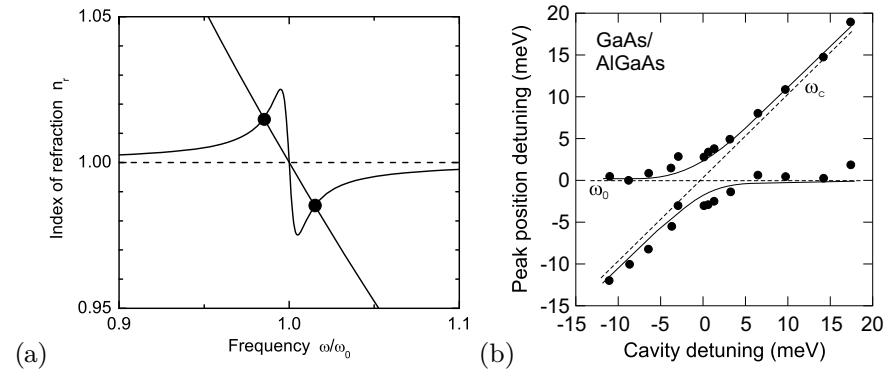

Fig. 19.19 **a** Graphical representation of (19.44) with the two solutions marked with *circles* for $n_\infty = 1$ (*dashed line*), $f = 10^{-3}$, $\Gamma/\omega_0 = 10^{-2}$ and $\omega_0 = \omega_m$. **b** Reflectance peak positions (experimental data (*circles*) at $T = 5\,\mathrm{K}$) versus cavity detuning $\omega_c - \omega_0$ for a cavity with two GaAs/(Al,Ga)As Bragg mirrors (24/33 pairs for the front/bottom mirror) and five embedded quantum wells whose resonances are closely matched. *Solid lines* are a theoretical fit according to (19.47) with $\Omega_0 = 4.3\,\mathrm{meV}$. The *dashed lines* show the electronic resonance ω_0 and the cavity resonance ω_c. Part (**b**) based on data from [1622]

For small $k_\parallel$ this leads to an (in-plane) effective photon 'rest mass', applying (6.38),

$$\frac{1}{m^*_{\mathrm{ph}}} = \frac{1}{\hbar^2}\,\frac{\partial^2 E_{\mathrm{ph}}}{\partial k^2}\ . \tag{19.50}$$

We find

$$m^*_{\mathrm{ph}} = \frac{\hbar k_z}{c} = \frac{\hbar\,\omega(k_\parallel = 0)}{c^2}\ . \tag{19.51}$$

Now we assume the electronic oscillator to be in resonance with the photon dispersion at $k_\parallel = 0$, i.e. $E_{\mathrm{el}} = \hbar\omega(k_\parallel = 0)$. The electronic resonance shall have vanishing dispersion for simplicity since the exciton mass is much larger than (19.51). The eigenwert equation of the coupled system, resembling (6.61), is

$$\begin{vmatrix} E - E_{\mathrm{ph}} & V \\ V & E - E_{\mathrm{el}} \end{vmatrix} = 0\ , \tag{19.52}$$

with two solutions, called the upper and lower cavity polariton branch, visualized in Fig. 19.20. Their splitting at $k_\parallel = 0$ is $2V$. Thus the coupling parameter $V = \hbar\Omega_0/2$ corresponds [1623] to the Rabi frequency (19.45). Experimental values for the splitting of 3–15meV in (In,Al,Ga)As based [1622, 1625–1628], 17–44meV in (Cd,Zn)(Te,Se) based [1629], 6–60meV in (Al,In,Ga)N based [1630–1634] and 78 meV in ZnO based [1635] microcavities were found. It is possible to condensate cavity polaritons in the minimum of the dispersion around $k_\parallel = 0$ (Bose-Einstein condensation). In [1636] stimulated scattering and gain from cavity polaritons have been reported. Further details on cavity polaritons can be found in [1637, 1638].

19.1.10 Hyperbolic Optical Metamaterials

A special class of uniaxial materials, termed hyperbolic metamaterials (HMM), has a (relative) dielectric function of the form (cf. Table 9.2)

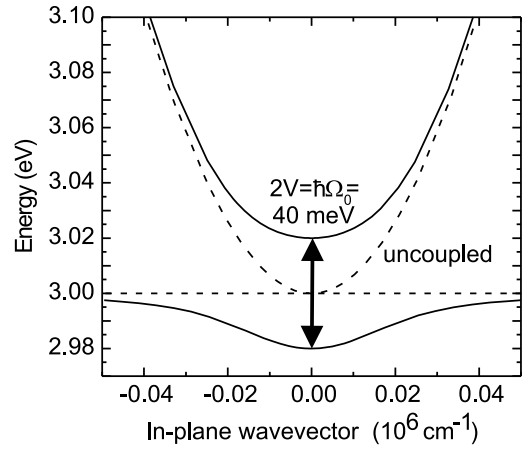

Fig. 19.20 Dispersion of cavity photon mode and electronic resonance at $E_{\mathrm{el}} = 3.0\,\mathrm{eV}$ (*dashed lines*) and coupled modes (*solid lines*) for $2V = 40\,\mathrm{meV}$

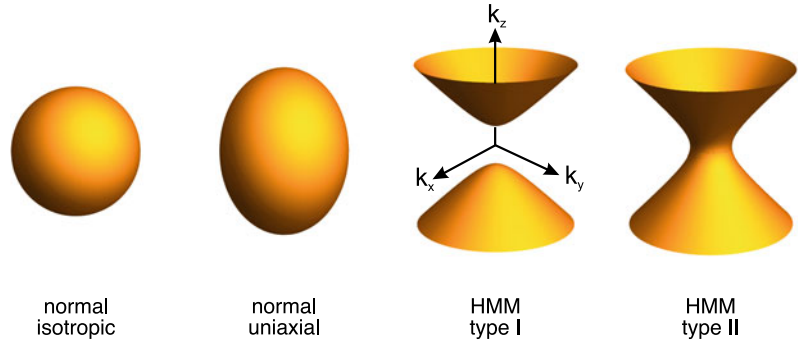

Fig. 19.21 Equifrequency surfaces (19.54) for a 'normal' isotropic ($\epsilon_\parallel = \epsilon_\perp > 0$) and uniaxial ($\epsilon_\parallel > 0, \epsilon_\perp > 0$, here shown for $\epsilon_\perp > \epsilon_\parallel$) optical medium and type I ($\epsilon_\parallel < 0$, $\epsilon_\perp > 0$) and type II ($\epsilon_\parallel > 0, \epsilon_\perp < 0$) hyberbolic metamaterials

$$\boldsymbol{\epsilon} = \begin{pmatrix} \epsilon_\parallel & 0 & 0 \\ 0 & \epsilon_\parallel & 0 \\ 0 & 0 & \epsilon_\perp \end{pmatrix} \tag{19.53}$$

with $\epsilon_\parallel \epsilon_\perp < 0$. A negative dielectric function is known from metals below the plasma frequency (cf. Sect. 9.9.1). From the conventional formula $\omega^2 = \boldsymbol{k}^2 c^2 / n^2$ in a isotropic medium, in an uniaxial medium the isofrequency surface is given by

$$\frac{\omega^2}{c^2} = \frac{k_x^2 + k_y^2}{\epsilon_\parallel} + \frac{k_z^2}{\epsilon_\perp} \tag{19.54}$$

and for 'normal' uniaxial materials an ellipsoid (or a sphere for isotropic materials, cmp. to band dispersions Fig. 6.35a, b). If one of the tensor elements is negative, two possible types of 'hyperbolic' metamaterials develop with $\epsilon_\parallel < 0$ (HMM type I) and with $\epsilon_\perp < 0$ (HMM type II). Their isofrequency surfaces (for TM waves) for the two types are depicted in Fig. 19.21.

Apart from homogeneous media, various geometries for HMM have been proposed and investigated [1639, 1640]. HMM can transport high-k waves and may enable devices for sub-wavelength resolution imaging. Also, the enhanced density of photonic states (within a restricted wavelength range) can be used for enhancement of spontaneous recombination rates (Purcell effect, cf. Sect. 19.2.2) [1641]. A possible epitaxial, almost perfectly lattice matched superlattice HMM system of alternating dielectric and metallic materials is MgO/TiN [1642]. Also HMM involving the anisotropic magnetic permittivity tensor have been considered [1643].

19.2 Microscopic Resonators

19.2.1 Microdiscs

A microdisc is a cylindrical resonator with a thickness d that is small compared to the radius R. It can be fabricated from semiconductors and semiconductor heterostructures using patterning and material-selective etching. With underetching a mostly free-standing disc can be made that resides on a post (Fig. 19.22).

The coordinate system is (ρ, ϕ, z) with the z direction being perpendicular to the disc area. Typically, the disc is so thin that there is only one node along z. Solving the wave equation in this geometry [1645], the modes are characterized by two numbers (m, l). m describes the number of zeros along the azimuthal direction ϕ with the field amplitude being proportional to $\exp(\pm im\phi)$. Thus, except for $m = 0$, the modes are simply degenerate. Modes with $E_z = 0$ are called TE modes. This is the preferred polarization of emission. The number l denotes the number of zeros in the radial direction. Only for modes with $|m| = 1$, is the intensity nonzero on the axis, i.e. for $\rho = 0$. All other modes have vanishing intensity in the disc center.

The light intensity in whispering gallery modes is preferentially concentrated along the circumference of the disc as shown in Fig. 19.23a. Since the light can only escape via evanescent waves, the light is well 'captured' in such a mode. The Q-factor (19.36) is extremely high and takes values of several

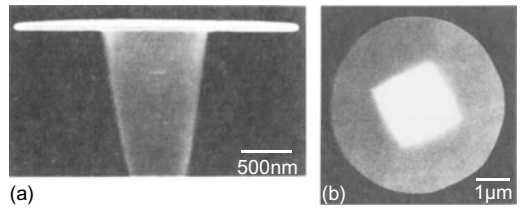

Fig. 19.22 **a** Side view of a 3-μm diameter disc containing one 10-nm InGaAs quantum well between 20-nm (In,Ga)(As,P) barriers standing on an InP pillar that has been selectively underetched using HCl. **b** Top view SEM image of a 5-μm diameter (In,Ga) (As,P) microdisc. The pedestal shape is a rhombus due to anisotropic etching of the HCl. Adapted from [1644], reprinted with permission, ©1992 AIP

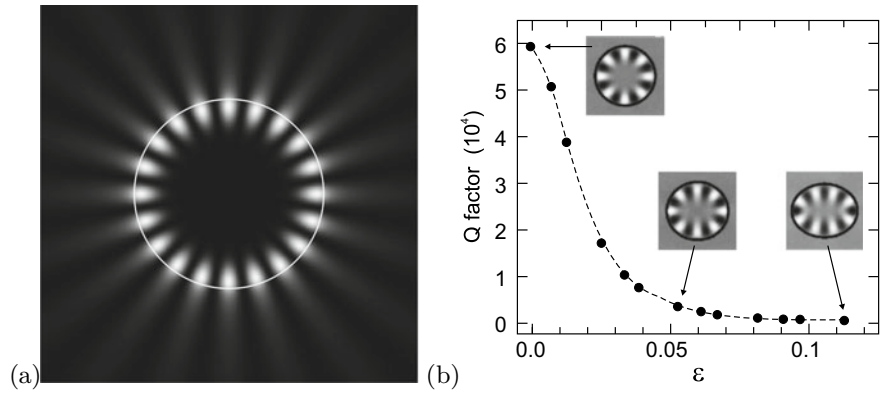

Fig. 19.23 **a** Field intensity for whispering gallery mode (10, 0) (TM-polarized) for a circle with 1 μm radius (shown as *white line*) and $n = 1.5$. The image size is $4 \times 4\,\mu m^2$. **b** Theoretical quality factor of a 2-μm InP microdisc as a function of the deformation parameter (19.56). The *insets* show (8,0) whispering gallery modes at a wavelength of 1.55 μm for $n = 3.4$. Part (**b**) adapted from [1647]

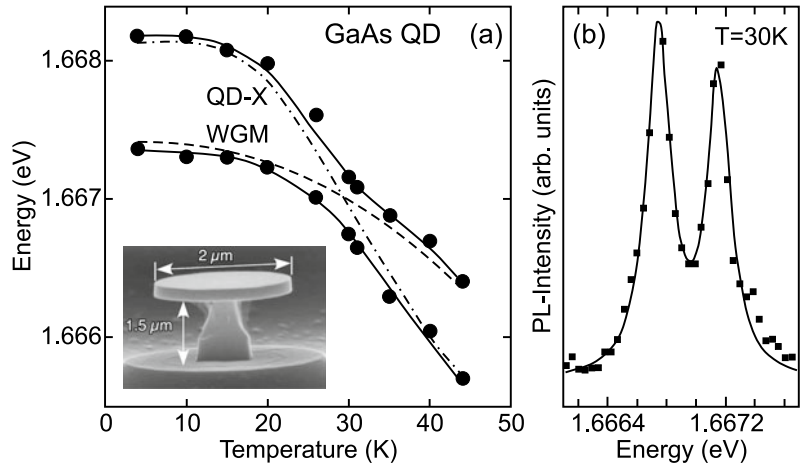

Fig. 19.24 Strong coupling of a single QD exciton (due to monolayer fluctuation in a 13 ML thick GaAs/$Al_{0.33}Ga_{0.67}As$ QW) with a WGM in a microdisk of 2 μm diameter (*inset*). (**a**) Anti-crossing of upper and lower peak for various temperatures. *Symbols* are data points, *solid lines* are theory considering coupling. The *dashed* (*dash-dotted*) line is the expected temperature shift of the WGM mode (exciton energy). (**b**) Photoluminescence spectrum at the anti-crossing point ($T = 30$ K). Experimental data (*squares*) and fit with two peaks (*solid line*). Adapted from [1648]

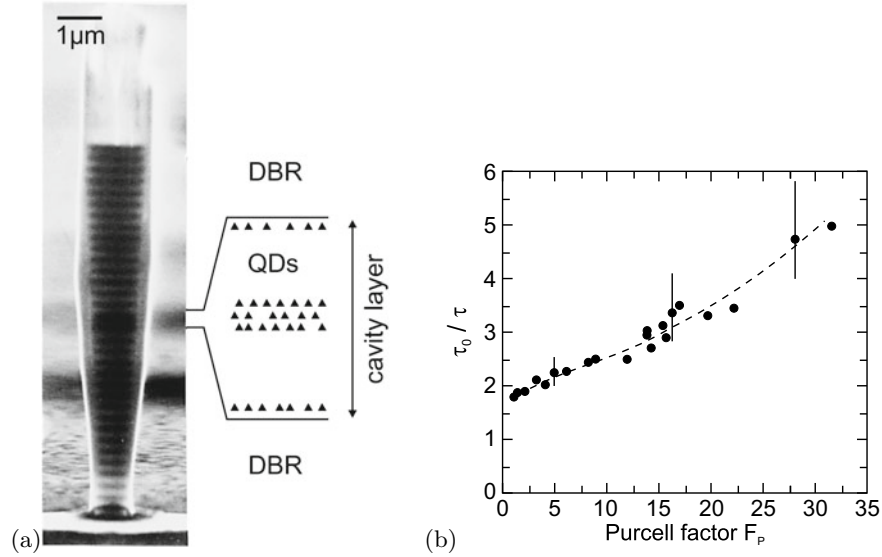

Fig. 19.25 **a** Micropillar with MBE-grown GaAs/AlAs DBRs and a cavity containing five layers of InAs quantum dots as indicated. The pillar has been prepared by reactive ion etching. Reprinted with permission from [1650], ©1998 APS. **b** Experimental decay time τ of on-resonance quantum dot luminescence scaled by off-resonance lifetime $\tau_0 = 1.1$ ns (close to lifetime in a QD in bulk) for a variety of micropillars with different Purcell factors F_P. The *error bars* correspond to the measurement accuracy of the decay time (±70 ps), the *dashed line* is a guide to the eye. Adapted from [1650]

10^4. In order to couple light out of such a disc, deformed resonators, e.g. with a defect in the form of protrusions [1646], were devised. Deformed resonators are discussed in more detail in the next section.

The strong coupling of a QD exciton to a whispering gallery mode is shown in Fig. 19.24 where anti-crossing behavior is observed at low temperatures. Tuning is achieved by temperature variation. Behavior of a similar system in the weak coupling regime is shown in Fig. 19.26.

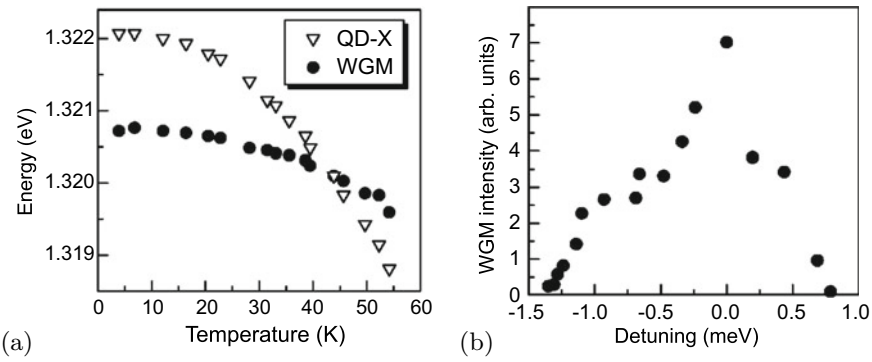

Fig. 19.26 **a** Temperature dependence of the energy positions of the whispering gallery mode (WGM) of a 5-μm diameter (Al,Ga)As/GaAs microdisc ($Q = 6500$) and the single-exciton resonance of a single InAs quantum dot contained within the disc. **b** Intensity of WGM mode as a function of the detuning $E_{\mathrm{WGM}} - E_{\mathrm{QD-X}}$ from the QD single exciton resonance. The excitation density was $15\,\mathrm{Wcm}^{-2}$ for all data. Adapted from [1651]

19.2.2 Purcell Effect

According to Fermi's golden rule (19.1), the probability of an optical transition depends on the density of available optical modes (final states). If the density of modes is enhanced compared to its vacuum value (19.2) at a resonance of an optical cavity, the lifetime of the electronic state decreases by the Purcell factor [1649],

$$F_{\mathrm{P}} = \frac{3}{4\pi^2}\, Q\, \frac{(\lambda/n)^3}{V}\ , \tag{19.55}$$

where n is the refractive index of the medium, Q is the quality factor of the cavity resonance and V is the effective mode volume.[3] Experiments on the emission of quantum dots (that generally provide small absorption and thus allow for the weak coupling regime) in etched micropillars containing a microcavity (Fig. 19.25a) have shown that indeed the luminescence decay is faster for cavities with large Purcell factor (Fig. 19.25b) [1650]. The resonance of cavity mode and emitter leads to an enhanced emission intensity as shown in Fig. 19.26 for the exciton emission of a single quantum dot in a microdisc [1651].

19.2.3 Deformed Resonators

The whispering gallery modes in circular (or spherical) cavities are long-lived and emission goes into all angles. Light escape is based only on the exponentially slow process of evanescent leakage (neglecting disorder effects such as surface roughness). In order to overcome the isotropic light emission, the resonator needs to be deformed. This can be accomplished with an ellipsoidal shape, i.e.

$$r(\phi) = R\ [1 + \epsilon\ \cos\phi]\ , \tag{19.56}$$

where $1+2\epsilon$ is the aspect ratio of the ellipse. The increased radiation leads to a decrease of the Q-factor as shown in Fig. 19.23b. Also, a new decay process, refractive escape, becomes possible. A ray that is initially in a whispering gallery trajectory diffuses in phase space until finally an angle smaller than the critical angle for total reflection (9.11) is reached. The ray dynamics becomes partially chaotic [1652].

[3] V is given by the spatial integral of the vacuum field intensity for the cavity mode, divided by its maximum value.

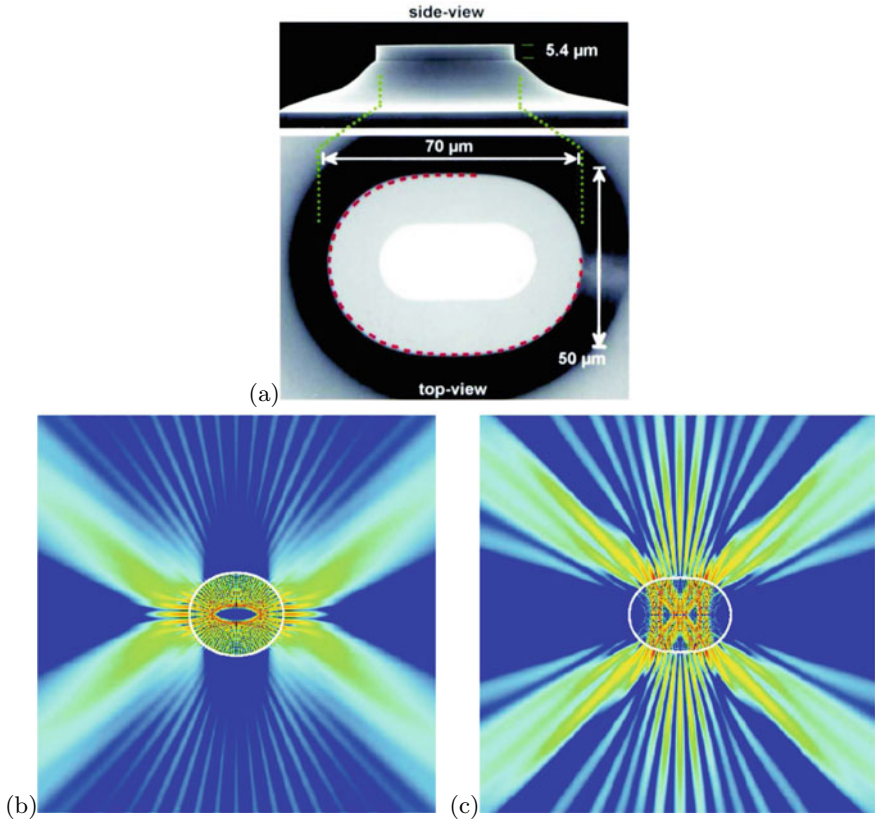

Fig. 19.27 **a** SEM image of a quadrupolar cylinder laser with deformation parameter $\epsilon \approx 0.16$ on a sloped InP pedestal. The *light grey area* in the top view is the electrical contact. **b** Simulated near-field intensity pattern of a chaotic whispering gallery mode for $\epsilon = 0.06$ and $n = 3.3$. **c** Simulated near-field intensity pattern of a bow-tie mode for $\epsilon = 0.15$. The length of the minor axis for (**b**) and (**c**) is 50 µm. Reprinted with permission from [1653], ©1998 AAAS

One other possible deformation of the circular disc geometry is a 'flattened quadrupole' as shown in Fig. 19.27a. This shape can be parameterized by a deformation parameter ϵ and the angle-dependent radius $r(\phi)$ given by

$$r(\phi) = R\left[1 + 2\epsilon\,\cos^2(2\phi)\right]^{1/2} . \tag{19.57}$$

For small deformation, the whispering gallery modes become chaotic and exhibit preferred emission along the long axis of the resonator (Fig. 19.27b). For larger deformations ($\epsilon \geq 0.14$), a stronger and qualitatively different directionality occurs in the shape of a bow-tie [1653] as shown in Fig. 19.27c. The optical laser power extracted from deformed resonators was found to increase exponentially with ϵ; for $\epsilon = 0.2$ it was 50 times larger than for the circular resonator.

Another modification that can be applied to the microdisc in order to increase outcoupling of light, is the spiral resonator [1654] as shown in Fig. 19.28a. The radius is parameterized by

$$r(\phi) = R\left[1 + \frac{\epsilon}{2\pi}\,\phi\right] . \tag{19.58}$$

The experimental emission pattern is displayed in Fig. 19.28b. It exhibits a maximum along the direction of the tangent at the radius step. The simulated near-field intensity of such an emission mode is shown in Fig. 19.28c. In a spiral laser, ray dynamics is also chaotic [1655].

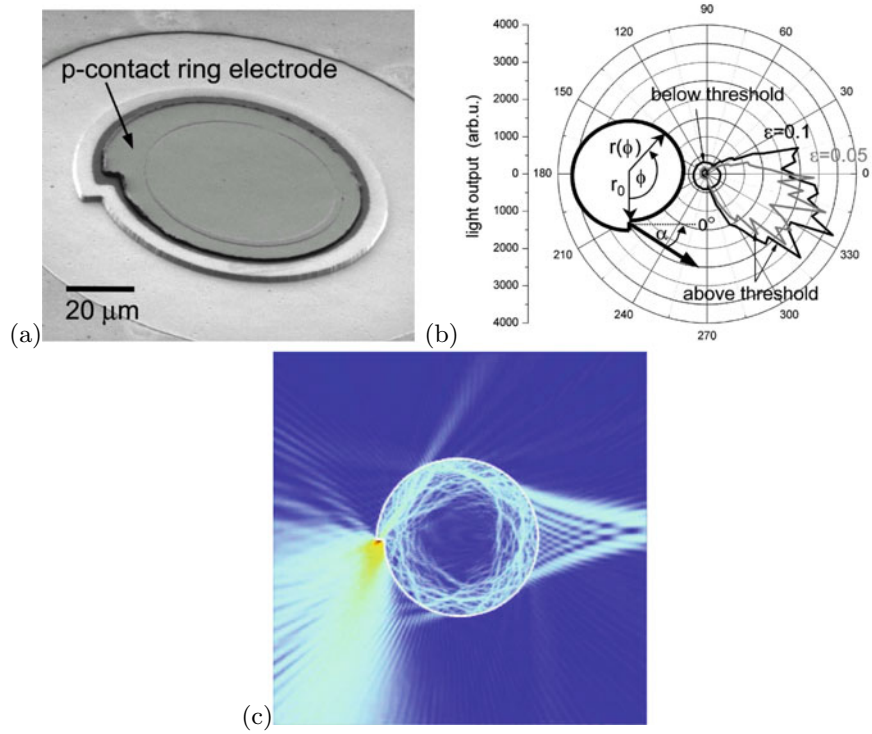

Fig. 19.28 **a** SEM image of a microcavity disc laser diode with a disc radius of 50 µm. The p-contact ring electrode defines the areas through which carriers are injected into the microdisc and where stimulated emission can take place. **b** Radial distribution of the light output from the spiral-shaped microdisc laser diode measured below and above threshold. The radius of the spiral microdisc was $r_0 = 250\,\mu\text{m}$ and the deformation parameters were $\epsilon = 0.05$ (*grey*) and $\epsilon = 0.10$ (*black*). An emission beam at an angle of $\alpha = 0°$ corresponds to a direction normal to the notch surface as shown in the *inset*. Below the laser threshold, the emission pattern is essentially isotropic and independent of the deformation parameter. Above the threshold, directional emission is clearly observed with the emission direction at a tilt angle $\alpha \approx 25°$. The measured divergence angle of the far-field pattern is $\sim 75°$ for $\epsilon = 0.10$ and $\sim 60°$ for $\epsilon = 0.05$. Reprinted with permission from [1656], ©2004 AIP. **c** Simulated near-field intensity pattern of an emission mode with $nkR \approx 200$ for deformation $\epsilon = 0.10$. Reprinted with permission from [1654], ©2003 AIP

19.2.4 Hexagonal Cavities

Hexagonal cavities develop, e.g., in microcrystals of wurtzite semiconductors (with the c-axis along the longitudinal axis of the pillar). In Fig. 19.29a, a ZnO tapered hexagonal resonator (needle) is shown. Whispering gallery modes modulate the intensity of the green ZnO luminescence [1657].[4] In a simple plane-wave model, the resonance condition is given by

$$6R_\text{i} = \frac{h\,c}{n\,E}\left[N + \frac{6}{\pi}\arctan\left(\beta\sqrt{3n^2-4}\right)\right], \tag{19.59}$$

where R_i is the radius of the inner circle (Fig. 19.29d), n is the index of refraction, N is the mode number and β is given by $\beta_\text{TM} = 1/n$ ($\beta_\text{TE} = n$) for TM (TE) polarization, respectively. Due to birefringence, $n_\parallel$ ($n_\perp$) has to be used as the index of refraction for TM (TE) polarization.

[4] We note that besides the green luminescence as in Fig. 10.20, an unstructured green band also occurs that is observed here. Its origin may be linked to the oxygen vacancy [1658].

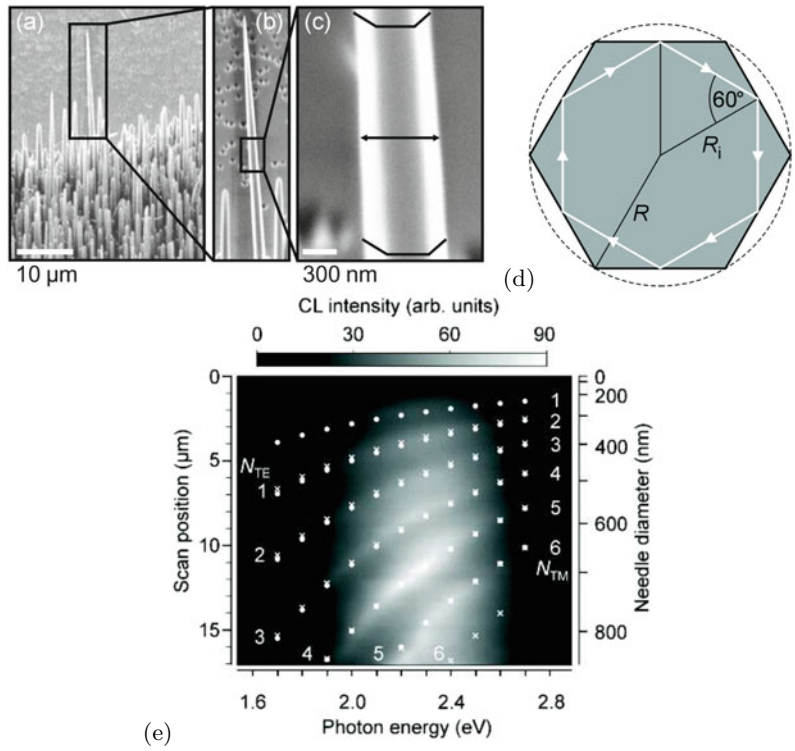

Fig. 19.29 **a–c** SEM images of ZnO nanoneedle fabricated by pulsed laser deposition. **d** Schematic geometry of cross-sectional plane. R_i (R) is the radius of the incircle (circumscribing circle). The circumference of the inscribed *white hexagon*, representing the path of a whispering gallery mode, has a length of $6R_i$. **e** Two-dimensional plot of spectra recorded along a linescan along the needle's longitudinal axis. The left vertical axis shows the linescan position x, the right one refers to the respective needle diameter D. The spectral maxima, i.e. the measured WGM energies, appear as bright belts going from the bottom left corner to the right upper one. With decreasing diameter, all resonances shift systematically to higher energies. The *white dots* give theoretical TM-resonance energy positions obtained from (19.59), *white crosses* give the same for TE-polarization. Reprinted with permission from [1657], ©2004 APS

A $N = 26$ whispering gallery mode of a hexagonal resonator is shown in Fig. 19.30c,d. The 6-fold symmetric emission stems from the edges of the hexagon. While whispering gallery resonators have typically mode numbers $N \gg 1$, in such hexagonal resonators the whispering gallery modes could be followed down to $N = 1$ [1657] as shown in Fig. 19.29a, b, e.

Under high optical pumping laser action occurs on the whispering gallery modes. The peak positions, close to the band gap in the spectral region of the electron-hole plasma, follow (19.59) [1660], as shown for various diameters in Fig. 19.31. Pumping threshold even at room temperature is below $100\,\mathrm{kW/cm^{-2}}$ [1661].

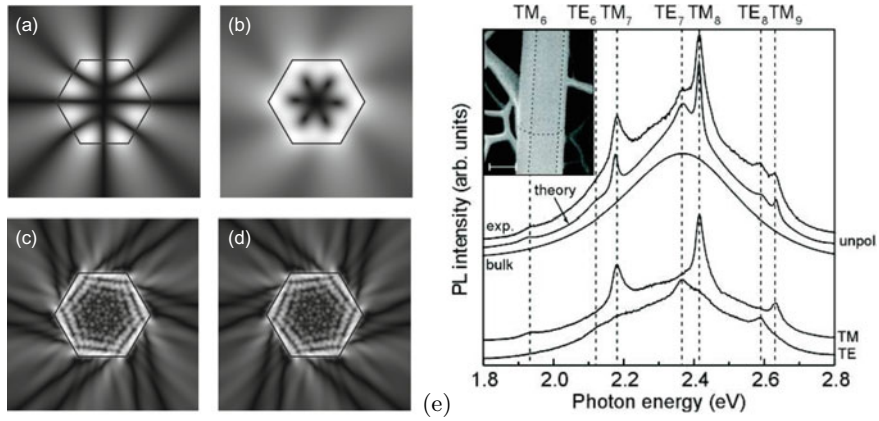

Fig. 19.30 Simulated near-field intensity pattern of modes in a cavity with hexagonal cross section (absolute value of electric field in linear grey scale): Modes ($N = 4$) with (**a**) symmetry $-a$ and (**b**) mode 4+ (nomenclature from [1659]) for $n = 2.1$ and $kR = 3.1553 - \mathrm{i}0.0748$. Modes (**c**) 26− and (**d**) 26+ for $n = 1.466$ and $kR = 22.8725 - \mathrm{i}0.1064$. The displayed modes have a chiral pattern. Emission originates mostly from the corners. **e** Micro-photoluminescence spectra of a single ZnO nanopillar. The three topmost curves are unpolarized. The curve labeled 'bulk' shows the unmodulated luminescence of the green luminescence in bulk. The line labeled 'exp.' shows the experimental μ-PL spectrum of the investigated nanopillar. The experimental spectra recorded for TM- and TE-polarization, respectively, are shown in the lowest two curves. The curve labeled 'theory' displays the theoretical luminescence spectra. *Dashed vertical lines* are guides to the eye referring to the spectral position of the dominating WGMs. The *inset* shows a SEM image of the investigated pillar, the scale bar has a length of 500 nm. The *dotted lines* show the position of the edges of the hexagonal resonator obtained from topography contrast

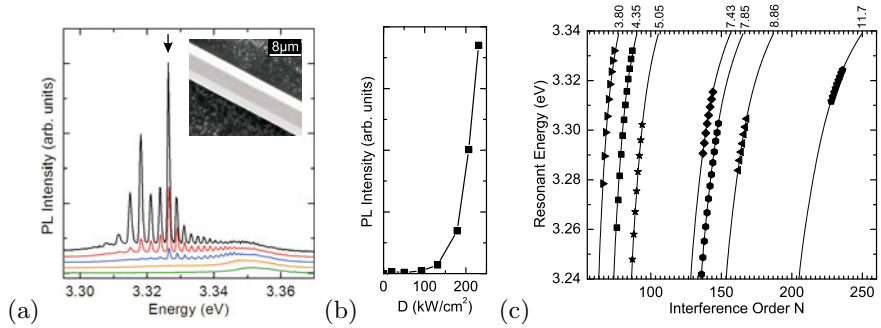

Fig. 19.31 **a** Photoluminescence spectra of a ZnO microwire with hexagonal cross section for various pump power densities (*lowest curve*: $D = 60\,\mathrm{kW/cm^2}$, *top curve*: $D = 250\,\mathrm{kW/cm^2}$) at $T = 10\,\mathrm{K}$. The inset shows the scanning electron microscopy image of a typical microwire ($d = 6.40\,\mu\mathrm{m}$). **b** Dependence of the emitted PL intensity of a selected lasing peak (denoted by an *arrow* in the spectrum in part (**a**)) on the excitation density D. *Lines* are guide to the eye. **c** Dependence of the resonant energies on the interference order N for wires with different diameters as labeled on top of the graph. *Lines* are the predicted theoretical values calculated from (19.59) using diameter values obtained from SEM measurements; the *symbols* represent the experimentally observed peaks. Adapted from [1660]

Chapter 20
Transparent Conductive Oxide Semiconductors

Many of the most important semi-conductors are oxides.

A.H Wilson, 1939 [72]

Abstract Typical materials in the class of transparent conductive oxides are mentioned. Their physical properties and the limits of conductivity versus transparency are discussed.

20.1 Introduction

Transparent conductive oxides (TCO) are semiconductors that are simultaneous transparent and highly conductive. Therefore they can serve as transparent contacts, e.g. as a solar cell front contact or in display applications. The materials are typically fabricated in the form of thin films on glass, polymers or similar substrates and devices. The crystallographic structure is polycrystalline or amorphous. The first TCO investigated was CdO in pressed powder [1662] and thin film form [38]. The recent historic development of the resistivity of the most important TCO materials in the last 30 years is shown in Fig. 20.1. Further information on TCO films can be found in [1663–1665].

20.2 Materials

Any wide-gap ($E_g > 3$ eV) semiconductor that is conductive, e.g. due to intrinsic defects or by chemical impurities (doping), can be considered to be a TCO. Pratically only a few, non-toxic materials that can be easily deposited are of importance. The first TCO application was heating of air plane windows. As always in semiconductor technology, price drives the suitability for applications. This in particular true for TCO applications since they include large area devices such as solar cells, displays and also large glass panes for electromagnetic shielding and architectural heat and IR transparency management. Therefore large quantities of TCO are needed. The popular ITO (indium-tin-oxide) suffers from large indium price and potential indium scarcity, opening the field for aluminum-doped ZnO (ZAO) which is abundant. Possible other compounds including Cd are of no practical interest due to toxicity. Conductive GaN has not been considered due to its large processing temperatures. All practical TCO materials contain either Zn, Sn or In (Fig. 20.2). A number of TCO materials is reviewed in [1666]. TCO are

M. Grundmann, *The Physics of Semiconductors*, Graduate Texts in Physics,
https://doi.org/10.1007/978-3-030-51569-0_20

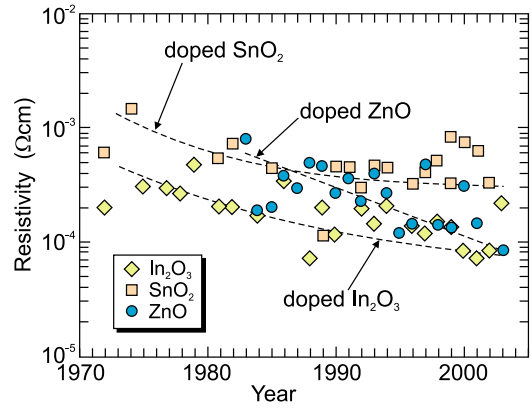

Fig. 20.1 Historical development of the resistivity of doped ZnO (*circles*), In_2O_3 (*squares*) and SnO_2 (*diamonds*) TCO films. Adapted from [1665]

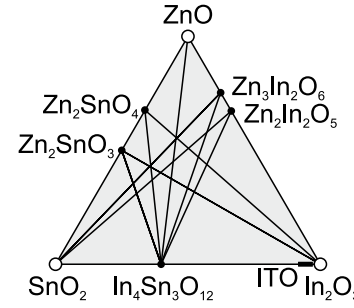

Fig. 20.2 Practical TCO materials

mostly n-conducting. Also p-conducting TCOs have been reported, e.g. $CuAlO_2$ delafossite [1667] with room temperature conductivity of $\sigma = 1\,\mathrm{S/cm}$, $ZnIr_2O_4$ [1668] with $\sigma = 2\,\mathrm{S/cm}$ and $ZnCo_2O_4$ spinel [1669] with $\sigma = 20\,\mathrm{S/cm}$. However, there has been so far no report on a practical transparent highly conductive p-type electrode.

The term ITO stands for a variety of Sn-doped indium oxide (In_2O_3) materials, the Sn content being typically in the 5–10% range but not strictly defined. The crystal structure of In_2O_3 [1670] is shown in Fig. 20.3. The effect of the replacement of indium by tin atoms in In_2O_3 on mechanical, electrical and optical properties of ITO has been calculated in [1671] using DFT. In Fig. 20.4 the band structures of pure In_2O_3 and $(Sn_{0.065}In_{0.935})_2O_3$ (one out of 16 indium atoms was replaced in the calculation) are compared [1672]. The fundamental band gap is slightly lowered, the high doping introduces a gigantic Burstein-Moss shift. Additionally another band gap opens that splits the lowest conduction band. Also the conduction mechanism in amorphous oxides has been discussed [151].

20.3 Properties

The best conductivity of TCOs is in the range of $10^{-4}\,\Omega\,\mathrm{cm}$ for the specific resistivity. Such value is about three orders of magnitude smaller than that of metals. However, the TCO meanwhile is highly transparent in the visible region, while metals become transparent only in the UV region because of their high plasma frequency (cf. Sect. 9.9.1).

The conduction mechanism in ZnO:Al is band transport in a highly doped semiconductor. The carrier concentration is typically around $10^{21}\,\mathrm{cm}^{-3}$. One of the best results is a (Hall) mobility of $47.6\,\mathrm{cm}^2/\mathrm{Vs}$, leading to a specific resistivity of $8.5 \times 10^{-5}\,\Omega\,\mathrm{cm}$ [1673]. The mobility is limited by

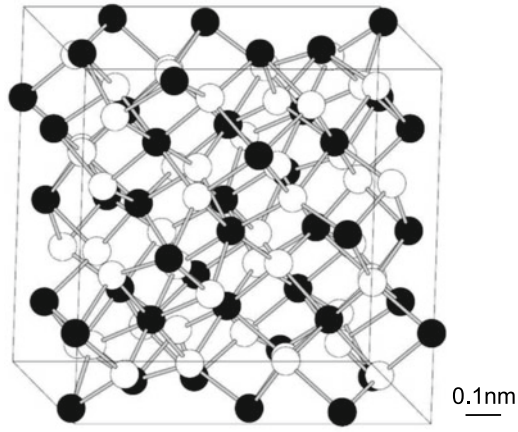

Fig. 20.3 The bixbyite crystal structure of indium oxide ($In_{32}O_{48}$) showing one unit cell where the indium and oxygen atoms are represented by the *full* and *empty circles*, respectively. Adapted from [1671]

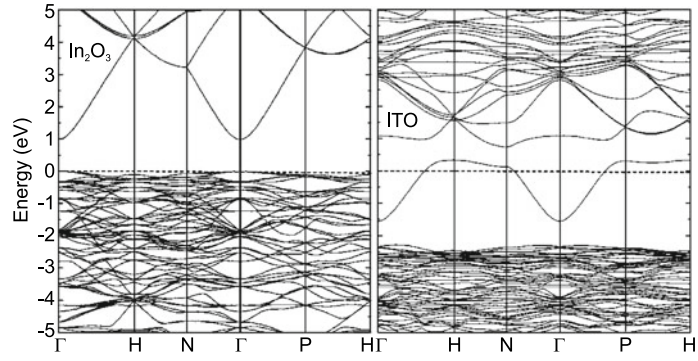

Fig. 20.4 Comparison of the band structure of In_2O_3 (*left*) and $(Sn_{0.065}In_{0.935})_2O_3$ (*right*). The position of the Fermi level is for both cases at $E = 0$. Adapted from [1672]

(doping level dependent) ionized impurity scattering (Sect. 8.3.3) as shown in Fig. 20.5 for various films. A detailed discussion of ionized impurity scattering in doped ZnO films can be found in [1674]. Also the mobility is correlated (Fig. 20.6) with scattering at structural defects such as grain boundaries [1675] (cf. Fig. 8.6). We note that the carrier mobility in a (polycrystalline) TCO is not very different from that in highly doped (crystalline) silicon (Fig. 8.9).

Conductivity and transparency are, however, linked. The high doping of the TCO leads to shifts in the band gap (renormalization and Burstein-Moss shift), band tails and the like that can introduce absorption in the visible spectral region. Also the infrared transparency is related to the conductivity by free carrier absorption and the plasma edge (Sect. 9.9.1). With increasing carrier density, the plasma edge shifts into the visible spectral range (Fig. 20.7a), limiting the possible maximum carrier density to several $10^{21}\,\mathrm{cm}^{-3}$, the exact value depending on the carrier mass.

In Fig. 20.7b the transparency spectra of two SnO_2 films with different conductivity are compared. The higher conductivity due to larger carrier concentration leads to reduced IR transparency. Generally, the transmission of a TCO is limited by the band edge on the high energy side of the spectrum and the plasma edge on the low energy side of the spectrum. The limited carrier concentration due to the onset of free carrier absorption in the visible spectral range ($\sim 3 \times 10^{21}\,\mathrm{cm}^{-3}$) and the limited mobility in the presence of such high impurity concentration (max. $50\,\mathrm{cm}^2/\mathrm{Vs}$) restrict the minimum resistivity of a TCO (or any transparent conductor) to about $4 \times 10^{-5}\,\Omega\,\mathrm{cm}$ [1677].

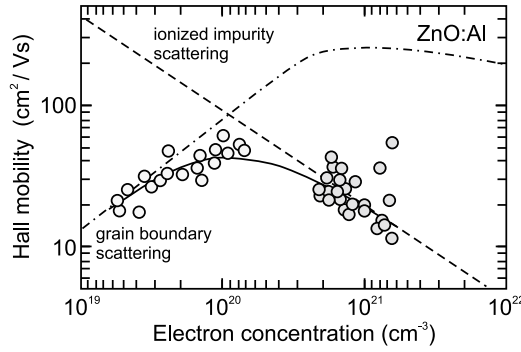

Fig. 20.5 Hall mobility for various ZnO:Al TCO thin films as a function of carrier (electron) concentration. The *dashed line* is the Brooks–Hering theory of ionized impurity scattering (taking into account non-parabolicity of the conduction band). The *dash-dotted* line is mobility in the presence of grain boundaries, the *solid line* is combined theory. *Symbols* are experimental data from two sets of samples. Adapted from [1665]

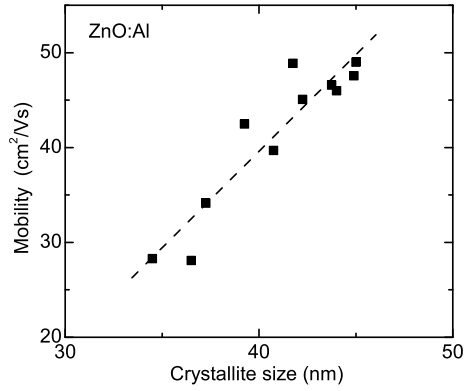

Fig. 20.6 Hall mobility of ZnO:Al films (of varying thickness) versus the crystallite size. Experimental data (from [1665]) are shown as *symbols*. The *dashed line* is a guide to the eye

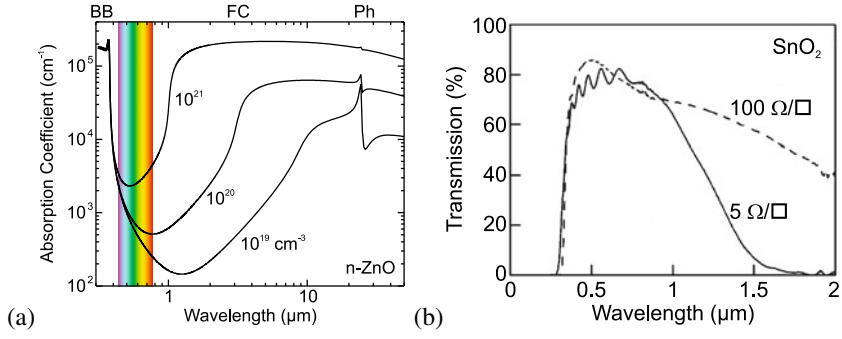

Fig. 20.7 **a** Absorption coefficient of n-type ZnO for various electron concentrations as labeled. Spectra synthesized from ellipsometric data of thin films. The visible spectral range is indicated. The contributing absorption processes are band-band transitions (BB), free carrier absorption (FC) and phonon-related absorption (Ph) as labeled. **b** Transparency versus wavelength spectra of two SnO_2 films with different conductivity as labeled. Adapted from [1676]

Part III
Applications

Chapter 21
Diodes

Abstract A thorough treatment of Schottky (metal-semiconductor) diodes, MIS (metal-insulator-semiconductor) diodes and (bipolar) pn-diodes is given, focussing on suitable materials, the formation of space charge layers and the forward and reverse current-voltage characteristics. Applications of such devices based on their rectifying properties are discussed.

21.1 Introduction

One of the simplest[1] semiconductor devices is the diode. It is a so-called two-terminal device, i.e. a device with two leads. The most prominent property of a diode is the rectifying current-voltage (I–V) characteristic. This function was initially realized with vacuum tubes (Fig. 21.1); a heated filament emits electrons that are transferred through vacuum to the anode if it is on a positive potential. The semiconductor diode technology led to a tremendous miniaturization, integration with other devices (in planar technology) and cost reduction.

We distinguish[2] *unipolar* diodes, for which the *majority* carriers cause the effects (e.g. metal-semiconductor diodes), and *bipolar* diodes in which *minority* carriers play the decisive role, e.g. in the pn junction diode.

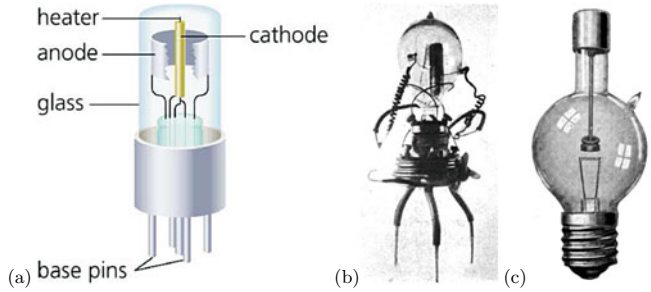

Fig. 21.1 **a** Schematic image of a vacuum diode. The electron current flows from the heated cathode to the anode when the latter is at a positive potential. **b** One of John A. Fleming's first diode 'valves', 1904. **c** Commercial 'tungar' rectifier, around 1916 [1679] (**b**, **c**). Adapted from [1678]

[1] The simplest device is a resistor made from a homogeneous piece of semiconductor, used, e.g., as a part of an integrated circuit or as a photoresistor as discussed in Sect. 22.2.

[2] This distinction is not only made for diodes but also many other semiconductor devices such as transistors, see Chap. 24.

M. Grundmann, *The Physics of Semiconductors*, Graduate Texts in Physics,
https://doi.org/10.1007/978-3-030-51569-0_21

Table 21.1 Typical current densities for various semiconductor devices

Device	j (A/cm^2)
Dark current of cooled CCD ($T \sim 200$ K)	$< 10^{-12}$
Dark current of CCD at room temperature	10^{-9}
3.6 nm SiOx gate dielectric (at 1 V)	10^{-9}
Photocurrent of Si solar cell (at 1 sun)	0.04
1.5 nm SiOx gate dielectric (at 1 V)	1
4-junction solar cell (at 508 sun)	6.5
Threshold of QD laser diodes	10
LED in typical operation	10
Threshold of QW laser diodes	10^2
LED in high power operation	10^2
Threshold of VCSEL	10^3
High power III–V laser diode in cw operation	10^3–10^4
High power III–V laser diode in pulsed operation	10^5
Resonant tunneling diode peak current	10^5
Power electronics transistors	10^5–10^7

Semiconductor devices carry vastly different currents depending on their design and eventual application. In Table 21.1, an overview of typical current densities is provided as a guide through the following chapters.

21.2 Metal-Semiconductor Contacts

The metal-semiconductor contact was investigated in 1874 by F. Braun (see Sect. 1.1). For metal sulfides, e.g. $CuFeS_2$, he found nonohmic behavior. We remark here that we treat first metal-semiconductor contacts with rectifying properties. Later it becomes understandable that metal-semiconductor contacts can also be used as ohmic contacts, i.e. contacts with a very small contact resistance. Rectifying metal-semiconductor contacts are also called Schottky diodes. A very important variation are metal-insulator-semiconductor diodes for which an insulator, mostly an oxide, is sandwiched between the metal and the semiconductor. Such diodes are treated in Sect. 21.3. An early treatment on 'crystal rectifiers' can be found in [1680]. Reviews on Schottky diodes can be found in [1681–1687].

21.2.1 Band Diagram in Equilibrium

The metal and the semiconductor have generally different positions of the Fermi levels relative to the vacuum level. When the metal is in contact with the semiconductor, charges will flow in such a way that in thermodynamic equilibrium the Fermi level is constant throughout the structure.[3] In the following we treat two limiting cases: The contact of a metal with a semiconductor without any surface states (Schottky-Mott model) and a contact where the semiconductor has a very high density of surface states (Bardeen model).

[3]This situation is similar to the heterostructure interface (Sect. 12.3.4), with the metal, however, having a very short screening length.

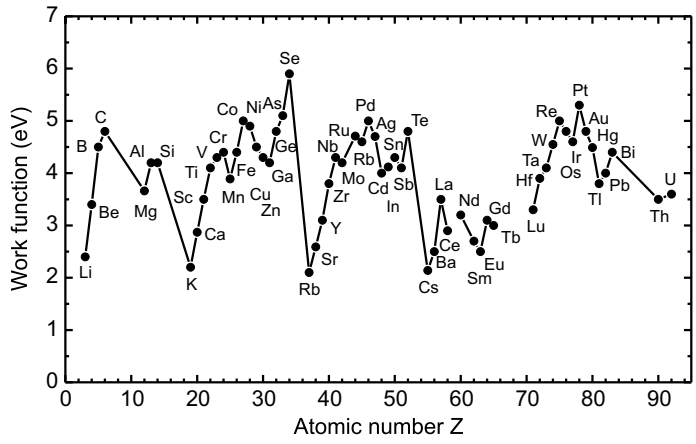

Fig. 21.2 Work function W_m of various metals

The position of the Fermi level in the metal is given by the work function W_m that is shown in Fig. 21.2 for various metals (see also Table 21.2). A recent review of published values of metal work functions is given in [1688]. The work function reflects the atomic shell structure; minima of the work function exist for group-I elements. The work function is the energy difference between the vacuum level (an electron is at rest in an infinite distance from the metal surface) and the metal Fermi level ($W_m > 0$). Since the electron density in the metal conduction band is very high, the position of the metal Fermi level does not change considerably when charge is exchanged between the metal and the semiconductor.

Since in a semiconductor the Fermi level depends strongly on the doping and temperature it is not useful to characterize the material itself. For semiconductors the electron affinity $\chi_{sc} = E_{vac} - E_C > 0$ is defined as the energy difference between the vacuum level and the conduction-band edge (see Fig. 12.21).

Ideal Band Diagram

When the metal and the semiconductor are not in contact (Fig. 21.3a), the metal is characterized by its work function $W_m = E_{vac} - E_F$ and the semiconductor by its electron affinity χ_{sc}. First, we assume that $W_m > \chi_{sc}$. For an n-type semiconductor, the energy difference between the Fermi level and the conduction band is denoted as

$$-e\,V_n = E_C - E_F \tag{21.1}$$

being negative, $V_n < 0$, for nondegenerate semiconductors. Thus, the position of the semiconductor Fermi level is given as

$$E_F = E_{vac} - \chi_{sc} + e\,V_n\ . \tag{21.2}$$

If the metal and semiconductor are brought into contact the Fermi levels will equilibrate. For the case of Fig. 21.3 ($E_{F,sc} > E_{F,m}$) electrons will flow from the semiconductor to the metal. The negative surface charge of the metal is compensated by a positive charge (due to D^+) in the semiconductor in the vicinity of the surface. Eventually a (Schottky) barrier of height[4] F_{Bn}

$$F_{Bn} = W_m - \chi_{sc} \tag{21.3}$$

[4]We denote the energy barrier height with $F_B = -e\phi_B$.

Table 21.2 Values of the work function W_m of various metals

Z	Element	W_m (eV)	Z	Element	W_m (eV)	Z	Element	W_m (eV)
3	Li	2.4	37	Rb	2.1	64	Gd	3.1
4	Be	3.4	38	Sr	2.59	65	Tb	3.0
5	B	4.5	39	Y	3.1	66	Dy	–
6	C	4.8	40	Zr	3.8	67	Ho	–
12	Mg	3.66	41	Nb	4.3	68	Er	–
13	Al	4.2	42	Mo	4.2	69	Tm	–
14	Si	4.2	44	Ru	4.71	70	Yb	–
19	K	2.2	45	Rh	4.6	71	Lu	3.3
20	Ca	2.87	46	Pd	5.0	72	Hf	3.9
21	Sc	3.5	47	Ag	4.7	73	Ta	4.1
22	Ti	4.1	48	Cd	4.0	74	W	4.55
23	V	4.3	49	In	4.12	75	Re	5.0
24	Cr	4.4	50	Sn	4.3	76	Os	4.8
25	Mn	3.89	51	Sb	4.1	77	Ir	4.6
26	Fe	4.4	52	Te	4.8	78	Pt	5.3
27	Co	5.0	55	Cs	2.14	79	Au	4.8
28	Ni	4.9	56	Ba	2.5	80	Hg	4.49
29	Cu	4.5	57	La	3.5	81	Tl	3.8
30	Zn	4.3	58	Ce	2.9	82	Pb	4.0
31	Ga	4.2	59	Pr	-	83	Bi	4.4
32	Ge	4.8	60	Nd	3.2	90	Th	3.5
33	As	5.1	62	Sm	2.7	92	U	3.6
34	Se	5.9	63	Eu	2.5			

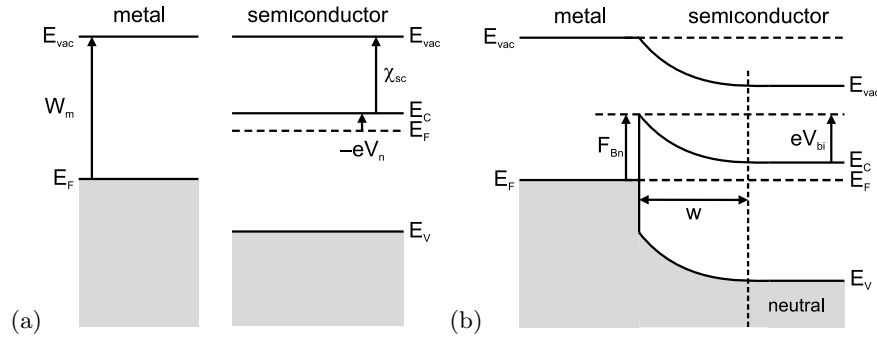

Fig. 21.3 Schematic band diagram of a metal-semiconductor junction that is dominated by bulk properties of the semiconductor. **a** no contact, **b** metal and semiconductor in contact. w denotes the width of the depletion layer. Outside the depletion layer the semiconductor is neutral. $F_{B,n}$ denotes the Schottky barrier height, V_{bi} denotes the built-in voltage (here $V_{bi} > 0$)

forms at the interface. The subscript 'n' stands for the contact on an n-type semiconductor. Surface/interface effects such as non-matching bonds, surface states, etc. are neglected at this point. In the semiconductor there exists a positively charged region that is called the *depletion layer* or space-charge region [1689]. Its extension (w in Fig. 21.3b) and properties will be discussed in Sect. 21.2.2. The space charge region in the metal is very thin due to the small screening length.

For a contact on a p-type semiconductor the barrier F_{Bp} (to the valence band) is (see Fig. 21.4d)

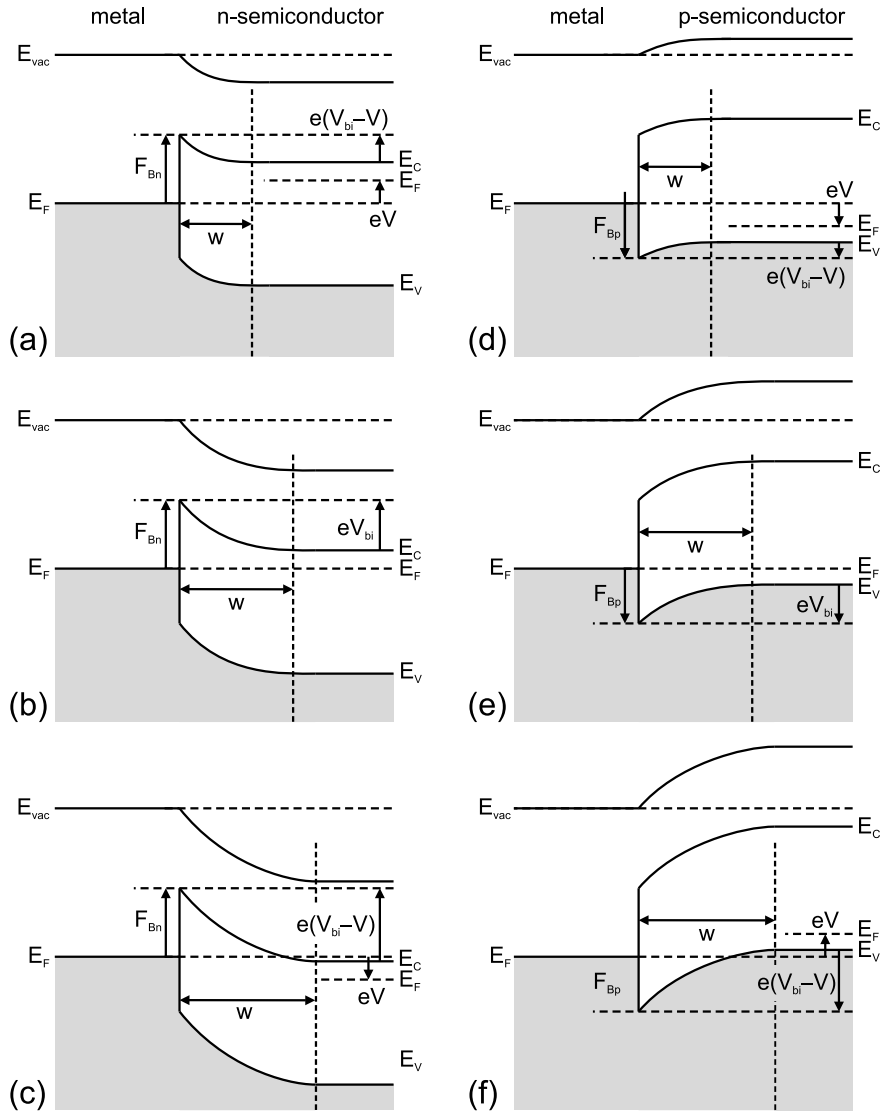

Fig. 21.4 Band diagrams of metal-semiconductor junctions for **a**, **b**, **c** an n-type semiconductor and **d**, **e**, **f** a p-type semiconductor (here $F_{\mathrm{Bp}} > 0$). (**b**, **e**) in thermodynamic equilibrium, (**a**, **d**) with forward bias ($V > 0$), (**c**, **f**) with reverse bias ($V < 0$)

$$F_{\mathrm{Bp}} = E_{\mathrm{g}} - (W_{\mathrm{m}} - \chi_{\mathrm{sc}}) \; . \tag{21.4}$$

Between the surface of the metal and the bulk part of the semiconductor there is a potential drop

$$V_{\mathrm{bi}} = \frac{F_{\mathrm{Bn}}}{e} + V_{\mathrm{n}} = \frac{W_{\mathrm{m}} - \chi_{\mathrm{sc}}}{e} + V_{\mathrm{n}} \; , \tag{21.5}$$

which is termed the built-in potential (or diffusion voltage). The exact form of the voltage drop, the so-called band bending, will be discussed in Sect. 21.2.2.

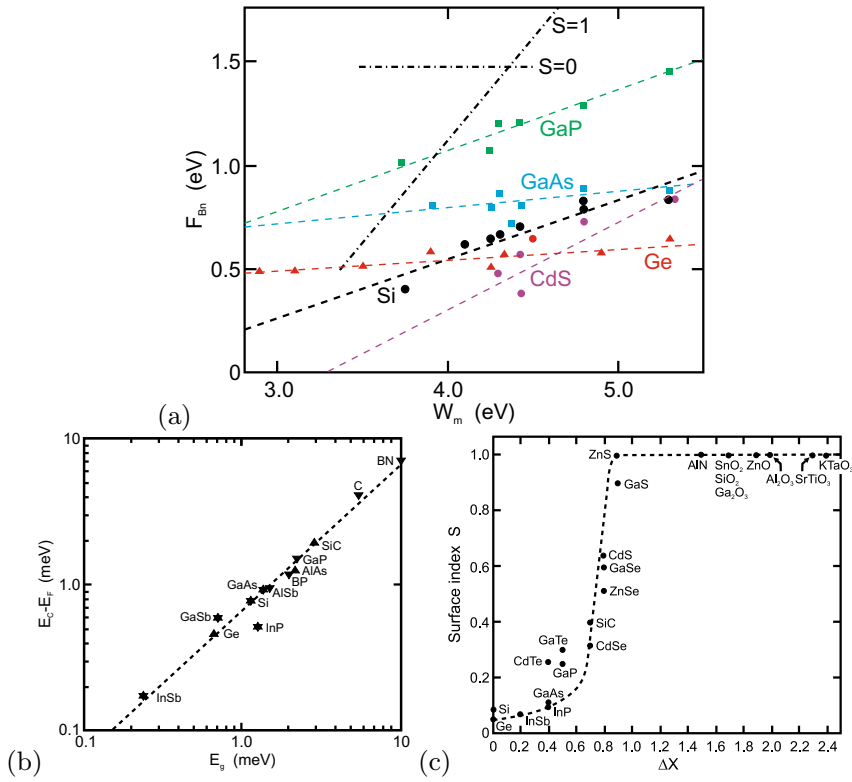

Fig. 21.5 **a** Experimental Schottky barrier heights F_{Bn} versus metal work function W_{m} for various metal-semiconductor junctions as labeled. *Dashed lines* are guides to the eye, *dash-dotted lines* indicate dependencies for the surface index (21.6) $S = 1$ and $S = 0$. Data from [1690, 1691]. **b** $E_{\mathrm{C}} - E_{\mathrm{F}}$ at the metal-semiconductor interface versus the band gap E_{g} for Au Schottky contacts on various semiconductors. The *dashed line* represents $E_{\mathrm{C}} - E_{\mathrm{F}} = 2E_{\mathrm{g}}/3$. Data from [1692]. **c**Surface index S versus the electronegativity difference ΔX between the species of compound semiconductors. *Dashed line* is a guide to the eye. Data from [1691, 1693]

The surface index is defined as

$$S = \frac{\partial F_{\mathrm{Bn}}}{\partial W_{\mathrm{m}}} \,. \tag{21.6}$$

From the present consideration (21.3), the same semiconductor with metals of varying work function should result in $S = 1$.

Band Diagram in the Presence of Surface States

Experimental data shown in Fig. 21.5a, however, show a different behavior with smaller slope. For GaAs, e.g., the barrier height is almost independent of the metal work function. Thus, a different model is needed for realistic Schottky diodes. A rule of thumb for the dominantly covalent semiconductors is that for n-type material the barrier height is 2/3 of the band gap and for p-type material 1/3 of the band gap, such that $E_{\mathrm{C}} - E_{\mathrm{F}} \approx 2E_{\mathrm{g}}/3$ (Fig. 21.5b). Only for ionic semiconductors $S \approx 1$ holds (Fig. 21.5c) [1694].

If the semiconductor has a large density of states at its surface ($\gtrsim 10^{12}\,\mathrm{cm}^{-2}$), there is a space-charge region already without the metal [1695]. Surface traps are filled up to the Fermi level (Fig. 21.6a). The size of the band bending in the semiconductor will be denoted as F_{Bn} since it will turn out below as the Schottky barrier height. If the density of surface states is very high, the charge carriers moving

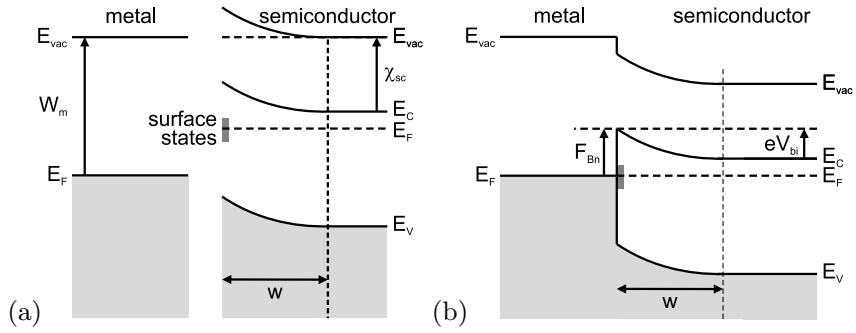

Fig. 21.6 Schematic band structure of a metal-semiconductor junction that is dominated by surface properties of the semiconductor. **a** no contact; due to pinning of the Fermi level at surface states of the semiconductor, a depletion-layer of width w is already present. **b** Metal and semiconductor in contact

from the semiconductor into the metal upon contact formation are accommodated in the surface states and the position of the Fermi level at the semiconductor surface changes only very little. Thus, the space-charge region is not modified and it is identical to the surface depletion region. The Schottky barrier height is then given by the band bending at the (bare) semiconductor surface F_{Bn} (Fig. 21.6d) and does not depend on the metal work function at all (Bardeen model [1695]). For this limiting case we find for the surface index $S = 0$.

For actual metal-semiconductor contacts the surface index S takes values between 0 and 1. A theory involving the semiconductor band structure and midgap (surface) states (MIGS) is needed [695, 1696]. For Si, the experimental result is $S = 0.27$; the corresponding density of surface states is $D_{\mathrm{s}} = 4 \times 10^{13}\,\mathrm{cm}^{-2}\,\mathrm{eV}^{-1}$.

21.2.2 Space-Charge Region

The width w of the space-charge region is calculated next. First, we make the so-called abrupt approximation. In this approximation (Schottky-Mott model), the charge density ρ in the space-charge region ($0 \le x \le w$) is given by the doping, i.e. $\rho = +eN_{\mathrm{D}}$. Outside the space-charge region the semiconductor is neutral, i.e. $\rho = 0$ and the electric field is zero, i.e. $\mathrm{d}\varphi/\mathrm{d}x = 0$. As further boundary conditions the potential at the interface is $\varphi(0) = -V_{\mathrm{bi}} < 0$. The potential drop in the space-charge region is determined by the one-dimensional Poisson equation

$$\frac{\mathrm{d}^2\varphi}{\mathrm{d}x^2} = -\frac{\rho}{\epsilon_{\mathrm{s}}}\,, \tag{21.7}$$

where $\epsilon_{\mathrm{s}} = \epsilon_{\mathrm{r}}\,\epsilon_0$ is the static dielectric constant of the semiconductor. Using the ansatz $\varphi(x) = \varphi_0 + \varphi_1 x + \varphi_2 x^2$ we find

$$\varphi(x) = -V_{\mathrm{bi}} + \frac{e\,N_{\mathrm{D}}}{\epsilon_{\mathrm{s}}}\left(w_0\,x - \frac{x^2}{2}\right)\,, \tag{21.8}$$

w_0 being the depletion layer width at zero bias.

The spatial dependence $E(x)$ of the electric field strength is

$$E(x) = -\frac{e\,N_{\mathrm{D}}}{\epsilon_{\mathrm{s}}}(w_0 - x) = E_{\mathrm{m}} + \frac{e\,N_{\mathrm{D}}}{\epsilon_{\mathrm{s}}}\,x\,, \tag{21.9}$$

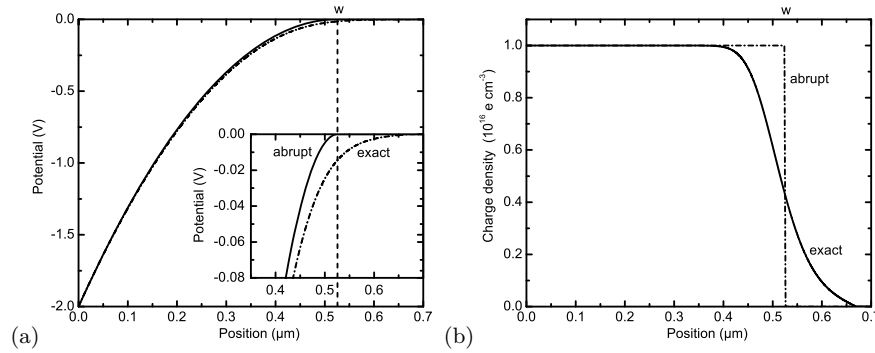

Fig. 21.7 **a** Potential φ and **b** charge density ρ across the depletion layer of a Schottky n-GaAs diode. Calculation parameters are $\epsilon_s = 12.5\,\epsilon_0$, $V_{bi} - V_{ext} = 2\,V$ (small reverse bias), $N_D = 1 \times 10^{16}\,cm^{-3}$, $T = 300\,K$. Abrupt approximation is shown as *solid lines*, exact (numerical) calculation as *dash-dotted line*. *Dashed line* in (**a**) indicates depletion layer width w_0 in the abrupt approximation

with the maximum field strength $E_m = -eN_D\,w_0/\epsilon_s < 0$ at $x = 0$. From the condition $\varphi(w_0) = 0$ we obtain w_0 as

$$w_0 = \sqrt{\frac{2\,\epsilon_s}{eN_D}\,V_{bi}}\ . \tag{21.10}$$

The charge density and the potential in the abrupt approximation are shown in Fig. 21.7 for GaAs material parameters.

Beyond the abrupt approximation

The thermal distribution of the majority carriers should be treated with a little more care. The dependence of the charge density $\rho = e(N_D^+ - n)$ on the potential φ (within the Boltzmann approximation) is ($\beta = e/kT$)

$$\rho(x) = e\,N_D\left[1 - \exp\left(\beta\,\varphi(x)\right)\right]\ . \tag{21.11}$$

The actual charge density and the potential, obtained from a numerical solution of (21.7), are shown in Fig. 21.7 in comparison with the abrupt approximation. Clearly, at the Schottky depletion layer width w_0, the charge varies continuously and the potential does not drop to zero.

We note that for the depletion layer $\varphi \le 0$ and $n \le N_D$. The charge difference $\Delta\rho$ (due to the tail of the thermal distribution of the majority charge carriers in the depletion layer) between the real distribution (21.11) to the abrupt approximation model with constant charge density ($\rho_0 = eN_D$) in the depletion layer is

$$\Delta\rho(x) = \rho(x) - \rho_0 = -e\,N_D\,\exp\left(\beta\,\varphi(x)\right)\ . \tag{21.12}$$

The integration of $\Delta\rho$ over the depletion layer yields that the voltage drop V_{bi} across the depletion layer needs to be corrected by ΔV

$$\Delta\varphi = \int_0^{w_0}\left[\int_0^x \frac{-\Delta\rho(x')}{\epsilon_s}\,dx'\right]dx = \frac{1}{\beta}\left[1 - \exp(-\beta\,V_{bi})\right] \approx \beta^{-1}\ . \tag{21.13}$$

The approximation is valid for $\beta V_{bi} \gg 1$. Therefore, (21.10) is corrected to

$$w_0 = \sqrt{\frac{2\,\epsilon_s}{e\,N_D}\,\left(V_{bi} - \beta^{-1}\right)}\,. \tag{21.14}$$

When a potential difference V_{ext} is applied externally to the diode, (21.14) is modified by the change in the interface boundary condition, $\varphi(0) = -V_{bi} + V_{ext}$. The band diagram is shown schematically in Fig. 21.4a for a forward bias and in Fig. 21.4c for a reverse bias. Therefore, we obtain for the depletion-layer width (within the abrupt approximation)

$$w(V_{ext}) = \sqrt{\frac{2\,\epsilon_s}{e\,N_D}\,\left(V_{bi} - V_{ext} - \beta^{-1}\right)}\,. \tag{21.15}$$

Now we can also give explicitly the value of the maximum electric field E_m (at $x = 0$)

$$\begin{aligned} E_m &= -\sqrt{\frac{2\,e\,N_D}{\epsilon_s}\,\left(V_{bi} - V_{ext} - \beta^{-1}\right)} \\ &= -\frac{2}{w}\,\left(V_{bi} - V_{ext} - \beta^{-1}\right)\,. \end{aligned} \tag{21.16}$$

We note that so far the barrier height is independent of the applied bias voltage. In the next section, it is shown that this is actually not the case.

An alternative approach to solve the Poisson equation is to consider the field as a function of the potential, $E(\phi)$. Then,

$$\frac{\mathrm{d}E^2}{\mathrm{d}\phi} = 2\,E\,\frac{\mathrm{d}E}{\mathrm{d}\phi}\,, \tag{21.17}$$

and

$$\frac{\mathrm{d}E}{\mathrm{d}\phi} = \frac{\mathrm{d}E}{\mathrm{d}x}\,\frac{\mathrm{d}x}{\mathrm{d}\phi} = -\frac{\mathrm{d}E}{\mathrm{d}x}\,\frac{1}{E} = -\frac{\mathrm{d}^2\phi}{\mathrm{d}x^2}\,\frac{1}{E}\,. \tag{21.18}$$

Combining these two equations and using (21.7) and (21.11) we find

$$\frac{\mathrm{d}E^2}{\mathrm{d}\phi} = -\frac{2\,e\,N_D}{\epsilon_s}\,\left[1 - \exp(\beta\,\phi)\right]\,. \tag{21.19}$$

The integration of this equation yields with the boundary condition $E(\phi = 0) = 0$,

$$E^2(\phi) = -\frac{2\,e\,N_D}{\epsilon_s}\,\left(\phi - \frac{\exp(\beta\,\phi)}{\beta} + \frac{1}{\beta}\right)\,. \tag{21.20}$$

At the interface $\phi(x = 0) = -(V_{bi} - V)$, and for sufficient voltage drop in the semiconductor $\exp\beta\,\phi \ll 1$, and therefore (21.16) for E_m is recovered without using the abrupt approximation or its correction (21.13).[5] Without approximation,

$$E_m = -\sqrt{\frac{2\,e\,N_D}{\epsilon_s}\,\left(V_{bi} - V_{ext} - \frac{1 - \exp[-\beta(V_{bi} - V_{ext})]}{\beta}\right)}\,. \tag{21.21}$$

[5]The functional integration method is limited to bijective potentials $\phi(x)$, i.e. strictly monotonously falling or rising potentials [1697] and thus covers monotonously varying doping density within the depletion layer.

21.2.3 Schottky Effect

The barrier height is reduced by the image-charge effect that has been neglected so far. This effect has been worked out for metals by Schottky [1698] and has been adapted to semiconductors [1699, 1700]. An electron (charge $q = -e$) at position x in the semiconductor is facing a metal surface at $x = 0$ (Fig. 21.8a). The potential distribution of the free charge is modified since the metal surface is an equipotential surface. The potential distribution outside the metal is identical to that if an *image* charge $-q$ was located at $-x$. This image charge exerts a force (image force F_{if}) on the electron

$$F_{\mathrm{if}} = -\frac{q^2}{16\,\pi\,\epsilon_{\mathrm{s}}\,x^2}\ , \tag{21.22}$$

where ϵ_{s} is again the relative dielectric constant of the semiconductor. In order to bring an electron from infinity to x the work E_{if},

$$E_{\mathrm{if}} = \int_{\infty}^{x} F_{\mathrm{if}}\,\mathrm{d}x = -\frac{q^2}{16\,\pi\,\epsilon_{\mathrm{s}}\,x}\ , \tag{21.23}$$

is needed. This image potential energy is shown in Fig. 21.8a. The total energy E_{tot} (solid line in Fig. 21.8a) of the electron in the presence of an electric field E is given by (F_{B_0} is the relabeled Schottky barrier (21.3) without image charge effect, $q = -e < 0$ and $E < 0$)

$$E_{\mathrm{tot}} = F_{\mathrm{B}_0} - q\,E\,x - \frac{q^2}{16\,\pi\,\epsilon_{\mathrm{s}}\,x}\ . \tag{21.24}$$

We note that the divergence at $x = 0$ stems from the continuum idealization of the problem. It can be removed by shifting the position of the image charge slightly against the interface or by using an extended charge [1188].

The maximum of this function ($\mathrm{d}E_{\mathrm{tot}}/\mathrm{d}x = 0$) is at x_{m},

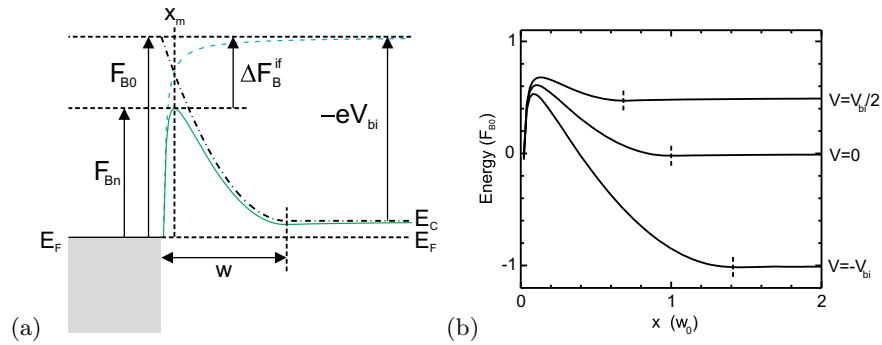

Fig. 21.8 **a** Energy of a particle with respect to the metal surface (*dashed line*), conduction band in semiconductor depletion layer (*dash-dotted line*) and combined effect (*solid line*). The image charge energy lowers the potential barrier F_{B_0} by the amount $\Delta F_{\mathrm{B}}^{\mathrm{if}}$ to F_{Bn}. **b** Conduction band on the semiconductor side of a metal-semiconductor junction at various bias voltages ($V = 0$, $+V_{\mathrm{bi}}/2$, and $-V_{\mathrm{bi}}$ as labeled) taking into account the Schottky effect. The width of the depletion layer is indicated with a *short vertical dashed line*. The barrier height without Schottky effect is $F_{\mathrm{B}0}$. The *dashed line* is the situation without Schottky effect for zero bias

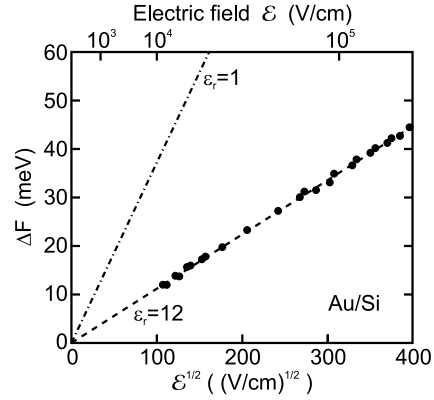

Fig. 21.9 Electric-field dependence of the image charge lowering of the Schottky barrier. *Dash-dotted* line is for vacuum dielectric constant, *dashed line* is (21.26) for $\epsilon_r = 12$. Adapted from [1701]

$$x_m = \sqrt{\frac{q}{16\,\pi\,\epsilon_s\,E}}\,. \tag{21.25}$$

The Schottky barrier F_{B_0} is thus reduced by $\Delta F_B^{if} > 0$ given by

$$\Delta F_B^{if} = -q\sqrt{\frac{q\,E}{4\pi\,\epsilon_s}} = 2\,q\,E\,x_m\,. \tag{21.26}$$

With the electrical field in the vicinity of the interface ($x_m \ll w$) given by E_m from (21.16), the barrier reduction is[6]

$$\Delta F_B^{if} = e\left[\frac{e^3\,N_D}{8\,\pi^2\,\epsilon_s^3}\left(V_{bi} - V_{ext} - \beta^{-1}\right)\right]^{1/4}\,. \tag{21.27}$$

For $\epsilon_s = \epsilon_0$ (vacuum) and a field strength of 10^5 V/cm, the maximum position is at $x_m = 6$ nm and the barrier reduction is $\Delta F_B^{if} = 0.12$ eV. For 10^7 V/cm, $x_m = 1$ nm and $\Delta F_B^{if} = 1.2$ eV. For semiconductors with $\epsilon_r \sim 10$ the effect is smaller (Fig. 21.9). The Schottky effect depends on the bias voltage as visualized in Fig. 21.8b and therefore the barrier height depends on the applied bias voltage.

21.2.4 Capacitance

The total space charge Q (per unit area) in the semiconductor is ($V = V_{ext}$)

$$Q(V) = e\,N_D\,w = \sqrt{2\,e\,N_D\,\epsilon_s\left(V_{bi} - V - \beta^{-1}\right)}\,. \tag{21.28}$$

and depends on the external voltage.

For measurement of the depletion layer capacitance first the external dc bias voltage V is set which defines the extension of the depletion layer. The (differential) capacitance is probed by an ac voltage with small amplitude $\delta V \ll V$. First we assume that the ac frequency ω is small compared to characteristic time constants of the electrically active impurities (quasi-static capacitance) and discuss

[6] The term ϵ_s^3 is technically $\epsilon_s\epsilon_d^2$ where ϵ_d is the image-force dielectric constant. ϵ_d is equal to ϵ_s if the transit time of an electron from the metal to the maximum of the potential energy is sufficiently long to build up the dielectric polarization of the semiconductor [1681].

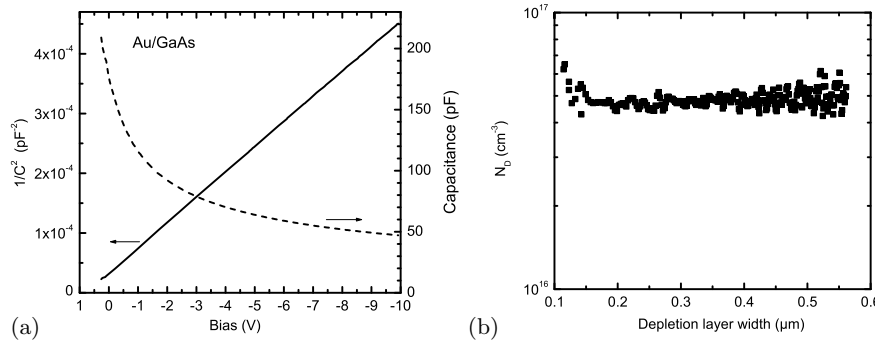

Fig. 21.10 **a** Capacitance C (*dashed line*) and $1/C^2$ (*solid line*) versus bias voltage dependence for an Au/GaAs Schottky diode (2-μm MOVPE-grown GaAs:Si on a n-GaAs substrate) at room temperature. From the extrapolation to $1/C^2 = 0$ and (21.30) we obtain $V_{\mathrm{bi}} = 804 \pm 3\,\mathrm{mV}$. **b** Donor concentration ($N_{\mathrm{D}} = 4.8 \times 10^{16}\,\mathrm{cm}^{-3}$) determined via (21.31) from the $1/C^2$ plot versus the depletion layer width (calculated using (21.29))

the bias dependence $C(V)$. Following we discuss the frequency and temperature dependence of the capacitance[7] $C(\omega, T)$, in particular when the measurement frequency is in the range of the (temperature dependent) electron capture or emission rate (10.42, 10.43).

Bias Dependence

From (21.28) the capacitance $C = |\mathrm{d}Q/\mathrm{d}V|$ (per unit area) of the space charge region is given by

$$C = \sqrt{\frac{e\,N_{\mathrm{D}}\,\epsilon_{\mathrm{s}}}{2\left(V_{\mathrm{bi}} - V - \beta^{-1}\right)}} = \frac{\epsilon_{\mathrm{s}}}{w}\,. \tag{21.29}$$

Equation (21.29) can also be written as

$$\frac{1}{C^2} = \frac{2\left(V_{\mathrm{bi}} - V - \beta^{-1}\right)}{e\,N_{\mathrm{D}}\,\epsilon_{\mathrm{s}}}\,. \tag{21.30}$$

If $1/C^2$ is measured as a function of the bias voltage (C–V spectroscopy), it should be linearly dependent on the bias voltage if the doping concentration is homogeneous (Fig. 21.10a). The doping concentration can be determined from the slope via

$$N_{\mathrm{D}} = -\frac{2}{e\,\epsilon_{\mathrm{s}}}\left[\frac{\mathrm{d}}{\mathrm{d}V}\left(\frac{1}{C^2}\right)\right]^{-1}\,, \tag{21.31}$$

(see Fig. 21.10b) and the built-in voltage V_{bi} from the extrapolation to $V = V'$ such that $1/C^2 = 0$, $V_{\mathrm{bi}} = V' + kT/e$. Using (21.5) the Schottky barrier height can be determined from this [1702] via

$$F_{\mathrm{B_n}} = e\,V' - e\,V_{\mathrm{n}} + kT - \Delta F_{\mathrm{B}}^{\mathrm{if}}\,, \tag{21.32}$$

where $\Delta F_{\mathrm{B}}^{\mathrm{if}}$ is the barrier lowering (21.27) due to the image force effect between the flat-band and the zero-bias cases.

We note that for inhomogeneous doping the depth profile of the doping can be determined by C–V spectroscopy. The $1/C^2$ versus bias curve is then no longer a straight line and exhibits a varying slope.

[7] Probing the capacitance as a function of the ac frequency is called admittance spectroscopy.

$N_D(w)$ is evaluated according to (21.31) using $w = \epsilon_s/C$ from (21.29) [1703],

$$N_D\left(w = \frac{\epsilon_s}{C}\right) = -\frac{2}{e\,\epsilon_s}\left[\frac{d}{dV}\left(\frac{1}{C^2}\right)\right]^{-1} , \tag{21.33}$$

Using functional integration, the capacitance of a depletion layer can be expressed in terms of $\varphi(0) = -(V_{bi} - V)$ without explicit knowledge of the potential $\varphi(x)$ [1697].[8] In the approximation $-e\varphi(0) \gg kT$ we obtain for homogeneous doping as refinement of (21.29)

$$C = \sqrt{\frac{e\,N_D\,\epsilon_s}{2\left(V_{bi} - V - \beta^{-1}\left(\frac{n_0}{N_D} - \ln\frac{n_0}{N_D}\right)\right)}} , \tag{21.34}$$

where n_0 is the electron concentration in the neutral region. Within this general treatment, the validity of (21.31) has been confirmed. Also, C does not diverge in the flatband case, for $V \to V_{bi}$, as for the abrupt approximation but exhibits a maximum [1697].

At a given bias voltage, the charge (ionized donors or acceptors) at the boundary of the space-charge region is tested by the capacitance measurement. However, this principle works only if the depth of the space-charge region actually changes with the bias voltage. The method can therefore not be directly applied to such systems like δ-doped layers or quantum wells.

Frequency and Temperature Dependence

The release of carriers from (and capture on) a donor occurs with a characteristic emission rate g_c (10.43) (capture rate r_c). This is true similarly for acceptors. Therefore, the capacitance depends on the sampling frequency (Fig. 21.11a). If the capacitance is probed with a frequency much smaller than the release rate, the system appears to be in equilibrium and has the (quasi-)static capacitance C_0. If the probe frequency is much higher, the system cannot follow and the donor does not contribute to the capacitance. The characteristic frequency $\hat{f}$ at the turning point of $C(f)$ is [1016, 1017]

$$2\pi\,\hat{f} = 2\,g_c , \tag{21.35}$$

with corrections of the simple factor of 2 discussed in [1704]. Since the emission rate depends exponentially on temperature, for a given frequency the capacitance depends on temperature [1705]. This is shown in Fig. 21.11b for ZnO which exhibits several donor levels. At low temperature shallow levels release their carriers, at higher temperature the deeper levels start to contribute. The DX center in AlGaAs (see Sect. 7.7.6) has been investigated in [1706] with this technique.

21.2.5 Current-Voltage Characteristic

The current transport through a metal-semiconductor junction is dominated by the majority charge carriers, i.e. electrons (holes) in the case of an n-type (p-type) semiconductor, respectively.

In Fig. 21.12, the possible transport mechanisms are visualized for an n-type semiconductor. Thermionic emission 'above' the barrier involves the hot electrons from the thermal distribution and will be important at least at high temperatures. Tunneling 'through' the barrier will be important for thin barriers, i.e. at high doping ($w \propto N_D^{-1/2}$, cf. (21.15)). 'Pure' tunneling for electrons close to the (quasi-) Fermi level, also called field emission, and thermionic field emission, i.e. tunneling of electrons

[8] This is valid as long as $\varphi(x)$ is strictly monotonous.

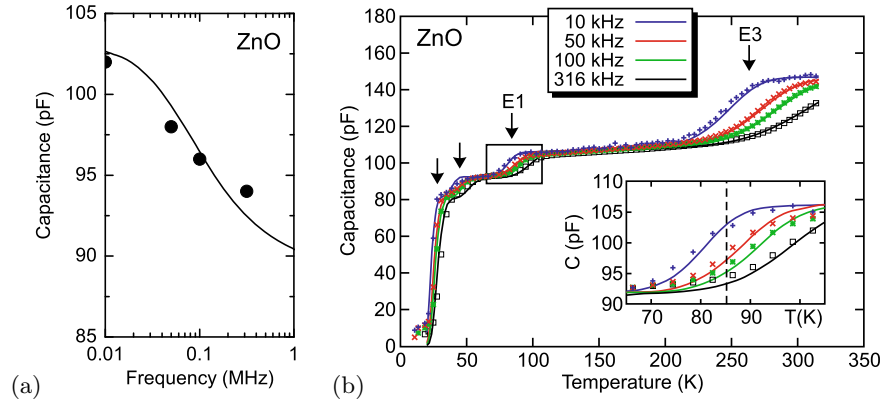

Fig. 21.11 **a** Capacitance versus probing frequency f for a Pd/ZnO Schottky diode (zero bias) at $T = 85$ K. Theoretical dependence (*solid line*) and experimental data (*circles*). **b** Capacitance of the same diode as a function of temperature (thermal admittance spectroscopy, TAS) for four different probing frequencies f =10, 50, 100 and 316 kHz (ac amplitude 50 mV). *Arrows* denote the release of carriers from four different defect levels, two shallow ones and the well-known defects E1 and E3 [737, 1707]. The *inset* shows the contribution of the E1 defect, indicated by a *rectangle* in the main graph, in more detail. *Symbols* are experimental data, *lines* are fit with four-level model (E1: $E_D = 116$ meV, E3: $E_D = 330$ meV) [1708]

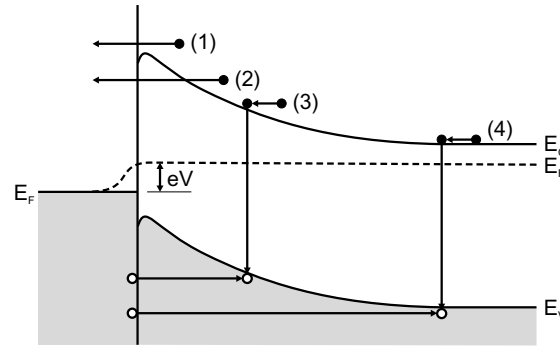

Fig. 21.12 Transport mechanisms at metal-semiconductor junctions. (**1**) Thermionic emission ('above' the barrier) (**2**) tunneling ('through' the barrier), (**3**) recombination in the depletion layer, (4) hole injection from metal

with higher energies, are distinguished. Also, recombination in the depletion layer and hole injection from the metal are possible.

The transport of electrons above the barrier can be described with diffusion theory [1709, 1710] or thermionic-emission theory [576]. A detailed treatment can be found in [1711, 1712]. In both cases the barrier height is large compared to kT. For thermionic emission (typically relevant for semiconductors with high mobility) the current is limited by the emission process and an equilibrium (constant electron quasi-Fermi level) is established throughout the depletion layer and ballistic transport is considered. In diffusion theory (for low mobility) a thermal equilibrium between metal and semiconductor electrons is established in the interface plane and the current is limited by diffusion and drift in the depletion region.

Thermionic Emission

The current density per unit area $j_{s\to m}$ of electrons that flow from the semiconductor into the metal is due to the hot electrons from the thermal distribution function

$$j_{s\to m} = -e \int_{E_F+F_{Bn}}^{\infty} v_x \, dn \, . \tag{21.36}$$

The integral starts at the lowest possible energy, the top of the Schottky barrier (no tunneling allowed in this model!). The electron density $\mathrm{d}n$ in a small energy interval $\mathrm{d}E$ is

$$\mathrm{d}n = D(E)\, f(E)\, \mathrm{d}E \ . \tag{21.37}$$

For a bulk semiconductor density of states (6.71) and the Boltzmann distribution ($F_\mathrm{B} \gg kT$)

$$\mathrm{d}n = \frac{1}{2\pi^2} \left(\frac{2m^*}{\hbar^2}\right)^{3/2} \sqrt{E - E_\mathrm{C}}\, \exp\left(-\frac{E - E_\mathrm{F}}{kT}\right) \mathrm{d}E \ . \tag{21.38}$$

For a given energy E, the carrier velocity v is determined by

$$E = E_\mathrm{C} + \frac{m^* v^2}{2} \ . \tag{21.39}$$

Thus we obtain

$$\sqrt{E - E_\mathrm{C}} = v \sqrt{m^*/2} \tag{21.40}$$

and

$$\mathrm{d}E = m^* v\, \mathrm{d}v \ . \tag{21.41}$$

Also, with (21.39) and (21.1),

$$E - E_\mathrm{F} = (E - E_\mathrm{C}) + (E_\mathrm{C} - E_\mathrm{F}) = \frac{m^* v^2}{2} - e\, V_\mathrm{n} \ . \tag{21.42}$$

Therefore we write (21.38) as

$$\mathrm{d}n = 2 \left(\frac{m^*}{h}\right)^3 \exp\left(\beta V_\mathrm{n}\right) \exp\left(-\frac{m^* v^2}{2\, kT}\right) 4\pi\, v^2\, \mathrm{d}v \ . \tag{21.43}$$

Then the one-dimensional integral over $4\pi v^2\, \mathrm{d}v$ is converted into a three-fold integral over $\mathrm{d}v_\mathrm{x}\, \mathrm{d}v_\mathrm{y}\, \mathrm{d}v_\mathrm{z}$. Integration over all velocities in y and z directions yields a factor $2\pi\, kT/m^*$. The integration over v_x runs from the minimum velocity $v_\mathrm{min,x}$ necessary to pass the barrier,

$$\int_{v_\mathrm{min,x}}^{\infty} \exp\left(-\frac{m^* v_x^2}{2\, kT}\right) v_\mathrm{x}\, \mathrm{d}v_\mathrm{x} = \frac{kT}{m^*} \exp\left(-\frac{m^* v_\mathrm{min,x}^2}{2\, kT}\right) \ , \tag{21.44}$$

with the minimum velocity determined by

$$\frac{m^* v_\mathrm{min,x}^2}{2} = e\, (V_\mathrm{bi} - V) \ . \tag{21.45}$$

Thus the current density is given as, using (21.5),

$$\begin{aligned} j_{\mathrm{s}\to\mathrm{m}} &= \frac{4\pi e\, m^* k^2}{h^3}\, T^2 \exp\left(-\beta (V_\mathrm{bi} - V_\mathrm{n})\right) \exp\left(\beta V\right) \\ &= A^* T^2 \exp\left(-\frac{F_\mathrm{Bn}}{kT}\right) \exp\left(\beta V\right) \ , \end{aligned} \tag{21.46}$$

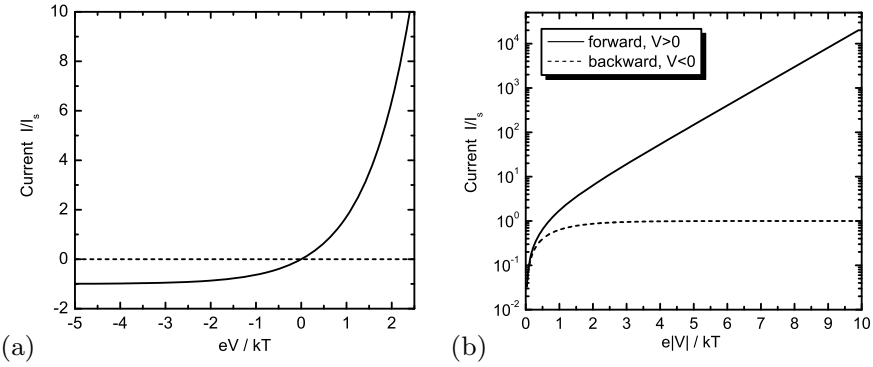

Fig. 21.13 Ideal diode I–V characteristics $I = I_\mathrm{s}(\exp(eV/kT) - 1)$ (**a**) in linear plot and (**b**) semilogarithmic plot

with A^* being the Richardson constant given by

$$A^* = \frac{4\pi e\, m^* k_\mathrm{B}^2}{h^3} = \frac{e\, N_\mathrm{C}\, \bar{v}}{4\, T^2}\ , \tag{21.47}$$

where $\bar{v}$ is the average thermal velocity in the semiconductor. A^* for electrons in vacuum is $120\,\mathrm{A\,cm^{-2}\,K^{-2}}$. A similar result is obtained for the thermionic emission of electrons from a metal (overcoming the work function) into vacuum.

If the bias is changed, the current from the semiconductor to the metal increases in the forward direction because the energy difference between the quasi-Fermi level and the top of the barrier is reduced. The current is reduced for reverse bias. The barrier from the metal into the semiconductor remains constant (except for the Schottky effect whose impact on the current-voltage characteristic is discussed next). Therefore the current $j_{\mathrm{m}\to\mathrm{s}}$ from the metal into the semiconductor is constant and can be obtained from the condition $j = j_{\mathrm{s}\to\mathrm{m}} + j_{\mathrm{m}\to\mathrm{s}} = 0$ for zero bias. Therefore the current-voltage characteristic in the thermionic-emission model is

$$\begin{aligned} j &= A^*\, T^2\, \exp\left(-\frac{F_\mathrm{Bn}}{kT}\right)\left[\exp\left(\beta V\right) - 1\right] \\ &= j_\mathrm{s}\left[\exp\left(\beta V\right) - 1\right]\ . \end{aligned} \tag{21.48}$$

The pre-factor

$$j_\mathrm{s} = A^*\, T^2 \exp\left(-\frac{F_\mathrm{Bn}}{kT}\right) \tag{21.49}$$

is called the saturation current density. The saturation current increases with increasing temperature.

The dependence (21.49) represents the ideal diode characteristic and is plotted in Fig. 21.13.

The temperature dependence of the saturation current j_s can be written as

$$\ln\left(\frac{j_\mathrm{s}}{T^2}\right) = \ln A^* - \frac{F_\mathrm{Bn}}{kT} \tag{21.50}$$

by transforming (21.49). The plot of $\ln(j_\mathrm{s}/T^2)$ to versus $1/T$ is called a Richardson plot and allows the barrier height and the Richardson constant to be determined from a linear fit (Fig. 21.14b).

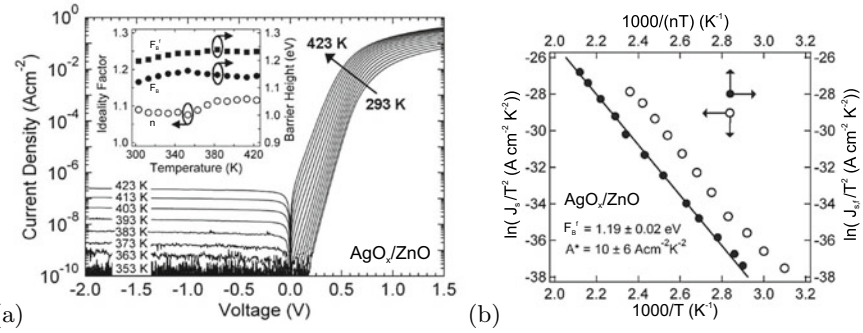

Fig. 21.14 Temperature dependent behavior of an AgO_x/ZnO Schottky diode. **a** I–V-characteristics. *Inset* depicts extracted parameters, ideality factor n, barrier height F_B and flatband barrier height F_B^f (21.54). **b** Richardson plots for the extracted barrier height and the calculated flatband barrier height with linear fit. Adapted from [1713]

Ideality Factor

If the Schottky (image force) effect, i.e. the change of barrier height with bias voltage, is considered, the semilogarithmic slope of the forward I–V characteristic is no longer $V_0^{-1} = e/kT$ but can be expressed as $V_0^{-1} = e/nkT$, n being a dimensionless parameter termed the ideality factor,[9]

$$j = j_s \left[\exp\left(\frac{e\,V}{n\,kT} \right) - 1 \right] . \tag{21.51}$$

n is given by

$$n = \left(1 - \frac{1}{e} \frac{\partial F_B}{\partial V} \right)^{-1} \approx 1 + \frac{1}{e} \frac{\partial F_B}{\partial V} . \tag{21.52}$$

The ideality factor due to the image force effect n_{if} (using (21.27) and the image force barrier lowering $\Delta F_B^{if,0}$ at zero bias) [1680] is

$$n_{if} = 1 + \frac{\Delta F_B^{if,0}}{4\,e\,V_{bi}} = 1 + \frac{x_m}{w_0} . \tag{21.53}$$

Typical values are smaller than 1.03. For GaAs and $N_D = 10^{17}\,cm^{-3}$, $n = 1.02$. With regard to V_0 and its temperature dependence, we refer also to Fig. 21.17 and the related discussion.

In Fig. 21.14a the temperature dependence of the I–V-characteristic of an almost ideal ZnO Schottky diode [1713] is depicted. The extracted barrier height is almost independent of temperature as it should be. Also the ideality factor is rather small (about 1.1) and also independent of temperature. The Richardson plot Fig. 21.14b according to (21.50) for this diode is a straight line. The extracted constant $A^* = (10 \pm 6)\,A\,cm^{-2}\,K^{-2}$ is reasonably close to the theoretical value of $32\,A\,cm^{-2}\,K^{-2}$ (using $m^* = 0.32$).

In order to gain a barrier height independent from non-idealities, in [1714] the flatband barrier height F_B^f is discussed which is calculated from the diode parameters via

$$F_B^f = n\,F_B - (n-1)\,\frac{kT}{e}\,\ln\left(\frac{N_C}{N_D} \right) , \tag{21.54}$$

[9] Obviously $n = 1$ for the ideal characteristic (21.48). Otherwise $n \geq 1$.

assuming all donors are ionized (otherwise N_D shall be replaced by the electron density n, not to be confused here with the ideality factor). Accordingly, the saturation current density (21.49) is rewritten as

$$j_{s,f} = A^* T^2 \exp\left(-\frac{F_B^f}{kT}\right) \tag{21.55}$$

Laterally Inhomogeneous Barrier

The increase of the ideality factor due to a spatially inhomogeneous barrier height has been proposed early on [1715–1719]. The barrier height $F_{Bn}(y, z)$ across the contact area is typically assumed to have a Gaussian probability distribution [1720] $p(F_{Bn})$ with a mean value $\bar{F}_{Bn}$ and a standard deviation σ_F.

It turns out that the barrier height F_{Bn}^C responsible for the capacitance, and thus the diffusion voltage determined by C–V spectroscopy, is given by the spatial average, i.e. $F_{Bn}^C = \bar{F}_{Bn}$. The barrier height F_{Bn}^j determining the current-voltage characteristics (cf. (21.48)) via

$$\begin{aligned} j &= A^* T^2 \left[\exp(\beta V) - 1\right] \int \exp\left(-\frac{F_{Bn}}{kT}\right) p(F_{Bn})\, \mathrm{d}F_{Bn} \\ &= A^* T^2 \exp\left(-\frac{F_{Bn}^j}{kT}\right) \left[\exp(\beta V) - 1\right] \end{aligned} \tag{21.56}$$

is given by

$$F_{Bn}^j = \bar{F}_{Bn} - \frac{\sigma_F^2}{2\,kT}\,. \tag{21.57}$$

Thus, the barrier height determined from the current-voltage characteristic underestimates the spatial average of the barrier height.[10] The Richardson plot (21.50) is now modified (and is nonlinear in $1/T$) to

$$\ln\left(\frac{j_s}{T^2}\right) = \ln A^* - \frac{F_{Bn}}{kT} + \frac{\sigma_F^2}{2\,k^2\,T^2}\,. \tag{21.58}$$

In [1721] the barrier nonuniformity due to the random distribution and discreteness of impurity charges in the depletion region is evaluated. This mechanism, yielding increasing barrier inhomogeneity for larger doping, represent a fundamental limit to the ideality of a Schottky diode.

If the distribution of barrier heights is discrete, at low voltages the current will first flow at certain spots with low barrier ('hot spots'). This leads to kinks in the I–V characteristics as found for SiC [1722] or ZnO [1723] (Fig. 21.15).

Temperature Dependence

Figure 21.16a shows the temperature-dependent I–V characteristics of a Pd/ZnO Schottky diode. A straightforward evaluation according to (21.48) results in a barrier height of about 700 meV and a Richardson constant that is orders of magnitude smaller than the theoretical value of 32 A K^{-2} cm^{-2} (for $m_e^* = 0.27$). A fit of the temperature-dependent data with (21.57), as shown in Fig. 21.16b, results in $\bar{F}_{Bn} = 1.1$ eV, in agreement with the (temperature-independent) value obtained from CV spectroscopy, and $\sigma_F = 0.13$ eV [1724].

The temperature dependence of the ideality factor n is given by [1725]

[10] This phenomenon is similar to the red-shift of luminescence lines (Stokes shift) due to thermalization in the presence of disorder, see Sect. 12.4.

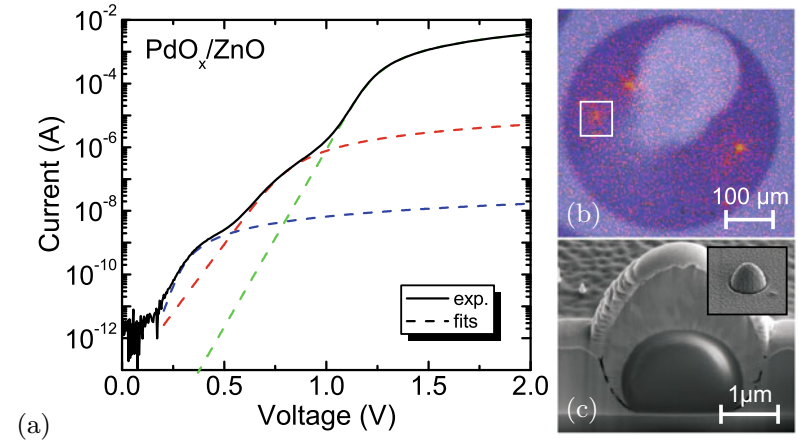

Fig. 21.15 **a** I–V characteristic of ZnO Schottky diode (*solid line*) with fits due to regions with three different barrier heights (*dashed lines*). **b** Thermography image at bias of 1 V. The *white square* marks the area where one hot spot was investigated in detail. **c** SEM image of FIB prepared cross section of a defect (Al_2O_3 particle) causing the lowest barrier hot spots, *inset*: plane view of such defect before preparation. Adapted from [1723]

$$n = \frac{1}{1 - \rho_2 + \rho_3/(2kT)} \,, \tag{21.59}$$

where ρ_2 (ρ_3) is the (temperature-independent) proportionality coefficient of the bias dependence of the mean barrier height (standard deviation), i.e.

$$\rho_2 = \frac{1}{e} \frac{\partial \bar{F}_{\mathrm{Bn}}}{\partial V} \tag{21.60a}$$

$$\rho_3 = \frac{1}{e} \frac{\partial \sigma_F^2}{\partial V} \,. \tag{21.60b}$$

The fit of $1/n - 1$ versus $1/T$ in Fig. 21.16c yields $\rho_2 = -0.025$ and $\rho_3 = -0.028\,\mathrm{eV}$ for the ZnO diodes under investigation.

The forward I–V characteristic of an Au/GaAs Schottky diode reported in [1726, 1727] is shown in Fig. 21.17a at various temperatures. The current amplitude decreases with decreasing temperature due to the temperature dependence of the saturation current (21.48). Also, the slope V_0^{-1} of the characteristic $j = j_s \exp(V/V_0)$ varies with temperature. Looking at the temperature dependence of V_0, it is described as $V_0 = k(T + T_0)/e$ rather than with an ideality factor n in the form of $V_0 = nkT/e$. In other words, the ideality factor follows a temperature dependence $n = 1 + T_0/T$. In view of (21.59), such behavior means for small T_0 that $n \approx 1/(1 - T_0/T)$ and thus $\rho_2 = 0$ and $\rho_3 = 2kT_0$. For $T_0 = 45\,\mathrm{K}$, ρ_3 is 0.008 eV, which is a fairly small value. Thus, the temperature behavior of the diode is due to the narrowing of the Gaussian distribution of barrier height with bias voltage [1720].

In a set of similar diodes with varying magnitude of barrier inhomogeneities, it is found that the effective barrier height and the ideality factor correlate [1728]. The extrapolation to $n = n_{\mathrm{if}}$ yields the limit of the barrier height for a homogeneous barrier (Fig. 21.18). For silicon, it is found that the surface orientation has a minor influence on the Schottky barrier height (Fig. 21.18b) for an unreconstructed surface. The presence of a reconstruction lowers the barrier height[11] (Fig. 21.18a).

[11] Reconstructions are accompanied by redistributions of the valence charge with respect to the undisturbed bulk (Sect. 11.4). The subsequent extra interface dipoles alter the barrier heights of reconstructed interfaces [1728].

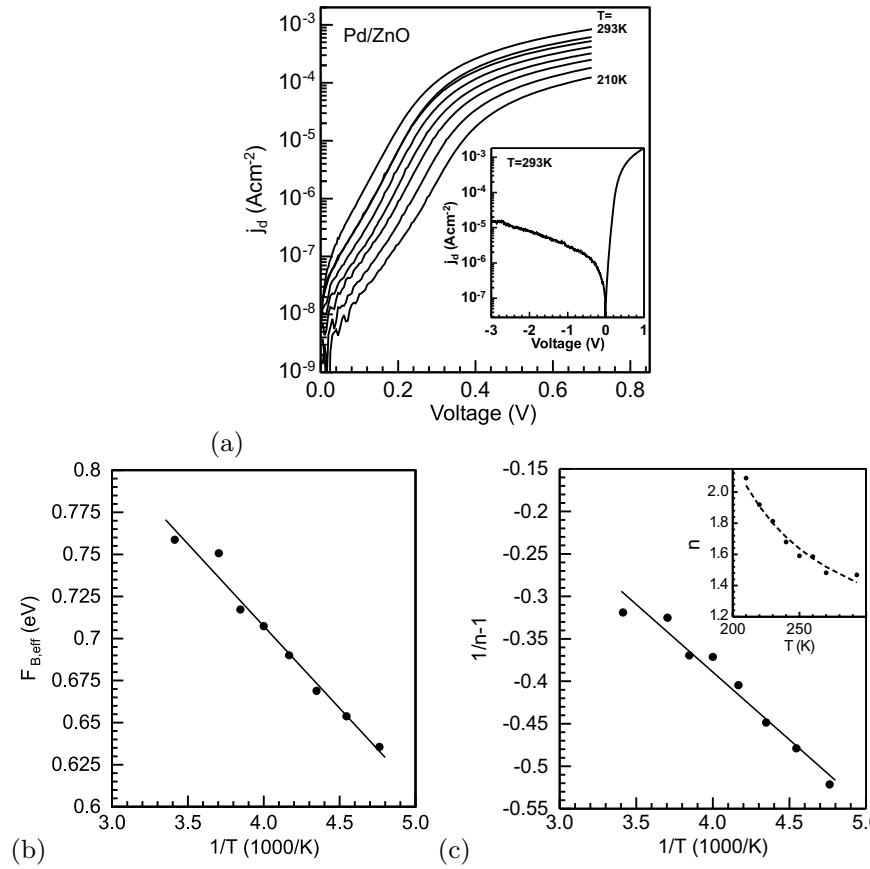

Fig. 21.16 **a** Forward I–V characteristic of Pd/ZnO Schottky diodes for various temperatures. Diode temperatures are 210, 220, 230, 240, 250, 260, 270, and 293 K. The *inset* shows the current density versus voltage for 293 K on a semilogarithmic scale. **b** Effective barrier height $F_{\mathrm{Bn}}^{\mathrm{j}}$ versus the inverse temperature. The *solid line* is a linear fit according to (21.57) yielding the standard deviation $\sigma_F = 0.13\,\mathrm{eV}$ and the mean barrier height $\bar{F}_{\mathrm{Bn}} = 1.1\,\mathrm{eV}$. (**c**) Plot of $1/n - 1$ versus the inverse temperature. The *solid line* is a linear fit of the data yielding the voltage deformation coefficients $\rho_2 = -0.025$ and $\rho_3 = -0.028\,\mathrm{eV}$. The *inset* shows the experimentally determined n factors and the n factors calculated from (21.59) using the voltage-deformation coefficients obtained from the linear fit (*dashed line*). Adapted from [1724]

Correlation of Barrier Height and Ideality Factor

Diffusion Theory

In diffusion theory the current density is considered in the presence of a carrier-density and electric-field gradient. In the Boltzmann approximation the electron current is given by (8.60a). In stationary equilibrium the current density is constant, i.e. independent of x. Assuming that the carrier density has its equilibrium values at $x = 0$ and $x = w$, we find after integration and using (21.8)

$$\begin{aligned} j &= -e\,\mu_n\,N_{\mathrm{C}}\,E_{\mathrm{m}}\,\exp\left(-\frac{F_{\mathrm{Bn}}}{kT}\right)\left[\exp\left(\beta V\right)-1\right] \\ &= j_{\mathrm{s}}\left[\exp\left(\beta V\right)-1\right]\,. \end{aligned} \tag{21.61}$$

Therefore, also in this case the ideal diode characteristic is obtained, however, with a different saturation current. The ideality factor in diffusion theory is $n = 1.06$ (for $F_{\mathrm{Bn}} \gtrsim 15\,kT$) [1684].

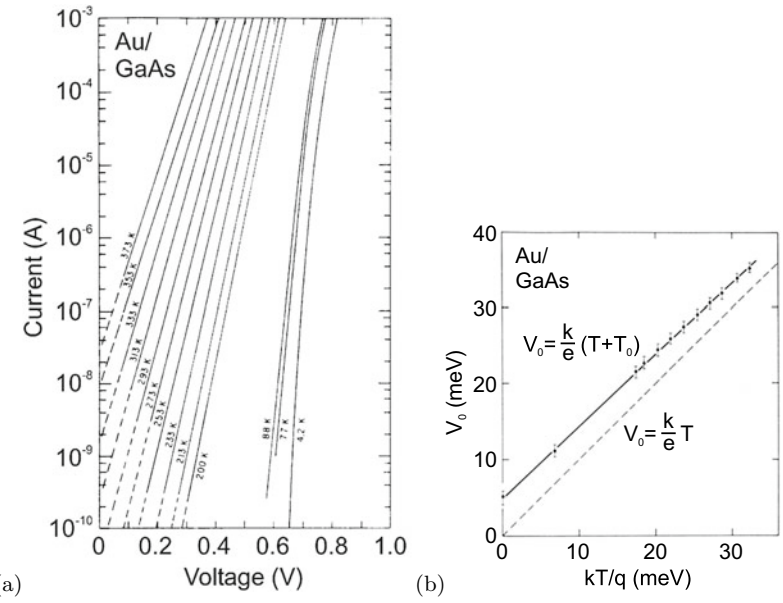

Fig. 21.17 **a** Forward I–V characteristic of Au/GaAs diode for various temperatures. **b** Temperature dependence of the voltage V_0. The experimental data are fitted with $T_0 = 45 \pm 8$ K. Adapted from [1726]

Combined Theory

A combination of both theories [1729] considers both mechanisms to be in series. The current can then be expressed as

$$j = \frac{eN_C v_r}{1 + v_r/v_D} \exp\left(-\frac{F_{Bn}}{kT}\right)\left[\exp(\beta V) - 1\right] \tag{21.62a}$$

$$= A^{**} T^2 \left[\exp(\beta V) - 1\right] \tag{21.62b}$$

$$= j_s \left[\exp(\beta V) - 1\right] .$$

Here $v_r = \bar{v}/4$ is a 'recombination velocity' [1730] at the top of the barrier according to $j = v_r(n - n_0)$, n_0 being the equilibrium electron density at the top of the barrier and $\bar{v}$ is the average thermal velocity in the semiconductor. v_D is an effective diffusion velocity describing the transport of electrons from the edge of the depletion layer ($x = w$) to the top of the barrier ($x = x_m$). It is defined as

$$v_D^{-1} = \int_{x_m}^{w} \frac{-e}{\mu_n kT} \exp\left(-\frac{F_{Bn} - E_C(x)}{kT}\right) dx . \tag{21.63}$$

In [1729] μ_n has been assumed to be independent of the electric field. This assumption is potentially not realistic. If $v_D \gg v_r$, thermionic theory applies and we obtain (21.48). The case $v_r \gg v_D \sim \mu_n E_m$ relates to diffusion theory and we recover (21.61).

The constant A^{**} in (21.62b) is called the effective Richardson constant. Its calculated dependence on the electric field is shown in Fig. 21.19 for Si. At room temperature for most Ge, Si and GaAs Schottky diodes the thermionic emission of majority carriers is the dominating process. The effect of lateral barrier height inhomogeneity in a diffusion model has been discussed in [1731].

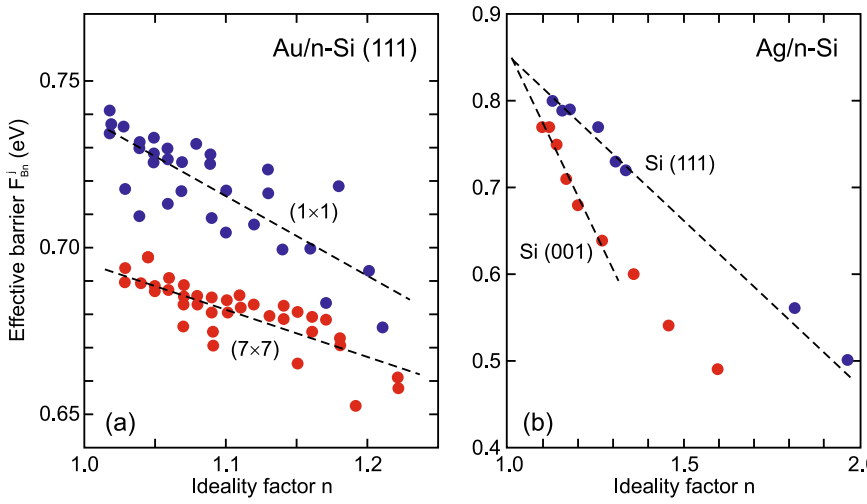

Fig. 21.18 **a** Effective barrier height versus ideality factor for Ag/n-Si Schottky diodes prepared on Si(111) surface with (7 × 7) reconstruction or unreconstructed (1 × 1) as labeled. The more ideal (1 × 1) surface exhibits the higher barrier. The *dashed lines* are linear fits. **b** Effective barrier height versus ideality factor for Au/n-Si Schottky diodes prepared on HF-dipped (1 × 1) unreconstructed (001) and (111) surfaces. The *dashed lines* are linear fits and extrapolation to $n = n_{if}$. Both surface orientations exhibit the same extrapolated homogeneous barrier height. Based on data compiled in [1728]

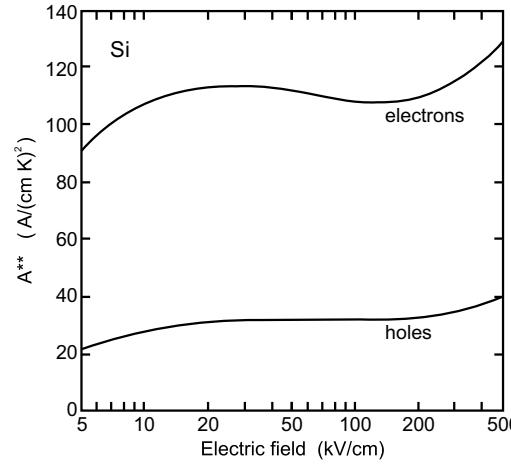

Fig. 21.19 Calculated effective Richardson constant A^{**} as a function of the electric field for a metal-Si diode at $T = 300\,\mathrm{K}$ for a (n-type or p-type) doping of $10^{16}\,\mathrm{cm}^{-3}$. Adapted from [1732]

Tunneling Current

At high doping the width of the depletion layer becomes small and tunneling processes become more probable. Also at low temperatures, when thermionic emission is very small, tunneling processes can dominate the transport between metal and semiconductor. One process is tunneling of electrons close to the Fermi level of the semiconductor. This process is called field emission (F) and is at least important for degenerate semiconductors at very low temperatures. If the temperature is raised, electrons are excited to higher energies where they encounter a thinner barrier. The tradeoff between thermal energy and barrier width selects an electron energy E_m above the conduction-band edge for which the current is largest. This process is known as thermionic field emission (TF). For very high temperatures enough carriers can overcome the barrier completely and we are back in the thermionic emission regime. The

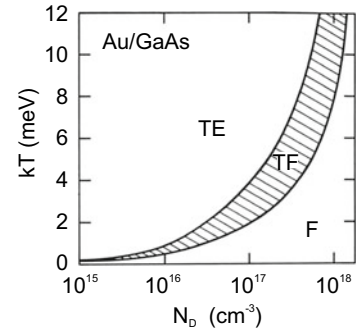

Fig. 21.20 Calculated conditions for thermionic field ('TF'), field ('F') and thermionic ('TE') emission in a Au/GaAs Schottky diode as a function of temperature and doping concentration. Adapted from [1684]

validity of the two regimes is shown in Fig. 21.20 for Au/GaAs Schottky diodes as a function of doping concentration (n-type) and temperature.

Tunneling through the image-charge effect rounded triangular Schottky barrier is discussed in detail in [1733]. In the field-emission regime the forward current is given by [1684]

$$j = j_s \exp\left(\frac{eV}{E_{00}}\right) , \tag{21.64}$$

with the characteristic energy parameter E_{00} given by

$$E_{00} = \frac{e\hbar}{2}\sqrt{\frac{N_D}{m^*\epsilon_s}} . \tag{21.65}$$

The saturation current is

$$j_s \propto \exp\left(-\frac{F_{Bn}}{E_{00}}\right) . \tag{21.66}$$

In Fig. 21.21, the forward characteristic of a highly doped Au/Si is shown. The experimental value of $E_{00} = 29\,\text{meV}$ agrees well with the theoretical expectation of $E_{00} = 29.5\,\text{meV}$. Note that at $T = 77\,\text{K}$ $kT = 7\,\text{meV}$, thus thermionic emission is excluded for the diode current.

In the reverse direction the I–V characteristic under field emission is given by [1684]

$$j = \frac{4\pi\, e\, m^*}{h^3} E_{00}^2 \frac{e\,(V_{bi} - V)}{F_{Bn}} \exp\left(-\frac{2\,F_{Bn}^{3/2}}{3E_{00}\sqrt{e(V_{bi} - V)}}\right) . \tag{21.67}$$

From Fig. 21.21b, a barrier height of 0.79 eV is deduced.

In the TF-emission regime the current-voltage characteristic is given by

$$j = j_s \exp\left(\frac{eV}{E_0}\right) , \tag{21.68}$$

with

$$E_0 = E_{00} \coth\left(\frac{E_{00}}{kT}\right) , \tag{21.69}$$

where E_{00} is given by (21.65). The energy for maximum TF emission E_m is given by $E_m = e(V_{bi} - V)/\cosh^2(E_{00}/kT)$. The coth-dependence of E_0 is shown in Fig. 21.22 for an Au/GaAs diode.

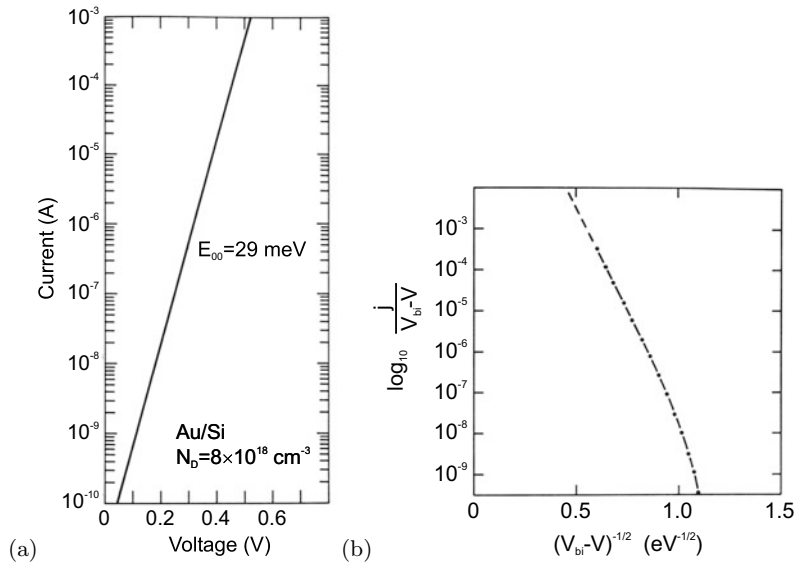

Fig. 21.21 **a** Forward and **b** reverse I–V characteristic of a Au/Si Schottky diode at 77 K. The doping concentration of the Si was $N_D = 8 \times 10^{18}\,\mathrm{cm}^{-3}$. Adapted from [1684]

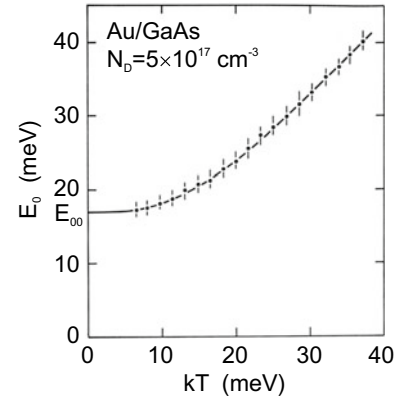

Fig. 21.22 Temperature dependence of E_0 of an Au/GaAs diode with $N_D = 5 \times 10^{17}\,\mathrm{cm}^{-3}$. The *solid line* is the theoretical dependence for thermionic emission according to (21.69) with $N_D = 6.5 \times 10^{17}\,\mathrm{cm}^{-3}$ and $m^* = 0.07$. Adapted from [1684]

A Schottky diode can suffer from non-idealities such as series and parallel ohmic resistance [1725]. These effects are discussed in some detail below for pn diodes in Sect. 21.4.4 and apply similarly to Schottky diodes.

21.2.6 Ohmic Contacts

Although an ohmic contact does not have a diode characteristic, it can be understood from the previous remarks. An ohmic contact will have a small contact resistance for both current directions. The voltage drop across the contact will be small compared to the voltage drop in the active layer (somewhere else). Details on electric contacts can be found in [1734].

The contact resistance R_c is defined as the differential resistance at $V = 0$

$$R_c = \left(\frac{\partial I}{\partial V} \right)^{-1}_{V=0} . \tag{21.70}$$

At low doping, the transport is dominated by thermionic emission (21.48). In this case R_c is given by

$$R_c = \frac{k}{e\,A^*\,T}\,\exp\left(\frac{F_{Bn}}{kT}\right)\,. \tag{21.71}$$

A small barrier height (Fig. 21.23a) will lead to small contact resistance. A negative Schottky barrier height, i.e. $W_m < E_{vac} - E_F$ for a n-type semiconductor, leads to an accumulation layer without a barrier for carrier transport (Fig. 21.23b).

For high doping R_c is determined by the tunneling current (Fig. 21.23c) and is proportional to

$$R_c \propto \exp\left(\frac{F_{Bn}}{E_{00}}\right)\,. \tag{21.72}$$

The contact resistance decreases exponentially with the doping. A theoretical calculation and experimental data are compared in Fig. 21.24 for contacts on Si.

The three mechanisms, low barrier height, accumulation layer and high doping, for the formation of Ohmic contacts are summarized schematically in Fig. 21.23. Ohmic contacts on wide band gap semiconductors are difficult, since metals with sufficiently small (large) work function for contacting n-type (p-type) material are mostly not available.

Although Schottky contact devices have their place in semiconductor technology, Ohmic contacts are indispensable for almost all devices.[12] Ohmic contacts are typically prepared by evaporating a contact metal containing the doping material for the semiconductor, e.g. Au/Zn for a contact on p-type GaAs [1737] and Au/Ge for a contact [1738] on n-type GaAs. The contact is alloyed around 400–500 °C (see Fig. 21.25) above the eutectic temperature of $T_{eu} = 360\,°C$ (for Au/Ge) to form a eutectic liquid in which the dopant can quickly diffuse. When the eutectic liquid cools it forms a solid, a highly doped semiconductor layer underneath the metal. The liquid-phase reactions can lead to inhomogeneous contacts. On n-type GaAs Pd/Ge/Au contacts have been reported to have superior structural quality [1739]. Ohmic contacts for a number of different semiconductors are reviewed in [1740, 1741].

The current-voltage characteristics of an intrinsic (low carrier density, trap-free) semiconductor with ohmic contacts is dominated by so-called *space-charge limited current* (SCLC) as proposed by Mott and Gurney [1743, 1744]. In a one-dimensional model, the semiconductor of length L is considered with ohmic contacts and applied voltage V_0 (applied electrical field $E_0 = V_0/L$). The thermal carriers shall be negligible compared to the injected ones. The space charge density ρ in the current density $j = \rho\,v = \rho\,\mu\,E$ is then in the space-charge limited regime due to the dependence of the electric field $\mathrm{d}E/\mathrm{d}x = \rho/\epsilon$ within the semiconductor (also $E = -\mathrm{d}V/\mathrm{d}x$). Therefore the current density can be written as

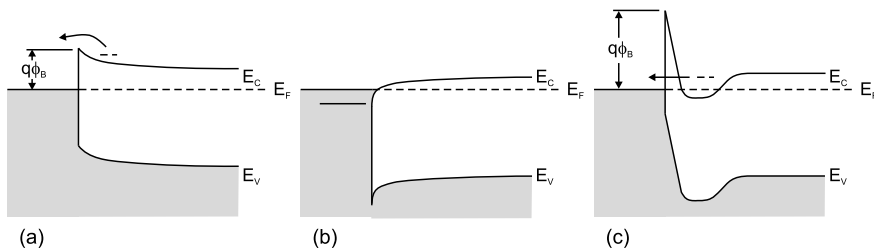

Fig. 21.23 Schematic conditions for the formation of an Ohmic contact, **a** low barrier height, **b** accumulation layer **c** high doping (thin depletion layer)

[12] Also a Schottky diode has an Ohmic back contact.

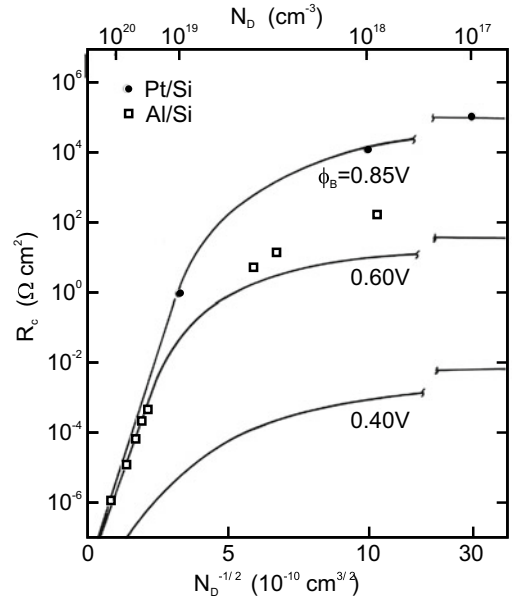

Fig. 21.24 Theoretical and experimental values of specific contact resistances at $T = 300\,\mathrm{K}$ for Al/n-Si [1735] and PtSi/n-Si [1736] contacts as a function of donor concentration. *Solid lines* are theoretical dependencies for different values of the barrier height as labeled. Adapted from [574]

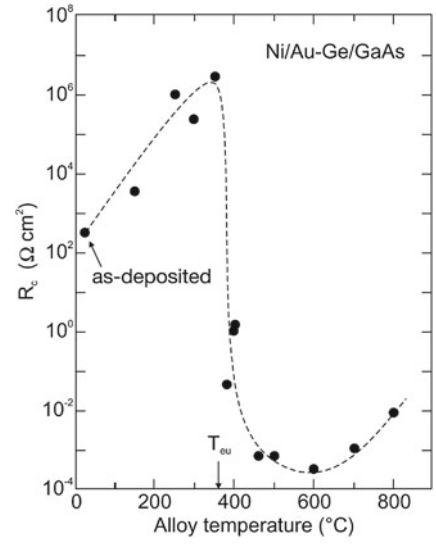

Fig. 21.25 Specific contact resistance for Ni/Au-Ge on n-type epitaxial GaAs for varying alloying temperatures (2 min). *Arrow* at T_{eu} denotes the eutectic temperature of Au-Ge. Adapted from [1742]

$$j = \epsilon\,\mu\,E\,\frac{\mathrm{d}E}{\mathrm{d}x}\,. \tag{21.73}$$

Integration (remember that j is independent of x) and the boundary condition $E(x=0)=0$ yields

$$E(x) = \left(\frac{2\,j}{\mu\,\epsilon}\right)^{1/2}\sqrt{x}\,. \tag{21.74}$$

We integrate again and find

$$V(x) = \frac{2}{3}\left(\frac{2\,j}{\mu\,\epsilon}\right)^{1/2} x^{3/2}\,, \tag{21.75}$$

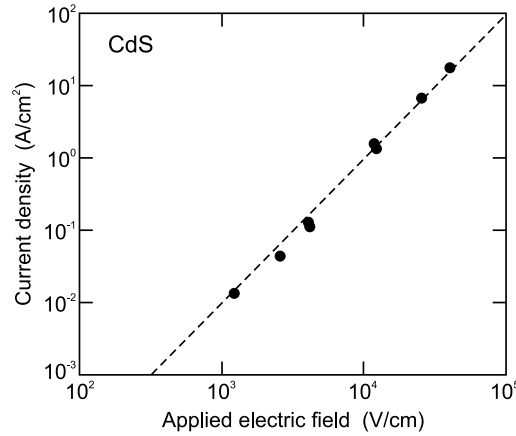

Fig. 21.26 Current density from the beginning ($\approx 100\,\mu$s) of a pulsed experiment versus applied field (applied voltage divided by sample thickness) for 50 μm thick CdS crystal between indium-tipped electrodes. The dashed line shows a V^2-dependence. Adapted from [1748]

and for j (and $E_0 = V_0/L$) therefore the Mott-Gurney law[13]

$$j = \frac{9}{8}\,\frac{\mu\,\epsilon}{L^3}\,V_0^2 = \frac{9}{8}\,\frac{\mu\,\epsilon}{L}\,E_0^2\,. \tag{21.76}$$

A quantum theory of space-charge limited current has been put forward in [1747]. For small voltages, Ohm's law $j \propto V_0$ is valid.

The $j \propto V^2$-dependence has been first observed for CdS [1748, 1749]. In order to avoid the effect of injected charge being trapped, pulsed measurements are applied [1748]; in this case, the V^2-dependence is well fulfilled (trap-free SCLC) (Fig. 21.26) while the steady-state current would be many orders of magnitude smaller. In [1750], an investigation of crystalline silicon and also a theory for bipolar transport can be found. Equation (21.76) can also serve to determine the mobility if the conditions for space-charge limited current are fulfilled. Modifications are necessary in the presence of traps as discussed in [1751] for the case of amorphous silicon.

21.2.7 Metal Contacts to Organic Semiconductors

Also, for organic semiconductors the metal contact plays a vital role, either for carrier injection or for manipulation of the space-charge region. The position of the Fermi level has been determined for various organic semiconductors as shown in Fig. 21.27. These data have been obtained from measurements on metal-semiconductor-metal structures (MSM, see also Sect. 22.3.5) as shown in Fig. 21.28a. The thin (50 nm) organic layer is fully depleted, thus the built-in field inside the semiconductor is constant. The built-in field is measured by applying an external dc bias and finding the external potential at which the electroabsorption signal vanishes. Figure 21.28b shows the measured electroabsorption signal $\Delta T/T$ (relative change of transmission T) and the optical density of an MEH-PPV film as a function of photon energy for an Al/MEH-PPV/Al structure. The exciton absorption peak is found at 2.25 eV. The bias at which the built-in field vanishes can then be determined for various other metals in metal/MEH-PPV/Al structures. Figure 21.27 summarizes such results for various metals and three organic semiconductors. The plot of the Fermi level position versus the metal work function (Fig. 21.28d,e) shows that the metals investigated do not introduce interface states in the single-particle gap that pin the Schottky

[13] For transport in vacuum where the electron motion is accelerated, $j \propto V_0^{3/2}$ was found earlier, [1745, 1746]

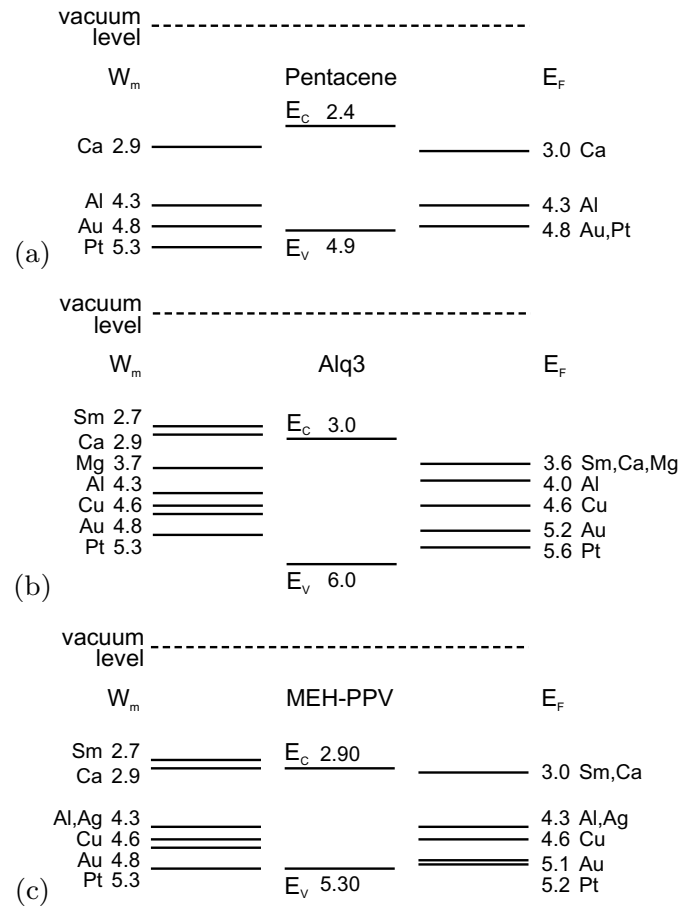

Fig. 21.27 Measured Fermi energies E_F (*labeled data* in eV) and the work functions W_m of various metals contacting (**a**) pentacene, (**b**) Alq_3 and (**c**) MEH-PPV. E_C (E_V) denotes the energy position of the electron (hole) polaron. Measured data for E_F for MEH-PPV from [1753], other from [1754]. Data for W_m from Table 21.2

barrier (see Fig. 21.5 for inorganic semiconductors). An electron trap, such as C_{60} in MEH-PPV, can pin the Fermi level of the n-contact metal and leads to a change of the built-in potential [1752].

Space-charge limited currents (see Sect. 21.2.6) are often observed in organic semiconductors. An analysis including the effects of traps has been reported in [1755].

21.3 Metal-Insulator-Semiconductor Diodes

In a metal-insulator-semiconductor (MIS) diode an insulator is sandwiched between the metal and the semiconductor. Subsequently, a MIS contact has zero dc conductance. The semiconductor typically has an ohmic back contact. As insulator, often the oxide of the respective semiconductor, is used. In particular SiO_2 on Si has been technologically advanced (Fig. 21.29). In the latter case, the diode is called a MOS (metal-oxide-semiconductor) diode. This structure has great importance for the investigation of semiconductor surfaces and overwhelming importance for semiconductor technology (planar integration of electronic circuits, CMOS technology). Also, CCDs (Sect. 22.3.8) are based on MIS diodes.

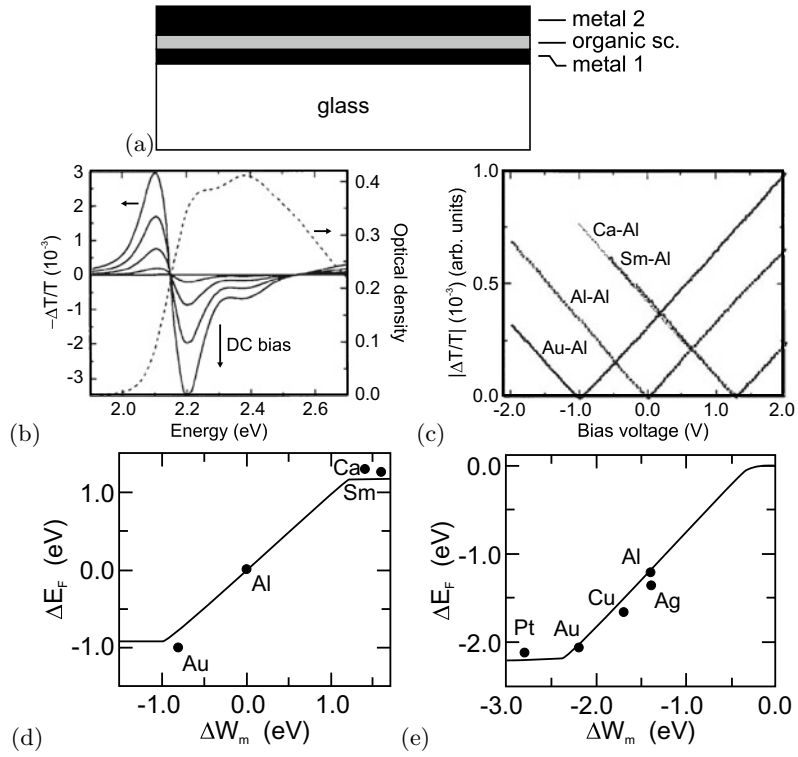

Fig. 21.28 **a** Schematic MSM structure with organic semiconductor (sc.) on transparent glass substrate. Metal 1 is thin and semitransparent. Thickness of organic semiconductor (polymer or small molecules) is about 50 nm. **b** Electroabsorption spectra of Al/MEH-PPV/Al structure at four dc bias voltages (*solid lines*) and optical density spectrum (*dashed line*). **c** Magnitude of the electroabsorption response at 2.1 eV as a function of bias for metal/MEH-PPV/Al structures. **d**, **e** Calculated (*solid lines*) and experimental (*points*) potential difference across (**d**) metal/MEH-PPV/Al structures and (**e**) metal/MEH-PPV/Ca structures as a function of the work-function difference of the contacts. Parts (**b**)–(**e**) adapted from [1753]

21.3.1 Band Diagram for Ideal MIS Diode

An ideal MIS diode has to fulfill the following three conditions:

(i) (as shown in Fig. 21.30) without external bias the energy difference W_{ms} between the work function of the metal and the semiconductor

$$W_{ms} = (-e)\,\phi_{ms} = W_m - \left(\chi_{sc} + \frac{E_g}{2} \pm e\,\Psi_B\right) \tag{21.77}$$

is zero ($\phi_{ms} = 0$). The '+' ('−') sign in (21.77) applies to a p-type, Fig. 21.30b (n-type, Fig. 21.30a) semiconductor. Ψ_B is the potential difference between the intrinsic and actual Fermi level, $\Psi_B = |E_i - E_F|/e > 0$.

(ii) The only charges present are those in the semiconductor and the opposite charge is on the metal surface close to the insulator.

(iii) There is no dc current between the metal and the semiconductor, i.e. the conductivity of the insulator is zero.

The quantity Ψ_B (Fig. 21.32) is given as (for a p-type material, using (7.18), the high temperature approximation (7.32) and (7.15))

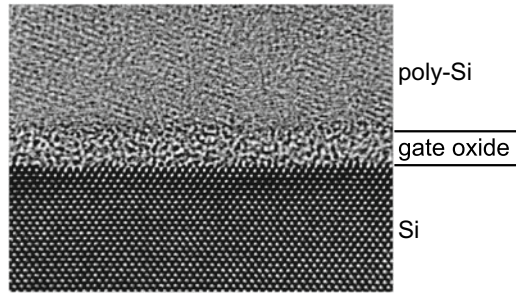

Fig. 21.29 High-resolution transmission electron microscopy image of a 1.6-nm thick gate oxide between poly-Si (cf. Sect. 24.5.4) and crystalline Si. From [1756]

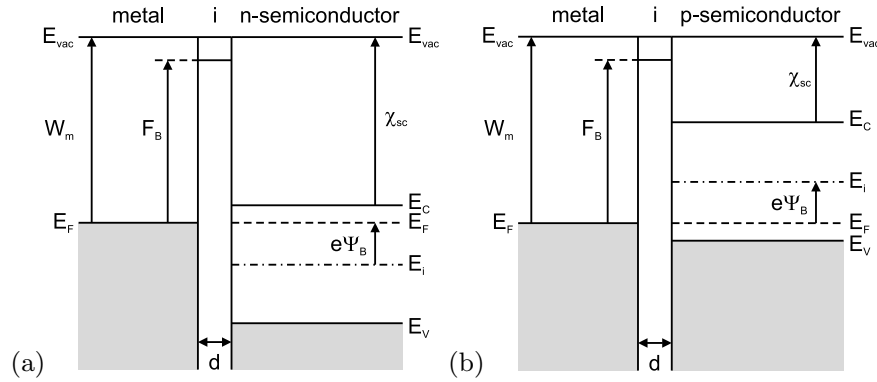

Fig. 21.30 Band diagram of an ideal MIS diode with **a** n- and **b** p-type semiconductor at external bias $V = 0$. The insulator ('i') thickness is d as labeled. The *dash-dotted line* represents the intrinsic Fermi level E_i

$$
\begin{aligned}
e\,\Psi_\mathrm{B} = E_\mathrm{i} - E_\mathrm{F} &= \left[\frac{E_\mathrm{C} + E_\mathrm{V}}{2} + \frac{kT}{2}\,\ln\left(\frac{N_\mathrm{V}}{N_\mathrm{C}}\right)\right] - \left[E_\mathrm{V} - kT\,\ln\left(\frac{N_\mathrm{A}}{N_\mathrm{V}}\right)\right] \\
&= \frac{E_\mathrm{g}}{2} + kT\,\ln\left(\frac{N_\mathrm{A}}{\sqrt{N_\mathrm{C}\,N_\mathrm{V}}}\right) = kT\,\ln\left(\frac{N_\mathrm{A}}{n_\mathrm{i}}\right)\,. \qquad (21.78)
\end{aligned}
$$

When an ideal MIS diode is biased, three general cases—accumulation, depletion and inversion— can occur (Fig. 21.35). We discuss these first for the p-type semiconductor.

Figure 21.35d shows the accumulation case for a negative voltage at the metal.[14] Part of the voltage drops across the insulator, the rest across the semiconductor. The valence band is bent upwards towards the Fermi level. The quasi-Fermi level in the semiconductor, however, is constant since no dc current flows (Fig. 21.31).[15]

Since the charge-carrier (hole) density depends exponentially on the energy separation $E_\mathrm{F} - E_\mathrm{V}$, a charge accumulation (of holes) occurs in the (p-type) semiconductor in the vicinity of the interface to the insulator.

[14] This poling is a forward bias of the respective Schottky diode since the positive pole is at the p-type semiconductor.

[15] We note that in order to reach the situations shown in Fig. 21.35 from the zero bias case of Fig. 21.30, a current must have flowed since charge carriers are redistributed. Figure 21.35 depicts the stationary equilibrium after transient voltage switch-on effects have subsided. The time, however, that is needed in order to reach such stationary equilibrium from zero bias (thermal equilibrium) may be very long (e.g. days, cf. Sect. 22.3.8).

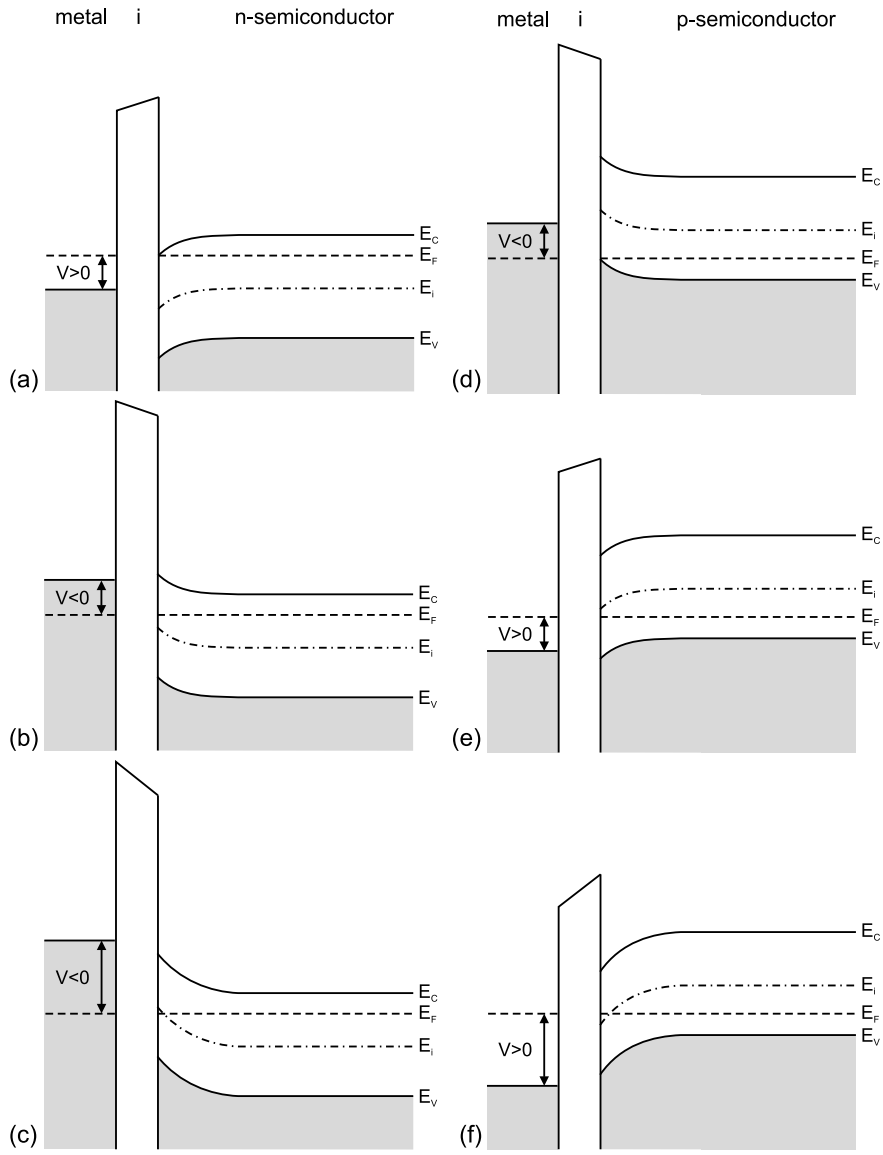

Fig. 21.31 Band diagram of ideal MIS diodes with **a**, **b**, **c** n-type and **d**, **e**, **f** p-type semiconductors for $V \neq 0$ in stationary equilibrium for the cases **a**, **d** accumulation, **b**, **e** depletion and **c**, **f** inversion

In Fig. 21.35e the depletion case is shown. Now a moderate reverse voltage, i.e. a positive bias to the metal, is applied. A depletion of majority charge carriers occurs in the semiconductor close to the insulator. The quasi-Fermi level in the semiconductor remains beneath the intrinsic level ($E_\mathrm{i} \approx E_\mathrm{C} + E_\mathrm{g}/2$), i.e. the semiconductor remains p-type everywhere. If the voltage is increased further to large values, the quasi-Fermi level intersects the intrinsic level and lies *above* E_i close to the insulator (Fig. 21.35f). In this region, the electron concentration becomes larger than the hole concentration and the inversion regime is reached. The inversion is called 'weak' if the Fermi level is still close to E_i. The inversion is called 'strong' when the Fermi level lies close to the conduction-band edge with an accordingly large inversion charge.

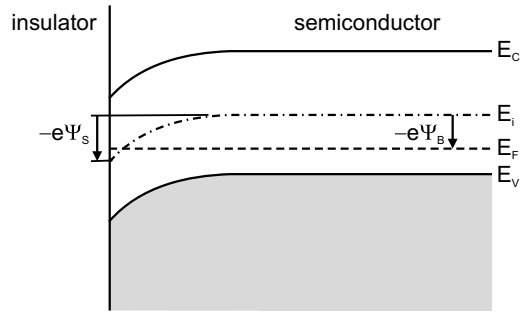

Fig. 21.32 Band diagram close to the interface of a p-type semiconductor MIS diode. Accumulation occurs for $\Psi_s < 0$, depletion for $\Psi_s > 0$ and inversion (as shown here) for $\Psi_s > \Psi_B > 0$

The corresponding phenomena occur for n-type semiconductors for the opposite signs of the voltage with electron accumulation and depletion. In the inversion case, $p > n$ close to the insulator (Fig. 21.35a–c).

21.3.2 Space-Charge Region

Now we calculate the charge and electric field distribution in an ideal MIS diode, following the treatment in [1757]. We introduce the potential Ψ that measures the separation of the intrinsic bulk Fermi level and the actual intrinsic level E_i, i.e. $-e\Psi(x) = E_i(x) - E_i(x \to \infty)$ (see Fig. 21.32). Its value at the surface is termed Ψ_s, the surface potential. The value is positive, i.e. $\Psi_s > 0$, if the intrinsic Fermi level at the surface is below the bulk Fermi level.

The electron and hole concentrations are given (for a p-type semiconductor) as

$$n_p = n_{p_0} \exp(\beta\Psi) \tag{21.79a}$$
$$p_p = p_{p_0} \exp(-\beta\Psi) \,, \tag{21.79b}$$

where n_{p_0} (p_{p_0}) are the bulk electron (hole) concentrations, respectively, and $\beta = e/kT > 0$.

Therefore, the net free charge is given by

$$n_p - p_p = n_{p_0} \exp(\beta\Psi) - p_{p_0} \exp(-\beta\Psi) \,. \tag{21.80}$$

The electron and hole concentrations at the surface are denoted with an index 's' and are given by[16]

$$n_s = n_{p_0} \exp(\beta\Psi_s) \tag{21.81a}$$
$$p_s = p_{p_0} \exp(-\beta\Psi_s) \,. \tag{21.81b}$$

We use the Poisson equation $\frac{d^2\Psi}{dx^2} = -\frac{\rho}{\epsilon_s}$ with the charge given by

$$\rho(x) = e\left[p_p(x) - n_p(x) + N_D^+(x) - N_A^-(x)\right] \,. \tag{21.82}$$

As boundary condition we employ that far away from the surface (for $x \to \infty$) there is charge neutrality (cf. (7.40)), i.e.

$$n_{p_0} - p_{p_0} = N_D^+ - N_A^- \,, \tag{21.83}$$

[16] Ψ_s represents the voltage drop across the semiconductor that will be discussed in more detail in Sect. 21.3.3. In this sense, Ψ_s for the MIS diode is related to $V_{bi} - V$ for the Schottky contact.

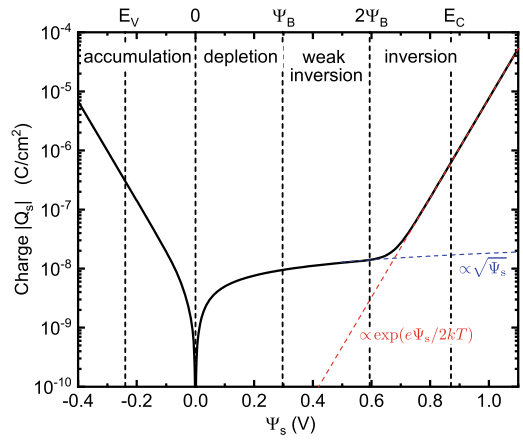

Fig. 21.33 Dependence of the space charge on the surface potential Ψ_s for p-type silicon with $N_A = 10^{15}\,\mathrm{cm}^{-3}$ at $T = 300\,\mathrm{K}$. The flat-band condition is present for $\Psi_s = 0$, strong inversion for $\Psi_s > 2\,\Psi_B$. The *dashed blue* (*red*) line is the dependence of the depletion (inversion) charge

and that $\Psi = 0$. The ionization of the dopants only depends on temperature which is everywhere the same[17]; thus $N_D^+ - N_A^-$ is constant throughout the homogeneous semiconductor. Therefore (21.83) (but not charge neutrality) holds everywhere in the semiconductor. Using (21.80) the Poisson equation reads

$$\frac{\partial^2 \Psi}{\partial x^2} = -\frac{e}{\epsilon_s}\{p_{p_0}\left[\exp(-\beta\Psi) - 1\right] - n_{p_0}\left[\exp(\beta\Psi) - 1\right]\}\,. \tag{21.84}$$

The Poisson equation is integrated and with the notations

$$\mathcal{F}(\Psi) = \sqrt{\left[\exp(-\beta\Psi) + \beta\Psi - 1\right] + \frac{n_{p_0}}{p_{p_0}}\left[\exp(\beta\Psi) - \beta\Psi - 1\right]} \tag{21.85a}$$

$$L_D = \sqrt{\frac{\epsilon_s\, kT}{e^2\, p_{p_0}}} = \sqrt{\frac{\epsilon_s}{e\,\beta\, p_{p_0}}}\,, \tag{21.85b}$$

with L_D being the Debye length (screening effect) for holes, the electric field can be written as

$$E = -\frac{\partial \Psi}{\partial x} = \pm\frac{\sqrt{2}\,kT}{e\,L_D}\mathcal{F}(\Psi)\,. \tag{21.86}$$

The positive (negative) sign is for $\Psi > 0$ ($\Psi < 0$), respectively. At the surface, Ψ_s will be taken as the value for Ψ. The total charge Q_s per unit area creating the surface field

$$E_s = -\left.\frac{\partial \Psi}{\partial x}\right|_{x=0} = \pm\frac{\sqrt{2}\,kT}{e\,L_D}\mathcal{F}(\Psi_s) \tag{21.87}$$

is given by the one-dimensional Gauss law as $Q_s = -\epsilon_s\, E_s$.

The dependence of the space-charge density from the surface potential[18] is depicted in Fig. 21.33. When Ψ_s is negative, $\mathcal{F}$ is dominated by the first term in (21.85a) and the space charge is positive (accumulation) and proportional to $Q_s \propto \exp(\beta|\Psi|/2)$. For $\Psi_s = 0$ the (ideal) MIS diode is under flat-band condition and the space charge is zero. For $\Psi_s > 0$ the space charge is negative. For $0 < \Psi_s \leq \Psi_B$

[17] The donor and acceptor ionization energies do not change upon Ψ.

[18] We note that we discuss the space-charge region now only with regard to Ψ_s, the voltage drop across the semiconductor, and the dependence of Ψ_s on the bias of the diode will be discussed in the next section.

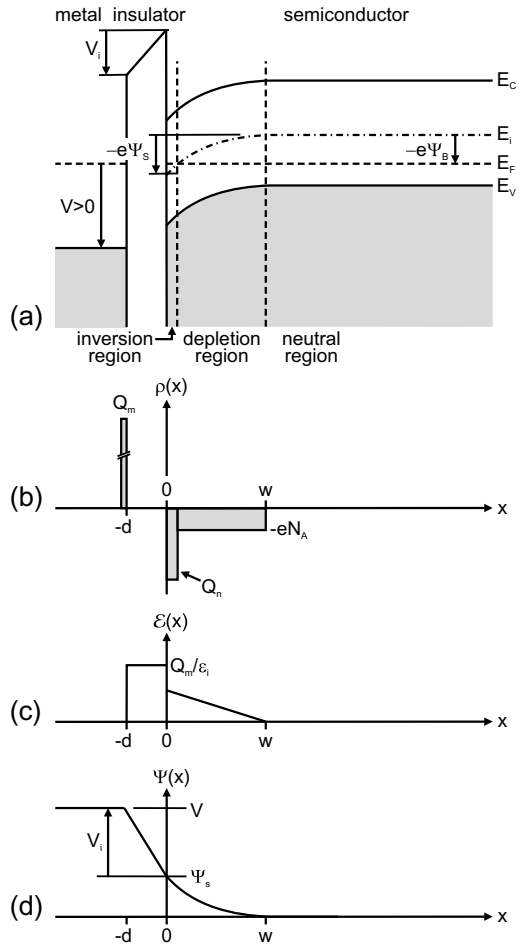

Fig. 21.34 Ideal MIS diode at inversion: **a** band diagram, **b** charge distribution, **c** electric field and **d** potential

the space charge is due to ionized impurities (depletion) and $\mathcal{F}$ is dominated by the second term in (21.85a), i.e. $\Psi_s \propto \sqrt{\Psi_s}$. For $\Psi_B \leq \Psi_s \leq 2\,\Psi_B$ the diode is in the weak inversion regime and still $\Psi_s \propto \sqrt{\Psi_s}$.

Eventually the dominating term of the second bracket in (21.85a) $f_1 = n_{p_0}/p_{p_0}\exp(\beta\Psi) = (n_i/N_A)^2\exp(\beta\Psi)$ becomes comparable and exponentially larger than the dominating term of the first bracket $f_2 = \beta\Psi$. Solving $f_1 = f_2$ for $\Psi = \gamma\,\Psi_B$ yields the equation $(N_A/n_i)^{\gamma-2} = \gamma\,\ln(N_A/n_i)$ and a value γ larger than and close[19] to 2. Thus for $\Psi_s > \Psi_s^{inv} \approx 2\,\Psi_B$ (using (21.78)),

$$\Psi_s^{inv} \approx \frac{2\,kT}{e}\,\ln\left(\frac{N_A}{n_i}\right)\,, \tag{21.88}$$

strong inversion starts and the space charge is given as $Q_s \propto -\exp(\beta\Psi/2)$. For the case of strong inversion the band diagram is shown in Fig. 21.34 together with the charge, field and potential.

The bias voltage V at the MIS diode (or the total voltage drop across the MIS diode) is

[19]For $N_A/n_i = 10^4$, 10^6 and 10^8, we find $\gamma = 2.33$, 2.25 and 2.20, respectively.

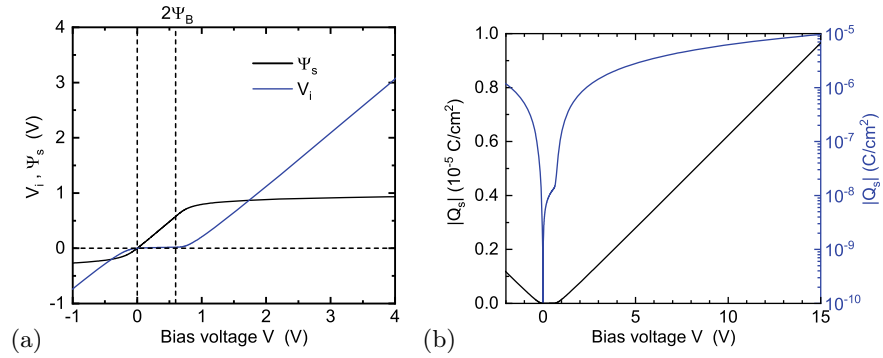

Fig. 21.35 Properties of the ideal MIS diode as a function of bias voltage V; same semiconductor parameters as in Fig. 21.33 with an amorphous SiO_2 ($\epsilon_r = 3.9$, $d = 5\,\text{nm}$) insulator (and $W_{ms} = 0$). **a** Voltage drops V_i (*blue*) across the insulator and Ψ_s (*black*) across the semiconductor. **b** Total charge (absolute values) in the semiconductor in linear (*black*) and logarithmic (*blue*) scale

$$V = V_i + \Psi_s \,, \tag{21.89}$$

with $V_i = Q_s/C_i$ being the voltage drop across the insulator. For the insulator capacitance (per area) C_i see (21.93). Both partial voltages are shown in Fig. 21.35a as a function of the bias. The voltage drop in the insulator becomes significant for $V > 2\,\Psi_B$.

In the case of inversion, the charge (per unit area) in the space-charge region

$$Q_s = Q_d + Q_n \tag{21.90}$$

is composed of the depletion charge (ionized acceptors)

$$Q_d = -e\,w\,N_A \,, \tag{21.91}$$

with w being the width of the depletion region, and the inversion charge Q_n, which is present only close to the interface. The charge as a function of bias is depicted in Fig. 21.35b where in the semi-logarithmic plot, the depletion and inversion charges can be distinguished. The charge becomes significant for $V > 2\,\Psi_B$.

The metal surface carries the opposite charge

$$Q_m = -Q_s \tag{21.92}$$

due to global charge neutrality. The insulator itself does not contribute charges in the case of an ideal MIS diode.

21.3.3 Capacitance

The insulator represents a capacitor with the dielectric constant ϵ_i and a thickness d. Therefore, the capacitance is

$$C_i = \frac{\epsilon_i}{d} \,. \tag{21.93}$$

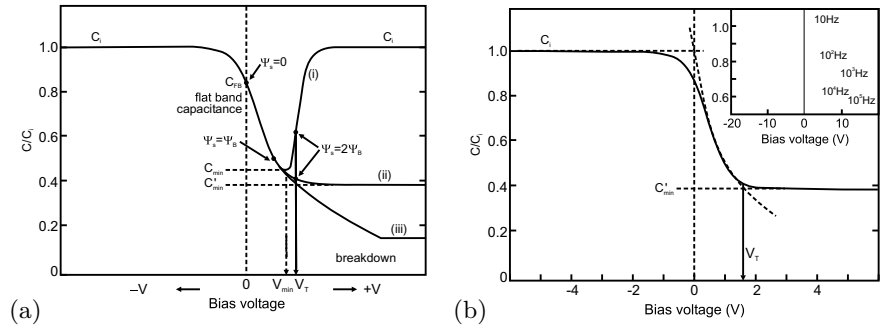

Fig. 21.36 **a** Schematic dependence of the capacitance of a MIS diode on the bias for (i) low frequencies, (ii) high frequencies and (iii) deep depletion. **b** High-frequency capacitance of a Si/SiO_2 diode. The *inset* shows the frequency dependence. Adapted from [1758]

Between the charges $-Q_s$ and Q_s the field strength E_i in the insulator is

$$E_i = \frac{|Q_s|}{\epsilon_i} \,. \tag{21.94}$$

The voltage drop V_i across the insulator is given by

$$V_i = E_i\, d = \frac{|Q_s|}{C_i} \,. \tag{21.95}$$

The total capacitance C of the MIS diode is given by the insulator capacitance in series with the capacitance C_d of the depletion layer

$$C = \frac{C_i\, C_d}{C_i + C_d} \,. \tag{21.96}$$

The capacitance of the space-charge region varies with the applied bias (Fig. 21.36). For forward bias (accumulation), the capacitance of the space-charge region is high. Therefore, the total capacitance of the MIS diode is given by the insulator capacitance $C \approx C_i$. When the voltage is reduced, the capacitance of the space-charge region drops to $C_d = \epsilon_s / L_D$ for the flat-band case ($\Psi_s = 0$). For a high reverse voltage, the semiconductor is inverted at the surface and the space-charge region capacitance is high again. In this case, the total capacitance is given by $C \approx C_i$ again.

The previous consideration assumes that the charge density in the semiconductor can follow changes of the bias sufficiently fast.[20] However, the inversion charge must be built up and then also disappear via recombination that is limited by the recombination time constant τ. For frequencies around τ^{-1} or faster, the charge in the inversion layer cannot follow and the capacitance of the semiconductor is given by the value $C_d \cong \epsilon_s / w_m$; w_m (Fig. 21.37) is the maximum depletion-layer width present at the beginning of inversion (cf. (21.10) and (21.88))

$$w_m \cong \sqrt{\frac{2\,\epsilon_s}{e\,N_A}\,\Psi_s^{inv}} = \sqrt{\frac{4\,\epsilon_s\,kT}{e^2\,N_A}\,\ln\left(\frac{N_A}{n_i}\right)} \,. \tag{21.97}$$

For further increased voltage (into the inversion regime), the electric field is screened by the inversion charge and the width of the depletion layer remains constant. Therefore, the total capacitance in the

[20] Typically, a dc bias voltage V is set and the capacitance is sampled with a small ac voltage of amplitude ΔV, with $\delta V \ll V$.

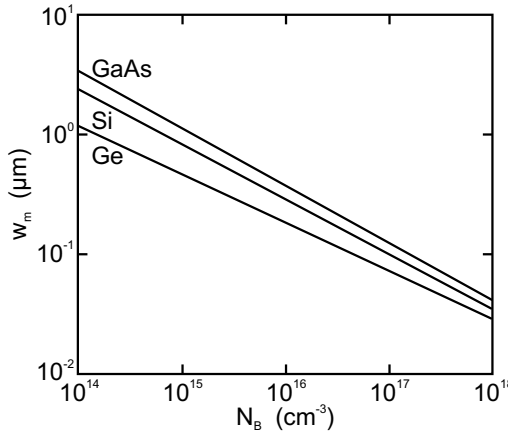

Fig. 21.37 Maximum width of the depletion layer w_m (21.97) at room temperature for deep depletion for GaAs, Si and Ge diodes as a function of bulk doping level

inversion regime is given by

$$C \cong \frac{\epsilon_i}{d + w_m\, \epsilon_i/\epsilon_s} \,. \tag{21.98}$$

21.3.4 Nonideal MIS Diode

In a real, i.e. nonideal, MIS diode, the difference ϕ_{ms} in the work functions of the metal and semiconductor (cf. (21.77)) is no longer zero. Therefore, the capacitance versus voltage relation is shifted with respect to the ideal MIS diode characteristic by the *flat-band voltage shift* V_{FB}

$$V_{FB} = \phi_{ms} - \frac{Q_{ox}}{C_i} \,. \tag{21.99}$$

Additionally, the flat-band voltage can be shifted by charges Q_{ox} in the oxide that have been neglected so far. Such charges can be trapped, i.e. fixed with regard to their spatial position, or mobile, e.g. ionic charges such as sodium.

For Al as metal ($\phi_m = 4.1\,\text{eV}$) and n-type Si ($\phi_s = 4.35\,\text{eV}$), the flat-band voltage shift is $\phi_{ms} = -0.25\,\text{V}$, as shown schematically in Fig. 21.38a for zero bias. V_{FB} is split into 0.2 eV and 0.05 eV for the oxide and the silicon, respectively. In Fig. 21.38b, the dependence of ϕ_{ms} on the doping, conductivity type and metal is shown for various SiO_2/Si MIS diodes. An Au-SiO_2/Si diode with p-type Si and $N_A \approx 10^{15}\,\text{cm}^{-3}$ fulfills the condition of an ideal MIS diode with regard to $\phi_{ms} = 0$.

21.4 Bipolar Diodes

A large class of diodes is based on pn junctions. In a homo pn junction an n-doped region is next to a p-doped region of the same semiconductor. Such a device is called *bipolar*. At the junction a depletion region forms. The transport properties are determined by the minority carriers. An important variation is the pin-diode in which an intrinsic (or lowly doped) region is between the doped region

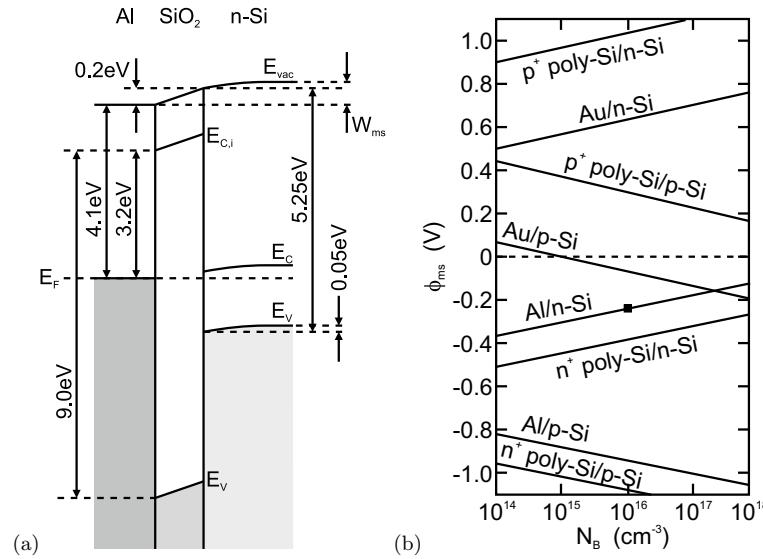

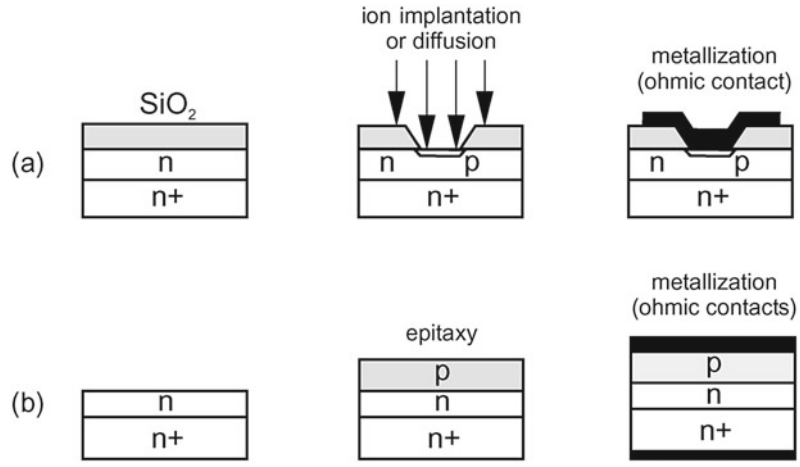

Fig. 21.38 **a** Schematic band diagram of an Al/SiO_2/Si (n-type) diode with 50 nm oxide thickness and $N_D = 10^{16}\,cm^{-3}$ for zero bias, $W_{ms} = 0.25\,eV$. Based on data from [1759]. **b** Difference of work functions $\phi_{ms} = -W_{ms}/e$ for SiO_2/Si MIS diodes and various doping levels and electrode materials (Al, Au and polycrystalline Si). The *square* represents the situation depicted in panel (**a**). Based on data from [1760]

Fig. 21.39 Schematic fabrication technologies for bipolar diodes: **a** Planar junction with local impurity incorporation (diffusion from gas phase or ion implantation) through mask and contact metallization, **b** epitaxial junction

(Sect. 21.5.8). If the differently doped regions belong to different semiconductor materials, the diode is a heterostructure pn diode (Sect. 21.4.6). Various schemes have been used to fabricate pn diodes (Fig. 21.39).

21.4.1 Band Diagram

If the doping profile is arbitrarily sharp, the junction is called *abrupt*. This geometry is the case for epitaxial pn junctions where the differently doped layers are grown on top of each other.[21] For

[21] The choices of dopants and the growth conditions, in particular the temperature, need to be made such that no or negligible interdiffusion of the dopants takes place.

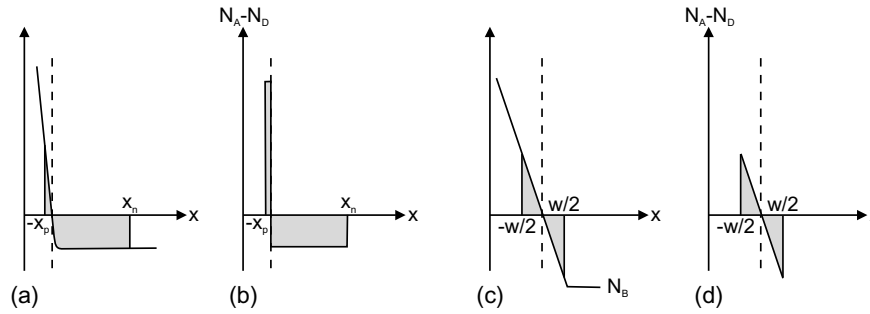

Fig. 21.40 Description of doping distribution with (**a**, **b**) abrupt approximation and with (**c**, **d**) linearly graded junction. (**a**, **c**) show real impurity concentration, (**b**, **d**) idealized doping profile

junctions that are fabricated by diffusion, the abrupt approximation is suitable for alloyed, ion-implanted and shallow-diffused junctions. For deep-diffused junctions a linearly graded approximation is better (Fig. 21.40), which is treated in more detail in [574]. If one doping level is much higher that the other, the junction is termed a *one-sided* (abrupt) junction. If $n \gg p$ ($p \gg n$), the junction is denoted as an n^+p-diode (p^+n-diode).

The thermodynamical equilibrium of a pn diode is considered here only for the electronic system. The thermodynamic stability of the atomic doping distribution is discussed in [1761]. Typically, thermodynamics works to randomize the chemical concentration gradient; the existence of a pn junction is due to the extremely low diffusion coefficient of dopants in the semiconductor lattice. Elevated temperatures can cause the destruction of the pn diode via enhanced dopant diffusion (Sect. 4.2.3). However, a thermodynamically stable concentration gradient and thus a built-in field can exist in a multi-component system [1761].

21.4.2 Space-Charge Region

In thermodynamical equilibrium the Fermi level is constant ($\nabla E_F = 0$). The built-in (positive) voltage V_{bi} is given by (see Fig. 21.41c)

$$e\,V_{bi} = E_g + e\,V_n + e\,V_p\,, \tag{21.100}$$

where V_n is the difference between conduction band and Fermi level on the n-side, $-eV_n = E_C - E_F$. V_p is the difference between valence band and Fermi level on the p-side, $-eV_p = E_F - E_V$. For the nondegenerate semiconductor V_n, $V_p < 0$ and (using (7.12), (7.10) and (7.11))

$$\begin{aligned} e\,V_{bi} &= kT\,\ln\left(\frac{N_C N_V}{n_i^2}\right) - \left[kT\,\ln\left(\frac{N_C}{n_{n_0}}\right) + kT\,\ln\left(\frac{N_V}{p_{p_0}}\right)\right] \\ &= kT\,\ln\left(\frac{p_{p_0}\,n_{n_0}}{n_i^2}\right) = kT\,\ln\left(\frac{p_{p_0}}{p_{n_0}}\right) = kT\,\ln\left(\frac{n_{n_0}}{n_{p_0}}\right) \qquad (21.101a) \\ &\cong kT\,\ln\left(\frac{N_A\,N_D}{n_i^2}\right)\,. \qquad (21.101b) \end{aligned}$$

The electron and hole densities on either side of the junction (n_{p_0} and p_{p_0} at $x = -x_p$ and n_{n_0} and p_{n_0} at $x = x_n$) are related to each other by (from rewriting (21.101a))

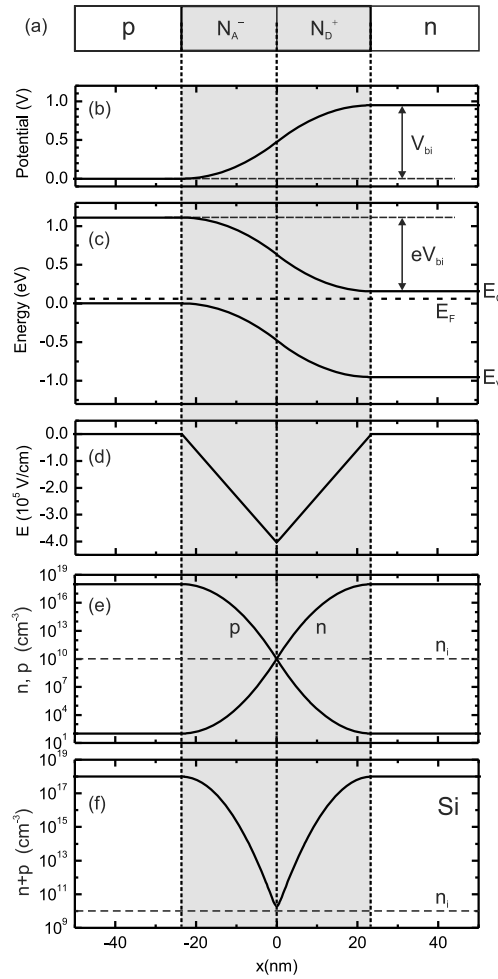

Fig. 21.41 pn junction (abrupt approximation) in thermal equilibrium (zero bias) for Si at room temperature and $N_A = N_D = 10^{18}\,\mathrm{cm}^{-3}$. **a** Schematic representation of p-doped and n-doped region with depletion layer (*grey area*) and fixed space charges, **b** diffusion potential, **c** band diagram with Fermi level (*dashed line*), **d** electric field, **e** free-carrier concentrations n and p and **f** total free-carrier density $n + p$

$$n_{p_0} = n_{n_0} \exp(-\beta V_{bi}) \tag{21.102a}$$

$$p_{n_0} = p_{p_0} \exp(-\beta V_{bi}) \ . \tag{21.102b}$$

Microscopically, the equilibration of the Fermi levels on the n- and p-side occurs via the diffusion of electrons and holes to the p- and n-side, respectively. The electrons and holes recombine in the depletion layer. Therefore, on the n-side the ionized donors and on the p-side the ionized acceptors remain (Fig. 21.41a). These charges build up an electric field (Fig. 21.41d) that works against the diffusion current. At thermal equilibrium the diffusion and drift currents cancel and the Fermi level is constant.

Values for the built-in potential are depicted in Fig. 21.42 for Si and GaAs diodes. The spatial dependence of the potential in the depletion layer is determined by the Poisson equation.

We assume here the complete ionization of the donors and acceptors. Also, we neglect at first majority carriers in the depletion layers on the n- and p-sides.[22] With these approximations, the Poisson equation in the depletion layers on the n- and p-side reads

[22] An abrupt decrease of the majority carrier density at the border of the space-charge region corresponds to zero temperature.

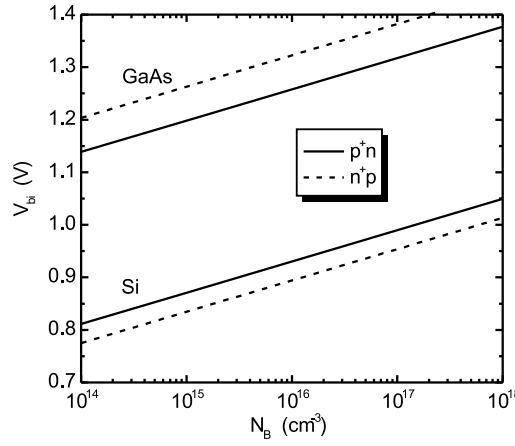

Fig. 21.42 Built-in voltage as a function of doping for one-sided Si and GaAs pn diodes

$$\frac{\partial^2 V}{\partial x^2} = -\frac{e\,N_\mathrm{D}}{\epsilon_\mathrm{s}},\ 0 \le x \le x_\mathrm{n} \tag{21.103a}$$

$$\frac{\partial^2 V}{\partial x^2} = \frac{e\,N_\mathrm{A}}{\epsilon_\mathrm{s}},\ -x_\mathrm{p} \le x \le 0\ . \tag{21.103b}$$

One integration yields (together with the boundary conditions that the field is zero at the boundaries of the depletion layer) the electric field in the two regions

$$E(x) = \frac{e}{\epsilon_\mathrm{s}}\,N_\mathrm{D}\,(x - x_\mathrm{n}),\ 0 \le x \le x_\mathrm{n} \tag{21.104a}$$

$$E(x) = -\frac{e}{\epsilon_\mathrm{s}}\,N_\mathrm{A}\,(x + x_\mathrm{p}),\ -x_\mathrm{p} \le x \le 0\ . \tag{21.104b}$$

The maximum field strength E_m is present at $x = 0$ and is given by

$$E_\mathrm{m} = -\frac{e\,N_\mathrm{D}\,x_\mathrm{n}}{\epsilon_\mathrm{s}} = -\frac{e\,N_\mathrm{A}\,x_\mathrm{p}}{\epsilon_\mathrm{s}}\ . \tag{21.105}$$

The continuity of the field at $x = 0$ is equivalent to the overall charge neutrality

$$N_\mathrm{D}\,x_\mathrm{n} = N_\mathrm{A}\,x_\mathrm{p}\ . \tag{21.106}$$

Another integration yields the potential (setting $V(x = 0) = 0$)

$$V(x) = -E_\mathrm{m}\left(x - \frac{x^2}{2x_\mathrm{n}}\right),\ 0 \le x \le x_\mathrm{n} \tag{21.107a}$$

$$V(x) = -E_\mathrm{m}\left(x + \frac{x^2}{2x_\mathrm{p}}\right),\ -x_\mathrm{p} \le x \le 0\ . \tag{21.107b}$$

The built-in potential $V_\mathrm{bi} = V(x_\mathrm{n}) - V(-x_\mathrm{p}) > 0$ is related to the maximum field via

$$V_\mathrm{bi} = -\frac{E_\mathrm{m}\,w}{2}\ , \tag{21.108}$$

where $w = x_n + x_p$ is the total width of the depletion layer. The elimination of E_m from (21.105) and (21.108) yields

$$w = \sqrt{\frac{2\,\epsilon_s}{e}\left(\frac{N_A + N_D}{N_A\,N_D}\right) V_{bi}} = x_n + x_p\ ; \tag{21.109}$$

the two parts of the depletion layer are given by

$$x_n = \frac{N_A}{N_A + N_D}\sqrt{\frac{2\,\epsilon_s}{e}\,\frac{N_A + N_D}{N_A\,N_D}\,V_{bi}} \tag{21.110a}$$

$$x_p = \frac{N_D}{N_A + N_D}\sqrt{\frac{2\,\epsilon_s}{e}\,\frac{N_A + N_D}{N_A\,N_D}\,V_{bi}}\ . \tag{21.110b}$$

For p^+n and n^+p junctions, the width of the depletion layer is determined by the lowly doped side of the junction

$$w = \sqrt{\frac{2\,\epsilon_s}{e\,N_B}\,V_{bi}}\ , \tag{21.111}$$

where N_B denotes the doping of the lowly doped side, i.e. N_A for a n^+p diode and N_D for a p^+n diode.

If the spatial variation of the majority carrier density is considered in more detail (and for finite temperature, cf. (21.13)), an additional term $-2kT/e = -2/\beta$ is added [1757] to V_{bi}

$$w = \sqrt{\frac{2\,\epsilon_s}{e}\left(\frac{N_A + N_D}{N_A\,N_D}\right)\left(V_{bi} - V - 2\beta^{-1}\right)}\ . \tag{21.112}$$

Also, the external bias V has been included in the formula. If w_0 denotes the depletion layer width at zero bias, the depletion layer width for a given voltage V can be written as

$$w(V) = w_0\sqrt{1 - \frac{V}{V_{bi} - 2/\beta}} \approx w_0\sqrt{1 - \frac{V}{V_{bi}}}\ . \tag{21.113}$$

Using the Debye length (cf. (21.85b))

$$L_D = \sqrt{\frac{\epsilon_s\,kT}{e^2\,N_B}}\ , \tag{21.114}$$

the depletion layer width for a one-sided diode can be written as (with $\beta = e/kT$)

$$w = L_D\sqrt{2\,(\beta V_{bi} - \beta V - 2)}\ . \tag{21.115}$$

The Debye length is a function of the doping level and is shown for Si in Fig. 21.43. For a doping level of $10^{16}\,cm^{-3}$ the Debye length in Si is 40 nm at room temperature. For one-sided junctions the depletion layer width is about 6 L_D for Ge, 8 L_D for Si and 10 L_D for GaAs.

The external bias is counted positive if the '+' ('−') pole is at the p-side (n-side). The reverse voltage has opposite polarity. If a reverse bias is applied, the depletion layer width is increased (Fig. 21.44).

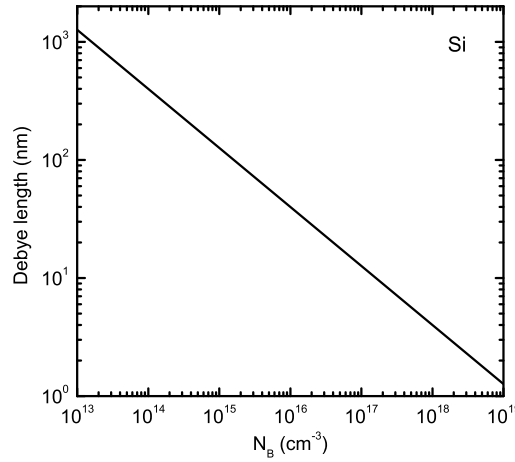

Fig. 21.43 Debye length in Si at room temperature as a function of the doping level N_B according to (21.114)

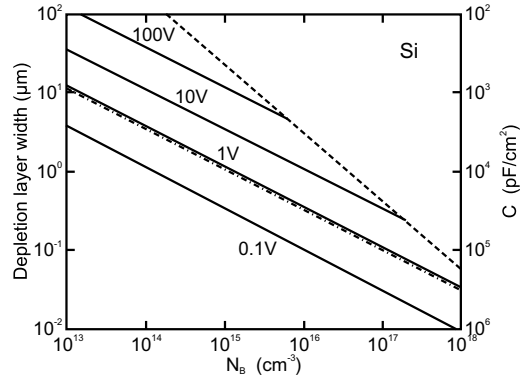

Fig. 21.44 Width of the depletion layer and capacitance per area for one-sided, abrupt Si junctions for various values of $V_{bi} - V - 2kT/e$ as labeled. The *dash-dotted line* is for zero bias, the *dashed line* is the limit due to avalanche breakdown. Adapted from [574]

21.4.3 Capacitance

The capacitance of the depletion layer is the charge change upon a change of the external bias. It is given as

$$C = \left|\frac{\mathrm{d}Q}{\mathrm{d}V}\right| = \frac{\mathrm{d}(eN_B w)}{\mathrm{d}(w^2 eN_B/2\epsilon_s)} = \frac{\epsilon_s}{w} = \frac{\epsilon_s}{\sqrt{2}\,L_D}\,\frac{1}{\sqrt{\beta V_{bi} - \beta V - 2}}\ . \tag{21.116}$$

Therefore, the capacitance of the depletion layer is inversely proportional to the depletion-layer width (see the two scales in Fig. 21.44). A detailed treatment has been given in [1762]. $1/C^2$ is proportional to the external bias

$$\frac{1}{C^2} = \frac{2\,L_D^2}{\epsilon_s^2}\,(\beta V_{bi} - \beta V - 2)\ . \tag{21.117}$$

From C–V spectroscopy the doping level can be obtained from the slope

$$\frac{\mathrm{d}(1/C^2)}{\mathrm{d}V} = \frac{2\,\beta\,L_D^2}{\epsilon_s^2} = \frac{2}{e\,\epsilon_s\,N_B}\ . \tag{21.118}$$

From the extrapolation to the voltage for which $1/C^2 = 0$ the built-in voltage can be obtained.

21.4.4 Current-Voltage Characteristics

Ideal Current-Voltage Characteristics

Now, the currents in thermodynamical equilibrium ($V = 0$) and under bias are discussed. A diode characteristic will be obtained. We work at first with the following assumptions: abrupt junction, Boltzmann approximation, low injection, i.e. the injected minority carrier density is small compared to the majority carrier density, and zero generation current in the depletion layer, i.e. the electron and hole currents are constant throughout the depletion layer. In the presence of a bias, electrons and holes have quasi-Fermi levels and the carrier densities are given by (cf. (7.55a, b))

$$n = N_{\mathrm{C}} \exp\left(\frac{F_{\mathrm{n}} - E_{\mathrm{C}}}{kT}\right) \tag{21.119a}$$

$$p = N_{\mathrm{V}} \exp\left(-\frac{F_{\mathrm{p}} - E_{\mathrm{V}}}{kT}\right) . \tag{21.119b}$$

Using the intrinsic carrier concentration (7.19,7.20), we can write

$$n = n_{\mathrm{i}} \exp\left(\frac{F_{\mathrm{n}} - E_{\mathrm{i}}}{kT}\right) = n_{\mathrm{i}} \exp\left[\beta(\psi - \phi_{\mathrm{n}})\right] \tag{21.120a}$$

$$p = n_{\mathrm{i}} \exp\left(-\frac{F_{\mathrm{p}} - E_{\mathrm{i}}}{kT}\right) = n_{\mathrm{i}} \exp\left[\beta(\phi_{\mathrm{p}} - \psi)\right] , \tag{21.120b}$$

where ϕ and ψ are the potentials related to the (quasi-) Fermi level and the intrinsic Fermi levels, $-e\phi_{\mathrm{n,p}} = F_{\mathrm{n,p}}$ and $-e\psi = E_{\mathrm{i}}$. The potentials ϕ_{n} and ϕ_{p} can also be written as

$$\phi_{\mathrm{n}} = \psi - \beta^{-1} \ln\left(\frac{n}{n_{\mathrm{i}}}\right) \tag{21.121a}$$

$$\phi_{\mathrm{p}} = \psi + \beta^{-1} \ln\left(\frac{p}{p_{\mathrm{i}}}\right) . \tag{21.121b}$$

The product np is given by

$$np = n_{\mathrm{i}}^2 \exp\left[\beta(\phi_{\mathrm{p}} - \phi_{\mathrm{n}})\right] . \tag{21.122}$$

Of course, at thermodynamical equilibrium (zero bias) $\phi_{\mathrm{p}} = \phi_{\mathrm{n}}$ and $np = n_{\mathrm{i}}^2$. For forward bias $\phi_{\mathrm{p}} - \phi_{\mathrm{n}} > 0$ (Fig. 21.45a) and $np > n_{\mathrm{i}}^2$. For reverse bias $\phi_{\mathrm{p}} - \phi_{\mathrm{n}} < 0$ (Fig. 21.45b) and $np < n_{\mathrm{i}}^2$.

The electron current density (per unit area) is given by (8.60a) that reads here with $\mathbf{E} = -\nabla\psi$ and n given by (21.120a) as[23]

$$\mathbf{j}_{\mathrm{n}} = -e\,\mu_{\mathrm{n}} \left(n\,\mathbf{E} + \beta^{-1}\,\nabla n\right) = e\,n\,\mu_{\mathrm{n}}\,\nabla\phi_{\mathrm{n}} . \tag{21.123}$$

Similarly, we obtain for the hole current density (using (8.60b) and (21.120b))

$$\mathbf{j}_{\mathrm{p}} = e\,\mu_{\mathrm{p}} \left(p\,\mathbf{E} - \beta^{-1}\,\nabla p\right) = -e\,p\,\mu_{\mathrm{p}}\,\nabla\phi_{\mathrm{p}} . \tag{21.124}$$

Both these currents through the depletion/space-charge region are constant since no recombination/generation is assumed for now. The gradient of the quasi-Fermi levels in the depletion layer

[23] We remind the reader that μ_{n} was defined as a negative number.

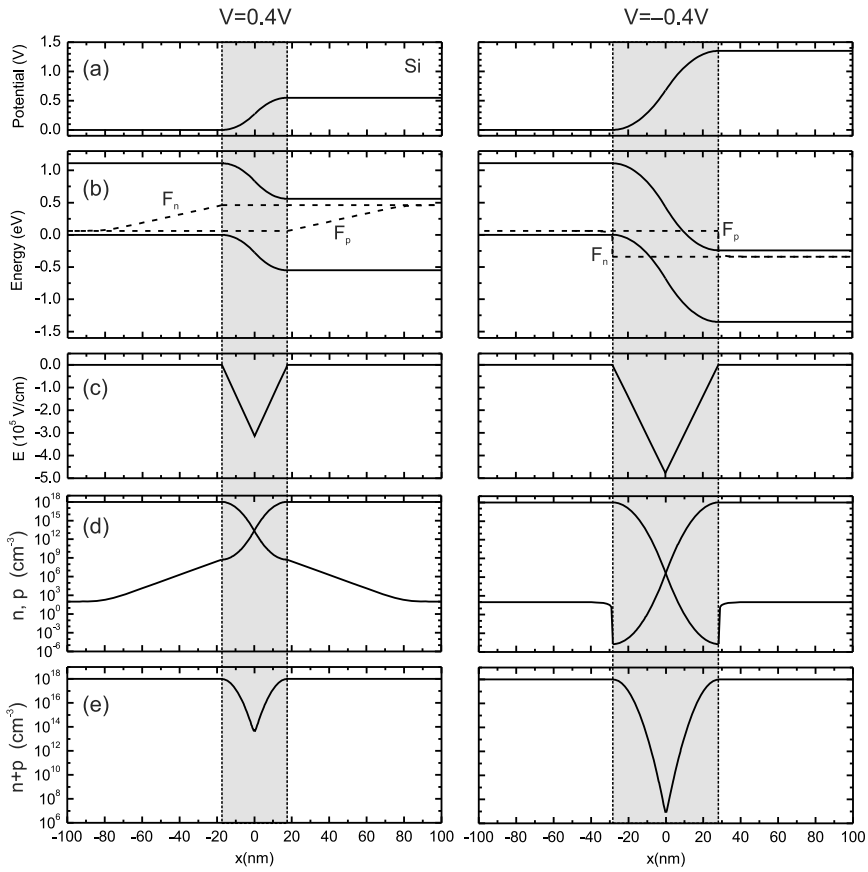

Fig. 21.45 **a** Diffusion potential, **b** band diagram, **c** electric field, **d** electron and hole concentrations and **e** $n + p$ under forward bias $+0.4\,\mathrm{V}$ (*left panel*) and reverse bias (*right panel*) $-0.4\,\mathrm{V}$ for a silicon pn diode at room temperature with $N_\mathrm{A} = N_\mathrm{D} = 10^{18}\,\mathrm{cm}^{-3}$ (same as in Fig. 21.41). The *dashed lines* in (**b**) are the electron and hole quasi-Fermi levels F_n and F_p. The depletion layer is shown as the *grey area*. The diffusion length in the n- and p-type material is taken as 4 nm. This value is much smaller than the actual diffusion length (μm-range) and is chosen here only to show the carrier concentration in the depletion layer and the neutral region in a single graph

is very small and the quasi-Fermi levels $\phi_{\mathrm{n,p}}$ are practically constant. The electron and hole currents are shown in Fig. 21.46 together with the carrier densities; a more detailed calculation of currents than presented here can be found in [1763]. The change of carrier density in the depletion layer is mostly due to the variation of ψ (or E_i).

Therefore, the voltage drop across the depletion layer is $V = \phi_\mathrm{p} - \phi_\mathrm{n}$ and (21.122) reads

$$n\,p = n_\mathrm{i}^2\,\exp\left(\beta V\right)\ . \tag{21.125}$$

The electron density at the boundary of the depletion layer on the p-side (at $x = -x_\mathrm{p}$) is (using (21.125))

$$n_\mathrm{p} = \frac{n_\mathrm{i}^2}{p_\mathrm{p}}\,\exp\left(\beta V\right) = n_{\mathrm{p}_0}\,\exp\left(\beta V\right)\ . \tag{21.126}$$

Similarly, the hole density on the n-side at $x = x_\mathrm{n}$ is given by

$$p_\mathrm{n} = p_{\mathrm{n}_0}\,\exp\left(\beta V\right)\ . \tag{21.127}$$

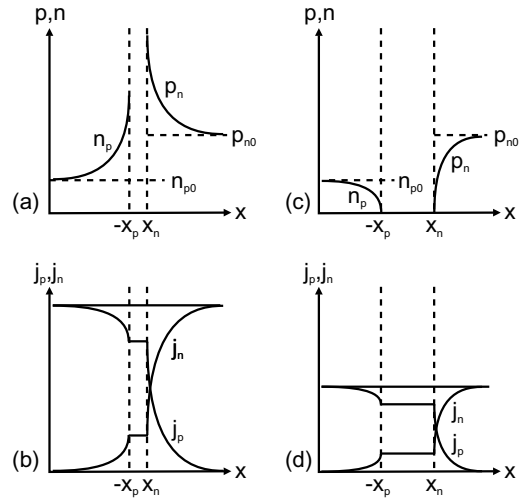

Fig. 21.46 Carrier densities (**a**, **c**) and current densities (**b**, **d**) (linear scales) in a pn diode under (**a**, **b**) forward bias and (**c**, **d**) reverse bias

From the continuity equation and the boundary condition that far away from the depletion layer the hole density is p_{n_0}, the hole density on the n-side is given by

$$\delta p_n(x) = p_{\mathrm{n}}(x) - p_{\mathrm{n}_0} = p_{\mathrm{n}_0} \left[\exp(\beta V) - 1\right] \exp\left(-\frac{x - x_{\mathrm{n}}}{L_{\mathrm{p}}}\right) , \tag{21.128}$$

where $L_{\mathrm{p}} = \sqrt{D_{\mathrm{p}} \tau_{\mathrm{p}}}$ is the hole (minority carrier) diffusion length. In [1763] it is argued from analytical and numerical analysis that the majority carrier density follows $\delta n_n(x) = \delta p_n(x)$.

The hole current density at the boundary of the depletion layer on the n-side is

$$j_{\mathrm{p}}(x_{\mathrm{n}}) = -e\, D_{\mathrm{p}} \frac{\partial p_{\mathrm{n}}}{\partial x}|_{x_{\mathrm{n}}} = \frac{e\, D_{\mathrm{p}}\, p_{\mathrm{n}_0}}{L_{\mathrm{p}}} \left[\exp(\beta V) - 1\right] . \tag{21.129}$$

Similarly, the electron current (again $\delta p_p(x) = \delta n_p(x)$ in the neutral region [1763]) in the depletion layer is

$$j_{\mathrm{n}}(-x_{\mathrm{p}}) = \frac{e\, D_{\mathrm{n}}\, n_{\mathrm{p}_0}}{L_{\mathrm{n}}} \left[\exp(\beta V) - 1\right] . \tag{21.130}$$

The total current due to diffusion is

$$j_{\mathrm{d}} = j_{\mathrm{p}}(x_{\mathrm{n}}) + j_{\mathrm{n}}(-x_{\mathrm{p}}) = j_{\mathrm{s}} \left[\exp(\beta V) - 1\right] , \tag{21.131}$$

with the saturation current given by

$$j_{\mathrm{s}}^{\mathrm{d}} = \frac{e\, D_{\mathrm{p}}\, p_{\mathrm{n}_0}}{L_{\mathrm{p}}} + \frac{e\, D_{\mathrm{n}}\, n_{\mathrm{p}_0}}{L_{\mathrm{n}}} . \tag{21.132}$$

This dependence represents the ideal diode characteristic and the famous result from Shockley. Here, only the minority diffusion currents have been considered; a more in-depth discussion is delivered in [1763] where also the majority carrier density and majority carrier drift and diffusion currents are analyzed (minority drift currents can be neglected altogether). However, the analysis leads to the same result (21.131) and (21.132).

For a one-sided (p^+n-) diode, the saturation current is (here $N_B = N_D$)

$$j_s^d \cong \frac{e\, D_p\, p_{n_0}}{L_p} \cong e \left(\frac{D_p}{\tau_p}\right)^{1/2} \frac{n_i^2}{N_B} \,. \tag{21.133}$$

The saturation depends via D_p/τ_p weakly on the temperature. The term n_i^2 depends on T, proportional to $T^3 \exp(-E_g/kT)$, which is dominated by the exponential function.

If the minority carrier lifetime is given by the radiative recombination (10.19), the hole diffusion length is

$$L_p = \sqrt{\frac{D_p}{B\, n_{n_0}}} \,. \tag{21.134}$$

For GaAs (Tables 8.2 and 10.1) with $N_D = 10^{18}\,\mathrm{cm}^{-3}$, we find $\tau_p = 10\,\mathrm{ns}$ and $L_p \approx 3\,\mu\mathrm{m}$. For L_n we find 14 µm, however, the lifetime at room temperature can be significantly shorter due to nonradiative recombination and subsequently also the diffusion length will be shorter (by about a factor of 10). For $L \sim 1\,\mu\mathrm{m}$, the diffusion saturation current is $j_s^d \sim 4 \times 10^{-20}\,\mathrm{A/cm}^2$.

The radiative recombination rate (band-band recombination, b–b) in the neutral n-region (as relevant for LEDs, see Sect. 23.3) is $B(np - n_i^2) \approx B n_{n_0}(p_n(x) - p_{n_0})$. Therefore, the recombination current $j_{d,n}^{b-b}$ in the neutral n-region is (using (21.128))

$$\begin{aligned} j_{d,n}^{b-b} &= e \int_{x_n}^{\infty} B\, n_i^2 \left[\exp(\beta V) - 1\right] \exp\left(-\frac{x - x_n}{L_p}\right) \mathrm{d}x \\ &= e\, B\, L_p\, n_i^2 \left[\exp(\beta V) - 1\right] \,. \end{aligned} \tag{21.135}$$

For the neutral region on the p-side a similar expression results. The total radiative recombination current from the neutral regions is

$$j_d^{b-b} = e\, B\, (L_n + L_p)\, n_i^2 \left[\exp(\beta V) - 1\right] \,. \tag{21.136}$$

For GaAs, the saturation current for the radiative recombination in the neutral region

$$j_s^{r,b-b} = e\, B\, (L_n + L_p)\, n_i^2 \tag{21.137}$$

is (Tables 7.1 and 10.1) for a diffusion length of 1 µm of $j_s^{r,b-b} \sim 4 \times 10^{-21}\,\mathrm{A/cm}^2$.

Since the (radiative) minority carrier lifetime is inversely proportional to the majority carrier density, the relevant diffusion length is that of the side with the lower doping level and is given by

$$L = \frac{1}{n_i} \sqrt{\frac{D_B\, N_B}{B}} \,, \tag{21.138}$$

where D_B is the minority carrier diffusion coefficient on the lowly doped side. The radiative recombination current from the neutral region can be written as

$$j_d^{b-b} = e \sqrt{B\, D_B\, N_B}\, n_i \left[\exp(\beta V) - 1\right] \,. \tag{21.139}$$

The I–V characteristic for pn diodes from two semiconductors with different band gap are shown in Fig. 21.47a (for Ge and Si). The Si diode has the much smaller saturation current. The saturation current

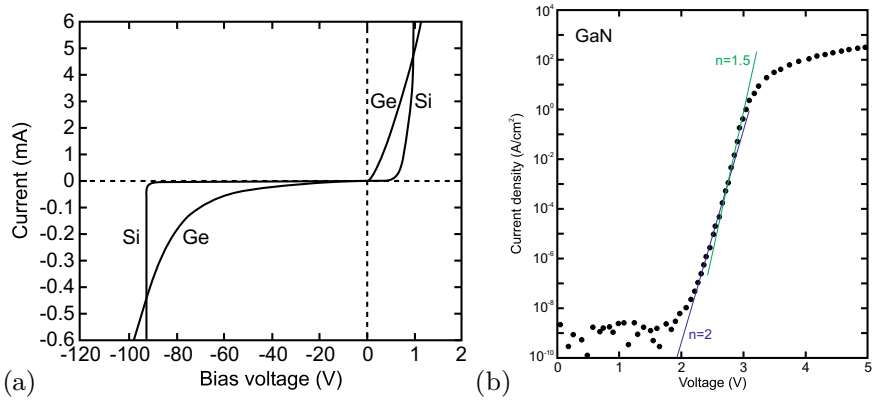

Fig. 21.47 Comparison of the characteristics of **a** Ge and Si and **b** GaN pn diodes at room temperature. Note the different scales in the forward and reverse regime in (**a**). The *lines* in (**b**) are related to ideality factors 2 and 1.5 as labeled. Adapted from [1764]

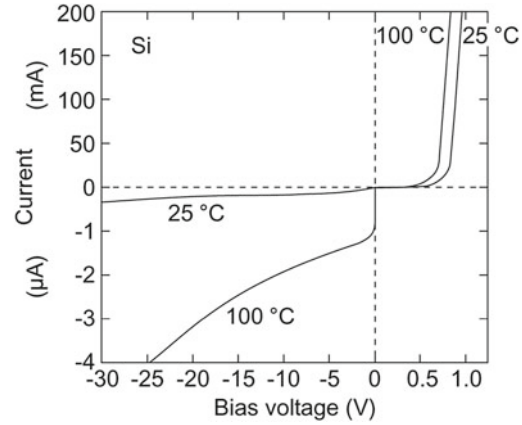

Fig. 21.48 Characteristics of a Si power diode at two temperatures, 25 °C and 100 °C

increases at higher temperature (Fig. 21.48). A wide-gap pn diode (GaN) exhibits small saturation currents (The $n = 1.5$ part of the GaN in Fig. 21.47b belongs to a saturation current density of 7×10^{-27} A/cm^2, the $n = 1.5$ part to $\approx 10^{-34}$ A/cm^2) and displays sizable current (density) only for larger voltages.

Real I–V Characteristics

Besides the ideal I–V characteristics due to diffusion several effects contribute to the characteristics of real bipolar diodes:

- a generation-recombination (G–R) current is present due to traps in the depletion layer
- already for fairly small forward voltages, high injection conditions are present, i.e. $p_n \ll n_n$ is no longer valid
- the series resistance R_s of the diode is finite (ideally $R_s = 0$)
- the diode has a finite parallel (shunt) resistance R_p (ideally $R_p = \infty$)
- at high reverse voltage the junction breaks down; this phenomenon is treated in Sect. 21.4.5

First, we consider the generation-recombination current due to band-impurity (b–i) processes (see Sect. 10.9). Such recombination is nonradiative or at least does not produce photons with an energy close to the band gap. The impact on the I–V diode characteristic has first been considered in [1765].

The net b–i recombination rate is given by (10.52). For reverse voltage, the generation dominates the G–R current. For $n < n_i$ and $p < n_i$, the net recombination rate r is

$$r \cong \frac{\sigma_\mathrm{n}\,\sigma_\mathrm{p}\,v_\mathrm{th}\,N_\mathrm{t}}{\sigma_\mathrm{n}\,\exp\left(\frac{E_\mathrm{t}-E_\mathrm{i}}{kT}\right)+\sigma_\mathrm{p}\,\exp\left(\frac{E_\mathrm{i}-E_\mathrm{t}}{kT}\right)}\,n_\mathrm{i} \equiv \frac{n_\mathrm{i}}{\tau_\mathrm{e}}\,, \tag{21.140}$$

where τ_e is the effective electron lifetime. The generation current density is given by

$$j_\mathrm{g} = \frac{e\,n_\mathrm{i}\,w}{\tau_\mathrm{e}}\,. \tag{21.141}$$

Since the width of the depletion layer varies with the applied reverse bias V, we expect a dependence

$$j_\mathrm{g} \propto \sqrt{V_\mathrm{bi}+|V|}\,. \tag{21.142}$$

The saturation current is given by the sum of the diffusion and generation parts

$$j_\mathrm{s} = e\sqrt{\frac{D_\mathrm{p}}{\tau_\mathrm{p}}}\,\frac{n_\mathrm{i}^2}{N_\mathrm{D}} + \frac{e\,n_\mathrm{i}\,w}{\tau_\mathrm{e}}\,. \tag{21.143}$$

In semiconductors with large n_i (narrow band gap, e.g. Ge) the diffusion current will dominate; in Si (larger band gap) the generation current can dominate.

The maximum of the recombination rate is present for $E_\mathrm{t} \approx E_\mathrm{i}$ (10.57). Then $n_\mathrm{t} = p_\mathrm{t} = n_\mathrm{i}$ in (10.52). Assuming $\sigma = \sigma_\mathrm{n} = \sigma_\mathrm{p}$, the recombination rate is

$$r_\mathrm{b-i} = \sigma\,v_\mathrm{th}\,N_\mathrm{t}\,\frac{n\,p-n_\mathrm{i}^2}{n+p+2\,n_\mathrm{i}}\,. \tag{21.144}$$

Using (21.122) we can write

$$r_\mathrm{b-i} = \sigma\,v_\mathrm{th}\,N_\mathrm{t}\,n_\mathrm{i}\,\frac{n_\mathrm{i}}{n+p+2\,n_\mathrm{i}}\left[\exp\left(\beta V\right)-1\right]\,. \tag{21.145}$$

The term $\zeta = \frac{n_\mathrm{i}}{n+p+2n_\mathrm{i}}$ is maximal for $n = p$, which is given (from (21.125)) by

$$n_\mathrm{mr} = p_\mathrm{mr} = n_\mathrm{i}\,\exp\left(\beta V/2\right)\,. \tag{21.146}$$

The function $\zeta(x)$ cannot be integrated analytically. In order to evaluate the integral of ζ over the depletion layer

$$\chi = \int_{-x_\mathrm{p}}^{x_\mathrm{n}} \zeta\,\mathrm{d}x\,, \tag{21.147}$$

the maximum rate

$$\zeta_\mathrm{mr} = \frac{n_\mathrm{i}}{n_\mathrm{mr}+p_\mathrm{mr}+2\,n_\mathrm{i}} = \frac{1}{2}\,\frac{1}{1+\exp\left(\beta V/2\right)} \tag{21.148}$$

can be integrated over the depletion layer as an approximation [574], $\chi \approx \zeta_\mathrm{mr}\,w$. This approach yields a recombination current

$$j_\mathrm{mr} = \frac{e\,\sigma\,v_\mathrm{th}\,N_\mathrm{t}\,w\,n_\mathrm{i}}{2}\,\frac{\exp\left(\beta V\right)-1}{\exp\left(\beta V/2\right)+1} \cong j_\mathrm{s}^\mathrm{mr}\,\exp\left(\frac{\beta V}{2}\right)\,, \tag{21.149}$$

with $j_s^{mr} = e\sigma v_{th} N_t w n_i/2$ and the approximation being valid for $eV/kT \gg 1$. Thus the nonradiative band-impurity recombination is often said to cause an ideality factor of $n = 2$.

For a better approximation of χ, the dependence of the potential $\varphi(x)$ can be approximated as linear (constant-field approximation), i.e. using the local field E_{mr} at the position where $n = p$ [1766]. For a symmetric diode with $n_{n_0} = p_{p_0}$, this position is at $x = 0$; for a one-sided junction on the lower-doped side. E_{mr} is given for $p_{p_0} \leq n_{n_0}$ by

$$E_{mr} = -\frac{\sqrt{2}}{w}\,(V_{bi} - V)\,\sqrt{1 + \frac{1}{\beta\,(V_{bi} - V)}\,\ln\frac{p_{p_0}}{n_{n_0}}}\,\sqrt{1 + \frac{p_{p_0}}{n_{n_0}}}\,. \tag{21.150}$$

For a symmetric diode (21.151a) holds, for a one-sided diode the approximation in (21.151b) holds

$$E_{mr} = -\frac{2}{w}\,(V_{bi} - V) \propto \sqrt{V_{bi} - V} \tag{21.151a}$$

$$E_{mr} \cong -\frac{\sqrt{2}}{w}\,(V_{bi} - V) \propto \sqrt{V_{bi} - V}\,. \tag{21.151b}$$

We note that for zero bias ($V = 0$), (21.108) is recovered from (21.151a). Using the above approximation ζ is given by

$$\zeta(x) = \frac{1}{2}\,\frac{1}{1 + \exp(\beta V/2)\,\cosh(\beta E_{mr} x)}\,. \tag{21.152}$$

Since ζ decreases sufficiently fast within the depletion layer, the integration over the depletion layer can be extended to $\pm\infty$ and we obtain

$$\chi = \frac{2}{\beta E_{mr}}\,\frac{1}{\sqrt{\exp(\beta V) - 1}}\,\arctan\left[\sqrt{\frac{\exp(\beta V/2) - 1}{\exp(\beta V/2) + 1}}\right]\,. \tag{21.153}$$

We note that for $V = 0$, the integral takes the value $\chi = (\beta E_{mr})^{-1}$. The recombination current is now given by [1766]

$$j_{r,b-i} = \frac{2\,\sigma\,v_{th}\,N_t\,n_i\,kT}{E_{mr}}\,\arctan\left[\sqrt{\frac{\exp(\beta V/2) - 1}{\exp(\beta V/2) + 1}}\right]\,\sqrt{\exp(\beta V) - 1}\,. \tag{21.154}$$

For large voltage the arctan term becomes $\pi/4$. For $eV/kT \gg 1$ the nonradiative recombination current can be written as

$$j_{r,b-i} = j_s^{r,b-i}\,\exp\left(\frac{\beta V}{n}\right)\,, \tag{21.155}$$

with $j_s^{r,b-i} = e\sigma v_{th} N_t n_i kT\pi/(2E_{mr})$. The voltage-dependent ideality factor n (semilogarithmic slope $n = \beta j_r(V)/j_r'(V)$) is close but not identical to 2 and is shown in Fig. 21.49 for various values of V_{bi}. The built-in voltage influences the logarithmic slope via the factor $1/E_{mr}$ in (21.154).

In the case of radiative band-band (b–b) recombination, the recombination rate is given by (10.14). Together with (21.125) and integrated over the depletion layer, the recombination current in the depletion layer is given by (cf. (21.136))

$$j_{r,b-b} = e\,B\,w\,n_i^2\,\left[\exp(\beta V) - 1\right]\,, \tag{21.156}$$

and exhibits an ideality factor of $n = 1$. Comparing (21.136) and (21.156), the dominating radiative-

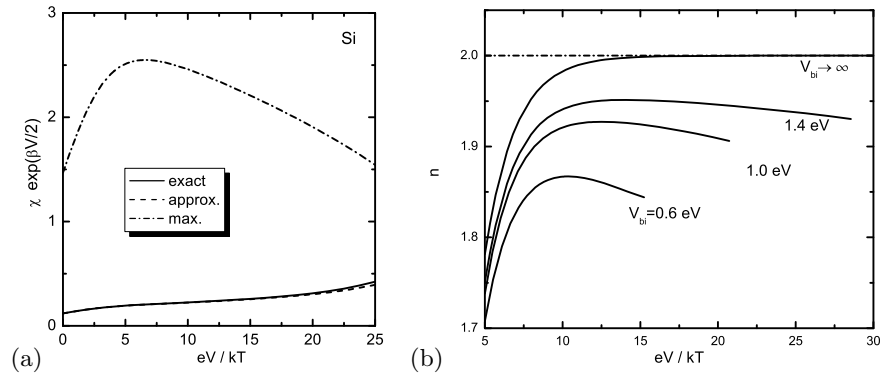

Fig. 21.49 **a** Integral χ (21.147) multiplied by $\exp(\beta V/2)$ in order to extract the differences on a linear scale. *Solid line*: Exact numerical calculation, *dash-dotted line*: standard approximation with constant maximum rate, *dashed line*: this work (approximation with constant field). As material parameters we have used room temperature and $n_i = 10^{10}\,\mathrm{cm}^{-3}$ (Si), $n_{n_0} = 10^{18}\,\mathrm{cm}^{-3}$ and $p_{p_0} = 10^{17}\,\mathrm{cm}^{-3}$. **b** Logarithmic slope of band-impurity recombination current in the forward bias regime for various values of the built-in voltage $V_{bi} = 0.6$, 1.0, and 1.4 eV and in the limit $V_{bi} \to \infty$. Adapted from [1766]

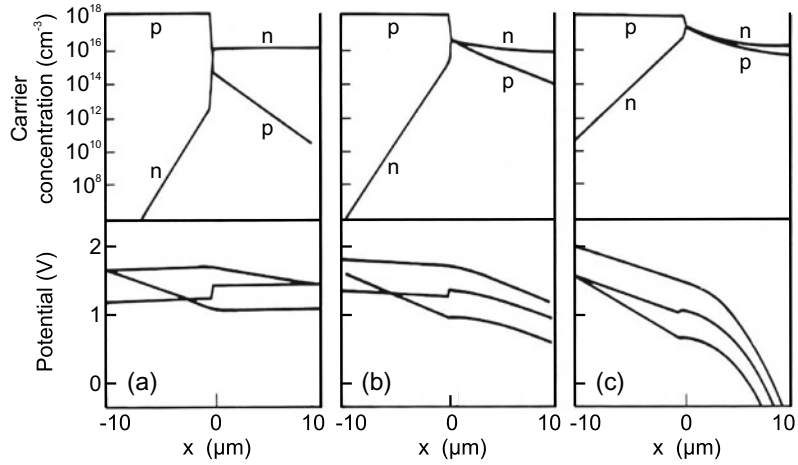

Fig. 21.50 Theoretical modeling of charge-carrier concentration, intrinsic Fermi level (potential) ψ and quasi-Fermi levels (with arbitrary offset) for a Si p^+n diode for various current densities: **a** $10\,\mathrm{A\,cm}^{-2}$, **b** $10^3\,\mathrm{A\,cm}^{-2}$ and **c** $10^4\,\mathrm{A\,cm}^{-2}$. $N_A = 10^{18}\,\mathrm{cm}^{-3}$, $N_D = 10^{16}\,\mathrm{cm}^{-3}$, $\tau_n = 0.3\,\mathrm{ns}$, $\tau_p = 0.84\,\mathrm{ns}$. Adapted from [1767]

recombination current is determined by the ratio of w and $L_n + L_p$. Since in the forward direction, the depletion-layer width tends towards zero (for flat-band conditions), the radiative-recombination current is dominated by the recombination in the neutral region(s).

For high injection current (under forward bias), the injected minority carrier density can become comparable with the majority carrier density. In this case, diffusion *and* drift need to be considered. At large current density, the voltage drop across the junction is small compared to the ohmic voltage drop across the current path. In the simulation (Fig. 21.50), the high-injection effects start on the n-doped side because it has been modeled with the lower doping ($N_D < N_A$).

The series resistance R_s (typically a few Ohms) also effects the characteristic at low injection. The voltage drop across the junction is reduced by $R_s I$. Thus, the I–V characteristic taking into account the effect of the series resistance is

$$I = I_s \left(\exp\left[\frac{e\,(V - R_s\,I)}{n\,kT} \right] - 1 \right) . \tag{21.157}$$

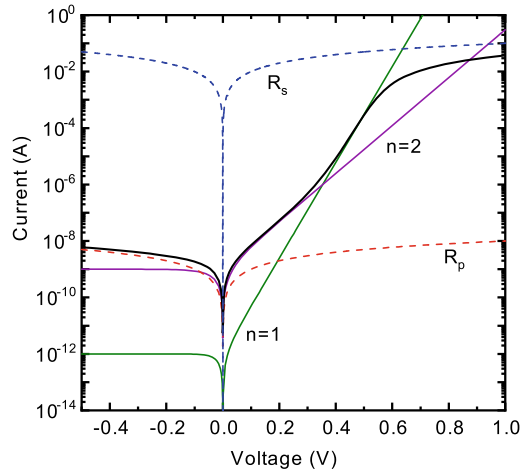

Fig. 21.51 Theoretical I–V characteristic of a diode at room temperature with saturation currents for the $n = 1$ and $n = 2$ processes of $I_s^{n=1} = 10^{-12}$ A and $I_s^{n=2} = 10^{-9}$ A and resistances $R_s = 10\,\Omega$, $R_p = 100\,\mathrm{M}\Omega$. *Green line*: Ideal diode with $n = 1$ characteristic only, *Purple line*: only $n = 2$ process, *dashed red line*: only parallel ohmic resistance R_p, *dashed blue line*: only series ohmic resistance R_s, *solid black line*: all effects combined as in (21.159)

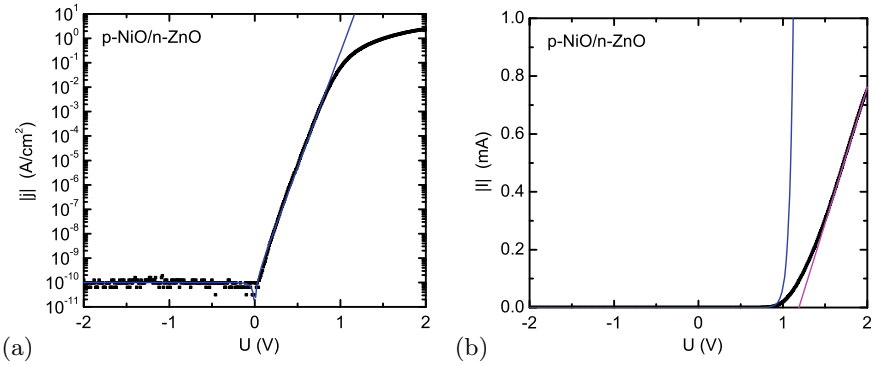

Fig. 21.52 **a** jV-characteristic of NiO/ZnO bipolar diode (cmp. Sect. 21.4.6) in half-logarithmic plot. The *blue line* is a fit with ideality factor $n = 1.8$. **b** IV-characteristic in linear plot. The *purple line* in (**b**) is a linear fit (with $R_s = 1.06\,\mathrm{k}\Omega$) for the range where the series resistance dominates

This equation is implicit with regard to I and can only be solved numerically. At high current, the resistance of the junction becomes very small (Fig. 21.51a); then the I–V characteristic deviates from the exponential behavior (Fig. 21.52a); finally it is dominated by the series resistance and becomes linear (Fig. 21.52b). Sometimes the extrapolated voltage from the linear range (1.19 V in Fig. 21.52b) is called 'threshold' voltage, but this is a wrong term for this behavior.

The diode can also exhibit a parallel (shunt) resistance R_p, e.g. due to surface conduction between the contacts. Including the shunt resistance, the diode characteristic is

$$I = I_s \left(\exp\left[\frac{e\,(V - R_s\,I)}{n\,kT} \right] - 1 \right) + \frac{V - R_s\,I}{R_p} \,. \tag{21.158}$$

The shunt resistance can be evaluated best from the differential conductance in the reverse-voltage regime [1725]. Due to a high surface-state density, the passivation of GaAs diodes can be difficult. Si can be very well passivated with low leakage current and high reliability.

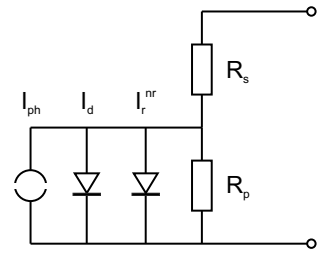

Fig. 21.53 Equivalent circuit of a pn diode. Serial (R_s) and parallel (R_p) resistance and diode currents: I_d (due to diffusion, $n \approx 1$), I_r^{nr} (nonradiative recombination due to band-impurity recombination, $n \approx 2$) and an ideal current source due to photogeneration (as discussed in Sect. 22.3)

Often, a clear distinction between the $n = 1$ and $n = 2$ regimes cannot be made. In this case, an intermediate ideality factor $1 \leq n \leq 2$ is fitted to the I–V characteristic as in (21.158). If the current can be separated into a $n = 1$ (diffusion) and a $n = 2$ (recombination-generation) process, the characteristic is given by (see Fig. 21.51)

$$I = I_s^{n=1}\left(\exp\left[\frac{e\,(V - R_s\,I)}{kT}\right] - 1\right) + I_s^{n=2}\left(\exp\left[\frac{e\,(V - R_s\,I)}{2\,kT}\right] - 1\right) + \frac{V - R_s\,I}{R_p}\,. \tag{21.159}$$

In summary, the pn diode has the equivalent circuit given in Fig. 21.53; the photocurrent source I_{ph} is discussed below in Sect. 22.3.

21.4.5 Breakdown

If a large voltage is applied in the reverse direction, the pn junction breaks down. At breakdown, a small voltage increase leads to a dramatic increase of the current. There are three mechanisms that lead to breakdown: thermal instability, tunneling, and avalanche multiplication [1768–1770]. Defects cause localized pre-breakdown sites [1770, 1771].

Thermal Instability

The reverse current at large applied voltage leads to a power dissipation and heating of the junction. This temperature increase leads to a further increase of the saturation current (21.133). If the heat sink, e.g. the mounting of the chip, is not able to transport the heat away from the device, the current increases indefinitely. If not limited by a resistor, such a current can destroy the device. The thermal instability is particularly important for diodes with high saturation current, e.g. Ge at room temperature.

Tunneling

At large reverse bias, charge carriers can tunnel between conduction and valence band through the junction. A more detailed discussion will be given below in Sect. 21.5.9 about the tunneling diode. Since for the tunneling effect a thin barrier is necessary, breakdown due to tunneling is important for diodes where both sides are highly doped. For Si and Ge diodes, tunneling dominates the breakdown if the breakdown voltage V_{br} is $V_{br} < 4E_g/e$. For $V_{br} > 6E_g/e$ avalanche multiplication dominates. The intermediate regime is a mixed case.

With increasing temperature, the tunneling current can be achieved already with a smaller field (since the band gap decreases with increasing temperature), thus the breakdown voltage *decreases* (negative temperature coefficient).

Avalanche Multiplication

Avalanche multiplication due to impact ionization is the most important mechanism for the breakdown of pn diodes. It limits the maximum reverse voltage for most diodes and also the collector voltage in a bipolar transistor or the drain voltage in a field-effect transistor. Avalanche multiplication can be used for the generation of microwave radiation or for photon counting (cf. Sect. 22.3.6).

Impact ionization was discussed in Sect. 8.4.4. The most important parameters are the electron and hole ionization coefficients α_n and α_p. For discussion of the diode breakdown, we assume that at $x = 0$ a hole current I_{p_0} enters the depletion layer. This current is amplified by the field in the depletion layer and impact ionization. At the end of the depletion layer ($x = w$), it is $M_\mathrm{p} I_{\mathrm{p}_0}$, i.e. $M_\mathrm{p} = I_\mathrm{p}(w)/I_\mathrm{p}(0)$. Similarly, an electron current is increased on its way from w to $x = 0$. The incremental change of the hole current due to electron-hole pairs generated along a line element $\mathrm{d}x$ is

$$\mathrm{d}I_\mathrm{p} = (I_\mathrm{p}\,\alpha_\mathrm{p} + I_\mathrm{n}\,\alpha_\mathrm{n})\,\mathrm{d}x \ . \tag{21.160}$$

The total current in the depletion layer is $I = I_\mathrm{p} + I_\mathrm{n}$ and is constant in stationary equilibrium. Therefore,

$$\frac{\mathrm{d}I_\mathrm{p}}{\mathrm{d}x} - \left(\alpha_\mathrm{p} - \alpha_\mathrm{n}\right)\, I_\mathrm{p} = \alpha_\mathrm{n}\, I \ . \tag{21.161}$$

The solution is

$$I_\mathrm{p}(x) = I \frac{\frac{1}{M_\mathrm{p}} + \int\limits_0^x \alpha_\mathrm{n}\, \exp\left[-\int\limits_0^x (\alpha_\mathrm{p} - \alpha_\mathrm{n})\,\mathrm{d}x'\right] \mathrm{d}x}{\exp\left[-\int\limits_0^x (\alpha_\mathrm{p} - \alpha_\mathrm{n})\,\mathrm{d}x'\right]} \ . \tag{21.162}$$

For $x = w$ we find for the multiplication factor

$$1 - \frac{1}{M_\mathrm{p}} = \int\limits_0^w \alpha_\mathrm{n}\, \exp\left[-\int\limits_0^x (\alpha_\mathrm{p} - \alpha_\mathrm{n})\,\mathrm{d}x'\right] \mathrm{d}x \ . \tag{21.163}$$

Avalanche breakdown is reached for $M_\mathrm{p} \to \infty$, i.e. when

$$\int\limits_0^w \alpha_\mathrm{n}\, \exp\left[-\int\limits_0^x (\alpha_\mathrm{p} - \alpha_\mathrm{n})\,\mathrm{d}x'\right] \mathrm{d}x = 1 \ . \tag{21.164}$$

A corresponding and equivalent equation is obtained when the consideration is started with the electron current. If $\alpha_\mathrm{p} = \alpha_\mathrm{n} = \alpha$, (21.164) simplifies to

$$\int\limits_0^w \alpha\,\mathrm{d}x = 1 \ . \tag{21.165}$$

This means that per transit of one carrier through the depletion layer, on average another carrier is created such that the process just starts to diverge. The breakdown voltage for various semiconductor materials is shown in Fig. 21.54a as a function of the doping level. The depletion-layer width w at breakdown and the maximum electric field E_m are depicted in Fig. 21.54b.

The average impact ionization coefficient α has been given as [1773]

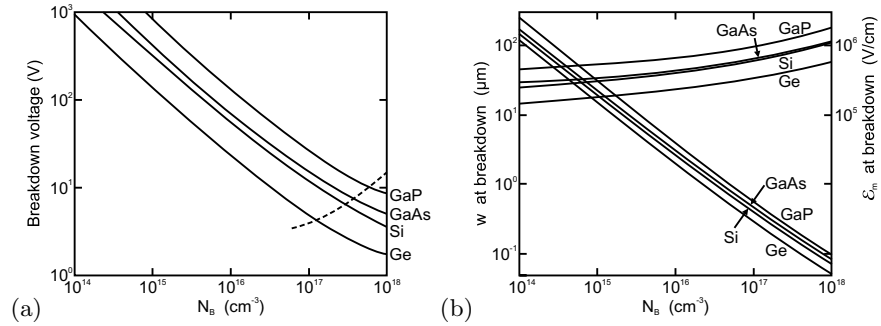

Fig. 21.54 **a** Avalanche breakdown voltage for one-sided abrupt junctions in Ge, Si, (100)-GaAs and GaP at $T = 300\,\mathrm{K}$. The *dashed line* indicates the limit of avalanche breakdown at high doping due to tunneling breakdown. **b** Depletion-layer width w at breakdown and maximum electric field E_m for the same junctions. Adapted from [1772]

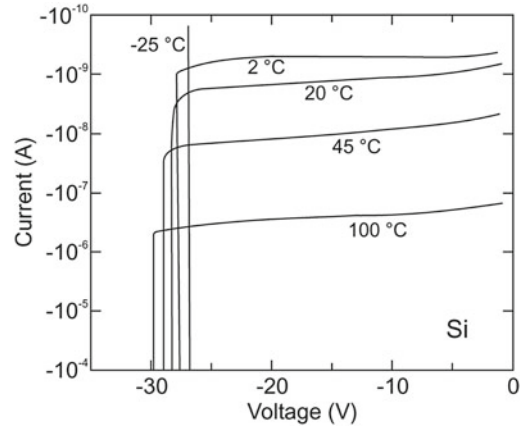

Fig. 21.55 Temperature dependence of a n^+p Si-diode with $N_\mathrm{B} = 2.5 \times 10^{16}\,\mathrm{cm}^{-3}$ and a guard-ring structure (see Fig. 21.56d). The temperature coefficient $\partial V_\mathrm{br}/\partial T$ is 0.024 V/K. Adapted from [1776]

$$\alpha = A\,E^7\ . \tag{21.166}$$

for silicon with $A = 1.8 \times 10^{-35}\,(\mathrm{cm/V})^7\ \mathrm{cm}^{-1}$. For the breakdown condition (21.165), using (21.9) and (21.166) the depletion layer width at breakdown w_B (w_B in cm, N_D in cm^3) is found to be

$$w_\mathrm{B} = 2.67 \times 10^{10}\,N_\mathrm{D}^{-7/8}\ . \tag{21.167}$$

From this the breakdown voltage can be calculated with (21.15) (V_B in V, N_D in cm^3) [1774]

$$V_\mathrm{B} = 6.40 \times 10^{13}\,N_\mathrm{D}^{-3/4}\ . \tag{21.168}$$

In GaAs, the impact-ionization coefficients and therefore the breakdown voltage are direction dependent. At a doping of $N_\mathrm{B} = 10^{16}\,\mathrm{cm}^{-3}$, the breakdown voltage is the same for (001) and (111) orientation; for smaller doping the breakdown voltage of (001)-oriented GaAs is smaller, for larger doping that of GaAs (111) [1775].

At higher temperatures, the charge carriers release their excess energy faster to the lattice.[24] Thus, less energy is available for impact ionization and the required electric field is higher. Therefore, the

[24]The scattering rate becomes higher with increasing temperature and, e.g., the mobility decreases, see Sect. 8.3.11, and the drift saturation velocity decreases, see Sect. 8.4.1.

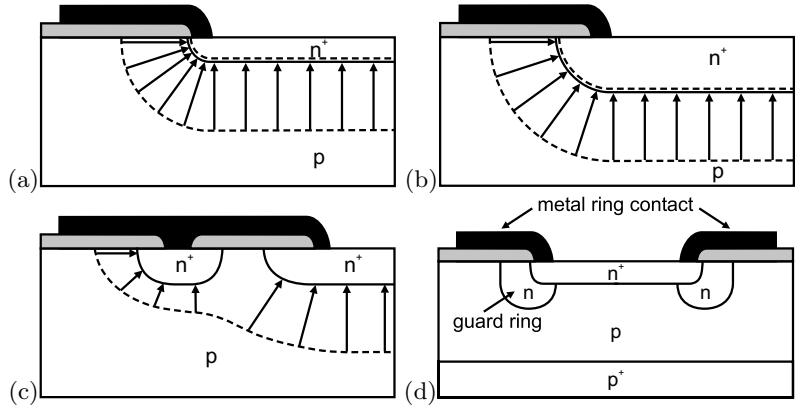

Fig. 21.56 **a** Large electric fields at large curvatures in a shallow junction. Avoidance of regions with large electric fields by **b** deep junction and **c** field-ring structure. **d** shows a guard-ring structure with circular, low-doped n region. *Grey area* denotes insulating material, arrows indicate field lines and the *dashed lines* indicate the extension of the depletion layers

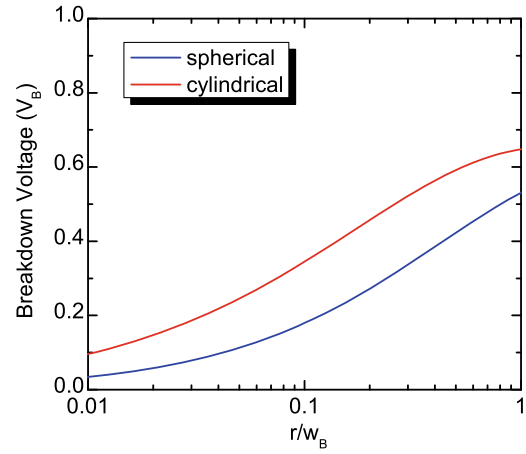

Fig. 21.57 Breakdown voltage (in units of the breakdown voltage V_B of a plane junction) for cylindrical and spherical junctions as a function of the curvature radius (in units of the depletion layer width at breakdown W_B for a plane junction). Data from [1774]

breakdown voltage *increases* with the temperature (Fig. 21.55). This behavior is opposite to tunneling diodes and the two processes can be distinguished in this way.

In planar structures (Fig. 21.56a), high electric fields as present in high power devices will occur at the parts with large curvature. At these sites breakdown will occur first and at much lower voltages than expected for a perfectly planar (infinite) structure [1777, 1778]. For devices that require high breakdown voltage, design changes have to be made. These include deep junctions (Fig. 21.56b) with a smaller curvature, a field-ring structure (Fig. 21.56c) in which an additional depletion layer is used to smooth the field lines and the often used guard ring (Fig. 21.56d) for which a circular region of low doping (and thus high breakdown voltage) is incorporated.

The decrease of breakdown voltage in a junction with cylindrical and spherical geometry has been numerically calculated as a function of curvature [1779] (Fig. 21.57). Analytical formulas in terms of the ratio of radius of curvature and the depletion layer width at breakdown for a plane junction r/w_B have been given later [1774].

Defects

In material with extended defects such as polycrystalline silicon breakdown can occur locally at lower voltage than in the corresponding defect-free bulk material ('pre-breakdown') [1771]. This effect typically occurs at certain grain boundaries and probably involves mid-gap states. It is also accompanied with electroluminescence by which it can be detected with high spatial resolution (Fig. 21.58).

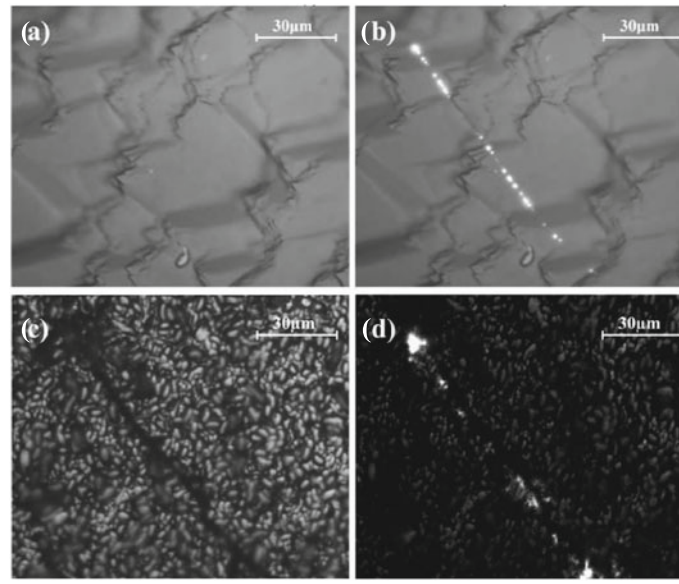

Fig. 21.58 Microscopic (**a**) forward bias electroluminescence and (**b**) microscopic reverse bias electroluminescence (µ-ReBEL) image of an alkaline texturized solar cell (cmp. Fig. 22.61) in a region without specific surface features at $U = -17$ V. The bulk defects at these positions are revealed topographically in the neighboring acidic texturized solar cell in the microscopic (**c**) image. Their ReBEL pattern appears similarly in the corresponding EL image (**d**). Adapted from [1771]

21.4.6 Heterostructure Diodes

In a heterostructure diode, the n- and p-regions are made of different semiconductors. Such structures are discussed in detail in [1780].

Type-I Heterostructure Diodes

In Fig. 21.59, the band diagram is shown for a type-I heterostructure with the n (p) region having the larger (smaller) band gap. Additionally to the built-in voltage, the barrier in the valence band is increased. Such a diode finds application in particular as an injection (emitter-base) diode in heterostructure bipolar transistors (Sect. 24.2.7). In such diode the (mostly undesired) hole current from the p- to the n-side is reduced. The peak in the conduction band poses potentially a greater barrier for electron transport across the interface than the diffusion potential itself. The spike can be reduced by grading the materials across the heterojunction and creating a smooth transition of E_g between the materials. The effect of grading on the properties of the heterojunction is discussed in detail in [1781].

Type-II Heterostructure Diodes

Many semiconductors can only be doped n-type or p-type (cmp. Sect. 7.4.2). Bipolar heterostructures can be formed and, depending on the position of the bands relativ to the vacuum level, can form a type-II heterostructure. Examples are p-NiO/n-ZnO or p-CuI/n-ZnO; the band diagram of the latter is depicted in Fig. 21.60a for a typical situation (p^+-n diode) [568, 1782]. Rectification for such device can be very high ($> 10^{10}$, Fig. 21.60b). Minority carrier injection is excluded due to the high barriers. The current across the interface is a recombination current, presumably via interface defects, which exhibits an ideality factor around 2 [1783].

21.4.7 Organic Semiconductor Diodes

A bipolar diode from organic semiconductors consists of the p-conductive hole transport layer (HTL) and the n-conductive electron transport layer (ETL). The low conductivity of organic semiconductors

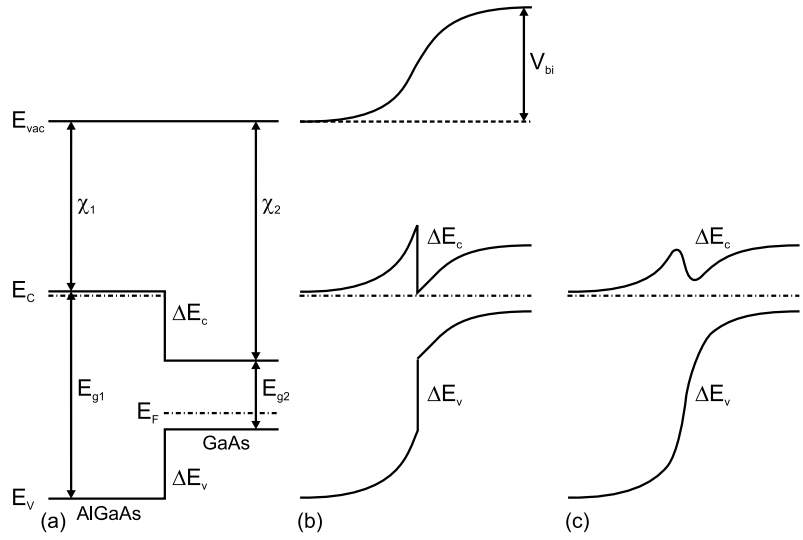

Fig. 21.59 Schematic band diagram of a n-AlGaAs/p-GaAs diode **a** without contact of the n- and p-materials, **b** in thermodynamic equilibrium, and **c** with graded Al composition at the heterointerface

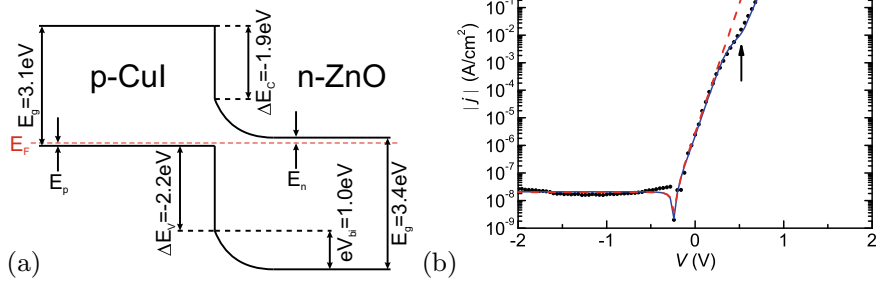

Fig. 21.60 **a** Schematic band diagram of a p-CuI/n-ZnO diode. Adapted from [1782]. **b** jV-characteristics (room temperature) of type-II epitaxial CuI/ZnO heterojunction bipolar diode (*symbols*) and fit (*red dashed line*) with $j_s = 2\times10^{-8}$ A/cm^2 and ideality factor $n = 1.8$. The other fit (*blue line*) takes into account additionally a barrier inhomogeneity and the series resistance. Adapted from [1784]

causes the applied voltage to drop over the entire structure [1785–1787] (Fig. 21.61c) while in a typical silicon diode for sufficient forward bias (and moderate injection, cmp. Fig. 21.50) flat-band conditions are present (Fig. 21.61b). The first organic homodiode was reported only in 2005 for zinc-phthalocyanine (ZnPc) doped with $[Ru(terpy)_2]^0$ (n-type) and F_4-TCNQ (p-type, cmp. Fig. 18.7b) [1788]. Deviation from ideal Shockley behavior is discussed in this report.

The hole injecting contact is often made from ITO, the electron injection contact from low work function metals such as Al, Mg or Ca. Specially designed layers for efficient charge injection (HIL, hole injection layer [1789] and EIL, electron injection layer [1790]) can be introduced between the contact metal and the transport layers (Fig. 21.62c). The particular level lineup of the HTL and HTL as shown in Fig. 21.61c (also Fig. 21.62a) leads to a barrier for electrons and holes. The hole and/or electron blocking is beneficial for recombination in the vicinity of the interface and prevents exciton diffusion to the contacts. In organic light emitting diodes (Sect. 23.3.7) an additional layer (EML, emission layer) designed for efficient radiative recombination (Sect. 18.6) is introduced between HTL and ETL (Fig. 21.62b).

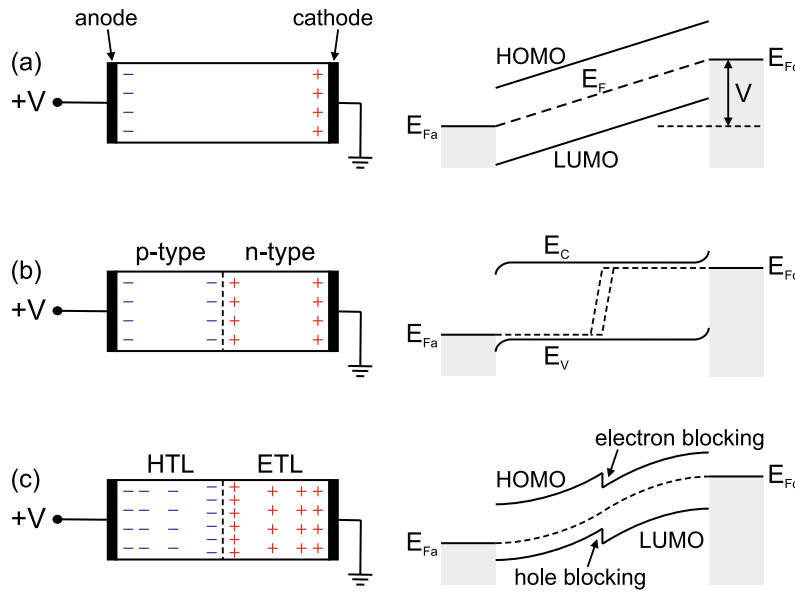

Fig. 21.61 Schematic sample geometry and charge distribution (*left*) and energy diagram (*right*) for **a** an ideal insulator, **b** a typical inorganic semiconductor pn diode and **c** a double layer organic diode under forward bias V. Adapted from [1787]

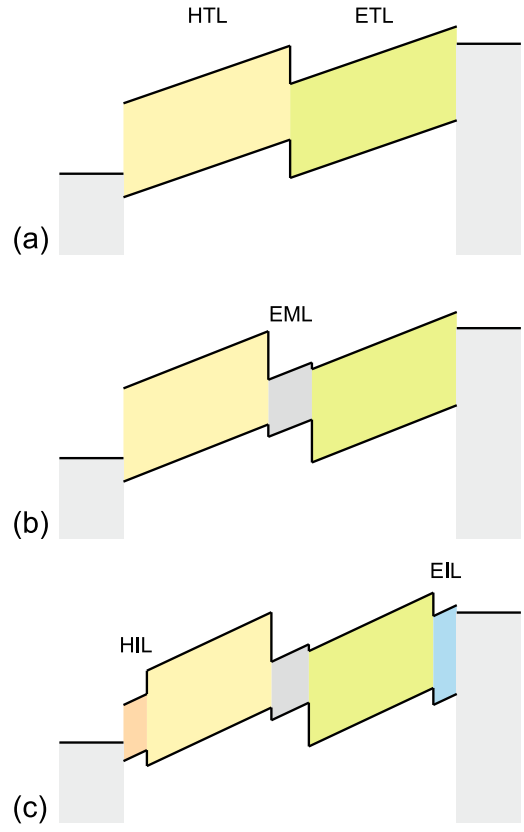

Fig. 21.62 Schematic energy diagram for **a** dual layer organic diode (HTL, ETL), **b** with additional emission layer (EML) and **c** with further hole and electron injection layers (HIL, EIL)

21.5 Applications and Special Diode Devices

In the following, various electronic applications of diodes are discussed. The most important special diode types are introduced. Optoelectronic applications (involving absorption and emission of photons) are treated below (Sect. 22). The applications of Schottky diodes are discussed in [1791].

21.5.1 Rectification

In a rectifier, the diode has to supply a high resistivity for one polarity of the bias and a low one to the other polarity. In Fig. 21.63a, a single-path rectification method is shown. Only the positive half-wave can pass the load resistor R_L (Fig. 21.63b). In Fig. 21.63c, the characteristic of a Si diode is shown. Of course, the voltage drop across the diode can only range in the 1-V regime. In order to make the setup work, the load resistor has to be considered. The total current is given by $I = I_\mathrm{s}[\exp(eU_\mathrm{d}/nkT) - 1]$. The total voltage U is split between the voltage drop across the diode U_d and that over the load resistance $U_\mathrm{L} = R_\mathrm{L} I$. The current is therefore given by

$$I = \frac{U - U_\mathrm{d}}{R_\mathrm{L}} \,. \tag{21.169}$$

For sizeable currents the voltage drop across the diode U_d is between 0.7 and 1 V. The characteristic is linear between about 1 and 220 V (Fig. 21.63d). Typically, the voltage U_L is low-pass filtered with a capacitor parallel to the load resistor. The effective voltage is the peak voltage divided by 2.

The drawback of the single diode rectifier is that only the positive half-wave contributes to a dc signal. The setup in Fig. 21.63e (bridge rectifier) allows both half-waves to contribute to the dc signal. The effective voltage in this case is the peak voltage divided by $\sqrt{2}$.

The forward resistance in the static (R_f) and dynamic (r_f) case are (for $\beta V_\mathrm{f} > 3$)

$$R_\mathrm{f} = \frac{V_\mathrm{f}}{I_\mathrm{f}} \cong \frac{V_\mathrm{f}}{I_\mathrm{s}} \exp\left(-\frac{e\,V_\mathrm{f}}{n\,kT}\right) \tag{21.170a}$$

$$r_\mathrm{f} = \frac{\partial V_\mathrm{f}}{\partial I_\mathrm{f}} = \frac{n\,kT}{e\,I_\mathrm{s}} \exp\left(\frac{e\,V_\mathrm{f}}{n\,kT}\right) \cong \frac{n\,kT}{e\,I_\mathrm{f}} \,. \tag{21.170b}$$

For reverse bias we have ($\beta|V_\mathrm{r}| > 3$)

$$R_\mathrm{r} = \frac{V_\mathrm{r}}{I_\mathrm{r}} \cong \frac{V_\mathrm{r}}{I_\mathrm{s}} \tag{21.171a}$$

$$r_\mathrm{r} = \frac{\partial V_\mathrm{r}}{\partial I_\mathrm{r}} = \frac{nkT}{eI_\mathrm{s}} \exp\left(\frac{e\,|V_\mathrm{r}|}{n\,kT}\right) \,. \tag{21.171b}$$

Thus, the dc and ac rectifications ratios are given by

$$\frac{R_\mathrm{r}}{R_\mathrm{f}} = \exp\left(\frac{e\,V_\mathrm{f}}{n\,kT}\right) \tag{21.172a}$$

$$\frac{r_\mathrm{r}}{r_\mathrm{f}} = \frac{I_\mathrm{f}}{I_\mathrm{s} \exp\left(\frac{e\,|V_\mathrm{r}|}{n\,kT}\right)} \,. \tag{21.172b}$$

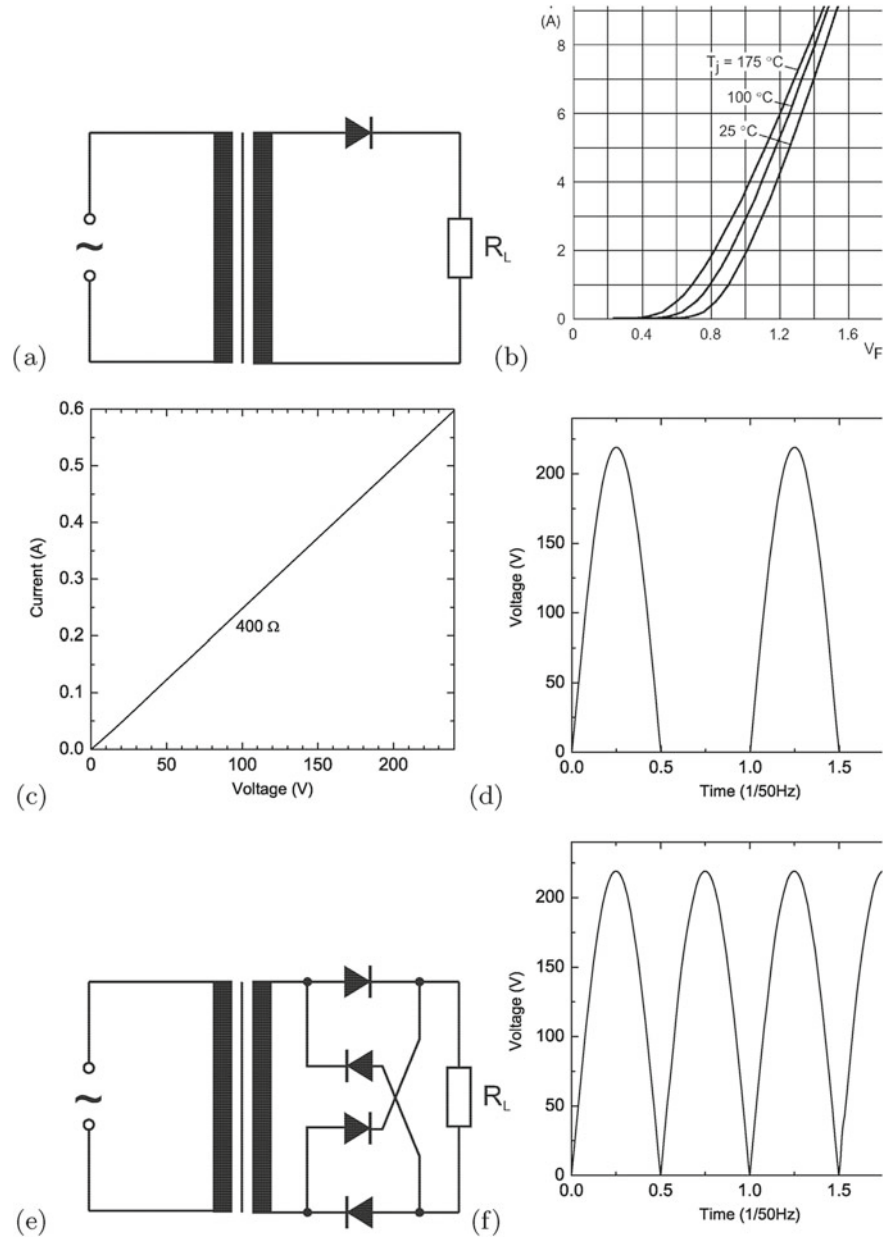

Fig. 21.63 **a** Single-path mains rectifier, **b** characteristics of Si diode (BYD127, Philips), **c** load characteristics of the mains rectifier ($R_L = 400\,\Omega$), **d** voltage output of single-path mains rectifier. **e** depicts the schematic circuit of a bridge rectifier that works for both half-waves, **f** the resulting voltage output

Rectifiers generally have slow switching speeds. A significant time delay arises from the necessary charge-carrier recombination when the diode switches from low (forward) to high (reverse) impedance. This poses typically no problem for line-frequency (50–60 Hz) applications. For fast applications, however, the minority carrier lifetime needs to be reduced, e.g. by doping Si with Au (see Sect. 10.9).

21.5.2 Frequency Mixing

The nonlinear characteristic of the diode allows the mixing of frequencies, e.g. for second- (or higher-) harmonic generation, upconversion or demodulating of radio-frequency (RF) signals. A single balanced mixer is shown in Fig. 21.64a, b. The RF signal consists of a RF carrier frequency f_0 modulated with an intermediate frequency (IF) signal $f_{\mathrm{IF}}(t)$. It is mixed with a local oscillator (LO) that has a constant frequency f_{LO} outside the RF modulation bandwidth $f_0 \pm f_{\mathrm{IF}}$. The IF signal can be detected from the setup in Fig. 21.64a if filtered through a low-pass filter to avoid loss of power to the IF amplifier. The temperature dependence of the diode characteristic (via j_{s} and β) on mixing efficiency is typically less than 0.5 dB for a 100-K change in temperature.

Problems of single-diode mixers are the radiation of local-oscillator power from the RF input port,[25] loss of sensitivity by absorption of input power in the local oscillator circuit, loss of input power in the intermediate frequency amplifier, and the generation of spurious output frequencies by harmonic mixing. Some of these problems can be solved by circuit techniques, but these circuits often introduce new problems. Most mixers therefore use multiple-diode techniques to provide a better solution of these problems. In Fig. 21.64c, the circuit diagram of a double balance mixer is shown. Even-order harmonics of both the LO and the signal frequency are rejected. This mixer does not require a low-pass filter to isolate the IF circuit. The three ports are isolated from each other by the symmetry of the circuit. These mixers usually cover a broader frequency band than the others. Ratios as high as 1000:1 are available. Microwave equivalents (working at $f \gg 1\,\mathrm{GHz}$) of such mixer circuits are available. Bandwidth ratios as high as 40:1 are available at microwave frequencies in MMICs (millimeter-wave integrated circuits).

The common drawback of MMIC diodes is that they are obtained from the Schottky barriers used in field-effect transistors, that have inferior performance compared to discrete diodes. The use of pHEMT technology[26] for millimeter-wave applications provides diodes that differently from regular Schottky diodes, since they consist of a Schottky barrier in series with a heterojunction. In Fig. 21.64d, a MMIC 45 GHz mixer is shown using fast GaAs-based pHEMTs.

21.5.3 Voltage Regulator

In a voltage regulator, the large variation of resistance with applied bias is used. This effect occurs in the forward direction and close to the breakdown voltage.

In Fig. 21.65a, a simple circuit is shown. When the input voltage V_{in} is increased, the current increases. The preresistor $R_1 = 5\,\mathrm{k\Omega}$ and the load resistor represent a voltage divider with $V_{\mathrm{in}} = I R_1 + V_{\mathrm{out}}$. The total current I is given by the two currents through the diode and the load resistor $I = I_{\mathrm{s}}[\exp(\beta V_{\mathrm{out}}/n) - 1] + V_{\mathrm{out}}/R_{\mathrm{L}}$. Therefore, the output voltage is implicitly given by

[25] That in military applications could make the mixer detectable by the enemy.

[26] Pseudomorphic high electron mobility transistors, cf. Sect. 24.5.8.

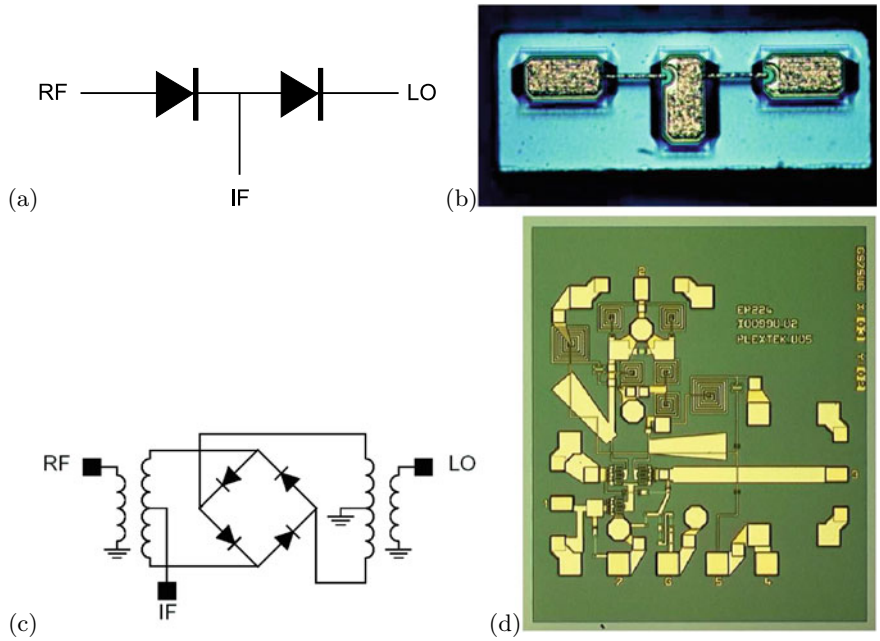

Fig. 21.64 **a** Schematic circuit of single balanced mixer with input (RF: radio frequency, LO: local oscillator) and output (IF: intermediate frequency). **b** Optical plan-view image ($300 \times 125\ \mu m^2$) of a high-speed single balanced mixer with two GaAs Schottky diodes with opposite poling. The device properties are $R_s = 5\,\Omega$, for $I = 1\ \mu A$ a forward and reverse voltage of 0.7 and 6 V, respectively; the capacitance of each diode is 8 fF. Reprinted with permission from [1792]. **c** Schematic circuit of a double balanced mixer. **d** Optical image ($1.65\,mm^2$) of 40–45 GHz MMIC (Gilbert cell) mixer on GaAs basis using pHEMTs. Reprinted with permission from [1793]

$$V_{out}\left(1+\frac{R_1}{R_L}\right) = V_{in} - R_1\, I_s\left[\exp\left(\frac{\beta V_{out}}{n}\right) - 1\right]. \tag{21.173}$$

A large current change is related to a fairly small change of the voltage across the diode, which at the same time is the output voltage. Therefore, a change in the input voltage causes only a small change in the output voltage.

We assume a diode with $n = 1$ and $I_S = 10^{-14}\,A$ with the characteristic shown in Fig. 21.65a. The numerical example in Fig. 21.65c is calculated for $R_L = 2\,k\Omega$ and $4\,k\Omega$, respectively. The output voltage varies by about 0.02 V if the input varies between 5 and 9 V. In Fig. 21.65d, the differential voltage change $\alpha = \frac{V_{in}}{V_{out}}\frac{\partial V_{out}}{\partial V_{in}}$ is shown.

In this way, voltage peaks can be filtered from the input voltage. If two antiparallel diodes are used, this principle works for both polarities. Instead of a diode in the forward direction, the very steep slope of the diode I–V characteristic at the breakdown can be used. Just before breakdown, the diode has a high resistance and the voltage drops at the load resistor. If the input voltage increases a little, the diode becomes conductive and shorts the additional voltage (the maximum allowed breakdown current needs to be observed!). Due to its small saturation current, typically Si diodes are used. The breakdown voltage can be designed via the diode parameters. Such diodes with defined breakdown voltage are called Z- or Zener diodes (see next section).

If the breakdown is due to tunneling (avalanche multiplication), the breakdown voltage decreases (increases) with temperature. If two diodes with positive and negative temperature coefficient are put in series, a very good temperature stability of the breakdown voltage of 0.002%/K can be achieved. Such diodes can be used to realize a reference voltage.

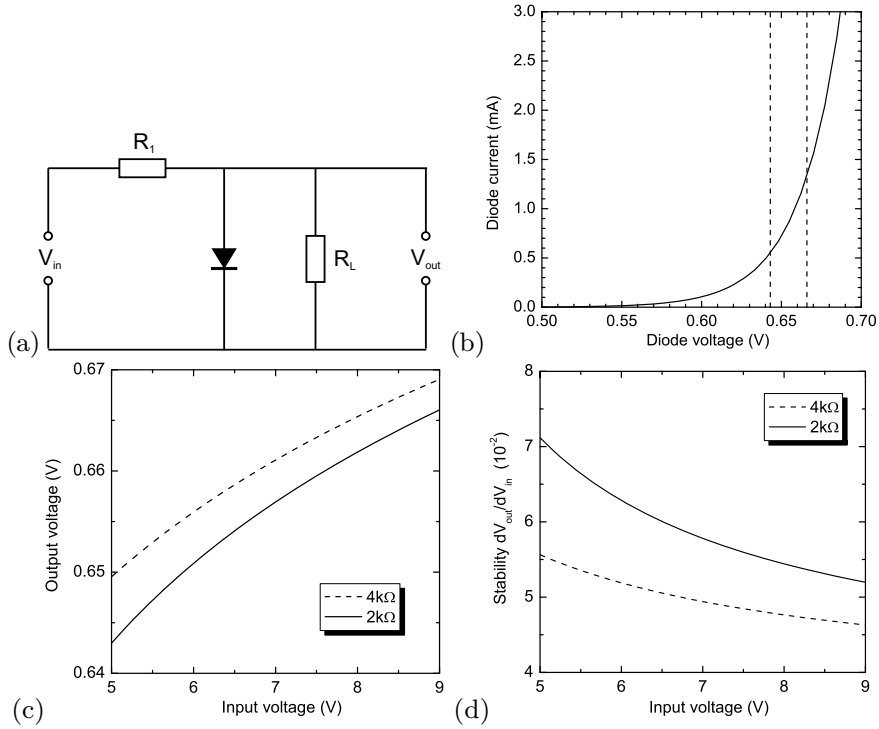

Fig. 21.65 **a** Circuit diagram of a voltage regulator, **b** diode characteristic ($n = 1$). The *vertical dashed lines* show the operation conditions for $R_L = 2\,\mathrm{k\Omega}$ and $U_E = 5$ and 9 V and thus the principle of voltage stabilization. **c** Output versus input voltage and **d** stability (differential voltage ratio α, see text) for input voltage between 5 and 9 V

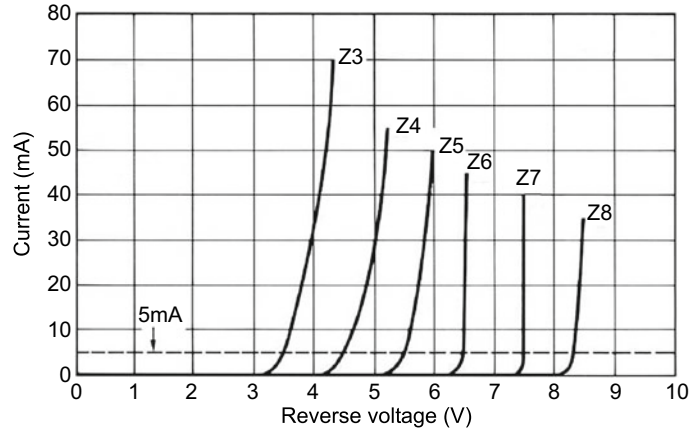

Fig. 21.66 Characteristics of a field of Zener diodes (at room temperature)

21.5.4 Zener Diodes

A Zener diode is designed to have a defined breakdown voltage. Zener diodes are available with a number of different standard breakdown voltages. Their characteristic is shown for reverse bias with the current shown positive. The characteristics of various Zener diodes for different breakdown voltages are shown in Fig. 21.66.

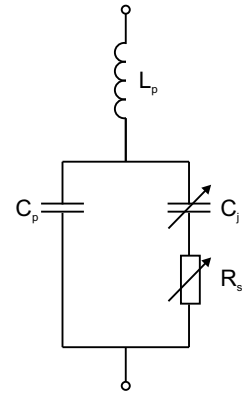

Fig. 21.67 Equivalent circuit of a varactor diode with parasitic capacitance C_p and inductance L_p and variable capacitance C_j and resistance R_s

21.5.5 Varactors

A diode exhibits a voltage-dependent capacitance. This effect can be used to tune an oscillator using the diode bias (voltage-controlled oscillator, VCO). The equivalent circuit is shown in Fig. 21.67. The capacitance consists of a parasitic capacitance C_p due to mounting and bonding. This effect also causes a parasitic inductance. The series resistance due to mounting can typically be neglected. The variable junction capacitance C_j and the ohmic resistance R_s are bias dependent.

The $C(V)$ dependence has generally a power law with an exponent γ (which itself may depend on the bias voltage)

$$C = \frac{C_0}{(1 + V/V_\mathrm{bi})^\gamma} \,, \tag{21.174}$$

where C_0 is the-zero bias capacitance. Since the frequency f of an LC oscillator circuit depends on $C^{-1/2}$ the frequency, f depends on the voltage as $f \propto V^{\gamma/2}$. Therefore, a $\gamma = 2$ dependence is most desirable.

For uniformly doped profiles, the capacitance depends with an inverse square root law on the applied voltage (21.117), i.e. $\gamma = 0.5$. Hyperabrupt junctions are typically made by ion implantation or epitaxy with graded impurity incorporation to create a special nonuniform doping profile (Fig. 21.68a). For a doping profile

$$N_\mathrm{B}(z) = \hat{N}_\mathrm{B} \left(\frac{z}{z_0}\right)^m \tag{21.175}$$

the capacitance is given as

$$C = \left[\frac{e\,\hat{N}_\mathrm{B}\,\epsilon_\mathrm{s}^{m+1}}{(m+2)\,z_0^m\,(V_\mathrm{bi} - V)}\right]^{\frac{1}{m+2}} = \frac{C_0}{(1 + V/V_\mathrm{bi})^{1/(m+2)}} \,. \tag{21.176}$$

Ideally, $m = -3/2$ results is a linear frequency versus voltage relation. The C–V characteristic of an implanted, hyperabrupt diode exhibits a part that has an exponent $\gamma = 2$ (Fig. 21.68b). A $\gamma = 2$ $C(V)$ dependence and therefore a linear $f(V)$ curve can be achieved over more than one octave using computer-controlled variable epitaxial-layer doping (Fig. 21.68c).

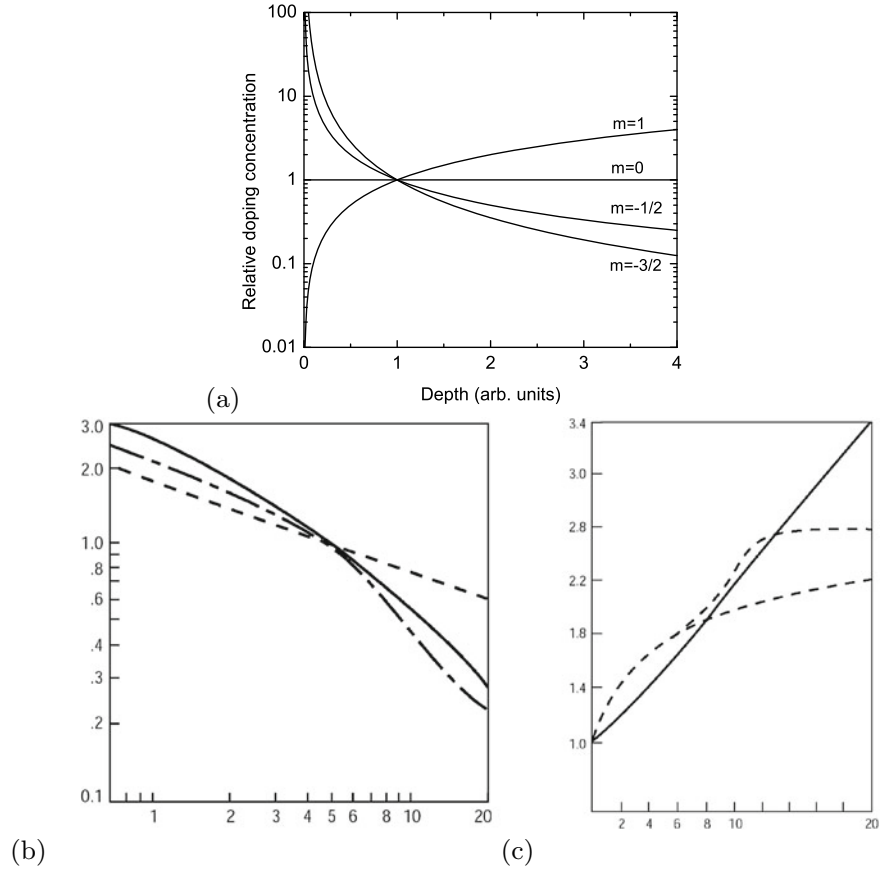

Fig. 21.68 **a** Donor-doping profile according to (21.175) in p^+n or Schottky diodes for $m = 0$ (abrupt junction), $m = 1$ (linearly graded junction) and two values with $m < 0$ (hyperabrupt junctions). **b** Bias dependence of capacitance for diodes with abrupt junction ('A', $\gamma = 0.5$), hyperabrupt junction ('H', $\gamma > 0.5$) and 'epilinear' junction ('L', $\gamma = 2$). **c** Frequency-voltage tuning characteristics (scaled to 1.0 for $V = 0$) for the three diode types. Parts (**b**) and (**c**) adapted from [1794], reprinted with permission

21.5.6 Fast-Recovery Diodes

Fast-recovery diodes are designed for high switching speeds. The switching speed from the forward to the reverse regime is given by the time $t_0 = t_1 + t_2$ with t_1 being the time to reduce the minority carrier density to the equilibrium value (e.g. $p_n \rightarrow p_{n_0}$) and t_2 being the time in which the current decreased exponentially (Fig. 21.69). The time t_1 can be drastically reduced by incorporation of deep levels that act as recombination centers. A prominent example is Si:Au. However, this concept is limited since the reverse generation current, e.g. (21.154), depends on the trap density. For direct semiconductors, recombination times are short, e.g. 0.1 ns or less for GaAs. In silicon, they can be extremely long (up to ms) or at least 1–5 ns. Schottky diodes are suitable for high-speed applications since they are majority carrier devices and minority charge carrier storage can be neglected.

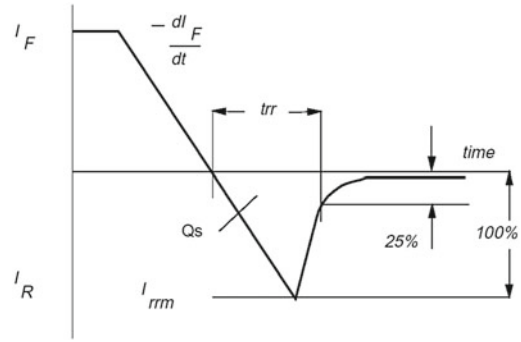

Fig. 21.69 Current versus time trace for a (soft) fast-recovery diode. Reprinted with permission from [1795]

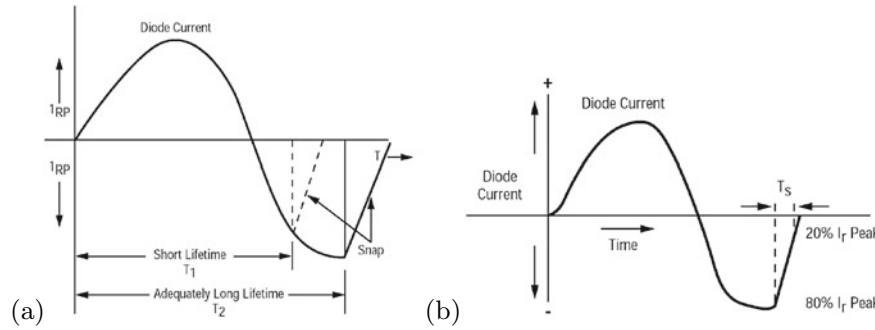

Fig. 21.70 **a** Current versus time trace for a step-recovery diode and sinusoidal voltage input. The lifetime must be sufficiently large such that a current peak is reached. **b** Definition of the snapback time T_s. Reprinted with permission from [1796]

21.5.7 Step-Recovery Diodes

This type of diode is designed to store charge in the forward direction. If polarity is reversed, the charge will allow conductance for a short while, ideally until a current peak is reached (Fig. 21.70a), and then cutoff the current very rapidly during the so-called snapback time T_s (Fig. 21.70b). The cutoff can be quite rapid, in the ps regime. These properties are used for pulse (comb) generation or as a gate in fast sampling oscilloscopes. In Si, only 0.5–5 µs are reached (fast-recovery diode, see previous section) while GaAs diodes can be used in the several tens of GHz regime.

Using a heterostructure GaAs/AlGaAs diode (cf. Sect. 21.4.6), as shown schematically in Fig. 21.71a, a steepening of a 15-V, 70-ps (10% to 90%) pulse to a fall time of 12 ps was observed (Fig. 21.71c). The forward current of the diode was 40 mA, supplied via a bias tee.

21.5.8 Pin-Diodes

In a pin-diode, an intrinsic (i), i.e. undoped region (with higher resistivity) is located between the n- and the p-regions. Often, also a region with low n- or p-doping is used. In this case, the center region is denoted as a ν- or π-region, respectively. The fabrication of arbitrary doping profiles and an intrinsic region poses little problem for epitaxial diodes.

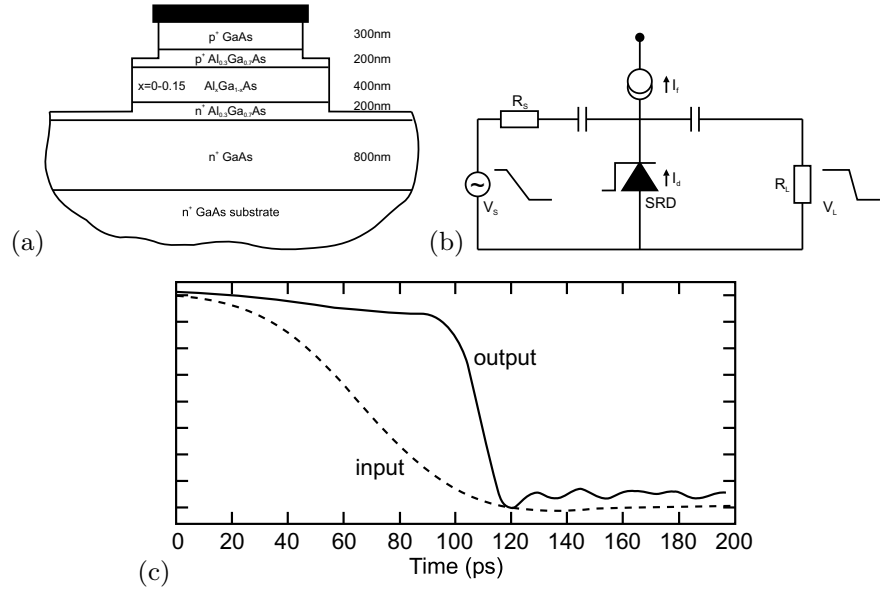

Fig. 21.71 **a** Schematic layer sequence for fast GaAs/AlGaAs step-recovery diode. **b** Circuit with input and output pulse. **c** Input (*dashed line*) and output (*solid line*) waveforms. Vertical division is 2 V. Adapted from [1797]

Via the Poisson equation, the charge in the intrinsic layer is related to the electric field. If no dopants are present, there is a constant (maximum) field in the i-region at zero bias. If there is low doping, a field gradient exists.

The capacitance for reverse bias is $\epsilon_s A/w$ and is constant starting at fairly small reverse bias (10 V). The series resistance is given by $R_s = R_i + R_c$. The contact resistance R_c dominates the series resistance for large forward bias (Fig. 21.72).

21.5.9 Tunneling Diodes

For the invention of the tunneling diode and the explanation of its mechanism the 1973 Nobel Prize in Physics was awarded to Esaki [1798]. Eventually, the tunneling diode did not make the commercial breakthrough due to its high basis capacitance. It is used for special microwave applications with low power consumption, for frequency stabilization and possibly in tunneling field-effect transistors (Sect. 24.5.6). Reviews can be found in [1799, 1800].

First, the tunneling diode is a pn diode. While the tunnel effect [1801] has already been discussed for Schottky diodes, it has not yet been considered by us for pn diodes. We expect the tunnel effect to be important if the depletion-layer is thin, i.e. when the doping of both sides is high.

The doping is so high that the quasi-Fermi levels lie within the respective bands (Fig. 21.73). The degeneracy is typically several kT and the depletion layer width is in the 10 nm range.

In the forward direction, the I–V characteristic of the tunneling diode exhibits a maximum followed by a minimum and subsequently an exponential increase (Fig. 21.74a). As shown in Fig. 21.74b, the total current consists of three currents, the band-to-band tunneling current, the excess current and the thermal (normal thermionic diode) current.

The $V = 0$ situation is again shown in Fig. 21.75b. Upon application of a small forward bias, electrons can tunnel from populated conduction-band states on the n-doped side into empty valance-

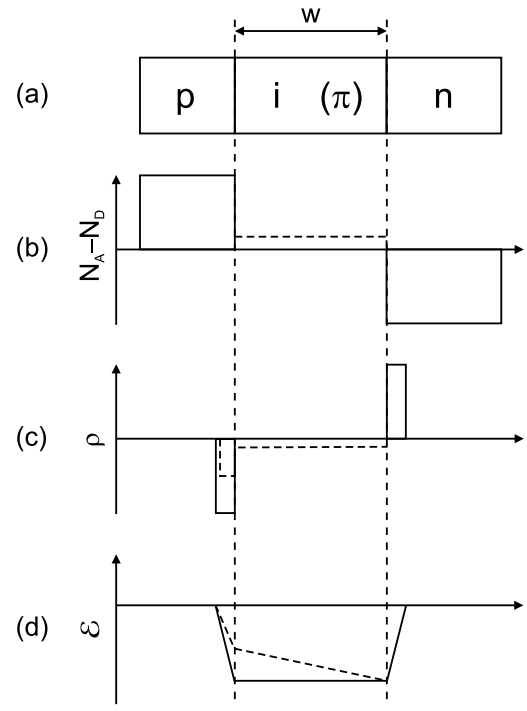

Fig. 21.72 **a** Schematic layer sequence of pin-diode ('i': intrinsic, 'π': lowly p-doped), **b** net impurity distribution $N_A - N_D$, **c** space charge and **d** electric field in a pin (*solid lines*) and a p–π–n (*dashed lines*) diode

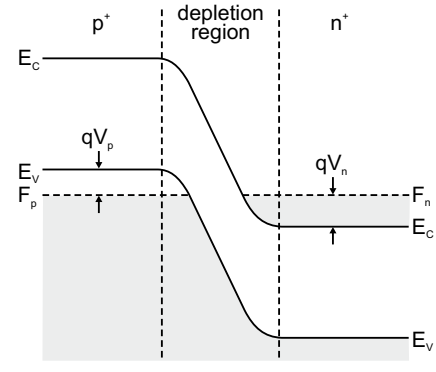

Fig. 21.73 Band diagram of a tunneling diode in thermodynamic equilibrium ($V = 0$). V_n and V_p characterize the degeneracies on the n- and p-side, respectively

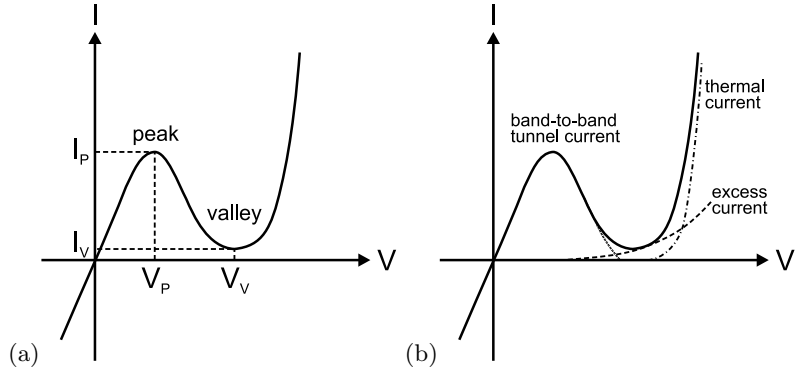

Fig. 21.74 **a** Static current-voltage characteristics of a typical tunneling diode. Peak and valley current and voltage are labeled. **b** The three components of the current (*short dashed*: band-to-band tunnel current, *dashed*: excess current, *dash-dotted*: thermal current) are shown separately. Adapted from [574], ©1981 Wiley

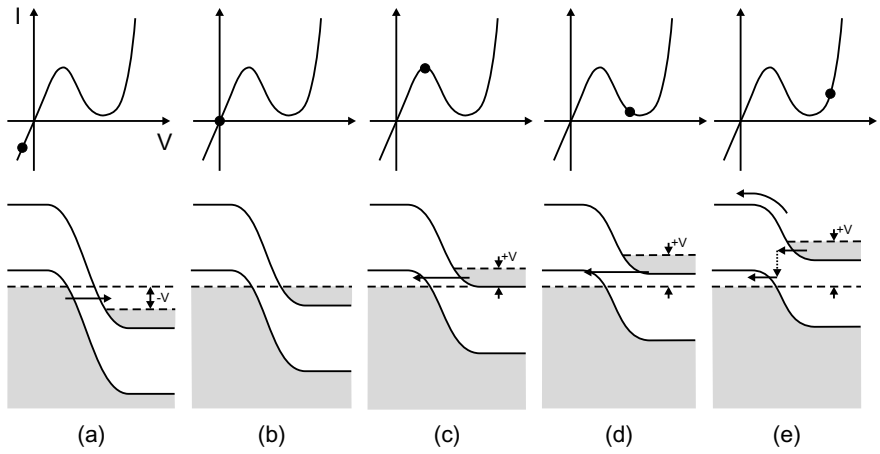

Fig. 21.75 I–V characteristics (*upper row*) and simplified band structure (*lower row*) of a tunneling diode at various bias voltages as indicated with a *dot* in the I–V plot. **a** Reverse bias, **b** in thermodynamic equilibrium ($V = 0$), **c** in the maximum of the tunneling current, **d** close to the valley and **e** forward bias with dominating thermal current. The tunneling current is indicated with *straight arrows*. In (**e**) the thermionic emission current (*curved arrow*) and the excess current with inelastic tunneling (*dotted arrow*) are shown

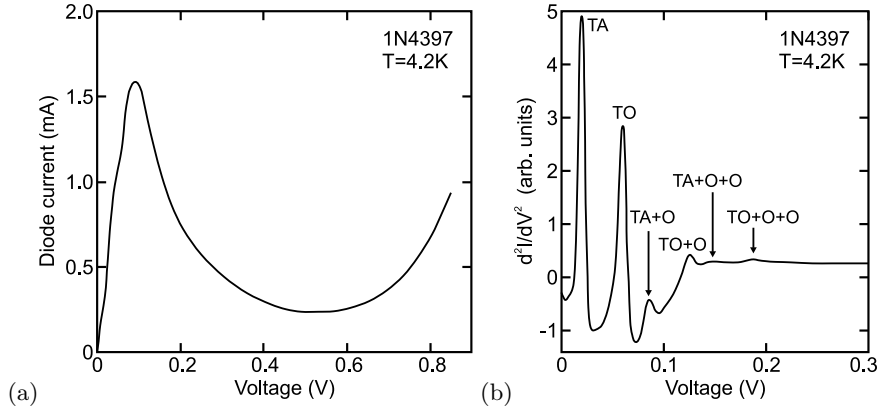

Fig. 21.76 **a** Current-voltage characteristic of silicon tunneling diode (model 1N4397 from American Microsemiconductor [1807]) at low temperature ($T = 4.2\,\mathrm{K}$). **b** $\mathrm{d}^2I/\mathrm{d}V^2$ for small forward voltages, exhibiting characteristic phonon energies. Adapted from [1805]

band states (filled with holes) on the p-doped side (Fig. 21.75c). We note that this tunneling process is usually considered elastic. However, signatures at characteristic phonon and multi-phonon energies are found (at low temperature) in the forward current [1802, 1803] and are best seen in a $\mathrm{d}^2I/\mathrm{d}V^2$-plot [1804, 1805] (Fig. 21.76). Peaks appear at typical phonon energies of silicon.[27]

A similar situation, now with electrons tunneling for the valence band on the p-side into the conduction band on the n-side, is present for small reverse bias (Fig. 21.75a). Thus the rectifying behavior of the diode is lost. This property makes it suitable for the monolithic ohmic connection of two pn diodes which is technologically used e.g. in multi-junction solar cells (cmp. Sect. 22.4.6).

For larger forward bias, the bands are separated so far that the electrons coming from the n-doped side do not find final states on the p-doped side. Thus the tunneling current ceases (Fig. 21.75d). The

[27] We note that for the 1N4396 silicon tunneling diode [1806] the phonon structure of germanium was found in [1805].

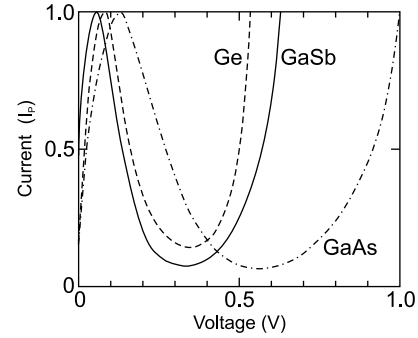

Fig. 21.77 Comparison of tunneling characteristic (room temperature) of diodes based on Ge, GaSb and GaAs. Peak-to-valley ratios are 8 (Ge) and 12 (GaSb, GaAs). Adapted from [574]

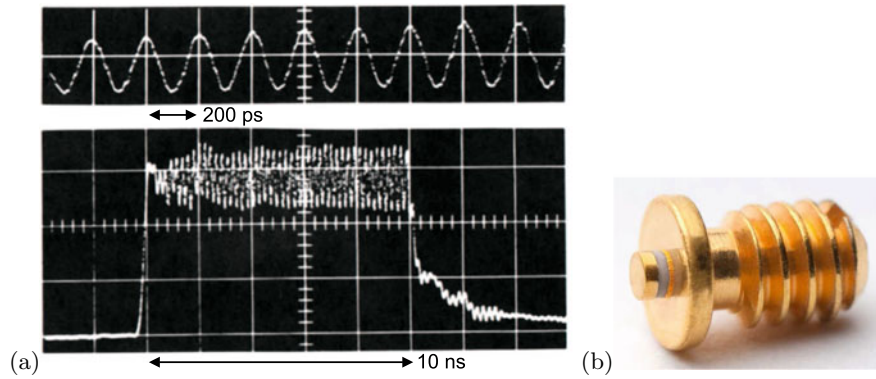

Fig. 21.78 **a** Current traces upon excitation of a 25 μm thick piece of n-type GaAs with a voltage pulse (amplitude 16 V and duration 10 ns). The upper trace is an expanded view of the lower trace. The oscillation period is 4.5 GHz. Adapted from [134]. **b** Image of packaged Gunn diode (Linwave DC1276G-T for 26–40 GHz), outer diameter 3 mm

current minimum is at a voltage $V = V_n + V_p > 0$. The thermal current is the normal diode diffusion current (Fig. 21.75e). Therefore, a minimum is present in the I–V characteristic. The excess current is due to inelastic tunneling processes through states in the band gap and causes the minimum to not drop down to almost zero current.

The peak (V_p, I_p) and valley (V_v, I_v) structure of the characteristic leads to a region of negative differential resistance (NDR). I_p/I_v is termed the peak-to-valley ratio (Fig. 21.77). Peak-to-valley ratios of 8 (Ge), 12 (GaSb, GaAs), 4 (Si), 5 (InP) or 2 (InAs) have been reported (all at room temperature).

21.5.10 Backward Diodes

When the doping in a tunneling diode is nearly or not quite degenerate, the peak-to-valley ratio can be very small. Then the tunnel current flows mostly in the reverse direction (low resistance) and the forward direction has a higher resistance (with or without the NDR regime). Such diodes are called backward diodes. Since there is no minority charge carrier storage, such diodes are useful for high-frequency applications.

21.5.11 Gunn Diodes

The Gunn diode is not really a diode and thus more appropriately called *Gunn element*. It allows to generate microwave radiation in the frequency range of 1–100 GHz [1808] and beyond [1809] using GaAs and in the THz-regime using GaN [1810]. Extracting higher harmonics, frequencies of several 100 GHz can be realized [1811, 1812].

The Gunn element relies on the negative differential resistance (NDR) occurring in semiconductors with two valleys of different mobility such as GaAs or InP (cmp. Sect. 8.4.2). At high fields, the electrons are scattered from the Γ-valley into the upper valley (L-valley for most materials). Accordingly, the Gunn element is also called *transferred electron device* (TED). Details on Gunn elements can be found in [1813].

The Gunn effect was discovered by and named after J.B. Gunn [134]. The spontaneous oscillation of current in a n-type semiconductor occurs when a sufficiently large voltage (pulse) is applied that causes the electric field in the semiconductor to reach the NDR regime (Fig. 21.78). The applied average field of $E = 16\,\mathrm{V}/25\,\mu\,m = 6.4\,\mathrm{kV/cm}$ [134] is larger than the threshold field of $E_\mathrm{T} = 3.2\,\mathrm{kV/cm}$ for NDR in GaAs (Table 8.4).

The self-started oscillations are due the inherent instability introduced by NDR. A homogeneous (uniform) electric field and electron distribution is unstable and a thin high-field domain with bipolar charge distribution (Gunn domain, predicted in [764]) can develop and drift through the device. After reaching the anode, another domain can form, causing a periodically fluctuating current. The highest frequencies can be achieved with the so-called limited-space-charge accumulation (LSA) mode which operates without domains. Optimal performance requires non-homogeneous doping profiles. A detailed discussion of the various oscillation mechanisms can be found in [765, 1808, 1814].

Discussion of further microwave diode devices such as the IMPATT diode can be found in [574, 1815].

Chapter 22
Light-to-Electricity Conversion

Abstract The use of diodes for the conversion of electromagnetic radiation (light) into electrical signals is discussed with many examples for devices such as photoconductors, pn-, pin-, MSM- and avalanche photodiodes and charge-coupled devices. Energy conversion with solar cells is explained and standard and advanced solar cells concepts are introduced.

22.1 Photocatalysis

The absorption of light in a semiconductor across the band gap creates free electrons and holes. In particular, for small particle size in powders[1] these charge carriers can reach the surface of the semiconductor. At the surface they can react with chemicals. The hole can form •OH radicals from OH^- attached to the bead. The electron can form $O_2\bullet^-$. These radicals can subsequently attack and detoxify, e.g., noxious organic pollutants in the solution surrounding the semiconductor. Such photocatalytic activity has been found, e.g., for TiO_2 and ZnO powders. A review of photocatalysis, in particular with TiO_2 particles and their surface modifications with metals and other semiconductors, is found in [1816].

The efficiency of the photocatalytic activity depends on the efficiency of the charge separation (Fig. 22.1). Any electron-hole pair that recombines within the bulk or the surface of the particle is lost for the catalytic activity. Thus, surfaces must exhibit a small density of recombination centers. Surface traps, however, can be beneficial for charge-carrier separation when they 'store' the charge-carrier rather than letting it recombine. Small particles are expected to exhibit more efficient charge-carrier separation than larger ones. Electrons at the surface can be donated and reduce an electron acceptor, typically oxygen, $A \rightarrow A^-$. A hole at the surface can oxidize a donor species, $D \rightarrow D^+$.

An example of increased photocatalytic activity are TiO_2 powders with deposited metal particles (such as Pt) for H_2 evolution and metal-oxide particles (such as RuO_2) for O_2 evolution. Such a system behaves as a short-circuited microscopic photoelectrochemical cell in which Pt is the cathode and RuO_2 is the anode [1817]. Excitation with light energy above the band gap in the TiO_2 particle (3.2 eV) injects electrons into the Pt particles and holes into the RuO_2 particles. Trapped electrons in Pt reduce water to hydrogen and trapped holes in RuO_2 oxidize water to oxygen.

The photocatalytic activity is also tied to the geometrical shape of the semiconductor. Generally, powders with nanosized grains have much higher activity than those with microsized particles [1818]. In Fig. 22.2 it is shown that nanosized objects with high surface-to-volume ratio are more effective catalysts than rather compact surfaces.

[1] 'Small' is here in relation to the diffusion length and does not need to be in the range where quantization effects (quantum dots) are present.

M. Grundmann, *The Physics of Semiconductors*, Graduate Texts in Physics,
https://doi.org/10.1007/978-3-030-51569-0_22

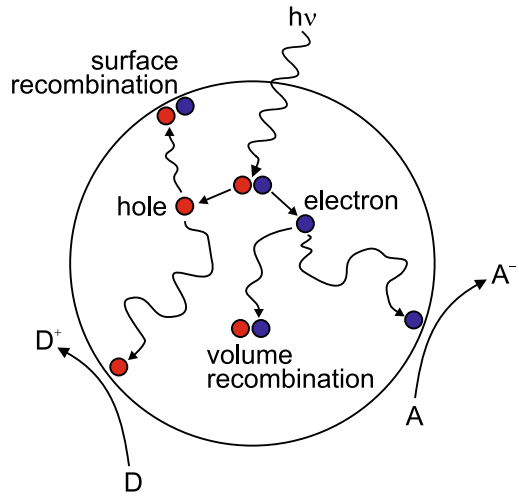

Fig. 22.1 Principle of photocatalytic activity. Light absorption creates an electron-hole pair. The electron and hole diffuse and can recombine in the bulk or at the surface. Free carriers can react at the surface with species from the surrounding solution, reducing an electron acceptor or oxidizing a donor species. Adapted from [1816]

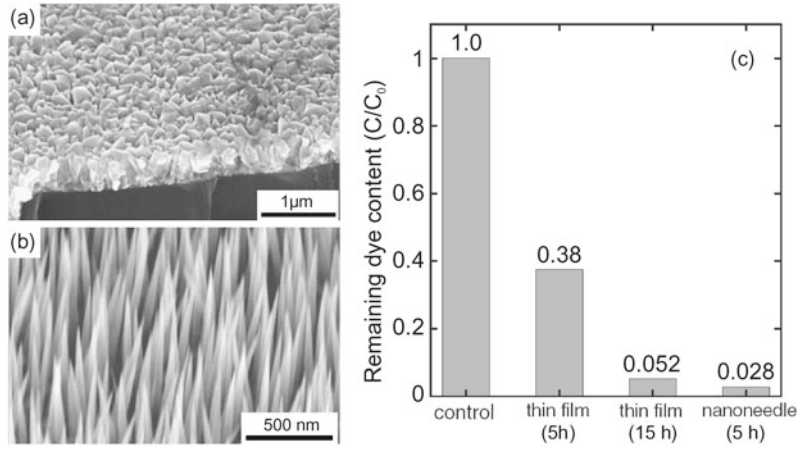

Fig. 22.2 SEM images of MOCVD-grown **a** ZnO thin film and **b** ZnO nanoneedle layer. **c** Comparison of the photocatalytic activity (decoloration of the dye Orange II in aqueous solution) of the ZnO thin film (irradiation with a Hg lamp for 5 h and 15 h) and the ZnO nanoneedles (irradiation 5 h). The sample labeled 'control' (scaled to 100%) is the start situation (absorption of the dye Orange II) without photocatalytic process. Adapted from [1819], reprinted with permission

In sun-protection cream only the UV absorption is wanted in UVA (330–420 nm) and UVB (260–330 nm) ranges. Subsequent photocatalysis on the skin and the presence of radicals are unwanted. Thus the semiconductor particles (∼10–200 nm diameter) are encapsulated in microbeads (∼1–10 μm diameter) of silica, PMMA or urethane, also improving ease of dispersion, aggregation, stability and skin feel.

22.2 Photoconductors

22.2.1 Introduction

Charge carriers can be generated in the semiconductor through the absorption of light with a photon energy above or below the band gap (Fig. 22.3). Absorption involving impurities occurs typically in the mid- and far-infrared spectral regimes (cf. Sect. 9.8). The additional charge carriers cause an increase in the conductivity (8.11).

22.2.2 Photoconductivity Detectors

In stationary equilibrium for constant illumination of power P_{opt} and photon energy $E = h\nu$ the generation rate G is given by

$$G = \frac{n}{\tau} = \eta \, \frac{P_{\text{opt}}/h\nu}{V} \, , \tag{22.1}$$

where V is the volume ($V = wdL$, see Fig. 22.4) and τ denotes the charge-carrier lifetime. η is the quantum efficiency, i.e. the average number of electron-hole pairs generated per incoming photon. The photocurrent between the electrodes is

$$I_{\text{ph}} = \sigma \, E \, w \, d \approx e \, \mu_{\text{n}} \, n \, E \, w \, d \, , \tag{22.2}$$

assuming that $\mu_{\text{n}} \gg \mu_{\text{p}}$ and with $E = V/L$ denoting the electric field in the photoconductor, V being the voltage across the photoconductor. We can then also write

$$I_{\text{ph}} = e \left(\eta \, \frac{P_{\text{opt}}}{h\nu} \right) \left(\frac{\mu_{\text{n}} \, \tau \, E}{L} \right) = g \, I_{\text{p}} \, . \tag{22.3}$$

With the primary photocurrent $I_{\text{p}} = e \left(\eta \frac{P_{\text{opt}}}{h\nu} \right)$ we deduce a gain

$$g = \frac{I_{\text{ph}}}{I_{\text{p}}} = \frac{\mu_{\text{n}} \, \tau \, E}{L} = \frac{\tau}{t_{\text{r}}} \, , \tag{22.4}$$

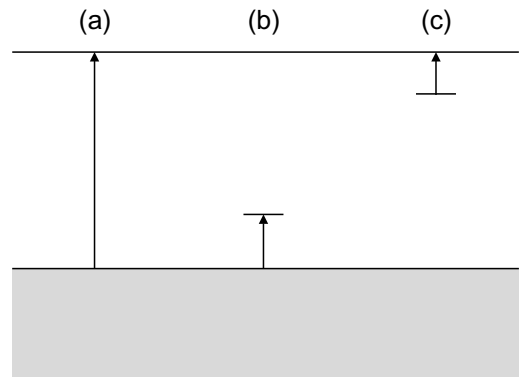

Fig. 22.3 Absorption and charge-carrier generation in a photoconductor: **a** band-band transition, **b** valence-band to acceptor and **c** donor to conduction-band transition

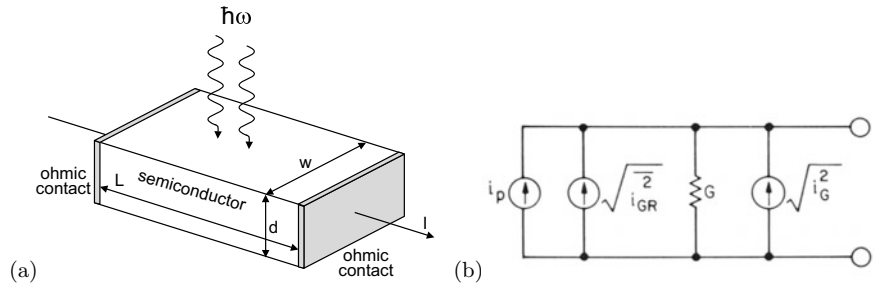

Fig. 22.4 **a** Scheme of photoconductor. **b** Equivalent circuit of photoconductor

where $t_r = L/v_d$ is the transit time through the photoconductor.

Now we consider a modulated light intensity

$$P(\omega) = P_{opt}\left[1 + m\exp(i\omega t)\right] , \tag{22.5}$$

where m is between 0 and 1. For $m = 0$ it is a constant light power, for $m = 1$ the intensity is sinusoidally modulated between 0 and $P_{max} = 2P_{opt}$. The rms optical power[2] is given by $\sqrt{2}m\,P_{opt}$. In the case of $m = 1$ this is equal to $P_{max}/\sqrt{2}$.

The rms photocurrent ($i^2 = \langle I^2\rangle - \langle I\rangle^2$) is

$$i_{ph} \approx \frac{e\,\eta\,m\,P_{opt}}{\sqrt{2}h\nu}\,\frac{\tau}{t_r}\,\frac{1}{\sqrt{1+\omega^2\tau^2}} . \tag{22.6}$$

Besides the photocurrent which is considered the signal, several sources of noise must be considered. Noise is in this case a fluctuation current i_n with $\langle i_n\rangle = 0$ (see Appendix K).

The thermal noise (Appendix K.3.1) at a conductivity $G = 1/R$ is[3]

$$i_G^2 = 4\,k\,T\,G\,B , \tag{22.7}$$

with B being the bandwidth over which the noise spectrum is integrated. The thermal noise at a resistor was experimentally found by Johnson [1820, 1821] and theoretically explained by Nyquist [1822].[4]

The statistical nature (Poisson statistics) of photon arrival (and absorption) and equally that of recombination of (photo-) excited electrons leads to fluctuations of the carrier density and consequently to fluctuating conductivity and gain. This so-called generation-recombination noise (Appendix K.3.4) is given by [1823]

$$i_{GR}^2 = 4\,e\,I_{ph}\,B\,g\,\frac{1}{1+\omega^2\,\tau^2} \tag{22.8}$$

for the modulation frequency ω, I_{ph} being the photocurrent in steady state (22.3). The equivalent circuit with the ideal photocurrent source and the noise currents is depicted in Fig. 22.4b. A detailed treatment can be found in [1824].

The signal-to-noise ratio of the power is then given by

[2]The rms value is the square root of the time average of the square of the power, $\sqrt{\langle P^2\rangle}$.

[3]For frequencies $h\nu \ll kT$; at room temperature kT/h is in the THz regime.

[4]The formula for thermal noise (22.7) is the fluctuation-dissipation theorem in statistical physics, providing a general relation between the response of an equilibrium system to small external perturbations and its spontaneous fluctuations.

$$S/N = \frac{i_{\rm ph}^2}{i_{\rm G}^2 + i_{\rm GR}^2} = \frac{\eta\, m^2\, (P_{\rm opt}/h\nu)}{8\, B} \left[1 + \beta^{-1} \frac{t_{\rm r}}{\tau}(1 + \omega^2\tau^2)\, \frac{G}{I_0}\right]^{-1} . \tag{22.9}$$

An important quantity is the noise equivalent power (NEP). This is the light power ($m\, P_{\rm opt}/\sqrt{2}$) for which the S/N ratio is equal to 1 (for $B = 1$). The responsivity of a detector to light has been termed 'detectivity' and is the inverse of the noise equivalent power. It typically depends on the square root of the detector area A and the bandwidth B [1825]. Thus the detectivity D^* (D star) has been introduced defined by [1826]

$$D^* = \frac{\sqrt{A\, B}}{\rm NEP} , \tag{22.10}$$

in order to make various detectors comparable. The unit of D^* is $\rm cm\, Hz^{1/2}\, W^{-1}$, also known as Jones. The detectivity should be stated together with the modulation frequency. It can be given for monochromatic radiation of a particular wavelength λ or a blackbody spectrum of given temperature T. As refined measure for detectivity, D^{**} (D double star) has been defined to take into account the solid angle Ω from which radiation can reach the detector [1827],

$$D^{**} = \sqrt{\Omega/\pi}\; D^* ; \tag{22.11}$$

for a Lambertian characteristic $D^{**} = D^*$.

22.2.3 Electrophotography

The principle of the Xerox copy machine is based on a photoconductive layer (Fig. 22.5). This layer is normally insulating such that both sides of the layer can be oppositely charged. If light hits the layer it becomes photoconductive and neutralizes locally. This requires a small lateral diffusion of charge carriers. Initially amorphous selenium ($E_{\rm g} = 1.8\,{\rm eV}$) was used. The conductivity in the dark of a-Se is $10^{16}\ \Omega$/cm. Se was subsequently replaced by organic material. The highest performance is currently achieved with amorphous silicon.

On the charged areas of the photo-sensitive layer toner can be attached. The toner pattern is subsequently transferred to the copy sheet and fixated. A copy takes typically more than one rotation of the drum. The principle was invented in 1938 by Chester F. Carlson (1906–1968) with sulfur as the photoconductor.[5]

22.2.4 QWIPs

Quantum-well intersubband photodetectors (QWIPs) are based on the absorption of photons between two quantum well subbands (Fig. 22.6). A review can be found in [1829]. Quantized electron or hole states can be used. Besides an oscillator strength for this transition, the lower level must be populated and the upper level must be empty in order to allow this process. The Fermi level is typically chosen by appropriate doping such that the lower subband is populated.

[5] In 1947 the Haloid company bought the rights to this process, renamed itself XeroX and brought the first copy machine to the market in 1958 based on amorphous selenium. The word 'xerography' stems from the Greek word $\xi\acute{\epsilon}\rho o\varsigma$ (dry). The last 'X' in XeroX was added to mimic the name of the KodaK corporation.

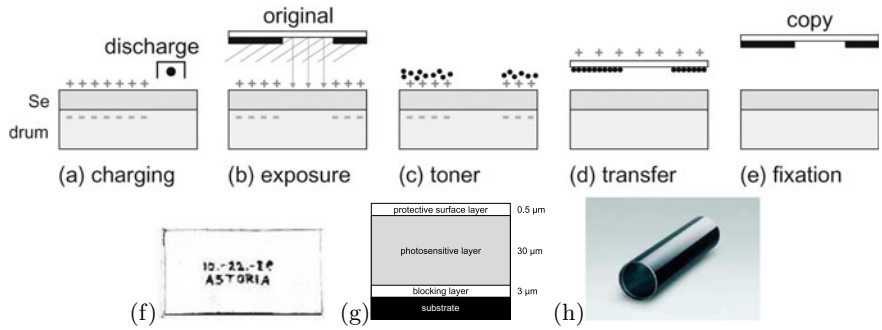

Fig. 22.5 Principle of xerography: **a** charging of the selenium-covered drum, **b** (reflection) exposure of the Se, exposed areas become uncharged, **c** toner addition, **d** toner transfer to paper for copy, and **e** fixation of the toner on the copy and preparation of drum for the next cycle. **f** First xerox copy (Oct. 22nd 1938). **g** Schematic cross section of coating of photo-sensitive drum. The indicated thicknesses are approximate. **h** Image of drum with photo-sensitive layer made from amorphous silicon. Part (**h**) from [1828]

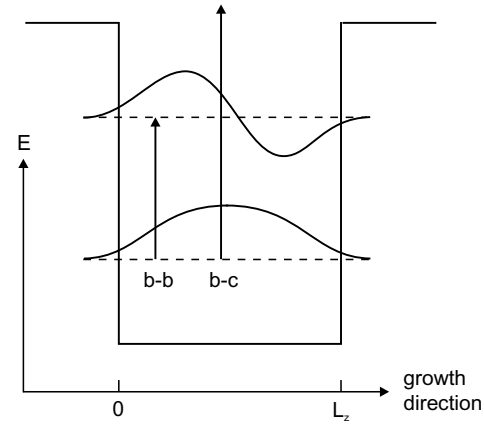

Fig. 22.6 Schematic level diagram of a quantum well. Optical intersubband transitions between the first and second quantized level (b–b) and the ground state and the continuum (b–c)

For infinite barrier height the energy separation between the first and second quantized levels (in the effective-mass theory) is (cf. (12.6))

$$E_2 - E_1 = 3\,\frac{\hbar^2}{2m^*}\,\frac{\pi^2}{L_z^2}\,. \tag{22.12}$$

For real materials the barrier height determines the maximum transition energy. Typical absorption and transmission spectra of a QWIP structure are shown in Fig. 22.7. The spectral response is in the mid- or far-infrared.

The dipole matrix element $\langle z\rangle = \langle\Psi_2|z|\Psi_1\rangle$ can be easily calculated to be

$$\langle z\rangle = \frac{16}{9\pi^2}\,L_z\,. \tag{22.13}$$

The oscillator strength is about 0.96. The polarization selection rule causes the absorption to vary $\propto \cos^2\phi$, where ϕ is the angle between the electric-field vector and the z direction (Fig. 22.8). This means that for vertical incidence ($\phi = 90°$) the absorption vanishes. Thus schemes have been developed to allow for skew entry of the radiation (Fig. 22.9a). The strict selection rule can be relaxed by using asymmetric potential wells (breaking of mirror symmetry/parity), strained materials (band mixing) or

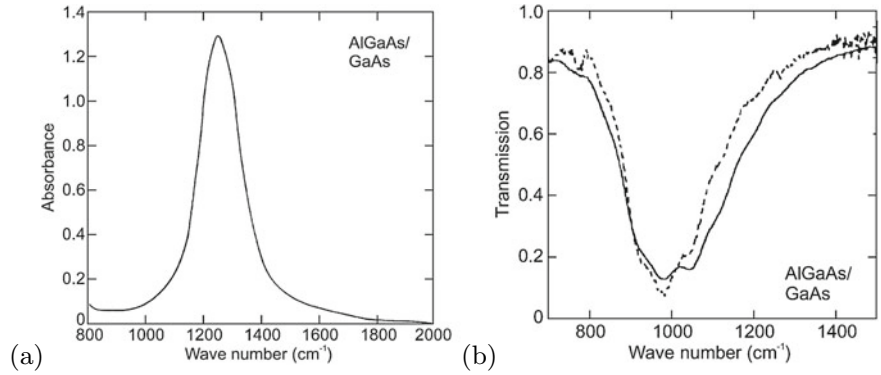

Fig. 22.7 **a** AlGaAs/GaAs QWIP absorption spectrum for multiple reflection geometry. Adapted from [1829]. **b** Transmission of AlGaAs/GaAs QWIP (100 QWs) in double reflection geometry (45° angle of incidence). The well doping is $1.0 \times 10^{12}\,\mathrm{cm}^{-2}$ (*dashed line*) and $1.5 \times 10^{12}\,\mathrm{cm}^{-2}$ (*solid line*). Adapted from [1830]

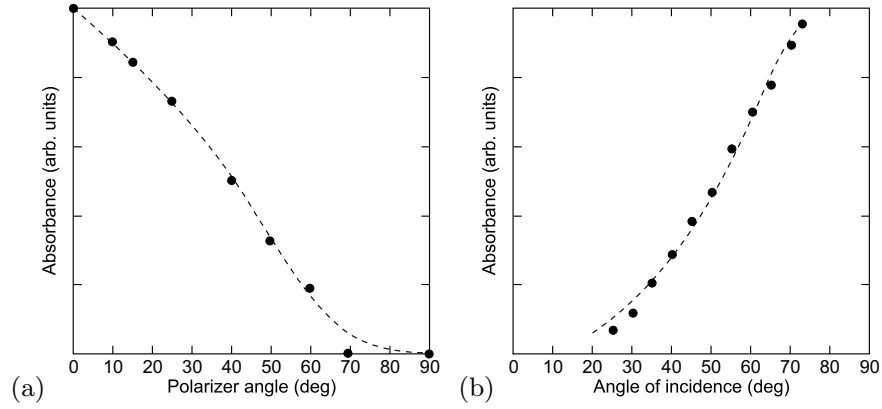

Fig. 22.8 Dependence of the QWIP response on **a** polarization and **b** angle of incidence. *Dashed lines* are guides to the eye. Adapted from [1829]

quantum dots (lateral confinement). Also, a grating can be used to create a finite angle of incidence (Fig. 22.9b).

Besides a useful detectivity ($2 \times 10^{10}\,\mathrm{cm\,Hz^{1/2}/W}$ at 77 K) QWIPs have the advantage, e.g. against HgCdTe interband absorbers, that the highly developed GaAs planar technology is available for the fabrication of focal plane arrays (FPA) as shown in Fig. 22.10. A FPA is an image sensor (in the focal plane of an imaging infrared optics) and is used, e.g., for the detection of heat leaks in buildings or night surveillance. In particular, night vision support in cars may become a major market. A competing technology are bolometric arrays with thermally insulated pixels based on MEMS technology. A review of FPA technologies can be found in [1831].

The carriers that have been optically excited into the upper state leave the QW by tunneling or thermionic emission. Also, a QWIP can be made based on the direct transfer from the (populated) subband into the continuum.

The incoming infrared radiation creates a photocurrent density of

$$i_{\mathrm{ph}} = e\,\eta_{\mathrm{w}}\,\Phi\ , \tag{22.14}$$

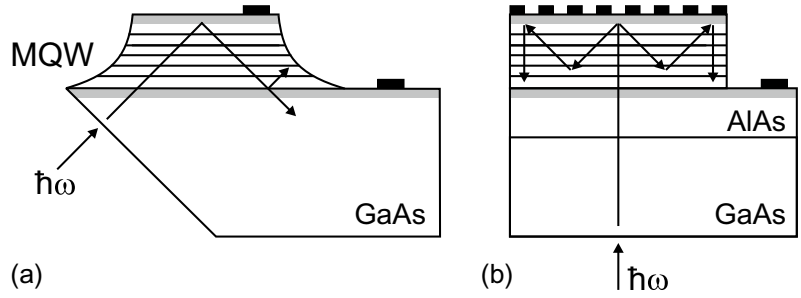

Fig. 22.9 QWIP geometries: **a** 45° edge coupled with multiple quantum-well (MQW) absorber and **b** grating coupled with GaAs substrate, AlAs reflector and metal grating on top. *Grey areas* are highly n-doped contact layers

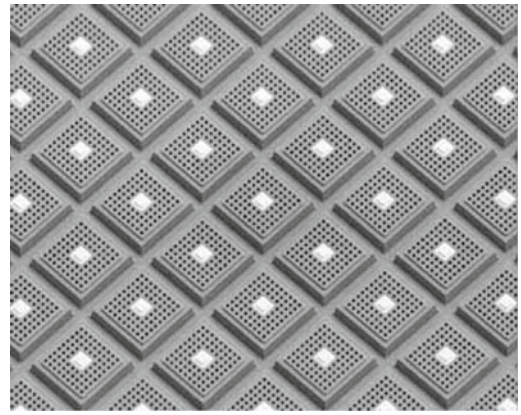

Fig. 22.10 Part of a 256 × 256 QWIP focal plane array (FPA) with grating coupler (area of one pixel: 37 μ m^2). From [1832]

where η_w is the quantum efficiency of a single quantum well (including the escape rate) and Φ is the photon flux per time and unit area. During the transport of the charge carriers through the barrier they can be (re-)captured by the QW with the probability p_c. The capture probability decreases exponentially with the applied bias. The total photocurrent (including generation and recapture) is

$$I_{ph} = (1 - p_c)\, I_{ph} + i_{ph} = \frac{i_{ph}}{p_c} \,. \tag{22.15}$$

If the quantum efficiency is small, the efficiency of N_w quantum wells $\eta \approx N_w \times \eta_w$. With this approximation the total photocurrent of N_w quantum wells is given by

$$I_{ph} = e\, \eta\, \Phi\, g \,, \tag{22.16}$$

where g is termed the gain of the structure and is given by

$$g = \frac{1}{p_c}\, \frac{\eta_w}{\eta} \approx \frac{1}{N_w\, p_c} \,. \tag{22.17}$$

The dark current can be calculated from thermionic emission and agrees fairly well with experiment (Fig. 22.11a). When the voltage is increased further, avalanche multiplication can occur while the carriers are transported through the barrier(s). This mechanism provides further gain as shown in Fig. 22.11b.

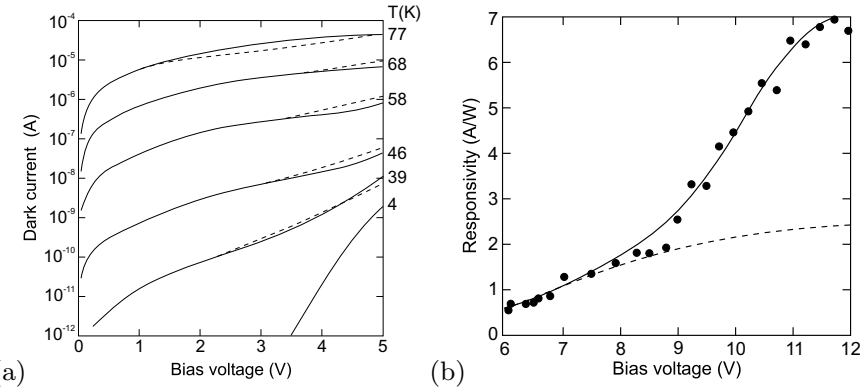

Fig. 22.11 **a** Dark current of a QWIP at 10.7 μ m, experimental (*solid lines*) and theoretical (*dashed lines*) response. **b** QWIP responsivity as a function of the applied voltage. The *solid line* (*dashed line*) is the theoretical dependence with (without) the effect of avalanche multiplication. Adapted from [1829]

22.2.5 Blocked Impurity-Band Detectors

Impurity absorption allows photoconductivity detectors in the mid- and far-infrared regions to be made. In particular, for THz spectroscopy in medicine and astronomy the extension to longer wavelengths is interesting. For conventional photoconductors the impurity concentration is well below the critical dopant concentration (cf. Sect. 7.5.7). Long-wavelength response can be achieved by going to impurity/host systems with smaller ionization energy, such as Si:B (45 meV) → Ge:As (12.7 meV) → GaAs:Te (5.7 meV). By applying stress to Ge the energy separation between impurity and conduction bands can be lowered and subsequently the detector response is shifted towards longer wavelengths.

For high doping the impurity level broadens to an impurity band and thus allows smaller ionization energy and thus stronger long-wavelength detector response. However, conduction in the impurity band leads to dark current and makes such detectors unfeasible. In a blocked impurity band (BIB) detector [1833–1835] an additional intrinsic blocking layer is sandwiched between the absorption layer and the contact (Fig. 22.12a). Such a structure is similar to a MIS diode, the insulator being the intrinsic semiconductor. We assume in the following an n-type semiconductor, such as Si:As or GaAs:Te, but also p-type BIBs can be made, e.g., from Ge:Ga.

The semiconductor is highly doped (N_D) and partly compensated (N_A). Typically, the acceptor concentration must be small, about $10^{12}\,cm^{-3}$, and controls the formation of the electric field as shown below. The doping is so high that the impurities form an impurity band. Some of the electrons recombine with the acceptors $N_A^- = N_A$ and leave some donors charged $N_D^+ = N_A$. For GaAs, e.g., the donor concentration in the doped semiconductor is $>10^{16}\,cm^{-3}$ and $\sim 10^{13}\,cm^{-3}$ in the i-layer.

Under an external forward bias V, i.e. the positive pole is at the insulator, part of the applied voltage drops over the blocking layer of thickness b. If ideally no charges are present here, the electric field is constant. In the n-doped material electrons move in the impurity band towards the insulator, forming neutral donors in an electron accumulation layer of thickness w in the presence of the charged acceptors N_A^-. This layer is the absorption layer. The mechanism can also be considered as if positive charge (the charged donors, N_D^+) moves (via hopping conduction) towards the back contact. In the literature the layer close to the insulator is thus also termed a 'depletion layer'. The band diagram and the electric field are shown in Fig. 22.12b, c. Due to the blocking layer the carriers on the donors in the n-type material cannot spill via the impurity band into the contact but must be lifted (by photoabsorption) into the conduction band.

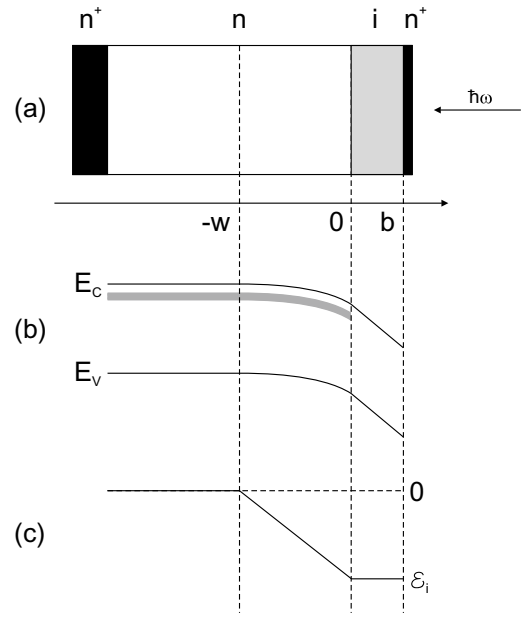

Fig. 22.12 **a** Structure of BIB photodetectors. Highly doped contact layers (*black*), doped semiconductor (*white*) and blocking (intrinsic) layer (*grey*). **b** Band diagram under small forward bias. *Shaded area* represents the donor impurity band. **c** Electric field in the structure

From the Poisson equation the electric field is given by

$$E(x) = -\frac{e}{\epsilon_\mathrm{s}} N_\mathrm{A}\,(w + x)\,,\ -w \le x \le 0 \tag{22.18a}$$

$$E(x) = -\frac{e}{\epsilon_\mathrm{s}} N_\mathrm{A}\, w = E_\mathrm{i},\ 0 \le x \le b\,. \tag{22.18b}$$

The voltage drops across the blocking layer V_b and the doped semiconductor V_s fulfill

$$V = V_\mathrm{b} + V_\mathrm{s}\,. \tag{22.19}$$

Integration of the fields yields

$$V_\mathrm{s} = \frac{e}{\epsilon_\mathrm{s}} N_\mathrm{A}\,\frac{w^2}{2} \tag{22.20a}$$

$$V_\mathrm{b} = \frac{e}{\epsilon_\mathrm{s}} N_\mathrm{A}\, w\, b\,. \tag{22.20b}$$

Substituting (22.20a,b) into (22.19) results in the width of the 'depletion layer'

$$w = \sqrt{\frac{2\,\epsilon_\mathrm{s}\,V}{e\,N_\mathrm{A}} + b^2}\ - b\,. \tag{22.21}$$

The high dopant concentration allows for much thinner absorption layers than in a conventional photoconductivity detector, making it less susceptible to background high-energy cosmic radiation. The recombination in the depletion layer is negligible. Detector performance is modeled in [1836].

22.3 Photodiodes

22.3.1 Introduction

The principle of the photodiode is the interband absorption of light in the depletion layer of a diode (or the i-zone of a pin-diode) and the subsequent separation of electrons and holes by the electric field. There are opposite requirements for fast detectors (thin depletion layer) and efficient detectors (complete light absorption, sufficiently thick depletion layer). For this reason generally semiconductors with high absorption coefficient are most suited (Fig. 22.13). In Fig. 22.14 the quantum efficiency and detectivity D^* of various semiconductor detectors are compared.

A diode can be operated without bias (photovoltaic mode) using the built-in field. An improvement in the speed of a pn-diode is achieved with a reverse bias since it increases the field strength in the depletion layer. However, the reverse bias is below the breakdown voltage. Operation near breakdown is exploited in the avalanche photodiode (APD). In the following we will discuss pn-, pin-, MS- (Schottky-), MSM- and heterostructure-diodes and APDs.

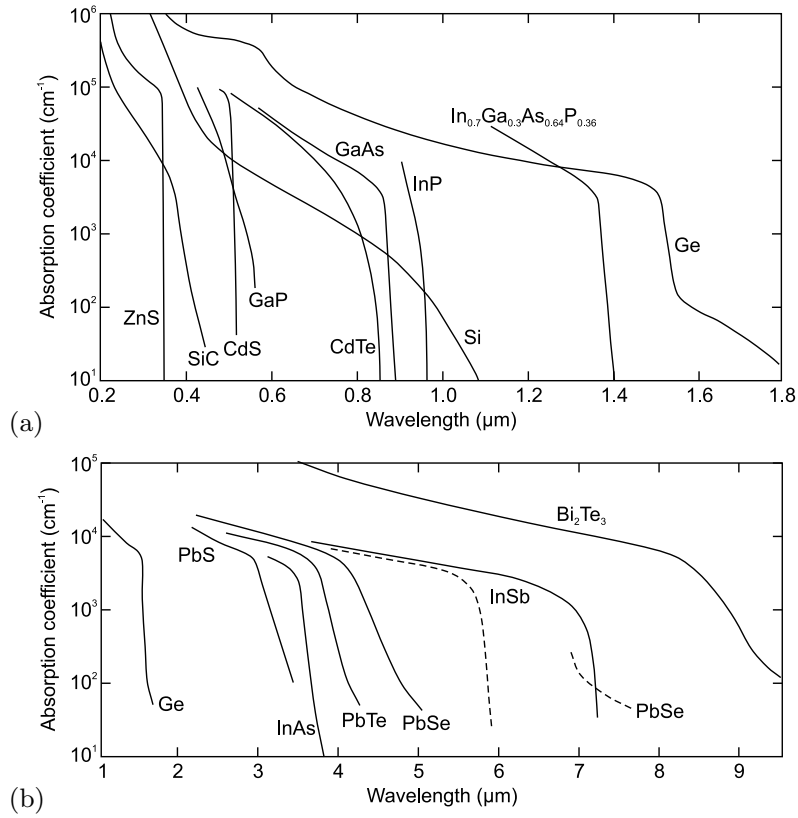

Fig. 22.13 Optical absorption coefficient of various semiconductor materials (as labeled) used for photodetectors **a** in the UV, visible and near-infrared range (at room temperature) and **b** in the mid-infrared spectral range at room temperature (*solid lines*) and at 77 K (*dashed lines*). Based on [1837]

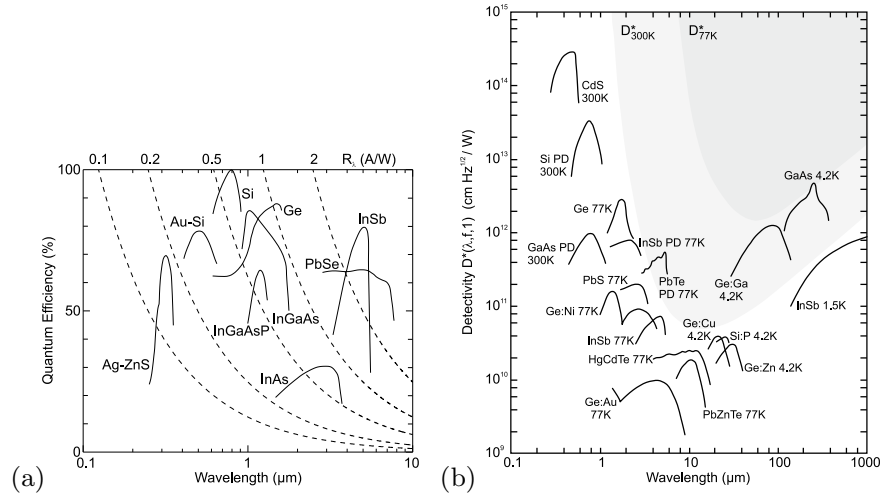

Fig. 22.14 **a** Quantum efficiency of various photodetectors. The *dashed lines* depict lines of equal responsivity (R_λ in A/W) as labeled on top of the panel. **b** Detectivity D^* of various photoconductors and photodiodes (PD). The *lighter* (*darker*) *shaded area* indicates the range unachievable at 300 K (77 K) due to background radiation. Adapted from [574]

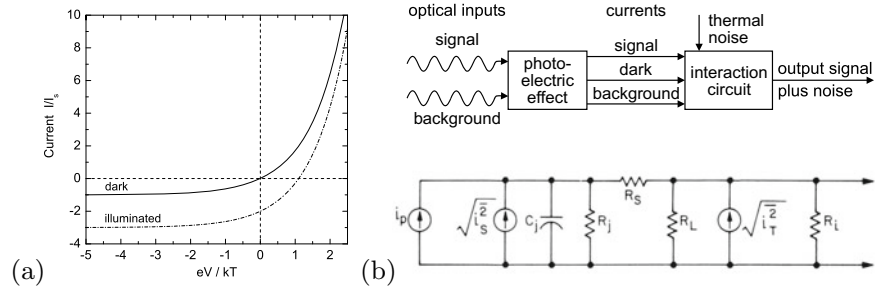

Fig. 22.15 **a** Schematic dark and illuminated I–V-characteristics of a photodiode (for the case $j_p = -2j_s$). **b** Schematic representation of currents in a photodiode and equivalent circuit. Part **b** adapted from [1838]

22.3.2 Pn Photodiodes

The most important figures of merit are the quantum efficiency, responsivity, noise equivalent power (NEP) and the response speed.

If the depletion layer is hit by a photon flux with a generation rate G_0 (i.e. electron-hole pairs per unit volume per unit time) the photogenerated current is added to the diffusion current. The photocurrent density j_p (per unit area) is

$$j_p = -e\, G_0\, L_p \tag{22.22}$$

for a p^+n-diode. In order to obtain this result the diffusion and continuity equations have to be solved for the depletion region.[6] Equation (22.22) means that the dark I–V characteristic is shifted by j_p as shown in Fig. 22.15a. The number of electron-hole pairs that are generated per photon of energy $h\nu$ by the absorption of the (monochromatic) light power P_{opt} is

[6]This derivation is done in Sect. 22.3.3. Equation (22.22) is obtained from (22.33) for vanishing thickness w and $\alpha L_p \ll 1$.

$$\eta = \frac{I_{\mathrm{ph}}/e}{P_{\mathrm{opt}}/(h\nu)} \ , \tag{22.23}$$

where $I_{\mathrm{ph}} = A j_{\mathrm{ph}}$ is the photogenerated current over the surface A. The *responsivity* R_λ of the photodiode (for monochromatic radiation) is defined as

$$R_\lambda = \frac{I_{\mathrm{ph}}}{P_{\mathrm{opt}}} = \frac{e}{h\nu}\,\eta \approx \frac{\lambda}{1.24\,\mu\mathrm{m}}\,\eta \ . \tag{22.24}$$

For a modulated light intensity P_{opt} must be replaced by $m\,P_{\mathrm{opt}}/\sqrt{2}$. The equivalent circuit including noise sources for a photodiode is shown in Fig. 22.15b.

Random processes lead to shot noise $\langle i_{\mathrm{S}}^2 \rangle$ (Sect. K.3.3). Besides the photocurrent I_{ph} itself, the background radiation (I_{B}, in particular for infrared detectors) and the thermal generation (dark current, I_{D}) of carriers contribute:

$$\langle i_{\mathrm{S}}^2 \rangle = 2\,e\,\left(I_{\mathrm{ph}} + I_{\mathrm{B}} + I_{\mathrm{D}}\right)\,B \ , \tag{22.25}$$

with B being the bandwidth. Additionally, the parallel resistances cause thermal noise

$$\langle i_{\mathrm{T}}^2 \rangle = 4\,kT\,B/R_{\mathrm{eq}} \ . \tag{22.26}$$

The resistance R_{eq} is given by the resistance of the depletion layer (junction) R_{j}, the load R_{L} and the input of the amplifier R_{i} as $R_{\mathrm{eq}}^{-1} = R_{\mathrm{j}}^{-1} + R_{\mathrm{L}}^{-1} + R_{\mathrm{i}}^{-1}$. The series resistance R_{s} of the photodiode can be usually ignored in this context.

For a fully modulated signal the signal-to-noise ratio of the photodiode is given by

$$S/N = \frac{i_{\mathrm{ph}}^2}{\langle i_{\mathrm{S}}^2 \rangle + \langle i_{\mathrm{T}}^2 \rangle} = \frac{\left(e\,\eta\,P_{\mathrm{opt}}/h\nu\right)^2/2}{2e\,\left(I_{\mathrm{ph}} + I_{\mathrm{B}} + I_{\mathrm{D}}\right)\,B + 4\,kT\,B/R_{\mathrm{eq}}} \ . \tag{22.27}$$

Therefore the NEP is given by

$$\mathrm{NEP} = \frac{2\,h\nu\,B}{\eta}\left[1 + \sqrt{1 + \frac{I_{\mathrm{eq}}}{e\,B}}\right] \ . \tag{22.28}$$

The current I_{eq} is given by $I_{\mathrm{eq}} = I_{\mathrm{B}} + I_{\mathrm{D}} + 2kT/(eR_{\mathrm{eq}})$. If $I_{\mathrm{eq}}/eB \ll 1$, the NEP is determined by the shot noise of the signal itself. In the other limit $I_{\mathrm{eq}}/eB \gg 1$ the detection is limited by the background radiation or thermal noise. In this case, the NEP is (for $B = 1\,\mathrm{Hz}$, in $\mathrm{W\,cm^2\,Hz^{1/2}}$)

$$\mathrm{NEP} = \sqrt{2}\,\frac{h\nu}{\eta}\,\sqrt{\frac{I_{\mathrm{eq}}}{e}} \ . \tag{22.29}$$

In Fig. 22.16 the situation is shown for a silicon photodiode as a function of R_{eq}. The diode has a quantum efficiency of 75% at $\lambda = 0.77\,\mu\mathrm{m}$. A high value of $R_{\mathrm{eq}} \sim 1\,\mathrm{G\Omega}$ is necessary to ensure detection limited by dark current.

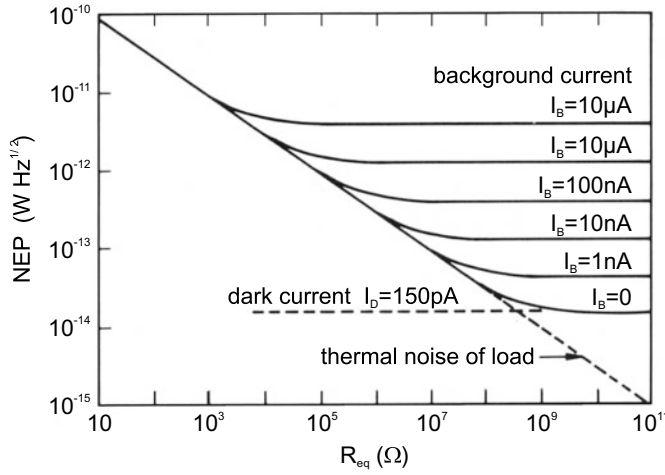

Fig. 22.16 NEP as a function of the resistance R_{eq} for a Si photodiode. From [1838]

22.3.3 Pin Photodiodes

The depletion layer in pn-diodes is relatively thin such that the incident light is not completely absorbed. An almost complete absorption of light can be achieved by using a thick intrinsic absorption layer. The field in the intrinsic region is constant or slowly varying linearly (Fig. 21.72). The generation rate per unit area decreases exponentially following the Lambert-Beer law (9.16) as shown in Fig. 22.17c:

$$G(x) = G_0 \, \exp(-\alpha \, x) \; . \tag{22.30}$$

The initial generation rate $G_0 = \Phi_0 \alpha$ is given by the incident photon flux per unit area Φ_0 and the reflectance of the surface R as $\Phi_0 = P_{\mathrm{opt}}(1 - R)/(Ah\nu)$.

The drift current in the i-region collects all those carriers (if recombination in the depletion layer is neglected). The electron drift current is given by

$$j_{\mathrm{dr}} = -e \int_0^w G(x) \, \mathrm{d}x = e \, \Phi_0 \left[1 - \exp(-\alpha \, w)\right] \; , \tag{22.31}$$

with w being the thickness of the depletion layer that is approximately the same as the thickness of the i-region. In the bulk (neutral) region ($x > w$) the minority-carrier density is determined by drift and diffusion[7] (10.78). The diffusion current density at $x = w$ is thus given by

$$j_{\mathrm{diff}} = e \, \Phi_0 \exp(-\alpha \, w) \, \frac{\alpha \, L_{\mathrm{p}}}{1 + \alpha \, L_{\mathrm{p}}} + e \, p_{\mathrm{n}_0} \, \frac{D_{\mathrm{p}}}{L_{\mathrm{p}}} \; . \tag{22.32}$$

The first term is due to the diffusion current of photo-generated carriers (10.78), the second term due to thermally generated carriers (21.133). The total current $j_{\mathrm{tot}} = j_{\mathrm{diff}} + j_{\mathrm{dr}}$ is given by

[7] At the edge of the depletion layer, $x = w$, all photo-generated carriers are transported away instantly, thus the excess carrier density from photo-generated carriers is zero there and (10.78) applies.

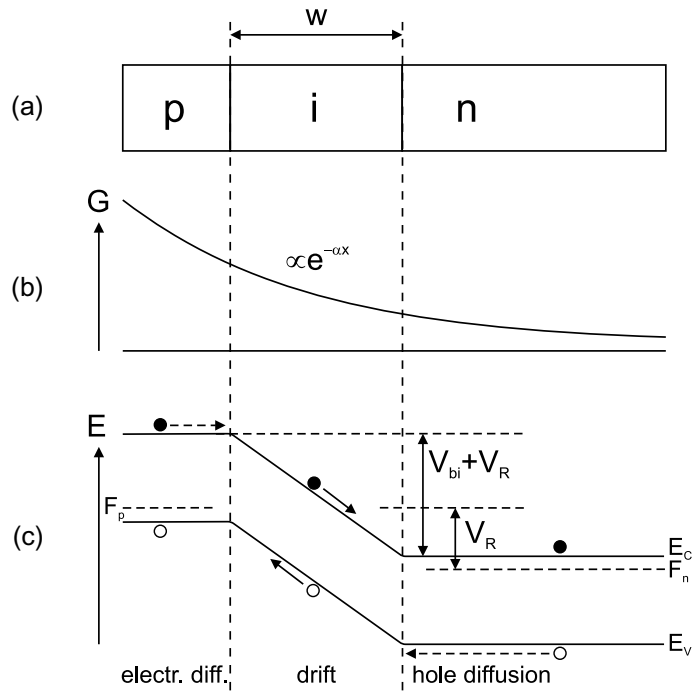

Fig. 22.17 **a** Schematic cross section of pin-diode, **b** profile of carrier generation due to light absorption and **c** schematic band structure under reverse bias. The generation of three electron-hole pairs is shown; subsequent drift (diffusive) transport is indicated with *solid* (*dashed*) *arrows*

$$j_{\text{tot}} = e\,\Phi_0\left[1 - \frac{\exp(-\alpha\, w)}{1+\alpha\, L_\text{p}}\right] + e\, p_{\text{n}_0}\,\frac{D_\text{p}}{L_\text{p}}\,. \tag{22.33}$$

The first term is due to the photocurrent, the second term is due to the diffusion current known from the p$^+$n-diode. In normal operation, the second can be neglected compared to the first. The quantum efficiency is

$$\eta = \frac{j_{\text{tot}}/e}{P_{\text{opt}}/h\nu} = (1-R)\left[1 - \frac{\exp(-\alpha\, w)}{1+\alpha\, L_\text{p}}\right]\,. \tag{22.34}$$

For a high quantum efficiency, of course low reflectance and high absorption coefficient, i.e. $\alpha w \gg 1$, are necessary.

However, for $w \gg 1/\alpha$ the transit time through the depletion layer $t_\text{r} \approx w/v_\text{s}$ (at sufficiently high field, v_s being the drift-saturation velocity) increases too much. The 3 dB cutoff frequency $f_{3\,\text{dB}}$ (Fig. 22.18) is

$$f_{3\,\text{dB}} \cong \frac{2.4}{2\pi\, t_\text{r}} \cong \frac{0.4\, v_\text{s}}{w}\,. \tag{22.35}$$

Therefore a tradeoff exists between the quantum efficiency and the response speed of the pin-photodiode (Fig. 22.18). Choosing $w \cong 1/\alpha$ is a good compromise.

22.3.4 Position-Sensing Detector

In a position-sensing detector (PSD) two electrodes are placed at opposite edges of a photodetector. The current output depends linearly on the beam position in between the electrodes, similar to a voltage

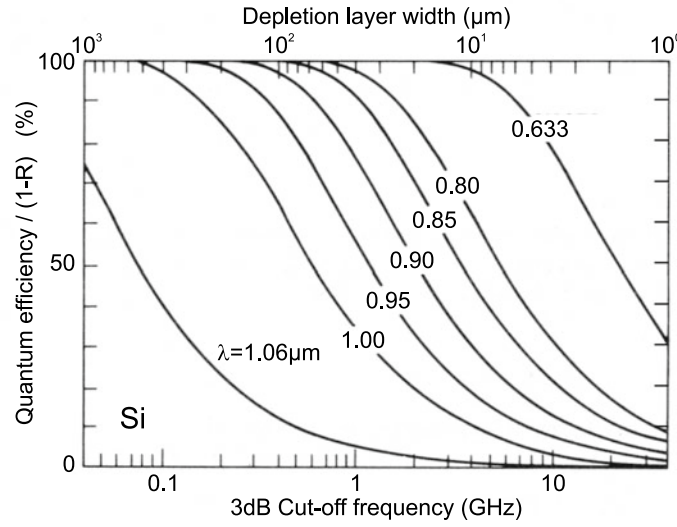

Fig. 22.18 Quantum efficiency and 3 dB cutoff frequency of a Si pin-diode at $T = 300\,\mathrm{K}$ for various wavelengths of input radiation. Adapted from [1838]

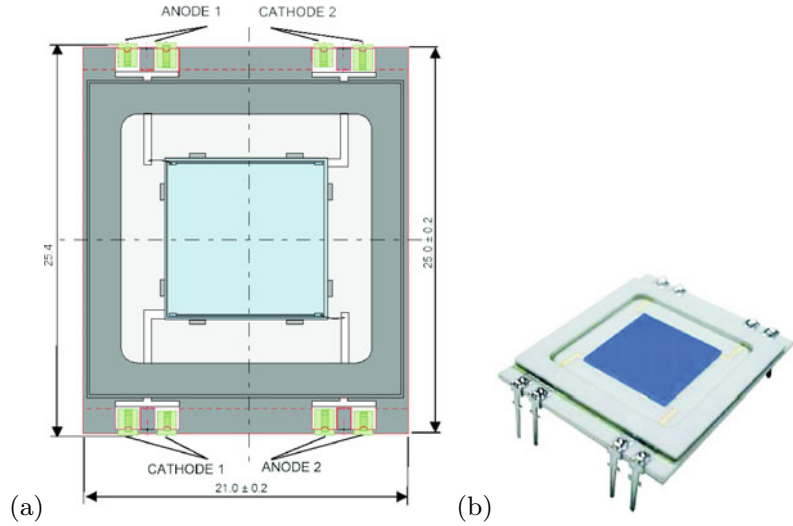

Fig. 22.19 **a** Scheme of two-dimensional position-sensing detector (PSD), **b** image of PSD. From [1839]

divider. If two pairs of electrodes, one on the front and one on the back of the detector, are fabricated in orthogonal directions (Fig. 22.19a), the beam position can be measured in both x and y directions.

22.3.5 MSM Photodiodes

A MSM photodiode consists of a piece of semiconductor between two Schottky contacts (MS contacts). These are typically arranged laterally (as shown in Fig. 22.24b) but will first be considered at the front and back of the semiconductor [1840]. The band structure in thermodynamic equilibrium is shown in Fig. 22.20.

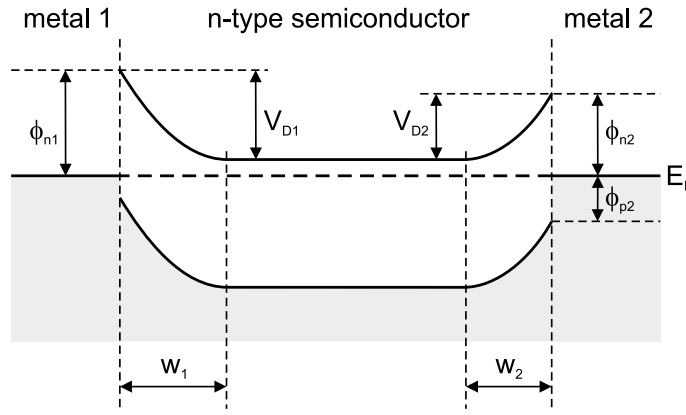

Fig. 22.20 Band diagram of a MSM structure with an n-type semiconductor in thermal equilibrium. In the general case, two different metals cause two different Schottky barrier heights and related depletion layer widths. Adapted from [1840]

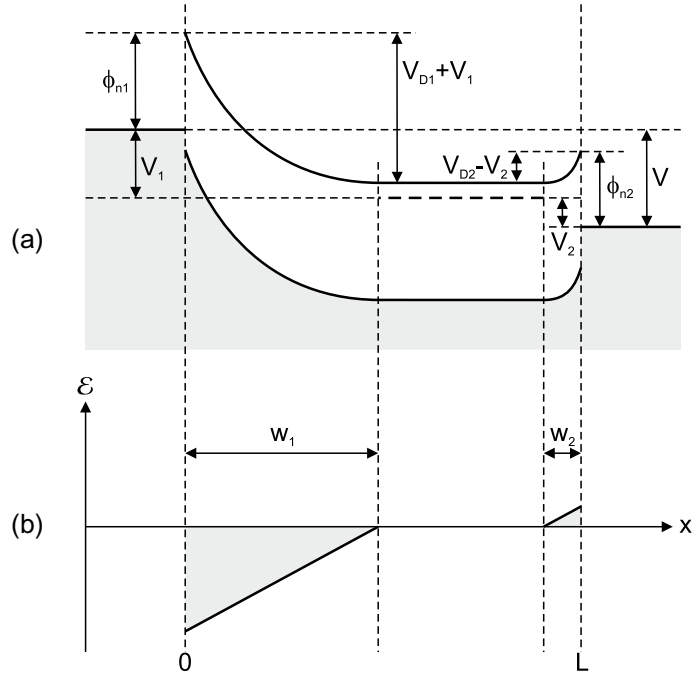

Fig. 22.21 **a** Band diagram for a MSM structure under bias ($V < V_{RT}$), **b** electric field distribution. Adapted from [1840]

In the general case two different metals with two different barriers ϕ_{n1}, ϕ_{n2} and built-in voltage V_{D1}, V_{D2} are considered. If a voltage is applied across the MSM diode, one of the junctions is biased in the forward, the other in the reverse direction. We assume in Fig. 22.21 that the voltage biases the first contact in the reverse direction, i.e. the '+' pole is on the left contact. The applied voltage V is split between the two contacts, the larger voltage will drop at the reverse-biased contact (here: $V_1 > V_2$)

$$V = V_1 + V_2 \, . \tag{22.36}$$

The electron current arises from thermionic emission at contact 2. Due to current continuity (without recombination since we inject majority charge carriers) this is also the current through contact 1, i.e.

$$j_{n1} = j_{n2} \, . \tag{22.37}$$

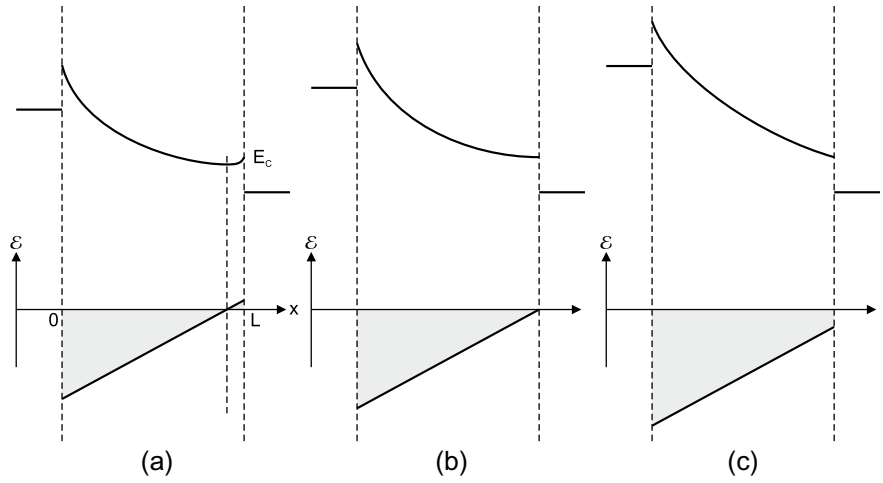

Fig. 22.22 Band diagram (*upper parts*) and electric field distribution (*lower parts*) in a MSM diode for various bias conditions: **a** at reach-through voltage V_{RT}, **b** at flat-band voltage V_{FB} and **c** for $V > V_{FB}$. Adapted from [1840]

The reverse current at contact 1 is

$$j_{n1} = A_n^* T^2 \exp(-\beta\phi_{n1}) \exp(\beta\Delta\phi_{n1}) \left[1 - \exp(-\beta V_1)\right] , \tag{22.38}$$

where $\Delta\phi_{n1}$ is the barrier reduction due to the Schottky effect (Sect. 21.2.3 and (21.27)). The forward current at contact 2 is

$$j_{n2} = -A_n^* T^2 \exp(-\beta\phi_{n2}) \exp(\beta\Delta\phi_{n2}) \left[1 - \exp(\beta V_2)\right] . \tag{22.39}$$

For a symmetric structure, i.e. $\phi_{n1} = \phi_{n2}$ and $V_{D1} = V_{D2} = V_D$, (22.37)–(22.39) yield together with (21.27)

$$\left(\frac{e^3 N_D}{8\pi^2 \epsilon_s^3}\right)^{1/4} \left[(V_D + V_1)^{1/4} - (V_D - V_2)^{1/4}\right] = \frac{1}{\beta} \ln\left[\frac{\exp(\beta V_2) - 1}{1 - \exp(-\beta V_1)}\right] . \tag{22.40}$$

Together with (22.36) a numerical or graphical solution can be found. Initially (for small voltages) the injected hole current (from contact 2) is much smaller than the electron current and diffusion occurs in the neutral region.

The reach-through voltage V_{RT} is reached when the width of the neutral region is reduced to zero (Fig. 22.22a). At the juncture of the two depletion regions inside the semiconductor material the electric field is zero and changes sign. For a larger voltage V_{FB} flat-band conditions are present at contact 2, i.e. the electric field is zero at contact 2 (Fig. 22.22b). At even larger voltage V_B breakdown occurs.

At $V = V_{RT}$ we have

$$w_1 = \left[\frac{2\epsilon_s}{e N_D} (V_1 + V_{D1})\right]^{1/2} \tag{22.41a}$$

$$w_2 = \left[\frac{2\epsilon_s}{e N_D} (V_{D2} - V_2)\right]^{1/2} \tag{22.41b}$$

$$L = w_1 + w_2 , \tag{22.41c}$$

and therefore (with (22.36))

$$V_{\mathrm{RT}} = \frac{e\,N_{\mathrm{D}}}{2\,\epsilon_{\mathrm{s}}}\,L^2 - L\left[\frac{2\,e\,N_{\mathrm{D}}}{\epsilon_{\mathrm{s}}}\,(V_{\mathrm{D2}} - V_2)\right] - \Delta V_{\mathrm{D}}\ , \tag{22.42}$$

with $\Delta V_{\mathrm{D}} = (V_{\mathrm{D1}} - V_{\mathrm{D2}})$, vanishing for a symmetric MSM structure. At and after reach-through the electric field varies linearly from 0 to L within the semiconductor. The point of zero electric field shifts towards contact 2. At the flat-band voltage this point has reached the contact 2 and the width of the depletion layer at contact 2 is zero. This condition leads (as long as no breakdown occurred) to

$$V_{\mathrm{FB}} = \frac{e\,N_{\mathrm{D}}}{2\,\epsilon_{\mathrm{s}}}\,L^2 - \Delta V_{\mathrm{D}}\ . \tag{22.43}$$

The maximum electric field is at contact 1 and is given (for $V > V_{\mathrm{FB}}$) by

$$E_{\mathrm{m1}} = \frac{V + V_{\mathrm{FB}} + 2\,\Delta V_{\mathrm{D}}}{L}\ . \tag{22.44}$$

If in a part of the structure the critical field E_{B} for impact ionization is reached (this will be at contact 1, since the field is highest there), the diode breaks down. Therefore the breakdown voltage is given by

$$V_{\mathrm{B}} \approx E_{\mathrm{B}}\,L - V_{\mathrm{FB}} - 2\,\Delta V_{\mathrm{D}}\ . \tag{22.45}$$

The current-voltage characteristic for a Si-MSM structure is shown in Fig. 22.23. At small voltages only small currents flow since one contact is in reverse bias. The hole current is much smaller than the electron current. Only those holes that diffuse through the neutral region contribute to the hole current. After reach-through the barrier $\phi_{\mathrm{p2}} + V_{\mathrm{D2}} - V_2$ for hole injection is strongly reduced that leads to strong hole injection. Beyond the flat-band voltage the hole current increases only weakly since a lowering of the barrier occurs only via the Schottky effect. For high fields ($V > V_{\mathrm{FB}}$, before breakdown) the hole current is

$$j_{\mathrm{p1}} = A_{\mathrm{p}}^{*}\,T^2\,\exp\left(-\beta\phi_{\mathrm{p2}}\right)\,\exp\left(\beta\Delta\phi_{\mathrm{p2}}\right) = j_{\mathrm{p,s}}\,\exp\left(\beta\Delta\phi_{\mathrm{p2}}\right)\ , \tag{22.46}$$

and the total current is

$$j = j_{\mathrm{n,s}}\,\exp\left(\beta\Delta\phi_{\mathrm{n1}}\right) + j_{\mathrm{p,s}}\,\exp\left(\beta\Delta\phi_{\mathrm{p2}}\right)\ , \tag{22.47}$$

with $j_{\mathrm{n,s}} = A_{\mathrm{n}}^{*}T^2\exp(-\beta\phi_{\mathrm{n1}})$ and $j_{\mathrm{p,s}} = A_{\mathrm{p}}^{*}T^2\exp(-\beta\phi_{\mathrm{p2}})$.

In a MSM photodetector the metal contacts are typically formed in an interdigitated structure on the semiconductor surface (Fig. 22.24). These contacts shield some of the active area from photons. An increase in quantum efficiency can be achieved with transparent contacts (e.g. ZnO or ITO) and an antireflection (AR) coating.

The dark current is given by (22.47) and is minimal when electron and hole saturation currents are identical. This conditions leads to the optimal barrier height

$$\phi_{\mathrm{n}} = E_{\mathrm{g}} - \phi_{\mathrm{ph}} = \frac{1}{2}\,\beta^{-1}\,\ln\left(\frac{m_{\mathrm{e}}}{m_{\mathrm{hh}}}\right) + \frac{1}{2}\,E_{\mathrm{g}} \tag{22.48}$$

close to middle of the band gap. For InP and optimal barrier $\phi_{\mathrm{n}} = 0.645\,\mathrm{eV}$ a dark current of $0.36\,\mathrm{pA/cm^2}$ is expected for a field of $10\,\mathrm{V/\mu m}$. For deviating barrier height the current increases exponentially. The current-voltage characteristic of an InGaAs:Fe MSM photodetector is shown in Fig. 22.25 for a dark environment and various illumination levels.

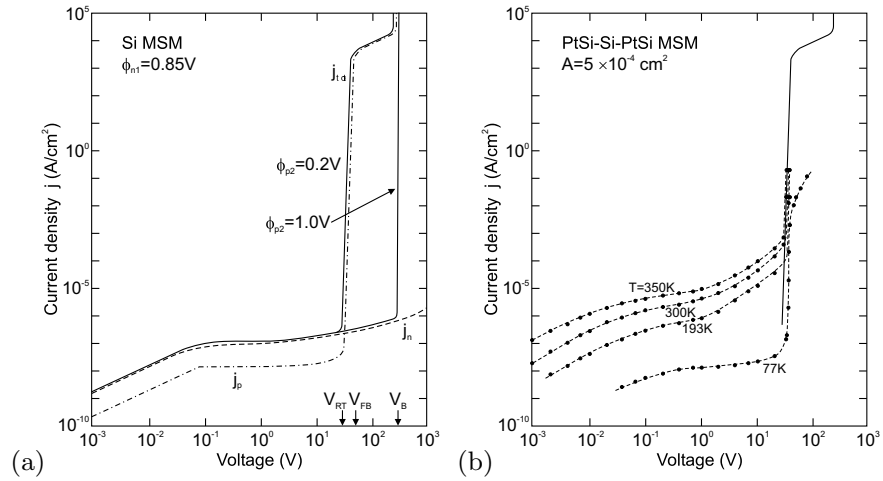

Fig. 22.23 Current-voltage characteristics of a Si MSM structure, $N_D = 4 \times 10^{14}\,\mathrm{cm}^{-3}$, $L = 12$ μ m (thin, polished, ⟨111⟩-oriented wafer), $T = 300\,\mathrm{K}$. **a** Theory for two different values of ϕ_{p_2}, **b** experiment (for $\phi_{p_2} = 0.2\,\mathrm{V}$). Adapted from [1840]

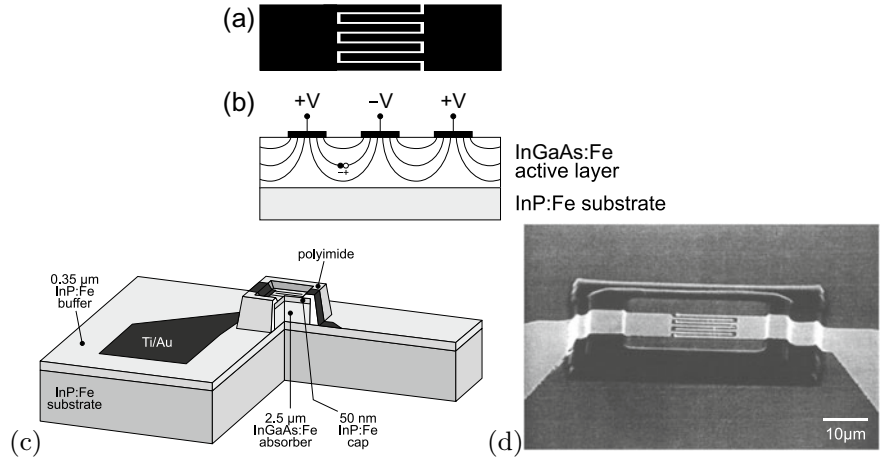

Fig. 22.24 Scheme of MSM photodetector with interdigital contacts in **a** plan view and **b** cross section. In part (**b**), the electric field lines are shown schematically together with an electron-hole pair ready to be separated. **c** Scheme of a MSM mesa structure, **d** SEM image of an InGaAs/InP MSM mesa photodetector. Parts **c** and **d** adapted from [1841]

The time-dependent response of a MSM photodetector depends on the drift time of the carriers, i.e. the time that a created electron and hole need to arrive at their respective contacts. In Fig. 22.26 a simulation is shown for a MSM detector. The current has two components, a fast one due to the electrons and a slow one due to the holes that have the lower mobility and smaller drift saturation velocity. A similar dependence is found in experiment (Fig. 22.27a). For longer wavelengths the detector is slower since they penetrate deeper into the material and thus the charge carriers have a longer path to the contacts (cf. scheme in Fig. 22.24b). An important role is played by the finger separation; smaller finger separation ensures a more rapid carrier collection (Fig. 22.27b). In [1842] a bandwidth of 300 GHz was demonstrated for 100 nm/100 nm finger width and separation for LT-GaAs[8] and bulk GaAs, limited by

[8]LT: grown at *low temperature*, i.e. containing many defects that reduce the carrier lifetime.

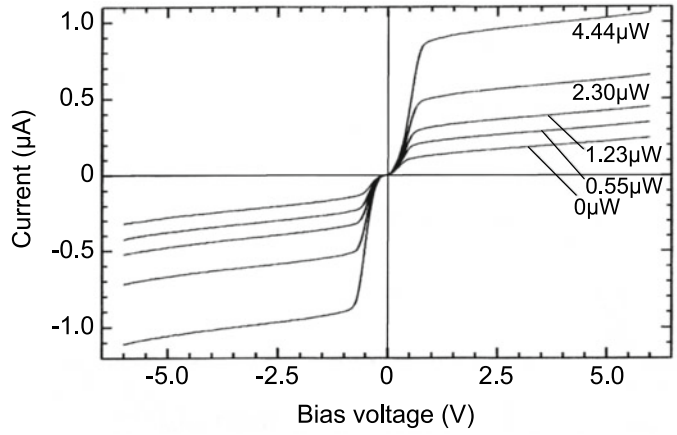

Fig. 22.25 dc I–V characteristic of an InGaAs/InP MSM photodetector (InP:Fe/InGaAs:Fe/InP:Fe, finger separation 1 μ m, $\lambda = 1.3$ μ m) under illumination for dark environment (0 μ W) and various illumination levels as labeled. Adapted from [1841]

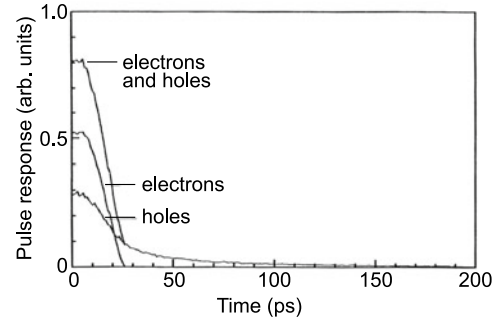

Fig. 22.26 Simulation of the time-dependent response of an InGaAs:Fe MSM photodetector to a short light pulse. Adapted from [1841]

the RC time constant. For 300 nm/300 nm fingers and a LT-GaAs a bandwidth of 510 GHz (pulsewidth of 0.87 ps) was reported, which is faster than the intrinsic transit time (1.1 ps) and not limited by the RC time constant (expected pulse width 0.52 ps), due to the recombination time (estimated to be 0.2 ps).

22.3.6 Avalanche Photodiodes

In an avalanche photodiode (APD) intrinsic amplification due to carrier multiplication (through impact ionization) in a region with high electric field is used to increase the photocurrent. The field is generated by a high reverse bias in the diode. In an ideal APD only one type of carrier is multiplied, resulting in the lowest noise. If electrons are injected into the field region at $x = 0$ (Fig. 22.28a), the multiplication factor for electrons is

$$M_\mathrm{n} = \exp(\alpha_\mathrm{n}\, w)\ , \tag{22.49}$$

for $\alpha_\mathrm{p} = 0$. Typically, both carrier types suffer multiplication. If the electron and hole impact ionization coefficients are the same ($\alpha_\mathrm{n} = \alpha_\mathrm{p} = \alpha$), the multiplication factor for electrons and holes M is given by

$$M = \frac{1}{1 - \alpha\, w}\ . \tag{22.50}$$

The rms value of the current noise is the same as in the case of the pn-diode (22.25), only that now the gain M is added

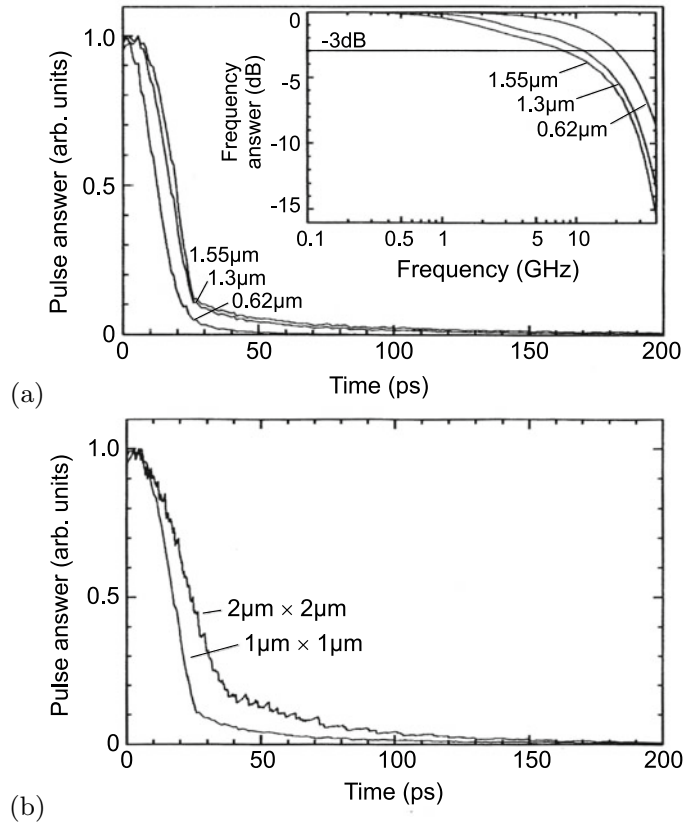

Fig. 22.27 **a** Experimental time-dependent response of an InGaAs:Fe MSM photodetector to a short light pulse for three different wavelengths, *inset* shows the frequency response from a Fourier transform. **b** Response of the MSM for two different finger widths and separations (both 1 or 2 μ m, respectively), InGaAs layer thickness 2 μ m, $\lambda = 1.3$ μ m and bias voltage 10 V. Adapted from [1841]

$$\langle i_S^2 \rangle = 2\,e\,\left(I_{\rm ph} + I_B + I_D\right)\,\langle M^2 \rangle\,B\ . \tag{22.51}$$

The term $\langle M^2 \rangle$ is written as $\langle M \rangle^2\,F(M)$ with $F(M) = \langle M^2 \rangle / \langle M \rangle^2$ being the excess noise factor that describes the additional noise introduced by the random nature of the impact ionization. For multiplication started with electron injection, it is given by [1843]

$$F(M) = k\,M + (1-k)\left(2 - \frac{1}{M}\right)\ , \tag{22.52}$$

with $k = \alpha_p/\alpha_n$. For hole injection starting the multiplication (22.52) holds with k substituted by $k' = \alpha_n/\alpha_p$. In Fig. 22.29a the excess noise factor is shown vs. the average multiplication for various values of k and k'.

Experimental data are shown in Fig. 22.29b for a Si APD. For short wavelengths absorption is preferential at the surface (n-region) and we have the case of hole injection. The data for the excess noise factor are fairly well fit with $k' \approx 5$. For longer wavelengths, the data for electron injection are fit by $k \approx 0.2 = 1/k'$.

For a fully modulated signal the signal-to-noise ratio is given by

$$S/N = \frac{(e\,\eta\,P_{\rm opt}/h\nu)^2/2}{2\,e\,\left(I_{\rm ph} + I_B + I_D\right)\,F(M)\,B + 4\,kT\,B/(R_{\rm eq}\,M^2)}\ . \tag{22.53}$$

If S/N is limited by thermal noise, the APD concept leads to a drastic improvement of noise.

The APD can used for single photon detection; then the variation in pulse height (with reasonable limits) plays no role for the count rate. The number of dark counts can be reduced by cooling the APD. Using constant fraction triggering, also the arrival time of the photon can be determined, allowing time resolution typically in the 100 ps regime.

A particular APD structure is known as a *solid-state multiplier*. It has separate absorption and amplification regions (SAM structure). In the low-field region the light is absorbed. One type of carrier is transported with the drift field E_d to the multiplication region in which a large field E_m is present and multiplication occurs. In Fig. 22.30a a homo-APD with SAM structure is shown. Regions with different electric field are created by a special doping profile.[9] A π-p-π structure leads to regions with homogeneous low and high field strengths.

The performance of a commercial silicon APD is depicted in Fig. 22.31. With increasing reverse bias, both the dark current and the multiplication factor increase. Before breakdown at about 77 V, the best ratio of M and I_{dark} is found. This particular diode has a typical excess noise factor of $F = 2$ for $M = 100$. Using (22.52), this shows that only one kind of carriers is multiplied.

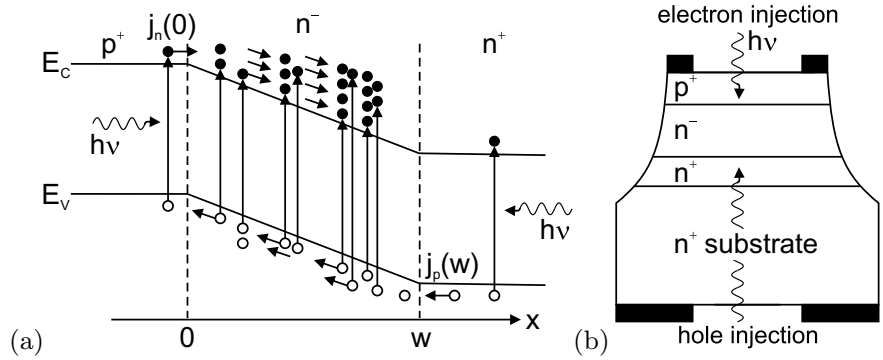

Fig. 22.28 Schematic band structure **a** and schematic device setup **b** of an avalanche photodiode (APD). From [1185]

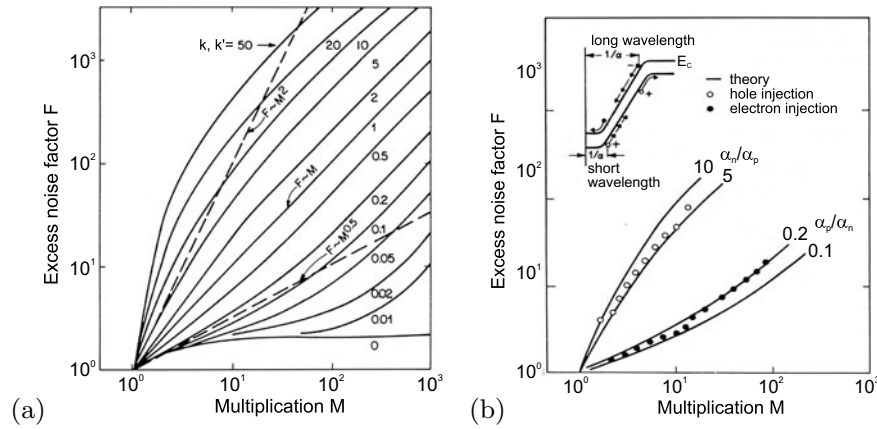

Fig. 22.29 **a** Excess noise factor for various values of the ratio of ionization coefficients k or k'. Adapted from [1843]. **b** Experimental results for F for a Si APD with 0.1 μ A primary current. The *empty* (*full*) symbols are for short (long) wavelengths [primary hole (electron) current]. The *inset* shows the schematic band diagram of the np-diode under reverse bias. Adapted from [1844]

[9] Employing spatially inhomogeneous Poisson's equation $\partial(\epsilon_s(x)E(x))/\partial x = \rho(x)$.

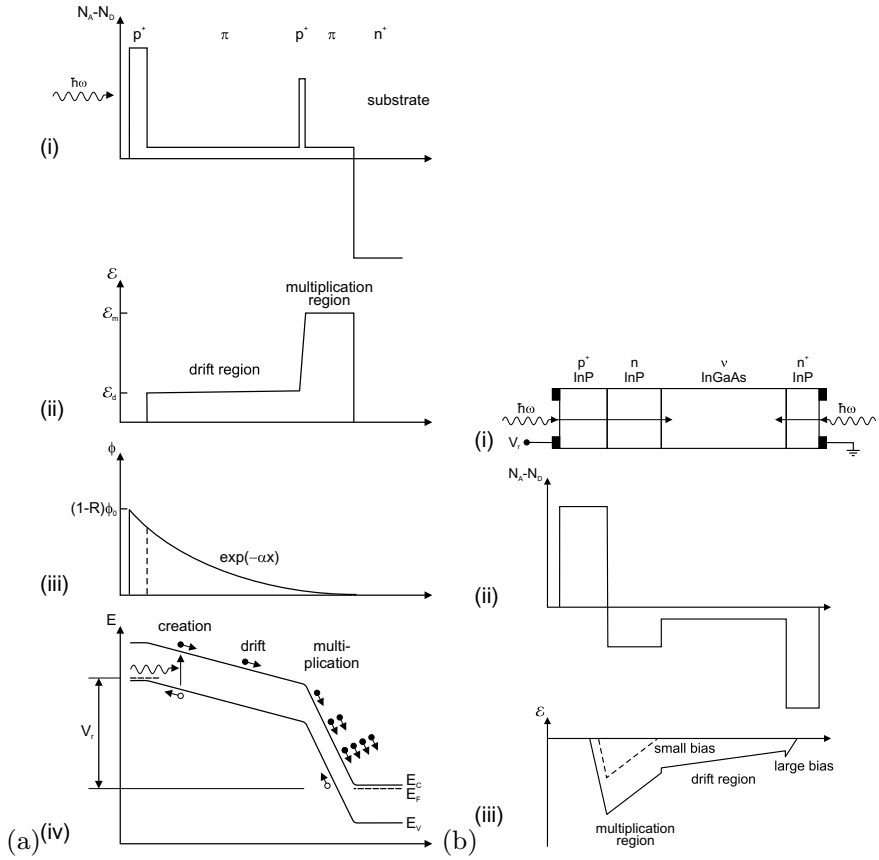

Fig. 22.30 **a** Homo-APD with SAM structure. (**i**) doping profile, (**ii**) electric field, (**iii**) photon flux or electron-hole pair generation rate and (**iv**) schematic band diagram under reverse voltage V_r with charge-carrier transport. The multiplication is for $\alpha_n \gg \alpha_p$. Adapted from [574]. **b** (**i**) Scheme of an InP/InGaAs hetero-APD with SAM structure, (**ii**) doping profile and (**iii**) electric field for small (*dashed line*) and large (*solid line*) reverse bias V_r. Adapted from [1185]

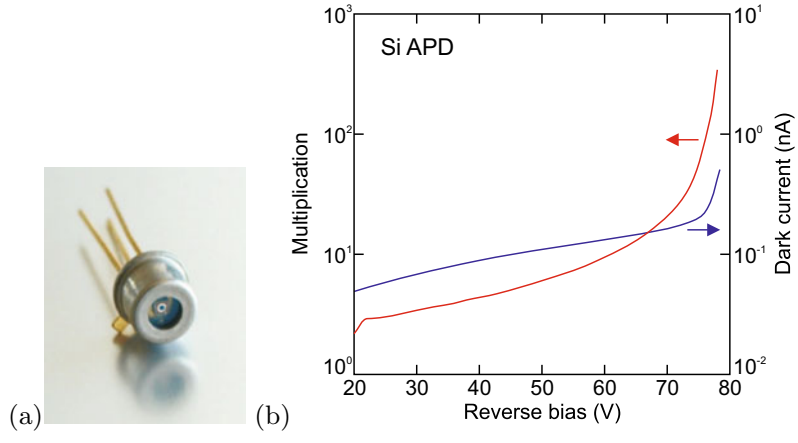

Fig. 22.31 **a** TO casing of Si APD. **b** Dark current (*blue*) (active area 0.2 mm^2) and multiplication factor (*red*) as a function of reverse bias (at 23°C). Adapted from [1845]

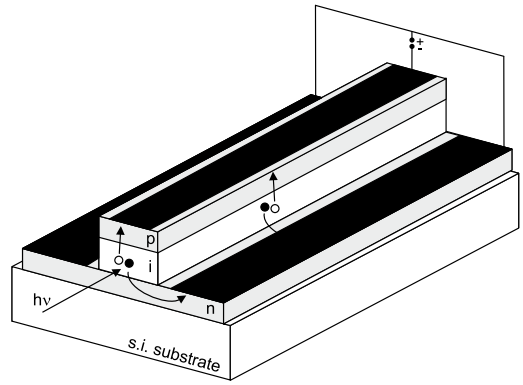

Fig. 22.32 Scheme of a traveling-wave photodetector with pin structure and coplanar contacts

In the case of a heterostructure-APD with SAM structure (Fig. 22.30b) absorption (of light with sufficiently long wavelength with an energy smaller the the InP band gap) takes place only in the InGaAs layer. Since no light is absorbed in the multiplication region, the device functions similarly for front and back illumination. In [1846] a multi-stage InGaAs-based APD on InP is described that is optimized for electron multiplication in ten subsequent gain sections; a total gain of 10^3 is achieved with an excess noise factor F of about 40, belonging to an effective ionization ratio of $k = 0.036$.

22.3.7 Traveling-Wave Photodetectors

In a standard photodetector there was a tradeoff between the thickness of the absorption layer and the speed of the detector. In a traveling-wave photodetector the light absorption occurs in a waveguide such that for sufficient length L all incident light is absorbed. Complete absorption is achieved ('long' waveguide) if $L \gg (\Gamma\alpha)^{-1}$, α being the absorption coefficient and $\Gamma \leq 1$ being the optical confinement factor, the geometrical overlap of the optical mode with the cross section of the absorbing medium (cf. also Sect. 23.4.4).

The electrical connections are designed along this waveguide on the sides (coplanar layout, Fig. 22.32). The bandwidth limitation due to a RC time constant is now replaced by the velocity match of the light wave $v_{\text{opt}} = c/n$ and the traveling electric wave in the contact lines $v_{\text{el}} \approx 1/\sqrt{LC}$. While the two waves travel along the waveguide, energy is transferred from the light wave to the electric wave. The 3 dB bandwidth due to velocity mismatch B_{vm} (for impedance- matched, long waveguides) is given by [1847]

$$B_{\text{vm}} = \frac{\Gamma\,\alpha}{2\pi}\,\frac{v_{\text{opt}}\,v_{\text{el}}}{v_{\text{opt}} - v_{\text{el}}}\,. \tag{22.54}$$

For a MSM structure, whose electrode separation has been designed with a self-aligned process (without extensive effort in lateral patterning) by an etch depth of a few 100 nm (Fig. 22.33), 3 dB cutoff frequencies beyond 500 GHz have been achieved (Fig. 22.34). The quantum efficiency of this detector was still 8.1%.

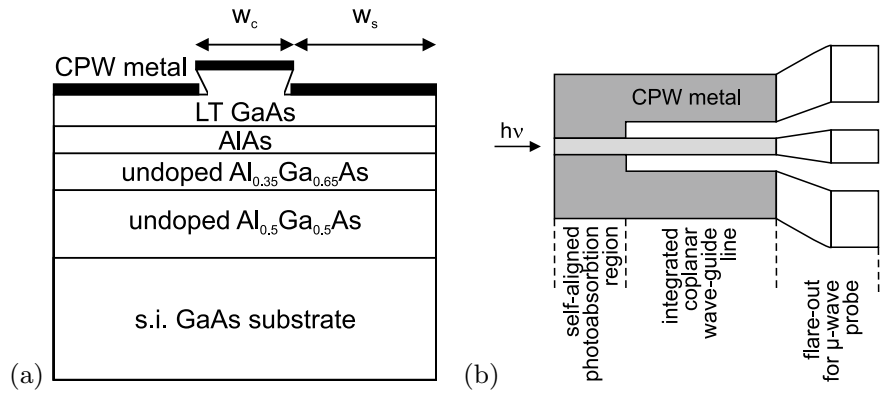

Fig. 22.33 Scheme of a MSM traveling-wave photodetector in **a** cross section and **b** plan view. Adapted from [1848]

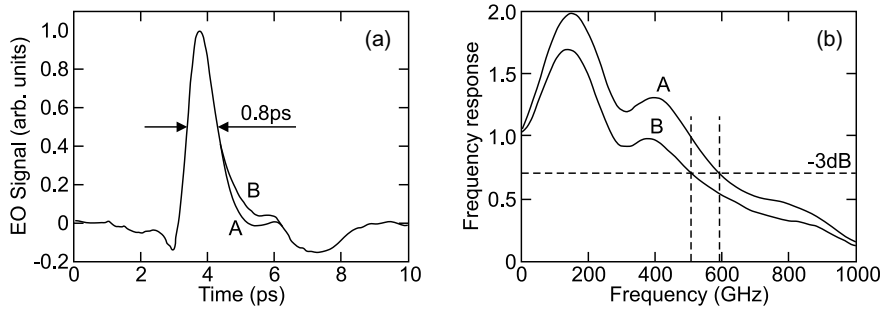

Fig. 22.34 **a** Pulse response (FWHM=0.8 ps) and **b** frequency response (Fourier transform of time response) of a MSM traveling-wave photodetector (bias 5 V) for various illumination intensities, A: 1 mW, B: 2.2 mW. Adapted from [1848]

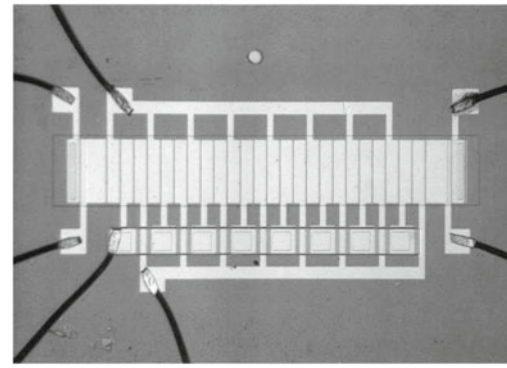

Fig. 22.35 First 8-bit charge coupled device (1970). The chip (size: 1.5 × 2.5 mm^2) consists of 24 closely packed MOS capacitors (narrow rectangles in the center grid). The thick rectangles at either end of the grid are input/output terminals

22.3.8 Charge Coupled Devices

The concept of the charge coupled device (CCD), an array of connected photodetectors serving as an image sensor, was devised by W.S. Boyle and G.E. Smith [143] (Fig. 22.35) and realized [144]. As textbook for further details [1849, 1850] may serve.

A MIS diode (mostly a silicon-based MOS diode) can be designed as a light detector. The diode is operated in deep depletion. When a large reverse voltage is applied, initially a depletion layer is formed and the bands are strongly bent as shown in Fig. 22.36b. We note that in this situation the

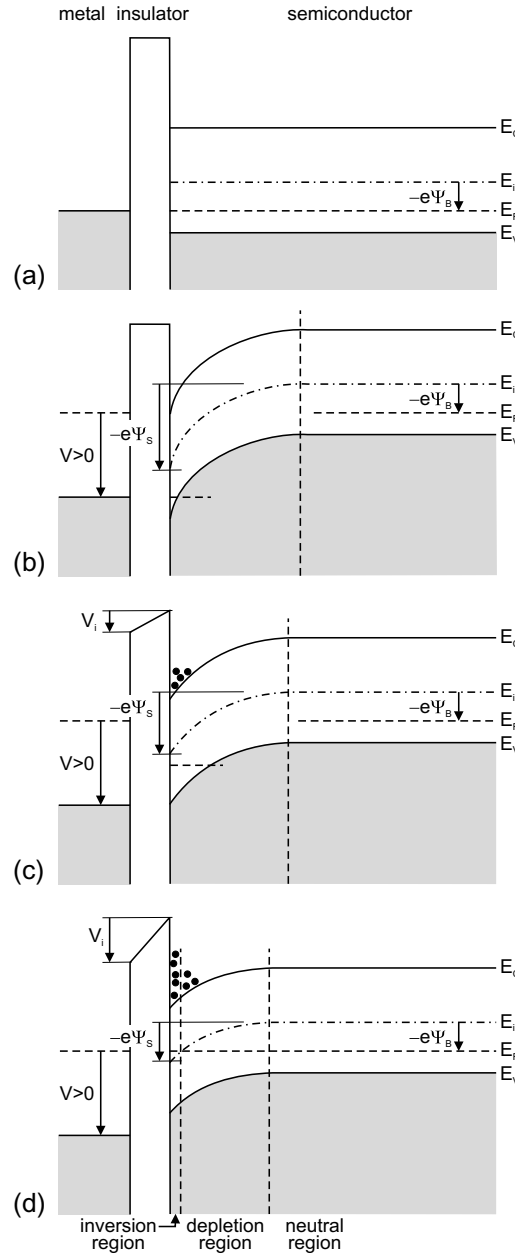

Fig. 22.36 Ideal MIS-diode (with p-type semiconductor) as photodetector (principle of a CCD pixel). **a** Without bias (see Fig. 21.30b). **b** Immediately after an external (reversely poled) voltage $V > 0$ has been applied, the surface potential is $\Psi_s = V$ and no charges have moved yet. **c** Strong depletion (still not in thermodynamic equilibrium) with signal charge and reduced surface potential $\Psi_s < V$. **d** The semiconductor in equilibrium (E_F is constant) with depletion and inversion layer (see Fig. 21.34). For all diagrams, $V = V - i + \Psi_s$

semiconductor is not in thermodynamic equilibrium (as it is in Fig. 22.36d) when the quasi-Fermi level is constant throughout the semiconductor. The inversion charge has yet to build up.

There are three mechanisms to generate the inversion charge. (a) generation-recombination, (b) diffusion from the depletion-layer boundary and (c) carrier generation by light absorption. Mechanisms (a) and (b) represent dark currents for the photodetector. The conductivity due to these two processes is shown in Fig. 22.37 and slowly builds up the inversion charge. Two temperature regimes are obvious; at low temperatures the generation dominates ($\propto n_i \propto \exp(-E_g/2kT)$), at high temperatures the

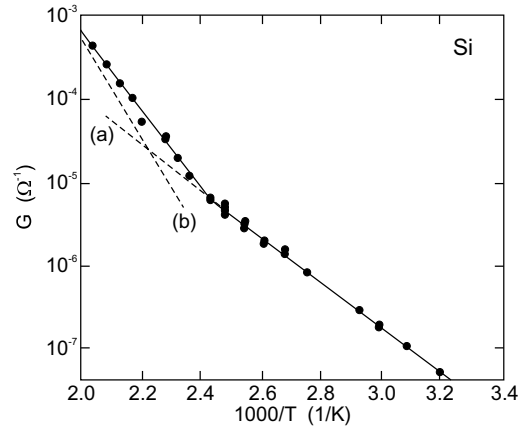

Fig. 22.37 Conductivity of a n-Si/SiO_2-diode as a function of temperature ($1/T$). The slope of the *dashed lines* is (a) $\sim 0.56\,\mathrm{eV}$ ($\approx E_g/2$) and (b) $\sim 1.17\,\mathrm{eV}$ ($\approx E_g$). Adapted from [1851]

diffusion ($\propto n_i^2 \propto \exp(-E_g/kT)$). The latter process can be strongly suppressed by cooling the device.

The gate voltage V_G and the surface potential Ψ_s are related to each other via

$$V_G - V_{FB} = V_i + \Psi_s = \frac{e\,N_A\,w}{C_i} + \frac{eN_A w^2}{2\epsilon_s}\,, \tag{22.55}$$

where w is the width of the depletion layer. w will be larger than w_m in thermodynamic equilibrium. The first term in the sum is $|Q_s|/C_i$ and the second is obtained by integrating the Poisson equation for the constant charge density $-eN_A$ across the depletion layer. The elimination of w yields

$$V_G - V_{FB} = \Psi_s + \frac{1}{C_i}\sqrt{2e\epsilon_s N_A \Psi_s}\,. \tag{22.56}$$

If light is absorbed in the depletion layer (process (c)), the hole (for p-Si) drifts towards the bulk material. The electron is stored as part of the signal charge Q_{sig} close to the oxide semiconductor interface (Fig. 22.36b).

$$V_G - V_{FB} = \frac{Q_{sig}}{C_i} + \frac{eN_A w}{C_i} + \Psi_s\,. \tag{22.57}$$

As a consequence of the increase in signal charge the potential well becomes shallower (22.57). For each gate voltage there is a maximum charge (well capacity). The maximum signal charge is reached for $\Psi_s \approx 2\Psi_B$ (Fig. 22.38).

In a charge coupled device (CCD) many light-sensitive MIS diodes, as described above, are fabricated in matrix form to create an image sensor. Upon application of a gate voltage they accumulate charge depending on the local exposure to light. The read out of this charge occurs by shifting the charge through the array to a read-out circuit. Therefore charge is transferred from one pixel to the next. Several schemes have been developed for this task. The three-phase clocking is shown schematically in Fig. 22.39. Other clocking schemes involve four, two or only one electrode per pixel [1853].

Since the CCD sensor has many pixels (e.g. up to 4096) along a line, the charge transfer must be highly efficient. The transfer of charge carriers occurs via thermal (regular) diffusion, self-induced drift and the effect of the fringing field (inset of Fig. 22.40). The time constant with which the charge carriers move due to diffusion (in a p-type semiconductor) is

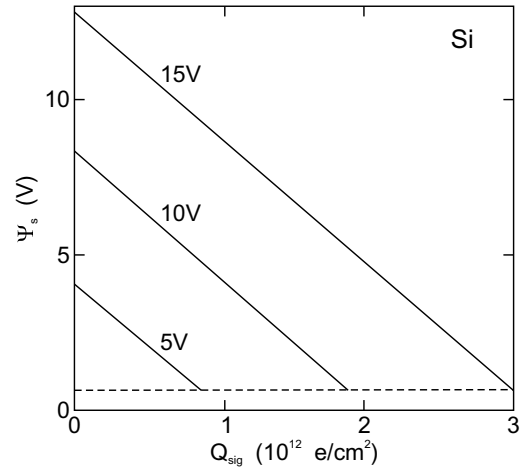

Fig. 22.38 Surface potential as a function of the signal charge Q_{sig} for various values of the bias $V_G - V_{FB}$ as labeled for a SiO_2/p-Si diode with $N_A = 10^{15}\,cm^{-3}$ and an oxide thickness of 100 nm. The *dashed line* represents the limit for inversion given by $\Psi_s = 2\Psi_B \approx 0.6\,V$. Adapted from [1852]

$$\tau_{th} = \frac{4\,L^2}{\pi^2\,D_n}\,, \tag{22.58}$$

where L is the length of the electrode. For a sufficiently large charge packet the self-induced drift due to Coulomb repulsion is important. The decay of charge is then given by

$$\frac{Q(t)}{Q(0)} = \frac{t_0}{t + t_0}\,, \tag{22.59}$$

with $t_0 = \pi\,L^3\,W_e C_i/(2\mu_n Q(0))$. W_e is the width of the electrode. This dependence is shown as a dashed line in Fig. 22.40a. The last electrons are efficiently transferred by the drift induced by the fringing field of the electrodes (solid line in Fig. 22.40a). The origin of the fringing field is schematically shown in Fig. 22.40b; the minimum fringing field shown is 2×10^3 V/cm. In about 1–2 ns practically all $(1 - 10^{-5})$ charges are transferred. This enables clock rates of several 10 MHz.

For the clocking of the CCD the lateral variation of potential depth with the applied gate voltage is used. In Fig. 22.41 it is shown how a lateral variation of doping or oxide thickness creates a lateral potential well. Such structures are used to confine the row of pixels against the neighboring rows (channel stops, Fig. 22.42). In order to avoid carrier loss at the interface between the oxide and the semiconductor a buried-channel structure is used (Fig. 22.43).

For front illumination parts of the contact electrodes shield the active area of the device. Higher sensitivity (in particular in the UV) is achieved for back illumination. For this purpose the chip is thinned (polished). This process is expensive and makes the chip mechanically less stable. For red/infrared wavelengths typically interference fringes occur for such thinned chips due to the small thickness. An increase in efficiency for front illumination can be achieved with an on-chip microlens (Fig. 22.44).

For color imaging the CCD is covered with a three-color Bayer mask [1858] (Fig. 22.45a). On average there are one blue and one red pixel and two green pixels since green is the most prominent color in typical lighting situations. Thus each pixel delivers monochromatic information; RGB images are generated using suitable image software. Alternatives in high-end products are the use of a beam splitter, static color filters and three CCD chips, one for each color (Fig. 22.45b), or the time-sequential recording of three monochromatic images using one CCD chip and a rotating color-filter wheel (Fig. 22.45c). Another method is to shift (by piezoelectric actors) the CCD by half or full pixels and take sequential exposures, increasing spatial and color resolution for still objects.

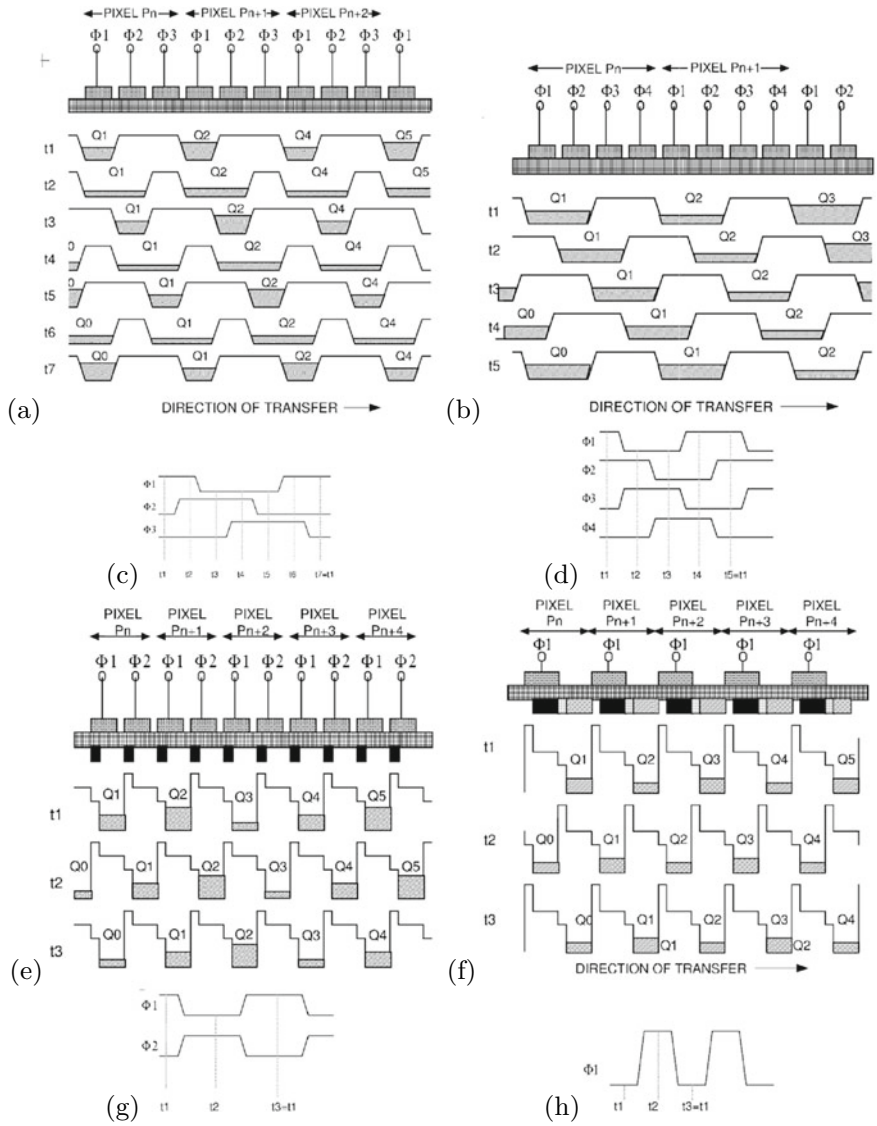

Fig. 22.39 **a** Three-phase CCD. Each pixel has three electrodes that can be switched independently (phases 1–3). **b**, **e**, **f** Schematic of CCDs with four, two or one phase, respectively. **c** (t_1) Charge accumulated after light exposure. A lateral potential well is formed along the row of pixels by the voltages at the three electrodes, e.g. $P_1 = P_3 = 5\,\mathrm{V}$, $P_2 = 10$,V. (t_2–t_7) transfer of charge, (t_7) has the same voltages as (t_1), the charge has been moved one pixel to the right. **d**, **g**, **h** Timing schemes for 4-, 2- and 1-phase CCDs, respectively. From [1853]

22.3.9 Photodiode Arrays

An array of photodiodes is also suitable to create an image sensor. During illumination each diode charges a capacitor that is read out with suitable electronics. Based on CMOS technology (cf. Sect. 24.5.4), economic image sensors can be made (CMOS image sensors, CIS) [1859, 1860]. For a long time they exhibited inferior performance to CCDs but progress in readout and noise suppression has made them the image sensor of choice for many camera applications including the smart phone

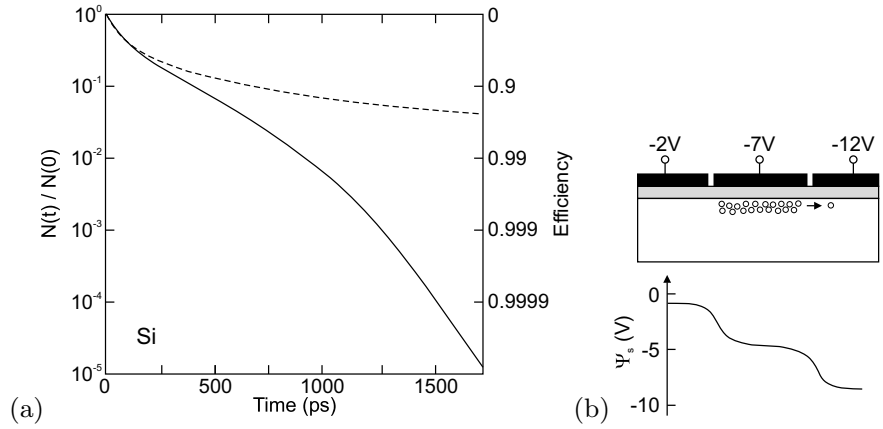

Fig. 22.40 **a** Efficiency of charge transfer with (*solid* line) and without (*dashed* line) the effect of the fringing field. **b** Schematic plot of the CCD electrodes and bias with the fringing field for a three-electrode CCD, oxide thickness 200 nm, doping $N_D = 10^{15}\,cm^{-3}$. The electrode pitch is 4 μ m and the gap between electrodes is 200 nm wide. Adapted from [1854]

Fig. 22.41 Creation of a lateral potential well (barrier) in a MIS structure with **a** varying doping via diffusion or implantation and **b** varying (stepped) oxide thickness. *Upper row* shows schematic geometry, *lower row* depicts schematic lateral variation of the surface potential

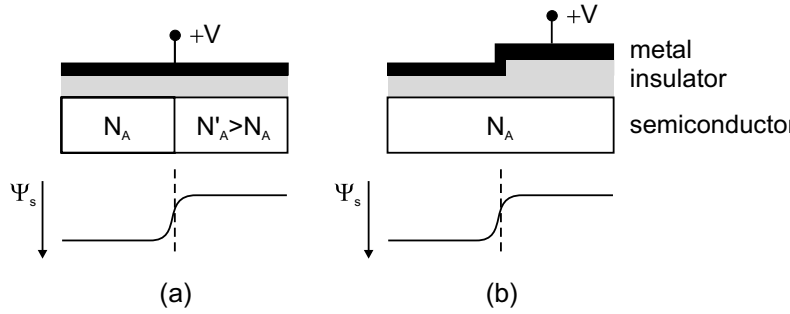

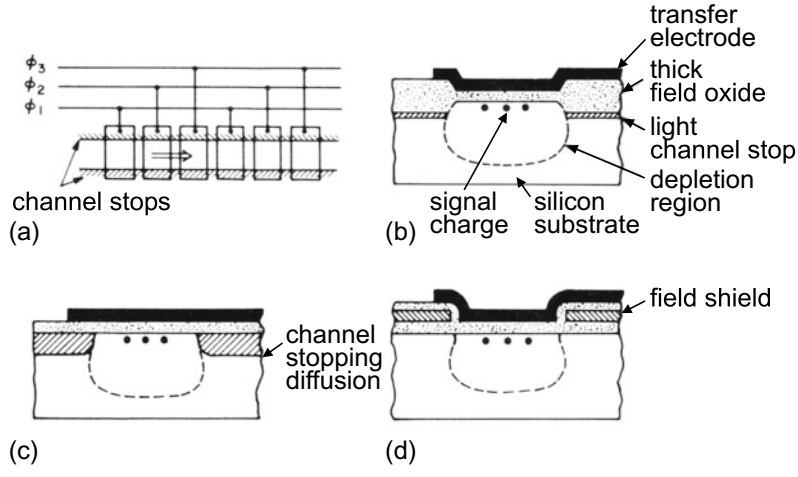

Fig. 22.42 **a** Schematic image of channel isolation. Cross section for channel isolation by **b** variation of oxide thickness, **c** highly doped region and **d** field effect. Adapted from [1855]

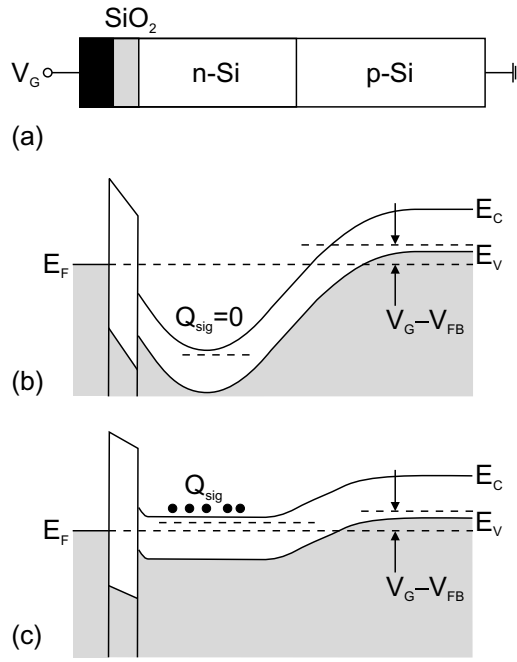

Fig. 22.43 **a** Schematic layers of MIS diode with buried-channel structure. Band diagram **b** after application of reverse voltage V_G and **c** with signal charge Q_{sig}. Adapted from [1856]

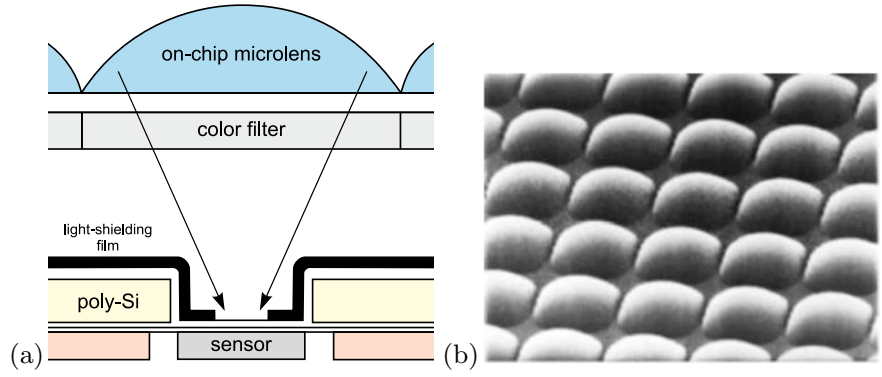

Fig. 22.44 **a** Scheme for enhancement of CCD efficiency for front illumination by application of an onchip microlens. **b** SEM image of an array of such microlenses. From [1857]

market. The built-in electronics allows simple outward connections (Fig. 22.46) and with several transistors per pixel even on-chip image processing.

The three-color CCD image sensor does not offer RGB color information at each pixel. Therefore the spatial resolution of a color image is not directly given by the pixel distance. This is not a very dramatic drawback since human vision is more sensitive to intensity contrast than color contrast. However, RGB color information for each pixel would be desirable, giving higher resolution, in particular in professional photography. Such a sensor has been fabricated employing the wavelength dependence of the silicon absorption coefficient (Fig. 22.13). Blue light has the shortest and red light the largest penetration depth. By stacking three photodiodes on top of each other (Fig. 22.47) photocurrents at different penetration depth are recorded that can be used to generate a RGB value for each pixel.

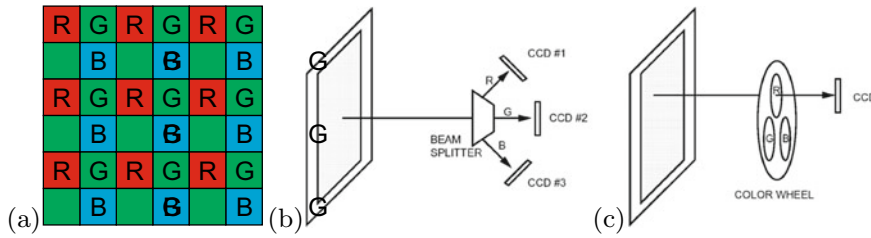

Fig. 22.45 **a** Arrangement of colors in a CCD Bayer [1858] color filter ('R': red, 'G': green, 'B': blue). Color splitting with **b** static color filters and **c** rotating color wheel. Parts **b** and **c** from [1853]

In Fig. 22.48a a 16-channel array of silicon avalanche photodiodes is shown. It features a quantum efficiency of $> 80\%$ between 760 and 910 nm. The pixel size is $648 \times 208\,\mu m^2$ on a 320 µ m pitch. The gain is 100 and the rise time 2 ns.

The InGaAs photodiode array in Fig. 22.48b is hybridized with CMOS read-out integrated circuits. It is useful for detection in the spectral range 0.8–1.7 µ m. The asymmetric diode size of $25 \times 500\,\mu m$ is designed for use in the focal plane of a monochromator.

Another special type of photodiode array is the four-quadrant detector. A light beam generates four photocurrents I_a, I_b, I_c, I_d of the respective parts (Fig. 22.49a). A beam deviation in the horizontal or vertical direction can be detected from the (signed) signals $(I_a + I_d) - (I_b + I_c)$ or $(I_a + I_b) - (I_c + I_d)$, respectively. We note that these signals can also be normalized to the total beam intensity $I_a + I_b + I_c + I_d$.

A further improvement of the microlens technology (cmp. Fig. 22.44) is achieved with additional tapered light pipes [1867], guiding obliquely incoming light to the photo-sensitive pixel in an optimized

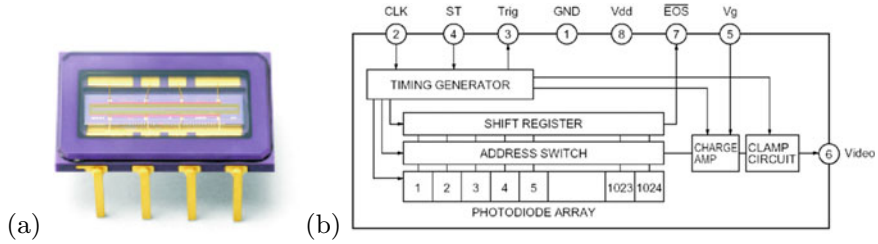

Fig. 22.46 (**a**) CMOS linear array sensor in a 8-pin package. **b** Block diagram, the built-in timing generator allows operation only with start and clock pulse inputs. Reprinted with permission from [1861]

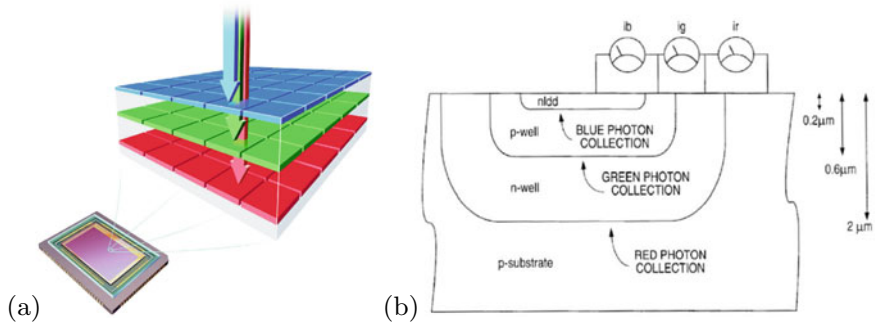

Fig. 22.47 **a** Scheme of image sensor with depth-dependent light detection. From [1862]. **b** Schematic layer sequence for three-color pixel. i_b, i_g and i_r denote the photocurrents for blue, green and red light, respectively. Adapted from [1863]

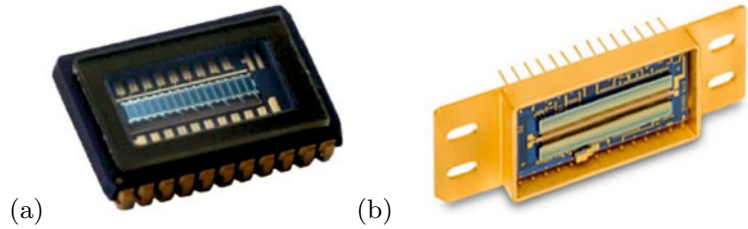

Fig. 22.48 **a** Array of 16-pixel ($1000 \times 405\,\mu m^2$) silicon APDs (width of housing: 15 mm). From [1864]. **b** 1024-pixel ($25 \times 500\,\mu m^2$) InGaAs photodiode array (width of array: 1 inch). From [1865]

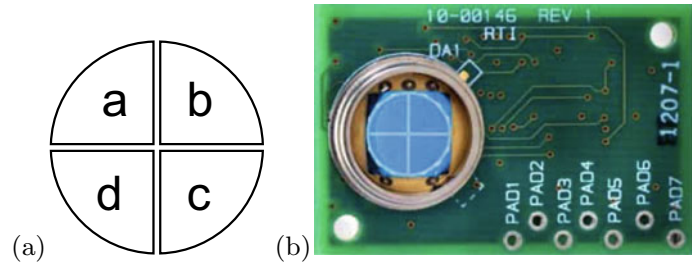

Fig. 22.49 **a** Scheme of four-quadrant photodetector with sections 'a', 'b', 'c' and 'd'. **b** image of four-quadrant silicon photodetector with circuit board (diameter of active area: 8 mm, gap between sectors: 0.2 mm). From [1866].

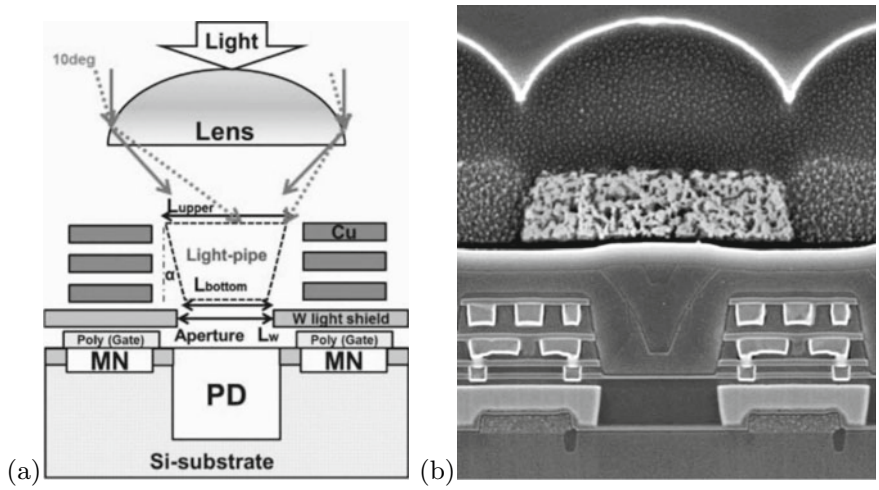

Fig. 22.50 **a** Schematic cross-section of global shutter pixel with light pipe for optimized collection. α denotes the taper angle, PD: photodiode, MN: buried memory node to store the charges until readout. **b** Cross-section SEM image of such pixel. Adapted from [1867]

fashion (Fig. 22.50). This so-called 'global shutter' pixel is connected to a local memory cell that allows simultaneous intermediate signal storage of all individual pixels in order to enable high framerate (slow-motion) video operation without spatio-temporal distortions due to a sequential read-out sequence. For such fast signal management, a three-layer scheme has been developed fusing three wafers for the photodiodes, the dynamic random access memory (DRAM) and the logic layer for the image signal processing (Fig. 22.51) [1868].

A special CMOS image sensor has built-in grating structures to allow detection of the linear polarization state [1869]. As depicted in Fig. 22.52, each pixel is subdivided in four with gratings in 0°, 90°, and ±45° directions between the on-chip lenses and the photodiodes to create sensitivity to the linear polarization state of the incoming light.

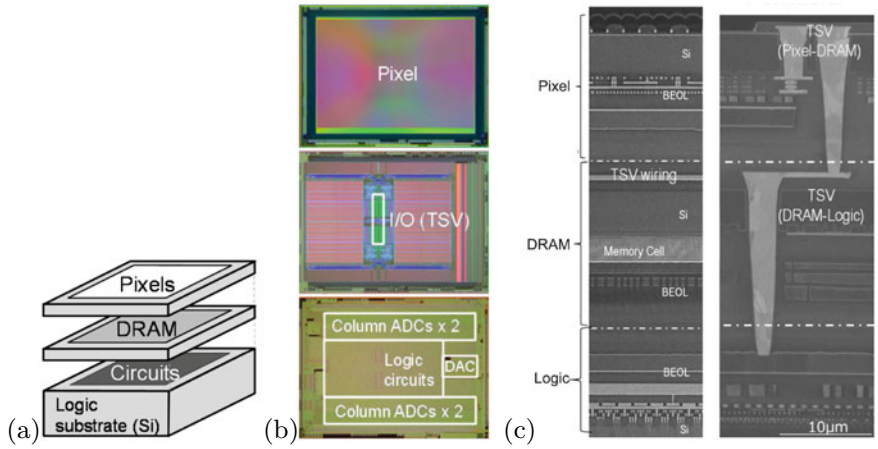

Fig. 22.51 **a** Scheme of stacking three wafers for global shutter CMOS image sensor. **b** Plane-view of the three chips, back-illuminated photodiodes, DRAM (30 nm process), and Logic (40 nm process). **c** Cross-section SEM image of the structure at position of pixel (left) and periphery (right). Adapted from [1868]

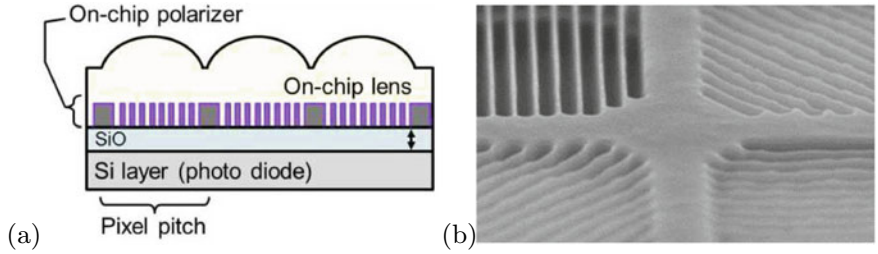

Fig. 22.52 **a** Scheme of polarization sensitive CMOS image sensor and **b** SEM image of grating pattern in SONY Polarsens™sensor. Adapted from [1869]

22.4 Solar Cells

Solar cells are light detectors, mostly photodiodes, that are optimized for the (large-area) conversion of solar radiation (light) into electrical energy. A 1993 review of the historic development of photovoltaics is given in [1870]. The latest data on solar cell efficiencies are compiled in the Solar Cell Efficiency Tables [1871].

22.4.1 Solar Radiation

The sun has three major zones, the core with a temperature of 1.56×10^7 K and a density of 100 g/cm^3 in which 40% of the mass is concentrated and 90% of the energy is generated, the convective zone with a temperature of 1.3×10^5 K and a density of 0.07 g/cm^3, and the photosphere with a temperature of 5800 K and low density ($\sim 10^{-8}$ g/cm^3). The radius is 6.96×10^8 m and is about 100 times larger than that of the earth (6.38×10^6 m). The distance sun–earth is 1.496×10^{11} m. The angle under which the sun disk appears on earth is 0.54°. An energy density of 1367 ± 7 W/m^2 arrives at the earth in front of its atmosphere.

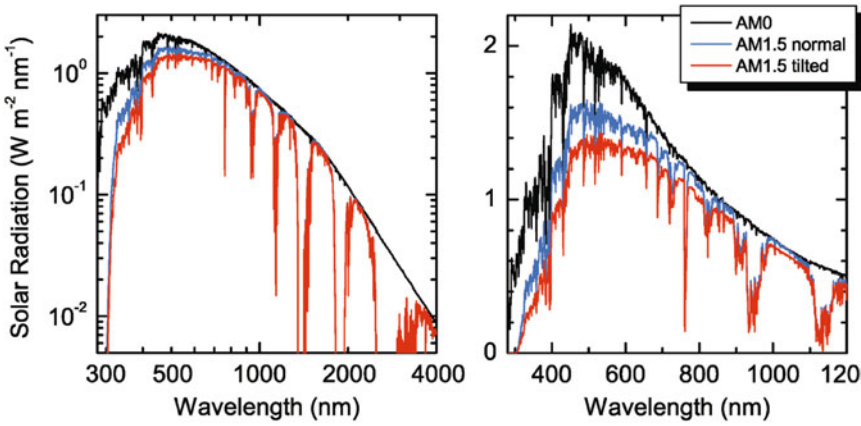

Fig. 22.53 Solar spectra (power per area and wavelength interval) for AM0 (*black line*, extraterrestrial irradiance) and AM1.5 (sun at 41.8° elevation above horizon) for direct normal irradiance (*blue line*) and global total irradiance (*red line*) on a sun facing surface (tilted 37° towards the equator). Left (right) graph in log-log (linear) scales

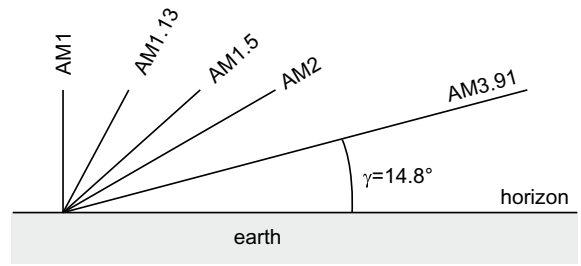

Fig. 22.54 Schematic path of sunlight through the atmosphere and definition of the air mass AMx

This value and the according spectrum of the sun's emission, which is similar to a blackbody with temperature 5800 K (Fig. 22.53), is termed air mass zero (AM0). The total energy that reaches the earth from the sun is 1.8×10^{17} W per year. This value is 10^4 times the world's primary energy need.

Air mass zero (AM0) is important for solar cells in satellites. When the solar spectrum passes the earth's atmosphere, it is changed with regard to its shape and the total energy density due to gas absorption (ozone, water, CO_2, ...). Depending on the meridian of the sun γ (Fig. 22.54), the spectrum on the surface of the earth is termed AMx with $x = 1/\sin\gamma$. In spring and fall (March 21st and September 21st), Leipzig (51°42′N latitude) has about AM1.61. At the summer (June 21st) and winter (December 21st) solstices the air mass in Leipzig is AM1.13 ($\gamma = 61.8°$) and AM3.91 ($\gamma = 14.8°$), respectively. Additionally, the duration of sunshine and thus the light power density is regionally different across the earth due to climate and weather (Fig. 22.55). For AM1.5, the incident power density is 844 W/m^2.

The global radiation reaching a photovoltaic cell has three components: (i) the direct radiation, (ii) diffuse radiation and (iii) reflected radiation. The relative amounts and their spectra depend on details such as the climate (e.g. humidity) or the environment (e.g. outdoors vs. urban).

22.4.2 Ideal Solar Cells

When a solar cell made from a semiconductor with a band gap E_g is irradiated by the sun, only photons with $h\nu > E_g$ contribute to the photocurrent and the output power. The I–V characteristic under

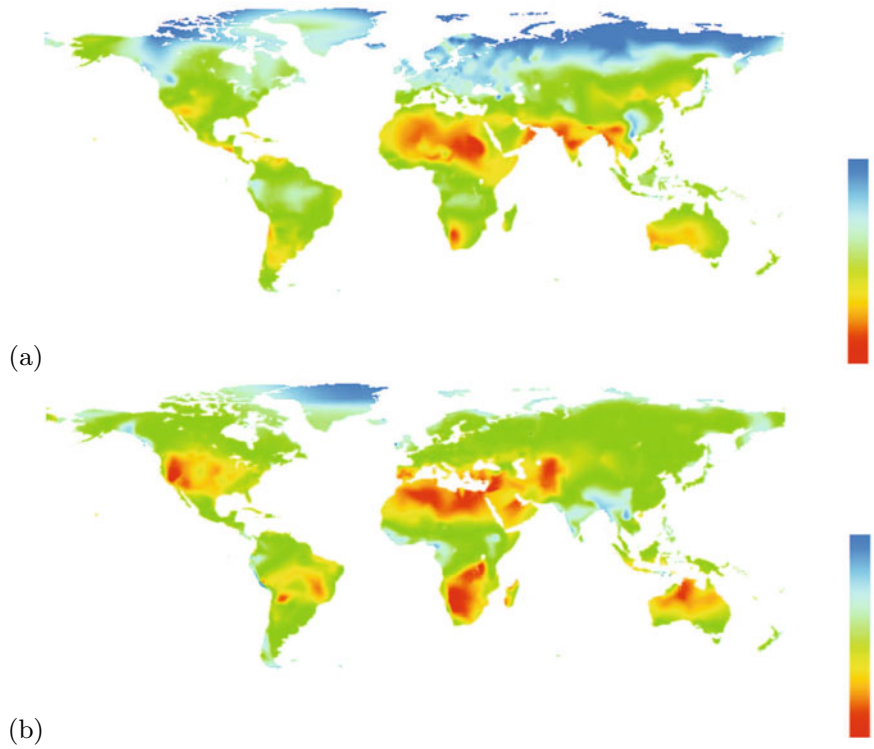

Fig. 22.55 Global sunshine distribution in **a** January and **b** July. The sunshine fraction is the actual number of bright sunshine hours over the potential number, and is thus expressed as a percentage figure. The color scale reaches from 0 to 100%. The sunshine data are in a 0.5 degree grid based on data from [1872]

illumination (Fig. 22.56) is given by

$$I = I_s \left[\exp(\beta V) - 1\right] - I_L \,, \tag{22.60}$$

with I_L being the current due to generation of excess carriers by the absorption of the sunlight. Assuming a simple n^+p-diode solar cell model, the current consists of two components: the depletion layer current j_{DL} from carriers absorbed in the depletion layer (field region) and the diffusion current j_D from absorption in the neutral region ($j = I/A$).

For the drift current out of the depletion layer of width w it can be assumed that it is collected fast and recombination plays no role. Thus (cmp. (22.31))

$$j_{DL}(\lambda) = e\, n_{ph}(\lambda)\,[1 - R(\lambda)]\,[1 - \exp(-\alpha(\lambda)\, w)] \,, \tag{22.61}$$

where λ is the wavelength of the incident radiation, R the reflectance of the surface, α the absorption coefficient and $n_{ph}(\lambda)$ the photon flux (number of photons per area and time) at the given wavelength. For a solar spectrum, an integral needs to be performed over the spectral distribution:

$$j_{DL} = \int j_{DL}(\lambda)\, \mathrm{d}\lambda \,, \tag{22.62}$$

the total photon flux being $n_{ph} = \int n_{ph}(\lambda)\, \mathrm{d}\lambda$.

The diffusion current collected at the back contact is obtained from solving (10.73) (now for electrons in p-type material) with the appropriate boundary conditions (reversely bias depletion layer, $n_p(w) = 0$, $\Delta n_p(\infty) = n_p(\infty) - n_{p_0} = 0$ [1873]):

$$j_D(\lambda) = e\, n_{ph}(\lambda)\,[1 - R(\lambda)]\,\frac{\alpha\, L_n}{1 + \alpha\, L_n}\,\exp(-\alpha\, w) + e\, n_0\,\frac{D_n}{L_n}\,, \tag{22.63}$$

Dropping the wavelength dependence and neglecting the dark term, the usual formula is obtained,

$$j_L = e\, n_{ph}\,(1 - R)\left[1 - \frac{\exp(-\alpha\, w)}{1 + \alpha\, L_n}\right]\,, \tag{22.64}$$

The last bracket represents the quantum efficiency [1874]. The model can be extended for taking into account a non-zero surface recombination velocity at the back contact at finite distance [1875].

Here a voltage *independent* photo-generated current I_L is assumed. If the diffusion length is small compared to the transport path, the carrier collection efficiency η_c becomes voltage dependent [1874]. The reduction of the diffusion potential for forward voltage decreases the carrier collection efficiency [1876], possibly to zero close to the built-in voltage.

The saturation current density is given by (21.132) and (21.133)

$$j_s = \frac{I_s}{A} = e\, N_C\, N_V \left(\frac{1}{N_A}\sqrt{\frac{D_n}{\tau_n}} + \frac{1}{N_D}\sqrt{\frac{D_p}{\tau_p}}\right)\exp\left(-\frac{E_g}{kT}\right)\,, \tag{22.65}$$

with A being the cell area.

The voltage at $I = 0$ is termed the *open-circuit* voltage V_{oc}, the current at $V = 0$ is termed the *short-circuit* current $I_{sc} = I_L$ (Fig. 22.56). Only a part of the rectangle $I_{sc} \times V_{oc}$ can be used for power conversion. By choice of the load resistance R_L, the work point is set. At I_m and V_m, the generated power $P_m = I_m V_m$ is maximal. The filling factor F is defined as the ratio

$$F = \frac{I_m\, V_m}{I_{sc}\, V_{oc}}\,. \tag{22.66}$$

The open-circuit voltage is given by

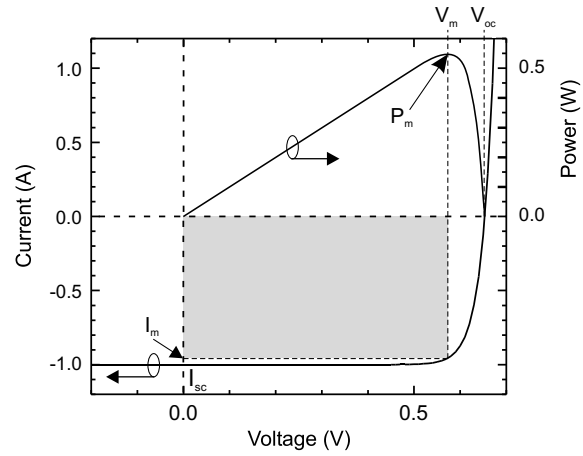

Fig. 22.56 Schematic I–V characteristics of a solar cell under illumination (*left scale*) and extracted power (*right scale*). The *grey area* is the maximum power rectangle with $P_m = I_m V_m$

$$V_{oc} = \frac{1}{\beta} \ln\left(\frac{I_L}{I_s} + 1\right) \cong \frac{1}{\beta} \ln\left(\frac{I_L}{I_s}\right) \tag{22.67}$$

and increases with increasing light power and decreasing dark current. The output power is

$$P = I\,V = I_s\,V\ (\exp(\beta V) - 1) - I_L\,V\ . \tag{22.68}$$

The condition $\mathrm{d}P/\mathrm{d}V = 0$ yields the optimal voltage at which the solar cell has to be operated and is given by the implicit equation

$$V_m = \frac{1}{\beta} \ln\left(\frac{I_L/I_s + 1}{1 + \beta V_m}\right) = V_{oc} - \frac{1}{\beta} \ln(1 + \beta V_m)\ . \tag{22.69}$$

The current at maximum power is

$$I_m = I_L \left(1 - \frac{1 - \beta V_m\, I_s/I_L}{1 + \beta V_m}\right) \cong I_L \left(1 - \frac{1}{\beta V_m}\right)\ . \tag{22.70}$$

E_m is the energy that is delivered per photon at the load resistor at the power maximum. The maximum power is $P_m = I_L E_m/e$ and E_m is given by

$$E_m \cong e \left[V_{oc} - \frac{1}{\beta} \ln(1 + \beta V_m) - \frac{1}{\beta}\right]\ . \tag{22.71}$$

The ideal solar cell has a (power) conversion efficiency $\eta = P_m/P_{in}$ that can be determined from Fig. 22.57a.

The right curve (1) in Fig. 22.57a shows the integral number n_{ph} of photons in the solar spectrum (per area and time) with an energy larger than a given one (E_g). For a given value of n_{ph}, the left curve

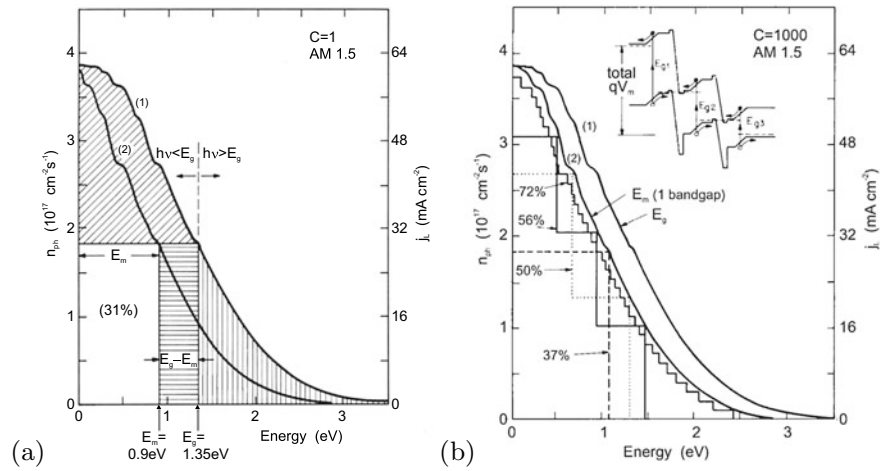

Fig. 22.57 **a** Number of photons n_{ph} per area and time in the sun spectrum (AM1.5, $C = 1$ sun) with an energy larger than a cutoff energy (*curve* 1) and graphical method to determine the quantum efficiency (from *curve* 2). Adapted from [1877]. **b** Number of photons in concentrated solar spectrum (AM1.5, $C = 1000$ sun) with an energy larger than a given energy and graphical method to determine the quantum efficiency of multi-junction solar cells. Adapted from [574] after [1877]

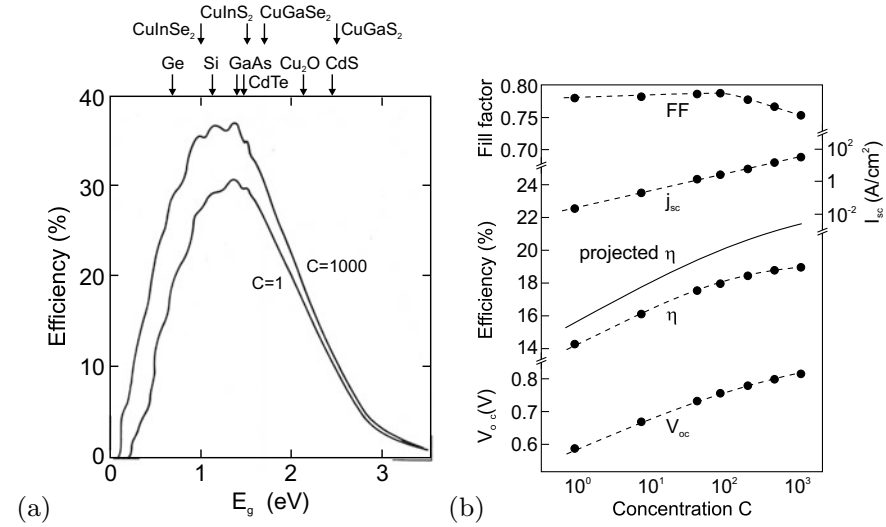

Fig. 22.58 **a** Ideal quantum efficiency of solar cells (single junction) as a function of band gap and light concentration C. The band gaps of some important semiconductors are denoted by *arrows*. Adapted from [1877]. **b** Properties of a silicon solar cell (water cooled) as a function of light concentration. *Solid line* is theoretically projected efficiency, *dashed lines* are guides to the eye. Adapted from [574]

(2) represents the value of E_m. The efficiency is the ratio of $E_m n_{ph}$ and the area under curve (1). The efficiency as a function of the band gap is shown in Fig. 22.58a. It has a fairly broad maximum such that many semiconductors can be used for solar cells, in principle. The maximum theoretical efficiency for a single junction is 31% for nonconcentrated sunlight (AM1.5). This limit corresponds to the classic Shockley-Queisser limit [1878–1880], assuming radiative recombination as the only charge-carrier recombination mechanism. In [1881], the limit for a single material is found to be 43% for an optimally tailored band structure that allows carrier multiplication by optically excited hot carriers. The solar cell as a heat engine is dicussed in [1882].

When the sunlight is concentrated, e.g. by a lens, the efficiency increases (Fig. 22.58b). The short-circuit current increases linearly. The effect is mostly due to the increase of the open-circuit voltage. For $C = 1000$, the maximum theoretical efficiency for a single-junction solar cell is 38%.

A further increase of efficiency can be achieved with multiple junctions using various materials for absorption. In a tandem cell (two junctions), the upper layer absorbs the higher-energy photons in a wide band gap material. The material with the lower band gap makes use of the low-energy photons. Thus, the cell works with two different values of E_m (Fig. 22.57b). With band gaps of 1.56 eV and 0.84 eV, an efficiency of 50% can be reached theoretically. With three materials 56%, and for a large number of materials 72% is the limit. Between the junctions, tunneling diodes (Sect. 21.5.9) must be used to allow carrier transport through the entire structure. It is a nontrivial task to fabricate multiple heterojunctions due to incompatibilities of the lattice constants. Besides heteroepitaxy, wafer bonding can also be used for fabrication. A lattice-matched InGaP/GaAs/InGaAsN cell seems a viable solution for high-efficiency solar cells.

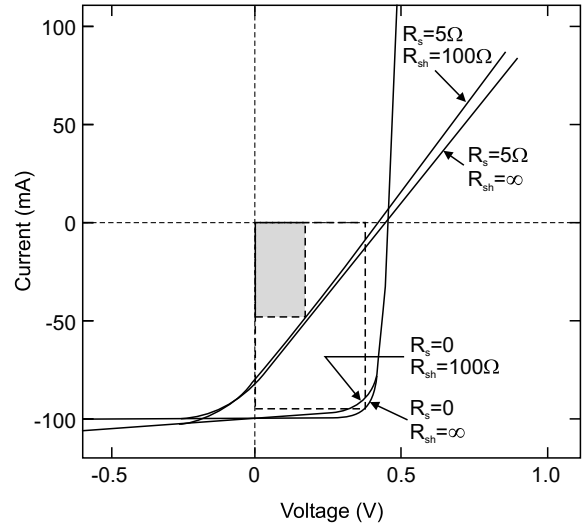

Fig. 22.59 I–V characteristics of a solar cell considering shunt and series resistances R_s and R_sh, respectively. The efficiency of the real cell (*shaded* power rectangle) is less than 30% of that of the ideal cell. Adapted from [1883]

22.4.3 Real Solar Cells

For a real solar cell, the effect of parallel resistance R_sh (shunt resistance due to leakage current, e.g. by local shorts of the solar cell) and serial resistance R_s (due to ohmic loss) must be considered. The I–V characteristic is then (cf. (21.158))

$$\ln\left(\frac{I+I_\mathrm{L}}{I_\mathrm{s}}-\frac{V-I\,R_\mathrm{s}}{I_\mathrm{s}\,R_\mathrm{sh}}+1\right)=\beta\ (V-I\,R_\mathrm{s})\ . \tag{22.72}$$

The serial resistance affects the efficiency more strongly than the shunt resistance (Fig. 22.59). Therefore, it is frequently enough to consider R_s only and use (cf. (21.157))

$$I=I_\mathrm{s}\,\exp\left(\beta(V-I\,R_\mathrm{s})\right)-I_\mathrm{L}\ . \tag{22.73}$$

In the example of Fig. 22.59, a serial resistance of 5 Ω reduces the filling factor by a factor of about four.

At open circuit voltage the photo-generated carriers have nowhere to go; in an ideal solar cell, the only process is the radiative recombination and the photon escape. Certainly, the internal quantum efficiency should be high and the non-radiative recombination rate small compared to the radiative one (cf. Sect. 10.10). The open circuit voltage and thus the energy conversion efficiency depends also on the light extraction efficiency χ_ex which will be discussed in greater detail in the context of LEDs (Sect. 23.3.3). Based on [1884, 1885], the open circuit voltage V'_oc of a real solar cell is *reduced* ($\chi_\mathrm{ex}\le 1$) from the ideal value V_oc given in (22.67),

$$V'_\mathrm{oc}=V_\mathrm{oc}+\beta^{-1}\ \ln\chi_\mathrm{ex}\ . \tag{22.74}$$

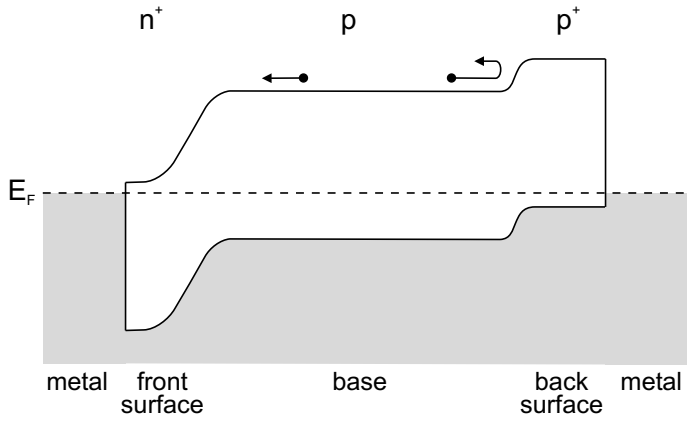

Fig. 22.60 Increase of the carrier collection efficiency by a back surface field. Adapted from [1886]

22.4.4 Design Refinements

In order to collect electrons most efficiently, a back surface field is used (Fig. 22.60). A higher-doped region at the back contact creates a potential barrier and reflects electrons back to the front contact.

An important point for optimization is the management of the reflection at the solar cell surface. First, a dielectric antireflection (AR) layer (or multi-layers) can be used. These layers should have a broad AR spectrum. Additionally, a textured surface reduces reflection (Fig. 22.61d), giving reflected photons a second chance for penetration (Fig. 22.61c). The reflectance of bare Si, 35%, can be reduced to 2%. An AM0 efficiency of over 15% was reached using textured multi-crystalline cells. Alkaline KOH-based etches attack Si (001) anisotropically and yield pyramidal structures (Fig. 22.61b) with {111} facets. Recently an acidic HF/HNO_3-based process has been established [1887], resulting in a worm-like surface pattern on multi-crystalline silicon wafers (Fig. 22.61a) with superior anti-reflection properties.

During its course over the sky during the day, the sun changes its angle towards a fixed solar cell.[10] A tracking mechanism can optimize the angle of incidence during the day and increase the overall efficiency of the solar cell (Fig. 22.62).

22.4.5 Modules

In order to cover a large area and supply certain values of output voltage and current, several solar cells are connected into modules. Arrays are built up from several modules (Fig. 22.63). If solar cells are connected in parallel, the total current increases; if they are connected in series, the output voltage increases. We note that in partially shadowed modules the reverse characteristics of solar cells are important [1892, 1893]; local breakdown can lead to hot spots and irreversible degradation.

[10] We are of course aware that the earth rather rotates around the sun.

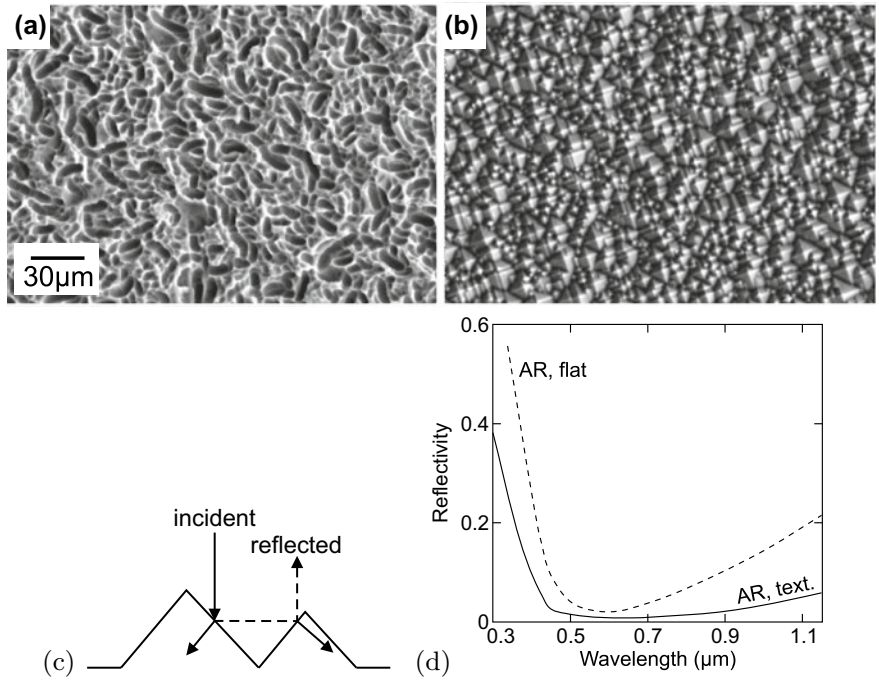

Fig. 22.61 **a** SEM image of topology of acidically etched multi-crystalline silicon wafer. **b** SEM image of alkaline etched mono-crystalline silicon wafer. **c** Exemplary light path. **d** Reflectance of antireflection-coated flat (*dashed line*) and textured (*solid line*) surface). Parts **a** and **b** adapted from [1888], part **d** adapted from [1889]

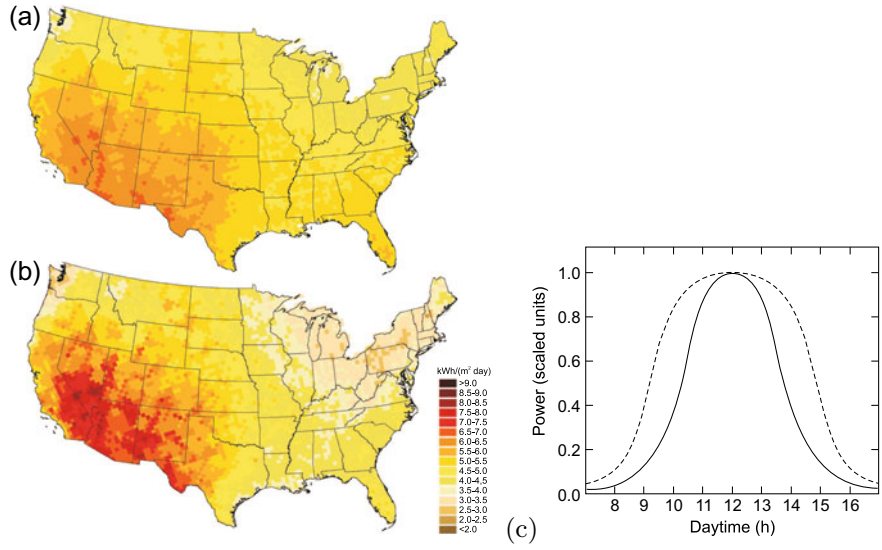

Fig. 22.62 Annual average solar energy (in kWh/(m^2 day)) for **a** an optimally tilted south-facing fixed panel and **b** an optimally two-axis tracked panel (in mainland US). Adapted from [1890]. **c** Power generation of a solar cell vs. time (in daytime hours) for a stationary setup facing the sun at constant angle (*solid line*) and mounting with tracking (*dashed line*) to optimize the angle towards the sun. Adapted from [1891]

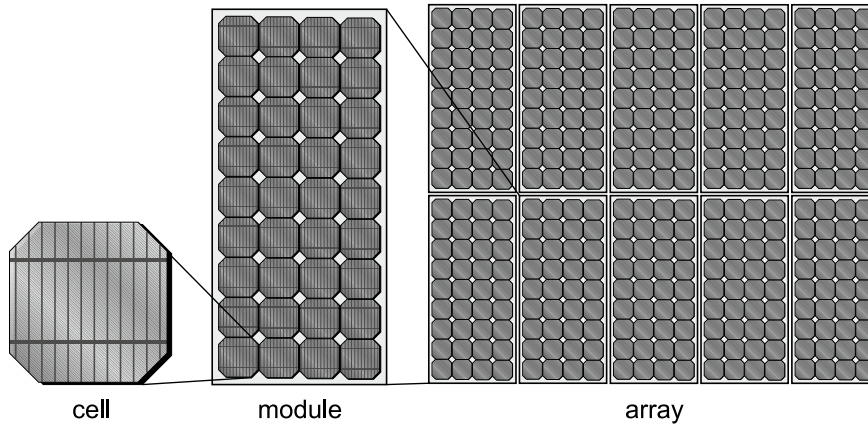

Fig. 22.63 Schematic drawing of a solar cell (with contact grid), a module (36 cells) and an array of ten modules

22.4.6 Solar-Cell Types

First Generation Photovoltaics

Silicon is the most frequently used material for solar cells. Cells based on single-crystalline silicon (wafers) have the highest efficiency but are the most expensive (Fig. 22.65a). The state-of-the-art industrial crystalline silicon solar cells technology and achievements (in 2014) has been reported in [1894]. The efficiencies of various solar cells are compiled in Table 22.1. Polycrystalline (for large grains also called multi-crystalline) silicon (Fig. 22.65b) is cheaper but offers less performance. Material design is oriented towards increasing the grain size and/or reducing their electrical activity. Grain boundaries act as recombination centers with a surface (i.e. interface) recombination velocity of 10^2 cm/s [1895] for particular, electrically fairly inactive grain boundaries, several 10^3 cm/s [1896], several 10^4 cm/s [1897] or even 10^5–10^7 cm/s [1898]. The grain boundaries reduce the effective diffusion length and thus carriers recombine before they can reach the contacts. A detailed theory of solar cell performance for polycrystalline material has been worked out in [1897] and explains the reduction of efficiency with decreasing grain size as shown in Fig. 22.64.

These solar cells are also called 'first-generation' photovoltaics. Thin sheets of crystalline silicon drawn from a melt between two seed crystals in a modified CZ growth (sheet silicon or ribbon silicon) allow cheaper production compared to cells based on 'traditional' polished wafers cut from a large silicon rod. Silicon made particularly for solar cell use is called 'solar-grade' silicon.

Second Generation Photovoltaics

Even cheaper are solar cells from amorphous silicon (Fig. 22.65c). Since silicon is an indirect semiconductor, a fairly thick layer is needed for light absorption. If direct band gap semiconductors are used, a thin layer ($d \approx 1$ μ m) is sufficient for complete light absorption. Such cells are called thin-film solar cells [1901]. A typical material class used in this type of cell are chalcopyrites, such as $CuInSe_2$ (CIS). The band gap is around 1 eV, which is not optimal. An improvement can be achieved by adding Ga and/or S which increases the band gap, $Cu(In,Ga)(Se,S)_2$ (CIGS), to 1.2–1.6 eV. Using CIGS, an efficiency of over 19% has been reported in laboratory samples; 12–13% seeming realistic for production

Table 22.1 Record efficiency of various solar cells (AM1.5, 1000 W/cm^2, 25° unless noted otherwise). Most data from [1871], additional data for 3J (conc.) [1899, 1900]. Date is that of (mostly certified) measurement

Cell material/type	Efficiency (%)	V_{oc} (V)	j_{sc} (mA/cm^2)	FF (%)	date m/y
Si (crystalline)	26.7 ± 0.5	0.738	42.65	84.9	3/2017
Si (multicrystalline)	22.3 ± 0.4	0.6742	41.08	80.5	8/2017
Si (amorphous)	10.2 ± 0.3	0.896	16.36	69.8	7/2014
GaAs (crystalline)	25.9 ± 0.8	1.038	29.4	84.7	12/2007
GaAs (thin film)	29.1 ± 0.6	1.1272	29.78	86.7	10/2018
GaAs (multicrystalline)	18.4 ± 0.5	0.994	23.2	79.7	11/1995
CIGS	22.9 ± 0.5	0.744	38.77	79.5	11/2017
CdTe	21.0 ± 0.4	0.8759	30.25	79.4	8/2014
perosvkite	20.9 ± 0.7	1.125	24.92	74.5	7/2017
dye sensitized	11.9 ± 0.4	0.744	22.47	71.2	9/2012
organic (thin film)	11.2 ± 0.3	0.780	19.3	74.2	10/2015
2J (GaInP/GaAs)	32.8 ± 1.4	2.568	14.56	87.7	9/2017
3J (GaInP/GaAs/Ge)	32.0 ± 1.5	2.622	14.4	85.0	1/2003
3J (GaInP/GaAs/InGaAs)	37.9 ± 1.2	3.065	14.27	86.7	2/2013
5J (bonded)	38.8 ± 1.2	4.767	9.564	85.2	7/2013
2J (conc., 38 suns)	35.5 ± 1.2				10/2017
3J (conc., 240 suns)	40.7 ± 2.4	2.911	3832	87.5	9/2006
3J (conc., 306 suns)	43.5				5/2012
4J (conc., 508 suns)	46.0 ± 2.2	4.227	6498	85.1	10/2014

[1902]. Also CdTe is a viable absorber mostly sputtered on glass with over 16% efficiency demonstrated and 9–10% realistic in production. Thin-film solar cells can be fabricated on glass substrate or on flexible polymer substrate such as Kapton[11] (Fig. 22.66a, b). Also here, optimization of the grain size is important (Fig. 22.66b). As the front contact, a transparent conductive oxide (TCO), such as ITO ($InSnO_2$) or ZnO:Al, is used. If the front surface is given by the glass substrate, as can be the case for CdTe/glass solar cells, the glass is actually termed 'superstrate'. Thin-film and amorphous silicon

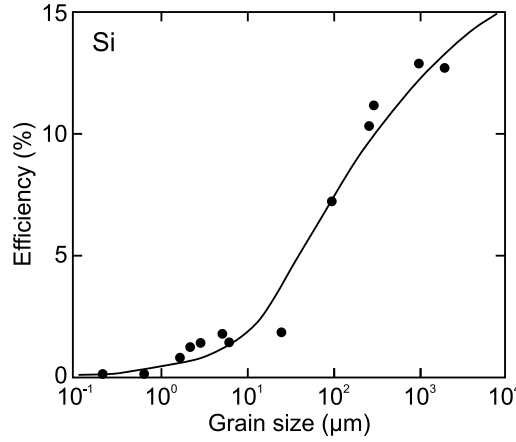

Fig. 22.64 Theoretical dependence of the effect of grain size on efficiency of polycrystalline solar cells (*solid line*) with experimental data points (*circles*). Adapted from [1897]

[11] Kapton® is a polyimide and a product and registered trademark of DuPont.

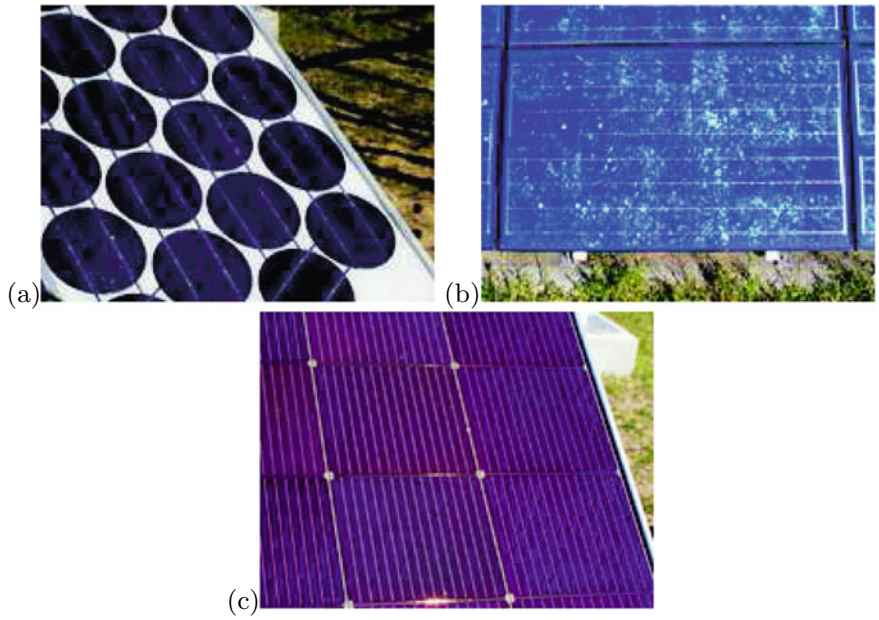

Fig. 22.65 Various types of solar cells: **a** monocrystalline silicon solar cell, **b** polycrystalline solar cell, **c** amorphous silicon solar cell. From [1891]

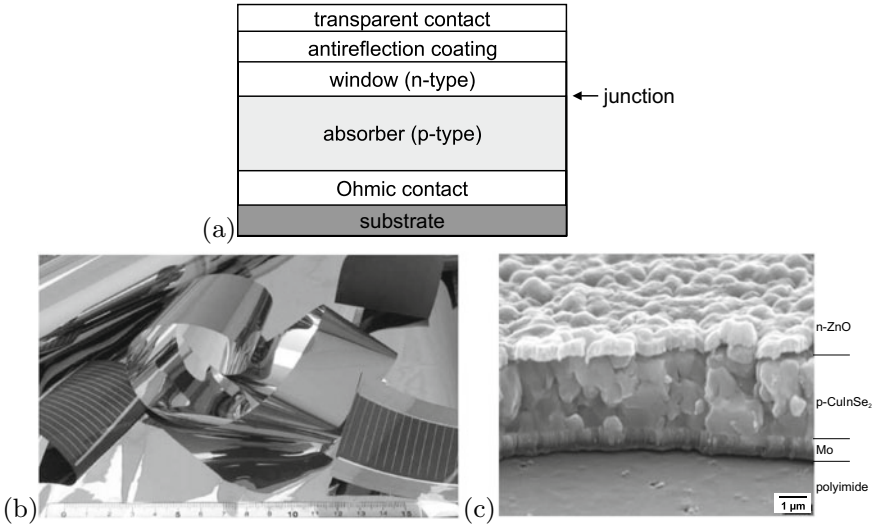

Fig. 22.66 **a** Schematic cross section of a polycrystalline thin-film solar cell. **b** Rolled sheets of CIS thin film solar cell on flexible Kapton foil. **c** SEM cross section of CIS thin-film solar cell. Parts **b** and **c** reprinted with permission from [1906]

solar cells are also termed 'second-generation' photovoltaics. Also organic materials can be used for solar cells [1903], promising low-cost production at acceptable performance, in 2004 2.5% [1904] and in 2006 about 4% maximum efficiency [1905].

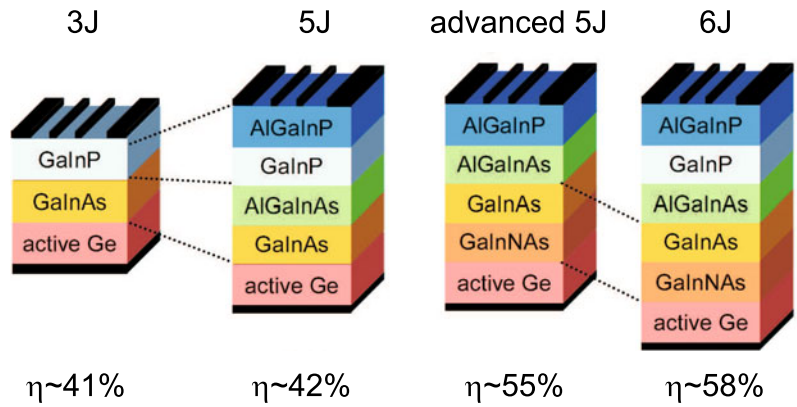

Fig. 22.67 Schematic layer stacking of multi-junction solar cells and expected efficiency. Adapted from [1914]

Third Generation Photovoltaics

'Third-generation' photovoltaics attempt to go beyond the 30% limit and comprise of multi-junction solar cells, concentration of sunlight, use of hot-carrier excess energy as discussed above and possibly other concepts including photon conversion [1907, 1908], intermediate band absorption [1909–1911], multi-exciton generation [1912] or the use of quantum dots [1913].

In multi-junction cells the different absorber layers are stacked on the substrate with increasing band gap and connected via (highly doped) tunneling junctions (Sect. 21.5.9). Under 500-fold AM1.5 illumination a three junction (3J) cell (GaInP/GaInAs/Ge) is expected to exhibit up to 41% efficiency, for 5J 42% or up to 55% using GaInNAs and with 6J up to 59% [1914, 1915] (Fig. 22.67). For a 3J cell the record efficienvy is 40.7% (240 suns) using the layer structure as shown in Fig. 22.68 [1899]. Details on modeling of III–V multi-junction solar cells can be found in [1916]. In a monolithic cell the absorbers must be tuned such that the same current (Kirchhoff's law) can pass through all layers. Multi-junction solar cells are heteroepitaxial devices and thus expensive; the use of concentration is economically mandatory.

A recent novel route is a tandem cell comprising of a bottom silicon cell and a top perovskite cell. Organo-metal halide peroskites, e.g. of the ammonium trihalogen plumbates type, R-N_3PbI_3, have exhibited quite high conversion efficiencies [1919, 1920] and can be tuned with regard to their absorption range.

Another concept targeting increased efficiency ands better use of otherwise wasted photons is the 'intermediate band' solar cell. Here, levels within the band gap of the host, e.g. created by a high doping with suitable elements or quantum dot levels, shall help absorb below band gap photons and pump them into the conduction band of the host. A review on this concept and experimental, results can be found in [1921].

22.4.7 Economic Issues

The cost[12] of producing photovoltaic (PV) modules, in constant dollars, has fallen from as much as $50 per peak watt in 1980 to as little as 3$/Wp in 2004. The cost of about 0.2 $/Wp in 2020, a third of the cost in 2012, is realistic and competitive in many applications (Fig. 22.69). The price of solar power followed for a while Swanson's law [1925], i.e. a reduction in price by 22% for a doubling of

[12] Some of the following information is based on [1922–1924].

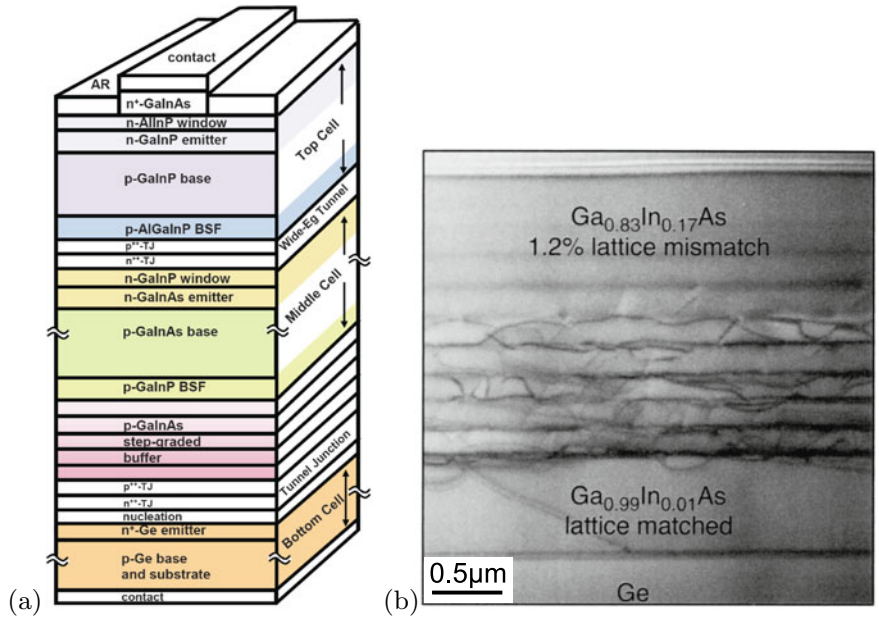

Fig. 22.68 **a** Schematic layer stacking of three-junction (3J) solar cell. The step-graded buffer (metamorphic buffer) changes the in-plane lattice constant for the following layers. Adapted from [1917]. **b** Cross-section TEM image of metamorphic InGaAs buffer on Ge. Adapted from [1918]

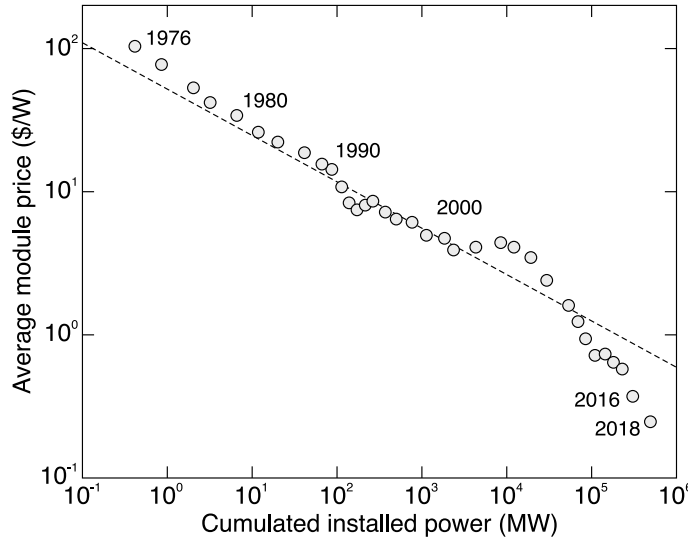

Fig. 22.69 Photovoltaic module price (US$/W) (adjusted to 2002 dollars) vs. the cumulated production. The *dashed line* represents Swanson's law. Most data from [1924]; data for 2016 and 2018 added from various sources

the installed (cumulated) solar power (dashed line in Fig. 22.69). After 2005, a rise in silicon cost has lead to a deviation for a few years, but recently the trend has shown even faster cost reductions.

The energy payback period is also dropping rapidly. For example, it took 2010 typical crystalline silicon module about 4 years to generate more energy than went into making the module in the first place. The next generation of silicon modules, employing a different grade of silicon and use thinner layers of semiconductor material, had 2011 an energy payback of about 2 years [1926]; energy payback time of course also depends on solar irradiation and it reduces from about 2 years in northern Europe

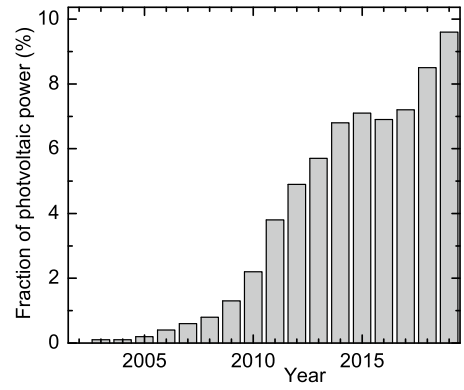

Fig. 22.70 Fraction of photovoltaic power of the total energy from power plants in the public grid in Germany. Data from [1927]

to 1.5 y or less in southern Europe [1927]. Thin-film modules bring the payback down to one year or less [1926, 1927]. However, market growth of thin-film modules is currently not faster than the total marker. This means that these modules will produce 'free' and clean energy for the remaining 29 years of their expected life.

PV technology can meet electricity demand on any scale. The solar energy resource in a 100 mile-square area of Nevada could supply the United States with all its electricity (about 800 GW), using modestly efficient (10%) commercial PV modules. A more realistic scenario involves distributing these same PV systems throughout the 50 states. Currently available sites, such as vacant land, parking lots, and rooftops, could be used. The land requirement to produce 800 GW would average out to be about 17×17 miles per state. Alternatively, PV systems built in the 'brownfields', the estimated 5 million acres of abandoned industrial sites in the US, could supply 90% of America's current electricity. Solar power is expected to contribute 10% of the US energy need in 2030. For Germany, more than 2% in 2020 was predicted (in 2004) to be probable. In the first half of 2019, photovoltaics actually contributed a total of 9.5% (25.05 TWh); the historic increase is depicted in Fig.22.70. In June 2019, solar power represented the largest fraction of all anergy carriers with 19.1% (7.17 TWh) in Germany [1927]. The maximum harvested solar power was 33.4 GW (52.4%) on June 29, 2019.

In 2001, PV module shipments in the US approached the 400 MW mark, representing a $2.5 to $3 billion market. The US-based industry itself is now approaching $1 billion per year and provides 25 000 jobs. It is expected to grow to the $10–$15 billion level in the next 20 years, providing 300 000 jobs by 2025. The actual number of jobs in 2018 was 242,000. The newly installed power in 2016 was almost 15 GW for a total of just above 40 GW. In 2017, a total of 50 GW were installed. In 2018, solar power provided 1.66% of total US electricity.

Chapter 23
Electricity-to-Light Conversion

Abstract Light emitting diodes (LEDs) and laser diodes are the focus of this chapter. For LEDs materials choices, the concepts of internal and external quantum efficiency as well as device design are treated. Special devices such as white LEDs, quantum dot and organic LEDs are introduced. For laser diodes the concepts of gain, loss and threshold, various heterostructures for modern device design and laser emission properties such as mode spectrum, far field, dynamics and tunability are discussed. Finally special devices such as the hot hole laser, the cascade laser and semiconductor optical amplifiers are mentioned.

23.1 Radiometric and Photometric Quantities

23.1.1 Radiometric Quantities

The radiometric quantities are derived from the radiant flux (power) Φ_e (or usually simply Φ) that is the total power (energy per time) emitted by a source, measured in Watts. The radiant intensity I_e is the radiant flux emitted by a point source into a solid angle,[1] measured in Watts per steradian (or W/sr). The irradiance E_e is the radiant flux per area incident on a given plane, measured in W/m^2. The radiance L_e is the radiant flux per area and solid angle as, e.g., emitted by an extended source, measured in W/(m^2 sr).

23.1.2 Photometric Quantities

The photometric quantities are related to the visual impression and are derived from the radiometric quantities by weighting them with the $V(\lambda)$ curve.

The luminous flux (luminosity or visible brightness) Φ_v of a source with the radiant flux (spectral power distribution) $\Phi(\lambda)$ is given by

[1] A solid angle Ω is the ratio of the spherical surface area A and the square of the sphere's radius r, i.e. $\Omega = A/r^2$.

M. Grundmann, *The Physics of Semiconductors*, Graduate Texts in Physics,
https://doi.org/10.1007/978-3-030-51569-0_23

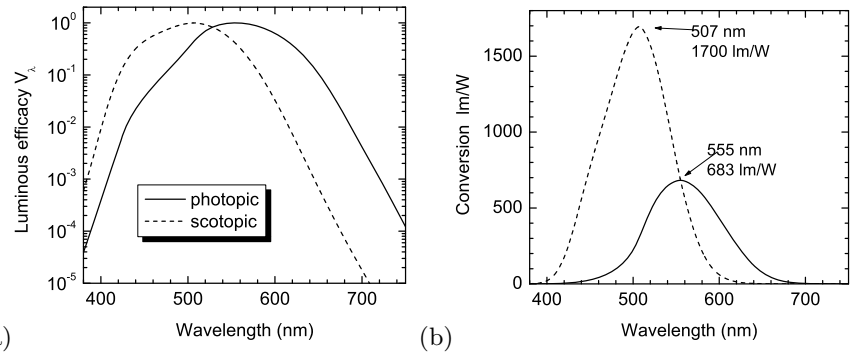

Fig. 23.1 **a** Relative eye sensitivity curves for photopic (light adapted, *solid line*) and (dark adapted, *dashed line*) vision. **b** Conversion of lumen to Watt for light- and dark-adapted vision

Table 23.1 Radiometric and photometric quantities and units. The photometric units are lumen (lm), lux (lx = lm/m^2) and candela (cd = lm/sr)

Radiometric			Photometric		
Quantity	Symbol	Unit	Quantity	Symbol	Unit
Radiant flux	Φ_e	W	Luminous flux	Φ_v	lm
Radiant intensity	I_e	W/sr	Luminous intensity	I_v	cd
Irradiance	E_e	W/m^2	Illuminance	E_v	lx
Radiance	L_e	W/m^2/sr	Luminance	L_v	lm/m^2/sr

$$\Phi_v = K_m \int_0^\infty \Phi(\lambda)\, V(\lambda)\, d\lambda \,, \tag{23.1}$$

with $K_m = 683\,\text{lm/W}$. This formula is also the definition of the unit 'lumen'. In Fig. 23.1b, the conversion function[2] $V(\lambda)$ is shown for light and dark adapted vision.[3]

Further derived photometric quantities are luminous intensity (luminous flux per solid angle), measured in candela (cd), the illuminance (luminous flux per area), measured in lux (lx), and the luminance (luminous flux per area and solid angle). The latter is particularly important if the radiation enters an optical system, e.g. for refocusing. The radiometric and photometric quantities are summarized in Table 23.1.

[2]The $V(\lambda)$ curve has been experimentally determined by letting several observers adjust (decrease) the perceived brightness of a monochromatic light source at 555 nm to that of light sources of the same absolute radiation power at other wavelengths with so-called heterochromatic flicker photometry. The 'relative sensitivity curve for the CIE Standard Observer' was determined in 1924. The 'standard observer' is neither a real observer nor an average human observer. The curve has shortcomings, e.g., due to the used spectral band width (20–30 nm) of the light sources and the comparison of spectral power instead of the photon flux.

[3]While photopic vision is due to cones, the scotopic (dark-adapted) vision is due to rods. Rods are more than one thousand times as sensitive as the cones and can reportedly be triggered by individual photons under optimal conditions. Rods predominate in the peripheral vision and are not color sensitive.

23.2 Scintillators

A scintillator (or phosphor) is a material that converts impacting high-energy radiation into photons [1928]. Besides a high conversion efficiency, the spectrum and decay time constant of the scintillator are important for display applications. For display purposes, the photons are directly used for forming the image for the observer. For radiation detection, the photons are fed to a photomultiplier tube and counted.

The most prominent applications, involving the conversion of electrons, are the screens of cathode ray tubes (CRT) (acceleration voltage $> 10\,\mathrm{kV}$) and of flat panel devices, such as field-effect displays (using a low voltage for excitation, typically $< 1\,\mathrm{kV}$) or plasma displays (using the UV light from the discharge of a plasma placed between two electrodes for excitation). Further details on electroluminescent displays can be found in [1929]. Other forms of radiation detected with scintillators are α-, β-, and γ-radiation, X-rays and neutrons [1930]. Different excitation conditions require different phosphors for optimal performance.

23.2.1 CIE Chromaticity Diagram

The CIE[4] procedure converts the spectral power distribution (SPD) of light from an object into a brightness parameter Y and two chromaticity coordinates x and y. The chromaticity coordinates map the color[5] with respect to hue and saturation on the two-dimensional CIE chromaticity diagram. The procedure for obtaining the chromaticity coordinates for a given colored object involves determination of its spectral power distribution $P(\lambda)$ at each wavelength, multiplication by each of the three color-matching functions $\bar{x}(\lambda)$, $\bar{y}(\lambda)$, and $\bar{z}(\lambda)$ (Fig. 23.2a) and integration (or summation) of the three tristimulus values X, Y, Z

$$X = \int_{380\,\mathrm{nm}}^{780\,\mathrm{nm}} P(\lambda)\,\bar{x}(\lambda)\,\mathrm{d}\lambda \tag{23.2a}$$

$$Y = \int_{380\,\mathrm{nm}}^{780\,\mathrm{nm}} P(\lambda)\,\bar{y}(\lambda)\,\mathrm{d}\lambda \tag{23.2b}$$

$$Z = \int_{380\,\mathrm{nm}}^{780\,\mathrm{nm}} P(\lambda)\,\bar{z}(\lambda)\,\mathrm{d}\lambda\ . \tag{23.2c}$$

Y gives the brightness. The tristimulus values are normalized to yield the chromaticity coordinates, e.g. $x = X/(X+Y+Z)$. x and y obtained in this way are the chromaticity coordinates. The third coordinate $z = 1-x-y$ offers no additional information and is redundant. Therefore, the color is represented in a

[4] Commission Internationale de l'Éclairage. The color space can be described by different coordinate systems, and the three most widely used color systems, Munsell, Ostwald, and CIE, describe the color space with different parameters. The Munsell system uses hue, value, and chroma and the Ostwald system uses dominant wavelength, purity, and luminance. The more precise CIE system uses a parameter Y to measure brightness and parameters x and y to specify the chromaticity that covers the properties hue and saturation on a two-dimensional chromaticity diagram.

[5] This definition is motivated by the color vision of the eye. Two light sources will have the same color, even if they have different SPDs, when they evoke the same color impression to the human eye.

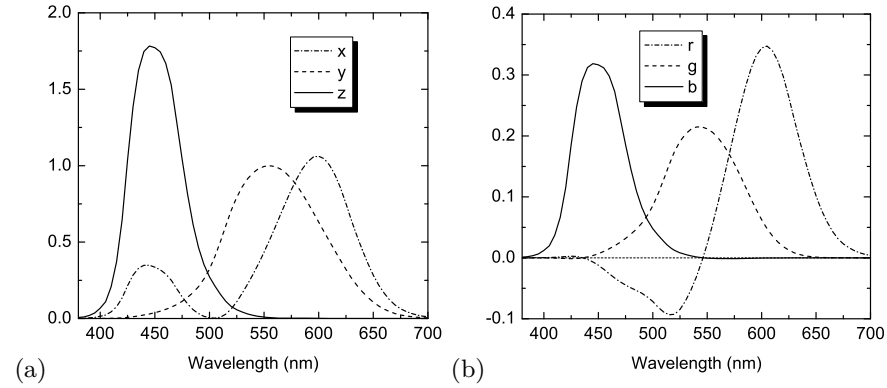

Fig. 23.2 **a** Color-matching functions $\bar{x}$, $\bar{y}$, and $\bar{z}$ for the calculation of the CIE chromaticity, **b** color-matching functions $\bar{r}$, $\bar{g}$, and $\bar{b}$ for the calculation of RGB values

two-dimensional diagram, the CIE chromaticity diagram[6] as shown in Fig. 23.3a. White is represented by $x = y = z = 1/3$. In order to relate the differences between colors as perceived by the human eye more closely to the geometrical distance in the chart, a revision was made (Fig. 23.3b) with new coordinates

$$u' = 4x/(-2x + 12y + 3) \tag{23.3a}$$

$$v' = 9y/(-2x + 12y + 3)\ . \tag{23.3b}$$

For CRTs the red-green-blue (RGB) color space is used.[7] The color matching functions for RGB values are shown in Fig. 23.2b. The RGB values are related to the XYZ values according to

$$\begin{pmatrix} R \\ G \\ B \end{pmatrix} = \begin{pmatrix} 2.36461 & -0.89654 & -0.46807 \\ -0.51517 & 1.42641 & 0.08876 \\ 0.00520 & -0.01441 & 1.00920 \end{pmatrix} \begin{pmatrix} X \\ Y \\ Z \end{pmatrix}\ . \tag{23.4}$$

The CIE RGB primaries from 1931 are at 700, 546.1, and 435.8 nm with the relative intensities 1.0, 4.5907, and 0.0601. A display device using three phosphors can only display colors in the triangular area of the CIE chart between the three chromaticity coordinates. For sRGB,[8] the 1931 CIE primaries and the NTSC[9] norm the coordinates are given in Table 23.2 and visualized in Fig. 23.3c. An optimal coverage of the CIE chart involves monochromatic sources (for laser TV or LED displays) at about 680, 520 and 440 nm.

[6]The coloring of the chart is provided for an understanding of color relationships. CRT monitors and printed materials cannot reproduce the full gamut of the color spectrum as perceived in human vision. The color areas that are shown only depict rough categories and are not precise statements of color.

[7]RGB is an additive color system. However, printing devices use a subtractive color system. This means that the ink absorbs a particular color, and the visible impression stems from what is reflected (not absorbed). When inks are combined, they absorb a combination of colors, and hence the reflected colors are reduced, or subtracted. The subtractive primaries are cyan, magenta and yellow (CMY) and are related to RGB via $(C, M, Y) = (1 - R, 1 - G, 1 - B)$.

[8]Standard RGB color space as defined mainly by Hewlett-Packard and Microsoft, almost identical to PAL/SECAM European television phosphors.

[9]National television standard colors, US norm.

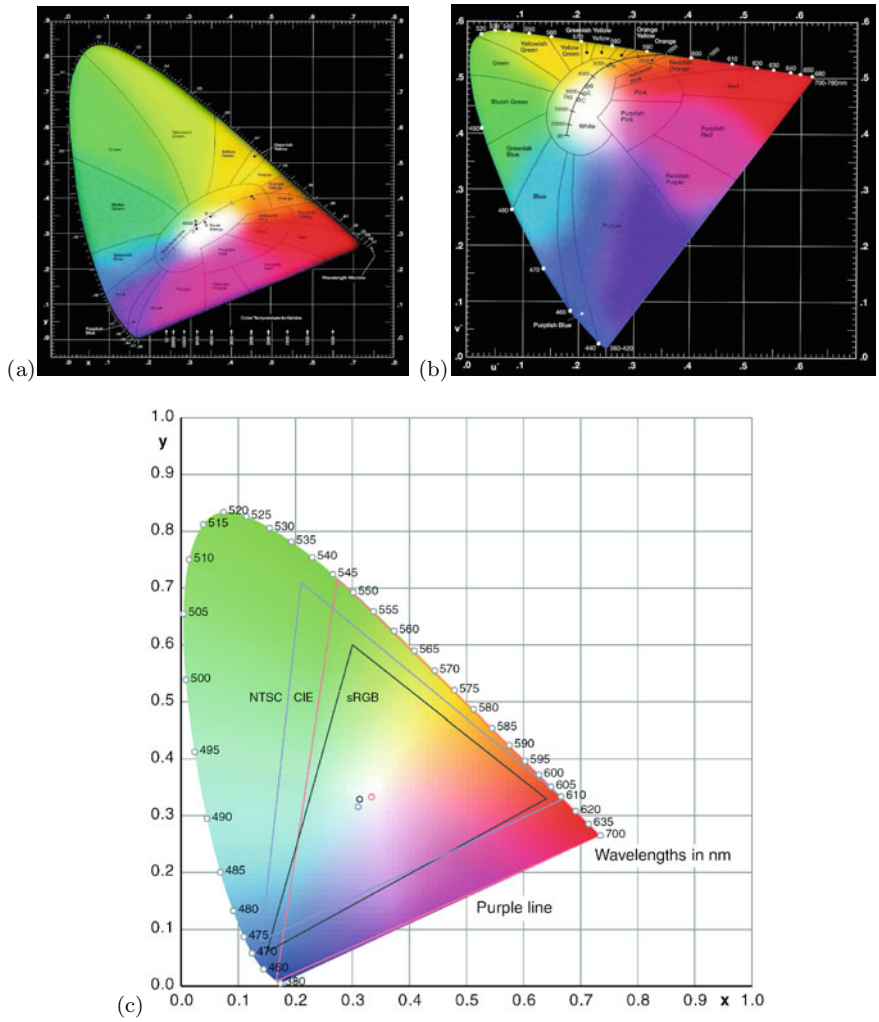

Fig. 23.3 CIE chromaticity diagram from 1931 **a** in the coordinates x and y and from 1976 **b** in the coordinates u' and v' (23.3b). The curved upper boundary is called the 'spectrum locus' and contains monochromatic colors, the straight line at the lower left is termed the 'purple boundary'. In the graph also the color of blackbody radiation is given, $T = 5440\,\mathrm{K}$ corresponds to $x = y = 1/3$. 'A', 'B', 'C', and 'E' are standard illuminants, 'D65' denotes daylight with color temperature $T = 6500\,\mathrm{K}$. **c** CIE chart with the color ranges of sRGB, CIE and NTSC. Part **c** adapted from [1931]

Table 23.2 Primaries and white points for sRGB, CIE and NTSC

Primary	Red		Green		Blue		White	
CIE	0.73467	0.26533	0.27376	0.71741	0.16658	0.00886	0.33333	0.33333
NTSC	0.6700	0.3300	0.2100	0.7100	0.1400	0.0800	0.3100	0.3160
sRGB	0.6400	0.3300	0.3000	0.6000	0.1500	0.0600	0.3127	0.3290

23.2.2 Display Applications

The once ubiquitous amber-colored monochrome displays are mostly fabricated using ZnS:Mn [1929], having broad emission (540–680 nm) with its spectral peak at 585 nm ($x = 0.50$, $y = 0.50$) with an efficiency of 2–4 lm/W. In color television (and similar applications such as color computer monitors, tubes for aviation use, projection television) the image is reproduced by selective and time-multiplexed cathode excitation of three phosphors (blue, green and red) deposited on the internal face of the screen. The chromaticity coordinates of the standard CRT phosphors P-22B, P-22G and P-22R are given in Table 23.3. They cover about the color range labeled 'sRGB' in Fig. 23.3c. For blue and green ZnS:Ag ($x = 0.157$, $y = 0.069$), ZnS:Ag,Cl, ZnS:Ag,Al and ZnS:Cu,Al ($x = 0.312$, $y = 0.597$), ZnS:Cu,Au,Al are used as phosphors, respectively. Y_2O_2S:Eu ($x = 0.624$, $y = 0.337$) activated with trivalent europium (Eu^{3+}) facilitated such a gain in the brilliance of red over ZnS:Ag (more than doubled it) that it has totally replaced it at about one fifth of the cost. For reproducible image quality, precise grain-size control (median size for CRT phosphors is about 8 µm), dispersion control and surface treatment are necessary. Flat-panel displays with their lower excitation voltage require different phosphors for optimal efficiency.

23.2.3 Radiation Detection

The most commonly used scintillation detector for alpha measurements is ZnS activated with silver, ZnS:Ag. This material is not very transparent to light and is usually prepared as a large number of crystals with sub-mm size attached with an adhesive to a flat piece of plastic or other material. The flat screen is optically coupled to a photomultiplier tube that is attached to associated electronics. The voltage and discriminator levels are selected so that the detector is sensitive to the rather large pulses from alpha interactions but insensitive to beta- or gamma-induced pulses. The alpha particles deposit all of their energies in a small thickness of material compared to beta and gamma radiations.

Scintillation detectors for beta radiation are often made from organic materials. In an organic scintillator, the light emission occurs as a result of fluorescence when a molecule relaxes from an excited level following excitation by energy absorption from ionizing radiation. Molecules such as anthracene, trans-stilbene, para-terphenyl, and phenyl oxazole derivatives are among the many organic species that have useful scintillation properties. The organic molecules are dissolved in organic solvents and used as liquid scintillators. A classic application is in the measurement of low-energy beta radiation from, e.g. tritium, ^{14}C, or ^{35}S. In such cases, the sample containing the radioactive beta emitter is dissolved in, or in some cases suspended in, the liquid scintillation solution. The emitted beta radiation transfers energy through the solvent to the scintillator molecule that emits light, subsequently detected by photomultiplier tubes. Organic scintillator molecules can also be dissolved in an organic monomer that can then be polymerized to produce a plastic scintillator in a wide variety of shapes and sizes. Very thin scintillators have been used for alpha detection, somewhat thicker scintillators for beta detection.

Table 23.3 CIE color coordinates, peak emission wavelength and decay time (10%) of standard CRT phosphors

Phosphor	x	y	λ_p (nm)	Decay time
P-22B	0.148	0.062	440	~20 µs
P-22G	0.310	0.594	540	~60 µs
P-22R	0.661	0.332	625	1 ms

Table 23.4 Emission peak wavelength and decay time of various scintillator materials

Material	λ_p (nm)	Decay time
Zn_2SiO_4:Mn	525	24 ms
ZnS:Cu	543	35–100 µs
$CdWO_4$	475	5 µs
CsI:Tl	540	1 µs
CsI:Na	425	630 ns
$Y_3Al_5O_{12}$:Ce	550	65 ns
Lu_2SiO_5:Ce	400	40 ns
$YAlO_3$:Ce	365	30 ns
ZnO:Ga	385	2 ns

Large-volume plastic scintillators have been used in gamma detection, particularly for dose-related measurements.

Other inorganic crystalline scintillators, especially sodium iodide activated with thallium, NaI:Tl, have been used for gamma-ray energy measurements. Such detectors can be grown as large single crystals that have a reasonably high efficiency for absorbing all of the energy from incident gamma rays. There exists a rather large number of inorganic scintillators; some examples of these include cesium iodide activated with thallium, CsI:Tl, bismuth germanate, $Bi_4Ge_3O_{12}$, and barium fluoride, BaF_2. These are mostly used for gamma measurements but can also be prepared with thin windows and have been used for charged particle (e.g. alpha and beta) counting. A number of scintillator materials including tungstates like $CdWO_4$ has been reviewed in [1932].

In Table 23.4, the peak emission wavelength and the characteristic decay time are listed for a variety of scintillator materials. Direct semiconductors, although not offering the highest efficiency, are particularly useful for high time resolution in, e.g., time-of-flight measurements or fast scanning electron microscopy.

23.2.4 Luminescence Mechanisms

Self-Trapped Excitons

In a strongly ionic crystal, such as NaI, a hole becomes localized to an atomic site via the polaron effect. A spatially diffuse electron is attracted, and a self-trapped exciton is formed that can recombine radiatively.

Self-Activated Scintillator

In such material, the luminescent species is a constituent of the crystal. The emission involves an intraionic transition, e.g. 6p→6s in Bi^{3+} of $Bi_4Ge_3O_{12}$, or a charge-transfer transition in the case of $(WO_4)^{2-}$ in $CaWO_4$. At room temperature, nonradiative competing processes limit the efficiency.

Activator Ions

For dopant ions such as Eu^{2+} in YO_2S:Eu, Ce^{3+} in $YAlO_3$:Ce or Tl^+ in NaI:Tl, the hole and electron excited by the radiation are sequentially trapped by the same ion that then undergoes a radiative transition, in the case of Eu and Ce[10] 5d→4f, for Tl $^3P_{0,1} \rightarrow S_0$. CsI:Tl has one of the highest efficiencies of 64.8 photons/keV [1933].

[10]This transition is dipole allowed for Ce and partially forbidden for Eu.

Core–Valence Luminescence
In some materials, e.g., BaF_2, CsF, $BaLu_2F_8$ the energy gap between the valence band and the top core band is less than the fundamental band gap. A radiative transition occurs when an electron from the valence band fills a hole in the top core band that has been created by the radiation. The light yield is limited to about 2 photons/keV.

Semiconductor Recombination Processes
Free excitons or excitons bound to impurities can recombine radiatively. This process is most efficient at low temperatures. At room temperature, the emission is typically much weaker ($\gtrsim 10\times$) since excitons become unbound or dissociated. Highly doped n-type semiconductors, e.g. CdS:In, exhibit recombination between donor-band electrons and holes. ZnO:Ga has an efficiency of about 15 photons/keV and a fast response (with 2.4 photons/keV emitted in the first 100 ps). Luminescence can also stem from donor–acceptor pair transitions, e.g. in PbI_2 with an efficiency of 3 photons/keV at 10 K. Isoelectronic impurities such as nitrogen in GaP:N and tellurium in CdS:Te attract an electron and subsequently a hole. In ZnS:Ag and ZnS:Cu (conduction) band to trap recombination is dominant. In a codoping scheme like CdS:In,Te, In supplies electrons in an impurity band that can recombine with holes trapped at Te.

23.3 Light-Emitting Diodes

23.3.1 Introduction

Light-emitting diodes (LEDs) are semiconductor devices in which injected carriers recombine radiatively. The recombination process leading to light emission can be of intrinsic nature, i.e. band–band recombination, or extrinsic, e.g. impurity-bound excitons. Impurity-related luminescence can also be excited via impact excitation. For an extensive treatment of LEDs see [1934, 1935], for a review of the early field [1936] and for recent reviews [1937, 1938]. Mostly LEDs are pn-diodes although also some MIS-based devices have been reported [1939, 1940].

23.3.2 Spectral Ranges

Applications for LEDs can be sorted by the color of emission. In Fig. 23.4, the standard sensitivity $V(\lambda)$ of the human eye is shown (see Fig. 23.1a). In the visible spectral region (about 400–750 nm) the perceived brightness of the LED depends on the eye sensitivity. It is largest in the green (at 555 nm) and drops strongly towards the red and blue.

The most important spectral regions and applications are:

- infrared ($\lambda > 800$ nm): remote controls, optocouplers, low-cost data transmission, IR interface
- visible: indicator LED, lighting[11] (room, buildings, cars), white LED for broad spectrum
- ultraviolet ($\lambda < 400$ nm): pumping of phosphors for white LEDs, biotechnology

In Fig. 23.4, potentially useful semiconductors for the various spectral regions are shown. The semiconductors that are currently used for the various colors of the visible spectrum are

- red–yellow: Ga(As,P)/GaAs, now (Al,In,Ga)P/GaP
- yellow–green: GaAsP:N, GaP:N

[11] Penetration of white LEDs into the general lighting market could translate (globally) into cost savings of $\$10^{11}$ or a reduction of power generation capacity of 120 GW.

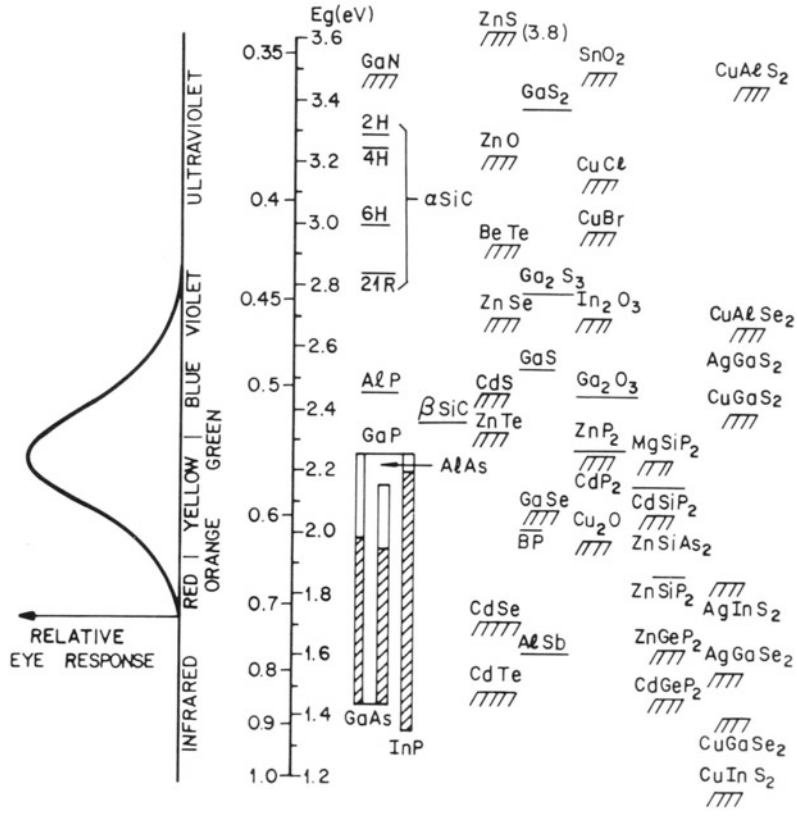

Fig. 23.4 Spectral coverage by various semiconductor materials. Reprinted with permission from [574], ©1981 Wiley

- green–blue: SiC, now GaN, (In,Ga)N
- violet: GaN
- ultraviolet: (Al,Ga)N

23.3.3 Efficiencies

External Quantum Efficiency

The *external* (or total) quantum efficiency η_{ext} is the number of photons emitted from the device per injected electron–hole pair. It is given by the product of the *internal* quantum efficiency η_{int} and the light extraction efficiency χ_{ex}:

$$\eta_{\text{ext}} = \chi_{\text{ex}}\, \eta_{\text{int}} \,. \tag{23.5}$$

In a commercial device another factor, the packaging efficiency may enter which accounts for photon loss due to packaging the LED dice into its housing.

Wall-Plug Efficiency

The wall-plug efficiency η_{w} is the power conversion ratio of the electrical power and the light output P_{out},

$$\eta_{\text{w}} = \frac{P_{\text{out}}}{I\,V} = \frac{\hbar\omega}{e\,V}\,\eta_{\text{ext}} \,. \tag{23.6}$$

At first it seems reasonable to assume that always $\eta_w < 1$. However, it has been reported that at small current and at elevated temperature the wall-plug efficiency is found larger than 100% due to the electrical work pumping heat from the lattice to the photon field in a GaSb-based diode[1941]. The groundwork for such effect was laid in [1942], essentially predicting that $\hbar\omega > e\,V$ is possible.

Internal Quantum Efficiency
The internal quantum efficiency is the number of photons generated (inside the semiconductor) per injected electron–hole pair. High material quality, low defect density and low trap concentration are important for a large value of η_{int}. The recombination current in the pn-diode is given in (21.136).

Light Extraction Efficiency
The light extraction efficiency of the LED chip is ratio of the number of photons leaving the device and the total number of generated photons.[12] The geometry of the LED is of prime importance to optimize χ_{ex}. Due to the large index of refraction of the semiconductors ($n_s \sim 2.5$–3.5), light can leave the semiconductor only under a small angle θ_c from the surface normal due to total reflection (cf. (9.11) and see right part of Fig. 9.4). Against air ($n_1 \approx 1$) the critical angle is

$$\theta_c = \sin^{-1}(1/n_s) \ . \tag{23.7}$$

The critical angle for total reflection is 16° for GaAs and 17° for GaP. Additionally, a portion of the photons that do not suffer total reflection is reflected back from the surface with the reflectance R given by (cf. (9.15))

$$R = \left(\frac{n_s - 1}{n_s + 1}\right)^2 \ . \tag{23.8}$$

We note that the above formula is valid strictly for vertical incidence. For the GaAs/air interface, the surface reflectance (for normal incidence) is about 30%. Thus, the light extraction efficiency for a LED is given by (1–R) and the critical angle by

$$\chi_{ex} \cong \frac{4\,n_1\,n_s}{(n_1 + n_s)^2}\,(1 - \cos\theta_c) \approx \frac{4\,n_s}{(n_s + 1)^2}\,(1 - \cos\theta_c) \ . \tag{23.9}$$

The latter approximation is valid when the outer medium is air. For GaAs, the light extraction efficiency is $0.7 \times 4\% \approx 2.7\%$. Thus, for this simple geometry, only a small fraction of generated photons can leave the device and contribute to the LED emission.

23.3.4 Device Design

In the following subsections the strategies that have allowed significant improvement of the extraction efficiency (Fig. 23.5) and thus LED performance are briefly discussed. The record by 2014 for light extraction efficiency is 89% [1943], however not for a mass-produced device.

Nonplanar Surfaces
With curved surfaces, the problem of total reflection can be (partially) circumvented (Fig. 23.6). Spherically polished chips are feasible, but, very expensive. The epoxy seal of the standard LED case (Fig.23.7a) and its shape play a similar role, however, with a smaller index of refraction than the semiconductor, and are important for the beam shape.

[12] Note that the light extraction efficiency is also important for solar cells, cf. Sect. 22.4.3.

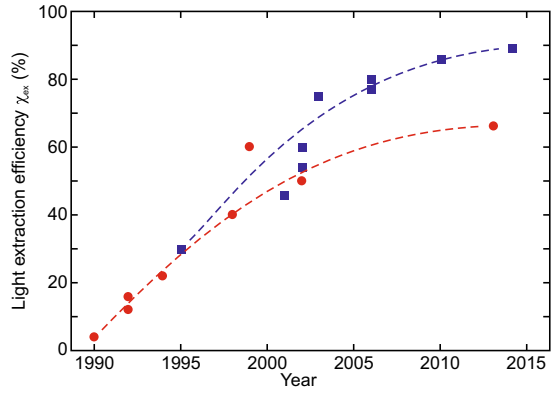

Fig. 23.5 Historic development of maximum light extraction efficiency for AlGaInP (*red circles*) and (In,Ga)N (*blue squares*) LEDs. *Dashed lines* are guides to the eye. Adapted from [1938, 1944]

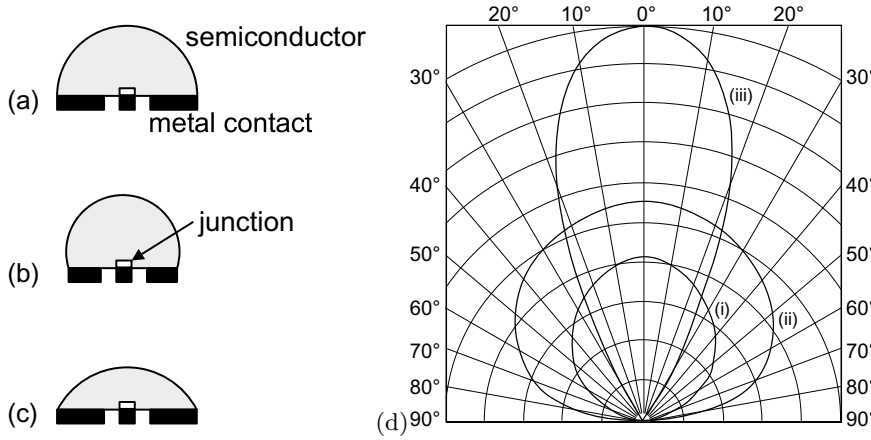

Fig. 23.6 Form of various LED casings with **a** hemispherical, **b** truncated sphere and **c** parabolic geometry. Adapted from [1945]. **d** Emission characteristics for rectangular (**i**), hemispheric (**ii**) and parabolic (**iii**) geometry. Adapted from [1946]

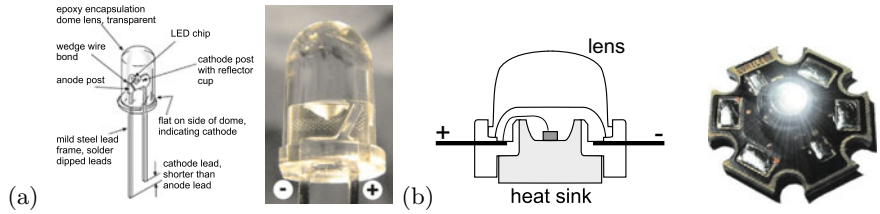

Fig. 23.7 **a** Standard LED casing (schematic drawing and macrophoto), **b** high-power mounting (schematic drawing and image of Luxeon® LED)

Thick-Window Chip Geometry

An increase in light extraction efficiency to about 10–12% can be achieved if the top layer is fabricated with a much larger thickness (Fig. 23.8b) of 50–70 µm instead of a few µm. However, such approach is not scalable since larger device area would demand even larger thickness.

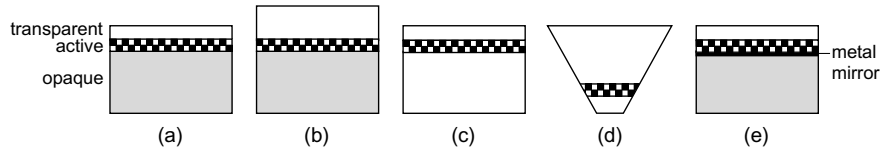

Fig. 23.8 **a** Standard LED layer sequence with opaque substrate (*grey*), active layer (*checkered*) and transparent top, **b** thick window design with thick top layer (50–70 µm). **c** Transparent substrate (by rebonding, see Fig. 23.9, **d** chip shaping (cf. also Fig. 23.11). **e** Thin-film LED with metal mirror (*black*) and rebonding (cf. also Fig. 23.12)

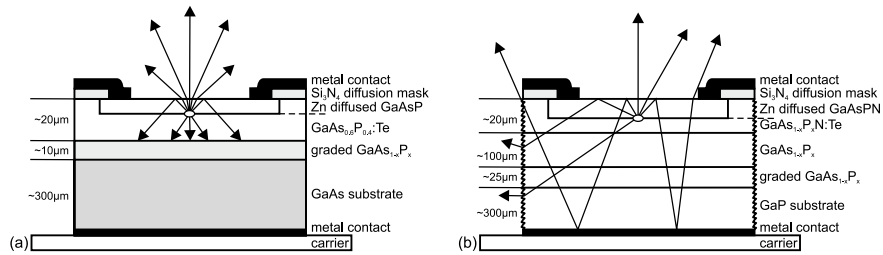

Fig. 23.9 Comparison of light paths in a GaAsP-based LED with **a** opaque (GaAs) and **b** transparent (GaP) substrate (side facets roughened). Adapted from [1947]

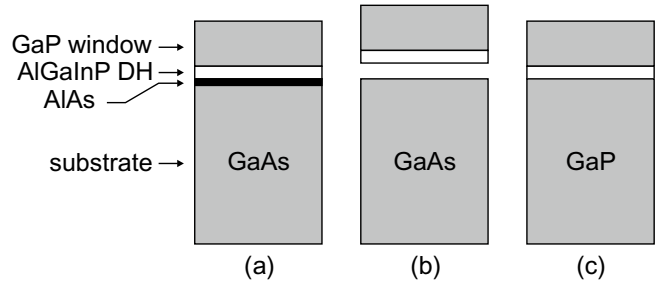

Fig. 23.10 Scheme of fabrication for red high brightness LED: **a** AlGaInP double heterostructure (DH) with GaP window on GaAs substrate (growth with MOCVD). **b** Lift-off using HF etch of sacrificial AlAs layer. **c** Wafer bonding on GaP (transparent for red light)

Transparent Substrate

Reflection of photons is not so detrimental if they are not lost later due to absorption in the substrate. In Fig. 23.8, the evolution of LED chip design is shown schematically. In Fig. 23.9, the light path is compared for opaque and transparent substrates. The latter provides higher light extraction efficiency due to the 'photon recycling' effect. Efficiencies of 20–25% are possible. In Fig. 23.10, the technological steps are shown to fabricate a GaP LED with an AlGaInP active layer. The active layer is initially grown on GaAs due to lattice-match conditions.

Nonrectangular Chip Geometry

If the chip is made with an inverted structure and mounted on a mirror, a high light extraction efficiency ($> 50\%$) can be achieved. Typical commercial designs are shown in Fig. 23.11.

The increase in quantum efficiency allows the devices to run on much higher output power. While initially LEDs delivered power only in the mW regime, now output power in the $\sim$ 1 W regime is possible (high brightness LEDs). The higher currents made a redesign of the LED mount towards better heat sinks necessary (Fig. 23.7b). While the standard case has a thermal resistance of 220 K/W (chip size $(0.25\,\text{mm})^2$ for 0.05–0.1 W and 0.2–2 lm), the high-power case has 15 K/W (chip size $(0.5\,\text{mm})^2$ for

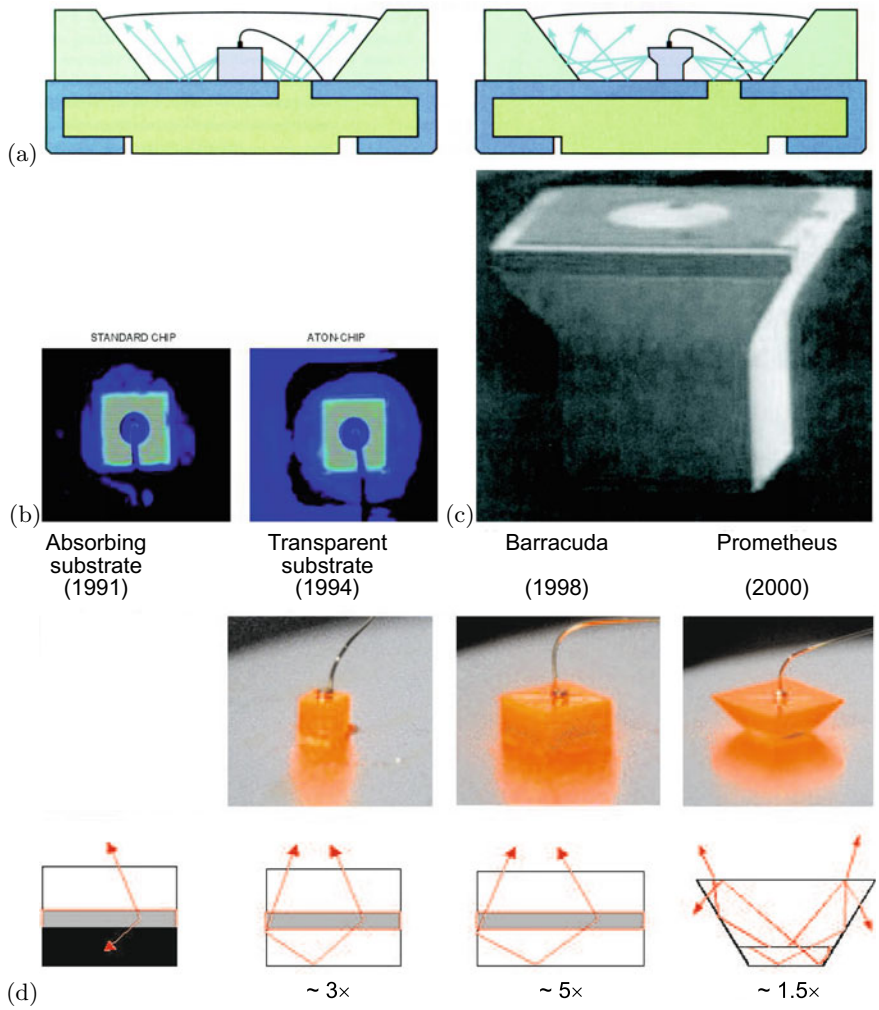

Fig. 23.11 Optimization of light exit by 3D design of the LED chip, **a** scheme, **b** emission pattern comparison and **c** SEM image of the ATON chip. Reprinted with permission from [1948]. **d** Development stages towards the truncated inverted pyramid (Prometheus) chip. From [1949]

0.5–2 W and 10–100 lm). An epoxy-free technique for encapsulation also enhances the color uniformity and maintains the brightness.

Thin-Film LED

In the thin-film LED design [1950], as schematically shown in Fig. 23.12a, a metal mirror is evaporated on the LED layers. In a flip-chip design, subsequently the metal side is wafer bonded to another metallized substrate and the original substrate is removed. Additionally, the LED surface can be patterned (before bonding) into an (hexagonal) array of (hexagonal) microprism mesas with an insulating (e.g. silicon nitride) layer with openings in order to optimize the current path. The microprisms are optimized to allow efficient reflection of light towards the emitting surface. This technology is scalable to large areas without loss in efficiency.

In order to avoid bonding from the top which leads to partial shielding of the emitted radiation and is a mechanical process, contact schemes for flip-chip LEDs have been devised for contacting both the n- and the p-layer from the same side [1952]. In Fig. 23.13 a schematic cross-section and an emission

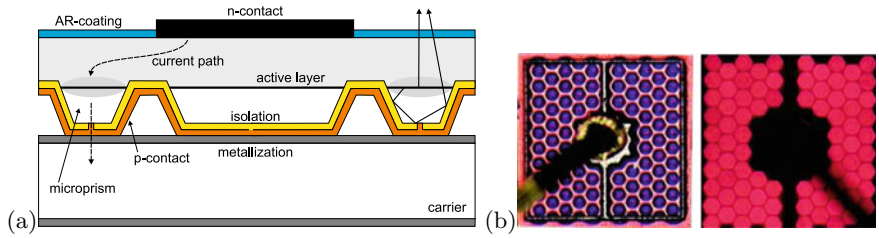

Fig. 23.12 **a** Scheme of thin-film flip-chip LED with microprisms. **b** image and luminescence image of thin film AlInGaP LED (chip length: 320 µm). Reprinted with permission from [1951]

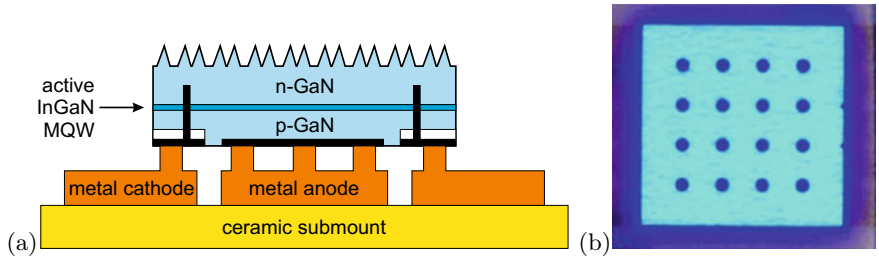

Fig. 23.13 **a** Scheme of thin-film flip-chip LED with rough surface and contacts from one side. **b** Emission image of $1 \times 1\,\mathrm{cm}^2$ chip. Adapted from [1952]

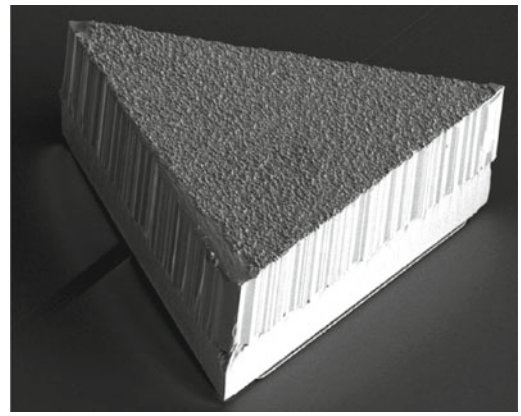

Fig. 23.14 Triangular GaN LED chip with high extraction efficiency. Both the p- and n-contact are on the bottom. Adapted from [1943]

image are shown. Here, the n-contact runs through a via hole with insulated side walls. In the emission image the array of via holes can be seen.

Bulk Flip-Chip

In the GaN material system a LED based on a triangular chip with 400 µm side length using a bulk substrate with 150 µm thickness has been presented that exhibits the so far highest extraction efficiency of almost 90% (Fig.23.14) [1943, 1953]. The top and all side facets are rough.

Cascaded LEDs

Similar to the use of tunneling junctions in multi-junction solar cells (Sect. 22.4.6), the monolithic serial connection of several LED layers has been proposed [1954] (Fig. 23.15). For a given output power P at forward voltage V_F and current density j of a single junction LED, ideally a LED with N identical stacks and $N-1$ tunneling junctions provides the same output power P at the N-fold forward voltage, as reported for $N = 2, 3$ in [1955], and the current density j/N. Since the internal quantum

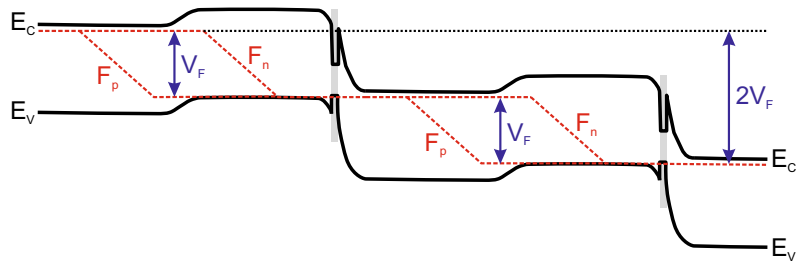

Fig. 23.15 Schematic band structure of cascaded LED. The *grey area* denotes an additional heterostructure for reduction of the series resistance of the tunnel junctions. Adapted from [1954]

efficiency of LEDs decreases with increasing current density (*droop*), such stacked LED design holds promise for increased wall-plug efficiency if the series resistance of the tunneling junctions is small. The quantum efficiency of such device is then larger than N times the efficiency of the single stack LED and thus way larger than 100% (similar to quantum cascade lasers, Sect. 23.4.16).

Historic Development

In Fig. 23.16, the historic development of the LED luminous efficacy (luminous flux per electrical input power) is shown for various material systems. While the luminosity has increased by a factor of 20 per decade in the last 40 years, the price has decreased by a factor of ten per decade (Fig. 23.17). Currently, there is a need for the development of more efficient LEDs in the green spectral range [1956] since their luminosity is small compared to devices for the blue and red spectral regions (Fig. 23.18).

23.3.5 White LEDs

There are different possibilities to generate white light with an LED as shown schematically in Fig. 23.19. The highest color gamut and a tunable white point can be achieved by combining a red, a green and a blue LED (Fig. 23.19a). Using a blue LED and a yellow phosphor (Figs. 23.19b and 23.20a,b), a white spectrum can be achieved that is, however, not very close to a blackbody spectrum (Fig. 23.20c). A better color rendering can be obtained with the combination of two phosphors [1958].

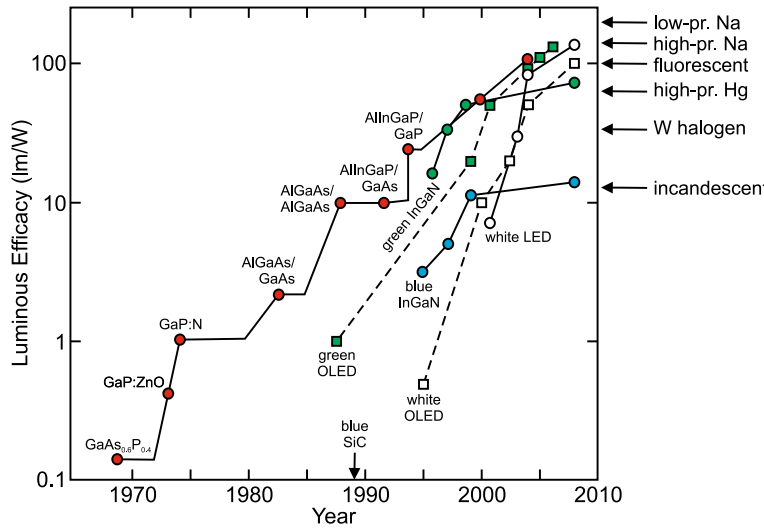

Fig. 23.16 Historic development of the luminous efficacy of semiconductor LEDs and OLEDs. Based on [1957] with the addition of data on OLEDs and recent data on LEDs. The arrows on the right indicate efficacy of various other light sources

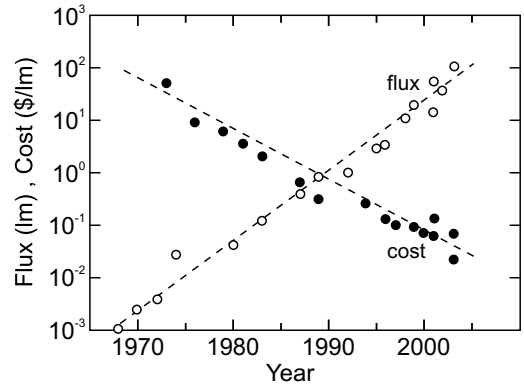

Fig. 23.17 Historic development of the flux (in lumen) and cost (in $/lm) for semiconductor LEDs. Data from [1949]

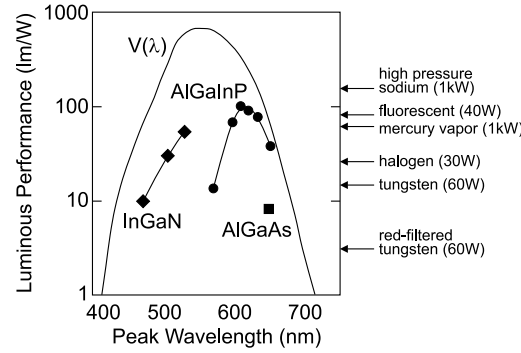

Fig. 23.18 Luminous performance of various LED materials in comparison with other light sources. Adapted from [1957]

With an UV LED that is itself invisible (and must be shielded so no UV radiation leaves the LED), phosphors with various colors can be pumped (Fig. 23.19c). The mix of phosphors determines the white point.

Using a blue-emitting LED based on (In,Ga)N material, phosphors (similar to those used in fluorescence lamps) can be pumped. Blue light is converted into green, yellow or red light such that the resulting total spectrum appears white to the human eye. Also, a broad range of other colors can be designed (color on demand), e.g. pink or particular corporate colors.

The color of a white LED depends on the operation conditions. In Fig. 23.21a the intensity vs. dc driving current characteristic of a white LED is shown. In Fig. 23.21b the chromaticity coordinates are shown for various dc currents. A change of wavelength with forward voltage occurs for the blue-emitting (In,Ga)N material due to filling of low-energy states (Fig. 23.22). In order to avoid this effect, the LED is driven with pulses of a fixed current amplitude and a repetition frequency that is high enough

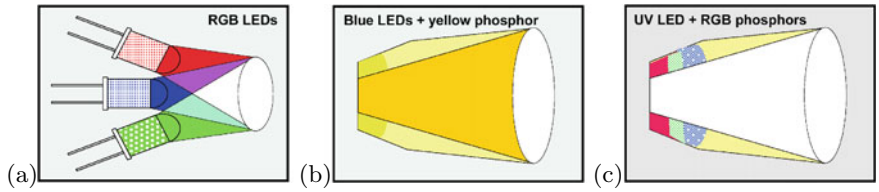

Fig. 23.19 Different strategies to generate white light with LEDs. **a** Additive mixing of R, G, and B LEDs, **b** blue LED and yellow phosphor, **c** UV LED (invisible) and R, G, and B phosphors. From [1949]

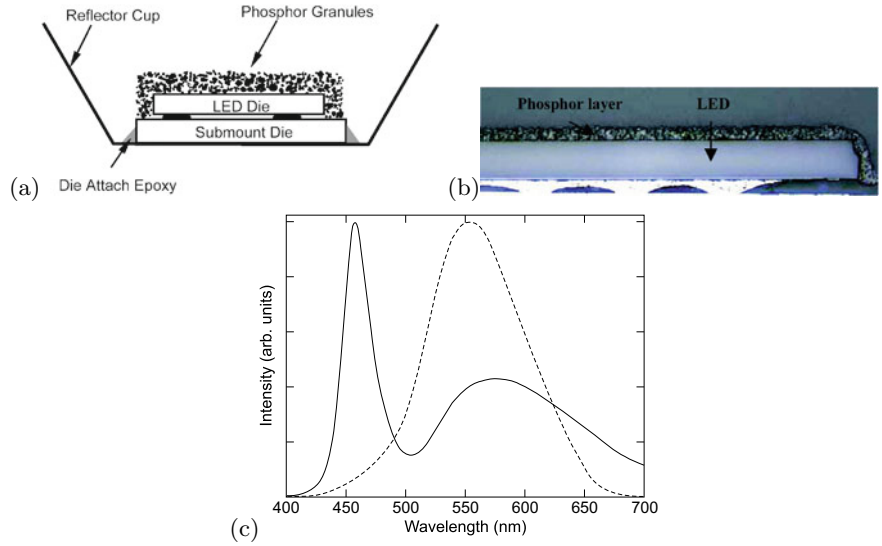

Fig. 23.20 **a** Scheme and **b** image of color conversion Luxeon® LED. From [1949]. **c** Spectrum (*solid line*) of white LED with blue LED pumping a yellow phosphor together with eye-sensitivity curve $V(\lambda)$ (*dashed line*). Adapted from [1951]

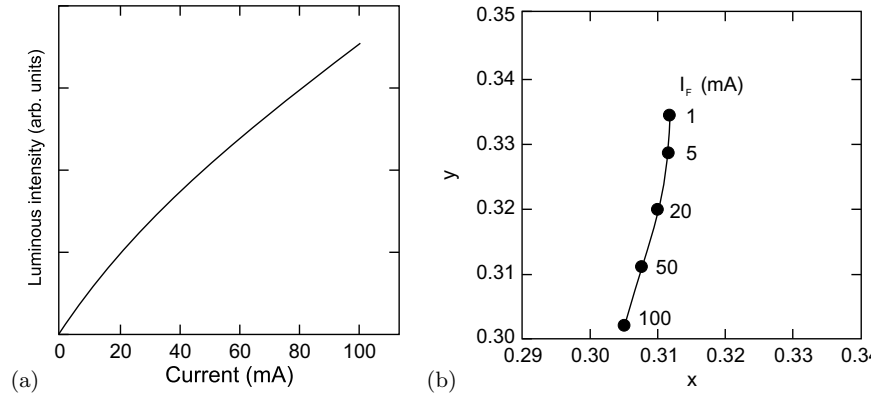

Fig. 23.21 **a** Luminous intensity of white LED (NSCW215) vs. dc forward current. **b** CIE chromaticity coordinates for various dc driving conditions as labeled. Data taken from [1959]

to provide a flicker-free image to the human eye, e.g. 100 Hz. The intensity of the LED is modulated via the pulse width, i.e. between 0–10 ms in this case (PWM, pulsewidth modulation).

The direct light from white LEDs is visually appealing and cannot be distinguished from a blackbody source of matching temperature. But since the spectral power distribution of white LEDs is different from natural light, objects illuminated by such light source can appear in 'wrong' colors. For the spectrum of Fig. 23.20c, in particular green is reproduced poorly. A quantitative measure for the ability of a light source to reproduce the colors of an illuminated object faithfully compared with a natural (blackbody) light source is the *color rendering index* (CRI).

A major advantage of LEDs for display and lighting applications is their long lifetime compared to halogen (about 2000 h), xenon (10,000 h) or fluorescent (6000–10,000 h) lights. Philips Lumileds projects (for white LUXEON® K2 LEDs) 70% lumen maintenance at given current (1 A) at 50,000 h for junction temperature $T_j \leq 120°$ [1961]. Similar values are given by OSRAM [1964] for white

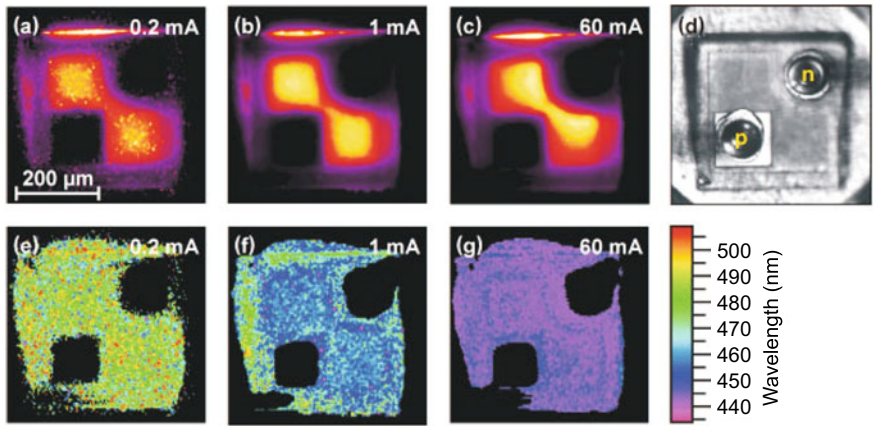

Fig. 23.22 **a–c** Electroluminescence intensity map of (In,Ga)N LED at different currents as labeled. **d** Optical image of the LED chip (top view). **e–g** Wavelength images (wavelength of spectral emission maximum) for different currents. Adapted from [1960]

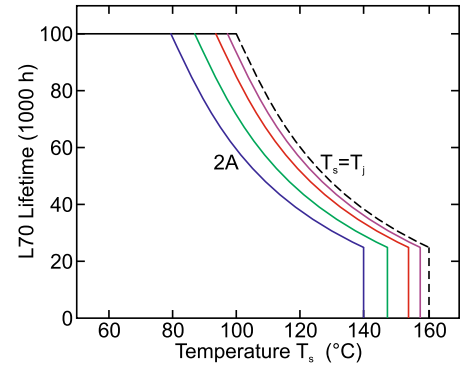

Fig. 23.23 Lifetime for 70% lumen as a function of solder temperature T_s (for white Diamond Dragon® LED) for various driving currents (0.3, 0.7, 1.4 and 2.0 A, *solid lines* from right to left). The *dashed line* is for low driving current and $T_s = T_j$. Adapted from [1964]

high power LEDs (Fig. 23.23). A current problem is the decrease of efficiency with increasing current density termed *droop*, probably due to Auger recombination [1962, 1963].

23.3.6 Quantum Dot LEDs

Quantum dots are an interesting active medium for LEDs due to their spectroscopic properties (Sect. 14.4.4).

Ultranarrow Spectral Emission

A LED based on a single QD exhibits a rather unique spectrum consisting of a single spectral line, at least at low temperatures [1965], due to exciton recombination as shown in Fig. 23.24. Such device can deliver single photons on demand and be a photon source for quantum cryptographic communication. At higher current also biexciton recombination appears. In [1966, 1967] the triggered emission of photon pairs from cascade-like XX and X recombination in a single dot and their polarization entanglement is reported. Entanglement is related to degenerate X and XX emission energy [1968] (cmp. Fig. 14.44).

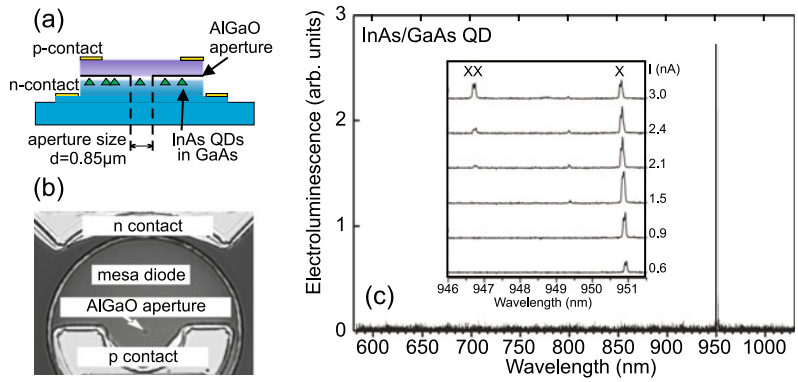

Fig. 23.24 **a** Schematic cross-section of QD LED. Current is fed to a single QD via an oxide aperture. **b** Plan-view SEM image of QD LED. **c** Electroluminescence (EL) spectrum ($T = 10\,\mathrm{K}$, $U = 1.65\,\mathrm{V}$, $I = 0.87\,\mathrm{nA}$) of single InGaAs/GaAs QD LED (diameter of oxide aperture 0.85 µm, thickness 60 nm). The single line is due to (neutral) exciton recombination. The *inset* shows dependence of EL spectrum on injection current; at higher currents a second peak due to biexciton recombination (XX→X) appears. Adapted from [1969]

Fig. 23.25 Electroluminescence spectrum of a quantum dot LED designed for broad spectral range (at $5\,\mathrm{kA/cm^2}$). Adapted from [1971]

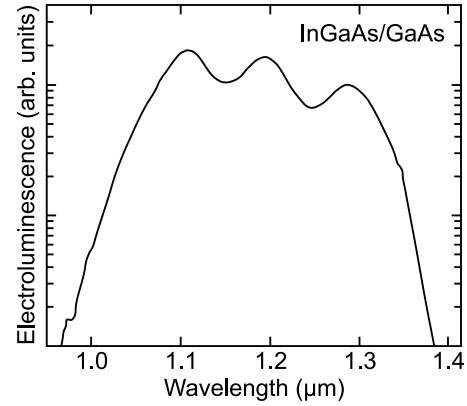

Ultrabroad Spectral Emission

An LED based on the emission from a quantum dot ensemble exhibits a fairly broad spectrum because of inhomogeneous broadening due to size fluctuations of the quantum dots (cmp. Fig. 14.47). Additionally several ensembles of QDs with different mean emission wavelength can be incorporated in a device, e.g. in stacked layers [1970]. This way ultrabroad electroluminescence spectra can be realized (Fig. 23.25). Also emission on the ground and excited state can be used for broad spectral emission.

23.3.7 Organic LEDs

An organic light emitting diode (OLED) is made from organic semiconductors. The pioneering work was made by Tang and Van Slyke [1789, 1972]. Typical layer sequences are depicted in Fig. 21.62. The light emission occurs through the anode (and the transparent ITO layer) while the metal cathode is opaque. Two major configurations are possible, emission through the transparent substrate (glass) or top emission (Fig. 23.26).

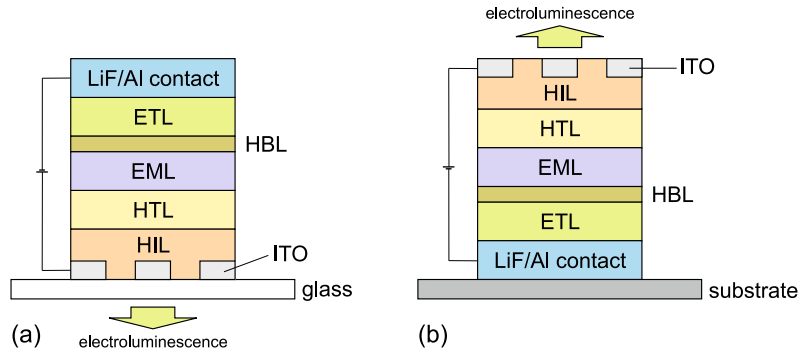

Fig. 23.26 Typical OLED design for **a** bottom and **b** top emission

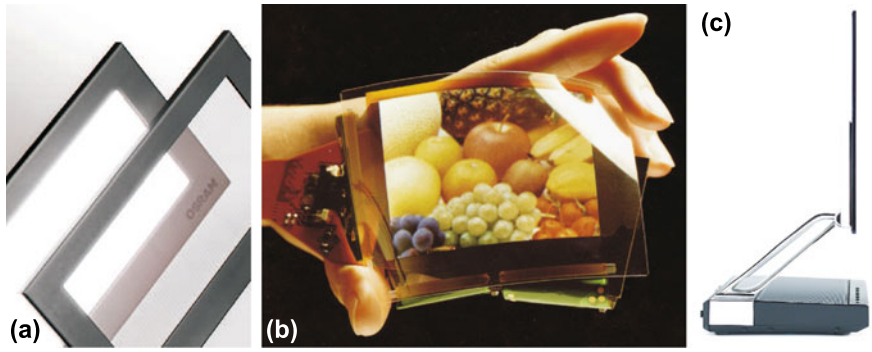

Fig. 23.27 **a** Transparent OLED panel. From [1973]. **b** Flexible OLED display. From [1974]. **c** 3 mm thin, 11 inch diagonal OLED TV. From [1975]

The optimization of materials for the various functional layers is ongoing. The emission layer (EML) is optimized for efficient radiative recombination for the design wavelength or wavelength range. The highest efficacy of over 100 lm/W (Fig. 23.16) is achieved using phosphorescent materials (Sect. 18.6). The contacts are optimized for high carrier injection efficiency and the transport layers are optimized for high conductivity.

End of 2007 a transparent white OLED panel was introduced [1973] (Fig. 23.27a). Its transparency is 55% and shall be improved in the future. A crucial point is the protection of the organic films against moisture and air. The encapsulation by glass is very good. Flexible OLED panels with polymer substrate and encapsulation have been demonstrated (Fig. 23.27b). OLED technology is currently used for small displays in digital cameras and cellular phones. It enables very thin TV panels, only a few mm thick (Fig. 23.27c) entering the mass market in 2010. An increase of the lifetime from 30,000 to beyond 50,000 h is expected.

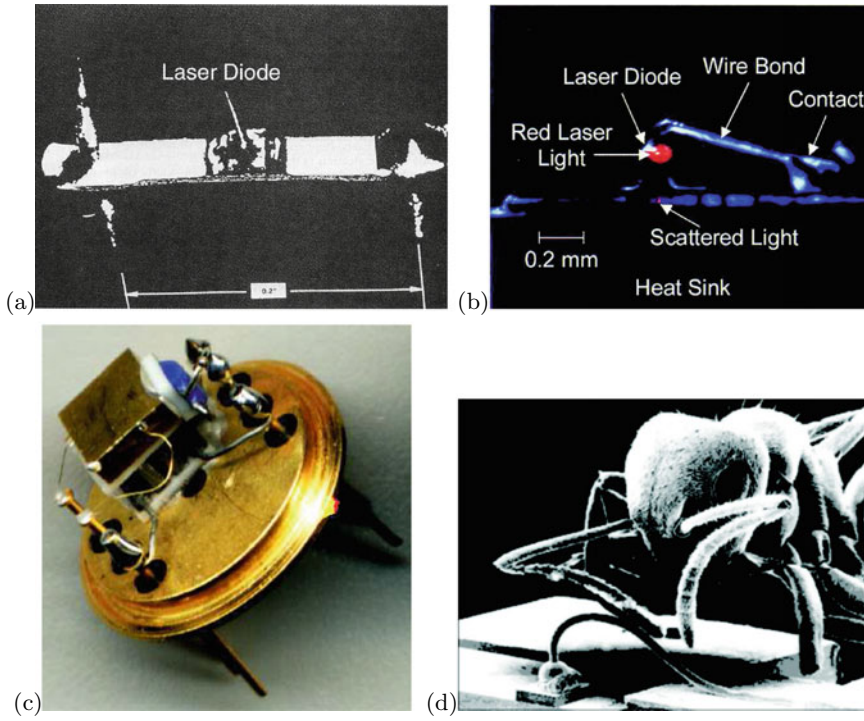

Fig. 23.28 Images of the first semiconductor lasers, 1962: **a** GaAs laser, Lincoln Laboratories and **b** GaInP laser, N. Holonyak and S.F. Bevacqua, Urbana Champaign. **c** Laser (at the end of gold bond wire) mounted on Peltier heat sink and a TO chip, Universität Leipzig. **d** Size comparison of an ant with a laser chip (underneath the bond wire)

23.4 Lasers

23.4.1 Introduction

Semiconductor lasers[13] [1976, 1977] contain a zone (mostly called the *active layer*) that has gain if sufficiently pumped and that overlaps with an optical wave. The wave bounces back and forth in an optical cavity that leads to optical feedback. The part of the wave that exits the semiconductor forms the laser beam. Some of the first semiconductor lasers and a mounting design are shown in Fig. 23.28.

Generally, two main geometrical laser types, *edge* emitters (Fig. 23.29a) and *surface* emitters (Fig. 23.29b), are distinguished. The emission of the edge emitter exits through cleaved {110} side facets[14] ($\approx 30\%$ reflectance), of which an opposite pair acts as a Fabry–Perot optical cavity. The surface emission is directed along (001), since this is the (standard) growth direction of the heterostructure sequence making up the laser. The mirrors in a vertical-cavity surface-emitting laser (VCSEL) are made from dielectric Bragg mirrors (cf. Sect. 19.1.4) with typically $R > 99.6\%$. Using antireflection coating

[13] The term 'laser' is an acronym for 'light amplification by stimulated emission of radiation'. The amplification relies on stimulated emission, theoretically predicted by Einstein in 1917. The laser concept was first explored in the microwave wavelength region (1954, MASER using ammonia, Ch.H. Townes, Nobel prize 1964). The first optical laser (1958, US patent No. 2,929,922 awarded 1960, A.L. Schawlow, Ch.H. Townes) was the ruby laser developed in 1960 by Th. Maiman. A device is a laser when it emits stimulated light. This light must neither be monochromatic nor be emitted in a narrow, directed beam.

[14] Or etched facets in possibly any direction.

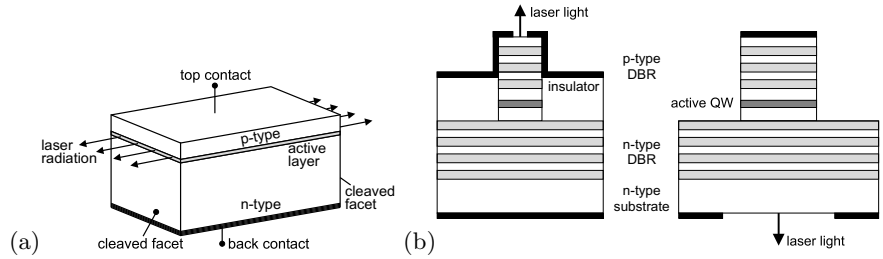

Fig. 23.29 **a** Schematic drawing of edge-emitting semiconductor laser. **b** Schematic drawings of vertical-cavity surface-emitting lasers with top emission (*left*) and emission through the substrate (*right*). *Black areas* are metal contacts

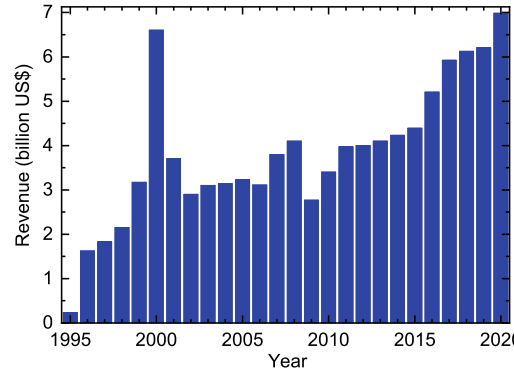

Fig. 23.30 Revenue in worldwide diode laser market. Based on numbers from [1978], data for 2020 estimated

on one facet, semiconductor lasers can be set up with an external cavity.[15] If both facets are antireflection coated, feedback is missing and the chip can be used as an optical amplifier (cf. Sect. 23.5).

Most lasers are pn-diodes and are then called laser diodes. They rely on the gain of interband transitions and the emission wavelength is determined and (more or less) given by the band gap of the semiconductor. The cascade laser [149] (Sect. 23.4.16) is a unipolar structure with a superlattice as active layer. Here, the intersubband transitions (mostly in the conduction band but also in the valence band) carry the gain. The emission wavelength depends on the subband separation and lies typically in the far- and mid-infrared. Extensions to the THz regime and also to shorter wavelengths are possible. A third type of laser is the 'hot-hole' laser (Sect. 23.4.17), typically fabricated with p-doped Ge, which can be viewed as unipolar and functions only in a magnetic field; its emission is in the THz regime.

23.4.2 Applications

In Fig. 23.30, the revenue in the worldwide diode laser market is shown. The drop after 2000 is due to the burst of the 'internet bubble'. Nondiode laser (gas, ruby, excimer, …) revenue is currently stable at around 2 billion US$, thus semiconductor lasers account for the largest share of all laser types sold.

The following applications rely on semiconductor lasers:

- optical communication, mostly optical fiber based (senders), typically at 10 GBit/s, in special situations also 40 GBit/s data rate.

[15] Such external cavities can be used for manipulation of the laser properties such as wavelength tuning.

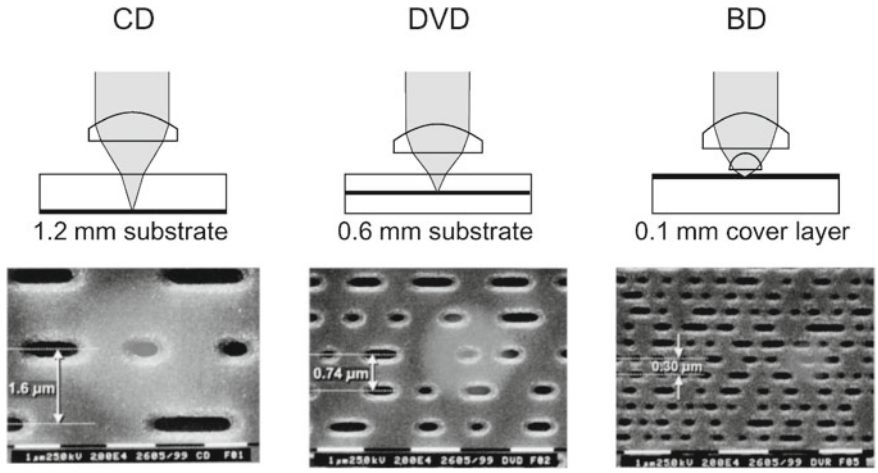

Fig. 23.31 Evolution of optical data storage technology, 'CD': compact disk (laser: 780 nm, pitch: 1.6 µm, capacity: 0.7 GB), 'DVD': digital versatile disk (laser: 635–650 nm, pitch: 0.74 µm, capacity: 4.7 GB for one layer), 'BD': 'Blu-ray' disk (laser: 405 nm, pitch: 0.32 µm, capacity: 27 GB for one layer)

- optical information storage and retrieval (CD, DVD, BD[16]) with as short of a wavelength as possible, as shown in Fig. 23.31, currently 405 nm.
- pumping of solid-state lasers, typically 910 or 940 nm for pumping Nd:YAG
- portable projectors, laser TV, entertainment.
- laser pointers, see Fig. 23.32. A red laser pointer simply uses the collimated red emission of a GaAs-based diode. In a green laser pointer, an infrared diode pumps a Nd:YAG or Nd:YVO_4 crystal. The emitted beam is then frequency doubled, typically with a $KTiOPO_4$ (KTP) crystal.
- medical instruments with a variety of wavelengths in ophthalmology, dermatology, cosmetics (hair removal, tattoo removal).
- various other uses, such as remote control, position detection, distance measurement, printing, scientific instrumentation.

The market for photonic devices is much more dynamic than the electronics market. An example is the rapid change of dominating laser applications. For diode lasers, the two most prominent applications are telecommunication (77% market share in 2000, 25% in 2003, 45% in 2008) and optical data storage (17% market share in 2000, 60% in 2003, 44% in 2008).

23.4.3 Gain

Due to current injection,[17] a nonequilibrium carrier distribution is created. After fast thermalization processes (phonon scattering), it can mostly described by quasi-Fermi levels. Sufficiently strong pumping leads to inversion, i.e. conduction-band states are more strongly populated with electrons than valence-band states (Fig. 23.33). In this case, the stimulated emission rate is stronger than the absorption rate (cf. Sect. 10.2.6). The thermodynamic laser condition (cf. (10.23)) requires the difference of

[16] 16 million 405 nm laser diodes were shipped in 2006–2008. 85% of those are built into SONY's PS3, the rest into HD-DVD and other Blu-ray™disc (BD) players.

[17] or due to optical pumping. If electrical contacts are not available, the laser action can be invoked by supplying a high-intensity light beam, possibly in a stripe-like shape. For optically pumped semiconductor lasers see Sect. 23.4.15.

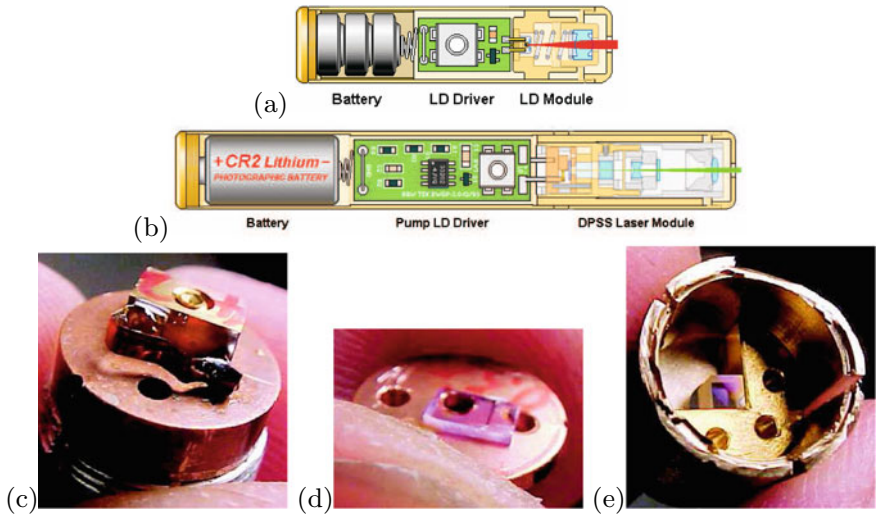

Fig. 23.32 **a** Scheme of red laser pointer, **b** scheme of green laser pointer. Parts of a green laser pointer: **c** pump laser diode, **d** YVO_4 crystal, **e** KTP doubler

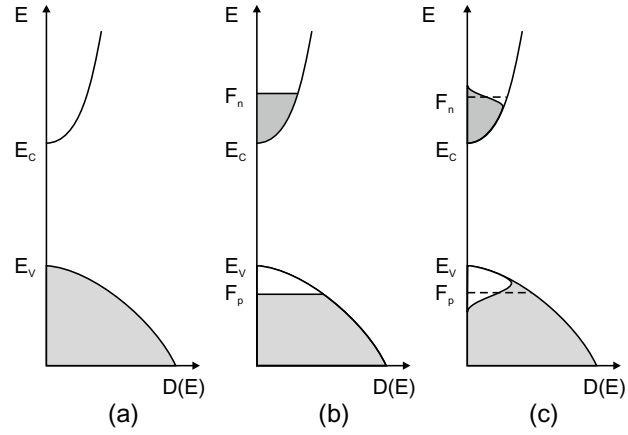

Fig. 23.33 Population **a** in thermodynamic equilibrium $T = 0\,\mathrm{K}$, **b** under inversion for $T = 0\,\mathrm{K}$, **c** under inversion for $T > 0\,\mathrm{K}$. *Shaded areas* are populated with electrons

the quasi-Fermi levels to be larger than the band gap.

$$F_\mathrm{n} - F_\mathrm{p} > E_\mathrm{g} \tag{23.10}$$

The gain is defined as the (frequency-dependent) coefficient $g(\hbar\omega)$ that describes the light intensity along a path L according to

$$I(L) = I(0)\,\exp(g\,L)\ . \tag{23.11}$$

The gain spectrum as a function of the photon energy $\hbar\omega$ is given for non-k-conserving recombination by (cf. (10.5) and (10.6))

$$g(\hbar\omega) = \int_0^{\hbar\omega - E_\mathrm{g}} D_\mathrm{e}(E) D_\mathrm{h}(E') \left[f_\mathrm{e}(E) f_\mathrm{h}(E') - (1 - f_\mathrm{e}(E))(1 - f_\mathrm{h}(E')) \right] \mathrm{d}E\ , \tag{23.12}$$

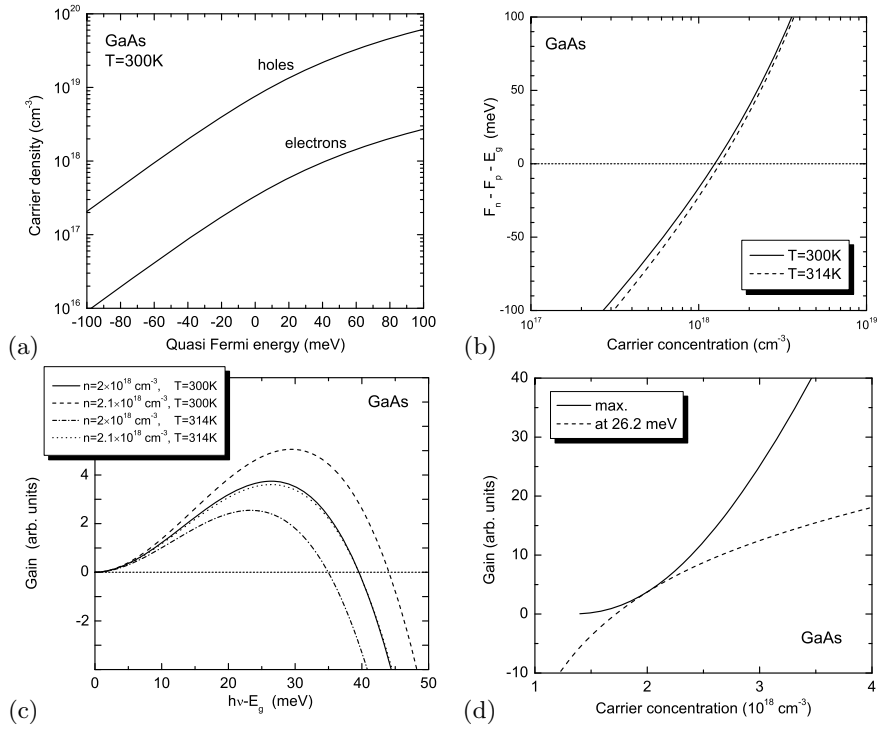

Fig. 23.34 Gain in the two-band model for GaAs. **a** Electron and hole concentrations at $T = 300\,\mathrm{K}$ as a function of the quasi-Fermi energies counted relative to the band edges, i.e. $F_\mathrm{n} - E_\mathrm{C}$ and $E_\mathrm{V} - F_\mathrm{p}$. **b** Difference of quasi-Fermi levels as a function of carrier concentration ($n = p$) for GaAs at two different temperatures. **c** Gain spectra according to (23.12) for $n = 2 \times 10^{18}$ and $T = 300\,\mathrm{K}$ (*solid line*), increased carrier density $n = 2.1 \times 10^{18}$ and $T = 300\,\mathrm{K}$ (*dashed line*), higher temperature $n = 2 \times 10^{18}$ and $T = 314\,\mathrm{K}$ (*dash-dotted line*) and same difference of the quasi-Fermi levels as for the *solid line*, $n = 2.1 \times 10^{18}$ and $T = 314\,\mathrm{K}$ (*dotted line*). **d** Maximum gain (*solid line*) and gain at a particular energy (*dashed line*, for photon energy $E_\mathrm{g} + 26.2\,\mathrm{meV}$ for which the gain is maximal for $n = 2 \times 10^{18}$ and $T = 300\,\mathrm{K}$, see *solid line* in part **c**)

with $E' = \hbar\omega - E_\mathrm{g} - E$. The gain is positive for those photon energies for which light is amplified and negative for those that are absorbed. In Fig. 23.34a, the electron and hole concentrations are shown for GaAs as a function of the quasi-Fermi energies. In Fig. 23.34b, the difference of the quasi-Fermi energies is shown as a function of the carrier density (for neutrality $n = p$). The gain spectrum is shown in Fig. 23.34c for a simple two-band model.[18] For a more elaborate discussion of such matters we refer to [1979]. In the case of inversion, the gain is positive for energies between E_g and $F_\mathrm{n} - F_\mathrm{p}$. At $\hbar\omega = F_\mathrm{n} - F_\mathrm{p}$, the gain is zero (transparency) and for larger energies negative (positive absorption coefficient). The agreement of experimental gain spectra of quantum wells with theoretical considerations, including carrier collision effects at the level of quantum kinetic theory in the Markovian limit, is very good (Fig. 23.35a) [1980].

For a given fixed energy, the gain increases with increasing pumping and increasing carrier density n (Fig. 23.34d). For very small density, it is given as $g(n \to 0) = -\alpha$. The gain rises around transparency approximately linearly with the pumping intensity. At transparency carrier density n_tr, the gain is zero. Therefore, the relation $g(n)$ can be approximated as (linear gain model)

[18] One electron and one hole band are considered; the heavy and light hole bands are taken into account via the mass according to (6.73).

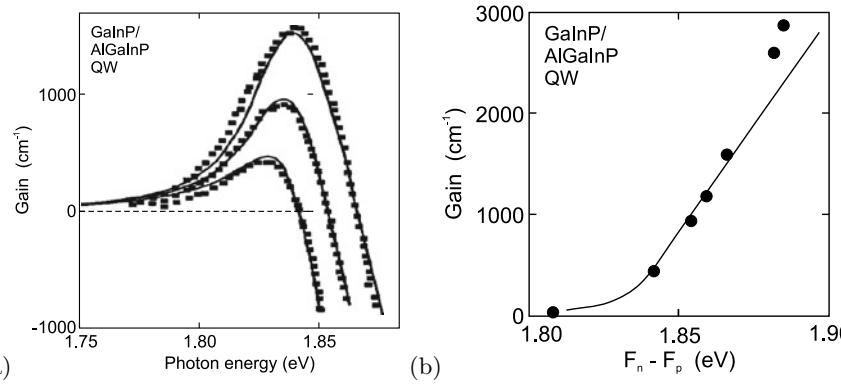

Fig. 23.35 **a** Gain spectra of a 6.8 nm thick $Ga_{0.41}In_{0.59}P/(Al_{0.5}Ga_{0.5})_{0.51}\ In_{0.49}P$ quantum well, experimental data (*symbols*) and theory (*lines*) for three different sheet carrier densities $n_{2D} = 2.2$, 2.7, and $3.2 \times 10^{12}\,\mathrm{cm}^{-2}$. **b** Maximum gain as a function of the separation of the quasi-Fermi levels, experimental data (*symbols*) and theory (*lines*). Adapted from [1980]

$$g(n) \cong \hat{\alpha}\,\frac{n - n_{\mathrm{tr}}}{n_{\mathrm{tr}}}\ . \tag{23.13}$$

For large carrier density, the gain saturates (at a value similar to α). The onset of positive gain is related to the separation of the quasi-Fermi levels being larger than the band gap (23.10), Fig. 23.35b. The gain in quantum dot lasers [150] has been discussed in [1981].

23.4.4 Optical Mode

The light wave that is amplified must be guided in the laser. An optical cavity is needed to provide optical feedback such that the photons travel several times through the gain medium and contribute to amplification. We explain the light-wave management for the edge emitter first:

Vertical Mode Guiding

In the course of the historical development of the semiconductor laser, the most significant improvements (reduction of lasing threshold current) have been achieved through the improvement of the overlap of the optical wave with the gain medium, as shown in Fig. 23.36. From homojunctions over the single heterojunction, eventually the double heterostructure (DHS) design could reduce the laser threshold current density to the $1\,\mathrm{kA/cm}^2$ level.

The band diagram of a double heterostructure is shown in Fig. 23.37 for zero and forward bias. In the DHS, the optical mode is guided by total reflection within the low band gap center layer (core), which has a larger index of refraction than the outer, large band gap layer (cladding).[19] When the layer thickness is in the range of λ/n_{r}, the form of the optical mode is determined by the (one-dimensional) wave equation (19.3) for the electrical field E_z. In Fig. 23.38a, the shape of the optical mode for $GaAs/Al_{0.3}Ga_{0.7}As$ DHS with different GaAs thickness is shown.

The optical confinement factor Γ is the part of the wave that has geometrical overlap with the gain medium, i.e. is subject to amplification. It is shown for $GaAs/Al_xGa_{1-x}As$ DHS with different GaAs thickness and different Al concentration in Fig. 23.38b. The modal gain g_{mod} that is responsible for light amplification in the cavity consists of the material gain g_{mat} due to inversion and the optical confinement factor.

[19] A smaller band gap coincides in many cases with a larger index of refraction.

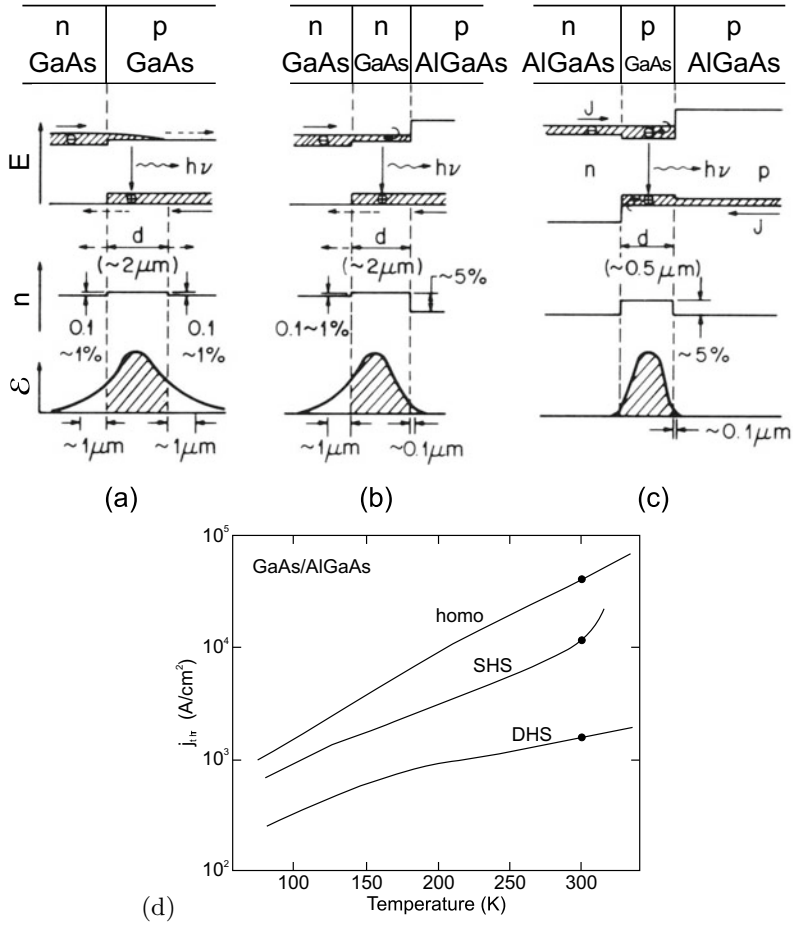

Fig. 23.36 Laser with **a** homojunction, **b** single heterostructure (SHS), **c** double heterostructure ('DHS'), **d** reduction of threshold current with design progress ('SHS': $d = 2\,\mu$m, 'DHS': $d = 0.5\,\mu$m). Adapted from [1982]

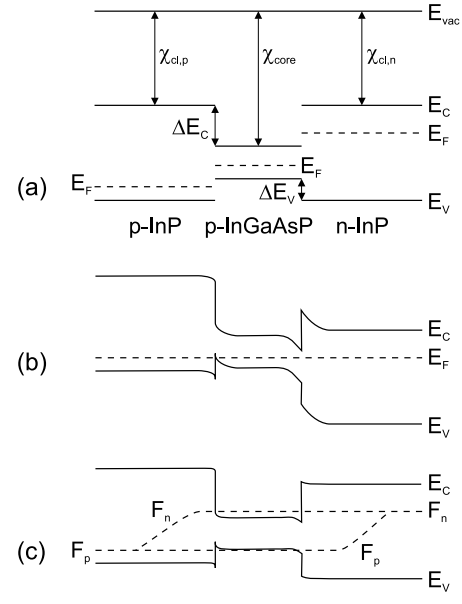

Fig. 23.37 Schematic band diagram of a pn double heterostructure (DHS) diode (InP/InGaAsP/InP) **a** before contact of the materials, **b** in thermodynamic equilibrium (zero bias, *dashed line* is Fermi level E_F = const.), **c** with forward bias close to flat-band conditions, *dashed lines* are quasi-Fermi levels. χ_{core} denotes the electron affinity of the core material, χ_{cl} that of the cladding layers

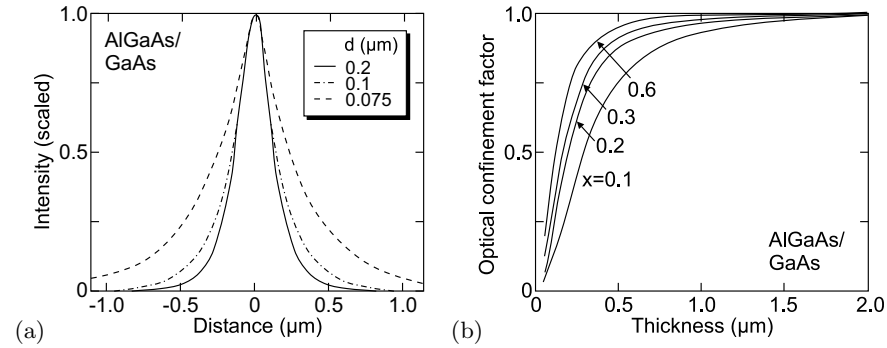

Fig. 23.38 **a** Optical mode (relative intensity) for various values of the thickness d of the active layer as labeled of a GaAs/$Al_{0.3}Ga_{0.7}As$ DHS laser, **b** Optical confinement factor Γ as a function of the thickness of the active layer and the Al concentration x of the barrier as labeled in a GaAs/$Al_xGa_{1-x}As$ DHS laser. Adapted from [1976]

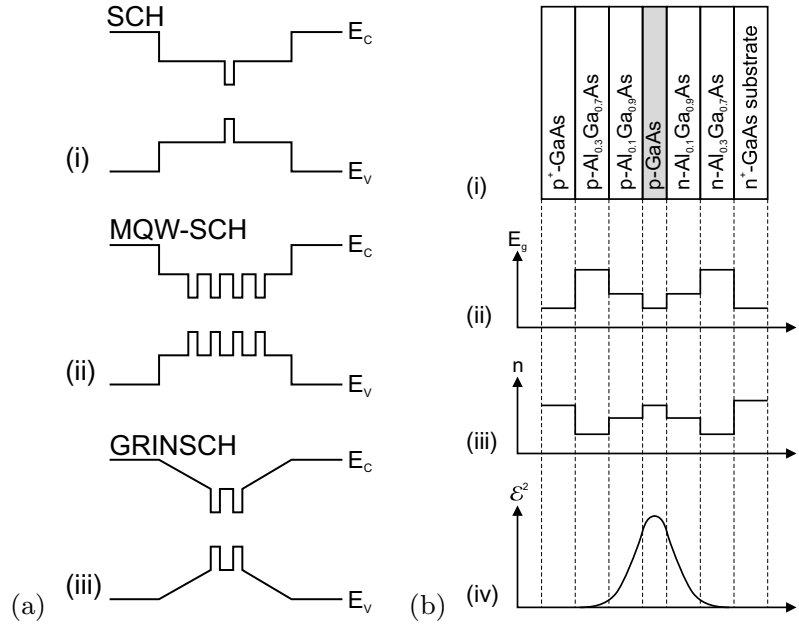

Fig. 23.39 **a** Various geometries of the active layer of a DHS laser with quantum wells as active medium, (**i**) single QW (separate confinement heterostructure, SCH), (**ii**) multiple QW SCH, and **c** GRINSCH (graded-index SCH) structure. **b** Layer sequence for a separate confinement heterostructure laser

$$g_{\mathrm{mod}} = \Gamma\, g_{\mathrm{mat}} \,. \tag{23.14}$$

In order to allow simultaneous optimization of the light mode and the carrier confinement, the separate confinement heterostructure (SCH) has been designed. Here, a single or multiple quantum well of a third material with even smaller band gap is the active medium (Fig. 23.39a,b,d). A single quantum well has an optical confinement factor of a few per cent only. It offers, however, efficient carrier capture and efficient radiative recombination. An increase in the carrier capture efficiency can be achieved using a graded index in the barrier (GRINSCH, Fig. 23.39c).

The thin wave-guiding layer leads to large divergence of the laser beam along the vertical direction, typically about 90°. The strong confinement of light also limits the maximum achievable output power due to catastrophic optical damage (COD). Several ideas have been realized to overcome this problem and achieve much smaller divergence of about 18°. The waveguide can be designed to be very thick (large optical cavity, LOC) that leads to an increase of threshold. Other schemes are insertion of a

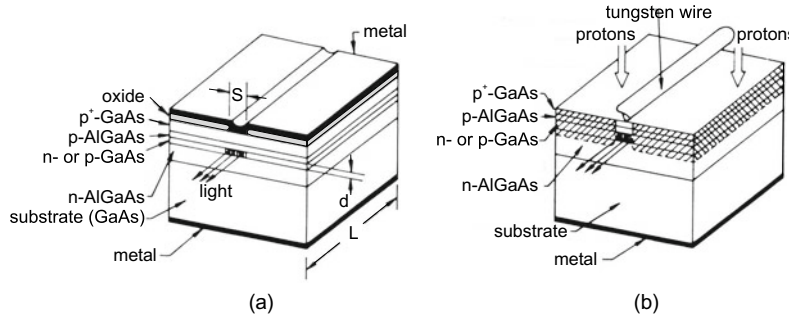

Fig. 23.40 Scheme of gain-guided lasers with stripe contact: **a** oxide stripe, **b** proton implanted with shadow mask from tungsten wire ($\sim 10\,\mu m$). Adapted from [1983]

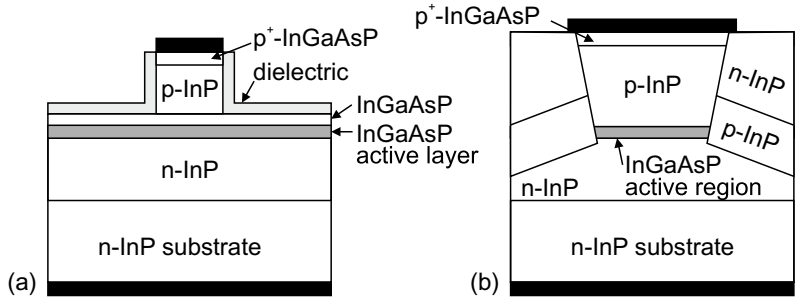

Fig. 23.41 Schematic cross section of index-guided lasers: **a** shallow ridge, **b** deep etch and regrowth. *Black areas* are metal contacts

low-index layer into the confinement layer, insertion of a high-index layer into the cladding layer or the use of high-index quarter-wavelength reflecting layers [1984].

Lateral Mode Guiding

Lateral waveguiding can be achieved with gain guiding and index guiding (or a mixture of the two). In the gain-guiding scheme (Fig. 23.40), the current path that is defined by the stripe contact and the current spreading underneath it, defines the gain region and therefore the volume of amplification that guides the optical wave. Since a high carrier density reduces the index of refraction, a competing antiguiding effect can occur. For index guiding, the lateral light confinement is caused by a lateral increase of the index of refraction. This index modulation can be achieved by using a mesa-like contact stripe (Fig. 23.41a). A shallow mesa reaches down into the upper cladding, a deep mesa reaches down into or through the active layer. Possible problems with surface recombination can be avoided by regrowth of the structure (Fig. 23.41b) with a wide band gap material (compared to the active layer). Optimization of regrowth is targeted to achieve a well-defined surface for subsequent contact processing. A lateral pn-diode can be incorporated that avoids current spreading in the upper part of the structure.

Depending on the width of the lateral mode, it can be monomode or multimode (Fig. 23.42a,b). For laterally monomode lasers, the stripe width may only be a few μm. In particular for such lasers, the current spreading must be controlled. Problems can arise for wide stripe widths due to current filamentation and inhomogeneous laser emission from the facet. Since the optical mode is typically more confined in the growth direction than in the lateral direction, the far field is asymmetric (Fig. 23.43a,b). The vertical axis has the higher divergence and is called the fast axis. The lateral axis is called the slow axis. The asymmetric beam shape is detrimental when the laser needs to be coupled into an optical fiber or a symmetric beam profile is needed for subsequent optics. The beam can be made symmetric using special optic components such as anamorphic prisms (Fig. 23.43c) and graded-index lenses. The beam from a laterally monomode laser is diffraction limited and can therefore generally be refocused efficiently (beam quality $M^2 \gtrsim 1$).

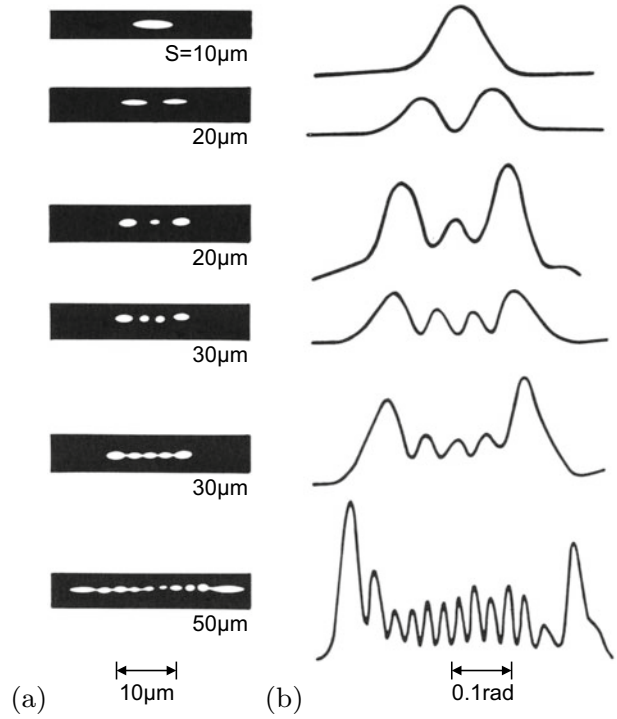

Fig. 23.42 Lateral near field **a** and far field **b** of lasers with various width S of the injection stripe as labeled. Adapted from [1985]

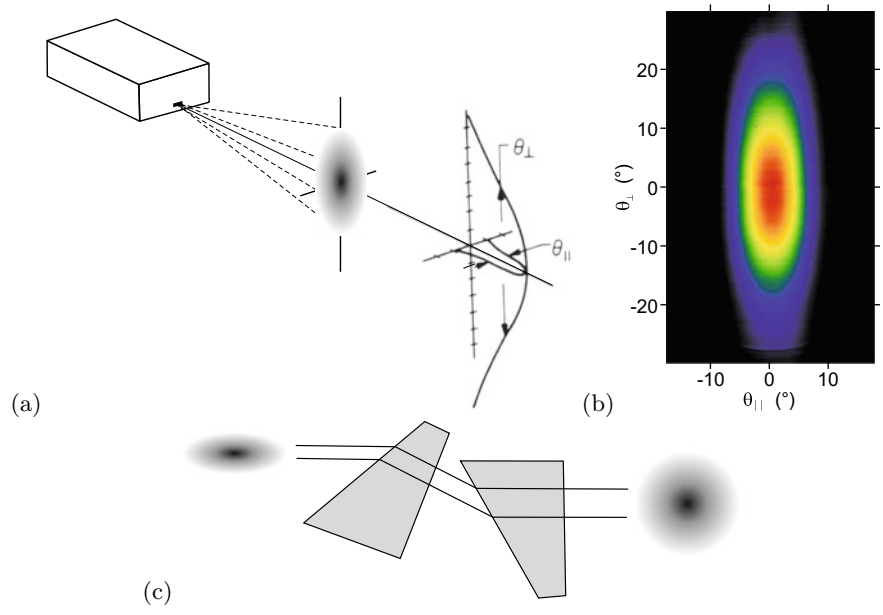

Fig. 23.43 **a** Schematics of the asymmetric far field of an edge emitter. Adapted from [574]. **b** Far-field distribution of violet GaN-based laser. Adapted from [1986]. **c** Correction of asymmetric far field with a pair of anamorphic prisms

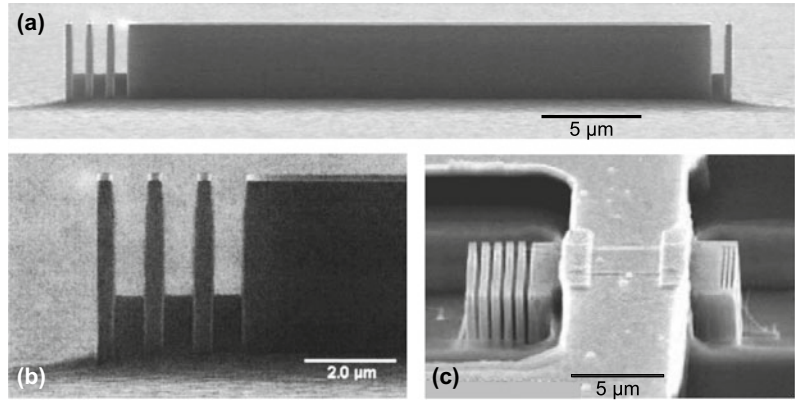

Fig. 23.44 SEM image of **a** an InP microlaser with third-order Bragg mirrors, **b** magnified view of the front facet with three slabs, **c** a 12-µm long microlaser with five third-order mirrors on the rear side and three first-order mirrors on the front side with top contact. From [1988]; part **b** reprinted with permission from [1987], ©2001 AIP

Longitudinal Modes

The spectral positions of the laser modes for a cavity with length L is given by the condition (cf. (19.39))

$$L = \frac{m\,\lambda}{2\,n_\mathrm{r}(\lambda)}\ , \tag{23.15}$$

where m is a natural number and $n(\lambda)$ is the dispersion of the index of refraction. The distance of neighboring modes is given by (for large m)

$$\Delta\lambda = \frac{\lambda^2}{2\,n_\mathrm{r}\,L\left(1 - \frac{\lambda}{n_\mathrm{r}}\frac{\mathrm{d}n_\mathrm{r}}{\mathrm{d}\lambda}\right)}\ . \tag{23.16}$$

The dispersion $\mathrm{d}n_\mathrm{r}/\mathrm{d}\lambda$ can sometimes be neglected.

The facets of edge-emitting lasers are typically cleaved. Cleaving bears the danger of mechanical breakage and tends to have poor reproducibility, low yield and therefore high cost. Etched facets are another possibility to form the cavity mirror. The etch process, typically reactive ion dry etching, must yield sufficiently smooth surfaces to avoid scattering losses. A highly efficient distributed Bragg mirror (cf. Sect. 19.1.4) with only a few periods can be created by using the large index contrast between the semiconductor and air. As shown in Fig. 23.44, slabs can be etched that make a Bragg mirror with the air gaps [1987]. In this way, very short longitudinal cavities can be made ($\approx 10\,\mu\mathrm{m}$).

23.4.5 Loss Mechanisms

While the light travels through the cavity, it is not only amplified but it also suffers losses. The internal loss α_i and the mirror loss α_m contribute to the total loss α_tot

$$\alpha_\mathrm{tot} = \alpha_\mathrm{i} + \alpha_\mathrm{m}\ . \tag{23.17}$$

The internal loss is due to absorption in the cladding, scattering at waveguide inhomogeneities and possibly other processes. It can be written as

$$\alpha_\mathrm{i} = \alpha_0\,\Gamma + \alpha_\mathrm{g}\,(1 - \Gamma)\ , \tag{23.18}$$

where α_0 is the loss coefficient in the active medium and α_g is the loss coefficient outside the active medium.

The mirror loss is due to the incomplete reflection of the optical wave at the laser facets. This condition is necessary, however, to observe a laser beam outside the cavity. R_1 and R_2 are the values of reflectance of the two facets, respectively. An as-cleaved facet has a reflectance of about 30% (cf. (23.8)). Using dielectric layers on the facets, the reflectance can be increased (high reflection, HR-coating) or decreased (antireflection, AR-coating). One round-trip through the cavity of length L has the length $2L$. The intensity loss due to reflection at the facets is expressed via $\exp(-2\alpha_m L) = R_1\, R_2$

$$\alpha_m = \frac{1}{2L} \ln\left(\frac{1}{R_1\, R_2}\right) . \tag{23.19}$$

If both mirrors have the same reflectance R, we have $\alpha_m = -L^{-1} \ln R$. For $R = 0.3$ a 1-mm cavity has a loss of $12\,\mathrm{cm}^{-1}$. For the internal loss a typical value is $10\,\mathrm{cm}^{-1}$, very good waveguides go down to $1\text{–}2\,\mathrm{cm}^{-1}$.

Lasing is only possible if the gain overcomes all losses (at least for one wavelength), i.e.

$$g_{mod} = g_{mat}\, \Gamma \geq \alpha_{tot} . \tag{23.20}$$

23.4.6 Threshold

When the laser reaches threshold, the (material) gain is pinned at the threshold value

$$g_{thr} = \frac{\alpha_i + \alpha_m}{\Gamma} . \tag{23.21}$$

Since $g \propto n$, the carrier density is also pinned at its threshold value and does not increase further with increasing injection current. Instead, additional carriers are quickly converted into photons by stimulated emission. The threshold carrier density is (using the linear gain model, cf. (23.13))

$$n_{thr} = n_{tr} + \frac{\alpha_i + \alpha_m}{\hat{\alpha}\, \Gamma} . \tag{23.22}$$

For an active layer of thickness d, the threshold current density is

$$j_{thr} \cong \frac{e\, d\, n_{thr}}{\tau(n_{thr})} , \tag{23.23}$$

where $\tau(n_{thr})$ is the (minority) carrier lifetime at the threshold carrier density (cmp. Sect. 10.10) from

$$\tau(n) = \frac{1}{A + B\, n + C\, n^2} . \tag{23.24}$$

Using (23.22), we can write (for $R = R_1 = R_2$)

$$j_{thr} = j_{tr} + \frac{e\, d}{\tau\, \hat{\alpha}\, \Gamma} \left(\alpha_i - \frac{1}{L} \ln R\right) , \tag{23.25}$$

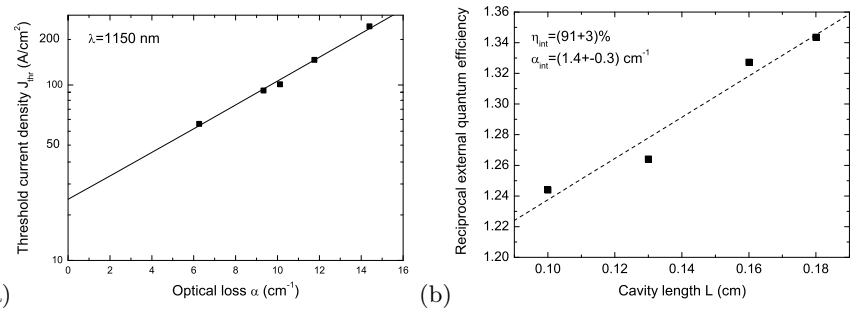

Fig. 23.45 **a** Threshold current density for (three-fold InGaAs/GaAs QD stack) laser ($\lambda = 1150\,\text{nm}$) at 10°C with different cavity length vs. the optical loss ($\propto 1/L$). The extrapolated transparency current density is $21.5 \pm 0.9\,\text{A/cm}^2$. **b** Inverse external quantum efficiency versus cavity length. The internal quantum efficiency determined from the plot is 91% and the internal loss is $1.4\,\text{cm}^{-1}$

where the transparency current density is $j_{\text{tr}} = e\,d\,n_{\text{tr}}/\tau$. Thus, the plot of j_{thr} versus $1/L$ (or the optical loss) should be linear and can be extrapolated towards the transparency current density (cf. Fig. 23.45a).

Any additional increase of the current j leads to stimulated emission with the rate

$$r_{\text{st}} = d\,v_{\text{g}}\,g_{\text{thr}}\,N_{\text{ph}}\ , \tag{23.26}$$

where v_{g} is the group velocity (mostly c_0/n_{r}) and N_{ph} is the photon density (per length) in the cavity. The photon density increases linearly beyond the threshold

$$N_{\text{ph}} = \frac{1}{e\,d\,v_{\text{g}}\,g_{\text{thr}}}\,(j - j_{\text{thr}})\ . \tag{23.27}$$

The photon lifetime

$$\frac{1}{\tau_{\text{ph}}} = v_{\text{g}}\,(\alpha_{\text{i}} + \alpha_{\text{m}}) = v_{\text{g}}\,\Gamma\,g_{\text{thr}} \tag{23.28}$$

is introduced that describes the loss rate of photons. $v_{\text{g}}\,\alpha_{\text{m}}$ describes the escape rate of photons from the cavity into the laser beam(s). Therefore,

$$N_{\text{ph}} = \frac{\tau_{\text{ph}}\,\Gamma}{e\,d}\,(j - j_{\text{thr}})\ . \tag{23.29}$$

Since the threshold depends on the carrier density, it is advantageous to reduce the active volume further and further. In this way, the same *amount* of injected carriers creates a larger carrier *density*. Figure 23.46 shows the historic development of laser threshold due to design improvements.

23.4.7 Spontaneous Emission Factor

The spontaneous emission factor β is the fraction of spontaneous emission (emitted into all angles) that is emitted into laser modes. For Fabry–Perot lasers, β is typically in the order of 10^{-4}–10^{-5}. The design of a microcavity can increase β drastically by several orders of magnitude to ≈ 0.1 [1989] or above and thus reduce the threshold current. The photon number as a function of the pump current can

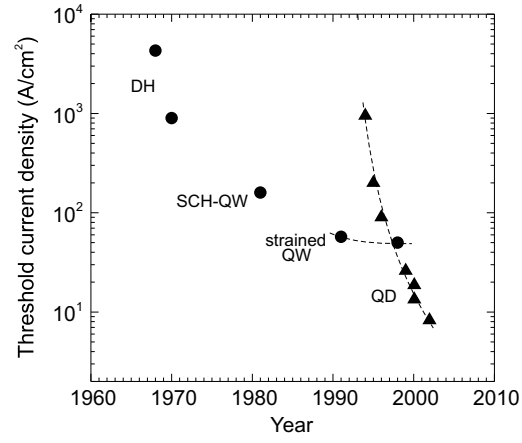

Fig. 23.46 Historic development of threshold current density (at room temperature, extrapolated for infinite cavity length and injection stripe width) for various laser designs, 'DH': double heterostructure, 'SCH–QW': separate confinement heterostructure with quantum wells. 'QD': quantum dots. *Dashed lines* are guides to the eye

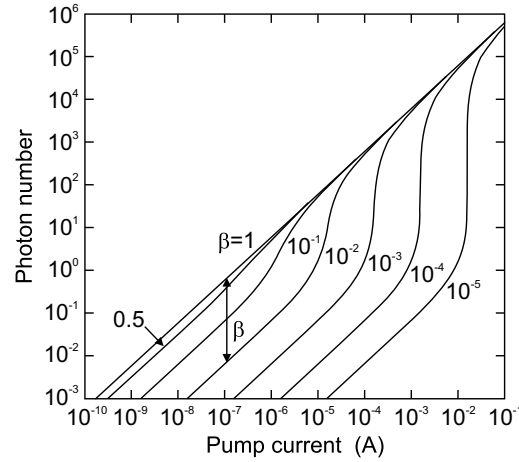

Fig. 23.47 Photon number versus pump current for a model laser. Adapted from [1991]

be calculated from the laser rate equations and is depicted in Fig. 23.47. For $\beta = 1$, all emitted power goes into the laser mode regardless of whether emission is spontaneous or stimulated. The definition of threshold in such 'nonclassical' lasers with large β is discussed in detail in [1990].

23.4.8 Output Power

The output power is given by the product of photon energy, the photon density in the cavity, the effective mode volume and the escape rate:

$$P_{\text{out}} = \hbar\omega\, N_{\text{ph}}\, \frac{L\, w\, d}{\Gamma}\, v_{\text{g}}\, \alpha_{\text{m}}\ . \tag{23.30}$$

Thus, it is given by

$$P_{\text{out}} = \hbar\omega\, v_{\text{g}}\, \alpha_{\text{m}}\, \frac{\tau_{\text{ph}}}{e}\, L\, w\ (j - j_{\text{thr}}) = \frac{\hbar\omega}{e}\, \frac{\alpha_{\text{m}}}{\alpha_{\text{m}} + \alpha_{\text{i}}}\ (I - I_{\text{thr}})\ . \tag{23.31}$$

To this equation, the factor η_{int} must be added. The internal quantum efficiency describes the efficiency of the conversion of electron–hole pairs into photons (cmp. (10.59)):

$$\eta_{\text{int}} = \frac{B\,n^2 + v_{\text{g}}\,g_{\text{thr}}\,N_{\text{ph}}}{A\,n + B\,n^2 + C\,n^3 + v_{\text{g}}\,g_{\text{thr}}\,N_{\text{ph}}} \,. \tag{23.32}$$

All in all, now (see Fig. 23.49a)

$$P_{\text{out}} = \frac{\hbar\omega}{e}\,\frac{\alpha_{\text{m}}}{\alpha_{\text{m}} + \alpha_{\text{i}}}\,\eta_{\text{int}}\,(I - I_{\text{thr}}) \,. \tag{23.33}$$

The differential (or slope) quantum efficiency, also called the external quantum efficiency η_{ext}, is the slope of the P_{out} curve versus the current in the lasing regime. It is given by

$$\eta_{\text{ext}} = \frac{\mathrm{d}P_{\text{out}}/\mathrm{d}I}{\hbar\omega/e} = \eta_{\text{int}}\,\frac{\alpha_{\text{m}}}{\alpha_{\text{m}} + \alpha_{\text{i}}} \,. \tag{23.34}$$

The external quantum efficiency can also be written as

$$\frac{1}{\eta_{\text{ext}}} = \frac{1}{\eta_{\text{int}}}\left(1 + \frac{\alpha_{\text{i}}}{\alpha_{\text{m}}}\right) = \frac{1}{\eta_{\text{int}}}\,[1 - 2\alpha_{\text{i}}\,L\,\ln(R_1 R_2)] \,. \tag{23.35}$$

Therefore, if η_{ext}^{-1} is plotted for similar lasers with different cavity length (see Fig. 23.45b), a straight line should arise from which the internal quantum efficiency (extrapolation to $L \to 0$) and the internal loss ($\propto$ slope) can be determined experimentally.

The threshold current for a given laser is typically determined from the P–I characteristic via extrapolation of the linear regime as shown in Fig. 23.49a. Other measures of the threshold current can be the change in junction resistance, the narrow peak in excess noise or the peak in the logarithmic derivative of mode power. The S-shaped curve of the power in the dominant mode (of a single-mode laser) as a function of voltage (Fig. 23.48), similar to the S-shaped curves of Fig. 23.47 has been discussed in [1992]. A related discussion of laser dynamics (cmp. Sect. 23.4.13) can be found in [1993].

Record values for the threshold current density are often given for the limit $L \to \infty$. Due to current spreading, the threshold current density also depends on the width of the injection stripe. Record low thresholds are therefore often given for the limit $w \to \infty$.

The total quantum efficiency is given by

$$\eta_{\text{tot}} = \frac{P_{\text{out}}/I}{\hbar\omega/e} \,. \tag{23.36}$$

This quantity is shown in Fig. 23.49b for a laser as a function of the current. For a linear P–I lasing characteristic, the total quantum efficiency converges towards the external quantum efficiency for high currents because the low quantum efficiency subthreshold regime no longer plays any role. Another important figure of merit is the wall-plug efficiency η_{w} that describes the power conversion:

$$\eta_{\text{w}} = \frac{P_{\text{out}}}{U\,I} \,. \tag{23.37}$$

Additionally to the current balance discussed so far, typically a leakage current exists that flows without contributing to recombination or lasing. Carriers not captured into or escaping from the active layers can contribute to this current. The present record for wall-plug efficiency of high-power laser diodes is above 70% [1994, 1995], employing careful control of band alignment (graded junctions, avoiding

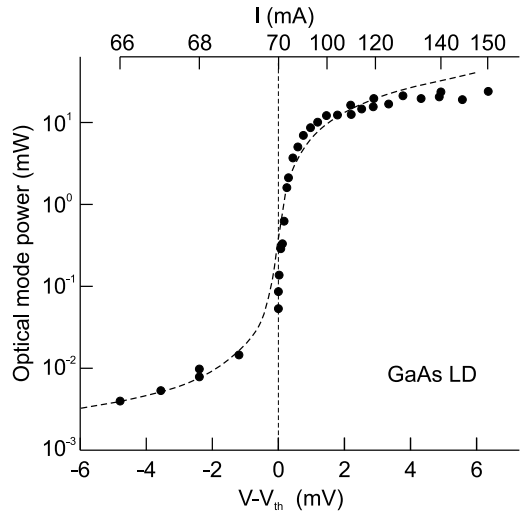

Fig. 23.48 Optical power (experimental data and modelling) in the dominant mode of a single-mode GaAs laser diode (Hitachi HLP 1400) as a function of voltage (in pulsed operation in order to avoid heating effects) around the threshold voltage V_{th}. Adapted from [1992]

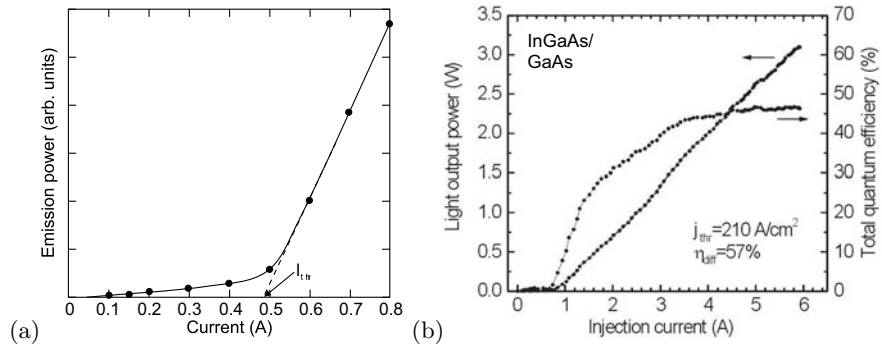

Fig. 23.49 **a** Typical P–I characteristic of a semiconductor laser. Adapted from [574]. **b** Output power and total quantum efficiency of a quantum dot laser (3 stacks of InGaAs/GaAs QDs, $L = 2\,\mathrm{mm}$, $w = 200\,\mu\mathrm{m}$, $\lambda = 1100\,\mathrm{nm}$, $T = 293\,\mathrm{K}$) versus injection current

voltage barriers), optical losses, Joule heating, spontaneous emission and carrier leakage. It seems possible to achieve η_{w} of 80%.

The P–I characteristic is not linear to arbitrary high currents. Generally, the output power will saturate or even decrease for increasing current. These effects can be due to increasing leakage current, increasing internal loss at high current or temperature effects, e.g. an increase of threshold with increasing temperature (cf. Sect. 23.4.9) and therefore a reduction of total efficiency. All nonradiative losses will eventually show up as heat in the laser that must be managed with a heat sink.

A radical effect is catastrophic optical damage (COD) at which the laser facet is irreversible (partially) destructed. Antioxidation or protective layers can increase the damage threshold to $>$ 20 MW/cm^2. The record power from a single edge emitter is $\sim$ 12 W (200 µm stripe width). For a lateral monomode laser, cw power of about 1.2 W has been reached from a 1480-nm InGaAsP/InP double quantum-well lasers with 3–5 µm stripes and 3 mm cavity length [1996]. About 500 mW can be coupled into a single-mode fiber [1997].

23.4.9 Temperature Dependence

The threshold of a laser typically increases with increasing temperature as shown in Fig. 23.50a. Empirically, in the vicinity of a temperature T_1 the threshold follows an exponential law (see Fig. 23.50b)

$$j_{\mathrm{thr}}(T) = j_{\mathrm{thr}}(T_1)\,\exp\left(\frac{T-T_1}{T_0}\right) \propto \exp\left(\frac{T}{T_0}\right)\,, \tag{23.38}$$

with T_0 being the so-called characteristic temperature.[20] It is the inverse logarithmic slope, $T_0^{-1} = \mathrm{d}\ln j_{\mathrm{thr}}/\mathrm{d}T$.

T_0 summarizes the temperature-dependent loss and the carrier redistribution in **k**-space due to the change of the Fermi distribution with temperature. With increasing temperature, populated states below the quasi-Fermi level become unpopulated and nonlasing states become populated. Therefore, the gain decreases with increasing temperature. This redistribution must be compensated by an increase of the quasi-Fermi energy, i.e. stronger pumping. This effect is present for (even ideal) bulk, quantum well

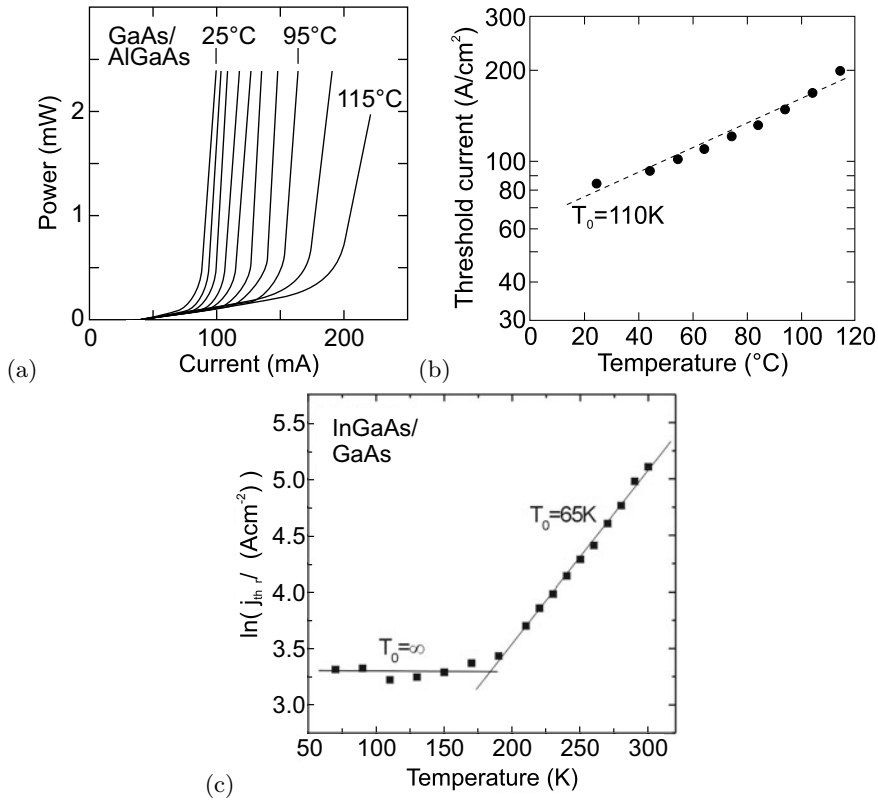

Fig. 23.50 **a** P–I characteristic (cw output power per mirror facet) of stripe-buried heterostructure laser at various temperatures of the heat sink between 25 °C and 115 °C in steps of 10 K. **b** Threshold current (in logarithmic scale) of this laser as a function of heat-sink temperature and exponential fit (*dashed line*) with $T_0 = 110$ K. Parts **a** and **b** adapted from [1998]. **c** Temperature dependence of the threshold current density of a quantum dot laser (3 stacks of InGaAs/GaAs QDs, $\lambda = 1150$ nm) with T_0 (*solid lines* are fits) given in the figure

[20] Since T_0 has the dimension of a temperature difference, it can be expressed in °C or K. For the sake of unambiguity it should be given in K.

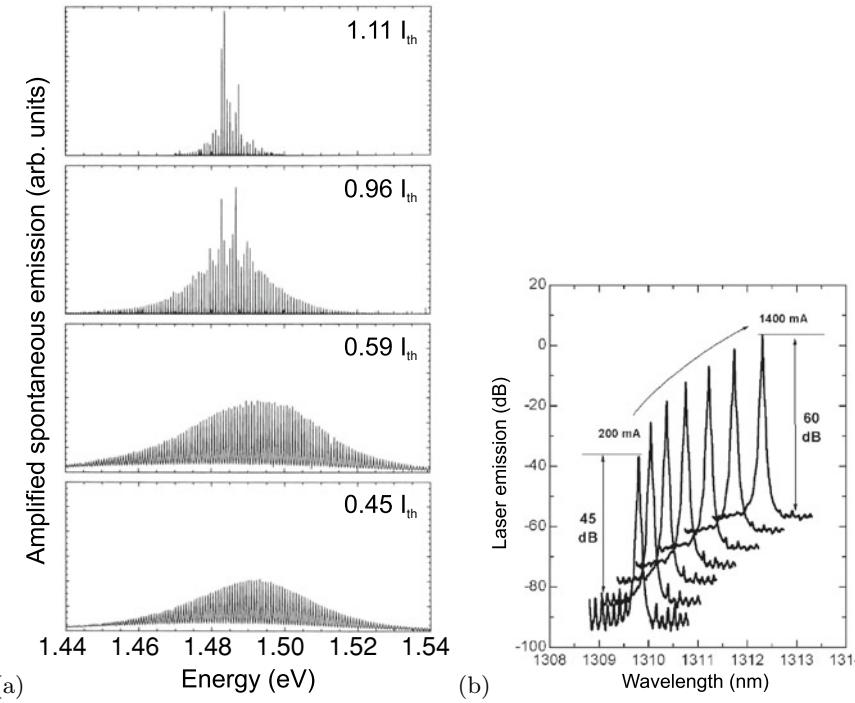

Fig. 23.51 **a** Mode spectra of a Fabry–Perot laser, under, at and above threshold ($I_{\text{thr}} = 13.5\,\text{mA}$). Adapted from [1185]. **b** Mode spectra of a cw DFB InGaAs/InP laser with 2 mm cavity length at various currents of 200, 400, . . ., 1400 mA ($I_{\text{thr}} = 65\,\text{mA}$), SSR>40 dB at $T = 293\,\text{K}$. Adapted from [1999], reproduced with permission from SPIE

and quantum wire lasers. Only for quantum dots with a δ-like density of states is the change of Fermi distribution irrelevant as long as excited states are energetically well separated from the (lasing) ground state. In Fig. 23.50c, the threshold of a quantum dot laser is indeed temperature independent ($T_0 = \infty$) as long as excited states are not thermally populated (for $T < 170\,\text{K}$ for the present laser).

23.4.10 Mode Spectrum

In Fig. 23.51a, the mode spectrum of a typical edge-emitting laser is shown. Below threshold, the amplified spontaneous emission (ASE) spectrum exhibits a comb-like structure due to the Fabry–Perot modes. Above threshold, some modes grow much faster than others, possibly resulting in single longitudinal mode operation at high injection. The relative strength of the strongest side mode is expressed through the side-mode suppression ratio (SSR) in dB

$$SSR = 10\,\log\left(\frac{I_{\text{mm}}}{I_{\text{sm}}}\right)\,, \tag{23.39}$$

where I_{mm} (I_{sm}) is the intensity of the maximum (strongest side) mode in the lasing spectrum.

As a tendency a DHS or QW semiconductor laser above threshold develops a narrow spectrum since the pump power is channeled into one or few modes with large gain. A quantum dot laser behaves differently when pumped largely above threshold. Since the gain of individual QDs in an inhomogeneously broadened ensemble (due to different QD sizes) is independent, a broad gain spectrum is

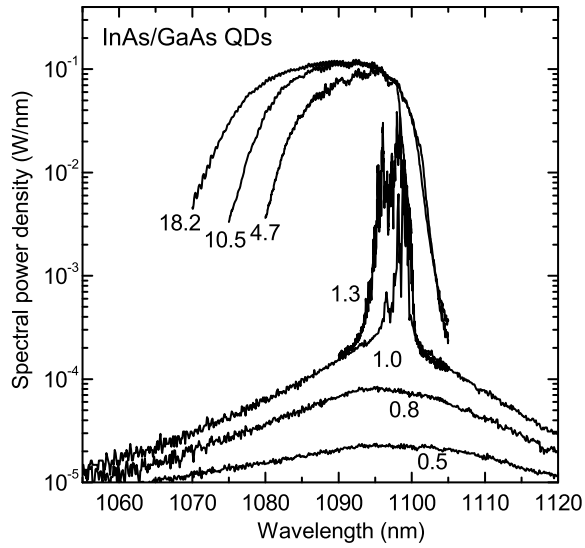

Fig. 23.52 Lasing spectra of quantum dot laser ($L = 1.2\,\text{mm}$, stripe width $w = 75\,\mu\text{m}$) at room temperature. The active medium is a three-fold stack of InGaAs/GaAs QDs. The current density as labeled is given in units of the threshold current density ($j_{\text{thr}} = 230\,\text{A/cm}^2$). Adapted from [2000]

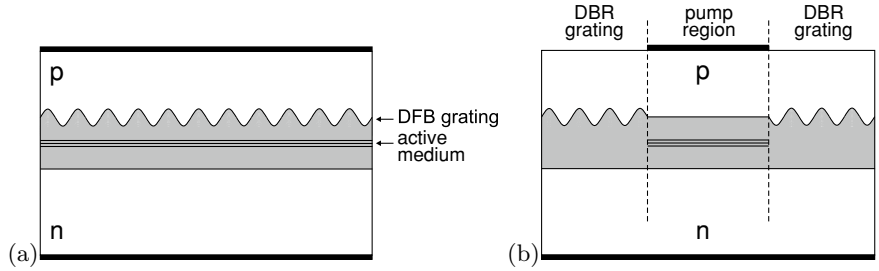

Fig. 23.53 Schematic drawing of **a** DFB (distributed feedback) and **b** DBR (distributed Bragg reflection) lasers. The active medium is schematically shown as a triple quantum well, the waveguide is shown as a *grey area*

present [2001]. The lasing spectrum takes a hat-like shape when homogeneous broadening is small compared to the inhomogeneous broadening[2000, 2002] (Fig. 23.52) as predicted theoretically [2001, 2003].

23.4.11 Longitudinal Single-Mode Lasers

In order to achieve a high SSR or single longitudinal mode lasing, the feedback must offer a higher wavelength selectivity than a simple mirror. A preferential feedback for certain modes can be obtained using a periodic dielectric structure that 'fits' to a particular wavelength, similar to a Bragg mirror. The periodic modulation of the refractive index can be made within the cavity (distributed feedback, DFB, Fig. 23.53a) or at the mirror (distributed reflection, DBR, Fig. 23.53b). In this way, monochromatic lasers with SSR $\gg 30\,\text{dB}$ are possible (Fig. 23.51b).

It is possible to couple several hundred mW optical power of a laterally and spectrally monomode laser into a monomode optical fiber [2004] (Fig. 23.54).

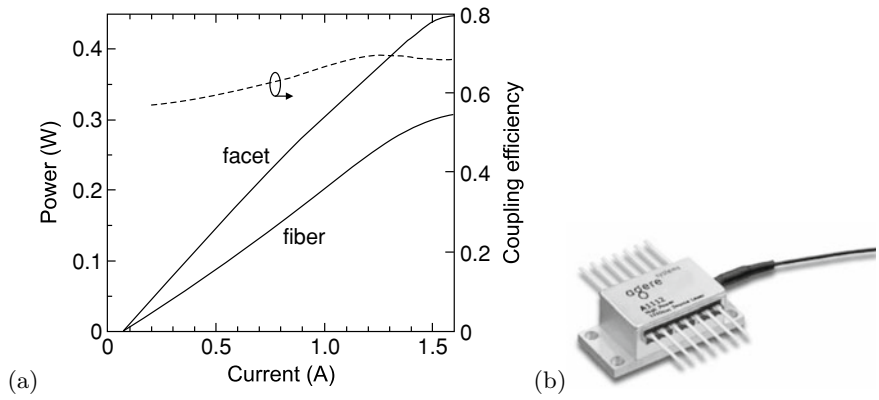

Fig. 23.54 **a** Output power of an InGaAsP/InP cw single-mode DFB laser at 1427 nm with 2 mm cavity length from the facet and coupled to a single-mode fiber versus driving current ($T = 293$ K). The *dashed* line represents the coupling efficiency to the fiber (right scale). Adapted from [2004]. **b** Package with pigtail of fiber coupled 1550 nm DFB laser with 40 mW output power in the fiber. From [2005]

23.4.12 Tunability

The tunability of the emission wavelength [2006] is important for several applications such as wavelength division multiplexing[21] and spectroscopy.

The simplest possibility to tune a laser is to vary its temperature and thus its band gap. This method is particularly used for lead salt lasers in the mid-infrared region,[22] as shown in Fig. 23.55.

For monomode lasers, mode hopping, i.e. the discontinuous shift of lasing wavelength (or gain maximum) from one mode to the next, poses a problem for continuous tuning, as shown in Fig. 23.56. The continuous shift of emission wavelength is due to the temperature dependence of the index of

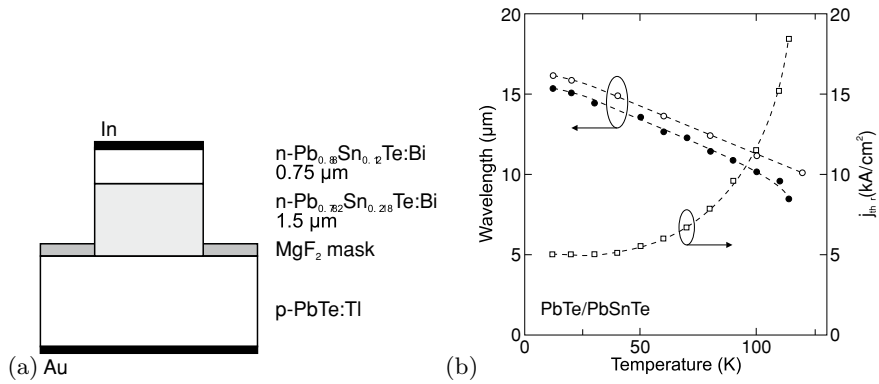

Fig. 23.55 **a** Schematic drawing of PbTe lead salt laser. **b** Tuning characteristics of such laser: Emission wavelength (*left scale*, *filled circles*: emission wavelength at cw threshold, *empty circles*: emission maximum under pulsed operation) and cw threshold current density (*right scale*) as a function of the heat-sink temperature. *Symbols* are experimental data, *dashed lines* are guides to the eye. Adapted from [2007]

[21] In order to make better use of the high bandwidth of the optical fiber several information channels with closely lying wavelengths are transmitted.

[22] Note the anomalous positive coefficient $\mathrm{d}E_\mathrm{g}/\mathrm{d}T$ as discussed in Sect. 6.7.

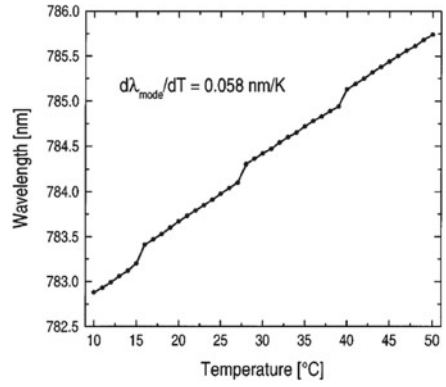

Fig. 23.56 Wavelength as a function of temperature (with mode hopping) for a GaAs-based DFB laser

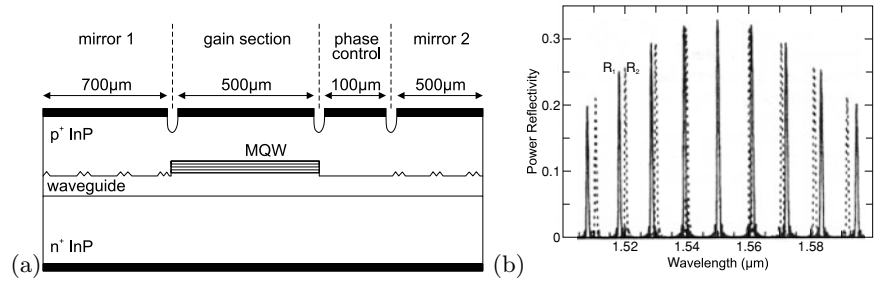

Fig. 23.57 **a** Schematic representation of SGDBR (sampled-grating DBR) laser with four sections. Adapted from [2008]. **b** Reflectance of two sampled gratings DBR mirrors

refraction and subsequently the longitudinal modes. The index of refraction increases with increasing temperature at typically $\sim 3 \times 10^{-4}\,\mathrm{K}^{-1}$. Generally, a red-shift is the consequence.

Another possibility to vary the index of refraction (and thus the optical path length) is a variation of the carrier density. The coefficient $\mathrm{d}n_\mathrm{r}/\mathrm{d}n$ is about $-10^{-20}\,\mathrm{cm}^3$. In a two-section laser, separate regions (with separately controlled currents) for gain and tuning are present. The regions are separated with deep-etched trenches to avoid crosstalk. The tuning range is limited to about 10 nm. For a mode-hopping free tuning, the control of the phase in the cavity is important and requires an additional section for the phase control. Such a three-section laser has separate regions (and current control) for the reflection, phase and amplification (or gain) region.

Using sampled gratings, the tuning range can be strongly increased to about 100 nm. A sampled grating is a nonperiodic lattice that has several ($\sim$ 10) reflection peaks. The laser structure has four sections (Fig. 23.57) with two mirrors that have slightly different sampled gratings. Via the carrier densities in the two mirror sections, different maxima can be brought to overlap (Vernier effect) and the position of the selected maximum can be tuned over a wide spectral range (Fig. 23.58).

23.4.13 Dynamics and Modulation

For transmission of information in the time domain, the laser intensity must be modulated. This can be accomplished by *direct* modulation, i.e. modulation of the injection current, or *external* modulators, for example using the voltage-induced shift of the absorption spectrum due to QCSE (cf. Sect. 15.1.2).

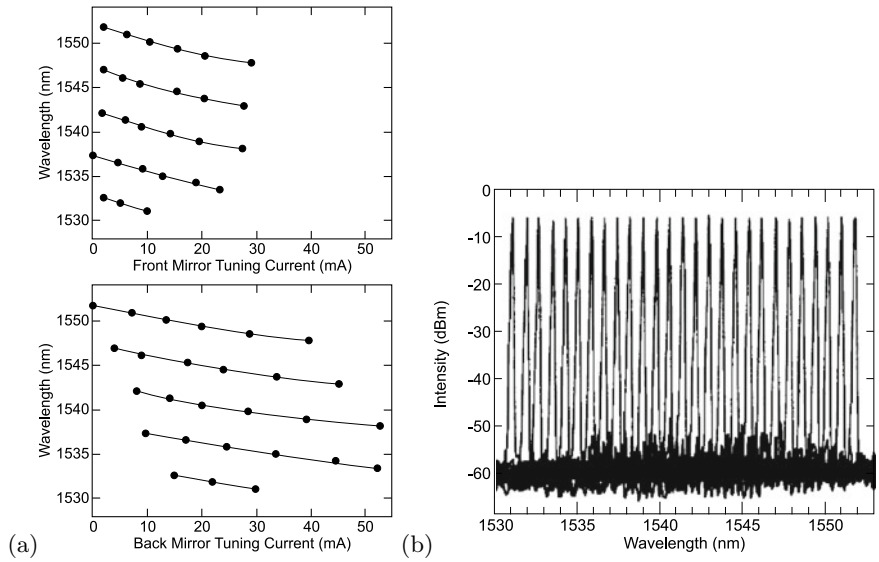

Fig. 23.58 **a** Tuning curves of two sampled gratings DBR mirrors for the front and back mirror current. **b** 27 wavelength channels (1531.12 to 1551.72 nm) with a channel separation of 1 nm. Adapted from [2009]

For direct modulation, small- and large-signal modulation are distinguished. Detailed treatments of laser dynamics and modulation can be found in [1993, 2010, 2011].

Laser Dynamics

The dynamical properties of the laser are described by the coupled rate equations for the carrier density n and the photon density (per volume) S (for a single mode):

$$\frac{\mathrm{d}n}{\mathrm{d}t} = \frac{j}{e\,d} - \frac{n}{\tau(n)} - \Gamma\, g(n,S)\, v_\mathrm{g}\, S \tag{23.40a}$$

$$\frac{\mathrm{d}S}{\mathrm{d}t} = \Gamma\, g(n,S)\, v_\mathrm{g}\, S + \beta\, B\, n^2 - \frac{S}{\tau_\mathrm{ph}}\,. \tag{23.40b}$$

The first term in (23.40a) describes the electrical injection[23] ($= I/(e\,V)$), the second one the recombination (all channels) and the third one the carrier conversion to photons through stimulated emission via the gain g. In the photon dynamics (23.40b), the first term represents the gain term, the second one the photons in the laser mode from the recombination (spontaneous emission, cmp. Sect. 23.4.7) and the third term the photon loss (due to internal losses and the mirrors). The recombination rate $n/\tau(n)$ is typically given by (23.24). The photon lifetime τ_ph is given by (23.28). If several optical modes are present, (23.40b) must be written down for each mode S_i and (23.40a) must be summed over all modes.

For the gain, various models are used. A simple one, going beyond (23.13), considering gain compression due to spectral hole burning, i.e. depletion of carriers due to stimulated emission, is

$$g(n,S) = g'\,\frac{n - n_\mathrm{thr}}{1 + \epsilon_S\, S}\,, \tag{23.41}$$

g' being the differential gain, $g' = \partial g/\partial n|_{S=0}$, and ϵ_S being the gain compression coefficient.

[23] This term can be multiplied by the injection efficiency η_inj to account for leakage currents.

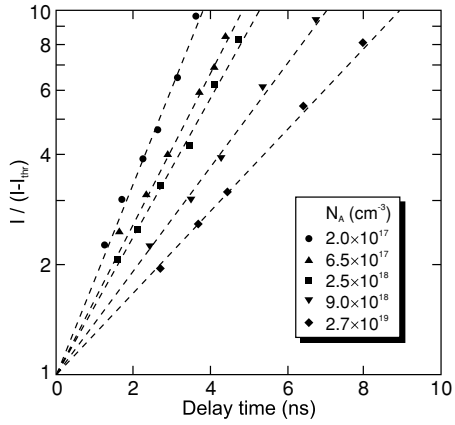

Fig. 23.59 Variation of turn-on delay time with the injected current for a laser at room temperature. Adapted from [2012]

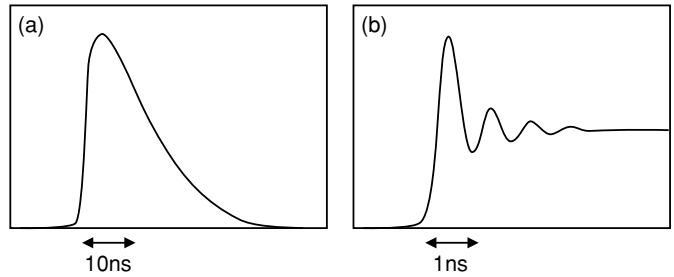

Fig. 23.60 Schematic response of **a** LED to current pulse and **b** of laser to current step

Large-Signal Modulation

If a current pulse is fed to the laser, the laser radiation is emitted with a short time delay, the so-called turn-on delay (TOD) time. This time is needed to build up the carrier density for inversion. The time dependence of the density is (neglecting the density dependence of the lifetime)

$$n(t) = \frac{I\,\tau}{e\,A\,d}\left[1 - \exp\left(-\frac{t}{\tau}\right)\right] . \tag{23.42}$$

The TOD time to reach the threshold density (using (23.23)) is

$$\tau_{\mathrm{TOD}} = \tau\,\ln\left(\frac{I}{I - I_{\mathrm{thr}}}\right) . \tag{23.43}$$

We note that $\tau_{\mathrm{TOD}} > 0$ for $I > I_{\mathrm{thr}}$. Such a dependence is found experimentally (Fig. 23.59). The turn-on delay time decreases with increasing pump current but typically is at least 1 ns. In order to circumvent this limitation for more than about 1 GHz pulse repetition rate, the laser is biased slightly below threshold.

In Fig. 23.60a, the response (light emission) of a LED to a short current pulse is shown schematically. The monotonously decreasing transient (that is more or less exponential) corresponds to the carrier recombination dynamics. When a laser is excited with a steep (long) current pulse, the response

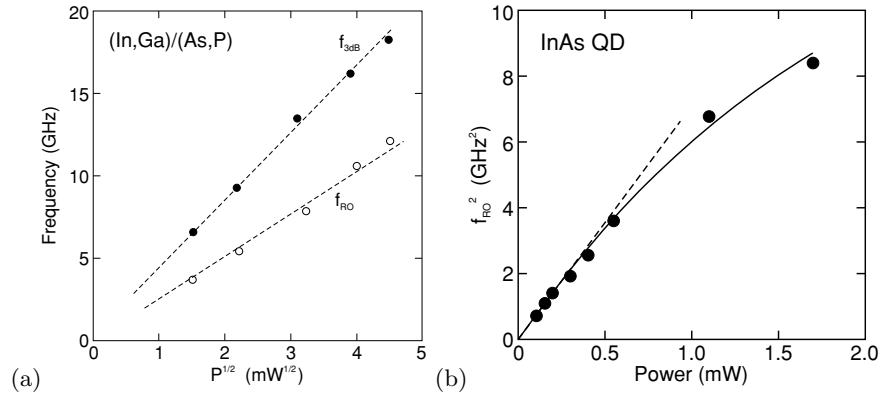

Fig. 23.61 **a** Dependence of small-signal 3 dB cutoff frequency $f_{3\mathrm{dB}}$ (*filled symbols*) and relaxation oscillation frequency f_{RO} (*empty symbols*) on the square root of the output power P for a DFB-laser. Adapted from [2013]. **b** Relaxation oscillation frequency f_{RO}^2 versus power for an InAs/GaAs QD laser. The *solid line* is a model including gain compression ($P_{\mathrm{sat}} = 3.3\,\mathrm{mW}$), the *dashed line* is the linear relation (23.44) for small power. Adapted from [2014]

exhibits so-called relaxation oscillations (RO) before the steady-state (cw) intensity level is reached (Fig. 23.60b).

In the laser, first the carrier density is built up. It surpasses the threshold density that leads to a build-up of the photon density. The laser pulse depletes the carrier density faster below threshold than the current can supply further carriers. Therefore, the laser intensity drops below the cw level. From the solution of the coupled rate equations for the electron and photon densities n and S (23.40a,b), the frequency of the relaxation oscillations is found as

$$f_{\mathrm{RO}} = \frac{1}{2\pi}\left(\frac{v_{\mathrm{g}}\,\Gamma\,g'\,S_0}{\tau_{\mathrm{ph}}}\right)^{1/2}\,, \tag{23.44}$$

where $\Gamma g'$ is the differential modal gain as defined in (23.41) and S_0 is the steady-state photon density per volume that is proportional to the laser power P. The dependence $f_{\mathrm{RO}} \propto S_0^{1/2}$ is also found experimentally (Fig. 23.61a). For higher power the relation $f_{\mathrm{RO}}^2 \propto S_0$ becomes non-linear (Fig. 23.61b) due to gain compression; in this case S_0 is replaced with $S_0/(1+\epsilon_S\,S_0) \propto P/(1+P/P_{\mathrm{sat}})$, with P_{sat} being the saturation power.

Pattern Response

For digital data transmission, the laser is driven with pulse sequences (bit patterns). The response to a random bit pattern is called an 'eye pattern' and is shown in Fig. 23.62. The pattern consists of traces of the type shown in Fig. 23.60b. A clear distinction with well-defined trigger thresholds between 'on'- and 'off'-states can only be made if the eye formed by the overlay of all possible traces remains open. From the eye patterns in Fig. 23.62, it can be seen that the RO overshoot can be suppressed by driving the laser with a dc offset current well above threshold.

Small-Signal Modulation

In small-signal modulation, the injection current I is varied periodically by a small amount δI with $\delta I \ll I$ in the lasing regime. The current modulation leads to a corresponding variation of the output intensity. The frequency response is limited by the differential gain and the gain compression coefficient. The frequency response shifts to higher frequency with increasing laser power as shown in Fig. 23.63b.

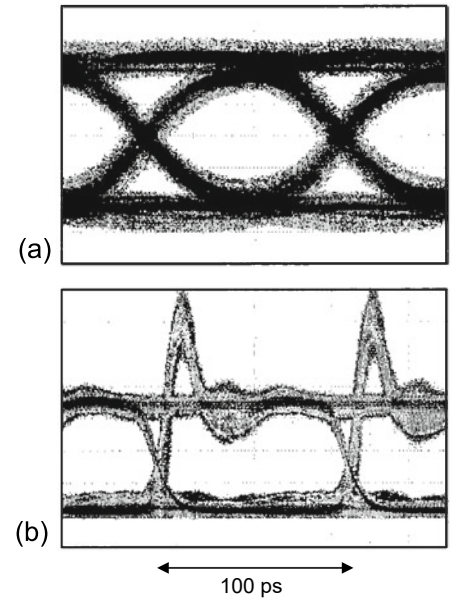

Fig. 23.62 Eye pattern of a single-mode VCSEL in response to a 10 Gb/s random bit pattern. The patterns are measured **a** with an offset current well above threshold and **b** with an offset current above but close to threshold. Adapted from [2015]

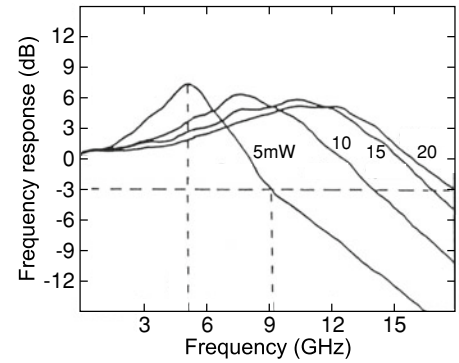

Fig. 23.63 Frequency response of a DFB-laser for various output powers as labeled. Adapted from [2013]

α Factor

Another important quantity is the α factor, also called the linewidth enhancement factor [2016, 2017]. Due to the coupling of amplitude and phase fluctuations in the laser, the linewidth Δf is larger than expected.

$$\Delta f = \frac{\hbar\omega\, v_g\, R_{\text{spont}}\, \ln R}{8\pi\, P_{\text{out}}\, L}(1+\alpha^2)\ . \tag{23.45}$$

The linewidth enhancement is described via $(1+\alpha^2)$ with

$$\alpha = \frac{\mathrm{d}n_r/\mathrm{d}n}{\mathrm{d}\kappa/\mathrm{d}n} = -\frac{4\pi}{\lambda}\frac{\mathrm{d}n_r/\mathrm{d}n}{g'}\ , \tag{23.46}$$

where κ denotes the imaginary part of the index of refraction (9.4). Typical values for α are between 1 and 10. The linewidth is inversely proportional to the output power (Fig. 23.64).

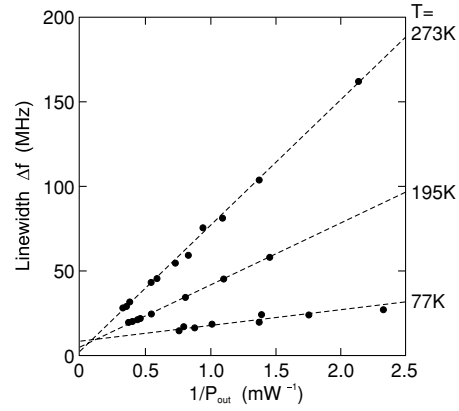

Fig. 23.64 Linewidth Δf of a cw GaAs/AlGaAs laser diode at various temperatures as a function of the inverse output power P_{out}^{-1}. At room temperature $\alpha \approx 5$. Adapted from [2018]

23.4.14 Surface-Emitting Lasers

Surface-emitting lasers emit their beam normal to the surface. They can be fabricated from horizontal (edge-) emitters by reflecting the beam with a suitable mirror into the surface direction. This technology requires tilted facets or micro-optical components but allows for high power per area. In Fig. 23.65, a schematic cross section of a horizontal-cavity surface-emitting laser (HCSEL) and the light emission from an array of 220 such lasers are shown. The laser contains a 45° mirror that steers the light through the substrate and a Bragg mirror to provide the cavity mirror. The facet can also be fabricated such that the emission is to the top surface (Fig. 23.66). Another possibility to couple the beam out of a horizontal cavity is a surface grating.

Now, surface-emitting lasers with vertical-cavity (VCSEL), as shown in Fig. 23.29b, will be discussed. A detailed treatment can be found in [2021]. VCSELs are of increasing importance after many issues regarding their technology and fabrication have been solved. VCSEL fabrication is essentially a planar technology and VCSELs can be fabricated as arrays (Fig. 23.68). An on-wafer test of their properties is possible. They offer a symmetrical (or possibly a controlled asymmetrical) beam profile (Fig. 23.67) with possible polarization control or fixation.

The cavity is formed by two highly reflecting Bragg mirrors with a distance of $\lambda/2$ or $3\lambda/2$ forming a microcavity (see Sect. 19.1.7). A high index contrast can be obtained from GaAs/AlAs Bragg mirrors in which the AlAs layers have been selectively oxidized in a hot moist atmosphere. Pure semiconductor Bragg mirrors suffer typically from small index contrast and require many pairs. This poses a problem,

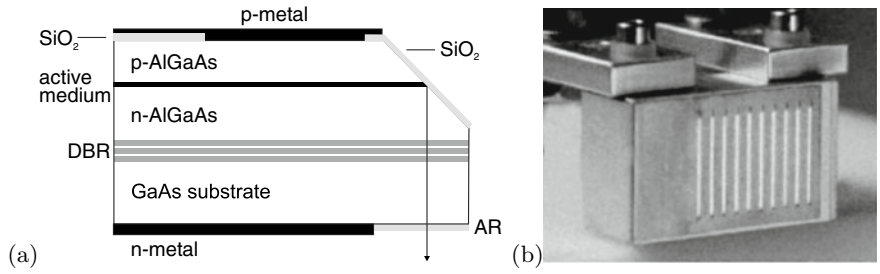

Fig. 23.65 **a** Principle of a surface-emitting laser. Light generated in the active region is internally reflected by the 45° angled mirror and directed through the substrate; 'AR': antireflection coating, 'DBR': epitaxial Bragg mirror. **b** Light emission from a 10 × 22 surface-emitting diode array. The light emission appears as stripes due to the broad beam divergence in the vertical direction. Part **b** reprinted with permission from [2019]

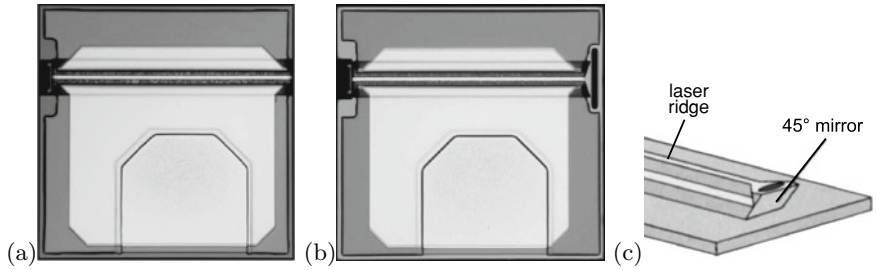

Fig. 23.66 **a** Horizontal Fabry–Perot cavity InP-based laser with 1310 nm emission length and 10 mW output power for modulation at 2.5 GB/s. The right facet is formed as DBR, emission is to the left. The trapezoid area in the center bottom of the image is the bond pad for the top contact. **b** Horizontal-cavity surface-emitting laser. Compared to **a**, the right facet is replaced with a 45° mirror, leading to surface emission. **c** Schematic drawing of the tilted facet. Parts **a** and **b** from [2020]

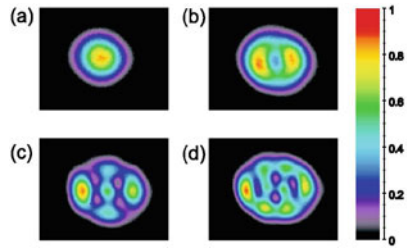

Fig. 23.67 In-plane near field of a VCSEL with 6 µm oxide aperture at various currents, **a** 3.0 mA, **b**, 6.2 mA, **c** 14.7 mA, **d** 18 mA

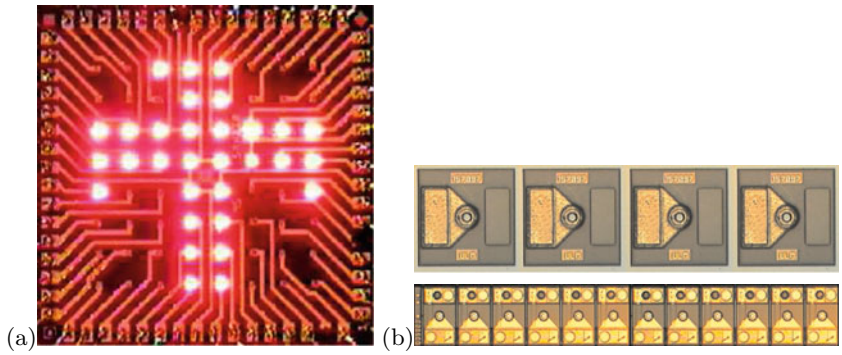

Fig. 23.68 **a**, **b** VCSEL arrays. Part **a** reprinted from [2022] with permission, part **b** reprinted from [2023] with permission

e.g. for InP-based VCSELs. In Fig. 23.69, the distribution of light intensity along a $3\lambda/2$ cavity is shown. In the stop band of the mirrors, there is only one optical mode, the cavity mode, that can propagate along the vertical (z) direction.

The current path through the active layer can be defined with an oxide aperture. This aperture is fabricated by selective oxidation of an AlAs layer, leaving a circular opening in the center of the VCSEL pillar as shown in Fig. 23.70. The current can be injected through the mirrors if they are doped. Alternatively, the current can be directly fed to the active layer by so-called intracavity contacts.

The emission wavelength of a VCSEL can be shifted via a variation of temperature or pump power. Tuning of the VCSEL emission can also be accomplished by leaving an air gap between the cavity

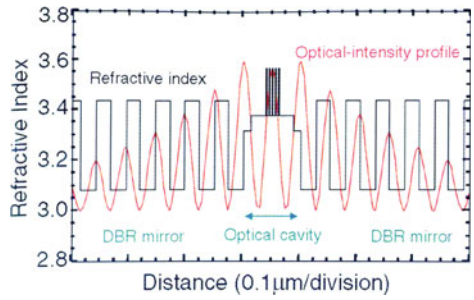

Fig. 23.69 Simulation of the longitudinal distribution of the optical field in a VCSEL structure. The active medium are five quantum wells in the center. Reproduced from [2024] by permission from the MRS Bulletin

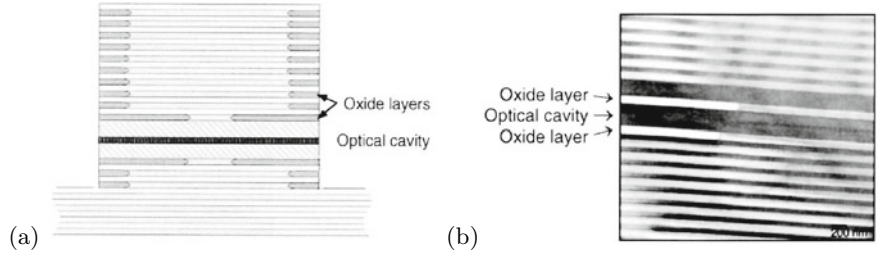

Fig. 23.70 **a** Schematic cross section of VCSEL with oxide aperture, **b** TEM image of cross section. Reproduced from [2024] by permission from the MRS Bulletin

and the upper mirror [2025]. Applying a voltage to the lever arm with the top mirror, the width of the air gap can be varied. This variation leads to a shift of the cavity mode and therefore of the laser emission wavelength (Fig. 23.71). A VCSEL with air gap and particularly a high contrast Bragg mirror is achieved with InP/air as shown in Fig. 23.72.

23.4.15 Optically Pumped Semiconductor Lasers

An easy way to pump semiconductor lasers is optical pumping. This technique is similar to diode-pumped solid-state lasers (DPSS). A (semiconductor) pump diode illuminates a suitable semiconductor structure (Fig. 23.73). The resonator is built between the bottom Bragg mirror of the semiconductor and the output coupler. The semiconductor structure contains suitable absorption layers (barriers) that absorb the pump light and quantum wells that emit laser radiation. This radiation is intracavity frequency doubled. In order to reach, e.g., a 488-nm output laser beam, a standard 808-nm pump diode is employed. The InGaAs/GaAs quantum wells are designed to emit at 976 nm. Other design wavelengths of the quantum wells allow for other output wavelengths. This technology allows compact lasers with little heat dissipation [2028]. The optically pumped semiconductor laser (OPSL) is also known as a semiconductor disc laser.

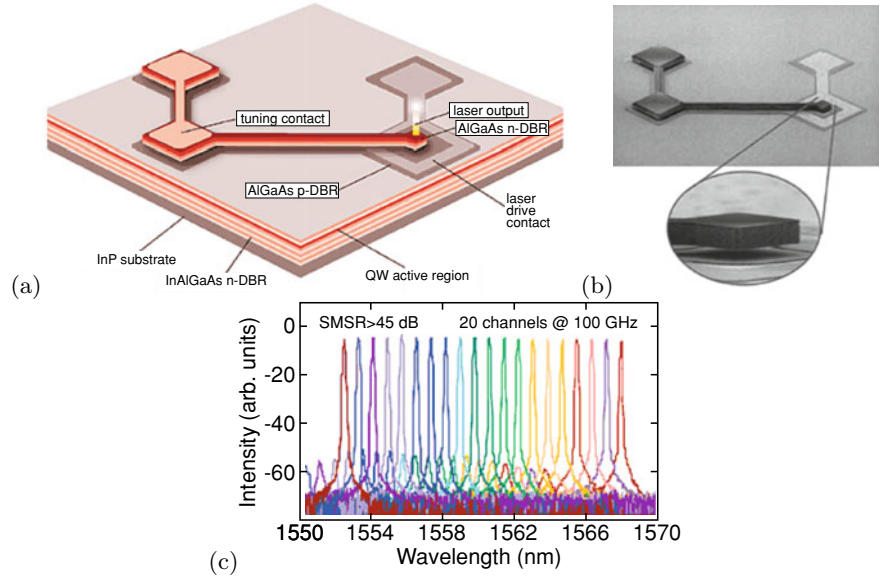

Fig. 23.71 **a** Schematic setup and **b** SEM image of VCSEL with air gap between active layer and top Bragg mirror, **c** spectra for different tuning conditions (via the width of the air gap). From [2026]

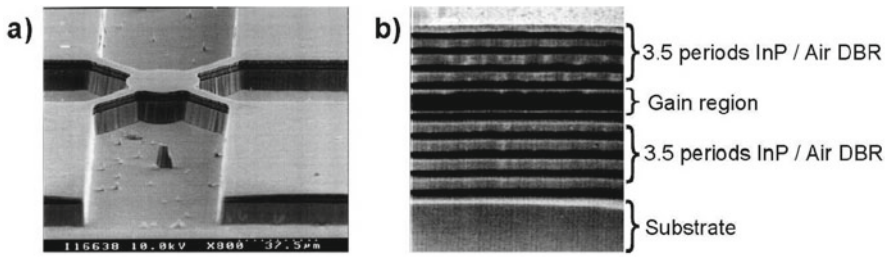

Fig. 23.72 **a** VCSEL with air gap and **b** Bragg mirror with high dielectric contrast InP/air interfaces. Reprinted with permission from [2027], ©2002 IEEE

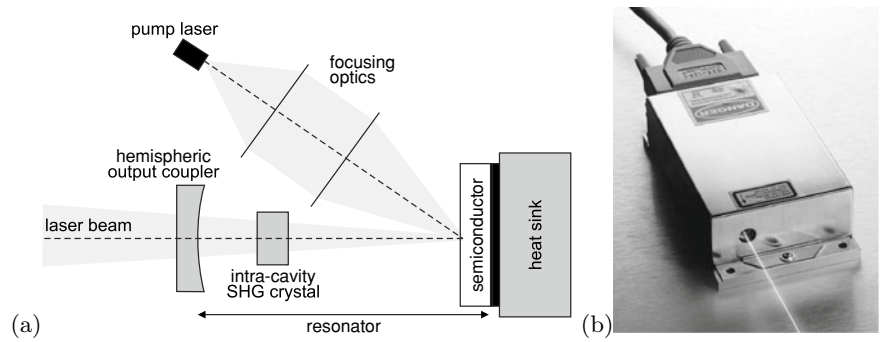

Fig. 23.73 **a** Schematic setup of optically pumped semiconductor laser (OPSL). The semiconductor chip consists of a Bragg mirror on the bottom, multiple quantum wells and an antireflection coating on the top. Adapted from [2028]. **b** OPSL source (488 nm, 20 mW, footprint: $125 \times 70\,\mathrm{mm}^2$). Reprinted with permission from [2029]

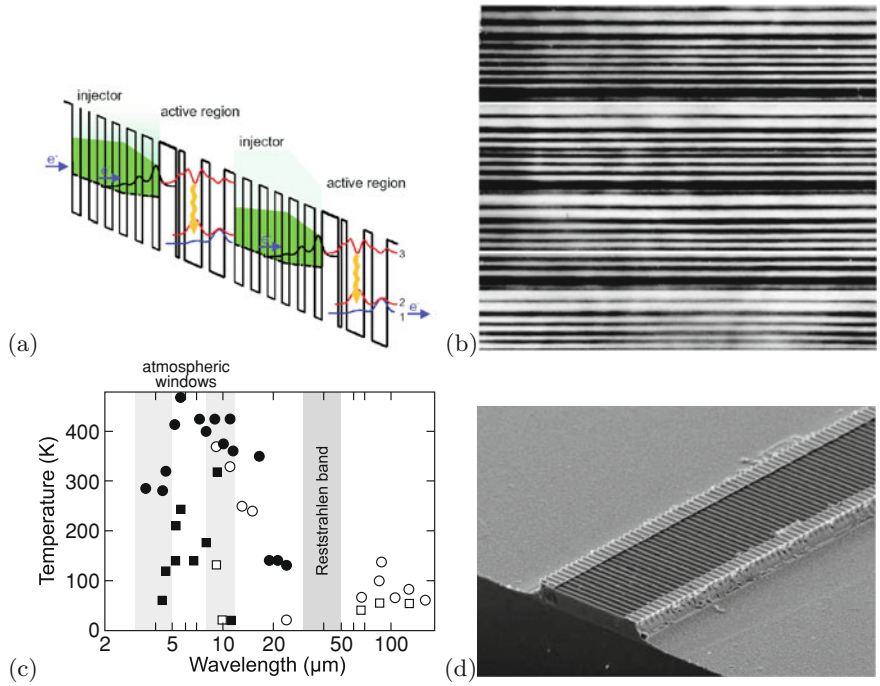

Fig. 23.74 **a** Schematic band diagram of quantum cascade laser. **b** Cross sectional TEM of cascade layer sequence. The periodicity of the vertical layer sequence is 45 nm. From [2030]. **c** Laser emission wavelengths and operation temperatures for various realized quantum cascade lasers (*squares*: cw, *circles*: pulsed operation, *solid symbols*: InP-, *empty symbols*: GaAs-based). Data from [2031]. **d** SEM image of a quantum cascade DFB laser (grating period: 1.6 μm). From [2031]

23.4.16 Quantum Cascade Lasers

In a quantum cascade laser (QCL), the gain stems from an intersubband transition. The concept was conceived in 1971 [145, 2032] and realized in 1994 [149]. In Fig. 23.74a, the schematic conduction-band structure at operation is shown. The injector supplies electrons into the active region. The electron is removed quickly from the lower level in order to allow inversion. The electron is then extracted into the next injector. The laser medium consists of several such units as shown in Fig. 23.74b. Since every unit can deliver a photon per electron (with efficiency η_1), the total quantum efficiency of N units $\eta = N\,\eta_1$ can be larger than 1.

The emission wavelength is in the far- or mid-infrared, depending only on the designed layer thicknesses and *not* on the band gap of the material (Fig. 23.74d). In the mid-infrared, room-temperature operation has been achieved while operation in the far-infrared requires cooling so far. Extensions to the THz-range and the infrared spectral region (telecommunication wavelengths of 1.3 and 1.55 μm) seem feasible. The cascade laser concept can also be combined with the DFB technology to create single-mode laser emission (Fig. 23.74d).

23.4.17 Hot-Hole Lasers

The hot-hole laser, which is mostly realized with p-doped Ge, is based on a population inversion between the light- and heavy-hole valence subbands. The laser operates with crossed electric and magnetic fields (Voigt configuration, typically $E = 0.5$–$3\,\mathrm{kV/cm}$, $B = 0.3$–$2\,\mathrm{T}$) and at cryogenic temperatures ($T = 4$–$40\,\mathrm{K}$) [2033–2035].

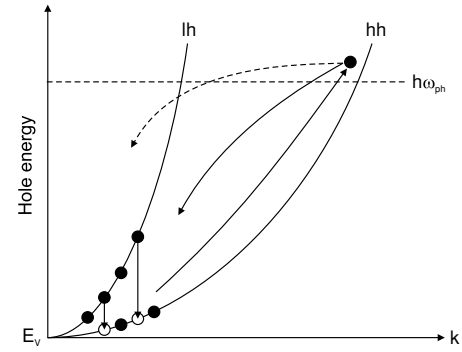

Fig. 23.75 Schematic cycle of hole motion in a hot-hole laser. *Filled* (*empty*) circles represent populated (unpopulated) hole states. The *solid lines* represent streaming motion of heavy hole, the *dashed line* represents scattering into the light hole band. *Arrows* denote radiative intervalence-band transitions

A significant scattering process of hot carriers is interaction with optical phonons, mainly optical phonon emission. This process has a threshold in carrier energy given by the optical phonon energy. For sufficiently high electric fields and at low temperature, hot carriers accelerate without acoustical phonon interaction (ballistic transport) along the crystallographic direction in which the electric field is applied. These hot carriers reach the optical phonon energy and lose all their energy due to emission of an optical phonon. They accelerate again, repeating this directional motion in momentum space. This motion is called *streaming motion*.

For $|E/B|$ ratios of about 1.5 kV/cmT, the heavy holes are accelerated up to energies above the optical phonon energy (37 meV in germanium) and consequently are scattered strongly by these phonons. Under these conditions, a few per cent of the heavy holes are scattered into the light-hole band. The light holes remain at much lower energies and are accumulated at the bottom of the light-hole band below the optical phonon energy as sketched in Fig. 23.75. The continuous pumping of heavy holes into the light-hole band can lead to a population inversion. Consequently, laser radiation is emitted from optical (radiative) intervalence-band transitions (cf. Sect. 9.9.3). The emission wavelength is in the far-infrared around 100 µm. Typical p-Ge lasers span the frequency range 1–4 THz (300–70 µm) [2036] and deliver 1–10 W peak output power for 1 cm^3 typical active volume.

Since the applied electric field causes considerable heating, the temperature of the laser crystal rises quickly, within a few µs, up to 40 K. Then the laser action stops. Thus the duration of the electric-field excitation is limited to 1–5 µs (limiting the emission power) and the repetition frequency is only a few Hertz due to the necessary cooling. Research is underway towards high duty cycle (possibly cw) operation by using smaller volumes and planar vertical-cavities [2037, 2038].

23.5 Semiconductor Optical Amplifiers

If the facets of a laser cavity are antireflection coated, a laser gain medium can be used as a semiconductor optical amplifier (SOA). A textbook on this subject is [2039]. Optical feedback from facets can also be avoided using tilted facets [2040].

A tapered amplifier geometry, as shown in Fig. 23.76a, allows for laterally monomode input and a preservation of the lateral beam quality during the propagation of the optical wave through the gain medium. The active medium is an 8-nm compressively strained InGaAs quantum well. A typical taper angle is 5–10°. The input aperture is between 5 and 7 µm. The amplifier length is 2040 µm. More than 20 dB optical amplification can be obtained (Fig. 23.76b). The self-oscillation is suppressed for

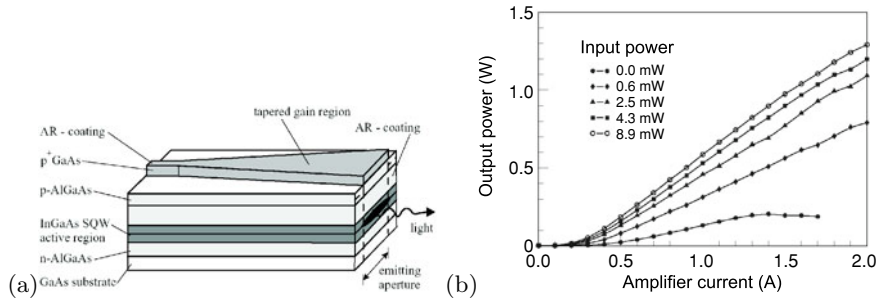

Fig. 23.76 **a** Schematic geometry of tapered semiconductor amplifier. **b** Optical output power versus amplifier current for various values of the optical input power, taper angle was 5°. For zero input power only spontaneous and amplified spontaneous emission is observed. Reprinted with permission from [2041]

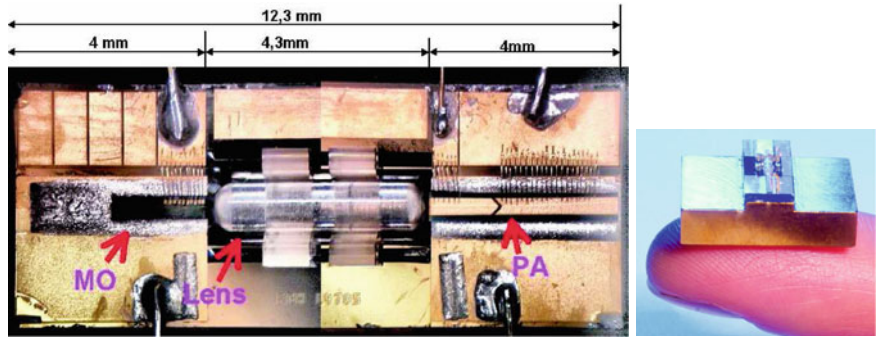

Fig. 23.77 Photographs of a MOPA arrangement of a laser (master oscillator, 'MO'), glass lens and tapered amplifier (power amplifier, 'PA') on a silicon micro-optical 'bench'. Reprinted with permission from [2042]

currents up to 2 A by AR facet coating of 10^{-4} in a 70 nm band. The wall-plug efficiency of the discussed amplifier is up to over 40%. If such an amplifier is arranged together with a seed laser diode (master oscillator), the setup is called MOPA (master oscillator power amplifier), as shown in Fig. 23.77. A modulated input also leads to a modulated output.

Quantum dot arrays can be a useful gain medium in a SOA [2043, 2044] due to their fast gain dynamics [2045] and broad spectrum (Sect. 23.3.6).

Chapter 24
Transistors

Frequently, I have been asked if an experiment I have planned is pure or applied research; to me it is more important to know if the experiment will yield new and probably enduring knowledge about nature. If it is likely to yield such knowledge, it is, in my opinion, good fundamental research; and this is much more important than whether the motivation is purely esthetic satisfaction on the part of the experimenter on the one hand or the improvement of the stability of a high-power transistor on the other.

W.B. Shockley [2046, 2047]

Abstract The device functionalities of bipolar, heterobipolar and field effect transistors (JFET, MESFET and MOSFET) are explained. Within physical models for drift, diffusion and recombination given earlier in the book, the characteristics of these devices are derived. Remarks on integrated circuits, miniaturization and thin film transistors finish this chapter.

24.1 Introduction

Transistors[1] are the key elements for electronic circuits such as amplifiers, memories and microprocessors. Transistors can be realized in bipolar technology (bipolar junction transistor (BJT), Sect. 24.2) or as unipolar devices using the field effect (field-effect transistor (FET), Sect. 24.3) [574, 2048]. The equivalent in vacuum-tube technology to the transistor is the triode (Fig. 24.1a). Transistors can be optimized for their properties in analog circuits such as linearity and frequency response or their properties in digital circuits such as switching speed and power consumption. Transistors for microwave applications are discussed in [1815]. Early commercial models are shown in Fig. 24.2.

24.2 Bipolar Transistors

Bipolar transistors consist of a pnp or npn sequence (Fig. 24.3). The layers (or parts) are named emitter (highly doped), base (thin, highly doped) and collector (normal doping level). The transistor can be considered to consist of two diodes (emitter–base and base–collector) back to back. However, the

[1]The term 'transistor' was coined from the combination of 'transconductance' or 'transfer' and 'varistor' after initially such devices were termed 'semiconductor triodes'. The major breakthrough was achieved in 1947 when the first transistor was realized that showed gain (Figs. 1.9 and 24.1b).

M. Grundmann, *The Physics of Semiconductors*, Graduate Texts in Physics,
https://doi.org/10.1007/978-3-030-51569-0_24

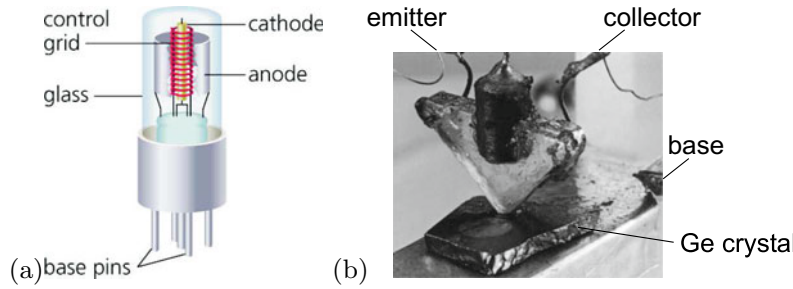

Fig. 24.1 **a** Schematic image of a vacuum triode. The electron current flows from the heated cathode to the anode when the latter is at a positive potential. The flow of electrons is controlled with the grid voltage. **b** Bell Laboratories' first (experimental) transistor, 1947

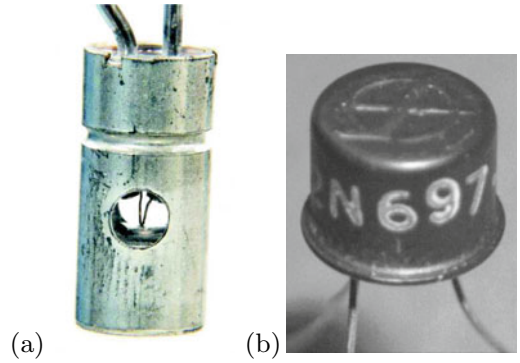

Fig. 24.2 **a** First commercial, developmental (point contact) transistor from BTL (Bell Telephone Laboratories) with access holes for adjustment of the whiskers pressing on a piece of Ge, diameter 7/32"=5 mm, 1948. **b** First high-performance silicon transistor (npn mesa technology), model 2N697 from Fairchild Semiconductor, 1958 (at $200, in 1960 $28.50). The product number is still in use (now $0.95)

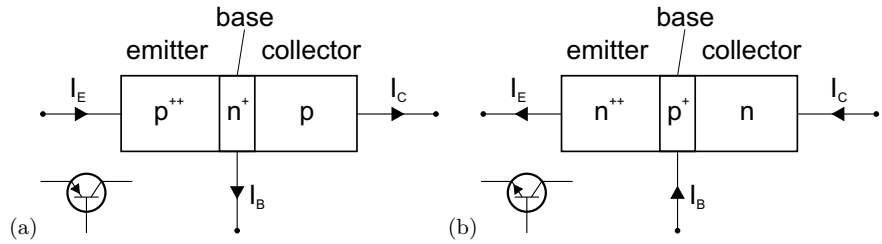

Fig. 24.3 Schematic structure and circuit symbol for **a** pnp and **b** npn transistors

important point is that the base is sufficiently thin (in relation to its minority carrier diffusion length) and carriers from the emitter (which are minority carriers in the base) can dominantly reach the collector by diffusion.

In Fig. 24.4, the three basic circuits with a transistor are shown. They are classified by the common contact for the input and output circuit. The space charges and band diagram for a pnp transistor in the base circuit configuration are depicted in Fig. 24.5. The emitter–base diode is switched in the forward direction to inject electrons into the base. The base–collector diode is switched in the reverse direction. The electrons that diffuse through the base and reach the neutral region of the collector were transported by the high drift field away from the base.

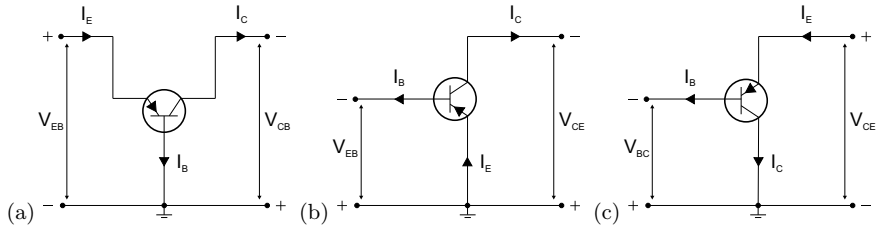

Fig. 24.4 Basic transistor circuits, named after the common contact: **a** Common base circuit, **b** common emitter circuit and **c** common collector circuit

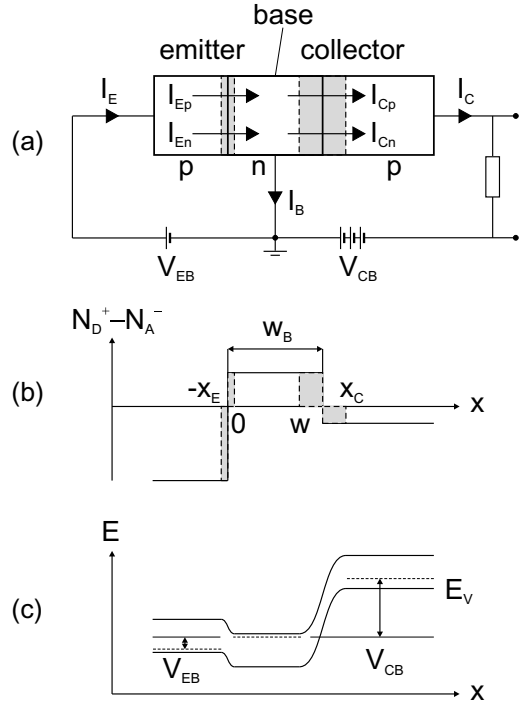

Fig. 24.5 pnp transistor in **a** base circuit. **b** Doping profile and space charges (abrupt approximation) and **c** band diagram for typical operation conditions

24.2.1 Carrier Density and Currents

The modeling of transistors is a complex topic. We treat the transistor on the level of the abrupt junction. As an approximation, we assume that all voltages drop at the junctions. Series resistances, capacities and stray capacities and other parasitic impedances are neglected at this point.

The major result is that the emitter–base current from the forward-biased emitter–base diode will be transferred to the collector. The current flowing from the base contact is small compared to the collector current. This explains the most prominent property of the transistor, the current amplification.

For the neutral part of the base region of a pnp transistor, the stationary equations for diffusion and continuity are

$$0 = D_\mathrm{B}\frac{\partial^2 p}{\partial x^2} - \frac{p - p_\mathrm{B}}{\tau_\mathrm{B}} \tag{24.1a}$$

$$j_\mathrm{p} = -eD_\mathrm{B}\frac{\partial p}{\partial x} \tag{24.1b}$$

$$j_{\text{tot}} = j_{\text{n}} + j_{\text{p}} \,, \tag{24.1c}$$

where p_{B} is the equilibrium minority carrier density in the base. From the discussion of the pn-diode, we know that at the boundary of the depletion layer the minority carrier density is increased by $\exp(eV/kT)$ (cf. (21.102a,b)). At the boundaries of the emitter–base diode (for geometry see Fig. 24.5a)

$$\delta p(0) = p(0) - p_{\text{B}} = p_{\text{B}} \left[\exp\left(\beta V_{\text{EB}}\right) - 1\right] \tag{24.2a}$$

$$\delta n(-x_{\text{E}}) = n(-x_{\text{E}}) - n_{\text{E}} = n_{\text{E}} \left[\exp\left(\beta V_{\text{EB}}\right) - 1\right] \,, \tag{24.2b}$$

where n_{E} and p_{B} are the equilibrium minority-carrier densities in the emitter and base, respectively. Accordingly, at the boundaries of the base–collector diode we have

$$\delta p(w) = p(w) - p_{\text{B}} = p_{\text{B}} \left[\exp\left(\beta V_{\text{CB}}\right) - 1\right] \tag{24.3a}$$

$$\delta n(x_{\text{C}}) = n(x_{\text{C}}) - n_{\text{C}} = n_{\text{C}} \left[\exp\left(\beta V_{\text{CB}}\right) - 1\right] \,. \tag{24.3b}$$

These are the boundary conditions for the diffusion equations in the p-doped layers and in the neutral region of the n-doped base. For the p-layers (with infinitely long contacts), the solution is (similar to (21.128)) for $x < -x_{\text{E}}$ and $x > -x_{\text{C}}$, respectively

$$n(x) = n_{\text{E}} + \delta n(-x_{\text{E}}) \, \exp\left(\frac{x + x_{\text{E}}}{L_{\text{E}}}\right) \tag{24.4a}$$

$$n(x) = n_{\text{C}} + \delta n(x_{\text{C}}) \, \exp\left(-\frac{x - x_{\text{C}}}{L_{\text{C}}}\right) \,. \tag{24.4b}$$

L_{E} and L_{C} are the minority carrier (electron) diffusion lengths in the emitter and collector, respectively. The solution for the hole density in the neutral region in the base ($0 < x < w$) is

$$\begin{aligned} p(x) = p_{\text{B}} &+ \left[\frac{\delta p(w) - \delta p(0) \exp\left(-w/L_{\text{B}}\right)}{2 \sinh\left(w/L_{\text{B}}\right)}\right] \exp\left(\frac{x}{L_{\text{B}}}\right) \\ &- \left[\frac{\delta p(w) - \delta p(0) \exp\left(w/L_{\text{B}}\right)}{2 \sinh\left(w/L_{\text{B}}\right)}\right] \exp\left(-\frac{x}{L_{\text{B}}}\right) \,. \end{aligned} \tag{24.5}$$

We shall denote the excess hole density at $x = 0$ and $x = w$ as $\delta p_{\text{E}} = \delta p(0)$ and $\delta p_{\text{C}} = \delta p(w)$, respectively. Typical ('normal') operation condition in the common base circuit is that $\delta p_{\text{C}} = 0$ (Fig. 24.8a). In the 'inverted' configuration, the role of emitter and collector are reversed and $\delta p_{\text{E}} = 0$. We can write (24.5) also as

$$p(x) = p_{\text{B}} + \delta p_{\text{E}} \, \frac{\sinh[(w - x)/L_{\text{B}}]}{\sinh\left[w/L_{\text{B}}\right]} + \delta p_{\text{C}} \, \frac{\sinh\left[/L_{\text{B}}\right)]}{\sinh\left[w/L_{\text{B}}\right]} \,. \tag{24.6}$$

If the base is thick, i.e. $w \to \infty$, or at least large compared to the diffusion length ($w/L_{\text{B}} \gg 1$), the carrier concentration is given by

$$p(x) = p_{\text{B}} + \delta p(0) \exp\left(-\frac{x}{L_{\text{B}}}\right) \tag{24.7}$$

and does not depend on the collector. In this case there is no transistor effect. A 'coupling' between emitter and collector currents that are given by the derivative $\partial p/\partial x$ at 0 and w, respectively, is only present for a sufficiently thin base.

From (24.6), the hole current densities at $x = 0$ and $x = w$ are given as[2]

$$j_{\mathrm{Ep}} = j_{\mathrm{p}}(0) = e\frac{D_{\mathrm{B}}}{L_{\mathrm{B}}}\left[\delta p_{\mathrm{E}}\ \coth\left(\frac{w}{L_{\mathrm{B}}}\right) - \delta p_{\mathrm{C}}\,\mathrm{csch}\left(\frac{w}{L_{\mathrm{B}}}\right)\right] \tag{24.8a}$$

$$j_{\mathrm{Cp}} = j_{\mathrm{p}}(w) = e\frac{D_{\mathrm{B}}}{L_{\mathrm{B}}}\left[\delta p_{\mathrm{E}}\,\mathrm{csch}\left(\frac{w}{L_{\mathrm{B}}}\right) - \delta p_{\mathrm{C}}\ \coth\left(\frac{w}{L_{\mathrm{B}}}\right)\right] . \tag{24.8b}$$

From (24.4a,b), the electron current densities at $x = -x_{\mathrm{E}}$ and $x = x_{\mathrm{C}}$ are given (with $\delta n_{\mathrm{E}} = \delta n(-x_{\mathrm{E}})$ and $\delta n_{\mathrm{C}} = \delta n(x_{\mathrm{C}})$) by

$$j_{\mathrm{En}} = j_{\mathrm{n}}(-x_{\mathrm{E}}) = e\,\frac{D_{\mathrm{E}}}{L_{\mathrm{E}}}\,\delta n_{\mathrm{E}} \tag{24.9a}$$

$$j_{\mathrm{Cn}} = j_{\mathrm{n}}(x_{\mathrm{C}}) = -e\,\frac{D_{\mathrm{C}}}{L_{\mathrm{C}}}\,\delta n_{\mathrm{C}} . \tag{24.9b}$$

The emitter current density is (similar to (21.131))

$$\begin{aligned} j_{\mathrm{E}} &= j_{\mathrm{p}}(0) + j_{\mathrm{n}}(-x_{\mathrm{E}}) \\ &= e\,\frac{D_{\mathrm{B}}}{L_{\mathrm{B}}}\left[\delta p_{\mathrm{E}}\ \coth\left(\frac{w}{L_{\mathrm{B}}}\right) - \delta p_{\mathrm{C}}\,\mathrm{csch}\left(\frac{w}{L_{\mathrm{B}}}\right)\right] + e\,\frac{D_{\mathrm{E}}}{L_{\mathrm{E}}}\,\delta n_{\mathrm{E}} . \end{aligned} \tag{24.10}$$

The collector current density is given as

$$\begin{aligned} j_{\mathrm{C}} &= j_{\mathrm{p}}(w) + j_{\mathrm{n}}(x_{\mathrm{C}}) \\ &= e\,\frac{D_{\mathrm{B}}}{L_{\mathrm{B}}}\left[\delta p_{\mathrm{E}}\,\mathrm{csch}\left(\frac{w}{L_{\mathrm{B}}}\right) - \delta p_{\mathrm{C}}\ \coth\left(\frac{w}{L_{\mathrm{B}}}\right)\right] - e\,\frac{D_{\mathrm{C}}}{L_{\mathrm{C}}}\,\delta n_{\mathrm{C}} . \end{aligned} \tag{24.11}$$

In these equations, only the diffusion currents are considered. Additionally, the recombination currents in the depletion layers must be considered, in particular at small junction voltages.

24.2.2 Current Amplification

The emitter current consists of two parts, the hole current I_{pE} injected from the base and the electron current I_{nE} that flows from the emitter to the base (Fig. 24.5a). Similarly, the collector current is made up from the hole and electron currents I_{pC} and I_{pC}, respectively.

The total emitter current splits into the base and collector currents

$$I_{\mathrm{E}} = I_{\mathrm{B}} + I_{\mathrm{C}} . \tag{24.12}$$

The amplification (gain) in common base circuits

$$\alpha_0 = h_{\mathrm{FB}} = \frac{\partial I_{\mathrm{C}}}{\partial I_{\mathrm{E}}} = \frac{\partial I_{\mathrm{Ep}}}{\partial I_{\mathrm{E}}}\,\frac{\partial I_{\mathrm{Cp}}}{\partial I_{\mathrm{Ep}}}\,\frac{\partial I_{\mathrm{C}}}{\partial I_{\mathrm{Cp}}} = \gamma\,\alpha_{\mathrm{T}}\,M , \tag{24.13}$$

[2] $\coth x \equiv \cosh x/\sinh x$, $\mathrm{csch} x \equiv 1/\sinh x$.

where γ is the emitter efficiency, α_T the base transport factor and M the collector multiplication factor. Since the collector is normally operated below the threshold for avalanche multiplication, $M = 1$.

The current amplification in the common emitter circuit is

$$\beta_0 = h_{FE} = \frac{\partial I_C}{\partial I_B} . \tag{24.14}$$

Using (24.12), we find

$$\beta_0 = \frac{\partial I_E}{\partial I_B} - 1 = \frac{\partial I_E}{\partial I_C}\frac{\partial I_C}{\partial I_B} - 1 = \frac{1}{\alpha_0}\beta_0 - 1 = \frac{\alpha_0}{1-\alpha_0} . \tag{24.15}$$

Since α_0 is close to 1 for a well-designed transistor, β_0 is a large number, e.g. $\beta_0 = 99$ for $\alpha_0 = 0.99$.

The emitter efficiency is (A denotes the device area)

$$\gamma = \frac{A\, j_{Ep}}{I_E} = \left[1 + \frac{n_E}{p_B}\frac{D_E}{D_B}\frac{L_B}{L_E}\tanh\left(\frac{w}{L_B}\right)\right]^{-1} . \tag{24.16}$$

The base transport factor, i.e. the ratio of minority carriers reaching the collector and the total number of injected minority carriers, is (for reverse bias $|\beta U_{CB}| \gg kT$)

$$\begin{aligned}\alpha_T = \frac{j_{Cp}}{j_{Ep}} &= \frac{\exp(\beta U_{EB}) - 1 + \cosh w/L_B}{1 + (\exp(\beta U_{EB}) - 1)\,\cosh w/L_B} \\ &\approx \frac{1}{\cosh(w/L_B)} \approx 1 - \frac{w^2}{2L_B^2} .\end{aligned} \tag{24.17}$$

The first approximation is for $\beta U_{EB} \gg 1$ (emitter diode injecting in forward direction), the second approximation is for $w \ll L_B$. If the base length is a tenth of the diffusion length, the base transport factor is $\alpha_T > 0.995$. M is also very close to 1; for reverse bias U_{CB} and $w \ll L_B$ we find

$$M \approx 1 + \frac{w}{L_C}\frac{D_C}{D_B}\frac{\delta n_C}{\delta p_C - \delta p_E} \approx 1 + \frac{w}{L_C}\frac{D_C}{D_B}\frac{n_C}{p_B}\exp(-\beta U_{EB}) . \tag{24.18}$$

Thus for $w \ll L_B$, α_0 is dominated by γ and given as (approximating (24.16))

$$\alpha_0 \approx \gamma \approx 1 - \frac{w}{L_E}\frac{n_E}{p_B}\frac{D_E}{D_B} . \tag{24.19}$$

The gain β_0 is then also determined by γ:

$$\beta_0 = h_{FE} \approx \frac{\gamma}{1-\gamma} \approx \frac{1}{1-\gamma} \propto \frac{N_E}{N_B}\frac{L_E}{w} , \tag{24.20}$$

N_E and N_B being the doping levels in the emitter and base, respectively. The base and collector current are shown in Fig. 24.6 as a function of the emitter–base voltage, i.e. the voltage at the injection diode. The collector current is close to the emitter–base diode current and displays a dependence $\propto \exp(eV_{EB}/kT)$. The base current shows a similar slope but is orders of magnitude smaller in amplitude. For small forward voltages of the emitter–base diode, the current is typically dominated by a nonradiative recombination current that flows through the base contact and has an ideality factor (m in Fig. 24.6) close to 2.

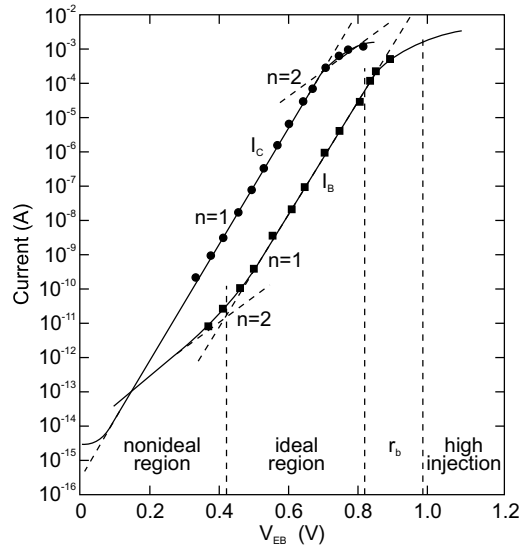

Fig. 24.6 Collector current I_C and base current I_B as a function of the emitter–base voltage V_{EB} (Gummel plot). Adapted from [2049]

24.2.3 Ebers-Moll Model

The Ebers-Moll model (Fig. 24.7) was developed in 1954 and is a relatively simple transistor model that needs, at its simplest level (Fig. 24.7a) just three parameters. It can (and must) be refined (Figs. 24.7b,c). The model considers two ideal diodes ('F' (forward) and 'R' (reverse)) back to back, each feeding a current source. The F diode represents the emitter–base diode and and the R diode the collector–base diode. The currents are

$$I_F = I_{F0}\left[\exp\left(\beta V_{EB}\right) - 1\right] \tag{24.21a}$$
$$I_R = I_{R0}\left[\exp\left(\beta V_{CB}\right) - 1\right] . \tag{24.21b}$$

Using (24.8a,b)–(24.11), the emitter and collector currents are

$$I_E = \hat{a}_{11}\left[\exp\left(\beta V_{EB}\right) - 1\right] + \hat{a}_{12}\left[\exp\left(\beta V_{CB}\right) - 1\right] \tag{24.22a}$$
$$I_C = \hat{a}_{21}\left[\exp\left(\beta V_{EB}\right) - 1\right] + \hat{a}_{22}\left[\exp\left(\beta V_{CB}\right) - 1\right] , \tag{24.22b}$$

with

$$\hat{a}_{11} = eA\left[p_B\frac{D_B}{L_B}\coth\left(\frac{w}{L_B}\right) + n_E\frac{D_E}{L_E}\right] \tag{24.23a}$$
$$\hat{a}_{12} = -eAp_B\frac{D_B}{L_B}\operatorname{csch}\left(\frac{w}{L_B}\right) \tag{24.23b}$$
$$\hat{a}_{21} = eAp_B\frac{D_B}{L_B}\operatorname{csch}\left(\frac{w}{L_B}\right) = -\hat{a}_{12} \tag{24.23c}$$
$$\hat{a}_{22} = -eA\left[p_B\frac{D_B}{L_B}\coth\left(\frac{w}{L_B}\right) + n_C\frac{D_C}{L_C}\right] . \tag{24.23d}$$

The currents at the three contacts are

$$I_E = I_F - \alpha_I I_R \tag{24.24a}$$

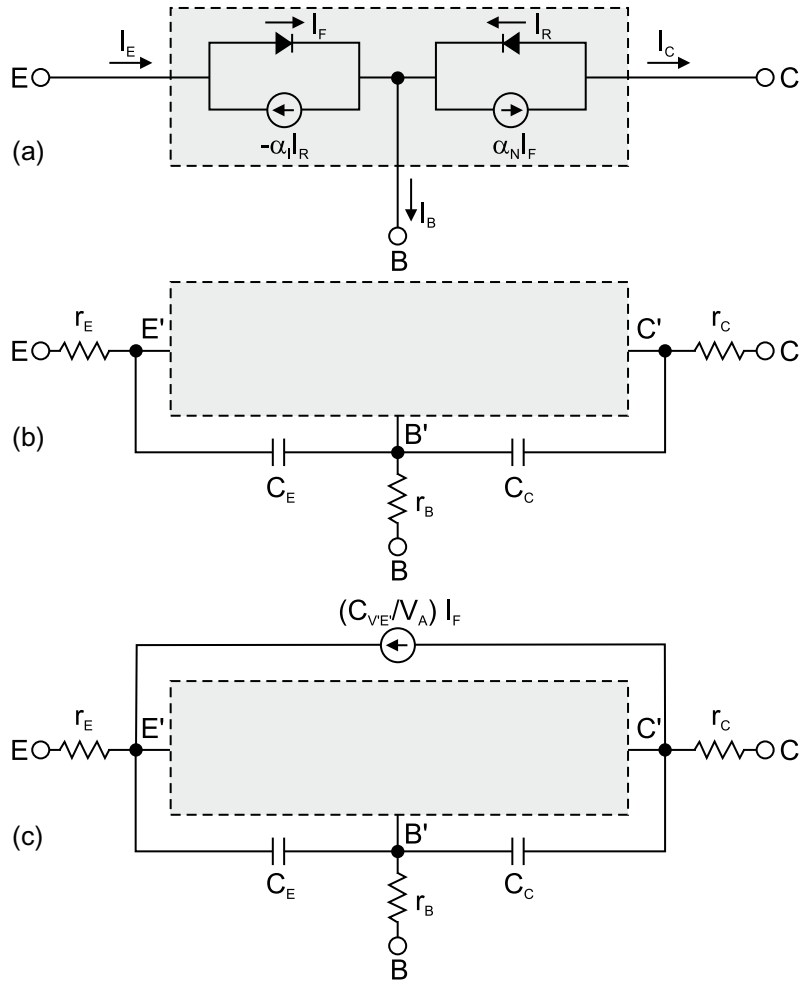

Fig. 24.7 Ebers-Moll model of a transistor, 'E': emitter, 'C': collector and 'B': base. Currents are shown for a pnp transistor. **a** Basic model (*grey area* in **b**, **c**), **b** model with series resistances and depletion-layer capacitances, **c** model additionally including the Early effect (V_A: Early voltage)

$$I_C = \alpha_N I_F - I_R \tag{24.24b}$$

$$I_B = (1-\alpha_N) I_F + (1-\alpha_I) I_R \ . \tag{24.24c}$$

The last equation is obtained from (24.24a,b) using (24.12). By comparison with (24.21a,b) and (24.23a–d) we find

$$I_{F0} = \hat{a}_{11} \tag{24.25a}$$

$$I_{R0} = -\hat{a}_{22} \tag{24.25b}$$

$$\alpha_I = \hat{a}_{12}/I_{R0} \tag{24.25c}$$

$$\alpha_N = \hat{a}_{21}/I_{F0} = -\hat{a}_{12}/I_{F0} = -\alpha_I I_{R0}/I_{F0} \ . \tag{24.25d}$$

The constants α_N and α_I are the forward ('normal') ($\alpha_N = \alpha_0$ from (24.13)) and reverse ('inverted') gains in the common base circuit, respectively. Both constants are larger than zero. Typically, $\alpha_N \approx 0.98 \ldots 0.998 \lessapprox 1$ and $\alpha_I \approx 0.5 \ldots 0.9 < \alpha_N$. The model has three independent parameters, e.g. α_N, I_{F0} and I_{R0}. Equations (24.24a,b) can be rewritten as

$$I_E = \alpha_I\, I_C + (1 - \alpha_I\, \alpha_N)\, I_F \tag{24.26a}$$
$$I_C = \alpha_N\, I_E - (1 - \alpha_I\, \alpha_N)\, I_R\ . \tag{24.26b}$$

Under normal operation we have

$$I_E = I_F \tag{24.27a}$$
$$I_C = \alpha_N\, I_E\ . \tag{24.27b}$$

The model can be refined and made more realistic by including the effect of series resistances and depletion-layer capacitances, increasing the number of parameters to eight. The Early effect (see next section) can be included by adding a further current source. This level is the 'standard' Ebers-Moll model with a total of nine parameters. Further parameters can be added. However, as is always the case with simulations, there is a tradeoff between the simplicity of the model and to what detail a real situation is approximated.

24.2.4 Current–Voltage Characteristics

In Fig. 24.8, the hole density in the base (of a pnp transistor) is shown for various voltage conditions. In Fig. 24.9, the I–V characteristics of a bipolar transistor in common base and common collector circuit are shown. In the common base circuit (Fig. 24.9a), the collector current is practically equal to the emitter current and is almost independent of the collector–base voltage. From (24.26b), the dependence of the collector current on the collector–base voltage is given (within the Ebers-Moll model) as

$$I_C = \alpha_N I_E - (1 - \alpha_I \alpha_N) I_{R0} \left[\exp\left(\beta V_{CB}\right) - 1\right]\ . \tag{24.28}$$

V_{CB} is in the reverse direction. Therefore, the second term is zero for normal operating conditions. Since $\alpha_N \lessapprox 1$, the collector current is almost equal to the emitter current.

Even at $V_{CB} = 0$ (the case of (Fig. 24.8c), holes are extracted from the base since $\partial p/\partial x|_{x=w} > 0$. A small forward voltage must be applied to the collector–base diode in order to make the current zero,

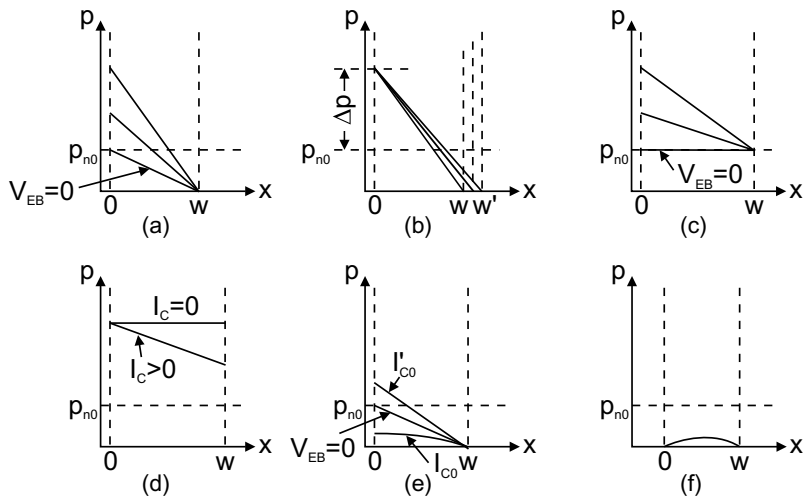

Fig. 24.8 Hole density (linear scale) in the base region (the neutral part of the base ranges from 0 to w) of a pnp transistor for various voltages. **a** normal voltages, $V_{CB} = \text{const.}$ and various V_{EB} (in forward direction). **b** $V_{EB} = \text{const.}$ and various values of V_{CB}. **c** Various values of $V_{EB} > 0$, $V_{CB} = 0$. **d** Both pn-junctions in forward direction. **e** Conditions for I_{C0} and I'_{C0}. **f** both junctions in reverse direction. Adapted from [574]

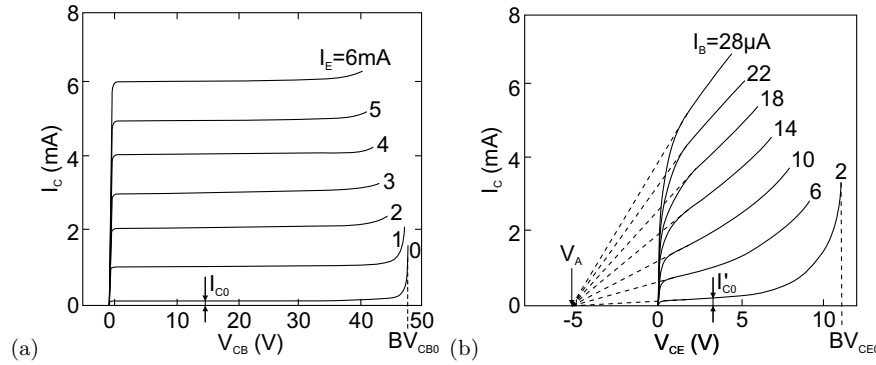

Fig. 24.9 Characteristics (I_C vs. V_{CB}) of a pnp transistor in **a** common base (CB) circuit (Fig. 24.4a) for various values of the emitter current as labeled. Adapted from [2050]. **b** Characteristics in common emitter (CE) circuit (Fig. 24.4b). Adapted from [2051]

i.e. $\partial p/\partial x|_{x=w} = 0$ (Fig. 24.8d). The collector saturation current I_{C0} is measured with an open emitter side. This current is smaller than the saturation current of the CB diode, since at the emitter side of the basis a vanishing gradient of the hole density is present (Fig. 24.8e). This reduces the gradient (and thus the current) at the collector side. The current I_{C0} is therefore smaller than the collector current for shorted emitter–base contact ($V_{EB} = 0$). At high collector voltage, the current increases rapidly at BV_{CB0} due to breakdown of the collector–base diode. It can also occur that the width of the neutral base region w becomes zero (punch-through). In this case, the emitter and collector are short-circuited.

In the common emitter circuit (Fig. 24.9b), there is a high current amplification I_C/I_B. Note that the collector current is given in mA and the base current in μA. The current increases with increasing V_{CE} because the base width w decreases and β_0 increases. There is no saturation of the I–V characteristics (Early effect [2052]). Instead, the I–V curves look as if they start at a negative collector–emitter voltage, the so-called Early voltage V_A. In the linear regime, the characteristic can be approximated by

$$I_C = \left(1 + \frac{V_{CE}}{V_A}\right) \beta_0 \, I_B \; . \tag{24.29}$$

Here, β_0 is the current gain for $V_{CE} \approx 0$.

The physical reason for the increase of the collector current with increasing V_{CE} is the increasing reverse voltage at the collector–base diode that causes the so-called 'base-width modulation', as shown in Fig. 24.8b. The expansion of the CB depletion layer leads subsequently to a reduction of the neutral base width w. w will be smaller and smaller compared to the geometrical base width w_B. When w is reduced, the common base gain α_0 (24.19) becomes closer to 1 and the current gain increases. Therefore, the collector current increases with V_{CE} for a given (fixed) base current. The Early voltage is the coefficient of the increase of collector current with V_{CE},

$$\frac{\beta_0 \, I_B}{V_A} = \frac{\partial I_C}{\partial V_{CE}} = \frac{\partial I_C}{\partial V_{CB}} \frac{\partial V_{CB}}{\partial V_{CE}} \approx \frac{\partial I_C}{\partial V_{CB}} \; . \tag{24.30}$$

For constant base current, the emitter-base voltage is almost constant and the approximation in (24.30) holds. The dependence of the CB depletion layer width on the base side x_C^n on U_{CB} is given by (21.110a) for a pnp-transistor. Typical values for the Early voltage are 50–300 V. The modeling of the Early effect in the SPICE simulation program is discussed in [2053].

For small collector–emitter voltage, the current quickly drops to zero. V_{CE} is typically split in such a way that the emitter–base diode is well biased forward and the CB diode has a high reverse voltage. If V_{CE} drops below a certain value (≈ 1 V for silicon transistors), there is no longer any bias at the CB diode. A further reduction of V_{CE} biases the CB diode in the forward direction and quickly brings the collector current down to zero.

24.2.5 Basic Circuits

24.2.5.1 Common Base Circuit

In the common base configuration, there is no current amplification since the currents flowing through emitter and base are almost the same. However, there is voltage gain since the collector current causes a large voltage drop across the load resistor.

24.2.5.2 Common Emitter Circuit

The input resistance of the common emitter circuit (Fig. 24.10b) depends on the emitter–base diode and varies between a value of the order of 100 kΩ at small current and a few Ω at larger current and high V_{EB}. The voltage gain is

$$r_V = \frac{V_{CE}}{V_{EB}} = \frac{I_C}{V_{EB}} R_L \,, \tag{24.31}$$

where R_L is the load resistance in the output circuit (see Fig. 24.4b). The ratio $g_m = I_C / V_{EB}$ is called the forward transconductance. Also, the differential transconductance $g'_m = \partial I_C / \partial V_{EB}$ is used. The voltage gain of the common emitter circuit is typically 10^2–10^3. Since current *and* voltage are amplified, this circuit has the highest power gain.

If the input voltage V_{EB} is increased, the collector current rises. This increase causes an increase of the voltage drop across the load resistance R_L and a decrease of the output voltage V_{CE}. Therefore, the phase of the input signal is reversed and the amplifier is inverting.

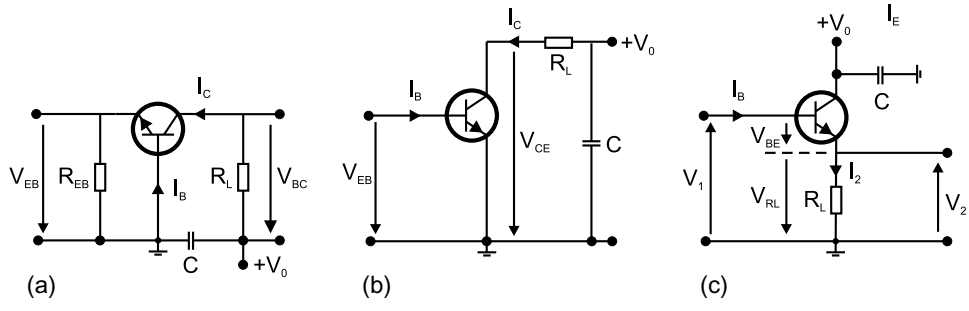

Fig. 24.10 **a** Common base, **b** common emitter and **c** common collector circuits with external loads

24.2.5.3 Common Collector Circuit

In Fig. 24.10c, the collector is connected to mass for alternating currents. Input and output current flow through the load resistance at which part of the input voltage drops. The input voltage is divided between the load resistor R_L and the emitter–base diode. At the transistor, the voltage $V_{BE} = V_1 - V_{RL}$ is applied. If the input voltage ($V_1 = V_{BC}$) is increased, I_2 increases. This leads to a larger voltage drop at the load resistor and therefore to a decrease of V_{BE}, working against the original increase. The input resistance R_1 is large despite a small load resistance, $R_1 \approx \beta_0 R_L$. The input voltage is larger than V_{RL}, thus no voltage gain occurs (actually it is a little smaller than 1). The current amplification is $(\beta + 1)$. The output resistance R_2 is small, $R_2 = V_2/I_2 = R_L \approx R_1/\beta_0$. Therefore, this circuit is also called an impedance amplifier that allows high-impedance sources to be connected low-impedance loads. Since an increase of the input voltage leads to an increase of the output voltage that is present at the emitter, this circuit is a direct amplifier and is also called an emitter follower.

24.2.6 High-Frequency Properties

Transistors for amplification of high-frequency signals are typically chosen as npn transistors since electrons, the minority carriers in the base, have higher mobility than holes. The active area and parasitic capacitance must be minimized. The emitter is formed in the shape of a stripe, nowadays in the 100 nm regime. The base width is in the 10 nm range. High p-doping of GaAs with low diffusion of the dopant is accomplished with carbon. Defects that would short emitter and collector at such thin base width must be avoided.

An important figure of merit is the cutoff frequency f_T for which h_{FE} is unity in the common emitter configuration. The cutoff frequency is related to the emitter–collector delay time τ_{EC} by

$$f_T = \frac{1}{2\pi\,\tau_{EC}} \,. \tag{24.32}$$

The delay time is determined by the charging time of the emitter–base depletion layer, the base capacitance, and the transport through the base–collector depletion layer. It is favorable if all times are short and similar. It does not help to minimize only one or two of the three processes since the longest time determines the transistor performance.

Another important figure of merit is the maximum frequency with which the transistor can oscillate in a feedback circuit with zero loss. This frequency is denoted by f_{max}. Approximately,

$$f_{max} \simeq \sqrt{\frac{f_T}{8\pi\,R_B\,C_{CB}}} \,, \tag{24.33}$$

where R_B is the base resistance and C_{CB} is the collector–base capacitance. f_{max} is larger than f_T, by a factor of the order of three.

24.2.7 Heterojunction Bipolar Transistors

In a heterojunction bipolar transistor (HBT), the emitter–base diode is formed with a heterostructure diode. The desired functionality is obtained when the emitter is made from the higher-bandgap material

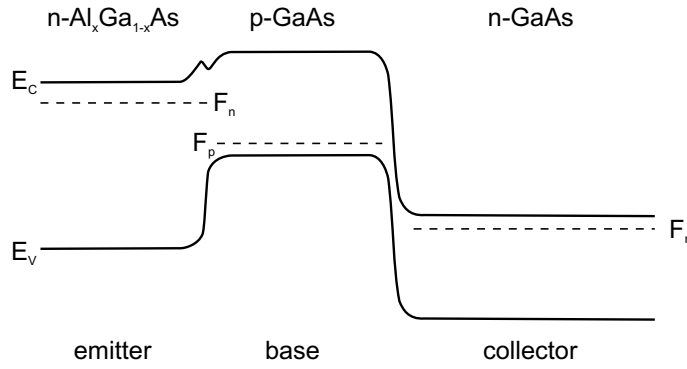

Fig. 24.11 Schematic band diagram of a heterojunction bipolar transistor

and the base from the lower-bandgap material. The schematic band diagram is shown in Fig. 24.11 (see Fig. 21.59c for the emitter–base diode).

The higher discontinuity in the valence band, compared to a homojunction with the base material, provides a higher barrier for hole transport from the base to the emitter. Thus, the emitter efficiency is increased. Another advantage is the possibility for higher doping of the base without loss of emitter efficiency. This reduces the base series resistance and leads to better high-frequency behavior due to higher current gain and a smaller RC time constant. Also, operation at higher temperature is possible when the emitter has a larger band gap. Current InP/InGaAs-based HBTs have cutoff frequencies beyond 30 GHz, SiGe-HBTs beyond 80 GHz. The high-frequency performance is influenced by the velocity-overshoot effect (cf. Sect. 8.4.3) [2054].

In Fig. 24.12, an InAlAs/InGaAs HBT is shown [2056]. The cutoff frequency is 90 GHz. For the layer design, a fairly thick collector with low doping was chosen. This design allows a broad depletion layer with fairly small maximum electric field and thus a high breakdown voltage of $BV_{CE0} > 8.5$ V. The base is not too thin (80 instead of maybe 60 nm) to reduce the series resistance. A graded region between emitter and base was chosen to avoid a spike occurring in the conduction band (Fig. 21.59b) and keep the turn-on voltage low.

24.2.8 Light-Emitting Transistors

The base current has two components. One is the recombination current in the neutral region of the emitter; this current can be suppressed in the HBT. The other is the recombination in the base region itself.[3] If quantum wells are introduced into the base region, this recombination can occur radiatively between electrons and holes captured into the quantum well (Fig. 24.13). The spectrum exhibits two peaks from the QWs and the GaAs barrier.

24.3 Field-Effect Transistors

Next to the bipolar transistors, the field-effect transistors (FET) are another large class of transistors. FETs were historically conceptualized first but due to technological difficulties with semiconductor

[3] Also, a recombination current in the emitter–base depletion region is possible. However, since in normal operating conditions this diode is forward biased, the depletion layer is short and the associated recombination current is small, cf. p. 614.

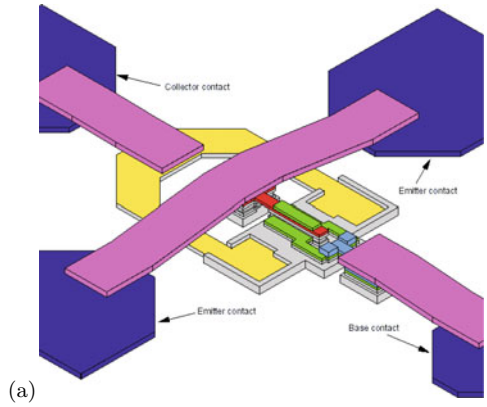

(a)

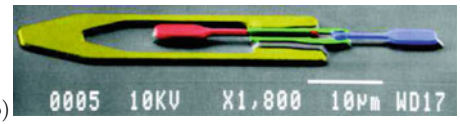

(b)

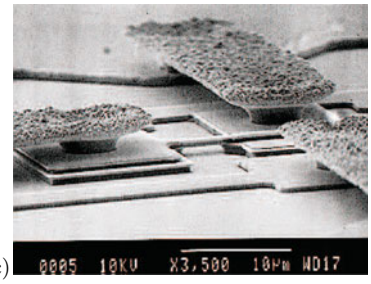

(c)

Material	d (nm)	type	function
(In,Ga)As	75	n^+	emitter cap
(In,Al)As	45	N^+	emitter cap
(In,Al)As	100	N	emitter
(In,Al,Ga)As	45	N	grade
(In,Ga)As	80	p^+	base
(In,Ga)As	700	n^-	collector
(In,Ga)As	430	n^+	subcollector
InP substrate			

(d)

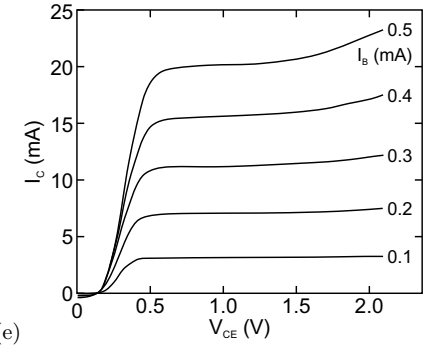

(e)

Fig. 24.12 **a** Schematic layout of a high-frequency HBT and SEM images **b** without and **c** with contacts. **d** Epitaxial layer sequence and **e** static performance data. Parts **a**, **b** from [2055], parts **d**, **e** from [2056]

surfaces, realized second. The principle is fairly simple: A current flows through a channel from source to drain. The current is varied via the channel conductivity upon the change of the gate voltage. The gate needs to make a nonohmic contact to the semiconductor. Since the conductivity in the channel is a property related to the majority charge carriers, FETs are called unipolar transistors. FETs feature a higher input impedance than bipolar transistors, a good linearity, and a negative temperature coefficient and thus a more homogeneous temperature distribution. According to the structure of the gate diode we distinguish JFETs, MESFETs and MOSFETs, as discussed in the following:

In the junction FET (JFET), the variation of channel conductivity is accomplished via the extension of the depletion layer of the pn-junction formed by the gate and the channel material (Fig. 24.14a). The JFET was analyzed by Schottky in 1952 [108] and realized by Dacey and Ross in 1953 [109]. The JFET can be made with a heterostructure gate to improve the frequency response.

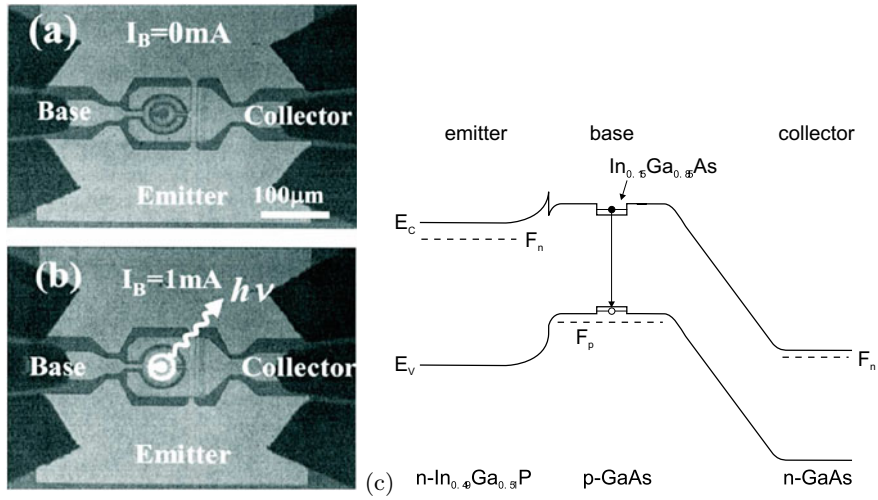

Fig. 24.13 Microscopic image of an InGaP/GaAs HBT with two 5-nm InGaAs/GaAs QWs in the 30-nm wide base at **a** zero base current and **b** at 1 mA base current in the common emitter configuration with Si CCD image of light emission. **c** Schematic band diagram of a HBT with a single InGaAs/GaAs quantum well in the base. Parts **a**, **b** from [2057], part **c** adapted from [2057]

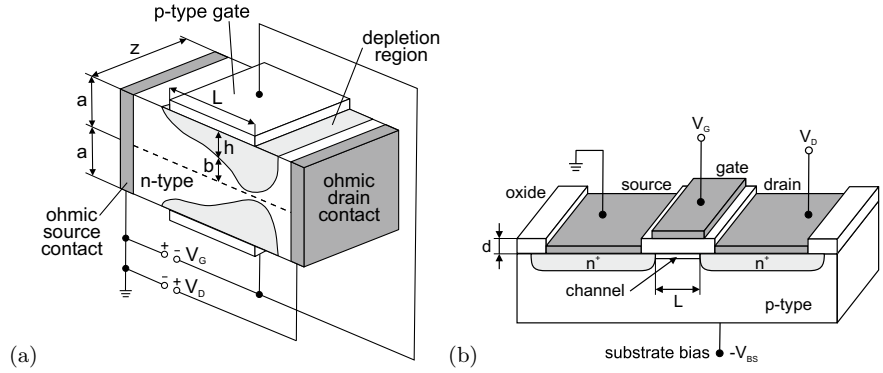

Fig. 24.14 **a** Shockley's model of a JFET. The *dashed line* represents the middle of the symmetric channel of total thickness $2a$. The *light grey area* is the depletion layer with thickness h. The gate length is L. The *dark grey* areas are ohmic metal contacts. Based on [109]. **b** Scheme of a MOSFET with channel length L and oxide thickness d. The *dark grey* areas are ohmic metal contacts. Adapted from [574]

In a MESFET, a metal–semiconductor diode (Schottky diode) is used as rectifying contact instead of a pn-diode. Otherwise, the principle is the same as that of the JFET. After the proposal by Mead in 1966 [135], the first (epitaxial) GaAs MESFET was realized by Hooper and Lehrer in 1967 [138]. The MESFET offers some advantages, such as the fabrication of the metal gate at lower temperature than necessary for the (diffusion or epitaxy of the) pn-diode, lower resistance, good thermal contact.

In a MISFET, the gate diode is a metal–insulator–semiconductor diode (Fig. 24.14b). If the insulator is an oxide, the related FET is a MOSFET. When the gate is put at a positive voltage (for a p-channel), an inversion layer is formed close to the insulator–semiconductor interface. This layer is an n-conducting channel allowing conduction between the two oppositely biased pn-diodes. It can carry a high current. The MOSFET was theoretically envisioned early by Lilienfeld in 1925 [55] and realized only in 1960 by Kahng and Atalla [121].

FETs come in 'n' and 'p' flavors, depending on the conductivity type of the channel. For high-frequency applications, typically an n-channel is used due to the higher mobility or drift velocity. In CMOS (complementary MOS) technology, both n-FETs and p-FETs are integrated in high density, allowing the effective realization of logic gates with minimized power consumption.

24.4 JFET and MESFET

24.4.1 General Principle

The principal characteristic of a JFET is shown in Fig. 24.15. At $V_D = 0$ and $V_G = 0$, the transistor is in thermodynamic equilibrium and there are no net currents. Underneath the gate diode, a depletion layer is present. If for zero gate voltage the source–drain voltage is applied to the channel, the current increases linearly. The positive voltage at the drain contact causes the expansion of the depletion layer of the (reversely biased) gate–drain pn-diode. When the two (the upper and the lower) depletion regions meet (pinch-off), the current saturates. The respective source–drain voltage is denoted as $V_{D,sat}$. For high gate–drain (reverse) voltage V_D, breakdown occurs with a strong increase of the source–drain current. A variation of the gate voltage V_G leads to a variation of the source–drain current. A reverse voltage leads to a reduction of the saturation current and saturation at lower source–drain voltage. For a certain gate voltage V_P, the pinch-off voltage, no current can flow in the channel any longer since pinch-off exists even for $V_D = 0$.

24.4.2 Static Characteristics

Here, we will calculate the general static behavior outlined in the previous section. We assume a long channel ($L \gg a$), the abrupt approximation for the depletion layer, the gradual channel approximation, i.e. the depletion layer depth changes slowly along x, and a field-independent, constant mobility. In

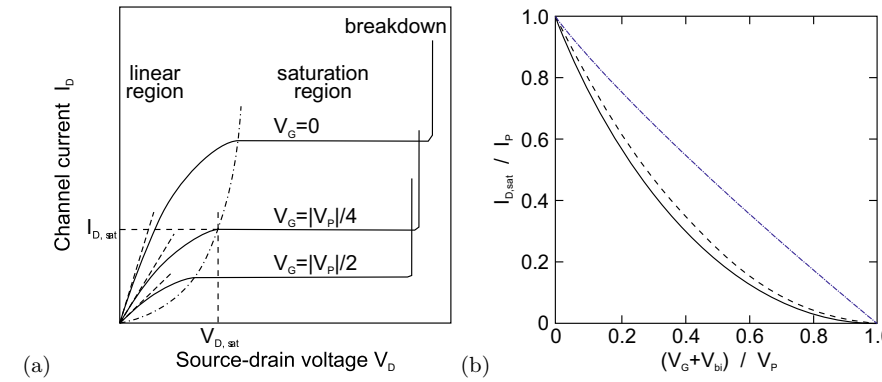

Fig. 24.15 **a** Principal characteristics of a JFET. The channel current I_D is shown as a function of the source–drain voltage V_D for three different values of the (absolute value of the) gate voltage V_G. The saturation values $V_{D,sat}$ and $I_{D,sat}$ are indicated for one curve. The intersections with the *dash-dotted* line yield the saturation voltage. Adapted from [574]. **b** Transfer behavior of a JFET for two different carrier distributions, homogeneous (*solid* line) and δ-like (*dashed* line). The *blue, dash-dotted* line is $\sqrt{I_D/I_P}$ vs. the gate voltage. After [2058, 2059]

this case, the two-dimensional Poisson equation for the potential distribution V can be used by solving it along the y direction (channel depth) for all x-positions (adiabatic approximation),

$$\frac{\partial^2 V}{\partial y^2} = -\frac{\rho(y)}{\epsilon_\mathrm{s}} \,. \tag{24.34}$$

The geometry is shown in the inset of Fig. 24.15b.

The depth h of the depletion layer in the abrupt approximation is given by (cf. (21.111), reverse voltages are counted as positive here)

$$h = \sqrt{\frac{2\epsilon_\mathrm{s}}{e N_\mathrm{D}} \left(V_\mathrm{bi} + V_\mathrm{G} + V(x)\right)} \,. \tag{24.35}$$

Here, we have assumed homogeneous doping, i.e. N_D does not depend on y (or x). The built-in voltage (for a $\mathrm{p^+n}$ gate diode) is given by $V_\mathrm{bi} = \beta^{-1} \ln(N_\mathrm{D}/n_\mathrm{i})$ (21.101a). The voltage V is the applied source–drain voltage in relation to the source. The depth of the depletion layer at $x = 0$ (source) and $x = L$ (drain) is given by

$$y_1 = h(0) = \sqrt{\frac{2\,\epsilon_\mathrm{s}}{e\,N_\mathrm{D}} \left(V_\mathrm{bi} + V_\mathrm{G}\right)} \tag{24.36a}$$

$$y_2 = h(L) = \sqrt{\frac{2\,\epsilon_\mathrm{s}}{e\,N_\mathrm{D}} \left(V_\mathrm{bi} + V_\mathrm{G} + V_\mathrm{D}\right)} \,. \tag{24.36b}$$

The maximum value of h is a. Therefore, the pinch-off voltage V_P, at which $V_\mathrm{P} = V_\mathrm{bi} + V_\mathrm{G} + V_\mathrm{D}$ is such that $h = a$, is given by

$$V_\mathrm{P} = \frac{e\,N_\mathrm{D}\,a^2}{2\,\epsilon_\mathrm{s}} \,. \tag{24.37}$$

The (drift) current density along x is given by (cf. (8.54a))

$$j_x = -e\,N_\mathrm{D}\,\mu_\mathrm{n}\,E_x = e\,N_\mathrm{D}\,\mu_\mathrm{n}\,\frac{\partial V}{\partial x} \tag{24.38}$$

for the neutral part of the semiconductor. Therefore, the current in the upper half of the channel is given by

$$I_\mathrm{D} = e\,N_\mathrm{D}\,\mu_\mathrm{n}\,\frac{\partial V(x)}{\partial x}\,Z\,\left[a - h(x)\right] \,, \tag{24.39}$$

where Z is the width of the channel (Fig. 24.14a). Although it seems that I_D depends on x, it is of course constant along the channel due to Kirchhoff's law.[4] Using the triviality $\int_0^L I_\mathrm{D}\mathrm{d}x = L\,I_\mathrm{D}$ and $\frac{\partial V}{\partial x} = \frac{\partial V}{\partial h}\,\frac{\partial h}{\partial x}$ with $\frac{\partial V}{\partial h} = eN_\mathrm{D}h/\epsilon_\mathrm{s}$ from (24.35), we find from (24.39)

$$I_\mathrm{D} = \frac{e^2\,\mu_\mathrm{n}\,N_\mathrm{D}^2\,Z\,a^3}{6\,\epsilon_\mathrm{s}\,L} \left[\frac{3}{a^2}\left(y_2^2 - y_1^2\right) - \frac{2}{a^3}\left(y_1^3 - y_2^3\right)\right] \,. \tag{24.40}$$

[4] We neglect recombination, in particular since the current is a majority-carrier current.

This equation can also be written, using (24.37) and

$$I_P = \frac{e^2\,\mu_n\,N_D^2\,Z\,a^3}{6\,\epsilon_s\,L}\ , \tag{24.41}$$

as

$$I_D = I_P\left[\frac{3V_D}{V_P} - 2\,\frac{(V_{bi}+V_G+V_D)^{3/2} - (V_{bi}+V_G)^{3/2}}{V_P^{3/2}}\right]\ . \tag{24.42}$$

The saturation current is reached for $y_2 = a$ or $V_{bi} + V_G + V_D = V_P$ and is given by

$$I_{D,sat} = I_P\left[1 - 3\,\frac{V_{bi}+V_G}{V_P} + 2\left(\frac{V_{bi}+V_G}{V_P}\right)^{3/2}\right]\ . \tag{24.43}$$

The dependence of the saturation current on $(V_G + V_{bi})/V_P$ is depicted in Fig. 24.15b. For the threshold (gate) voltage of

$$V_T = V_P - V_{bi}\ , \tag{24.44}$$

the saturation current is zero since then $V_D = 0$.[5] Around the threshold voltage, the drain saturation current is given in lowest order of V_G as

$$I_{D,sat} \approx \frac{3\,I_P}{4}\left(\frac{V_G - V_T}{V_P}\right)^2\ . \tag{24.45}$$

Thus, in order to experimentally determine the threshold voltage, $\sqrt{I_D}$ is plotted versus the gate voltage and extrapolated to $I_D = 0$ (dash-dotted line in Fig. 24.15 and Fig. 24.16).

The source–drain voltage at the saturation point decreases with decreasing saturation current, shown as dashed parabola-like line in Fig. 24.15a.

If the charge-carrier distribution differs from the homogeneous distribution assumed so far, a change of transistor properties arises, as shown in Fig. 24.15b for a δ-like carrier distribution. The I–V characteristic is slightly less curved, but not linear. A linear characteristic is only achievable in the drift velocity saturation regime (cf. Sect. 24.4.4).

For high source–drain voltage $V_D > V_P - V_{bi} - V_G$, the current remains essentially at its saturation value. For very high source–drain voltage, breakdown in the gate–drain diode can occur, when the maximum voltage, which is given by $V_G + V_D$ at the end of the channel, is equal to the breakdown voltage V_B.

The forward transconductance g_m and the drain transconductance g_D are given by

$$g_m = \left.\frac{\partial I_D}{\partial V_G}\right|_{V_D=const.} = g_{max}\left[\sqrt{\frac{V_{bi}+V_G}{V_P}} - \sqrt{\frac{V_{bi}+V_G+V_D}{V_P}}\right] \tag{24.46}$$

$$g_D = \left.\frac{\partial I_D}{\partial V_D}\right|_{V_G=const.} = g_{max}\left[1 - \sqrt{\frac{V_{bi}+V_G+V_D}{V_P}}\right]\ , \tag{24.47}$$

where

$$g_{max} = \frac{3\,I_P}{V_P} = \frac{e\,N_D\,\mu_n\,Z\,a}{L}\ . \tag{24.48}$$

[5] The threshold voltage can also be obtained from the condition $g_{D0} = 0$ (cf. (24.49)).

In more detail, the mobility used in (24.45), (24.46) and (24.47) must be distinguished as saturation, field-effect and effective mobility (cmp. more details given for MOSFETs on p. 780).

The drain transconductance for $V_D \to 0$ (linear regime, dashed straight lines in Fig. 24.15a) is given by

$$g_{D0} = g_{max}\left[1 - \sqrt{\frac{V_{bi} + V_G}{V_P}}\right] = g_{m,sat} \ , \tag{24.49}$$

which is equal[6] to the forward transconductance in the saturation regime $g_{m,sat} = \partial I_{D,sat}/\partial V_G$.

24.4.3 Normally On and Normally Off FETs

The JFET discussed so far had an n-conductive channel and was conductive at $V_G = 0$. It is termed an 'n-type, normally on' (or depletion) FET. If the channel is p-conductive, the FET is called 'p-type'. A FET that has a nonconductive channel at $V_G = 0$ is called 'normally off' (or accumulation) FET. In this case, the built-in voltage must be large enough to cause pinch-off. For a positive gate voltage (in the forward direction of the gate–drain diode), current begins to flow. The I–V characteristics of the four FET-types are depicted in Fig. 24.16. The circuit symbols for the four different FET types are shown in Fig. 24.17.

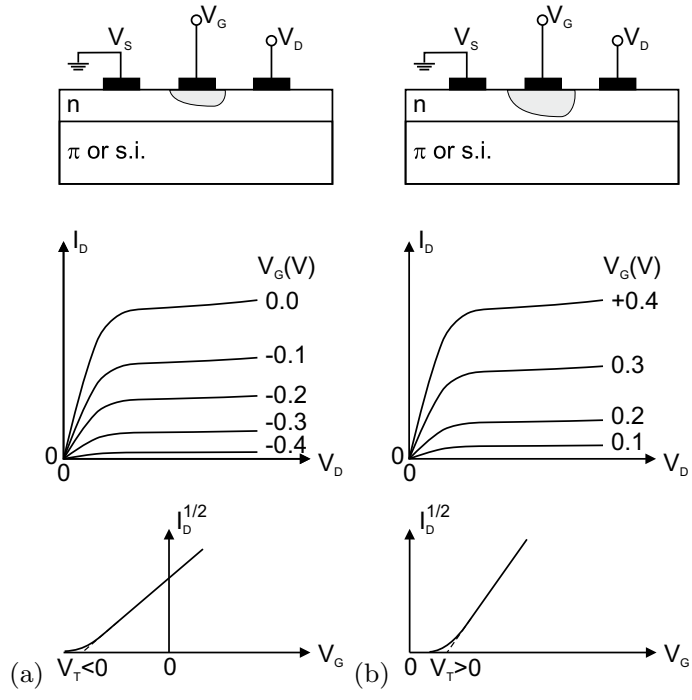

Fig. 24.16 Scheme (*top*), I_D vs. V_D (*center*) and $I_D^{1/2}$ vs. V_G (*bottom*) I–V characteristics for **a** normally on (depletion) and **b** normally off (accumulation) n-type JFET. Adapted from [574]

[6] Technically, here $g_{D0} = -g_{m,sat}$, however, we had counted V_G positive for the reverse direction.

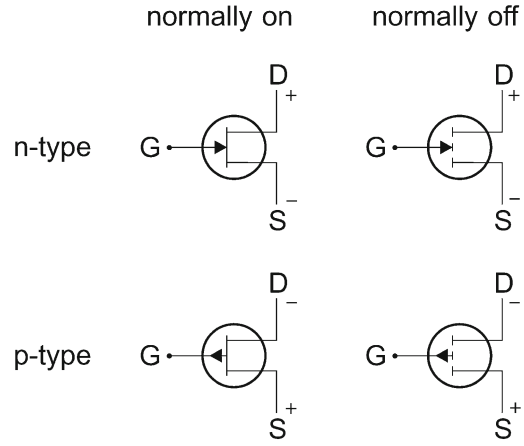

Fig. 24.17 Circuit symbols for various types of FETs

24.4.4 Field-Dependent Mobility

So far, we have considered FETs with long channels ($L \gg a$). This situation is often not the case, in particular for high-integration or high-frequency applications. For short channels, the I–V characteristics exhibit changes. The theory needs to be modified to take into account, among other effects, the electric-field dependence of the mobility (Fig. 8.13) that was discussed in Sect. 8.4.1.

Drift-Velocity Saturation

A material without negative differential mobility, such as Si or Ge, can be described with a drift-velocity model

$$v_\mathrm{d} = \mu\, E\, \frac{1}{1+\mu\, E/v_\mathrm{s}}\ . \tag{24.50}$$

In this model, μ denotes the low-field (ohmic) mobility and v_s the drift-saturation velocity reached for $E \gg v_\mathrm{s}/\mu$. The fraction in (24.50) describes the drift-velocity saturation.

By inserting (24.50) into (24.39), we obtain (for a n-channel)

$$I_\mathrm{D} = -e\, N_\mathrm{D}\, \mu_\mathrm{n}\, E(x)\, \frac{1}{1+\mu\, E(x)/v_\mathrm{s}}\, [a-h(x)]\, Z\ , \tag{24.51}$$

and after a short calculation the drain current is given by (cf. (24.42))

$$I_\mathrm{D} = I_\mathrm{P} \left(1+\frac{\mu\, V_\mathrm{G}}{v_\mathrm{s}\, L}\right)^{-1} \left[\frac{3V_\mathrm{D}}{V_\mathrm{P}} - 2\,\frac{(V_\mathrm{bi}+V_\mathrm{G}+V_\mathrm{D})^{3/2}-(V_\mathrm{bi}+V_\mathrm{G})^{3/2}}{V_\mathrm{P}^{3/2}}\right]\ . \tag{24.52}$$

The factor $1/(1+z)$ with $z = \mu V_\mathrm{G}/v_\mathrm{s}L$ reduces the channel current due to the drift saturation effect. The effect of the parameter z is depicted in Fig. 24.18 in comparison to $z = 0$, i.e. without the drift saturation effect (or $v_\mathrm{s} \to \infty$). The forward conductance $g_\mathrm{m,sat}$ decreases with increasing z, as shown in Fig. 24.19.

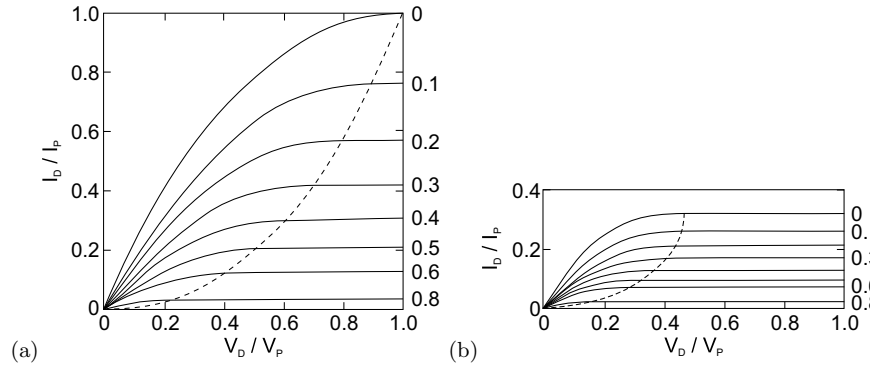

Fig. 24.18 I–V characteristic **a** without consideration of drift saturation ($z = 0$) and **b** with drift saturation ($z = 3$) for various values of $(V_G + V_{bi})/V_P$ =0, 0.1, 0.2, 0.3, 0.4, 0.5, 0.6, 0.8 as indicated at the right side. The intersections of the *dashed line* and the *solid lines* indicate the beginning of saturation. Adapted from [2060]

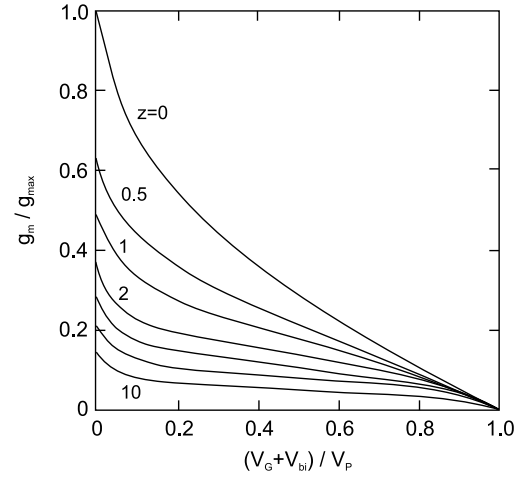

Fig. 24.19 Decrease of (saturated) forward conductance with gate voltage (according to (24.49)) and parametric dependence on z for $z = 0$, 0.5, 1, 2, 3, 5 and 10. Adapted from [2060]

Two-Region Model

In order to model the GaAs drift velocity vs. field characteristic, a two-region model is used. In the front region of the channel (region I), the field is small enough and a constant mobility μ is used. In the back region of the channel (region II) is the high-field region where a constant drift velocity v_s is used. With increasing source–drain voltage, the region II (I) increases (decreases) in length. The relative width of region II is also increased with decreasing channel length.

Saturated-Drift Model

Here, the drift velocity is taken everywhere as v_s, i.e. complete drift saturation. This is a good approximation for short channels (high fields) that are in current saturation. In this case, the current is given by

$$I_D = -e\, N_D\, v_s\, [a - h(x)]\; Z\;. \tag{24.53}$$

Equation (24.53) is valid for homogeneous doping. For other doping profiles, the current is given by

$$I_{\mathrm{D}} = v_{\mathrm{s}}\, Z \int_{h}^{a} \rho(y)\, \mathrm{d}y \ . \tag{24.54}$$

The forward conductance is given by

$$g_{\mathrm{m}} = \frac{v_{\mathrm{s}}\, Z\, \epsilon_{\mathrm{s}}}{h(V_{\mathrm{G}})} \ . \tag{24.55}$$

The transistor is more linear if the depletion-layer depth only weakly depends on the gate voltage. This can be accomplished with a doping profile with increasing doping with depth. An increase with a power law and a step-wise or exponential increase lead to a more linear $I(V)$-dependence. In the limit of δ-like doping, a linear $I_{\mathrm{D,sat}}$ vs. V_{G} relation develops. Indeed, FETs with graded or stepped doping profiles exhibit improved linearity and are used for analog circuits.

Nonequilibrium Velocity

Below the electric field for which the drift velocity in GaAs peaks, the carriers can be considered to be in equilibrium. If the field is higher, velocity overshoot (Sect. 8.4.3 and Fig. 8.16) occurs. The carriers have a higher velocity (and ballistic transport) before they relax to the lower equilibrium (or steady-state) velocity after intervalley scattering. This effect will shorten the transit time in short-channel FETs.

24.4.5 High-Frequency Properties

Two factors limit the high-frequency performance of a FET: The transit time and the RC time constant. The transit time t_{r} is the time that the carrier needs to go from source to drain. For the case of constant mobility (long channel) and constant drift velocity (short channel), the transit time is given by (24.56a and b), respectively.

$$t_{\mathrm{r}} = \frac{L}{\mu\, E} \approx \frac{L^2}{\mu\, V_{\mathrm{G}}} \tag{24.56a}$$

$$t_{\mathrm{r}} = \frac{L}{v_{\mathrm{s}}} \ . \tag{24.56b}$$

For a 1-μm long gate in a GaAs FET, the transit time is of the order of 10 ps. This time is typically small compared to the RC time constant due to the capacitance C_{GS} and transconductance. The cutoff frequency is given by

$$f_{\mathrm{T}} = \frac{g_{\mathrm{m}}}{2\pi\, C_{\mathrm{GS}}} \ . \tag{24.57}$$

24.5 MOSFETs

The MOSFET has four terminals. In Fig. 24.14b, two n-type regions (source and drain) are within a p-type substrate. The n-type channel (length L) forms underneath a MIS diode. A forth electrode sets the substrate bias. The source electrode is considered to be at zero potential. The important parameters

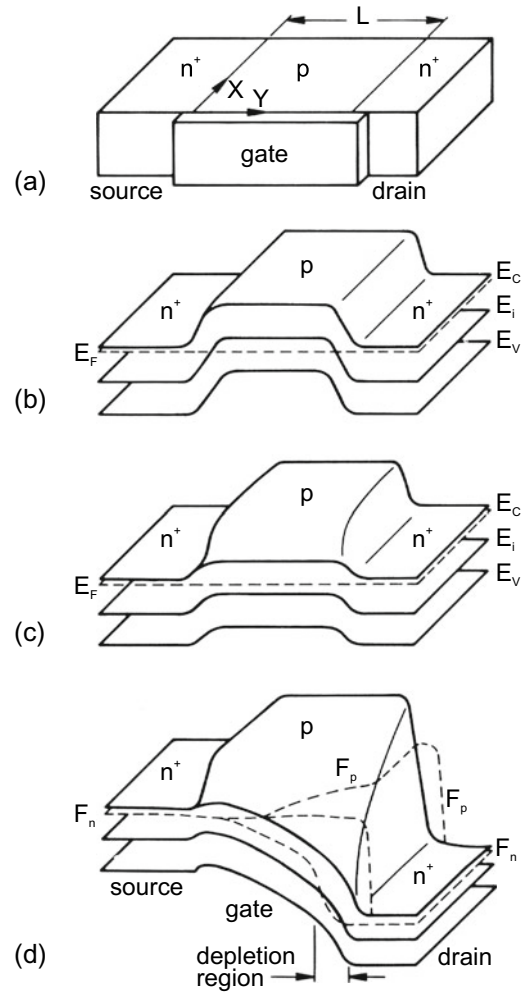

Fig. 24.20 **a** Schematic geometry of a MOSFET and its band diagram for **b** flat-band conditions for zero gate voltage (and $V_D = 0$), **c** thermodynamic equilibrium with reverse gate voltage (weak inversion, still $V_D = 0$) and **d** nonequilibrium with nonzero drain voltage and gate voltages (with most of the channel being inverted, the depletion region is indicated). Adapted from [2061]

are the substrate doping N_A, the insulator thickness d and the depth r_j of the n-type regions. Around the MOSFET structure is an oxide to insulate the transistor from neighboring devices.

24.5.1 Operation Principle

When there is no applied gate voltage, only the saturation current of the pn-diode(s) between source and drain flows. In thermodynamic equilibrium (Fig. 24.20c), the necessary surface potential for inversion at the MIS diode is $\Psi_s^{inv} \approx 2\Psi_B$. If there is a finite drain voltage, a current flows and there is no longer equilibrium. In this case, the quasi-Fermi level of the electrons (or generally of the minority carriers) is lowered and a higher gate voltage is needed to create inversion. The situation at the drain is depicted in Fig. 24.21.

In nonequilibrium, the depletion layer width is a function of the drain voltage V_D. In order to reach strong inversion at the drain, the surface potential must be at least $\Psi_s^{inv} \approx V_D + 2\Psi_B$.

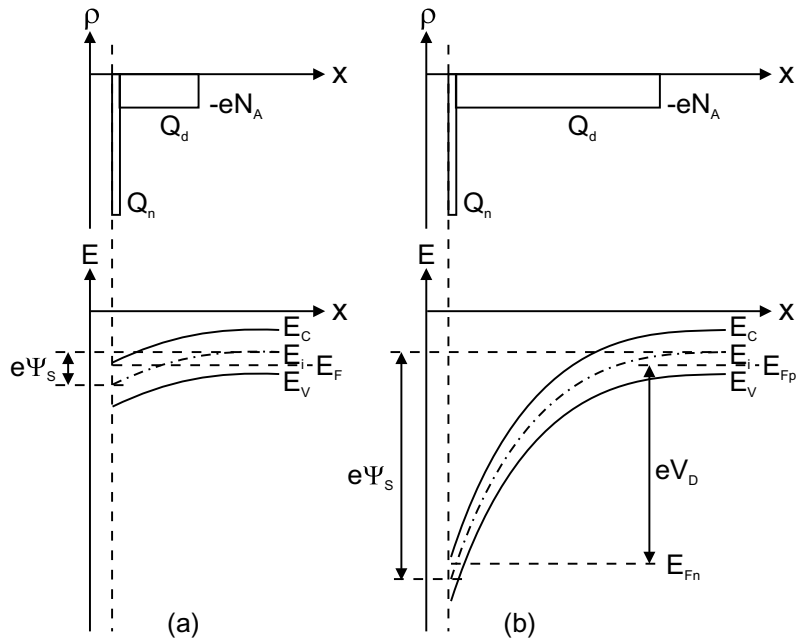

Fig. 24.21 Charge-carrier distribution (*top*) and band diagram (*bottom*) at the inverted p-region of a MOSFET for **a** thermodynamic equilibrium ($V_D = 0$) and **b** nonequilibrium at drain

If the gate voltage is such that an inversion channel is present from source to drain, a current will flow for a small drain voltage (Fig. 24.22a). Initially, the current will increase linearly with V_D, depending on the conductivity of the channel. With increasing drain voltage, the quasi-Fermi level of the electrons is lowered until, finally at $V_D = V_{D,sat}$, the inversion channel depth becomes zero (pinch-off at the point denoted with an arrow in Fig. 24.22b). The current at this condition is denoted as $I_{D,sat}$. For a further increase of V_D, the pinch-off point moves closer to the source contact and the channel length (inverted region) is shortened (arrow in Fig. 24.22c). The voltage at the pinch-off point remains $V_{D,sat}$ and thus the current in the channel remains constant at $I_{D,sat}$.

24.5.2 Current–Voltage Characteristics

We assume now that the potential $V(y)$ varies along the channel from $V = 0$ at $y = 0$ to $V = V_D$ at $y = L$. In the gradual-channel approximation, the voltage drop V_i across the oxide is

$$V_i(y) = V_G - \Psi_s(y) \,, \tag{24.58}$$

where Ψ_s is the surface potential in the semiconductor (see Fig. 21.34). The total charge induced in the semiconductor (per unit area) is, using (21.92), given by

$$Q_s(y) = -\left[V_G - \Psi_s(y)\right] C_i \,, \tag{24.59}$$

with C_i being the insulator capacitance (per unit area), as given in (21.93).

The inversion surface potential can be approximated by $\Psi_s(y) \approx 2\Psi_B + V(y)$ (see Fig. 24.21). With (21.97) the depletion-layer charge is

$$Q_d(y) = -e\, N_A\, w_m = -\sqrt{2\,\epsilon_s\, e\, N_A\, [2\Psi_B + V(y)]} \,, \tag{24.60}$$

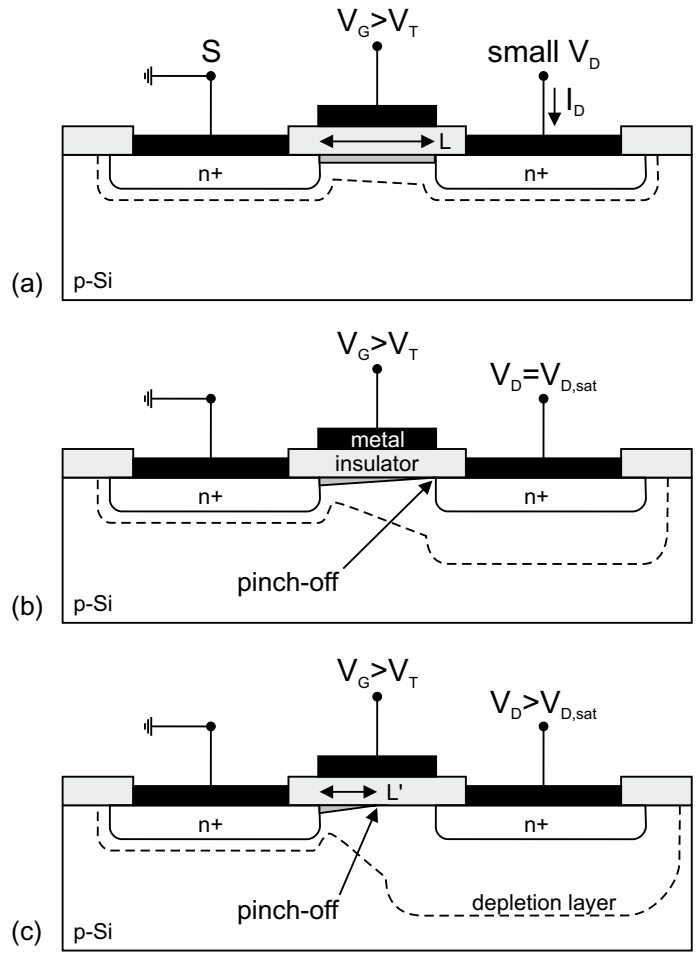

Fig. 24.22 **a** MOSFET with inverted channel (*dark grey*) of length L for small source–drain voltage V_D in linear regime, **b** at the start of saturation at pinch-off, **c** in the saturation regime with reduced channel length L'. The pinch-off point is denoted by an arrow in **b** and **c**. The *dashed lines* denote the extension of the depletion region. Adapted from [574]

such that, using (24.59), the inversion layer charge is

$$\begin{aligned} Q_\mathrm{n}(y) &= Q_\mathrm{s}(y) - Q_\mathrm{d}(y) \\ &= -\left[V_\mathrm{G} - V(y) - 2\Psi_\mathrm{B}\right] C_\mathrm{i} + \sqrt{2\,\epsilon_\mathrm{s}\, e\, N_\mathrm{A}\,\left[2\Psi_\mathrm{B} + V(y)\right]}\,. \end{aligned} \tag{24.61}$$

For the calculation of the drain current, we consider the increase of channel resistance $\mathrm{d}R(y)$ along a line element $\mathrm{d}y$ of the channel. The integral of the conductivity over the cross section A of the channel (width Z) is

$$\iint\limits_A \sigma(x,z)\mathrm{d}x\,\mathrm{d}z = -e\,\mu_\mathrm{n} \iint\limits_A n(x,z)\,\mathrm{d}x\,\mathrm{d}z = Z\,\mu_\mathrm{n}\,|Q_\mathrm{n}(y)|\,. \tag{24.62}$$

Therefore,

$$\mathrm{d}R(y) = \mathrm{d}y\,\frac{1}{Z\,\mu_\mathrm{n}\,|Q_\mathrm{n}(y)|}\,. \tag{24.63}$$

Here we have assumed that the mobility is constant along the channel, i.e. not field dependent. The change of voltage across the line element $\mathrm{d}x$ is

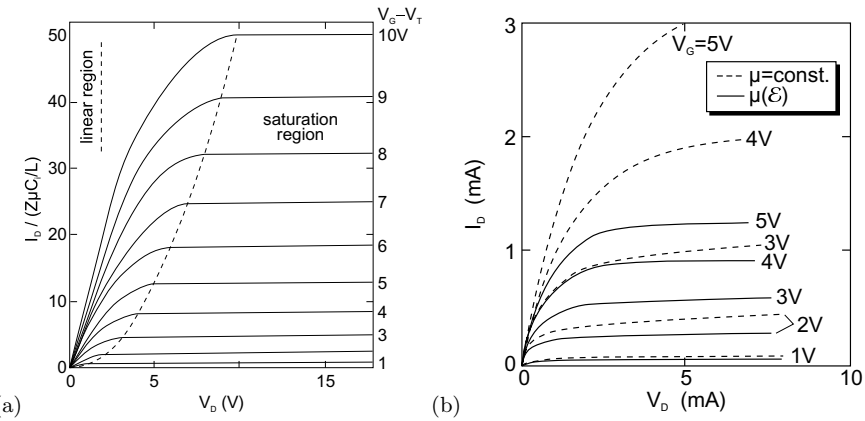

Fig. 24.23 **a** Idealized I–V characteristics for a MOSFET with constant mobility. The *dashed line* visualizes the drain (saturation) voltage for which the current is equal to $I_{\mathrm{D,sat}}$. The *solid lines* are for various values of the gate voltage $V_{\mathrm{G}} - V_{\mathrm{T}}$ =1–10 V. Adapted from [574] **b** I–V characteristics taking into account the effect of field-dependent mobility (*solid lines*) in comparison to the constant-mobility model (*dashed lines*) for various gate voltages as labeled. Adapted from [2062]

$$\mathrm{d}V(y) = I_{\mathrm{D}}\,\mathrm{d}R = \frac{I_{\mathrm{D}}\,\mathrm{d}y}{Z\,\mu_{\mathrm{n}}\,|Q_{\mathrm{n}}(y)|}\ . \tag{24.64}$$

We note the drain current is independent of x. Using (24.61) and performing the integral of (24.64) from $V(y=0) = 0$ to $V(y=L) = V_{\mathrm{D}}$, we find

$$I_{\mathrm{D}} = \mu_{\mathrm{n}}\,C_{\mathrm{i}}\,\frac{Z}{L}\left\{\left(V_{\mathrm{G}} - 2\Psi_{\mathrm{B}} - \frac{V_{\mathrm{D}}}{2}\right) - \frac{2}{3}\frac{\sqrt{2e\epsilon_{\mathrm{s}}N_{\mathrm{A}}}}{C_{\mathrm{i}}}\left[(V_{\mathrm{D}} + 2\Psi_{\mathrm{B}})^{3/2} - (2\Psi_{\mathrm{B}})^{3/2}\right]\right\}\ . \tag{24.65}$$

This characteristic is depicted in Fig. 24.23a. In the linear regime (small drain voltage, $V_{\mathrm{D}} \ll (V_{\mathrm{G}} - V_{\mathrm{T}})$), the drain current is given by

$$I_{\mathrm{D}} \cong \mu_{\mathrm{n}}\,C_{\mathrm{i}}\,\frac{Z}{L}\,(V_{\mathrm{G}} - V_{\mathrm{T}})\,V_{\mathrm{D}}\ . \tag{24.66}$$

The threshold voltage V_{T}, i.e. the gate voltage for which the channel is opened and a current can flow, is given for small drain voltage (linear regime) by

$$V_{\mathrm{T}} = 2\,\Psi_{\mathrm{B}} + \frac{\sqrt{4\,e\,\epsilon_{\mathrm{s}}\,N_{\mathrm{A}}\,\Psi_{\mathrm{B}}}}{C_{\mathrm{i}}}\ . \tag{24.67}$$

The transconductances in the linear regime are easily obtained as (cmp. (24.46), (24.47))

$$g_{\mathrm{m}} = \mu_{\mathrm{n}}\,C_{\mathrm{i}}\,\frac{Z}{L}\,V_{\mathrm{D}} \tag{24.68a}$$

$$g_{\mathrm{D}} = \mu_{\mathrm{n}}\,C_{\mathrm{i}}\,\frac{Z}{L}\,(V_{\mathrm{G}} - V_{\mathrm{T}})\ . \tag{24.68b}$$

The mobility extracted from evaluation of a characteristic using (24.68b) is termed *effective* mobility (μ_{eff}). The mobility extracted from (24.68a) is termed *field effect* mobility (μ_{FE}). The experimentally

measured field effect mobility is typically smaller than the effective mobility. The difference between the effective and the field effect mobility is related to the gate voltage dependence of the effective mobility; in the linear regime,

$$\mu_{\mathrm{FE}} \approx \mu_{\mathrm{eff}} + (V_{\mathrm{G}} - V_{\mathrm{T}}) \left.\frac{\partial \mu_{\mathrm{eff}}}{\partial V_{\mathrm{G}}}\right|_{V_{\mathrm{D}}=const.} . \tag{24.69}$$

The saturation current is approximately

$$I_{\mathrm{D,sat}} \cong \mu_{\mathrm{n}} C_{\mathrm{i}} \frac{m Z}{L} (V_{\mathrm{G}} - V_{\mathrm{T}})^2 , \tag{24.70}$$

where m depends on the doping concentration and is about 0.5 for low doping. The mobility extracted from (24.70) is termed *saturation* mobility (μ_{sat}). Due to the neglect of the gate voltage dependence in the definition for the saturation mobility, the experimental results usually yield $\mu_{\mathrm{sat}} < \mu_{\mathrm{eff}}$. For low p-doping of the substrate, the threshold voltage in (24.70) for the saturation regime is also given by (24.67). At higher doping, the threshold voltage becomes dependent on the gate voltage. C_{i} denotes the insulator capacitance

$$C_{\mathrm{i}} = \epsilon_{\mathrm{i}}/d_{\mathrm{i}} . \tag{24.71}$$

The forward transconductance in the saturation regime is

$$g_{\mathrm{m,sat}} = \mu_{\mathrm{n}} C_{\mathrm{i}} \frac{2 m Z}{L} (V_{\mathrm{G}} - V_{\mathrm{T}}) . \tag{24.72}$$

For constant drift velocity (Fig. 24.23b for field-dependent mobility), the saturation current is given by

$$I_{\mathrm{D,sat}} = Z C_{\mathrm{i}} v_{\mathrm{s}} (V_{\mathrm{G}} - V_{\mathrm{T}}) , \tag{24.73}$$

and the forward transconductance in the saturation regime is

$$g_{\mathrm{m,sat}} = Z C_{\mathrm{i}} v_{\mathrm{s}} . \tag{24.74}$$

We note that the transistor properties depend on and can be separated into the geometry factor (Z/L) and the material properties ($\mu C_{\mathrm{i}} = \mu \epsilon_{\mathrm{i}}/d_{\mathrm{i}}$).

The threshold voltage can be changed by the substrate bias V_{BS} as ($\beta = e/kT$)

$$\Delta V_{\mathrm{T}} = \frac{a}{\sqrt{\beta}} \left(\sqrt{2\Psi_{\mathrm{B}} + V_{\mathrm{BS}}} - \sqrt{2\Psi_{\mathrm{B}}} \right) , \tag{24.75}$$

with (L_{D} being the Debye length (cf. 21.85b))

$$a = 2 \frac{\epsilon_{\mathrm{s}}}{\epsilon_{\mathrm{i}}} \frac{d}{L_{\mathrm{D}}} . \tag{24.76}$$

Experimental data are shown in Fig. 24.24. For a Si/SiO_2 gate diode, $a = 1$ for, e.g., $d_{\mathrm{i}} = 10\,\mathrm{nm}$ and $N_{\mathrm{A}} = 10^{16}\,\mathrm{cm}^{-3}$. For gate voltages below V_{T}, the current is given by the diffusion current, similar to a npn transistor. This regime is important for low-voltage, low-power conditions. The related drain current is termed the *subthreshold* current and is given by

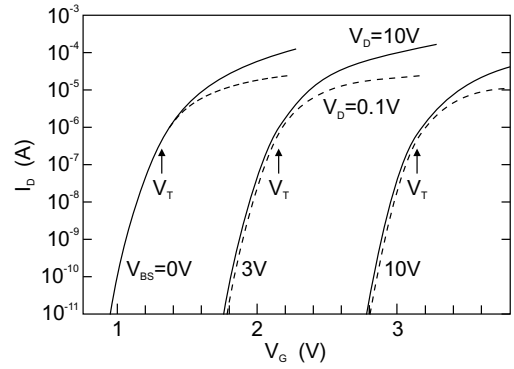

Fig. 24.24 Experimental subthreshold I–V characteristic of a MOSFET device with long channel (15.5 µm). *Solid lines* for $V_D = 10\,V$, *dashed lines* for $V_D = 0.1\,V$. Adapted from [2063]

$$I_D = \mu_n \frac{Z\,a\,C_i\,n_i^2}{2\,L\,\beta^2\,N_A^2} \left[1 - \exp\left(-\beta V_D\right)\right] \exp\left(-\beta\Psi_s\right)\,(\beta\Psi_s)^{-1/2}\ . \tag{24.77}$$

The drain current therefore increases exponentially with V_G, as shown in Fig. 24.24. V_G is approximately linear proportional to Ψ_B:

$$\Psi_s = (V_G - V_{FB}) - \frac{a^2}{2\beta}\left(\sqrt{1 + \frac{4}{a^2}\,(\beta V_G - \beta V_{FB} - 1)} - 1\right)\ , \tag{24.78}$$

where V_{FB} is the flat-band voltage of the gate MIS diode. The drain current is independent of V_D for $V_D \gtrsim 3kT/e$.

24.5.3 MOSFET Types

MOSFETs can have an n-type channel (on a p-substrate) or a p-channel (on an n-type substrate). So far, we have discussed the normally off MOSFET. If there is a conductive channel even without a gate voltage, the MOSFET is normally on. Here, a negative gate voltage must be applied to close the channel. Therefore, similar to the JFET, a total of four different types of MOSFET exist, see Fig. 24.25.

24.5.4 Complementary MOS

Complementary metal–oxide–semiconductor technology (CMOS) is the dominating technology for highly integrated circuits. In such devices, MOSFETs with n-channel (NMOS) and p-channel (PMOS) are used on the same chip. The basic structure of logic circuits, the inverter, can be realized with a pair of NMOS and PMOS transistors, as shown in Fig. 24.26a with two normally off transistors. The load capacitor represents the capacitance of the following elements.

If the input voltage is $V_{in} = 0$, the NMOS transistor is nonconductive ('off'). The (positive) voltage V_{DD} is at the PMOS transistor source, thus the gate is negative in relation to the source and the transistor is conductive ('on') since $-V_{DD} = V_{Gp} < V_{Tp} < 0$ (see Fig. 24.25). The current flows through the capacitor that becomes charged to $V_{out} = V_{DD}$. The current then subsides, since V_D at the PMOS becomes zero. If the input voltage is set to V_{DD}, the NMOS transistor has a positive gate–source voltage larger than the threshold $V_{Tn} < V_{Gn} = V_{DD}$ and becomes conductive. The charge from the

capacitor flows over the NMOS to ground. The PMOS transistor has zero gate–source voltage and is in the 'off' state. In this case, the voltage V_{DD} drops entirely across the PMOS and the capacitor is uncharged with $V_{out} = 0$.

In both its logic states, the CMOS inverter does not consume power. No current[7] flows in either of the two steady states since one of the two transistors is in both cases in the 'off' state. Current flows only during the switching operation. Therefore, the CMOS scheme allows for low power consumption.

The middle voltage for which $V_{in} = V_{out}$ can be calculated from the MOSFET characteristics. Both are, for this condition, in saturation and the currents are given by (cf. (24.70))

$$I_{Dn} = \mu_n C_{ox} \frac{Z_n}{2L_n} (V_M - V_{Tn})^2 \tag{24.79a}$$

$$I_{Dp} = \mu_p C_{ox} \frac{Z_p}{2L_p} \left(V_{DD} - V_M - V_{Tp}\right)^2 . \tag{24.79b}$$

With $\gamma = \frac{Z_p}{Z_n} \frac{L_n}{L_p} \frac{\mu_p}{(-\mu_n)}$, we find from $I_{Dn} = -I_{Dp}$,

$$V_M = \frac{V_{Tn} + \gamma \left(V_{DD} + V_{Tp}\right)}{1 + \gamma} . \tag{24.80}$$

As gate material, often polycrystalline silicon (poly-Si) is used (cf. Fig. 21.29). It is used instead of metals because its work function matches that of silicon closely. Also, poly-Si is more resistant to temperature. Despite its high doping, the resistance of poly-Si is two orders of magnitude larger than that of metals. Since it is easily oxidized, it cannot be used with high-k oxide dielectrics.[8]

For optimized ohmic contacts on the n- and p-Si, different metals are used to create a small barrier height (Fig. 21.23a) and low contact resistance (cf. Sect. 21.2.6). Figure 24.27 visualizes the band edges of silicon in relation to the work functions of various metals (see Table 21.2). For example, the work function of titanium matches the electron affinity of n-Si closely. However, a direct deposition of Ti on Si results in a Schottky barrier of 0.5 eV [1690]. A surface passivation with a group-VI element such as Se can help reduce this value to 0.19 eV [2065].

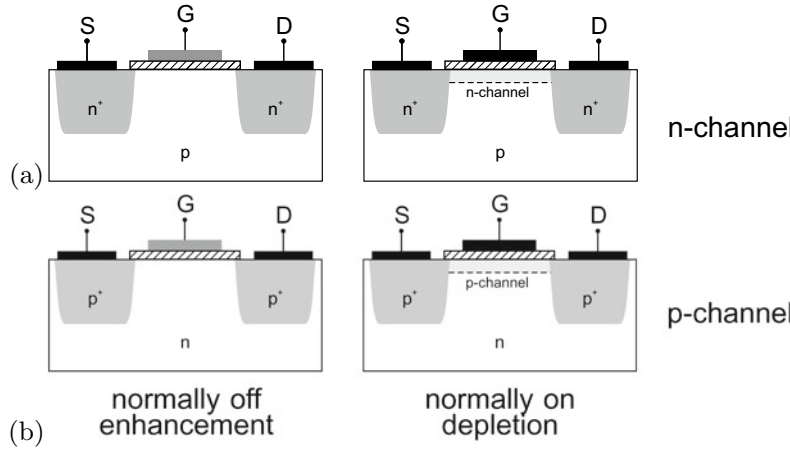

Fig. 24.25 The four MOSFET types. **a** Enhancement and **b** depletion type with n-channel (*top row*) and p-channel (*bottom row*)

[7] except for the subthreshold current and other leakage currents. These need to be reduced further since the dissipated power limits chip performance (speed and device density) and battery lifetime in handheld applications.

[8] The term 'high-k dielectric' means a dielectric material with large dielectric constant ϵ.

In the latest generation of CMOS ICs the PMOS (NMOS) device has a built-in compressive (tensile) channel strain for modifying the effective mass (cf. Sect. 6.12.2), both allowing higher drive current due to higher mobility. A detailed treatment can be found in [2066].

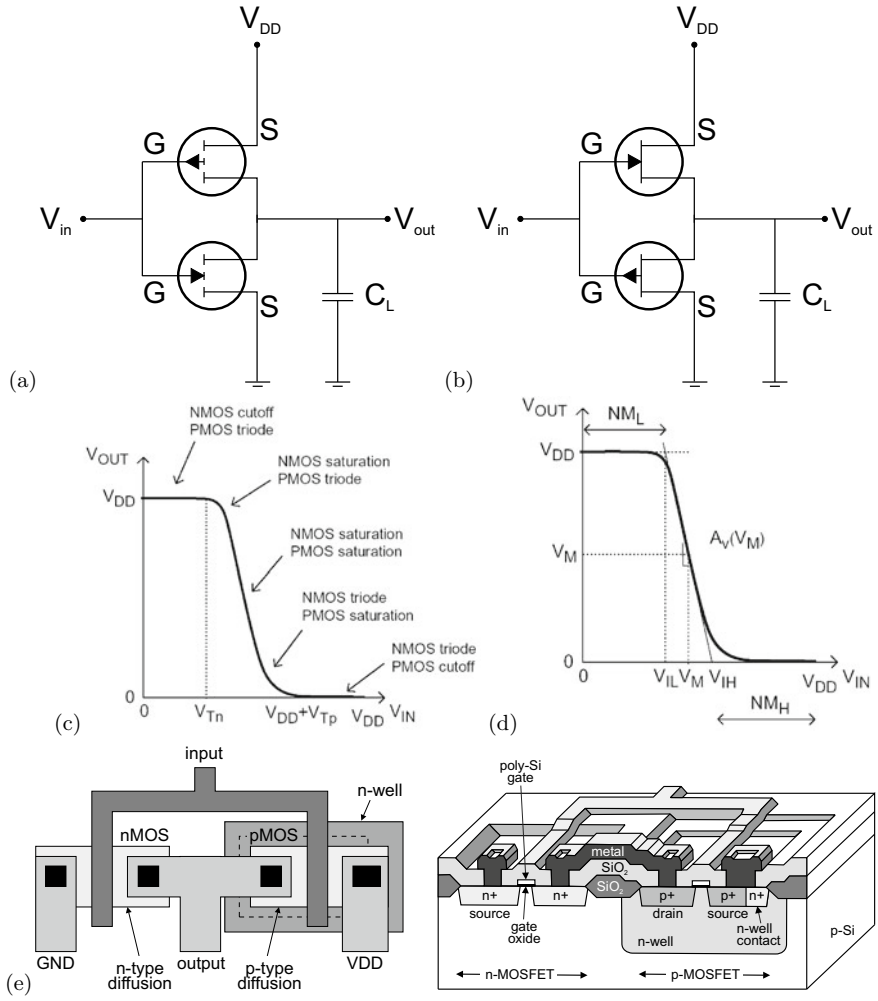

Fig. 24.26 Circuit diagram of **a** inverter with n-type (bottom) and p-type (normally off, enhancement mode) FETs and **b** inverter with p-type (bottom) and n-type (normally on, depletion mode) FETs. **c** Inverter characteristic with the transistor thresholds indicated, **d** inverter characteristic with middle voltage V_M indicated. $NM_{L,H}$ denotes the low- and high-noise margins, respectively, i.e. the voltage by which the input voltage can fluctuate without leading to switching. **e** Composite layout (*left panel*) and cross-sectional view (*right panel*) of CMOS inverter. Part **e** adapted from [2064]

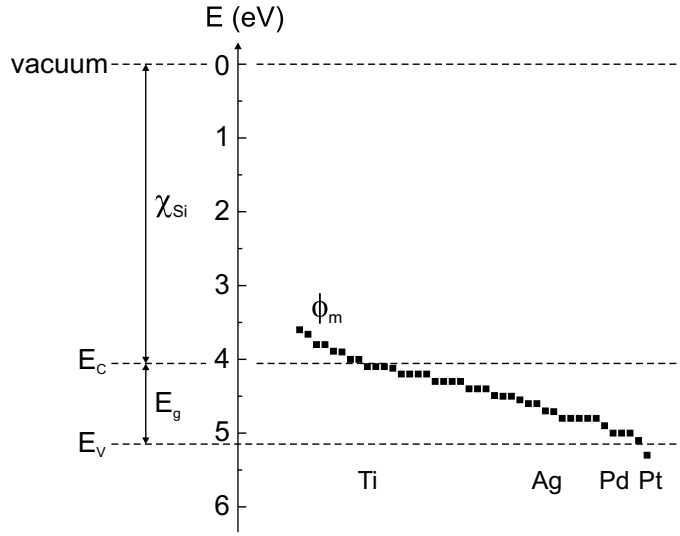

Fig. 24.27 Silicon band edges in relation to different metals and their work functions

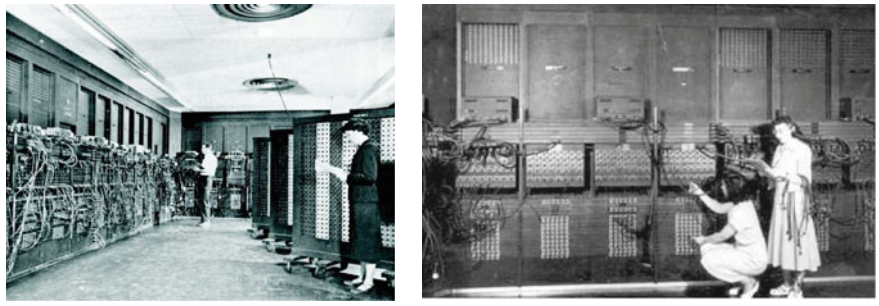

Fig. 24.28 ENIAC, the first electronic computer (J.P. Eckert, J.W. Mauchly, 1944/5). The images show only a small part of the 18 000 vacuum tubes

24.5.5 Large-Scale Integration

Historic Development

Compared to the first computers on the basis of vacuum tubes (triodes), e.g. ENIAC (Fig. 24.28), today's devices are extremely miniaturized and need many orders of magnitude less power per operation. ENIAC needed 174 kW of power. A comparable computing power was reached in 1971 with the few cm^2 large Intel 4004 microprocessor (Fig. 24.29b) consuming only several Watts with 2300 transistors. In 2004 about 42 million transistors were integrated in the Pentium 4 microprocessor (Fig. 24.30). Also, memory chips started to become highly integrated (Fig. 24.29a).

The development of electronic circuit integration is empirically described by Moore's 'law' [2067] that has been valid since the 1970s. According to this law, the number of transistors doubles every 20 months (Fig. 24.31a). At the same time, the performance has been improved by an increase of the clock speed (Fig. 24.31b).[9]

[9] After year 2003 data for maximum clock rate are not for highest integration density processors.

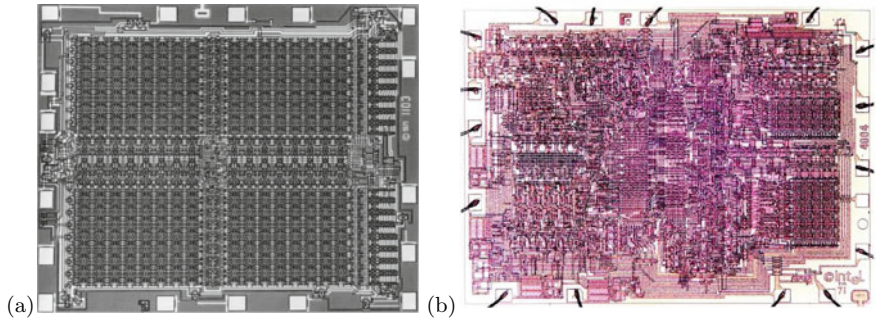

Fig. 24.29 **a** Intel^{TM} 1103 1 KByte (1024 memory cells) dynamic random access memory (RAM), arranged in four grids with 32 rows and columns (1970), chip size: 2.9 $\times$ 3.5 mm^2. **b** Intel^{TM} 4004 microprocessor (1971), chip size: 2.8 $\times$ 3.8 mm^2, circuit lines: 10 µm, 2,300 MOS transistors, clock speed: 108 kHz

Fig. 24.30 The Intel^{TM} Pentium 4 microprocessor (2000), circuit lines: 0.18 µm, 42 million transistors, clock speed: 1.5 GHz

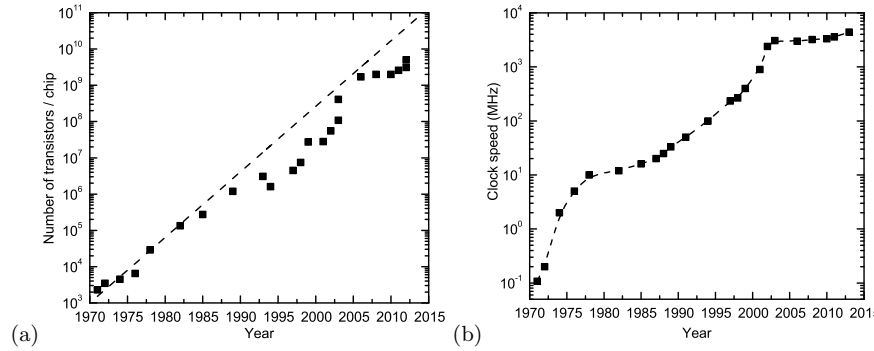

Fig. 24.31 **a** Moore's law on the exponential increase of transistors per chip (for Intel^{TM} processor chips). *Dashed line* corresponds to doubling in 20 months. **b** Historical increase of maximum clock speed, *dashed line* is guide to the eye. Note the almost constant rate of 10 MHz from the mid-1970s to the mid-1980s and another plateau developing after 2000

Interconnects

Moore's second law says that the cost of production also doubles for each new chip generation and is currently (2004) in the multi-billion US$ range. Most of the cost saved by integration is due to efficient *wiring* (interconnects) of the components, in 2004 (65 nm node) in eight layers above the active elements (transistors and capacitors) (Fig. 24.33), in 2008 (45 nm node) in eleven layers. Plane-view images of the first three layers of the interconnects are shown in Fig. 24.34. The Cu interconnects are fabricated with the so-called damascene process [2068–2070]. Barrier layers (e.g. TaN or TiN) are required to avoid out-diffusion of Cu into the silicon or other parts of the circuit. Three effects limit the conductivity: The interconnect metal line width and height approaches the mean free path of carriers ($d_{\mathrm{Cu}} \approx 40$ nm) [715, 2071], grain boundary scattering can limit mobility since grain size is reduced for thinner lines, and the (high resistivity) barrier reduces space for the conductive part of the metal line. In Fig. 24.32 the increase of the resistivity of copper with reduced dimension is shown as a function of film thickness t and for a 100 nm-film as a function of line width w. In a simplified approach, the line resistivity ρ_{line} is given as [2071]

$$\frac{\rho_{\mathrm{line}}}{\rho_0} = 1 + \frac{3}{8}(1-p)\left(\frac{d}{t} + \frac{d}{w}\right) , \tag{24.81}$$

ρ_0 denoting the bulk resistivity (1.7 μΩ cm for Cu), d being the mean free path (8.7) and p being the electron scattering parameter ($p = 0$ for diffuse scattering).

In order to achieve the best high frequency performance the material between the metal interconnects should have low dielectric constant ('low-k' dielectric). Alternative materials to the standard SiO_2 ($\epsilon_r \approx 4.1$) are investigated such as SiOF (≈ 3.8), SiCOH (≈ 3.0), porous materials (≈ 2.5) and air gaps [2072].

CMOS Scaling

Using planar technologies, LSI (large-scale integration), VLSI (very large-scale integration), ULSI (ultra large-scale integration) and further generations of devices have been conceived, driven by high-density electronic memory devices. Subsequently also logic devices are produced with reduced device size.

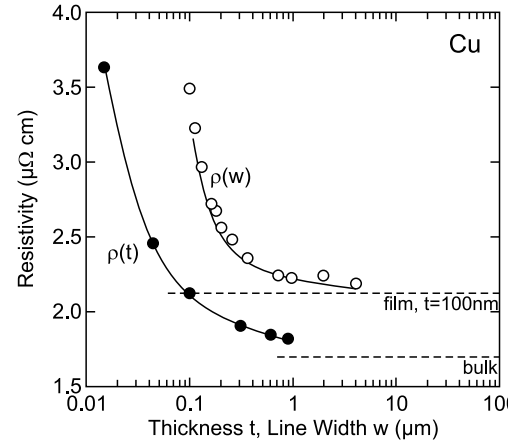

Fig. 24.32 Resistivity of copper at room temperature for various film thickness (*solid circles*), and for a 100 nm-film as a function of line width w (*empty circles*). *Solid lines* are theoretical dependence according to (24.81). The *dashed lines* indicate the limits for bulk material ($t \to \infty$) and for large line thickness ($d = 100\,\text{nm}$, $w \to \infty$). Adapted from [2071]

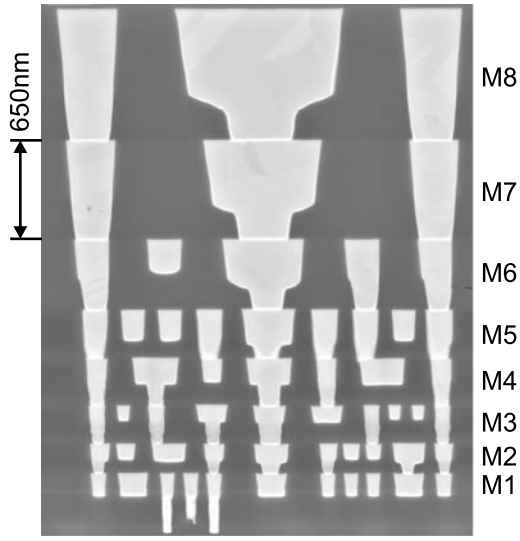

Fig. 24.33 Cross section through a logic chip (65 nm technology, 35 nm gate length) with eight layers of dual damascene Cu interconnects (M1–M8) with low-k carbon-doped oxide ($\epsilon_r = 2.9$) inter-level dielectric above the active elements. Adapted from [2073]

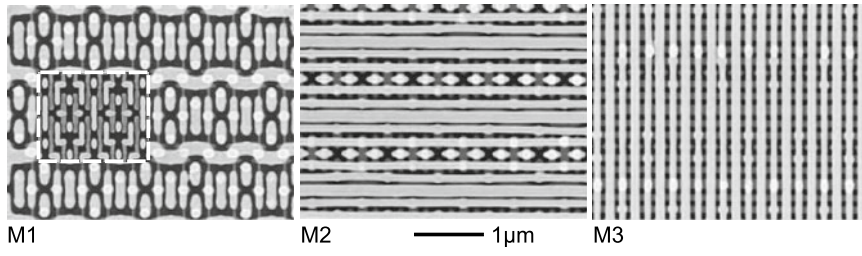

Fig. 24.34 Plane-view of the first three interconnect layers of a 45 nm node SRAM array (Intel® Xeon®). In the image of the M1 layer the gate layer metal connects are shown in the *inset*, framed with a *white dashed line*. Adapted from [2074]

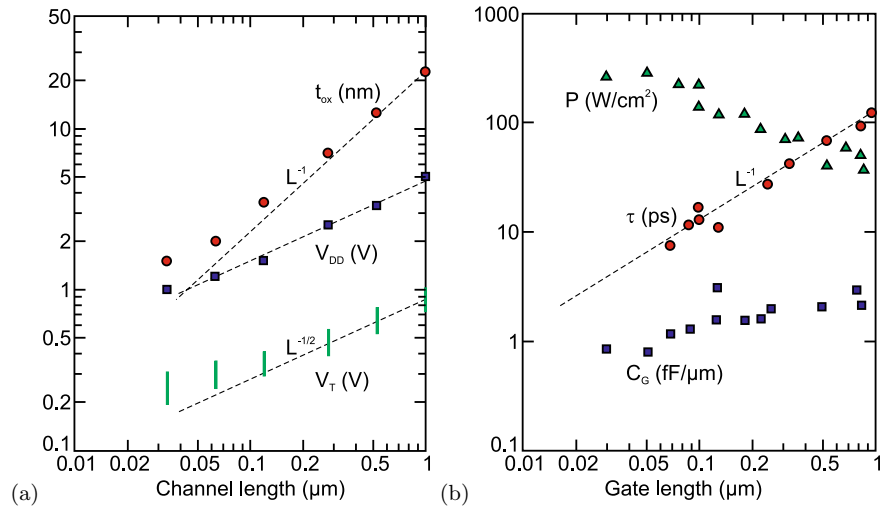

Fig. 24.35 Scaling of MOSFET parameters gate oxide thickness t_{ox}, power supply voltage V_{DD} (across source–drain), threshold voltage V_T, total power loss per area P, gate capacitance per channel width C_G and inverter delay τ, the time required to propagate a transition through a single inverter driving a second, identical inverter, commonly used as a means of gauging the speed of CMOS transistors. Data for **a** from [2075] and for **b** selected from [2076]

The increase of the number of transistors per area requires the scaling of their geometrical properties. This impacts many other properties of the transistor and their scaling needs to be considered as well. From a general perspective, the physical properties scale while the thermal energy kT remains constant for room-temperature electronics.

If channel width Z and channel length L of a transistor are scaled down by a factor of $s > 1$, $Z' = Z/s$ and $L' = L/s$, the area obviously scales as $A' = A/s^2$. In subsequent transistor generations $s = \sqrt{2}$, i.e. doubling of the number of devices per area. In order to maintain the aspect ratio of the device also the oxide thickness (d_i) is scaled, $t'_{ox} = t_{ox}/s$ ('classical scaling').

The ultimate design criteria are maximum temperature and maximum power loss. The maximum temperature needs to be obeyed, the worst case usually taken as 100°C. The power loss per area, e.g. heating, needs to stay constant at an appropriate maximum level around 200 kW/m^2 (Fig. 24.35b) unless higher (and more expensive) efforts on cooling are made. At the same time the device performance needs to be maintained if not improved, e.g. for lower power dissipation in battery operated devices. Very important is the reduction of operation voltage V_{DD} in order to keep electric fields and power consumption small enough (Fig. 24.35). The power consumption in stand-by mode P_{off} depends on V_{DD} and the subthreshold (off) current

$$P_{off} = W_{tot}\, V_{DD}\, I_{off} \ , \tag{24.82}$$

where W_{tot} is the total width of the turned-off devices and I_{off} is the average off-current per device per width. The latter increases exponentially with reduced threshold voltage V_T,

$$I_{off} = I_0 \exp\left(-\frac{e\, V_T}{n\, kT}\right) \ , \tag{24.83}$$

with ideality factor $n \approx 1.2$ and $I_0 \approx 1$–$10\,\mu A/\mu m$ [2075]. A well-functioning MOSFET requires a ratio of V_T/V_{DD} of < 0.3.

The power consumption in active mode P_{ac} depends also on the clock speed (frequency f) that increases with higher integration due to shorter gate length,

$$P_{ac} = C_{sw}\, V_{DD}^2\, f \ , \tag{24.84}$$

where C_{sw} is the total node capacitance being charged and decharged in a clock cycle.

Historically the oxide thickness has been reduced less than the channel length [2075] (Fig. 24.35a) leading to increased local fields. The reduction of the physical gate oxide thickness is limited due to gate leakage through tunneling [2077]. While for a gate voltage of 1.5 V and oxide thickness $t_{ox} = 3.6$ nm the leakage current is only about 10^{-8} A/cm^2, it is about 1 A/cm^2 for $t_{ox} = 2.0$ nm and about 10^4 A/cm^2 for $t_{ox} = 1.0$ nm. Obviously variations of oxide thickness are more harmful at small average thickness. 1.2 nm physical SiO_2 thickness has been used in the 90 nm (gate length) logic node.

The technological solution for further reduction of oxide thickness is the use of geometrically thicker layers, to suppress tunneling, with higher dielectric constant ('high-k dielectrics'), e.g. HfO_2 [2078], to maintain reasonable gate capacitance per gate width

$$C_G = \frac{\epsilon_{ox}}{t_{ox}}\, L \ , \tag{24.85}$$

(cmp. (24.71)) at a value of about 1.0–1.5 fF/μm (Fig. 24.35)b. For the 45 nm technology node a 0.7-fold reduction in electrical oxide thickness was achieved while reducing gate leakage 1000× for the PMOS and 25× for the NMOS transistors [2079].

Materials

The electronics industry is based on silicon as the material for transistors. However, many other materials are incorporated in the technology. Traditionally silicon dioxide gate oxide is used, silicon nitride for insulation layers and polysilicon for gate contacts. For wiring aluminum has been used. Silicides were introduced as contact materials around 1986.

Progress was made with copper interconnects (IBM, 1997), replacing aluminum. The better electrical and heat conductivity could previously not be used since Cu is a deep level in Si (cf. Fig. 7.6). The key to success was an improved barrier technology based on amorphous TaN- or TiN-based barrier layers to prevent the diffusion of Cu into the silicon and dielectric layers. The first chip from series production, incorporating the Cu technology, was the PowerPC 750 (400 MHz) in 1998. Since 2000 high-k, i.e. large ϵ_r, Hf-containing gate dielectrics are used (Fig. 24.36). HfO_2 has a dielectric constant of 25–30. 45 nm node technology probably uses HfZrO, HfSiO or HfSiON [2080] gate dielectrics with $k \sim 12$ and an electrical thickness of $t_{ox}\epsilon_{SiO_2}/\epsilon_{ox} = 1.0$ nm.

Germanium is reintroduced into mainstream semiconductor technology via SiGe stressors in the source and drain for PMOS. Uniaxial compressive strain in the channel region leads to 30% increased saturation current [2082] mostly due to reduced effective masses [749, 2083, 2084] (Sect. 8.3.14) for 90 nm transistors. Similarly, uniaxial tensile strain in NMOS, introduced by SiN caps or more recently tensile trench contacts [2079], allows for 10% higher saturation current [2082] (Fig. 24.37). The enhanced electron mobility is due to strain-induced splitting of the X-valley and change of electron mass [2085]. Further improvement to 18% (NMOS) and 50% (PMOS) increase in $I_{D,sat}$ compared to unstrained Si have been made in 65 nm transistors [2073].

The end of the miniaturization has been theoretically predicted many times and for various feature sizes. Today, only fundamental limits such as the size of an atom seems to limit circuit design.[10] Such

[10] Only commercial profit, rather than testing physical limits, drives the miniaturization. Insufficient economic advantages or low yield of further chip generations possibly can limit or slow down large-scale integration.

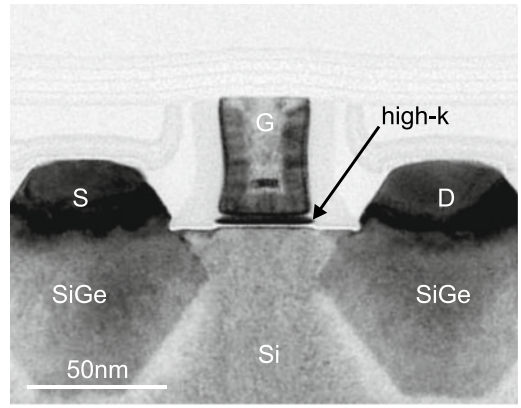

Fig. 24.36 Cross-section TEM image of 45 nm node PMOS transistor with high-k Hf-containing gate oxide (*dark*) above a thin SiO_2 layer (*white*). The role of the stressor SiGe pockets is explained in Fig. 24.35. Adapted from [2081]

limits (and the effects in nanostructures in the few-nm regime) will be reached beyond 2010, projected at about 2020. Up to then, it is probable that at least a few companies will follow the road map for further miniaturization, as laid out by the Semiconductor Industry Association[11] (SIA).

24.5.6 Tunneling FETs

A decisive parameter for FET performance is low leakage current. With shrinking device dimensions it increases rapidly for conventional FET design. A novel type of FET has thus been conceptualized, the tunneling FET (TFET) [2088]. It is a lateral p-i-n diode with a MOS gate (Fig. 24.38). The leakage current is minimized due to the reverse biased p-i-n structure. A low leakage current (per gate width) of less than 10^{-14} A/μm has been realized [2089, 2090]. The channel current is due to band-to-band tunneling as in an Esaki diode (Sect. 21.5.9) and can be controlled by the gate voltage [2091]. The surface tunneling junction is close to the source electrode. The use of germanium instead of silicon allows further performance enhancements [2092].

24.5.7 Nonvolatile Memories

Floating Gate Memories

When the gate electrode of a MOSFET is modified in such a way that a (semi-) permanent charge can be stored in the gate, a nonvolatile electronic memory can be fabricated. In the floating-gate structure (Fig. 24.39a), an insulator–metal–insulator structure is used where charge is stored in the metal and cannot escape through the insulating barriers. The 'metal' is often realized by poly-Si. In the MIOS structure (Fig. 24.39b), the insulator–oxide interface is charged. The charge can be removed by UV light (EPROM, erasable programmable read-only memory) or by a sufficient voltage across the oxide at which the charge carriers can tunnel out (Fowler–Nordheim tunneling) (EEPROM, E^2PROM, electrically erasable programmable read-only memory).

Nowadays, a special type of EEPROM is used for the so-called *flash* memories. The stored gate charge causes a change in the MOSFET threshold voltage and is designed to switch between the on

[11] www.semichips.org.

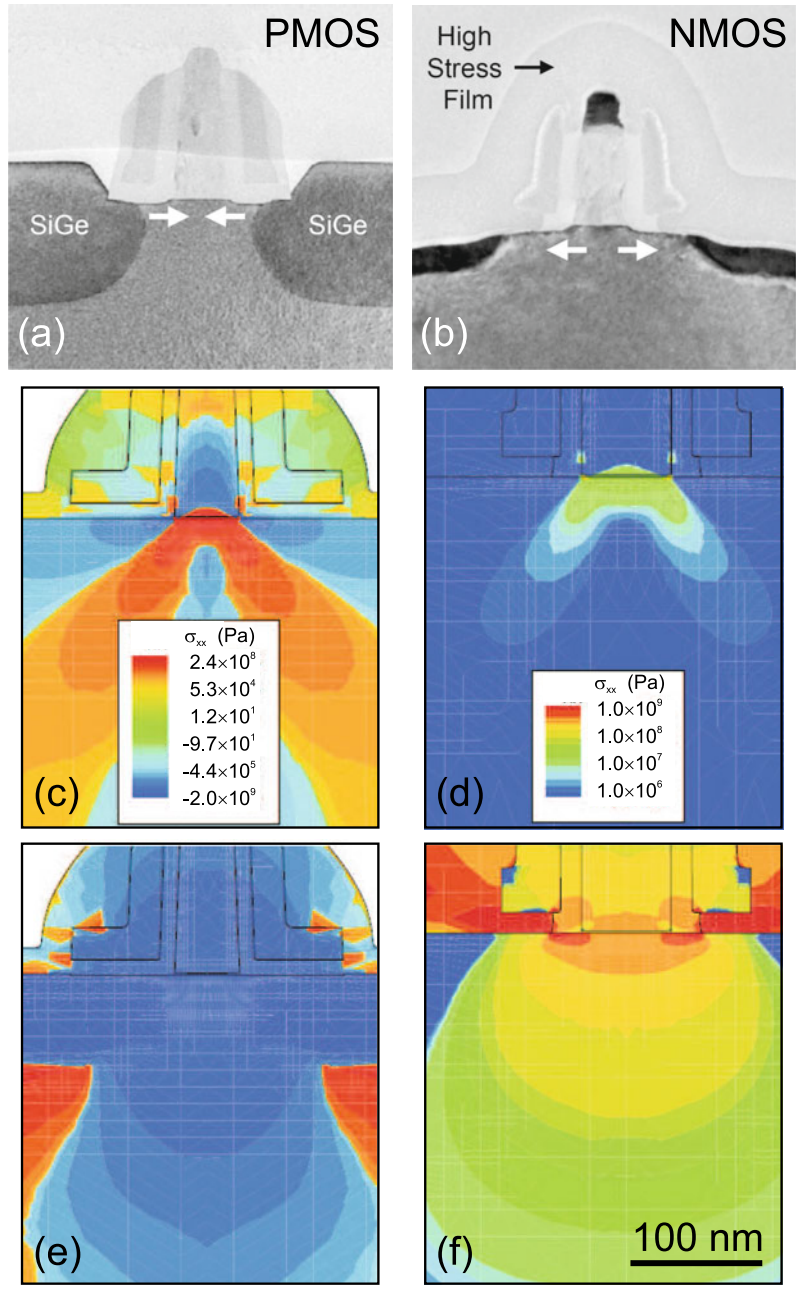

Fig. 24.37 Cross-section TEM images of strained **a** PMOS and **b** NMOS transistors. Adapted from [2086]. **c**–**f** Modelling of strain distribution: PMOS without **c** and with **e** $Si_{0.83}Ge_{0.17}$ pockets, NMOS without **d** and with **f** tensile cap layer. Adapted from [2087]

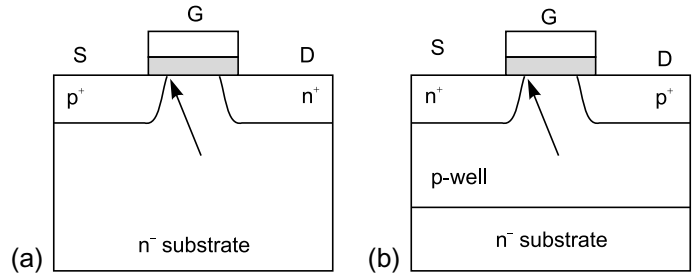

Fig. 24.38 Schematic of a **a** n-type and **b** p-type tunneling FET (TFET). D is reversely biased, i.e. positive for NTFET and negative for PTFET. The *grey areas* represent the gate oxide, the *arrows* denote the spatial position of tunneling (surface tunneling juction) for sufficient (NTFET: positive, PTFET: negative) gate voltage

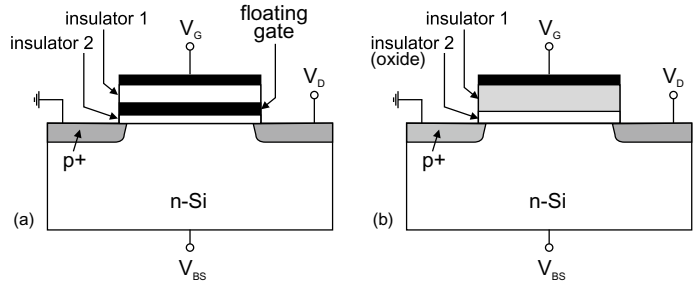

Fig. 24.39 MOSFET with **a** floating gate and **b** MIOS structure

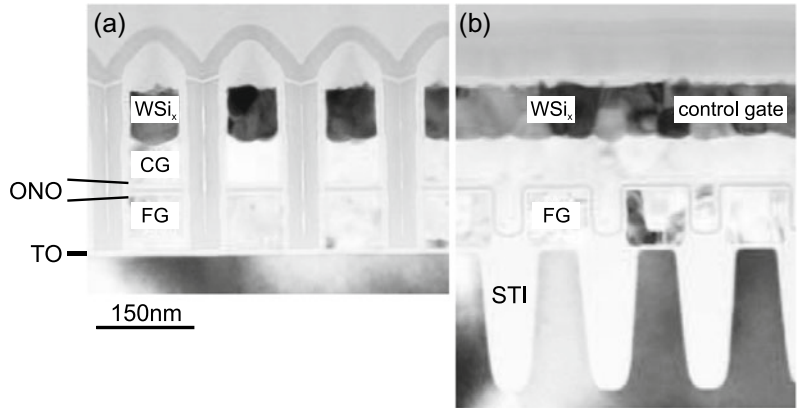

Fig. 24.40 Cross sections **a** perpendicular and **b** parallel to the control gate line of a 4 Gb, 73 nm SLC flash memory (Samsung K9F4G08U0M). 'CG' denotes the control gate, 'FG' the floating gate, 'TO' the tunneling oxide, 'ONO' the oxide/nitride/oxide insulator stack, and 'STI' the shallow trench insulation. Adapted from [2074]

and off state. The storage time of the charge can be of the order of 100 years. Since tunneling limits the charge retention, the oxide must be sufficiently thick. In Fig. 24.40 a cross section of a 4 Gb, 73 nm SLC (single-level cell) flash memory is shown. The lower insulator (tunneling oxide at the channel) consist of 7.2 nm SiO_2, the upper insulator (insulator 1 in Fig. 24.39a) is a 18 nm thick oxide/nitride/oxide (ONO) stack. The floating gate has a $90 \times 90\,\text{nm}^2$ footprint, is about 86 nm high and consists of two polysilicon layers.

In a SLC memory the floating gate has two states, a certain charge value and the erased state. In a MLC (multi-level cell) the gate can store several charge states which can be sensed as different logic states, e.g. $2^2 = 4$ states. This increases the storage density, lowering cost per bit, but also increases the complexity. Typical endurance of SLC is at least 10^6 program–erase cycles. SLC cells so far have about ten times higher endurance (possible number of read–write cycles) and lower power consumption than MLC. Generally SLC flash memory is considered industrial grade and MLC flash is considered

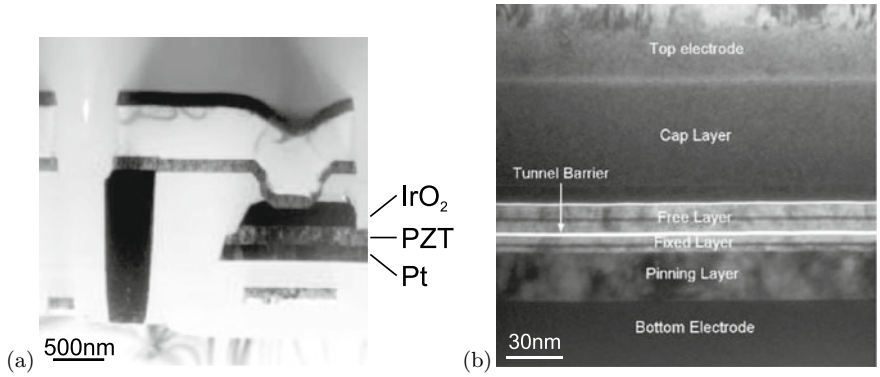

Fig. 24.41 **a** Cross-section TEM image of a cell from a Ramtron 4 Mb FeRAM. The information is stored in the electric polarization of a polycrystalline $Pb(Ti_xZr_{1-x})O_3$ (PZT) island, contacted on the bottom and top with platinum and iridium oxide, respectively. Adapted from [2074]. **b** Cross-section TEM of the magnetic tunneling junction from a Freescale 4.2 Mb MRAM, located between the M4 and M5 interconnect layers. The magnetization of the free layer can be switched, that of the fixed layer remains constant. Adapted from [2074]

consumer grade. Recently also triple level cells (TLC), storing 3 bit (8 states) are commercialized, however the increased storage density comes at high cost of reliability [2093].

The ultimate limit, explored currently, is to use a single electron charge to cause such an effect in the single-electron transistor (SET).

Future Concepts

Memory concepts beyond the storage of free charges include information storage via

- the static polarization in a ferroelectric material (either crystalline or polymer) (FeRAM [2094], Fig. 24.41a) which can be switched by an electric field.
- the phase change between amorphous and polycrystalline phases in a chalcogenide layer (typically GeSb [2095] or $Ge_2Sb_2Te_5$, GST [2096, 2097] with an $\alpha \leftrightarrow$ c transition, Fig. 24.42) upon local heating (similar to a rewritable DVD) and the related change is resistivity (PCM, phase change memory).
- the storage of magnetization direction (MRAM [2098, 2099]) and subsequent resistance change of a magneto-tunneling junction (MTJ) whose resistance depends on the relative magnetization (parallel or perpendicular) of two magnetic layers separated by a thin tunneling insulator (Fig. 24.41b). The largest TMR (tunnel-magnetoresistance) effect has been achieved with MgO as insulator [2099]. The magnetization of the bottom magnetic layer of the MTJ is fixed. The magnetization directions $\pm 45°$ are written into the free layer with the magnetic fields of two perpendicular high current wires in two subsequent back-end interconnect layers sandwiching the MTJ.
- resistance change based on solid electrolytes (PMC, programmable metallization cell memory). The lowering of the resistance is attained by the reduction of ions in a fairly high resistivity electrolyte (e.g. from the system Cu,Ag–Ge–Se,S,O [2100, 2101] or oxides [2102]) to form a conducting bridge between the electrodes. The resistance is returned to the high value via the application of a reverse bias that results in the breaking of the conducting pathway.
- resistance change in transition metal oxides such as perovskites, e.g. $SrTiO_3$:Cr [2103, 2104] or NiO:Ti (RRAM). Electrical pulses of opposite polarity switch the resistance reversibly between a high- and a low-resistance state. Oxygen-vacancy drift modulates the valence of the mixed-valence transition-metal ion (e.g. Ti^{3+}–Ti^{4+}) and thus the conducting state [2105].

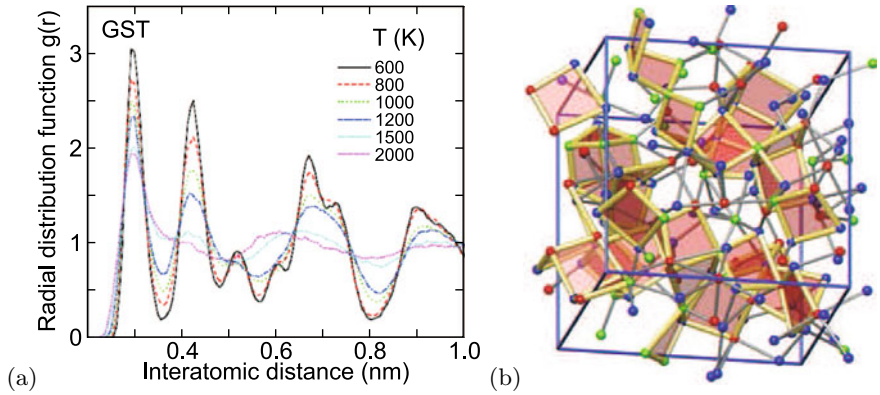

Fig. 24.42 **a** Radial distribution function of ions in $Ge_2Sb_2Te_5$ (GST) for various temperatures (cmp. Fig. 3.14b). Adapted from [2096]. **b** Atom arrangement in the amorphous phase of GST with square units highlighted that nucleate crystallization. Adapted from [2097]

- a molecular configuration change (e.g. redox reaction) between crossed wire lines (molecular electronics [2106–2108].

24.5.8 Heterojunction FETs

Several types of field-effect transistors have been devised that use heterojunctions (HJFET).

HIGFET

As conducting channel, the two-dimensional electron gas at an undoped heterointerface is used. Such a transistor is called a heterojunction insulating gate FET (HIGFET). With forward or backward gate voltage, an electron or hole gas can be created (channel enhancement mode), as visualized in Fig. 24.43. Thus, a complementary logic can be realized. However, the p-channel suffers from low hole mobility.

HEMT

If the top wide-bandgap layer is n-doped, a modulation-doped FET (MODFET) is made (see Sect. 12.3.4). This structure is also called a HEMT (high electron mobility transistor) or TEGFET (two-dimensional electron gas FET) (Fig. 24.44). A thin undoped AlGaAs spacer layer is introduced between the doped AlGaAs and the undoped GaAs to reduce impurity scattering from carriers that tunnel into the barrier. With increasing gate voltage, a parallel conduction channel in the AlGaAs is opened. The natural idea would be to increase the Al fraction in the AlGaAs to increase the quantum-well barrier height. Unfortunately, the barrier height is limited to 160 meV for an aluminum concentration of about 20%. For Al content higher than about 22%, the DX center (cf. Sect. 7.7.6) forms a deep level such that the apparent ionization energy increases drastically and no shallow donors can be used for modulation doping. An improvement for the barrier conduction problem is the use of δ-doping [2109], i.e. the introduction of a highly doped thin (mono-)layer (Fig. 24.45), which results in higher channel carrier concentration.

Pseudomorphic HEMTs

Instead of increasing the height of the barrier, the depth of the well can be increased by using a low-bandgap material. On GaAs substrate, InGaAs is used (Fig. 24.46). However, strain is introduced in this case and the InGaAs layer thickness is limited by the onset of dislocation formation (cf. Sect. 5.4.1) (which reduces the channel mobility and the device reliability). For $In_{0.15}Ga_{0.85}As$ (thickness about 10–20 nm), a total barrier height of about 400 meV can be obtained. A barrier height of 500 meV can be reached with an InAlAs/InGaAs structure on InP (Fig. 24.47). The InAlAs does not suffer from the problem related to DX centers. The channel indium concentration is typically 50%. The mobility increases with increasing indium concentration. This InP-based HEMT structure is widely used in satellite receivers for its excellent high-speed and low-noise properties in the 100–500 GHz range and beyond.

However, the InP technology is economically less favorable than GaAs due to smaller available substrate size and higher cost (2001: 4" InP substrate: $ 1000, 6" GaAs substrate: $ 450).

Metamorphic HEMTs

A unification of the InAlAs/InGaAs structure with the best figure of merit and the GaAs substrate is achieved with the metamorphic HEMT (MHEMT). Here, a relaxed buffer is used to bring the in-plane lattice constant from that of GaAs to about that of InP. It is key that the defects occurring are confined to the relaxed buffer and do not enter the active device structure (see Fig. 24.48). The relaxed buffer is typically about 1 µm thick. It can be grown, e.g., with a graded $In_x(Ga,Al)_{1-x}As$ layer with x =0–42% or with a stepped structure with piecewise constant indium concentration in each layer. It is important that a smooth interface of the channel is achieved in order to avoid additional scattering mechanisms. For high-frequency operation, the fabrication of a small gate length is important, as shown in Fig. 24.49 for a 70-nm gate of a f_T =293 GHz, f_{max} = 337 GHz transistor [2110]. SiGe channels,

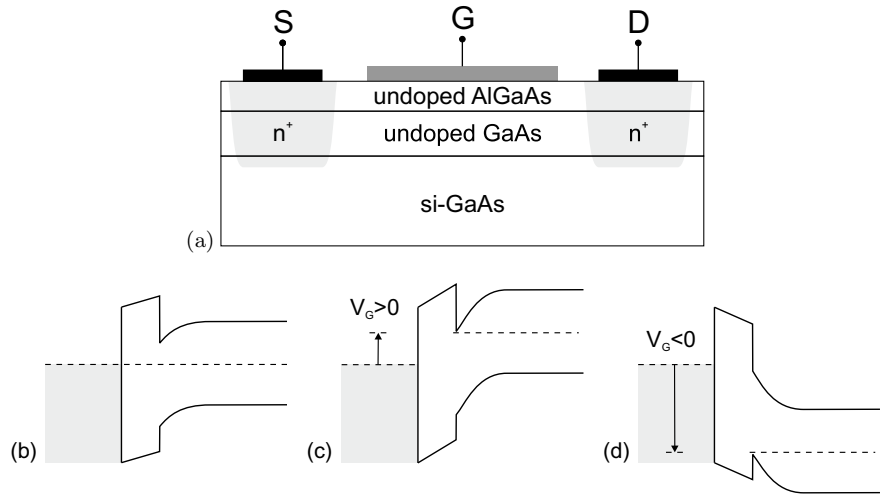

Fig. 24.43 **a** Scheme of a HIGFET structure with metal gate and undoped AlGaAs/GaAs heterointerface on semi-insulating GaAs. The source and drain contacts are n-doped such that this structure can be used as an n-HIGFET (see part **c**). **b** Band diagram for zero gate voltage. **c** Band diagram for positive gate voltage and n-channel, **d** for negative gate voltage and p-channel

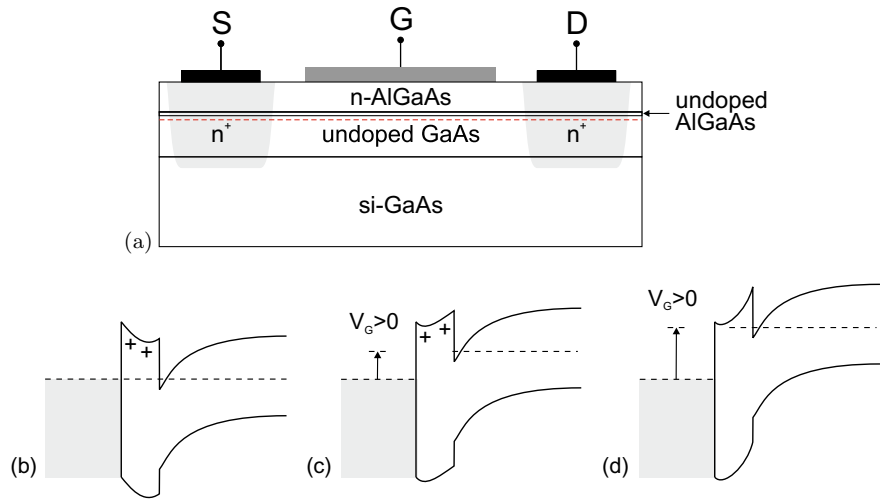

Fig. 24.44 **a** Scheme of a HEMT structure with n-AlGaAs/GaAs heterointerface on semi-insulating GaAs. The source and drain contacts are n-doped such that this structure can be used as an n-channel (normally-on) HEMT. The *horizontal dashed line* represents schematically the position of the 2DEG at the heterointerface on the GaAs side. **b** Band diagram at zero gate voltage. **c** Band diagram at positive gate voltage, increase of channel carrier concentration. **d** Band diagram at even larger positive gate voltage, formation of conducting channel in the AlGaAs layer

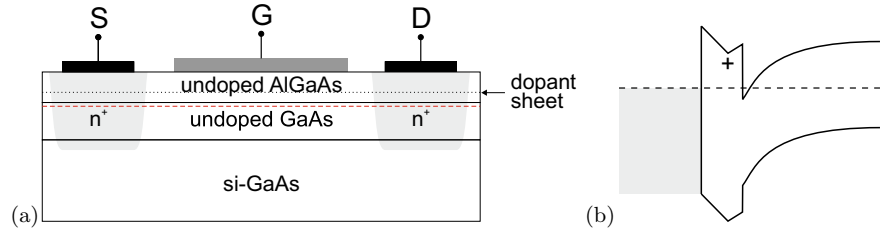

Fig. 24.45 **a** Scheme of a δ-doped HEMT structure with AlGaAs/GaAs heterointerface on semi-insulating GaAs. The source and drain contacts are n-doped such that this structure can be used as an n-channel HEMT. The *horizontal dashed line* represents schematically the position of the 2DEG in the GaAs layer. **b** Band diagram at zero gate voltage

providing higher mobility than pure Si, can be fabricated using graded or stepped SiGe buffer layers on Si substrate. With such Si-based MHEMTs frequencies up to 100 GHz can be achieved.

24.6 Thin-Film Transistors

Thin-film transistors (TFTs) are field-effect transistors with a channel formed as thin film on insulating substrate. A detailed treatment is available in [2112]. TFTs are typically fabricated as large-area arrays from thin layers of polycrystalline or amorphous silicon [2113] or organic semiconductors [2114–2117] on cheap substrates such as glass. Their most prominent use is driving pixels in active-matrix displays such as electroluminescence (EL) displays or twisted nematic liquid crystal displays (LCD) [2118]. Various gates and gate geometries have been reported as depicted in Fig. 24.50.

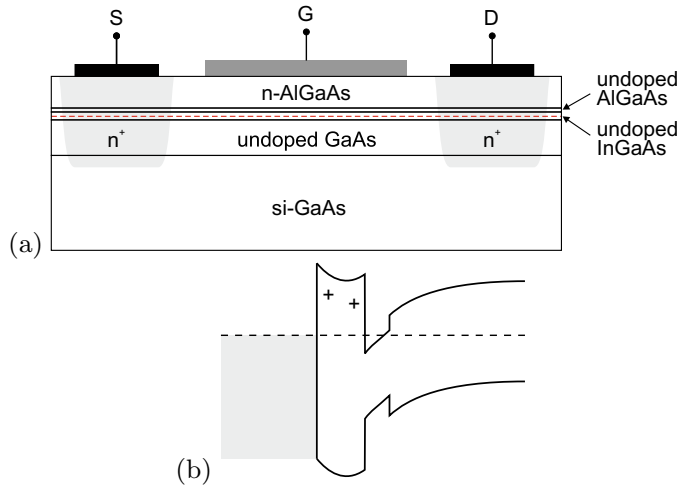

Fig. 24.46 **a** Scheme of a PHEMT structure with n-AlGaAs/InGaAs heterointerface on semi-insulating GaAs. The source and drain contacts are n-doped such that this structure can be used as an n-channel HEMT. The *horizontal dashed line* represents schematically the position of the 2DEG in the InGaAs layer. **b** Band diagram at zero gate voltage

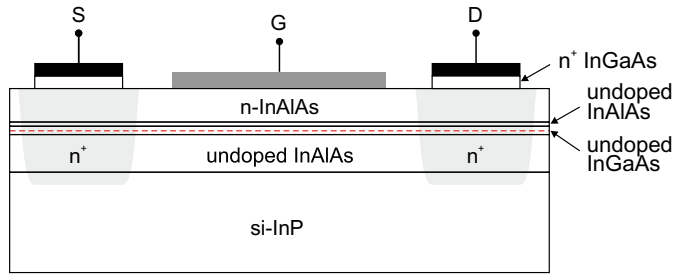

Fig. 24.47 Scheme of a PHEMT structure with n-AlInAs/InGaAs/InAlAs structure on semi-insulating InP. The source and drain contacts (with a highly doped InGaAs contact layer) are an n-doped such that this structure can be used as an n-channel HEMT. The *horizontal dashed line* represents schematically the position of the 2DEG in the InGaAs layer

24.6.1 Annealing of Amorphous Silicon

Since the mobility in polycrystalline silicon is much higher (up to several hundred cm^2/Vs depending on grain size, see Sect. 8.3.8) than in amorphous silicon ($< 1\,cm^2/Vs$), such material is much more desirable as channel in TFTs. However, it requires high deposition temperatures. In order to achieve polycrystalline silicon with large grain size from amorphous silicon films that can be deposited at low temperature (down to room temperature) several schemes have been developed, the most important being thermal annealing and (excimer) laser annealing (ELA). Crystallization occurs by thermally activated nucleation and growth processes [2119]. Polycrystalline layers with small grain size can be made amorphous with implantation of Si (self-implantation) and a subsequent optimized (re-)crystallization processes.

In laser annealing energy is locally introduced during short pulses (several 10 ns or even fs); subsequent material change occurs on a sub-µs time scale [2120]. Laser induced crystallization enables the use of inexpensive low-temperature substrates, such as plastic or glass, since it involves the ultrafast melting and resolidification of the near-surface region of the sample, and minimal heating of the substrate. Local processing is also possible using laser crystallization.

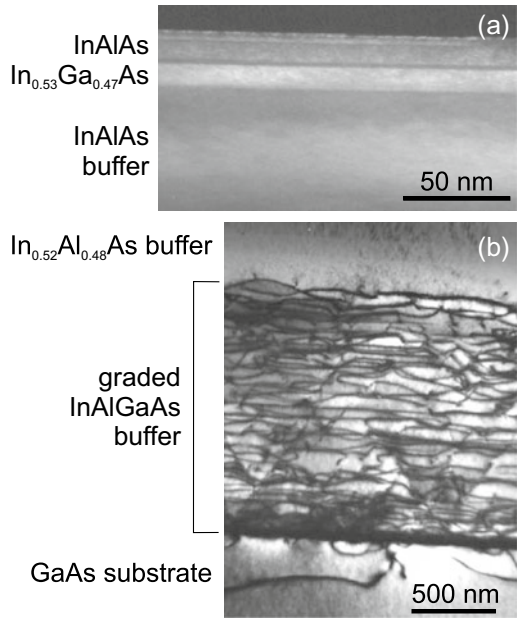

Fig. 24.48 Cross-sectional TEM image of an InAlAs/InGaAs MHEMT: **a** Active layer with rms surface roughness of 2.0 nm (from AFM), **b** graded InGaAlAs buffer layer (1.5 μm) on GaAs substrate. Adapted from [2111]

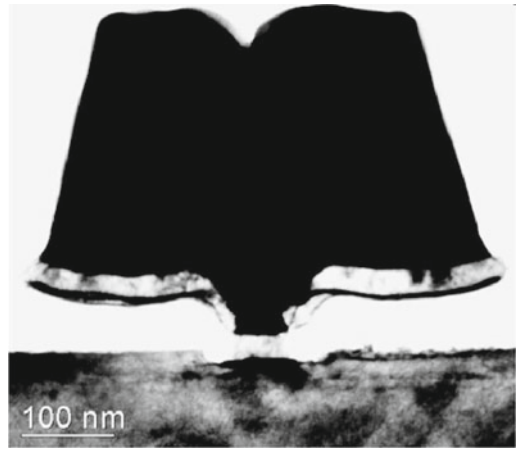

Fig. 24.49 Cross-sectional TEM image of the 70-nm gate of an InAlAs MHEMT on GaAs substrate. From [2110]

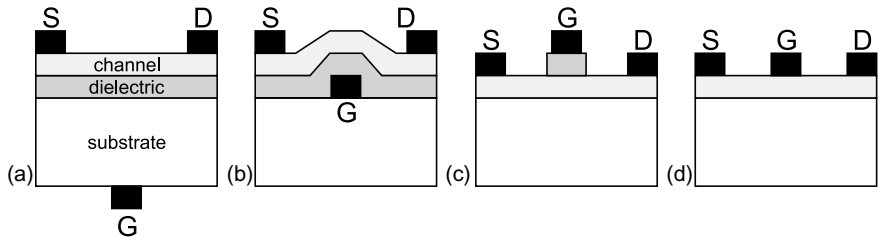

Fig. 24.50 Schematic geometries of TFTs: **a**–**c** MISFETs, **d** MESFET with **a**, **b** bottom gate and **c**, **d** top gate. Semiconductor channel layer (*light grey*), insulating dielectric (*dark grey*) and metals (*black*)

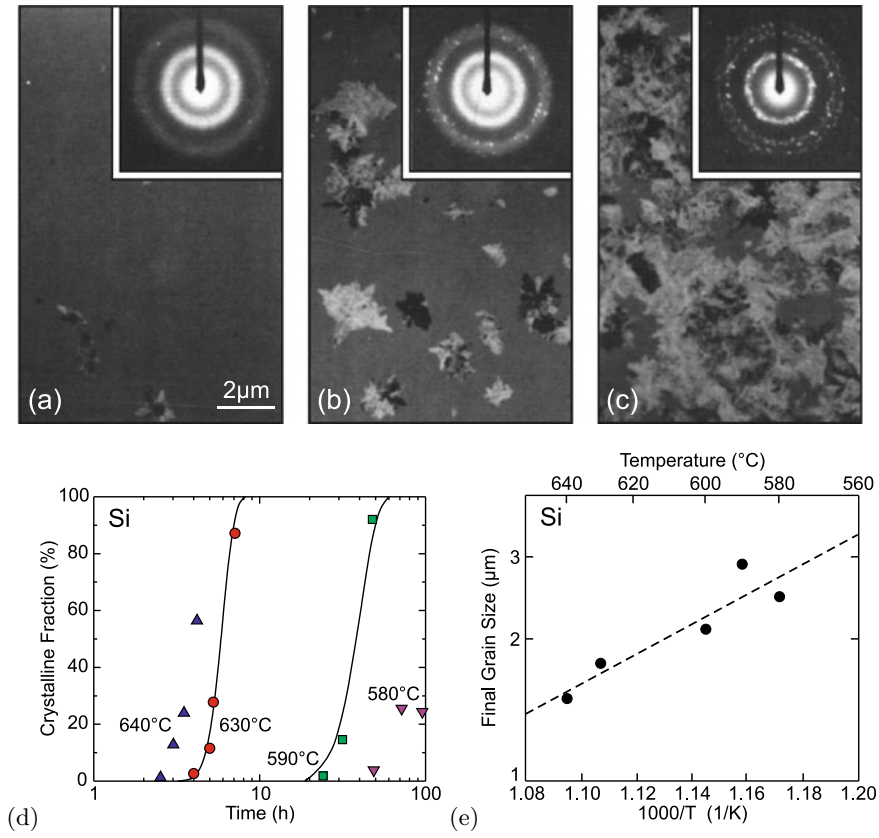

Fig. 24.51 Thermal annealing of 100 nm thick film of amorphous silicon (fabricated from LPCVD and amorphized by 100 keV Si^+ implantation with a dose of $5 \times 10^{15}\,cm^{-2}$). TEM images and diffraction patterns (*insets*) for amorphized Si after **a** 4 h, **b** 5.25 h and **c** 7.1 h annealing at $T = 630°C$. The crystalline fractions are 2%, 28% and 87%, respectively. **d** Crystalline fraction as a function of annealing time for various annealing temperatures as labeled. *Symbols* are experimental data, *solid lines* depict theory considering grain nucleation and growth. **e** Final grain size for various annealing temperature. *Dashed line* is exponential with a slope of 0.6 eV. Adapted from [2121]

In Fig. 24.51 the effect of thermal annealing of amorphous silicon is shown. The annealing time necessary to convert the amorphous phase completely to polycrystalline, e.g. 10 h at 640°C, depends largely on temperature as detailed in [2121, 2122] (Fig. 24.51a) with a large activation energy of 3.9 eV. Also the final grain size is temperature dependent (Fig. 24.51b).

The introduction of certain metals like Pd [2123], Al [2124], Au [2125] or Ni [2126] induces crystallization and allows for much lower annealing temperatures. Pd and Ni create silicides that play an important role for the grain nucleation or growth front. Au and Al are solved in the bulk but have a similar effect. For example, using Pd complete crystallization of a 150 nm thick a-Si film deposited at 480°C can be achieved by thermal annealing after 10 h at only 500°C [2127] (using metal-induced lateral crystallization, MILC).

24.6.2 TFT Devices

A schematic cross section of an amorphous silicon-based TFT is shown in Fig. 24.52a. Carriers in amorphous silicon have a low mobility typically less than $1\,cm^2/Vs$ [2128, 2129]. As-grown polycrys-

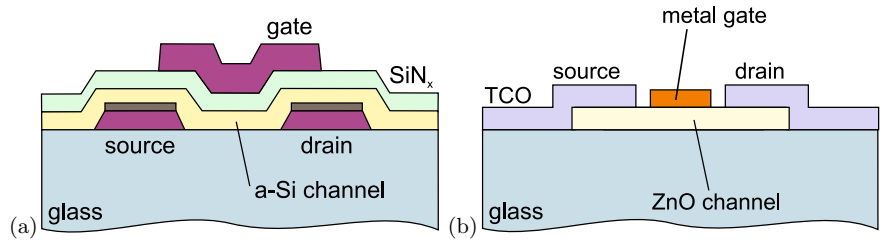

Fig. 24.52 **a** Schematic cross section of a top-gate amorphous silicon (a-Si) thin-film transistor (MISFET) on glass substrate. **b** Schematic cross section of a transparent ZnO thin-film transistor (MESFET)

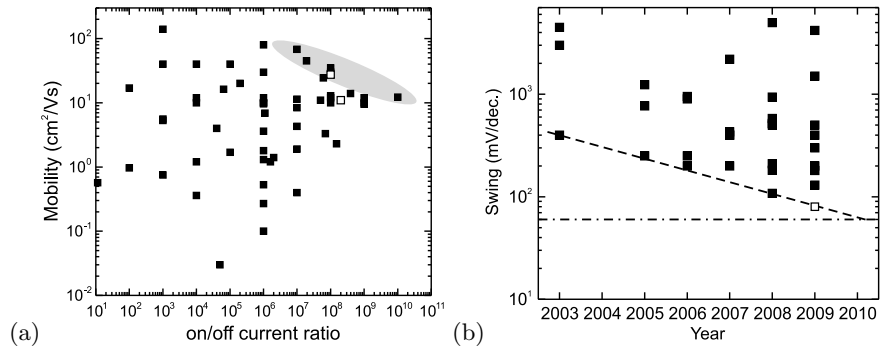

Fig. 24.53 **a** Field effect mobility and on/off current ratio for oxide channel transistors. *Filled squares* represent MISFET transistors; *open squares* are for MESFETs from [2135]. The *shaded area* indicates best performance. **b** Voltage swing for MISFETs (*filled squares*, subthreshold voltage swing) and MESFET (*empty square*, above turn-on voltage from [2135]) with TSO channels. The *dashed line* is guide to the eye for the trend of best performance. The *dash-dotted line* indicates the thermodynamic limit of about 60 meV/decade for the swing [2138]. Adapted from [2136]

talline silicon has a mobility of typically less than 10 cm^2/Vs. With the use of laser irradiation or thermal annealing, amorphous or small-grain polycrystalline silicon layers can be recrystallized, increasing the mobility up to several 100 cm^2/Vs, improving transistor performance [2128, 2130, 2131]. However, for display applications a mobility of 10 cm^2/Vs is large enough.

The main optimization criteria for thin-film transistors are high on-off ratio, long-term stability, good uniformity and reproducibility, and low cost. Recently, flexible (on polymer substrate) and transparent TFTs (TFET, transparent FET), e.g. with polycrystalline ZnO or GaInZnO (GIZO) channel (Fig. 24.52b), are being investigated for advanced applications such as all-transparent electronics and displays [151, 2132–2135]. A compilation of recent results on transparent semiconducting oxide (TSO) channel FETs can be found in [2136]. In Fig. 24.53 performance data for various TSO channel FETs are visualized. In Fig. 24.54 a transparent inverter based on ZnO-MESFETs is depicted [2137].

24.6.3 Transistors with 2D Materials

The ultimate thin film transistor is one with a single monolayer as channel. Various 2D materials (cf. Sect. 13) as mono- or multi-layers have been investigated in transistors [2140, 2141]. The channel mobility for conventional layers decreases typically for thickness d below 10 nm and strongly below 5 nm. The idea to use 2D materials is to avoid a rough surface and interface defects towards the gate. A single layer MoS_2 transistor with HfO_2 gate and Au ohmic contacts has been reported in [2142] with a (field effect) mobility above 200 cm^2/Vs, low sub-threshold voltage swing and high on/off ratios above

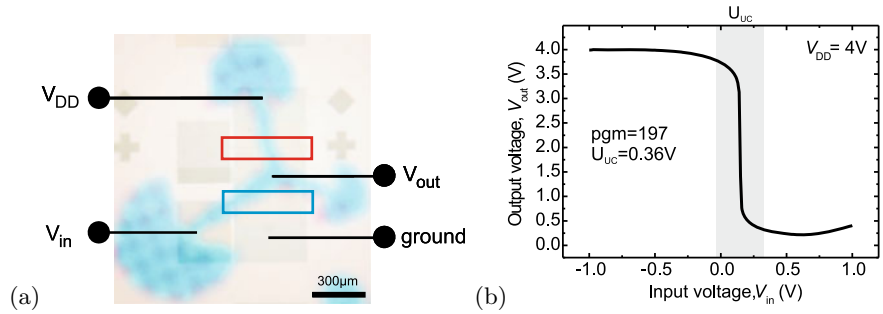

Fig. 24.54 **a** Optical image of transparent MESFET inverter based on ZnO. The *two rectangles* indicate the two gates. **b** Transfer characteristic for supply voltage V_{DD}=4 V

10^6. Also, a thinner channel allows further gate size scaling. However, the realities are complicated [2143, 2144] and clear performance gains have not been achieved yet. Also, the upscaling to wafer size is an unresolved issue.

24.6.4 OFETs

Organic field effect transistors (OFETs) [2139, 2145–2147] are transistors for which at least the channel consists of an organic material. Most work is done on thin film transistors, although some work on OFETs using bulk organic semiconductors has been reported [2148, 2149]. Organic materials are also used for the insulator and the contact materials. Often organic and flexible substrates are used. Applications are in low cost electronics, e.g. for driving display pixels or RFID tags (typically operating at 13.56 MHz or 900 MHz). Processes like spin-on and printing can be used. Due to their larger chemical stability against oxidation, mostly p-type channel materials are used. The highest mobilities are reached for pentacene (6 cm^2/Vs) and sexithiophene (1 cm^2/Vs); n-type organic semiconductors exhibit field mobility below 0.1 cm^2/Vs [2145].

Appendix A
Tensors

A.1 Introduction

A physical quantity $T_{ij\ldots m}$ with a total of k indices that is independent of translations of the coordinate system and transforms with respect to all indices like a vector is called a tensor of rank k.

Often, Einstein's sum convention is used; a sum is built over indices with the same symbol. For example, $x_i' = D_{ij}\, x_j$ shall be read as $x_i' = \sum_{j=1}^{3} D_{ij}\, x_j$.

A.2 Rotation of Coordinate System

A rotation of the coordinate system is a transformation $\mathbf{x} \to \mathbf{x}'$ that is written in components as

$$x_i' = D_{ij}\, x_j \ . \tag{A.1}$$

$\mathbf{D}$ is called the rotation matrix. The inverse of the rotation matrix is $\mathbf{D}^{-1}$ with

$$D_{kl}^{-1} = D_{lk} \ , \tag{A.2}$$

i.e. it is the transpose of matrix $\mathbf{D}$. The inverse transformation is $x_j = D_{ij}\, x_i'$. Thus,

$$D_{ij}\, D_{kj} = \delta_{ij} \ . \tag{A.3}$$

A simple example is the azimuthal rotation around the z-axis by an angle ϕ (in the mathematically positive direction)

$$\mathbf{D} = \begin{pmatrix} \cos\phi & -\sin\phi & 0 \\ \sin\phi & \cos\phi & 0 \\ 0 & 0 & 1 \end{pmatrix} \ . \tag{A.4}$$

For the description of an arbitrary rotation $(x, y, z) \to (X, Y, Z)$, generally three angles are necessary. Typically, the Euler angles (ϕ, θ, ψ) are used (Fig. A.1). First, the system is rotated by ϕ around the z-axis. The y-axis becomes the u-axis. Then, the system is tilted by θ around the u-axis and the z-axis becomes the Z-axis. Finally, the system is rotated by ψ around the Z-axis.

M. Grundmann, *The Physics of Semiconductors*, Graduate Texts in Physics,
https://doi.org/10.1007/978-3-030-51569-0

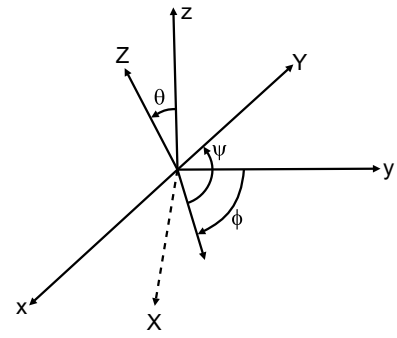

Fig. A.1 Rotation of a coordinate system (x, y, z) by the Euler angles (ϕ, θ, ψ) into the system (X, Y, Z)

The matrix for the general rotation by the Euler angles is

$$\begin{pmatrix} \cos\psi\cos\theta\cos\phi - \sin\psi\sin\phi & -\sin\phi\cos\theta\cos\psi - \cos\phi\sin\psi & \sin\theta\cos\psi \\ \cos\phi\cos\theta\sin\psi + \sin\phi\cos\psi & -\sin\psi\cos\theta\sin\phi + \cos\psi\cos\phi & \sin\theta\sin\psi \\ -\cos\phi\sin\theta & \sin\phi\sin\theta & \cos\theta \end{pmatrix} . \tag{A.5}$$

A.3 Rank-*n* Tensors

Rank-0 Tensors

A tensor of rank 0 is also called a scalar. For example, the length $v_1^2+v_2^2+v_3^2$ of the vector $\mathbf{v} = (v_1, v_2, v_3)$ is a scalar since it is invariant under rotation of the coordinate system. However, 'scalar' is not equivalent to 'number' since, e.g. the number $v_1^2 + v_2^2$ is not rotationally invariant.

Rank-1 Tensors

A tensor of rank 1 is a vector. It transforms under coordinate rotation $\mathbf{D}$ as

$$v_i' = D_{ij}\, v_j \ . \tag{A.6}$$

Rank-2 Tensors

A tensor of rank 2 is also called a dyade and is a 3×3 matrix $\mathbf{T}$ that transforms under coordinate rotation as

$$T_{ij}' = D_{ik}\, D_{jl}\, T_{kl} \ . \tag{A.7}$$

The physical meaning is the following: Two vectors $\mathbf{s}$ and $\mathbf{r}$ shall be related to each other via $s_i = T_{ij} r_j$. This could be, e.g., the current $\mathbf{j}$ and the electric field $\mathbf{E}$ that are connected via the tensor of conductivity $\boldsymbol{\sigma}$, i.e. $j_i = \sigma_{ij} E_j$.

Such an equation only makes physical sense if it is also valid in a (any) rotated coordination system. The tensor $\mathbf{T}'$ in the rotated coordinate system must fulfill $s'_i = T'_{ij} r'_j$. This implies the transformation law (A.7). $s'_k = D_{ki} s_i = D_{ki} T_{ij} r_j$ and also $s'_k = T'_{km} r'_m = T'_{km} D_{mj} r_j$. Thus, $T'_{km} D_{mj} = D_{ki} T_{ij}$ since the previous relations are valid for arbitrary $\mathbf{r}$. Multiplication by D_{lj} yields $T'_{km} D_{mj} D_{lj} = T'_{km} \delta_{ml} = T'_{kl} = D_{ki} D_{lj} T_{ij}$.

The trace of a rank-2 tensor is defined as $\mathrm{tr}\mathbf{T} = T_{ii} = T_{11} + T_{22} + T_{33}$. It is a scalar, i.e. invariant under coordinate rotation, since $T'_{kk} = D_{ki} D_{kj} T_{ij} = \delta_{ij} T_{ij} = T_{ii}$. Next to the trace invariant, rank-2 tensors have two more invariants independent:

$$I_1 = \mathrm{tr}\,\mathbf{T} = T_{11} + T_{22} + T_{33} \tag{A.8a}$$

$$I_2 = [(\mathrm{tr}\,\mathbf{T})^2 - \mathrm{tr}\,(\mathbf{T}^2)]/2 = T_{11}T_{22} + T_{22}T_{33} + T_{11}T_{33} - T_{12}T_{21} - T_{23}T_{32} - T_{13}T_{31} \tag{A.8b}$$

$$I_3 = \det(\mathbf{T}) = T_{13}T_{22}T_{31} + T_{12}T_{23}T_{31} + T_{13}T_{21}T_{32} - T_{11}T_{23}T_{32} - T_{12}T_{21}T_{33} + T_{11}T_{22}T_{33}\ . \tag{A.8c}$$

Of course any function of the invariants is also invariant. In terms of the eigenvalues λ_1, λ_2, and λ_3 of $\mathbf{T}$, the invariants are given by

$$I_1 = \lambda_1 + \lambda_2 + \lambda_3 \tag{A.9a}$$

$$I_2 = \lambda_1\,\lambda_2 + \lambda_1\,\lambda_3 + \lambda_2\,\lambda_3 \tag{A.9b}$$

$$I_3 = \lambda_1\,\lambda_2\,\lambda_3\ . \tag{A.9c}$$

It shall be noted that the relation

$$\mathbf{T}^3 = I_1\,\mathbf{T}^2 - I_2\,\mathbf{T} + I_3\mathbf{1} \tag{A.10}$$

holds, $\mathbf{1}$ being the unity matrix. Further information on tensor invariants can be found in [2150].

A rank-2 tensor can be separated into a symmetric part $\mathbf{T}^S$ and an antisymmetric part $\mathbf{T}^A$, i.e. $T^S_{ji} = T^S_{ij}$ and $T^A_{ji} = -T^A_{ij}$ with

$$\mathbf{T} = \mathbf{T}^S + \mathbf{T}^A \tag{A.11a}$$

$$T^S_{ij} = \frac{T_{ij} + T_{ji}}{2} \tag{A.11b}$$

$$T^A_{ij} = \frac{T_{ij} - T_{ji}}{2}\ . \tag{A.11c}$$

A rank-2 tensor can be separated into an isotropic (spherical) part $\mathbf{T}^I$ and a deviatoric part $\mathbf{T}^D$. The isotropic part is invariant under coordinate rotation.

$$\mathbf{T} = \mathbf{T}^I + \mathbf{T}^D \tag{A.12a}$$

$$T^I_{ij} = \delta_{ij}\frac{\mathrm{tr}\,\mathbf{T}}{3} \tag{A.12b}$$

$$T^D_{ij} = T_{ij} - \delta_{ij}\frac{\mathrm{tr}\,\mathbf{T}}{3}\ . \tag{A.12c}$$

The trace of $\mathbf{T}$ is the same as that of $\mathbf{T}^I$. The trace of $\mathbf{T}^D$ is zero.

Rank-3 Tensors

A tensor of rank 3 transforms according to

$$T'_{ijk} = D_{il}\, D_{jm}\, D_{kn} T_{lmn}\ . \tag{A.13}$$

An example is the tensor **e** of piezoelectric constants that relates the rank-2 tensor of the strains ϵ with the polarization vector **P**, i.e. $P_i = e_{ijk}\epsilon_{jk}$.

Rank-4 Tensors

A tensor of rank 4 transforms according to

$$T'_{ijkl} = D_{im}\, D_{jn}\, D_{ko}\, D_{lp}\, T_{mnop}\ . \tag{A.14}$$

An example is the tensor **C** of elastic constants that relates the rank 2 tensors $\boldsymbol{\epsilon}$ and $\boldsymbol{\sigma}$ of the elastic strains and stresses, i.e. $\sigma_{ij} = C_{ijkl}\epsilon_{kl}$. The reduction of the rotation of a rank-4 tensor to a 6×6 matrix problem is discussed in [2151].

Appendix B
Point and Space Groups

Table B.1 The 10 two-dimensional point groups in full and abbreviated international notation. N_{sg} denotes the number of space groups

Group	Notation		N_{sg}	Symmetry elements
	Full	Abbreviated		
	International			
C_1	1	1	1	C_1
D_1	1 m	m	3	C_1, m
C_2	2	2	1	C_2
D_2	2 mm	mm	4	C_2, 2 m
C_3	3	3	1	C_3
D_3	3 m	3 m	2	C_3, 3 m
C_4	4	4	1	C_4
D_4	4 mm	4 m	2	C_4, 2 m
C_6	6	6	1	C_6
D_6	6 mm	6 m	1	C_6, 6 m

M. Grundmann, *The Physics of Semiconductors*, Graduate Texts in Physics,
https://doi.org/10.1007/978-3-030-51569-0

Table B.2 The 32 point groups in Schönfließ and international notation. N_{sg} denotes the number of space groups

System	Class		N_{sg}	Symmetry elements
	International	Schönfließ		
Triclinic	1	C_1	1	E
	$\bar{1}$	C_i	1	$E\ i$
Monoclinic	m	C_s	3	$E\ \sigma_h$
	2	C_2	4	$E\ C_2$
	2/m	C_{2h}	6	$E\ C_2\ i\ \sigma_h$
Orthorhombic	2 mm	C_{2v}	9	$E\ C_2\ \sigma_v'\ \sigma_v''$
	222	D_2	22	$E\ C_2\ C_2'\ C_2''$
	mmm	D_{2h}	28	$E\ C_2\ C_2'\ C_2''\ i\ \sigma_h\ \sigma_v'\ \sigma_v''$
Tetragonal	4	C_4	6	$E\ 2C_4\ C_2$
	$\bar{4}$	S_4	2	$E\ 2S_4\ C_2$
	4/m	C_{4h}	6	$E\ 2C_4\ C_2\ i\ 2S_4\ \sigma_h$
	4 mm	C_{4v}	10	$E\ 2C_4\ C_2\ 2\sigma_v'\ 2\sigma_d$
	$\bar{4}$2 m	D_{2d}	12	$E\ C_2\ C_2'\ C_2''\ 2\sigma_d\ 2S_4$
	422	D_4	12	$E\ 2C_4\ C_2\ 2C_2'\ 2C_2''$
	4/mmm	D_{4h}	20	$E\ 2C_4\ C_2\ 2C_2'\ 2C_2''\ i\ 2S_4\ \sigma_h\ 2\sigma_v'\ 2\sigma_h$
Trigonal (rhombohedral)	3	C_3	4	$E\ 2C_3$
	$\bar{3}$	S_6	2	$E\ 2C_3\ i\ 2S_6$
	3 m	C_{3v}	7	$E\ 2C_3\ 3\sigma_v$
	32	D_3	6	$E\ 2C_3\ 3C_2$
	$\bar{3}$ m	D_{3d}	6	$E\ 2C_3\ 3C_2\ i\ 2S_6\ 3\sigma_d$
Hexagonal	$\bar{6}$	C_{3h}	6	$E\ 2C_3\ \sigma_h\ 2S_3$
	6	C_6	1	$E\ 2C_6\ 2C_3\ C_2$
	6/m	C_{6h}	2	$E\ 2C_6\ 2C_3\ C_2\ i\ 2S_3\ 2S_6\ \sigma_h$
	$\bar{6}$ m2	D_{3h}	6	$E\ 2C_3\ 3C_2\ \sigma_h\ 2S_3\ 3\sigma_v$
	6 mm	C_{6v}	4	$E\ 2C_6\ 2C_3\ C_2\ 3\sigma_v\ 3\sigma_d$
	622	D_6	4	$E\ 2C_6\ 2C_3\ C_2\ 3C_2'\ 3C_2''$
	6/mmm	D_{6h}	4	$E\ 2C_6\ 2C_3\ C_2\ 3C_2'\ 3C_2''\ i\ 2S_3$ $2S_6\ \sigma_h\ 3\sigma_d\ 3\sigma_v$
Cubic	23	T	5	$E\ 4C_3\ 4C_3^2\ 3C_2$
	$m3$	T_h	7	$E\ 4C_3\ 4C_3^2\ 3C_2\ i\ 8S_6\ 3\sigma_h$
	$\bar{4}3$ m	T_d	8	$E\ 8C_3\ 3C_2\ 6\sigma_d\ 6S_4$
	432	O	6	$E\ 8C_3\ 3C_2\ 6C_2'\ 6C_4$
	$m3$ m	O_h	10	$E\ 8C_3\ 3C_2\ 6C_2\ 6C_4\ i\ 8S_6\ 3\sigma_h\ 6\sigma_d\ 6S_4$

Table B.3 Space group numbers and corresponding space group symbols in standard international notation

1	P1	2	$P\bar{1}$	3	P2	4	$P2_1$	5	C2
6	Pm	7	Pc	8	Cm	9	Cc	10	P2/m
11	$P2_1/m$	12	C2/m	13	P2/c	14	$P2_1/c$	15	C2/c
16	P222	17	$P222_1$	18	$P2_12_12$	19	$P2_12_12_1$	20	$C222_1$
21	C222	22	F222	23	I222	24	$I2_12_12_1$	25	Pmm2
26	$Pmc2_1$	27	Pcc2	28	Pma2	29	$Pca2_1$	30	Pnc2
31	$Pmn2_1$	32	Pba2	33	$Pna2_1$	34	Pnn2	35	Cmm2
36	$Cmc2_1$	37	Ccc2	38	Amm2	39	Abm2	40	Ama2
41	Aba2	4_2	Fmm2	43	Fdd2	44	Imm2	45	Iba2
46	Ima2	47	Pmmm	48	Pnnn	49	Pccm	50	Pban
51	Pmma	52	Pnna	53	Pmna	54	Pcca	55	Pbam
56	Pccn	57	Pbcm	58	Pnnm	59	Pmmn	60	Pbcn
61	Pbca	62	Pnma	63	Cmcm	64	Cmca	65	Cmmm
66	Cccm	67	Cmma	68	Ccca	69	Fmmm	70	Fddd
71	Immm	72	Ibam	73	Ibca	74	Imma	75	P4
76	$P4_1$	77	$P4_2$	78	$P4_3$	79	I4	80	$I4_1$
81	$P\bar{4}$	82	$I\bar{4}$	83	P4/m	84	$P4_2/m$	85	P4/n
86	$P4_2/n$	87	I4/m	88	$I4_1/a$	89	P422	90	$P42_12$
91	P4122	92	$P412_12$	93	$P4_222$	94	$P4_22_12$	95	$P4_322$
96	$P4_32_12$	97	I422	98	$I4_122$	99	P4mm	100	P4bm
101	$P4_2cm$	102	$P4_2nm$	103	P4cc	104	P4nc	105	$P4_2mc$
106	$P4_2bc$	107	I4mm	108	I4cm	109	$I4_1md$	110	$I4_1cd$
111	$P\bar{4}2m$	112	$P\bar{4}2c$	113	$P\bar{4}2_1m$	114	$P\bar{4}2_1c$	115	$P\bar{4}m2$
116	$P\bar{4}c2$	117	$P\bar{4}b2$	118	$P\bar{4}n2$	119	$I\bar{4}m2$	120	$I\bar{4}c2$
121	$I\bar{4}2m$	122	$I\bar{4}2d$	123	P4/mmm	124	P4/mcc	125	P4/nbm
126	P4/nnc	127	P4/mbm	128	P4/mnc	129	P4/nmm	130	P4/ncc
131	$P4_2/mmc$	132	$P4_2/mcm$	133	$P4_2/nbc$	134	$P4_2/nnm$	135	$P4_2/mbc$
136	$P4_2/mnm$	137	$P4_2/nmc$	138	$P4_2/ncm$	139	I4/mmm	140	I4/mcm
141	$I4_1/amd$	142	$I4_1/acd$	143	P3	144	$P3_1$	145	$P3_2$
146	R3	147	$P\bar{3}$	148	$R\bar{3}$	149	P312	150	P321
151	$P3_112$	152	$P3_121$	153	$P3_212$	154	$P3_221$	155	R32
156	P3m1	157	P31m	158	P3c1	159	P31c	160	R3m
161	R3c	162	$P\bar{3}1m$	163	$P\bar{3}1c$	164	$P\bar{3}m1$	165	$P\bar{3}c1$
166	$R\bar{3}m$	167	$R\bar{3}c$	168	P6	169	$P6_1$	170	$P6_5$
171	$P6_2$	172	$P6_4$	173	$P6_3$	174	$P\bar{6}$	175	P6/m
176	$P6_3/m$	177	P622	178	$P6_122$	179	$P6_522$	180	$P6_222$
181	$P6_422$	182	$P6_322$	183	P6mm	184	P6cc	185	$P6_3cm$
186	$P6_3mc$	187	$P\bar{6}m2$	188	$P\bar{6}c2$	189	$P\bar{6}2m$	190	$P\bar{6}2c$
191	P6/mmm	192	P6/mcc	193	$P6_3/mcm$	194	$P6_3/mmc$	195	P23
196	F23	197	I23	198	$P2_13$	199	$I2_13$	200	$Pm\bar{3}$
201	$Pn\bar{3}$	202	$Fm\bar{3}$	203	$Fd\bar{3}$	204	$Im\bar{3}$	205	$Pa\bar{3}$
206	$Ia\bar{3}$	207	P432	208	$P4_232$	209	F432	210	$F4_132$
211	I432	212	$P4_332$	213	$P4_132$	214	$I4_132$	215	$P\bar{4}3m$
216	$F\bar{4}3m$	217	$I\bar{4}3m$	218	$P\bar{4}3n$	219	$F\bar{4}\ 3c$	220	$I\bar{4}3d$
221	$Pm\bar{3}m$	222	$Pn\bar{3}n$	223	$Pm\bar{3}n$	224	$Pn\bar{3}m$	225	$Fm\bar{3}m$
226	$Fm\bar{3}c$	227	$Fd\bar{3}m$	228	$Fd\bar{3}c$	229	$Im\bar{3}m$	230	$Ia\bar{3}d$

Appendix C
Kramers–Kronig Relations

The Kramers–Kronig relations (KKR) are relations between the real and imaginary part of the dielectric function. They are of a general nature and are based on the properties of a complex, analytical response function $f(\omega) = f_1(\omega) + \mathrm{i} f_2(\omega)$ fulfilling the following conditions[1]:

- The poles of $f(\omega)$ are below the real axis.
- The integral of $f(\omega)/\omega$ along a semicircle with infinite radius in the upper half of the complex plane vanishes.
- The function $f_1(\omega)$ is even and the function $f_2(\omega)$ is odd for real values of the argument.

The integral of $f(s)/(s-\omega)\mathrm{d}s$ along the real axis and an infinite semicircle in the upper half of the complex plane is zero because the path is a closed line. The integral along a semicircle above the pole at $s = \omega$ yields $-\pi \mathrm{i} f(\omega)$, the integral over the infinite semicircle is zero. Therefore the value of $f(\omega)$ is given by[2]

$$f(\omega) = \frac{1}{\pi \mathrm{i}} \Pr \int_{-\infty}^{\infty} \frac{f(s)}{s-\omega} \mathrm{d}s \,. \tag{C.1}$$

Equating the real and imaginary parts of (C.1) yields for the real part

$$f_1(\omega) = \frac{1}{\pi} \Pr \int_{-\infty}^{\infty} \frac{f_2(s)}{s-\omega} \mathrm{d}s \,. \tag{C.2}$$

Splitting the integral into two parts $\int_0^\infty$ and $\int_{-\infty}^0$, going from s to $-s$ in the latter and using $f_2(-\omega) = -f_2(\omega)$ and $\frac{1}{s-\omega} + \frac{1}{s+\omega} = \frac{2s}{s^2-\omega^2}$ yields (C.3a)

$$f_1(\omega) = \frac{2}{\pi} \Pr \int_0^{\infty} \frac{s\, f_2(s)}{s^2-\omega^2} \mathrm{d}s \tag{C.3a}$$

$$f_2(\omega) = -\frac{2}{\pi} \Pr \int_0^{\infty} \frac{f_1(s)}{s^2-\omega^2} \mathrm{d}s \,. \tag{C.3b}$$

[1] The requirements for the function f to which the KKR apply can be interpreted as that the function must represent the Fourier transform of a linear and causal physical process.

[2] The Cauchy principal value Pr of the integral is the limit for $\delta \to 0$ of the sum of the integrals over $-\infty < s < \omega - \delta$ and $\omega + \delta < s < \infty$.

M. Grundmann, *The Physics of Semiconductors*, Graduate Texts in Physics,
https://doi.org/10.1007/978-3-030-51569-0

In a similar way, (C.3b) is obtained. These two relations are the Kramers–Kronig relations [2152, 2153]. They are most often applied to the dielectric function ϵ. In this case, they apply to the susceptibility, i.e. $f(\omega) = \chi(\omega) = \epsilon(\omega)/\epsilon_0 - 1$. The susceptibility can be interpreted as the Fourier transform of the time-dependent polarization in the semiconductor after an infinitely short pulsed electric field, i.e. the impulse response of the polarization. For the dielectric function $\epsilon = \epsilon_1 + \mathrm{i}\epsilon_2$, the following KKR relations hold:

$$\epsilon_1(\omega) = \epsilon_0 + \frac{2}{\pi} \Pr \int_0^\infty \frac{s\,\epsilon_2(s)}{s^2 - \omega^2} \mathrm{d}s \tag{C.4a}$$

$$\epsilon_2(\omega) = -\frac{2\omega}{\pi} \Pr \int_0^\infty \frac{\epsilon_1(s) - \epsilon_0}{s^2 - \omega^2} \mathrm{d}s\,. \tag{C.4b}$$

The static dielectric constant is thus given by

$$\epsilon(0) = \epsilon_0 + \frac{2}{\pi} \Pr \int_0^\infty \frac{\epsilon_2(s)}{s} \mathrm{d}s\,. \tag{C.5}$$

The integral does not diverge since ϵ_2 is an odd function and zero at $\omega = 0$. Generally the j-th momentum M_j of the imaginary part of the dielectric function is

$$M_j = \int_0^\infty \epsilon_2(\omega)\,\omega^j\,\mathrm{d}\omega\,. \tag{C.6}$$

Thus, $M_{-1} = \pi[\epsilon(0) - \epsilon_0]/2$.

Other KKRs are, e.g., the relation between the index of refraction n_r and the absorption coefficient α:

$$n_\mathrm{r}(\lambda) = \frac{1}{\pi} \Pr \int_0^\infty \frac{\alpha(s)}{1 - s^2/\lambda^2} \mathrm{d}s\,. \tag{C.7}$$

If the imaginary (real) part of the dielectric function is known (for all frequencies), the real (imaginary) part can be calculated via the KKR. If the dependence is not known for the entire frequency range, assumptions about the dielectric function in the unknown spectral regions must be made that limit the reliability of the transformation.

Appendix D
Oscillator Strength

The response of an oscillator to an electric field **E** is formulated with the dielectric function. The resulting polarization **P** is related to the electric field via

$$\mathbf{P} = \epsilon_0 \, \chi \, \mathbf{E} \, , \tag{D.1}$$

with χ being the electric susceptibility, and the displacement field **D** is given by

$$\mathbf{D} = \epsilon_0 \, \mathbf{E} + \mathbf{P} = \epsilon_0 \, \epsilon \, \mathbf{E} \, . \tag{D.2}$$

Thus the (relative) dielectric constant is

$$\epsilon = 1 + \chi \, . \tag{D.3}$$

We assume a harmonic oscillator model for an electron, i.e. an equation of motion for the amplitude $x = x_0 \exp(\mathrm{i}\omega t)$

$$m \, \ddot{x} = -C \, x \, . \tag{D.4}$$

The resonance frequency is $\omega_0^2 = C/m$. The presence of a harmonic electric field E of frequency ω and amplitude E_0 adds a force eE. Thus,

$$-\, m \, \omega^2 \, x = -m \, \omega_0^2 \, x + e \, E \, . \tag{D.5}$$

The polarization ex_0 is given by

$$e \, x_0 = \frac{e^2}{m} \, \frac{1}{\omega_0^2 - \omega^2} \, E_0 = \frac{e^2}{m \, \omega_0^2} \, \frac{1}{1 - \omega^2/\omega_0^2} \, E_0 \, . \tag{D.6}$$

The pre-factor is called the (dimensionless) *oscillator strength* and will be denoted as

$$f = \frac{e^2}{\epsilon_0 \, m \, \omega_0^2} \tag{D.7}$$

in the following. The frequency-dependent dielectric function of the resonance is thus

$$\epsilon(\omega) = 1 + \frac{f}{1 - \omega^2/\omega_0^2} \, . \tag{D.8}$$

M. Grundmann, *The Physics of Semiconductors*, Graduate Texts in Physics,
https://doi.org/10.1007/978-3-030-51569-0

In the low-frequency limit, the dielectric function is $\epsilon(0) = 1+f$, in the high-frequency limit $\epsilon(\infty) = 1$. The oscillator strength is the difference of ϵ for frequencies below and above the resonance.

For all systems, the high-frequency limit of ϵ is 1. This means that $\chi = 0$, i.e. there are no more oscillators to be polarized. The low-frequency limit includes all possible oscillators. If there are further oscillators between frequencies well above ω_0 and $\omega \to \infty$, these are summarized as the high-frequency dielectric constant $\epsilon_\infty > 1$. Equation (D.8) then reads

$$\epsilon(\omega) = \epsilon(\infty) + \frac{\hat{f}}{1 - \omega^2/\omega_0^2} \,. \tag{D.9}$$

The limit $\epsilon \to \epsilon(\infty)$ is only valid for frequencies above ω_0 but smaller than the next resonance(s) at higher frequencies.[3] Another common form is to include the background dielectric constant via

$$\epsilon(\omega) = \epsilon(\infty)\left[1 + \frac{f}{1 - \omega^2/\omega_0^2}\right] \,. \tag{D.10}$$

Obviously, $f = \hat{f}/\epsilon(\infty)$, making the two forms equivalent.

In order to discuss the lineshape, not only for ϵ but also for the index of refraction $n^* = n_\mathrm{r} + \mathrm{i}\kappa = \sqrt{\epsilon}$, we introduce damping to our calculation by adding a term $-m\Gamma\dot{x}$ to the left side of (D.5). This term is something like a 'friction' and would cause the oscillation amplitude to decay exponentially with a time constant $\tau = 2/\Gamma$ without external stimulus. The dielectric constant is

$$\epsilon(\omega) = \epsilon(\infty)\left[1 + \frac{f}{1 - (\omega^2 + \mathrm{i}\,\omega\Gamma)/\omega_0^2}\right] = \epsilon' + \mathrm{i}\epsilon'' \,. \tag{D.11}$$

The real and imaginary part fulfill the Kramers–Kronig relations (C.3a) and (C.3b). For the oscillator strength, the regimes of large oscillator strength ($f \sim 1$) and small oscillator strength ($f \ll 1$) are distinguished. For the damping, two regimes should be distinguished: Small damping ($\Gamma \ll \omega_0$) and strong damping ($\Gamma \gtrsim \omega_0$). Typical lineshapes are shown in Figs. D.1 and D.2.

For small oscillator strength, i.e. $f \ll 1$, the index of refraction $n^* = \sqrt{\epsilon} = n_\mathrm{r} + \mathrm{i}\kappa$ is given by ($n_\infty = \sqrt{\epsilon(\infty)}$)

$$n_\mathrm{r} = n_\infty\left[1 + \frac{f}{2}\,\frac{\omega_0^2\,(\omega_0^2 - \omega^2)}{(\omega_0^2 - \omega^2)^2 + \Gamma^2\,\omega^2}\right] \tag{D.12a}$$

$$\kappa = n_\infty\,\frac{f}{2}\,\frac{\Gamma\,\omega_0\,(\omega_0^2 - \omega^2)}{(\omega_0^2 - \omega^2)^2 + \Gamma^2\,\omega^2} \,. \tag{D.12b}$$

For small detuning from the resonance frequency, i.e. $\omega = \omega_0 + \delta\omega$ with $|\delta\omega|/\omega_0 \ll 1$, the index of refraction is given by

$$n_\mathrm{r} = n_\infty\left[1 - \frac{f}{4}\,\frac{\omega_0\,\delta\omega}{(\delta\omega)^2 + \Gamma^2/4}\right] \tag{D.13a}$$

$$\kappa = n_\infty\,\frac{f}{4}\,\frac{\omega_0\,\Gamma/2}{(\delta\omega)^2 + \Gamma^2/4} \,. \tag{D.13b}$$

The maximum absorption is given as

[3] For ω going to infinite values (beyond the X-ray regime), ϵ always goes towards one.

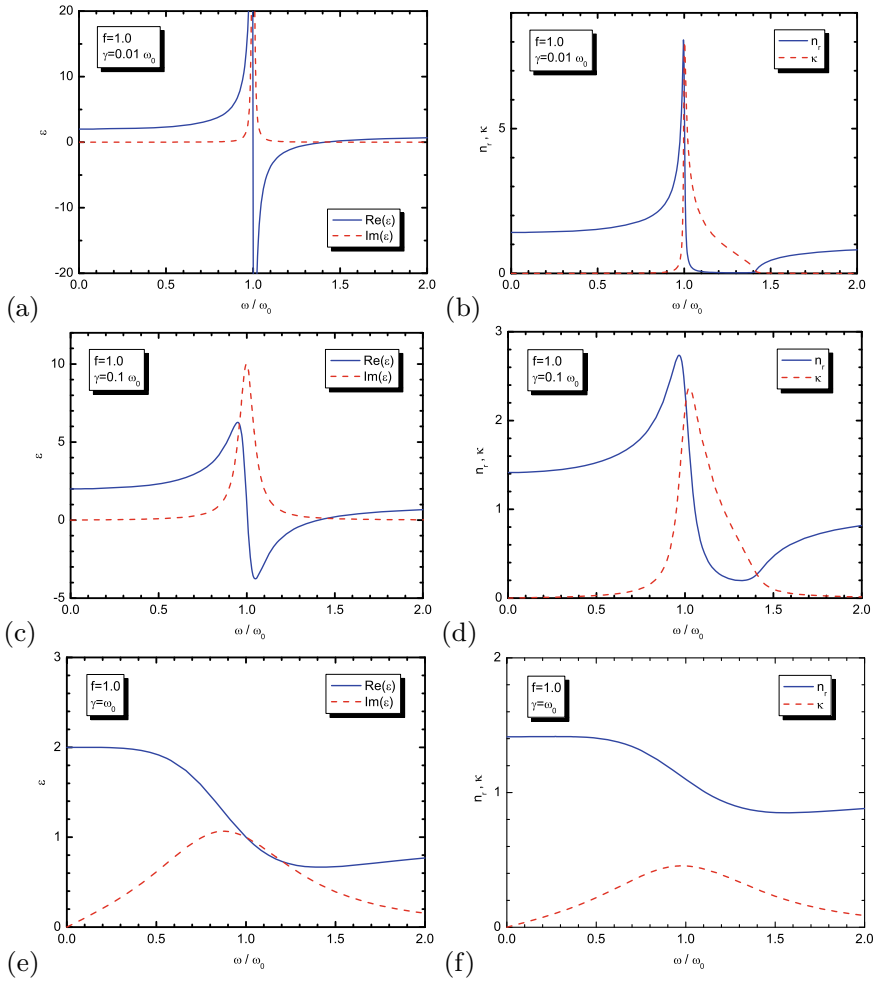

Fig. D.1 Real (*solid lines*) and imaginary (*dashed lines*) parts of the dielectric constant (**a**, **c**, **e**) and index of refraction (**b**, **d**, **f**) (D.11) for oscillator strength $f = 1$ and various values of damping: (**a**, **b**) $\Gamma = 10^{-2}\omega_0$, (**c**, **d**) $\Gamma = 10^{-1}\omega_0$, and (**e**, **f**) $\Gamma = \omega_0$

$$\alpha_{\mathrm{m}} = 2\,\frac{\omega_0}{c}\,\kappa(\omega_0) = f\,\frac{\omega_0^2}{\Gamma}\,\frac{n_\infty}{c}\,. \tag{D.14}$$

For zero damping, the dielectric function has a zero at

$$\omega_0' = \omega_0\sqrt{1+f} \approx \omega_0\left(1+\frac{f}{2}\right)\,. \tag{D.15}$$

The latter approximation is valid for $f \ll 1$. In the region between ω_0 and ω_0', the real part of the index of refraction is very small (for the physically unrealistic case of $\Gamma \equiv 0$ it is exactly zero since $\epsilon < 0$). The reflectance (for vertical incidence $R = [(1-n^*)/(1+n^*)]^2$) in this region (width: $f\omega_0/2$) is thus very high. For larger damping (and small oscillator strength), this effect is washed out.

The frequency $\omega_{\epsilon'',\max}$ of the maximum of the imaginary part of ϵ'' of the dielectric function ($\hat{\Gamma} = \Gamma/\omega_0$) is

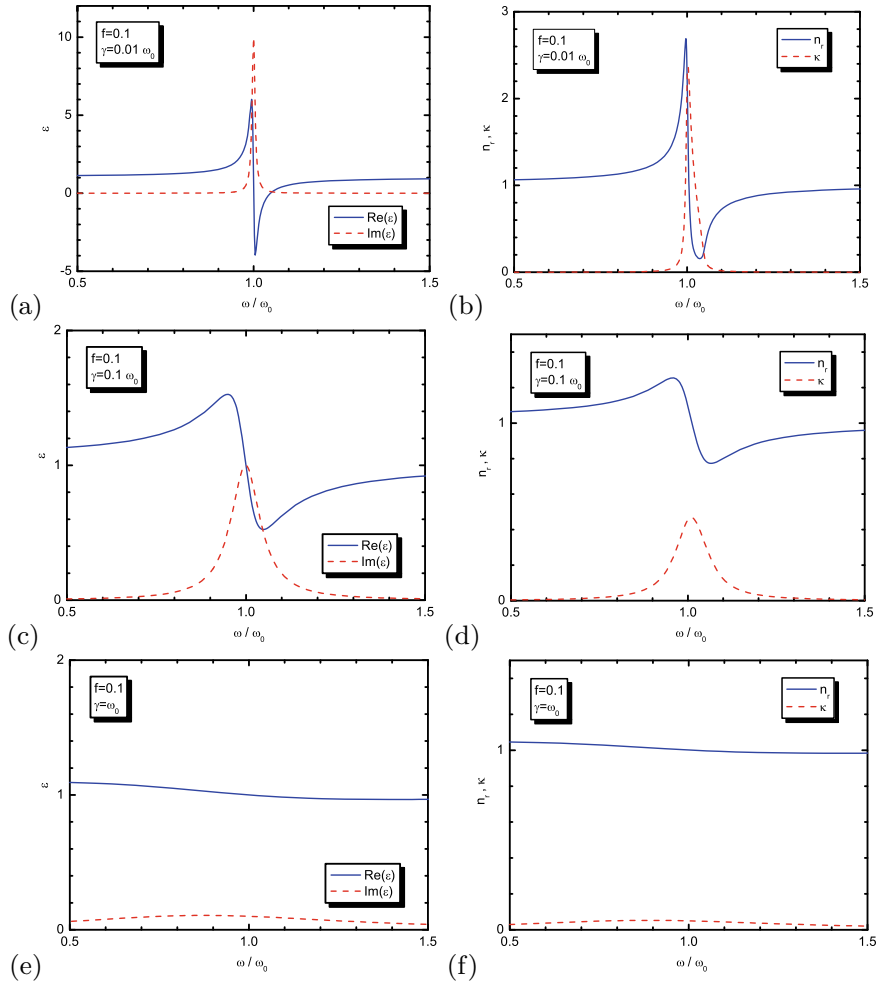

Fig. D.2 Real (*solid lines*) and imaginary (*dashed lines*) parts of the dielectric constant (**a**, **c**, **e**) and index of refraction (**b**, **d**, **f**) (D.11) for oscillator strength $f = 10^{-1}$ and various values of damping: (**a**, **b**) $\Gamma = 10^{-2}\omega_0$, (**c**, **d**) $\Gamma = 10^{-1}\omega_0$, and (**e**, **f**) $\Gamma = \omega_0$

$$\omega^2_{\epsilon'',\max} = \omega_0^2 \frac{2 - \hat{\Gamma}^2 + \sqrt{16 - 4\hat{\Gamma}^2 + \hat{\Gamma}^4}}{6} \approx \omega_0^2 \left[1 - \left(\frac{\Gamma}{2\omega_0}\right)^2\right] . \tag{D.16}$$

The approximation is valid for small damping $\Gamma \ll \omega_0$. In this case, the detuned frequency of the maximum is close to ω_0 (Fig. D.3). The frequency position of the maximum of $\tan\delta = \epsilon''/\epsilon'$ is

$$\omega^2_{\tan\delta,\max} = \omega_0^2 \frac{2 + f - \hat{\Gamma}^2 + \Lambda^2}{6} \tag{D.17}$$

$$\Lambda^2 = \sqrt{12\,(1+f) + \left(2 + f - \hat{\Gamma}^2\right)^2} .$$

The value of $\tan\delta$ at its maximum is (Λ has the same meaning as in (D.17))

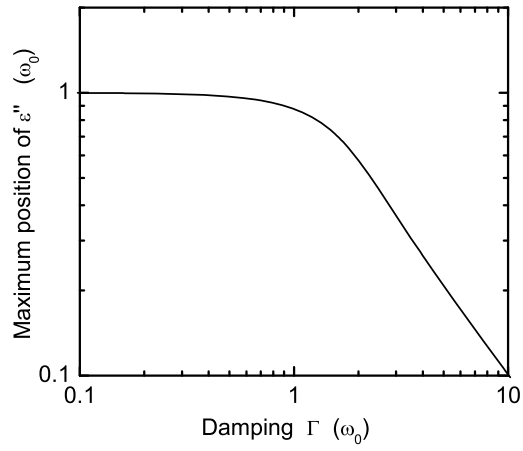

Fig. D.3 Frequency position of the maximum of ϵ as a function of the damping

$$(\tan\delta)_{\max} = \frac{-3\sqrt{\frac{3}{2}}\, f\, \hat{\Gamma}\sqrt{2+f-\hat{\Gamma}^2+\Lambda^2}}{-8-8\,f+f^2-4\,\hat{\Gamma}^2-2\,f\,\hat{\Gamma}^2+\hat{\Gamma}^4+\left(2+f-\hat{\Gamma}^2\right)\Lambda^2}\,. \tag{D.18}$$

Appendix E
Quantum Statistics

E.1 Introduction

Bosons are particles with integer spin $s = n$, fermions are particles with spin $s = n + 1/2$ with n being an integer including zero. The fundamental quantum-mechanical property of the wavefunction of a system with N such particles is that under exchange of any two particles, the wavefunction is symmetric in the case of bosons and antisymmetric in the case of fermions. For two particles, these conditions read

$$\Psi(q_1, q_2) = \Psi(q_2, q_1) \tag{E.1a}$$

$$\Psi(q_1, q_2) = -\Psi(q_2, q_1) \ , \tag{E.1b}$$

where (E.1a) holds for bosons and (E.1b) holds for fermions. The variables q_i denote the coordinates and spin of the i-th particle. The Pauli principle allows bosons to populate the same single particle state with an arbitrary number of particles (at least more than one). For fermions, the exclusion principle holds that each single particle state can only be populated once.

E.2 Partition Sum

We consider a gas of N identical particles in a volume V in equilibrium at a temperature T. The possible quantum-mechanical states of a particle is denoted as r. The energy of a particle in the state r is ϵ_r, the number of particles in the state r is n_r.

For vanishing interaction of the particles, the total energy of the gas in the state R (with n_r particles in the state r) is

$$E_R = \sum_r n_r \, \epsilon_r \ . \tag{E.2}$$

The sum runs over all possible states r. The total number of particles imposes the condition

$$N = \sum_r n_r \ . \tag{E.3}$$

In order to calculate the thermodynamic potentials, the partition sum Z needs to be calculated

M. Grundmann, *The Physics of Semiconductors*, Graduate Texts in Physics,
https://doi.org/10.1007/978-3-030-51569-0

$$Z = \sum_R \exp(-\beta E_R) \ , \tag{E.4}$$

with $\beta = 1/(kT)$. The sum runs over all possible microscopic states R of the gas, i.e. all combinations of the n_r that fulfill (E.3). The probability P_S to find the system in a particular state S is given by (canonical ensemble)

$$P_S = \frac{\exp(-\beta E_S)}{Z} \ . \tag{E.5}$$

The average number $\bar{n}_s$ of particles in a state s is given by

$$\bar{n}_s = \frac{\sum_R n_s \exp(-\beta E_R)}{Z} = -\frac{1}{\beta Z}\frac{\partial Z}{\partial \epsilon_\mathrm{s}} = -\frac{1}{\beta}\frac{\partial \ln Z}{\partial \epsilon_\mathrm{s}} \ . \tag{E.6}$$

We note that the average deviation $\overline{(\Delta n_s)^2} = \overline{n_s^2 - \bar{n}_s^2} = \overline{n_s^2} - \bar{n}_s^2$ is given by

$$\overline{(\Delta n_s)^2} = \frac{1}{\beta^2}\frac{\partial^2 \ln Z}{\partial \epsilon_\mathrm{s}^2} = -\frac{1}{\beta}\frac{\partial \bar{n}_s}{\partial \epsilon_\mathrm{s}} \ . \tag{E.7}$$

In the Bose–Einstein statistics (for bosons), the particles are fundamentally indistinguishable. Thus, a set of $(n_1, n_2, \ldots)$ uniquely describes the system. In the case of fermions, for each state n_r is either 0 or 1. In both cases, (E.3) needs to be fulfilled.

E.3 Photon Statistics

This case is the Bose–Einstein statistics (cf. (E.24)) with undefined particle number. We rewrite (E.6) as

$$\bar{n}_s = \frac{\sum_{n_s} n_s \exp(-\beta n_s \epsilon_\mathrm{s}) \sum^{(s)}_{n_1,n_2,\ldots} \exp(-\beta(n_1\epsilon_1 + n_2\epsilon_2 + \ldots))}{\sum_{n_s} \exp(-\beta n_s \epsilon_\mathrm{s}) \sum^{(s)}_{n_1,n_2,\ldots} \exp(-\beta(n_1\epsilon_1 + n_2\epsilon_2 + \ldots))} \ , \tag{E.8}$$

where $\sum^{(s)}$ denotes a summation that does not include the index s. In the case of photons, the values n_r can take any value (integers including zero) without restriction and therefore the sums $\sum^{(s)}$ in the numerator and denominator of (E.8) are identical. After some calculation we find

$$\bar{n}_s = -\frac{1}{\beta}\frac{\partial}{\partial \epsilon_\mathrm{s}} \ln\left(\sum_{n_s=0}^{\infty} \exp(-\beta n_s \epsilon_\mathrm{s})\right) \ . \tag{E.9}$$

The argument of the logarithm is a geometrical series with the limit $[1 - \exp(-\beta\epsilon_\mathrm{s})]^{-1}$. This leads to the so-called Planck distribution

$$\bar{n}_s = \frac{1}{\exp(\beta\epsilon_\mathrm{s}) - 1} \ . \tag{E.10}$$

E.4 Fermi–Dirac Statistics

Now, the particle number is fixed to N. For the sum $\sum^{(s)}$ from (E.6), we introduce the term $Z_S(M)$

$$Z_s(M) = \sum_{n_1,n_2,\ldots}{}^{(s)} \exp(-\beta(n_1\epsilon_1 + n_2\epsilon_2 + \ldots)) \ , \tag{E.11}$$

when M particles are to be distributed over all states except s ($\sum_r^{(s)} n_r = M$). M is either $N-1$ if $n_s = 1$ and N if $n_s = 0$. Using Z_s, we can write

$$\bar{n}_s = \frac{1}{\frac{Z_s(N)}{Z_s(N-1)} \exp(\beta\epsilon_s) + 1} \ . \tag{E.12}$$

We evaluate $Z_s(N-1)$

$$\ln Z_s(N - \Delta N) = \ln Z_s(N) - \frac{\partial \ln Z_s}{\partial N}|_N \ \Delta N \ , \tag{E.13}$$

or

$$Z_s(N - \Delta N) = Z_s(N) \exp(-\gamma_s \Delta N) \ , \tag{E.14}$$

with

$$\gamma_s = \frac{\partial \ln Z_s}{\partial N} \ . \tag{E.15}$$

Since Z_s runs over many states, the derivative is approximately equal to

$$\gamma = \frac{\partial \ln Z}{\partial N} \ , \tag{E.16}$$

as will be shown below. Thus, we obtained so far

$$\bar{n}_s = \frac{1}{\exp(\gamma + \beta\epsilon_s) + 1} \ . \tag{E.17}$$

Equation (E.3) holds also for the average values $\bar{n}_s$, i.e.

$$N = \sum_r \bar{n}_r = \sum_r \frac{1}{\exp(\gamma + \beta\epsilon_s) + 1} \ , \tag{E.18}$$

from which the value of γ can be calculated. Given that the free energy is given as $F = -kT \ln Z$, we find that

$$\gamma = -\frac{1}{kT} \frac{\partial F}{\partial N} = -\beta\mu \ , \tag{E.19}$$

where μ is the chemical potential by definition. Therefore, the distribution function for the Fermi–Dirac statistics (also called the Fermi function) is

$$\bar{n}_s = \frac{1}{\exp(\beta(\epsilon_s - \mu)) + 1} \ . \tag{E.20}$$

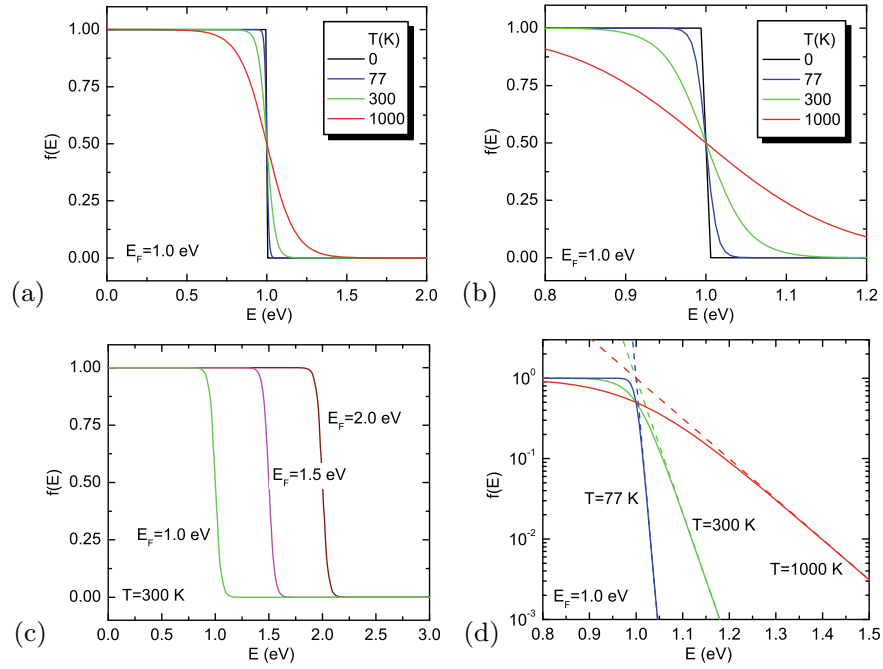

Fig. E.1 Fermi function for **a**, **b** different temperatures (for $E_\mathrm{F} = 1.0\,\mathrm{eV}$) and **c** for different chemical potentials (for $T = 300\,\mathrm{K}$). **d** Fermi function (*solid lines*) compared with Boltzmann approximation (*dashed lines*) for various temperatures and $E_\mathrm{F} = 1.0\,\mathrm{eV}$ on semilogarithmic plot

Now, we briefly revisit the approximation $\gamma = \gamma_s$. Exactly, γ fulfills

$$\gamma = \gamma_s - n_s \frac{\partial \gamma}{\partial N} \,. \tag{E.21}$$

Thus, the approximation is valid if $n_s \frac{\partial \gamma}{\partial N} \ll \gamma$. Since $n_s < 1$, this means that the chemical potential does not change significantly upon addition of another particle.

The Fermi–Dirac distribution function (E.20) for electrons is typically written as

$$f_\mathrm{e}(E) = \frac{1}{\exp\left(\frac{E-E_\mathrm{F}}{kT}\right) + 1} \,, \tag{E.22}$$

where k (or k_B) denotes the Boltzmann constant, T is the temperature, and E_F is the Fermi level, which is called the chemical potential μ in thermodynamics. The Fermi distribution is shown in Fig. E.1 for various parameters. The distribution function gives the probability that a state at energy E is populated in thermodynamic equilibrium. For $E = E_\mathrm{F}$ the population is $1/2$ for all temperatures. At (the unrealistic case of) $T = 0$, the function makes a step from 1 (for $E < E_\mathrm{F}$) to 0.

The high-energy tail of the Fermi distribution, i.e. for $E - E_\mathrm{F} \gg kT$, can be approximated by the Boltzmann distribution:

$$f_\mathrm{e}(E) \cong \exp\left(-\frac{E - E_\mathrm{F}}{kT}\right) \,. \tag{E.23}$$

E.5 Bose–Einstein Distribution

Executing (E.8) with the approximation $\gamma = \gamma_s$, the Bose–Einstein distribution is found to be

$$\bar{n}_s = \frac{1}{\exp(\beta(\epsilon_s - \mu)) - 1} \,. \tag{E.24}$$

Appendix F
Kronig-Penney Model

The Kronig-Penney model [71] is a simple, one-dimensional analytically solvable model that visualizes the effect of the periodic potential on the dispersion relation of electrons, i.e. the formation of a band structure.

A one-dimensional periodic hard-wall potential of finite height is assumed (Fig. F.1). The well width is a, the barrier width b and thus the period $P = a + b$. The potential is zero in the well (regions $(0, a) + nP$) and $+U_0$ in the barrier. The Schrödinger equation

$$-\frac{\hbar^2}{2m}\frac{\partial^2\Psi}{\partial x^2} + U(x)\,\Psi = E\,\Psi \tag{F.1}$$

has to be solved. The solutions for a single hard-wall potential well are well known. In the well, they have oscillatory character, i.e. $\Psi \propto \exp(\mathrm{i}kx)$ with real k. In the barrier, they have exponential character, i.e. $\Psi \propto \exp(\kappa x)$ with real κ. Thus we chose

$$\Psi(x) = A\exp(\mathrm{i}Kx) + B\exp(-\mathrm{i}Kx) \tag{F.2a}$$

$$\Psi(x) = C\exp(\kappa x) + D\exp(-\kappa x)\ . \tag{F.2b}$$

The wavefunction from (F.2a) is for the well between 0 and a with $E = \hbar^2K^2/2m$. The wavefunction from (F.2b) is for the barrier between a and $a + b$ with $U_0 - E = \hbar^2\kappa^2/2m$. From the periodicity and Bloch's theorem (6.3) the wavefunction at $x = -b$ must have the form $\Psi(-b) = \exp(-\mathrm{i}kP)\Psi(a)$, i.e. between the two wavefunctions is only a phase factor. The wavevector k of the Bloch function (plane-wave part of the solution) is a new quantity and must be carefully distinguished from K and κ, both coding the eigenenergy.

As boundary conditions, the continuity of Ψ and Ψ' are used.[4] At $x = 0$ and $x = a$ this yields

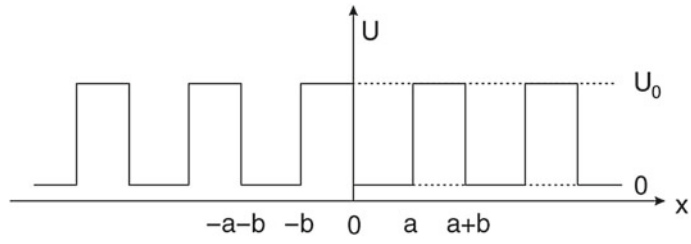

Fig. F.1 One-dimensional periodic hard-wall potential (Kronig-Penney model)

[4] Generally, Ψ'/m should be continuous, however, in the present example the mass is assumed constant throughout the structure.

M. Grundmann, *The Physics of Semiconductors*, Graduate Texts in Physics,
https://doi.org/10.1007/978-3-030-51569-0

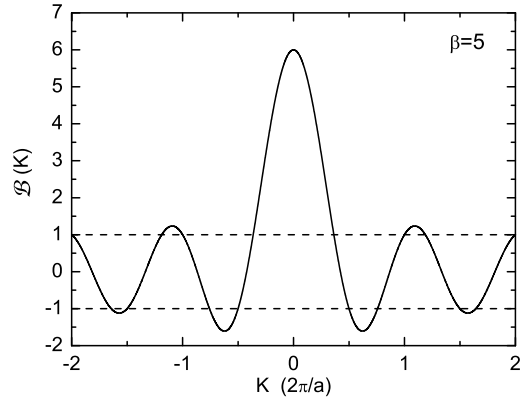

Fig. F.2 Transcendental function $\mathcal{B}(K)$ from (F.5) for $\beta = 5$. The *dashed lines* indicate the $[-1, 1]$ interval for which solutions exist for (F.5)

$$A + B = C + D \tag{F.3a}$$
$$\mathrm{i}KA - \mathrm{i}KB = \kappa C - \kappa D \tag{F.3b}$$
$$A\exp(\mathrm{i}Ka) + B\exp(-\mathrm{i}Ka) = C\exp(\kappa a) + D\exp(-\kappa a) \tag{F.3c}$$
$$\mathrm{i}KA\exp(\mathrm{i}Ka) - \mathrm{i}KB\exp(-\mathrm{i}Ka) = \kappa C\exp(\kappa a) - \kappa D\exp(-\kappa a). \tag{F.3d}$$

The continuity of Ψ and Ψ' at $x = -b$ is used in the left sides of (F.3c, F.3d). A nontrivial solution arises only if the determinant of the coefficient matrix is zero. This leads (after some tedious algebra) to

$$\cos(kP) = \left[\frac{\kappa^2 - K^2}{2\kappa K}\right]\sinh(\kappa b)\,\sin(Ka) + \cosh(\kappa b)\,\cos(Ka)\ . \tag{F.4}$$

Further simplification are obtained by letting the barrier thickness $b \to 0$ and $U_0 \to \infty$; then $P \to a$. The limit, however, is performed in such a way that the barrier 'strength' $U_0 b \propto \kappa^2 b$ remains constant and finite, i.e. $U(x) \propto \sum_n \delta(n\,a)$. Equation (F.4) then reads (for $\kappa b \to 0$: $\sinh(\kappa b) \to \kappa b$ and $\coth(\kappa b) \to 1$):

$$\cos(ka) = \beta\,\frac{\sin(Ka)}{Ka} + \cos(Ka) = \mathcal{B}(K)\ . \tag{F.5}$$

The dimensionless coupling parameter $\beta = \kappa^2 ba/2$ represents the strength of the barrier. Equation (F.5) only has a solution if the right side is in the interval $[-1, 1]$ (Fig. F.2). The function $\sin(x)/x$ oscillates with decreasing amplitude such that for sufficiently high values of Ka a solution can always be found ($\mathcal{B}(0) = \beta + 1$). The resulting dispersion is shown in Fig. F.3a, b for two different values of β. The dispersion is different from the free-electron dispersion (for $\beta = 0$, i.e. $k = K + 2\pi n$) and has several bands separated by gaps. The band gaps are related to the K-values for which (F.5) cannot be fulfilled. At the center ($k = 0$, Γ-point) and the zone boundary (X-point), ($k = \pi/a$) the bands are split and the tangent is horizontal ($\mathrm{d}E/\mathrm{d}k = 0$). The form of the dispersion is similar to the arccos function. The first band has the value $E_\mathrm{X} = \hbar^2\pi^2/(2ma^2)$ at the X-point for all values of β.

The band gap $E_{12}(X)$ between the first and the second subband (at the X-point) is shown in Fig. F.4. For large coupling between the potential wells (small β, $\beta \lesssim 1$) it is $E_{12} = (4\beta/\pi^2)E_\mathrm{X}$. In this case, the width of the subbands is wide. For small coupling (large β) the band gap E_{12} converges towards $3E_\mathrm{X}$, as expected for decoupled potential wells with energy levels $E_n = n^2 E_\mathrm{X}$. In this case, the width of the bands is small. Also, the character of the wavefunction is that of the solution for the individual quantum wells, i.e. even or s-type (for $n = 1, 3, \ldots$) or odd or p-type (for $n = 2, 4, \ldots$).

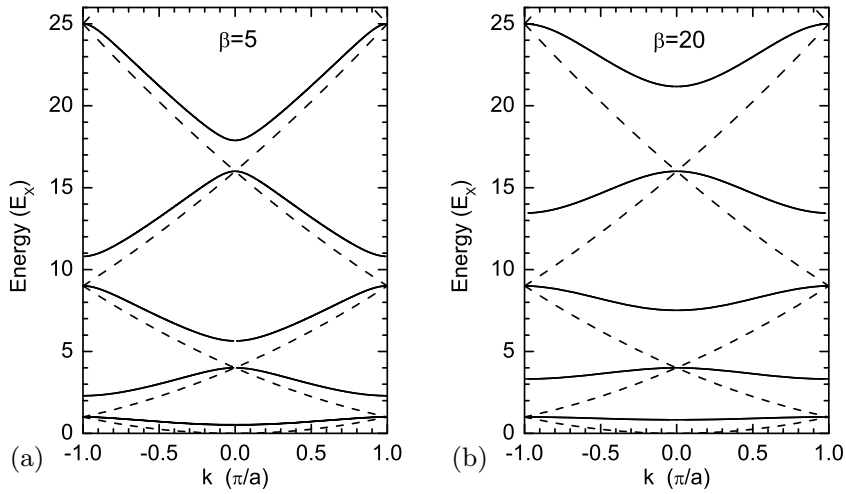

Fig. F.3 Energy dispersion of Kronig-Penney model (in units of $E_X = \hbar^2\pi^2/(2ma^2)$) as a function of the superlattice wavevector k for (**a**) $\beta = 5$ and (**b**) $\beta = 20$ in (F.5). The *dashed lines* are the free-electron dispersion (for $\beta = 0$) (cf. Fig. 6.2a)

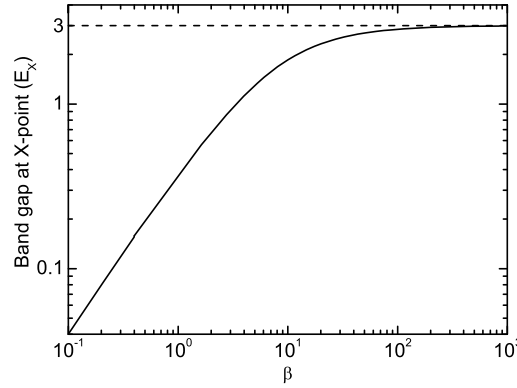

Fig. F.4 Band gap between first and second subband (at X-point, in units of $E_X = \hbar^2\pi^2/(2ma^2)$) as a function of β. For small $\beta \ll 10$, the band gap is $\propto \beta$. For thick barriers ($\beta \to \infty$) the band gap saturates towards $3E_X$ as expected for uncoupled wells

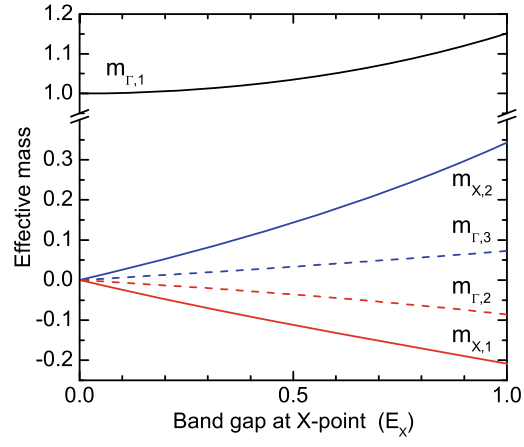

Fig. F.5 Effective mass (in units of m) of the first band extrema at the Γ- and X-points ($k = 0$ and π/a, respectively) as a function of the band gap at the X-point (in units of $E_X = \hbar^2\pi^2/(2ma^2)$). The number in the index of the mass denotes the band

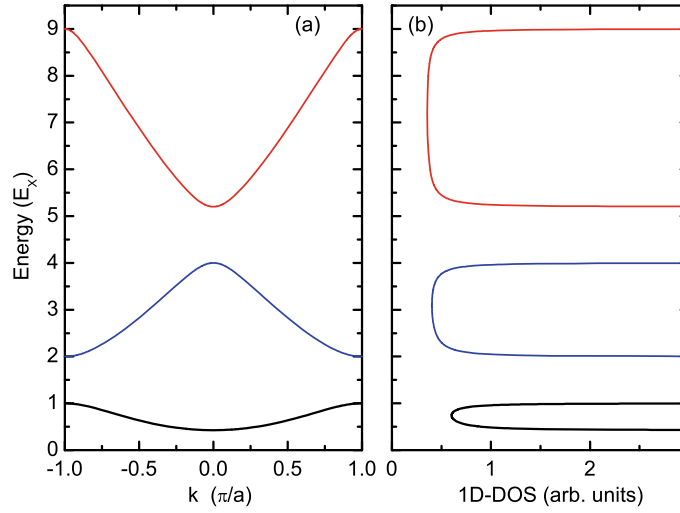

Fig. F.6 **a** Band dispersion and **b** density of states from the Kronig-Penney model for the first band gap being equal to E_X ($b \approx 3.382$)

Other interesting quantities related to real bandstructures are the width of the valence band $E_{12}(\Gamma)$ and the fundamental bandgap $E_{23}(\Gamma)$. Typical values of $E_{23}(\Gamma)/E_{12}(\Gamma) \approx \beta/10$ (for $\beta < 5$) of real semiconductors are in the range of 0.03–0.3, i.e. for $\beta = 0.3$–3.

In Fig. F.5 the effective masses are shown for the first five band extrema. The mass at the lowest minimum remains close to 1, i.e. keeps the carrier mass m from (F.1). Around the first gaps at the X- and the Γ-point, the effective masses are pairwise positive and negative, according to the character of the extremum as minimum or maximum, respectively. The absolute values are smaller than 1 for the given range of gaps. The mass increases initially linearly from zero with increasing gap.

The one-dimensional density of states (1D-DOS) has peaks (poles) at the band edges and is flat throughout most of the bands where the dispersion is linear (Fig. F.6).

Appendix G
Tight-Binding Model

G.1 Concept

The tight-binding model of electronic states rests on the concept of linear combination of atomic orbitals for finding a solution of the Hamiltonian of a periodic lattice. The ingredients of the model are the lattice structure and overlap matrix elements.[5]

Let us for now assume that there is one atom per lattice site. The atomic Hamiltonian $\boldsymbol{H}_{\mathbf{atom}}$ has the solutions $\phi_n(\boldsymbol{r})$ with

$$\boldsymbol{H}_{\mathbf{atom}}\,\phi_n(\boldsymbol{r}) = E_n\,\phi_n(\boldsymbol{r})\ , \tag{G.1}$$

where E_n the energy of the n-th energy level ($n = 1, 2, \ldots$) of the free atom.

The lattice shall be spanned by the lattice vectors $\boldsymbol{R_i}$ with the index i running over all N sites. For bulk-like solutions, a Bloch-type wave function, fulfilling (6.3), can be constructed from the atomic orbitals,

$$\Psi_{n\boldsymbol{k}}(\boldsymbol{r}) = \frac{1}{\sqrt{N}}\sum_i \exp(\imath\,\boldsymbol{k}\,\boldsymbol{R_i})\,\phi_n(\boldsymbol{r}-\boldsymbol{R_i})\ , \tag{G.2}$$

and will be taken as Ansatz for the solution of the crystal Hamiltonian $\boldsymbol{H}$ that is the sum of the atomic Hamiltonians plus a deviation $\boldsymbol{H'}$ due to the crystal, which is small at the atomic site.

For now we consider only a single atomic state[6] $n = n_0$ forming the band structure and write simple $\phi = \phi_{n_0}$. The single particle energy in the crystal is then given by

$$E(\boldsymbol{k}) = \int \Psi^*_{\boldsymbol{k}}(\boldsymbol{r})\,\boldsymbol{H}\,\Psi_{\boldsymbol{k}}(\boldsymbol{r})\,\mathrm{d}^3\boldsymbol{r} = \langle\Psi^*_{\boldsymbol{k}}(\boldsymbol{r})|\boldsymbol{H}|\Psi_{\boldsymbol{k}}(\boldsymbol{r})\rangle\ . \tag{G.3}$$

Equation (G.3) contains a double sum over the lattice sites i and j,

$$E(\boldsymbol{k}) = \frac{1}{N}\sum_{i,j}\exp(\imath\boldsymbol{k}(\boldsymbol{R_j}-\boldsymbol{R_i}))\int\phi^*(\boldsymbol{r}-\boldsymbol{R_j})\boldsymbol{H}\phi(\boldsymbol{r}-\boldsymbol{R_i})\,\mathrm{d}^3\boldsymbol{r} \tag{G.4}$$

$$= \frac{1}{N}\sum_{i,j}\exp(\imath\boldsymbol{k}(\boldsymbol{R_j}-\boldsymbol{R_i}))\,H_{ij}\ . \tag{G.5}$$

[5] In the framework of second quantization with creation and annihilation operators the theory is more elegant but we go here 'zu Fuß'.

[6] Often this is a s-type state but, e.g., for graphene the important bands around the Fermi level are formed by p-type states.

M. Grundmann, *The Physics of Semiconductors*, Graduate Texts in Physics,
https://doi.org/10.1007/978-3-030-51569-0

Now, for $i = j$, i.e. $\boldsymbol{R'} = \boldsymbol{R_j} - \boldsymbol{R_i} = 0$, the matrix element H_{ii} gives a value α,

$$H_{ii} = \alpha = \langle \phi^*(\boldsymbol{r}) | \boldsymbol{H} | \phi(\boldsymbol{r}) \rangle \ , \tag{G.6}$$

which is nothing else but the atomic energy level E_1. Since the wave function ϕ decays (rather quickly) with increasing distance R' from the atom, the matrix elements will decrease as well. In the nearest-neighbor approximation, the sum of the $\boldsymbol{R'}$ runs only over the m (equivalent) nearest neighbors $\boldsymbol{\tau_m}$ and we only consider one more matrix element $H_{ij} = \gamma$, when i and j are neighboring sites. This matrix element is not calculated explicitly but adjusted empirically to match experiments (empirical tight-binding model). Thus we find the energy dispersion

$$E(\boldsymbol{k}) = \alpha + \gamma \, \Delta(\boldsymbol{k}) \ , \tag{G.7}$$

with the sum

$$\Delta(\boldsymbol{k}) = \sum_m \exp(\imath \, \boldsymbol{k} \, \boldsymbol{\tau_m}) \ , \tag{G.8}$$

running over the nearest-neighbor sites. Extensions of the model consider second or even third next-neighbor sites with parameters γ' and γ''. Also, a larger number of atomic orbitals than a single one can be included, forming further bands.

G.2 One-Dimensional Model

In a one-dimensional model, $\boldsymbol{R_i} = i\boldsymbol{a} = ia\boldsymbol{e}$, $\boldsymbol{e}$ being the unit vector. The nearest neighbors to the atom at $i = 0$ are at $i = \pm 1$ and $\boldsymbol{\tau_{1,2}} = \pm a\boldsymbol{e}$. Therefore, $\Delta(\boldsymbol{k})$ (G.8) is given by ($\boldsymbol{k} = k\boldsymbol{e}$)

$$\Delta(\boldsymbol{k}) = \exp(+\imath \, \boldsymbol{k} \, \boldsymbol{a}) + \exp(-\imath \, \boldsymbol{k} \, \boldsymbol{a}) = 2 \, \cos(k \, a) \ , \tag{G.9}$$

and the dispersion relation represents a band of width 4γ with extrema at $k = 0$ and $k = \pm \pi / a$,

$$E(\boldsymbol{k}) = \alpha + 2 \, \gamma \, \cos(k \, a) \ . \tag{G.10}$$

It is straightforward to extend this scheme to the case of a two-dimensional square lattice with four nearest neighbors (Appendix G.3.1) or to three-dimensional cubic lattices.

In the usual semiconductor cases, the basis has more than one atom; here we consider a two-atom basis with an A- and a B-site (like Fig. 5.5). Two different (the sites A and B having the same atom is a special case discussed below) atomic Hamiltonians $\boldsymbol{H_A}$ and $\boldsymbol{H_B}$ exist with sets of eigenfunctions $\phi_{\mathrm{A},n}$ and $\phi_{\mathrm{B},n}$. We again consider only a single state at this point, i.e. we use ϕ^{A} and ϕ^{B}. Bloch-like functions (6.3) with these two orbitals are,

$$\Psi^{\mathrm{A}}_{\boldsymbol{k}}(\boldsymbol{r}) = \frac{1}{\sqrt{N}} \sum_i \exp(\imath \, \boldsymbol{k} \, \boldsymbol{R_i}) \, \phi^{\mathrm{A}}(\boldsymbol{r} - \boldsymbol{R_i}) \tag{G.11}$$

$$\Psi^{\mathrm{B}}_{\boldsymbol{k}}(\boldsymbol{r}) = \frac{1}{\sqrt{N}} \sum_i \exp(\imath \, \boldsymbol{k} \, \boldsymbol{R_i}) \, \phi^{\mathrm{B}}(\boldsymbol{r} - \boldsymbol{R_i} + \boldsymbol{\delta}) \ , \tag{G.12}$$

according to (G.2) with $\boldsymbol{\delta}$ being the vector pointing from the A- to the B-site. The total wave function is given by

$$\Psi_{\boldsymbol{k}}(\boldsymbol{r}) = c_{\mathrm{A}}(\boldsymbol{k})\,\Psi_{\boldsymbol{k}}^{\mathrm{A}} + c_{\mathrm{B}}(\boldsymbol{k})\,\Psi_{\boldsymbol{k}}^{\mathrm{B}} \tag{G.13}$$

with complex coefficients c_{A} and c_{B}, denoting amplitudes and phases on the A- and B-site. This scheme can be generalized to larger number of atoms in the unit cell. Multiplying $\boldsymbol{H}\Psi_{\boldsymbol{k}} = E(\boldsymbol{k})\Psi_{\boldsymbol{k}}$ with $\Psi_{\boldsymbol{k}}^{\mathrm{A}*}$ and $\Psi_{\boldsymbol{k}}^{\mathrm{B}*}$ from the left side, respectively, and integration leads to the equation system,

$$\begin{pmatrix} \langle\Psi_{\boldsymbol{k}}^{\mathrm{A}*}|\boldsymbol{H}|\Psi_{\boldsymbol{k}}^{\mathrm{A}}\rangle & \langle\Psi_{\boldsymbol{k}}^{\mathrm{A}*}|\boldsymbol{H}|\Psi_{\boldsymbol{k}}^{\mathrm{B}}\rangle \\ \langle\Psi_{\boldsymbol{k}}^{\mathrm{B}*}|\boldsymbol{H}|\Psi_{\boldsymbol{k}}^{\mathrm{A}}\rangle & \langle\Psi_{\boldsymbol{k}}^{\mathrm{B}*}|\boldsymbol{H}|\Psi_{\boldsymbol{k}}^{\mathrm{B}}\rangle \end{pmatrix} \begin{pmatrix} c_{\mathrm{A}} \\ c_{\mathrm{B}} \end{pmatrix} = \begin{pmatrix} \hat{H}_{\mathrm{AA}} & \hat{H}_{\mathrm{AB}} \\ \hat{H}_{\mathrm{BA}} & \hat{H}_{\mathrm{BB}} \end{pmatrix} \begin{pmatrix} c_{\mathrm{A}} \\ c_{\mathrm{B}} \end{pmatrix} = \tag{G.14}$$

$$E(\boldsymbol{k}) \begin{pmatrix} \langle\Psi_{\boldsymbol{k}}^{\mathrm{A}*}|\Psi_{\boldsymbol{k}}^{\mathrm{A}}\rangle & \langle\Psi_{\boldsymbol{k}}^{\mathrm{A}*}|\Psi_{\boldsymbol{k}}^{\mathrm{B}}\rangle \\ \langle\Psi_{\boldsymbol{k}}^{\mathrm{B}*}|\Psi_{\boldsymbol{k}}^{\mathrm{A}}\rangle & \langle\Psi_{\boldsymbol{k}}^{\mathrm{B}*}|\Psi_{\boldsymbol{k}}^{\mathrm{B}}\rangle \end{pmatrix} \begin{pmatrix} c_{\mathrm{A}} \\ c_{\mathrm{B}} \end{pmatrix} = E(\boldsymbol{k}) \begin{pmatrix} S_{\mathrm{AA}} & S_{\mathrm{AB}} \\ S_{\mathrm{AB}}^{*} & S_{\mathrm{BB}} \end{pmatrix} \begin{pmatrix} c_{\mathrm{A}} \\ c_{\mathrm{B}} \end{pmatrix} . \tag{G.15}$$

The overlap matrix $\boldsymbol{S}$ is approximately the unity matrix $\mathbf{1}$, assuming the overlap integral of the atomic A and B wave functions $S_{\mathrm{AB}} = 0$ (of course, always $S_{\mathrm{AA}} = S_{\mathrm{BB}} = 1$). The matrix $\hat{\boldsymbol{H}}$ belongs to the Hamiltonian in the $\boldsymbol{k}$-representation. A non-trivial solution is only possible if the determinant fulfills,

$$\begin{vmatrix} \hat{H}_{\mathrm{AA}} - E(\boldsymbol{k}) & \hat{H}_{\mathrm{AB}} \\ \hat{H}_{\mathrm{BA}} & \hat{H}_{\mathrm{BB}} - E(\boldsymbol{k}) \end{vmatrix} = 0 \,, \tag{G.16}$$

With $\hat{H}_{\mathrm{BA}} = \hat{H}_{\mathrm{AB}}^{*}$, the solutions are

$$E(\boldsymbol{k}) = \frac{\hat{H}_{\mathrm{AA}} + \hat{H}_{\mathrm{BB}}}{2} \pm \frac{1}{2}\sqrt{(\hat{H}_{\mathrm{AA}} - \hat{H}_{\mathrm{BB}})^2 + 4|\hat{H}_{\mathrm{AB}}|^2} \,. \tag{G.17}$$

G.3 Two-Dimensional Lattices

G.3.1 Square Lattice

The nearest neighbors in the square lattice (with simple base) with lattice constants a and b, are in orthogonal directions,

$$\boldsymbol{\tau}_{\mathbf{1,2}} = \pm a\,(1,0) \,, \quad \boldsymbol{\tau}_{\mathbf{3,4}} = \pm a\,(0,1) \,. \tag{G.18}$$

Thus $\Delta(\boldsymbol{k})$ from (G.8) is given as

$$\Delta(\boldsymbol{k}) = 2\,\big(\cos(k_x\,a) + \cos(k_y\,a)\big) \,, \tag{G.19}$$

yielding the dispersion relation,

$$E(\boldsymbol{k}) = \alpha + 2\,\gamma\,\big(\cos(k_x\,a) + \cos(k_y\,a)\big) \,. \tag{G.20}$$

It should be mentioned that such model with an additional magnetic field perpendicular to the plane was treated by Hofstadter [1471] leading to a fractal behavior as function of the tight-binding energy γ and the magnetic field ('Hofstadter butterfly'). Experiments on moiré graphene bilayers (cf. Sect. 13.3) seemingly show such effects. Also the Hofstadter butterfly is the blueprint for assigning topological quantum numbers to the quantum Hall phases (cf. Sect. 15.2.8) [1472].

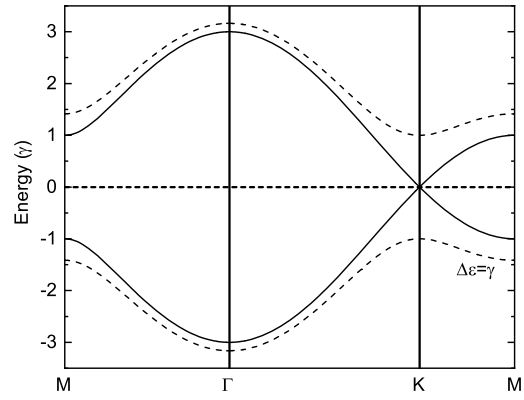

Fig. G.1 Tight-binding model band structure for honeycomb lattice with A = B according to (G.24) (solid line) and A≠B according to (G.25) with $\Delta\epsilon = \gamma$ (*dashed line*)

G.3.2 Honeycomb Lattice

We now look at the honeycomb lattice which is a model for graphene or other two-dimensional semiconductors (cf. Fig. 13.1a). For an A-atom, the three vectors to the neighboring B-sites are

$$\boldsymbol{\tau_{1,2}} = -\frac{a}{2}\left(1, \pm\sqrt{3}\right) \ , \quad \boldsymbol{\tau_3} = a\ (1,0) \ . \tag{G.21}$$

$\Delta(\boldsymbol{k})$ from (G.8) is given by

$$\Delta(\boldsymbol{k}) = \exp(-\imath\, k_x\, a)\left[1 + 2\,\exp\left(\frac{3}{2}\,\imath\, k_x\, a\right)\cos\left(\frac{\sqrt{3}}{2}\,k_y\, a\right)\right] . \tag{G.22}$$

For the A- and B-atoms being the same (as for graphene), $\hat{H}_{\mathrm{AA}} = \hat{H}_{\mathrm{BB}} = \alpha$, giving a constant part to the energy that is ignored in the following. The square root in (G.17) yields a band structure (cf. Fig. G.1)

$$\begin{aligned} E(\boldsymbol{k}) &= \pm\gamma\,|\Delta(\boldsymbol{k})| \\ &= \pm\gamma\sqrt{1 + 4\cos\left(\frac{3\,a\,k_x}{2}\right)\cos\left(\frac{\sqrt{3}\,a\,k_y}{2}\right) + 4\cos^2\left(\frac{\sqrt{3}\,a\,k_y}{2}\right)} \ . \end{aligned} \tag{G.23}$$

The energy is zero for at the K-points $\boldsymbol{K}, \boldsymbol{K'} = 2\pi/(3a)(1, \pm 1/\sqrt{3})$ and their other equivalents (cmp. Fig. 13.1b). The band gap at the M-point is 2γ. Around the K-points, the energy can be expanded with $\boldsymbol{k} - (\boldsymbol{K}, \boldsymbol{K'}) = \boldsymbol{q} = q(\cos\phi, \sin\phi)$. We find

$$E_{\boldsymbol{K},\boldsymbol{K'}}(\boldsymbol{q}) = \pm\gamma\left(\frac{3\,a}{2}\,q \mp \frac{3\,a^2}{8}\,q^2\,\sin(3\,\phi)\right) . \tag{G.24}$$

This shows that the dispersion is linear and isotropic around the K- and K'-points (Dirac points) and (further away) has threefold symmetry (triangular warping, cmp. Sect. 6.10.2). The dispersion at the Dirac points is often written as $E(q) = \pm\hbar q v_{\mathrm{F}}$ with $v_{\mathrm{F}} = 3\gamma a/(2\hbar)$. Also, the K- and K'-points are non-equivalent, reflecting the two-atomic base. The winding sense in the $\mp q^2$-term around K and K' is opposite which leads to further 'pseudo-spin' physics.

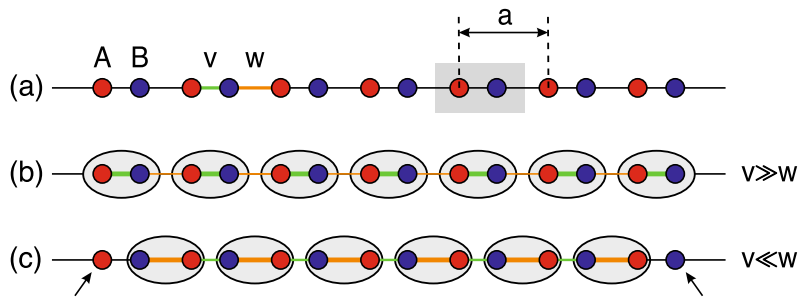

Fig. G.2 Schematic of the Su-Schrieffer-Heeger (SSH) model. (**a**) One-dimensional chain of unit cells (*grey area*) with A- and B-sites. The lattice constant is a. The hopping potentials v (intra-base, *green line*) and w (inter-base, *orange line*) are indicated. Dimers (*grey ellipses*) are shown for the cases (**b**) $v \gg w$ and (**c**) $v \ll w$

For the case of the A- and B-sites being non-identical (e.g. for BN), $\Delta\epsilon = \hat{H}_{\mathrm{AA}} - \hat{H}_{\mathrm{BB}} \neq 0$, the (non-constant part of the dispersion) is,

$$E(\boldsymbol{k}) = \pm\sqrt{\Delta\epsilon^2 + \gamma^2\,|\Delta(\boldsymbol{k})|^2}\,. \tag{G.25}$$

Thus a gap of $2|\Delta\epsilon|$ opens up at the K- and K'-points. Developing the solution around the K-points yields

$$E_{\boldsymbol{K},\boldsymbol{K}'}(\boldsymbol{q}) = \pm|\Delta\epsilon|\left[1 + \left(\frac{3\,\gamma^2}{2\,\Delta\epsilon^2}\right)^2\left(\frac{1}{2}\,a^2\,q^2 \mp \frac{1}{4}\,a^3\,q^3\,\sin(3\,\phi)\right)\right]\,, \tag{G.26}$$

and therefore (isotropic) parabolic extrema close to K and K'; the different winding sense of K and K' appears in the $\mp q^3$-term.

G.4 Edge States and Topological Aspects

G.4.1 One-Dimensional Model

The Su-Schrieffer-Heeger (SSH) model [370, 2154, 2155] is a tight-binding model very much like the one in Appendix G.2, describing a single spin-less electron on a one-dimensional lattice with a two-sites (A and B) unit cell (Fig. G.2a), suitable e.g. to describe an polyacetylene molecule. One electron per unit cell is assumed such that states are half filled. Also, the length of the chain will eventually be finite (N unit cells). The model has no on-site potential, which means that the constant energy parts H_{AA} and H_{BB} in (G.16) are now considered non-essential. The momentum-space Hamiltonian can be then written as

$$\hat{\boldsymbol{H}}(\boldsymbol{k}) = \begin{pmatrix} 0 & v + w\,\exp(-\mathrm{i}\,k\,a) \\ v + w\,\exp(\mathrm{i}\,k\,a) & 0 \end{pmatrix}\,, \tag{G.27}$$

with the energy eigenvalues[7] given by

$$E(\boldsymbol{k}) = \pm|v + w\,\exp(-\mathrm{i}\,k\,a)| = \pm\sqrt{v^2 + w^2 + 2\,v\,w\,\cos(k\,a)}\,. \tag{G.28}$$

[7] The eigenvectors are $(\pm\exp -\mathrm{i}\phi(k),\,1)/\sqrt{2}$ with $\phi = \arctan(d_y/d_x)$ (G.31).

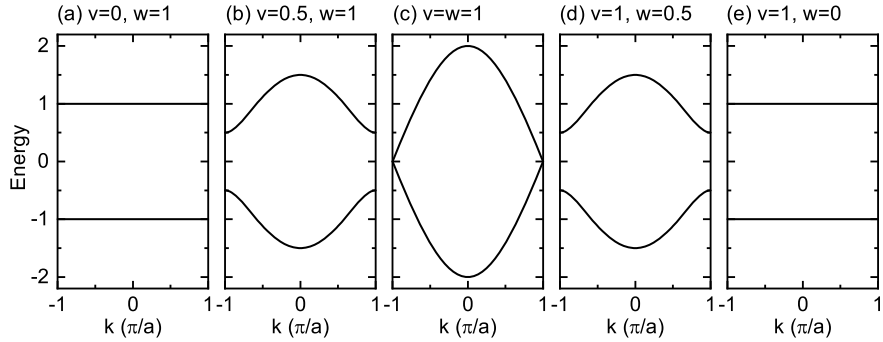

Fig. G.3 Band structure of the SSH model (G.28) for the cases $v = 0$, $v < w$, $v = w$, $v > w$ and $w = 0$, as labeled

The parameters v and w are real positive numbers[8]; v denotes the intra-base hopping amplitude between A and B, while w denotes the hopping between A and B belonging to different lattice points, i.e. from B to the right-neighbor A (Fig. G.2a). The band structure from (G.28) is shown in Fig. G.3 for which we discuss five cases: in (a) $v = 0$ ($w \neq 0$) and (e) $w = 0$ ($v \neq 0$), the bands are flat with a gap (of size $2v$ or $2w$). For (c) $v = w$, the bands have no gap (similar to the graphene case). For the last two cases, (b) $v < w$ and (d) $v > w$, the bands are curved with a gap (of size $2|v - w|$).

The point is now that the two seemingly similar cases Fig. G.3b and d result in the same band structure (i.e. the same eigenvalues), but they are different in other, maybe more subtle but actually very fundamental aspects, namely their eigenstates and eventually their topology.

The Hamiltonian for this two-band model (G.27) can be rewritten using the Pauli matrices,

$$\boldsymbol{\sigma_0} = \begin{pmatrix} 1 & 0 \\ 0 & 1 \end{pmatrix}, \ \boldsymbol{\sigma_x} = \begin{pmatrix} 0 & 1 \\ 1 & 0 \end{pmatrix}, \ \boldsymbol{\sigma_y} = \begin{pmatrix} 0 & -\mathrm{i} \\ \mathrm{i} & 0 \end{pmatrix}, \ \boldsymbol{\sigma_z} = \begin{pmatrix} 1 & 0 \\ 0 & -1 \end{pmatrix}, \tag{G.29}$$

as

$$\hat{\boldsymbol{H}}(\boldsymbol{k}) = d_x \, \boldsymbol{\sigma_x} + d_y \, \boldsymbol{\sigma_y} + d_z \, \boldsymbol{\sigma_z} = \boldsymbol{d}(\boldsymbol{k}) \, \boldsymbol{\sigma} \ , \tag{G.30}$$

with the vector

$$\boldsymbol{d}(\boldsymbol{k}) = (v + w \, \cos(k\,a), w \, \sin(k\,a), 0) \ . \tag{G.31}$$

The coefficient of $\boldsymbol{\sigma_0}$ is zero in the SSH model (zero potential). Also $d_z = 0$ (due to 'chiral' symmetry,[9] $d_z \neq 0$ would open a gap[10] for $v = w$). Generally, the normalized vector $\hat{\boldsymbol{d}} = \boldsymbol{d}/d$ can be displayed on the Bloch sphere. In Fig. G.4 the mapping of the Brillouin (torus, cf. Fig. 6.6) to the Bloch sphere to represent a unit vector.

Here, the vector $\boldsymbol{d}$ is two-dimensional and its length is equal to $E(\boldsymbol{k})$ (positive value). While $\boldsymbol{k}$ runs through the entire Brillouin zone, i.e. from $-\pi$ to π, $\boldsymbol{d}$ forms a circle of radius w around the point $(v, 0)$; it is visualized in Fig. G.5 for the cases (b) and (d).

The main and *qualitative* difference of the two trajectories is that the origin ($\boldsymbol{k} = 0$) is contained or not contained in the circle. Note, that for $v = w$, the circle touches the origin and the case (c) is undefined with that respect; such material, however, does not have a gap and is no insulator but a metal. Now, a number as topological invariant can be defined as the number of rotations that $\boldsymbol{d}$ makes

[8] This choice is not limiting the generality since other phases or signs can be moved into the wave functions.

[9] This means that the Hamiltonian does not induce any transitions from a site on one sublattice (i.e. the A-sites or B-sites) to any site on the *same* sublattice. Refer to [370] for further details.

[10] This is similar to the trivial gap in the diatomic linear chain model opening for $M_1 \neq M_2$ when $C_1 = C_2$, cf. Sect. 5.2.3.

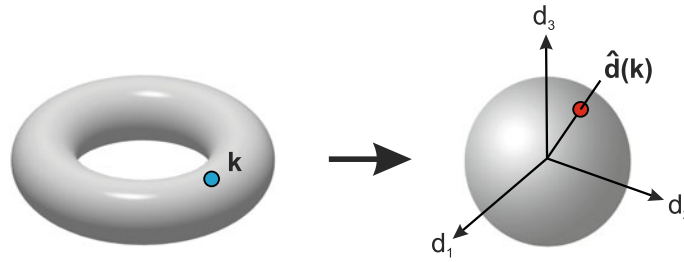

Fig. G.4 Mapping of the $\boldsymbol{k}$-values from a 2D Brillouin zone (torus) to the vectors $\hat{\boldsymbol{d}}$ (Bloch sphere). Designed after a graph in [2157]

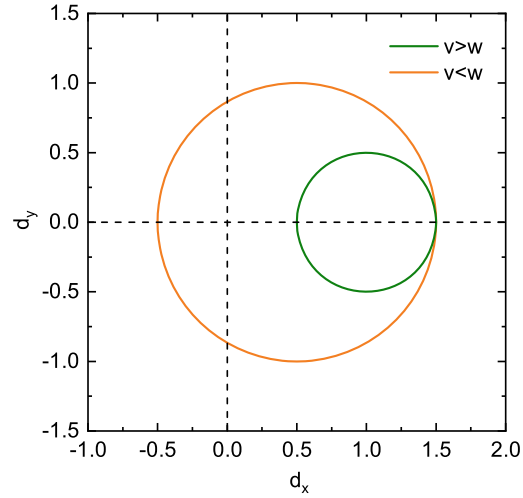

Fig. G.5 Vector $\boldsymbol{d}$ according to (G.30) for the cases $v > w$ (*green*, $v = 1$, $w = 0.5$) and $v < w$ (*orange*, $v = 0.5$, $w = 1$)

in the (d_x, d_y)-plane around the origin (while $\boldsymbol{k}$ runs through the entire Brillouin zone and avoids the origin for any wave vector since the material should have a gap); this quantity should be termed the 'bulk winding number' ν. We note that in general, the trajectory of $\boldsymbol{d}$ will be deformed from a circle, but it will be a closed loop due to the periodicity of the bulk $\boldsymbol{k}$-space. Also, it might wind more than once around the origin. The calculation of the winding number can be generalized to an integral in reciprocal space,

$$\nu = \frac{1}{2\pi} \int_{\mathrm{BZ}} \left(\boldsymbol{d}_{\mathrm{n}}(\boldsymbol{k}) \times \frac{\mathrm{d}}{\mathrm{d}\boldsymbol{k}} \boldsymbol{d}_{\mathrm{n}}(\boldsymbol{k}) \right)_z \mathrm{d}\boldsymbol{k} \ . \tag{G.32}$$

A look at the states of a finite chain model reveals another important distinction between the two cases $\nu = 0$ and $\nu = 1$. Going to the extreme cases (a) and (e), the situation can be cartooned as shown in Fig. G.2b, c. For $v \gg w$, the coupling within the base is strong and the chain disintegrates in N bases; this is called the 'dimerized limit'. Then N identical uncoupled (or very weakly coupled) bases, split into their symmetric and anti-symmetric state, make up the flat bands. In the case $v \ll w$, the dimers group differently, giving the same flat bulk band structure. But, for a finite chain, at the edges two sites, indicated by arrows in Fig. G.2c remain unconnected to the bulk of the chain. Their energy is zero (since no on-site potentials are used in the SSH model). The discussed model is the simplest one to generate edge states. The edge states are only present for $\nu = 1$ and not for the 'topologically trivial' case $\nu = 0$.

For finite N, the problem must be solved numerically. The Schrödinger equation (G.27) leads to the matrix eigenvalue problem,

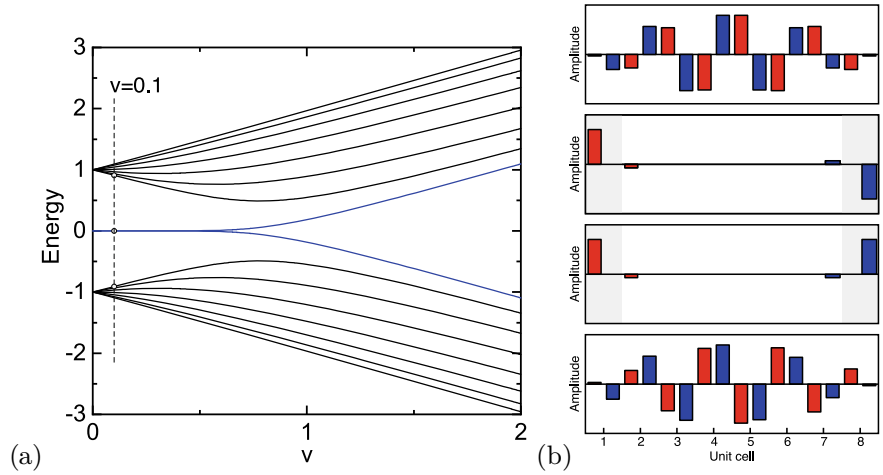

Fig. G.6 **a** Eigenvalues for SSH finite chain model (G.33) with $N = 8$ and $w = 1$. For sufficiently small v, two zero energy edge states (*blue lines*) develop. The case $v = 0.1$ is highlighted with a *dashed line* and the HOMO, the LUMO and the two edge states are indicated by *circles*. **b** Mode patterns (for $v = 0.1$) of the two edge states (center graphs) (energy: $\pm 10^{-8}$) and the HOMO (bottom graph) and LUMO (top graph) (energy: ± 0.909) as indicated in panel (**a**). The *red* (*blue*) bars denote the amplitude on the A (B) sites. The *greyed areas* denote the first and last unit cell of the chain

$$\begin{pmatrix} 0 & v & 0 & 0 & 0 & & 0 & 0 & 0 \\ v & 0 & w & 0 & 0 & & 0 & 0 & 0 \\ 0 & w & 0 & v & 0 & & 0 & 0 & 0 \\ 0 & 0 & v & 0 & w & & 0 & 0 & 0 \\ & & & & & \cdots & & & \\ 0 & 0 & 0 & 0 & 0 & & w & 0 & v \\ 0 & 0 & 0 & 0 & 0 & & 0 & v & 0 \end{pmatrix} \begin{pmatrix} a(k)\ \exp \mathrm{i}k \\ b(k)\ \exp \mathrm{i}k \\ a(k)\ \exp \mathrm{i}2k \\ b(k)\ \exp \mathrm{i}2k \\ \cdots \\ a(k)\ \exp \mathrm{i}Nk \\ b(k)\ \exp \mathrm{i}Nk \end{pmatrix} = E(k) \begin{pmatrix} a(k)\ \exp \mathrm{i}k \\ b(k)\ \exp \mathrm{i}k \\ a(k)\ \exp \mathrm{i}2k \\ b(k)\ \exp \mathrm{i}2k \\ \cdots \\ a(k)\ \exp \mathrm{i}Nk \\ b(k)\ \exp \mathrm{i}Nk \end{pmatrix} . \tag{G.33}$$

The eigenvalues for constant $w = 1$ and v varying between 0 and 2 are shown in Fig. G.6a for a chain with $N = 8$ bases. For $v \to 0$, two edges states develop with zero energy in the gap. For $N \to \infty$, the edge states develop for $v < 1$. The wave function amplitudes of the edge states are shown together with those of the HOMO/LUMO in Fig. G.6b. The edge states have significant amplitude only on the A- or B-site and are strongly localized at the edges.

For a system with periodic boundary conditions, the upper right and the lower left element in the matrix of (G.33) are equal to w and no edge states are present.

G.4.2 Two-Dimensional Models

Topological edge states in two-dimensional lattices with alternating hopping potentials have been investigated for square and honeycomb lattices in [2156, 2158]. Topological aspects of graphene are discussed in [2159, 2160]. The gap due to breaking parity symmetry (graphene → BN as discussed above) has been described in [2161]. It is topologically trivial while gaps in graphene due to next-nearest neighbor coupling [1616] or spin-orbit interaction [2162] lead to non-trivial bulks. Two-dimensional topological insulators with arbitrary Chern number can be constructed with the scheme given in [2163].

It was also found that zigzag graphene ribbons (cmp. Fig. 14.16) feature zero energy edge states, while armchair ribbons do not [2164].

Appendix H
k · p Perturbation Theory

The $\mathbf{k}\cdot\mathbf{p}$ method is described in great detail in [461] for various crystal symmetries. The solutions of the Schrödinger equation (cf. Sect. 6.2.1)

$$H\,\Psi_{n\mathbf{k}}(\mathbf{r}) = \left(-\frac{\hbar^2}{2m}\nabla^2 + U(\mathbf{r})\right)\Psi_{n\mathbf{k}}(\mathbf{r}) = E_n(\mathbf{k})\,\Psi_{n\mathbf{k}}(\mathbf{r})\ , \tag{H.1}$$

with a lattice periodic potential U, i.e. $U(\mathbf{r}) = U(\mathbf{r}+\mathbf{R})$ for direct lattice vectors $\mathbf{R}$, are Bloch waves of the form

$$\Psi_{n\mathbf{k}}(\mathbf{r}) = \exp(\mathrm{i}\,\mathbf{k}\,\mathbf{r})\,u_{n\mathbf{k}}(\mathbf{r})\ , \tag{H.2}$$

with the lattice periodic Bloch function $u_{n\mathbf{k}}(\mathbf{r}) = u_{n\mathbf{k}}(\mathbf{r}+\mathbf{R})$.

Inserting the Bloch wave into (H.1), the following equation is obtained for the periodic Bloch function:

$$\left(-\frac{\hbar^2}{2m}\nabla^2 + U(\mathbf{r}) + \frac{\hbar}{m}\mathbf{k}\cdot\mathbf{p}\right)u_{n\mathbf{k}}(\mathbf{r}) = \left(E_n(\mathbf{k}) - \frac{\hbar^2k^2}{2m}\right)u_{n\mathbf{k}}(\mathbf{r})\ . \tag{H.3}$$

For simplicity, we assume a band edge $E_n(0)$ at $\mathbf{k}=0$. In its vicinity, the $\mathbf{k}\cdot\mathbf{p}$ term can be treated as a perturbation. The dispersion for a nondegenerate band[11] is given up to second order in k

$$E_n(\mathbf{k}) = E_n(0) + \sum_{i,j=1}^{3}\left(\frac{\hbar^2}{2m}\,\delta_{ij} + \frac{\hbar^2}{m}\sum_{l\neq n}\frac{p^i_{nl}\,p^j_{ln}}{E_n(0)-E_l(0)}\right)k_i\,k_j\ , \tag{H.4}$$

with l running over other, so-called *remote* bands. The momentum matrix element is given by $p^i_{nl} = \langle u_{n0}|p_i|u_{l0}\rangle$ (cf. (6.39)). The coefficients in front of the quadratic terms are the components of the dimensionless inverse effective-mass tensor (cf. (6.43))

$$\left(\frac{m}{m^*}\right)_{ij} = \delta_{ij} + \frac{2}{m}\sum_{l\neq n}\frac{p^i_{nl}\,p^j_{ln}}{E_n(0)-E_l(0)}\ . \tag{H.5}$$

For degenerate bands, the $p^i_{nn'}$ vanish when n and n' belong to the degenerate set and also the first-order correction is zero. In the Löwdin perturbation theory [2165], the bands are separated into the close-by degenerate or nearly degenerate bands and the remote bands. The effect of the remote bands is taken into account by an effective perturbation

[11] apart from the spin degeneracy.

M. Grundmann, *The Physics of Semiconductors*, Graduate Texts in Physics,
https://doi.org/10.1007/978-3-030-51569-0

Table H.1 Basis set that diagonalizes the spin-orbit interaction

$\|J, m_j\rangle$	Wavefunction	Symmetry
$\|\frac{1}{2}, \frac{1}{2}\rangle$	$\mathrm{i}\|s\uparrow\rangle$	Γ_6
$\|\frac{1}{2}, -\frac{1}{2}\rangle$	$\mathrm{i}\|s\downarrow\rangle$	Γ_6
$\|\frac{3}{2}, \frac{3}{2}\rangle$	$\frac{1}{\sqrt{2}}\|(x+\mathrm{i}y)\uparrow\rangle$	Γ_8
$\|\frac{3}{2}, \frac{1}{2}\rangle$	$\frac{1}{\sqrt{6}}\|(x+\mathrm{i}y)\downarrow\rangle - \sqrt{\frac{2}{3}}\|z\uparrow\rangle$	Γ_8
$\|\frac{3}{2}, -\frac{1}{2}\rangle$	$-\frac{1}{\sqrt{6}}\|(x-\mathrm{i}y)\uparrow\rangle - \sqrt{\frac{2}{3}}\|z\downarrow\rangle$	Γ_8
$\|\frac{3}{2}, -\frac{3}{2}\rangle$	$\frac{1}{\sqrt{2}}\|(x-\mathrm{i}y)\uparrow\rangle$	Γ_8
$\|\frac{1}{2}, \frac{1}{2}\rangle$	$\frac{1}{\sqrt{3}}\|(x+\mathrm{i}y)\downarrow\rangle + \sqrt{\frac{1}{3}}\|z\uparrow\rangle$	Γ_7
$\|\frac{1}{2}, -\frac{1}{2}\rangle$	$-\frac{1}{\sqrt{3}}\|(x-\mathrm{i}y)\uparrow\rangle + \sqrt{\frac{1}{3}}\|z\downarrow\rangle$	Γ_7

$$\mathbf{k}\cdot\mathbf{p} + \mathbf{k}\cdot\mathbf{p}\sum_{l\neq n}\frac{|l\rangle\langle l|}{E_n(0)-E_l(0)}\mathbf{k}\cdot\mathbf{p}\,, \tag{H.6}$$

with the index l running over all bands not being in the degenerate set. The dispersion relation is obtained by diagonalization of the Hamiltonian (H.3) in the degenerate basis but with the perturbation given by (H.6).

The spin-orbit interaction [1547] adds an additional term

$$H_{\mathrm{so}} = \frac{\hbar}{4\,m^2\,c^2}\,(\boldsymbol{\sigma}\times\nabla U)\;\mathbf{p} \tag{H.7}$$

to the Hamiltonian, where $\boldsymbol{\sigma}$ are the Pauli spin matrices and c the vacuum speed of light. In the Schrödinger equation for the Bloch functions two new terms arise:

$$\begin{aligned}&\Big(-\tfrac{\hbar^2}{2m}\nabla^2 + U(\mathbf{r}) + \tfrac{\hbar}{4m^2c^2}\,(\boldsymbol{\sigma}\times\nabla U)\;\mathbf{p}+\\ &\quad\tfrac{\hbar}{m}\mathbf{k}\left[\mathbf{p} + \tfrac{\hbar}{4m^2c^2}\,(\boldsymbol{\sigma}\times\nabla U)\right]\Big)\,u_{n\mathbf{k}}(\mathbf{r}) = \left(E_n(\mathbf{k}) - \tfrac{\hbar^2k^2}{2m}\right)u_{n\mathbf{k}}(\mathbf{r})\,.\end{aligned} \tag{H.8}$$

The linear term in $\mathbf{k}$ is again treated as a perturbation. The first spin-orbit term in (H.8) is lattice periodic, thus the solutions at $\mathbf{k}=0$ are still periodic Bloch functions, however, different ones from previously. If the band edge is not degenerate, the momentum operator in (H.3) is simply replaced by

$$\boldsymbol{\pi} = \mathbf{p} + \frac{\hbar}{4\,m^2\,c^2}\,(\boldsymbol{\sigma}\times\nabla U)\;, \tag{H.9}$$

and the band edge is still parabolic. For a degenerate band edge, the effect can be more profound, in particular it can lead to the lifting of a degeneracy.

In the 8-band Kane model [510], four bands (lowest conduction band, heavy, light and split-off hole band) are treated explicitly and the others through Löwdin perturbation theory. The basis is chosen to be diagonal in the spin-orbit interaction leaving the spin-orbit interaction Δ_0 as parameter. The band- edge Bloch functions are denoted as $|i\uparrow\rangle$, where the index $i = s, x, y, z$ labels the symmetry of the different bands. The linear combinations that diagonalize the spin-orbit interaction are given in Table H.1. The band gap and the spin-orbit interaction are given by

$$E_g = E_{\Gamma_6} - E_{\Gamma_8} \tag{H.10a}$$
$$\Delta_0 = E_{\Gamma_8} - E_{\Gamma_7} \, . \tag{H.10b}$$

The Hamiltonian in the basis states of Table H.1 is given by

$$\begin{bmatrix}
k^2+E_g & 0 & \sqrt{2}Pk_+ & -\sqrt{\frac{2}{3}}Pk_z & -\sqrt{\frac{2}{3}}Pk_- & 0 & \sqrt{\frac{1}{3}}Pk_z & -\sqrt{\frac{4}{3}}Pk_- \\
0 & k^2+E_g & 0 & \sqrt{\frac{2}{3}}Pk_+ & -\sqrt{\frac{2}{3}}Pk_z & \sqrt{2}Pk_- & \sqrt{\frac{4}{3}}Pk_+ & \sqrt{\frac{1}{3}}Pk_z \\
\sqrt{2}Pk_- & 0 & k^2 & 0 & 0 & 0 & 0 & 0 \\
-\sqrt{\frac{2}{3}}Pk_z & \sqrt{\frac{2}{3}}Pk_- & 0 & k^2 & 0 & 0 & 0 & 0 \\
-\sqrt{\frac{2}{3}}Pk_+ & -\sqrt{\frac{2}{3}}Pk_z & 0 & 0 & k^2 & 0 & 0 & 0 \\
0 & \sqrt{2}Pk_+ & 0 & 0 & 0 & k^2 & 0 & 0 \\
\sqrt{\frac{1}{3}}Pk_z & \sqrt{\frac{4}{3}}Pk_- & 0 & 0 & 0 & 0 & k^2-\Delta_0 & 0 \\
-\sqrt{\frac{4}{3}}Pk_+ & \sqrt{\frac{1}{3}}Pk_z & 0 & 0 & 0 & 0 & 0 & k^2-\Delta_0
\end{bmatrix} \tag{H.11}$$

with the energy measured from the valence-band edge in units of $\hbar^2/(2m)$ and

$$\frac{1}{2}\,\mathrm{i}\,\hbar P = \langle s|\pi_x|x\rangle = \langle s|\pi_y|y\rangle = \langle s|\pi_z|z\rangle \tag{H.12a}$$
$$k_\pm = k_x \pm \mathrm{i}k_y \, . \tag{H.12b}$$

The inclusion of remote bands renormalizes the above Hamiltonian to

$$\begin{bmatrix}
Dk^2+E_g & 0 & \sqrt{2}Pk_+ & -\sqrt{\frac{2}{3}}Pk_z & -\sqrt{\frac{2}{3}}Pk_- & 0 & \sqrt{\frac{1}{3}}Pk_z & -\sqrt{\frac{4}{3}}Pk_- \\
0 & Dk^2+E_g & 0 & \sqrt{\frac{2}{3}}Pk_+ & -\sqrt{\frac{2}{3}}Pk_z & \sqrt{2}Pk_- & \sqrt{\frac{4}{3}}Pk_+ & \sqrt{\frac{1}{3}}Pk_z \\
\sqrt{2}Pk_- & 0 & H_h & R & S & 0 & \frac{\mathrm{i}}{\sqrt{2}}R & -\mathrm{i}\sqrt{2}S \\
-\sqrt{\frac{2}{3}}Pk_z & \sqrt{\frac{2}{3}}Pk_- & R^* & H_l & 0 & S & \frac{H_h-H_l}{\sqrt{2}\mathrm{i}} & \mathrm{i}\sqrt{\frac{3}{2}}R \\
-\sqrt{\frac{2}{3}}Pk_+ & -\sqrt{\frac{2}{3}}Pk_z & S^* & 0 & H_l & -R & -\mathrm{i}\sqrt{\frac{3}{2}}R^* & \frac{H_h-H_l}{\sqrt{2}\mathrm{i}} \\
0 & \sqrt{2}Pk_+ & 0 & S^* & -R^* & H_h & -\mathrm{i}\sqrt{2}S^* & -\frac{\mathrm{i}}{\sqrt{2}}R^* \\
\sqrt{\frac{1}{3}}Pk_z & \sqrt{\frac{4}{3}}Pk_- & -\frac{\mathrm{i}}{\sqrt{2}}R^* & -\frac{H_h-H_l}{\sqrt{2}\mathrm{i}} & \mathrm{i}\sqrt{\frac{3}{2}}R & \mathrm{i}\sqrt{2}S & \frac{H_h+H_l}{\sqrt{2}}-\Delta_0 & 0 \\
-\sqrt{\frac{4}{3}}Pk_+ & \sqrt{\frac{1}{3}}Pk_z & \mathrm{i}\sqrt{2}S^* & -\mathrm{i}\sqrt{\frac{3}{2}}R^* & -\frac{H_h-H_l}{\sqrt{2}\mathrm{i}} & \frac{\mathrm{i}}{\sqrt{2}}R & 0 & \frac{H_h+H_l}{\sqrt{2}}-\Delta_0
\end{bmatrix} \tag{H.13}$$

with

$$D = 1 + \frac{2}{m}\sum_{l\neq n}\frac{|\langle s|\pi_x|l\rangle|^2}{E_g - E_l(0)} \tag{H.14a}$$
$$\gamma_1' = \left[1 + \frac{2}{m}\sum_{l\neq n}\frac{|p_{xl}^x|^2}{E_n(0) - E_l(0)}\right] - \frac{2P^2}{3E_g} \tag{H.14b}$$
$$\gamma_2' = \left[1 + \frac{2}{m}\sum_{l\neq n}\frac{|p_{xl}^y|^2}{E_n(0) - E_l(0)}\right] - \frac{P^2}{3E_g} \tag{H.14c}$$
$$\gamma_3' = \left[\frac{2}{m}\sum_{l\neq n}\frac{p_{xl}^x p_{ly}^y + p_{xl}^y p_{ly}^x}{E_n(0) - E_l(0)}\right] - \frac{P^2}{3E_g} \tag{H.14d}$$
$$H_h = (\gamma_1' + \gamma_2')(k_x^2 + k_y^2) + (\gamma_1' - 2\gamma_2')k_z^2 \tag{H.14e}$$

$$H_{\mathrm{l}} = (\gamma_1' - \gamma_2')(k_x^2 + k_y^2) + (\gamma_1' + 2\gamma_2')k_z^2 \tag{H.14f}$$

$$R = -2\sqrt{3}\gamma_3' k_- k_z \tag{H.14g}$$

$$S = \sqrt{3}\gamma_2'(k_x^2 - k_y^2) + 2\sqrt{3}\gamma_3' \mathrm{i} k_x k_y \,. \tag{H.14h}$$

The Hamiltonian in the presence of inhomogeneous strain is given in [536]. The hole bands decouple from the conduction band for $E_{\mathrm{g}} \to \infty$ (six-band model [1423]). The heavy and light holes can be treated separately for $\Delta_0 \to \infty$ (Luttinger Hamiltonian). For the Γ_8 states, the Hamiltonian is then given by

$$\begin{bmatrix} H_{\mathrm{h}} & R & S & 0 \\ R^* & H_{\mathrm{l}} & 0 & S \\ S^* & 0 & H_{\mathrm{l}} & -R \\ 0 & S^* & -R^* & H_{\mathrm{h}} \end{bmatrix} . \tag{H.15}$$

Appendix I
Effective-Mass Theory

The effective-mass theory or approximation (EMA), also termed the envelope function approximation, is widely used for calculating the electronic properties of carriers in potentials in an otherwise periodic crystal. The strength of the method is that the complexities of the periodic potential are hidden in the effective-mass tensor m^*_{ij}. The effective-mass theory is a useful approximation for the treatment of shallow impurities (Sect. 7.5) or quantum wells (Sect. 12.3.2) with a potential that is slowly varying with respect to the scale of the lattice constant.

For the lattice-periodic potential, the Schrödinger equation

$$H_0\, \Psi_{n\mathbf{k}} = E_n(\mathbf{k})\, \Psi_{\mathrm{n}\mathbf{k}} \tag{I.1}$$

is solved by the Bloch wave $\Psi_{n\mathbf{k}}$. With a perturbing potential V, the Schrödinger equation reads

$$(H_0 + V)\ \Psi_{n\mathbf{k}} = E_n(\mathbf{k})\, \Psi_{\mathrm{n}\mathbf{k}}\ . \tag{I.2}$$

According to Wannier's theorem [2166], the solution is approximated by the solution of the equation

$$(E_n(-\mathrm{i}\nabla) + V)\, \Phi_n = E\, \Phi_n\ . \tag{I.3}$$

The dispersion relation is expanded to second order as described in Appendix H. The function Φ_n is termed the *envelope function* since it varies slowly compared to the lattice constant and the exact wavefunction is approximated (in lowest order) by

$$\Psi(\mathbf{r}) = \Phi_n(\mathbf{r})\ \exp(\mathrm{i}\,\mathbf{k}\,\mathbf{r})\, u_{n0}(\mathbf{r})\ . \tag{I.4}$$

M. Grundmann, *The Physics of Semiconductors*, Graduate Texts in Physics,
https://doi.org/10.1007/978-3-030-51569-0

Appendix J
Boltzmann Transport Theory

J.1 Boltzmann Transport Equation

The Boltzmann treatment of transport in semiconductors goes beyond the relaxation time approximation (cmp. Sect. 8.2) and contains this approach as its simplest approximation. The distribution function of carriers $f(\mathbf{r}, \mathbf{p}, t)$ is considered with regard to their momentum $\mathbf{p} = (p_x, p_y, p_z)$, their position $(r) = (x, y, z)$ and time t. Via the dispersion relation(s) the momentum distribution also determines the energy distribution.

In thermodynamical equilibrium, the distribution function shall be termed $f_0(\mathbf{p})$. In a homogeneous semiconductor it should be independent of $\mathbf{r}$, not depend explicitly on time and the momentum distribution be such that the resulting energy distribution should match the Fermi-Dirac distribution.

In non-equilibrium, the flow of electrons and heat is determined by the external forces $\mathbf{F}$ (electrical and magnetic fields) and the scattering of charge carriers via various processes (termed here collisions). In a (non-equilibrium) steady-state situation with constant forces, the distribution function f is constant in time; thus in a given time interval δt the change δf is zero,

$$\frac{\delta f}{\delta t} = 0 \,. \tag{J.1}$$

Within the time interval δt the momenta change as $\mathbf{p} \to \mathbf{p} + \mathbf{F}\,\delta t$ and the coordinates as $\mathbf{r} \to \mathbf{r} + \mathbf{p}/m^*\,\delta t$. We assume here for simplicity an isotropic mass and also the particle energy given by $E = \mathbf{p}^2/(2\,m^*)$. The condition (J.1) written in partial derivatives reads

$$\left(\frac{\partial}{\partial t} + \frac{1}{m^*}\,\mathbf{p}\cdot\nabla_{\mathbf{r}} + \mathbf{F}\cdot\nabla_{\mathbf{p}}\right) f(\mathbf{p}, \mathbf{r}, t) = 0 \,. \tag{J.2}$$

The force may be taken as the Lorentz force. So far no collisions have been considered. Without giving an explicit form for the microscopic details of the collisions, the change of the distribution function due to collisions is written as

$$\left(\frac{\partial f}{\partial t}\right)_{\text{coll}} \,. \tag{J.3}$$

Assuming that only two-particle collisions play a role, sample boundaries play no role and that position and velocity of particles are uncorrelated, the collision term can be written as

$$\left(\frac{\partial f}{\partial t}\right)_{\text{coll}} = \iiint \left[f(\mathbf{p}', \mathbf{r}, t)\, P(\mathbf{p}', \mathbf{p}) - f(\mathbf{p}, \mathbf{r}, t)\, P(\mathbf{p}, \mathbf{p}')\right] \mathrm{d}\mathbf{p}' \,. \tag{J.4}$$

M. Grundmann, *The Physics of Semiconductors*, Graduate Texts in Physics,
https://doi.org/10.1007/978-3-030-51569-0

with $P(\mathbf{p}, \mathbf{p}')$ being the transition probability per time that a momentum $\mathbf{p}$ is changed into $\mathbf{p}'$ by collisions. The collision integral must be calculated explicitly using microscopic and eventually quantum mechanical models. This leads now to the Boltzmann transport equation

$$\left(\frac{\partial}{\partial t} + \frac{1}{m^*}\mathbf{p}\cdot\nabla_{\mathbf{r}} + \mathbf{F}\cdot\nabla_{\mathbf{p}}\right) f(\mathbf{p},\mathbf{r},t) = \left(\frac{\partial f}{\partial t}\right)_{\text{coll}} . \tag{J.5}$$

Under certain circumstances, the collision term can be effectively written as (for a homogeneous semiconductor and homogeneous fields, neglecting the spatial dependence of f)

$$\left(\frac{\partial f}{\partial t}\right)_{\text{coll}} = -\frac{f(\mathbf{p}) - f_0}{\tau(\mathbf{p})} . \tag{J.6}$$

Compared to the relaxation time approximation, the major difference on the level of (J.6) here is the consideration of the momentum (and energy) dependence of the distribution function and the relaxation time.

J.2 Conductivity

In thermodynamical equilibrium the number of electronic states per unit volume associated with an element $\mathrm{d}\mathbf{p} = \mathrm{d}p_x\,\mathrm{d}p_y\,\mathrm{d}p_z$, including spin degeneracy of 2 is

$$\frac{2}{h^3}\, f_0(\mathbf{p})\,\mathrm{d}\mathbf{p} . \tag{J.7}$$

In the presence of an electric field $\mathbf{E}$, which we assume here in x-direction, a steady-state current will arise and the number of electronic states changes to

$$\frac{2}{h^3}\, f(\mathbf{p})\,\mathrm{d}\mathbf{p} , \tag{J.8}$$

making the (electron) current density (along x-direction)

$$j_x = -\frac{2e}{h^3}\iiint v_x\,[f(\mathbf{p}) - f_0(\mathbf{p})]\,\mathrm{d}\mathbf{p} . \tag{J.9}$$

This is a generalization of (8.4). The Boltzmann transport equation (J.5) with (J.6) simplifies to

$$-\frac{f(\mathbf{p}) - f_0}{\tau(\mathbf{p})} = -e\,E_x\,\frac{\partial f}{\partial p_x} \approx -e\,E_x\,\frac{\partial f_0}{\partial p_x} . \tag{J.10}$$

The last approximation is valid for small fields and makes j_x proportional to E_x (ohmic regime). The derivative with respect to p_x is converted to a derivative with respect to energy, yielding

$$\frac{f(\mathbf{p}) - f_0}{\tau(\mathbf{p})} = e\,v_x\,E_x\,\frac{\partial f_0}{\partial E} . \tag{J.11}$$

We note that for the Fermi-Dirac distribution (E.22) $f_0(E)$:

$$\frac{\partial f_0}{\partial E} = -\frac{1}{kT}\, f_0\,[1 - f_0]\,, \tag{J.12}$$

and in the case of a non-degenerate semiconductor (Boltzmann approximation), the right-hand side simplyfies to

$$\frac{\partial f_0}{\partial E} \approx -\frac{1}{kT}\, f_0 = -\frac{1}{kT}\, \exp\left(-\frac{E - E_\mathrm{F}}{kT}\right)\,, \tag{J.13}$$

Now the current density is given as

$$j_x = -\frac{2\,e^2}{h^3}\, E_x \iiint v_x^2\, \tau(\mathbf{p})\, \frac{\partial f_0}{\partial E}\, \mathrm{d}\mathbf{p}\,. \tag{J.14}$$

If we assume that τ depends only on the momentum and not its direction[12], and replace v_x^2 by $v^2/3$ assuming isotropy, the integral reads[13]

$$j_x = -\frac{8\pi\, e^2}{3\,h^3}\, E_x \int_0^\infty v^2\, \tau(p)\, \frac{\partial f_0}{\partial E}\, p^2\, \mathrm{d}p\,. \tag{J.15}$$

The quantity $8\pi p^2 \mathrm{d}p f_0/h^3$ (cmp. J.7) denotes the number $\mathrm{d}n$ of electrons with momentum in the range $\mathrm{d}p$. Thus the integral can also be written as (in Boltzmann approximation)

$$j_x = \frac{e^2}{3\,kT}\, E_x \int_0^\infty v^2\, \tau\, \mathrm{d}n\,. \tag{J.16}$$

Denoting the average of a quantity a over the electron distribution with $\langle a \rangle$ according to

$$\langle a \rangle = \frac{\int a\, \mathrm{d}n}{n}\,, \tag{J.17}$$

the equation (J.16) can be written as

$$j_x = \frac{n\, e^2}{3\,kT}\, E_x\, \langle v^2 \tau \rangle\,. \tag{J.18}$$

Using $m^* \langle v^2 \rangle = 3\,kT$, we thus have obtained

$$\sigma = \frac{n\, e^2}{m^*}\, \frac{\langle v^2 \tau \rangle}{\langle v^2 \rangle}\,, \tag{J.19}$$

and with $\sigma = n\,(-e)\,\mu$ (for electrons), the mobility

$$\mu = -\frac{e}{m^*}\, \frac{\langle v^2 \tau \rangle}{\langle v^2 \rangle}\,. \tag{J.20}$$

[12] This might be incorrect e.g. for piezoelectric scattering.

[13] using $\mathrm{d}\mathbf{p} = 4\pi p^2 \mathrm{d}p$.

For degenerate semiconductors, similar as for metals, the derivative of f_0 in (J.15) has a significant value only in the few-kT vicinity of the Fermi level. In an approximation we can evaluate the integral by replacing $E^{3/2}$ and τ by their values at the Fermi level and find[14] (using (6.70))

$$\sigma = \frac{j_x}{E_x} = \frac{n\, e^2\, \tau_\mathrm{F}}{m^*} \,. \tag{J.21}$$

Starting again with (J.15), using the density of states (6.71) in the form (per volume)

$$D(E) = m^* \, \frac{8\,\pi}{h^3} \, \sqrt{2\, m^* E} \,, \tag{J.22}$$

and $\mathrm{d}p/\mathrm{d}E = \sqrt{2m^*/E}$ we write

$$j_x = -\frac{e^2}{3} \, E_x \int\limits_0^\infty D(E)\, v^2\, \tau(E) \, \frac{\partial f_0}{\partial E} \, \mathrm{d}E \,. \tag{J.23}$$

Using an energy-dependent mobility, in the spirit of (J.20) defined as

$$\mu(E) = -e \, \frac{v^2\, \tau(E)}{3\, kT} \,, \tag{J.24}$$

the conductivity can be written in a generalized form integrating over single electron states [2167] (neglecting correlation effects):

$$\begin{aligned} \sigma &= e \int D(E)\, \mu(E)\, kT \, \frac{\partial f_0}{\partial E} \, \mathrm{d}E \\ &= -e \int D(E)\, \mu(E)\, f_0(E)\, [1 - f_0(E)] \, \mathrm{d}E \,. \end{aligned} \tag{J.25}$$

J.3 Hall Effect

Treating the Hall effect with the Boltzmann transport equation and making the assumptions of isotropy, one obtains (cmp. (15.12) and (15.22))

$$R_\mathrm{H} = \frac{1}{q\, n} \, \frac{\langle v^2 \tau^2 \rangle \, \langle v^2 \rangle}{\langle v^2 \tau \rangle^2} \,. \tag{J.26}$$

The Hall mobility determined from the Hall coefficient is

$$\mu_\mathrm{H} = \sigma \, R_\mathrm{H} = \frac{e}{m^*} \, \frac{\langle v^2 \tau^2 \rangle}{\langle v^2 \tau \rangle^2} \,, \tag{J.27}$$

and thus different from the field mobility (J.20).

[14] $\int_0^\infty \frac{\partial f_0}{\partial E} \mathrm{d}E = -1 + [1 + \exp(E_\mathrm{F}/kT)]^{-1} \approx -1$ for $E_\mathrm{F} \gg kT$.

J.4 Thermopower

The electronic energy transported per electron is $E - E_F$. Writing (J.25) as $\sigma = \int \sigma(E)\mathrm{d}E$, the weighing factor for electrons at energy E contributing to conduction is $\sigma(E)\mathrm{d}E/\sigma$. Therefore the Seebeck coefficient (thermopower) can be written [823]

$$S = -\frac{k}{e}\int \left(\frac{E - E_F}{kT}\right)\frac{\sigma(E)}{\sigma}\,\mathrm{d}E\ . \tag{J.28}$$

or

$$S = -\frac{k}{e}\frac{\int D(E)\,\mu(E)\,[(E - E_F)/kT]f\,(1-f)\,\mathrm{d}E}{\int D(E)\,\mu(E)\,f\,(1-f)\,\mathrm{d}E}\ . \tag{J.29}$$

For band conduction the thermopower is obtained by integrating (J.29) for electrons (S_n) and holes (S_p) (using the Boltzmann approximation) as [823]

$$S_n = -\frac{k}{e}\left(\frac{E_C - E_F}{kT} + T_C\right) \tag{J.30a}$$

$$S_p = \frac{k}{e}\left(\frac{E_F - E_V}{kT} + T_V\right)\ , \tag{J.30b}$$

where A_i are constants depending on the energy dependence of the density of states and the mobility,

$$T_C = \frac{\int_0^\infty (E'/kT)\,\sigma(E')\,\mathrm{d}E'}{\int_0^\infty \sigma(E')\,\mathrm{d}E'}\ ,\ E' = E - E_C \tag{J.31a}$$

$$T_V = \frac{\int_{-\infty}^0 (E'/kT)\,\sigma(E')\,\mathrm{d}E'}{\int_{-\infty}^0 \sigma(E')\,\mathrm{d}E'}\ ,\ E' = E_V - E\ . \tag{J.31b}$$

If the product of the density of states and the mobility $D\mu$ depends on the energy like E^γ, the constant is $A = 1+\gamma$ (for $\gamma > -1$). For a parabolic band ($D \propto E^{1/2}$) and acoustic deformation potential scattering $\mu \propto E^{-1/2}$ (Sect. 8.3.4), A=1; for moderate ionized impurity scattering $\mu \propto E^{3/2}$ (Sect. 8.3.3) and $A = 3$.

For two-band conduction, when electrons *and* holes contribute to transport,

$$S = \frac{S_n\,\sigma_n + S_p\,\sigma_p}{\sigma_n + \sigma_p}\ . \tag{J.32}$$

At low temperatures the interaction of the phonon flow with the current via electron-phonon scattering (phonon-drag effect) leads to an increase of thermopower [825, 2168–2170].

Appendix K
Noise

Noise is a general phenomenon effecting every measurement process and the performance of semiconductor devices [2171–2178]. Eventually, always a signal-to-noise ratio is measured instead of a 'signal'. Electrical noise fundamentally limits the sensitivity and resolution of communication, navigation, measurement, and other electronic systems [2176].

Behind the fluctuating signal stand microscopic classical and quantum mechanical processes that inherently contain randomness. From the physical standpoint, seemingly constant physical quantities even in thermodynamical equilibrium such as the free carrier density or the density of carriers on a trap are subject to fluctuations, e.g. leading to generation-recombination noise. Also the random motion of carriers, in equilibrium without net charge transport, leads to fluctuations, e.g. thermal noise on a resistor.

In this appendix necessary definitions, some mathematical basics and simple physical examples regarding noise are given.

K.1 Fluctuating signals

The noisy signal under consideration can be 'analog', for example in the case of a fluctuating current, voltage or power or it can be 'digital' for example a photon count rate.

Let $A(t)$ be an analog signal that fluctuates in time. Even under constant experimental conditions, it will fluctuate due to possibly many reasons, at least due to thermal fluctuations. We note that another, identically set-up experiment will have another signal $B(t)$. The time average (of first moment) of the signal within a time interval $2T$ (symmetric around $t = 0$) is defined as

$$\langle A \rangle_T = \frac{1}{2\,T} \int_{-T}^{T} A(t)\,\mathrm{d}t \ . \tag{K.1}$$

The time average of the signal $\langle A \rangle$ in general is the limit for large times,

$$\langle A \rangle = \lim_{T\to\infty} \frac{1}{2\,T} \int_{-T}^{T} A(t)\,\mathrm{d}t \ . \tag{K.2}$$

Two identical experiments will (should) share the same limits, i.e. $\langle A \rangle = \langle B \rangle$. The fluctuation or noise of A is defined as $a(t)$ via

M. Grundmann, *The Physics of Semiconductors*, Graduate Texts in Physics,
https://doi.org/10.1007/978-3-030-51569-0

$$a(t) = A(t) - \langle A \rangle \ , \tag{K.3}$$

thus evidently $\langle a \rangle = 0$. For an identical but different experiment, $a(t) \neq b(t)$ as stated before.

The *variance* σ^2 (or second moment) of the signal is the average of the squared fluctuation,

$$\sigma^2 = \langle a^2 \rangle = \lim_{T\to\infty} \frac{1}{2\,T} \int_{-T}^{T} a(t)^2 \,\mathrm{d}t = \langle A^2 \rangle - \langle A \rangle^2 \ . \tag{K.4}$$

The *effective value* of the noise quantity a is the square root of the variance, also termed the 'root mean square' (or rms-value),

$$\sigma = \langle a^2 \rangle^{1/2} = \sqrt{\langle A^2 \rangle - \langle A \rangle^2} \ . \tag{K.5}$$

The quantity σ^2 is a measure of the noise power, where $\langle A \rangle^2$ is a measure of the dc power.[15]

In a measurement procedure, the noise of a signal can be reduced by integrating or averaging over time; however, the time for a specific measurement is always finite and maybe constricted by many conditions. Given a fixed (finite) averaging time of T_0, the measured signals T_{T_0} in a series of such subsequent identical measurements will still exhibit a fluctuation. How large this remaining fluctuation is depends on the choice of T_0 and the noise spectrum discussed below.

In the case of a digital signal, e.g. the count rate of a photomultiplier or from a scintillator, the signal consists of (integer) numbers $N(t_i)$ aggregated at times t_i, $i = 0, 1, \ldots, m$. The average is then defined as

$$\langle N \rangle = \lim_{m\to\infty} \frac{1}{m} \sum_{i=0}^{m} N(t_i) \ . \tag{K.6}$$

The definition of the variance and rms are analog to this definition. A well known result for photon counting, based on the Poisson statistics of classical light is $\sigma^2 = \langle N \rangle = \bar{N}$.

K.2 Correlations

If a measurable quantity is subject to two fluctuating quantities $a_1(t)$ and $a_2(t)$, the time average of $a_1 + a_2$ is

$$\langle (a_1 + a_2)^2 \rangle = \langle a_1^2 \rangle + \langle a_2^2 \rangle + 2\langle a_1\, a_2 \rangle \ . \tag{K.7}$$

The third term is the decisive one; the correlation coefficient of noise quantities a_1 and a_2 is defined as

$$c_{12} = \frac{\langle a_1\, a_2 \rangle}{\sqrt{a_1^2\, a_2^2}} = \frac{\langle a_1\, a_2 \rangle}{\sigma_1\, \sigma_2} \ . \tag{K.8}$$

If the two noise quantities are independent of each other they are termed *uncorrelated* and $c_{12} = 0$. In the following it will become clear that this is a necessary but not sufficient condition for two noise sources to be uncorrelated. In the case $c_{12} = 0$, the noise powers of the two processes are simply added,

[15] Imagine a fluctuating current $I(t) = \langle I \rangle + i(t)$ leading to Joule heating ($\propto I^2$) at a resistor. Comparing the heating from I and $\langle I \rangle = \langle I \rangle$ (from a low noise current source) can yield the noise power. Also $\langle i^2 \rangle$ could be determined by first compensating I with $\langle I \rangle$ (from a low noise current source) and then measuring the temperature increase at the resistor.

$$\langle (a_1 + a_2)^2 \rangle = \langle a_1^2 \rangle + \langle a_2^2 \rangle \ . \tag{K.9}$$

This concept can be generalized to several noise sources.

A more general concept to determine correlation of two functions a_1 and a_2 is the *cross correlation* function, defined by

$$\rho_{12}(\tau) = \langle a_1(t)\, a_2(t+\tau) \rangle \ , \tag{K.10}$$

which is the average of function a_1 and time-shifted function a_2. Often $t = 0$ is used when the nature of the fluctuations does not change with time. An important time-shift is $\tau = 0$, and it follows that

$$c_{12} = \frac{\rho_{12}(0)}{\sigma_1\, \sigma_2} \ , \tag{K.11}$$

Two noise quantities a_1 and a_2 are uncorrelated if $\rho_{12}(\tau) = 0$ holds for all times τ; thus $c_{12} = 0$ is a special but important case.[16]

If a_1 and a_2 are the same function, i.e. $a = a_1 = a_2$, (K.10) becomes the *auto correlation* function,

$$\rho(\tau) = \langle a(t)\, a(t+\tau) \rangle \ , \tag{K.12}$$

In stationary processes the auto correlation function must be symmetric with regard to τ,

$$\rho(\tau) = \rho(-\tau) \ . \tag{K.13}$$

The value at $\tau = 0$ is

$$\rho(0) = \langle a^2 \rangle = \sigma^2 \ . \tag{K.14}$$

Typically, $\rho(\tau \to \infty) = 0$ in a statistic (non-repetitive) process. For uncorrelated processes, the auto correlation function of the sum, is the sum of the individual auto correlation functions.

K.3 Noise spectrum

Since the function $a(t)$ is not known, the noise spectrum cannot be calculated from its Fourier transform. However, this is also unnecessary since we are not interested in the Fourier transform of a itself but rather the spectral power density for a given frequency $W(\nu)$, with

$$\int_0^\infty W(\nu)\, \mathrm{d}\nu = \langle a^2 \rangle \ . \tag{K.15}$$

Since the quantity $\langle a^2 \rangle$ is finite and the spectral power density $W(\nu)$ is positive, for high frequencies, $W(\nu)$ must decrease to zero. Starting from the auto correlation function ρ, its Fourier transform shall be denoted w,

$$w(\nu) = \int_{-\infty}^\infty \rho(\tau)\ \exp(-2\pi\, \mathrm{i}\, \nu\, \tau)\, \mathrm{d}\tau \ . \tag{K.16}$$

[16] A simply example of correlated noise sources with $c_{12} = 0$ are the voltages at a resistor and a capacitance in series; the fact that they are 90° out of phase makes $c_{12} = 0$ although the fluctuations of the voltages, due to fluctuations of the driving current, are obviously correlated.

Also,

$$\rho(\tau) = \int_{-\infty}^{\infty} w(\nu)\, \exp(2\pi\, \mathrm{i}\, \nu\, \tau)\, \mathrm{d}\nu\ . \tag{K.17}$$

Using $\tau = 0$ in this equation, we have obtained an equation similar to (K.15). With (K.12) $w(\nu)$ can be identified as a spectral power density. Due to (K.13), w is a real and even function and we find for the noise power spectrum W in (K.15) $W = 2\, w$ (Wiener–Khintchine theorem),

$$W(\nu) = 2 \int_{-\infty}^{\infty} \rho(\tau)\, \exp(-2\pi\, \mathrm{i}\, \nu\, \tau)\, \mathrm{d}\tau = 4 \int_{0}^{\infty} \rho(\tau)\, \cos(-2\pi\, \nu\, \tau)\, \mathrm{d}\tau\ . \tag{K.18}$$

The noise power is practically measured in a finite frequency range, often in a narrow band of width B (with varying central frequency). If the frequency dependence of W can be neglected within B around the frequency ν_0, the variance is given by

$$\langle a^2 \rangle(\nu_0, B) = \int_{\nu_0 - B/2}^{\nu_0 + B/2} W(\nu)\, \mathrm{d}\nu \approx W(\nu_0)\, B\ . \tag{K.19}$$

Typical noise mechanisms and spectra are discussed in the following sections.

K.3.1 Thermal Noise

Finite temperature induces random motion of particles, e.g. as known from the theory of ideal gases and diffusion. In the case of charge carriers such motions lead to fluctuations of current or at a resistor to fluctuation of voltage. This happens also in the case of zero bias (no external fields). Such 'thermal noise' at a resistor was experimentally found by Johnson [1820, 1821] and theoretically derived by Nyquist [1822].

Using the general result from Langevin theory of motion under a fluctuating force, the mobility[17] is given as

$$\mu(\omega) = \frac{e}{kT} \int_{0}^{\infty} \langle v(t)\, v(0) \rangle\, \exp(\mathrm{i}\omega t)\, \mathrm{d}t\ . \tag{K.20}$$

Now we restrict ourselves to times much longer than the relaxation time constant, and subsequently to frequencies much smaller than $1/\tau$. In this case the conductivity $\sigma(\omega) = e\, n\, \mu(\omega)$ does not depend on frequency and can be taken as its low frequency limit σ_0 (cmp. Sect. 8.5). In a conductor (resistor) of length L and cross section A shall be N electrons ($n = N/(AL)$). With the electron velocities $v_i(t)$, the current is

$$I(t) = \frac{e}{L} \sum_i v_i(t)\ . \tag{K.21}$$

Without external field, $\langle v_i(t) \rangle = 0$ and $\langle I(t) \rangle = 0$ and we name this fluctuating current $i(t)$. If all electrons move independently of each other,

[17] In the Langevin theory the mobility is the ratio of velocity v and the force K, here the mobility is the ratio of v and the field E with $K = -e\, E$.

$$\langle i(\tau)\, i(0)\rangle = N\, \frac{e^2}{L^2}\, \langle v(\tau)\, v(0)\rangle \ . \tag{K.22}$$

The power spectrum of $i(t)$ is according to (K.18),

$$\begin{aligned} W(\omega) &= 2 \int_{-\infty}^{\infty} \langle i(\tau)\, i(0)\rangle \, \exp(\mathrm{i}\omega\tau)\, \mathrm{d}\tau = 4\, N\, \frac{e^2}{L^2} \int_{0}^{\infty} \langle v(\tau)\, v(0)\rangle \, \exp(\mathrm{i}\omega\tau)\, \mathrm{d}\tau \\ &= 4\, \frac{N\, e^2}{L^2}\, \frac{\mu\, kT}{e} = 4\, \frac{N\, e^2}{L^2}\, \frac{\sigma_0\, kT\, A\, L}{e^2\, N} = 4\, \sigma_0\, \frac{A}{L}\, kT \ . \end{aligned} \tag{K.23}$$

Then, using the conductance $G = R^{-1} = \sigma_0\, A/L$, we find the frequency independent spectral power

$$W = 4\, kT\, G \ . \tag{K.24}$$

Therefore the fluctuation of the current induced by the thermal motion is

$$\langle i^2 \rangle = 4\, kT\, G\, B \ , \tag{K.25}$$

and the variance of the fluctuating voltage at a resistor with resistance R in a frequency range B is ($i = u/R$)

$$\langle u^2 \rangle = 4\, kT\, R\, B \ . \tag{K.26}$$

At room temperature ($T_0 = 293\,\mathrm{K}$), the quantity $k\, T_0$ is about 26 meV; in the context here, the unit W s=W/Hz is the appropriate one, and $k\, T_0 = 4.04 \times 10^{-21}$ W/Hz. This represents a fundamental limit to noise in devices. Since the power density is independent of frequency, this noise is 'white' noise. The formulas (K.26) and (K.25) are valid for frequencies $h\, \nu \ll kT$; for larger frequencies the quantum nature of electromagnetic radiation and photon statistics play a role. For practical purposes even cooled devices at $T = 4\,\mathrm{K}$ fulfill the limit condition for frequencies up in the 100 GHz regime. In the cases of heated electron (or hole) gases (cmp. Fig.10.3), the lattice temperature must be replaced by the temperature of the carrier gas.

For a RC low pass, the power spectrum $W_i = 4kT\,G$ at the resistor is converted using $u^2 = |Z|^2 i^2$ to $W_u = 4kT\,R/[1 + (\omega RC)^2]$.

K.3.2 1/f Noise

For many processes a frequency dependent noise spectral power following a ν^α-law is found with α close to -1. Such noise is termed 'pink noise', $1/f$-noise or Flicker noise. The microscopic reasons for such behavior can be manifold and various models have been proposed [2179, 2180]. As an example, the noise spectrum of a RuO_2 thick film resistor is depicted in Fig. K.1a; for this system, the fluctuation of tunneling current in metal-insulator-metal units was used to explain the observed frequency (and temperature) dependence of the $1/f$-noise. At high frequencies, the $1/f$ spectral power vanishes and other noise sources such as thermal noise dominate, as depicted in Fig. K.1b for an a-Si thin film transistor. The $1/f$-dependence of the noise spectral power (of a carbon sheet resistor) has been detected for frequencies down to 3×10^{-6} Hz [2181].

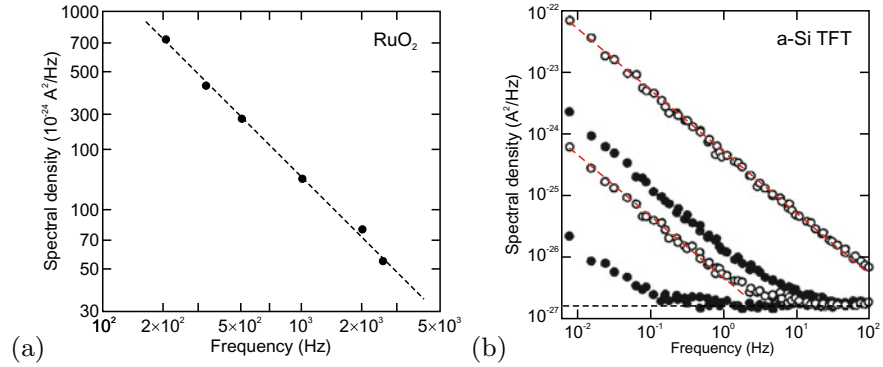

Fig. K.1 **a** Noise current density spectrum of a ruthenium oxide resistor (at $T = 300\,\mathrm{K}$ and current of $I = 1\,\mathrm{mA}$), experimental data (*symbols*) and $1/f$-dependency (*dashed line*). Adapted from [2182]. **b** Noise current density spectrum of an amorphous silicon thin film transistor, experimental data (*symbols*) for various source-drain voltages, thermal noise (*horizontal dashed line*) and $1/f$-dependency (*red dashed lines*). Adapted from [2183]

K.3.3 Shot Noise

A dc current $\langle i \rangle = I_0$ through a resistor is a sequence of electron transfers from one contact to the other. The transit time t_{tr} is given by the length L and the drift velocity v_{D} as $t_{\mathrm{tr}} = L/v_{\mathrm{D}} = L^2/(\mu V)$. The event times of these transits are random and thus lead to a noise (ac) component on top of the dc current. This is termed 'shot' noise, after the crackling arrival of shot pellets on a target. For low frequencies ($f \ll t_{\mathrm{tr}}^{-1}$), the noise power is

$$W = 2\,e\,I_0\,, \tag{K.27}$$

and the current noise thus is given by

$$\langle i^2 \rangle = 2\,e\,I_0\,B\,, \tag{K.28}$$

This noise term has been first found for vacuum diodes in the saturation regime which also serve as noise normals according to (K.28). It is important for the validity of (K.28) that in each event a full charge e is transferred. The situation in a semiconductor diode is more complicated since various currents contribute; if scattering events occur during transit, also fractional transferred charges can occur. The reverse current of an asymmetric diode if originating from the lowly doped region is due to carriers crossing the depletion layer. If generation in the depletion layer plays no role, the noise is also determined by the shot noise (K.28).

The maximal noise level (K.28) is present in absence of all correlations (Poisson process), both in the injection process as well as in the subsequent transport. Such value has been found, e.g., for intrinsic germanium in [2184] and in the limit of large currents for CdTe detectors [2185] (Fig. K.2). In a metallic conductor (or degenerate semiconductor) the noise is reduced to a third of that value due to correlations induced by the Pauli exclusion principle [2186]. The modification in non-degenerate semiconductors on length scales intermediate between the elastic and inelastic mean free paths is discussed in [2187]. The case of shot noise in semiconductors in the presence of transport of electrons and holes has been treated in [2184, 2188].

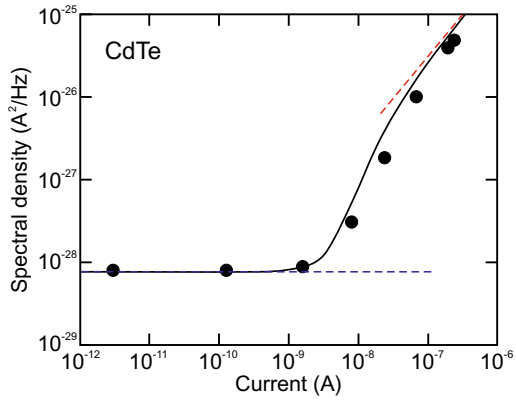

Fig. K.2 Noise of semi-insulating (dark) CdTe detector at $T = 323\,\mathrm{K}$ (at a frequency of about 1–2 kHz when $1/f$-noise plays no role). Experimental data (*symbols*) and detailed theory (*black line*). The *dashed blue line* represents the thermal noise (K.25), the *dashed red line* the shot noise (K.28). Adapted from [2185]

K.3.4 Generation-Recombination Noise

It is a semiconductor specific property that the carrier density is subject to fluctuations due to generation and recombination.[18] A fluctuation in majority carrier density leads to a change of conductivity which will lead to a change in current if a constant voltage is applied. Typical examples of transitions leading to a fluctuation of the carrier density are between bands and localized levels and in between the conduction and valence bands. Usually, the sample remains neutral. Detailed treatments are given in [2189, 2190].

A simple example is the effect of carrier number fluctuation due to transitions between a conduction band and donor levels. This is manifested in the noise spectrum of a n-Si sample at $T = 78\,\mathrm{K}$ (Fig. K.3a) with the plateau at 10^6–$10^7\,\mathrm{Hz}$ on top of the $1/f$ noise [2191] (The plateau at 10^8–$10^9\,\mathrm{Hz}$ is due to velocity fluctuations). The spectral power of the generation-recombination noise contribution is given by

$$W = I_0^2 \, \frac{\langle \delta n^2 \rangle}{\langle n \rangle^2} \, \frac{4\,\tau_0}{1 + (\omega\,\tau_0)^2} \,, \tag{K.29}$$

where τ_0 is the characteristic relaxation time, $\langle n \rangle = \bar{n}$ is the average carrier density (average carrier number per given volume) and $\langle \delta n^2 \rangle = \langle (n - \bar{n})^2 \rangle$ is the fluctuation of the carrier density. In order to better visualize the generation-recombination noise with respect to the $1/f$ noise, the quantity $W \times \omega$ can be plotted (Fig. K.3b) which takes the shape of a peak (for logarithmic frequency axis) [2192].

For a partially compensated semiconductor with $N_\mathrm{D} > N_\mathrm{A}$ it is found (if holes can be neglected) [2190]

$$\frac{\langle \delta n^2 \rangle}{\langle n \rangle^2} = \left[1 + \frac{\bar{n}\,N_\mathrm{D}}{(\bar{n} + N_\mathrm{A})\,(N_\mathrm{D} - N_\mathrm{A} - \bar{n})} \right]^{-1} \leq 1 \,. \tag{K.30}$$

The fluctuation $\langle \delta n^2 \rangle / \langle n \rangle^2$ is typically smaller than the Poisson value of 1; such sub-Poissonian statistics is typical of a repulsive correlation. For the case $N_\mathrm{D} \gg N_\mathrm{A}$ [2190], (K.30) simplifies to

$$\frac{\langle \delta n^2 \rangle}{\langle n \rangle^2} = \left[1 + \frac{N_\mathrm{D}}{N_\mathrm{D} - \bar{n}} \right]^{-1} = \frac{N_\mathrm{D} - \bar{n}}{2\,N_\mathrm{D} - \bar{n}} \,. \tag{K.31}$$

[18] A metal exhibits a constant carrier density.

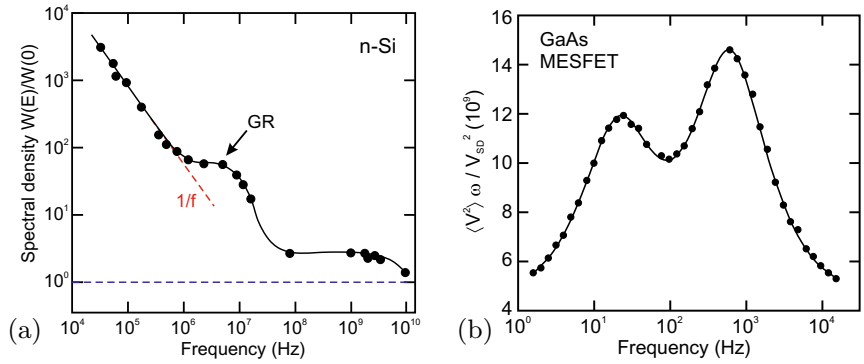

Fig. K.3 **a** Current noise spectrum of n-type Si ($T = 78\,\mathrm{K}$, $n = 3 \times 10^{13}\,\mathrm{cm}^{-3}$) for an electric field of $E = 200\,\mathrm{V/cm}$ along the ⟨100⟩ direction, in relative units to the noise spectrum for $E = 0$. The *dashed blue line* indicates the level of thermal noise, The *arrow* labeled 'GR' denotes the contribution of generation-recombination noise. Adapted from [2191]. **b** Voltage noise power times frequency of a GaAs MESFET. Experimental data (*symbols*) and fit (*solid line*) including two generation-recombination noise terms of the type (K.29) (times ω) for two different traps. Adapted from [2192]

In the ambipolar regime, typically close to intrinsic conditions, when only free electrons and holes are important, it is found [2190] ($\mu_\mathrm{n} < 0$)

$$\frac{\langle \delta n^2 \rangle}{\langle n \rangle^2} = \frac{\bar{n}^2\, \bar{p}\, (\mu_\mathrm{p} - \mu_\mathrm{n})^2}{(\bar{n} + \bar{p})\, (\bar{p}\, \mu_\mathrm{p} - \bar{n}\, \mu_\mathrm{n})^2}\ . \tag{K.32}$$

which simplifies to

$$\frac{\langle \delta n^2 \rangle}{\langle n \rangle^2} = \frac{1}{2}\ . \tag{K.33}$$

in the intrinsic case ($\bar{n} = \bar{p}$).

References

1. J.R. Chelikowsky, M.L. Cohen, Semiconductors: A pillar of pure and applied physics. J. Appl. Phys. **117**, 112812, 1–8 (2015). 10.1063/1.4913838
2. J.M. Bishop, *How to Win the Nobel Prize: An Unexpected Life in Science* (Harvard University Press, Cambridge, 2003)
3. G. Busch, Early history of the physics and chemistry of semiconductors—From doubts to fact in a hundred years. Eur. J. Phys. **10**, 254–264 (1989). 10.1088/0143-0807/10/4/002
4. L. Hoddeson, E. Braun, J. Teichmann, S. Weart, eds., *Out of the Crystal Maze* (Oxford University Press, Oxford, 1992)
5. K.C. Handel, *Anfänge der Halbleiterforschung und -entwicklung. Dargestellt an den Biographien von vier deutschen Halbleiterpionieren*, Ph.D. Thesis, RWTH Aachen (1999)
6. R.S. Feigelson, ed., *50 Years Progress in Crystal Growth* (Elsevier, Amsterdam, 2004)
7. P.R. Morris, A history of the world semiconductor industry, in *IEE History of Technology Series*, vol. 12 (Peter Peregrinus Ltd., London, 1990). 10.1049/PBHT012E
8. D. Holbrook, W.M. Cohen, D.A. Hounshell, S. Klepper, The nature, sources, and consequences of firm differences in the early history of the semiconductor industry. Strat. Mgmt. J. **21**, 1017–1041 (2000). 10.1002/1097-0266(200010/11)21:10/11<1017::AID-SMJ131>3.0.CO;2-G
9. S.M. Sze, ed., *Semiconductor Devices: Pioneering Papers* (World Scientific, Singapore, 1991). 10.1142/1087
10. A. Volta, Del modo di render sensibilissima la più debole Elettricità sia Naturale, sia Artificiale. Phil. Trans. Roy. Soc. London **72**, 237–280 (1782) (followed by an English translation *Of the Method of rendering very sensible the weakest Natural and Artificial Electricity*). 10.1098/rstl.1782.0018
11. T.J. Seebeck, Magnetische Polarisation der Metalle und Erze durch Temperaturdifferenz. Abhandl. Deut. Akad. Wiss. Berlin (Physik. Klasse) 265–373 (1822)
12. T.J. Seebeck, Über die magnetische Polarisation der Metalle und Erze durch Temperaturdifferenz. Ann. Physik **82**, 1–20, 133–160, 253–286 (1826). 10.1002/andp.18260820102; 10.1002/andp.18260820202; 10.1002/andp.18260820302
13. M. Faraday, Experimental Researches in Electricity, §10. On Conduction Power generally. Phil. Trans. Roy. Soc. London **123**, 507–522 (1833) (Series IV, paragraph 434, p. 519). 10.1098/rstl.1833.0022
14. E. Becquerel, Recherches sur les effets de la radiation chimique de la lumière solaire au moyen des courants électriques. **9**, 145–149 (1839)
15. E. Becquerel, Mémoire sur les effects électriques produits sous l'influence des rayons solaires. Comptes Rendus de L'Académie des Sciences **9**, 561–567 (1839)
16. E. Becquerel, Untersuchungen über die Wirkungen der chemischen Strahlen des Sonnenlichts mittelst elektrischer Ströme. Ann. Physik **130**, 18–35 (1841). 10.1002/andp.18411300903
17. E. Becquerel, Ueber die elektrischen Wirkungen unter Einfluss der Sonnenstrahlen. Ann. Physik **130**, 35–42 (1841). 10.1002/andp.18411300904
18. J. Peltier, Nouvelles Expériences sur la Caloricité des courans électriques. Ann. Chim. **LVI**, 371–387 (1834)
19. W. Smith, The Action of Light on Selenium. J. Soc. Telegraph Engrs. **2**, 31–33 (1873). 10.1049/jste-1.1873.0023
20. W. Smith, Effect of light on selenium during the passage of an electric current. Nature **7**, 303 (1873). 10.1038/007303e0
21. S. Bidwell, On the sensitiveness of selenium to light, and the development of a similar property in sulphur. Proc. Phys. Soc. **7**, 129–145 (1885). 10.1088/1478-7814/7/1/319

M. Grundmann, *The Physics of Semiconductors*, Graduate Texts in Physics,
https://doi.org/10.1007/978-3-030-51569-0

22. S. Bidwell, The electrical properties of selenium. Proc. Phys. Soc. **13**, 552–579 (1894). 10.1088/1478-7814/13/1/348
23. W. Schreier, Ferdinand Braun in Leipzig, Zum 150. Geburtstag des Entdeckers des Halbleitereffektes und des Erfinders der Kathodenstrahlröhre, NTM Zeitschrift für Geschichte der Wissenschaften, Technik und Medizin **8**, 201–208 (2000). 10.1007/BF02914193
24. F. Braun, Über die Stromleitung durch Schwefelmetalle. Ann. Phys. Chem. **153**, 556–563 (1874). 10.1002/andp.18752291207
25. W.G. Adams, R.E. Day, The action of light on selenium. Proc. Roy. Soc. Lond. A **25**, 113–117 (1876). 10.1098/rspl.1876.0024
26. W. Siemens, On the influence of light upon the conductivity of crystalline selenium. Phil. Mag. **50**, 416 (1875). 10.1080/14786447508641313
27. C.E. Fritts, On a new form of selenium cell, and some electrical discoveries made by its use. Am. J. Sci. **26**, 465–472 (1883). 10.2475/ajs.s3-26.156.465
28. E.H. Hall, On a new action of the magnet on electric currents. Am. J. Math. **2**, 287–292 (1879). 10.2307/2369245
29. E.H. Hall, On a new action of the magnet on electric currents. Philos. Mag. **9**, 225–230 (1879). 10.1080/14786448008626828
30. H.A. Rowland, Preliminary notes on Mr. Hall's recent discovery. Philos. Mag. **9**, 432–434 (1880). 10.1080/14786448008626865
31. J.Z. Buchwald, The Hall effect and Maxwellian electrodynamics in the 1880's. Part I: Discovery of a new electric field. Centaurus **23**, 51–99 (1979). 10.1111/j.1600-0498.1979.tb00360.x
32. J.Z. Buchwald, The Hall effect and Maxwellian electrodynamics in the 1880's. Part II: The unification of theory, 1881–1893. Centaurus **23**, 118–162 (1979). 10.1111/j.1600-0498.1979.tb00227.x
33. J.C. Bose, *Detector for Electrical Disturbances*, US patent 755, 860, filed 1901, awarded 1904
34. G.W. Pickard, *Means for Receiving Intelligence Communicated by Electric Waves*, US patent 836, 531, filed 1906, awarded 1906
35. G.W. Pickard, *Oscillation-Receiver*, US patent 888, 191, filed 1907, awarded 1908
36. T. Jenkins, A brief history of ... semiconductors. Phys. Edu. **40**, 430–439 (2005). 10.1088/0031-9120/40/5/002
37. H.J. Round, A note on carborundum. Electron World **19**, 309 (1907). 10.1142/9789814503464_0116
38. K. Bädeker, Über die elektrische Leitfähigkeit und die thermoelektrische Kraft einiger Schwermetallverbindungen, Ann. Physik **327**, 749–766 (1907) and Habilitationsschrift. Universität Leipzig. 10.1002/andp.19073270409
39. W. Kaiser, Karl Bädekers Beitrag zur Halbleiterforschung. Centaurus **22**, 187–200 (1978). 10.1111/j.1600-0498.1979.tb00588.x
40. M. Grundmann, Karl Bädeker (1877–1914) and the discovery of transparent conductive materials. Phys. Status Solidi A **212**, 1409–1426 (2015). 10.1002/pssa.201431921
41. K. Bädeker, Über eine eigentümliche Form elektrischen Leitvermögens bei festen Körpern. Ann. Physik **334**, 566–584 (1909). 10.1002/andp.19093340807
42. K. Steinberg, Über den Halleffekt bei jodhaltigem Kupferjodür. Ann. Physik **340**, 1009–1033 (1911). 10.1002/andp.19113401010
43. G.W. Pickard, The discovery of the oscillating crystal. Radio News **6**(7) (1925 issue), 1166, 1270 (1925)
44. J.A. Ratcliffe, William Henry Eccles. 1875-1966. Biogr. Memoirs Fell. Roy. Soc. **17**, 195–214 (1971). 10.1098/rsbm.1971.0008
45. W.H. Eccles, On an oscillation detector actuated solely by resistance-temperature variations. Proc. Phys. Soc. **22**, 360–368 (1910). 10.1088/1478-7814/22/1/326
46. J. Weiss, *Experimentelle Beiträge zur Elektronentheorie aus dem Gebiet der Thermoelektrizität*, Ph.D. Thesis, Albert-Ludwigs Universität Freiburg i.Br. (1910)
47. J. Königsberger, J. Weiss, Über die thermoelektrischen Effekte (Thermokräfte, Thomsonwärme) und die Wärmeleitung in einigen Elementen und Verbindungen und über die experimentelle Prüfung der Elektronentheorien. Ann. Physik **340**, 1–46 (1911). 10.1002/andp.19113400602
48. F. Friedrich, P. Knipping, M. von Laue, Interferenzerscheinungen bei Röntgenstrahlen, Bayerische Akademie der Wissenschaften, Mathematisch-Physikalische Klasse, Sitzungsberichte (1912), pp. 303–322 and Ann. Physik **346**, 971–988 (1913). 10.1002/andp.19133461004
49. M. von Laue, Eine quantitative Prüfung der Theorie für die Interferenz-Erscheinungen bei Röntgenstrahlen, Bayerische Akademie der Wissenschaften, Mathematisch-Physikalische Klasse, Sitzungsberichte (1912), pp. 363–373 and Ann. Physik **346**, 989–1002 (1913). 10.1002/andp.19133461005
50. G. Dörfel, *Julius Edgar Lilienfeld und William David Coolidge - Ihre Röntgenröhren und ihre Konflikte* (Max-Planck-Institut für Wissenschaftsgeschichte, Berlin, 2006)
51. Th.L. Thomas, The Twenty Lost Years of Solid-State Physics, Analog (Science Fact → Science Fiction) **LXXV**(1) (March 1965 issue), pp. 8–13, 81 (1965) (Erroneously this article places Universität Leipzig into Poland.)
52. C. Kleint, Julius Edgar Lilienfeld: Life and profession. Progr. Surf. Sci. **57**, 253–327 (1998). 10.1016/S0079-6816(98)80026-9
53. J.E. Lilienfeld, *Method and Apparatus Controlling Electric Currents*, US patent 1,745, 175, filed 1926, awarded 1930

54. B.E. Crawford, *The Invention of the Transistor* (University of Vermont, Burlington, 1991). M.Sc. Thesis
55. J.E. Lilienfeld, *Device for Controlling Electric Current*, US patent 1,900,018, filed 1928, awarded 1933
56. J.E. Lilienfeld, *Amplifier for Electric Currents*, US patent 1,877,140, filed 1928, awarded 1932
57. W. Gosling, The pre-history of the transistor. Radio Electron. Eng. **43**, 10 (1973)
58. A. Schleede, H. Buggisch, Untersuchungen am Bleiglanz- und Pyritdetektor. Z. Anorg. Allg. Chemie **161**, 85–107 (1927). 10.1002/zaac.19271610107
59. E. Körner, *Über die Darstellungsmethoden und die Lumineszenzfähigkeit reinsten Zinksulfids und Zinkoxydes*, Ph.D. Thesis, Universität Greifswald (1930)
60. A. Schleede, Über den strukturellen Bau der Leuchtzentren in den Zink- und Cadmium-Sulfid-Leuchtstoffen. Chem. Ber. **90**, 1162–1175 (1957). 10.1002/cber.19570900642
61. F. Bloch, Über die Quantenmechanik der Elektronen in Kristallgittern. Z. Phys. **52**, 555–560 (1928). 10.1007/BF01339455
62. E.E. Loebner, Subhistories of the light emitting diode. IEEE Trans. Electron Dev. **23**, 675–699 (1976). 10.1109/T-ED.1976.18472
63. M.A. Nivikov, Oleg Vladimirovich Losev: Pioneer of semiconductor electronics. Fiz. Tverd. Tela **46**, 5–9 (2004) [Phys. Solid State **46**, 1–4 (2004)]. 10.1134/1.1641908
64. N. Zheludev, The life and times of the LED—a 100-year history. Nat. Photon. **1**, 189–192 (2007). 10.1038/nphoton.2007.34
65. O.V. Lossev, Luminous carborundum detector and detection effect and oscillations with crystals. Philos. Mag. Series 7 **6**(39), 1024–1044 (1928). 10.1080/14786441108564683
66. R. Peierls, Zur Theorie der galvanomagnetischen Effekte. Zeitschr. f. Physik **53**, 255–266 (1929). 10.1007/BF01339727
67. R.E. Peierls, Zur Theorie des Hall-Effekts. Phys. Zeitschrift **30**, 273–274 (1929)
68. M.J.O. Strutt, Zur Wellenmechanik des Atomgitters. Ann. Physik **391**, 319–324 (1928). 10.1002/andp.19283911006
69. R. Peierls, Zur Theorie der elektrischen und thermischen Leitfähigkeit von Metallen. Ann. Physik **396**, 121–148 (1930). 10.1002/andp.19303960202
70. W. Heisenberg, Zum Paulischen Ausschließungsprinzip. Ann. Physik **402**, 888–904 (1931). 10.1002/andp.19314020710
71. R. de L. Kronig, W.G. Penney, Quantum mechanics of electrons in crystal lattices. Proc. R. Soc. Lond. A **130**, 499–513 (1931). 10.1098/rspa.1931.0019
72. A.H. Wilson, *Semi-Conductors and Metals, An Introduction to the Electron Theory of Metals* (Cambridge University Press, Cambridge, 1939)
73. R.W. Cahn, Silicon: Child and progenitor of revolution, in *Into the Nano Era, Moore's Law Beyond Planar Silicon CMOS*, ed. by H.R. Huff, pp. 3–10 (Springer, Berlin, 2009). 10.1007/978-3-540-74559-4_1
74. A.H. Wilson, The theory of electronic semi-conductors. Proc. R. Soc. Lond. A **133**, 458–491 (1931). 10.1098/rspa.1931.0162
75. A.H. Wilson, The theory of electronic semi-conductors II. Proc. R. Soc. Lond. A **134**, 277–287 (1931). 10.1098/rspa.1931.0196
76. H. Schmalzried, Carl Wagner, Berichte der Bunsengesellschaft für Physikalische Chemie **95**, 936–949 (1991). 10.1002/bbpc.19910950816
77. C. Wagner, W. Schottky, Theorie der geordneten Mischphasen. Z. Phys. Chem. **11B**, 163–210 (1930)
78. C. Wagner, Theorie der geordneten Mischphasen II. Diffusionsvorgänge. Z. Phys. Chem. **1931A** (issue supplement), 177–186 (1931). 10.1515/zpch-1931-s120
79. C. Wagner, Theorie der geordneten Mischphasen III. Fehlordnungserscheinungen in polaren Verbindungen als Grundlage für Ionen- und Elektronenleitung. Z. Phys. Chem. **22B**, 181–194 (1933). 10.1515/zpch-1933-2213
80. H.H. v. Baumbach, C. Wagner, Die elektrische Leitfähigkeit von Zinkoxyd und Cadmiumoxyd. Z. Phys. Chem. **22B**, 199–211 (1933). 10.1515/zpch-1933-2215
81. C. Zener, A theory of electrical breakdown of solid dielectrics. Proc. R. Soc. Lond. A **145**, 523–529 (1934). 10.1098/rspa.1934.0116
82. J. Frenkel, On the absorption of light and the trapping of electrons and positive holes in crystalline dielectrics. Phys. Z. Sowjetunion **9**, 158–186 (1936)
83. B.I. Davydov, On the rectification of current at the boundary between two semiconductors. Dokl. Acad. Nauk SSSR (C.R. Acad. Sci. USSR) **20**, 279–282 (1938)
84. B.I. Davydov, On the theory of solid rectifiers. Dokl. Acad. Nauk SSSR (C.R. Acad. Sci. USSR) **20**, 283–285 (1938)
85. W. Schottky, Halbleitertheorie der Sperrschicht. Naturwissenschaften **26**, 843 (1938). 10.1007/BF01774216
86. N.F. Mott, Note on the contact between a metal and an insulator or semiconductor. Proc. Camb. Philos. Soc. **34**, 568–572 (1938). 10.1017/S0305004100020570
87. N.F. Mott, The theory of crystal rectifiers. Proc. R. Soc. Lond. A **171**, 27–38 (1939). 10.1098/rspa.1939.0051

88. R. Hilsch, R.W. Pohl, Steuerung von Elektronenströmen mit einem Dreielektrodenkristall und ein Modell einer Sperrschicht. Z. Phys. **111**, 399–408 (1938). 10.1007/BF01342357
89. R.S. Ohl, *Light-Sensitive Electric Device*, US patent 2,402,662, filed 1941, awarded 1946
90. J.H. Scaff, The role of metallurgy in the technology of electronic materials. Metall. Mater. Trans. B **1**, 561–573 (1970). 10.1007/BF02811579
91. M. Riordan, L. Hoddeson, The origins of the pn junction. IEEE Spectrum **34**(6), 46–51 (1997). 10.1109/6.591664
92. R.S. Ohl, *Alternating Current Rectifier*, US patent 2,402,661, filed 1941, awarded 1946
93. J. Scaff, R.S. Ohl, The development of silicon crystal rectifiers for microwave radar receivers. Bell Syst. Tech. J. **26**, 1–30 (1947). 10.1002/j.1538-7305.1947.tb01310.x
94. K. Clusius, E. Holz, H. Welker, *Elektrische Gleichrichteranordnung mit Germanium als Halbleiter und Verfahren zur Herstellung von Germanium für eine solche Gleichrichteranordnung*, German patent DBP 966 387, 21g, 11/02 (1942)
95. H. Welker, *Halbleiteranordnung zur kapazitiven Steuerung von Strömen in einem Halbleiterkristall*, German patent DBP 980 084, 21g, 11/02 (1945)
96. J. Bardeen, W.H. Brattain, *Three-electrode circuit element utilizing semiconductor materials*, US patent 2,524,035, filed 1948, awarded 1950
97. M. Riordan, L. Hoddeson, C. Herring, The invention of the transistor. Rev. Mod. Phys. **71**, S336–S345 (1999). 10.1103/RevModPhys.71.S336
98. J. Bardeen, W.H. Brittain, Physical principles involved in transistor action. Phys. Rev. **75**, 1208–1225 (1949). 10.1103/PhysRev.75.1208
99. J. Bardeen, W.H. Brittain, The transistor, a semi-conductor triode. Phys. Rev. **74**, 230–231 (1948). 10.1103/PhysRev.74.230
100. W.F. Brinkman, D.E. Haggan, W.W. Troutman, A history of the invention of the transistor and where it will lead us. IEEE J. Solid-State Circ. **32**, 1858–1865 (1997). 10.1109/4.643644
101. W.B. Shockley, *Circuit Element Utilizing Semiconductor Material*, US patent 2,569,347, filed 1948, awarded 1951
102. N.A. Goryunova, *Grey Tin*, Ph.D. Thesis (in Russian), Leningrad State University (1951)
103. N.A. Goryunova, *The Chemistry of Diamond-Like Semiconductors* (Chapman and Hall, London, 1965) (translation of her book that was published 1963 in Leningrad)
104. H. Welker, *Verfahren zur Herstellung eines Halbleiterkristalls mit Zonen verschiedenen Leitungstyps bei A_{III}-B_V-Verbindungen*, German patent DBP 976 709, 21g, 11/02 (1952)
105. H. Welker, *Verfahren zur Herstellung eines Halbleiterkristalls aus einer A_{III}-B_V-Verbindung mit Zonen verschiedenen Leitungstyps*, German patent DBP 976 791, 12c, 2 (1952)
106. H. Welker, *Semiconductor devices and methods of their manufacture*, US patent 2,798,989, filed 1952, awarded 1957
107. H. Welker, Über neue halbleitende Verbindungen. Z. Naturf. **7a**, 744–749 (1952). 10.1515/zna-1952-1110
108. W. Shockley, A unipolar "field-effect" transistor. Proc. IRE **40**, 1365–1376 (1952). 10.1109/JRPROC.1952.273964
109. G.C. Dacey, I.M. Ross, Unipolar "field-effect" transistor. Proc. IRE **41**, 970–979 (1953). 10.1109/JRPROC.1953.274285
110. D.M. Chapin, C.S. Fuller, G.L. Pearson, A new silicon p-n junction photocell for converting solar radiation into electrical power. J. Appl. Phys. **25**, 676–677 (1954). 10.1063/1.1721711
111. J.S. Kilby, *Miniaturized electronic circuits*, US patent 3,138,743, filed 1959, awarded 1964
112. R.N. Noyce, *Semiconductor device-and-lead structure*, US patent 2,981,877, filed 1959, awarded 1961
113. A.N. Saxena, *Invention of Integrated Circuits—Untold Important Facts* (World Scientific, Singapore, 2009). 10.1142/6850
114. G. Mortenson, D.O. Relin, *Three Cups of Tea: One Man's Mission to Fight Terrorism and Build Nations ... One School at a Time* (Viking Penguin, New York, 2006)
115. J.A. Hoerni, *Method of manufacturing semiconductor devices*, US patent 3,025,589, filed 1959, awarded 1962
116. J.A. Hoerni, *Semiconductor device*, US patent 3,064,167, filed 1959, awarded 1962
117. J.A. Hoerni, Planar silicon diodes and transistors, in *International Electron Devices Meeting* (Washington, D.C., 1960), p. 50. 10.1109/IEDM.1960.187178
118. J.A. Hoerni, Planar silicon diodes and transistors. IRE Trans. Electron Dev. **8**, 178 (1961). 10.1109/T-ED.1961.14755
119. M. Riordan, The silicon dioxide solution: How physicist Jean Hoerni built the bridge from the transistor to the integrated circuit. IEEE Spectrum **44**(12), 50–56 (2007). 10.1109/MSPEC.2007.4390023
120. Datasheet *2N1613, Silicon npn transistor*, Fairchild Semiconductor
121. D. Kahng, M.M. Atalla, Silicon-silicon dioxide field induced surface device, in *IRE Solid-State Device Research Conference* (Carnegie Institute of Technology, Pittsburgh, PA, 1960). 10.1142/9789814503464_0076
122. D. Kahng, *Electric field controlled semiconductor device*, US patent 3,102,230, filed 1960, awarded 1963

123. R.N. Hall, G.E. Fenner, J.D. Kingsley, T.J. Soltys, R.O. Carlson, Coherent light emission from GaAs junctions. Phys. Rev. Lett. **9**, 366–368 (1962). 10.1103/PhysRevLett.9.366
124. R.N. Hall, *Stimulated Emission Semiconductor Devices*, US patent 3,245,002, filed 1962, awarded 1966
125. M.I. Nathan, W.P. Dumke, G. Burns, F.H. Dill Jr., G. Lasher, Stimulated emission of radiation from GaAs p-n junctions. Appl. Phys. Lett. **1**, 62–64 (1962). 10.1063/1.1777371
126. T.M. Quist, R.H. Rediker, R.J. Keyes, W.E. Krag, B. Lax, A.L. McWhorter, H.J. Zeigler, Semiconductor maser in GaAs. Appl. Phys. Lett. **1**, 91–92 (1962). 10.1063/1.1753710
127. N. Holonyak Jr., S.F. Bevacqua, Coherent (visible) light emission from $Ga(As_{1-x}P_x)$ junctions. Appl. Phys. Lett. **1**, 82–83 (1962). 10.1063/1.1753706
128. Remembering the laser diode. Nat. Photon. **6**, 795 (2012). 10.1038/nphoton.2012.310
129. J.J. Coleman, The development of the semiconductor laser diode after the first demonstration in 1962. Semicond. Sci. Technol. **27**, 090207:1–10 (2012). 10.1088/0268-1242/27/9/090207
130. Zh.I. Alferov, R.F. Kasarinov, *Semiconductor laser with electric pumping*, Inventor's Certificate No. 181737 (in Russian), Application No. 950840 (1963)
131. ZhI Alferov, Nobel Lecture: The double heterostructure concept and its applications in physics, electronics, and technology. Rev. Mod. Phys. **73**, 767–782 (2001). 10.1103/RevModPhys.73.767
132. H. Kroemer, A proposed class of heterojunction injection lasers. Proc. IEEE **51**, 1782–1783 (1963). 10.1109/PROC.1963.2706
133. H. Kroemer, Nobel Lecture: Quasielectric fields and band offsets: Teaching electrons new tricks. Rev. Mod. Phys. **73**, 783–793 (2001). 10.1103/RevModPhys.73.783
134. J.B. Gunn, Microwave oscillations of current in III-V semiconductors. Solid State Commun. **1**, 88–91 (1963). 10.1016/0038-1098(93)90262-L
135. C.A. Mead, Schottky barrier gate field effect transistor. Proc. IEEE **54**, 307–308 (1966). 10.1109/PROC.1966.4661
136. Zh.I. Alferov, V.I. Korol'kov, V.I. Maslov, A.V. Lishina, M.K. Trukan, A.A. Yakovenko, Investigation of current-voltage characteristics of diffused p-n junctions in $GaAs_{0.65}P_{0.35}$, Fizika i Tekn. Poluprovodn. **1**, 260–264 (1967) [Sov. Phys. Semicond. **1**, 206–209 (1967)]
137. Zh.I. Alferov, D.Z. Garbuzov, V.S. Grigor'ev, Yu.V. Zhilyaev, L.V. Kradinova, V.I. Korol'kov, E.P. Morozov, O.A. Ninua, E.L. Portnoy, V.D. Prochukhan, M.K. Trukan, Injection luminescence of epitaxial heterojunctions in the GaP–GaAs system. Fiz. Tverd. Tela **9**, 279–282 (1967) [Sov. Phys. Solid State **9**, 208–210 (1967)]
138. W.W. Hooper, W.I. Lehrer, An epitaxial GaAs field effect transistor. Proc. IEEE **55**, 1237–1238 (1967). 10.1109/PROC.1967.5817
139. Zh.I. Alferov, V.M. Andreev, E.L. Portnoi, M.K. Trukan, AlAs–GaAs heterojunction injection lasers with a low room-temperature threshold. Fizika i. Tekn. Poluprovodn. **3**, 1328-1332 (1969) [Sov. Phys. Semicond. **3**, 1107–1110 (1970)]
140. I. Hayashi, Heterostructure lasers. IEEE Trans. Electron Dev. **31**, 1630–1642 (1984). 10.1109/T-ED.1984.21764
141. R.A. Logan, H.G. White, W. Wiegmann, Efficient green electroluminescence in nitrogen-doped GaP p-n junctions. Appl. Phys. Lett. **13**, 139–141 (1968). 10.1063/1.1652543
142. R.M. Potter, J.M. Blank, A. Addamiano, Silicon carbide light-emitting diodes. J. Appl. Phys. **40**, 2253–2257 (1969). 10.1063/1.1657967
143. W.S. Boyle, G.E. Smith, Charge coupled semiconductor devices. Bell Syst. Tech. J. **49**, 587–593 (1970). 10.1002/j.1538-7305.1970.tb01790.x
144. G.F. Amelio, M.F. Tompsett, G.E. Smith, Experimental verification of the charge coupled device concept. Bell Syst. Tech. J. **49**, 593–600 (1970). 10.1002/j.1538-7305.1970.tb01791.x
145. R.F. Kazarinov, R.A. Suris, Possibility of the Amplification of Electromagnetic Waves in a Semiconductor with a Superlattice. Fiz. Tekh. Poluprovodn. **5**, 797–800 (1971) [Sov. Phys. Semicond. **5**, 707–709 (1971)]
146. R.S. Pengelly, J.A. Turner, Monolithic broadband GaAs F.E.T. amplifiers. Electron. Lett. **12**, 251–252 (1976). 10.1049/el:19760193
147. S. Nakamura, *Crystal Growth Method for Gallium Nitride-Based Compound Semiconductor*, US patent 5,290,393, filed 1992, awarded 1994
148. S. Nakamura, M. Senoh, N. Iwasa, S. Nagahama, High-brightness InGaN blue, green and yellow light-emitting diodes with quantum-well structures. Jpn. J. Appl. Phys. **34**, L797–L799 (1995). 10.1143/JJAP.34.L797
149. J. Faist, F. Capasso, D.L. Sivco, C. Sirtori, A.L. Hutchinson, A.Y. Cho, Quantum cascade laser. Science **264**, 553–556 (1994). 10.1126/science.264.5158.553
150. N. Kirstaedter, N.N. Ledentsov, M. Grundmann, D. Bimberg, V.M. Ustinov, S.S. Ruvimov, M.V. Maximov, P.S. Kop'ev, ZhI Alferov, U. Richter, P. Werner, U. Gösele, J. Heydenreich, Low threshold, large T_0 injection laser emission from (InGa)As quantum dots. Electron. Lett. **30**, 1416 (1994). 10.1049/el:19940939
151. K. Nomura, H. Ohta, A. Takagi, T. Kamiya, M. Hirano, H. Hosono, Room-temperature fabrication of transparent flexible thin-film transistors using amorphous oxide semiconductors. Nature **432**, 488–492 (2004). 10.1038/nature03090
152. A.J. Moses, Optical materials properties, in *Handbook of Electronic Materials*, vol. 1 (Plenum, New York, 1971). 10.1007/978-1-4684-6159-6

153. M. Neuberger, III–V Semiconducting Compounds, in *Handbook of Electronic Materials*, vol. 2 (Plenum, New York, 1971). 10.1007/978-1-4615-9606-6
154. J.T. Milek, Silicon nitride for microelectronic applications. Part 1 Preparation and properties, in *Handbook of Electronic Materials*, vol. 3 (Plenum, New York, 1971). 10.1007/978-1-4684-6162-6
155. M. Neuberger, D.L. Grigsby, W.H. Veazie Jr., Niobium alloys and compounds, in *Handbook of Electronic Materials*, vol. 4 (Plenum, New York, 1972). 10.1007/978-1-4757-6001-9
156. M. Neuberger, Group IV semiconducting materials, in *Handbook of Electronic Materials*, vol. 5 (Plenum, New York, 1972). 10.1007/978-1-4684-7917-1
157. J.T. Milek, Silicon nitride for microelectronic applications. Part 2 Applications and devices, in *Handbook of Electronic Materials*, vol. 6 (Plenum, New York, 1972). 10.1007/978-1-4615-9609-7
158. O. Madelung, *Semiconductors: Data Handbook*, 3rd edn. (Springer, Berlin, 2004). 10.1007/978-3-642-18865-7
159. W. Martienssen, Semiconductors, in *Springer Handbook of Condensed Matter and Materials Data*, W. Martienssen, H. Warlimont, eds. (Springer, Berlin, 2005), pp. 575–694. 10.1007/3-540-30437-1_9
160. S. Adachi, *Handbook on Physical Properties of Semiconductors*, vol. 1 (Group IV Elemental Semiconductors) (Kluwer, New York, 2004)
161. S. Adachi, *Handbook on Physical Properties of Semiconductors*, vol. 2 (III-V Compound Semiconductors) (Kluwer, New York, 2004)
162. S. Adachi, *Handbook on Physical Properties of Semiconductors*, vol. 3 (II–VI Compound Semiconductors) (Kluwer, New York, 2004). 10.1007/1-4020-7821-8
163. S. Adachi, *Optical Constants of Crystalline and Amorphous Semiconductors. Numerical Data and Graphical Information* (Springer, New York, 1999). 10.1007/978-1-4615-5247-5
164. Landolt-Börnstein, *Numerical Data and Functional Relationships in Science and Technology*, New Series, vol. 17, *Semiconductors*, O. Madelung, M. Schulz, H. Weiss, eds. (Springer, Berlin, 1982)
165. S. Adachi, *Properties of Group-IV, III-V and II-VI Semiconductors* (Wiley, Chichester, 2005). 10.1002/0470090340
166. S. Adachi, *Properties of Semiconductor Alloys: Group-IV, III-V and II-VI Semiconductors* (Wiley, Chichester, 2009). 10.1002/9780470744383
167. M. Dayah, www.dayah.com
168. B. Bryson, *A Short History of Nearly Everything* (Doubleday, London, 2003)
169. J.C. Phillips, *Bonds and Bands in Semiconductors* (Academic Press. New York, 1973). 10.1016/B978-0-12-553350-8.X5001-5
170. J.C. Phillips, G. Lucovsky, *Bonds and Bands in Semiconductors*, 2nd edn. (Momentum Press, New York, 2009)
171. P. Evers, *Die wundersame Welt der Atomis: 10 Jahre in den Physikalischen Blättern* (Wiley-VCH, Weinheim, 2002)
172. M.T. Yin, M.L. Cohen, Microscopic theory of the phase transformation and lattice dynamics of Si. Phys. Rev. Lett. **45**, 1004–1007 (1980). 10.1103/PhysRevLett.45.1004
173. J. Bardeen, W. Shockley, Deformation potentials and mobilities in non-polar crystals. Phys. Rev. **80**, 72–80 (1950). 10.1103/PhysRev.80.72
174. G.E. Kimball, The electronic structure of diamond. J. Chem. Phys. **3**, 560–564 (1935). 10.1063/1.1749729
175. N. Bernstein, M.J. Mehl, D.A. Papaconstantopoulos, N.I. Papanicolaou, M.Z. Bazant, E. Kaxiras, Energetic, vibrational, and electronic properties of silicon using a nonorthogonal tight-binding model. Phys. Rev. B **62**, 4477–4487 (2000). 10.1103/PhysRevB.62.4477 Erratum: Phys. Rev. B **65**, 249902 (2002). 10.1103/PhysRevB.65.249902
176. R.M. Roberts, *Serendipity, Accidental Discoveries in Science* (Wiley, New York, 1989), pp. 75–81
177. Y. Liu, P. Kilby, T.J. Frankcombe, T.W. Schmidt, The electronic structure of benzene from a tiling of the correlated 126-dimensional wavefunction. Nat. Commun. **11**, 1210:1–5 (2020). 10.1038/s41467-020-15039-9
178. H.J.F. Jansen, A.J. Freeman, Structural properties and electron density of NaCl. Phys. Rev. B **33**, 8629–8631 (1986). 10.1103/PhysRevB.33.8629
179. T. Soma, T. Umenai, Madelung energies of tetragonal and orthorhombic systems. Phys. Status Solidi B **78**, 229–240 (1976). 10.1002/pssb.2220780122
180. J.A. Van Vechten, Quantum dielectric theory of electronegativity in covalent systems. I. electronic dielectric constant. Phys. Rev. **182**, 891–905 (1969). 10.1103/PhysRev.182.891
181. J.C. Phillips, J.A. Van Vechten, Dielectric classification of crystal structures, ionization potentials, and band structures. Phys. Rev. Lett. **22**, 705–708 (1969). 10.1103/PhysRevLett.22.705
182. C.R.A. Catlow, A.M. Stoneham, Ionicity in solids. J. Phys. C: Solid State Phys. **16**, 4321–4338 (1983). 10.1088/0022-3719/16/22/010
183. H.B. Callen, Electric breakdown in ionic solids. Phys. Rev. **76**, 1394–1402 (1949). 10.1103/PhysRev.76.1394
184. J.C. Phillips, J.A. Van Vechten, Charge redistribution and piezoelectric constants. Phys. Rev. Lett. **23**, 1115–1117 (1969). 10.1103/PhysRevLett.23.1115
185. S. Takeuchi, K. Suzuki, Stacking fault energies of tetrahedrally coordinated crystals. Phys. Status Solidi A **171**, 99–103 (1999). 10.1002/(SICI)1521-396X(199901)171:1<99::AID-PSSA99>3.0.CO;2-B

186. J.-B. Romé de l'Isle, *Cristallographie, ou Description Des Formes Propre a Tous les Corps du Regne Minéral*, vol. 1, p. 91 (1783)
187. M.S. Dresselhaus, G. Dresselhaus, A. Jorio, *Group Theory, Application to the Physics of Condensed Matter* (Springer, Berlin, 2008). 10.1007/978-3-540-32899-5
188. M.A. Bravais, Mémoire sur les systèmes formés par des points distribués régulièrement sur un plan ou dans l'éspace. J. L'Ecole Polytechnique **19**, 1–128 (1850)
189. M.A. Bravais, *Études Cristallographiques* (Gauthier-Villars, Paris, 1866)
190. H.G.F. Winkler, Hundert Jahre Bravais Gitter. Die Naturwissenschaften **37**, 385–390 (1950). 10.1007/BF00738360
191. D. Shechtman, I. Blech, D. Gratias, J.W. Cahn, Metallic phase with long-range orientational order and no translational symmetry. Phys. Rev. Lett. **53**, 1951–1953 (1984). 10.1103/PhysRevLett.53.1951
192. I.R. Fisher, K.O. Cheon, A.F. Panchula, P.C. Canfield, M. Chernikov, H.R. Ott, K. Dennis, Magnetic and transport properties of single-grain R-Mg-Zn icosahedral quasicrystals [R=Y, ($Y_{1-x}Gd_x$), ($Y_{1-x}Tb_x$), Tb, Dy, Ho, and Er]. Phys. Rev. B **59**, 308–321 (1999). 10.1103/PhysRevB.59.308
193. K. Kimura, A. Hori, M. Takeda, H. Yamashita, H. Ino, Possibility of semiconducting quasicrystal in boron-rich solids. J. Non-Cryst. Solids **153&154**, 398–402 (1993). 10.1016/0022-3093(93)90382-8
194. K. Kirihara, K. Kimura, Covalency, semiconductor-like and thermoelectric properties of Al-based quasicrystals: Icosahedral cluster solids. Sci. Technol. Adv. Mat. **1**, 227–236 (2000). 10.1016/S1468-6996(00)00021-8
195. G. Burns, A.M. Glazer, *Space Groups for Solid State Scientists*, 3rd edn. (Academic Press, San Diego, 2013). 10.1016/C2011-0-05712-5
196. R.E. Proano, D.G. Ast, Effects of the presence/absence of HCl during gate oxidation on the electrical and structural properties of polycrystalline silicon thin film transistors. J. Appl. Phys. **66**, 2189–2199 (1989). 10.1063/1.344317
197. A.H. Clark, Electrical and optical properties of amorphous germanium. Phys. Rev. **154**, 750–757 (1967). 10.1103/PhysRev.154.750
198. R.C. Chittick, J.H. Alexander, H.F. Sterling, The preparation and properties of amorphous silicon. J. Electrochem. Soc. **116**, 77–81 (1969). 10.1149/1.2411779
199. E.P. Denton, H. Rawson, J.E. Stanworth, Vanadate glasses. Nature **173**, 1030–1032 (1954). 10.1038/1731030b0
200. H. Hosono, Ionic amorphous oxide semiconductors: Material design, carrier transport, and device application. J. Non-Cryst. Solids **352**, 851–858 (2006). 10.1016/j.jnoncrysol.2006.01.073
201. C.S. Schnohr, M.C. Ridgway, eds., *X-Ray Absorption Spectroscopy of Semiconductors* (Springer, Heidelberg, 2015). 10.1007/978-3-662-44362-0
202. D.E. Sayers, F.W. Lytle, E.A. Stern, Structure determination of amorphous Ge, GeO_2 and GeSe by Fourier analysis of extended X-ray absorption fine structure (EXAFS). J. Non-Cryst. Solids **8–10**, 401–447 (1972). 10.1016/0022-3093(72)90167-6
203. M.H. Brodsky, ed., *Amorphous Semiconductors*, Topics in Applied Physics 36 (Springer, Berlin, 1979). 10.1007/3-540-16008-6
204. B. Kramer, Electronic structure and optical properties of amorphous semiconductors. Adv. Solid State Phys. (Festkörperprobleme) **12**, 133–182 (1972). 10.1007/BFb0107701
205. R. Hull, ed., *Properties of Crystalline Silicon* (IET, London, 1999)
206. A.J. Haq, P.R. Munroe, Phase transformations in (111) Si after spherical indentation. J. Mater. Res. **24**, 1967–1975 (2009). 10.1557/jmr.2009.0249
207. G.A. Busch, R. Kern, Semiconducting properties of gray tin. Solid State Phys. **11**, 1–40 (1960). 10.1016/S0081-1947(08)60166-6
208. J.R. Chelikowski, Chemical trends in the structural stability of binary crystals. Phys. Rev. B **34**, 5295–5304 (1986). 10.1103/PhysRevB.34.5295
209. J.M. Besson, J.P. Itié, A. Polian, G. Weill, J.L. Mansot, J. Gonzalez, High-pressure phase transition and phase diagram of gallium arsenide. Phys. Rev. B **44**, 4214–4234 (1991). 10.1103/PhysRevB.44.4214
210. P. Lawaetz, Stability of the wurtzite structure. Phys. Rev. B **5**, 4039–4045 (1972). 10.1103/PhysRevB.5.4039
211. R.F. Davis, M.S. Shur, *GaN-based Materials And Devices: Growth, Fabrication, Characterization and Performance* (World Scientific, Singapore, 2004). 10.1142/5539
212. C. Jagadish, S.J. Pearton, eds., *Zinc Oxide Bulk, Thin Films and Nanostructures: Processing, Properties and Applications* (Elsevier, Amsterdam, 2006). 10.1016/B978-0-08-044722-3.X5000-3
213. M. Shur, S. Rumyantsev, M. Levinshtein, eds., *SiC Materials And Devices*, vol. 1 (World Scientific, Singapore, 2006). 10.1142/S0129156405003399 also: Int. J. High Speed Electronics and Systems **15**, 705–1033 (2005)]; M. Shur, S. Rumyantsev, M. Levinshtein, eds., *SiC Materials And Devices*, vol. 2 (World Scientific, Singapore, 2007). 10.1142/S0129156406004004 also: Int. J. High Speed Electronics and Systems **16**, 751–881 (2006)] 10.1142/6134, 10.1142/6311
214. S. Siebentritt, U. Rau, eds., *Wide-Gap Chalcopyrites* (Springer, Berlin, 2006). 10.1007/b105644
215. J.L. Shay, J.H. Wernick, *Ternary Chalcopyrites* (Pergamon, Oxford, 1975)
216. A. Zunger, Order-disorder transformation in ternary tetrahedral semiconductors. Appl. Phys. Lett. **50**, 164–166 (1987). 10.1063/1.97649

217. J.E. Jaffe, A. Zunger, Theory of the band-gap anomaly in ABC_2 chalcopyrite semiconductors. Phys. Rev. B **29**, 1882–1906 (1984). 10.1103/PhysRevB.29.1882
218. H.F. Liu, A.S.W. Wong, G.X. Hu, H. Gong, Observation of interfacial reactions and recrystallization of extrinsic phases in epitaxial grown ZnO/GaAs heterostructures. J. Cryst. Growth **310**, 4305–4308 (2008). 10.1016/j.jcrysgro.2008.07.062
219. K.-W. Park, Y.-H. Yun, S.-C. Choi, Photoluminescence characteristics of $ZnGa_2O_4$ thin films prepared by chemical solution method. Solid State Ionics **177**, 1875–1878 (2006). 10.1016/j.ssi.2006.05.049
220. T. Maitra, R. Valentí, Ferromagnetism in the Fe-substituted spinel semiconductor $ZnGa_2O_4$, J. Phys.: Cond. Matter **17**, 7417–7431 (2005). 10.1088/0953-8984/17/46/025
221. K.E. Sickafus, J.M. Wills, N.W. Grimes, Structure of spinel. J. Am. Ceram. Soc. **82**, 3279–3292 (1999). 10.1111/j.1151-2916.1999.tb02241.x
222. H.St.C. O'Neill, A. Navrotsky, Simple spinels: Crystallographic parameters, cation radii, lattice energies, and cation distribution. Am. Mineralogist. **68**, 181–194 (1983)
223. J.E. Jaffe, R.A. Bachorz, M. Gutowski, Low-temperature polymorphs of ZrO_2 and HfO_2: A density-functional theory study. Phys. Rev. B **72**, 144107:1–9 (2005). 10.1103/PhysRevB.72.144107
224. P. Duwez, F.H. Brown Jr., F. Odell, The zirconia-yttria system. J. Electrochem. Soc. **98**, 356–362 (1951). 10.1149/1.2778219
225. R. Ruh, K.S. Mazdiyasni, P.G. Valentine, H.O. Bielstein, Phase relations in the system ZrO_2–Y_2O_3 at low Y_2O_3 contents. J. Am. Ceram. Soc. **67**, C-190–C-192 (1984). 10.1111/j.1151-2916.1984.tb19618.x
226. X. Nie, S.-H. Wei, S.B. Zhang, Bipolar doping and band-gap anomalies in delafossite transparent conductive oxides. Phys. Rev. Lett. **88**, 066405, 1–4 (2002). 10.1103/PhysRevLett.88.066405
227. C.Y. Yang, Z.R. Huang, W.H. Yang, Y.Q. Zhou, K.K. Fung, Crystallographic study of lanthanum aluminate by convergent-beam electron diffraction. Acta Cryst. A **47**, 703–706 (1991). 10.1107/S0108767391005603
228. M.M. Lee, J. Teuscher, T. Miyasaka, T.N. Murakami, H.J. Snaith, Efficient hybrid solar cells based on meso-superstructured organometal halide perovskites. Science **338**, 643–647 (2012). 10.1126/science.1228604
229. A. Fakharuddin, U. Shabbir, W. Qiu, T. Iqbal, M. Sultan, P. Heremans, L. Schmidt-Mende, Inorganic and layered perovskites for optoelectronic devices. Adv. Mater. **31**, 1807095:1–39 (2019). 10.1002/adma.201807095
230. J. Deng, J. Li, Z. Yang, M. Wang, All-inorganic lead halide perovskites: A promising choice for photovoltaics and detectors. J. Mater. Chem. C **7**, 12415–12440 (2019). 10.1039/c9tc04164h
231. Q. Sun, W.-J. Yin, Thermodynamic stability trend of cubic perovskites. J. Am. Chem. Soc. **139**, 14905–14908 (2017). 10.1021/jacs.7b09379
232. B. Parida, S. Yoon, S.M. Jeong, J.S. Cho, J.-K. Kim, D.-W. Kang, Recent progress on cesium lead/tin halide-based inorganic perovskites for stable and efficient solar cells: A review. Solar Energy Mater. Solar Cells **204**, 110212:1–29 (2020). 10.1016/j.solmat.2019.110212
233. A. Guivarc'h, R. Guérin, J. Caulet, A. Poudoulec, J. Fontanille, Metallurgical study of Ni/GaAs contacts. II. Interfacial reactions of Ni thin films on (111) and (001) GaAs. J. Appl. Phys. **66**, 2129–2136 (1989). 10.1063/1.344308
234. S. Yoshioka, H. Hayashi, A. Kuwabara, F. Oba, K. Matsunaga, I. Tanaka, Structures and energetics of Ga_2O_3 polymorphs. J. Phys.: Cond. Matter **19**, 346211:1–11 (2007). 10.1088/0953-8984/19/34/346211
235. M. Higashiwaki, S. Fujita, eds., *Gallium Oxide. Materials Properties, Crystal Growth, and Devices* (Springer, Cham, 2020). 10.1007/978-3-030-37153-1
236. E.S. Dana, W.E. Ford, *A Textbook of Mineralogy with an Extended Treatise on Crystallography and Physical Mineralogy*, 3rd edn. (Wiley, New York, 1922)
237. W. Borchardt-Ott, *Kristallographie: Eine Einführung für Naturwissenschaftler*, 8th edn. (Springer, Berlin, 2013). 10.1007/978-3-662-22076-4
238. W. Borchardt-Ott, R.O. Gould, *Crystallography*, 3rd edn. (Springer, Berlin, 2012). 10.1007/978-3-642-16452-1
239. *International Tables for Crystallography, Volume A: Space-Group Symmetry*, 5th edn., Th. Hahn, ed., (Springer, Dordrecht, 2002). 10.1107/97809553602060000100
240. Naval Research Laboratory
241. Thomas Höche, private communication (2008)
242. Y. Lifshitz, X.F. Duan, N.G. Shang, Q. Li, L. Wan, I. Bello, S.T. Lee, Epitaxial diamond polytypes on silicon. Nature **412**, 404 (2001). 10.1038/35086656
243. M.J. Kozielski, Polytype single crystals of $Zn_{1-x}Cd_xS$ and $ZnS_{1-x}Se_x$ solid solutions grown from the melt under high argon pressure by Bridgman's method. J. Cryst. Growth **30**, 86–92 (1975). 10.1016/0022-0248(75)90203-1
244. S.J. Pearton, J. Yang, P.H. Cary, F. Ren, J. Kim, M.J. Tadjer, M.A. Mastro, A review of Ga_2O_3 materials, processing, and devices. Appl. Phys. Rev. **5**, 011301:1–56 (2018). 10.1063/1.5006941
245. P.F. Fewster, *X-Ray Scattering from Semiconductors* (Imperial College Press. London (2003). 10.1142/p289
246. W.H. Miller, *Treatise on Crystallography* (Deighton, Cambridge, 1839)
247. J.F. Zheng, J.D. Walker, M.B. Salmeron, E.R. Weber, Interface segregation and clustering in strained-layer InGaAs/GaAs heterostructures studied by cross-section scanning tunneling microscopy. Phys. Rev. Lett. **72**, 2414–2417 (1994). 10.1103/PhysRevLett.72.2414

248. K.-J. Chao, Ch-K Shih, D.W. Gotthold, B.G. Streeman, Determination of 2D pair correlations and pair interaction energies of in atoms in molecular beam epitaxially grown InGaAs alloys. Phys. Rev. Lett. **79**, 4822–4825 (1997). 10.1103/PhysRevLett.79.4822
249. C. Bundesmann, M. Schubert, D. Spemann, A. Rahm, H. Hochmuth, M. Lorenz, M. Grundmann, Infrared dielectric function and phonon modes of Mg-rich cubic $Mg_xZn_{1-x}O$ ($x \geq 0.67$) thin films on sapphire (0001). Appl. Phys. Lett. **85**, 905–907 (2004). 10.1063/1.1777797
250. M.M. Kreitman, D.L. Barnett, Probability tables for clusters of foreign atoms in simple lattices assuming next-nearest-neighbor interactions. J. Chem. Phys. **43**, 364–371 (1965). 10.1063/1.1696753
251. O. Okada, Magnetic Susceptibilities of $Mg_{1-p}Mn_pTe_2$. J. Phys. Soc. Jpn. **48**, 391–398 (1980). 10.1143/JPSJ.48.391
252. S.-H. Wei, L.G. Ferreira, A. Zunger, First-principles calculation of temperature-composition phase diagrams of semiconductor alloys. Phys. Rev. B **41**, 8240–8269 (1990). 10.1103/PhysRevB.41.8240
253. I.-H. Ho, G.B. Stringfellow, Solid phase immiscibility in GaInN. Appl. Phys. Lett. **69**, 2701–2703 (1996). 10.1063/1.117683
254. I.V. Maznichenko, A. Ernst, M. Bouhassoune, J. Henk, M. Däne, M. Lüders, P. Bruno, W. Hergert, I. Mertig, Z. Szotek, W.M. Temmerman, Structural phase transitions and fundamental band gaps of $Mg_xZn_{1-x}O$ alloys from first principles. Phys. Rev. B **80**, 144101:1–11 (2009). 10.1103/PhysRevB.80.144101
255. J.C. Mikkelsen Jr., J.B. Boyce, Atomic-scale structure of random solid solutions: Extended X-ray absorption fine-structure study of $Ga_{1-x}In_xAs$. Phys. Rev. Lett. **49**, 1412–1415 (1982). 10.1103/PhysRevLett.49.1412
256. J.C. Mikkelsen Jr., J.B. Boyce, Extended x-ray absorption fine-structure study of $Ga_{1-x}In_xAs$ random solid solutions. Phys. Rev. B **28**, 7130–7140 (1983). 10.1103/PhysRevB.28.7130
257. O. Ambacher, M. Eickhoff, A. Link, M. Hermann, M. Stutzmann, F. Bernardini, V. Fiorentini, Y. Smorchkova, J. Speck, U. Mishra, W. Schaff, V. Tilak, L.F. Eastman, Electronics and sensors based on pyroelectric AlGaN/GaN heterostructures, Part A: Polarization and pyroelectronics. Phys. Status Solidi C **0**, 1878–1907 (2003). 10.1002/pssc.200303138
258. A. Zunger, S. Mahajan, *Atomic Ordering and Phase Separation in III-V Alloys, Handbook on Semiconductors*, vol. 3 (Elsevier, Amsterdam, 1994), pp. 1399–1513
259. H.S. Lee, J.Y. Lee, T.W. Kim, D.U. Lee, D.C. Choo, H.L. Park, Coexistence behavior of the $CuPt_B$-type and the CuAu-I-type ordered structures in highly strained $Cd_xZn_{1-x}Te$/GaAs heterostructures. Appl. Phys. Lett. **79**, 1637–1639 (2001). 10.1063/1.1398617
260. C.J. Humphreys, STEM imaging of crystals and defects, in *Introduction to Analytical Electron Microscopy*, J.J. Hren, J.I. Goldstein, D.C. Joy, eds. (Springer, New York, 1979). 10.1007/978-1-4757-5581-7
261. C. Domke, Ph Ebert, M. Heinrich, K. Urban, Direct determination of the interaction between vacancies on InP(110) surfaces. Phys. Rev. B **54**, 10288–10291 (1996). 10.1103/PhysRevLett.76.2089
262. Ph Ebert, X. Chen, M. Heinrich, M. Simon, K. Urban, M.G. Lagally, Direct determination of the interaction between vacancies on InP(110) surfaces. Phys. Rev. Lett. **76**, 2089–2092 (1996). 10.1103/PhysRevLett.76.2089
263. R.M. Feenstra, J.M. Woodall, G.D. Pettit, Observation of bulk defects by scanning tunneling microscopy and spectroscopy: Arsenic antisite defects in GaAs. Phys. Rev. Lett. **71**, 1176–1179 (1993). 10.1103/PhysRevLett.71.1176
264. R.B. Capaz, K. Cho, J.D. Joannopoulos, Signatures of bulk and surface arsenic antisite defects in GaAs(110). Phys. Rev. Lett. **75**, 1811–1814 (1995). 10.1103/PhysRevLett.75.1811
265. R. Jones, A. Carvalho, J.P. Goss, P.R. Briddon, The self-interstitial in silicon and germanium. Mater. Sci. Eng. B **159**, 112–116 (2008). 10.1016/j.mseb.2008.09.013
266. S.J. Clark, *Complex structure in tetrahedral semiconductors*, Ph.D. Thesis, University of Edinburgh (1994)
267. M. Lannoo, J. Bourgoin, *Point Defects in Semiconductors I* (Springer, Berlin, 1981). 10.1007/978-3-642-81574-4
268. H. Bracht, N.A. Stolwijk, H. Mehrer, Properties of intrinsic point defects in silicon determined by zinc diffusion experiments under nonequilibrium conditions. Phys. Rev. B **52**, 16542–16560 (1995). 10.1103/PhysRevB.52.16542
269. V. Ranki, K. Saarinen, Formation of thermal vacancies in highly As and P doped Si. Phys. Rev. Lett. **93**, 255502:1–4 (2004). 10.1103/PhysRevLett.93.255502
270. J. Gebauer, M. Lausmann, F. Redmann, R. Krause-Rehberg, H.S. Leipner, E.R. Weber, Ph. Ebert, Determination of the Gibbs free energy of formation of Ga vacancies in GaAs by positron annihilation. Phys. Rev. B **67**, 235207:1–8 (2003). 10.1103/PhysRevB.67.235207
271. F. Morehead, N. Stolwijk, W. Meyberg, U. Gösele, Self-interstitial and vacancy contributions to silicon self-diffusion determined from the diffusion of gold in silicon. Appl. Phys. Lett. **42**, 690–692 (1983). 10.1063/1.94074
272. S. Dannefaer, P. Mascher, D. Kerr, Monovacancy formation enthalpy in silicon. Phys. Rev. Lett. **56**, 2195–2198 (1986). 10.1103/PhysRevLett.56.2195
273. P.M. Fahey, P.B. Griffin, J.D. Plummer, Point defects and dopant diffusion in silicon. Rev. Mod. Phys. **61**, 289–384 (1989). 10.1103/RevModPhys.61.289
274. P. Pichler, *Intrinsic Point Defects, Impurities, and Their Diffusion in Silicon* (Springer, Berlin, 2004). 10.1007/978-3-7091-0597-9

275. G.D. Watkins, The vacancy in silicon: Identical diffusion properties at cryogenic and elevated temperatures. J. Appl. Phys. **103**, 106106:1–2 (2008). 10.1063/1.2937198
276. Y. Shimizu, M. Uematsu, K.M. Itoh, Experimental evidence of the vacancy-mediated silicon self-diffusion in single-crystalline silicon. Phys. Rev. Lett. **98**, 095901:1–4 (2007). 10.1103/PhysRevLett.98.095901
277. C.S. Nichols, C.G. Van der Walle, S.T. Pantelides, Mechanisms of dopant impurity diffusion in silicon. Phys. Rev. B **40**, 5484–5496 (1989). 10.1103/PhysRevB.40.5484
278. A. Ural, P.B. Griffin, J.D. Plummer, Fractional contributions of microscopic diffusion mechanisms for common dopants and self-diffusion in silicon. J. Appl. Phys. **85**, 6440–6446 (1999). 10.1063/1.370285
279. J.-W. Jeong, A. Oshiyama, Atomic and electronic structures of a boron impurity and its diffusion pathways in crystalline Si. Phys. Rev. B **64**, 235204:1–9 (2001). 10.1103/PhysRevB.64.235204
280. W. Windl, Concentration dependence of self-interstitial and boron diffusion in silicon. Appl. Phys. Lett. **92**, 202104:1–3 (2008). 10.1063/1.2936081
281. K.-S. Yoon, C.-O. Wang, J.-H. Yoo, T. Won, First-principles investigation of indium diffusion in a silicon substrate. J. Korean Phys. Soc. **48**, 535–539 (2006)
282. X.-Y. Liu, W. Windl, K.M. Beardmore, M.P. Masquelier, First-principles study of phosphorus diffusion in silicon: Interstitial- and vacancy-mediated diffusion mechanisms. Appl. Phys. Lett. **82**, 1839–1841 (2003). 10.1063/1.1562342
283. L. Rayleigh, On the distillation of binary mixtures. Philos. Mag. **4**, 521–537 (1902). 10.1080/14786440209462876
284. C.H. Li, Normal freezing of ideal ternary liquid solutions of the pseudobinary type. J. Phys. D: Appl. Phys. **7**, 2003–2008 (1974). 10.1088/0022-3727/7/14/319
285. W. Zulehner, The growth of highly pure silicon crystals. Metrologia **31**, 255–261 (1994). 10.1088/0026-1394/31/3/012
286. I. Yonenaga, T. Ayuzawa, Segregation coefficients of various dopants in $Si_x Ge_{1-x}$ ($0.93 < x < 0.96$) single crystals. J. Cryst. Growth **297**, 14–19 (2006). 10.1016/j.jcrysgro.2006.08.044
287. W.C. O'Mara, R.B. Herring, L.P. Hunt, eds., *Handbook of Semiconductor Silicon Technology* (Noyes, Berkshire, 1990)
288. J.J. Dowd, R.L. Rouse, Distribution coefficient of indium in germanium on crystallization. Proc. Phys. Soc. B **66**, 60–61 (1953). 10.1088/0370-1301/66/1/110
289. W.W. Tyler, R. Newman, H.H. Woodbury, Properties of germanium doped with nickel. Phys. Rev. **98**, 461–465 (1955). 10.1103/PhysRev.98.461
290. W.C. Dunlap Jr., Gold as acceptor in germanium. Phys. Rev. **97**, 614–629 (1955). 10.1103/PhysRev.97.614
291. W.G. Pfann, Techniques of zone melting and crystal growing. Solid State Phys. **4**, 423–521 (1957). 10.1016/S0081-1947(08)60158-7
292. M. Nastasi, J.W. Mayer, *Ion Implantation and Synthesis of Materials* (Springer, Berlin, 2006). 10.1007/978-3-540-45298-0
293. A. Benninghoven, F.G. Rudenauer, H.W. Werner, eds., *Secondary Ion Mass Spectrometry* (Wiley, New York, 1987)
294. P. van der Heide, *Secondary Ion Mass Spectrometry: An Introduction to Principles and Practices* (Wiley, New York, 2014)
295. S. Uppal, A.F.W. Willoughby, J.M. Bonar, A.G.R. Evans, N.E.B. Cowern, R. Morris, M.G. Dowsett, Diffusion of ion-implanted boron in germanium. J. Appl. Phys. **90**, 4293–4295 (2001). 10.1063/1.1402664
296. R.F. Lever, K.W. Brannon, A low energy limit to boron channeling in silicon. J. Appl. Phys. **69**, 6369–6372 (1991). 10.1063/1.348838
297. www.srim.org
298. J.F. Ziegler, M.D. Ziegler, J.P. Biersack, SRIM—the stopping and range of ions in matter. Nucl. Instrum. Meth. B **218**, 1818–1823 (2010). 10.1016/j.nimb.2010.02.091
299. K. Kimura, Y. Oota, K. Nakajima, T.H. Büyüklimanli, High-resolution depth profiling of ultrashallow boron implants in silicon using high-resolution RBS. Current Appl. Phys. **3**, 9–11 (2003). 10.1016/S1567-1739(02)00227-4
300. R. Wittmann, *Miniaturization Problems in CMOS Technology: Investigation of Doping Profiles and Reliability*, Ph.D. Thesis, Technische Universität Wien (2007)
301. J. Yokota, Lattice distorsion around charged impurities in semiconductors. J. Phys. Soc. Jpn. **19**, 1487 (1964). 10.1143/JPSJ.19.1487
302. J.A. Vergés, D. Glötzel, M. Cardona, O.K. Andersen, Absolute hydrostatic deformation potentials of tetrahedral semiconductors. Phys. Status Solidi B **113**, 519–534 (1982). 10.1002/pssb.2221130217
303. M. Cardona, N.E. Christensen, Acoustic deformation potentials and heterostructure band offsets in semiconductors. Phys. Rev. B **35**, 6182–6194 (1987). 10.1103/PhysRevB.35.6182
304. D.A.W. Soarez, C.A. Pimentel, Precision interplanar spacing measurements of boron-doped silicon. J. Appl. Cryst. **16**, 486–492 (1983). 10.1107/S0021889883010870
305. J.L. Hastings, S.K. Estreicher, P.A. Fedders, Vacancy aggregates in silicon. Phys. Rev. B **56**, 10215–10220 (1997). 10.1103/PhysRevB.56.10215

306. M. Albrecht, R. Schewski, K. Irmscher, Z. Galazka, T. Markurt, M. Naumann, T. Schulz, R. Uecker, R. Fornari, S. Meuret, M. Kociak, Coloration and oxygen vacancies in wide band gap oxide semiconductors: Absorption at metallic nanoparticles induced by vacancy clustering—a case study on indium oxide. J. Appl. Phys. **115**, 053504:1–12 (2014). 10.1063/1.4863211
307. S. Lee, G.S. Hwang, Theoretical determination of stable fourfold coordinated vacancy clusters in silicon. Phys. Rev. B **78**, 125310:1–6 (2008). 10.1103/PhysRevB.78.125310
308. H.R. Vydyanath, J.S. Lorenzo, F.A. Kröger, Defect pairing diffusion, and solubility studies in selenium-doped silicon. J. Appl. Phys. **49**, 5928–5937 (1978). 10.1063/1.324560
309. P. Deák, A. Gali, A. Sólynom, A. Buruzs, Th. Fraunheim, Electronic structure of boron-interstitial clusters in silicon. J. Phys.: Cond. Matter **17**, S2141–S2153 (2005) and references therein. 10.1088/0953-8984/17/22/001
310. B.P. Uberuaga, G. Henkelman, H. Jónsson, S.T. Dunham, W. Windl, R. Stumpf, Theoretical studies of self-diffusion and dopant clustering in semiconductors. Phys. Status Solidi B **233**, 24–30 (2002). 10.1002/1521-3951(200209)233:1%3C24::AID-PSSB24%3E3.0.CO;2-5
311. M.J. Caturla, M.D. Johnson, T.D. de la Rubia, The fraction of substitutional boron in silicon during ion implantation and thermal annealing. Appl. Phys. Lett. **72**, 2736–2738 (1998). 10.1063/1.121075
312. F.A. Trumbore, Solid solubilities of impurity elements in germanium and silicon. Bell Syst. Tech. J. **39**, 205–233 (1960). 10.1002/j.1538-7305.1960.tb03928.x
313. V.E. Borisenko, S.G. Yudin, Steady-state solubility of substitutional impurities in silicon. Phys. Status Solidi A **101**, 123–127 (1987). 10.1002/pssa.2211010113
314. H.-J. Queisser, Deep impurities. Adv. Solid State Phys. (Festkörperprobleme) **11**, 45–64 (1971). 10.1007/BFb0107682
315. J. Adey, R. Jones, P.R. Briddon, Enhanced dopant solubility in strained silicon. J. Phys.: Cond. Matter **16**, 9117–9126 (2004). 10.1088/0953-8984/16/50/002
316. S. Fischler, Correlation between maximum solid solubility and distribution coefficient for impurities in Ge and Si. J. Appl. Phys. **33**, 1615 (1962). 10.1063/1.1728792
317. F.S. Shishiyanu, V.G. Gheorghiu, S.K. Palazov, Diffusion, solubility, and electrical activity of Co and Fe in InP. Phys. Status Solidi A **40**, 29–35 (1977). 10.1002/pssa.2210400103
318. M. Luysberg, R. Göbel, H. Janning, FeP precipitates in hydride-vapor phase epitaxially grown InP:Fe. J. Vac. Sci. Technol. B **12**, 2305–2309 (1994). 10.1116/1.587757
319. N.A. Smith, I.R. Harris, B. Cockayne, W.R. MacEwan, The identification of precipitate phases in Fe-Doped InP single crystals. J. Cryst. Growth **68**, 517–522 (1984). 10.1016/0022-0248(84)90458-5
320. J.P. Hirth, A brief history of dislocation theory. Metall. Mat. Trans. A **16**, 2085–2090 (1985). doi:10.1007/BF02670413
321. S. Kret, Pawel Dłużewski, Piotr Dłużewski, J.-Y. Laval, On the measurement of dislocation core distributions in a GaAs/ZnTe/CdTe heterostructure by high-resolution transmission electron microscopy. Philos. Mag. **83**, 231–244 (2003). 10.1080/0141861021000020095
322. A.R. Smith, V. Ramachandran, R.M. Feenstra, D.W. Greve, M.-S. Shin, M. Skowronski, J. Neugebauer, J.E. Northrup, Wurtzite GaN surface structures studied by scanning tunneling microscopy and reflection high energy electron diffraction. J. Vac. Sci. Technol. A **16**, 1641–1645 (1998). 10.1116/1.581134
323. S.N.G. Chu, W.T. Tsang, T.H. Chiu, A.T. Macrander, Lattice-mismatch-generated dislocation structures and their confinement using superlattices in heteroepitaxial GaAs/InP and InP/GaAs grown by chemical beam epitaxy. J. Appl. Phys. **66**, 520–530 (1989). 10.1063/1.343568
324. A.M. Smirnov, E.C. Young, V.E. Bougrov, J.S. Speck, A.E. Romanov, Critical thickness for the formation of misfit dislocations originating from prismatic slip in semipolar and nonpolar III-nitride heterostructures. APL Mater. **4**, 016105:1–8 (2016). 10.1063/1.4939907
325. M. Grundmann, Universal relation for the orientation of dislocations from prismatic slip systems in hexagonal and rhombohedral strained heterostructures. Appl. Phys. Lett. **116**, 082104:1–3 (2020). 10.1063/1.5140977
326. M. Grundmann, M. Lorenz, Epitaxial growth and strain relaxation of corundum-phase $(Al,Ga)_2O_3$ thin films from pulsed laser deposition at 1000°C on r-plane Al_2O_3. Appl. Phys. Lett. **117**, 242102:1–4 (2020). 10.1063/5.0030675
327. M. Horn-von Hoegen, F.K. LeGoues, M. Copel, M.C. Reuter, R.M. Tromp, Defect self-annihilation in surfactant-mediated epitaxial growth. Phys. Rev. Lett. **67**, 1130–1133 (1991). 10.1103/PhysRevLett.67.1130
328. R.B. Heimann, Auflösung von Kristallen, Theorie und technische Anwendung, in *Applied Mineralogy*, vol. 8 (Springer, Wien, 1975). 10.1007/978-3-7091-3402-3
329. K. Sato, M. Shikida, T. Yamashiro, K. Asaumi, Y. Iriye, M. Yamamoto, Anisotropic etching rates of single-crystal silicon for TMAH water solution as a function of crystallographic orientation. Sens. Actuators **73**, 131–137 (1999). 10.1016/S0924-4247(98)00271-4
330. J.G. Grabmaier, C.B. Watson, Dislocation etch pits in single crystal GaAs. Phys. Status Solidi **32**, K13–K15 (1969). 10.1002/pssb.19690320155
331. H. Richter, M. Schulz, Versetzungsnachweis auf {100}-Flächen von GaAs-Einkristallen. Kristall und Technik **9**, 1041–1050 (1974). 10.1002/crat.19740090909

332. K. Ishida, H. Kawano, Different etch pit shapes revealed by molten KOH etching on the (001) GaAs surface and their dependence on the Burgers vectors. Phys. Status Solidi A **98**, 175–181 (1986). 10.1002/pssa.2210980119
333. J.L. Weyher, J. van de Ven, Selective etching and photoetching of GaAs in CrO_3–HF aqueous solutions. III. Interpretation of defect-related etch figures. J. Cryst. Growth **78**, 191–217 (1986). 10.1016/0022-0248(86)90055-2
334. A.F. Bogenschütz, *Ätzpraxis für Halbleiter* (Carl Hanser, München, 1967)
335. M. Köhler, *Etching in Microsystem Technology* (Wiley-VCH, Weinheim, 1999). 10.1002/9783527613786
336. A.R. Clawson, Guide to references on III-V semiconductor chemical etching. Mater. Sci. Eng. **31**, 1–438 (2001). 10.1016/S0927-796X(00)00027-9
337. J. Frühauf, *Shape and Functional Elements of the Bulk Silicon Microtechnique: A Manual of Wet-Etched Silicon Structures* (Springer, Berlin, 2005). 10.1007/b138230
338. D.M. Manos, D.L. Flamm, eds., *Plasma Etching: An Introduction* (Academic Press, San Diego, 1989)
339. G.S. May, C.J. Spanos, *Fundamentals of Semiconductor Manufacturing and Process Control* (Wiley, Hoboken, 2006). 10.1002/0471790281
340. J.W. Coburn, *Plasma Etching and Reactive Ion Etching: Fundamentals and Applications, American Vacuum Society Monograph Series* (AVS, New York, 1982)
341. V.M. Donnelly, A. Kornblit, Plasma etching: Yesterday, today, and tomorrow. J. Vac. Sci. Technol. A **31**, 050825:1–47 (2013). 10.1116/1.4819316
342. V. Smaminathan, A.S. Jordan, Dislocations in III/V compounds. Semicond. Semimet. **38**, 293–341 (1993). 10.1016/S0080-8784(08)62803-3
343. T. Kamejima, J. Matsui, Y. Seki, H. Watanabe, Transmission electron microscopy study of microdefects in dislocation-free GaAs and InP crystals. J. Appl. Phys. **50**, 3312–3321 (1979). 10.1063/1.326372
344. L. Wang, W. Jie, Y. Yang, G. Xu, L. Fu, Defect characterization and composition distributions of mercury indium telluride single crystals. J. Cryst. Growth **310**, 2810–2814 (2008). 10.1016/j.jcrysgro.2008.01.060
345. NREL, www.nrel.gov/measurements/trans.html
346. Z. Liliental-Weber, H. Sohn, J. Washburn, Structural defects in epitaxial III/V layers. Semicond. Semimet. **38**, 397–447 (1993). 10.1016/S0080-8784(08)62805-7
347. Y. Hao, G. Meng, ZhL Wang, Ch. Ye, L. Zhang, Periodically twinned nanowires and polytypic nanobelts of ZnS: the role of mass diffusion in vapor-liquid-solid growth. Nano Lett. **6**, 1650–1655 (2006). 10.1021/nl060695n
348. S. Mader, A.E. Blakeslee, Extended dislocations in $GaAs_{0.7}P_{0.3}$. Appl. Phys. Lett. **25**, 365–367 (1974). 10.1063/1.1655510
349. M. Sato, K. Sumino, K. Hiraga, Impurity effect in stacking fault energy of silicon crystals studied by high resolution electron microscopy. Phys. Status Solidi A **68**, 567–577 (1981). 10.1002/pssa.2210680228
350. A. Gomez, D.J.H. Cockayne, P.B. Hirsch, V. Vitek, Dissociation of near-screw dislocations in germanium and silicon. Philos. Mag. **31**, 105–113 (1975). 10.1080/14786437508229289
351. D. Gerthsen, C.B. Carter, Stacking-fault energies of GaAs. Phys. Status Solidi A **136**, 29–43 (1993). 10.1002/pssa.2211360104
352. P. Pirouz, D.J.H. Cockayne, N. Shimada, P. Hirsch, A.R. Lang, Dissociation of dislocations in diamond. Proc. Roy. Soc. Lond. A **386**, 241–249 (1983). 10.1098/rspa.1983.0034
353. H. Gottschalk, G. Patzer, H. Alexander, Stacking fault energy and ionicity of cubic III-V compounds. Phys. Status Solidi A **45**, 207–217 (1978). 10.1002/pssa.2210450125
354. S. Takeuchi, K. Suzuki, K. Maeda, Stacking-fault energy of II-VI compounds. Philos. Mag. A **50**, 171–178 (1984). 10.1080/01418618408244220
355. S. Amelinckx, W. Dekeyser, The structure and properties of grain boundaries. Solid State Phys. **8**, 325–499 (1959). 10.1016/S0081-1947(08)60482-8
356. C.R.M. Grovenor, Grain boundaries in semiconductors. J. Phys. C: Solid State Phys. **18**, 4079–4119 (1985). 10.1088/0022-3719/18/21/008
357. C. Fontaine, D.A. Smith, On the atomic structure of the Σ=3 112 twin in silicon. Appl. Phys. Lett. **40**, 153–154 (1982). 10.1063/1.93019
358. H. Sawada, H. Ichinose, M. Kohyama, Imaging of a single atomic column in silicon grain boundary. J. Electron Microscopy **51**, 353–357 (2002). 10.1093/jmicro/51.6.353
359. F.L. Vogel, W.G. Pfann, H.E. Corey, E.E. Thomas, Observations of dislocations in lineage boundaries in germanium. Phys. Rev. **90**, 489–490 (1953). 10.1103/PhysRev.90.489
360. H. Föll, Universität Kiel. http://www.tf.uni-kiel.de/matwis/amat/def_en/kap_7/backbone/r7_2_2.html
361. H. Föll, D. Ast, TEM observations on grain boundaries in sintered silicon. Philos. Mag. A **40**, 589–610 (1979). 10.1080/01418617908234861
362. M. Grundmann, A. Krost, D. Bimberg, LP-MOVPE growth of antiphase domain free InP on (001) Si using low temperature processing. J. Cryst. Growth **107**, 494–495 (1991). 10.1016/0022-0248(91)90509-4
363. Wolfgang Mader, private communication (2006)
364. F. Wolf, W. Mader, Microdomain structure in Fe_2O_3-doped ZnO and the formation of spinel. Optik **110**(Suppl. 8), 66 (1999)

365. F. Wolf, B.H. Freitag, W. Mader, Inversion domain boundaries in ZnO with additions of Fe_2O_3 studied by high-resolution ADF imaging. Micron **38**, 549–552 (2007). 10.1016/j.micron.2006.07.021
366. G.P. Srivastava, *The Physics of Phonons* (Taylor and Francis, New York, 1990)
367. N. Ashcroft, D. Mermin, *Solid State Physics* (Harcourt College Publishers, Fort Worth, 1976)
368. C. Kittel, *Introduction to Solid State Physics*, 8th edn. (Wiley, Chichester, 2004)
369. M.V. Berry, Quantal phase factors accompanying adiabatic changes. Proc. Roy. Soc. Lond. A **392**, 45–57 (1984). 10.1098/rspa.1984.0023
370. J.K. Asbóth, L. Oroszlány, A. Pályi, A short course on topological insulators, band-structure topology and edge states in one and two dimensions, in *Lecture Notes in Physics*, vol. 919 (Springer, 2016). 10.1007/978-3-319-25607-8
371. R. Süsstrunk, S.D. Huber, Classification of topological phonons in linear mechanical metamaterials. PNAS **113**, E4767–E4775 (2016). 10.1073/pnas.1605462113
372. H. Montgomery, The symmetry of lattice vibrations in the zincblende and diamond structures. Proc. Roy. Soc. Lond. A **309**, 521–549 (1969). 10.1098/rspa.1969.0055
373. J.L.T. Waugh, G. Dolling, Crystal dynamics of gallium arsenide. Phys. Rev. **132**, 2410–2412 (1963). 10.1103/PhysRev.132.2410
374. P.H. Borcherds, K. Kunc, G.F. Alfrey, R.L. Hall, The lattice dynamics of gallium phosphide. J. Phys. C: Solid State Phys. **12**, 4699–4706 (1979). 10.1088/0022-3719/12/22/012
375. J.L.Yarnell, J.L.Warren, R.G.Wenzel, P.J.Dean, Lattice dynamics of gallium phosphide, in *Neutron Inelastic Scattering*, vol. 1 (IAEA, Vienna, 1968), pp. 301–313
376. S. Bağcı, S. Duman, H.M. Tütüncü, G.P. Srivastava, G. Uğur, Ab initio calculation of the structural and dynamical properties of the zinc-blende BN and its (110) surface. Diamond Rel. Mater. **15**, 1161–1165 (2006). 10.1016/j.diamond.2005.10.038
377. T. Tomoyose, A. Fukuchi, M. Kobayashi, Influence of quadrupolar deformability on phonon dispersion in silver and copper halides. Solid State Ionics **167**, 83–90 (2004). 10.1016/j.ssi.2003.12.007
378. E. Ruiz, S. Alvarez, P. Alemany, Electronic structure and properties of AlN. Phys. Rev. B **49**, 7115–7123 (1994). 10.1103/PhysRevB.49.7115
379. A. Göbel, T. Ruf, A. Fischer, K. Eberl, M. Cardona, J.P. Silveira, F. Briones, Optical phonons in isotope superlattices of GaAs, GaP, and GaSb studied by Raman scattering. Phys. Rev. B **59**, 12612–12621 (1999). 10.1103/PhysRevB.59.12612
380. Mathias Schubert, private communication (2006)
381. A.S. Barker Jr., A.J. Sievers, Optical studies of the vibrational properties of disordered solids. Rev. Mod. Phys. **47**, Suppl. No. 2, S1–S179 (1975). 10.1103/RevModPhys.47.S1.2
382. R.C. Newman, Local Vibrational mode spectroscopy of defects in III/V compounds. Semicond. Semimet. **38**, 117–187 (1993). 10.1016/S0080-8784(08)62800-8
383. M. Stavola, Vibrational spectroscopy of light element impurities in semiconductors. Semicond. Semimet. **51B**, 153–224 (1999). 10.1016/S0080-8784(08)62976-2
384. M.D. McCluskey, Local vibrational modes of impurities in semiconductors. J. Appl. Phys. **87**, 3593–3617 (2000). 10.1063/1.372453
385. L. Hoffmann, J.C. Bach, B. Bech Nielsen, P. Leary, R. Jones, S. Öberg, Substitutional carbon in germanium. Phys. Rev. B **55**, 11167–11173 (1997). 10.1103/PhysRevB.55.11167
386. F. Thompson, R.C. Newman, Localized vibrational modes of light impurities in gallium phosphide. J. Phys. C: Solid State Phys. **4**, 3249–3257 (1971). 10.1088/0022-3719/4/18/030
387. M. Vandevyver, D.N. Talwar, Green's-function theory of impurity vibrations due to defect complexes in elemental and compound semiconductors. Phys. Rev. B **21**, 3405–3431 (1980). 10.1103/PhysRevB.21.3405
388. L. Genzel, T.P. Martin, C.H. Perry, Model for long-wavelength optical-phonon modes of mixed crystals. Phys. Status Solidi B **62**, 83–92 (1974). 10.1002/pssb.2220620108
389. I.F. Chang, S.S. Mitra, Application of a modified random-element-isodisplacement model to long-wavelength optic phonons of mixed crystals. Phys. Rev. **172**, 924–933 (1968). 10.1103/PhysRev.172.924
390. L.I. Deych, A. Yamilov, A.A. Lisyansky, Concept of local polaritons and optical properties of mixed polar crystals. Phys. Rev. B **62**, 6301–6316 (2000). 10.1103/PhysRevB.62.6301
391. H. von Wenckstern, R. Schmidt-Grund, C. Bundesmann, A. Müller, C.P. Dietrich, M. Stölzel, M. Lange, M. Grundmann, The (Mg,Zn)O alloy, in *Handbook of Zinc Oxide and Related Materials*, vol. 1 Materials, ed. by Z.C. Feng (Taylor and Francis/CRC Press, Florida, USA, 2012), pp. 257–320. 10.1201/b13072-14
392. Z.G. Hu, M. Strassburg, N. Dietz, A.G.U. Perera, A. Asghar, I.T. Ferguson, Composition dependence of the infrared dielectric functions in Si-doped hexagonal $Al_xGa_{1-x}N$ films on c-plane sapphire substrates. Phys. Rev. B **72**, 245326:1–10 (2005). 10.1103/PhysRevB.72.245326
393. M. Grundmann, Topological states of the diatomic linear chain: Effect of impedance matching to the fixed ends. New J. Phys. **22**, 083076:1–7 (2020). 10.1088/1367-2630/aba918
394. H.M. Kayaga, T. Soma, Temperature dependence of the linear thermal expansion coefficient for Si and Ge. Phys. Status Solidi B **129**, K5–K8 (1985). 10.1002/pssb.2221290149

395. A.S. Saada, *Elasticity, Theory and Applications* (Pergamon, New York, 1974)
396. P.N. Keating, Effect of invariance requirements on the elastic strain energy of crystals with application to the diamond structure. Phys. Rev. **145**, 637–645 (1966). 10.1103/PhysRev.145.637
397. A.-B. Chen, A. Sher, W.T. Yost, Elastic constants and related properties of semiconductor compounds and their alloys. Semicond. Semimet. **37**, 1–77 (1992). 10.1016/S0080-8784(08)62513-2
398. R.S. Lakes, Foam structures with a negative Poisson's ratio. Science **235**, 1038–1040 (1987). 10.1126/science.235.4792.1038
399. K.E. Evans, M.A. Nkansah, I.J. Hutchinson, S.C. Rogers, Molecular network design. Nature **353**, 124 (1991). 10.1038/353124a0
400. R.H. Baughman, Auxetic materials: Avoiding the shrink. Nature **425**, 667 (2003). 10.1038/425667a
401. R. Gatt, J.N. Grima, Negative compressibility. Phys. Status Solidi RRL **2**, 236–238 (2008). 10.1002/pssr.200802101
402. R.M. Martin, Elastic properties of ZnS structure semiconductors. Phys. Rev. B **1**, 4005–4011 (1970). 10.1103/PhysRevB.1.4005
403. R.M. Martin, Relation between elastic tensors of wurtzite and zinc-blende structure material. Phys. Rev. B **6**, 4546–4553 (1972). 10.1103/PhysRevB.6.4546 Erratum: Phys. Rev. B **20**, 818 (1979). 10.1103/PhysRevB.20.818.2
404. K. Kim, W.R.L. Lambrecht, B. Segall, Elastic constants and related properties of tetrahedrally bonded BN, AlN, GaN, and InN. Phys. Rev. B **53**, 16310–16326 (1996). 10.1103/PhysRevB.53.16310
405. A. Polian, M. Grimsditch, I. Grzegory, Elastic constants of gallium nitride. J. Appl. Phys. **79**, 3343–3344 (1996). 10.1063/1.361236
406. L.E. McNeil, M. Grimsditch, R.H. French, Vibrational spectroscopy of aluminum nitride. J. Am. Ceram. Soc. **76**, 1132–1136 (1993). 10.1111/j.1151-2916.1993.tb03730.x
407. C.F. Cline, H.L. Dunegan, G.W. Henderson, Elastic constants of hexagonal BeO, ZnS, and CdSe. J. Appl. Phys. **38**, 1944–1948 (1967). 10.1063/1.1709787
408. G. Carlotti, D. Fioretto, G. Socino, E. Verona, Brillouin scattering determination of the whole set of elastic constants of a single transparent film of hexagonal symmetry. J. Phys.: Cond. Matter **7**, 9147–9153 (1995). 10.1088/0953-8984/7/48/006
409. Ch.G. Van de Walle, Band lineups and deformation potentials in the model-solid theory. Phys. Rev. B **39**, 1871–1883 (1989). 10.1103/PhysRevB.39.1871
410. A.E. Romanov, T.J. Baker, S. Nakamura, J.S. Speck, Strain-induced polarization in wurtzite III-nitride semipolar layers. J. Appl. Phys. **100**, 023522:1–10 (2006). 10.1063/1.2218385
411. M. Grundmann, J. Zúñiga-Pérez, Pseudomorphic ZnO-based heterostructures: From polar through all semipolar to nonpolar orientations. Phys. Status Solidi B **253**, 351–360 (2016). 10.1002/pssb.201552535
412. M. Grundmann, Elastic Theory of pseudomorphic monoclinic and rhombohedral heterostructures. J. Appl. Phys. **124**, 185302:1–10 (2018). 10.1063/1.5045845
413. M. Lorenz, S. Hohenberger, E. Rose, M. Grundmann, Atomically stepped, pseudomorphic, corundum-phase $(Al_{1-x}Ga_x)_2O_3$ thin films ($0 \leq x < 0.08$) grown on R-plane sapphire. Appl. Phys. Lett. **113**, 231902:1–5 (2018). 10.1063/1.5059374
414. M. Grundmann, Strain in pseudomorphic monoclinic Ga_2O_3-based heterostructures. Phys. Status Solidi B **254**, 1700134:1–7 (2017). pssb.201700134
415. M. Grundmann, A most general and facile recipe for the calculation of heteroepitaxial strain. Phys. Status Solidi B **257**, 2000323:1–5 (2020). 10.1002/pssb.202000323
416. J.D. Eshelby, The determination of the elastic field of an ellipsoidal inclusion and related problems. Proc. Roy. Soc. Lond. A **241**, 376–396 (1957). 10.1098/rspa.1957.0133
417. M. Grundmann, O. Stier, D. Bimberg, InAs/GaAs pyramidal quantum dots: Strain distribution, optical phonons, and electronic structure. Phys. Rev. B **52**, 11969–11981 (1995). 10.1103/PhysRevB.52.11969
418. L.B. Freund, J.A. Floro, E. Chason, Extensions of the Stoney formula for substrate curvature to configurations with thin substrates or large deformations. Appl. Phys. Lett. **74**, 1987–1989 (1999). 10.1063/1.123722
419. M. Grundmann, Nanoscroll formation from strained layer heterostructures. Appl. Phys. Lett. **83**, 2444–2446 (2003). 10.1063/1.1613366
420. G.G. Stoney, The tension of metallic films deposited by electrolysis. Proc. Roy. Soc. Lond. A **82**, 172–175 (1909). 10.1098/rspa.1909.0021
421. R. Beresford, J. Yin, K. Tetz, E. Chason, Real-time measurements of stress relaxation in InGaAs/GaAs. J. Vac. Sci. Technol. B **18**, 1431–1434 (2000). 10.1116/1.591397
422. A. Krost, A. Dadgar, F. Schulze, R. Clos, K. Haberland, T. Zettler, Heteroepitaxy of GaN on silicon: In Situ measurements. Mat. Sci. Forum **483–485**, 1051–1056 (2005). 10.4028/www.scientific.net/MSF.483-485.1051
423. V.Y. Prinz, V.A. Seleznev, A.K. Gutakovsky, Self-formed InGaAs/GaAs nanotubes: Concept, fabrication, properties, in *Proceedings 24th International Conference Physics of Semiconductors* (Jerusalem, Israel, 1998) (World Scientific, Singapore, 1998), Th3-D5
424. X. Li, Strain induced semiconductor nanotubes: From formation process to device applications. J. Phys. C: Solid State Phys. **41**, 193001:1–12 (2008). 10.1088/0022-3727/41/19/193001

425. B. Schmidt, Minimal energy configurations of strained multi-layers. Calc. Var. **30**, 477–497 (2007). 10.1007/s00526-007-0099-4
426. O.G. Schmidt, N. Schmarje, C. Deneke, C. Müller, N.-Y. Jin-Phillipp, Three-dimensional nano-objects evolving from a two-dimensional layer technology. Adv. Mater. **13**, 756–759 (2001). 10.1002/1521-4095(200105)13:10%3C756::AID-ADMA756%3E3.0.CO;2-F
427. L. Zhang, E. Ruh, D. Grützmacher, L. Dong, D.J. Bell, B.J. Nelson, C. Schönenberger, Anomalous coiling of SiGe/Si and SiGe/Si/Cr helical nanobelts. Nano Lett. **6**, 1311–1317 (2006). 10.1021/nl052340u
428. J. Zang, F. Liu, Modified Timoshenko formula for bending of ultrathin strained bilayer films. Appl. Phys. Lett. **92**, 021905:1–3 (2008). 10.1063/1.2828043
429. Stefan Mendach, private communication (2006)
430. J.C. Bean, L.C. Feldman, A.T. Fiory, S. Nakahara, I.K. Robinson, Ge_xSi_{1-x}/Si strained-layer superlattice grown by molecular beam epitaxy. J. Vac. Sci. Technol. A **2**, 436–440 (1984). 10.1116/1.572361
431. R. Hull, J.C. Bean, Nucleation of misfit dislocations in strained-layer epitaxy in the Ge_xSi_{1-x}/Si system. J. Vac. Sci. Technol. A **7**, 2580–2585 (1989). 10.1116/1.575800
432. J.W. Matthews, A.E. Blakeslee, Defects in epitaxial multilayers. I. Misfit dislocations. J. Cryst. Growth **27**, 118–125 (1974). 10.1016/S0022-0248(74)80055-2
433. J.W. Matthews, A.E. Blakeslee, Defects in epitaxial multilayers. II. Dislocation pile-ups, threading dislocations, slip lines and cracks. J. Cryst. Growth **29**, 273–280 (1975). 10.1016/0022-0248(75)90171-2
434. R. People, J.C. Bean, Calculation of critical layer thickness versus lattice mismatch for Ge_xSi_{1-x}/Si strained-layer heterostructures. Appl. Phys. Lett. **47**, 322–324 (1985). 10.1063/1.96206
435. F.C. Frank, J. van der Merwe, One-dimensional dislocations. I. Static theory. Proc. Roy. Soc. Lond. A **198**, 205–216 (1949). 10.1098/rspa.1949.0095
436. F.C. Frank, J. van der Merwe, One-dimensional dislocations. II. Misfitting monolayers and oriented overgrowth. Proc. Roy. Soc. Lond. A **198**, 216–225 (1949). 10.1098/rspa.1949.0096
437. J.H. van der Merwe, Crystal interfaces. Part II. Finite overgrowths. J. Appl. Phys. **34**, 123–127 (1962). 10.1063/1.1729051 Erratum: J. Appl. Phys. **34**, 3420 (1963). 10.1063/1.1729218
438. J.R. Willis, S.C. Jain, R. Bullough, The energy of an array of dislocations: Implications for strain relaxation in semiconductor heterostructures. Philos. Mag. A **62**, 115–129 (1990). 10.1080/01418619008244339
439. B.W. Dodson, J.Y. Tsao, Relaxation of strained-layer semiconductor structures via plastic flow. Appl. Phys. Lett. **51**, 1325–1327 (1987). 10.1063/1.98667
440. E. Kasper, H.J. Herzog, H. Kibbel, A one-dimensional SiGe superlattice grown by UHV epitaxy. Appl. Phys. **8**, 199–205 (1975). 10.1007/BF00896611
441. K.L. Kavanagh, M.A. Capano, L.W. Hobbs, J.C. Barbour, P.M.J. Marée, W. Schaff, J.W. Mayer, D. Pettit, J.M. Woodall, J.A. Stroscio, R.M. Feenstra, Asymmetries in dislocation densities, surface morphology, and strain of GalnAs/GaAs single heterolayers. J. Appl. Phys. **64**, 4843–4852 (1988). 10.1063/1.341232
442. M. Grundmann, U. Lienert, D. Bimberg, A. Fischer-Colbrie, J.N. Miller, Anisotropic and inhomogeneous strain relaxation in pseudomorphic $In_{0.23}Ga_{0.77}As$/GaAs quantum wells. Appl. Phys. Lett. **55**, 1765–1767 (1989). 10.1063/1.102212
443. M. Grundmann, Universal relation for the orientation of dislocations from prismatic glide systems in hexagonal and rhombohedral strained heterostructures. Appl. Phys. Lett. **116**, 082104:1–3 (2020). 10.1063/1.5140977
444. P. Quadbeck, Ph. Ebert, K. Urban, J. Gebauer, R. Krause-Rehberg, Effect of dopant atoms on the roughness of III-V semiconductor cleavage surfaces. Appl. Phys. Lett. **76**, 300–302 (2000). 10.1063/1.125726
445. J.E. Ayers, Compliant substrates for heteroepitaxial semiconductor devices: Theory, experiment, and current directions. J. Electr. Mater. **37**, 1511–1523 (2008). 10.1007/s11664-008-0504-6
446. Eike Weber, private communication
447. X.F. Brun, S.N. Melkote, Analysis of stresses and breakage of crystalline silicon wafers during handling and transport. Solar Energy Mater. Solar Cells **93**, 1238–1247 (2009). 10.1016/j.solmat.2009.01.016
448. H.J. Möller, C. Funke, M. Rinio, S. Scholz, Multicrystalline silicon for solar cells. Thin Solid Films **487**, 179–187 (2005). 10.1016/j.tsf.2005.01.061
449. P.S. Dominguez, J.M. Fernandez, Introduction of thinner monocrystalline silicon wafers in an industrial cell-manufacturing facility, in *Proceedings 20th EU PVSEC* (Barcelona, Spain, 2005), pp. 903–905
450. P.-Y. Chen, M.-H. Tsai, W.-K. Yeh, M.-H. Jing, Y. Chang, Investigation of the relationship between whole-wafer strength and control of its edge engineering. Jpn. J. Appl. Phys. **48**, 126503:1–6 (2009). 10.1143/JJAP.48.126503
451. C. Kittel, *Quantum Theory of Solids*, 2nd edn. (Wiley, New York, 1987)
452. G. Dresselhaus, Spin-orbit coupling effects in zinc blende structures. Phys. Rev. **100**, 580–586 (1955). 10.1103/PhysRev.100.580
453. J.-W. Luo, G. Bester, A. Zunger, Full-zone spin splitting for electrons and holes in bulk GaAs and GaSb. Phys. Rev. Lett. **102**, 056405:1–4 (2009). 10.1103/PhysRevLett.102.056405
454. E.I. Rashba, Properties of semiconductors with an extremum loop. I. Cyclotron and combinatorial resonance in a magnetic field perpendicular to the plane of the loop. Fiz. Tverd. Tela **2**, 1224–1238 (1960) [Sov. Phys. Solid State **2**, 1109–1122 (1960)]

455. Yu.A. Bychkov, É.I. Rashba, Properties of a 2D electron gas with lifted spectral degeneracy. Pis'ma Zh. Èksp. Teor. Fiz. **39**, 66 (1984) [JETP Lett. **39**, 78–81 (1984)]
456. S.G. Ganichev, L.E. Golub, Interplay of Rashba/Dresselhaus spin splittings probed by photogalvanic spectroscopy—A review. Phys. Status Solidi B **251**, 1801–1823 (2014). 10.1002/pssb.201350261
457. G.F. Koster, J.O. Dimmock, R.G. Wheeler, H. Statz, *Properties of the Thirty-Two Point Groups* (MIT, Cambridge, 1963)
458. D.G. Bell, Group theory and crystal lattices. Rev. Mod. Phys. **26**, 311–320 (1954). 10.1103/RevModPhys.26.311
459. R.H. Parmentier, Symmetry properties of the energy bands of the zinc blende structure. Phys. Rev. **100**, 573–579 (1955). 10.1103/PhysRev.100.573
460. M. Glasser, Symmetry properties of the wurtzite structure. J. Phys. Chem. Solids **10**, 229–241 (1959). 10.1016/0022-3697(59)90080-0
461. L.C.L.Y. Voon, M. Willatzen, *The k · p Method* (Springer, Berlin, 2009). 10.1007/978-3-540-92872-0
462. L.P. Bouckaert, R. Smoluchowski, E. Wigner, Theory of Brillouin zones and symmetry properties of wave functions in crystals. Phys. Rev. **50**, 58–67 (1936). 10.1103/PhysRev.50.58
463. M.Z. Hasan, C.L. Kane, Topological insulators. Rev. Mod. Phys. **82**, 3045–3067 (2010). 10.1103/RevModPhys.82.3045
464. S.-Q. Shen, *Topological Insulators, Dirac Equation in Condensed Matter*, 2nd edn. (Springer Nature, Singapore, 2017). 10.1007/978-981-10-4606-3
465. J. Zak, Berry's phase for energy bands in solids. Phys. Rev. Lett. **62**, 2747–2750 (1989). 10.1103/PhysRevLett.62.2747
466. D. Shin, S.A. Sato, H. Hübener, U. De Giovannini, J. Kima, N. Park, A. Rubio, Unraveling materials Berry curvature and Chern numbers from real-time evolution of Bloch states. PNAS **116**, 4135–4140 (2019). 10.1073/pnas.1816904116
467. J.R. Chelikowsky, M.L. Cohen, Nonlocal pseudopotential calculations for the electronic structure of eleven diamond and zinc-blende semiconductors. Phys. Rev. B **14**, 556–582 (1976). 10.1103/PhysRevB.14.556
468. R. Dalven, Electronic structure of PbS, PbSe, and PbTe. Solid State Phys. **28**, 179–224 (1973). 10.1016/S0081-1947(08)60203-9
469. A. Schleife, F. Fuchs, J. Furthmüller, F. Bechstedt, First-principles study of ground- and excited-state properties of MgO, ZnO, and CdO polymorphs. Phys. Rev. B **73**, 245212:1–14 (2006). 10.1103/PhysRevB.73.245212
470. H. Dixit, R. Saniz, S. Cottenier, D. Lamoen, B. Partoens, Electronic structure of transparent oxides with the Tran–Blaha modified Becke–Johnson potential. J. Phys.: Cond. Matter **24**, 205503:1–9 (2012). 10.1088/0953-8984/24/20/205503
471. J.E. Jaffe, A. Zunger, Electronic structure of the ternary chalcopyrite semiconductors $CuAlS_2$, $CuGaS_2$, $CuInS_2$, $CuAlSe_2$, $CuGaSe_2$, and $CuInSe_2$. Phys. Rev. B **28**, 5822–5847 (1983). 10.1103/PhysRevB.28.5822
472. S. Limpijumnong, S.N. Rashkeev, W.R.L. Lambrecht, Electronic structure and optical properties of $ZnGeN_2$. MRS Internet J. Nitride Semicond. Res. **4**(S1), 600–605 (1999). 10.1557/S1092578300003112
473. W. Rehwald, Band structure of spinel-type semiconductors. Phys. Rev. **155**, 861–868 (1967). 10.1103/PhysRev.155.861
474. H. Dixit, N. Tandon, S. Cottenier, R. Saniz, D. Lamoen, B. Partoens, V. Van Speybroeck, M. Waroquier, Electronic structure and band gap of zinc spinel oxides beyond LDA: $ZnAl_2O_4$, $ZnGa_2O_4$ and $ZnIn_2O_4$. New J. Phys. **13**, 063002:1–11 (2011). 10.1088/1367-2630/13/6/063002
475. R. Ahuja, O. Eriksson, B. Johansson, Electronic and optical properties of $BaTiO_3$ and $SrTiO_3$. J. Appl. Phys. **90**, 1854–1859 (2001). 10.1063/1.1384862
476. E.D. Indari, T.D.K. Wungu, R. Hidayat, Ab-Initio calculation of electronic structure of lead halide perovskites with formamidinium cation as an active material for perovskite solar cells. IOP Conf Ser.: J. Phys.: Conf. Ser. **877**, 012054:1–6 (2017). 10.1088/1742-6596/877/1/012054
477. P. Pitriana, T.D.K. Wungu, Herman, R. Hidayat, The characteristics of band structures and crystal binding in all-inorganic perovskite $APbBr_3$ studied by the first principle calculations using the Density Functional Theory (DFT) method. Results Phys. **15**, 102592:1–7 (2019). 10.1016/j.rinp.2019.102592
478. S. Tao, I. Schmidt, G. Brocks, J. Jiang, I. Tranca, K. Meerholz, S. Olthof, Absolute energy level positions in tin- and lead-based halide perovskites. Nature Commun. **10**, 2560:1–10 (2019). 10.1038/s41467-019-10468-7
479. L. Protesescu, S. Yakunin, M.I. Bodnarchuk, F. Krieg, R. Caputo, C.H. Hendon, R.X. Yang, A. Walsh, M.V. Kovalenko, Nanocrystals of cesium lead halide perovskites ($CsPbX_3$, X=Cl, Br, and I): Novel optoelectronic materials showing bright emission with wide color gamut. Nano Lett. **15**, 3592–3696 (2015). 10.1021/nl5048779
480. Y. Iso, T. Isobe, Review - Synthesis, luminescent properties, and stabilities of cesium lead halide perovskite nanocrystals. ECS. J. Solid State Sci. Technol. **7**, R3040–R3045 (2018). 10.1149/2.0101801jss
481. B. Seraphin, Über ein ein-dimensionales Modell halbleitender Verbindungen vom Typus $A^{III}B^{V}$, Z. Naturf. **9a**, 450–456 (1954). 10.1515/zna-1954-0511
482. D.S. Saxon, R.A. Hutner, Some electronic properties of a one-dimensional crystal model. Philips Res. Rep. **4**, 81–122 (1949)

483. I. Adawi, One-dimensional treatment of the effective mass in semiconductors. Phys. Rev. **105**, 789–792 (1957). 10.1103/PhysRev.105.789
484. J. Wu, W. Walukiewicz, Band gaps of InN and group III nitride alloys. Superlatt. Microstruct. **34**, 63–75 (2003). 10.1016/j.spmi.2004.03.069
485. J.E. Bernard, A. Zunger, Electronic Structure of ZnS, ZnSe, ZnTe, and their pseudobinary alloys. Phys. Rev. B **36**, 3199–3228 (1987). 10.1103/PhysRevB.36.3199
486. E.W. Williams, V. Rehn, Electroreflectance Studies of InAs, GaAs and (Ga, In)As alloys. Phys. Rev. **172**, 798–810 (1968). 10.1103/PhysRev.172.798
487. K.-R. Schulze, H. Neumann, K. Unger, Band structure of $Ga_{1-x}In_xAs$. Phys. Status Solidi B **75**, 493–500 (1976). 10.1002/pssb.2220750211
488. J. Wu, W. Walukiewicz, K.M. Yu, J.W. Ager III, S.X. Li, E.E. Haller, H. Lu, W.J. Schaff, Universal bandgap bowing in group-III nitride alloys. Solid State Commun. **127**, 411–414 (2003). 10.1016/S0038-1098(03)00457-5
489. R. Braunstein, A.R. Moore, F. Herman, Intrinsic optical absorption in germanium-silicon alloys. Phys. Rev. **109**, 695–710 (1958). 10.1103/PhysRev.109.695
490. D.J. Wolford, W.Y. Hsu, J.D. Dow, B.G. Streetman, Nitrogen trap in the semiconductor alloys $GaAs_{1-x}P_x$ and $Al_xGa_{1-x}As$. J. Lumin. **18**(19), 863–867 (1979). 10.1016/0022-2313(79)90252-7
491. R. Schmidt, B. Rheinländer, M. Schubert, D. Spemann, T. Butz, J. Lenzner, E.M. Kaidashev, M. Lorenz, M. Grundmann, Dielectric functions (1 to 5 eV) of wurtzite $Mg_xZn_{1-x}O$ ($x \leq 0.29$) thin films. Appl. Phys. Lett. **82**, 2260–2262 (2003). 10.1063/1.1565185
492. R. Schmidt-Grund, A. Carstens, B. Rheinländer, D. Spemann, H. Hochmut, G. Zimmermann, M. Lorenz, M. Grundmann, C.M. Herzinger, M. Schubert, Refractive indices and band-gap properties of rocksalt $Mg_xZn_{1-x}O$ ($0.68 \leq x \leq 1$). J. Appl. Phys. **99**, 123701:1–7 (2006). 10.1063/1.2205350
493. S. Larach, R.E. Shrader, C.F. Stocker, Anomalous variation of band gap with composition in zinc sulfo- and seleno-tellurides. Phys. Rev. **108**, 587–589 (1957). 10.1103/PhysRev.108.587
494. S. Merita, T. Krämer, B. Mogwitz, B. Franz, A. Polity, B.K. Meyer, Oxygen in sputter-deposited ZnTe thin films. Phys. Status Solidi C **3**, 960–963 (2006). 10.1002/pssc.200564637
495. B. Kramer, A pseudopotential approach for the Green's function of electrons in amorphous solids. Phys. Status Solidi **41**, 649–658 (1970). 10.1002/pssb.19700410220
496. B. Kramer, Electronic structure and optical properties of amorphous germanium and silicon. Phys. Status Solidi B **47**, 501–510 (1971). 10.1002/pssb.2220470215
497. J.A. van Vechten, *A Simple Man's View of the Thermochemistry of Semiconductors, Handbook on Semiconductors*, vol. 3 (North Holland, Amsterdam, 1980), pp. 1–111
498. J. Hartung, L.Å. Hansson, J. Weber, Temperature dependence of the indirect gap in silicon, in *Proceedings of the 20th International Conference on the Physics of Semiconductors Thessaloniki, Greece*, E.M. Anastassakis, J.D. Joannopoulos, eds. (World Scientific, Singapore, 1990), pp. 1875–1878
499. Y.W. Tsang, M.L. Cohen, Calculation of the temperature dependence of the energy gaps of PbTe and SnTe. Phys. Rev. B **3**, 1254–1261 (1971). 10.1103/PhysRevB.3.1254
500. I. Tanaka, K. Sugimoto, D. Kim, H. Nishimura, M. Nakayama, Control of temperature dependence of exciton energies in CuI-CuBr alloy thin films grown by vacuum deposition. Int. J. Mod. Phys. B **15**, 3977–3980 (2001). 10.1142/S0217979201009141
501. J. Serrano, Ch. Schweitzer, C.T. Lin, K. Reinmann, M. Cardona, D. Fröhlich, Electron-phonon renormalization of the absorption edge of the cuprous halides. Phys. Rev. B **65**, 125110:1–7 (2002). 10.1103/PhysRevB.65.125110
502. J. Bhosale, A.K. Ramdas, A. Burger, A. Muñoz, A.H. Romero, M. Cardona, R. Lauck, R.K. Kremer, Temperature dependence of band gaps in semiconductors: Electron-phonon interaction. Phys. Rev. B **86**, 195208:1–10 (2012). 10.1103/PhysRevB.86.195208
503. Y. Varshni, Temperature dependence of the energy gap in semiconductors. Physica **34**, 149–154 (1967). 10.1016/0031-8914(67)90062-6
504. L. Viña, S. Logothetidis, M. Cardona, Temperature dependence of the dielectric function of germanium. Phys. Rev. B **30**, 1979–1991 (1984). 10.1103/PhysRevB.30.1979
505. K.P. O'Donnell, X. Chen, Temperature dependence of semiconductor band gaps. Appl. Phys. Lett. **58**, 2924–2926 (1991). 10.1063/1.104723
506. R. Pässler, Dispersion-related description of temperature dependencies of band gaps in semiconductors. Phys. Rev. B **66**, 085201:1–18 (2002) 10.1103/PhysRevB.66.085201
507. D. Brunner, H. Angerer, E. Bustarret, F. Freudenberg, R. Höpler, R. Dimitrov, O. Ambacher, M. Stutzmann, Optical constants of epitaxial AlGaN films and their temperature dependence. J. Appl. Phys. **82**, 5090–5096 (1997). 10.1063/1.366309
508. R. Schmidt-Grund, N. Ashkenov, M.M. Schubert, W. Czakai, D. Faltermeier, G. Benndorf, H. Hochmuth, M. Lorenz, M. Grundmann, Temperature-dependence of the refractive index and the optical transitions at the fundamental band-gap of ZnO. AIP Conf. Proc. **893**, 271–272 (2007). 10.1063/1.2729872

509. N. Garro, A. Cantarero, M. Cardona, A. Göbel, T. Ruf, K. Eberl, Dependence of the lattice parameters and the energy gap of zinc-blende-type semiconductors on isotopic masses. Phys. Rev. B **54**, 4732–4740 (1996). 10.1103/PhysRevB.54.4732
510. E.O. Kane, Band structure of indium antimonide. J. Phys. Chem. Solids **1**, 249–261 (1957). 10.1016/0022-3697(57)90013-6
511. C. Hermann, C. Weisbuch, $\overrightarrow{k} \cdot \overrightarrow{p}$ perturbation theory in III-V compounds and alloys: A reexamination. Phys. Rev. B **15**, 823–833 (1977). 10.1103/PhysRevB.15.823
512. Y.-N. Xu, W.Y. Ching, Electronic, optical, and structural properties of some wurtzite crystals. Phys. Rev. B **48**, 4335–4351 (1993). 10.1103/PhysRevB.48.4335
513. M. Oshikiri, F. Aryasetiawan, Y. Imanaka, G. Kido, Quasiparticle effective-mass theory in semiconductors. Phys. Rev. B **66**, 125204:1–4 (2002). 10.1103/PhysRevB.66.125204
514. F. Nava, C. Canali, C. Jacoboni, L. Reggiani, S.F. Kozlov, Electron effective masses and lattice scattering in natural diamond. Solid State Commun. **33**, 475–477 (1980). 10.1016/0038-1098(80)90447-0
515. G. Dresselhaus, A.F. Kip, C. Kittel, Cyclotron resonance of electrons and holes in silicon and germanium crystals. Phys. Rev. **98**, 368–384 (1955). 10.1103/PhysRev.98.368
516. S. Shokhovets, G. Gobsch, O. Ambacher, Conduction band parameters of ZnO. Superlatt. Microstruct. **39**, 299–305 (2006). 10.1016/j.spmi.2005.08.052
517. W.S. Baer, R.N. Dexter, Electron cyclotron resonance in CdS. Phys. Rev. **135**, A1388–A1393 (1964). 10.1103/PhysRev.135.A1388
518. W. Shockley, Cyclotron resonance, magnetoresistance, and Brillouin zones in semiconductors. Phys. Rev. **90**, 491 (1953). 10.1103/PhysRev.90.491
519. P. Pfeffer, W. Zawadzki, Conduction electrons in GaAs: Five-level $k \cdot p$ theory and polaron effects. Phys. Rev. B **41**, 1561–1576 (1990). 10.1103/PhysRevB.41.1561
520. M. Cardona, N.E. Christensen, G. Fasol, Relativistic band structure and spin-orbit splitting of zinc-blende-type semiconductors. Phys. Rev. B **38**, 1806–1827 (1988). 10.1103/PhysRevB.38.1806
521. Dieter Bimberg, private communication, original authorship unknown
522. G. Ottaviani, L. Reggiani, C. Canali, F. Nava, A. Alberigi-Quaranta, Hole drift velocity in silicon. Phys. Rev. B **12**, 3318–3329 (1975). 10.1103/PhysRevB.12.3318
523. M. Cardona, F.H. Pollak, Energy-band structure of germanium and silicon: The $k \cdot p$ method. Phys. Rev. **142**, 530–543 (1966). 10.1103/PhysRev.142.530
524. M.I. Eremets, Semiconducting diamond. Semicond. Sci. Technol. **6**, 439–444 (1991). 10.1088/0268-1242/6/6/004
525. J.J. Hopfield, Fine structure in the optical absorption edge of anisotropic crystals. J. Phys. Chem. Solids **15**, 97–107 (1960). 10.1016/0022-3697(60)90105-0
526. J.L. Shay, B. Tell, L.M. Schiavone, H.M. Kasper, F. Thiel, Energy bands of $AgInS_2$ in the chalcopyrite and orthorhombic structures. Phys. Rev. B **9**, 1719–1723 (1974). 10.1103/PhysRevB.9.1719
527. D.L. Carter, R.T. Bates, eds., *Physics of Semimetals and Narrow-Gap Semiconductors* (Pergamon Press, 1971)
528. G.A. Saunders, Semimetals and narrow gap semiconductors. Contemp. Phys. **14**, 149–166 (1973). 10.1080/00107517308213730
529. W. Feng, D. Xiao, J. Ding, Y. Yuo, Three-dimensional topological insulators in I–III–VI_2 and II–IV–V_2 chalcopyrite semiconductors. Phys. Rev. Lett. **106**, 016402:1–4 (2011). 10.1103/PhysRevLett.106.016402
530. G. Bastard, Dielectric anomalies in extremely non-parabolic zero-gap semiconductors. J. Phys. C: Solid State Phys. **14**, 839–845 (1981). 10.1088/0022-3719/14/6/010
531. F. Teppe, M. Marcinkiewicz, S.S. Krishtopenko, S. Ruffenach, C. Consejo, A.M. Kadykov, W. Desrat, D. But, W. Knap, J. Ludwig, S. Moon, D. Smirnov, M. Orlita, Z. Jiang, S.V. Morozov, V.I. Gavrilenko, N.N. Mikhailov, S.A. Dvoretskii, Temperature-driven massless Kane fermions in HgCdTe crystals. Nature Commun. **7**, 12576:1–6 (2016). 10.1038/ncomms12576
532. J.O. Dimmock, I. Melngailis, A.J. Strauss, Band structure and laser action in $Pb_xSn_{1-x}Te$. Phys. Rev. Lett. **16**, 1193–1196 (1966). 10.1103/PhysRevLett.16.1193
533. G.L. Bir, G.E. Pikus, *Symmetry and Strain-induced Effects in Semiconductors* (Wiley, New York, 1974)
534. G.E. Pikus, G.L. Bir, Effect of Deformation on the Hole Energy Spectrum of Germanium and Silicon. Fiz. Tverd. Tela **1**, 1642–1658 (1956) [Sov. Phys. Solid State **1**, 1502–1517 (1959)]
535. N.E. Christensen, Electronic structure of GaAs under strain. Phys. Rev. B **30**, 5753–5765 (1984). 10.1103/PhysRevB.30.5753
536. Y. Zhang, Motion of electrons in semiconductors under inhomogeneous strain with application to laterally confined quantum wells. Phys. Rev. B **49**, 14352–14366 (1994). 10.1103/PhysRevB.49.14352
537. A.R. Goñi, K. Strössner, K. Syassen, M. Cardona, Pressure dependence of direct and indirect optical absorption in GaAs. Phys. Rev. B **36**, 1581–1587 (1987). 10.1103/PhysRevB.36.1581
538. W. Shan, W. Walukiewicz, J.W. Ager III, E.E. Haller, J.F. Geisz, D.J. Friedman, J.M. Olson, S.R. Kurtz, Band anticrossing in GaInNAs alloys. Phys. Rev. Lett. **82**, 1221–1224 (1999). 10.1103/PhysRevLett.82.1221

539. S.L. Chuang, C.S. Chang, $k \cdot p$ method for strained wurtzite semiconductors. Phys. Rev. B **54**, 2491–2504 (1996). 10.1103/PhysRevB.54.2491
540. M. Kumagai, S.L. Chuang, H. Ando, Analytical solutions of the block-diagonalized Hamiltonian for strained wurtzite semiconductors. Phys. Rev. B **57**, 15303–15314 (1998). 10.1103/PhysRevB.57.15303
541. C. Herring, E. Vogt, Transport and deformation-potential theory for many-valley semiconductors with anisotropic scattering. Phys. Rev. **101**, 944–961 (1956). 10.1103/PhysRev.101.944
542. M.V. Fischetti, S.E. Laux, Band structure, deformation potentials, and carrier mobility in strained Si, Ge, and SiGe alloys. J. Appl. Phys. **80**, 2234–2252 (1996). 10.1063/1.363052
543. D. Aspnes, M. Cardona, Strain dependence of effective masses in tetrahedral semiconductors. Phys. Rev. B **17**, 726–740 (1978). 10.1103/PhysRevB.17.726
544. P.R.C. Kent, A. Zunger, Theory of electronic structure evolution in GaAsN and GaPN alloys. Phys. Rev. B **64**, 115208:1–23 (2001). 10.1103/PhysRevB.64.115208
545. J. Wu, W. Shan, W. Walukiewicz, Band anticrossing in highly mismatched III-V semiconductor alloys. Semicond. Sci. Technol. **17**, 860–869 (2002). 10.1088/0268-1242/17/8/315
546. J. Chelikowsky, D.J. Chadi, M.L. Cohen, Calculated valence-band densities of states and photoemission spectra of diamond and zinc-blende semiconductors. Phys. Rev. B **8**, 2786–2794 (1973). 10.1103/PhysRevB.8.2786
547. N.F. Mott, Electrons in disordered structures. Advances in Phys. **16**, 49–144 (1967). 10.1080/00018736700101265
548. M.H. Cohen, H. Fritzsche, S.R. Ovshinsky, Simple band model for amorphous semiconductor alloys. Phys. Rev. Lett. **22**, 1065–1068 (1969). 10.1103/PhysRevLett.22.1065
549. E.A. Davis, N.F. Mott, Conduction in non-crystalline systems. V. Conductivity, optical absorption and photoconductivity in amorphous semiconductors, Philos. Mag. **22**, 903–922 (1970). 10.1080/14786437008221061
550. J.M. Marshall, A.E. Owen, Drift mobility studies in vitreous arsenic triselenide. Philos. Mag. **24**, 1281–1305 (1971). 10.1080/14786437108217413
551. D.A. Drabold, U. Stephan, J. Dong, S.M. Nakhmanson, The structure of electronic states in amorphous silicon. J. Molec. Graphics and Modelling **17**, 285–291, 330–332 (1999). 10.1016/S1093-3263(99)00036-4
552. W. Körner, C. Elsässer, Density-functional theory study of stability and subgap states of crystalline and amorphous Zn-Sn-O. Thin Solid Films **555**, 81–86 (2014). 10.1016/j.tsf.2013.05.146
553. S. Sallis, K.T. Butler, N.F. Quackenbush, D.S. Williams, M. Junda, D.A. Fischer, J.C. Woicik, N.J. Podraza, B.E. White, Jr., A. Walsh, L.F.J. Piper, Origin of deep subgap states in amorphous indium gallium zinc oxide: Chemically disordered coordination of oxygen. Appl. Phys. Lett. **104**, 232108:1–4 (2014). 10.1063/1.4883257
554. W. Pauli 1931 in a letter from New York to R. Peierls, in: Wolfgang Pauli, Scientific Correspondence with Bohr, Einstein, Heisenberg a.o. Volume II: 1930–1939, K. von Meyenn, ed. (Springer, Berlin, 1985), Nr. 287, p. 94; Lateron Pauli complains to Peierls "... daß Sie immer noch nicht von der Physik des festen Körpers losgekommen sind." (ibid, Nr. 310, p. 163). 10.1007/978-3-540-78801-0
555. W. Shockley, *Electrons and Holes in Semiconductors with Applications to Transistor Electronics* (D. van Nostrand, New York, 1950)
556. D. Bednarczyk, J. Bernarczyk, The approximation of the Fermi-Dirac integral $F_{1/2}(\eta)$. Phys. Lett. **64A**, 409–401 (1978). 10.1016/0375-9601(78)90283-9
557. X. Aymerich-Humet, F. Serra-Mestres, J. Millán, An analytical approximation for the Fermi-Dirac integral $F_{3/2}(\eta)$. Solid State Electron. **24**, 981–982 (1981). 10.1016/0038-1101(81)90121-0
558. X. Aymerich-Humet, F. Serra-Mestres, J. Millán, A generalized approximation of the Fermi-Dirac integrals. J. Appl. Phys. **54**, 2850–2851 (1983). 10.1063/1.332276
559. K. Unger, Reversible formulae to approximate Fermi integrals. Phys. Status Solidi B **149**, K141–K144 (1988). 10.1002/pssb.2221490254
560. J. McDougall, E.C. Stoner, The computation of Fermi-Dirac functions. Phil. Trans. Roy. Soc. Lond.**237**, 67–104 (1938). 10.1098/rsta.1938.0004
561. A.J. MacLeod, Algorithm 779: Fermi-Dirac functions of order $-1/2$, $1/2$, $3/2$, $5/2$. ACM Trans. Math. Softw. **24**, 1–12 (1998). 10.1145/285861.285862
562. A.B. Sproul, M.A. Green, J. Zhao, Improved value for the silicon intrinsic carrier concentration at 300 K. Appl. Phys. Lett. **57**, 255–257 (1990). 10.1063/1.349645
563. A.B. Sproul, M.A. Green, Intrinsic carrier concentration and minority-carrier mobility of silicon from 77 to 300 K. J. Appl. Phys. **73**, 1214–1225 (1993). 10.1063/1.353288
564. M.A. Green, Intrinsic concentration, effective densities of states, and effective mass in silicon. J. Appl. Phys. **67**, 2944–2954 (1990). 10.1063/1.345414
565. K. Misiakos, D. Tsamakis, Accurate measurements of the silicon intrinsic carrier density from 78 to 340 K. J. Appl. Phys. **74**, 3293–3297 (1993). 10.1063/1.354551
566. B. Gudden, *Über die Elektrizitätsleitung in Halbleitern*, Sitzungsber. Phys.-Med. Soz. Erlangen **62**, 289–302 (1930)
567. B. Gudden, Elektrische Leitfähigkeit elektronischer Halbleiter, in: *Ergebnisse der Exakten Naturwissenschaften*, ed. by Schriftleitung der "Naturwissenschaften" (Springer, Berlin, 1934), pp. 223–256. 10.1007/978-3-642-94250-1_5

568. M. Grundmann, F.-L. Schein, M. Lorenz, T. Böntgen, J. Lenzner, H. von Wenckstern, Cuprous iodide - a p-type transparent semiconductor: history and novel applications. Phys. Status Solidi A **210**, 1671–1703 (2013). 10.1002/pssa.201329349
569. A. Zunger, Practical doping principles. Appl. Phys. Lett. **83**, 57–59 (2003). 10.1063/1.1584074
570. M. Ramamoorthy, S.T. Pantelides, Complex dynamical phenomena in heavily arsenic doped silicon. Phys. Rev. Lett. **76**, 4753–4756 (1996). 10.1103/PhysRevLett.76.4753
571. S. Lany, J. Osorio-Guillén, A. Zunger, Origins of the doping asymmetry in oxides: Hole doping in NiO versus electron doping in ZnO. Phys. Rev. B **75**, 241203:1–4 (2007). 10.1103/PhysRevB.75.241203
572. W. Kohn, Shallow impurity states in semiconductors—The early years. Physica B **146**, 1–5 (1987). 10.1016/0378-4363(87)90046-5
573. A.K. Ramdas, Spectroscopy of shallow centers in semiconductors: Progress since 1960. Physica B **146**, 6–18 (1987). 10.1016/0378-4363(87)90047-7
574. S.M. Sze, K.K. Ng, *Physics of Semiconductor Devices*, 3rd edn. (Wiley, New York, 2007)
575. E.F. Schubert, *Doping in III–V Semiconductors* (Cambridge University Press, Cambridge, 1993). 10.1017/CBO9780511599828
576. H.A. Bethe, Theory of the boundary layer of crystal rectifiers. MIT Radiation Lab. Rep. **43–12**, 1–26 (1942)
577. U. Heim, Evidence for donor-acceptor recombination in InP by time-resolved photoluminescence spectroscopy. Solid State Commun. **7**, 445–447 (1969). 10.1016/0038-1098(69)90893-X
578. W. Kohn, J.M. Luttinger, Theory of donor states in silicon. Phys. Rev. **98**, 915–922 (1955). 10.1103/PhysRev.98.915
579. G. Feher, D.K. Wilson, E.A. Gere, Electron spin resonance experiments on shallow donors in germanium. Phys. Rev. Lett. **3**, 25–28 (1959). 10.1103/PhysRevLett.3.25
580. R. Kalish, The search for donors in diamond. Diamond Rel. Mater. **10**, 1749–1755 (2001). 10.1016/S0925-9635(01)00426-5
581. V.A. Karasyuk, D.G.S. Beckett, M.K. Nissen, A. Villemarie, T.W. Steiner, M.L.W. Thewalt, Fourier-transform magnetoluminescence spectroscopy of donor-bound excitons in GaAs. Phys. Rev. B **49**, 16381–16397 (1994). 10.1103/PhysRevB.49.16381
582. U. Kaufmann, J. Schneider, Point defects in GaP, GaAs, and InP. Adv. Electron. Electr. Phys. **58**, 81–141 (1982). 10.1016/S0065-2539(08)61022-7
583. W. Götz, N.M. Johnson, C. Chen, H. Liu, C. Kuo, W. Imler, Activation energies of Si donors in GaN. Appl. Phys. Lett. **68**, 3144–3146 (1996). 10.1063/1.115805
584. A.J. Ptak, L.J. Holbert, L. Ting, C.H. Swartz, M. Moldovan, N.C. Giles, T.H. Myersa, P. Van Lierde, C. Tian, R.A. Hockett, S. Mitha, A.E. Wickenden, D.D. Koleske, R.L. Henry, Controlled oxygen doping of GaN using plasma assisted molecular-beam epitaxy. Appl. Phys. Lett. **79**, 2740–2742 (2001). 10.1063/1.1403276
585. S. Teitler, R.F. Wallis, Note on semiconductor statistics. J. Phys. Chem. Solids **16**, 71–75 (1960). 10.1016/0022-3697(60)90074-3
586. B. Šantić, On the determination of the statistical characteristics of the magnesium acceptor in GaN. Superlatt. Microstruct. **36**, 445–453 (2004). 10.1016/j.spmi.2004.09.008
587. R.M. Dickstein, S.L. Titcomb, R.L. Anderson, Carrier concentration model for n-type silicon at low temperatures. J. Appl. Phys. **66**, 2437–2441 (1989). 10.1063/1.344253
588. J.S. Blakemore, Radiative Capture by Impurities in Semiconductors. Phys. Rev. **163**, 809–815 (1967). 10.1103/PhysRev.163.809
589. H.B. Bebb, Comments on radiative capture by impurities in semiconductors. Phys. Rev. B **5**, 4201–4203 (1972). 10.1103/PhysRevB.5.4201
590. J.W. Harrison, J.R. Hauser, Alloy scattering in ternary III-V compounds. Phys. Rev. B **13**, 5347–5350 (1976). 10.1103/PhysRevB.13.5347
591. V.W.L. Chin, T.L. Tansley, Alloy scattering and lattice strain effects on the electron mobility in $In_{1-x}Ga_xAs$. Solid State Electron. **34**, 1055–1063 (1991). 10.1016/0038-1101(91)90100-D
592. W. Zhao, D. Jena, Dipole scattering in highly polar semiconductor alloys. J. Appl. Phys. **96**, 2095–2101 (2004). 10.1063/1.1767615
593. R. Stratton, Dipole scattering from ion pairs in compensated semiconductors. J. Phys. Chem. Solids **23**, 1011–1017 (1962). 10.1016/0022-3697(62)90159-2
594. P.P. Debye, E.M. Conwell, Electrical properties of n-type germanium. Phys. Rev. **93**, 693–706 (1954). 10.1103/PhysRev.93.693
595. G.W. Brown, H. Grube, M.E. Hawley, Observation of buried phosphorus dopants near clean Si(100)-(2 × 1) surfaces with scanning tunneling microscopy. Phys. Rev. B **70**, 121301:1–4 (2004). 10.1103/PhysRevB.70.121301
596. A.T. Collins, A.W.S. Williams, The nature of the acceptor centre in semiconducting diamond. J. Phys. C: Solid State Phys. **4**, 1789–1800 (1971). 10.1088/0022-3719/4/13/030
597. K. Thonke, The boron acceptor in diamond. Semicond. Sci. Technol. **18**, S20–S26 (2003). 10.1088/0268-1242/18/3/303

598. H. Alves, *Defects, Doping and Compensation in Wide Bandgap Semiconductors*, Ph.D. Thesis, Universität Giessen (2003)
599. S. Fischer, C. Wetzel, E.E. Haller, B.K. Meyer, On p-type doping in GaN—Acceptor binding energies. Appl. Phys. Lett. **67**, 1298–1300 (1995). 10.1063/1.114403
600. W. Kohn, Shallow impurity states in silicon and germanium. Solid State Phys. **5**, 257–320 (1957). 10.1016/S0081-1947(08)60104-6
601. K.Ya. Shtivel'man, R.G. Useinov, Degeneracy multiplicity of the states of two-charge acceptors in semiconductors. Soviet Phys. J. **17**, 1439–1440 (1974). 10.1007/BF00891303
602. D.C. Look, *Electrical Characterization of GaAs Materials and Devices* (Wiley, New York, 1989)
603. E.M. Conwell, Hall effect and density of states in germanium. Phys. Rev. **99**, 1195–1198 (1955). 10.1103/PhysRev.99.1195
604. E.E. Haller, W.L. Hansen, F.S. Goulding, Physics of ultra-pure germanium. Adv. Phys. **30**, 93–138 (1981). 10.1080/00018738100101357
605. M.B. Johnson, O. Albrektsen, R.M. Feenstra, H.W.M. Salemink, Direct imaging of dopants in GaAs with cross-sectional scanning tunneling microscopy. Appl. Phys. Lett. **63**, 2923–2925 (1993). 10.1063/1.110274 Erratum: Appl. Phys. Lett. **64**, 1454 (1994). 10.1063/1.111999
606. A.M. Yakunin, A.Yu. Silov, P.M. Koenraad, J.H. Wolter, W. Van Roy, J. De Boeck, J.-M. Tang, M.E. Flatté, Spatial structure of an individual Mn acceptor in GaAs. Phys. Rev. Lett. **92**, 216806:1–4 (2004). 10.1103/PhysRevLett.92.216806
607. J.-M. Tang, M. Flatté, Multiband tight-binding model of local magnetism in $Ga_{1-x}Mn_xAs$. Phys. Rev. Lett. **92**, 047201:1–4 (2004). 10.1103/PhysRevLett.92.047201
608. J.S. Blakemore, *Semiconductor Statistics* (Pergamon Press, Oxford, 1962)
609. N.B. Hannay ed., *Semiconductors* (Reinhold Publ. Corp, New York, 1959)
610. G. Leibiger, *A^{III} B^{V}-Mischkristallbildung mit Stickstoff und Bor*, Ph.D. Thesis, Universität Leipzig (2003)
611. E. Ziegler, W. Siegel, Determination of two donor (majority) levels in semiconductors from Hall effect measurements. Crystal Res. Technol. **17**, 1015–1024 (1982). 10.1002/crat.2170170822
612. H.-J. Hoffmann, Defect-level analysis of semiconductors by a new differential evaluation of $n(1/t)$-characteristics. Appl. Phys. **19**, 307–312 (1979). 10.1007/BF00900474
613. M. Tao, A kinetic model for metalorganic chemical vapor deposition from trimethylgallium and arsine. J. Appl. Phys. **87**, 3554–3562 (2000). 10.1063/1.372380
614. G. Weyer, J.W. Petersen, S. Damgaard, H.L. Nielsen, J. Heinemeier, Site-selective doping of compound semiconductors by ion implantation of radioactive nuclei. Phys. Rev. Lett. **44**, 155–157 (1980). 10.1103/PhysRevLett.44.155
615. E. Antoncik, B.L. Gu, On the Mössbauer isomer shift studies of the electronic structure of Sn implanted $A^{III}B^{V}$ compounds. Hyperfine Interactions **14**, 257–269 (1983). 10.1007/BF02043477
616. R. Noufi, R. Axton, C. Herrington, S.K. Deb, Electronic properties versus composition of thin films of $CuInSe_2$. Appl. Phys. Lett. **45**, 668–670 (1994). 10.1063/1.95350
617. T.R. Paudel, A. Zakutayev, S. Lany, M. d'Avezac, A. Zunger, Doping rules and doping prototypes in A_2BO_4 spinel oxides. Adv. Funct. Mater. **21**, 4493–4501 (2011). 10.1002/adfm.201101469
618. J.D. Perkins, T.R. Paudel, A. Zakutayev, P. Ndione, P.A. Parilla, S. Lany, D.S. Ginley, Y. Shi, J.S. Bettinger, M.F. Toney, Inverse design approach to hole doping in ternary oxides: Enhancing p-type conductivity in cobalt oxide spinels. Phys. Rev. B **84**, 205207:1–8 (2011). 10.1103/PhysRevB.84.205207
619. N.F. Mott, *Metal-insulator Transitions* (Taylor and Francis, London, 1990)
620. V.I. Fistul, *Highly Doped Semiconductors* (Springer, New York, 1969). 10.1007/978-1-4684-8821-0
621. B.L. Crowder, W.N. Hammer, Shallow acceptor states in ZnTe and CdTe. Phys. Rev. **150**, 541–545 (1966). 10.1103/PhysRev.150.541
622. G.L. Pearson, J. Bardeen, electrical properties of pure silicon and silicon alloys containing boron and phosphorous. Phys. Rev. **75**, 865–883 (1949). 10.1103/PhysRev.75.865
623. G.E. Stillman, L.W. Cook, T.J. Roth, T.S. Low, B.J. Skromme, High-purity material, in *GaInAsP Alloy Semiconductors*, ed. by T.P. Pearsall (Wiley, New York, 1982), pp. 121–166
624. T.F. Lee, T.C. McGill, Variation of impurity-to-band activation energies with impurity density. J. Appl. Phys. **46**, 373–380 (1975). 10.1063/1.321346
625. M.L. Young, S.J. Bass, The electrical properties of undoped and oxygen- doped GaP grown by the liquid encapsulation technique. J. Phys. D: Appl. Phys. **4**, 995–1005 (1971). 10.1088/0022-3727/4/7/317
626. H.C. Casey Jr., F. Ermanis, K.B. Wolfstirn, Variation of electrical properties with Zn concentration in GaP. J. Appl. Phys. **40**, 2945–2958 (1969). 10.1063/1.1658106
627. K. Pakula, M. Wojdak, M. Palczewska, B. Suchanek, J.M. Baranowski, Luminescence and ESR spectra of GaN:Si below and above Mott transition. MRS Internet J. Nitride Semicond. Res. **3**, e34:1–4 (1998). 10.1557/S109257830000106X

628. G.R. James, A.W.R. Leitch, F. Omnès, M.C. Wagener, M. Leroux, Correlation of transport and optical properties of Si-doped $Al_{0.23}Ga_{0.77}N$. J. Appl. Phys. **96**, 1047–1052 (2004) (The printed paper title reads '$Al_{0.23}G_{0.77}N$'). 10.1063/1.1760235
629. M. Brandt, H. von Wenckstern, C. Meinecke, T. Butz, H. Hochmuth, M. Lorenz, M. Grundmann, Dopant activation in homoepitaxial MgZnO:P thin films. J. Vac. Sci. Technol. B **27**, 1604–1608 (2009). 10.1116/1.3086657
630. H. Kato, M. Sano, K. Miyamoto, T. Yao, Growth and characterization of Ga-doped ZnO layers on a-plane sapphire substrates grown by molecular beam epitaxy. J. Cryst. Growth **237–239**, 538–543 (2002). 10.1016/S0022-0248(01)01972-8
631. H. Kato, A. Ogawa, H. Kotani, M. Sano, T. Yao, Effects of polarity on MBE growth of undoped, Ga- and N-doped ZnO films, MRS Fall Meeting 2006, Boston, Symp. K ('Zinc Oxide and Related Materials'), K5.6 (2006)
632. Z.-L. Lu, W.-Q. Zou, M.-X. Xu, F.-M. Zhang, Y.-W. Du, Structural and electrical properties of single crystalline Ga-doped ZnO thin films grown by molecular beam epitaxy. Chin. Phys. Lett. **26**, 116102:1–4 (2009). 10.1088/0256-307X/26/11/116102
633. M.C. Wu, Y.K. Su, K.Y. Cheng, C.Y. Chang, Electrical and optical properties of heavily doped Mg- and Te-GaAs grown by liquid-phase epitaxy. Solid State Electron. **31**, 251–256 (1988). 10.1016/0038-1101(88)90137-2
634. M. Ogawa, T. Baba, Heavily Si-doped GaAs and AlAs/n-GaAs superlattice grown by molecular epitaxy. Jpn. J. Appl. Phys. **24**, L572–L574 (1985). 10.1143/JJAP.24.L572
635. T. Yamada, E. Tokumitsu, K. Saito, T. Akatsuka, M. Miyauchi, M. Konagai, K. Takahashi, Heavily carbon doped p-Type GaAs and GaAlAs grown by metalorganic molecular beam epitaxy. J. Cryst. Growth **95**, 145–149 (1989). 10.1016/0022-0248(89)90369-2
636. J.L. Liévin, F. Alexandre, C. Dubon-Chevallier, Molecular beam epitaxy of $Ga_{0.99}Be_{0.01}As$ for very high speed heterojunction bipolar transistors, in: *Properties of Impurity States in Superlattice Semiconductors*, NATO ASI Series B: Physics, Vol. 183, C.Y. Fong, I.P. Batra, S. Ciraci, eds. (Plenum, New York, 1988), pp. 19–28. 10.1007/978-1-4684-5553-3_3
637. W. Yang, J. Mathews, J.S. Williams, Hyperdoping of Si by ion implantation and pulsed laser melting. Mat. Sci. Semicond. Processing **62**, 103–114 (2017). 10.1016/j.mssp.2016.11.005
638. S. Zhou, F. Liu, S. Prucnal, K. Gao, M. Khalid, C. Baehtz, M. Posselt, W. Skorupa, M. Helm, Hyperdoping silicon with selenium: Solid versus liquid phase epitaxy. Sci. Rep. **5**, 8329:1–7 (2015). 10.1038/srep08329
639. J. Bourgoin, M. Lannoo, *Point Defects in Semiconductors II* (Springer, Berlin, 1983). 10.1007/978-3-642-81832-5
640. S.T. Pantelides, ed., *Deep Centers in Semiconductors* (Gordon and Breach, New York, 1986)
641. J.-W. Chen, A.G. Milnes, Energy levels in silicon. Ann. Rev. Mat. Sci. **10**, 157–228 (1980). 10.1146/annurev.ms.10.080180.001105
642. K. Lischka, Deep level defects in narrow gap semiconductors. Phys. Status Solidi B **133**, 17–46 (1986). 10.1002/pssb.2221330104
643. J.-M. Spaeth, H. Overhof, P*oint Defects in Semiconductors and Insulators, Determination of Atomic and Electronic Structure from Paramagnetic Hyperfine Interactions* (Springer, Berlin, 2003). 10.1007/978-3-642-55615-9
644. P.T. Landsberg, Degeneracy factors of traps from solubility data for semiconductors. J. Phys. D: Appl. Phys. **10**, 2467–2471 (1977). 10.1088/0022-3727/10/18/011
645. H.I. Ralph, The degeneracy factor of the gold acceptor level in silicon. J. Appl. Phys. **49**, 672–675 (1978). 10.1063/1.324642
646. R. Kassing, L. Cohausz, P. van Staa, W. Mackert, H.J. Hoffman, Determination of the entropy-factor of the gold donor level in silicon by resistivity and DLTS measurements. Appl. Phys. A **34**, 41–47 (1984). 10.1007/BF00617573
647. H.H. Woodbury, G.W. Ludwig, Spin resonance of transition metals in silicon. Phys. Rev. **117**, 102–108 (1960). 10.1103/PhysRev.117.102
648. S. Greulich-Weber, J.R. Niklas, E.R. Weber, J.M. Spaeth, Electron nuclear double resonance of interstitial iron in silicon. Phys. Rev. B **30**, 6292–6299 (1984). 10.1103/PhysRevB.30.6292
649. H. Feichtinger, J. Waltl, A. Gschwandtner, Localization of the Fe°-level in silicon. Solid State Commun. **27**, 867–871 (1978). 10.1016/0038-1098(78)90194-1
650. Y.H. Lee, R.L. Kleinhenz, J.W. Corbett, EPR of a thermally induced defect in silicon. Appl. Phys. Lett. **31**, 142–144 (1977). 10.1063/1.89630
651. H.G. Grimmeiss, E. Janzén, H. Ennen, O. Schirmer, J. Schneider, R. Wörner, C. Holm, E. Sirtl, P. Wagner, Tellurium donors in silicon. Phys. Rev. B **24**, 4571–4586 (1981). 10.1103/PhysRevB.24.4571
652. H.G. Grimmeiss, L. Montelius, K. Larsson, Chalcogens in germanium. Phys. Rev. B **37**, 6916–6928 (1988). 10.1103/PhysRevB.37.6916
653. R.K. Franks, J.B. Robertson, Magnesium as a donor impurity in silicon. Solid State Commun. **5**, 479–481 (1967). 10.1016/0038-1098(67)90598-4
654. U. Kaufmann, J. Schneider, R. Wörner, T.A. Kennedy, N.D. Wilsey, The deep double donor P_{Ga} in GaP. J. Phys. C: Solid State Phys. **14**, L951–L955 (1981). 10.1088/0022-3719/14/31/005
655. R.J. Wagner, J.J. Krebs, G.H. Strauss, A.M. White, Submillimeter EPR evidence for the As antisite defect in GaAs. Solid State Commun. **36**, 15–17 (1980). 10.1016/0038-1098(93)90263-M

656. C.H. Champness, The statistics of divalent impurity centres in a semiconductor. Proc. Phys. Soc. B **69**, 1335–1339 (1956). 10.1088/0370-1301/69/12/421
657. R. Schaub, G. Pensl, M. Schulz, C. Holm, Donor states in tellurium-doped silicon. Appl. Phys. A **34**, 215–222 (1984). 10.1007/BF00616575
658. R.O. Carlson, Double-acceptor behavior of zinc in silicon. Phys. Rev. **108**, 1390–1393 (1957). 10.1103/PhysRev.108.1390
659. W.W. Tyler, H.H. Woodbury, Scattering of carriers from doubly charged impurity sites in germanium. Phys. Rev. **102**, 647–655 (1956). 10.1103/PhysRev.102.647
660. M.D. Sturge, The Jahn-Teller effect in solids. Solid State Phys. **20**, 91–211 (1968). 10.1016/S0081-1947(08)60218-0
661. G.D. Watkins, Negative-U properties for defects in solids. Adv. Solid State Phys. (Festkörperprobleme) **24**, 163–189 (1984). 10.1007/BFb0107450
662. G.D. Watkins, J.R. Troxell, Negative-U properties for point defects in silicon. Phys. Rev. Lett. **44**, 593–596 (1980). 10.1103/PhysRevLett.44.593
663. P.W. Anderson, Model for the electronic structure of amorphous semiconductors. Phys. Rev. Lett. **34**, 953–955 (1975). 10.1103/PhysRevLett.34.953
664. R.D. Harris, J.L. Newton, G.D. Watkins, Negative-*U* defect: Interstitial boron in silicon. Phys. Rev. B **36**, 1094–1104 (1987). 10.1103/PhysRevB.36.1094
665. G.A. Baraff, E.O. Kane, M. Schlüter, Theory of the silicon vacancy: An Anderson negative-*U* system. Phys. Rev. B **21**, 5662–5686 (1980). 10.1103/PhysRevB.21.5662
666. M. Sprenger, S.H. Muller, E.G. Sieverts, C.A.J. Ammerlaan, Vacancy in silicon: Hyperfine interactions from electron-nuclear double resonance measurements. Phys. Rev. B **35**, 1566–1581 (1987). 10.1103/PhysRevB.35.1566
667. A.F. Wright, Density-functional-theory calculations for the silicon vacancy. Phys. Rev. B **74**, 165116:1–8 (2006). 10.1103/PhysRevB.74.165116
668. A. Fazzio, A. Janotti, A.J.R. da Silva, Microscopic picture of the single vacancy in germanium. Phys. Rev. B **61**, R2401–R2404 (2000). 10.1103/PhysRevB.61.R2401
669. P.M. Mooney, N.S. Caswell, S.L. Wright, The capture barrier of the DX center in Si-doped $Al_xGa_{1-x}As$. J. Appl. Phys. **62**, 4786–4797 (1987). 10.1063/1.338981
670. P.M. Mooney, Deep donor levels (DX centers) in III-V semiconductors. J. Appl. Phys. **67**, R1–R26 (1990). 10.1063/1.345628
671. J.C. Bourgoin, ed., *Physics of DX Centers in GaAs Alloys* (Sci-Tech, Lake Isabella, CA, 1990). 10.4028/www.scientific.net/SSP.10
672. D.V. Lang, R.A. Logan, Large-lattice-relaxation model for persistent photoconductivity in compound semiconductors. Phys. Rev. Lett. **39**, 635–639 (1977). 10.1103/PhysRevLett.39.635
673. J. Mäkinen, T. Laine, K. Saarinen, P. Hautojärvi, C. Corbel, V.M. Airaksinen, J. Nagle, Microscopic structure of the DX center in Si-doped $Al_xGa_{1-x}As$: Observation of a vacancy by positron-annihilation spectroscopy. Phys. Rev. B **52**, 4870–4883 (1995). 10.1103/PhysRevB.52.4870
674. J. Dabrowski, M. Scheffler, Isolated arsenic-antisite defect in GaAs and the properties of EL2. Phys. Rev. B **40**, 10391–10401 (1989). 10.1103/PhysRevB.40.10391
675. G.M. Martin, Optical assessment of the main electron trap in bulk semi-insulating GaAs. Appl. Phys. Lett. **39**, 747–748 (1981). 10.1063/1.92852
676. J.S. Blakemore, Semiconducting and other major properties of gallium arsenide. J. Appl. Phys. **53**, R123–R181 (1982). 10.1063/1.331665
677. A. Rohatgi, R.H. Hopkins, J.R. Davis, R.B. Campbell, H.C. Mollenkopf, J.R. McCormick, The impact of molybdenum on silicon and silicon solar cell performance. Solid State Electron. **23**, 1185–1190 (1980). 10.1016/0038-1101(80)90032-5
678. D.C. Look, The electrical characterization of semi-insulating GaAs: A correlation with mass-spectrographic analysis. J. Appl. Phys. **48**, 5141–5148 (1977). 10.1063/1.323593
679. O. Mizuno, H. Watanabe, Semi-insulating properties of Fe-doped InP. Electron. Lett. **11**, 118–119 (1975). 10.1049/el:19750089
680. Y. Toudic, B. Lambert, R. Coquille, G. Grandpierre, M. Gauneau, Chromium-doped p-type semi-insulating InP. Semicond. Sci. Technol. **3**, 464–468 (1988). 10.1088/0268-1242/3/5/008
681. R.P. Tapster, M.S. Skolnick, R.G. Humphreys, P.J. Dean, B. Cockayne, W.T. MacEwan, Optical and capacitance spectroscopy of InP:Fe. J. Phys. C: Solid State Phys. **14**, 5069–5079 (1981). 10.1088/0022-3719/14/33/016
682. A. Juhl, A. Hoffmann, D. Bimberg, H.J. Schulz, Bound-exciton-related fine structure in charge transfer spectra of InP:Fe detected by calorimetric absorption spectroscopy. Appl. Phys. Lett. **50**, 1292–1294 (1987). 10.1063/1.97888
683. A.M. Hennel, Transition metals in III/V compounds. Semicond. Semimet. **38**, 189–234 (1993). 10.1016/S0080-8784(08)62801-X

684. H.J. Schulz, Optical properties of 3d transition metals in II-VI compounds. J. Cryst. Growth **59**, 65–80 (1982). 10.1016/0022-0248(82)90308-6
685. J. Cheng, S.R. Forrest, B. Tell, D. Wilt, B. Schwartz, P.D. Wright, Semi-insulating properties of Fe-implanted InP. I. Current-limiting properties of n^+-semi-insulating-n^+ structures. J. Appl. Phys. **58**, 1780–1786 (1985). 10.1063/1.336028
686. D.G. Knight, W.T. Moore, R. Bruce, Growth of semi-insulating InGaAsP alloys using low-pressure MOCVD. J. Cryst. Growth **124**, 352–357 (1992). 10.1016/0022-0248(92)90483-Y
687. A. Dadgar, O. Stenzel, A. Näser, M. Zafar Iqbal, D. Bimberg, H. Schumann, Ruthenium: A superior compensator of InP. Appl. Phys. Lett. **73**, 3878–3880 (1998) 10.1063/1.122898
688. D. Söderström, G. Fornuto, A. Buccieri, Studies on InP:Fe growth in a close-spaced showerhead MOVPE reactor, in *Proceedings 10th European Workshop on MOVPE* (Lecce, Italy, 2003), PS.IV.01:1–4. 10.1285/i9788883050088p153
689. R.A. Faulkner, Toward a theory of isoelectronic impurities in semiconductors. Phys. Rev. **175**, 991–1009 (1968). 10.1103/PhysRev.175.991
690. P.J. Dean, Recombination processes associated with "Deep States" in gallium phosphide. J. Lumin. **1–2**, 398–419 (1970). 10.1016/0022-2313(70)90054-2
691. R. Schwabe, W. Seifert, F. Bugge, R. Bindemann, V.F. Agekyan, S.V. Pogarev, Photoluminescence of nitrogen-doped VPE GaAs. Solid State Commun. **55**, 167–173 (1985). 10.1016/0038-1098(85)90272-8
692. X. Liu, M.-E. Pistol, L. Samuelson, Excitons bound to nitrogen pairs in GaAs. Phys. Rev. B **42**, 7504–7512 (1990). 10.1103/PhysRevB.42.7504
693. B. Gil, J.P. Albert, J. Camassel, H. Mathieu, C. Benoit à la Guillaume, Model calculation of nitrogen properties in III–V compounds. Phys. Rev. B **33**, 2701–2712 (1986). 10.1103/PhysRevB.33.2701
694. D.G. Thomas, J.J. Hopfield, Isoelectronic traps due to nitrogen in gallium phosphide. Phys. Rev. **150**, 680–689 (1966). 10.1103/PhysRev.150.680
695. W. Mönch, *Semiconductor Surfaces and Interfaces* (Springer, Berlin, 2001). 10.1007/978-3-662-04459-9
696. Y. Rosenwaks, R. Shikler, Th. Glatzel, S. Sadewasser, Kelvin probe force microscopy of semiconductor surface defects. Phys. Rev. B **70**, 085320:1–7 (2004). 10.1103/PhysRevB.70.085320
697. W. Mönch, Branch-point energies and the band-structure lineup at Schottky contacts and heterostrucures. J. Appl. Phys. **109**, 113724:1–10 (2011). 10.1063/1.3592978
698. J. Tersoff, Theory of semiconductor heterojunctions: The role of quantum dipoles. Phys. Rev. B **30**, 4874–4877 (1984). 10.1103/PhysRevB.30.4874
699. E.P. Shapera, A. Schleife, Database-driven materials selection for semiconductor heterojunction design. Adv. Theory and Simul. **2018**, 1800075:1–13 (2018). 10.1002/adts.201800075
700. W. Walukiewicz, Amphoteric native defects in semiconductors. Appl. Phys. Lett. **54**, 2094–2096 (1989). 10.1063/1.101174
701. E. Mollwo, Die Wirkung von Wasserstoff auf die Leitfähigkeit und Lumineszenz von Zinkoxydkristallen. Z. Phys. **138**, 478–488 (1954). 10.1007/BF01340694
702. J.I. Pankove, N.M. Johnson, eds., Hydrogen in Semiconductors. Semicond. Semimet. **34**, (1991). 10.1016/S0080-8784(08)62855-0
703. S.J. Pearton, J.W. Corbett, M. Stavola, *Hydrogen in Crystalline Semiconductors* (Springer, Berlin, 1992). 10.1007/978-3-642-84778-3
704. T. Sakurai, H.D. Hagstrum, Hydrogen chemisorption on the silicon (110) 5×1 surface. J. Vac. Sci. Technol. **13**, 807–809 (1976). 10.1116/1.568994
705. J.I. Pankove, Photoluminescence recovery in rehydrogenated amorphous silicon. Appl. Phys. Lett. **32**, 812–813 (1978). 10.1063/1.89925
706. M.H. Brodsky, M. Cardona, J.J. Cuomo, Infrared and Raman spectra of the silicon-hydrogen bonds in amorphous silicon prepared by glow discharge and sputtering. Phys. Rev. B **16**, 3556–3571 (1977). 10.1103/PhysRevB.16.3556
707. P.J.H. Denteneer, C.G. Van de Walle, S.T. Pantelides, Microscopic structure of hydrogen-boron complex in crystalline silicon. Phys. Rev. B **39**, 10809–10824 (1989). 10.1103/PhysRevB.39.10809
708. C.P. Herrero, M. Stutzmann, Microscopic structure of boron-hydrogen complexes in crystalline silicon. Phys. Rev. B **38**, 12668–12671 (1988). 10.1103/PhysRevB.38.12668
709. M. Stavola, K. Bergmann, S.J. Pearton, J. Lopata, Hydrogen motion in defect complexes: reorientation kinetics of the B-H complex in silicon. Phys. Rev. Lett. **61**, 2786–2789 (1988). 10.1103/PhysRevLett.61.2786
710. V.P. Markevich, A.R. Peaker, J. Coutinho, R. Jones, V.J.B. Torres, S. Öberg, P.R. Briddon, L.I. Murin, L. Dobaczewski, N.V. Abrosimov, Structure and properties of vacancy-oxygen complexes in $Si_{1-x}Ge_x$ alloys. Phys. Rev. B **69**, 125218:1–11 (2004). 10.1103/PhysRevB.69.125218
711. V.P. Markevich, L.I. Murin, M. Suezawa, J.L. Lindström, J. Coutinho, R. Jones, P.R. Briddon, S. Öberg, Observation and theory of the V-O-H_2 complex in silicon. Phys. Rev. B **61**, 12964–12969 (2000). 10.1103/PhysRevB.61.12964

712. A.S. Yapsir, P. Deák, R.K. Singh, L.C. Snyder, J.W. Corbett, T.-M. Lu, Hydrogen passivation of a substitutional sulfur defect in silicon. Phys. Rev. B **38**, 9936–9940 (1988). 10.1103/PhysRevB.38.9936
713. K. Seeger, *Semiconductor Physics, An Introduction*, 9th edn. (Springer, Berlin, 2004). 10.1007/978-3-662-09855-4
714. M. Lundstrom, *Fundamentals of Carrier Transport*, 2nd edn. (Cambridge University Press, Cambridge, 2000). 10.1017/CBO9780511618611
715. H.-D. Liu, Y.-P. Zhao, G. Ramanath, S.P. Murarka, G.-C. Wang, Thickness dependent electrical resistivity of ultrathin (<40 nm) Cu films. Thin Solid Films **384**, 151–156 (2001). 10.1016/S0040-6090(00)01818-6
716. C. Jacoboni, L. Reggiani, Bulk hot-electron properties of cubic semiconductors. Adv. Phys. **28**, 493–553 (1979). 10.1080/00018737900101405
717. E.M. Conwell, V. Weisskopf, Theory of impurity scattering in semiconductors. Phys. Rev. **77**, 388–390 (1950). 10.1103/PhysRev.77.388
718. H. Brooks, Scattering by ionized impurities in semiconductors. Phys. Rev. **83**, 879 (1951). 10.1103/PhysRev.83.868
719. B.K. Ridley, Reconciliation of the Conwell-Weisskopf and Brooks-Herring formulae for charged-impurity scattering in semiconductors: Third-body interference. J. Phys. C: Solid State Phys. **10**, 1589–1593 (1977). 10.1088/0022-3719/10/10/003
720. D.C. Chattopadhyay, H.J. Queisser, Electron scattering by ionized impurities in semiconductors. Rev. Mod. Phys. **53**, 745–768 (1981). 10.1103/RevModPhys.53.745
721. B.K. Ridley, *Quantum Processes in Semiconductors*, 5th edn. (Clarendon Press, Oxford, 2013). 10.1093/acprof:oso/9780199677214.001.0001
722. D.B.M. Klaasen, A unified model for device simulation-I. Model equations and concentration dependence. Solid State Electron. **35**, 953–959 (1992). 10.1016/0038-1101(92)90325-7
723. D.B.M. Klaasen, A unified model for device simulation-II. Temperature dependence of carrier mobility and lifetime. Solid State Electron. **35**, 961–967 (1992). 10.1016/0038-1101(92)90326-8
724. J.H. You, H.T. Johnson, Effect of dislocations on electrical and optical properties of GaAs and GaN. Solid State Phys. **61**, 143–261 (2009). 10.1016/S0081-1947(09)00003-4
725. G.L. Pearson, W.T. Read, F.J. Morin, Dislocations in plastically deformed germanium. Phys. Rev. **93**, 666–667 (1954). 10.1103/PhysRev.93.666
726. W.T. Read, Theory of dislocations in germanium. Philos. Mag. **45**, 775–796 (1954). 10.1080/14786440808520491
727. W.T. Read, Scattering of electrons by charged dislocations in semiconductors. Philos. Mag. **46**, 111–131 (1954). 10.1080/14786440208520556
728. B. Pödör, Electron mobility in plastically deformed germanium. Phys. Status Solidi **16**, K167–K170 (1966). 10.1002/pssb.19660160264
729. H.W. Choi, J. Zhang, S.J. Chua, Dislocation scattering in n-GaN. Mat. Sci. Semicond. Processing **4**, 567–570 (2001). 10.1016/S1369-8001(02)00019-7
730. J.Y.W. Seto, The electrical properties of polycrystalline silicon films. J. Appl. Phys. **46**, 5247–5254 (1975). 10.1063/1.321593
731. C.H. Seager, T.G. Castner, Zero-bias resistance of grain boundaries in neutron-transmutation-doped polycrystalline silicon. J. Appl. Phys. **49**, 3879–3889 (1978). 10.1063/1.325394
732. M.R. Murti, K.V. Reddy, Grain boundary effects on the carrier mobility of polysilicon. Phys. Status Solidi A **119**, 237–240 (1990). 10.1002/pssa.2211190128
733. J.W. Orton, M.J. Powell, The Hall effect in polycrystalline and powdered semiconductors. Rep. Prog. Phys. **43**, 1263–1307 (1980). 10.1088/0034-4885/43/11/001
734. N. Gupta, B.P. Tyagi, An analytical model of the influence of grain size on the mobility and transfer characteristics of polysilicon thin-film transistors (TFTs). Physica Scripta **71**, 225–228 (2005). 10.1238/Physica.Regular.071a00225
735. R.L. Petritz, Theory of photoconductivity in semiconductor films. Phys. Rev. **104**, 1508–1516 (1956). 10.1103/PhysRev.104.1508
736. C.M. Wolfe, G.E. Stillman, W.T. Lindley, Electron mobility in high-purity GaAs. J. Appl. Phys. **41**, 3088–3091 (1970). 10.1063/1.1659368
737. H. v. Wenckstern, S. Weinhold, G. Biehne, R. Pickenhain, H. Schmidt, H. Hochmuth, M. Grundmann, Donor levels in ZnO. Adv. Solid State Phys. (Festkörperprobleme) **45**, 263–274 (2006). 10.1007/11423256_21
738. H.K. Sy, D.K. Desai, C.K. Ong, Electron screening and mobility in heavily doped silicon. Phys. Status Solidi B **130**, 787–792 (1985). 10.1002/pssb.2221300244
739. G. Masetti, M. Severi, S. Solmi, Modeling of carrier mobility against carrier concentration in arsenic-, phosphorus-, and boron-doped silicon. IEEE Trans. Electron Devices **30**, 764–769 (1983). 10.1109/T-ED.1983.21207
740. V.L. Gurevich, A.I. Larkin, Yu.A. Firsov, Possibility of superconductivity in semiconductors. Fiz. Tverd. Tela (Leningrad) **4**, 185 (1962) [Sov. Phys. Solid State **4**, 131 (1962)]
741. M.L. Cohen, Superconductivity in many-valley semiconductors and in semimetals. Phys. Rev. **134**, A511–A521 (1964). 10.1103/PhysRev.134.A511

742. C.S. Koonce, M.L. Cohen, Theory of superconducting semiconductors and semimetals. Phys. Rev. **177**, 707–719 (1969). 10.1103/PhysRev.177.707
743. J.K. Hulm, M. Ashkin, D.W. Deis, C.K. Jones, Superconductivity in semiconductors and semi-metals. Prog. Low Temp. Physics **6**, 205–242 (1970). 10.1016/S0079-6417(08)60064-5
744. E. Bustarret, Superconductivity in doped semiconductors. Physica C **514**, 36–45 (2005). 10.1016/j.physc.2015.02.021
745. X. Blase, E. Bustarret, C. Chapelier, T. Klein, C. Marcenat, Superconducting group-IV semiconductors. Nat. Mater. **8**, 375–382 (2009). 10.1038/nmat2425
746. E. Ekimov, V. Sidorov, E. Bauer, N.N. Mel'nik, N.J. Curro, J.D. Thompson, S.M. Stishov, Superconductivity in diamond. Nature **428**, 542–545 (2004). 10.1038/nature02449
747. E. Bustarret, C. Marcenat, P. Achatz, J. Kačmarčik, F. Lévy, A. Huxley, L. Ortéga, E. Bourgeois, X. Blase, D. Débarre, J. Boulmer, Superconductivity in doped cubic silicon. Nature **444**, 465–468 (2006). 10.1038/nature05340
748. T. Herrmannsdörfer, V. Heera, O. Ignatchik, M. Uhlarz, A. Mücklich, M. Posselt, H. Reuther, B. Schmidt, K.-H. Heinig, W. Skorupa, M. Voelskow, C. Wündisch, R. Skrotzki, M. Helm, J. Wosnitza, Superconducting state in a gallium-doped germanium layer at low temperatures. Phys. Rev. Lett. **102**, 217003:1–4 (2009). 10.1103/PhysRevLett.102.217003
749. C.S. Smith, Piezoresistance effect in germanium and silicon. Phys. Rev. **94**, 42–49 (1954). 10.1103/PhysRev.94.42
750. R.W. Keyes, The effect of elastic deformation on the electrical conductivity of semiconductors. Solid State Phys. **11**, 149–221 (1960). 10.1016/S0081-1947(08)60168-X
751. Y. Ohmura, Piezoresistance effect in p-type Si. Phys. Rev. B **42**, 9178–9181 (1990). 10.1103/PhysRevB.42.9178
752. Y. Kanda, A graphical representation of the piezoresistance coefficients in silicon. IEEE Trans. Electron Dev. **29**, 64–70 (1982). 10.1109/T-ED.1982.20659
753. M. Zerbst, Piezowiderstandseffekt in Galliumarsenid. Z. Naturf. **17a**, 649–651 (1962). 10.1515/zna-1962-0804
754. A. Sagar, Piezoresistance in n-type GaAs. Phys. Rev. **112**, 1533 (1958). 10.1103/PhysRev.112.1533
755. G. Bauer, Determination of electron temperatures and of hot electron distribution functions in semiconductors. Solid-State Phys., Springer Tracts Modern Phys. **74**, 1–106 (1974). 10.1007/BFb0041386
756. T. Kunikiyo, M. Takenaka, Y. Kamakura, M. Yamaji, H. Mizuno, M. Morifuji, K. Taniguchi, C. Hamaguchi, A Monte Carlo simulation of anisotropic electron transport in silicon including full band structure and anisotropic impact-ionization model. J. Appl. Phys. **75**, 297–312 (1994). 10.1063/1.355849
757. E.M. Conwell, *High Field Transport in Semiconductors* (Academic Press, New York, 1967)
758. C. Canali, C. Jacoboni, F. Nava, G. Ottaviani, A. Alberigi-Quaranta, Electron drift velocity in silicon. Phys. Rev. B **12**, 2265–2284 (1975). 10.1103/PhysRevB.12.2265
759. C. Jacoboni, C. Canali, G. Ottaviani, A. Alberigi-Quaranta, A review of some charge transport properties of silicon. Solid State Electron. **20**, 77–89 (1977). 10.1016/0038-1101(77)90054-5
760. C. Jacoboni, F. Nava, C. Canali, G. Ottaviani, Electron drift velocity and diffusivity in germanium. Phys. Rev. B **24**, 1014–1026 (1981). 10.1103/PhysRevB.24.1014
761. T. González Sánchez, J.E. Velázquez Pérez, P.M. Gutiérrez Conde, D. Pardo Collantes, Electron transport in InP under high electric field conditions. Semicond. Sci. Technol. **7**, 31–36 (1992). 10.1088/0268-1242/7/1/006
762. V. Balynas, A. Krotkus, A. Stalnionis, A.T. Gorelionok, N.M. Shmidt, J.A. Tellefsen, Time-resolved, hot-electron conductivity measurement using an electro-optic sampling technique. Appl. Phys. A **51**, 357–360 (1990). 10.1007/BF00324321
763. J.D. Albrecht, P.P. Ruden, S. Limpijumnong, W.R. Lambrecht, K.F. Brennan, High field electron transport properties of bulk ZnO. J. Appl. Phys. **86**, 6864–6867 (1999). 10.1063/1.371764
764. B.K. Ridley, T.B. Watkins, The possibility of negative resistance effects in semiconductors. Proc. Phys. Soc. **78**, 293–304 (1961). 10.1088/0370-1328/78/2/315
765. P.N. Butcher, The Gunn effect. Rep. Prog. Phys. **30**, 97–148 (1967). 10.1088/0034-4885/30/1/303
766. T.K. Ishii, ed., *Handbook of Microwave Technology* (Academic Press, San Diego, 1995) (Two volumes, Vol. 1: *Components and Devices*, Vol. 2: *Applications*)
767. J. Požela, A. Reklaitis, Electron transport properties in GaAs at high electric fields. Solid State Electron. **23**, 927–933 (1980). 10.1016/0038-1101(80)90057-X
768. B. Kramer, A. Mircea, Determination of saturated electron velocity in GaAs. Appl. Phys. Lett. **26**, 623–625 (1975). 10.1063/1.88001
769. S. Sridharan, P.D. Yoder, Anisotropic transient and stationary electron velocity in bulk wurtzite GaN. IEEE Electr. Dev. Lett. **29**, 1190–1192 (2008). 10.1109/LED.2008.2005433
770. C.L. Anderson, C.R. Crowell, Threshold energies for electron-hole pair production by impact ionization in semiconductors. Phys. Rev. B **5**, 2267–2272 (1972). 10.1103/PhysRevB.5.2267
771. T. Pearsall, Threshold energies for impact ionization by electrons and holes in InP. Appl. Phys. Lett. **35**, 168–170 (1979). 10.1063/1.91068
772. Y. Kamakura, H. Mizuno, M. Yamaji, M. Morifuji, K. Taniguchi, C. Hamaguchi, T. Kunikiyo, M. Takenaka, Impact ionization model for full band Monte Carlo simulation. J. Appl. Phys. **75**, 3500–3506 (1994). 10.1063/1.356112

773. T. Kunikiyo, M. Takenaka, M. Morifuji, K. Taniguchi, C. Hamaguchi, A model of impact ionization due to the primary hole in silicon for a full band Monte Carlo simulation. J. Appl. Phys. **79**, 7718–7725 (1996). 10.1063/1.362375
774. A. Kuligk, N. Fitzer, R. Redmer, Ab initio impact ionization rate in GaAs, GaN, and ZnS. Phys. Rev. B **71**, 085201:1–6 (2005). 10.1103/PhysRevB.71.085201
775. C.S. Hung, J.R. Gliessman, The resistivity and Hall effect of germanium at low temperatures. Phys. Rev. **79** 726–727 (1950). 10.1103/PhysRev.79.726
776. C.S. Hung, Theory of resistivity and Hall effect at very low temperatures. Phys. Rev. **79**, 727–728 (1950). 10.1103/PhysRev.79.727
777. C.S. Hung, J.R. Gliessman, Resistivity and Hall effect of germanium at low temperatures. Phys. Rev. **96**, 1226–1236 (1954). 10.1103/PhysRev.96.1226
778. T. Słupiński, J. Caban, K. Moskalik, Hole transport in impurity band and valence bands studied in moderately doped GaAs:Mn single crystals. Acta Phys. Polon. **112**, 325–330 (2007). 10.12693/APhysPolA.112.325
779. Z. Kabilova, C. Kurdak, R.L. Peterson, Observation of impurity band conduction and variable range hopping in heavily doped (010) β-Ga_2O_3. Semicond. Sci. Technol. **34**, 03LT02:1–7 (2019). 10.1088/1361-6641/ab0150
780. D.J. Thouless, Electrons in disordered systems and the theory of localization. Phys. Rep. **13**, 93–142 (1974). 10.1016/0370-1573(74)90029-5
781. T.F. Rosenbaum, K. Andres, G.A. Thomas, R.N. Bhatt, Sharp metal-insulator transition in a random solid. Phys. Rev. Lett. **45**, 1723–1726 (1980). 10.1103/PhysRevLett.45.1723
782. P.W. Anderson, Absence of diffusion in certain random lattices. Phys. Rev. **109**, 1492–1505 (1958). 10.1103/PhysRev.109.1492
783. N.F. Mott, The metal-insulator transition in an impurity band. J. Phys. Colloques **37**, C4-301–C4-306 (1976). 10.1051/jphyscol:1976453
784. J.T. Devreese, Polarons, digital Encycl. Appl. Phys. 383–413 (2003). 10.1002/3527600434.eap347
785. D. Emin, *Polarons* (Cambridge University Press, Cambridge, 2013)
786. J. Appel, Polarons. Solid State Phys. **21**, 193–391 (1968). 10.1016/S0081-1947(08)60741-9
787. R.P. Feynman, Slow electrons in a polar crystal. Phys. Rev. **97**, 660–665 (1955). 10.1103/PhysRev.97.660
788. G.D. Mahan, *Many-Particle Physics* (Springer. New York, 2000). 10.1007/978-1-4757-5714-9
789. H. Fröhlich, H. Pelzer, S. Zienau, Properties of slow electrons in polar materials. Philos. Mag. **41**, 221–242 (1950). 10.1080/14786445008521794
790. T.D. Schultz, Slow electrons in polar crystals: Self-energy, mass, and mobility. Phys. Rev. **116**, 526–543 (1959). 10.1103/PhysRev.116.526
791. O.F. Schirmer, O^- bound small polarons in oxide materials. J. Phys.: Cond. Matter **18**, R667–R704 (2006). 10.1088/0953-8984/18/43/R01
792. M. Albrecht, J. Varley, T. Remmele, Z. Gałaska, R. Uecker, C. Van de Walle, R. Fornari, In-situ observation of small polarons in gallium oxide by aberration corrected high resolution transmission electron microscopy, in *15th European Microscopy Congress* (Manchester, UK, 2012). PS2.3:1–2
793. B.J. Morgan, D.O. Scanlon, G.W. Watson, Small polarons in Nb- and Ta-doped rutile and anatase TiO_2. J. Mater. Chem. **19**, 5175–5178 (2009). 10.1039/B905028K
794. S.J.F. Byrnes, *Basic Theory and Phenomenology of Polarons* (2008). online at http://sjbyrnes.com/FinalPaper--Polarons.pdf
795. N.F. Mott, E.A. Davis, *Electronic Properties in Non-Crystalline Materials* (Clarendon Press, Oxford, 1971)
796. A.L. Efros, B.I. Shklovskii, *Electronic Properties of Doped Semiconductors* (Springer, Berlin, 1984). 10.1007/978-3-662-02403-4
797. M. Pollak, B.I. Shklovskii, eds., *Hopping Transport in Solids* (Elsevier/North-Holland, Amsterdam, 1990)
798. J.J. Hauser, Electrical properties and anisotropy in amorphous Si and $Si_{0.5}Ge_{0.5}$ alloy. Phys. Rev. B **8**, 3817–3823 (1973). 10.1103/PhysRevB.8.3817
799. N.F. Mott, Conduction in glasses containing transition metal ions. J. Non-Cryst. Solids **1**, 1–17 (1968). 10.1016/0022-3093(68)90002-1
800. A.L. Efros, B.I. Shklovskii, Coulomb gap and low temperature conductivity of disordered system. J. Phys. C: Solid State Phys. **8**, L49–L51 (1975). 10.1088/0022-3719/8/4/003
801. A. Yildiz, N. Serin, T. Serin, M. Kasap, Crossover from nearest-neighbor hopping conduction to Efros–Shklovskii variable-range hopping conduction in hydrogenated amorphous silicon films. Jpn. J. Appl. Phys. **48**, 111203:1–5 (2009). 10.1143/JJAP.48.111203
802. N. Mott, The mobility edge since 1967. J. Phys. C: Solid State Phys. **20**, 3075–3102 (1987). 10.1088/0022-3719/20/21/008
803. B.C.H. Steele, A. Heinzel, Materials for fuel-cell technologies. Nature **414**, 345–352 (2001). 10.1038/35104620
804. N. Sata, K. Eberman, K. Eberl, J. Maier, Mesoscopic fast ion conduction in nanometre-scale planar heterostructures. Nature **408**, 946–949 (2000). 10.1038/35050047

805. J. Garcia-Barriocanal, A. Rivera-Calzada, M. Varela, Z. Sefrioui, E. Iborra, C. Leon, S.J. Pennycook, J. Santamaria, Colossal ionic conductivity at interfaces of epitaxial ZrO_2:Y_2O_3/$SrTiO_3$ heterostructures. Science **321**, 676–680 (2008). 10.1126/science.1156393
806. J.X.M. Zheng-Johansson, R.L. McGreevy, A molecular dynamics study of ionic conduction in CuI. II. Local ionic motion and conduction mechanisms. Solid State Ionics **83**, 35–48 (1996). 10.1016/0167-2738(95)00218-9
807. M. Yashima, Q. Xu, A. Yoshiasa, S. Wada, Crystal structure, electron density and diffusion path of the fast-ion conductor copper iodide CuI. J. Mater. Chem. **16**, 4393–4396 (2006). 10.1039/B610127E
808. T. Jow, J.B. Wagner, On the electrical properties of cuprous iodide. J. Electrochem. Soc. **125**, 613–620 (1978). 10.1149/1.2131511
809. P.T. Landsberg, On the diffusion theory of rectification. Proc. Roy. Soc. Lond. A **213**, 226–237 (1952). 10.1098/rspa.1952.0122
810. A.N. Chakravarti, B.R. Nag, Generalized Einstein relation for degenerate semiconductors having non-parabolic energy bands. Int. J. Electr. **37**, 281–284 (1974). 10.1080/00207217408900521
811. N.G. Nilsson, An accurate approximation of the generalized einstein relation for degenerate semiconductors. Phys. Status Solidi A **19**, K75–K78 (1973). 10.1002/pssa.2210190159
812. E. Spenke, *Elektronische Halbleiter, Eine Einführung in die Physik der Gleichrichter und Transistoren* (Springer, Berlin, 1955). 10.1007/978-3-662-01338-0
813. F.A. Lindholm, R.W. Ayers, Generalized Einstein relation for degenerate semiconductors. Proc. IEEE **56**, 371–372 (1968). 10.1109/PROC.1968.6320
814. H.S. Carslaw, J.C. Jaeger, *Conduction of Heat in Solids* (Clarendon Press, Oxford, 1959)
815. T.H. Geballe, G.W. Hull, Isotopic and other types of thermal resistance in germanium. Phys. Rev. **110**, 773–775 (1958). 10.1103/PhysRev.110.773
816. H.B.G. Casimir, Note on the conduction of heat in crystals. Physica **5**, 495–500 (1938). 10.1016/S0031-8914(38)80162-2
817. W.S. Capinski, H.J. Maris, E. Bauser, I. Silier, M. Asen-Palmer, T. Ruf, M. Cardona, E. Gmelin, Thermal conductivity of isotopically enriched Si. Appl. Phys. Lett. **71**, 2109–2111 (1997). 10.1063/1.119384
818. T. Ruf, R.W. Henn, M. Asen-Palmer, E. Gmelin, M. Cardona, H.J. Pohl, G.G. Devyatykh, P.G. Sennikov, Thermal conductivity of isotopically enriched silicon. Solid State Commun. **115**, 243–247 (2000). 10.1016/S0038-1098(00)00172-1
819. G.O. Mahan, Good thermoelectrics. Solid State Phys. **51**, 81–157 (1997). 10.1016/S0081-1947(08)60190-3
820. H. Böttner, G. Chen, R. Venkatasubramanian, Aspects of thin-film superlattice thermoelectric materials, devices, and applications. Dev. Appl. MRS Bull. **31**, 211–217 (2006). 10.1557/mrs2006.47
821. V.A. Johnson, K. Lark-Horowitz, Theory of thermoelectric power in semiconductors with applications to germanium. Phys. Rev. **92**, 226–232 (1953). 10.1103/PhysRev.92.226
822. T.H. Geballe, G.W. Hull, Seebeck effect in silicon. Phys. Rev. **98**, 940–947 (1955). 10.1103/PhysRev.98.940
823. H. Fritzsche, A general expression for the thermoelectric power. Solid State Commun. **9**, 1813–1815 (1971). 10.1016/0038-1098(71)90096-2
824. Z. Wang, S. Wang, S. Obukhov, N. Vast, J. Sjakste, V. Tjuterev, N. Mingo, Thermoelectric transport properties of silicon: Toward an ab initio approach. Phys. Rev. B **83**, 205208:1–5 (2011). 10.1103/PhysRevB.83.205208
825. G.D. Mahan, L. Lindsay, D.A. Broido, The Seebeck coefficient and phonon drag in silicon. J. Appl. Phys. **116**, 245102:1–7 (2014). 10.1063/1.4904925
826. I. Newton, *Opticks* (London, 1704), Book 3, Query 5, p. 133
827. C. Kranert, C. Sturm, R. Schmidt-Grund, M. Grundmann, Raman tensor formalism for optically anisotropic crystals. Phys. Rev. Lett. **116**, 127401:1–5 (2016). 10.1103/PhysRevLett.116.127401
828. C. Sturm, J. Furthmüller, F. Bechstedt, R. Schmidt-Grund, M. Grundmann, Dielectric tensor of monoclinic Ga_2O_3 single crystals in the spectral range 0.5–8.5 eV. APL Mater. **3**, 106106:1–9 (2015). 10.1063/1.4934705
829. C. Sturm, R. Schmidt-Grund, C. Kranert, J. Furthmüller, F. Bechstedt, M. Grundmann, Dipole analysis of the dielectric function of color dispersive materials: Application to monoclinic Ga_2O_3. Phys. Rev. B **94**, 035148:1–11 (2016). 10.1103/PhysRevB.94.035148
830. W. Voigt, Beiträge zur Aufklärung der Eigenschaften pleochroitischer Kristalle. Ann. Physik **314**, 367–416 (1902). 10.1002/andp.19023141006
831. C. Sturm, M. Grundmann, The singular optical axes in biaxial crystals and analysis of their spectral dispersion effects in β-Ga_2O_3. Phys. Rev. A **93**, 053839:1–8 (2016). 10.1103/PhysRevA.93.053839
832. C. Sturm, V. Zviagin, M. Grundmann, Applicability of the constitutive equations for the determination of the material properties of optically active materials. Opt. Lett. **44**, 1351–1354 (2019). 10.1364/OL.44.001351
833. A. Kwan, J. Dudley, E. Lantz, Who really discovered Snell's law? Physics World **15**, 64 (2002). 10.1088/2058-7058/15/4/44
834. A. Fresnel, *Œuvres complètes d'Augustin Fresnel*, H. de Senarmont, É. Verdet, L. Fresnel, eds. (Imprimerie Impériale, Paris, 1866-1870, 3 vols.)
835. M. Bouguer, *Essai d'optique sur la gradation de la lumière* (Claude Jombert, Paris, 1729)

836. A. Beer, Bestimmung der Absorption des rothen Lichts in farbigen Flüssigkeiten. Ann. Phys. Chem. **162**, 78–88 (1852). 10.1002/andp.18521620505
837. Ch.M. Wolfe, N. Holonyak Jr., G.E. Stillman, *Physical Properties of Semiconductors* (Prentice Hall, Englewood Cliffs, NJ, 1989)
838. M. Born, K. Huang, *Dynamical Theory of Crystal Lattices* (Clarendon Press, Oxford, 1954)
839. R.H. Lyddane, R.G. Sachs, E. Teller, On the polar vibrations of alkali halides. Phys. Rev. **59**, 673–676 (1941). 10.1103/PhysRev.59.673
840. B. Jogai, Absorption coefficient of wurtzite GaN calculated from an empirical tight binding model. Solid State Commun. **116**, 153–157 (2000). 10.1016/S0038-1098(00)00305-7
841. M. Cardona, Modulation spectroscopy of semiconductors. Adv. Solid State Phys. (Festkörperprobleme) **10**, 125–173 (1970). 10.1007/BFb0108433
842. M.D. Sturge, Optical absorption of gallium arsenide between 0.6 and 2.75 eV. Phys. Rev. **127**, 768–773 (1962). 10.1103/PhysRev.127.768 Erratum: Phys. Rev. **129**, 2835 (1963). 10.1103/PhysRev.129.2835.3
843. R.G. Ulbrich, Band edge spectra of highly excited gallium arsenide. Adv. Solid State Phys. (Festkörperprobleme) **25**, 299–307 (1985). 10.1007/BFb0108162
844. T. Matsuyama, H. Horinaka, K. Wada, T. Kondo, M. Hangyo, T. Nakanishi, S. Okumi, K. Togowa, Spin-dependent luminescence of highly polarized electrons generated by two-photon absorption in semiconductors. Jpn. J. Appl. Phys. **40**, L555–L557 (2001). 10.1143/JJAP.40.L555
845. P.J. Dean, D.G. Thomas, Intrinsic absorption-edge spectrum of gallium phosphide. Phys. Rev. **150**, 690–703 (1966). 10.1103/PhysRev.150.690
846. L.H. Hall, J. Bardeen, F.J. Blatt, Infrared absorption spectrum of germanium. Phys. Rev. **95**, 559–560 (1954). 10.1103/PhysRev.95.559
847. J. Geist, A. Migdall, H.P. Baltes, Analytic representation of the silicon absorption coefficient in the indirect transition region. Appl. Optics **27**, 3777–3779 (1988). 10.1364/AO.27.003777
848. G.G. Macfarlane, V. Roberts, Infrared absorption of germanium near the lattice edge. Phys. Rev. **97**, 1714–1716 (1955). 10.1103/PhysRev.97.1714.2
849. G.G. Macfarlane, T.P. McLean, J.E. Quarrington, V. Roberts, Fine structure in the absorption-edge spectrum of Si. Phys. Rev. **111**, 1245–1254 (1958). 10.1103/PhysRev.111.1245
850. B.N. Brockhouse, Lattice vibrations in silicon and germanium. Phys. Rev. Lett. **2**, 256–258 (1959). 10.1103/PhysRevLett.2.256
851. J.I. Pankove, P. Aigrain, Optical absorption of arsenic-doped degenerate germanium. Phys. Rev. **126**, 956–962 (1962). 10.1103/PhysRev.126.956
852. G.A. Cox, G.G. Roberts, R.H. Tredgold, The optical absorption edge of barium titanate. Br. J. Appl. Phys. **17**, 743–745 (1966). 10.1088/0508-3443/17/6/305
853. F. Urbach, The long-wavelength edge of photographic sensitivity and of the electronic absorption of solids. Phys. Rev. **92**, 1324 (1953). 10.1103/PhysRev.92.1324
854. S.R. Johnson, T. Tiedje, Temperature dependence of the Urbach edge in GaAs. J. Appl. Phys. **78**, 5609–5613 (1995). 10.1063/1.359683
855. M. Beaudoin, A.J.G. DeVries, S.R. Johnson, H. Laman, T. Tiedje, Optical absorption edge of semi-insulating GaAs and InP at high temperatures. Appl. Phys. Lett. **70**, 3540–3542 (1997). 10.1063/1.119226
856. T.S. Moss, T.D.F. Hawking, Infrared absorption in gallium arsenide. Infrared Phys. **1**, 111–115 (1961). 10.1016/0020-0891(61)90014-8
857. J. Stuke, Review of optical and electrical properties of amorphous semiconductors. J. Non-Cryst. Solids **4**, 1–26 (1970). 10.1016/0022-3093(70)90015-3
858. A. Baldereschi, N.O. Lipari, Energy levels of direct excitons in semiconductors with degenerate bands. Phys. Rev. B **3**, 439–451 (1971). 10.1103/PhysRevB.3.439
859. N.O. Lipari, M. Altarelli, Theory of indirect excitons in semiconductors. Phys. Rev. B **15**, 4883–4897 (1977). 10.1103/PhysRevB.15.4883
860. N.O. Lipari, Exciton energy levels in wurtzite-type crystals. Phys. Rev. B **4**, 4535–4538 (1971). 10.1103/PhysRevB.4.4535
861. D. Birkedal, J. Singh, V.G. Lyssenko, J. Erland, J.M. Hvam, Binding of quasi-two-dimensional biexcitons. Phys. Rev. Lett. **76**, 672–675 (1996). 10.1103/PhysRevLett.76.672
862. E.F. Gross, Excitons and their motion in crystal lattices. Usp. Fiz. Nauk **76**, 433–466 (1962) [Sov. Phys. Usp. **5**, 195–218 (1962)]. 10.1070/PU1962v005n02ABEH003407
863. T. Kazimierczuk, D. Fröhlich, S. Scheel, H. Stolz, M. Bayer, Giant Rydberg excitons in the copper oxide Cu_2O. Nature **514**, 343–347 (2014). 10.1038/nature13832
864. Ch. Uihlein, D. Fröhlich, R. Kenklies, Investigation of exciton fine structure in Cu_2O. Phys. Rev. B **23**, 2731–2740 (1981). 10.1103/PhysRevB.23.2731
865. R.J. Elliott, Intensity of optical absorption by excitons. Phys. Rev. **108**, 1384–1389 (1957). 10.1103/PhysRev.108.1384

866. A. Shikanai, T. Azuhata, T. Sota, S. Chichibu, A. Kuramata, K. Horino, S. Nakamura, Biaxial strain dependence of exciton resonance energies in wurtzite GaN. J. Appl. Phys. **81**, 417–424 (1997). 10.1063/1.364074
867. S. Rudin, T.L. Reinecke, B. Segall, Temperature-dependent exciton linewidths in semiconductors. Phys. Rev. B **42**, 11218–11231 (1990). 10.1103/PhysRevB.42.11218
868. A.J. Fischer, W. Shan, J.J. Song, Y.C. Chang, R. Horning, B. Goldenberg, Temperature-dependent absorption measurements of excitons in GaN epilayers. Appl. Phys. Lett. **71**, 1981–1983 (1997). 10.1063/1.119761
869. A.J. Fischer, D.S. Kim, J. Hays, W. Shan, J.J. Song, D.B. Eason, J. Ren, J.F. Schetzina, H. Luo, J.K. Furdyna, Z.Q. Zhu, T. Yao, W. Schäfer, Femtosecond coherent spectroscopy of bulk ZnSe and ZnCdSe/ZnSe quantum wells. Phys. Rev. Lett. **73**, 2368–2371 (1994). 10.1103/PhysRevLett.73.2368
870. A.K. Viswanath, J.I. Lee, D. Kim, C.R. Lee, J.Y. Leem, Exciton-phonon interactions, exciton binding energy, and their importance in the realization of room-temperature semiconductor lasers based on GaN. Phys. Rev. B **58**, 16333–16339 (1998). 10.1103/PhysRevB.58.16333
871. D.-S. Kim, J. Shah, J.E. Cunnigham, T.C. Damen, W. Schäfer, M. Hartmann, S. Schmitt-Rink, Giant exciton resonance in time-resolved four-wave mixing in quantum wells. Phys. Rev. Lett. **68**, 1006–1009 (1992). 10.1103/PhysRevLett.68.1006
872. R. Hauschild, H. Priller, M. Decker, J. Brückner, H. Kalt, C. Klingshirn, Temperature dependent band gap and homogeneous line broadening of the exciton emission in ZnO. Phys. Status Solidi C **3**, 976–979 (2006). 10.1002/pssc.200564643
873. J.J. Hopfield, D.G. Thomas, Polariton absorption lines. Phys. Rev. Lett. **15**, 22–25 (1965). 10.1103/PhysRevLett.15.22
874. J.J. Hopfield, Resonant scattering of polaritons as composite particles. Phys. Rev. **182**, 945–952 (1969). 10.1103/PhysRev.182.945
875. A.A. Maradudin, D.L. Mills, Effect of spatial dispersion on the properties of a semi-infinite dielectric. Phys. Rev. B **7**, 2787–2810 (1973). 10.1103/PhysRevB.7.2787
876. Y. Toyozawa, On the dynamical behavior of an exciton. Prog. Theor. Phys., Suppl. **12**, 111–140 (1959). 10.1143/PTPS.12.111
877. U. Heim, P. Wiesner, Direct evidence for a bottleneck of exciton-polariton relaxation in CdO. Phys. Rev. Lett. **30**, 1205–1207 (1973). 10.1103/PhysRevLett.30.1205
878. B. Gil, Oscillator strengths of A, B, and C excitons in ZnO films. Phys. Rev. B **64**, 201310:1–3 (2001). 10.1103/PhysRevB.64.201310
879. T. Soma, H.-M. Kagaya, The metallic and ionic contributions to lattice vibrations of III-V covalent crystals. Phys. Status Solidi B **118**, 245–254 (1983). 10.1002/pssb.2221180130
880. A. Göldner, *Nichtstrahlende Relaxationsprozesse bandkantennaher Zustände in II-VI- und III-V-Halbleiterstrukturen*, Ph.D. Thesis, Technische Universität Berlin (2000) (Wissenschaft und Technik Verlag, Berlin, 2000)
881. I. Broser, M. Rosenzweig, Determination of excitonic parameters of the A polariton in CdS from magnetoreflectance spectroscopy. Phys. Rev. B **22**, 2000–2007 (1980). 10.1103/PhysRevB.22.2000
882. M. Rosenzweig, *Exzitonische Polaritonen in CdS—Optische Eigenschaften räumlich dispersiver Medien*, Ph.D. Thesis, Technische Universität Berlin (1982)
883. G. Blattner, G. Kurtze, G. Schmieder, C. Klingshirn, Influence of magnetic fields up to 20 T on excitons and polaritons in CdS and ZnO. Phys. Rev. B **25**, 7413–7427 (1982). 10.1103/PhysRevB.25.7413
884. B. Gil, S. Clur, O. Briot, The exciton-polariton effect on the photoluminescence of GaN on sapphire. Solid State Commun. **104**, 267–270 (1997). 10.1016/S0038-1098(97)00284-6
885. A.E. Yunovich, Radiative recombination and optical properties of GaP, in *Radiative Recombination in Semiconductors*, ed. by Ya. E. Pokrovskii (Moscow, 1972) (in Russian). A.E. Yunovich, Strahlende Rekombination und optische Eigenschaften von GaP. Fortschritte der Physik **23**, 317–398 (1975). 10.1002/prop.19750230602
886. V. Vashishta, R.K. Kalia, Universal behavior of exchange-correlation energy in electron-hole liquid. Phys. Rev. B **25**, 6492–6495 (1982). 10.1103/PhysRevB.25.6492
887. R. Zimmermann, Nonlinear optics and the Mott transition in semiconductors. Phys. Status Solidi B **146**, 371–384 (1988). 10.1002/pssb.2221460140
888. H.-E. Swoboda, M. Sence, F.A. Majumder, M. Rinker, J.-Y. Bigot, J.B. Grun, C. Klingshirn, Properties of electron-hole plasma in II-VI compounds as a function of temperature. Phys. Rev. B **39**, 11019–11027 (1989). 10.1103/PhysRevB.39.11019
889. J.P. Löwenau, S. Schmitt-Rink, H. Haug, Many-body theory of optical bistability in semiconductors. Phys. Rev. Lett. **49**, 1511–1514 (1982). 10.1103/PhysRevLett.49.1511
890. L.V. Keldysh, Concluding remarks [for IXth International Conference on the Physics of Semiconductors], in *Proceedings of the 9th International Conference on the Physics of Semiconductors* (Moscow, Nauka, Leningrad, 1968), pp. 1303–1312
891. W.F. Brinkman, T.M. Rice, P.W. Anderson, S.T. Chui, Metallic state of the electron-hole liquid, particularly in germanium. Phys. Rev. Lett. **28**, 961–964 (1972). 10.1103/PhysRevLett.28.961

892. G.A. Thomas, T.M. Rice, J.C. Hensel, Liquid-gas phase diagram of an electron-hole fluid. Phys. Rev. Lett. **33**, 219–222 (1974). 10.1103/PhysRevLett.33.219
893. T.L. Reinecke, S.C. Ying, Droplet model of electron-hole liquid condensation in semiconductors. Phys. Rev. Lett. **35**, 311–315 (1975). 10.1103/PhysRevLett.35.311 Erratum: Phys. Rev. Lett. **35**, 547 (1975). 10.1103/PhysRevLett.35.547.2
894. R.S. Markiewicz, J.P. Wolfe, C.D. Jeffries, Strain-confined electron-hole liquid in germanium. Phys. Rev. B **15**, 1988–2005 (1977). 10.1103/PhysRevB.15.1988
895. L.V. Butov, C.W. Lai, A.L. Ivanov, A.C. Gossard, D.S. Chemla, Towards Bose-Einstein condensation of excitons in potential traps. Nature **417**, 47–52 (2002). 10.1038/417047a
896. L.V. Butov, A.C. Gossard, D.S. Chemla, Macroscopically ordered state in an exciton system. Nature **418**, 751–754 (2002). 10.1038/nature00943
897. K.E. O'Hara, L.Ó. Súilleabháin, J.P. Wolfe, Strong nonradiative recombination of excitons in Cu_2O and its impact on Bose-Einstein statistics. Phys. Rev. B **60**, 10565–10568 (1999). 10.1103/PhysRevB.60.10565
898. M. Skolnick, A.I. Tartakovskii, R. Butté, R.M. Stevenson, J.J. Baumberg, D.M. Whittaker, High occupancy effects and condensation phenomena in semiconductor microcavities and bulk semiconductors, in *Nano-Optoelectronics, Concepts, Physics and Devices*, ed. by M. Grundmann (Springer, Berlin, 2002), pp. 273–296. 10.1007/978-3-642-56149-8_11
899. H. Mahr, Two-photon absorption spectroscopy, in *Quantum Electronics: A Treatise*, H. Rabin, C.L. Tang, eds. vol. I, Part A (Academic, New York, 1975), pp. 285–361. 10.1016/B978-0-12-574001-2.50010-1
900. H.J. Fossum, D.B. Chang, Two-photon excitation rate in indium antimonide. Phys. Rev. B **8**, 2842–2849 (1973). 10.1103/PhysRevB.8.2842
901. J.P. van der Ziel, Two-photon absorption spectra of GaAs with $2\hbar\omega_1$ near the direct band gap. Phys. Rev. B **16**, 2775–2780 (1977). 10.1103/PhysRevB.16.2775
902. C.J. Summers, R. Dingle, D.E. Hill, Far-infrared donor absorption and photoconductivity in epitaxial n-type GaAs. Phys. Rev. B **1**, 1603–1606 (1970). 10.1103/PhysRevB.1.1603
903. ShM Kogan, T.M. Lifshits, Photoelectric spectroscopy—A new method of analysis of impurities in semiconductors. Phys. Status Solidi A **39**, 11–39 (1977). 10.1002/pssa.2210390102
904. L.T. Ho, A.K. Ramdas, Excitation spectra and piezospectroscopic effects of magnesium donors in silicon. Phys. Rev. B **5**, 462–474 (1972). 10.1103/PhysRevB.5.462
905. R.A. Cooke, R.A. Hoult, R.F. Kirkman, R.A. Stradling, The characterisation of the donors in GaAs epitaxial films by far-infrared photoconductive techniques. J. Phys. D: Appl. Phys. **11**, 945–953 (1978). 10.1088/0022-3727/11/6/014
906. B.L. Cardozo, E.E. Haller, L.A. Reichertz, J.W. Beemann, Far-infrared absorption in GaAs:Te liquid phase epitaxial films. Appl. Phys. Lett. **83**, 3990–3992 (2003). 10.1063/1.1624491
907. M. Kleverman, K. Bergmann, H.G. Grimmeiss, Photothermal investigations of magnesium-related donors in silicon. Semicond. Sci. Technol. **1**, 49–52 (1986). 10.1088/0268-1242/1/1/006
908. U. Fano, Sullo spettro di assorbimento dei gas nobili presso il limite dello spettro d'arco. Nuovo Cimento **12**, 154–160 (1935). 10.6028/jres.110.083 English translation: U. Fano, G. Pupillo, A. Zannoni, C.W. Clark, On the absorption spectrum of noble gases at the arc spectrum limit, J. Res. NIST 110, 583-587 (2005). 10.1007/BF02958288
909. G. Breit, E. Wigner, Capture of slow neutrons. Phys. Rev. **49**, 519–531 (1936). 10.1103/PhysRev.49.519
910. G. Lucovsky, On the photoionization of deep impurity centers in semiconductors. Solid State Commun. **3**, 299–302 (1965). 10.1016/0038-1098(65)90039-6
911. P. Drude, Zur Ionentheorie der Metalle. Z. Phys. **1**, 161–165 (1900)
912. C.R. Pidgeon, *Free Carrier Optical Properties of Semiconductors, Handbook on Semiconductors*, vol. 2 (North Holland, Amsterdam, 1980), pp. 223–328
913. H.Y. Fan, Effects of free carriers on the optical properties. Semicond. Semimet. **3**, 405–419 (1967). 10.1016/S0080-8784(08)60321-X
914. W.P. Dumke, Quantum theory of free carrier absorption. Phys. Rev. **124**, 1813 (1961). 10.1103/PhysRev.124.1813
915. R. von Baltz, W. Escher, Quantum theory of free carrier absorption. Phys. Status Solidi B **51**, 499–507 (1972). 10.1002/pssb.2220510209
916. P. Kleinert, M. Giehler, Theory of free-carrier infrared absorption in GaAs. Phys. Status Solidi B **136**, 763–777 (1986). 10.1002/pssb.2221360246
917. Z.G. Hu, M.B.M. Rinzan, S.G. Matsik, A.G.U. Perera, G. Von Winckel, A. Stintz, S. Krishna, Optical characterizations of heavily doped p-type $Al_xGa_{1-x}As$ and GaAs epitaxial films at terahertz frequencies. J. Appl. Phys. **97**, 093529:1–7 (2005). 10.1063/1.1894581
918. H.R. Chandrasekhar, A.K. Ramdas, Nonparabolicity of the conduction band and the coupled plasmon-phonon modes in n-GaAs. Phys. Rev. B **21**, 1511–1515 (1980). 10.1103/PhysRevB.21.1511
919. E. Burstein, Anomalous optical absorption limit in InSb. Phys. Rev. **93**, 632–633 (1954). 10.1103/PhysRev.93.632
920. T.S. Moss, The interpretation of the properties of indium antimonide. Proc. Phys. Soc. B **76**, 775–782 (1954). 10.1088/0370-1301/67/10/306

921. T.J. Coutts, D.L. Young, X. Li, Characterization of transparent conducting oxides. MRS Bull. **25**, 58–65 (2000). 10.1557/mrs2000.152
922. S. Kim, J. Park, S. Kim, Y. Lee, S. Ahn, J. Cho, M. Ju, N. Lakshminarayan, V.A. Dao, J. Yi, Free-carrier absorption and Burstein-Moss shift effect on quantum efficiency in heterojunction silicon solar cells. Vacuum **108**, 39–44 (2014). 10.1016/j.vacuum.2014.05.015
923. G.N. Childs, S. Brand, R.A. Abram, Intervalence band absorption in semiconductor laser materials. Semicond. Sci. Technol. **1**, 116–120 (1986). 10.1088/0268-1242/1/2/004
924. J. Taylor, V. Tolstikhin, Intervalence band absorption in InP and related materials for optoelectronic device modeling. J. Appl. Phys. **87**, 1054–1059 (2000). 10.1063/1.371979
925. R. Braunstein, E.O. Kane, The valence band structure of the III-V compounds. J. Phys. Chem. Solids **23**, 1423–1431 (1962). 10.1016/0022-3697(62)90195-6
926. A. Chandola, R. Pino, P.S. Dutta, Below bandgap optical absorption in tellurium-doped GaSb. Semicond. Sci. Technol. **20**, 886–893 (2005). 10.1088/0268-1242/20/8/046
927. W.P. Dumke, M.R. Lorenz, G.D. Pettit, Intra- and interband free-carrier absorption and the fundamental absorption edge in n-type InP. Phys. Rev. B **1**, 4668–4673 (1970). 10.1103/PhysRevB.1.4668
928. H. Peelaers, E. Kioupakis, C.G. Van de Walle, Fundamental limits on optical transparency of transparent conducting oxides: Free-carrier absorption in SnO_2. Appl. Phys. Lett. **100**, 011914:1–3 (2012) 10.1063/1.3671162
929. A. Schleife, J.B. Varley, F. Fuchs, C. Rödl, F. Bechstedt, P. Rinke, A. Janotti, C.G. Van de Walle, Tin dioxide from first principles: Quasiparticle electronic states and optical properties. Phys. Rev. B **83**, 035116:1–9 (2011). 10.1103/PhysRevB.83.035116
930. H. Peelaers, C.G. Van de Walle, Sub-band-gap absorption in Ga_2O_3. Appl. Phys. Lett. **111**, 182104:1–5 (2017). 10.1063/1.5001323
931. R. Zallen, *Crystal Structures, Handbook on Semiconductors*, vol. 1 (North Holland, Amsterdam, 1980), pp. 1–27
932. R.J. Collins, H.Y. Fan, Infrared lattice absorption bands in germanium, silicon, and diamond. Phys. Rev. **93**, 674–678 (1954). 10.1103/PhysRev.93.674
933. F.A. Johnson, Lattice absorption bands in silicon. Proc. Phys. Soc. **73**, 265–272 (1959). 10.1088/0370-1328/73/2/315
934. W.G. Spitzer, Multiphonon lattice absorption. Semicond. Semimet. **3**, 17–69 (1967). 10.1016/S0080-8784(08)60314-2
935. E.S. Koteles, W.R. Datars, Two-phonon absorption in InSb, InAs, and GaAs. Can. J. Phys. **54**, 1676–1682 (1976). 10.1139/p76-199
936. A. Mooradian, G.B. Wright, Observation of the interaction of plasmons with longitudinal optical phonons in GaAs. Phys. Rev. Lett. **16**, 999–1001 (1966). 10.1103/PhysRevLett.16.999
937. P.T. Landsberg, *Recombination in Semiconductors* (Cambridge Univ. Press, Cambridge, 1992). 10.1017/CBO9780511470769
938. G. Göbel, Recombination without k-selection rules in dense electron-hole plasmas in high-purity GaAs lasers. Appl. Phys. Lett. **24**, 492–494 (1974). 10.1063/1.1655025
939. X. Sun, J. Liu, L.C. Kimerling, J. Michel, Direct gap photoluminescence of n-type tensile-strained Ge-on-Si. Appl. Phys. Lett. **95**, 011911:1–3 (2009). 10.1063/1.3170870
940. J. Shah, R.C.C. Leite, Radiative recombination from photoexcited hot carriers in GaAs. Phys. Rev. Lett. **22**, 1304–1307 (1969). 10.1103/PhysRevLett.22.1304
941. W. Michaelis, M. Pilkuhn, Radiative recombination in silicon p-n junctions. Phys. Status Solidi **36**, 311–319 (1969). 10.1002/pssb.19690360132
942. W. Shockley, W.T. Read Jr., Statistics of the recombination of holes and electrons. Phys. Rev. **87**, 835–842 (1952). 10.1103/PhysRev.87.835
943. R.N. Hall, Electron-hole recombination in germanium. Phys. Rev. **87**, 387 (1952). 10.1103/PhysRev.87.387
944. V.K. Malyutenko, Negative luminescence in semiconductors: A retrospective view. Physica E **20**, 553–557 (2004). 10.1016/j.physe.2003.09.008
945. J.F. Muth, J.H. Lee, I.K. Shmagin, R.M. Kolbas, H.C. Casey Jr., B.P. Keller, U.K. Mishra, S.P. DenBaars, Absorption coefficient, energy gap, exciton binding energy, and recombination lifetime of GaN obtained from transmission measurements. Appl. Phys. Lett. **71**, 2572–2774 (1997). 10.1063/1.120191
946. W. Gerlach, H. Schlangenotto, H. Maeder, On the radiative recombination rate in silicon. Phys. Status Solidi A **13**, 277–283 (1972). 10.1002/pssa.2210130129
947. A. Galeckas, J. Linnros, V. Grivickas, U. Lindefelt, C. Hallin, Auger recombination in 4H-SiC: Unusual temperature behavior. Appl. Phys. Lett. **71**, 3269–3271 (1997). 10.1063/1.120309
948. V. Palankovski, *Simulation of Heterojunction Bipolar Transistors*, Ph.D. Thesis, Technische Universität Wien (2002)
949. R.K. Akrenkiel, Minority-carrier lifetime in III-V semiconductors. Semicond. Semimet. **39**, 39–150 (1993). 10.1016/S0080-8784(08)62594-6
950. P.J. Dean, J.R. Haynes, W.F. Flood, New radiative recombination processes involving neutral donors and acceptors in silicon and germanium. Phys. Rev. **161**, 711–729 (1967). 10.1103/PhysRev.161.711

951. G. Davies, The optical properties of luminescence centres in silicon. Phys. Rep. **176**, 83–188 (1989). 10.1016/0370-1573(89)90064-1
952. G.D. Gilliland, Photoluminescence spectroscopy of crystalline semiconductors. Mater. Sci. Engin. R **18**, 99–400 (1997). 10.1016/S0927-796X(97)80003-4
953. P.J. Dean, D.C. Herbert, *Bound Excitons in Semiconductors*, in: *Excitons*, K. Cho, ed. (Springer, Berlin, 1979), pp. 55–182. 10.1007/978-3-642-81368-9_3
954. P.J. Dean, Lithium donors and the binding of excitons at neutral donors and acceptors in gallium phosphide, in *Luminescence of Crystals, Molecules and Solutions*, ed. by F. Williams (Plenum, New York, 1973), pp. 538–552. 10.1007/978-1-4684-2043-2_75
955. S. Permogorov, A. Reznitsky, A. Naumov, H. Stolz, W. von der Osten, Localisation of excitons at small Te clusters in diluted $ZnSe_{1-x}Te_x$ solid solutions. J. Phys.: Cond. Matter **1**, 5125–5137 (1989). 10.1088/0953-8984/1/31/011
956. T. Skettrup, M. Suffczynski, W. Gorzkowski, Properties of excitons bound to ionized donors. Phys. Rev. B **4**, 512–517 (1971). 10.1103/PhysRevB.4.512
957. R.G. Ulbrich, Low density photoexcitation phenomena in semiconductors: Aspects of theory and experiment. Solid State Electron. **21**, 51–59 (1978). 10.1016/0038-1101(78)90114-4
958. D.E. Hill, Exciton recombination radiation of GaAs:Zn. Phys. Rev. B **1**, 1863–1864 (1970). 10.1103/PhysRevB.1.1863
959. D.C. Reynolds, D.C. Look, B. Jogai, V.M. Phanse, R.P. Vaudo, Identification of an ionized-donor-bound-exciton transition in GaN. Solid State Commun. **103**, 533–535 (1997). 10.1016/S0038-1098(97)00231-7
960. N. Nepal, M.L. Nakarmi, K.B. Nam, J.Y. Lin, H.X. Jiang, Acceptor-bound exciton transition in Mg-doped AlN epilayer. Appl. Phys. Lett. **85**, 2271–2273 (2004). 10.1063/1.1796521
961. D.G. Thomas, J.J. Hopfield, Optical properties of bound exciton complexes in cadmium sulfide. Phys. Rev. **128**, 2135–2148 (1962). 10.1103/PhysRev.128.2135
962. J.L. Merz, H. Kukimoto, K. Nassau, J.W. Shiever, Optical properties of substitutional donors in ZnSe. Phys. Rev. B **6**, 545–556 (1972). 10.1103/PhysRevB.6.545
963. P.J. Dean, D.C. Herbert, C.J. Werkhoven, B.J. Fitzpatrick, R.N. Bhargava, Donor bound-exciton excited states in zinc selenide. Phys. Rev. B **23**, 4888–4901 (1981). 10.1103/PhysRevB.23.4888
964. B.K. Meyer, J. Sann, S. Lautenschläger, M.R. Wagner, A. Hoffmann, Ionized and neutral donor-bound excitons in ZnO. Phys. Rev. B **76**, 184120:1–4 (2007). 10.1103/PhysRevB.76.184120
965. J.R. Haynes, Experimental proof of the existence of a new electronic complex in silicon. Phys. Rev. Lett. **4**, 361–363 (1960). 10.1103/PhysRevLett.4.361
966. B.K. Meyer, H. Alves, D.M. Hofmann, W. Kriegseis, D. Forster, F. Bertram, J. Christen, A. Hoffmann, M. Straßburg, M. Dworzak, U. Haboeck, A.V. Rodina, Bound exciton and donor-acceptor pair recombinations in ZnO. Phys. Status Solidi B **241**, 231–260 (2004). 10.1002/pssb.200301962
967. S. Müller, D. Stichtenoth, M. Uhrmacher, H. Hofsäss, C. Ronning, J. Röder, Unambiguous identification of the PL-I_9 line in zinc oxide. Appl. Phys. Lett. **90**, 012107:1–3 (2007). 10.1063/1.2430483
968. P.J. Dean, M. Skolnick, Donor discrimination and bound exciton spectra in InP. J. Appl. Phys. **54**, 346–359 (1983). 10.1063/1.331709
969. F.A.J.M. Driessen, H.G.M. Lochs, S.M. Olsthoorn, L.J. Giling, An analysis of the two electron satellite spectrum of GaAs in high magnetic fields. J. Appl. Phys. **69**, 906–912 (1991). 10.1063/1.347332
970. D. Karaiskaj, M.L.W. Thewalt, T. Ruf, M. Cardona, H.-J. Pohl, G.G. Deviatych, P.G. Senniko, H. Riemann, Photoluminescence of isotopically purified silicon: How sharp are bound exciton transitions? Phys. Rev. Lett. **86**, 6010–6013 (2001). 10.1103/PhysRevLett.86.6010
971. D. Karaiskaj, M.L.W Thewalt, T. Ruf, M. Cardona, M. Konuma, "Intrinsic" acceptor ground state splitting in silicon: an isotopic effect. Phys. Rev. Lett. **89**, 016401:1–4 (2002). 10.1103/PhysRevLett.89.016401
972. V.A. Karasyuk, M.L.W. Thewalt, S. An, E.C. Lightowlers, A.S. Kaminskii, Fourier-transform photoluminescence spectroscopy of excitons bound to group-III acceptors in silicon: Zeeman effect. Phys. Rev. B **54**, 10543–10558 (1996). 10.1103/PhysRevB.54.10543
973. M.L.W. Thewalt, A. Yang, M. Steger, D. Karaiskaj, M. Cardona, H. Riemann, N.V. Abrosimov, A.V. Gusev, A.D. Bulanov, I.D. Kovalev, A.K. Kaliteevskii, O.N. Godisov, P. Becker, H.J. Pohl, E.E. Haller, J.W. Ager III, K.M. Itoh, Direct observation of the donor nuclear spin in a near-gap bound exciton transition: ^{31}P in highly enriched ^{28}Si. J. Appl. Phys. **101**, 081724:1–5 (2007). 10.1063/1.2723181
974. J.D. Cuthbert, D.G. Thomas, Fluorescent decay times of excitons bound to isoelectronic traps in GaP and ZnTe. Phys. Rev. **154**, 763–771 (1967). 10.1103/PhysRev.154.763
975. J.P. Laurenti, P. Roentgen, K. Wolter, K. Seibert, H. Kurz, J. Camassel, Indium-doped GaAs: A very dilute alloy system. Phys. Rev. B **37**, 4155–4163 (1988). 10.1103/PhysRevB.37.4155
976. D. Bimberg, M. Sondergeld, E. Grobe, Thermal dissociation of excitons bound to neutral acceptors in high-purity GaAs. Phys. Rev. B **4**, 3451–3455 (1971). 10.1103/PhysRevB.4.3451
977. M. Grundmann, C.P. Dietrich, Lineshape theory of photoluminescence from semiconductor alloys. J. Appl. Phys. **106**, 123521:1–10 (2009). 10.1063/1.3267875

978. D.G. Chtchekine, Z.C. Feng, S.J. Chua, G.D. Gilliland, Temperature-varied photoluminescence and magnetospectroscopy study of near-band-edge emissions in GaN. Phys. Rev. B **63**, 125211:1–7 (2001). 10.1103/PhysRevB.63.125211
979. V.D. Kulakovskiĭ, G.E. Pikus, V.B. Timofeev, Multiexciton complexes in semiconductors. Usp. Fiz. Nauk **135**, 237–284 (1981) [Sov. Phys. Usp. **24**, 815–840 (1981)]. 10.1070/PU1981v024n10ABEH004805
980. A.S. Kaminskiĭ, Ya.E. Pokrovskiĭ, Recombination radiation of the condensed phase on nonequilibrium carriers in silicon. Pis'ma Zh. Eksp. Teor. Fiz. **11**, 381 (1970) [JETP Lett. **11**, 255–257 (1970)]
981. M.L.W. Thewalt, Details of the structure of bound excitons and bound multiexciton complexes in Si. Can. J. Phys. **55**, 1463–1480 (1977). 10.1139/p77-186 Erratum: Can. J. Phys. **56**, 310 (1978). 10.1139/p78-038
982. M.L.W. Thewalt, J.A. Rostworowski, G. Kirczenow, Piezospectroscopic studies of phosphorus-, boron-, and lithium-doped silicon. Can. J. Phys. **57**, 1898–1923 (1979). 10.1139/p79-262
983. O. Goede, L. John, D. Hennig, Compositional disorder-induced broadening for free excitons in II-VI semiconducting mixed crystals. Phys. Status Solidi B **89**, K183–K186 (1978). 10.1002/pssb.2220890262
984. E.F. Schubert, E.O. Göbel, Y. Horikoshi, K. Ploog, H.J. Queisser, Alloy broadening in photoluminescence spectra of $Al_xGa_{1-x}As$. Phys. Rev. B **30**, 813–820 (1984). 10.1103/PhysRevB.30.813
985. S. Heitsch, G. Zimmermann, D. Fritsch, C. Sturm, R. Schmidt-Grund, C. Schulz, H. Hochmuth, D. Spemann, G. Benndorf, B. Rheinländer, Th. Nobis, M. Lorenz, M. Grundmann, Luminescence and surface properties of $Mg_xZn_{1-x}O$ thin films grown by pulsed laser deposition. J. Appl. Phys. **101**, 083521:1–6 (2007). 10.1063/1.2719010
986. R. Zimmermann, Theory of the exciton linewidth in II-VI semiconductor mixed crystals. J. Cryst. Growth **101**, 346–349 (1990). 10.1016/0022-0248(90)90993-U
987. J.M. Langer, R. Buczko, A.M. Stoneham, Alloy broadening of the near-gap luminescence and the natural band offset in semiconductor alloys. Semicond. Sci. Technol. **7**, 547–551 (1992). 10.1088/0268-1242/7/4/018
988. A. Müller, M. Stölzel, G. Benndorf, M. Lorenz, M. Grundmann, Origin of the near-band-edge luminescence in $Mg_xZn_{1-x}O$ alloys. J. Appl. Phys. **107**, 013704:1–6 (2010). 10.1063/1.3270431
989. M.C. Wagener, G.R. James, A.W.R. Leitch, F. Omnès, On the nature of Si-doping in AlGaN alloys. Phys. Status Solidi C **1**, 2322–2327 (2004). 10.1002/pssc.200404838
990. B. Segall, G.D. Mahan, Phonon-assisted recombination of free excitons in compound semiconductors. Phys. Rev. **171**, 935–948 (1968). 10.1103/PhysRev.171.935
991. J. Conradi, R.R. Haering, Oscillatory exciton emission in CdS. Phys. Rev. Lett. **20**, 1344–1346 (1968). 10.1103/PhysRevLett.20.1344
992. Y.S. Park, J.R. Schneider, Oscillations in exciton emission in the excitation spectra of ZnSe and CdS. Phys. Rev. Lett. **21**, 798–800 (1968). 10.1103/PhysRevLett.21.798
993. D. Kovalev, B. Averboukh, D. Volm, B.K. Meyer, H. Amano, I. Akasaki, Free exciton emission in GaN. Phys. Rev. B **54**, 2518–2522 (1996). 10.1103/PhysRevB.54.2518
994. S. Permogorov, Optical emission due to exciton scattering by LO phonons in semiconductors, in *Excitons*, E.I. Rashba, M.D. Sturge, eds. (North-Holland, 1982)
995. M. Wojdak, A. Wysmołek, K. Pakuła, J.M. Baranowski, Emission due to exciton scattering by LO-phonons in gallium nitride. Phys. Status Solidi B **216**, 95–99 (1999). 10.1002/(SICI)1521-3951(199911)216:1%3C95::AID-PSSB95%3E3.0.CO;2-R
996. R. Dingle, Luminescent transitions associated with divalent copper impurities and the green emission from semiconducting zinc oxide. Phys. Rev. Lett. **23**, 579–581 (1969). 10.1103/PhysRevLett.23.579
997. Th Agne, *Identifikation und Untersuchung von Defekten in ZnO Einkristallen*. Ph.D. Thesis, Universität des Saarlandes, Saarbrücken, (2004)
998. K. Huang, A. Rhys, Theory of light absorption and non-radiative transitions in F-centres. Proc. Roy. Soc. Lond. A **204**, 406–423 (1950). 10.1098/rspa.1950.0184
999. J.J. Hopfield, A theory of edge-emission phenomena in CdS, ZnS and ZnO. J. Phys. Chem. Solids **10**, 110–119 (1959). 10.1016/0022-3697(59)90064-2
1000. M. Lax, The Franck-Condon principle and its application to crystals. J. Chem. Phys. **20**, 1752–1760 (1952). 10.1063/1.1700283
1001. J.L. Merz, Isoelectronic oxygen trap in ZnTe. Phys. Rev. **176**, 961–968 (1968). 10.1103/PhysRev.176.961
1002. C. Klingshirn, The luminescence of ZnO under high one- and two-quantum excitation. Phys. Status Solidi B **71**, 547–556 (1975). 10.1002/pssb.2220710216
1003. P.J. Dean, C.H. Henry, C.J. Frosch, Infrared donor-acceptor pair spectra involving the deep oxygen donor in gallium phosphide. Phys. Rev. **168**, 812–816 (1968). 10.1103/PhysRev.168.812
1004. A. Juhl, *Calorimetrische Absorptionsspektroskopie (CAS)—Eine neue Methode zur Charakterisierung der optischen Eigenschaften von Halbleitersystemen*, Ph.D. Thesis, Technische Universität Berlin (1987)
1005. W.H. Koschel, U. Kaufmann, S.G. Bishop, Optical an ESR analysis of the fe acceptor in InP. Solid State Commun. **21**, 1069–1072 (1977). 10.1016/0038-1098(77)90308-8
1006. F. Jelezko J. Wrachtrup, Single defect centres in diamond: A review. Phys. Status Solidi A **203**, 3207–3225 (2006). 10.1002/pssa.200671403

1007. R. Schirhagl, K. Chang, M. Loretz, C.L. Degen, Nitrogen-vacancy centers in diamond: Nanoscale sensors for physics and biology. Ann. Rev. Phys. Chem. **65**, 83–105 (2014). 10.1146/annurev-physchem-040513-103659
1008. G. Balasubramanian, I.Y. Chan, R. Kolesov, M. Al-Hmoud, J. Tisler, C. Shin, C. Kim, A. Wojcik, P.R. Hemmer, A. Krueger, T. Hanke, A. Leitenstorfer, R. Bratschitsch, F. Jelezko, J. Wrachtrup, Nanoscale imaging magnetometry with diamond spins under ambient conditions. Nature **455**, 648–651 (2008). 10.1038/nature07278
1009. E. Abe, K. Sasaki, Tutorial: Magnetic resonance with nitrogen-vacancy centers in diamond—Microwave engineering, materials science, and magnetometry. J. Appl. Phys. **123**, 161101:1–14 (2018). 10.1063/1.5011231
1010. W. Lochmann, A. Haug, Phonon-assisted auger recombination in Si with direct calculation of the overlap integrals. Solid State Commun. **35**, 553–556 (1980). 10.1016/0038-1098(80)90896-0
1011. M. Takeshima, Theory of phonon-assisted Auger recombination in semiconductors. Phys. Rev. B **23**, 6625–6637 (1981). 10.1103/PhysRevB.23.6625
1012. M. Takeshima, Phonon-assisted Auger recombination in a quasi-two-dimensional structure semiconductor. Phys. Rev. B **30**, 3302–3308 (1984). 10.1103/PhysRevB.30.3302
1013. P.C. Findlay, C.R. Pidgeon, H. Pellemans, R. Kotitschke, B.N. Murdin, T. Ashley, A.D. Johnson, A.M. White, C.T. Elliott, Auger recombination dynamics of $In_xGa_{1-x}Sb$. Semicond. Sci. Technol. **14**, 1026–1030 (1999). 10.1088/0268-1242/14/12/302
1014. D. Vignaud, J.F. Lampin, E. Lefebvre, M. Zaknoune, F. Mollot, Electron lifetime of heavily Be-doped $In_{0.53}Ga_{0.47}As$ as a function of growth temperature and doping density. Appl. Phys. Lett. **80**, 4151–4153 (2002). 10.1063/1.1483126
1015. D.B. Laks, G.F. Neumark, S.T. Pantelides, Accurate interband-Auger-recombination rates in silicon. Phys. Rev. B **42**, 5176–5185 (1990). 10.1103/PhysRevB.42.5176
1016. P. Blood, J.W. Orton, The electrical characterization of semiconductors. Rep. Progress Phys. **41**, 157–257 (1978). 10.1088/0034-4885/41/2/001
1017. P. Blood, J.W. Orton, *The Electrical Characterization of Semiconductors: Majority Carriers and Electron States* (Academic Press, San Diego, 1992)
1018. D. Macdonald, A. Cuevas, Validity of simplified Shockley-Read-Hall statistics for modeling carrier lifetimes in crystalline silicon. Phys. Rev. B **67**, 075203:1–7 (2003). 10.1103/PhysRevB.67.075203
1019. D.H. Auston, Picosecond photoconductivity: High-speed measurements of devices and materials. Semicond. Semimet. **28**, 85–134 (1990). 10.1016/S0080-8784(08)62785-4
1020. A.A. Istratov, E.R. Weber, Electrical properties and recombination activity of copper, nickel and cobalt in silicon. Appl. Phys. A **66**, 123–136 (1998). 10.1007/s003390050649
1021. A.A. Istratov, H. Hieslmair, E.R. Weber, Iron and its complexes in silicon. Appl. Phys. A **69**, 13–44 (1999). 10.1007/s003390050968
1022. A.A. Istratov, H. Hieslmair, E.R. Weber, Iron contamination in silicon technology. Appl. Phys. A **70**, 489–534 (2000). 10.1007/s003390051074
1023. J.S. Blakemore, Lifetime in p-type silicon. Phys. Rev. **110**, 1301–1308 (1958). 10.1103/PhysRev.110.1301
1024. M.S. Tyagi, R. van Overstraeten, Minority carrier recombination in heavily doped silicon. Solid State Electron. **26**, 577–597 (1983). 10.1016/0038-1101(83)90174-0
1025. G. Bemski, Lifetime of electrons in p-type silicon. Phys. Rev. **100**, 523–524 (1955). 10.1103/PhysRev.100.523
1026. Q. Dai, Q. Shan, J. Wang, S. Chhajed, J. Cho, E.F. Schubert, M.H. Crawford, D.D. Koleske, M.-H. Kim, Y. Park, Carrier recombination mechanisms and efficiency droop in GaInN/GaN light-emitting diodes. Appl. Phys. Lett. 97, 133507:1–3 (2010). 10.1063/1.3493654
1027. S. Karpov, ABC-model for interpretation of internal quantum efficiency and its droop in III-nitride LEDs: a review. Opt. Quant. Electron. **47**, 1293–1303 (2015). 10.1007/s11082-014-0042-9
1028. J. Frenkel, On pre-breakdown phenomena in insulators and electronic semi-conductors. Phys. Rev. **54**, 647–648 (1938). 10.1103/PhysRev.54.647
1029. R.D. Harris, J.L. Newton, G.D. Watkins, Negative-U properties for interstitial boron in silicon. Phys. Rev. Lett. **48**, 1271–1274 (1982). 10.1103/PhysRevLett.48.1271
1030. S. Bothra, S. Tyagi, S.K. Chandhi, J.M. Borrego, Surface recombination velocity and lifetime in InP. Solid State Electron. **34**, 47–50 (1991). 10.1016/0038-1101(91)90199-9
1031. J. Schmidt, A.G. Aberle, Accurate method for the determination of bulk minority-carrier lifetimes of mono- and multicrystalline silicon wafers. J. Appl. Phys. **81**, 6186–6199 (1997). 10.1063/1.364403
1032. M.J. Kerr, J. Schmidt, A. Cuevas, J.H. Bultman, Surface recombination velocity of phosphorus-diffused silicon solar cell emitters passivated with plasma enhanced chemical vapor deposited silicon nitride and thermal silicon oxide. J. Appl. Phys. **89**, 3821–3826 (2001). 10.1063/1.1350633
1033. O. Hahneiser, M. Kunst, Theoretical and experimental study of charge carrier kinetics in crystalline silicon. J. Appl. Phys. **85**, 7741–7754 (1999). 10.1063/1.370579
1034. D.E. Aspnes, Recombination at semiconductor surfaces and interfaces. Surf. Sci. **132**, 406–421 (1983). 10.1016/0039-6028(83)90550-2
1035. L. Zhou, B. Bo, X. Yan, C. Wang, Y. Chi, X. Yang, Brief review of surface passivation on III-V semiconductor. Crystals **8**, 226:1–14 (2018). 10.3390/cryst8050226

1036. C. Donolato, Theory of beam induced current characterization of grain boundaries in polycrystalline solar cells. J. Appl. Phys. **54**, 1314–1322 (1983). 10.1063/1.332205
1037. T. Kieliba, S. Riepe, W. Warta, Effect of dislocations on minority carrier diffusion length in practical silicon solar cells. J. Appl. Phys. **100**, 063706:1–12 (2006). 10.1063/1.2338126
1038. J. Palm, Local investigation of recombination at grain boundaries in silicon by grain boundary-electron beam induced current. J. Appl. Phys. **74**, 1169–1178 (1993). 10.1063/1.354917
1039. T.F. Ciszek, T.H. Wang, R.W. Burrows, X. Wu, J. Alleman, Y.S. Tsuo, T. Bekkedahl, Grain boundary and dislocation effects on the PV performance of high-purity silicon, in *23th IEEE Photovoltaic Specialists Conference Rec.* (IEEE, New York, 1993), pp. 101–105. 10.1109/PVSC.1993.347071
1040. R. Corkish, T. Puzzer, A.B. Sproul, K.L. Luke, Quantitative interpretation of electron-beam-induced current grain boundary contrast profiles with application to silicon. J. Appl. Phys. **84**, 5473–5481 (1998). 10.1063/1.368310
1041. J.D. Major, Grain boundaries in CdTe thin film solar cells: A review. Semicond. Sci. Technol. **31**, 093001:1–19 (2016). 10.1088/0268-1242/31/9/093001
1042. A.D. Kurtz, S.A. Kulin, B.L. Averbach, Effect of dislocations on the minority carrier lifetime in semiconductors. Phys. Rev. **101**, 1285–1291 (1956). 10.1103/PhysRev.101.1285
1043. E.A. Fitzgerald, D.G. Ast, P.D. Kirchner, G.D. Pettit, J.M. Woodall, Structure and recombination in InGaAs/GaAs heterostructures. J. Appl. Phys. **63**, 693–703 (1988). 10.1063/1.340059
1044. M. Grundmann, J. Christen, D. Bimberg, A. Fischer-Colbrie, R. Hull, Misfit dislocations in pseudomorphic $In_{0.23}Ga_{0.77}As/GaAs$ quantum wells: Influence on lifetime and diffusion of excess excitons. J. Appl. Phys. **66**, 2214–2216 (1989). 10.1063/1.344288
1045. H. Dember, Über eine photoelektronische Kraft in Kupferoxydul-Kristallen. Phys. Zeitschrift **32**, 554–556 (1931)
1046. H. Dember, Über eine Kristallphotozelle. Phys. Zeitschrift **32**, 856–858 (1931)
1047. H. Dember, Über die Vorwärtsbewegung von Elektronen durch Licht. Phys. Zeitschrift **33**, 207–208 (1932)
1048. M. Krčmar, W.M. Saslow, Exact surface solutions for semiconductors: The Dember effect and partial currents. Phys. Rev. B **65**, 233313:1–4 (2002). 10.1103/PhysRevB.65.233313
1049. S.R. Goldman, K. Kalikstein, B. Kramer, Dember-effect theory. J. Appl. Phys. **49**, 2849–2854 (1978). 10.1063/1.325166
1050. S.K. Chattopadhyaya, V.K. Mathur, Normal and anomalous Dember effect. J. Appl. Phys. **40**, 1930–1933 (1969). 10.1063/1.1657868
1051. M. Ni, M.K.H. Leung, D.Y.C. Leung, K. Sumathy, A review and recent developments in photocatalytic water-splitting using TiO_2 for hydrogen production. Renew. Sustain. Energy Rev. **11**, 401–425 (2007). 10.1016/j.rser.2005.01.009
1052. S. Cho, J.-W. Jang, K.-H. Lee, J.S. Lee, Research update: Strategies for efficient photoelectrochemical water splitting using metal oxide photoanodes. APL Mater. **2**, 010703:1–14 (2014). 10.1063/1.4861798
1053. J. Watson, The tin oxide gas sensor and its applications. Sens. Act. **5**, 29–42 (1984). 10.1016/0250-6874(84)87004-3
1054. G. Eranna, B.C. Joshi, D.P. Runthala, R.P. Gupta, Oxide materials for development of integrated gas sensors—A comprehensive review. Crit. Rev. Solid State Mater. Sci. **29**, 111–188 (2004). 10.1080/10408430490888977
1055. X. Liu, S. Cheng, H. Liu, S. Hu, D. Zhang, H. Ning, A survey on gas sensing technology. Sensors **12**, 9635–9665 (2012). 10.3390/s120709635
1056. H. Ibach, *Physics of Surfaces and Interfaces* (Springer, Berlin, 2006). 10.1007/3-540-34710-0
1057. A. Zangwill, *Physics at Surfaces* (Cambridge University Press, Cambridge, 2012). 10.1017/CBO9780511622564
1058. R.H. Kingston, *Semiconductor Surface Physics* (Literary Licensing, Whitefish, 2012)
1059. P.J. Morandi, *Symmetry Groups: The Classification of Wallpaper Patterns, From Group Cohomology to Escher's Tessellations* (New Mexico State University, 2007)
1060. A.A. Stekolnikov, F. Bechstedt, Shape of free and constrained group-IV crystallites: Influence of surface energies. Phys. Rev. B **72**, 125326:1–9 (2005). 10.1103/PhysRevB.72.125326
1061. J.M. Bermond, J.J. Métois, X. Egéa, F. Floret, The equilibrium shape of silicon. Surf. Sci. **330**, 48–60 (1995). 10.1016/0039-6028(95)00230-8
1062. C.B. Duke, Semiconductor surface reconstruction: The structural chemistry of two-dimensional surface compounds. Chem. Rev. **96**, 1237–1259 (1996). 10.1021/cr950212s
1063. J. Fritsch, U. Schröder, Density functional calculation of semiconductor surface phonons. Phys. Reports **309**, 209–331 (1999). 10.1016/S0370-1573(98)00034-9
1064. K. Hermann, *Fritz-Haber-Institut* (Berlin)
1065. W.G. Schmidt, F. Bechstedt, J. Bernholc, GaAs(001) surface reconstructions: Geometries, chemical bonding and optical properties. Appl. Surf. Sci. **190**, 264–268 (2002). 10.1016/S0169-4332(01)00862-5
1066. K. Takayanagi, Y. Tanishiro, S. Takahashi, M. Takahashi, Surface analysis of Si(111)-7×7. Surf. Sci. **164**, 367–392 (1985). 10.1016/0039-6028(85)90753-8
1067. R. Wiesendanger, G. Tarrach, L. Scandella, H.-J. Güntherodt, Scanning tunneling microscopy on laser- and thermal-annealed Si(111): Transitions from 7×7 reconstructed to disordered surface structures. Ultramicroscopy **32**, 291–295 (1990). 10.1016/0304-3991(90)90006-8

1068. F.J. Giessibl, S. Hembacher, H. Bielefeldt, J. Mannhart, Subatomic features on the silicon (111)-(7×7) surface observed by atomic force microscopy. Science **289**, 422–425 (2000). 10.1126/science.289.5478.422
1069. B.S. Swartzentruber, N. Kitamura, M.G. Lagally, M.B. Webb, Behavior of steps on Si(001) as a function of vicinality. Phys. Rev. B **47**, 13432–13441 (1993). 10.1103/PhysRevB.47.13432
1070. O. Dulub, L.A. Boatner, U. Diebold, STM study of the geometric and electronic structure of ZnO(0001)-Zn, $(000\bar{1})$-O, $(10\bar{1}0)$, and $(11\bar{2}0)$ surfaces. Surf. Sci. **519**, 201–217 (2002). 10.1016/S0039-6028(02)02211-2
1071. J.J. Métois, A. Saúl, P. Müller, Measuring the surface stress polar dependence. Nature Mater. **4**, 238–242 (2005). 10.1038/nmat1328
1072. M. Syväjärvi, R. Yakimova, E. Janzén, Step-bunching in SiC epitaxy: Anisotropy and influence of growth temperature. J. Cryst. Growth **236**, 297–304 (2002). 10.1016/S0022-0248(01)02331-4
1073. A.A. Baski, S.C. Erwin, L.J. Whitman, The structure of silicon surfaces from (001) to (111). Surf. Sci. **392**, 69–85 (1997). 10.1016/S0039-6028(97)00499-8
1074. R.H. Ritchie, Plasma losses by fast electrons in thin films. Phys. Rev. **106**, 874–881 (1957). 10.1103/PhysRev.106.874
1075. J.M. Pitarke, V.M. Silkin, E.V. Chulkov, P.M. Echenique, Theory of surface plasmons and surface-plasmon polaritons. Rep. Prog. Phys. **70**, 1–87 (2007). 10.1088/0034-4885/70/1/R01
1076. J. Zhang, L. Zhang, W. Xu, Surface plasmon polaritons: Physics and applications. J. Phys. D: Appl. Phys. **45**, 113001:1–19 (2012). 10.1088/0022-3727/45/11/113001
1077. https://www.wikipedia.de
1078. S. Kalusniak, S. Sadofev, F. Henneberger, ZnO as a tunable metal: New types of surface plasmon polaritons. Phys. Rev. Lett. **112**, 137401 (2014). 10.1103/PhysRevLett.112.137401
1079. J.E. Northrup, M.S. Hybertsen, S.G. Louie, Many-body calculation of the surface-state energies for Si(111)2×1. Phys. Rev. Lett. **66**, 500–503 (1991). 10.1103/PhysRevLett.66.500
1080. I. Ivanov, A. Mazur, J. Pollmann, The ideal (111), (110), and (100) surfaces of Si, Ge and GaAs: A comparison of their electronic structure. Surf. Sci. **92**, 365–384 (1980). 10.1016/0039-6028(80)90209-5
1081. R.I.G. Uhrberg, G.V. Hansson, Electronic structure of silicon surfaces: Clean and with ordered overlayers. Crit. Rev. Solid State Mater. Sci. **17**, 133–186 (1991). 10.1080/10408439108242191
1082. P. Mårtensson, W.-X. Ni, G.V. Hansson, J.M. Nicholls, B. Reihl, Surface electronic structure of Si(111)7×7-Ge and Si(111)5×5-Ge studied with photoemission and inverse photoemission. Phys. Rev. B **36**, 5974–5981 (1987). 10.1103/PhysRevB.36.5974
1083. S.R. Varier, P.S. Mandal, N. Sahadev, D.N. Biswas, K. Maiti, Study of the surface electronic structure of Si(111) surface using spin and angle resolved photoemission spectroscopy. AIP Conf. Proc. **1512**, 818–819 (2013). 10.1063/1.4791289
1084. Z. Zhu, Y. Cheng, U. Schwingenschlögl, Band inversion mechanism in topological insulators: A guideline for materials design. Phys. Rev. B **85**, 235401:1–5 (2012). 10.1103/PhysRevB.85.235401
1085. L. Fu, C.L. Kane, E.J. Mele, Topological insulators in three dimensions. Phys. Rev. Lett. **98**, 106803:1–4 (2007). 10.1103/PhysRevLett.98.106803
1086. H. Zhang, C.-X. Liu, X.-L. Qi, X. Dai, Zh Fang, S-Ch. Zhang, Topological insulators in Bi_2Se_3, Bi_2Te_3 and Sb_2Te_3 with a single Dirac cone on the surface. Nature Physics **5**, 438–442 (2009). 10.1038/nphys1270
1087. Y. Xia, D. Qian, D. Hsieh, L. Wray, A. Pal, H. Lin, A. Bansil, D. Grauer, Y.S. Hor, R.J. Cava, M.Z. Hasan, Observation of a large-gap topological-insulator class with a single Dirac cone on the surface. Nat. Phys. **5**, 398–402 (2009). 10.1038/nphys1274
1088. Y. Xia, *Photoemission studies of a new topological insulator class: Experimental discovery of the Bi_2X_3 topological insulator class*, Ph.D. Thesis, Princeton University (2010)
1089. J.E. Ayers, T. Kujofsa, P. Rago, J. Raphael, *Heteroepitaxy of Semiconductors: Theory, Growth, and Characterization*, 2nd edn. (CRC Press, Boca Raton, 2016)
1090. U. Pohl, *Epitaxy of Semiconductors* (Springer, Berlin, 2013). 10.1007/978-3-642-32970-8
1091. G. Dhanaraj, K. Byrappa, V. Prasad, M. Dudley, eds., *Springer Handbook of Crystal Growth* (Springer, Heidelberg, 2010). 10.1007/978-3-540-74761-1
1092. J.Y. Tsao, *Materials Fundamentals of Molecular Beam Epitaxy* (Academic Press, San Diego, 1993). 10.1016/C2009-0-22426-3
1093. M.L. Hitchman, K.F. Jensen, eds., *Chemical Vapor Deposition* (Academic Press, San Diego, 1993)
1094. P. George, *Chemical Vapor Deposition: Simulation and Optimization* (VDM Verlag Dr. Mueller, Saarbrücken, 2008)
1095. G. Stringfellow, *Organometallic Vapor-Phase Epitaxy: Theory and Practice* (Academic Press, San Diego, 1999). 10.1016/B978-0-12-673842-1.X5000-5
1096. C.S. Hwang, C.Y. Yoo, eds., *Atomic Layer Deposition for Semiconductors* (Springer, Berlin, 2014). 10.1007/978-1-4614-8054-9
1097. J. Valdez, ed., *Atomic Layer Deposition (ALD)* (Nova Science Publ., Hauppauge, 2015)
1098. R. Eason, ed., *Pulsed Laser Deposition of Thin Films: Applications-Led Growth of Functional Materials* (Wiley, Hoboken, 2006). 10.1002/0470052120

1099. P. Capper, M. Mauk, eds., *Liquid Phase Epitaxy of Electronic, Optical and Optoelectronic Materials* (Wiley, Chichester, 2007). 10.1002/9780470319505
1100. B.A. Joyce, J.H. Neave, P.J. Dobson, P.K. Larsen, Analysis of reflection high-energy electron-diffraction data from reconstructed semiconductor surfaces. Phys. Rev. B **29**, 814–819 (1984). 10.1103/PhysRevB.29.814
1101. J.-T. Zettler, W. Richter, K. Ploska, M. Zorn, J. Rumberg, C. Meyne, M. Pristovsek, Real time diagnostics of semiconductor surface modifications by reflectance anisotropy spectroscopy, in *Semiconductor Characterization—Present Status and Future Needs*, W.M. Bullis, D.G. Seiler, A.C. Diebold, eds. (AIP Press, Woodbury, 1996), pp. 537–543
1102. J.-T. Zettler, Characterization of epitaxial semiconductor growth by reflectance anisotropy spectroscopy and ellipsometry. Prog. Cryst. Growth Charact. Mater. **35**, 27–98 (1997). 10.1016/S0960-8974(97)00024-7
1103. W. Zulehner, Status and future of silicon crystal growth. Mater. Sci. Engin. B **4**, 1–10 (1989). 10.1016/0921-5107(89)90207-9
1104. W. Zulehner, Historical overview of silicon crystal pulling development. Mater. Sci. Engin. B **73**, 7–15 (2000). 10.1016/S0921-5107(99)00427-4
1105. B. Depuydt, A. Theuwis, I. Romandie, Germanium: From the first application of Czochralski crystal growth to large diameter dislocation-free wafers. Mat. Sci. Semicond. Process. **9**, 437–443 (2006). 10.1016/j.mssp.2006.08.002
1106. Virgina Semiconductor, www.virginiasemi.com
1107. J. Czochralski, Ein neues Verfahren zur Messung der Kristallisationsgeschwindigkeit der Metalle. Z. Phys. Chem. **92**, 219–221 (1918). 10.1515/zpch-1918-9212
1108. R. Uecker, The historical development of the Czochralski method. J. Cryst. Growth **401**, 7–24 (2014). 10.1016/j.jcrysgro.2013.11.095
1109. G.K. Teal, J.B. Little, Growth of germanium single crystals. Phys. Rev. **78**, 647 (1950). 10.1103/PhysRev.78.637
1110. G.K. Teal, M. Sparks, E. Buehler, Growth of germanium single crystals containing p-n junctions. Phys. Rev. **81**, 637 (1951). 10.1103/PhysRev.81.637
1111. W.R. Runyan, Growth of large diameter silicon and germanium crystals by the Teal-Little method. Rev. Sci. Instr. **30**, 535–540 (1959). 10.1063/1.1716676
1112. W.G. Pfann, *Zone Melting* (Wiley, New York, 1966)
1113. H.J. Scheel, T. Fukuda, eds., *Crystal Growth Technology* (Wiley, New York, 2004)
1114. Siltronic AG, München
1115. K.A. Reinhardt, W. Kern, *Handbook of Silicon Wafer Cleaning Technology*, 3rd edn. (William Andrew, New York, 2018)
1116. J. Ruzyllo, Semiconductor cleaning technology: Forty years in the making. Interface **19**, 44–46 (2010). 10.1149/2.F05101if
1117. W. Kern, Purifying Si and SiO_2 surfaces with hydrogen peroxide, in *Semiconductor International* (1984), pp. 94–99
1118. A. Ishizaka, Y. Shiraki, Low temperature surface cleaning of silicon and its application to silicon MBE. J. Electrochem. Soc. **133**, 666–671 (1986). 10.1149/1.2108651
1119. J.C. Kim, J.-Y. Ji, J.S. Kline, J.R. Tucker, T.-C. Shen, Preparation of atomically clean and flat Si(100) surfaces by low-energy ion sputtering and low-temperature annealing. Appl. Surf. Sci. **220**, 293–297 (2003). 10.1016/S0169-4332(03)00826-2
1120. H. Hartnagel, B.L. Weiss, A contribution to etch polishing of GaAs. J. Mat. Sci. **8**, 1061–1063 (1973). 10.1007/BF00756642
1121. Z.F. Tomashik, N.V. Kusyak, V.N. Tomashik, Chemical etching of InAs, InSb, and GaAs in H_2O_2-HBr solutions. Inorg. Mat. **38**, 434–437 (2002). 10.1023/A:1015402501421
1122. H. von Wenckstern, H. Schmidt, C. Hanisch, M. Brandt, C. Czekalla, G. Benndorf, G. Biehne, A. Rahm, H. Hochmuth, M. Lorenz, M. Grundmann, Homoepitaxy of ZnO by pulsed-laser deposition. Phys. Status Solidi RRL **1**, 129–131 (2007). 10.1002/pssr.200701052
1123. C. Weisbuch, Fundamental properties of III-V semiconductor two-dimensional quantized structures: the basis for optical and electronic device applications. Semicond. Semimet. **24**, 1–133 (1987). 10.1016/S0080-8784(08)62448-5
1124. C.H.J. van den Brekel, Growth rate anisotropy and morphology of autoepitaxial silicon films from $SiCl_4$. J. Cryst. Growth **23**, 259–266 (1974). 10.1016/0022-0248(74)90067-0
1125. J.-I. Nishizawa, T. Terasaki, M. Shimbo, Layer growth in silicon epitaxy. J. Cryst. Growth **13**(14), 297–301 (1972). 10.1016/0022-0248(72)90173-X
1126. J.G.E. Gardiniers, C.H. Klein Douwel, L.J. Giling, Reduced pressure silicon CVD on hemispherical substrates. J. Cryst. Growth **108**, 319–334 (1991). 10.1016/0022-0248(91)90380-N
1127. S. Nishino, Y. Nishio, Y. Masuda, Y. Chen, C. Jacob, Morphological stability of 6H-SiC epitaxial layer on hemispherical substrates prepared by chemical vapor deposition. Mat. Sci. Forum **338–342**, 197–200 (2000). 10.4028/www.scientific.net/MSF.338-342.197

1128. L. Hollan, C. Schiller, Étude de l'anisotropie de la croissance épitaxiale de GaAs en phase vapeur. J. Cryst. Growth **13**(14), 319–324 (1972). 10.1016/0022-0248(72)90177-7
1129. K. Morizane, Antiphase domain structures in GaP and GaAs epitaxial layers grown on Si and Ge. J. Cryst. Growth **38**, 249–254 (1977). 10.1016/0022-0248(77)90305-0
1130. M. Volmer, A. Weber, Keimbildung in übersättigten Gebilden. Z. Physikal. Chem. **119U**, 277–301 (1926). 10.1515/zpch-1926-11927
1131. I.N. Stranski, Zur Theorie der isomorphen Fortwachsung (orientierter Ausscheidung) von Ionenkristallen aufeinander. Z. Physikal. Chemie **142A**, 453–466 (1929). 10.1515/zpch-1929-14232
1132. I.N. Stranski, L. Krastanow, Zur Theorie der orientierten Ausscheidung von Ionenkristallen aufeinander, Monatshefte f. Chemie u. verwandte Teile anderer Wissenschaften **71**, 351–364 (1937). 10.1515/zpch-1929-14232
1133. E. Bauer, Phänomenologische Theorie der Kristallabscheidung an Oberflächen. I. Z. Kristallogr. **110**, 372–394 (1958). 10.1524/zkri.1958.110.16.372
1134. T. Shitara, D.D. Vvedensky, M.R. Wilby, J. Zhang, J.H. Neave, B.A. Joyce, Step-density variations and reflection high-energy electron-diffraction intensity oscillations during epitaxial growth on vicinal GaAs(001). Phys. Rev. B **46**, 6815–6824 (1992). 10.1103/PhysRevB.46.6815
1135. A. Pimpinelli, J. Villain, *Physics of Crystal Growth* (Cambridge Univ. Press, Cambridge, 1999). 10.1017/CBO9780511622526
1136. E. Ohshima, H. Ogino, I. Niikura, K. Maeda, M. Sato, M. Ito, T. Fukuda, Growth of the 2-in-size bulk ZnO single crystals by the hydrothermal method. J. Cryst. Growth **260**, 166–170 (2004). 10.1016/j.jcrysgro.2003.08.019
1137. F. Scholz, U. Kaiser, Universität Ulm
1138. S. Heitsch, C. Bundesmann, G. Wagner, G. Zimmermann, A. Rahm, H. Hochmuth, G. Benndorf, H. Schmidt, M. Schubert, M. Lorenz, M. Grundmann, Low temperature photoluminescence and infrared dielectric functions of pulsed laser deposited ZnO thin films on silicon. Thin Solid Films **496**, 234–239 (2006). 10.1016/j.tsf.2005.08.305
1139. M. Grundmann, T. Böntgen, M. Lorenz, Occurrence of rotation domains in heteroepitaxy. Phys. Rev. Lett. **105**, 146102:1–4 (2010). 10.1103/PhysRevLett.105.146102
1140. M. Grundmann, Formation of epitaxial domains: Unified theory and survey of experimental results. Phys. Status Solidi B **248**, 805–824 (2011). 10.1002/pssb.201046530
1141. Y. Zhang, C. McAleese, H. Xiu, C.J. Humphreys, R.R. Lieten, B. Degroote, G. Borghs, Misoriented domains in (0001)-GaN/(111)-Ge grown by molecular beam epitaxy. Appl. Phys. Lett. **91**, 092125:1–2 (2007) 10.1063/1.2779099
1142. H. Kawanami, A. Hatayama, Y. Hayashi, Antiphase boundary of GaAs films grown on Si(001) substrates by molecular beam epitaxy. J. Electr. Mater. **17**, 341–349 (1988). 10.1007/BF02652116
1143. J. Ohta, H. Fujioka, M. Oshima, K. Fujiwara, A. Ishii, Experimental and theoretical investigation on the structural properties of GaN grown on sapphire. Appl. Phys. Lett. **83**, 3075–3077 (2003). 10.1063/1.1618379
1144. H. Kato, M. Sano, K. Miyamoto, T. Yao, Polarity control of ZnO on c-plane sapphire by plasma-assisted MBE. J. Cryst. Growth **275**, e2459–e2465 (2005). 10.1016/j.jcrysgro.2004.11.377
1145. P.J. Schuck, M.D. Mason, R.D. Grober, O. Ambacher, A.P. Lima, C. Miskys, R. Dimitrov, M. Stutzmann, Spatially resolved photoluminescence of inversion domain boundaries in GaN-based lateral polarity heterostructures. Appl. Phys. Lett. **79**, 952–954 (2001). 10.1063/1.1390486
1146. B.J. Rodriguez, A. Gruveman, A.I. Kingon, R.J. Nemanich, O. Ambacher, Piezoresponse force microscopy for polarity imaging of GaN. Appl. Phys. Lett. **80**, 4166–4168 (2002). 10.1063/1.1483117
1147. T.S. Zheleva, S.A. Smith, D.B. Thomson, K.J. Linthicum, P. Rajagopal, R.F. Davis, Pendeo-epitaxy: A new approach for lateral growth of gallium nitride films. J. Electr. Mater. **28**, L5–L8 (1999). 10.1007/s11664-999-0239-z
1148. A. Strittmatter, S. Rodt, L. Reißmann, D. Bimberg, H. Schröder, E. Obermeier, T. Riemann, J. Christen, A. Krost, Maskless epitaxial lateral overgrowth of GaN layers on structured Si(111) substrates. Appl. Phys. Lett. **78**, 727–729 (2001). 10.1063/1.1347013
1149. H. Lahrèche, P. Vennéguès, B. Beaumont, P. Gibart, Growth of high-quality GaN by low-pressure metal-organic vapour phase epitaxy (LP-MOVPE) from 3D islands and lateral overgrowth. J. Cryst. Growth **205**, 245–252 (1999). 10.1016/S0022-0248(99)00299-7
1150. T. Riemann, T. Hempel, J. Christen, P. Veit, R. Clos, A. Dadgar, A. Krost, U. Haboeck, A. Hoffmann, Optical and structural microanalysis of GaN grown on SiN submonolayers. J. Appl. Phys. **99**, 123518:1–8 (2006). 10.1063/1.2150589
1151. H.G. Chen, T.S. Ko, S.C. Ling, T.C. Lu, H.C. Kuo, S.C. Wang, Y.H. Wu, L. Chang, Dislocation reduction in GaN grown on stripe patterned *r*-plane sapphire substrates. Appl. Phys. Lett. **91**, 021914:1–3 (2007). 10.1063/1.2754643
1152. N. Okada, K. Tadatomo, Characterization and growth mechanism of nonpolar and semipolar GaN layers grown on patterned sapphire substrates. Semicond. Sci. Technol. **27**, 024003:1–9 (2012). 10.1088/0268-1242/27/2/024003
1153. F. Tendille, P. De Mierry, P. Vennéguès, S. Chenot, M. Teisseire, Defect reduction method in (11–22) semipolar GaN grown on patterned sapphire substrate by MOCVD: Toward heteroepitaxial semipolar GaN free of basal stacking faults. J. Cryst. Growth **404**, 177–183 (2014). 10.1016/j.jcrysgro.2014.07.020

1154. Y.H. Lo, New approach to grow pseudomorphic structures over the critical thickness. Appl. Phys. Lett. **59**, 2311–2313 (2005). 10.1063/1.106053
1155. C. Lynch, E. Chason, R. Beresford, L.B. Freund, K. Tetz, K.W. Schwarz, Limits of strain relaxation in InGaAs/GaAs probed in real time by in situ wafer curvature measurement. J. Appl. Phys. **98**, 073532:1–7 (2005). 10.1063/1.2060947
1156. A. Dadgar, J. Bläsing, A. Diez, A. Alam, M. Heuken, A. Krost, Metalorganic chemical vapor phase epitaxy of crack-free GaN on Si(111) exceeding 1 μm thickness. Jpn. J. Appl. Phys. **39**, L1183–L1185 (2000). 10.1143/JJAP.39.L1183
1157. J. Bläsing, A. Reiher, A. Dadgar, A. Dietz, A. Krost, The origin of stress reduction by low-temperature AlN interlayers. Appl. Phys. Lett. **81**, 2722–2724 (2002). 10.1063/1.1512331
1158. K. Sakamoto, T. Sakamoto, S. Nagao, G. Hashiguchi, K. Kuniyoshi, Y. Bando, Reflection high-energy electron diffraction intensity oscillations during Ge_xSi_{1-x} MBE growth on Si(001) substrates. Jpn. J. Appl. Phys. **26**, 666–670 (1987). 10.1143/JJAP.26.666
1159. P.M.J. Marée, K. Nakagawa, F.M. Mulders, J.F. van der Veen, Thin epitaxial Ge-Si(111) films: Study and control of morphology. Surf. Sci. **191**, 305–328 (1987). 10.1016/S0039-6028(87)81180-9
1160. M. Copel, M.C. Reuter, E. Kaxiras, R.M. Tromp, Surfactants in epitaxial growth. Phys. Rev. Lett. **63**, 632–635 (1989). 10.1103/PhysRevLett.63.632
1161. D. Kandel, E. Kaxiras, The surfactant effect in semiconductor thin-film growth. Solid State Phys. **54**, 219–262 (2000). 10.1016/S0081-1947(08)60249-0
1162. M. Ilg, D. Eißler, C. Lange, K. Ploog, Surfactant-mediated molecular beam epitaxy of high-quality (111)B-GaAs. Appl. Phys. A **56**, 397–399 (1993). 10.1007/BF00324362
1163. X. Yang, M.J. Jurkovic, J.B. Heroux, W.I. Wang, Low threshold InGaAsN/GaAs single quantum well lasers grown by molecular beam epitaxy using Sb surfactant. Electron. Lett. **35**, 1082–1083 (1999). 10.1049/el:19990746
1164. T. Kageyama, T. Miyamoto, M. Ohta, T. Matsuura, Y. Matsui, T. Furuhata, F. Koyama, Sb surfactant effect on GaInAs/GaAs highly strained quantum well lasers emitting at 1200 nm range grown by molecular beam epitaxy. J. Appl. Phys. **96**, 44–48 (2004). 10.1063/1.1760841
1165. H.J. Osten, J. Klatt, G. Lippert, B. Dietrich, E. Bugiel, Surfactant-controlled solid phase epitaxy of germanium and silicon. Phys. Rev. Lett. **69**, 450–453 (1992). 10.1103/PhysRevLett.69.450
1166. H. Kroemer, Heterostructure devices: A device physicist looks at interfaces. Surf. Sci. **132**, 543–576 (1983). 10.1007/978-94-009-3073-5_7
1167. G. van der Ch, J. Walle, Neugebauer, Universal alignment of hydrogen levels in semiconductors, insulators and solutions. Nature **423**, 626–628 (2003). 10.1038/nature01665
1168. K. Xu, H. Sio, O.A. Kirillov, L. Dong, M. Xu, P.D. Ye, D. Gundlach, N.V. Nguyen, Band offset determination of atomic-layer-deposited Al_2O_3 and HfO_2 on InP by internal photoemission and spectroscopic ellipsometry. J. Appl. Phys. **113**, 024504:1–5 (2013). 10.1063/1.4774038
1169. K. Shi, D.B. Li, H.P. Song, Y. Guo, J. Wang, X.Q. Xu, J.M. Liu, A.L. Yang, H.Y. Wei, B. Zhang, S.Y. Yang, X.L. Liu, Q.S. Zhu, Z.G. Wang, Determination of InN/diamond heterojunction band offset by X-ray photoelectron spectroscopy. Nanoscale Res. Lett. **6**, 50:1–5 (2011). 10.1007/s11671-010-9796-6
1170. P.F. Zhang, X.L. Liu, R.Q. Zhang, H.B. Fan, H.P. Song, H.Y. Wei, C.M. Jiao, S.Y. Yang, Q.S. Zhu, Z.G. Wang, Valence band offset of MgO/InN heterojunction measured by X-ray photoelectron spectroscopy. Appl. Phys. Lett. **92**, 042906 (2008). 10.1063/1.2839611
1171. W. Wei, Z. Qin, S. Fan, Z. Li, K. Shi, Q. Zhu, G. Zhang, Valence band offset of β-Ga_2O_3wurtzite GaN heterostructure measured by X-ray photoelectron spectroscopy. Nanoscale Res. Lett. **7**, 562:1–5 (2013). 10.1186/1556-276X-7-562
1172. X. Zhang, Q. Zhang, F. Lu, Energy band alignment of an In_2O_3:Mo/Si heterostructure. Semicond. Sci. Technol. **22**, 900–904 (2007). 10.1088/0268-1242/22/8/013
1173. A. Walsh, J.L.F. Da Silva, S.-H. Wei, C. Körber, A. Klein, L.F.J. Piper, A. DeMasi, K.E. Smith, G. Panaccione, P. Rorelli, D.J. Payne, A. Bourlange, R.G. Egdell, Nature of the band gap of In_2O_3 revealed by first-principles calculations and X-ray spectroscopy. Phys. Rev. Lett. **100**, 167402:1–4 (2008). 10.1103/PhysRevLett.100.167402
1174. P.D.C. King, T.D. Veal, C.E. Kendrick, L.R. Bailey, S.M. Durbin, C.F. McConville, InN/GaN valence band offset: High-resolution x-ray photoemission spectroscopy measurements. Phys. Rev. B **78**, 033308:1–4 (2008). 10.1103/PhysRevB.78.033308
1175. K. Muraki, S. Fukatsu, Y. Shiraki, R. Ito, Surface segregation of In atoms during molecular beam epitaxy and its influence on the energy levels in InGaAs/GaAs quantum wells. Appl. Phys. Lett. **61**, 557–559 (1992). 10.1063/1.107835
1176. D. Hernández-Maldonado, M. Herrera, P. Alonso-González, Y. González, L. González, J. Gazquez, M. Varela, S.J. Pennycook, M. de la Paz Guerrero-Lebrero, J. Pizarro, P.L. Galindo, S.I. Molina, Compositional analysis with atomic column spatial resolution by 5th-order aberration-corrected scanning transmission electron microscopy. Microsc. Microanal. **17**, 578–581 (2011). 10.1017/S1431927611000213
1177. Volker Gottschalch, Günther Wagner, private communication (2006)

1178. P. Offermans, *Study of III-V semiconductor nanostructures by cross-sectional scanning tunneling microscopy*, Ph.D. Thesis, Technische Universiteit Eindhoven (2005). 10.6100/IR595006
1179. O. von Roos, Position-dependent effective masses in semiconductor theory. Phys. Rev. B **27**, 7547–7552 (1983). 10.1103/PhysRevB.27.7547
1180. D.J. BenDaniel, C.B. Duke, Space-charge effects on electron tunneling. Phys. Rev. **152**, 683–692 (1966). 10.1103/PhysRev.152.683
1181. P. Harrison, A. Valavanis, *Quantum Wells, Wires and Dots: Theoretical and Computational Physics of Semiconductor Nanostructures*, 4th edn. (Wiley, Chichester, 2016). 10.1002/9781118923337
1182. M. Ehrhardt, Th. Koprucki, eds., Multi-band effective mass approximations, in *Advanced Mathematical Models and Numerical Techniques*, vol. 94. *Lecture Notes in Computational Science and Engineering* (Springer, Heidelberg, 2014). 10.1007/978-3-319-01427-2
1183. Y.C. Chang, J.N. Schulman, Interband optical transitions in GaAs/$Ga_{1-x}Al_x$As and InAs-GaSb superlattices. Phys. Rev. B **31**, 2069–2079 (1985). 10.1103/PhysRevB.31.2069
1184. R.C. Miller, D.A. Kleinman, A.C. Gossard, Energy-gap discontinuities and effective masses for GaAs/Al_xGa_{1-x}As quantum wells. Phys. Rev. B **29**, 7085–7087 (1984). 10.1103/PhysRevB.29.7085
1185. S.L. Chuang, *Physics of Photonic Devices*, 2nd edn. (Wiley, New York, 2009)
1186. R.C. Miller, A.C. Gossard, W.T. Tsang, O. Munteanu, Extrinsic luminescence from GaAs quantum wells. Phys. Rev. B **25**, 3871–3877 (1982). 10.1103/PhysRevB.25.3871
1187. W.T. Masselink, Y.-Ch. Chang, H. Morkoç, Binding energy of acceptors in GaAs/Al_xGa_{1-x}As quantum wells. Phys. Rev. B **28**, 7373–7376 (1983). 10.1116/1.582827
1188. D.B. Tran Thoai, R. Zimmermann, M. Grundmann, D. Bimberg, Image charges in semiconductor quantum wells: Effect on exciton binding energy. Phys. Rev. B **42**, 5906–5909 (1990). 10.1103/PhysRevB.42.5906
1189. M.J.L.S. Haines, N. Ahmed, S.J.A. Adams, K. Mitchell, I.R. Agool, C.R. Pidgeon, B.C. Cavenett, E.P. O'Reilly, A. Ghiti, M.T. Emeny, Exciton-binding-energy maximum in $Ga_{1-x}In_x$As/GaAs quantum wells. Phys. Rev. B **43**, 11944–11949 (1991). 10.1103/PhysRevB.43.11944
1190. K.J. Moore, G. Duggan, K. Woodbridge, C. Roberts, Observations and calculations of the exciton binding energy in (In,Ga)As/GaAs strained-quantum-well heterostructures. Phys. Rev. B **41**, 1090–1094 (1990). 10.1103/PhysRevB.41.1 090
1191. L. Esaki, A perspective in quantum-structure development, in *NATO ASI Series (Series B: Physics)*, E.E. Mendez, K. von Klitzing, eds. vol. 170 (Springer, Boston, 1987). 10.1007/978-1-4684-5478-9_1
1192. R. Dingle, A.C. Gossard, W. Wiegmann, Direct observation of superlattice formation in a semiconductor heterostructure. Phys. Rev. Lett. **34**, 1327–1330 (1975). 10.1103/PhysRevLett.34.1327
1193. F. Stern, S. Das Sarma, Electron energy in GaAs-$Ga_{1-x}Al_x$ heterojunctions. Phys. Rev. B **30**, 840–848 (1984). 10.1103/PhysRevB.30.840
1194. A.L. Efros, F.G. Pikus, G.G. Samsonidze, Maximum low-temperature mobility of two-dimensional electrons in heterojunctions with a thick spacer layer. Phys. Rev. B **41**, 8295–8301 (1990). 10.1103/PhysRevB.41.8295
1195. L. Pfeiffer, K.W. West, The role of MBE in recent quantum Hall effect physics discoveries. Physica E **20**, 57–64 (2003). 10.1016/j.physe.2003.09.035
1196. B.A. Bernevig, T.L. Hughes, S.-C. Zhang, Quantum spin Hall effect and topological phase transition in HgTe quantum wells. Science **314**, 1757–1761 (2006). 10.1126/science.1133734
1197. M. König, S. Wiedmann, C. Brüne, A. Roth, H. Buhmann, L.W. Molenkamp, X.-L. Qi, S.-C. Zhang, Quantum spin Hall insulator state in HgTe quantum wells. Science **318**, 766–770 (2007). 10.1126/science.1148047
1198. A. Roth, C. Brüne, H. Buhmann, L.W. Molenkamp, J. Maciejko, X.-L. Qi, S.-C. Zhang, Nonlocal transport in the quantum spin Hall state. Science **325**, 294–297 (2009). 10.1126/science.1174736
1199. J. Christen, D. Bimberg, Line shapes of intersubband and excitonic recombination in quantum wells: Influence of final-state interaction, statistical broadening, and momentum conservation. Phys. Rev. B **42**, 7213–7219 (1990). 10.1103/PhysRevB.42.7213
1200. J. Feldmann, G. Peter, E.O. Göbel, P. Dawson, K. Moore, C. Foxon, R.J. Elliott, Linewidth dependence of radiative exciton lifetimes in quantum wells. Phys. Rev. Lett. **59**, 2337–2340 (1987). 10.1103/PhysRevLett.59.2337 Erratum: Phys. Rev. Lett. **60**, 243 (1988) 10.1103/PhysRevLett.60.243.4
1201. M.S. Skolnick, J.M. Rorison, K.J. Nash, D.J. Mowbray, P.R. Tapster, S.J. Bass, A.D. Pitt, Observation of a many-body edge singularity in quantum-well luminescence spectra. Phys. Rev. Lett. **58**, 2130–2133 (1987). 10.1103/PhysRevLett.58.2130
1202. D. Gammon, S. Rudin, T.L. Reinecke, D.S. Katzer, C.S. Kyono, Phonon broadening of excitons in GaAs/Al_xGa_{1-x}As quantum wells. Phys. Rev. B **51**, 16785–16789 (1995). 10.1103/PhysRevB.51.16785
1203. L. Béaur, T. Bretagnon, B. Gil, A. Kavokin, T. Guillet, C. Brimont, D. Tainoff, M. Teisseire, J.-M. Chauveau, Exciton radiative properties in nonpolar homoepitaxial ZnO/(Zn,Mg)O quantum wells. Phys. Rev. B **84**, 165312:1–8 (2011). 10.1103/PhysRevB.84.165312
1204. E. Runge, R. Zimmermann, Optical properties of localized excitons in nanostructures: Theoretical aspects. Adv. Solid State Phys. (Festkörperprobleme) **38**, 251–263 (1999). 10.1007/BFb0107622

1205. E. Runge, Excitons in semiconductor nanostructures. Solid State Phys. **57**, 149–305 (2002). 10.1016/S0081-1947(08)60180-0
1206. S.T. Davey, E.G. Scott, B. Wakefield, G.J. Davies, A photoluminescence study of $Ga_{1-x}In_xAs/Al_{1-y}In_yAs$ quantum wells grown by MBE. Semicond. Sci. Technol. **3**, 365–371 (1988). 10.1088/0268-1242/3/4/014
1207. M. Grassi Alessi, F. Fragano, A. Patané, M. Capizzi, E. Runge, R. Zimmermann, Competition between radiative decay and energy relaxation of carriers in disordered $In_xGa_{1-x}As/GaAs$ quantum wells. Phys. Rev. B **61**, 10985–10993 (2000). 10.1103/PhysRevB.61.10985
1208. Q. Li, S.J. Xu, W.C. Cheng, M.H. Xie, S.Y. Tong, C.M. Che, H. Yang, Thermal redistribution of localized excitons and its effect on the luminescence band in InGaN ternary alloys. Appl. Phys. Lett. **79**, 1810–1812 (2001). 10.1063/1.1403655
1209. J. Hegarty, L. Goldner, M.D. Sturge, Localized and delocalized two-dimensional excitons in GaAs-AlGaAs multiple-quantum-well structures. Phys. Rev. B **30**, 7346–7348 (1984). 10.1103/PhysRevB.30.7346
1210. N.F. Mott, E.A. Davies, *Electronic Processes in Noncrystalline Materials*, 2nd edn. (Oxford University Press, New York, 1979)
1211. T. Takeuchi, S. Sota, M. Katsuragawa, M. Komori, H. Takeuchi, H. Amano, I. Akasaki, Quantum-confined Stark effect due to piezoelectric fields in GaInN strained quantum wells. Jpn. J. Appl. Phys. **36**, Part 2, L382–L385 (1997). 10.1143/JJAP.36.L382
1212. S.F. Chichibu, A.C. Abare, M.S. Minsky, S. Keller, S.B. Fleischer, J.E. Bowers, E. Hu, U.K. Mishra, L.A. Coldren, S.P. DenBaars, Effective band gap inhomogeneity and piezoelectric field in InGaN/GaN multiquantum well structures. Appl. Phys. Lett. **73**, 2005–2008 (1998). 10.1063/1.122350
1213. C. Morhain, T. Bretagnon, P. Lefebvre, X. Tang, P. Valvin, T. Guillet, B. Gil, T. Taliercio, M. Teisseire-Doninelli, B. Vinter, C. Deparis, Internal electric field in wurtzite $ZnO/Zn_{0.78}Mg_{0.22}O$ quantum wells. Phys. Rev. B **72**, 241305(R):1–4 (2005). 10.1103/PhysRevB.72.241305
1214. J.A. Davis, L.V. Dao, X. Wen, C. Ticknor, P. Hannaford, V.A. Coleman, H.H. Tan, C. Jagadish, K. Koike, S. Sasa, M. Inoue, M. Yano, Suppression of the internal electric field effects in $ZnO/Zn_{0.7}Mg_{0.3}O$ quantum wells by ion-implantation induced intermixing. Nanotechnology **19**, 055205:1–4 (2008). 10.1088/0957-4484/19/05/055205
1215. E. Berkowicz, D. Gershoni, G. Bahir, E. Lakin, D. Shilo, E. Zolotoyabko, A.C. Abare, S.P. Denbaars, L.A. Coldren, Measured and calculated radiative lifetime and optical absorption of $In_xGa_{1-x}N/GaN$ quantum structures. Phys. Rev. B **61**, 10994–11008 (2000). 10.1103/PhysRevB.61.10994
1216. N. Akopian, G. Bahir, D. Gershoni, M.D. Craven, J.S. Speck, S.P. DenBaars, Optical evidence for lack of polarization in $(11\bar{2}0)$-oriented GaN/(AlGa)N quantum structures. Appl. Phys. Lett. **86**, 202104:1–3 (2005). 10.1063/1.1926406
1217. J. Spitzer, T. Ruf, M. Cardona, W. Dondl, R. Schorer, G. Abstreiter, E.E. Haller, Raman scattering by optical phonons in isotopic $^{70}(Ge)_n\,^{74}(Ge)_n$ superlattices. Phys. Rev. Lett. **72**, 1565–1568 (1994). 10.1103/PhysRevLett.72.1565
1218. A. Reznicek, R. Scholz, S. Senz, U. Gösele, Comparative TEM study of bonded silicon/silicon interfaces fabricated by hydrophilic, hydrophobic and UHV wafer bonding. Mater. Chem. Phys. **81**, 277–280 (2003). 10.1016/S0254-0584(02)00601-6
1219. P. Kopperschmidt, S. Senz, G. Kästner, D. Hesse, U.M. Gösele, Materials integration of gallium arsenide and silicon by wafer bonding. Appl. Phys. Lett. **72**, 3181–3183 (1998). 10.1063/1.121586
1220. Q.-Y. Tong, U. Gösele, *Semiconductor Wafer Bonding: Science and Technology* (Wiley, New York, 1998)
1221. U. Gösele, Q.-Y. Tong, Semiconductor Wafer Bonding. Ann. Rev. Mat. Sci. **28**, 215–241 (1998). 10.1146/annurev.matsci.28.1.215
1222. M. Alexe, U. Gösele, eds., *Wafer Bonding* (Springer, Berlin, 2004). 10.1007/978-3-662-10827-7
1223. A.K. Geim, Nobel Lecture: Random walk to graphene. Rev. Mod. Phys. **83**, 851–862 (2011). 10.1103/RevModPhys.83.851
1224. *2D Materials*, F. Iacopi, J.J. Boeckl, C. Jagadish, eds., Semicond. Semimet. **95** (2016). 10.1016/S0080-8784(16)30017-5
1225. P. Avouris, T.F. Heinz, T. Low, eds., *2D Materials, Properties and Devices* (Cambridge Univ. Press, Cambridge, 2017). 10.1017/9781316681619
1226. J. Li, Z. Wei, J. Kang, *Two-Dimensional Semiconductors, Synthesis Physical Properties and Applications* (Wiley-VCH, Weinheim, 2020)
1227. H.P. Boehm, R. Setton, E. Stumpp, Nomenclature and terminology of graphite intercalation compounds. Carbon **24**, 241–245 (1986). 10.1016/0008-6223(86)90126-0
1228. A.H. Castro Neto, F. Guinea, N.M.R. Peres, K.S. Novoselov, A.K. Geim, The electronic properties of graphene. Rev. Mod. Phys. **81**, 109–162 (2009). 10.1103/RevModPhys.81.109
1229. D.R. Dreyer, R.S. Ruoff, C.W. Bielawski, From conception to realization: An historial account of graphene and some perspectives for its future. Angew. Chemie Int. Ed. **49**, 9336–9344 (2010). 10.1002/anie.201003024
1230. *Ten years in two dimensions* (editorial), Nature Nanotechn. **9**, 725 (2014) and Focus issue 'Graphene applications' of Nature Nanotechnology **9** (2014). 10.1038/nnano.2014.244

1231. J. Yang, P. Hu, G. Yu, Perspective of graphene-based electronic devices: Graphene synthesis and diverse applications. APL Mater. **7**, 020901:1–7 (2019). 10.1063/1.5054823
1232. W. Choi, I. Lahiri, R. Seelaboyina, Y.S. Kang, Synthesis of graphene and its applications: A review. Crit. Rev. Solid State Mater. Sci. **35**, 52–71 (2010). 10.1063/1.5054823
1233. V.B. Mohan, K.-T. Lau, D. Hui, D. Battacharyya, Graphene-based materials and their composites: A review on production, applications and product limitations. Compos. B: Eng. **142**, 200–220 (2018). 10.1016/j.compositesb.2018.01.013
1234. R. Peierls, Bemerkungen über Umwandlungstemperaturen. Helvetica Phys. Acta **7**, 81–83 (1934). 10.5169/seals-110415
1235. N.D. Mermin, Crystalline order in two dimensions. Phys. Rev. **176**, 250–254 (1968), 10.1103/PhysRev.176.250 Errata: Phys. Rev. B **20**, 4762 (1979) 10.1103/PhysRevB.20.4762 and Phys. Rev. B **74**, 149902(E) (2006). 10.1103/PhysRevB.74.149902
1236. J.C. Meyer, A.K. Geim, M.I. Katsnelson, K.S. Novoselov, T.J. Booth, S. Roth, The structure of suspended graphene sheets. Nature **446**, 60–63 (2007). 10.1038/nature05545
1237. K.S. Novoselov, A.K. Geim, S.V. Morozov, D. Jiang, Y. Zhang, S.V. Dubonos, I.V. Grigorieva, A.A. Firsov, Electric field effect in atomically thin carbon films. Science **306**, 666–669 (2004). 10.1126/science.1102896
1238. K.S. Novoselov, D. Jiang, F. Schedin, T.J. Booth, V.V. Khotkevich, S.V. Morozov, A.K. Geim, Two-dimensional atomic crystals. PNAS **102**, 10451–10453 (2005). 10.1073/pnas.0502848102
1239. G.R. Yazdi, T. Iakimov, R. Yakimova, Epitaxial graphene on SiC: A review of growth and characterization. Crystals **6**, 53:1–45 (2016). 10.3390/cryst6050053
1240. University of Manchester, www.condmat.physics.manchester.ac.uk
1241. A.M. Valencia, M.J. Caldas, Single vacancy defect in graphene: Insights into its magnetic properties from theoretical modeling. Phys. Rev. B **96**, 125431:1–9 (2017). 10.1103/PhysRevB.96.125431
1242. J.S. Bunch, A.M. van der Zande, S.S. Verbridge, I.W. Frank, D.M. Tanenbaum, J.M. Parpia, H.G. Craighead, P.L. McEuen, Electromechanical resonators from graphene sheets. Science **315**, 490–493 (2007). 10.1126/science.1136836
1243. D.G. Papageorgiou, I.A. Kinloch, R.J. Young, Mechanical properties of graphene and graphene-based nanocomposites. Progr. Mat. Sci. **90**, 75–127 (2017). 10.1016/j.pmatsci.2017.07.004
1244. L. Wirtz, A. Rubio, The phonon dispersion of graphite revisited. Solid State Commun. **131**, 141–152 (2004). 10.1016/j.ssc.2004.04.042
1245. A.C. Ferrari, J.C. Meyer, V. Scardaci, C. Casiraghi, M. Lazzeri, F. Mauri, S. Piscanec, D. Jiang, K.S. Novoselov, S. Roth, A.K. Geim, Raman spectrum of graphene and graphene layers. Phys. Rev. Lett. **97**, 187401:1–4 (2006). 10.1103/PhysRevLett.97.187401
1246. M. Machón, S. Reich, C. Thomsen, D. Sánchez-Portal, P. Ordejón, Ab initio calculations of the optical properties of 4-Å-diameter single-walled nanotubes. Phys. Rev. B **66**, 155410:1–5 (2002). 10.1103/PhysRevB.66.155410
1247. S. Reich, C. Thomsen, J. Maultzsch, *Carbon Nanotubes: Basic Concepts and Physical Properties* (Wiley-VCH. Berlin (2004). 10.1002/9783527618040
1248. Ch.L. Kane, Erasing electron mass. Nature **438**, 168–170 (2005). 10.1038/438168a
1249. K.S. Novoselov, A.K. Geim, S.V. Morozov, D. Jiang, M.I. Katsnelson, I.V. Grigorieva, S.V. Dubonos, A.A. Firsov, Two-dimensional gas of massless Dirac fermions in graphene. Nature **438**, 197–200 (2005). 10.1038/nature04233
1250. P.R. Wallace, The band theory of graphite. Phys. Rev. **71**, 622–634 (1947). 10.1103/PhysRev.71.622
1251. C. Bena, G. Montambaux, Remarks on the tight-binding model of graphene. New J. Phys. **11**, 095003:1–15 (2009). 10.1088/1367-2630/11/9/095003
1252. S. Reich, J. Maultzsch, C. Thomsen, P. Ordejón, Tight-binding description of graphene. Phys. Rev. B **66**, 035412:1–5 (2002). 10.1103/PhysRevB.66.035412
1253. R.S. Deacon, K.-C. Chuang, R.J. Nicholas, K.S. Novoselov, A.K. Geim, Cyclotron resonance study of the electron and hole velocity in graphene monolayers. Phys. Rev. B **76**, 081406(R):1–4 (2007). 10.1103/PhysRevB.76.081406
1254. A. Bostwick, T. Ohta, Th. Seyller, K. Horn, E. Rotenberg, Quasiparticle dynamics in graphene. Nature Phys. **3**, 36–40 (2006). 10.1038/nphys477
1255. P. Miró, M. Audiffred, T. Heine, An atlas of two-dimensional materials. Chem. Soc. Rev. **43**, 6537–6554 (2014). 10.1039/c4cs00102h
1256. B. Partoens, F.M. Peeters, From graphene to graphite: Electronic structure around the *K* point. Phys. Rev. B **74**, 075404:1–11 (2006). 10.1103/PhysRevB.74.075404
1257. M. Aoki, H. Amawashi, Dependence of band structures on stacking and field in layered graphene. Solid State Commun. **142**, 123–127 (2007). 10.1016/j.ssc.2007.02.013
1258. T. Ohta, A. Bostwick, Th Seyller, K. Horn, E. Rotenberg, Controlling the electronic structure of bilayer graphene. Science **313**, 951–954 (2006). 10.1126/science.1130681
1259. S.V. Vonsovsky, M.I. Katsnelson, *Quantum Solid-State Physics* (Springer, New York, 1989)
1260. M.S. Sercheli, Y. Kopelevich, R. Ricardo da Silva, J.H.S. Torres, C. Rettori, Evidence for internal field in graphite: A conduction electron spin-resonance study. Solid State Commun. **121**, 579–583 (2002). 10.1016/S0038-1098(01)00465-3

1261. K.I. Bolotin, K.J. Sikes, Z. Jiang, M. Klima, G. Fudenberg, J. Hone, P. Kim, H.L. Störmer, Ultrahigh electron mobility in suspended graphene. Solid State Commun. **146**, 351–355 (2008). 10.1016/j.ssc.2008.02.024
1262. K.S. Novoselov, Z. Jiang, Y. Zhang, S.V. Morozov, H.L. Störmer, U. Zeitler, J.C. Maan, G.S. Boebinger, P. Kim, A.K. Geim, Room-temperature quantum Hall effect in graphene. Science **315**, 1379 (2007). 10.1126/science.1137201
1263. O. Klein, Die Reflexion von Elektronen an einem Potentialsprung nach der relativistischen Dynamik von Dirac. Z. Phys. **53**, 157–165 (1929). 10.1007/BF01339716
1264. A. Calogeracos, N. Dombey, History and physics of the Klein paradox. Contemporary Physics **40**, 313–321 (1999). 10.1080/001075199181387
1265. M.I. Katsnelson, K.S. Novoselov, A.K. Geim, Chiral tunnelling and the Klein paradox in graphene. Nat. Phys. **2**, 620–625 (2006). 10.1038/nphys384
1266. R.R. Nair, P. Blake, A.N. Grigorenko, K.S. Novoselov, T.J. Booth, T. Stauber, N.M.R. Peres, A.K. Geim, Fine structure constant defines visual transparency of graphene. Science **320**, 1308 (2008). 10.1126/science.1156965
1267. K.F. Mak, M.Y. Sfeir, Y. Wu, C.H. Lui, J.A. Misewich, T.F. Heinz, Measurement of the optical conductivity of graphene. Phys. Rev. Lett. **101**, 196405:1–4 (2008). 10.1103/PhysRevLett.101.196405
1268. T. Ando, Y. Zheng, H. Suzuura, Dynamical conductivity and zero-mode anomaly in honeycomb lattices. J. Phys. Soc. Jpn. **71**, 1318–1324 (2002). 10.1143/JPSJ.71.1318
1269. H. Falomir, M. Loewe, E. Muñoz, A. Raya, Optical conductivity and transparency in an effective model for graphene. Phys. Rev. B **98**, 195430:1–11 (2018). 10.1103/PhysRevB.98.195430
1270. B.G. Ghamsari, J. Tosado, M. Yamamoto, M.S. Fuhrer, S.M. Anlage, Measuring the complex optical conductivity of graphene by Fabry-Pérot reflectance spectroscopy. Sci. Rep. **6**(34166), 1–6 (2016). 10.1038/srep34166. Erratum: Sci. Rep. **7**, 40973 (2017). 10.1038/srep40973
1271. C. Tusche, H.L. Meyerheim, J. Kirschner, Observation of depolarized ZnO(0001) monolayers: Formation of unreconstructed planar sheets. Phys. Rev. Lett. **99**, 026102:1–4 (2007). 10.1103/PhysRevLett.99.026102
1272. S. Das, J.A. Robinson, M. Dubey, H. Terrones, M. Terrones, Beyond graphene: Progress in novel two-dimensional materials and van der Waals solids. Ann. Rev. Mater. Res. **45**, 1–27 (2015). 10.1146/annurev-matsci-070214-021034
1273. S. Manzeli, D. Ovchinnikov, D. Pasquier, O.V. Yazyev, A. Kis, 2D transition metal dichalcogenides. Nat. Rev. Mater. **2**, 17033:1–15 (2017) 10.1038/natrevmats.2017.33
1274. J. Zhou, J. Lin, X. Huang, Y. Zhou, Y. Chen, J. Xia, H. Wang, Y. Xie, H. Yu, J. Lei, D. Wu, F. Liu, Q. Fu, Q. Zeng, C.-H. Hsu, C. Yang, L. Lu, T. Yu, Z. Shen, H. Lin, B.I. Yakobson, Q. Liu, K. Suenaga, G. Liu, Z. Liu, A library of atomically thin metal chalcogenides. Nature **556**, 355–359 (2018). 10.1038/s41586-018-0008-3
1275. W. Zhou, X. Zou, S. Najmaei, Z. Liu, Y. Shi, J. Kong, J. Lou, P.M. Ajayan, B.I. Yakobson, J.-C. Idrobo, Intrinsic structural defects in monolayer molybdenum disulfide. Nano Lett. **13**, 2615–2622 (2013). 10.1021/nl4007479
1276. B. Ouyang, G. Lan, Y. Guo, Z. Mi, J. Song, Phase engineering of monolayer transition-metal dichalcogenide through coupled electron doping and lattice deformation. Appl. Phys. Lett. **107**, 191903:1–5 (2015). 10.1063/1.4934836
1277. Y.C. Cheng, Z.Y. Zhu, M. Tahir, U. Schwingenschlögl, Spin-orbit induced spin splittings in polar transition metal dichalcogenide monolayers. EPL **102**, 57001:1–6 (2013). 10.1209/0295-5075/102/57001
1278. H. Qiu, T. Xu, Z. Wang, W. Ren, H. Nan, Z. Ni, Q. Chen, S. Yuan, F. Miao, F. Song, G. Long, Y. Shi, L. Sun, J. Wang, X. Wang, Hopping transport through defect-induced localized states in molybdenum disulphide. Nature Commun. **4**, 2642:1–6 (2013). 10.1038/ncomms3642
1279. Y. Chen, J. Xi, D.O. Dumcenco, Z. Liu, K. Suenaga, D. Wang, Z. Shuai, Y.-S. Huang, L. Xie, Tunable Band gap photoluminescence from atomically thin transition-metal dichalcogenide alloys. ACS Nano **7**, 4610–4616 (2013). 10.1021/nn401420h
1280. J. Hong, Z. Hu, M. Probert, K. Li, D. Lv, X. Yang, L. Gu, N. Mao, Q. Feng, L. Xie, J. Zhang, D. Wu, Z. Zhang, C. Jin, W. Ji, X. Zhang, J. Yuan, Z. Zhang, Exploring atomic defects in molybdenum disulphide monolayers. Nature Commun. **6**, 6293:1–8 (2015). 10.1038/ncomms7293
1281. S. Najmaei, Z. Liu, W. Zhou, X. Zou, G. Shi, S. Lei, B.I. Yakobson, J.-C. Idrobo, P.M. Ajayan, J. Lou, Vapour phase growth and grain boundary structure of molybdenum disulphide atomic layers. Nat. Mater. **12**, 754–759 (2013). 10.1038/nmat3673
1282. Z. Li, X. Yan, Z. Tang, Z. Huo, G. Li, L. Jiao, L.-M. Liu, M. Zhang, J. Luo, J. Zhu, Direct observation of multiple rotational stacking faults coexisting in freestanding bilayer MoS_2, Sci. Rep. **7**, 8323:1–10 (2017). 10.1038/s41598-017-07615-9
1283. X. Duan, C. Wang, Z. Fan, G. Hao, L. Kou, U. Halim, H. Li, X. Wu, Y. Wang, J. Jiang, A. Pan, Y. Huang, R. Yu, X. Duan, Synthesis of $WS_{2x}Se_{2-2x}$ alloy nanosheets with composition-tunable electronic properties. Nano Lett. **16**, 264–269 (2016). 10.1021/acs.nanolett.5b03662
1284. D.H. Kim, H.S. Kim, M.W. Song, S. Lee, S.Y. Lee, Geometric and electronic structures of monolayer hexagonal boron nitride with multi-vacancy. Nano Convergence **4**, 13:1–8 (2017). 10.1186/s40580-017-0107-0
1285. Y. Miyamoto, M.L. Cohen, S.G. Louie, Ab initio calculation of phonon spectra for graphite, BN, and BC_2N sheets. Phys. Rev. B **52**, 14971–14975 (1995). 10.1103/PhysRevB.52.14971

1286. C. Lee, H. Yan, L.E. Brus, T.F. Heinz, J. Hone, S. Ryu, Anomalous lattice vibrations of single and few-layer MoS_2. ACS Nano **4**, 2695–2700 (2010). 10.1021/nn1003937
1287. A. Molina-Sánchez, L. Wirtz, Phonons in single-layer and few-layer MoS_2 and WS_2, Phys. Rev. B **84**, 155413:1–8 (2011). 10.1103/PhysRevB.84.155413
1288. K. Kaasbjerg, K.S. Thygesen, K.W. Jacobsen, Phonon-limited mobility in n-type single-layer MoS_2 from first principles. Phys. Rev. B **85**, 115317:1–16 (2012). 10.1103/PhysRevB.85.115317
1289. H. Tornatzky, R. Gillen, H. Uchiyama, J. Maultzsch, Phonon dispersion in MoS_2, Phys. Rev. B **99**, 144309:1–13 (2019). 10.1103/PhysRevB.99.144309
1290. F. Ferreira, A.J. Chaves, N.M.R. Peres, R.M. Ribeiro, Excitons in hexagonal boron nitride single-layer: A new platform for polaritonics in the ultraviolet. J. Opt. Soc. Am. B **36**, 674–683 (2019). 10.1364/JOSAB.36.000674
1291. K.F. Mak, C. Lee, J. Hone, J. Shan, T.F. Heinz, Atomically thin MoS_2: A new direct-gap semiconductor. Phys. Rev. Lett. **105**, 136805:1–4 (2010). 10.1103/PhysRevLett.105.136805
1292. K. Kośmider, J.W. González, J. Fernández-Rossier, Large spin splitting in the conduction band of transition metal dichalcogenide monolayers. Phys. Rev. B **88**, 245436:1–7 (2013). 10.1103/PhysRevB.88.245436
1293. A. Kormányos, G. Burkard, M. Gmitra, J. Fabian, V. Zólyomi, N.D. Drummond, V. Fal'ko, $\mathbf{k} \cdot \mathbf{p}$ theory for two-dimensional transition metal dichalcogenide semiconductors, 2D Mater. **2**, 02211:1–31 (2015). 10.1088/2053-1583/2/2/022001. Erratum: 2D Mater. **2**, 049501 (2015). 10.1088/2053-1583/2/4/049501
1294. G.-B. Liu, W.-Y. Shan, Y. Yao, W. Yao, D. Yiao, Three-band tight-binding model for monolayers of group-VIB transition metal dichalcogenides. Phys. Rev. B **88**, 085433:1–10 (2013). 10.1103/PhysRevB.88.085433. Erratum: Phys. Rev. B **89**, 039901 (2014). 10.1103/PhysRevB.89.039901
1295. J. Kang, S. Tongay, J. Zhou, J. Li, J. Wu, Band offsets and heterostructures of two- dimensional semiconductors. Appl. Phys. Lett. **102**, 012111:1–4 (2013). 10.1063/1.4774090
1296. Z.Y. Zhu, Y.C. Cheng, U. Schwingenschlögl, Giant spin-orbit-induced spin splitting in two-dimensional transition-metal dichalcogenide semiconductors. Phys. Rev. B **84**, 153402:1–5 (2011). 10.1103/PhysRevB.84.153402
1297. D. Le, A. Barinov, E. Preciado, M. Isarraraz, I. Tanabe, T. Komesu, C. Troha, L. Bartels, T.S. Rahman, P.A. Dowben, Spin-orbit coupling in the band structure of monolayer WSe_2. J. Phys.: Cond. Matter **27**, 182201:1–5 (2015). 10.1088/0953-8984/27/18/182201
1298. A. Arora, M. Koperski, K. Nogajewski, J. Marcus, C. Faugeras, M. Potemski, Excitonic resonances in thin films of WSe_2: From monolayer to bulk material. Nanoscale **7**, 10421–10429 (2015). 10.1039/c5nr01536g
1299. D.Y. Qiu, F.H. da Jornada, S.G. Louie, Optical spectrum of MoS_2: Many-body effects and diversity of exciton states. Phys. Rev. Lett. **111**, 216805:1–5 (2013). 10.1103/PhysRevLett.111.216805. Erratum: Phys. Rev. Lett. **115**, 119901:1-2 (2015). 10.1103/PhysRevLett.115.119901
1300. Cedric Robert, private communication (2019)
1301. D. Xiao, G.-B. Liu, W. Feng, X. Xu, W. Yao, Coupled spin and valley physics in monolayers of MoS_2 and other group-VI dichalcogenides. Phys. Rev. Lett. **108**, 196802:1–5 (2012). 10.1103/PhysRevLett.108.196802
1302. T. Cao, G. Wang, W. Han, H. Ye, C. Zhu, J. Shi, Q. Niu, P. Tan, E. Wang, B. Liu, J. Feng, Valley-selective circular dichroism of monolayer molybdenum disulphide. Nature Commun. **3**, 887:1–5 (2012). 10.1038/ncomms1882
1303. M.M. Glazov, E.L. Ivchenko, G. Wang, T. Amand, X. Marie, B. Urbaszek, B.L. Liu, Spin and valley dynamics of excitons in transition metal dichalcogenide monolayers. Phys. Status Solidi B **252**, 2349–2362 (2015). 10.1002/pssb.201552211
1304. A. Srivastava, M. Sidler, A.V. Allain, D.S. Lembke, A. Kis, A. Imamoğlu, Valley Zeeman effect in elementary optical excitations of monolayer WSe_2. Nature Phys. **11**, 141–147 (2015). 10.1038/NPHYS3203
1305. G. Aivazian, Z. Gong, A.M. Jones, R.-L. Chu, J. Yan, D.G. Mandrus, C. Zhang, D. Cobden, W. Yao, X. Xu, Magnetic control of valley pseudospin in monolayer WSe_2. Nat. Phys. **11**, 148–152 (2015). 10.1038/NPHYS3201
1306. X. L. Yang, S. H. Guo, F. T. Chan, K. W. Wong, and W. Y. Ching, Analytic solution of a two-dimensional hydrogen atom. I. Nonrelativistic theory. Phys. Rev. A **43**, 1186–1196 (1991). 10.1103/PhysRevA.43.1186
1307. D.G.W. Parfitt, M.E. Portnoi, The two-dimensional hydrogen atom revisited. J. Math. Phys. **43**, 4681–4691 (2002). 10.1063/1.1503868
1308. N.S. Rytova, The screened potential of a point charge in a thin film. Moscow Univ. Phys. Bull. **3**, 30–37 (1967) (in Russian), English translation at arXiv:1806.00976
1309. L.V. Keldysh, Coulomb interaction in thin semiconductor and semimetal films. JETP Lett. **29**, 658–660 (1979)
1310. D. Felbacq, E. Rousseau, Rigorous asymptotic study of the screened electrostatic potential in a thin dielectric slab. Ann. Physik **513**, 1800486:1–7 (2019). 10.1002/andp.201800486
1311. A. Chernikov, T.C. Berkelbach, H.M. Hill, A. Rigosi, Y. Li, O.B. Aslan, D.R. Reichman, M.S. Hybertsen, T.F. Heinz, Exciton binding energy and nonhydrogenic Rydberg series in monolayer WS_2. Phys. Rev. Lett. **113**, 076802:1–5 (2014). 10.1103/PhysRevLett.113.076802
1312. M.R. Molas, A.O. Slobodeniuk, K. Nogajewski, M. Bartos, Ł. Bala, A. Babiński, K. Watanabe, T. Taniguchi, C. Faugeras, M. Potemski, Energy spectrum of two-dimensional excitons in a nonuniform dielectric medium. Phys. Rev. Lett. **123**, 136801:1–6 (2019). 10.1103/PhysRevLett.123.136801

1313. M. Goryca, J. Li, A.V. Stier, T. Taniguchi, K. Watanabe, B. Urbaszek, X. Marie, S.A. Crooker, Revealing exciton masses and dielectric properties of monolayer semiconductors with high magnetic fields. Nature Commun. **10**, 4172:1–12 (2019). 10.1038/s41467-019-12180-y
1314. F.S. Ham, The quantum defect method. Solid State Phys. **1**, 127–192 (1955). 10.1016/S0081-1947(08)60678-5
1315. M. Koperski, M.R. Molas, A. Arora, K. Nogajewski, M. Bartos, J. Wyzula, D. Vaclavkova, P. Kossacki, M. Potemski, Orbital, spin and valley contributions to Zeeman splitting of excitonic resonances in $MoSe_2$, WSe_2 and WS_2 monolayers. 2D Mater. **6**, 015001:1–10 (2019). 10.1088/2053-1583/aae14b
1316. D.V. Rybkovskiy, I.C. Gerber, M.V. Durnev, Atomically inspired $\boldsymbol{k} \cdot \boldsymbol{p}$ approach and valley Zeeman effect in transition metal dichalcogenide monolayers. Phys. Rev. B **95**, 155406:1–9 (2017). 10.1103/PhysRevB.95.155406
1317. B. Zhu, X. Chen, X. Cui, Exciton binding energy of monolayer WS_2, Sci. Rep. **5**, 9218:1–5 (2015). 10.1038/srep09218
1318. T.P. Lyons, S. Dufferwiel, M. Brooks, F. Withers, T. Taniguchi, K. Watanabe, K.S. Novoselov, G. Burkard, A.I. Tartakovskii, The valley Zeeman effect in inter- and intra-valley trions in monolayer WSe_2. Nat. Commun. **10**, 2330:1–8 (2019). 10.1038/s41467-019-10228-7
1319. I.C. Gerber, X. Marie, Dependence of band structure and exciton properties of encapsulated WSe_2 monolayers on the hBN-layer thickness. Phys. Rev. B **98**, 245126:1–7 (2018). 10.1103/PhysRevB.98.245126
1320. A.V. Stier, N.P. Wilson, G. Clark, X. Xu, S.A. Crooker, Probing the influence of dielectric environment on excitons in monolayer WSe_2: insight from high magnetic fields. Nano Lett. **16**, 7054–7060 (2016). 10.1021/acs.nanolett.6b03276
1321. J.M.B. Lopes dos Santos, N.M.R. Peres, A.H. Castro Neto, Graphene bilayer with a twist: Electronic structure. Phys. Rev. Lett. **99**, 256802:1–4 (2007). 10.1103/PhysRevLett.99.256802
1322. E.J. Mele, Commensuration and interlayer coherence in twisted bilayer graphene. Phys. Rev. B **81**, 161405(R):1–4 (2010). 10.1103/PhysRevB.81.161405
1323. R. Bistritzer, A.H. MacDonald, Moiré bands in twisted double-layer graphene. PNAS **108**, 12233–12237 (2011). 10.1073/pnas.1108174108
1324. G. Jeong, B. Choi, D.-S. Kim, S. Ahn, B. Park, J.H. Kang, H. Min, B.H. Hong, Z.H. Kim, Mapping of Bernal and non-Bernal stacking domains in bilayer graphene using infrared nanoscopy. Nanoscale **9**, 4191–4195 (2017). 10.1039/c7nr00713b
1325. J. Liu, Z. Huang, F. Lai, L. Lin, Y. Xu, C. Zuo, W. Zheng, Y. Qu, Controllable growth of the graphene from millimeter-sized monolayer to multilayer on Cu by chemical vapor deposition. Nanoscale Res. Lett. **10**, 455:1–8 (2015). 10.1186/s11671-015-1164-0
1326. A.K. Geim, I.V. Griegorieva, Van der Waals heterostructures. Nature **499**, 419–425 (2013). 10.1038/nature12385
1327. K.S. Novoselov, A. Mishchenko, A. Carvalho, A.H. Castro Neto, 2D materials and van der Waals heterostructures. Science **353**, 461 (2016) and Science **353**, aac9439:1-11 (2016). 10.1126/science.aac9439
1328. J.C.W. Song, N.M. Gabor, Electron quantum metamaterials in van der Waals heterostructures. Nature Nanotechn. **13**, 986–993 (2018). 10.1038/s41565-018-0294-9
1329. S.J. Liang, B. Cheng, X. Cui, F. Miao, Van der Waals heterostructures for high-performance device applications: Challenges and opportunities. Adv. Mater. **2019**, 1903800:1–27 (2019). 10.1002/adma.201903800
1330. W. Liao, Y. Huang, H. Wang, H. Zhang, Van der Waals heterostructures for optoelectronics: Progress and prospects. Appl. Mater. Today **16**, 435–455 (2019). 10.1016/j.apmt.2019.07.004
1331. L. Wang, I. Meric, P.Y. Huang, Q. Gao, Y. Gao, H. Tran, T. Taniguchi, K. Watanabe, L.M. Campos, D.A. Muller, J. Guo, P. Kim, J. Hone, K.L. Shepard, C.R. Dean, One-dimensional electrical contact to a two-dimensional material. Science **342**, 614–617 (2013). 10.1126/science.1244358
1332. M. Yankowitz, Q. Ma, P. Jarillo-Herrero, B.L. LeRoy, Van der Waals heterostructures combining graphene and hexagonal boron nitride. Nat. Rev. Phys. **1**, 112–125 (2019). 10.1038/s42254-018-0016-0
1333. Z. Qiu, M. Trushin, H. Fang, I. Verzhbitskiy, S. Gao, E. Laksono, M. Yang, P. Lyu, J. Li, J. Su, M. Telychko, K. Watanabe, T. Taniguchi, J. Wu, A.H. Castro Neto, L. Yang, G, Eda, S. Adam, J. Lu, Giant gate-tunable bandgap renormalization and excitonic effects in a 2D semiconductor. Sci. Adv. **5**, eaaw2347:1–6 (2019). 10.1126/sciadv.aaw2347
1334. Y. Fu, D. He, J. He, A. Bian, L. Zhang, S. Liu, Y. Wang, H. Zhao, Effect of dielectric environment on excitonic dynamics in monolayer WS_2, Adv. Mater. Interf. **6**, 1901307:1–9 (2019). 10.1002/admi.201901307
1335. M. Le Ster, T. Maerkl, P.J. Kowalczyk, S.A. Brown, Moiré patterns in van der Waals heterostructures. Phys. Rev. B **99**, 075422:1–10 (2019). 10.1103/PhysRevB.99.075422
1336. K. Tran, G. Moody, F. Wu, X. Lu, J. Choi, K. Kim, A. Rai, D.A. Sanchez, J. Quan, A. Singh, J. Embley, A. Zepeda, M. Campbell, T. Autry, T. Taniguchi, K. Watanabe, N. Lu, S.K. Banerjee, K.L. Silverman, S. Kim, E. Tutuc, L. Yang, A.H. MacDonald, X. Li, Evidence for Moiré excitons in van der Waals heterostructures. Nature **567**, 71–75 (2019). 10.1038/s41586-019-0975-z
1337. Y. Cao, V. Fatemi, S. Fang, K. Watanabe, T. Taniguchi, E. Kaxiras, P. Jarillo-Herrero, Unconventional superconductivity in magic-angle graphene superlattices. Nature **556**, 43–55 (2018). 10.1038/nature26160

1338. R.P. Feynman, There's plenty of room at the bottom: An invitation to enter a new field of physics (After-dinner speech on December 29th 1959 at the annual meeting of the American Physical Society at the California Institute of Technology). Eng. Sci. **23**, 22–36 (1960)
1339. D. Bimberg, M. Grundmann, N.N. Ledentsov, *Quantum Dot Heterostructures* (Wiley, Chichester, 1999)
1340. M. Grundmann, ed., *Nano-Optoelectronics, Concepts, Physics and Devices* (Springer, Heidelberg, 2002). 10.1007/978-3-642-56149-8
1341. E. Kapon, M. Walther, J. Christen, M. Grundmann, C. Caneau, D.M. Hwang, E. Colas, R. Bhat, G.H. Song, D. Bimberg, Quantum wire heterostructures for optoelectronic applications. Superlatt. Microstruct. **12**, 491–499 (1992). 10.1016/0749-6036(92)90307-Q
1342. M. Grundmann, J. Christen, M. Joschko, O. Stier, D. Bimberg, E. Kapon, Recombination kinetics and intersubband relaxation in semiconductor quantum wires. Semicond. Sci. Technol. **9**, 1939–1945 (1994). 10.1088/0268-1242/9/11S/014
1343. L. Pfeiffer, K.W. West, H.L. Störmer, J.P. Eisenstein, K.W. Baldwin, D. Gershoni, J. Spector, Formation of a high quality two-dimensional electron gas on cleaved GaAs. Appl. Phys. Lett. **56**, 1697–1699 (1990). 10.1063/1.103121
1344. M. Grundmann, D. Bimberg, Formation of quantum dots in twofold cleaved edge overgrowth. Phys. Rev. B **55**, 4054–4056 (1997). 10.1103/PhysRevB.55.4054
1345. W. Wegscheider, G. Schedelbeck, G. Abstreiter, M. Rother, M. Bichler, Atomically precise GaAs/AlGaAs quantum dots fabricated by twofold cleaved edge overgrowth. Phys. Rev. Lett. **79**, 1917–1920 (1997). 10.1103/PhysRevLett.79.1917
1346. A.P. Levitt, ed., *Whisker Technology* (Wiley, New York, 1970)
1347. Zh.L. Wang, ed., *Nanowires and Nanobelts—Materials, Properties and Devices* (Kluwer Academic, Boston, 2004) (Two volumes, Vol. I: *Metal and Semiconductor Nanowires*, Vol. II: *Nanowires and Nanobelts of Functional Materials*) 10.1007/978-0-387-28745-4; 10.1007/978-0-387-28747-8
1348. M.T. Björk, B.J. Ohlsen, T. Sass, A.I. Perrson, C. Thelander, M.H. Magnusson, K. Deppert, L.R. Wallenberg, L. Samuelson, One-dimensional heterostructures in semiconductor nanowhiskers. Appl. Phys. Lett. **80**, 1058–1060 (2002). 10.1063/1.1447312
1349. J.-C. Harmand, G. Patriarche, F. Glas, F. Panciera, I. Florea, J.-L. Maurice, L. Travers, Y. Ollivier, Atomic step flow on a nanofacet. Phys. Rev. Lett. **121**, 166101:1–5 (2018). 10.1103/PhysRevLett.121.166101
1350. M.H. Huang, S. Mao, H. Feick, H. Yan, Y. Wu, H. Kind, E. Weber, R. Russo, P. Yang, Room-temperature ultraviolet nanowire nanolasers. Science **292**, 1897–1899 (2001). 10.1126/science.1060367
1351. X. Duan, Y. Huang, R. Agarwal, C. Lieber, Single-nanowire electrically driven lasers. Nature **421**, 241–245 (2003). 10.1038/nature01353
1352. ZhL Wang, J. Song, Piezoelectric nanogenerators based on zinc oxide nanowire arrays. Science **312**, 242–246 (2006). 10.1126/science.1124005
1353. M. Lorenz, J. Lenzner, E.M. Kaidashev, H. Hochmuth, M. Grundmann, Cathodoluminescence of selected single ZnO nanowires on sapphire. Ann. Physik **13**, 39–42 (2004). 10.1002/andp.200310040
1354. B.Q. Cao, J. Zúñiga-Pérez, N. Boukos, C. Czekalla, H. Hilmer, J. Lenzner, A. Travlos, M. Lorenz, M. Grundmann, Homogeneous core/shell ZnO/ZnMgO quantum well heterostructures on vertical ZnO nanowires. Nanotechnology **20**, 305701 (2009). 10.1088/0957-4484/20/30/305701
1355. M.V. Barton, The circular cylinder with a band of uniform pressure on a finite length of the surface. J. Appl. Mech. **8**, A97–A104 (1941)
1356. E. Ertekin, P.A. Greaney, D.C. Chrzan, T.D. Sands, Equilibrium limits of coherency in strained nanowire heterostructures. J. Appl. Phys. **97**, 114325:1–10 (2005). 10.1063/1.1903106
1357. F. Glas, Critical dimensions for the plastic relaxation of strained axial heterostructures in free-standing nanowires. Phys. Rev. B **74**, 121302:1–4 (2006). 10.1103/PhysRevB.74.121302
1358. X.Y. Kong, ZhL Wang, Polar-surface dominated ZnO nanobelts and the electrostatic energy induced nanohelixes, nanosprings, and nanospirals. Appl. Phys. Lett. **84**, 975–977 (2004). 10.1063/1.1646453
1359. Zh.L. Wang, Novel zinc oxide nanostructures discovery by electron microscopy. J. Phys.: Conf. Ser. **26**, 1–6 (2006). 10.1088/1742-6596/26/1/001
1360. M. Grundmann, E. Kapon, J. Christen, D. Bimberg, Electronic and optical properties of quasi one-dimensional carriers in quantum wires. J. Nonlinear Opt. Phys. Mater. **4**, 99–140 (1995). 10.1142/S0218863595000069
1361. M. Grundmann, O. Stier, D. Bimberg, Electronic states in strained cleaved-edge-overgrowth quantum wires and quantum dots. Phys. Rev. B **58**, 10557–10561 (1998). 10.1103/PhysRevB.58.10557
1362. H.J. Xiang, J. Yang, J.G. Hou, Q. Zhu, Piezoelectricity in ZnO nanowires: A first-principles study. Appl. Phys. Lett. **89**, 223111:1–3 (2006). 10.1063/1.2397013
1363. S. Iijima, Helical microtubules of graphitic carbon. Nature **354**, 56–58 (1991). 10.1038/354056a0
1364. S. Iijima, T. Ichihasi, Single-shell carbon nanotubes of 1-nm diameter. Nature **363**, 603–605 (1993). 10.1038/363603a0
1365. R. Saito, G. Dresselhaus, M.S. Dresselhaus, *Physical Properties of Carbon Nanotubes* (Imperial, London, 1998). 10.1142/p080

1366. J. Kürti, V. Zólyomi, M. Kertesz, G. Sun, The geometry and the radial breathing mode of carbon nanotubes: Beyond the ideal behaviour. New J. Phys. **5**, 125:1–21 (2003). 10.1088/1367-2630/5/1/125
1367. R. Saito, M. Fujita, G. Dresselhaus, M.S. Dresselhaus, Electronic structure of chiral graphene tubules. Appl. Phys. Lett. **60**, 2204–2206 (1992). 10.1063/1.107080
1368. M.-F. Yu, B.S. Files, S. Arepalli, R.S. Ruoff, Tensile loading of ropes of single wall carbon nanotubes and their mechanical properties. Phys. Rev. Lett. **84**, 5552–5555 (2000). 10.1103/PhysRevLett.84.5552
1369. S. Ogata, Y. Shibutani, Ideal tensile strength and band gap of single-walled carbon nanotubes. Phys. Rev. B **68**, 165409:1–4 (2003). 10.1103/PhysRevB.68.165409
1370. R. Saito, M. Fujita, G. Dresselhaus, M.S. Dresselhaus, Electronic structure of carbon fibers based on C_{60}. Proc. Mater. Res. Soc. **247**, 333–338 (1992). 10.1557/PROC-247-333
1371. N. Hamada, S.-I. Sawada, A. Oshiyama, New one-dimensional conductors: Graphitic microtubule. Phys. Rev. Lett. **68**, 1579–1581 (1992). 10.1103/PhysRevLett.68.1579
1372. X. Blase, L.X. Benedict, E.L. Shirley, S.G. Louie, Hybridization effects and metallicity in small radius carbon nanotubes. Phys. Rev. Lett. **72**, 1878–1881 (1994). 10.1103/PhysRevLett.72.1878
1373. J.W. Mintmire, C.T. White, Universal density of states for carbon nanotubes. Phys. Rev. Lett. **81**, 2506–2509 (1989). 10.1103/PhysRevLett.81.2506
1374. A. Grüneis, R. Saito, G.G. Samsonidze, T. Kimura, M.A. Pimenta, A. Jorio, A.G. Souza Filho, G. Dresselhaus, M.S. Dresselhaus, Inhomogeneous optical absorption around the *K* point in graphite and carbon nanotubes. Phys. Rev. B **67**, 165402:1–7 (2003). 10.1103/PhysRevB.67.165402
1375. S.M. Bachilo, M.S. Strano, C. Kittrell, R.H. Hauge, R.E. Smalley, R.B. Weisman, Structure-assigned optical spectra of single-walled carbon nanotubes. Science **298**, 2361–2366 (2002). 10.1126/science.1078727
1376. H. Telg, J. Maultzsch, S. Reich, F. Hennrich, C. Thomsen, Chirality distribution and transition energies of carbon nanotubes. Phys. Rev. Lett. **93**, 177401:1–4 (2004). 10.1103/PhysRevLett.93.177401
1377. C. Thomsen, S. Reich, Raman scattering in carbon nanotubes, in *Light Scattering in Solids IX*, M. Cardona, R. Merlin, eds. Topics Appl. Phys. vol. 108 (Springer, Berlin, 2007), pp. 115–234 10.1007/978-3-540-34436-0_3
1378. N.G. Chopra, R.J. Luyken, K. Cherrey, V.H. Crespi, M.L. Cohen, S.G. Louie, A. Zettl, Boron nitride nanotubes. Science **269**, 966–967 (1995). 10.1126/science.269.5226.966
1379. R.S. Lee, J. Gavillet, M.L. de la Chapelle, A. Loiseau, J.-L. Cochon, D. Pigache, J. Thibault, F. Willaime, Catalyst-free synthesis of boron nitride single-wall nanotubes with a preferred zig-zag configuration. Phys. Rev. B **64**, 121405(R):1–4 (2001). 10.1103/PhysRevB.64.121405
1380. A. Rubio, J.L. Corkill, M.L. Cohen, Theory of graphitic boron nitride nanotubes. Phys. Rev. B **49**, 5081–5084 (1994). 10.1103/PhysRevB.49.5081
1381. L. Wirtz, V. Olevano, A.G. Marinopoulos, L. Reining, A. Rubio, Optical absorption in small BN and C nanotubes. AIP Conf. Proc. **685**, 406–410 (2003). 10.1063/1.1628060
1382. O. Stier, M. Grundmann, D. Bimberg, Electronic and optical properties of strained quantum dots modeled by 8-band $k \cdot p$ theory. Phys. Rev. B **59**, 5688–5701 (1999). 10.1103/PhysRevB.59.5688
1383. R. Santoprete, B. Koiller, R.B. Capaz, P. Kratzer, Q.K.K. Liu, M. Scheffler, Tight-binding study of the influence of the strain on the electronic properties of InAs/GaAs quantum dots. Phys. Rev. B **68**, 235311:1–9 (2003). 10.1103/PhysRevB.68.235311
1384. Th. Maltezopoulos, A. Bolz, C. Meyer, C. Heyn, W. Hansen, M. Morgenstern, R. Wiesendanger, Wave-function mapping of InAs quantum dots by scanning tunneling spectroscopy. Phys. Rev. Lett. **91**, 196804:1–4 (2003). 10.1103/PhysRevLett.91.196804
1385. O. Stier, Theory of the optical properties of InGaAs/GaAs quantum dots, in *Nano-Optoelectronics, Concepts, Physics, Devices*, ed. by M. Grundmann (Springer, Berlin, 2002), pp. 167–202. 10.1007/978-3-642-56149-8_7
1386. L.P. Kouwenhoven, N.C. van der Vaart, A.T. Johnson, W. Kool, C.J.P.M. Harmans, J.G. Williamson, A.A.M. Staring, C.T. Foxon, Single electron charging effects in semiconductor quantum dots. Z. Phys. B **85**, 367–373 (1991). 10.1007/BF01307632
1387. Th. Heinzel, Single electron tunneling, in *Mesoscopic Electronics in Solid State Nanostructures* (Wiley, Weinheim, 2006), pp. 247–272. 10.1002/9783527618910.ch9
1388. X.-X. Song, D. Liu, V. Mosallanejad, J. You, T.-Y. Han, D.-T. Chen, H.-O. Li, G. Cao, M. Xiao, G.-C. Guo, G.-P. Guo, A gate defined quantum dot on the two-dimensional transition metal dichalcogenide semiconductor WSe_2. Nanoscale **7**, 16867–16873 (2015). 10.1039/C5NR04961J
1389. E.O. Göbel, Semiconductor applications in metrology. Adv. Solid State Phys. (Festkörperprobleme) **39**, 1–12 (1999). 10.1007/BFb0107460
1390. S.P. Giblin, M. Kataoka, J.D. Fletcher, P. See, T.J.B.M. Janssen, J.P. Griffiths, G.A.C. Jones, I. Farrer, D.A. Ritchie, Towards a quantum representation of the ampere using single electron pumps. Nat. Commun. **3**, 930:1–6 (2018). 10.1038/ncomms1935
1391. S. Tarucha, D.G. Austing, T. Honda, R.J. van der Hage, L.P. Kouwenhoven, Shell filling and spin effects in a few electron quantum dot. Phys. Rev. Lett. **77**, 3613–3616 (1996). 10.1103/PhysRevLett.77.3613
1392. N. Horiguchi, T. Futatsugi, Y. Nakata, N. Yokoyama, Electron transport properties through InAs self-assembled quantum dots in modulation doped structures. Appl. Phys. Lett. **70**, 2294–2296 (1997). 10.1063/1.118840

1393. R. Steffen, A. Forchel, T.L. Reinecke, T. Koch, M. Albrecht, J. Oshinowo, F. Faller, Single quantum dots as local probes of electronic properties of semiconductors. Phys. Rev. B **54**, 1510–1513 (1996). 10.1103/PhysRevB.54.1510
1394. K.C. Rajkumar, K. Kaviani, J. Chen, P. Chen, A. Madhukar, D. Rich, In-Situ growth of three-dimensionally confined structures on patterned GaAs (111)B substrates. Proc. Mater. Res. Soc. **263**, 163–167 (1992). 10.1557/PROC-263-163
1395. Wolfgang Weller, private communication (2006)
1396. M. Liu, G. Zhong, Y. Yin, J. Miao, K. Li, C. Wang, X. Xu, C. Shen, H. Meng, Aluminum-doped cesium lead bromide perovskite nanocrystals with stable blue photoluminescence used for display backlight. Adv. Sci. **4**, 1700335:1–8 (2017). 10.1002/advs.201700335
1397. M. Grundmann, Pseudomorphic InAs/GaAs quantum dots on low index planes. Adv. Solid State Phys. (Festkörperprobleme) **35**, 123–154 (1996). 10.1007/BFb0107543
1398. V.A. Shchukin, N.N. Ledentsov, D. Bimberg, *Epitaxy of Nanostructures* (Springer, Heidelberg, 2004). 10.1007/978-3-662-07066-6
1399. V.A. Shchukin, N.N. Ledentsov, P.S. Kop'ev, D. Bimberg, Spontaneous ordering of arrays of coherent strained islands. Phys. Rev. Lett. **75**, 2968–2971 (1995). 10.1103/PhysRevLett.75.2968
1400. N. Moll, M. Scheffler, E. Pehlke, Influence of surface stress on the equilibrium shape of strained quantum dots. Phys. Rev. B **58**, 4566–4571 (1998). 10.1103/PhysRevB.58.4566
1401. D. Leonard, M. Krishnamurthy, C.M. Reaves, S.P. Denbaars, P.M. Petroff, Direct formation of quantum-sized dots from uniform coherent islands of InGaAs on GaAs surfaces. Appl. Phys. Lett. **63**, 3203–3205 (1993). 10.1063/1.110199
1402. D.M. Bruls, P.M. Koenraad, H.W.M. Salemink, J.H. Wolter, M. Hopkinson, M.S. Skolnick, Stacked low-growth-rate InAs quantum dots studied at the atomic level by cross-sectional scanning tunneling microscopy. Appl. Phys. Lett. **82**, 3758–3760 (2003). 10.1063/1.1578709
1403. Q. Xie, A. Madhukar, P. Chen, N. Kobayashi, Vertically self-organized InAs quantum box islands on GaAs(100). Phys. Rev. Lett. **75**, 2542–2545 (1995). 10.1103/PhysRevLett.75.2542
1404. S. Facsko, T. Dekorsy, C. Koerdt, C. Trappe, H. Kurz, A. Vogt, H.L. Hartnagel, Formation of ordered nanoscale semiconductor dots by ion sputtering. Science **285**, 1551–1553 (1999). 10.1126/science.285.5433.1551
1405. F. Frost, A. Schindler, F. Bigl, Roughness evolution of ion sputtered rotating inp surfaces: Pattern formation and scaling laws. Phys. Rev. Lett. **85**, 4116–4419 (2000). 10.1103/PhysRevLett.85.4116
1406. R. Gago, L. Vásquez, R. Cuerno, M. Varela, C. Ballesteros, J.M. Albella, Production of ordered silicon nanocrystals by low-energy ion sputtering. Appl. Phys. Lett. **78**, 3316–3318 (2001). 10.1063/1.1372358
1407. R. Gago, L. Vásquez, O. Plantevin, T.H. Metzger, J. Muâoz-García, R. Cuerno, M. Castro, Order enhancement and coarsening of self-organized silicon nanodot patterns induced by ion-beam sputtering. Appl. Phys. Lett. **89**, 233101:1–3 (2006). 10.1063/1.2398916
1408. B. Ziberi, F. Frost, B. Rauschenbach, Th. Höche, Highly ordered self-organized dot patterns on Si surfaces by low-energy ion-beam erosion. Appl. Phys. Lett. **87**, 033113:1–3 (2005). 10.1063/1.2000342
1409. W.L. Chan, E. Chason, Making waves: Kinetic processes controlling surface evolution during low energy ion sputtering. J. Appl. Phys. **101**, 121301:1–46 (2007). 10.1063/1.2749198
1410. B. Ziberi, F. Frost, Th. Höche, B. Rauschenbach, Ripple pattern formation on silicon surfaces by low-energy ion-beam erosion: Experiment and theory. Phys. Rev. B **72**, 235310:1–7 (2005). 10.1103/PhysRevB.72.235310
1411. F. Findeis, A. Zrenner, G. Böhm, G. Abstreiter, Optical spectroscopy on a single InGaAs/GaAs quantum dot in the few-exciton limit. Solid State Commun. **114**, 227–230 (2000). 10.1016/S0038-1098(00)00019-3
1412. O. Stier, A. Schliwa, R. Heitz, M. Grundmann, D. Bimberg, Stability of biexcitons in pyramidal InAs/GaAs quantum dots. Phys. Status Solidi B **224**, 115–118 (2001). 10.1002/1521-3951(200103)224:1<115::AID-PSSB115>3.0.CO;2-B
1413. D.J.P. Ellis, R.M. Stevenson, R.J. Young, A.J. Shields, P. Atkinson, D.A. Ritchie, Control of fine-structure splitting of individual InAs quantum dots by rapid thermal annealing. Appl. Phys. Lett. **90**, 011907:1–3 (2007) 10.1063/1.2430489
1414. B. Urbaszek, R.J. Warburton, K. Karrai, B.D. Gerardot, P.M. Petroff, J.M. Garcia, Fine structure of highly charged excitons in semiconductor quantum dots. Phys. Rev. Lett. **90**, 247403:1–4 (2003). 10.1103/PhysRevLett.90.247403
1415. R.J. Warburton, C. Schäflein, D. Haft, F. Bickel, A. Lorke, K. Karrai, J.M. Garcia, W. Schoenfeld, P.M. Petroff, Optical emission from a charge-tunable quantum ring. Nature **405**, 926–929 (2000). 10.1038/35016030
1416. L. Besombes, Y. Léger, L. Maingault, D. Ferrand, H. Mariette, Probing the spin state of a single magnetic ion in an individual quantum dot. Phys. Rev. Lett. **93**, 207403:1–4 (2004). 10.1103/PhysRevLett.93.207403
1417. W. Franz, Einfluß eines elektrischen Feldes auf eine optische Absorptionskante. Z. Naturf. **13a**, 484–489 (1958). 10.1515/zna-1958-0609
1418. L.V. Keldysh, Behaviour of non-metallic crystals in strong electric fields. Soviet Phys. JETP **6**, 763–770 (1958)
1419. F. Duque-Gomez, J.E. Sipe, The Franz-Keldysh effect revisited: Electroabsorption including interband coupling and excitonic effects. J. Phys. Chem. Solids **76**, 138–152 (2015). 10.1016/j.jpcs.2014.07.023

1420. H. Shen, M. Dutta, Franz-Keldysh oscillations in modulation spectroscopy. J. Appl. Phys. **78**, 2151– (1995). 10.1063/1.360131
1421. A. Jaeger, *Exzitonen und Franz–Keldysh-Effekt im quaternären Halbleiter InGaAsP/InP*, Ph.D. Thesis, Phillips-Universität Marburg (1997)
1422. D.A.B. Miller, D.S. Chemla, T.C. Damen, A.C. Gossard, W. Wiegmann, T.H. Wood, C.A. Burrus, Electric field dependence of optical absorption near the band gap of quantum-well structures. Phys. Rev. B **32**, 1043–1060 (1985). 10.1103/PhysRevB.32.1043
1423. J.M. Luttinger, Quantum theory of cyclotron resonance in semiconductors: General theory. Phys. Rev. **102**, 1030–1041 (1956). 10.1103/PhysRev.102.1030
1424. N. Miura, *Physics of Semiconductors in High Magnetic Fields* (Oxford University Press, Oxford, 2008)
1425. M. Oestreich, S. Hallstein, A.P. Heberle, K. Eberl, E. Bauser, W.W. Rühle, Temperature and density dependence of the electron Landé g factor in semiconductors. Phys. Rev. B **53**, 7911–7916 (1996). 10.1103/PhysRevB.53.7911
1426. M.J. Snelling, E. Blackwood, C.J. McDonagh, R.T. Harley, C.T.B. Foxon, Exciton, heavy-hole, and electron g factors in type-I GaAs/$Al_xGa_{1-x}As$ quantum wells. Phys. Rev. B **45**, 3922–3925 (1992). 10.1103/PhysRevB.45.3922
1427. C.L. Chien, C.R. Westgate, eds., *The Hall Effect and its Application* (Plenum Press, New York, 1980). 10.1007/978-1-4757-1367-1
1428. H.-J. Lippmann, F. Kuhrt, Der Geometrieeinfluß auf den Hall-Effekt bei rechteckigen Halbleiterplatten. Z. Naturf. **13a**, 474–483 (1958). 10.1515/zna-1958-0608
1429. L.J. van der Pauw, A method of measuring specific resistivity and Hall effect of discs of arbitrary shape. Philips Res. Reports **13**, 1–9 (1958)
1430. L.J. van der Pauw, A method of measuring the resistivity and Hall coefficient on lamellae of arbitrary shape. Philips Tech. Rev. **20**, 220–224 (1958)
1431. D.S. Perloff, Four-point sheet resistance correction factors for thin rectangular samples. Solid State Electron. **20**, 681–687 (1977). 10.1016/0038-1101(77)90044-2
1432. O. Breitenstein, W. Warta, M. Langenkamp, *Lock-in Thermography, Basics and Use for Evaluating Electronic Devices and Materials*, 2nd edn. (Springer, Heidelberg, 2010) 10.1007/978-3-642-02417-7
1433. O. Madelung, H. Weiss, Die elektrischen Eigenschaften von Indiumantimonid II. Z. Naturf. **9a**, 527–534 (1954). 10.1515/zna-1954-0608
1434. H.G. Svavarsson, J.T. Gudmundsson, H.P. Gislason, Impurity band in lithium-diffused and annealed GaAs: Conductivity and Hall effect measurements. Phys. Rev. B **67**, 205213:1–6 (2003). 10.1103/PhysRevB.67.205213
1435. S. Meiboom, B. Abeles, Theory of the galvanomagnetic effects in n-germanium. Phys. Rev. **93**, 1121 (1954). 10.1103/PhysRev.93.1121
1436. B. Abeles, S. Meiboom, Theory of the galvanomagnetic effects in germanium. Phys. Rev. **95**, 31–37 (1954). 10.1103/PhysRev.95.31
1437. B. Arnaudov, T. Paskova, S. Evtimova, E. Valcheva, M. Heuken, B. Monemar, Multilayer model for Hall effect data analysis of semiconductor structures with step-changed conductivity. Phys. Rev. B **67**, 045314:1–10 (2003). 10.1103/PhysRevB.67.045314
1438. D.C. Look, J.R. Sizelove, Dislocation scattering in GaN. Phys. Rev. Lett. **82**, 1237–1240 (1999). 10.1103/PhysRevLett.82.1237
1439. H. von Wenckstern, M. Brandt, H. Schmidt, G. Biehne, R. Pickenhain, H. Hochmuth, M. Lorenz, M. Grundmann, Donor like defects in ZnO substrate materials and ZnO thin films. Appl. Phys. A **88**, 135–139 (2007). 10.1007/s00339-007-3966-0
1440. D.C. Look, Two-layer Hall-effect model with arbitrary surface-donor profiles: Application to ZnO. J. Appl. Phys. **104**, 063718:1–7 (2008). 10.1063/1.2986143
1441. J. Antoszweski, D.J. Seymour, L. Faraone, J.R. Meyer, C.A. Hoffmann, Magneto-transport characterization using quantitative mobility-spectrum analysis. J. Electr. Mater. **24**, 1255–1262 (1995). 10.1007/BF02653082
1442. I. Vurgaftman, J.R. Meyer, C.A. Hoffman, D. Redfern, J. Antoszewski, L. Faraone, J.R. Lindemuth, Improved quantitative mobility spectrum analysis for Hall characterization. J. Appl. Phys. **84**, 4966–4973 (1998). 10.1063/1.368741
1443. J. Rothman, J. Meilhan, G. Perrais, J.-P. Belle, O. Gravrand, Maximum entropy mobility spectrum analysis of HgCdTe heterostructures. J. Electr. Mater. **35**, 1174–1184 (2006). 10.1007/s11664-006-0238-2
1444. J. Antoszewski, L. Faraone, Quantitative mobility spectrum analysis (QMSA) in multi-layer semiconductor structures. Opto-Electr. Rev. **12**, 347–352 (2004)
1445. L. Friedman, T. Holstein, Studies of polaron motion. Part III: The Hall mobility of the small polaron. Ann. Phys. **21**, 494–549 (1963). 10.1016/0003-4916(63)90130-1
1446. Y.M. Gal'perin, E.P. German, V.G. Karpov, Hall effect under hopping conduction conditions. Zh. Eksp. Teor. Fiz. **99**, 343–356 (1991) [Sov. Phys. JETP **72**, 193–200 (1991)]
1447. P.G. Le Comber, D.I. Jones, W.E. Spear, Hall effect and impurity conduction in substitutionally doped amorphous silicon. Philos. Mag. **35**, 1173–1187 (1977). 10.1080/14786437708232943

1448. I. Crupi, S. Mirabella, D. D'Angelo, S. Gibilisco, A. Grasso, S. Di Marco, F. Simone, A. Terrasi, Anomalous and normal Hall effect in hydrogenated amorphous Si prepared by plasma enhanced chemical vapor deposition. J. Appl. Phys. **107**, 043503:1–6 (2010). 10.1063/1.3305805
1449. M. Grünewald, P. Thomas, D. Würtz, The sign anomaly of the Hall effect in amorphous tetrahedrally bonded semiconductors: A chemical-bond orbital approach. J. Phys. C: Solid State Phys. **14**, 4083–4093 (1981). 10.1088/0022-3719/14/28/010
1450. M. Schubert, *Infrared Ellipsometry on Semiconductor Layer Structures: Phonons, Plasmons and Polaritons* (Springer. Heidelberg (2004). 10.1007/b11964
1451. M. Schubert, T. Hofmann, C.M. Herzinger, Generalized far-infrared magneto-optic ellipsometry for semiconductor layer structures: determination of free-carrier effective-mass, mobility, and concentration parameters in n-type GaAs. J. Opt. Soc. Am. A **20**, 347–356 (2003). 10.1364/JOSAA.20.000347
1452. B. Lax, J.G. Mavroides, H.J. Zeiger, R.J. Keys, Cyclotron resonance in indium antimonide at high magnetic fields. Phys. Rev. **122**, 31–35 (1961). 10.1103/PhysRev.122.31
1453. K.L. Litvinenko, J.Li , N. Stavrias, A.J. Meaney, P.C.M. Christianen, H. Engelkamp, K.P. Homewood, C.R. Pidgeon, B.N. Murdin, The quadratic Zeeman effect used for state-radius determination in neutral donors and donor bound excitons in Si:P. Semicond. Sci. Technol. **31**, 045007:1–7 (2016). 10.1007/b11964
1454. S.N. Walck, T.L. Reinecke, Exciton diamagnetic shift in semiconductor nanostructures. Phys. Rev. B **57**, 9088–9096 (1998). 10.1103/PhysRevB.57.9088
1455. M. Grochol, F. Grosse, R. Zimmermann, Exciton wave function properties probed by diamagnetic shift in disordered quantum wells. Phys. Rev. B **71**, 125339:1–8 (2005). 10.1103/PhysRevB.71.125339
1456. W. Zawadski, R. Lassnig, Specific Heat and magneto-thermal oscillations of two-dimensional electron gas in a magnetic field. Solid State Commun. **50**, 537–539 (1984). 10.1016/0038-1098(84)90324-7
1457. H.L. Störmer, R. Dingle, A.C. Gossard, W. Wiegmann, R.A. Logan, Electronic properties of modulation-doped GaAs-$Al_xGa_{1-x}As$ superlattices. Inst. Phys. Conf. Ser. **43**, 557–560 (1979)
1458. A.B. Fowler, F.F. Fang, W.E. Howard, P.J. Stiles, Magneto-oscillatory conductance in silicon surfaces. Phys. Rev. Lett. **16**, 901–903 (1966). 10.1103/PhysRevLett.16.901
1459. M.A. Paalanen, D.C. Tsui, A.C. Gossard, Quantized Hall effect at low temperatures. Phys. Rev. B **25**, 5566–5569 (1982). 10.1103/PhysRevB.25.5566
1460. Physikalisch-Technische Bundesanstalt (PTB), Braunschweig
1461. K. von Klitzing, G. Dorda, M. Pepper, New method for high-accuracy determination of the fine-structure constant based on quantized Hall resistance. Phys. Rev. Lett. **45**, 494–497 (1980). 10.1103/PhysRevLett.45.494
1462. G. Landwehr, 25 Years quantum Hall effect: How it all came about. Physica E **20**, 1–13 (2003). 10.1016/j.physe.2003.09.015
1463. J. Falson, Y. Kozuka, M. Uchida, J.H. Smet, T.-h. Arima, A. Tsukazaki, M. Kawasaki, MgZnO/ZnO heterostructures with electron mobility exceeding 1×10^6 cm^2/Vs. Sci. Rep. **6**, 26598:1–8 (2016). 10.1038/srep26598
1464. J. Faslom, M. Kawasaki, A review of the quantum Hall effects in MgZnO/ZnO heterostructures. Rep. Prog. Phys. **81**, 056501:1–24 (2018). 10.1088/1361-6633/aaa978
1465. H. Bachmair, E.O. Göbel, G. Hein, J. Melcher, B. Schumacher, J. Schurr, L. Schweitzer, P. Warnecke, The von Klitzing resistance standard. Physica E **20**, 14–23 (2003). 10.1016/j.physe.2003.09.017
1466. J.K. Jain, *Composite Fermions* (Cambridge University Press, Cambridge, 2007). 10.1017/CBO9780511607561
1467. H. Aoki, T. Ando, Effect of localization of the Hall conductivity in the two-dimensional system in strong magnetic fields. Solid State Commun. **38**, 1079–1082 (1981). 10.1016/0038-1098(93)90276-S
1468. R.B. Laughlin, Quantized Hall conductivity in two dimensions. Phys. Rev. B **23**, 5632–5633 (1981). 10.1103/PhysRevB.23.5632
1469. D.J. Thouless, M. Kohmoto, M.P. Nightingale, M. den Nijs, Quantized Hall conductance in a two-dimensional periodic potential. Phys. Rev. Lett. **49**, 405–408 (1982). 10.1103/PhysRevLett.49.405
1470. Y. Hatsugai, Chern number and edge states in the integer quantum Hall effect. Phys. Rev. Lett. **71**, 3697–3700 (1993). 10.1103/PhysRevLett.71.3697
1471. D.R. Hofstadter, Energy levels and wave functions of Bloch electrons in rational and irrational magnetic fields. Phys. Rev. B **14**, 2239–2249 (1976). 10.1103/PhysRevB.14.2239
1472. D. Osadchy, J.E. Avron, Hofstadter butterfly as quantum phase diagram. J. Math. Phys. **42**, 5665–5671 (2001). 10.1063/1.1412464
1473. E. Ahlswede, P. Weitz, J. Weis, K. von Klitzing, K. Eberl, Hall potential profiles in the quantum Hall regime measured by a scanning force microscope. Physica B **298**, 562–566 (2001). 10.1016/S0921-4526(01)00383-0
1474. R.E. Prange, Quantized Hall resistance and the measurement of the fine-structure constant. Phys. Rev. B **23**, 4802–4805 (1981). 10.1103/PhysRevB.23.4802
1475. M. Büttiker, Absence of backscattering in the quantum Hall effect in multiprobe conductors. Phys. Rev. B **38**, 9375–9389 (1988). 10.1103/PhysRevB.38.9375
1476. K. Lier, R.R. Gerhardts, Self-consistent calculation of edge channels in laterally confined two-dimensional electron systems. Phys. Rev. B **50**, 7757–7767 (1994). 10.1103/PhysRevB.50.7757

1477. Y. Zhang, Y.-W. Tan, H.L. Stormer, P. Kim, Experimental observation of the quantum Hall effect and Berry's phase in graphene. Nature **438**, 201–204 (2005). 10.1038/nature04235
1478. M.O. Goerbig, The quantum Hall effect in graphene—A theoretical perspective. Comptes Rendus Phys. **12**, 369–378 (2011). 10.1016/j.crhy.2011.04.012
1479. Z. Jiang, Y. Zhang, Y.-W. Tan, H.L. Stormer, P. Kim, Quantum Hall effect in graphene. Solid State Commun. **143**, 14–19 (2007). 10.1016/j.ssc.2007.02.046
1480. J.P. Eisenstein, H.L. Störmer, The fractional quantum Hall effect. Science **248**, 1510–1516 (1990). 10.1126/science.248.4962.1510
1481. J.K. Jain, Composite-Fermion approach for the fractional quantum Hall effect. Phys. Rev. Lett. **63**, 199–202 (1989). 10.1103/PhysRevLett.63.199
1482. J.K. Jain, Theory of the fractional quantum Hall effect. Phys. Rev. B **41**, 7653–7665 (1990). 10.1103/PhysRevB.41.7653 Erratum: Phys. Rev. B **42**, 9193 (1990). 10.1103/PhysRevB.42.9193
1483. H.L. Störmer, D.C. Tsui, A.C. Gossard, The fractional quantum Hall effect. Rev. Mod. Phys. **71**, S298–S305 (1999). 10.1103/RevModPhys.71.S298
1484. D. Weiss, M.L. Roukes, A. Menschig, P. Frambow, K. von Klitzing, G. Weimann, Electron pinball and commensurate orbits in a periodic array of scatterers. Phys. Rev. Lett. **66**, 2790–2793 (1991). 10.1103/PhysRevLett.66.2790
1485. M. Fiebig, Revival of the magnetoelectric effect. J. Phys. D: Appl. Phys. **38**, R123–R152 (2005). 10.1088/0022-3727/38/8/R01
1486. W. Eerenstein, N.D. Mathur, J.F. Scott, Multiferroic and magnetoelectric materials. Nature **442**, 759–765 (2006). 10.1038/nature05023
1487. Nils Ashcroft, private communication (2006)
1488. V.M. Fridkin, *Ferroelectric Semiconductors (translated from Russian)* (Plenum, New York, 1980)
1489. Y. Xu, *Ferroelectric Materials and Their Applications* (North Holland, Amsterdam, 1991)
1490. K. Rabe, Ch.H. Ahn, J.-M. Triscone, eds., Physics of ferroelectrics, a modern perspective, *Topics in Applied Physics*, vol. 105 (Springer, Berlin, 2007). 10.1007/978-3-540-34591-6
1491. R. Comes, M. Lambert, A. Guinier, The chain structure of $BaTiO_3$ and $KNbO_3$. Solid State Commun. **6**, 715–719 (1968). 10.1016/0038-1098(68)90571-1
1492. R.E. Cohen, Origin of ferroelectricity in perovskite oxides. Nature **358**, 136–138 (1992). 10.1038/358136a0
1493. G. Shirane, S. Hoshino, On the phase transition in lead titanate. J. Phys. Soc. Jpn. **6**, 265–270 (1951). 10.1143/JPSJ.6.265
1494. W.J. Merz, The electric and optical behavior of $BaTiO_3$ single-domain crystals. Phys. Rev. **76**, 1221–1225 (1949). 10.1103/PhysRev.76.1221
1495. D.K. Agrawal, C.H. Perry, Long-wavelength optical phonons and phase transitions in SbSI. Phys. Rev. B **4**, 1893–1902 (1971). 10.1103/PhysRevB.4.1893
1496. G. Rupprecht, R.O. Bell, Dielectric constant in paraelectric perovskites. Phys. Rev. **135**, A748–A752 (1964). 10.1103/PhysRev.135.A748
1497. M.E. Lines, Statistical theory for displacement ferroelectrics. III. Comparison with experiment for lithium tantalate. Phys. Rev. **177**, 819–829 (1969). 10.1103/PhysRev.177.819
1498. W.J. Merz, Double hysteresis loop of $BaTiO_3$ at the Curie point. Phys. Rev. **91**, 513–517 (1953). 10.1103/PhysRev.91.513
1499. P.W. Forsbergh Jr., Domain structures and phase transitions in barium titanate. Phys. Rev. **76**, 1187–1201 (1949). 10.1103/PhysRev.76.1187
1500. Ch. Gähwiller, Einfluß des elektrischen Feldes auf die fundamentale Absorptionskante von Bariumtitanat. Phys. Kondens. Materie **6**, 269–289 (1967). 10.1007/BF02422508
1501. G. Arlt, P. Quadflieg, Piezoelectricity in III-V compounds with a phenomenological analysis of the piezoelectric effect. Phys. Status Solidi B **25**, 323–330 (1968). 10.1002/pssb.19680250131
1502. M. Grundmann, O. Stier, D. Bimberg, Symmetry breaking in pseudomorphic V-groove quantum wires. Phys. Rev. B **50**, 14187–14192 (1994). 10.1103/PhysRevB.50.14187
1503. D.L. Smith, C. Mailhiot, Piezoelectric effects in strained-layer superlattices. J. Appl. Phys. **63**, 2717–2719 (1988). 10.1063/1.340965
1504. T. Hanada, Basic properties of ZnO, GaN, and related materials, in *Oxide and Nitride Semiconductors: Processing, Properties and Applications*, T. Yao, S.-K. Hong, eds. (Springer, Heidelberg, 2009). 10.1007/978-3-540-88847-5_1
1505. M. Catti, Y. Noel, R. Dovesi, Full piezoelectric tensors of wurtzite and zinc blende ZnO and ZnS by first-principles calculations. J. Phys. Chem. Solids **64**, 2183–2190 (2003). 10.1016/S0022-3697(03)00219-1
1506. M.S. Shur, B. Gelmont, A. Khan, Electron mobility in two-dimensional electron gas in AlGaN/GaN heterostructures and in bulk GaN. J. Electr. Mater. **25**, 777–785 (1996). 10.1007/BF02666636
1507. F. Bernardini, V. Fiorentini, D. Vanderbilt, Spontaneous polarization and piezoelectric constants of III-V nitrides. Phys. Rev. B **56**, R10024–R10027 (1997). 10.1103/PhysRevB.56.R10024
1508. Oliver Ambacher, private communication (2005)

1509. P. Waltereit, O. Brandt, A. Trampert, H.T. Grahn, J. Menniger, M. Ramsteiner, M. Reiche, K.H. Ploog, Nitride semiconductors free of electrostatic fields for efficient white light-emitting diodes. Nature **406**, 865–868 (2000). 10.1038/35022529
1510. C.Q. Chen, V. Adivarahan, J.W. Yang, M. Shatalov, E. Kuokstis, M.A. Khan, Ultraviolet light emitting diodes using non-polar a-plane GaN-AlGaN multiple quantum wells. Jpn. J. Appl. Phys. **42**, Part 2, L1039–L1040 (2003). 10.1143/JJAP.42.L1039
1511. R. Sharma, P.M. Pattison, H. Masui, R.M. Farrel, T.J. Baker, B.A. Haskell, F. Wu, S.P. DenBaars, J.S. Speck, S. Nakamura, Demonstration of a semipolar $(10\bar{1}\bar{3})$ InGaN/GaN green light emitting diode. Appl. Phys. Lett. **87**, 231110:1–3 (2005). 10.1063/1.2139841
1512. S.-H. Park, Crystal orientation effects on electronic properties of wurtzite InGaN/GaN quantum wells. J. Appl. Phys. **91**, 9904–9908 (2002). 10.1063/1.1480465
1513. H. Sato, R.B. Chung, H. Hirasawa, N. Fellows, H. Masui, F. Wu, M. Saito, K. Fujito, J.S. Speck, S.P. DenBaars, S. Nakamura, Optical properties of yellow light-emitting diodes grown on semipolar $(11\bar{2}2)$ bulk GaN substrates. Appl. Phys. Lett. **92**, 221110:1–3 (2008). 10.1063/1.2938062
1514. M. Grundmann, Theory of semiconductor solid and hollow nano- and microwires with hexagonal cross-section under torsion. Phys. Status Solidi B **252**, 773–785 (2015). 10.1002/pssb.201451431
1515. A.D. Andreev, E.P. O'Reilly, Theory of the electronic structure of GaN/AlN hexagonal quantum dots. Phys. Rev. B **62**, 15851–15870 (2000). 10.1103/PhysRevB.62.15851
1516. J.K. Furdyna, Diluted magnetic semiconductors. J. Appl. Phys. **64**, R29–R64 (1988). 10.1063/1.341700
1517. J.K. Furdyna, J. Kossut, eds., Diluted magnetic semiconductors. Semicond. Semimet. **25**, (1988). 10.1016/S0080-8784(08)62411-4
1518. D. Awshalom, D. Loss, N. Samarth, eds., *Semiconductor Spintronics and Quantum Computation* (Springer, Berlin, 2002). 10.1007/978-3-662-05003-3
1519. S.J. Pearton, C.R. Abernathy, M.E. Overberg, G.T. Thaler, D.P. Norton, N. Theodoropoulou, A.F. Hebard, Y.D. Park, F. Ren, J. Kim, L.A. Boatner, Wide band gap ferromagnetic semiconductors and oxides. J. Appl. Phys. **93**, 1–13 (2003). 10.1063/1.1517164
1520. T. Dietl, H. Ohno, Dilute ferromagnetic semiconductors: Physics and spintronic structures. Rev. Mod. Phys. **86**, 187–251 (2014). 10.1103/RevModPhys.86.187
1521. I. Tsubokawa, On the magnetic properties of a $CrBr_3$ single crystal. J. Phys. Soc. Jpn. **15**, 1664–1668 (1960). 10.1143/JPSJ.15.1664
1522. B.T. Matthias, R.M. Bozorth, J.H. van Vleck, Ferromagnetic interaction in EuO. Phys. Rev. Lett. **7**, 160–161 (1961). 10.1103/PhysRevLett.7.160
1523. G. Güntherodt, Optical properties and electronic structure of europium chalcogenides. Phys. Cond. Matter **18**, 37–78 (1974). 10.1007/BF01950500
1524. P.G. Steeneken, *New light on EuO thin films: Preparation, transport, magnetism and spectroscopy of a ferromagnetic semiconductor*, Ph.D. Thesis, Rijksuniversiteit Groningen (2002)
1525. P. Wachter, Europium chalcogenides: EuO, EuS, EuSe, and EuTe, in: *Handbook on the Physics and Chemistry of Rare Earths*, K.A. Gschneider, Jr., L. Eyring, eds. (North-Holland, Amsterdam, 1979), pp. 507–574
1526. T. Fukumura, H. Toyosaki, Y. Yamada, Magnetic oxide semiconductors. Semicond. Sci. Technol. **20**, S103–S111 (2005). 10.1088/0268-1242/20/4/012
1527. W. Giriat, J.K. Furdyna, Crystal structure, composition, and materials preparation of diluted magnetic semiconductors in Ref. [1517], pp. 1–34. 10.1016/S0080-8784(08)62417-5
1528. C. Rigaux, Magnetooptics in narrow gap diluted magnetic semiconductors in Ref. [1517], pp. 229–274. 10.1016/S0080-8784(08)62422-9
1529. C. Domb, N.W. Dalton, Crystal statistics with long-range forces. I. The equivalent neighbour model. Proc. Phys. Soc. **89**, 859–871 (1966). 10.1088/0370-1328/89/4/311
1530. C. Zener, Interaction between the d-shells in the transition metals. Phys. Rev. **81**, 440–444 (1951). 10.1103/PhysRev.81.440
1531. H. Akai, Ferromagnetism and its stability in the diluted magnetic semiconductor (In, Mn)As. Phys. Rev. Lett. **81**, 3002–3005 (1998). 10.1103/PhysRevLett.81.3002
1532. T. Dietl, H. Ohno, F. Matsukura, J. Cibert, D. Ferrand, Zener model description of ferromagnetism in zinc-blende magnetic semiconductors. Science **287**, 1019–1022 (2000). 10.1126/science.287.5455.1019
1533. H. Munekata, H. Ohno, S. von Molnár, A. Segmüller, L.L. Chang, L. Esaki, Diluted magnetic III-V semiconductors. Phys. Rev. Lett. **63**, 1849–1852 (1989). 10.1103/PhysRevLett.63.1849
1534. H. Ohno, M. Munekata, T. Penney, S. von Molnár, L.L. Chang, Magnetotransport properties of p-type (In, Mn)As diluted magnetic III-V semiconductors. Phys. Rev. Lett. **68**, 2664–2667 (1992). 10.1103/PhysRevLett.68.2664
1535. H. Ohno, A. Shen, F. Matsukura, A. Oiwa, A. Endo, S. Katsumoto, Y. Iye, (Ga, Mn)As: A new diluted magnetic semiconductor based on GaAs. Appl. Phys. Lett. **69**, 363–365 (1996). 10.1063/1.118061
1536. Y.-J. Zhao, P. Mahadevan, A. Zunger, Comparison of predicted ferromagnetic tendencies of Mn substituting the Ga site in III-V's and in I-III-VI_2 chalcopyrite semiconductors. Appl. Phys. Lett. **84**, 3753–3755 (2004). 10.1063/1.1737466

1537. H. Ohno, D. Chiba, F. Matsukura, T. Omiya, E. Abe, T. Dietl, Y. Ohno, K. Ohtani, Electric-field control of ferromagnetism. Nature **408**, 944–946 (2000). 10.1038/35050040
1538. S.T.B. Goennenwein, Th.A. Wassner, H. Huebl, M.S. Brandt, J.B. Philipp, M. Opel, R. Gross, A. Koeder, W. Schoch, A. Waag, Hydrogen control of ferromagnetism in a dilute magnetic semiconductor. Phys. Rev. Lett. **92**, 227202:1–4 (2004). 10.1103/PhysRevLett.92.227202
1539. P. Sharma, A. Gupta, K.V. Rao, F.J. Owens, R. Sharma, R. Ahuja, J.M. Osorio Guillen, B. Johansson, G.A. Gehring, Ferromagnetism above room temperature in bulk and transparent thin films of Mn-doped ZnO. Nature Mater. **2**, 673–677 (2003). 10.1038/nmat984
1540. M. Diaconu, H. Schmidt, H. Hochmuth, M. Lorenz, G. Benndorf, D. Spemann, A. Setzer, P. Esquinazi, A. Pöppl, H. von Wenckstern, K.-W. Nielsen, R. Gross, H. Schmid, W. Mader, G. Wagner, M. Grundmann, Room-temperature ferromagnetic Mn-alloyed ZnO films obtained by pulsed laser deposition. J. Magn. Magn. Mat. **307**, 212–221 (2006). 10.1016/j.jmmm.2006.04.004
1541. E.H. Hall, On the "Rotational Coefficient" in nickel and cobalt. Philos. Mag. Series 5 **12**(74), 157–172 (1881). 10.1080/14786448108627086
1542. N. Nagaosa, J. Sinova, S. Onoda, A.H. MacDonald, N.P. Ong, Anomalous Hall effect. Rev. Mod. Phys. **82**, 1539–1592 (2010). 10.1103/RevModPhys.82.1539
1543. M.I. Miah, Pure anomalous Hall effect in nonmagnetic zinc-blende semiconductors. Opt. Quant. Electron. **40**, 1033–1042 (2008). 10.1007/s11082-009-9296-z
1544. C.-X. Liu, S.-C. Zhang, X.-L. Qi, The quantum anomalous Hall effect: Theory and experiment. Ann. Rev. Cond. Matter Phys. **7**, 301–321 (2016). 10.1146/annurev-conmatphys-031115-011417
1545. C.-Z. Chang, J. Zhang, X. Feng, J. Shen, Z. Zhang, M. Guo, K. Li, Y. Ou, P. Wei, L.-L. Wang, Z.-Q. Ji, Y. Feng, S. Ji, X. Chen, J. Jia, X. Dai, Z. Fang, S.-C. Zhang, K. He, Y. Wang, L. Lu, X.-C. Ma, Q.-K. Xue, Experimental observation of the quantum anomalous Hall effect in a magnetic topological insulator. Science **340**, 167–170 (2013). 10.1126/science.1234414
1546. Y. Deng, Y. Yu, M.Z. Shi, Z. Guo, Z. Xu, J. Wang, X.H. Chen, Y. Zhang, Quantum anomalous Hall effect in intrinsic magnetic topological insulator $MnBi_2Te_4$. Science **367**, 895–900 (2020). 10.1126/science.aax8156
1547. E.I. Rashba, Electron spin operation by electric fields: Spin dynamics and spin injection. Physica E **20**, 189–195 (2004). 10.1016/j.physe.2003.08.002
1548. M.I. D'yakonov, V.I. Perel', Spin relaxation of conduction electrons in noncentrosymetric semiconductors. Fiz. Tverd. Tela **13**, 3581–3585 (1971) [Sov. Phys. Solid State **13**, 3023–3026 (1972)]
1549. S. Datta, B. Das, Electronic analog of the electro-optic modulator. Appl. Phys. Lett. **56**, 665–667 (1990). 10.1063/1.102730
1550. A.T. Hanbicki, O.M.J. van 't Erve, R. Magno, G. Kioseoglou, C.H. Li, B.T. Jonker, Analysis of the transport process providing spin injection through an Fe/AlGaAs Schottky barrier. Appl. Phys. Lett. **82**, 4092–4094 (2003). 10.1063/1.1580631
1551. B.T. Jonker, S.C. Erwin, A. Petrou, A.G. Petukhov, Electrical spin injection and transport in semiconductor spintronic device. MRS Bull. **28**, 740–748 (2003). 10.1557/mrs2003.216
1552. N. Nishizawa, K. Nishibayashi, H. Munekata, Pure circular polarization electroluminescence at room temperature with spin-polarized light-emitting diodes. PNAS **114**, 1783–1788 (2017). 10.1073/pnas.1609839114
1553. C.L. Braun, *Organic Semiconductors, Handbook on Semiconductors*, vol. 3 (North Holland, Amsterdam, 1980), pp. 857–873
1554. *Physics of Organic Semiconductors*, 2nd edn., W. Brütting, C. Adachi, eds. (Wiley-VCH, Weinheim, 2012). 10.1002/9783527654949
1555. Th.U. Kampen, *Low Molecular Weight Organic Semiconductors* (Wiley-VCH. Weinheim (2009). 10.1002/9783527629978
1556. A. Curioni, W. Andreoni, R. Treusch, F.J. Himpsel, E. Haskal, P. Seidler, C. Heske, S. Kakar, T. van Buuren, L.J. Terminello, Atom-resolved electronic spectra for Alq_3 from theory and experiment. Appl. Phys. Lett. **72**, 1575–1577 (1998). 10.1063/1.121119
1557. D. Braun, A. Heeger, Visible light emission from semiconducting polymer diodes. Appl. Phys. Lett. **58**, 1982–1984 (1991). 10.1063/1.105039
1558. A.McL. Mathieson, J.M. Robertson, V.C. Sinclair, The crystal and molecular structure of anthracene. I. X-ray measurements. Acta Cryst. **3**, 245–250 (1950). 10.1107/S0365110X50000641
1559. J.M. Robertson, V.C. Sinclair, J. Trotter, The crystal and molecular structure of tetracene. Acta Cryst. **14**, 697–704 (1961). 10.1107/S0365110X61002151
1560. N. Karl, High purity organic molecular crystals, in *Crystals: Growth, Properties and Applications*, vol. 4, ed. by H.C. Freyhardt (Springer, Berlin, 1980), pp. 1–100. 10.1007/978-3-642-67764-9_1
1561. N. Karl, Growth and electrical properties of high purity organic molecular crystals. J. Cryst. Growth **99**, 1009–1016 (1990). 10.1016/S0022-0248(08)80072-3
1562. Ch. Kloc, P.G. Simpkins, T. Siegrist, R.A. Laudise, Physical vapor growth of centimeter-sized crystals of α-hexathiophene. J. Cryst. Growth **182**, 416–427 (1997). 10.1016/S0022-0248(97)00370-9

1563. R.A. Laudise, Ch. Kloc, P.G. Simpkins, T. Siegrist, Physical vapor growth of organic semiconductors. J. Cryst. Growth **187**, 449–454 (1998). 10.1016/S0022-0248(98)00034-7
1564. M. Mas-Torrent, M. Durkut, P. Hadley, X. Ribas, C. Rovira, High mobility of dithiophene-tetrathiafulvalene single-crystal organic field effect transistors. J. Am. Chem. Soc. **126**, 984–985 (2004). 10.1021/ja0393933
1565. M. Campione, R. Ruggerone, S. Tavazzi, M. Moret, Growth and characterisation of centimetre-sized single crystals of molecular organic materials. J. Mat. Chem. **15**, 2437–2443 (2005). 10.1039/B415912H
1566. M. Oehzelt, A. Aichholzer, R. Resel, G. Heimel, E. Venuti, R.G. Della Valle, Crystal structure of oligoacenes under high pressure. Phys. Rev. B **74**, 104103:1–7 (2006). 10.1103/PhysRevB.74.104103
1567. B. Part, A. Kahn, N. Koch, W. Gao, Electronic structure and electrical properties of interfaces between metals and π-conjugated molecular films. J. Polymer Sc. Polymer Phys. **41**, 2529–2548 (2003). 10.1002/polb.10642
1568. M. Pfeiffer, A. Beyer, T. Fritz, K. Leo, Controlled doping of phthalocyanine layers by cosublimation with acceptor molecules: A systematic Seebeck and conductivity study. Appl. Phys. Lett. **73**, 3202–3204 (1998). 10.1063/1.122718
1569. B.A. Gregg, S.-G. Chen, R.A. Cormier, Coulomb forces and doping in organic semiconductors. Chem. Mater. **16**, 4586–4599 (2004). 10.1021/cm049625c
1570. G.F. Neumark, Concentration and temperature dependence of impurity-to-band activation energies. Phys. Rev. B **5**, 408–414 (1972). 10.1103/PhysRevB.5.408
1571. B.A. Gregg, S.-G. Chen, H.M. Branz, On the superlinear increase in conductivity with dopant concentration in excitonic semiconductors. Appl. Phys. Lett. **84**, 1707–1709 (2004). 10.1063/1.1668326
1572. A.J. Heeger, S. Kivelson, J.R. Schrieffer, W.-P. Su, Solitons in conducting polymers. Rev. Mod. Phys. **60**, 781–850 (1988). 10.1103/RevModPhys.60.781
1573. P.W.M. Blom, M.C.J.M. Vissenberg, Charge transport in poly(p-phenylene vinylene) light-emitting diodes. Mater. Sci. Engin. **27**, 53–94 (2000). 10.1016/S0927-796X(00)00009-7
1574. L.B. Schein, Temperature independent drift mobility along the molecular direction of As_2Se_3. Phys. Rev. B **15**, 1024–1034 (1977). 10.1103/PhysRevB.15.1024
1575. L.B. Schein, C.B. Duke, A.R. McGhie, Observation of the band-hopping transition for electrons in naphthalene. Phys. Rev. Lett. **40**, 197–200 (1978). 10.1103/PhysRevLett.40.197
1576. L. Li, G. Meller, H. Kosina, Temperature and field-dependence of hopping conduction in organic semiconductors. Microelectr. J. **38**, 47–51 (2007). 10.1016/j.mejo.2006.09.022
1577. Y. Kawasumi, I. Akai, T. Karasawa, Photoluminescence and dynamics of excitons in Alq_3 single crystals. Int. J. Mod. Phys. B **15**, 3825–3828 (2001). 10.1142/S0217979201008767
1578. M.A. Baldo, S.R. Forrest, Transient analysis of organic electrophosphorescence: I. Transient analysis of triplet energy transfer. Phys. Rev. B **62**, 10958–10966 (2000). 10.1103/PhysRevB.62.10958
1579. W. Humbs, H. Zhang, M. Glasbeek, Femtosecond fluorescence upconversion spectroscopy of vapor-deposited tris(8-hydroxyquinoline) aluminum films. Chem. Phys. **254**, 319–327 (2000). 10.1016/S0301-0104(00)00044-6
1580. Z. Vardeny, E. Ehrenfreund, J. Shinar, F. Wudl, Photoexcitation spectroscopy of polythiophene. Phys. Rev. B **35**, 2498–2500 (1987). 10.1103/PhysRevB.35.2498
1581. J.-W. van der Horst, P.A. Bobbert, M.A.J. Michels, Electronic and optical excitations in crystalline conjugated polymers. Phys. Rev. B **66**, 035206:1–7 (2002). 10.1103/PhysRevB.66.035206
1582. A. Baldo, D.F. O'Brien, M.E. Thompson, S.R. Forrest, Excitonic singlet-triplet ratio in a semiconducting organic thin film. Phys. Rev. B **60**, 14422–14428 (1999). 10.1103/PhysRevB.60.14422
1583. A. Baldo, D.F. O'Brien, Y. You, A. Shoustikov, S. Sibley, M.E. Thompson, S.R. Forrest, Highly efficient phosphorescent emission from organic electroluminescent devices. Nature **395**, 151–154 (1998). 10.1038/25954
1584. C. Adachi, M.A. Baldo, M.E. Thompson, S.R. Forrest, Nearly 100% internal phosphorescence efficiency in an organic light emitting device. J. Appl. Phys. **90**, 5048–5051 (2001). 10.1063/1.1409582
1585. M.A. Baldo, S. Lamansky, P.E. Burrows, M.E. Thompson, S.R. Forrest, Very high-efficiency green organic light-emitting devices based on electrophosphorescence. Appl. Phys. Lett. **75**, 4–6 (1999). 10.1063/1.124258
1586. M.A. Baldo, M.E. Thompson, S.R. Forrest, High-efficiency fluorescent organic light-emitting devices using a phosphorescent sensitizer. Nature **403**, 750–753 (2000). 10.1038/35001541
1587. T. Förster, Transfer mechanisms of electron excitation. Discuss. Faraday Soc. **27**, 7–17 (1959). 10.2307/3583604
1588. R.R. Willey, *Practical Design and Production of Optical Thin Films* (CRC Press, London, 2002). 10.1201/9780203910467
1589. J.M. Bendickson, J.P. Dowling, M. Scalora, Analytic expressions for the electromagnetic mode density in finite, one-dimensional, photonic band-gap structures. Phys. Rev. E **53**, 4107–4121 (1996). 10.1103/PhysRevE.53.4107
1590. J. Gottmann, A. Husmann, T. Klotzbücher, E.W. Kreutz, Optical properties of alumina and zirconia thin films grown by pulsed laser deposition. Surface and Coatings Technol. **100–101**, 415–419 (1998). 10.1016/S0257-8972(97)00661-0
1591. J. Sellmann, Ch. Sturm, R. Schmidt-Grund, Ch. Czekalla, J. Lenzner, H. Hochmuth, B. Rheinländer, M. Lorenz, M. Grundmann, Structural and optical properties of ZrO_2 and Al_2O_3 thin films and Bragg reflectors grown by pulsed laser deposition. Phys. Status Solidi C **5**, 1240–1243 (2008). 10.1002/pssc.200777875

1592. Bernd Rauschenbach, private communication (2006)
1593. Norbert Kaiser, Fraunhofer-Institute for Applied Optics, Jena
1594. C.M. Soukoulis, ed., Photonic crystals and light localization in the 21st century, in *NATO Science Series C: Mathematical and Physical Sciences*, vol. 563 (Kluwer Academic Publishers, Dordrecht, 1996). 10.1007/978-94-010-0738-2
1595. J.D. Joannopoulos, R.D. Meade, J.N. Winn, *Photonic Crystals, Molding the Flow of Light* (Princeton University Press, Princeton, NJ, 1995)
1596. K. Busch, S. Lölkes, R.B. Wehrspohn, H. Föll, eds., *Photonic Crystals: Advances in Design, Fabrication, and Characterization* (Wiley-VCH, Berlin, 1994)
1597. E.-X. Ping, Transmission of electromagnetic waves in planar, cylindrical, and spherical dielectric layer systems and their applications. J. Appl. Phys. **76**, 7188–7194 (1994). 10.1063/1.357999
1598. K.M. Ho, C.T. Chan, C.M. Soukoulis, Existence of a photonic gap in periodic dielectric structures. Phys. Rev. Lett. **65**, 3152–3155 (1990). 10.1103/PhysRevLett.65.3152
1599. O. Toader, S. John, Proposed square spiral microfabrication architecture for large three-dimensional photonic band gap crystals. Science **292**, 1133–1135 (2001). 10.1126/science.1059479
1600. S.R. Kennedy, M.J. Brett, O. Toader, S. John, Fabrication of tetragonal square spiral photonic crystals. Nano Lett. **2**, 59–62 (2002). 10.1021/nl015635q
1601. K. Busch, S. John, Photonic band gap formation in certain self-organizing systems. Phys. Rev. E **58**, 3896–3908 (1998). 10.1103/PhysRevE.58.3896
1602. E. Yablonovitch, T.J. Gmitter, K.M. Leung, Photonic band structure: The face-centered-cubic case employing nonspherical atoms. Phys. Rev. Lett. **67**, 2295–2298 (1991). 10.1103/PhysRevLett.67.2295
1603. K.M. Ho, C.T. Chan, C.M. Soukoulis, R. Biswas, M. Sigalas, Photonic band gaps in three dimensions: New layer-by-layer periodic structures. Solid State Commun. **89**, 413–416 (1994). 10.1016/0038-1098(94)90202-X
1604. A. Chutinan, S. Noda, Spiral three-dimensional photonic-band-gap structure. Phys. Rev. B **57**, R2006–R2008 (1998). 10.1103/PhysRevB.57.R2006
1605. S. Fan, P.R. Villeneuve, R.D. Meade, J.D. Joannopoulos, Design of three-dimensional photonic crystals at submicron lengthscales. Appl. Phys. Lett. **65**, 1466–1468 (1994). 10.1063/1.112017
1606. H.S. Sözüer, J.W. Haus, Photonic bands: Simple-cubic lattice. J. Opt. Soc. Am. B **10**, 296–302 (1993). 10.1364/JOSAB.10.000296
1607. H.S. Sözüer, J.W. Haus, R. Inguva, Photonic bands: Convergence problems with the plane-wave method. Phys. Rev. B **45**, 13962–13972 (1992). 10.1103/PhysRevB.45.13962
1608. S. John, K. Busch, Photonic bandgap formation and tunability in certain self-organizing systems. IEEE J. Lightw. Techn. **17**, 1931–1943 (1999). 10.1109/50.802976
1609. F. García-Santamaria, C. López, F. Meseguer, F. López-Tejeira, J. Sánchez-Dehesa, H.T. Miyazaki, Opal-like photonic crystal with diamond lattice. Appl. Phys. Lett. **79**, 2309–2311 (2001). 10.1063/1.1406560
1610. A. Blanco, E. Chomski, S. Grabtchak, M. Ibisate, S. John, S.W. Leonard, C. Lopez, F. Meseguer, H. Miguez, J.P. Mondia, G.A. Ozin, O. Toader, H.M. van Driel, Large-scale synthesis of a silicon photonic crystal with a complete three-dimensional bandgap near 1.5 micrometres. Nature **405**, 437–440 (2000). 10.1038/35013024
1611. A.F. Koenderink, A. Lagendijk, W.L. Vos, Optical extinction due to intrinsic structural variations of photonic crystals. Phys. Rev. B **72**, 153102:1–4 (2005). 10.1103/PhysRevB.72.153102
1612. M. Lončar, D. Nedeljković, T. Doll, J. Vučović, A. Scherer, T.P. Pearsall, Waveguiding in planar photonic crystals. Appl. Phys. Lett. **77**, 1937–1939 (2000) 10.1063/1.1311604
1613. A.B. Khanikaev, G. Shvets, Two-dimensional topological photonics. Nature Photon. **11**, 763–773 (2017). 10.1038/s41566-017-0048-5
1614. S. Raghu, F.D.M. Haldane, Analogs of quantum-Hall-effect edge states in photonic crystals. Phys. Rev. A **78**, 033834:1–21 (2008). 10.1103/PhysRevA.78.033834
1615. B. Bahari, A. Ndao, F. Vallini, A. El Amili, Y. Fainman, B. Kanté, Nonreciprocal lasing in topological cavities of arbitrary geometries. Science **358**, 636–640 (2017). 10.1126/science.aao4551
1616. F.D.M. Haldane, Model for a quantum Hall effect without Landau levels: Condensed-matter realization of the "Parity Anomaly". Phys. Rev. Lett. **61**, 2015–2018 (1988). 10.1103/PhysRevLett.61.2015
1617. G. Harari, M.A. Bandres, Y. Lumer, M.C. Rechtsman, Y.D. Chong, M. Khajavikhan, D.N. Christodoulides, M. Segev, Topological insulator laser: Theory. Science **359**, 1230 and eaar4003:1–6 (2018). 10.1126/science.aar4003
1618. Y. Yang, Z.H. Hang, Topological whispering gallery modes in twodimensional photonic crystal cavities. Opt. Express **26**, 21235–21241 (2018). 10.1364/OE.26.021235
1619. M.A. Bandres, S. Wittek, G. Harari, M. Parto, J. Ren, M. Segev, D.N. Christodoulides, M. Khajavikhan, Topological insulator laser: Experiments. Science **359**, 1231 and eaar4005:1–5 (2018). 10.1126/science.aar4005
1620. Z.-K. Shao, H.-Z. Chen, S. Wang, X.-R. Mao, Z.-Q. Yang, S.-L. Wang, X.-X. Wang, X. Hu, R.-M. Ma, A high-performance topological bulk laser based on band-inversion-induced reflection. Nature Nanotechn. **15**, 67–72 (2020). 10.1038/s41565-019-0584-x
1621. Y. Zhu, Q. Wu, S. Morin, T.W. Mossberg, Observation of a two-photon gain feature in the strong-probe absorption spectrum of driven two-level atoms. Phys. Rev. Lett. **65**, 1200–1203 (1990). 10.1103/PhysRevLett.65.1200

1622. C. Weisbuch, M. Nishioka, A. Ishikawa, Y. Arakawa, Observation of the coupled exciton-photon mode splitting in a semiconductor quantum microcavity. Phys. Rev. Lett. **69**, 3314–3317 (1992). 10.1103/PhysRevLett.69.3314
1623. V. Savona, Z. Hradil, A. Quattropani, P. Schwendimann, Quantum theory of quantum-well polaritons in semiconductor microcavities. Phys. Rev. B **49**, 8774–8779 (1994). 10.1103/PhysRevB.49.8774
1624. G. Khitrova, H.M. Gibbs, F. Jahnke, M. Kira, S.W. Koch, Nonlinear optics of normal-mode-coupling semiconductor microcavities. Rev. Mod. Phys. **71**, 1591–1639 (1999). 10.1103/RevModPhys.71.1591
1625. M.S. Skolnick, T.A. Fisher, D.M. Whittaker, Strong coupling phenomena in quantum microcavity structures. Semicond. Sci. Technol. **13**, 645–669 (1998). 10.1088/0268-1242/13/7/003
1626. P.J. Klar, G. Rowland, P.J.S. Thomas, A. Onischenko, T.E. Sale, T.J.C. Hosea, R. Grey, Photomodulated reflectance study of $In_xGa_{1-x}As$/GaAs/AlAs microcavity vertical-cavity surface emitting laser structures in the weak-coupling regime: The cavity/ground-state-exciton resonance. Phys. Rev. B **59**, 2894–2901 (1999). 10.1103/PhysRevB.59.2894
1627. J.J. Baumberg, P.G. Savvidis, R.M. Stevenson, A.I. Tartakovskii, M.S. Skolnick, D.M. Whittaker, J.S. Roberts, Parametric oscillation in a vertical microcavity: A polariton condensate or micro-optical parametric oscillation. Phys. Rev. B **62**, R16247–R16250 (2000). 10.1103/PhysRevB.62.R16247
1628. A. Kavokin, G. Malpuech, B. Gil, Semiconductor microcavities: Towards polariton lasers. MRS Internet J. Nitride Semicond. Res. **8**, 3:1–25 (2003). 10.1557/S1092578300000466
1629. Le Si Dang, D. Heger, R. André, F. Bœuf, R. Romestain, Stimulation of polariton photoluminescence in semiconductor microcavity. Phys. Rev. Lett. **81**, 3920–3923 (1998). 10.1103/PhysRevLett.81.3920
1630. A. Pawlis, D.J. As, D. Schikora, J. Schörmann, K. Lischka, Photonic devices based on wide gap semiconductors for room temperature polariton emission. Phys. Status Solidi C **1**, S202–S209 (2004). 10.1002/pssc.200405141
1631. T. Tawara, H. Gotoh, T. Akasaka, N. Kobayashi, T. Saitoh, Cavity polaritons in InGaN microcavities at room temperature. Phys. Rev. Lett. **92**, 256402:1–4 (2004). 10.1103/PhysRevLett.92.256402
1632. N. Antoine-Vincent, F. Natali, D. Byrne, P. Disseix, A. Vasson, J. Leymarie, F. Semond, J. Massies, Potentialities of GaN-based microcavities in strong coupling regime at room temperature. Superlatt. Microstruct. **36**, 599–606 (2004). 10.1016/j.spmi.2004.09.017
1633. E. Feltin, G. Christmann, R. Butté, J.-F. Carlin, M. Mosca, N. Grandjean, Room temperature polariton luminescence from a GaN/AlGaN quantum well microcavity. Appl. Phys. Lett. **89**, 071107:1–3 (2006) 10.1063/1.2335404
1634. F. Semond, I. R. Sellers, F. Natali, D. Byrne, M. Leroux, J. Massies, N. Ollier, J. Leymarie, P. Disseix, A. Vasson, trong light-matter coupling at room temperature in simple geometry GaN microcavities grown on silicon. Appl. Phys. Lett. **87**, 021102:1–3 (2005). 10.1063/1.1994954
1635. R. Schmidt-Grund, B. Rheinländer, C. Czekalla, G. Benndorf, H. Hochmuth, M. Lorenz, M. Grundmann, Exciton-polariton formation at room temperature in a planar ZnO resonator structure. Appl. Phys. A **93**, 331–337 (2008). 10.1007/s00340-008-3160-x
1636. P.G. Savvidis, J.J. Baumberg, R.M. Stevenson, M.S. Skolnick, D.M. Whittaker, J.S. Roberts, Angle-Resonant stimulated polariton amplifier. Phys. Rev. Lett. **84**, 1547–1550 (2000). 10.1103/PhysRevLett.84.1547
1637. Y. Yamamoto, T. Tassone, H. Cao, *Semiconductor Cavity Quantum Electrodynamics* (Springer, Berlin, 2000). 10.1007/3-540-45515-9
1638. D. Sanvitto, V. Timofeev, *Exciton Polaritons in Microcavities* (Springer, Berlin, 2012). 10.1007/978-3-642-24186-4
1639. A. Poddubny, I. Iorsh, P. Belov, Y. Kivshar, Hyperbolic metamaterials. Nat. Photon. **7**, 958–967 (2013). 10.1038/nphoton.2013.243
1640. P. Huo, S. Zhang, Y. Liang, Y. Lu, T. Xu, Hyperbolic metamaterials and metasurfaces: Fundamentals and applications. Adv. Opt. Mater. **7**, 1801616:1–25 (2019). 10.1002/adom.201801616
1641. A. Poddubny, P. Belov, Y. Kivshar, Spontaneous radiation of a finite-size dipole emitter in hyperbolic media. Phys. Rev. A **84**, 023807:1–6 (2011). 10.1103/PhysRevA.84.023807
1642. G.V. Naik, B. Saha, J. Liu, S.M. Saber, E.A. Stach, J.M.K. Irudayaraj, T.D. Sands, V.M. Shalaev, A. Boltasseva, Epitaxial superlattices with titanium nitride as a plasmonic component for optical hyperbolic metamaterials. PNAS **111**, 7546–7551 (2014). 10.1073/pnas.1319446111
1643. S.S. Kruk, Z.J. Wong, E. Pshenay-Severin, K. O'Brien, D.N. Neshev, Y.S. Kivshar, X. Zhang, Magnetic hyperbolic optical metamaterials. Nat. Commun. **7**, 11329;1–7 (2016). 10.1038/ncomms11329
1644. S.L. McCall, A.F.J. Levi, R.E. Slusher, S.J. Pearton, R.A. Logan, Whispering-gallery mode microdisk lasers. Appl. Phys. Lett. **60**, 289–291 (1992). 10.1063/1.106688
1645. R.P. Wang, M.-M. Dumitrescu, Theory of optical modes in semiconductor microdisk lasers. J. Appl. Phys. **81**, 3391–3397 (1997). 10.1063/1.365034
1646. A.F.J. Levi, R.E. Slusher, S.L. McCall, J.L. Glass, S.J. Pearton, R.A. Logan, Directional light coupling from microdisk lasers. Appl. Phys. Lett. **62**, 561–563 (1993). 10.1063/1.108911
1647. S.-K. Kim, S.-H. Kim, G.-H. Kim, H.-G. Park, D.-J. Shin, Y.-H. Lee, Highly directional emission from few-micron-size elliptical microdisks. Appl. Phys. Lett. **84**, 861–863 (2004). 10.1063/1.1646459

1648. E. Peter, P. Senellart, D. Martrou, A. Lemaître, J. Hours, J. M. Gérard, J. Bloch, Exciton-photon strong-coupling regime for a single quantum dot embedded in a microcavity. Phys. Rev. Lett. **95**, 067401:1–4 (2005). 10.1103/PhysRevLett.95.067401
1649. E.M. Purcell, Spontaneous emission probabilities at radio frequencies. Phys. Rev. **69**, 681 (1946). 10.1103/PhysRev.69.674.2
1650. J.M. Gérard, B. Sermage, B. Gayral, B. Legrand, E. Costard, V. Thierry-Mieg, Enhanced spontaneous emission by quantum boxes in a monolithic optical microcavity. Phys. Rev. Lett. **81**, 1110–1113 (1998). 10.1103/PhysRevLett.81.1110
1651. A. Kiraz, P. Michler, C. Becher, B. Gayral, A. Imamoğlu, Lidong Zhang, E. Hu, W.V. Schoenfeld, P.M. Petroff, Cavity-quantum electrodynamics using a single InAs quantum dot in a microdisk structure. Appl. Phys. Lett. **78**, 3932–3934 (2001). 10.1063/1.1379987
1652. J.U. Nöckel, A.D. Stone, Ray and wave chaos in asymmetric resonant optical cavities. Nature **385**, 45–47 (1997). 10.1038/385045a0
1653. C. Gmachl, F. Capasso, E.E. Narimanov, J.U. Nöckel, A.D. Stone, J. Faist, D.L. Sivco, A.Y. Cho, High-power directional emission from microlasers with chaotic resonators. Science **280**, 1556–1564 (1998). 10.1126/science.280.5369.1556
1654. G.D. Chern, H.E. Tureci, A. Douglas Stone, R.K. Chang, M. Kneissl, N.M. Johnson, Unidirectional lasing from InGaN multiple-quantum-well spiral-shaped micropillars. Appl. Phys. Lett. **83**, 1710–1712 (2003). 10.1063/1.1605792
1655. S.-Y. Lee, S. Rim, J.-W. Ryu, T.-Y. Kwon, M. Choi, C.-M. Kim, Quasiscarred resonances in a spiral-shaped microcavity. Phys. Rev. Lett. **93**, 164102:1–4 (2004). 10.1103/PhysRevLett.93.164102
1656. M. Kneissl, M. Teepe, N. Miyashita, N.M. Johnson, G.D. Chern, R.K. Chang, Current-injection spiral-shaped microcavity disk laser diodes with unidirectional emission. Appl. Phys. Lett. **84**, 2485–2498 (2004). 10.1063/1.1691494
1657. T. Nobis, E.M. Kaidashev, A. Rahm, M. Lorenz, M. Grundmann, Whispering gallery modes in nanosized dielectric resonators with hexagonal cross section. Phys. Rev. Lett. **93**, 103903:1–4 (2004). 10.1103/PhysRevLett.93.103903
1658. F. Leiter, H. Zhou, F. Henecker, A. Hofstaetter, D.M. Hofmann, B.K. Meyer, Magnetic resonance experiments on the green emission in undoped ZnO crystals. Physica B **308–310**, 908–911 (2001). 10.1016/S0921-4526(01)00837-7
1659. J. Wiersig, Hexagonal dielectric resonators and microcrystal lasers. Phys. Rev. A **67**, 023807:1–12 (2003). 10.1103/PhysRevA.67.023807
1660. C. Czekalla, C. Sturm, R. Schmidt-Grund, B. Cao, M. Lorenz, M. Grundmann, Whispering gallery mode lasing in zinc oxide microwires. Appl. Phys. Lett. **92**, 241102:1–3 (2008). 10.1063/1.2946660
1661. C.P. Dietrich, M. Lange, T. Böntgen, M. Grundmann, The corner effect in hexagonal whispering gallery microresonators. Appl. Phys. Lett. **101**, 141116:1–5 (2012). 10.1063/1.4757572
1662. F. Streintz, Ueber die elektrische Leitfähigkeit vom gepressten Pulvern. Ann. Physik **314**, 854–885 (1902). 10.1002/andp.19023141207
1663. H.L. Hartnagel, A.L. Dawar, A.K. Jain, C. Jagadish, *Semiconducting Transparent Thin Films* (Institute of Physics Publishing, Philadelphia, 1995)
1664. MRS Bull. **25**(8), issue on *Transparent Conducting Oxides*. 10.1557/mrs2000.256
1665. T. Minami, Transparent conducting oxide semiconductors for transparent electrodes. Semicond. Sci. Technol. **20**, S35–S44 (2005). 10.1088/0268-1242/20/4/004
1666. R.G. Gordon, Criteria for choosing transparent conductors. MRS Bull. **25**, 52–57 (2000). 10.1557/mrs2000.151
1667. H. Kawazoe, M. Yasukawa, H. Hyodo, M. Kurita, H. Yanagi, H. Hosono, P-type electrical conduction in transparent thin films of $CuAlO_2$. Nature **389**, 939–942 (1997). 10.1038/40087
1668. M. Dekkers, G. Rijnders, D.H.A. Blank, $ZnIr_2O_4$, a p-type transparent oxide semiconductor in the class of spinel zinc-d^6-transition metal oxide. Appl. Phys. Lett. **90**, 021903:1–3 (2007). 10.1063/1.2431548
1669. F.-L. Schein, H. von Wenckstern, H. Frenzel, M. Grundmann, ZnO-based n-channel junction field-effect transistor with room-temperature-fabricated amorphous p-Type $ZnCo_2O_4$ gate. IEEE Electr. Dev. Lett. **33**, 676–678 (2012). 10.1109/LED.2012.2187633
1670. M. Marezio, Refinement of the crystal structure of In_2O_3 at two wavelengths. Acta Cryst. **20**, 723–728 (1966). 10.1107/S0365110X66001749
1671. S.H. Brewer, S. Franzen, Calculation of the electronic and optical properties of indium tin oxide by density functional theory. Chem. Phys. **300**, 285–293 (2004). 10.1016/j.chemphys.2003.11.039
1672. O.N. Mryasov, A.J. Freeman, Electronic band structure of indium tin oxide and criteria for transparent conducting behavior. Phys. Rev. B **64**, 233111:1–3 (2001). 10.1103/PhysRevB.64.233111
1673. H. Agura, A. Suzuki, T. Matsushita, T. Aoki, M. Okuda, Low resistivity transparent conducting Al-doped ZnO films prepared by pulsed laser deposition. Thin Solid Films **445**, 263–267 (2003). 10.1016/S0040-6090(03)01158-1
1674. K. Ellmer, Resistivity of polycrystalline zinc oxide films: Current status and physical limit. J. Phys. D: Appl. Phys. **34**, 3097–3108 (2001). 10.1088/0022-3727/34/21/301

1675. T. Minami, S. Suzuki, T. Miyata, Electrical conduction mechanism of highly transparent and conductive ZnO thin films. Proc. Mater. Res. Soc. **666**, F1.3.1 (2001). 10.1557/PROC-666-F1.3
1676. D.S. Ginley, C. Bright, Transparent conducting oxides. MRS Bull. **8**, 15–18 (2000). 10.1557/mrs2000.256
1677. J.R. Bellingham, W.A. Phillips, C.J. Adkins, Intrinsic performance limits in transparent conducting oxides. J. Mat. Sci. Lett. **11**, 263–265 (1992). 10.1007/BF00729407
1678. J.A. Fleming, *The Thermionic Valve and Its Developments in Radiotelegraphy and Telephony* (The Wireless Press, London, 1919)
1679. G.S. Meikle, The hot cathode argon gas filled rectifier. General Electric Rev. **XIX**, 297–304 (1916), see also. J. Franklin Inst. **181**, 704–705 (1916). 10.1016/S0016-0032(16)90633-1
1680. H.C. Torrey, C.A. Whitmer, *Crystal Rectifiers*, MIT Radiation Lab. Series, Vol. 15 (McGraw-Hill, New York, 1948)
1681. H.K. Henisch, Rectifying semiconductor contacts. J. Electrochem. Soc. **103**, 637–643 (1956). 10.1149/1.2430178
1682. H.K. Henisch, *Rectifying Semiconductor Contacts* (Clarendon Press, Oxford, 1957)
1683. J.R. Macdonald, Accurate solution of an idealized one-carrier metal-semiconductor junction problem. Solid State Electron. **5**, 11–37 (1962). 10.1016/0038-1101(62)90013-8
1684. F.A. Padovani, The voltage-current characteristic of metal-semiconductor contacts. Semicond. Semimet. **7A**, 75–146 (1971). 10.1016/S0080-8784(08)63007-0
1685. E.H. Rhoderick, R.H. Williams, *Metal-Semiconductor Contacts*, 2nd edn. (Oxford University Press, Oxford, 1988)
1686. R.T. Tung, Recent advances in Schottky barrier concepts. Mater. Sci. Engin. R **35**, 1–138 (2001). 10.1016/S0927-796X(01)00037-7
1687. L. Magaud, F. Cryot-Lackmann, Schottky barriers. Digital Encycl. Appl. Phys. 573–591 (2003). 10.1002/3527600434.eap406
1688. G.N. Derry, M.E. Kern, E.H. Worth, Recommended values of clean metal surface work functions. J. Vac. Sci. Technol. A **33**, 060801:1–9 (2015). 10.1116/1.4934685
1689. K.W. Boer, *Introduction to Space Charge Effects in Semiconductors* (Springer, Heidelberg. 2010). 10.1007/978-3-642-02236-4
1690. A.M. Cowley, S.M. Sze, Surface states and barrier height of metal-semiconductor systems. J. Appl. Phys. **36**, 3212–3220 (1965). 10.1063/1.1702952
1691. A. Dimoulas, P. Tsipas, A. Sotiropoulos, E.K. Evangelou, Fermi-level pinning and charge neutrality level in germanium. Appl. Phys. Lett. **89**, 252110:1–3 (2006). 10.1063/1.2410241
1692. C.A. Mead, W.G. Spitzer, Fermi level position at metal-semiconductor interfaces. Phys. Rev. **134**, A713–A716 (1964). 10.1103/PhysRev.134.A713
1693. S. Kurtin, T.C. McGill, C.A. Mead, Fundamental transition in the electronic nature of solids. Phys. Rev. Lett. **22**, 1433–1436 (1969). 10.1103/PhysRevLett.22.1433
1694. C.A. Mead, Surface barriers on ZnSe and ZnO. Phys. Lett. **18**, 218 (1965). 10.1016/0031-9163(65)90295-7
1695. J. Bardeen, Surface states and rectification at a metal-semiconductor contact. Phys. Rev. **71**, 717–727 (1947). 10.1103/PhysRev.71.717
1696. W. Mönch, 125 years of metal-semiconductor contacts: Where do we stand? Adv. Solid State Phys. (Festkörperprobleme) **39**, 13–24 (1999). 10.1007/BFb0107461
1697. M. Schmidt, R. Pickenhain, M. Grundmann, Exact solutions for the capacitance of space charge regions at semiconductor interfaces. Solid State Electron. **51**, 1002–1004 (2007). 10.1016/j.sse.2007.04.004
1698. W. Schottky, Über den Einfluß von Strukturwirkungen, besonders der Thomsonschen Bildkraft, auf die Elektronenemission der Metalle. Phys. Zeitschrift **15**, 872–878 (1914)
1699. E.D. Courant, Image force and tunnel effect in crystal rectifiers. Phys. Rev. **69**, 684 (1946). 10.1103/PhysRev.69.674.2
1700. W.E. Meyerhof, Contact potential difference in silicon crystal rectifiers. Phys. Rev. **71**, 727–735 (1947). 10.1103/PhysRev.71.727
1701. S.M. Sze, C.R. Crowell, D. Kahng, Photoelectric determination of the image force dielectric constant for hot electrons in schottky barriers. J. Appl. Phys. **35**, 2534–2536 (1964). 10.1063/1.1702894
1702. A.M. Goodman, Metal-semiconductor barrier height measurement by the differential capacitance method—Degenerate one-carrier system. J. Appl. Phys. **34**, 329–338 (1963). 10.1063/1.1713221
1703. C. van Opdorp, Evaluation of doping profiles from capacitance measurements. Solid State Electron. **11**, 397–406 (1968). 10.1016/0038-1101(68)90020-8
1704. S. Dueñas, M. Jaraiz, J. Vicente, E. Rubio, L. Bailón, J. Barbolla, Optical admittance spectroscopy: A new method for deep level characterization. J. Appl. Phys. **61**, 2541–2545 (1987). 10.1063/1.337930
1705. D.L. Losee, Admittance spectroscopy of impurity levels in Schottky barriers. J. Appl. Phys. **46**, 2204–2214 (1975). 10.1063/1.321865
1706. M.P. Verkhovodov, H.P. Peka, D.A. Pulemyotov, Capacitance behaviour of junctions with frozen dopant levels. Semicond. Sci. Technol. **8**, 1842–1847 (1993). 10.1088/0268-1242/8/10/009

1707. F.D. Auret, J.M. Nel, M. Hayes, L. Wu, W. Wesch, E. Wendler, Electrical characterization of growth-induced defects in bulk-grown ZnO. Superlatt. Microstruct. **39**, 17–23 (2006). 10.1016/j.spmi.2005.08.021
1708. M. Schmidt, M. Ellguth, C. Czekalla, H. von Wenckstern, R. Pickenhain, M. Grundmann, G. Brauer, W. Skorupa, M. Helm, Q. Gu, Ch.Ch. Ling, Defects in zinc-implanted ZnO thin films. J. Vac. Sci. Technol. B **27**, 1597–1600 (2009). 10.1116/1.3086659
1709. C. Wagner, Zur Theorie der Gleichrichterwirkung. Phys. Zeitschrift **32**, 641–645 (1931)
1710. W. Schottky, E. Spenke, Zur quantitativen Durchführung der Raumladungs- und Randschichttheorie der Kristallgleichrichter. Wiss. Veröff. Siemens Werke **18**, 225–291 (1939)
1711. P.T. Landsberg, The theory of direct-current characteristics of rectifiers. Proc. Roy. Soc. London A **206**, 463–477 (1951). 10.1098/rspa.1951.0082
1712. P.T. Landsberg, Contributions to the theory of heterogeneous barrier layer rectifiers. Proc. Roy. Soc. London A **206**, 477–488 (1951). 10.1098/rspa.1951.0083
1713. M.W. Allen, S.M. Durbin, X. Weng, J.M. Redwing, K. Sarpatwari, S.E. Mohney, H. von Wenckstern, M. Grundmann, Temperature-dependent properties of nearly ideal ZnO Schottky diodes. IEEE Trans. Electron Devices **56**, 2160–2164 (2009). 10.1109/TED.2009.2026393
1714. L.F. Wagner, R.W. Young, A. Sugerman, A note on the correlation between the Schottky diode barrier height and the ideality factor as determined from I-V measurements. IEEE Electr. Dev. Lett. **4**, 320–322 (1983). 10.1109/EDL.1983.25748
1715. H.J. Yearian, D.C. characteristics of Ge and Si crystal rectifiers. Phys. Rev. **69**, 682 (1946). 10.1103/PhysRev.69.674.2
1716. R.G. Sachs, Theory of crystal rectifiers. Phys. Rev. **69**, 682 (1946). 10.1103/PhysRev.69.674.2
1717. V.A. Johnson, R.N. Smith, H.J. Yearian, Semi-quantitative explanation of D.C. characteristics of crystal rectifiers. Phys. Rev. **69**, 682–683 (1946). 10.1103/PhysRev.69.674.2
1718. H.J. Yearian, D.C. characteristics of silicon and germanium point contact crystal rectifiers. Part I. Experimental. J. Appl. Phys. **21**, 214–221 (1950). 10.1063/1.1699637
1719. V.A. Johnson, R.N. Smith, H.J. Yearian, D.C. characteristics of silicon and germanium point contact crystal rectifiers. Part II. The multicontact theory. J. Appl. Phys. **21**, 283–289 (1950). 10.1063/1.1699654
1720. J.H. Werner, H.H. Güttler, Barrier inhomogeneities at Schottky contacts. J. Appl. Phys. **69**, 1522–1533 (1991). 10.1063/1.347243
1721. V.B. Bondarenko, YuA Kudinov, S.G. Ershov, V.V. Korablev, Natural nonuniformities in the height of a Schottky barrier. Semicond. **32**, 495–496 (1998). 10.1134/1.1187426
1722. D. Defives, O. Noblanc, C. Dua, C. Brylinski, M. Barthula, V. Aubry- Fortuna, F. Meyer, Barrier inhomogeneities and electrical characteristics of Ti/4H-SiC Schottky rectifiers. IEEE Trans. Electron Devices **46**, 449–455 (1999). 10.1109/16.748861
1723. S. Müller, H. von Wenckstern, O. Breitenstein, J. Lenzner, M. Grundmann, Microscopic identification of hot spots in multibarrier Schottky contacts on pulsed laser deposition grown zinc oxide thin films. IEEE Trans. Electron Devices **59**, 536–541 (2012). 10.1109/TED.2011.2177984
1724. H. von Wenckstern, G. Biehne, R. Abdel Rahman, H. Hochmuth, M. Lorenz, M. Grundmann, Mean barrier height of Pd Schottky contacts on ZnO thin films. Appl. Phys. Lett. **88**, 092102:1–3 (2006). 10.1063/1.2180445
1725. J.H. Werner, Schottky barrier and pn-junction I/V plots - Small signal evaluation. Appl. Phys. A **47**, 291–200 (1988). 10.1007/BF00615935
1726. F.A. Padovani, G.G. Sumner, Experimental study of gold-gallium arsenide Schottky barriers. J. Appl. Phys. **36**, 3744–3747 (1965). 10.1063/1.1713940
1727. F.A. Padovani, R. Stratton, Field and thermionic-field emission in Schottky barriers. Solid State Electron. **9**, 695–707 (1966). 10.1016/0038-1101(66)90097-9
1728. W. Mönch, Barrier heights of real Schottky contacts explained by metal-induced gap states and lateral inhomogeneities. J. Vac. Sci. Technol. B **17**, 1867–1876 (1999). 10.1116/1.590839
1729. C.R. Crowell, S.M. Sze, Current transport in metal-semiconductor barriers. Solid State Electron. **9**, 1035–1048 (1966). 10.1016/0038-1101(66)90127-4
1730. C.R. Crowell, M. Beguwala, Recombination velocity effects on current diffusion and imref in Schottky barriers. Solid State Electron. **14**, 1149–1157 (1971). 10.1016/0038-1101(71)90027-X
1731. A. Lajn, H. von Wenckstern, M. Grundmann, G. Wagner, P. Barquinha, E. Fortunato, R. Martins, Comparative study of transparent rectifying contacts on semiconducting oxide single crystals and amorphous thin films. J. Appl. Phys. **113**, 044511:1–13 (2013). 10.1063/1.4789000
1732. J.M. Andrews, M.P. Lepselter, Reverse current-voltage characteristics of metal-silicide Schottky diodes. Solid State Electron. **13**, 1011–1023 (1970). 10.1016/0038-1101(70)90098-5
1733. J.H.B. Deane, R.G. Forbes, The formal derivation of an exact series expansion for the principal Schottky-Nordheim barrier function v, using the Gauss hypergeometric differential equation. J. Phys. A: Math. Theor. **41**, 395301:1–9 (2008). 10.1088/1751-8113/41/39/395301
1734. R. Holm, *Electrical Contacts. Theory and Applications*, 4th edn. (Springer, Berlin, 1981) 10.1007/978-3-662-06688-1

1735. A.Y.C. Yu, Electron tunneling and contact resistance of metal-silicon contact barriers. Solid State Electron. **13**, 239–247 (1970). 10.1016/0038-1101(70)90056-0
1736. C.Y. Chang, Y.K. Fang, S.M. Sze, Specific contact resistance of metal-semiconductor barriers. Solid State Electron. **14**, 541–550 (1971). 10.1016/0038-1101(71)90129-8
1737. T. Sanada, O. Wada, Ohmic contacts to p-GaAs with Au/Zn/Au structure. Jpn. J. Appl. Phys. **19**, L491–L494 (1980). 10.1143/JJAP.19.L491
1738. N. Braslau, J.B. Gunn, J.L. Staples, Metal-semiconductor contacts for GaAs bulk effect devices. Solid State Electron. **10**, 381–383 (1967). 10.1016/0038-1101(67)90037-8
1739. C.L. Chen, L.J. Mahoney, M.C. Finn, R.C. Brooks, A. Chu, J.G. Mavroides, Low resistance Pd/Ge/Au and Ge/Pd/Au ohmic contacts to n-type GaAs. Appl. Phys. Lett. **48**, 535–537 (1986). 10.1063/1.96498
1740. V.L. Rideout, A review of the theory and technology for ohmic contacts to group III-V compound semiconductors. Solid State Electron. **18**, 541–550 (1975). 10.1016/0038-1101(75)90031-3
1741. B.C. Sharma, Ohmic contacts to III-V compound semiconductors. Semicond. Semimet. **15**, 1–38 (1981). 10.1016/S0080-8784(08)60284-7
1742. G.Y. Robinson, Metallurgical and electrical properties of alloyed Ni/Au-Ge Films on n-type GaAs. Solid State Electron. **18**, 331–342 (1975). 10.1016/0038-1101(75)90088-X
1743. N.F. Mott, R.W. Gurney, *Electronic Processes in Ionic Crystals* (Clarendon Press, Oxford, 1940), pp. 168–173
1744. P. Zhang, Á. Valfells, L.K. Ang, J.W. Luginsland, Y.Y. Lau, 100 years of the physics of diodes. Appl. Phys. Rev. **4**, 011304:1–29 (2017). 10.1063/1.4978231
1745. C.D. Child, Discharge from hot CaO. Phys. Rev. (Series I) **32**, 492–511 (1911). 10.1103/PhysRevSeriesI.32.492
1746. I. Langmuir, The effect of space charge and residual gases on thermionic currents in high vacuum. Phys. Rev. **2**, 450–486 (1913). 10.1103/PhysRev.2.450
1747. G. González, Quantum theory of space charge limited current in solids. J. Appl. Phys. **117**, 084306:1–3 (2015). 10.1063/1.4913512
1748. R.W. Smith, A. Rose, Space-charge-limited currents in single crystals of cadmium sulfide. Phys. Rev. **97**, 1531–1537 (1955). 10.1103/PhysRev.97.1531
1749. G.T. Wright, Space-charge limited currents in insulating materials. Nature **182**, 1296–1297 (1958). 10.1038/1821296a0
1750. U. Büget, G.T. Wright, Space-charge-limited current in silicon. Solid State Electron. **10**, 199–207 (1967). 10.1016/0038-1101(67)90074-3
1751. J.W. Orton, M.J. Powell, The relationship between space-charge-limited current and density of states in amorphous silicon. Philos. Mag. **50**, 11–21 (1984). 10.1080/13642818408238824
1752. C.M. Heller, I.H. Campbell, D.L. Smith, N.N. Barashkov, J.P. Ferraris, Chemical potential pinning due to equilibrium electron transfer at metal/C_{60}-doped polymer interfaces. J. Appl. Phys. **81**, 3227–3231 (1997). 10.1063/1.364154
1753. I.H. Campbell, T.W. Hagler, D.L. Smith, J.P. Ferraris, Direct measurement of conjugated polymer electronic excitation energies using metal/polymer/metal structures. Phys. Rev. Lett. **76**, 1900–1903 (1996). 10.1103/PhysRevLett.76.1900
1754. I.H. Campbell, D.L. Smith, Physics of organic electronic devices. Solid State Phys. **55**, 1–117 (2001). 10.1016/S0081-1947(01)80003-5
1755. P. Mark, W. Helfrich, Space-charge-limited currents in organic crystals. J. Appl. Phys. **33**, 205–215 (1962). 10.1063/1.1728487
1756. Frieder Baumann, Lucent Technologies Bell Labs
1757. C.G.B. Garrett, W.H. Brattain, Physical theory of semiconductor surfaces. Phys. Rev. **99**, 376–387 (1955). 10.1103/PhysRev.99.376
1758. A.S. Grove, B.E. Deal, E.H. Snow, C.T. Shah, Investigation of thermally oxidised silicon surfaces using metal-oxide-semiconductor structures. Solid State Electron. **8**, 145–163 (1965). 10.1016/0038-1101(65)90046-8
1759. B.E. Deal, E.H. Snow, C.A. Mead, Barrier energies in metal-silicon dioxide-silicon structures. J. Phys. Chem. Solids **27**, 1873–1879 (1966). 10.1016/0022-3697(66)90118-1
1760. W.M. Werner, The work function difference of the MOS-system with aluminum field plates and polycrystalline silicon field plates. Solid State Electron. **17**, 769–775 (1974). 10.1016/0038-1101(74)90023-9
1761. J.F. Guilleomoles, I. Lubomirsky, I. Riess, D. Cahen, Thermodynamic stability of p/n junctions. J. Phys. Chem. **99**, 14486–14493 (1995). 10.1021/j100039a041
1762. W.F. O'Hearn, Y.F. Chang, An analysis on the frequency dependence of the capacitance of abrupt p-n junction semiconductor devices. Solid State Electron. **13**, 473–483 (1970). 10.1016/0038-1101(70)90158-9
1763. J. Yang, Y. Zhang, W. Chen, G. Liu, p-n junction theory in view of excess majority carriers. EPL **120**, 28004:1–4 (2017). 10.1209/0295-5075/120/28004
1764. Y. Yoshizumi, S. Hashimoto, T. Tanabe, M. Kiyama, High-breakdown-voltage pn-junction diodes on GaN substrates. J. Cryst. Growth **298**, 875–878 (2007). 10.1016/j.jcrysgro.2006.10.246
1765. C.-T. Sah, R.N. Noyce, W. Shockley, Carrier generation and recombination in P-N junctions and P-N junction characteristics. Proc. IRE **45**, 1228–1243 (1957). 10.1109/JRPROC.1957.278528

1766. M. Grundmann, The bias dependence of the non-radiative recombination current in p-n diodes. Solid State Electron. **49**, 1446–1448 (2005). 10.1016/j.sse.2005.06.015
1767. H.K. Gummel, Hole-electron product of pn junctions. Solid State Electron. **10**, 209–212 (1967). 10.1016/0038-1101(67)90075-5
1768. J.L. Moll, *Physics of Semiconductors* (McGraw-Hill, New York, 1964)
1769. M.J.O. Strutt, Properties of semiconductor diodes, in *Semiconductor Devices*, vol. 1 (Academic Press, New York, 1966), English translation of W. Guggenbühl, M.J.O. Strutt, W. Wunderlin, *Halbleiterbauelemente, I. Halbleiter und Halbleiterdioden* (Springer, Basel, 1962). 10.1007/978-3-0348-6854-9
1770. S. Mahadevan, S.M. Hardas, G. Suryan, Electrical breakdown in semiconductors. Phys. Status Solidi A **8**, 335–374 (1971). 10.1002/pssa.2210080202
1771. D. Lausch, K. Petter, H. von Wenckstern, M. Grundmann, Correlation of pre-breakdown sites and bulk defects in multicrystalline silicon solar cells. Phys. Status Solidi RRL **3**, 70–72 (2009). 10.1002/pssr.200802264
1772. S.M. Sze, G. Gibbons, Avalanche breakdown voltages of abrupt and linearly graded p-n junctions in Ge, Si, GaAs and GaP. Appl. Phys. Lett. **8**, 111–113 (1966). 10.1063/1.1754511
1773. W. Fulop, Calculation of avalanche breakdown voltages of silicon p-n junctions. Solid State Electron. **10**, 39–43 (1967). 10.1016/0038-1101(67)90111-6
1774. B.J. Baliga, S.K. Ghandhi, Analytical solutions for the breakdown voltage of abrupt cylindrical and spherical junctions. Solid State Electron. **19**, 739–744 (1976). 10.1016/0038-1101(76)90152-0
1775. M.H. Lee, S.M. Sze, Orientation dependence of breakdown voltage in GaAs. Solid State Electron. **23**, 1007–1009 (1980). 10.1016/0038-1101(80)90072-6
1776. A. Goetzberger, B. McDonald, R.H. Haitz, R.M. Scarlet, Avalanche effects in silicon p-n junctions. II. Structurally perfect junctions. J. Appl. Phys. **34**, 1591–1600 (1963). 10.1063/1.1702640
1777. B.J. Baliga, *Modern Power Devices* (Wiley, New York, 1987)
1778. B.J. Baliga, *Fundamentals of Power Semiconductor Devices* (Springer, Berlin, 2008). 10.1007/978-0-387-47314-7
1779. S.M. Sze, G. Gibbons, Effect of junction curvature on breakdown voltage in semiconductors. Solid State Electron. **9**, 831–845 (1966). 10.1016/0038-1101(66)90033-5
1780. A.G. Milnes, D.L. Feucht, *Heterojunctions and Metal Semiconductor Junctions* (Academic Press, New York, 1972)
1781. H.J.A. Bluyssen, L.J. van Ruyven, F. Williams, Effects of quantum confinement and compositional grading on the band structure of heterojunctions. Solid State Electron. **22**, 573–579 (1979). 10.1016/0038-1101(79)90020-0
1782. F.-L. Schein, H. von Wenckstern, M. Grundmann, Transparent p-CuI/n-ZnO heterojunction diodes. Appl. Phys. Lett. **102**, 092109:1–4 (2013). 10.1063/1.4794532
1783. M. Grundmann, R. Karsthof, H. von Wenkstern, M. Grundmann, Interface recombination current in type II heterostructure bipolar diodes. ACS Appl. Mat. Interf. **6**, 14785–14789 (2014). 10.1021/am504454g
1784. C. Yang, M. Kneiß, F.-L- Schein, M. Lorenz, M. Grundmann, Room-temperature domain-epitaxy of copper iodide thin films for transparent CuI/ZnO heterojunctions with high rectification ratios larger than 10^9. Sci. Rep. **6**, 21937:1–8 (2016). 10.1038/srep21937
1785. J. Yang, J. Shen, Effects of discrete trap levels on organic light emitting diodes. J. Appl. Phys. **85**, 2699–2705 (1999). 10.1063/1.369587
1786. J. Staudigel, M. Stößel, F. Steuber, J. Simmerer, A quantitative numerical model of multilayer vapor-deposited organic light emitting diodes. J. Appl. Phys. **86**, 3895–3910 (1999). 10.1063/1.371306
1787. J. Blochwitz, *Organic light-emitting diodes with doped charge transport layers*, Ph.D. Thesis, Technische Universität Dresden (2001)
1788. K. Harada, A.G. Werner, M. Pfeiffer, C.J. Bloom, C.M. Elliott, K. Leo, Organic homojunction diodes with a high built-in potential: Interpretation of the current-voltage characteristics by a generalized Einstein relation. Phys. Rev. Lett. **94**, 036601:1–4 (2005). 10.1103/PhysRevLett.94.036601
1789. S.A. Van Slyke, C.H. Chen, C.W. Tang, Organic electroluminescent devices with improved stability. Appl. Phys. Lett. **69**, 2160–2162 (1996). 10.1063/1.117151
1790. T. Oyamada, H. Yoshizaki, H. Sasabe, C. Adachi, Efficient electron injection characteristics of triazine derivatives for transparent OLEDs (TOLEDs). Chemistry Lett. **33**, 1034–1035 (2004). 10.1246/cl.2004.1034
1791. B.L. Sharma, *Metal-Semiconductor Schottky Barrier Junctions and Their Applications* (Plenum Press, New York, 1984). 10.1007/978-1-4684-4655-5
1792. Virginia Diodes, Inc., www.virginiadiodes.com
1793. A. Dearn, L. Devlin, Plextek Ltd., UK
1794. *Tuning varactors*, Application Note, MicroMetrics Inc., Londonderry, NH, USA
1795. *BY329 Product Specifications*, Philips Semiconductors (1998)
1796. *Step recovery diodes*, Application Note, MicroMetrics Inc., Londonderry, NH, USA
1797. M.R.T. Tan, S.Y. Yang, D.E. Mars, J.L. Moll, *A 12 psec GaAs double heterostructure step recovery diode*, HPL-91-187:1–11 (Hewlett-Packard Co., Palo Alto, CA, 1991)
1798. L. Esaki, New phenomenon in narrow germanium p-n junctions. Phys. Rev. **109**, 603–604 (1958). 10.1103/PhysRev.109.603

1799. E.E. Mendez, L. Esaki, Resonant tunneling. Digital Encycl. Appl. Phys., pp. 437–454 (2003). 10.1002/3527600434.eap400
1800. A. Seabaugh, R. Lake, Tunnel diodes. Digital Encycl. Appl. Phys., pp. 335–359 (2003). 10.1002/3527600434.eap541
1801. E.O. Kane, Zener tunneling in semiconductors. J. Phys. Chem. Solids **12**, 181–188 (1959). 10.1016/0022-3697(60)90035-4
1802. L. Esaki, Y. Miyahara, A new device using the tunneling process in narrow p-n junctions. Solid State Electron. **1**, 13–21 (1960). 10.1016/0038-1101(60)90052-6
1803. N. Holonyak Jr., I.A. Lesk, R.N. Hall, J.J. Tiemann, H. Ehrenreich, Direct observation of phonons during tunneling in narrow junction diodes. Phys. Rev. Lett. **3**, 167–168 (1959). 10.1103/PhysRevLett.3.167
1804. A.G. Chynoweth, R.A. Logan, D.E. Thomas, Phonon-assisted tunneling in silicon and germanium Esaki junctions. Phys. Rev. **125**, 877–881 (1962). 10.1103/PhysRev.125.877
1805. M. Bao, K.L. Wang, Accurately measuring current-voltage characteristics of tunnel diodes. IEEE Trans. Electron Devices **53**, 2564–2568 (2006). 10.1109/TED.2006.882281
1806. Datasheet *Tunneling Diode 1N4396*, American Semiconductors, www.americanmicrosemi.com
1807. Datasheet *Tunneling Diode 1N4397*, American Semiconductors, www.americanmicrosemi.com
1808. P.J. Bulmann, G.S. Hobson, B.S. Taylor, *Transferred Electron Devices* (Academic, New York, 1972)
1809. A. Khalid, N.J. Pilgrim, G.M. Dunn, M.C. Holland, C.R. Stanley, I.G. Thayne, D.R.S. Cumming, A planar Gunn diode operating above 100 GHz. IEEE Electr. Dev. Lett. **28**, 849–851 (2007). 10.1109/LED.2007.904218
1810. V.N. Sokolov, K.W. Kim, V.A. Kochelap, D.L. Woolard, Terahertz generation in submicron GaN diodes within the limited space-charge accumulation regime. J. Appl. Phys. **98**, 064507:1–7 (2005). 10.1063/1.2060956
1811. A. Rydberg, High efficiency and output power from second and third-harmonic millimeter-wave InP-TED oscillators at frequencies above 170 GHz. IEEE Electr. Dev. Lett. **11**, 439–441 (1990). 10.1109/55.62989
1812. H. Eisele, Dual Gunn device oscillator with 10 mW at 280 GHz. Electron. Lett. **43**, 636–637 (2007). 10.1049/el:20070936
1813. S. Yngvesson, Transferred Electron Devices (TED)—Gunn devices. in Ref. [1815], pp. 23–58. 10.1007/978-1-4615-3970-4_2
1814. R. Van Zyl, W. Perold, R. Botha, The Gunn-diode: Fundamentals and fabrication, in *Proceedings 1998 South African Symposium on Communications and Signal Processing* (1998), pp. 407–412. 10.1109/COMSIG.1998.736992
1815. S. Yngvesson, Microwave semiconductor devices, in *Springer International Series in Engineering and Computer Science*, vol. 134 (Springer, New York, 1991). 10.1007/978-1-4615-3970-4
1816. A.L. Linsebigler, G. Lu, J.T. Yates, Photocatalysis on TiO_2 surfaces: Principles, mechanisms, and selected results. Chem. Rev. **95**, 735–758 (1995). 10.1021/cr00035a013
1817. D. Duonghong, E. Borgarello, M. Grätzel, Dynamics of light-induced water cleavage in colloidal systems. J. Am. Chem. Soc. **103**, 4685–4690 (1981). 10.1021/ja00406a004
1818. K.Y. Jung, YCh. Kang, S.B. Park, Photodegradation of trichloroethylene using nanometre-sized ZnO particles prepared by spray pyrolysis. J. Mater. Sci. Lett. **16**, 1848–1849 (1997). 10.1023/A:1018589206858
1819. J.L. Yang, S.J. An, W.I. Park, G-Ch. Yi, W. Choi, Photocatalysis using ZnO thin films and nanoneedles grown by metal-organic chemical vapor deposition. Adv. Mater. **16**, 1661–1664 (2004). :10.1002/adma.200306673
1820. J.B. Johnson, Thermal agitation of electricity in conductors. Nature **119**, 50–51 (1927). 10.1038/119050c0
1821. J.B. Johnson, Thermal agitation of electricity in conductors. Phys. Rev. **32**, 97 (1928). 10.1103/PhysRev.32.97
1822. H. Nyquist, Thermal agitation of electric charge in conductors. Phys. Rev. **32**, 110 (1928). 10.1103/PhysRev.32.110
1823. A. Van der Ziel, *Fluctuation Phenomena in Semiconductors* (Butterworth Scientific Publ., London, 1959)
1824. R.W. Boyd, *Radiometry and Detection of Optical Radiation* (Wiley, New York, 1983)
1825. S. Nudelman, The detectivity of infrared photodetectors. Appl. Optics **1**, 627–636 (1962). 10.1364/AO.1.000627
1826. R.C. Jones, Method of rating the performance of photoconductive cells. Proc. IRIS (Infrared Radiation Information Symposium) **2**, 9–12 (1957)
1827. R.C. Jones, Proposal of the detectivity D^{**} for detectors limited by radiation noise. J. Opt. Soc. Am. **50**, 1058 (1960). 10.1364/JOSA.50.001058
1828. Canon Inc., www.canon.com/technology
1829. B.F. Levine, Quantum-well infrared photodetectors. J. Appl. Phys. **74**, R1–R81 (1993). 10.1063/1.354252
1830. H.C. Liu, R. Dudek, A. Shen, E. Dupont, C.Y. Song, Z.R. Wasilewski, M. Buchanan, High absorption (>90%) quantum-well infrared photodetectors. Appl. Phys. Lett. **79**, 4237–4239 (2001). 10.1063/1.1425066
1831. A. Rogalski, Progress in focal plane array technologies. Prog. Quantum Electr. **36**, 342–473 (2012). 10.1016/j.pquantelec.2012.07.001
1832. Fraunhofer-Institut für Angewandte Festkörperphysik, Freiburg, www.iaf.fraunhofer.de
1833. M.D. Petroff, M.G. Stapelbroek, *Blocked impurity band detectors*, US Patent 4,568,960, filed 1980, awarded 1986
1834. N.M. Haegel, BIB detector development for the far infrared: From Ge to GaAs. Proc. SPIE **4999**, 182–194 (2003). 10.1117/12.479623

1835. L.A. Reichertz, J.W. Beeman, B.L. Cardozo, N.M. Haegel, E.E. Haller, G. Jakob, R. Katterloher, GaAs BIB photodetector development for far-infrared astronomy. Proc. SPIE **5543**, 231–238 (2004). 10.1117/12.560291
1836. F. Szmulowicz, F.L. Madarsz, Blocked impurity band detectors—An analytical model: Figures of merit. J. Appl. Phys. **62**, 2533–2540 (1987). 10.1063/1.339466
1837. H. Melchior, Demodulation and Photodetection Techniques, in *Laser Handbook*, vol. 1, F.T. Arecchi, E.O. Schulz-Dubois, eds. (North-Holland, Amsterdam, 1972), pp. 725–835
1838. G.E. Stillman, C.M. Wolfe, Avalanche photodiodes. Semicond. Semimet. **12**, 291–393 (1977). 10.1016/S0080-8784(08)60150-7
1839. Datasheet *Position Sensitive Photodiodes, DL-100-7-KER pin* (2002), Silicon Sensor GmbH, Berlin (Germany), www.silicon-sensor.com
1840. S.M. Sze, D.J. Coleman, A. Loya, Current transport in metal-semiconductor-metal (MSM) structures. Solid State Electron. **14**, 1209–1218 (1971). 10.1016/0038-1101(71)90109-2
1841. D. Kuhl, *Herstellung und Charakterisierung von MSM Detektoren*, Ph.D. Thesis, Technische Universität Berlin (1992)
1842. S.Y. Chou, M.Y. Liu, Nanoscale tera-hertz metal-semiconductor-metal photodetectors. IEEE J. Quantum Electr. **QE-28**, 2358–2368 (1992). 10.1109/3.159542
1843. R.J. McIntyre, Multiplication noise in uniform avalanche diodes. IEEE Trans. Electron Devices **13**, 164–168 (1966). 10.1109/T-ED.1966.15651
1844. R.D. Baertsch, Noise and ionization rate measurements in silicon photodiodes. IEEE Trans. Electron Devices **13**, 987 (1966). 10.1109/T-ED.1966.15880
1845. Datasheet APD Silicon Sensor AD500-12 TO, Silicon Sensor International AG (2010)
1846. G.M. Williams, M. Compton, D.A. Ramirez, M.M. Hayat, A.S. Huntington, Multi-gain-stage InGaAs avalanche photodiode with enhanced gain and reduced excess noise. IEEE J. Electr. Dev. Soc. **1**, 54–65 (2013). 10.1109/JEDS.2013.2258072
1847. K.S. Giboney, M.J.W. Rodwell, J.E. Bowers, Traveling-wave photodetectors. IEEE Phot. Technol. Lett. **4**, 1363–1365 (1992). 10.1109/68.180577
1848. J.-W. Shi, K.-G. Gan, Y.-J. Chiu, Y.-H. Chen, C.-K. Sun, Y.-J. Yang, J.E. Bowers, Metal-semiconductor-metal traveling-wave photodetectors. IEEE Phot. Technol. Lett. **16**, 623–635 (2001). 10.1109/68.924045
1849. J.D.E. Beynon, D.R. Lamb, eds., *Charge-coupled Devices and their Applications* (McGraw-Hill, Maidenhead, 1977)
1850. A.J.P. Theuwissen, *Solid-State Imaging with Charge-Coupled Devices* (Kluwer, New York, 1995). 10.1007/0-306-47119-1
1851. A. Goetzberger, E.H. Nicollian, Temperature dependence of inversion-layer frequency response in silicon. Bell Syst. Tech. J. **46**, 513–522 (1967). 10.1002/j.1538-7305.1967.tb04232.x
1852. J.D.E. Beynon, The basic principles of charge-coupled devices. Microelectron. **7**, 7–13 (1975)
1853. *Charge-coupled device (CCD) image sensors*, MTD/PS-0218, Rev. 2 (2008), Eastman Kodak Company, Rochester, NY, www.kodak.com
1854. J.E. Carnes, W.F. Kosonocky, E.G. Ramberg, Free charge transfer in charge-coupled devices. IEEE Trans. Electron Devices **19**, 798–808 (1972). 10.1109/T-ED.1972.17497
1855. C.H. Sequin, M.F. Tompsett, *Charge Transfer Devices* (Academic, New York, 1975)
1856. D.J. Burt, *Basic Operation of the Charge Coupled Device* (Int. Conf. Technol. Appl. CCD, University of Edinburgh, 1974), pp. 1–12
1857. SONY Corporation, www.sony.net
1858. B.E. Bayer, *Color imaging array*, US Patent 3,971,065, filed 1975, awarded 1976
1859. M. Bigas, E. Cabruja, J. Forest, J. Salvi, Review of CMOS image sensors. Microelectron. J. **37**, 433–451 (2006). 10.1016/j.mejo.2005.07.002
1860. A.J.P. Theuwissen, CMOS image sensors: State-of-the-art. Solid State Electron. **52**, 1401–1406 (2008). 10.1016/j.sse.2008.04.012
1861. Datasheet *CMOS linear image sensor, S9226* (2003), www.hamamatsu.com
1862. Foveon Inc., www.foveon.com
1863. R.B. Merrill, *Color separation in an active pixel cell imaging array using a triple-well structure*, US Patent 5,965,875, filed 1998, awarded 1999
1864. Datasheet *16 element APD array 16AA0.4-9 SMD* (2018), First Sensor AG, Berlin, www.first-sensor.com
1865. Datasheet *InGaAs Linear Photodiode Array, SU1024LE-1.7* (2019), Sensors Unlimited, Inc., www.sensorsinc.com
1866. Datasheet *Quadrant Photodiode with Position Sensing, QD50-0* (2019), OSI Optoelectronics, Hawthorne, CA, USA, www.osioptoelectronics.com
1867. T. Yokoyama, M. Tsutsui, Y. Nishi, I. Mizuno, V. Dmitry, A. Lahav, High performance 2.5um global shutter pixel with new designed light-pipe structure, in *Proceedings 2018 IEEE International Electron Devices Meeting (IEDM)* (IEEE, 2018), pp. 10.5.1–10.5.4. 10.1109/IEDM.2018.8614569

1868. H. Tsugawa, H. Takahashi, R. Nakamura, T. Umebayashi, T. Ogita, H. Okano, K. Iwase, H. Kawashima, T. Yamasaki, D. Yoneyama, J. Hashizume, T. Nakajima, K. Murata, Y. Kanaishi, K. Ikeda, K. Tatani, T. Nagano, H. Nakayama, T. Harutam, T. Nomoto, Pixel/DRAM/logic 3-layer stacked CMOS image sensor technology, in *Proceedings 2017 IEEE International Electron Devices Meeting (IEDM)* (IEEE, 2017), pp. 3.2.1–3.2.4. 10.1109/IEDM.2017.8268317
1869. IMX250MZRMYR flyer, SONY corporation, www.sony-semicon.co.jp
1870. J.J. Loferski, The first forty years: A brief history of the modern photovoltaic age. Prog. Photovolt.: Res. Appl. **1**, 67–78 (1993) 10.1002/pip.4670010109
1871. The most up to date table at printing can be found in M. Green, E. Dunlop, J. Hohl-Ebinger, M. Yoshita, N. Kopidakis, X. Hao, Solar cell efficiency tables (Version 57). Prog. Photovolt.: Res. Appl. **29**, 3–15 (2021). 10.1002/pip.3371
1872. R. Leemans, W.P. Cramer, *The IIASA database for mean monthly values of temperature, precipitation and cloudiness on a global terrestrial grid, Research Report RR-91-18* (International Institute of Applied Systems Analyses, Laxenburg, Austria, 1991)
1873. W.W. Gärtner, Depletion-layer photoeffects in semiconductors. Phys. Rev. **116**, 84–87 (1959). 10.1103/PhysRev.116.84
1874. X. Liu, J. Sites, Solar-cell collection efficiency and its variation with voltage. J. Appl. Phys. **75**, 577–581 (1994). 10.1063/1.355842
1875. H.H. Hovel, Carrier collection, spectral response, and photocurrent. Semicond. Semimet. **11**, 8–47 (1975). 10.1016/S0080-8784(08)62358-3
1876. S. Hegedus, D. Desai, C. Thompson, Voltage dependent photocurrent collection in CdTe/CdS solar cells. Prog. Photovolt.: Res. Appl. **15**, 587–602 (2007). 10.1002/pip.767
1877. C.H. Henry, Limiting efficiencies of ideal single and multiple energy gap terrestrial solar cells. J. Appl. Phys. **51**, 4494–4500 (1980). 10.1063/1.328272
1878. W. Shockley, H.-J. Queisser, Detailed balance limit of efficiency of p-n junction solar cells. J. Appl. Phys. **32**, 510–519 (1961). 10.1063/1.1736034
1879. H.-J. Queisser, Detailed balance limit for solar cell efficiency. Mater. Sci. Engin. B **159–160**, 322–328 (2008). 10.1016/j.mseb.2008.06.033
1880. Th Kirchartz, U. Rau, Detailed balance and reciprocity in solar cells. Phys. Status Solidi A **205**, 2737–2751 (2008). 10.1002/pssa.200880458
1881. J.H. Werner, S. Kolodinski, H.-J. Queisser, Novel optimization principles and efficiency limits for semiconductor solar cells. Phys. Rev. Lett. **72**, 3851–3854 (1994). 10.1103/PhysRevLett.72.3851
1882. T. Markvart, Solar cell as a heat engine: Energy-entropy analysis of photovoltaic conversion. Phys. Status Solidi A **205**, 2752–2756 (2008). 10.1002/pssa.200880460
1883. M.B. Prince, Silicon solar energy converters. J. Appl. Phys. **26**, 534–540 (1955). 10.1063/1.1722034
1884. R.T. Ross, Some thermodynamics of photochemical systems. J. Chem. Phys. **46**, 4590–4593 (1967). 10.1063/1.1840606
1885. O.D. Miller, E. Yablonovitch, S.R. Kurtz, Strong internal and external luminescence as solar cells approach the Shockley-Queisser limit. IEEE J. Photovoltaics **2**, 303–311 (2012). 10.1109/JPHOTOV.2012.2198434
1886. J. Mandelkorn, J.H. Lamneck, Simplified fabrication of back surface electric field silicon cells and novel characteristics of such cells. Solar Cells **29**, 121–130 (1990). reprinted from: Conf. Rec. 9th IEEE Photovoltaic Spec. Conf. (IEEE, New York, 1972), pp. 83–90. 10.1016/0379-6787(90)90021-V
1887. A. Hauser, I. Melnyk, P. Fath, S. Narayanan, S. Roberts, T.M. Bruton, A simplified process for isotropic texturing of mc-Si, in *Proceedings 3rd World Conference on Photovoltaic Energy Conversion*, vol. 2 (2003), pp. 1447–1450
1888. K. Wambach, S. Schlenker, I. Röver, Deutsche Solar AG, Freiberg
1889. R.A. Arndt, J.F. Allison, J.G. Haynos, A. Meulenberg, Jr., Optical properties of the COMSAT non-reflective cell, in *11th IEEE Photovoltaic Specialists Conference Rec.* (IEEE, New York, 1975), pp. 40–43
1890. NREL, www.nrel.gov/gis/solar.html
1891. Australian CRC for Renewable Energy Ltd. (ACRE), www.acre.murdoch.edu.au
1892. A. Woyte, J. Nijs, R. Belmans, Partial shadowing of photovoltaic arrays with different system configurations: literature review and field test results. Solar Energy **74**, 217–233 (2003). 10.1016/S0038-092X(03)00155-5
1893. J.W. Bishop, Computer simulation of the effects of electrical mismatches in photovoltaic cell interconnection circuits. Solar Cells **25**, 73–89 (1988). 10.1016/0379-6787(88)90059-2
1894. G. Hahn, S. Joos, State-of-the-art industrial crystalline silicon solar cells. Semicond. Semimet. **90**, 1–72 (2014). 10.1016/B978-0-12-388417-6.00005-2
1895. J.H. Werner, K. Taretto, U. Rau, Grain boundary recombination in thin-film silicon solar cells. Solid State Phenomena **80–81**, 299–304 (2001). 10.4028/www.scientific.net/SSP.80-81.299
1896. M. Imaizumi, T. Ito, M. Yamaguchi, K. Kaneko, Effect of grain size and dislocation density on the performance of thin film polycrystalline silicon solar cells. J. Appl. Phys. **81**, 7635–7640 (1997). 10.1063/1.365341
1897. A.K. Ghosh, C. Fishman, T. Feng, Theory of the electrical and photovoltaic properties of polycrystalline silicon. J. Appl. Phys. **51**, 446–454 (1980). 10.1063/1.327342

1898. K.R. Taretto, *Modeling and characterization of polycrystalline silicon for solar cells and microelectronics*, Ph.D. Thesis, Universität Stuttgart (2003)
1899. R.R. King, D.C. Law, K.M. Edmondson, C.M. Fetzer, G.S. Kinsey, H. Yoon, R.A. Sherif, N.H. Karam, 40% efficient metamorphic GaInP/GaInAs/Ge multijunction solar cells. Appl. Phys. Lett. **90**, 183516 (2007). 10.1063/1.2734507
1900. Sharp Corporation, https://global.sharp/corporate/news/120531.html
1901. B. Dimmler, Overview of thin-film solar cell technologies. Semicond. Semimet. **90**, 121–136 (2014). 10.1016/B978-0-12-388417-6.00004-0
1902. V. Probst, J. Palm, S. Visbeck, T. Niesen, R. Tölle, A. Lerchenberger, M. Wendl, H. Vogt, H. Calwer, W. Stetter, F. Karg, New developments in Cu(In, Ga)(S, Se)$_2$ thin film modules formed by rapid thermal processing of stacked elemental layers. Solar Energy Mater Solar Cells **90**, 3115–3123 (2006). 10.1016/j.solmat.2006.06.031
1903. H. Hoppe, N.S. Sariciftci, Organic solar cells: An overview. J. Mater. Res. **19**, 1924–1944 (2004). 10.1557/JMR.2004.0252
1904. S.E. Shaheen, C.J. Brabec, N.S. Sariciftci, F. Padinger, T. Fromherz, J.C. Hummelen, 2.5% efficient organic plastic solar cells. Appl. Phys. Lett. **78**, 841–843 (2001). 10.1063/1.1345834
1905. V. Shrotriya, G. Li, Y. Yao, T. Moriarty, K. Emery, Y. Yang, Accurate measurement and characterization of organic solar cells. Adv. Funct. Mater. **16**, 2016–2023 (2006). 10.1002/adfm.200600489
1906. Solarion AG, Leipzig (company closed)
1907. T. Trupke, M.A. Green, P. Würfel, Improving solar cell efficiencies by down-conversion of high-energy photons. J. Appl. Phys. **92**, 1668–1674 (2002). 10.1063/1.1492021
1908. T. Trupke, M.A. Green, P. Würfel, Improving solar cell efficiencies by up-conversion of sub-band-gap light. J. Appl. Phys. **92**, 4117–4122 (2002). 10.1063/1.1505677
1909. A. Luque, A. Martí, Increasing the efficiency of ideal solar cells by photon induced transitions at intermediate levels. Phys. Rev. Lett. **78**, 5014–5017 (1997). 10.1103/PhysRevLett.78.5014
1910. K.M. Yu, W. Walukiewicz, J. Wu, W. Shan, J.W. Beeman, M.A. Scarpulla, O.D. Dubon, P. Becla, Diluted II–VI oxide semiconductors with multiple band gaps. Phys. Rev. Lett. **91**, 246403:1–4 (2003). 10.1103/PhysRevLett.91.246403
1911. A. Franceschetti, S. Lanya, G. Bester, Quantum-dot intermediate-band solar cells with inverted band alignment. Physica E **41**, 15–17 (2008). 10.1016/j.physe.2008.05.023
1912. A. Luque, A. Martí, A.J. Nozik, Solar cells based on quantum dots: Multiple exciton generation and intermediate bands. MRS Bull. **32**, 236–241 (2007). 10.1557/mrs2007.28
1913. S. Suraprapapich, S. Thainoi, S. Kanjanachuchai, S. Panyakeow, Quantum dot integration in heterostructure solar cells. Solar Energy Mater. Solar Cells **90**, 2968–2974 (2006). 10.1016/j.solmat.2006.06.011
1914. F. Dimroth, High-efficiency solar cells from III-V compound semiconductors. Phys. Status Solidi C **3**, 373–379 (2006). 10.1002/pssc.200564172
1915. R.R. King, D.E. Joslin, H. Karam, *Multijunction photovoltaic cell with thin 1st (top) subcell and thick 2nd subcell of same or similar semiconductor material*, US patent 6,316,715, filed 2000, awarded 2001
1916. Gergö Létay, *Modellierung von III–V Solarzellen*, Ph.D. Thesis, Universität Konstanz (2003)
1917. Spectrolab, www.spectrolab.com
1918. F. Dimroth, S. Kurtz, High-efficiency multijunction solar cells. MRS Bull. **32**, 230–235 (2007). 10.1557/mrs2007.27
1919. M.A. Green, A. Ho-Baillie, H.J. Snaith, The emergence of perovskite solar cells. Nature Photonics **8**, 506–514 (2014). 10.1038/nphoton.2014.134
1920. H.J. Snaith, Perovskites: The emergence of a new era for low-cost, high-efficiency solar cells. Phys. Chem. Lett. **4**, 3623–3630 (2013). 10.1021/jz4020162
1921. Y. Okada, N.J. Ekins-Daukes, T. Kita, R. Tamaki, M. Yoshida, A. Pusch, O. Hess, C.C. Phillips, D.J. Farrell, K. Yoshida, N. Ahsan, Y. Shoji, T. Sogabe, J.-F. Guillemoles, Intermediate band solar cells: Recent progress and future directions. Appl. Phys. Rev. **2**, 0213021:1–48 (2015). 10.1063/1.4916561
1922. US Department of Energy, www.eere.energy.gov/solar
1923. J.H. Werner, Second and third generation photovoltaics - Dreams and reality. Adv. Solid State Phys. (Festkörperprobleme) **44**, 51–66 (2004). 10.1007/978-3-540-39970-4_5
1924. D. Lincot, The new paradigm of photovoltaics: From powering satellites to powering humanity. Comptes Rendus Physique **18**, 381–390 (2017). 10.1016/j.crhy.2017.09.003
1925. R.M. Swanson, A vision for crystalline silicon photovoltaics. Prog. Photovolt: Res. Appl. **14**, 443–453 (2006). 10.1002/pip.709
1926. M.J. de Wild-Scholten, Energy payback time and carbon footprint of commercial photovoltaic systems. Solar Energy Materials & Solar Cells **119**, 296–305 (2013). 10.1016/j.solmat.2013.08.037
1927. Fraunhofer-Institut für solare Energiesysteme (ISE), www.energy-charts.de (2019)
1928. S.E. Derenzo, M.J. Weber, E. Bourret-Courchesne, M.K. Klintenberg, The quest for the ideal inorganic scintillator. Nucl. Instrum. Meth. A **505**, 111–117 (2003). 10.1016/S0168-9002(03)01031-3

1929. Y.A. Ono, *Electroluminescent Displays* (World Scientific, Singapore, 1995). 10.1142/2504
1930. G.F. Knoll, *Radiation Detection and Measurement*, 4th edn. (Wiley, New York, 2010)
1931. G. Hoffmann, FH Emden
1932. M. Nikl, V.V. Laguta, A. Vedda, Complex oxide scintillators: Material defects and scintillation performance. Phys. Status Solidi B **245**, 1701–1722 (2008). 10.1002/pssb.200844039
1933. S.E. Derenzo, W.W. Moses, M.J. Weber, A.C. West, Methods for a systematic, comprehensive search for fast, heavy scintillator materials. Proc. Mater. Res. Soc. **348**, 39–49 (1994). 10.1557/PROC-348-39
1934. E.F. Schubert, *Light-Emitting Diodes*, 2nd edn. (Cambridge University Press, Cambridge, 2006). 10.1017/CBO9780511790546
1935. J. Li, G.Q. Zhang, eds., *Light-Emitting Diodes, Materials, Processes, Devices and Applications* (Springer, Cham, 2019). 10.1007/978-3-319-99211-2
1936. A.A. Bergh, P.J. Dean, Light-emitting diodes. Proc. IEEE **60**, 156–223 (1972). 10.1109/PROC.1972.8592
1937. M.R. Krames, O.B. Shchekin, R. Mueller-Mach, G.O. Mueller, L. Zhou, G. Harbers, M.G. Craford, Status and future of high-power light-emitting diodes for solid-state lighting. J. Display Technol. **3**, 160–175 (2007). 10.1109/JDT.2007.895339
1938. R.D. Dupuis, M.R. Krames, History, development, and applications of high-brightness visible light-emitting diodes. IEEE J. Lightw. Techn. **26**, 1154–1171 (2008). 10.1109/JLT.2008.923628
1939. H.P. Maruska, D.A. Stevenson, J.I. Pankove, Violet luminescence of Mg-doped GaN. Appl. Phys. Lett. **22**, 303–305 (1973). 10.1063/1.1654648
1940. N. Koide, H. Kato, S. Yamasaki, K. Manabe, M. Hashimoto, H. Amano, K. Hiramatsu, I. Aksaki, Doping of GaN with Si and properties of blue m/i/n/n^+ GaN LED with Si-doped n^+-layer by MOVPE. J. Cryst. Growth **115**, 639–642 (1991). 10.1016/0022-0248(91)90818-P
1941. P. Santhanam, D.J. Gray, Jr., R.J. Ram, Thermoelectrically pumped light-emitting diodes operating above unity efficiency. Phys. Rev. Lett. **108**, 097403:1–5 (2012). 10.1103/PhysRevLett.108.097403
1942. J. Tauc, The share of thermal energy taken from the surroundings in the electro-luminescent energy radiated from a p-n junction. Czech. J. Phys. **7**, 275–276 (1957). 10.1007/BF01688028
1943. A. David, C.A. Hurni, R.I. Aldaz, M.J. Cich, B. Ellis, K. Huang, F.M. Steranka, M.R. Krames, High light extraction efficiency in bulk-GaN based volumetric violet light-emitting diodes. Appl. Phys. Lett. **105**, 23111:1–5 (2014). 10.1063/1.4903297
1944. Soraa, www.soraa.com
1945. W.N. Carr, Photometric figures of merit for semiconductor luminescent sources operating in spontaneous mode. Infrared Phys. **6**, 1–19 (1966). 10.1016/0020-0891(66)90019-4
1946. S.V. Galginaitis, Improving the external efficiency of electroluminescent diodes. J. Appl. Phys. **36**, 460–461 (1965). 10.1063/1.1714011
1947. M.G. Craford, Recent developments in light-emitting-diode technology. IEEE Trans. Electron Devices **24**, 935–943 (1977). 10.1109/T-ED.1977.18854
1948. OSRAM Opto Semiconductors GmbH, Regensburg, Germany (2001), www.osram-os.com
1949. Lumileds Lighting, www.lumileds.com
1950. V. Haerle, B. Hahn, S. Kaiser, A. Weimar, S. Bader, F. Eberhard, A. Plössl, D. Eisert, High brightness LEDs for general lighting applications using the new ThinGaN™-technology. Phys. Status Solidi A **201**, 2736–2739 (2004). 10.1002/pssa.200405119
1951. OSRAM Opto Semiconductors GmbH, Regensburg, Germany (2003), www.osram-os.com
1952. O.B. Shchekin, J.E. Epler, T.A. Trottier, T. Margalith, D.A. Steigerwald, M.O. Holcomb, P.S. Martin, M.R. Krames, High performance thin-film flip-chip InGaN/GaN light-emitting diodes. Appl. Phys. Lett. **89**, 071109 (2006). 10.1063/1.2337007
1953. C.A. Hurni, A. David, M.J. Cich, R.I. Aldaz, B. Ellis, K. Huang, A. Tyagi, R.A. DeLille, M.D. Craven, F.M. Steranka, M.R. Krames, Bulk GaN flip-chip violet light-emitting diodes with optimized efficiency for high-power operation. Appl. Phys. Lett. **106**, 031101:1–4 (2015). 10.1063/1.4905873
1954. F. Akyol, S. Krishnamoorthy, Y. Zhang, S. Rajan, Tunneling-based carrier regeneration in cascaded GaN light emitting diodes to overcome efficiency droop. Appl. Phys. Lett. **103**, 081107:1–4 (2013) 10.1063/1.4819737
1955. F. Akyol, S. Krishnamoorthy, Y. Zhang, S. Rajan, GaN-based three-junction cascaded light-emitting diode with low-resistance InGaN tunnel junctions. Appl. Phys. Express **8**, 082103:1–3 (2015). 10.7567/APEX.8.082103
1956. M. Auf der Maur, A. Pecchia, G. Penazzi, W. Rodrigues, A. Di Carlo, Efficiency drop in green InGaN/GaN light emitting diodes: The role of random alloy fluctuations. Phys. Rev. Lett. **116**, 027401:1–5 (2016). 10.1103/PhysRevLett.116.027401
1957. M.G. Craford, Visible light-emitting diodes: Past, present, and very bright future. MRS Bull. **25**, 27–31 (2000). 10.1557/mrs2000.200
1958. R. Mueller-Mach, G. Mueller, M.R. Krames, H.A. Höppe, F. Stadler, W. Schnick, Th. Juestel, P. Schmidt, Highly efficient all-nitride phosphor-converted white light emitting diode. Phys. Status Solidi A **202**, 1727–1732 (2005). 10.1002/pssa.200520045

1959. *Balancing White Color*, Application note SE-AP00042:1–3, Nichia Corp. (2016)
1960. J. Christen, T. Riemann, F. Bertram, D. Rudloff, P. Fischer, A. Kaschner, U. Haboeck, A. Hoffmann, C. Thomsen, Optical micro-characterization of group-III-nitrides: Correlation of structural, electronic and optical properties. Phys. Status Solidi C 1795–1815 (2003). 10.1002/pssc.200303125
1961. *Power Light Source Luxeon© K2*, Technical Datasheet DS51 (6/08), Philips Lumileds Lighting Company (2008)
1962. Y.C. Shen, G.O. Mueller, S. Watanabe, N.F. Gardner, A. Munkholm, M.R. Krames, Auger recombination in InGaN measured by photoluminescence. Appl. Phys. Lett. **91**, 141101:1–3 (2007). 10.1063/1.2785135
1963. C. Weisbuch, M. Piccardo, L. Martinelli, J. Iveland, J. Peretti, J.S. Speck, The efficiency challenge of nitride light-emitting diodes for lighting. Phys. Status Solidi A **212**, 899–913 (2015). 10.1002/pssa.201431868
1964. S. Weise, Th. Zahner, Th. Lutz, A. Stich, *Reliability of the DRAGON® Product Family* (Application Note, Osram Opto Semiconductors, 2009)
1965. A. Lochmann, E. Stock, O. Schulz, F. Hopfer, D. Bimberg, V.A. Haisler, A.I. Toropov, A.K. Bakarov, A.K. Kalagin, Electrically driven single quantum dot polarised single photon emitter. Electron. Lett. **42**, 774–775 (2006). 10.1049/el:20061076
1966. R.M. Stevenson, R.J. Young, P. Atkinson, K. Cooper, D.A. Ritchie, A.J. Shields, A semiconductor source of triggered entangled photon pairs. Nature **439**, 179–182 (2006). 10.1038/nature04446
1967. R.J. Young, R.M. Stevenson, P. Atkinson, D.A. Ritchie, A.J. Shields, Improved fidelity of triggered entangled photons from single quantum dots. New J. Phys. **8**, 29 (2006). 10.1088/1367-2630/8/2/029
1968. A.J. Shields, Semiconductor quantum light sources. Nat. Photonics **1**, 215 (2007). 10.1038/nphoton.2007.46
1969. A. Lochmann, E. Stock, O. Schulz, F. Hopfer, D. Bimberg, V.A. Haisler, A.I. Toropov, A.K. Bakarov, M. Scholz, S. Büttner, O. Benson, Electrically driven quantum dot single photon source. Phys. Status Solidi C **4**, 547–550 (2007). 10.1002/pssc.200673201
1970. S.K. Ray, K.M. Groom, M.D. Beattie, H.Y. Liu, M. Hopkinson, R.A. Hogg, Broad-band superluminescent light-emitting diodes incorporating quantum dots in compositionally modulated quantum wells. IEEE Phot. Technol. Lett. **18**, 58–60 (2006). 10.1109/LPT.2005.860028
1971. E.U. Rafailov, M.A. Cataluna, W. Sibbett, Mode-locked quantum-dot lasers. Nat. Photonics **1**, 395–401 (2007). 10.1038/nphoton.2007.120
1972. C.W. Tang, S.A. Van Slyke, Organic electroluminescent diodes. Appl. Phys. Lett. **51**, 913–915 (1987). 10.1063/1.98799
1973. OSRAM Opto Semiconductors GmbH, Regensburg, Germany (2007), www.osram-os.com
1974. Pioneer Electronics, www.pioneerelectronics.com
1975. Sony Model XEL-1 (2009), www.sony.com
1976. H.C. Casey, Jr., M.B Panish, *Heterostructure Lasers* (Academic Press, New York, 1978) (Two volumes, Part A: *Fundamental Principles*, Part B: *Materials and Operating Characteristics*)
1977. H. Kressel, J. Butler, *Semiconductor Lasers and Heterojunction LEDs* (Academic Press, New York, 1977)
1978. Lasers and Photonics Marketplace Seminar, as published by Laser Focus World, www.laserfocusworld.com
1979. H. Haug, S.W. Koch, *Quantum Theory of the Optical and Electronic Properties of Semiconductors*, 5th edn. (World Scientific, Singapore, 2009). 10.1142/7184
1980. W.W. Chow, P.M. Smowton, P. Blood, A. Girndt, F. Jahnke, S.W. Koch, Comparison of experimental and theoretical GaInP quantum well gain spectra. Appl. Phys. Lett. **71**, 157–159 (1997). 10.1063/1.119489
1981. M. Grundmann, The present status of quantum dot lasers. Physica E **5**, 167–184 (2000). 10.1016/S1386-9477(99)00041-7
1982. M.B. Panish, I. Hayashi, S. Sumski, Double-heterostructure injection lasers with room-temperature thresholds as low as 2300 A/cm^2. Appl. Phys. Lett. **16**, 326–327 (1970). 10.1063/1.1653213
1983. L.A. D'Asaro, Advances in GaAs junction lasers with stripe geometry. J. Lumin. **7**, 310–337 (1973). 10.1016/0022-2313(73)90073-2
1984. H. Wenzel, F. Bugge, G. Erbert, R. Hülsewede, R. Staske, G. Tränkle, High-power diode lasers with small vertical beam divergence emitting at 808 nm. Electron. Lett. **37**, 1024–1026 (2001). 10.1049/el:20010712
1985. H. Yonezu, I. Sakuma, K. Kobayashi, T. Kamejima, M. Ueno, Y. Nannichi, A GaAs/Al$_x$Ga$_{1-x}$As double heterostructure planar stripe laser. Jpn. J. Appl. Phys. **12**, 1585–1592 (1973). 10.1143/JJAP.12.1585
1986. W.G. Scheibenzuber, *GaN-Based Laser Diodes: Towards Longer Wavelengths and Short Pulses* (Springer, Berlin, 2012). 10.1007/978-3-642-24538-1
1987. M. Kamp, J. Hofmann, A. Forchel, S. Lourdudoss, Ultrashort InGaAsP/InP lasers with deeply etched Bragg mirrors. Appl. Phys. Lett. **78**, 4074–4075 (2001). 10.1063/1.1377623
1988. Mathias Kamp, private communication
1989. M. Fujita, R. Ushigome, T. Baba, Large spontaneous emission factor of 0.1 in a microdisk injection laser. IEEE Phot. Technol. Lett. **13**, 403–405 (2001) 10.1109/68.920731
1990. G. Björk, A. Karlsson, Y. Yamamoto, Definition of a laser threshold. Phys. Rev. A **50**, 1675–1680 (1994). 10.1103/PhysRevA.50.1675
1991. Y. Yamamoto, S. Machida, G. Björk, Microcavity semiconductor laser with enhanced spontaneous emission. Phys. Rev. A **44**, 657–668 (1991). 10.1103/PhysRevA.44.657

1992. H.S. Sommers, Spectral characteristics of single-mode injection lasers: The power-gain curve from weak stimulation to full output. J. Appl. Phys. **52**, 156–160 (1982). 10.1063/1.331591
1993. T. Erneux, P. Glorieux, *Laser Dynamics* (Cambridge University Press, Cambridge, 2010), 10.1017/CBO9780511776908
1994. N.A. Pikhtin, S.O. Slipchenko, Z.N. Sokolova, A.L. Stankevich, D.A. Vinokurov, I.S. Tarasov, Zh.I. Alferov, 16 W continuous-wave output power from 100 μm-aperture laser with quantum well asymmetric heterostructure. Electron. Lett. **40**, 1413–1414 (2004). 10.1049/el:20045885
1995. A. Knigge, G. Erbert, J. Jonsson, W. Pittroff, R. Staske, B. Sumpf, M. Weyers, G. Tränkle, Passively cooled 940 nm laser bars with 73% wall-plug efficiency at 70 W and 25°C. Electron. Lett. **41**, 250–251 (2005). 10.1049/el:20058180
1996. D. Garbuzov, I. Kudryashov, A. Komissarov, M. Maiorov, W. Roff, J. Connolly, 14xx nm DFB InGaAsP/InP pump lasers with 500 mW CW output power for WDM combining, in *Optical Fiber Communication Conference, OSA Technical Digest Series, WD1* (Optical Society of America, Washington, D.C., 2003), pp. 486–487. 10.1109/OFC.2002.1036504
1997. T. Kimura, M. Nakae, J. Yoshida, S. Iizuka, A. Sato, 14XX nm over 1 W pump laser module with integrated PBC, in *Optical Fiber Communication Conference, OSA Technical Digest Series* (Optical Society of America, Washington, D.C., 2003), pp. 485–486. 10.1109/OFC.2002.1036503
1998. W.T. Tsang, R.A. Logan, J.P. Van der Ziel, Low-current-threshold strip-buried-heterostructure lasers with self-aligned current injection stripes. Appl. Phys. Lett. **34**, 644–647 (1979). 10.1063/1.90623
1999. D. Garbuzov, M. Maiorov, R. Menna, A. Komissarov, V. Khalfin, I. Kudryashov, A. Lunev, L. DiMarco, J. Connolly, High-power 1300-nm Fabry-Perot and DFB ridge-waveguide lasers. Proc. SPIE **4651**, 92–100 (2002). 10.1117/12.467937
2000. M. Grundmann, O. Stier, S. Bognár, C. Ribbat, F. Heinrichsdorff, D. Bimberg, Optical properties of self-organized quantum dots: Modeling and experiments. Phys. Status Solidi A **178**, 255–262 (2000). 10.1002/1521-396X(200003)178:1<255::AID-PSSA255>3.0.CO;2-Q
2001. M. Grundmann, How a quantum-dot laser turns on. Appl. Phys. Lett. **77**, 1428–1430 (2000). 10.1063/1.1290716
2002. F. Heinrichsdorff, C. Ribbat, M. Grundmann, D. Bimberg, High-power quantum-dot lasers at 1100 nm. Appl. Phys. Lett. **76**, 556–558 (2000). 10.1063/1.125816
2003. Ch. Ribbat, R. Sellin, M. Grundmann, D. Bimberg, High power quantum dot lasers at 1160 nm. Phys. Status Solidi B **224**, 819–822 (2001). 10.1002/(SICI)1521-3951(200104)224:3<819::AID-PSSB819>3.0.CO;2-1
2004. D. Garbuzov, I. Kudryashov, A. Tsekoun, A. Komissarov, W. Roff, M. Maiorov, R. Menna, A. Lunev, J. Connolly, 14xx nm DFB InGaAsP/InP pump lasers with 500 mw CW output power for WDM combining, in *Optical Fiber Communication Conference 2002, Technical Digest: ThN6* (2002). 10.1109/OFC.2002.1036504
2005. *High-Power 1550 nm DFB Source Lasers, A1112*, Datasheet DS00-281OPTO-1, Agere Systems (2001)
2006. M.-C. Amann, J. Buus, *Tunable Laser Diodes* (Artech House, Boston, 1998)
2007. J.N. Walpole, A.R. Calawa, T.C. Harman, S.H. Groves, Double-heterostructure PbSnTe lasers grown by molecular-beam epitaxy with cw operation up to 114 K. Appl. Phys. Lett. **28**, 552–554 (1976). 10.1063/1.88820
2008. S.-L. Lee, I.-F. Jang, C.-T. Pien, C.-Y. Wang, T.-T. Shih, Sampled grating DBR laser arrays with adjustable 0.8/1.6-nm wavelength spacing. IEEE Phot. Technol. Lett. **11**, 955–957 (1999). 10.1109/68.775311
2009. B. Mason, G.A. Fish, S.P. DenBaars, L.A. Coldren, Ridge waveguide sampled grating DBR lasers with 22-nm quasi-continuous tuning range. IEEE Phot. Technol. Lett. **10**, 1211–1213 (1998). 10.1109/68.705593
2010. K. Petermann, *Laser Diode Modulation and Noise* (Kluwer, Dordrecht, 1988). 10.1007/978-94-009-2907-4
2011. S. Wieczorek, B. Krauskopf, T.B. Simpson, D. Lenstra, The dynamical complexity of optically injected semiconductor lasers. Phys. Rep. **416**, 1–128 (2005). 10.1016/j.physrep.2005.06.003
2012. C.J. Hwang, J.C. Dyment, Dependence of threshold and electron lifetime on acceptor concentration in GaAs-$Ga_{1-x}Al_xAs$ lasers. J. Appl. Phys. **44**, 3240–3244 (1973). 10.1063/1.1662740
2013. N.K. Dutta, S.J. Wang, A.B. Piccirilli, R.F. Karlicek Jr., R.L. Brown, M. Washington, U.K. Chakrabarti, A. Gnauck, Wide-bandwidth and high-power InGaAsP distributed feedback lasers. J. Appl. Phys. **66**, 4640–4644 (1989). 10.1063/1.343820
2014. F. Grillot, B. Dagens, J.-G. Provost, H. Su, L.F. Lester, Gain Compression and above-threshold linewidth enhancement factor in 1.3-μm InAs-GaAs quantum-dot lasers. IEEE J. Quantum Electr. **44**, 946–951 (2008). 10.1109/JQE.2008.2003106
2015. J.S. Gustavsson, Å. Haglund, J. Bengtsson, A. Larsson, High-speed digital modulation characteristics of oxide-confined vertical-cavity surface-emitting lasers—Numerical simulations consistent with experimental results. IEEE J. Quantum Electr. **QE-38**, 1089–1096 (2002). 10.1109/JQE.2002.801009
2016. C.H. Henry, Theory of the linewidth of semiconductor lasers, IEEE J. Quantum Electr. **QE-18**, 259–264 (1982). 10.1109/JQE.1982.1071522
2017. Y. Yamamoto, H.A. Haus, Commutation relations and laser linewidth. Phys. Rev. A **41**, 5164–5170 (1990). 10.1103/PhysRevA.41.5164

2018. D. Welford, A. Mooradian, Output power and temperature dependence of the linewidth of single-frequency cw (GaAl)As diode lasers. Appl. Phys. Lett. **40**, 865–867 (1982). 10.1063/1.92945. Erratum: Appl. Phys. Lett. **41**, 1007 (1982). 10.1063/1.93718
2019. Quintessence Photonics Corporation, www.qpclasers.com
2020. BinOptics Corporation, Ithaca, NY, now MACOM, www.binoptics.com
2021. H.E. Li, K. Iga, eds., *Vertical-cavity Surface-emitting Laser Devices* (Springer, Berlin, 2003). 10.1007/978-3-662-05263-1
2022. Sandia National Laboratories, www.sandia.gov
2023. Ulm Photonics, now Philips, www.ulm-photonics.de, 10.1007/978-3-662-05263-1
2024. K.D. Choquette, Vertical-cavity surface-emitting lasers: Light for the information age. MRS Bull. **27**, 507–511 (2002). 10.1557/mrs2002.168
2025. C.J. Chang-Hasnain, Tunable VCSELs. IEEE J. Sel. Topics Quantum Electron. **6**, 978–987 (2000). 10.1109/2944.902146
2026. Bandwidth 9 (company closed 2005)
2027. F. Römer, C. Prott, J. Daleiden, S. Irmer, M. Strassner, A. Tarraf, H. Hillmer, Micromechanically tunable air gap resonators for long wavelength VCSEL's, in *IEEE LEOS International Semiconductor Laser Conference*. Garmisch/Germany, pp. 13–14 (2002). 10.1109/ISLC.2002.1041095
2028. M. Schulze, J.-M. Pelaprat, Efficiency experts. Photonics Spectra **35**(5), 150–151 (2001)
2029. *Sapphire*^{TM} *488-20 laser*, Datasheet MC-027-10-0M0111Rev.A, Coherent Inc. (2004)
2030. Federico Capasso, private communication
2031. Jérôme Faist, private communication
2032. F. Capasso, K. Mohammed, A.Y. Cho, Resonant tunneling through double barriers, perpendicular quantum transport phenomena in superlattices, and their device applications. IEEE J. Quantum Electr. **QE-22**, 1853–1869 (1986). 10.1109/JQE.1986.1073171
2033. H. Krömer, Proposed negative-mass microwave amplifier. Phys. Rev. **109**, 1856 (1958). 10.1103/PhysRev.109.1856
2034. A.A. Andronov, I.V. Zverev, V.A. Kozlov, Yu.N. Nozdrin, S.A. Pavlov, V. N. Shastin, Stimulated emission in the long-wavelength region from hot holes in Ge in crossed electric and magnetic fields. Pis'ma Zh. Eksp. Teor. Fiz. **40**, 69–72 (1984) [JETP Lett. **40**, 804–807 (1984)]
2035. Optical and Quantum Electronics **23**(2), Special Issue *Far-infrared Semiconductor Lasers*, E. Gornik, A.A. Andronov, eds. (Chapman and Hall, London, 1991). 10.1007/BF00619760
2036. E. Bründermann, Widely tunable far infrared hot hole semiconductor lasers, in *Long-wavelength Infrared Semiconductor Lasers*, ed. by H.K. Choi (Wiley, New York, 2004), pp. 279–350
2037. E. Bründermann, A.M. Linhart, H.P. Röser, O.D. Dubon, W.L. Hansen, E.E. Haller, Miniaturization of p-Ge lasers: Progress toward continuous wave operation. Appl. Phys. Lett. **68**, 1359–1361 (1996). 10.1063/1.116079
2038. E. Bründermann, D.R. Chamberlin, E.E. Haller, High duty cycle and continuous terahertz emission from germanium. Appl. Phys. Lett. **76**, 2991–2993 (2000). 10.1063/1.126555
2039. N.K. Dutta, Q. Wang, *Semiconductor Optical Amplifiers*, 2nd edn. (World Scientific, Singapore, 2013). 10.1142/8781
2040. A.J. Collar, G.D. Henshall, J. Farré, B. Mikkelsen, Z. Wang, L. Eskildsen, D.S. Olesen, K.E. Stubkjaer, Low residual reflectivity of angled-facet semiconductor laser amplifiers. IEEE Phot. Technol. Lett. **2**, 553–555 (1990). 10.1109/68.58046
2041. G. Jost, University of Ulm (Annual Report, Department of Optoelectronics, 1998), p. 64
2042. Ferdinand-Braun-Institut für Höchstfrequenztechnik, Berlin, www.fbh-berlin.de
2043. M. Sugawara, N. Hatori, M. Ishida, H. Ebe, Y. Arakawa, T. Akiyama, K. Otsubo, T. Yamamoto, Y. Nakata, Recent progress in self-assembled quantum-dot optical devices for optical telecommunication: Temperature-insensitive 10 Gb s^{-1} directly modulated lasers and 40 Gb s^{-1} signal-regenerative amplifiers. J. Phys. D: Appl. Phys. **38**, 2126–2134 (2005). 10.1088/0022-3727/38/13/008
2044. N. Yasuoka, K. Kawaguchi, H. Ebe, T. Akiyama, M. Ekawa, K. Morito, M. Sugawara, Y. Arakawa, Quantum-dot semiconductor optical amplifiers with polarization-independent gains in 1.5-μm wavelength bands. IEEE Phot. Technol. Lett. **20**, 1908–1910 (2008). 10.1109/LPT.2008.2004695
2045. P. Borri, S. Schneider, W. Langbein, U. Woggon, A.E. Zhukov, V.M. Ustinov, N.N. Ledentsov, Zh.I. Alferov, D. Ouyang, D. Bimberg, Ultrafast carrier dynamics and dephasing in InAs quantum-dot amplifiers emitting near 1.3-μm-wavelength at room temperature. Appl. Phys. Lett. **79**, 2633–2635 (2001). 10.1063/1.1411986
2046. W.B. Shockley, Transistor technology evokes new physics, Nobel Lecture (1956), in *Nobel Lectures, Physics* 1942–1962 (Elsevier, Amsterdam, 1964), pp. 344–374
2047. R.R. Nelson, The link between science and invention: The case of the transistor, in *The Rate and Direction of Inventive Activity: Economic and Social Factors* (Princeton University Press, Princeton, 1962), pp. 549–583
2048. Sh.S. Li, *Semiconductor Physical Electronics*, 2nd edn. (Springer, New York, 2006). 10.1007/0-387-37766-210.1007/0-387-37766-2

2049. P.G.A Jespers, Measurements for bipolar devices in: *Process and Device Modeling for Integrated Circuit Design*, ed. by F. van de Wiele, W.L. Engl, P.G. Jespers, NATO Science Series E, vol. 21 (Noordhoff, Leyden, 1977)
2050. M.J. Morant, *Introduction to Semiconductor Devices* (Addison-Wesley, Reading, MA, 1964)
2051. H.K. Gummel, H.C. Poon, An integral charge control model of bipolar transistors. Bell Syst. Tech. J. **49**, 827–852 (1970). 10.1002/j.1538-7305.1970.tb01803.x
2052. J.M. Early, Effects of space-charge layer widening in junction transistors. Proc. IRE **40**, 1401–1406 (1952). 10.1109/JRPROC.1952.273969
2053. C.C. McAndrew, L.W. Nagel, Early effect modeling in SPICE. IEEE J. Solid-State Circ. **31**, 136–138 (1996). 10.1109/4.485877
2054. D.C. Herbert, Extended velocity overshoot in GaAs HBT. Semicond. Sci. Technol. **10**, 682–686 (1995). 10.1088/0268-1242/10/5/019
2055. Solid State Electronics Laboratory, University of Michigan, www.eecs.umich.edu
2056. D. Cui, D. Sawdai, D. Pavlidis, S.H. Hsu, P. Chin, T. Block, High Power Performance Using InAlAs/InGaAs single heterojunction bipolar transistors, in *Proceedings of the 12th Int. Conf. on Indium Phosphide and Related Materials*, pp. 473–476 (2000). 10.1109/ICIPRM.2000.850336
2057. M. Feng, N. Holonyak Jr., R. Chan, Quantum-well-base heterojunction bipolar light-emitting transistor. Appl. Phys. Lett. **84**, 1952–1954 (2004). 10.1063/1.1669071
2058. R.R. Bockemuehl, Analysis of field effect transistors with arbitrary charge distribution. IEEE Trans. Electron Dev. **10**, 31–34 (1963). 10.1109/T-ED.1963.15076
2059. R.D. Middlebrook, I. Richer, Limits on the power-law exponent for field-effect transistor transfer characteristics. Solid State Electron. **6**, 542–544 (1963). 10.1016/0038-1101(63)90043-1
2060. K. Lehovec, R. Zuleeg, Voltage-current characteristics of GaAs-JFET's in the hot electron range. Solid State Electron. **13**, 1415–1425 (1970). 10.1016/0038-1101(70)90175-9
2061. H.C. Pao, C.T. Sah, Effects of diffusion current on characteristics of metal-oxide (insulator)-semiconductor transistors. Solid State Electron. **9**, 927–937 (1966). 10.1016/0038-1101(66)90068-2
2062. K. Yamaguchi, Field-dependent mobility model for two-dimensional numerical analysis of MOSFET's. IEEE Trans. Electron Dev. **26**, 1068–1074 (1979). 10.1109/T-ED.1979.19547
2063. R.R. Troutman, Subthreshold design considerations for insulated gate field-effect transistors. IEEE J. Solid-State Circ. **9**, 55–60 (1974). 10.1109/JSSC.1974.1050462
2064. W. Maly, *Atlas of IC technologies—An Introduction to VLSI Processes* (Benjamin/Cummings Publishing Company, San Francisco, 1987)
2065. D. Udeshi, E. Maldonado, Y. Xu, M. Tao, W.P. Kirk, Thermal stability of ohmic contacts between Ti and Se-passivated n-type Si(001). J. Appl. Phys. **95**, 4219–4222 (2004). 10.1063/1.1687047
2066. V. Sverdlov, *Strain-Induced Effects in Advanced MOSFETs* (Springer. Berlin (2011). 10.1007/978-3-7091-0382-1
2067. G.E. Moore, Cramming more components onto integrated circuits. Electronics **38**(8), 114–117 (1965). Reprinted. In: Proc. IEEE **86**, 82–85 (1998). 10.1109/JPROC.1998.658762
2068. M. Fayolle, F. Romagna, Copper CMP evaluation: Planarization issues. Microelectron. Eng. **37**, 135–141 (1997). 10.1016/S0167-9317(97)00104-4
2069. Z. Stavreva, D. Zeidler, M. Plötner, K. Drescher, Characteristics in chemical-mechanical polishing of copper: Comparison of polishing pads. Appl. Surf. Sci. **108**, 39–44 (1997). 10.1016/S0169-4332(96)00572-7
2070. C.-H. Tung, G.T.T. Sheng, C.-Y. Lu, *ULSI Semiconductor Technology Atlas* (Wiley, Hoboken, 2003). 10.1002/0471668796
2071. K. Hinode, Y. Hanaoka, K.-I. Takeda, S. Kondo, Resistivity increase in ultrafine-line copper conductor for ULSIs. Jpn. J. Appl. Phys. **40**, L1097–L1099 (2001). 10.1143/JJAP.40.L1097
2072. T. Harada, A. Ueki, K. Tomita, K. Hashimoto, J. Shibata, H. Okamura, K. Yoshikawa, T. Iseki, M. Higashi, S. Maejima, K. Nomura, K. Goto, T. Shono, S. Muranaka, N. Torazawa, S. Hirao, M. Matsumoto, T. Sasaki, S. Matsumoto, S. Ogawa, M. Fujisawa, A. Ishii, M. Matsuura, T. Ueda, Extremely low Keff (∼1.9) Cu interconnects with air gap formed using SiOC, in *IEEE International Interconnect Technology Conference (IITC)* (2007), pp. 141–143. 10.1109/IITC.2007.382364
2073. P. Bai, C. Auth, S. Balakrishnan, M. Bost, R. Brain, V. Chikarmane, R. Heussner, M. Hussein, J. Hwang, D. Ingerly, R. James, J. Jeong, C. Kenyon, E. Lee, S.-H. Lee, N. Lindert, M. Liu, Z. Ma, T. Marieb, A. Murthy, R. Nagisetty, S. Natarajan, J. Neirynck, A. Ott, C. Parker, J. Sebastian, R. Shaheed, S. Sivakumar, J. Steigerwald, S. Tyagi, C. Weber, B. Woolery, A. Yeoh, K. Zhang, M. Bohr, A 65nm logic technology featuring 35nm gate lengths, enhanced channel strain, 8 Cu interconnect layers, Low-k ILD and 0.57 μm^2 SRAM cell, in *IEDM Technical Digest* (IEEE, Piscataway, 2004), pp. 657–660. 10.1109/IEDM.2004.1419253
2074. www.chipworks.com
2075. Y. Taur, CMOS design near the limit of scaling. IBM J. Res. Dev. **46**, 213–222 (2002). 10.1147/rd.462.0213
2076. E.J. Nowak, Maintaining the benefits of CMOS scaling when scaling bogs down. IBM J. Res. Dev. **46**, 169–180 (2002). 10.1147/rd.462.0169
2077. S.-H. Lo, D.A. Buchanan, Y. Taur, W. Wang, Quantum-mechanical modeling of electron tunneling current from the inversion layer of ultra-thin-oxide nMOSFET's. IEEE Electr. Dev. Lett. **18**, 209–211 (1997). 10.1109/55.568766

2078. G.D. Wilk, R.M. Wallace, J.M. Anthony, Hafnium and zirconium silicates for advanced gate dielectrics. J. Appl. Phys. **87**, 484–492 (2000). 10.1063/1.371888
2079. Ch. Auth, M. Buehler, A. Cappellani, C.-H. Choi, G. Ding, W. Han, S. Joshi, B. McIntyre, M. Prince, P. Ranade, J. Sandford, Ch. Thomas, 45nm high-k + metal gate strain-enhanced transistors. Intel Techn. J. **12**, 77 (2008). 10.1535/itj.1201
2080. M.A. Quevedo-Lopez, S.A. Krishnan, D. Kirsch, C.H.J. Li, J.H. Sim, C. Huffman, J.J. Peterson, B.H. Lee, G. Pant, B.E. Gnade, M.J. Kim, R.M. Wallace, D. Guo, H. Bu, T.P. Ma, High performance gate first HfSiON dielectric satisfying 45nm node requirements, in *IEDM Technical Digest* (IEEE, Piscataway, 2005), pp. 425–428. 10.1109/IEDM.2005.1609369
2081. K. Mistry, C. Allen, C. Auth, B. Beattie, D. Bergstrom, M. Bost, M. Brazier, M. Buehler, A. Cappellani, R. Chau, C.-H. Choi, G. Ding, K. Fischer, T. Ghani, R. Grover, W. Han, D. Hanken, M. Hattendorf, J. He, J. Hicks, R. Heussner, D. Ingerly, P. Jain, R. James, L. Jong, S. Joshi, C. Kenyon, K. Kuhn, K. Lee, H. Liu, J. Maiz, B. McIntyre, P. Moon, J. Neirynck, S. Pae, C. Parker, D. Parsons, C. Prasad, L. Pipes, M. Prince, P. Ranade, T. Reynolds, J. Sandford, L. Shifren, J. Sebastian, J. Seiple, D. Simon, S. Sivakumar, P. Smith, C. Thomas, T. Troeger, P. Vandervoorn, S. Williams, K. Zawadzki, A 45nm logic technology with high-k+metal gate transistors, strained silicon, 9 Cu interconnect layers, 193nm dry patterning, and 100% Pb-free packaging, IEDM Technical Digest (IEEE, Piscataway, 2007), pp. 247–250. 10.1109/IEDM.2007.4418914
2082. K. Mistry, M. Armstrong, C. Auth, S. Cea, T. Coan, T. Ghani, T. Hoffmann, A. Murthy, J. Sandford, R. Shaheed, K. Zawadzki, K. Zhang, S. Thompson, M. Bohr, Delaying forever: uniaxial strained silicon transistors in a 90nm CMOS technology, Symp. VLSI Technology Digest (IEEE, Piscataway, 2004), pp. 50–51. 10.1109/VLSIT.2004.1345387
2083. T. Krishnamohan, C. Jungemann, D. Kim, E. Ungersboeck, S. Selberherr, A.-T. Pham, B. Meinerzhagen, P. Wong, Y. Nishi, K.C. Saraswat, High performance, uniaxially-strained, silicon and germanium, double-gate p-MOSFETs. Microelectron. Eng. **84**, 2063–2066 (2007). 10.1016/j.mee.2007.04.085
2084. T. Guillaume, M. Mouis, Calculations of hole mass in [110]-uniaxially strained silicon for the stress-engineering of p-MOS transistors. Solid State Electron. **50**, 701–708 (2006). 10.1016/j.sse.2006.03.040
2085. E. Ungersboeck, S. Dhar, G. Karlowatz, H. Kosina, S. Selberherr, Physical modeling of electron mobility enhancement for arbitrarily strained silicon. J. Comput. Electron. **6**, 55–58 (2007). 10.1007/s10825-006-0047-0
2086. M. Bohr, *The Invention of Uniaxial Strained Silicon Transistors at Intel* (Intel, 2007)
2087. Synopsys, Inc., www.synopsys.com/products/tcad/examples/strain2d.pdf
2088. W. Hansch, C. Fink, J. Schulze, I. Eisele, A vertical MOS-gated Esaki tunneling transistor in silicon. Thin Solid Films **369**, 387–389 (2000). 10.1016/S0040-6090(00)00896-8
2089. P.-F. Wang, K. Hilsenbeck, Th Nirschl, M. Oswald, Ch. Stepper, M. Weis, D. Schmitt-Landsiedel, W. Hansch, Complementary tunneling transistor for low power application. Solid State Electron. **48**, 2281–2286 (2004). 10.1016/j.sse.2004.04.006
2090. W.M. Reddick, G.A.J. Amaratunga, Silicon surface tunnel transistor. Appl. Phys. Lett. **67**, 494–496 (1995). 10.1063/1.114547
2091. P.-F. Wang, T. Nirschl, D. Schmitt-Landsiedel, W. Hansch, Simulation of the Esaki-tunneling FET. Solid State Electron. **47**, 1187–1192 (2003). 10.1016/S0038-1101(03)00045-5
2092. E.-H. Toh, G.H. Wang, G. Samudra, Y.-C. Yeo, Device physics and design of germanium tunneling field-effect transistor with source and drain engineering for low power and high performance applications. J. Appl. Phys. **103**, 104504:1–5 (2008). 10.1063/1.2924413
2093. L.M. Grupp, J.D. Davis, S. Swanson, The bleak future of NAND flash memory, in *Proceedings 10th USENIX Conferences File and Storage Technologies (FAST 2012)* (USENIX Association, Berkeley, USA, 2012), pp. 2:1–8
2094. G.R. Fox, R.Bailey, W.B. Kraus, F. Chu, S. Sun, T. Davenport, The current status of FeRAM, in *Ferroelectric Random Access Memories*, Topics in Applied Physics 93, H. Ishiwara, M. Okuyama, Y. Arimoto, eds. (Springer, Berlin, 2004), pp. 139–148. 10.1007/978-3-540-45163-1_10
2095. Y.C. Chen, C.T. Rettner, S. Raoux, G.W. Burr, S.H. Chen, R.M. Shelby, M. Salinga, W.P. Risk, T.D. Happ, G.M. McClelland, M. Breitwisch, A. Schrott, J.B. Philipp, M.H. Lee, R. Cheek, T. Nirschl, M. Lamorey, C.F. Chen, E. Joseph, S. Zaidi, B. Yee, H.L. Lung, R. Bergmann, C. Lam, Ultra-thin phase-change bridge memory device using GeSb, IEDM Technical Digest (IEEE, Piscataway, 2006), pp. 777–780. 10.1109/IEDM.2006.346910
2096. Z. Sun, J. Zhou, R. Ahuja, Unique melting behavior in phase-change materials for rewritable data storage. Phys. Rev. Lett. **98**, 055505:1–4 (2007). 10.1103/PhysRevLett.98.055505
2097. J. Hegedüs, S.R. Elliott, Microscopic origin of the fast crystallization ability of Ge-Sb-Te phase-change memory materials. Nat. Mater. **7**, 399–405 (2008). 10.1038/nmat2157
2098. P.K. Naji, M. Durlam, S. Tehrani, J. Calder, M.F. DeHerrera, A 256kb 3.0V 1T1MTJ nonvolatile magnetoresistive RAM, ISSCC Digest of Technical Papers (IEEE, Piscataway, 2001), pp. 122–124. 10.1109/ISSCC.2001.912570
2099. W.J. Gallagher, S.S.P. Parkin, Development of the magnetic tunnel junction MRAM at IBM: From first junctions to a 16-Mb MRAM demonstrator chip. IBM J. Res. Dev. **50**, 5–23 (2006). 10.1147/JRD.2006.5388775; Erratum: IBM J. Res. Dev. 50, 23A (2006). 10.1147/rd.501.0005

2100. M.N. Kozicki, C. Gopalan, M. Balakrishnan, M. Park, M. Mitkova, Non-volatile memory based on solid electrolytes, in *Proceedings IEEE Non-Volatile Memory Technology Symposium* (IEEE, Piscataway, 2004), pp. 10–17. 10.1109/NVMT.2004.1380792
2101. M.N. Kozicki, P. Mira, M. Mitkova, Nanoscale memory elements based on solid-state electrolytes. IEEE Trans. Nanotechnol. **4**, 331–338 (2005). 10.1109/TNANO.2005.846936
2102. K. Szot, W. Speier, G. Bihlmayer, R. Waser, Switching the electrical resistance of individual dislocations in single-crystalline $SrTiO_3$. Nat. Mater. **5**, 312–320 (2006). 10.1038/nmat1614
2103. A. Beck, J.G. Bednorz, Ch. Gerber, C. Rossel, D. Widmer, Reproducible switching effect in thin oxide films for memory applications. Appl. Phys. Lett. **77**, 139–141 (2000). 10.1063/1.126902
2104. S. Karg, G.I. Meijer, D. Widmer, R. Stutz, J.G. Bednorz, Ch. Rettner, Nanoscale resistive memory device using $SrTiO_3$ films, in *22nd IEEE Non-Volatile Semiconductor Memory Workshop, Monterey* (IEEE, Piscataway, 2007), pp. 68–70. 10.1109/NVSMW.2007.4290584
2105. M. Janousch, G.I. Meijer, U. Staub, B. Delley, S.F. Karg, B.P. Andreasson, Role of oxygen vacancies in Cr-doped $SrTiO_3$ for resistance-change memory. Adv. Mater. **19**, 2232–2235 (2007). 10.1002/adma.200602915
2106. M.A. Reed, C. Zhou, C.J. Muller, T.P. Burgin, J.M. Tour, Conductance of a molecular junction. Science **278**, 252–254 (1997). 10.1126/science.278.5336.252
2107. J.R. Heath, P.J. Kuekes, G.S. Snider, R.S. Williams, A defect-tolerant computer architecture: opportunities for nanotechnology. Science **280**, 1716–1721 (1998). 10.1126/science.280.5370.1716
2108. A. Aviram, M. Ratner, eds., Molecular electronics: Science and technology. Ann. N. Y. Acad. Sci. **852** (1998). 10.1111/j.1749-6632.1998.tb09860.x
2109. E.F. Schubert, Delta-doping of semiconductors: Electronic, optical and structural properties of materials and devices. Semicond. Semimet. **40**, 1–151 (1994). 10.1016/S0080-8784(08)62662-9
2110. M. Schlechtweg, A. Tessmann, A. Leuther, C. Schwörer, M. Lang, U. Nowotny, O. Kappeler, Integrated circuits based on 300 GHz f_T metamorphic HEMT technology for millimeter-wave and mixed-signal applications, in *Proceedings of the European Gallium Arsenide and other Compound Semiconductors Application Symposium (GAAS 2003)* (Horizon House, London, 2003), pp. 465–468
2111. D. Lubyshev, W.K. Liu, T.R. Stewart, A.B. Cornfeld, X.M. Fang, X. Xu, P. Specht, C. Kisielowski, M. Naidenkova, M.S. Goorsky, C.S. Whelan, W.E. Hoke, P.F. Marsh, J.M. Millunchick, S.P. Svensson, Strain relaxation and dislocation filtering in metamorphic high electron mobility transistor structures grown on GaAs substrates. J. Vac. Sci. Technol. B **19**, 1510–1514 (2001). 10.1116/1.1376384
2112. S.D. Brotherton, *Introduction to Thin Film Transistors. Physics and Technology of TFTs* (Springer, Heidelberg, 2013). 10.1007/978-3-319-00002-2
2113. Y. Kuo, ed., *Thin Film Transistors: Materials and Processes* (Kluwer, Boston, 2003) (Two volumes, Vol. 1: *Amorphous silicon thin film transistors*, Vol. 2: *Polycrystalline silicon thin film transistors*)
2114. G. Horowitz, Organic field-effect transistors. Adv. Mater. **10**, 365–377 (1998). 10.1002/(SICI)1521-4095(199803)10:5<365::AID-ADMA365>3.0.CO;2-U
2115. C.D. Dimitrakopoulos, P.R.L. Malenfant, Organic thin film transistors for large area electronics. Adv. Mater. **14**, 99–117 (2002). 10.1002/1521-4095(20020116)14:2<99::AID-ADMA99>3.0.CO;2-9
2116. BCh. Shekar, J. Lee, S.-W. Rhee, Organic thin film transistors: Materials, processes and devices. Korean J. Chem. Eng. **21**, 267–285 (2004). 10.1007/BF02705409
2117. Y.M. Sun, Y.Q. Liu, D.B. Zhu, Advances in organic field-effect transistors. J. Mater. Chem. **15**, 53–65 (2005). 10.1039/B411245H
2118. C.T. Liu, Revolution of the TFT LCD technology. J. Display Technol. **3**, 342–350 (2007). 10.1109/JDT.2007.908348
2119. U. Köster, Crystallization of amorphous silicon films. Phys. Status Solidi A **48**, 313–321 (1978). 10.1002/pssa.2210480207
2120. D. Toet, P.M. Smith, T.W. Sigmon, T. Takehara, C.C. Tsai, W.R. Harshbarger, M.O. Thompson, Laser crystallization and structural characterization of hydrogenated amorphous silicon thin films. J. Appl. Phys. **85**, 7914–7918 (1999). 10.1063/1.370607
2121. R.B. Iverson, R. Reif, Recrystallization of amorphized polycrystalline silicon films on SiO_2: Temperature dependence of the crystallization parameters. J. Appl. Phys. **62**, 1675–1681 (1987). 10.1063/1.339591
2122. N. Yamauchi, R. Reif, Polycrystalline silicon thin films processed with silicon ion implantation and subsequent solid-phase crystallization: Theory, experiments, and thin-film transistor applications. J. Appl. Phys. **75**, 3235–3257 (1994). 10.1063/1.356131
2123. G. Liu, S.J. Fonash, Polycrystalline silicon thin film transistors on Corning 7059 glass substrates using short time, low-temperature processing. Appl. Phys. Lett. **62**, 2554–2556 (1993). 10.1063/1.109294
2124. M.S. Haque, H.A. Naseem, W.D. Brown, Aluminum-induced crystallization and counter-doping of phosphorous-doped hydrogenated amorphous silicon at low temperatures. J. Appl. Phys. **79**, 7529–7536 (1996). 10.1063/1.362425

2125. L.H. Lee, Y.K. Fang, S.H. Fan, Au metal-induced lateral crystallisation (MILC) of hydrogenated amorphous silicon thin film with very low annealing temperature and fast MILC rate. Electron. Lett. **35**, 1108–1109 (1999). 10.1049/el:19990743
2126. T.K. Kim, T.H. Ihn, B.I. Lee, S.K. Joo, High-performance low-temperature poly-silicon thin film transistors fabricated by new metal-induced lateral crystallization process. Jpn. J. Appl. Phys. **37**, 4244–4247 (1998). 10.1143/JJAP.37.4244
2127. S.-W. Lee, Y.-C. Jeon, S.-K. Joo, Pd induced lateral crystallization of amorphous Si thin films. Appl. Phys. Lett. **66**, 1671–1673 (1995). 10.1063/1.113888
2128. K. Sera, F. Okumura, H. Uchida, S. Itoh, S. Kaneko, K. Hotta, High-performance TFTs fabricated by XeCl excimer laser annealing of hydrogenated amorphous-silicon film. IEEE Trans. Electron Dev. **36**, 2868–2872 (1989). 10.1109/16.40970
2129. H. Gleskova, S. Wagner, Electron mobility in amorphous silicon thin-film transistors under compressive strain. Appl. Phys. Lett. **79**, 3347–3349 (2001). 10.1063/1.1418254
2130. N. Yamauchi, N. Kakuda, T. Hisaki, Characteristics of high mobility polysilicon thin-film transistors using very thin sputter-deposited SiO_2 films. IEEE Trans. Electron Dev. **41**, 1882–1885 (1994). 10.1109/16.324606
2131. M. Zaghdoudi, R. Rogel, N. Alzaied, M. Fathallah, T. Mohammed-Brahim, High polysilicon TFT field effect mobility reached thanks to slight phosphorus content in the active layer. Mater. Sci. Engin. C **28**, 1010–1013 (2008). 10.1016/j.msec.2007.10.087
2132. J.F. Wager, Transparent electronics. Science **300**, 1245–1246 (2003). 10.1126/science.1085276
2133. K. Nomura, H. Ohta, K. Ueda, T. Kamiya, M. Hirano, H. Hosono, Thin-film transistor fabricated in single-crystalline transparent oxide semiconductor. Science **300**, 1269–1272 (2003). 10.1126/science.1083212
2134. E.M.C. Fortunato, P.M.C. Barquinha, A. Pimentel, A.M.F. Gonçalves, A.J.S. Marques, L.M.N. Pereira, R.F.P. Martins, Fully transparent ZnO thin-film transistor produced at room temperature. Adv. Mater. **17**, 590–594 (2005). 10.1002/adma.200400368
2135. H. Frenzel, A. Lajn, M. Brandt, H. von Wenckstern, G. Biehne, H. Hochmuth, M. Lorenz, M. Grundmann, ZnO metal-semiconductor field-effect transistors with Ag-Schottky gates. Appl. Phys. Lett. **92**, 192108:1–3 (2008). 10.1063/1.2926684
2136. M. Grundmann, H. Frenzel, A. Lajn, M. Lorenz, F. Schein, H. von Wenckstern, Transparent semiconducting oxides: Materials and devices. Phys. Status Solidi A **207**, 1437–1449 (2010). 10.1002/pssa.200983771
2137. H. Frenzel, A. Lajn, H. von Wenckstern, M. Grundmann, Ultrathin gate-contacts for metal-semiconductor field-effect transistor devices: An alternative approach in transparent electronics. J. Appl. Phys. **107**, 114515:1–6 (2010). 10.1063/1.3430988
2138. S. Jit, P.K. Pandey, P.K. Tiwari, Modeling of the subthreshold current and subthreshold swing of fully depleted short-channel Si-SOI-MESFETs. Solid State Electron. **53**, 57–62 (2009). 10.1016/j.sse.2008.09.013
2139. S.R. Forrest, Ultrathin organic films grown by organic molecular beam deposition and related techniques. Chem. Rev. **97**, 1793–1896 (1997). 10.1021/cr941014o
2140. D. Jariwala, V.K. Sangwan, L.J. Lauhon, T.J. Marks, M.C. Hersam, Emerging device applications for semiconducting two-dimensional transition metal dichalcogenides. ACS Nano **8**, 1102–1120 (2014). 10.1021/nn500064s
2141. Y. Liu, X. Duan, Y. Huang, X. Duan, Two-dimensional transistors beyond graphene and TMDCs. Chem. Soc. Rev. **47**, 6388–6409 (2018). 10.1039/c8cs00318a
2142. B. Radisavljevic, A. Radenovic, J. Brivio, V. Giacometti, A. Kis, Single-layer MoS_2 transistors. Nature Nanotechn. **6**, 147–150 (2011). 10.1038/nnano.2010.279
2143. S. Ahmed, J. Yi, Two-dimensional transition metal dichalcogenides and their charge carrier mobilities in field-effect transistors. Nano-Micro Lett. **9**, 50:1–23 (2017). 10.1007/s40820-017-0152-6
2144. Z. Yu, Z.-Y. Ong, S. Li, J.-B. Xu, G. Zhang, Y.-W. Zhang, Y. Shi, X. Wang, Analyzing the carrier mobility in transition-metal dichalcogenide MoS_2 field-effect transistors. Adv. Funct. Mater. **27**, 1604093:1–17 (2017). 10.1002/adfm.201604093
2145. G. Horowitz, Organic thin film transistors: From theory to real devices. J. Mater. Res. **19**, 1946–1962 (2004). 10.1557/JMR.2004.0266
2146. Z. Bao, J. Locklin, eds., *Organic Field-Effect Transistors* (CRC Press, New York, 2007)
2147. Ch. Wöll, ed., *Organic Electronics: Structural and Electronic Properties of OFETs* (Wiley-VCH, Weinheim, 2009). 10.1002/9783527627387
2148. G. Horowitz, F. Garnier, A. Yassar, R. Hajlaoui, F. Kouki, Field-effect transistor made with a sexithiophene single crystal. Adv. Mater. **8**, 52–54 (1996). 10.1002/adma.19960080109
2149. H.E. Katz, C. Kloc, V. Sundar, J. Zaumseil, A.L. Briseno, Z. Bao, Field-effect transistors made from macroscopic single crystals of tetracene and related semiconductors on polymer dielectrics. J. Mater. Res. **19**, 1995–1998 (2004). 10.1557/JMR.2004.0254
2150. G. Kindlmann, Tensor invariants and their gradients, in *Visualization and Processing of Tensor Fields*, J. Weickert, H. Hagen, eds. (Springer, Berlin, 2006), pp. 215-224. 10.1007/3-540-31272-2_12
2151. C.G. Koay, On the six-dimensional orthogonal tensor representation of the rotation in three dimensions: A simplified approach. Mech. Mater. **41**, 951–953 (2009). 10.1016/j.mechmat.2008.12.006

2152. H.A. Kramers, Some remarks on the theory of absorption and refraction of X-rays. Nature **117**, 775 (1926). 10.1038/117774a0
2153. R. de L. Kronig, On the theory of dispersion of X-rays. J. Opt. Soc. Am. **12**, 547–557 (1926). 10.1364/JOSA.12.000547
2154. W.P. Su, J.R. Schrieffer, A.J. Heeger, Solitons in polyacetylene. Phys. Rev. Lett. **42**, 1698–1701 (1979). 10.1103/PhysRevLett.42.1698
2155. N. Batra, G. Sheet, *Understanding Basic Concepts of Topological Insulators Through Su-Schrieffer-Heeger (SSH) Model*. arXiv:1906.08435
2156. F. Liu, K. Wakabayashi, Novel topological phase with a zero Berry curvature. Phys. Rev. Lett. **118**, 076803:1–5 (2017). 10.1103/PhysRevLett.118.076803
2157. J. Cayssol, Introduction to Dirac materials and topological insulators. Comptes Rendus Phys. **14**, 760–778 (2013). 10.1016/j.crhy.2013.09.012
2158. F. Liu, M. Yamamoto, K. Wakabayashi, Topological edge states of honeycomb lattices with zero Berry curvature. J. Phys. Soc. Jpn. **86**, 123707:1–4 (2017). 10.7566/JPSJ.86.123707
2159. Y. Hatsugai, T. Fukui, H. Aoki, Topological aspects of graphene, Dirac fermions and the bulk-edge correspondence in magnetic fields. Eur. Phys. J. Special Topics **148**, 133–141 (2007). 10.1140/epjst/e2007-00233-5
2160. Y. Hatsugai, Topological aspects of graphene. J. Phys.: Conf. Ser. **334**, 012004:1–14 (2011). 10.1088/1742-6596/334/1/012004
2161. G.W. Semenoff, Condensed-matter simulation of a three-dimensional anomaly. Phys. Rev. Lett. **53**, 2449–2452 (1984). 10.1103/PhysRevLett.53.2449
2162. C.L. Kane, E.J. Mele, Quantum spin Hall effect in graphene. Phys. Rev. Lett. **95**, 226801:1–4 (2005). 10.1103/PhysRevLett.95.226801
2163. D. Sticlet, F. Piéchon, J.-N. Fuchs, P. Kalugin, P. Simon, Geometrical engineering of a two-band Chern insulator in two dimensions with arbitrary topological index. Phys. Rev. B **85**, 165456:1–10 (2012). 10.1103/PhysRevB.85.165456
2164. O.A. Dobrescu, M. Apostol, Electronic edge states in graphene sheets. Romanian J. Phys. **60**, 466–480 (2015)
2165. P.-O. Löwdin, A note on the quantum-mechanical perturbation theory. J. Chem. Phys. **19**, 1396–1401 (1951). 10.1063/1.1748067
2166. G.H. Wannier, The structure of electronic excitation levels in insulating crystals. Phys. Rev. **52**, 191–197 (1937). 10.1103/PhysRev.52.191
2167. M. Cutler, N.F. Mott, Observation of Anderson localization in an electron gas. Phys. Rev. **181**, 1336–1340 (1969). 10.1103/PhysRev.181.1336
2168. C. Herring, Theory of the thermoelectric power of semiconductors. Phys. Rev. **96**, 1163–1187 (1954). 10.1103/PhysRev.96.1163
2169. E.D. Kriger, A.F. Kravchenko, B.V. Morozov, V.G. Polovinkin, E.M. Skok, Investigation of the phonon drag effect in n-GaAs. Phys. Status Solidi A **13**, 389–398 (1972). 10.1002/pssa.2210130207
2170. M.W. Wu, N.J.M Horing, H.L. Cui, Phonon-drag effects on thermoelectric power. Phys. Rev. B **54**, 5438–5443 (1996). 10.1103/PhysRevB.54.5438
2171. A. van der Ziel, *Noise Sources, Characterization, Measurement* (Prentice-Hall, Englewood Cliffs, 1970)
2172. A. van der Ziel, E.R. Chenette, Noise in solid state devices. Adv. Electron. Electr. Phys. **46**, 313–383 (1978). 10.1016/S0065-2539(08)60414-X
2173. J. Engberg, T. Larsen, *Noise Theory of Linear and Nonlinear Circuits* (Wiley, Chichester, 1995)
2174. Sh. Kogan, *Electronic Noise and Fluctuations in Solids* (Cambridge University Press, Cambridge, 1996). 10.1017/CBO9780511551666
2175. N.B. Lukyanchikova, *Noise Research in Semiconductor Physics* (Gordon and Breach, Amsterdam, 1996)
2176. B. Schiek, H.-J. Siweris, I. Rolfes, *Noise in High-Frequency Circuits and Oscillators* (Wiley, Hoboken, 2006). 10.1002/0470038942.fmatter
2177. R. Müller, *Rauschen*, 2nd edn. (Springer, Berlin, 2013). 10.1007/978-3-642-61501-6
2178. S. Yngvesson, Review of noise processes and noise concepts relevant to microwave semiconductor devices, in Ref. [1815], pp. 207–228. 10.1007/978-1-4615-3970-4_8
2179. P. Dutta, P.M. Horn, Low-frequency fluctuations in solids: $1/f$ noise. Rev. Mod. Phys. **53**, 497–516 (1981). 10.1103/RevModPhys.53.497
2180. M.B. Weissmann, $1/f$ noise and other slow, nonexponential kinetics in condensed matter. Rev. Mod. Phys. **60**, 537–571 (1988). 10.1103/RevModPhys.60.537
2181. T.G.M. Kleinpenning, A.H. de Kuijper, Relation between variance and sample duration of $1/f$ noise signals. J. Appl. Phys. **63**, 43–45 (1988). 10.1063/1.340460
2182. T.M. Chen, S.F. Su, D. Smith, $1/f$ Noise in Ru-based thick-film resistor. Solid State Electron. **25**, 821–827 (1982). 10.1016/0038-1101(82)90213-1
2183. J.M. Boudry, L.E. Antonuk, Current-noise-power spectra of amorphous silicon thin-film transistors. J. Appl. Phys. **76**, 2529–2534 (1994). 10.1063/1.357614

2184. J.E. Hill, K.M. van Vliet, Ambipolar transport of carrier density fluctuations in germanium. Physica **24**, 709–720 (1958). 10.1016/S0031-8914(58)80087-7
2185. G. Ferrari, M. Sampietro, G. Bertuccio, G. Gomila, L. Reggiani, On the origin of shot noise in CdTe detectors. Appl. Phys. Lett. **83**, 2450–2452 (2003). 10.1063/1.1611648
2186. C.W.J. Beenakker, M. Büttiker, Suppression of shot noise in metallic diffusive conductors. Phys. Rev. B **46**, 1889–1892 (1992). 10.1103/PhysRevB.46.1889
2187. H. Schomerus, E.G. Mishchenko, C.W.J. Beenakker, Shot-noise in non-degenerate semiconductors with energy-dependent elastic scattering, in *Statistical and Dynamical Aspects of Mesoscopic Systems*, D. Reguera, J.M. Rubí, G. Platero, L.L. Bonilla, eds., Lecture Notes in Physics, vol. 547, pp. 96–104 (Springer, Berlin, 2000). 10.1007/3-540-45557-4_9
2188. A. van der Ziel, Shot noise in semiconductors. J. Appl. Phys. **24**, 222–223 (1953). 10.1063/1.1721242
2189. R. Müller, Generation-recombination noise, in *Noise in Physical Systems*, ed. by D. Wolf, Springer Series in Electrophysics, vol. 2, pp. 13–25 (1978). 10.1007/978-3-642-87640-0_2
2190. V. Mitin, L. Reggiani, L. Varani, Generation-recombination noise in semiconductors, in: *Noise and Fluctuations Control in Electronic Devices*, ed. by A. Balandin (American Scientific Publishers, Valencia, USA, 2002), pp. 1–19 (Chap. 2)
2191. V. Bareikis, J. Liberis, I. Matulioniene, A. Matulionis, P. Sakalas, Experiments on hot electron noise in semiconductor materials for high-speed devices. IEEE Trans. Electron Dev. **41**, 2050–2060 (1994). 10.1109/16.333822
2192. B.K. Jones, Low-frequency noise spectroscopy. IEEE Trans. Electron Dev. **41**, 2188–2197 (1994). 10.1109/16.333840

Index

M. Grundmann, *The Physics of Semiconductors*, Graduate Texts in Physics,
https://doi.org/10.1007/978-3-030-51569-0